CODEN: JASMAN

ISSN: 0001-4966

The Journal of the Acoustical Society of America

Vol. 109, No. 6 June 2001

ACOUSTICAL NEWS—USA 2537

USA Meetings Calendar 2538

ACOUSTICAL NEWS—INTERNATIONAL 2539

International Meetings Calendar 2539

REPORTS OF RELATED MEETINGS 2541

OBITUARIES 2543

BOOK REVIEWS 2545

REVIEWS OF ACOUSTICAL PATENTS 2547

TUTORIAL PAPERS

Acoustical cavity excitation Harold Levine 2555

GENERAL LINEAR ACOUSTICS [20]

A staggered-grid finite-difference method with perfectly matched layers for poroelastic wave equations Yan Qing Zeng, Qing Huo Liu 2571

Pulse propagation in randomly fluctuating media Dalcio K. Dacol 2581

Multiple scattering in a reflecting cavity: Application to fish counting in a tank Julien De Rosny, Philippe Roux 2587

Reflectance properties of two-dimensional sonic band-gap crystals L. Sanchis, F. Cervera, J. Sánchez-Dehesa, J. V. Sánchez-Pérez, C. Rubio, R. Martínez-Sala 2598

Acoustically coupled gas bubbles in fluids: Time-domain phenomena Christopher Feuillade 2606

Time reversal for a single spherical scatterer David H. Chambers, A. K. Gautesen 2616

The surface motion due to a line force or dislocation within an anisotropic elastic half-space Kuang-Chong Wu 2625

Modeling elastic wave forward propagation and reflection using the complex screen method Xiao-Bi Xie, Ru-Shan Wu 2629

Mode counts in an aluminum foam Oleg I. Lobkis, Richard L. Weaver 2636

(Continued)

THE JOURNAL OF THE ACOUSTICAL SOCIETY OF AMERICA VOL. 109, NO. 6, JUNE 2001

CONTENTS—*Continued from preceding page*

NONLINEAR ACOUSTICS [25]

Acoustic nonlinearity of cracks partially filled with liquid: Cubic approximation — V. E. Nazarov — 2642

Weak nonlinear propagation of sound in a finite exponential horn — Philippe Béquin, Christopher L. Morfey — 2649

Numerical model for nonlinear standing waves and weak shocks in thermoviscous fluids — Christian Vanhille, Cleofé Campos-Pozuelo — 2660

Time-reversed sound beams of finite amplitude — Kevin B. Cunningham, Mark F. Hamilton, Andrew P. Brysev, Leonid M. Krutyansky — 2668

AEROACOUSTICS, ATMOSPHERIC SOUND [28]

Blast noise propagation above a snow cover — Donald G. Albert, Lars R. Hole — 2675

Acoustic sounding of wind velocity profiles in a stratified moving atmosphere — Vladimir E. Ostashev, Thomas M. Georges, Steven F. Clifford, George H. Goedecke — 2682

UNDERWATER SOUND [30]

On the stability of long-range sound propagation through a structured ocean — Michael A. Wolfson, Steven Tomsovic — 2693

Three-dimensional elasticity model for a decoupling coating on a rectangular plate immersed in a heavy fluid — A. Berry, O. Foin, J. P. Szabo — 2704

A modal Pritchard approximation for computing array element mutual impedance — C. L. Scandrett, J. L. Day, S. R. Baker — 2715

A multifrequency scintillation method for ocean flow measurement — I. Fuks, M. Charnotskii, K. Naugolnykh — 2730

ULTRASONICS, QUANTUM ACOUSTICS, AND PHYSICAL EFFECTS OF SOUND [35]

Stationary velocity and pressure gradients in a thermoacoustic stack — Roger Waxler — 2739

TRANSDUCTION [38]

Development of panel loudspeaker system: Design, evaluation and enhancement — Mingsian R. Bai, Talung Huang — 2751

STRUCTURAL ACOUSTICS AND VIBRATION [40]

Time-domain analyses of acoustics–structure interactions for piezoelectric transducers — Sung Yi, Shih Fu Ling, Ming Ying — 2762

Visualization of acoustic radiation from a vibrating bowling ball — Sean F. Wu, Nassif Rayess, Xiang Zhao — 2771

Experimental and numerical investigations of resonant vibration characteristics for piezoceramic plates — Chi-Hung Huang, Chien-Ching Ma — 2780

Transient response of an acoustic medium by an excited submerged spherical shell — U. Zakout — 2789

The surface variational principle applied to an acoustic cavity — F. Franco, K. A. Cunefare — 2797

NOISE: ITS EFFECTS AND CONTROL [50]

A theoretical study of passive control of duct noise using panels of varying compliance — Lixi Huang — 2805

A study of time-domain FXLMS algorithms with control output constraint — Xiaojun Qiu, Colin H. Hansen — 2815

(Continued)

THE JOURNAL OF THE ACOUSTICAL SOCIETY OF AMERICA VOL. 109, NO. 6, JUNE 2001

CONTENTS—*Continued from preceding page*

ACOUSTICAL MEASUREMENTS AND INSTRUMENTATION [58]

Orthogonal acoustical factors of a sound field in a bamboo forest — Hiroyuki Sakai, Shozo Shibata, Yoichi Ando — 2824

ACOUSTIC SIGNAL PROCESSING [60]

Minimum entropy deconvolution of pulse-echo signals acquired from attenuative layered media — Tomas Olofsson, Tadeusz Stepinski — 2831

PHYSIOLOGICAL ACOUSTICS [64]

A model for sound lateralization — Vered Aharonson, Miriam Furst — 2840

A computational algorithm for computing nonlinear auditory frequency selectivity — Ray Meddis, Lowel P. O'Mard, Enrique A. Lopez-Poveda — 2852

Sources of distortion product otoacoustic emissions revealed by suppression experiments and inverse fast Fourier transforms in normal ears — Dawn Konrad-Martin, Stephen T. Neely, Douglas H. Keefe, Patricia A. Dorn, Michael P. Gorga — 2862

PSYCHOLOGICAL ACOUSTICS [66]

Duration discrimination and subjective duration for ramped and damped sounds — Robert S. Schlauch, Dennis T. Ries, Jeffrey J. DiGiovanni — 2880

Children's detection of pure-tone signals with random multitone maskers — Eunmi L. Oh, Frederic Wightman, Robert A. Lutfi — 2888

Using statistical decision theory to predict speech intelligibility. I. Model structure — Hannes Müsch, Søren Buus — 2896

Using statistical decision theory to predict speech intelligibility. II. Measurement and prediction of consonant-discrimination performance — Hannes Müsch, Søren Buus — 2910

Psychophysical recovery from single-pulse forward masking in electric hearing — David A. Nelson, Gail S. Donaldson — 2921

Effects of temporal envelope modulation on acoustic signal recognition in a vocal fish, the plainfin midshipman — Jessica R. McKibben, Andrew H. Bass — 2934

Pitch strength and pitch dominance of iterated rippled noises in hearing-impaired listeners — Marjorie R. Leek, Van Summers — 2944

Aging and temporal discrimination in auditory sequences — Peter J. Fitzgibbons, Sandra Gordon-Salant — 2955

The effects of compression ratio, signal-to-noise ratio, and level on speech recognition in normal-hearing listeners — Benjamin W. Y. Hornsby, Todd A. Ricketts — 2964

SPEECH PRODUCTION [70]

Modeling the motion of the internal tongue from tagged cine-MRI images — Maureen Stone, Edward P. Davis, Andrew S. Douglas, Moriel NessAiver, Rao Gullapalli, William S. Levine, Andrew Lundberg — 2974

Verifying a vocal tract model with a closed side-branch — Michel Tah-Tung Jackson, Carol Espy-Wilson, Suzanne E. Boyce — 2983

The acoustic bases for gender identification from children's voices — Theodore L. Perry, Ralph N. Ohde, Daniel H. Ashmead — 2988

SPEECH PERCEPTION [71]

Providing low- and mid-frequency speech information to listeners with sensorineural hearing loss — Christopher W. Turner, Shea L. Brus — 2999

(Continued)

THE JOURNAL OF THE ACOUSTICAL SOCIETY OF AMERICA VOL. 109, NO. 6, JUNE 2001

CONTENTS—*Continued from preceding page*

SPEECH PROCESSING AND COMMUNICATION SYSTEMS [72]

Audio-visual enhancement of speech in noise — Laurent Girin, Jean-Luc Schwartz, Gang Feng — 3007

MUSIC AND MUSICAL INSTRUMENTS [75]

The speed of pitch resolution in a musical context — R. Ranvaud, W. F. Thompson, L. Silveira-Moriyama, L.-L. Balkwill — 3021

BIOACOUSTICS [80]

***In situ* source level and source position estimates of biological transient signals produced by snapping shrimp in an underwater environment** — Brian G. Ferguson, Jane L. Cleary — 3031

Localization and visual verification of a complex minke whale vocalization — Jason Gedamke, Daniel P. Costa, Andy Dunstan — 3038

Ultrasound detection by clupeiform fishes — David A. Mann, Dennis M. Higgs, William N. Tavolga, Marcy J. Souza, Arthur N. Popper — 3048

Ultrasound phased arrays for prostate treatment — Joseph S. Tan, Leon A. Frizzell, Narendra Sanghvi, Shih-jeh Wu, Ralf Seip, Jeffrey T. Kouzmanoff — 3055

LETTERS TO THE EDITOR

Enhanced weak integral formulation for the mixed ($\underline{u}$,p) poroelastic equations [20] — Noureddine Atalla, M. A. Hamdi, Raymond Panneton — 3065

Absorption of sound in the Martian atmosphere [35] — Henry E. Bass, James P. Chambers — 3069

Dynamic behavior of multistep cracked beams with varying cross section [40] — Q. S. Li — 3072

Hyperbolic location errors due to insufficient numbers of receivers [80] — John L. Spiesberger — 3076

Ants are deaf [80] — Flavio Roces, Jürgen Tautz — 3080

Response to ''Ants are deaf'' [J. Acoust. Soc. Am. 109, 3080 (2001)] [80] — Robert Hickling, Richard L. Brown — 3083

INDEX TO VOLUME 109

How To Use This Index — 3084

Classification of Subjects — 3084

Subject Index To Volume 109 — 3089

Author Index To Volume 109 — 3145

ACOUSTICAL NEWS—USA

Elaine Moran
Acoustical Society of America, Suite 1NO1, 2 Huntington Quadrangle, Melville, NY 11747-4502

Editor's Note: *Readers of this Journal are encouraged to submit news items on awards, appointments, and other activities about themselves or their colleagues. Deadline dates for news items and notices are 2 months prior to publication.*

New Fellows of the Acoustical Society of America

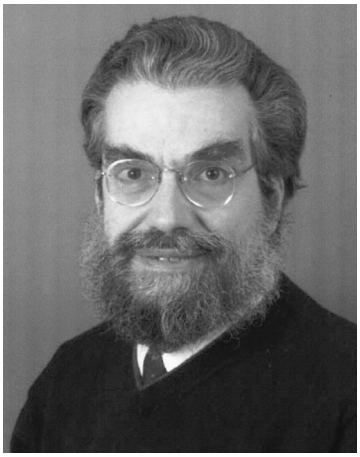

Paul J. Abbas—For contributions to the understanding of encoding in the auditory nerve.

John H. Grose—For contributions to the understanding of perception of sound in adults and children.

Paul C. Hines—For contributions to acoustic scattering at ocean boundaries.

Bernhard R. Tittmann—For contributions to acoustical microscopy and ultrasonic nondestructive evaluation.

Amy Neel receives ASHF Research Grant in Speech Science

ASA member Amy T. Neel, Assistant Professor at Purdue University, was awarded the Research Grant in Speech Science by the American Speech Language and Hearing Foundation. Her proposal was titled ''The Use of Formant Movement Details in Vowel Identification.'' This $5,000 grant is designed to further research activities in the areas of speech communication for individuals having received a doctoral degree within the last 5 years. This grant is supported by the Dennis Klatt Memorial Fund maintained by the American Speech Language and Hearing Foundation.

Previous recipients have been Yingyong Qi, Kathleen Ellen Cum-

 0001-4966/2001/109(6)/2537/2/$18.00

mings, Helen Hanson, and Michael S. Vitevitch. For further information about the award and application instructions visit <http://www.ashfoundation.org/funding.htm>.

Students receive awards from Robert Bradford Student Award Fund

Three students were selected to receive Robert Bradford Student Award medals in 2000 ''For Merit in Architectural Acoustics.''

Elizabeth Codero of the Massachusetts Institute of Technology (MIT), received the award for her project ''Acoustics in Restaurant Design,'' Michelle Leah Hoeffler, also of MIT, was awarded the medal for her project titled ''A Case Study: The Acoustical Design of a Performance Hall—from the Architect's Perspective,'' and William Neale of Washington University received the award for ''Acoustics in a Greenhouse/Day Care Center.''

The year 2000 marked the 15th year of the Robert Bradford Newman Student Award Medal Program. During those 15 years, 135 Newman Medals were awarded to students at 33 universities around the world.

The University of Texas at Austin dedicates the McKinney Wing of the Applied Research Laboratories

A formal dedication ceremony was held on 9 November 2000 to mark the naming of the McKinney Wing of the Applied Research Laboratories (ARL) at the J. J. Pickle Research Campus of The University of Texas at Austin, in honor of Chester McKinney.

Chester McKinney, a Fellow and Past President of the Acoustical Society of America, served as the ARL director from 1965 until his retirement in 1980. He was instrumental in establishing the high-resolution sonar program that remains one of the cornerstones of ARL research in acoustics today.

''Chester McKinney's administrative principles continue to guide the center,'' said Dr. Clark S. Penrod, ARL's executive director. ''He fostered an atmosphere in which the laboratories became known for technical excellence and for providing cost-effective solutions to some of the military's most difficult problems.''

McKinney, a native of Cooper, Texas, was born 29 January 1920. After his discharge from the U.S. Army Air Corps as a captain in 1946, he worked at the laboratories toward two degrees in physics, an M.S. in 1947 and a Ph.D. in 1950. He specialized in radar and sonar research, and his later work was primarily in the field of underwater acoustics. Since retiring from his director's post, he continues to serve as a consultant to ARL.

In the past 20 years, McKinney has served on several advisory committees to the U.S. Navy, including the Mine Advisory Committee, the Naval Studies Board, the Underwater Sound Advisory Group, and other similar groups. In 1983–84, he was a liaison scientist with the Office of Naval Research in London.

Chester McKinney has served ASA as Vice President (1983–84) and President (1987–88). He has also served as chair of the Medals and Awards Committee (1982–83), the Technical Committee on Underwater Acoustics (1960–61), and the Fall 1984 meeting held in Austin, Texas. He is an Honorary Fellow of the British Institute of Acoustics.

USA Meetings Calendar

Listed below is a summary of meetings related to acoustics to be held in the U.S. in the near future. The month/year notation refers to the issue in which a complete meeting announcement appeared.

2001

9–13 July	2001 SIAM Annual Meeting, San Diego, CA [Society for Industrial and Applied Mathematics (SIAM), Tel.: 215-382-9800; Fax: 215-386-7999; E-mail: meetings@siam.org; WWW: www.siam.org/meetings/an01/].
15–19 August	ClarinetFest 2001, New Orleans, LA [Dr. Keith Koons, ICA Research Presentation Committee Chair, Music Dept., Univ. of Central Florida, P.O. Box 161354, Orlando, FL 32816-1354, Tel.: 407-823-5116; E-mail: kkoons@pegasus.cc.ucf.edu].
19–24 August	Asilomar Conference on Implantable Auditory Prostheses, Pacific Grove, CA [Michael Dorman, Dept. of Speech and Hearing Science, Arizona State Univ., Tempe, AZ 85287-0102; Tel.: 480-965-3345; Fax: 480-965-0965; E-mail: mdorman@asu.edu].
4–6 October	Ninth Annual Conference on the Management of the Tinnitus Patient, Iowa City, IA [Rich Tyler, Tel.: 319-356-2471; E-mail: rich-tyler@uiowa.edu; WWW: www.medicine.uiowa.edu/otolaryngology/news/news].
7–10 October	2001 IEEE International Ultrasonics Symposium Joint with World Congress on Ultrasonics, Atlanta, GA [W. O'Brien, Electrical and Computer Engineering, Univ. of Illinois, 405 N. Mathews, Urbana, IL 61801; Fax: 217-244-0105; WWW: www.ieee-uffc.org/2001].
29–31 October	NOISE-CON 01, The 2001 National Conference and Exposition on Noise Control Engineering, Portland, ME [Institute of Noise Control Engineering, P.O. Box 3206 Arlington Branch, Poughkeepsie, NY 12603; Tel.: +1 914 462-4006; Fax: +1 914 462 4006; E-mail: omd@ince.org; WWW: users.aol.com/inceusa/ince.html].
15–18 November	American Speech Language Hearing Association Convention, New Orleans, LA [American Speech-Language-Hearing Association, 10801 Rockville Pike, Rockville, MD 20852; Tel.: 888-321-ASHA; E-mail: convention@asha.org; WWW: professional.asha.org/convention/abstracts/welcome.asp].
3–7 December	142nd Meeting of the Acoustical Society of America, Ft. Lauderdale, FL [Acoustical Society of America, Suite 1NO1, 2 Huntington Quadrangle, Melville, NY 11747-4502; Tel.: 516-576-2360; Fax: 516-576-2377; E-mail: asa@aip.org; WWW: asa.aip.org]. Deadline for submission of abstracts: 3 August 2001.

2002

21–23 February	National Hearing Conservation Association Annual Conference, Dallas, TX [NHCA, 9101 E. Kenyon Ave., Ste. 3000, Denver, CO 80237; Tel.: 303-224-9022; Fax: 303-770-1812; E-mail: nhca@gwami.com; WWW: www.hearingconservation.org/index.html].
10–13 March	Annual Meeting of American Institute for Ultrasound in Medicine, Nashville, TN [American Institute of Ultrasound In Medicine, 14750 Sweitzer Lane, Suite 100, Laurel, MD 20707-5906; Tel.: 301-498-4100 or 800-638-5352; Fax: 301-498-4450; E-mail: conv_edu@aium.org; WWW: www.aium.org].
3–7 June	143rd Meeting of the Acoustical Society of America, Pittsburgh, PA [Acoustical Society of America, Suite 1NO1, 2 Huntington Quadrangle, Melville, NY 11747-4502; Tel.: 516-576-2360; Fax: 516-576-2377; E-mail: asa@aip.org; WWW: asa.aip.org].
2–6 December	Joint Meeting: 144th Meeting of the Acoustical Society of America, 3rd Iberoamerican Congress of Acoustics and 9th Mexican Congress on Acoustics, Cancun, Mexico [Acoustical Society of America, Suite 1NO1, 2 Huntington Quadrangle, Melville, NY 11747-4502; Tel.: 516-576-2360; Fax: 516-576-2377; E-mail: asa@aip.org; WWW: asa.aip.org/cancun.html].

ACOUSTICAL NEWS—INTERNATIONAL

Walter G. Mayer
Physics Department, Georgetown University, Washington, DC 20057

Russian Acousticians honor L. M. Brekhovskikh

The Shirshov Institute of Oceanology of the Russian Academy of Sciences has taken the initiative in organizing a conference on Ocean Acoustics which will be held in honor of the 85th birthday of Academician Leonid M. Brekhovskikh. The conference will be held jointly with the 12th Meeting of the Russian Acoustical Society. The event will take place in Moscow in May 2002. Further details are available from Yu. A. Chepurin, P. P. Shirshov Institute of Oceanology, Russian Academy of Sciences, Nakhimovsky Prospekt 36, 117851 Moscow, Russia.

Papers published in *Acoustical Science and Technology* (Japan)

A listing of Invited Papers and Regular Papers appearing in the latest issue of the English language version of the Journal of the Acoustical Society of Japan, *Acoustical Science and Technology*, was published for the first time in the January 1995 issue of the journal. This listing is continued below.

The March 2001 issue, Vol. 22, No. 2, contains the following contributions:

T. Hikichi and N. Osaka, ''Sound timbre interpolation based on physical modeling''
T. Lawu, N. Tsutsumi, and M. Ueda, ''Evaluation of ultrasonic image quality by tissue second harmonic imaging using a computer generated phantom model''
I. Kinoshita, S. Emura, and M. Myoshi, ''Sound image rendering using a loudspeaker and a fully open-air headphone set''
S. Hayashi, Y. Kato, K. Tanaka, and H. Kobayashi, ''Acoustic emission from a sonoluminescing bubble''
T. Samejima and D. Yamamoto, ''Active control of a sound field with a state feedback electro-acoustic transducer''
K. Ogata and Y. Somoda, ''Articulatory measuring system by using magnetometer and optical sensors''
M. Aoki, M. Okamoto, S. Aoki, H. Matsui, T. Sakurai, and Y. Kaneda, ''Sound source segregation based on estimating incident angle of each frequency component of input signals acquired by multiple microphones''

EEAA—New Web site

The Eastern-European Acoustical Association, with headquarters in St. Petersburg, has recently opened a rather voluminous home page with text in Russian and in English. It contains information about the association and the contents of the journal *Technical Acoustics* EEAA publishes. The address for the EEAA is webcenter.ru/~eeaa; the home page of the journal *Technical Acoustics* is webcenter.ru/~eeaa/ejta.

International Meetings Calendar

Below are announcements of meetings to be held abroad. Entries preceded by an * are new or updated listings with full contact addresses given in parentheses. *Month/year* listings following other entries refer to meeting announcements, with full contact addresses, which were published in previous issues of the *Journal*.

June 2001

14–15 *__Swiss Acoustical Society Spring Meeting__, Lausanne, Switzerland. (SGA-SSA, c/o Akustik, Suva, P.O. Box 4358, 6002 Luzern, Switzerland; Fax: +41 419 6213; Web: www.sga-ssa.ch)

July 2001

2–5 __Ultrasonics International Conference (UI01)__, Delft. (Fax: +1 607 255 9179; Web: www.ccmr.comell.edu/~ui01/) *12/00*

2–6 __8th International Congress on Sound and Vibration__, Kowloon, Hong Kong. (Fax: +852 2365 4703; Web: www.iiav.org) *8/00*

23–24 __2nd Symposium on Underwater Bio-Sonar Systems and Bioacoustics__, Loughborough. (Fax: +44 1509 22 7053; Web: sonar-fs.lboro.ac.uk/uag/ioa) *4/01*

August 2001

9–11 *__Meeting of the Society for Music Perception and Cognition (SMPC2001)__, Kingston, Ontario, Canada. (L. Cuddy, Department of Psychology, Queen's University, Kingston, Ontario K7L 3N6, Canada; Fax: +1 613 533 2499; Web: psyc.queensu.ca/~smpc/)

28–30 __INTER-NOISE 2001__, The Hague. (Web: internoise2001.tudelft.nl) *6/99*

September 2001

2–7 __17th International Congress on Acoustics (ICA)__, Rome. (Fax: +39 6 4976 6932; Web: www.ica2001.it) *10/98*

10–14 __International Symposium on Musical Acoustics (ISMA 2001)__, Perugia. (Fax: +39 75 577 2255; Web: www.cini.ve.cnr.it/ISMA2001) *10/99*

30–5 __Conference on Microgravity Transport Processes in Fluid, Thermal, Materials, and Biological Sciences__, Banff. (Fax: +1 212 591 7441; Web: www.engfnd.org/engfnd/lay.html) *4/01*

October 2001

1–3 *__Acoustics Conference in Canada 2001__, Nottawasaga Resort, Ontario, Canada. (D. Giusti, Jade Acoustics, Inc., 545 North Rivermede Road, Ste. 203, Concord, Ontario L4K 4H1, Canada; Fax: +1 905 660 4110; Web: www.caa2001.com)

17–19 __32nd Meeting of the Spanish Acoustical Society__, La Rioja. (Fax: +34 91 411 76 51; Web: www.ia.csic.es/sea/index.html) *10/99*

25–26 __Fall Meeting of the Swiss Acoustical Society__, Wallis/Valais. (Web: www.sga-ssa.ch) *02/01*

November 2001

14–15 *__Institute of Acoustics Autumn Conference__, Stratford-upon-Avon, UK. (Institute of Acoustics, 77A St. Peter's Street, St. Albans, Herts. AL1 3BN, UK; Fax: +44 172 785 0553; Web: www.ioa.org.uk)

16–18 *__Reproduced Sound 17__, Stratford-upon-Avon, UK. (Institute of Acoustics, 77A St. Peter's Street, St. Albans, Herts. AL1 3BN, UK; Fax: +44 172 785 0553; Web: www.ioa.org.uk)

19–23 *__Russian Acoustical Society Meeting__, Moscow, Russia. (RAS, N. N. Andreyev Acoustics Institute, ul. Shvernika 4, Moscow 117036, Russia; Fax: +7 095 126 8411; Web: www.akin.ru/e_rao.htm)

21–23 __Australian Acoustical Society Annual Meeting__, Canberra. (e-mail: m.burgess@adfa.edu.au; Web: www.users.bigpond.com/Acoustics) *02/01*

 0001-4966/2001/109(6)/2539/2/$18.00

March 2002

4–8 **German Acoustical Society Meeting (DAGA 2002)**, Bochum. (Web: www.ika.ruhr-uni-bochum.de) *10/00*

May 2002

27–30 *__Joint Meeting: Russian Acoustical Society and Conference on Ocean Acoustics__, Moscow, Russia. (Yu. A. Chepurin, P. P. Shirshov Institute of Oceanology, Russian Academy of Sciences, Nakhimovsky Prospekt 36, 117851 Moscow, Russia; Fax: +7 095 124 5983; Web: rav.sio.rssi.ru/Ixconf.html)

June 2002

4–6 **6th International Symposium on Transport Noise and Vibration**, St. Petersburg. (Fax: +7 812 127 9323; e-mail: noise@mail.rcom.ru) *02/01*

10–14 **Acoustics in Fisheries and Aquatic Ecology**, Montpellier. (Web: www.ices.dk/symposia/) *12/00*

August 2002

19–23 **16th International Symposium on Nonlinear Acoustics (ISNA16)**, Moscow. (Fax: +7 095 126 8411; Web: acs366b.phys.msu.su/isna) *12/00*

September 2002

16–21 **Forum Acusticum 2002 (Joint EAA-SEA-ASJ Meeting)**, Sevilla. (Fax: +34 91 411 7651; Web: www.cica.es/aliens/forum2002) *2/00*

December 2002

2–6 **Joint Meeting: 9th Mexican Congress on Acoustics, 144th Meeting of the Acoustical Society of America, and 3rd Iberoamerican Congress on Acoustics**. Cancún. (e-mail: sberista@maya.esimez.ipn.mx; Web: asa.aip.org) *10/00*

April 2004

5–9 **18th International Congress on Acoustics (ICA2004)**, Kyoto, Japan. (Web: ica2004.or.jp) *4/01*

REPORTS OF RELATED MEETINGS

This Journal department provides concise reports of meetings that have been held by other organizations concerned with acoustical subjects; and of meetings co-sponsored by the Acoustical Society but planned primarily by other co-sponsors.

ASME International Mechanical Engineering Congress and Exposition

The ASME held its 2000 International Mechanical Engineering Congress and Exposition (IMECE) on 5–10 November in Orlando, FL. At this IMECE, the Noise Control and Acoustics Division (NCAD) sponsored six symposia that consisted of 16 sessions of 54 papers. These symposia covered a wide range of topics including (1) Computational Acoustics; (2) Macrosonics; (3) Novel Sensing Techniques; (4) Pump Unsteady Flows and Acoustics; (5) The Use of Sound and Vibration for System Characterization; and (6) Vibration and Noise Control with Multifunctional Materials. Also, the NCAD presented the Rayleigh Lecture on ''Quiet Flow: Emerging Design Methods,'' given by Dr. William K. Blake, and two tutorial lectures on ''Acoustic Properties of Materials,'' given by Dr. Mardi C. Hastings, and on ''Acoustic Holography as a Noise Diagnostic Tool,'' given by Dr. Sean F. Wu. On behalf of the NCAD the ASME issued the 2000 Per Bruel Gold Medal to Dr. Michael Howe of Boston University for his outstanding contributions to acoustics and noise control. The NCAD also presented the Best Paper Award to Joseph W. Gregory, Richard F. Keltie, and F. Donald Caulfield for their paper entitled, ''Realization of a Minimum-Order Power Flow Model and SEA Model Updating Using Time Domain Measurements.'' The 2001 ASME IMECE will be held at New York Hilton Hotel & Towers and Sheraton New York Hotel & Towers in New York on 11–16 November 2001.

Sean F. Wu
Chair, ASME Noise Control and Acoustics Division

NHCA's 26th Annual Hearing Conservation Conference

On 22–24 February 2001 in Raleigh, NC, the National Hearing Conservation Association (NHCA) held its 26th Annual Hearing Conservation Conference, chaired by ASA member Mary McDaniel, Vice President of NHCA.

The conference, which was attended by approximately 240 hearing conservation professionals, included four concurrent half-day workshops from which attendees could select two. The workshops covered otoacoustic emissions, hearing protection selection, noise measurements, and decisions and analyses regarding hearing-critical jobs. The program, diverse as usual, included a retrospective lecture by Alf Axelsson on the relationship between listening to rock music and hearing loss, and the first-ever named presentation, the Don Gasaway Lecture, delivered by Elliott Berger, entitled *The Ardent Hearing Conservationist.* Other aspects of the broad-ranging program were an encore presentation of NHCA's practical pop-ups (short 10-min. to-the-point presentations), 13 posters, two forums, a series of round table breakfast discussions, and a number of allied committee and American National Standards Institute (ANSI) working group meetings. The luncheon lecture, *The Importance of Natural Soundscapes to Life on Planet Earth*, which played to rave reviews, was delivered by Bernie Krause of the Wild Sanctuary. Of course there was ample time to visit and socialize during the exhibitor receptions, and the new action event—a live auction, at which a fun time was had by all.

The lectures covered topics such as the Mine Safety and Health Administration's (MSHA) approach to noise control in the mining industry, presentations by Jerry Goodman and Beth Cooper on space station acoustics and NASA's Glenn Acoustics Research Center, an analysis of the performance of active-noise reduction (ANR) earmuffs by John Casali, and a presentation of both the quick SIN (speech in noise) test by Laurel Christensen and the HINT (hearing in noise) test by Sig Soli. The posters were equally as varied, covering issues like workers' compensation claims, hearing loss prevention programs for children, hearing loss in commercial motor vehicle operators, and noise levels and noise reduction during functional magnetic resonance imaging.

Internationally renowned researcher Alf Axelsson received the Outstanding Hearing Conservationist award for his leadership in basic cochlear research, the epidemiology of noise-induced hearing loss, investigations of tinnitus prevalence and treatment, and international collaborative efforts.

For those who missed this exciting event, the technical information can be recaptured in the loose-leaf proceedings available from the NHCA Executive Offices in Denver, CO (303-224-9022, E-mail: nhca@gwami.com), or the abstracts can be reviewed on the NHCA website at www.hearingconservation.org. Next year's meeting will be held in Dallas from 21–23 February.

Elliott H. Berger
Senior Scientist, Auditory Research
E·A·R
7911 Zionsville Rd.
Indianapolis, IN 46268-1657

 0001-4966/2001/109(6)/2541/1/$18.00

OBITUARIES

Bruce Hartmann • 1938–2000

Bruce Hartmann, a fellow of the Acoustical Society of America, died after a heart attack on 16 August 2000 in Nags Head, NC; he was stricken while scuba diving at a beach resort. A polymer scientist, he was a leading authority on the design and use of polymers to dampen vibrations and to absorb sound. He was born in 1938 in St. Louis, MO, but spent the major portion of his childhood in Washington, DC, where he graduated from the Archbishop Carroll High School. He subsequently attended the Catholic University of America and graduated in 1960 with a B.S. in physics. After graduation, he joined the Naval Ordinance Laboratory (NOL) and began a long and distinguished 40-year association as a research scientist with that institution and with the Carderock Division of the Naval Surface Weapons Center, which continued NOL's functions. The Naval Ordinance Laboratory then had the policy of sending selected employees to graduate school as part of their duties. This policy enabled Hartmann to receive a M.S. in physics from the University of Maryland and, in 1970, a doctorate in physics from the American University.

Dr. Hartmann was a prolific research scientist who coauthored over 120 technical publications, many of which were published in *The Journal of the Acoustical Society of America*. The Carderock Division of the Naval Surface Warfare Center (NSWC) recognized his accomplishments by awarding him its most prestigious recognition, the David W. Taylor Award. It also conferred upon him the title of Distinguished Scientist, which is the highest technical grade within the civilian service of the Government. Many of Hartmann's publications are considered as standard references in several areas of polymer science. His analysis of structure-property relations in polyurethanes is the basis of numerous developments in this area. The additive property analysis he developed is now referred to as the ''Hartmann function'' and is the basis for calculating acoustic properties of polymers.

His research was of great importance to Navy efforts to produce quiet submarines. Examples of his contributions were his leadership in research and development efforts on major Navy programs including the Advanced Special Hull Treatment (ASHT) for the Seawolf submarine and the Virginia Class Submarine.

GUILLERMO C. GAUNAURD
JOHN D. LEE

Earl D. Schubert • 1916–1999

Earl D. Schubert, a Fellow of the Acoustical Society of America, passed away in his home in Stanford, CA, on 1 December 1999, after a lengthy battle with lupus. He was a leading authority on psychological acoustics, especially musical psychological acoustics and binaural hearing. He was born on 8 November 1916 on a farm near Fostoria, OH. When he was very young his father died, and he was subsequently raised in an orphanage at which his mother worked. He developed an interest in music in his early years which he sustained throughout his life. His undergraduate education was received from Manchester College in North Manchester, IN, in 1938, where he majored in music and mathematics, apparently with the intent of becoming a high school teacher. After graduation he taught mathematics at a high school in Indiana and also directed the school band, but within a year or two, he began graduate work at the University of Iowa, where he majored in music; his principal professors there were Arnold Small, Sr., and Carl Seashore. This graduate work was interrupted for one year while he again did high school teaching, in Fort Wayne, IN. In 1942, he received his Master's degree.

Shortly after the beginning of World War II, Schubert was drafted into the Army and subsequently served from 1942 through 1946. During this period he first worked on a project on speech communication under high levels of noise in Waco, TX; among his co-workers at this time was James F. Curtis, who subsequently became an eminent speech communication scientist and also a Fellow of the ASA. During the later war years, he worked on a communications survey project in the South Pacific with Donald Lewis, who was a faculty member in the psychology department at the University of Iowa. Possibly influenced by his association with Lewis, Schubert returned to Iowa and began work toward a doctorate in experimental psychology and statistics following his discharge from the Army. His principal concentration was on audition, his thesis advisor was Lewis, and he received his Ph.D. in 1948.

After completion of his doctoral work, Schubert began a life long career in academia with the University of Michigan. It was while Schubert was at Michigan that he published his first paper in The *Journal of the Acoustical Society of America*, this appearing in the July 1950 issue on the effect of thermal masking noise on pitch of a pure tone. He stayed at Michigan four years, and then returned to the University of Iowa in 1951. During this period at Iowa he continued to do experimental work relating to pitch shifts; one notes for example a presentation at the Spring 1953 meeting of the Acoustical Society on pitch shifts as they relate to hearing losses. A paper on a similar subject coauthored with a former doctoral student J. C. Webster appeared in the September 1954 issue. The July 1955 issue carried a letter to the editor on a phenomenon in which speech fed alternatively to the two ears can become unintelligible at certain rates, even though it would be intelligible at one ear if the switching did not occur. In 1955, Schubert left Iowa to assume the position of Director of the Cleveland Hearing and Speech Center and continued to conduct research on the association of the intelligibility of speech with the time interval between the ears. During the Cleveland period, Schubert undertook a ''volunteer job'' for the Acoustical Society for which the Society is very grateful. Beginning with the March 1957 issue, Schubert became co-editor, first with Robert N. Thurston, then with Frederick Elmer White, of the ''References to Contemporary Papers on Acoustics'' section of the *Journal*. This continued for 14 years, up through the September 1970 issue.

Schubert left Cleveland in 1960 to take on a professorial position at Indiana University; he stayed there for four years, moving to Stanford University in 1964, with an appointment in the Medical School in the program of hearing and speech sciences. There he conducted a sustained and productive research program and guided the work of several generations of students. Research topics addressed binaural hearing, with focus on temporal cues, and normal and delayed auditorial sidetone. He also worked with computers to develop an audiological data bank to predict the relative danger of noise pollution. During this period he published extensively; among the publications best remembered is Vol. 14 in the prestigious series *Benchmark Papers in Acoustics*, a series initiated by R. Bruce Lindsay. Schubert edited the volume on psychoacoustics, which appeared in 1979. After his formal retirement from Stanford in 1987, he continued to work with students and to do research, switching his energies to Stanford's Center for Computer Research in Music and Acoustics.

Frederick Elmer White • 1909–2000

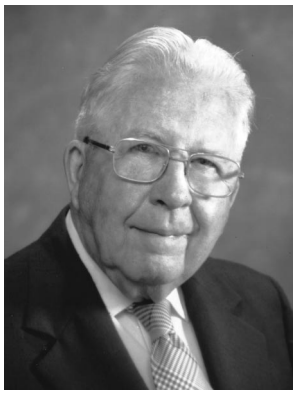

Frederick Elmer White, a Fellow of the Acoustical Society of America, passed away on 5 August 2000. He was born on 21 January 1909 in Peabody, MA, received an A.B. from Boston University in 1930, and, as a student of the late R. Bruce Lindsay, received an M.S. in 1932 and a Ph.D. in 1934 from Brown University. All of his degrees were in physics.

White served as Professor of Physics at Boston College from 1949 to 1974 where he taught advanced courses in acoustics. At various times he served as dean of Boston College's graduate school of arts and sciences, acting chairman of its physics department, and member of its premedical and predental advisory committees. After his retirement in 1974, he taught at the Pinetree School in Hamilton, MA, for several years.

During World War II, Dr. White worked at Duke University in the military research program under the direction of the National Defense Research Committee (NDRC) on studies involving sound ranging for artillery.

 0001-4966/2001/109(6)/2543/2/$18.00

It is generally believed that, during this period, he produced several significant reports that were never published because the material was classified.

Dr. White joined the Acoustical Society of America in 1943 and was elected a Fellow in 1964. He served as Associate Editor of *The Journal of the Acoustical Society of America* for References to Contemporary Papers in Acoustics (RCPA) for over 25 years, from 1962 to 1989. In his role as Associate Editor, White poured through dozens of journals which were delivered to his home each month, from which he extracted relevant articles for publication in RCPA. In recognition of this service, the Society awarded him the Distinguished Service Citation in 1987 ''for long and devoted service as Associate Editor for References to Contemporary Papers on Acoustics.''

He is survived by his wife Anna who frequently accompanied him to Acoustical Society meetings.

ELAINE MORAN
ROBERT T. BEYER

BOOK REVIEWS

P. L. Marston
Physics Department, Washington State University, Pullman, Washington 99164

These reviews of books and other forms of information express the opinions of the individual reviewers and are not necessarily endorsed by the Editorial Board of this Journal.

Editorial Policy: *If there is a negative review, the author of the book will be given a chance to respond to the review in this section of the Journal and the reviewer will be allowed to respond to the author's comments. [See "Book Reviews Editor's Note," J. Acoust. Soc. Am.* ***81****, 1651 (May 1987).]*

Structural Acoustics and Vibration

R. Ohayon and C. Soize

Academic Press, 1998.
242 pp. Price: $74.00 hc. ISBN 0125249454.

As the front cover announces, this book covers mechanical models, variational formulations, and discretization of structural systems loaded by internal and external acoustic fluids. This book is concerned with the prediction of the linear dynamic response of structures of arbitrary shape. Its focus is on the specialized methods necessary for efficient spanning of both low-frequency and mid-frequency ranges of numerical structural acoustics. This is quite likely the only monograph that tackles all of these topics; it attempts (and usually succeeds) to achieve its coverage in an elegant and succinct fashion.

The reader is carefully conveyed through the three topics of structural acoustics, namely structural vibrations, internal and external acoustics, and finally coupled structural acoustics modeling (considering both internal and externally loaded structures). The final chapter of the book presents the theory of substructures with statistical variations in their parameters (fuzzy structures). A major theme of the book is the distinction between low-frequency and mid-frequency modeling of finite domain problems (those with modal structure) along with appropriate approximation techniques for both frequency ranges. This work presents the reduced order modeling and substructure synthesis techniques needed to efficiently model complex systems (presenting some techniques never seen in book form previously). Since the structural and acoustical domains are taken to be arbitrary, approximate solutions are requisite. The continuous variational equations serve as the basis for finite dimensional approximations of each problem, leading either to a finite element approximation for internal acoustics and the elastodynamics problems or a boundary element approximation for exterior acoustics simulations. However, no details on the implementation are given (the reader is referred to classic texts or papers on these topics).

The book is organized into 15 chapters. Chapter 1 serves to introduce the book and provide an outline. In Chapter 2 (Basic Notions on Variational Formulations) the strong form (governing differential equations, boundary, and initial conditions) and weak form (based on the variational equations) for the Helmholtz equation are given as a model problem. The allowed function spaces for both strong and weak solutions including restrictions on the continuity of the forcing functions are given. Definitions and manipulations of continuous and discrete operators, topics heavily relied on in the text, are outlined in this chapter. Convergence issues of finite element approximations are briefly noted.

The style of writing begun in Chapter 2 (and continued throughout the book) somewhat obscures the presentation. The extensive use of footnotes to provide the reader the mathematical details of the various formulations is distracting. While the authors recommend that the reader ignore these if uninterested in such details, this is nearly impossible as the footnotes pervade nearly every page of the text. Existence and uniqueness of solutions are absolutely essential to numerical and analytic solution. Therefore, it is crucial to present the requirements on the solutions and forcing functions. Also, these continuity requirements are conveyed to the approximate solutions and are thus important. But because no proofs of convergence of the methods are given in the book (nor do I believe such proofs have a place in this book), the level of functional analysis presented is not really indicated. While the authors are careful to use the function spaces, definitions are sometimes lacking or difficult to find. For instance, the notation of Sobolev spaces is used on footnote on page 10. However, I couldn't find $H^1(\Omega)$ labeled as a Sobolev space until page 110 and I never found a definition. While this is not an impediment to readers who have a functional analysis background, it is precisely the readers who do not, who will likely find this treatment most burdensome.

Structural dynamics modeling techniques are presented in Chapters 3–9. In Chapter 3 (Linearized Vibrations and Structural Modes), the governing equations for conservative elastodynamics are given. First the strong form is given, followed by the weak form and subsequent approximation by a finite dimensional subspace. A fairly standard discussion about the spectral qualities of the eigenvalue problem is followed by an extremely succinct presentation of the analysis of structures with cyclic symmetry and substructure synthesis. Their presentation represents perhaps the most elegant representation (especially of the substructuring problem) that I have seen—however, the didactic nature of the presentation is somewhat lacking due to the notation used. A main problem is that proofs are given without a good roadmap of where they are going (which eventually is a very good place). The summaries of the various methods (if there are any summary) are usually too brief to be help in clarifying the procedures. Finally, no examples of the procedures are given—again detracting from the presentation. Alternatively, an algorithmic flowchart would be helpful.

In Chapter 4 (Dissipative Constitutive Equation for the Master Structure), standard viscoelasticity theory is nicely reviewed. Both frequency dependent and independent damping coefficients are presented along with their relation to phenomenological models in the time domain. In Chapters 5–8, methods for extracting the frequency response of the structure and constructing reduced order models are presented. The novel technique of shifting the frequency response from a higher band to be centered at zero frequency, then converting the frequency domain equations to time domain equations is beautifully presented. The resulting time domain formulation can then be integrated by standard techniques, presumably in a more efficient fashion than through frequency by frequency solution. However, no analysis is given as to the nature of the efficiency gained by this technique; guidelines for the time stepping parameters would be a great help. In Chapter 8, reduced order modeling is presented along with procedures to obtain the modes and an energy analysis to determine when to truncate the summation. A single degree of freedom model is the system given as a model problem. Again no specific results are given even for this simple system. Such a simple problem would show clearly how the method is to proceed for the more complicated multi-degree of freedom problem thereby addressing the trade-off issues of synthesizing the low-frequency and mid-frequency results. In Chapter 9, the response to deterministic and random forcing is given.

In Chapter 10 (Linear Acoustic Equations), both inviscid and viscous wave equations are developed along with appropriate representations of the boundary equations. The classical absorption coefficient is succinctly derived and integrated into the wave equation. A velocity potential is used to represent the acoustic fluctuations. A novel gauge function is used, but not explained (the reader is referenced to works by Ohayon and Morand)—hence the book does not stand alone in this regard. This nonzero but spatially constant function enters into the variational equations at every step. It is not until the last section of Chapter 13 where the novelty of this gauge function is mentioned (where it is stated that this takes into account volume changes in the internal fluid—a term apparently not taken into account by

 0001-4966/2001/109(6)/2545/2/$18.00

other workers). For exterior loading only, apparently, this function can be taken as zero. It would be helpful to know what is the benefit of keeping this term and whether the other methods are strictly wrong in having different gauge function (one with a different physical interpretation like the hydrostatic pressure, for instance).

In Chapter 11 the internal acoustics formulation is given. The variational equations are given. The finite domain problem is solved via the finite element method. Eigenvalue analysis is introduced along the same lines as for structural analysis. The focus on differentiating between the low- and mid-frequency domains is maintained for acoustics with parallel methods to those applied for the structural problem developed here. The external acoustics problem is presented in Chapter 12. Single layer and double layer potentials are given along with the corresponding integral equations to solve for the velocity potential given boundary data. Issues of uniqueness are addressed nicely. A unique variational approach is given along with proofs.

Chapters 13 and 14 are concerned with modeling the structural acoustic system. The continuous operator formulation for the coupled response of the system (in terms of structural displacement vector, fluid velocity potential, and a variable that is closely related to the fluid pressure) is given followed by the discrete and reduced order modeling of the system in the low-frequency and mid-frequency regions. One trade-off with the symmetric approach put forth here is that use of the velocity potential requires the introduction of a third variable in the fluid structure interaction problem (not needed when fluid pressure is used as the primary variable). Of course, in the time domain if the fluid pressure is used as a primary variable, then the resulting system is nonsymmetric. The cases of internal, external and combined internal–external loading are treated.

In Chapter 15 (Fuzzy Structure Theory), Soize's approach to introducing uncertainty and complexity into substructures in a consistent and measurable way is given. The statistical underpinnings of the method are described. A recursive algorithm for computing realizations of the response are presented along with identification schemes for the various coefficients of the method.

This is an ambitious monograph that is incredibly dense in the amount of information contained. It is likely to be difficult reading for someone not well acquainted with finite element modeling techniques; however, there are jewels of information for those willing to dig deeply. The notation in the book is somewhat nonstandard and constant interjection of footnotes makes the book hard to follow—but these detriments can be overcome by careful reading. One possible improvement of the book would be the inclusion of a model problem with examples to showcase strengths and weaknesses of these techniques. I recommend this book as an excellent and intense research monograph on structural acoustics. It represents perhaps the only treatment of modern reduced order modeling techniques applied to structural acoustics problems. It is highly recommended for structural dynamicists and structural acousticians interested in modeling arbitrarily shaped structures with complex attachments.

KARL GROSH
Mechanical Engineering Department
University of Michigan
Ann Arbor, Michigan 48109

REVIEWS OF ACOUSTICAL PATENTS

Lloyd Rice
11222 Flatiron Drive, Lafayette, Colorado 80026

The purpose of these acoustical patent reviews is to provide enough information for a Journal reader to decide whether to seek more information from the patent itself. Any opinions expressed here are those of reviewers as individuals and are not legal opinions. Printed copies of United States Patents may be ordered at $3.00 each from the Commissioner of Patents and Trademarks, Washington, DC 20231. Patents are available via the Internet at http://www.uspto.gov.

Reviewers for this issue:

KEVIN P. SHEPHERD, *M.S. 463, NASA Langley Research Center, Hampton, Virginia 23681*
WILLIAM THOMPSON, JR., *601 Glenn Road, State College, Pennsylvania 16803*
ERIC E. UNGAR, *Acentech, Incorporated, 33 Moulton Street, Cambridge, Massachusetts 02138*

6,119,808

43.20.Ye TRANSPORTABLE ACOUSTIC SCREENING CHAMBER FOR TESTING SOUND EMITTERS

James B. Steedman and Hans J. Forschner, both of Fullerton, California
19 September 2000 (Class 181/295); filed 19 August 1998

This patent pertains to a small reverberation chamber that weighs less than about 150 lb and that has overall external dimensions that do not exceed approximately 6 ft. It consists of a double-wall arrangement, with the acoustically reflective walls separated by foam or a similar material, and it includes vibration isolation elements between the interior and exterior floors and under the entire chamber. A boom that permits several microphones to be rotated about a centrally mounted test object is also provided.—EEU

5,985,001

43.25.Qp SEPARATION OF A GAS

Michael Ernest Garrett and Alberto I. LaCava, assignors to The BOC Group PLC
16 November 1999 (Class 95/29); filed in the United Kingdom 23 May 1997

An apparatus is described for separating a gas mixture of oxygen and nitrogen into two gas streams, one of which is relatively rich in the more readily adsorbed constituent of the mixture (the oxygen) and the other containing the less readily adsorbed constituent. The gas mixture enters a columnar vessel **2** containing a bed of carbon from reservoir **8**. The pressure in the vessel is alternately raised and lowered by the vibrations of a multitude of conventional, low frequency, loudspeakers **4** mounted on all faces of the column **2** and driven in-phase with one another. Additionally, two more loudspeakers **6** at the top and bottom of the column are driven at the same frequency as the others but 180 degrees out-of-phase from each other so as

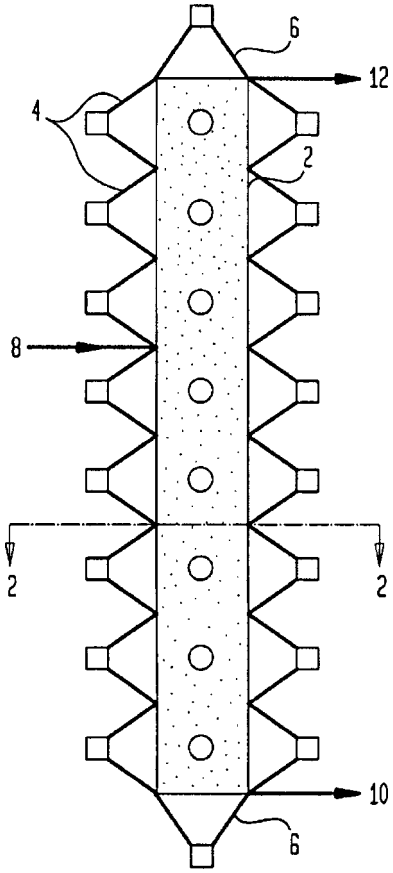

to promote a net incremental translation of the nitrogen upward to reservoir **12** and a net incremental translation of the oxygen downward to reservoir **10**.—WT

6,109,566

43.28.Py VIBRATION-DRIVEN ACOUSTIC JET CONTROLLING BOUNDARY LAYER SEPARATION

Robin Mihekun Miller and Roman N. Tunkel, assignors to United Technologies Corporation
29 August 2000 (Class 244/207); filed 25 February 1999

In order to delay separation of the boundary layer on an airfoil, such as on a helicopter rotor blade, an oscillating jet flow is introduced approxi-

 0001-4966/2001/109(6)/2547/8/$18.00

mately tangentially on the low-pressure surface of the blade. A cavity within the airfoil communicates with this surface via one or more essentially tangential slots. One wall of this cavity consists of a membrane to which a mass is attached. As the blade vibrates, the membrane oscillates to pump air through the slots, thus generating the desired oscillating jet flows.—EEU

5,992,077

43.30.Ky NOSE CONE AND METHOD FOR ACOUSTICALLY SHIELDING AN UNDERWATER VEHICLE SONAR ARRAY

Neil J. Dubois, assignor to the United States of America as represented by the Secretary of the Navy
30 November 1999 (Class 42/293); filed 18 March 1998

A more or less cylindrically shaped nose cone assembly is described, fashioned from closed-cell elastomeric foam and used to cover the nose portion of an underwater vehicle such as a torpedo. The purpose of the assembly is to shield a transducer array mounted in the nose of the vehicle from acoustic signals that are generated in the surrounding medium in order to assess the sensitivity of the transducer array to other signals such as structure borne sound.—WT

6,109,108

43.35.Zc ELECTROMAGNETIC ACOUSTIC TRANSDUCER EMAT AND INSPECTION SYSTEM WITH EMAR

Toshihiro Ohtani *et al.*, assignors to Ebara Corporation
29 August 2000 (Class 73/599); filed in Japan 13 December 1995

This patent pertains to an electromagnetic acoustic transducer (EMAT) for detection of damage and residual stresses in an electrically conductive material and for measurement of some characteristics of that material. It also relates to the prediction of fatigue life based on electromagnetic ultrasonic resonance (EMAR) measurement. Magnets placed near the surface of the object to be inspected induce a steady magnetic field in the object. A dual flat coil is situated between the aforementioned magnets and the test object. A burst of radio-frequency current in one part of the coil induces eddy currents on the surface of the object, and these interact with the steady magnetic field to generate a Lorentz force. This force induces motions in the direction perpendicular to the direction of the steady magnetic field and to the current, resulting in shear waves that propagate through the object and eventually are reflected back toward the surface near the coil. There the shear waves interact with the magnetic field to generate eddy currents, which are detected by the second part of the flat coil. A controller and processor are used to provide the current pulse and to analyze the received current to develop the desired information. —EEU

6,109,109

43.35.Zc HIGH ENERGY, LOW FREQUENCY, ULTRASONIC TRANSDUCER

Albert E. Brown, assignor to The Regents of the University of California
29 August 2000 (Class 73/632); filed 19 October 1998

This transducer is intended for inspection of reinforcing rods in concrete structures (and the like), where only one end of the rod is exposed. The transducer consists of a stack of annular piezoelectric discs, separated by thin members, and arranged around the protruding length of the rod to be inspected. The piezoelectric elements are mechanically in series and are connected electrically in parallel, so that the total displacement obtained is the sum of the individual displacements. The acoustic impedance of the transducer array is matched to the rod's impedance for maximum transfer of acoustic energy. Ultrasonic reflections at points along the rod where the rod diameter changes by one percent of the wavelength are detected and reconstructed by signal processing into an image of the rod.—EEU

6,116,080

43.35.Zc APPARATUS AND METHODS FOR PERFORMING ACOUSTICAL MEASUREMENTS

Raymond C. Logue *et al.*, assignors to Lorex Industries, Incorporated
12 September 2000 (Class 73/24.05); filed 17 April 1998

This patent relates generally to acoustical measurements of component concentrations in gas mixtures and/or volumetric or mass flow ratios. It makes use of measurements of the speed of sound in the ultrasonic range and applies cross-correlation and Fourier analysis methods to process the data, applying thermodynamic relations to determine the desired information. The patent discusses the transducers, electronics, signal processing, and some measured results in considerable detail.—EEU

6,046,962

43.38.Dv ELECTRODYNAMIC TRANSDUCER FOR UNDERWATER ACOUSTICS

Vito Suppa and Jean Bertheas, assignors to Thomson Marconi Sonar SAS
4 April 2000 (Class 367/172); filed in France 27 May 1997

The device in question is a body of revolution about the extreme right hand vertical center-line of the cross sectional sketch shown. Part **106** is a permanent magnet while **104** and **105** are pole pieces defining air gap **107**. Hemispherical dome **109** of carbon fiber embedded in a resin matrix supports the radiating horn **110** of syntactic foam. The lower legs of dome **109** support a coil of windings **120** situated in the air gap **107**. Rubber membrane **115** keeps the indicated oil out of the interior of the transducer. The dome-horn structure is stiffened by a series of ribs **116** spaced circumferentially

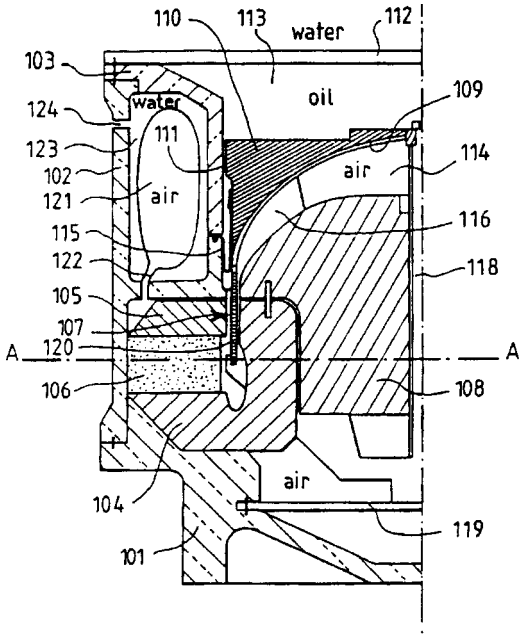

around the dome. These ribs are free to slide in slots in the core piece **108**; they also function as heat sinks to help dissipate heat generated in the coil **120**. Centering shaft **118** connects the dome-horn structure to a support disc spring **119** at the bottom of the transducer. Hydrostatic pressure compensation is provided via the air-filled rubber bladder **121**; the hydrostatic pressure communicates to the cylindrical chamber **123** containing the bladder via a series of holes **124** in the outer chamber wall.—WT

6,119,522

43.40.Le ELECTROMAGNETIC ACOUSTIC TRANSDUCER AND METHODS OF DETERMINING PHYSICAL PROPERTIES OF CYLINDRICAL BODIES USING AN ELECTROMAGNETIC ACOUSTIC TRANSDUCER

Ward L. Johnson *et al.*, assignors to the United States of America as represented by the Secretary of Commerce
19 September 2000 (Class 73/643); filed 2 August 1994

An array of magnets **22** and a wire coil **24** are placed around an essentially circular cylindrical test object **200**. The oscillating current in the coil is adjusted to produce resonant vibrations of the test object. The arrangement shown in the figure is intended to induce axial shear vibrations;

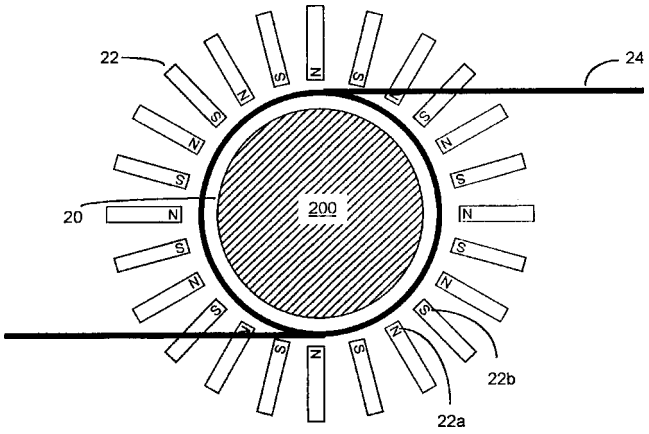

other coil arrangements relative to the magnets and test object permit the generation of torsional, radial, or axial vibrations. The observed resonance frequencies and the decay rates of vibrations at natural frequencies can be used to determine various physical properties of the test object.—EEU

6,138,791

43.50.Gf MUFFLER SLEEVE, AND METHOD AND APPARATUS FOR MANUFACTURING SAME

Daniel Edward Zanzie, assignor to Bay Industries, Incorporated
31 October 2000 (Class 181/252); filed 10 March 1998

This patent is primarily concerned with a description of a machine for the assembly of automobile mufflers. Sound absorbing material, **212**, used in mufflers is typically loose fiberglass. It is proposed that the fiberglass be

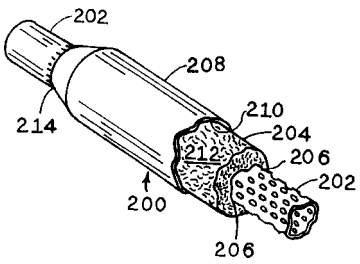

infused with a thermosetting hardening agent such as sodium silicate and kaolin clay. This creates a fairly rigid structure, making for easier muffler assembly, but the material remains porous and resilient.—KPS

6,116,090

43.58.Ls MULTIEYED ACOUSTICAL MICROSCOPIC LENS SYSTEM

Roman Gr. Maev *et al.*, assignors to DaimlerChrysler Corporation
12 September 2000 (Class 73/625); filed 30 April 1999

This acoustical microscope, intended for the inspection of welds in production, uses several acoustical transducers to generate independent beams of acoustic energy, with each beam aimed at a different point on the target. The beams from the various transducers are produced sequentially and for a short time, so that no transducer transmits while a reflection is being received. The transducer array is moved across the test specimen, allowing it to be inspected in a relatively short time.—EEU

6,146,147

43.70.Dn INTERACTIVE SOUND AWARENESS SKILLS IMPROVEMENT SYSTEM AND METHOD

Jan Wasowicz, assignor to Cognitive Concepts, Incorporated
14 November 2000 (Class 434/169); filed 13 March 1998

The argument made here, and said to be supported by decades of clinical experience, is that an artificial presentation of phonetic sounds can provide a better language learning experience than normal day-to-day life. It could be true. The patent discloses a game console which presents various phonetic sounds coordinated with a visual display. Standard game-playing strategies are followed, such as increasing the difficulty level as the player progresses. Video display details are available on a separate microfiche obtainable from the patent office.—DLR

6,126,447

43.70.Fq COLOR-ASSONANT PHONETICS SYSTEM

L. Eve Engelbrite of Chandler, Arizona
3 October 2000 (Class 434/167); filed 8 December 1997

This patent presents a system of colored text characters designed to ease the task of learning to read English text. The system uses bold, slanted and thin letters to indicate particular consonant and vowel qualities, but the primary association the system makes is to use specific colors for each vowel quality. The vowel sound is always the sound in the color word used, such as /æ/ in tan, /i/ in green, /e/ in red, /ey/ in gray or /ay/ in lime. All consonants are black. Color figures are available from the patent office for a fee.—DLR

6,134,526

43.70.Kv APPARATUS AND METHOD FOR REPRODUCING RECORDED SIGNALS BY USING RECORDING MEDIUM

Yong Ho Kim, assignor to Samsung Electronics Company, Limited
17 October 2000 (Class 704/246); filed in Republic of Korea 13 May 1997

The device described here is a kind of karaoke processor to be used with movies rather than music. The intended application is for learning a foreign language. The language learner would continuously control whether his own voice or the original actor's voice was played back and would also be able to hear a recorded version of his voice dubbed into the movie track. In addition to isolating and silencing the original actor's voice, there is also a limited provision for silencing certain background sounds from the movie track.—DLR

6,134,524

43.72.Ar METHOD AND APPARATUS TO DETECT AND DELIMIT FOREGROUND SPEECH

Stephen Douglas Peters and Daniel Boies, assignors to Nortel Networks Corporation
17 October 2000 (Class 704/233); filed 24 October 1997

This patent presents an improved method of detecting speech, or more precisely, detecting the begin and endpoints of the speech signal, in a noisy environment. Up and down counters operate on an amplitude-like transformation of the signal energy to provide running estimates of high and low quantiles of the energy level. These are shown in the figure as **HQE** and

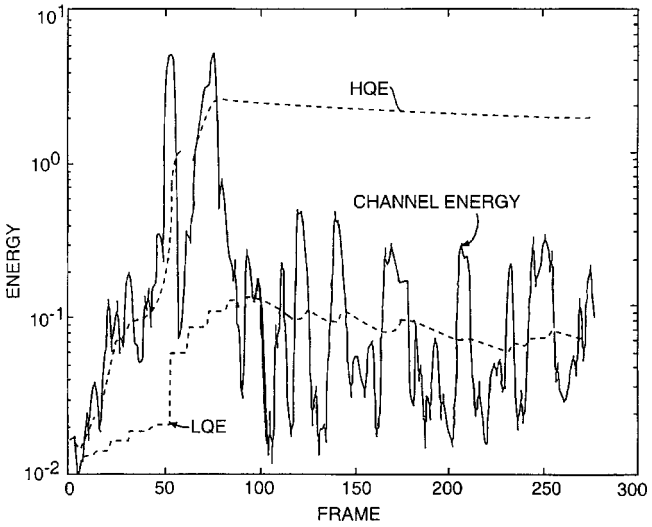

LQE. An offset value, called the mask, is added to both high and low quantiles. This offset is adapted to maintain a predetermined ratio of the offset quantiles. The standard deviation of the mask offset provides the desired speech endpoint measure.—DLR

6,131,083

43.72.Gy METHOD OF ENCODING AND DECODING SPEECH USING MODIFIED LOGARITHMIC TRANSFORMATION WITH OFFSET OF LINE SPECTRAL FREQUENCY

Kimio Miseki and Katsumi Tsuchiya, assignors to Kabushiki Kaisha Toshiba
10 October 2000 (Class 704/217); filed in Japan 24 December 1997

Previous vocoding systems have used a codebook for encoding the speech spectral information in the form of line spectral frequency (LSF) parameters. This system improves the coding accuracy by computing the codebook error based on a log scale conversion of the LSF parameters. This results in a reduction of the perceptual error for a given number of bits used to transmit the spectral code.—DLR

6,138,092

43.72.Gy CELP SPEECH SYNTHESIZER WITH EPOCH-ADAPTIVE HARMONIC GENERATOR FOR PITCH HARMONICS BELOW VOICING CUTOFF FREQUENCY

Richard Louis Zinser, Jr. *et al.*, assignors to Lockheed Martin Corporation
24 October 2000 (Class 704/223); filed 13 July 1998

This vocoder, identified as a CELP synthesizer, also uses vector quantization to code a line spectral frequency form of the linear prediction spectral envelope. Enhancements include mixing of simultaneous pulse and noise excitations and transmission of a parameter indicating a high-frequency cutoff point for harmonics generated by the pulse excitation source.—DLR

6,125,346

43.72.Ja SPEECH SYNTHESIZING SYSTEM AND REDUNDANCY-REDUCED WAVEFORM DATABASE THEREFOR

Hirofumi Nishimura *et al.*, assignors to Matsushita Electric Industrial Company, Limited
26 September 2000 (Class 704/258); filed in Japan 10 December 1996

Systems for speech synthesis based on concatenation of wave form segments typically use subword segments with length on the order of that of a phoneme, such as diphones or triphones. In this patented system, the smallest unit is a pitch period. A large number of pitch period segments is

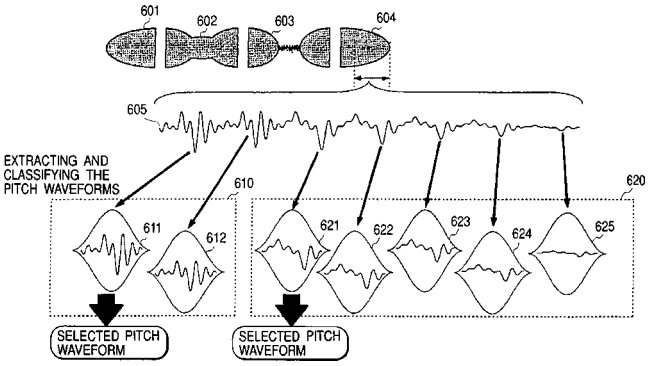

collected and these are classified into similarity groups. A central segment is chosen to represent each group and all other segments in the group are discarded. A pointer table allows a selected segment to be retrieved quickly.—DLR

6,134,528

43.72.Ja METHOD DEVICE AND ARTICLE OF MANUFACTURE FOR NEURAL-NETWORK BASED GENERATION OF POSTLEXICAL PRONUNCIATIONS FROM LEXICAL PRONUNCIATIONS

Corey Andrew Miller *et al.*, assignors to Motorola, Incorporated
17 October 2000 (Class 704/258); filed 13 June 1997

This speech synthesis system uses a neural network based on phonetic units to adjust the phonetic output stream to correspond more closely with alternate pronunciations as occur in natural, fluent speech. These alternate pronunciations are referred to as ''post-lexical'' phonetic sequences and include effects such as coarticulation, speech rate effects, dialect variations, and others. The neural network training procedures require labeled speech sequences covering all of the alternate pronunciations to be learned.—DLR

6,144,939

43.72.Ja FORMANT-BASED SPEECH SYNTHESIZER EMPLOYING DEMI-SYLLABLE CONCATENATION WITH INDEPENDENT CROSS FADE IN THE FILTER PARAMETER AND SOURCE DOMAINS

Steve Pearson *et al.*, assignors to Matsushita Electric Industrial Company, Limited
7 November 2000 (Class 704/258); filed 25 November 1998

This speech synthesis system uses a formant synthesizer, such as the Klatt model, and stores an inventory of demisyllable parameter sets collected from human speech. Because the glottal source and filter parameters for the synthesizer are kept separate, various strategies of smoothing, interpolation, and cross fading can be applied separately in the two domains.—DLR

6,141,415

43.72.Kb METHOD AND APPARATUS FOR DETECTING SPEECH AT A NEAR-END OF A COMMUNICATIONS SYSTEM, A SPEAKER-PHONE SYSTEM, OR THE LIKE

Tandhoni S. Rao, assignor to Texas Instruments, Incorporated
31 October 2000 (Class 379/410); filed 11 October 1996

This patent presents an interesting method for a speakerphone to determine whether a signal picked up by the room microphone was produced by the phone loudspeaker or whether it represents a sound from within the room. Loudspeaker output is modified by filtering with a very narrow notch

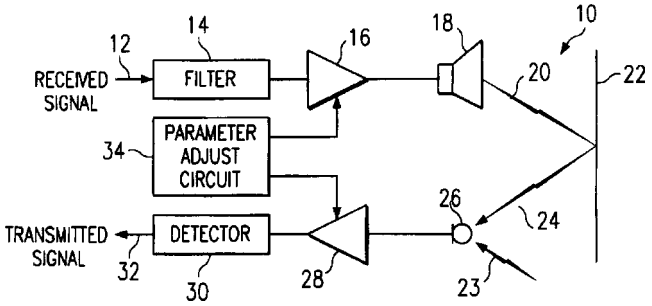

filter, perhaps in the frequency range of 2 to 5 KHz. Detection at the microphone of a signal with such a notch causes that signal to be used as an adaptor to reduce microphone feedback.—DLR

6,125,345

43.72.Ne METHOD AND APPARATUS FOR DISCRIMINATIVE UTTERANCE VERIFICATION USING MULTIPLE CONFIDENCE MEASURES

Piyush C. Modi and Mazin G. Rahim, assignors to AT&T Corporation
26 September 2000 (Class 704/240); filed 19 September 1997

In speech recognition, several different methods have been tried for evaluating the confidence in a particular result. These methods include maximum likelihood, minimum classification error minimizing either the empirical error rate or the expected error rate, and minimum verification

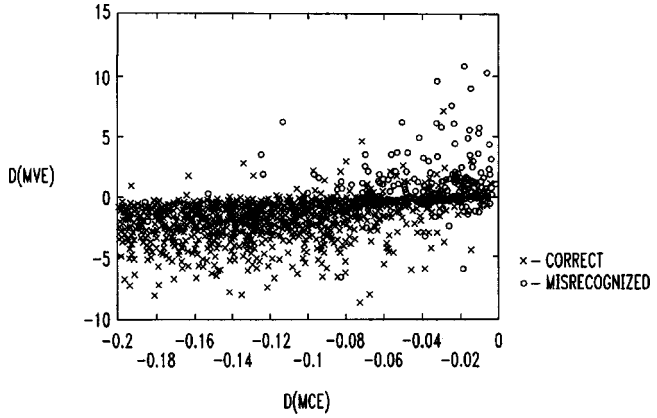

error. Each of these methods has certain advantages under certain conditions. This patent describes a recognizer which evaluates the confidence using a number of different methods and then combines the results of these methods using a neural network classifier.—DLR

6,125,347

43.72.Ne SYSTEM FOR CONTROLLING MULTIPLE USER APPLICATION PROGRAMS BY SPOKEN INPUT

William F. Cote *et al.*, assignors to L & H Applications USA, Incorporated
26 September 2000 (Class 704/275); filed 29 September 1993

For use with a multi-tasking operating system, this speech recognition system maintains a database of recognized text events (TEs). The TE database also records the task to which the TE was directed. The database is organized so as to maximally simplify the process of correcting erroneously recognized inputs and to minimize the impact of such errors on the various tasks running in the system. The speech recognition system is itself one of the system tasks.—DLR

6,128,594

43.72.Ne PROCESS OF VOICE RECOGNITION IN A HARSH ENVIRONMENT, AND DEVICE FOR IMPLEMENTATION

Christian Gulli *et al.*, assignors to Sextant Avionique
3 October 2000 (Class 704/244); filed in France 26 January 1996

The patent describes a multitude of problems facing the designer of a speech recognizer for use in a military aircraft cockpit. They include monophonic delivery, high noise levels, pilot stress, interference and echoes, to name just a few. Facing these severe hurdles, this recognizer restricts the vocabulary to perhaps 100 words and provides a dual decoding, by words and by phonetic sequences. The results of the two decodings are compared and also subjected to an analysis to determine the possible relevance of the utterance to the current flight status.—DLR

6,128,595

43.72.Ne METHOD OF DETERMINING A RELIABILITY MEASURE

Bernhard J. Rüber, assignor to U.S. Philips Corporation
3 October 2000 (Class 704/255); filed in Germany 12 September 1997

When using speech recognition for data entry, it may be the case that only a portion of the spoken utterance contains the relevant data items, although that item may be spoken in different ways. An example is given of the entry of a date, which may be spoken in many alternate ways, but which

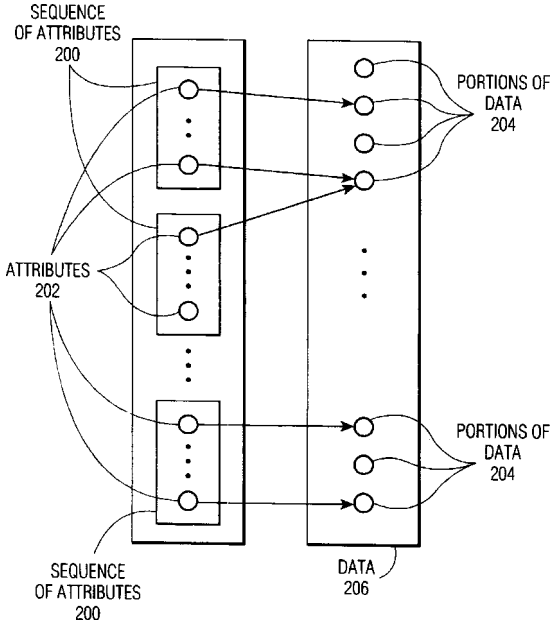

are somewhat constrained by the surrounding context. This recognizer attempts to reduce any such phrase to the underlying concept, which is then recoded into a standard form for database use.—DLR

6,134,525

43.72.Ne IDENTIFICATION-FUNCTION CALCULATOR, IDENTIFICATION-FUNCTION CALCULATING METHOD, IDENTIFICATION UNIT, IDENTIFICATION METHOD, AND SPEECH RECOGNITION SYSTEM

Naoto Iwahashi, assignor to Sony Corporation
17 October 2000 (Class 704/236); filed in Japan 26 September 1995

This patent describes several methods for adjusting the input classifier of a speech recognition system so as to adapt the classification to the speech of a new, unknown speaker. For example, the classifier could analyze the speech into a phoneme sequence. In order to perform the adaptation with a small number of speech items from the unknown speaker, acoustic vectors from the unknown speech and of the same item from a known speaker are used together to adapt the input classifier. This is done by maximizing the log likelihood or the maximum likelihood classification. The patent presentation is in a very general style, making it much more difficult to understand the application of the method to a specific type of recognizer.—DLR

6,134,527

43.72.Ne METHOD OF TESTING A VOCABULARY WORD BEING ENROLLED IN A SPEECH RECOGNITION SYSTEM

Jeffrey Arthur Meunier *et al.*, assignors to Motorola, Incorporated
17 October 2000 (Class 704/247); filed 30 January 1998

This patent covers strategies for training vocabulary items for a limited vocabulary speech recognition system. The training process consists of two steps, creating a recognition model for the new item, and testing the new item for possible conflicts with previously trained items. These two steps are carried out together so as to minimize the delay before the user is notified of a possible conflict.—DLR

6,134,529

43.72.Ne SPEECH RECOGNITION APPARATUS AND METHOD FOR LEARNING

Martin Rothenberg, assignor to Syracuse Language Systems, Incorporated
17 October 2000 (Class 704/270); filed 9 February 1998

This speech recognition system is designed to teach reading and writing skills in a native or foreign language. In other words, it does not perform a phonetic evaluation of the user's pronunciation. Instead, the user is presented with questions or statements in the language which contain true and false information. This sort of constraint on the user's possible speech responses is sufficient to allow the system to determine whether the user has responded appropriately.—DLR

6,137,863

43.72.Ne STATISTICAL DATABASE CORRECTION OF ALPHANUMERIC ACCOUNT NUMBERS FOR SPEECH RECOGNITION AND TOUCH-TONE RECOGNITION

Deborah W. Brown *et al.*, assignors to AT&T Corporation
24 October 2000 (Class 379/88.01); filed 13 December 1996

This speech recognition system is arranged to improve the accuracy of word identities, such as passwords for access to priveleged information or services. A confusion matrix of phonetic units is used to compute the overall likely confusions between the phonetic sequence detected in the input item and all stored reference items. Acceptence of the entered password occurs only if the correct reference item has the best overall confusion score.—DLR

6,138,094

43.72.Ne SPEECH RECOGNITION METHOD AND SYSTEM IN WHICH SAID METHOD IS IMPLEMENTED

Gilles Miet and Benoit Guilhaumon, assignors to U.S. Philips Corporation
24 October 2000 (Class 704/233); filed in France 3 February 1997

This is like reading a patent from the 1970s. A small-vocabulary recognizer forms a vector consisting of FFT spectra, concatenated across all frames of the utterance. There is no mention of how to start or stop speech collection and no provision for time adjustments. A Hamming distance is computed between the input and all references. If the shortest distance is less than a noise-level-dependent threshold, the item is recognized.—DLR

6,138,095

43.72.Ne SPEECH RECOGNITION

Sunil K. Gupta and Frank Kao-Ping Soong, assignors to Lucent Technologies, Incorporated
24 October 2000 (Class 704/234); filed 3 September 1998

This patent for a speech recognition system is entirely centered around the notion that the rejection threshold should be dependent upon the length of the utterance. A single spectral density model trained on the entire training database represents an alternative hypothesis in the comparison of test utterances against reference items. Since the single state model is not utterance length dependent, the distance computation for test inputs is weighted accordingly.—DLR

6,138,097

43.72.Ne METHOD OF LEARNING IN A SPEECH RECOGNITION SYSTEM

Philip Lockwood *et al.*, assignors to Matra Nortel Communications
24 October 2000 (Class 704/256); filed in France 29 September 1997

The latest trend is that cell phone manufacturers are discovering speech recognition. Recently issued patents would suggest that, in the process, they are also rediscovering 20- and 30-year-old recognition techniques. In this patent, the training system for a small vocabulary recognizer stores an average of the spectral densities from the analysis of a few initial utterances and then runs the recognizer to determine whether additional training is required. A few additional utterances are checked against the previously stored densities and against all other reference utterances in the system. The user is warned of a potential conflict.—DLR

6,138,098

43.72.Ne COMMAND PARSING AND REWRITE SYSTEM

Stuart M. Shieber *et al.*, assignors to Lernout & Hauspie Speech Products N.V.
24 October 2000 (Class 704/257); filed 30 June 1997

This patent describes a speech recognition control strategy intended for use with any of several commercially available PC-based recognizers. The control system is able to generate keyboard emulation commands for a variety of PC software applications, particularly word processors. The text

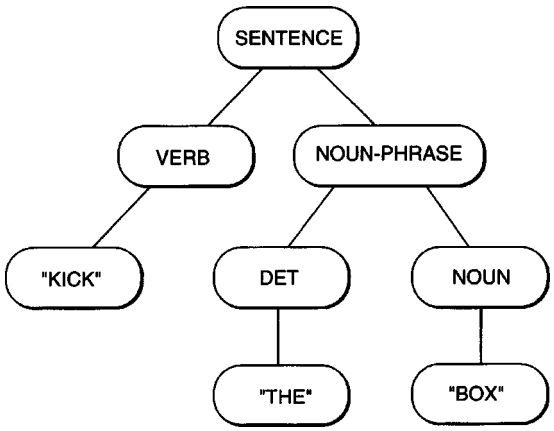

string produced by the recognizer is analyzed by a context-free grammar parser using easily modified grammar rules which describe the possible utterances. The grammar rule set also includes, as terminal nodes, keyboard command sequences to be produced when a phrase is recognized.—DLR

6,138,099

43.72.Ne AUTOMATICALLY UPDATING LANGUAGE MODELS

James R. Lewis and Maria Smith, assignors to International Business Machines Corporation
24 October 2000 (Class 704/257); filed 19 October 1998

This speech recognition system allows the user to enter new words or phrases, to be used to modify the recognition language model. When a modified item is recognized, the new item is compared to the previous language model item. A close match indicates that the new item is merely an alternate pronunciation and a model update proceeds. If the difference is large, the user is queried for confirmation before the update occurs.—DLR

6,141,641

43.72.Ne DYNAMICALLY CONFIGURABLE ACOUSTIC MODEL FOR SPEECH RECOGNITION SYSTEM

Mei-Yuh Hwang and Xuedong D. Huang, assignors to Microsoft Corporation
31 October 2000 (Class 704/243); filed 15 April 1998

This patent discloses a method of grading the various components of a speech recognition language model to determine their relative contributions to overall recognition accuracy. Using such a scale, the less valuable components can be selectively eliminated, allowing the resulting language model to fit within the memory limitations of a small computer system.—DLR

6,148,105

43.72.Ne CHARACTER RECOGNIZING AND TRANSLATING SYSTEM AND VOICE RECOGNIZING AND TRANSLATING SYSTEM

Shinji Wakisaka and Hiroko Sato, assignors to Hitachi, Limited
14 November 2000 (Class 382/190); filed in Japan 15 November 1995

The patented device is a hand-held translator intended for use by a tourist or other traveller. The unit performs speech recognition on audio inputs from a microphone as well as text recognition from images captured

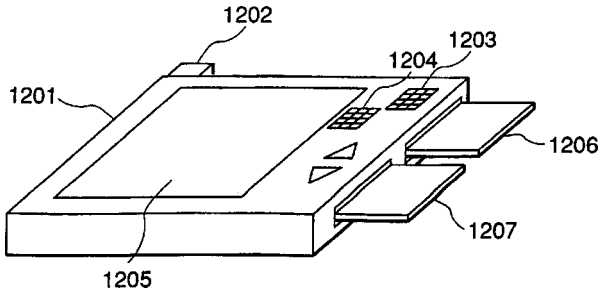

by an embedded camera. Foreign language material arriving at either input is translated to the target language and spoken and/or displayed for the user.—DLR

6,148,284

43.72.Ne METHOD AND APPARATUS FOR AUTOMATIC SPEECH RECOGNITION USING MARKOV PROCESSES ON CURVES

Lawrence Kevin Saul, assignor to AT&T Corporation
14 November 2000 (Class 704/256); filed 23 February 1998

Any signal which can be represented as a sequence of vectors, such as speech acoustic analysis vectors, can be thought of as a point moving through a multidimensional space. This patent makes the argument that the ''intrinsic geometric properties'' of the resulting curve through the multidimensional space are of greater value for recognition than the traditional

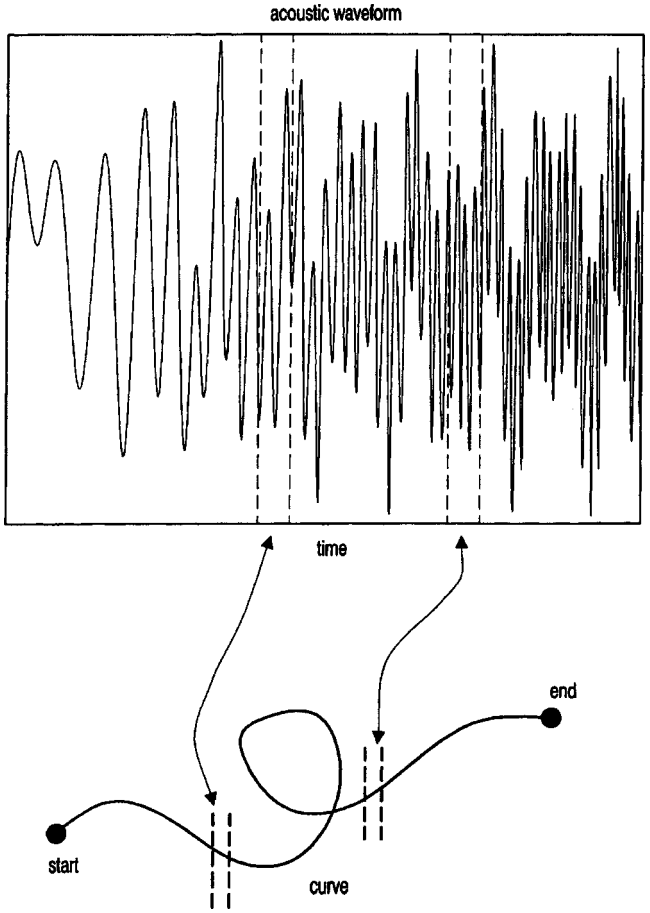

forms of analysis. For example, it is said that properties, such as arc length or radius, do not depend on the rate at which they are traversed. By adjusting the analysis so as to take the arc length into account, better consonant recognition is said to be achieved.—DLR

6,151,572

43.72.Ne AUTOMATIC AND ATTENDANT SPEECH TO TEXT CONVERSION IN A SELECTIVE CALL RADIO SYSTEM AND METHOD

Yan-Ming Cheng *et al.*, assignors to Motorola, Incorporated
21 November 2000 (Class 704/235); filed 27 April 1998

The patent presents a voice processing system for use by a pager or selective calling radio service provider. The goal of the system is to convert callers' messages to text for distribution to subscribers' pager units. In order to achieve better accuracy than the recognition system alone could provide, a human operator provides a backup check. Alerted by a low recognition confidence result, the operator can listen to the utterance and edit the text result or ask the caller for a repetition. The preferred recognition system uses a method which is essentially a normalized cepstral vector analyzer.—DLR

6,151,573

43.72.Ne SOURCE NORMALIZATION TRAINING FOR HMM MODELING OF SPEECH

Yifan Gong, assignor to Texas Instruments, Incorporated
21 November 2000 (Class 704/256); filed 17 September 1997

This patent discloses a method of extracting a background noise signature from the audio input signal and using that information to normalize the hidden Markov speaker models for improving the speech recognition performance in noisy environments. The method is said to work for additive noise sources, such as background sounds or microphone characteristics. It would not work well for convolutive effects, such as room reverberation.—DLR

6,141,644

43.72.Pf SPEAKER VERIFICATION AND SPEAKER IDENTIFICATION BASED ON EIGENVOICES

Roland Kuhn *et al.*, assignors to Matsushita Electric Industrial Company, Limited
31 October 2000 (Class 704/273); filed 4 September 1998

A method is described for computing a characterization of a person's voice, to be used for speaker identification or verification. A speaker model is first constructed just as for use in a speech recognition system, such as, for example, a hidden Markov model. The model parameters for all density functions are then concatenated into a single supervector. The set of supervectors for all enrolled speakers is reduced by any of several matrix techniques, such as principal components analysis, factor analysis, or singular value decomposition. Any later speaker model can then be mapped to a point in the resulting reduced-dimensional space by generating its supervector. Distances in the space correspond to differences between speakers.—DLR

Acoustical cavity excitation

Harold Levine
Mathematics Department, Stanford University, Stanford, California 94305

(Received 3 March 2001; accepted for publication 3 March 2001)

A tutorial exposition is given of cavity excitations and it is shown that relatively simple analytical solutions for the excitation of acoustic fields in cavities with lossy walls can be obtained for a broad class of such cavities. The standard analytic procedure whereby one expresses the acoustic field as a sum over the eigenmodes of the cavity is reviewed and its limitations are pointed out. An alternate procedure is to seek to make use of Green's functions depending on a single coordinate and to not express such Green's functions as sums over eigenfunctions. Instead, one expresses the Green's function as a closed form function that has a discontinuous slope at the value of the coordinate corresponding to the source location. Although the class of cavities for which this approach is possible is limited, it is sufficiently broad to be of intrinsic interest and the results may be helpful to those seeking benchmark solutions and analytic insight. Displayed examples are for cavities whose shapes are spheres and cylinders, with interior monopole, dipole, line, and distributed sources. The formulation yields simple expressions for the total power absorbed by the cavity walls.
 [DOI: 10.1121/1.1367246]

PACS numbers: 43.10.Ln, 43.20.Ks, 43.55.Ka [ADP]

I. INTRODUCTION

The nature and consequences of acoustic fields within closed regions, generically referred to here as cavities, are topics of enduring importance in fundamental acoustics and in its practical applications. The literature abounds with many papers in which topics (room acoustics being a prime example) involving cavities are of principal focus. Examples presented within the recent issues of this journal include the papers by Chen (1996), Easwaran and Craggs (1996), Franzoni and Labrozzi (1999), Kang and Moo (2000), Kim and Kim (1999), Kokkarakis and Roumeliotis (1999), Lobkis and Weaver (2000), Missaoui and Cheng (1997), Schaffner (1999), and Sumbatyan, *et al.* (2000). In much of the more practical recent literature, the work is extensively numerical and relies on standard generic finite-element programs. Such, while appropriate to addressing specific examples, tends to preclude generalization and to inhibit insight. There is also the worrisome thought that the computer implementation may have some undetected ''mistakes'' and that results may not be wholly correct. Such fears can, however, be largely offset if one has some standard benchmark solutions, preferably analytic, against which the numerical implementation can be tested.

Regarding analytic solutions, there are very few that are wholly so, and these are for specialized geometries and idealizations. There does exist, nevertheless, a standard ''textbook solution'' that is formally analytic, although its actual implementation could involve extensive numerical calculations. Such, which one finds discussed in books such as those by Pierce (1981) and by Morse and Ingard (1968), involves a sum over the natural modes of the cavity, with the individual terms involving the eigenfunctions and modal eigenvalues for the cavity. The formulation gives a prominent role to a Green's function which incorporates these characteristic quantities. The quantities are relatively easy to express if the cavity is of regular shape (e.g., a rectangular box) and if the boundary conditions at the wall are especially simple (e.g., perfectly rigid), but the required sum is still formidible to evaluate, especially in the vicinity of a localized source, where the convergence is slow.

What is relatively poorly, if not entirely, unknown to the general acoustics community, is that there is a broad class of idealized cavity problems in which the cavity boundaries need not be so highly idealized and for which the modal sums can be either completely summed or considerably simplified. The present paper deals with such cases. Because of the vast existing literature concerned with boundary value problems involving the Helmholtz equation, no wide-sweeping claims are here made as to novelty. However, a tutorial paper with a strong effort toward clarity of presentation should be of some interest to this journal's readers.

To explain the general subject matter of the paper, it is appropriate to first review what might be termed the standard ''textbook'' solution for the excitation of an acoustic cavity by a distributed source. The primarily desired descriptor of the acoustic field is taken here as the complex amplitude $\phi(\mathbf{r})$ of the velocity potential, given that the time dependence is $e^{-i\omega t}$. The acoustic part of the pressure has complex amplitude $p=-i\omega\rho\phi$ and the associated vector fluid velocity has complex amplitude $\mathbf{v}=-\nabla\phi$. Within a cavity (domain D), except at the location of the source, ϕ satisfies the Helmholtz equation. The walls are locally reacting, with a wall impedance $p/v_n=\rho c/\eta$, where η is a convenient dimensionless descriptor of the cavity wall admittance. Here v_n is the component of the fluid velocity directed normally into the bounding wall (out of the cavity).

The construction of solutions in terms of eigenmodes of the cavity makes use of modal wave functions that are everywhere regular solutions of the homogeneous Helmholtz equation

$$(\nabla^2+k_m^2)\phi_m(\mathbf{r})=0 \tag{1}$$

subject to the admittance boundary condition at the cavity wall

$$\frac{\partial}{\partial n}\phi_m = ik\eta\phi_m, \tag{2}$$

wherein the symbolism $\partial/\partial n$ implies a normal derivative directed outward from the cavity interior. Here η is the admittance parameter mentioned above and $k=\omega/c$ is the wave number. The ϕ_n are the eigenfunctions and the k_n^2 are the eigenvalues. Both are, in general, complex, and the set of all such eigenfunctions is a complete set.

As shown in various standard textbooks, the Green's function corresponding to a point source located at a point $\mathbf{r}'$ in the cavity can be taken as

$$G(\mathbf{r},\mathbf{r}') = \sum_{(m)} \frac{\phi_m(\mathbf{r})\phi_m(\mathbf{r}')}{k_m^2 - k^2}. \tag{3}$$

This result embodies the derivable fact that the eigenfunctions are orthogonal and presumes that they are normalized, so that

$$\int_D \phi_{m_1}(\mathbf{r})\phi_{m_2}(\mathbf{r})dV = \delta_{m_1 m_2}. \tag{4}$$

The Green's function satisfies a version of the inhomogeneous Helmholtz equation, namely

$$(\nabla^2 + k^2)G = -\delta(\mathbf{r}-\mathbf{r}'). \tag{5}$$

(Other definitions of the Green's function that are used in different texts differ according to the choice of the coefficient of the delta function on the right side.) This Green's function (or point source function) can be used to formally express the solution of the general inhomogeneous Helmholz equation with a source term on the right side, this equation being

$$(\nabla^2 + k^2)\phi = -q(\mathbf{r}). \tag{6}$$

This governs the spatial variation, $\phi(\mathbf{r})$, of an acoustical response due to a given time-periodic source distribution $\mathrm{Re}[q(\mathbf{r})e^{-i\omega t}]$, $\omega = kc$, inside the cavity. This quantity q may be thought of as the complex amplitude of the time rate at which additional volume of fluid is being added to the medium per unit time (volume velocity per unit volume). With such an inhomogeneous source and with both ϕ and the Green's function satisfying the same admittance boundary condition at the cavity walls, the solution for ϕ is given by

$$\phi(\mathbf{r}) = \int_D G(\mathbf{r},\mathbf{r}')q(\mathbf{r}')dV' = \sum_{(m)} \frac{\phi_m(\mathbf{r})}{k_m^2 - k^2}\int_D q(\mathbf{r}')\phi_m(\mathbf{r}')dV'. \tag{7}$$

One should note that the satisfaction of the linear boundary condition (2) follows automatically from the fact that each of the eigenfunctions satisfies this boundary condition.

The formal solution just outlined nevertheless has a marked shortcoming in terms of analytical and computational convenience because it implies that one should first find each of the modal eigenvalues and eigenfunctions. If the admittance boundary condition is imposed in a nontrivial manner, then the individual eigenvalues k_n^2, even for cavities of simple shape, are roots of transcendental equations, and an analytical evaluation of the indicated sum is not *a priori* obvious.

II. SIMPLE ALTERNATIVE GREEN'S FUNCTIONS

A simple example involving a spherical cavity suffices to demonstrate that one can at times find an alternative form of the cavity Green's function that does not involve the normal mode functions or eigenvalues.

A. Source in the center of a sphere

For a point source in the center of a sphere of radius a with perfectly soft (pressure release) walls, the natural modal eigenfunctions of the cavity that contribute to the resulting spherically symmetric disturbance are

$$\phi_n(r) = \frac{1}{(2\pi a)^{1/2}}\frac{\sin(n\pi r/a)}{r} \tag{8}$$

and these conform to the orthonormality condition

$$4\pi\int_0^a r^2\phi_n^2(r)dr = 1. \tag{9}$$

Here the wall boundary condition is taken as

$$\phi_n(a) = 0 \tag{10}$$

and the corresponding eigenvalues are

$$k_m = \frac{n\pi}{a}, \quad n = 1,2,\ldots\ . \tag{11}$$

In the standard ''textbook'' solution alluded to above, the constructed Green's function for a source distributed over the surface of a spherical shell within the sphere is

$$G(r,r') = \frac{1}{2\pi a}\sum_{n=1}^{\infty}\frac{1}{(n\pi/a)^2 - k^2} \times \frac{\sin(n\pi r/a)}{r}\frac{\sin(n\pi r'/a)}{r'}. \tag{12}$$

If one allows r' to shrink to zero, one obtains a cavity excitation function

$$\phi(r) = G(r,0) = \frac{1}{2\pi a r}\sum_{n=1}^{\infty}\frac{n\pi/a}{(n\pi/a)^2 - k^2}\sin(n\pi r/a) \tag{13}$$

associated with a source (singularity) at the sphere's center. This limit is seen to be such that the function $\phi(r)$ so obtained satisfies the condition

$$\lim_{\epsilon\to 0}\left(-4\pi\epsilon^2\left(\frac{d\phi}{dr}\right)_{r=\epsilon}\right) = 1. \tag{14}$$

What might be at first sight surprising is that the nonuniformly convergent trigonometric series that appears in Eq. (13) can actually be evaluated in closed form, with the especially simple result:

$$\phi(r)=\frac{1}{4\pi r}\frac{\sin k(a-r)}{\sin ka}. \tag{15}$$

That this is indeed the correct result for the sum is confirmed by the facts that it satisfies the Helmholtz equation, that it satisfies the boundary condition of Eq. (10), and that it satisfies the singularity condition (14).

B. Green's function with discontinuous slope

As indicated by the mathematical preamble in the introduction to this paper, the Green's function that appears in Eq. (12) should be the solution to the ordinary differential equation

$$\left[\frac{1}{r^2}\frac{d}{dr}\left(\frac{r^2 d}{dr}\right)+k^2\right]G=-\frac{\delta(r-r')}{4\pi r^2}, \quad 0<r, \quad r'<a, \tag{16a}$$

with the boundary condition

$$G(a,r')=0 \tag{16b}$$

at the outer surface, and with the requirement of regular behavior at the sphere center, this being

$$G(0,r') \quad \text{finite}. \tag{16c}$$

The differential equation is homogeneous on the two sides of the singularity location r', and it is a relatively simple matter to patch together solutions from the two regions to obtain the exact solution

$$G(r,r')=\frac{1}{4\pi k}\frac{1}{\sin ka}\frac{\sin kr_<}{r_<}\frac{\sin k(a-r_>)}{r_>}, \tag{17}$$

where $(r_<,r_>)$ designate the smaller/larger of r,r', respectively.

[The details of the derivation are more fully aired in a subsequent section of this paper. The method is frequently seen in textbook discussions of the Green's function for the vibrating string, as, for example, in the book by Mathews and Walker (1970). The result for the vibrating string appeared in the first (1877), and subsequent editions, of Rayleigh's *Theory of Sound* (1945). Rayleigh in turn refers to an 1870 work by Donkin. It is not clear to what extent Donkin's work was actually published, as Rayleigh, in his introduction, alludes to the premature death of Donkin and includes the statement that ''the first part of his *Acoustics*, although little more than a fragment, is sufficient to shew that my labours would have been unnecessary had Professor Donkin lived to complete his work.'']

Given the Green's function displayed above, one can readily take the same limit as was entailed in going from Eq. (12) to Eq. (13), and what results is

$$\phi(r)=G(r,0)=\frac{1}{4\pi r}\frac{\sin k(a-r)}{\sin ka}, \tag{18}$$

which is the same as what appears in Eq. (15). The relevant point here is that one can arrive at this result without ever determining the modal eigenfunctions or the eigenvalues (which are actually defined by the zeros of the trigonometric factor, $\sin ka$, in the denominator of the Green's function representation).

C. Strategy for the present paper

What should be evident from the example above is that a simplication is possible when the relevant mathematics reduces, at least in part, to the solution of an ordinary differential equation. This in turn implies that the technique is at first sight restricted to examples where the bounding surfaces of the cavity are natural surfaces in a coordinate system for which the Helmholtz equation is separable. The set of coordinate systems for which this is so is limited and has been exhibited by Eisenhart (1934), with the results summarized by Morse and Feshbach (1953). For cavities, the only coordinate systems of intrinsic interest in this respect are rectangular coordinates, spherical coordinates, cylindrical coordinates, spheroidal coordinates, ellipsoidal coordinates, and elliptic cylinder coordinates. There is, however, an additional class of cavities in which the bounding surface is such that the solutions of the Helmholtz equation can be made of sums over products, one factor being a solution of an ordinary differential equation and the other being a solution of a partial differential equation with only two (rather than three) independent variables. This class would include cylindrical cavities, where the cross sections are neither circles or ellipses. For simplicity and brevity, the examples treated here are for spheres and circular cylinders.

Given an intrinsic interest in cavities for which at least a portion of the boundary surface is lossy and described by an impedance (or admittance) boundary condition analogous to Eq. (2), the class of examples that are applicable is further restricted, as the boundary conditions must be amenable to separability also.

The idea of taking the Green's function to be such that one of the factors (in either a sum or an integral) is a single function, but with discontinuous slope has considerable precedent in acoustics. For example, one can see it appears in essence in the context of a source in layered media (sound speed depending only on the depth coordinate in the ocean) in an early paper by Pekeris (1946). An example with analogous scope but with greater generality and elegance appears in a somewhat later paper by Haskell (1951). The use of ''depth-dependent'' kernels in Green's functions represented as integrals over a horizontal wave number k, with the kernels (depth-dependent Green's functions) having discontinuous slope in the depth coordinate is presently extensive in underwater acoustics and is the basis of the fast-field program conceived by Marsh and Elam and developed by DiNapoli, the theory of which is given by DiNapoli and Deavenport (1980).

For exterior problems, such as point sources outside rigid spheres or line sources outside rigid cylinders, in an otherwise unbounded space, the use of Green's functions which involve ''radial-distance-dependent'' Green's functions which have discontinuous slope at the radial coordinate of the source is standard and one can find an extensive summary of the relevant results in the compilation by Bowman *et al.* (1987). In this context, however, the idea of natural modes is inapplicable so one is not enticed to even consider a sum over ''eigenfunctions.''

For interior problems (i.e., cavities) the implications of using analogous Green's functions are relatively unexplored,

especially when the surface is lossy (impedance boundary condition). The plan here is to teach by way of example rather than attempt an exhaustive general treatment of all such problems.

There are two immediate advantages of using such alternative Green's functions in cavity problems. One is the derivation of fields due to multipole sources, such as point dipoles. The other is the calculation of the energy loss at the walls of the cavity. Examples illustrating these advantages appear further below.

III. CAVITIES WITH LOSSY WALLS

In what follows a number of Green's functions are constructed for spherical and cylindrical cavities whose walls are characterized by boundary admittances. The benefits of formulations such as were alluded to the previous section are illustrated by the explicit consideration of different primary source types (e.g., monopoles, dipoles, and extended sources).

A. Source at center of spherical cavity

When a field is excited by a time-periodic source with volume velocity amplitude Q at the center of a spherical cavity, the velocity potential satisfies the inhomogeneous wave equation

$$\left(\nabla^2-\frac{1}{c^2}\frac{\partial^2}{\partial t^2}\right)\Phi=-\frac{Q}{4\pi r^2}\,\delta(r)\cos\omega t$$

$$=-\mathrm{Re}\left\{\frac{Q\,\delta(r)}{4\pi r^2}e^{-i\omega t}\right\},\quad 0<r<a. \tag{19}$$

Alternately, one can regard $\delta(r)/(4\pi r^2)$ as equivalent to $\delta(x)\,\delta(y)\,\delta(z)$ because both expressions have the same volume integral.

To determine the complex amplitude of the velocity potential one sets

$$\Phi=\mathrm{Re}\{\phi(r)e^{-i\omega t}\} \tag{20}$$

and doing so yields the Helmholtz equation

$$\left[\frac{1}{r^2}\frac{d}{dr}\left(r^2\frac{d}{dr}\right)+k^2\right]\phi=-Q\,\frac{\delta(r)}{4\pi r^2},\quad 0<r<a. \tag{21}$$

By integration over a small sphere of radius ϵ and and subsequently taking a limit, one discovers that the delta function term on the right is equivalent to the boundary condition

$$\lim_{\epsilon\to 0}\int_{r=\epsilon}\left(-\frac{d\phi}{dr}\right)dS=Q. \tag{22}$$

The other boundary condition on the ordinary differential equation in Eq. (21) is taken as the admittance boundary condition

$$\frac{d\phi}{dr}=ik\eta\phi,\quad r=a, \tag{23}$$

where η represents an admittance parameter for the boundary surface at $r=a$.

To solve the problem just posed, one defines a Green's function $G(r,r')$ which is bounded for all r in $0\leqslant r\leqslant a, r'$ arbitrary, and has a discontinuous r-derivative at $r=r'$. This Green's function is required to satisfy the relations

$$\left[\frac{1}{r^2}\frac{d}{dr}\left(r^2\frac{d}{dr}\right)+k^2\right]G(r,r')=-\frac{\delta(r-r')}{4\pi r^2}, \tag{24a}$$

$$G(0,r')\quad \text{finite}, \tag{24b}$$

$$\frac{dG}{dr}=ik\eta G,\quad r=a. \tag{24c}$$

It is a consequence of the differential equation that $G(r,r')$ must be continuous at r' and this is achieved if the solution has the form

$$G(r,r')=Cf_1(r_<)f_2(r_>), \tag{25}$$

where $r_<, r_>$ designate the smaller/larger of r, r', respectively, and where C is a constant.

Satisfaction of the homogeneous differential equation and of the boundary conditions (24b) and (24c) for the two distinct regions $r<r'$ and $r>r'$ is achieved with the identification of the two functions $f_1(r)$ and $f_2(r)$ as

$$f_1(r)=\frac{\sin kr}{r}, \tag{26a}$$

$$f_2(r)=\frac{ka\cos k(a-r)-[1+ika\,\eta]\sin k(a-r)}{r}. \tag{26b}$$

The constant C is subsequently derived by integrating both sides of Eq. (24a) over a narrow region of r that is centered at r', this integration yielding

$$r'^2\frac{d}{dr}G\bigg|_{r=r'-0}^{r=r'+0}=-\frac{1}{4\pi}. \tag{27}$$

Such suffices to fix the scale factor C in Eq. (25), so that

$$C=\frac{1}{4\pi k}\left[\frac{1}{ka\cos ka-(1+ika\,\eta)\sin ka}\right]. \tag{28}$$

The values of ka which are such that the denominator vanishes in this expression for C are precisely the eigenvalues that are associated with the spherically symmetric modes of the cavity when the boundary condition (23) is imposed. The condition for the denominator vanishing can be alternately expressed as

$$i\eta j_0(ka)-j_0'(ka)=0, \tag{29}$$

where

$$j_0(z)=\frac{\sin z}{z} \tag{30}$$

and

$$j_0'(z)=\frac{d}{dz}j_0(z)=-j_1(z)=-\frac{\sin z}{z^2}+\frac{\cos z}{z}, \tag{31}$$

with $j_0(z)$ and $j_1(z)$ denoting spherical Bessel functions.

The Green's function as defined by Eqs. (24a), (24b), (24c) is thus explicitly given by

$$G(r,r')=\frac{1}{4\pi k}\frac{\sin kr_<}{r_<}\times\left[\frac{ka\cos k(a-r_>)-(1+ika\eta)\sin k(a-r_>)}{ka\cos ka-(1+ika\eta)\sin ka}\right]\frac{1}{r_>}. \tag{32}$$

Solution of the the originally posed problem for the velocity potential ϕ is subsequently achieved with the aid of Green's integral theorem (ϵ being an arbitrary inner radius), which states

$$\begin{aligned}\int_{\epsilon<r<a}[\phi\nabla^2 G-G\nabla^2\phi]dV&=-\frac{1}{4\pi}\int_{\epsilon<r<a}\phi(r)\frac{\delta(r-r')}{r^2}dV\\&=\int_{r=\epsilon}\left[\phi\frac{\partial}{\partial n}G-G\frac{\partial}{\partial n}\phi\right]dS\\&\quad+\int_{r=a}\left[\phi\frac{\partial}{\partial n}G-G\frac{\partial}{\partial n}\phi\right]dS.\end{aligned} \tag{33}$$

The result that emerges is

$$-\phi(r')=\lim_{\epsilon\to 0}\int_{r=\epsilon}G\frac{d\phi}{dr}dS=-QG(0,r') \tag{34a}$$

or

$$\begin{aligned}\phi(r)&=QG(0,r)\\&=QCf_2(r)\\&=\frac{Q}{2\pi r}\left[\frac{ka\cos k(a-r)-1(1+ika\eta)\sin k(a-r)}{ka\cos ka-(1+ika\eta)\sin ka}\right].\end{aligned} \tag{34b}$$

In the limit of small r, the result so obtained reduces to

$$\phi(r)\to\frac{Q}{4\pi r},\quad r\to 0, \tag{35}$$

and this substantiates the assertion that Q is the monopole source strength, the amplitude to the oscillating total volume velocity of the source. [The radial velocity is the negative of $d\phi/dr$ and this times the surface area $4\pi r^2$ of a sphere surrounding the sphere does indeed equal Q in the limit of small r.]

B. Distributed source within sphere

An instructive generalization of the problem addressed above is that where the source, rather than be concentrated at a point, is uniformly distributed over a spherical volume with radius δ. In such a case one defines a source density q (volume velocity per unit volume), this being given by

$$q(r)=\frac{Q}{(4/3)\pi\delta^3},\quad 0<r<\delta, \tag{36a}$$

$$q(r)=0,\quad \delta<r<a. \tag{36b}$$

For such a distributed source, Green's theorem leads to the following modification of the result that appears in Eq. (34b):

$$\phi(r)=\frac{Q}{(4/3)\pi\delta^3}\int_{0<r<\delta}G(r,r')dV'. \tag{37}$$

This in turn integrates, for $r>\delta$, to

$$\phi(r)=\frac{Q}{4\pi r}F(k\delta)\times\left[\frac{ka\cos k(a-r)-(1+ika\eta)\sin k(a-r)}{ka\cos ka-(1+ika\eta)\sin ka}\right],\quad a>r>\delta. \tag{38}$$

The only distinction of this from the point source result in Eq. (34b) is the appearance of an interference factor $F(k\delta)$ where

$$F(z)=\frac{3[\sin z-z\cos z]}{z^3}=3\frac{j_1(z)}{r}. \tag{39}$$

This function has the asymptotic limits

$$F(z)\sim 1,\quad z\to 0, \tag{40a}$$

$$F(z)\sim\frac{3\cos z}{z^2},\quad z\gg 1. \tag{40b}$$

Since the argument of F is $k\delta$, the interference factor depends on the ratio of the source radius δ to the wave length $\lambda=2\pi/k$ of sound of angular frequency ω.

C. Radially oscillating inner sphere

The derivations in either of the previous sections can be readily modified to yield the solution of a related boundary value problem where the cavity excitation is presumed to be caused by an the radial oscillations of a spherical surface within the cavity, this surface being centered at the center of the sphere and having radius δ. If the total volume velocity is Q then the imposed radial velocity on this inner surface is

$$-\frac{d}{dr}\phi=\frac{Q}{4\pi\delta^2},\quad r=\delta. \tag{41}$$

In the region outside the surface of the interior sphere, the Helmholtz equation is applicable, so one has the differential equation

$$\left[\frac{1}{r^2}\frac{d}{dr}\left(r^2\frac{d}{dr}\right)+k^2\right]\phi=0,\quad \delta<r<a, \tag{42a}$$

and the boundary condition at the outer surface of the cavity remains the same as before, this being

$$\frac{d}{dr}\phi=ik\eta\phi,\quad r=a. \tag{42b}$$

The problem as posed above, which is a two-part boundary value problem for an ordinary differential equation, is easily solved without explicit use of Green's functions, but it is nevertheless instructive to see how the general formalism used in the previous sections applies here. The suitable Green's function for the concentric spherical domain $\delta<r<a$ must satisfy the differential equation (24a) therein, but now with the understanding that r' is between δ and a. The condition that G be finite at the origin is no longer relevant and is replaced by the Neumann boundary condition

$$\frac{dG}{dr}=0, \quad r=\delta. \tag{43a}$$

But G continues to be required to satisfy the admittance boundary condition

$$\frac{dG}{dr}=ik\eta G, \quad r=a \tag{43b}$$

at the outer surface of the cavity. In a manner similar to that described in the derivation of Eqs. (26), (27), and (28), the Green's function is found to have the explicit form

$$G(r,r')=-\frac{1}{4\pi k}\frac{1}{\Delta}\frac{f_1(r_<)}{r_<}\frac{f_2(r_>)}{r_>} \tag{44}$$

with

$$f_1(r)=\sin k(r-\delta)+k\delta\cos k(r-\delta), \tag{45a}$$

$$f_2(r)=ka\cos k(a-r)-(1+ika\eta)\sin k(a-r), \tag{45b}$$

and

$$\Delta=(1+ika\eta)[\sin k(a-\delta)+k\delta\cos k(a-\delta)] + ka[k\delta\sin k(a-\delta)-\cos k(a-\delta)]. \tag{46}$$

It follows directly from an application of Green's integral theorem that

$$\phi(r)=QG(r,\delta), \quad \delta<r<a, \tag{47a}$$

$$\phi(r)=-\frac{Q}{4\pi r}\frac{1}{\Delta}[ka\cos k(a-r) - (1+ika\eta)\sin k(a-r)] \tag{47b}$$

and, in the limit $\delta\to 0$, the prior result of Eq. (34b) for excitation by a point source is recovered.

D. Dipole at the center of a sphere

To determine the field of a dipole, it is first necessary to find an appropriate boundary condition that applies at the center of the sphere. To this purpose, it is sufficient to consider a dipole in an unbounded space, where the monopole field is given by the familiar $R^{-1}\exp ikR$. If a point source is located at the origin in an unbounded space and the source has a dipolar nature, the dipole having its axis along the z-axis (from which the polar angle θ is measured), then the velocity potential, here denoted as $\chi(r,\theta)$, at small radial distance from the origin should have the form

$$\chi(r,\theta)=\frac{D}{4\pi}\left\{\frac{\partial}{\partial z'}\left(\frac{\exp[ik[x^2+y^2+(z-z')^2]^{1/2}]}{[x^2+y^2+(z-z')^2]^{1/2}}\right)\right\}_{z'=0} \sim\frac{Q}{4\pi}\left\{\frac{z-z'}{R^3}\right\}_{z'=0}\sim\frac{D}{4\pi}\frac{\cos\theta}{r^2}, \quad r\to 0. \tag{48}$$

Here D is the dipole source amplitude and can be regarded as the product of a large monopole amplitude Q times the small distance d between monopoles of amplitude Q and $-Q$.

The presence of the factor $\cos\theta$ in this limit, given a rudimentary knowledge of separable solutions of the Helmholtz equation in spherical coordinates, suggests that the velocity potential be taken of the general form

$$\chi(r,\theta)=\phi(r)\cos\theta, \tag{49}$$

where the radially dependent factor $\phi(r)$ remains to be determined. Such a substitution into the Helmholtz equation yields the ordinary differential equation

$$\left[\frac{1}{r^2}\frac{d}{dr}\left(r^2\frac{d}{dr}\right)+k^2-\frac{2}{r^2}\right]\phi=0, \quad 0<r<a, \tag{50a}$$

while the limiting form of Eq. (48) yields the inner boundary condition

$$\phi\to\frac{D}{4\pi r^2}, \quad r\to 0. \tag{50b}$$

At the outer surface of the cavity the admittance boundary condition is once again applied, and this is unaffected by the factor θ, so one has

$$\frac{d}{dr}\phi=ik\eta\phi, \quad r=a \tag{50c}$$

as the outer boundary condition on ϕ.

An effective Green's function for integration of the system Eq. (50) obeys the system of equations

$$\left[\frac{1}{r^2}\frac{d}{dr}\left(r^2\frac{d}{dr}\right)+k^2-\frac{2}{r^2}\right]G=-\frac{\delta(r-r')}{4\pi r^2}, \tag{51a}$$

$$G(0,r')=0, \quad \frac{dG}{dr}=ik\eta G, \quad r=a. \tag{51b}$$

To determine the Green's function, one follows the general methodology of the previous sections and sets

$$G(r,r')=Cf_1(r_<)f_2(r_>) \tag{52}$$

as in Eq. (25). Taking into account the known solutions of the homogenous version of the ordinary differential equation (51a) and of the outer boundary conditions, one finds that the function $f_1(r)$ that appears in Eq. (52) can be taken as

$$f_1(r)=j_1(kr), \tag{53}$$

which has the asymptotic behavior

$$f_1(r)\sim\tfrac{1}{3}kr, \quad kr\to 0. \tag{54}$$

Similarly, the other function $f_2(r)$ can be taken as

$$f_2(r)=[n_1'(ka)-i\eta n_1(ka)]j_1(kr) - [j_1'(ka)-i\eta j_1(ka)]n_1(kr). \tag{55}$$

Here the results involve the first-order spherical Bessel and Neumann functions, together with their argument derivatives (symbolized by a prime).

As in the previous examples, the constant C is determined from the derivative jump condition

$$r'^2 \frac{d}{dr} G \Big|_{r=r'-0}^{r=r'+0} = -\frac{1}{4\pi}. \tag{56}$$

The intricate expression that results when the explicit form of Eq. (52) for the Green's function is inserted here is simplified with the following relations (the first of which holds for either j_m or n_m)

$$\frac{d}{dz} j_m(z) = \frac{1}{2m+1}[m j_{m-1}(z) - (m+1) j_{m+1}(z)], \tag{57a}$$

$$n_{m-1}(z) j_m(z) - n_m(z) j_{m-1}(z) = \frac{1}{z^2}. \tag{57b}$$

It follows after some algebra that the scale factor C in Eq. (52) is expressed by

$$C = -\frac{k}{4\pi}\left[\frac{1}{i\eta j_1(ka) - j_1'(ka)}\right]. \tag{58}$$

The resulting Green's function is

$$\begin{aligned} G(r,r') = \frac{1}{4\pi}&\left[\frac{k j_1(kr_<)}{j_1'(ka) - i\eta j_1(ka)}\right] \\ &\times\{[n_1'(ka) - i\eta n_1(ka)] j_1(kr_>) \\ &-[j_1'(ka) - i\eta j_1(ka)] n_1(kr_>)\}. \end{aligned} \tag{59}$$

The denominator in this expression indicates what are the appropriate eigenvalues for a class of eigenfunctions of the Helmholtz equation within the spherical cavity, each such eigenfunction having the separated form

$$\chi_n(r,\theta) = \phi_n(r)\cos\theta \tag{60}$$

and satisfying the admittance boundary condition Eq. (50c). The equation for determining the eigenfunctions is accordingly

$$j_1'(k_n a) = i\eta j_1(k_n a). \tag{61}$$

A one-dimensional counterpart of Green's theorem can be deduced from the differential equations for ϕ, G, and from their common boundary condition at $r=a$. With the aid of this theorem, one obtains

$$\begin{aligned} -\frac{1}{4\pi}\phi(r') &= \lim_{r\to 0}\left\{ r^2\left(G\frac{d}{dr}\phi - \phi\frac{d}{dr}G\right)\right\} \\ &= -\frac{kD}{4\pi} C f_2(r'). \end{aligned} \tag{62}$$

The evaluation of the limit results with the help of Eqs. (50b) and (59). Hence

$$\phi(r) = kCf_2(r) = Dk^2 \frac{[n_1'(ka) - i\eta n_1(ka)] j_1(kr) + [i\eta j_1(ka) - j_1'(ka)] n_1(kr)}{4\pi[j_1'(ka) - i\eta j_1(ka)]}. \tag{63}$$

That this does indeed have the requisite behavior

$$\phi(r) \to \frac{Q}{4\pi r^2}, \quad r\to 0 \tag{64}$$

is confirmed when one makes use of the asymptotic relations

$$j_1(z)\to 0, \quad n_1(z)\to -\frac{1}{z^2}, \quad z\to 0. \tag{65}$$

E. Off-center point source in a sphere

Consider next the placement of a monopolar point source at the distance $\delta(<a)$ from the center of a spherical cavity, along the direction of the polar axis whereupon $\theta = 0$. Let

$$\begin{aligned} R &= [r^2 \sin^2\theta + (r\cos\theta - \delta)^2]^{1/2} \\ &= [r^2 + \delta^2 - 2r\delta\cos\theta]^{1/2} \end{aligned} \tag{66}$$

denote the distance from the source in terms of δ and of the spherical coordinates at point P; and note the representation for an isolated (free space) source function (omitting the time factor $e^{-\omega t}$),

$$\begin{aligned} Q\frac{e^{ikR}}{4\pi R} = \frac{ikQ}{4\pi}&\sum_{m=0}^{\infty}(2m+1) j_m(kr_<) \\ &\times h_m^{(1)}(kr_>) P_m(\cos\theta), \end{aligned} \tag{67}$$

where $r_<, r_>$ correspond to the smaller/larger of δ, r respectively. The functions

$$h_m^{(1)}(z) = j_m(z) + i n_m(z) \tag{68}$$

are spherical Hankel functions of the first kind and of order m. The functions P_m are Legendre polynomials.

With the above expression as a guide, it is evident that within the cavity it is appropriate to express the spatial wave form by a sum

$$\chi(r,\theta)=\sum_{m=0}^{\infty}\phi_m(r)P_m(\cos\theta). \tag{69}$$

Substitution into the Helmholtz equation in spherical coordinates indicates that the radial functions obey the equation

$$\left[\frac{1}{r^2}\frac{d}{dr}\left(r^2\frac{d}{dr}\right)+k^2-\frac{m(m+1)}{r^2}\right]\phi_m(r)=0,\quad 0<r<a. \tag{70}$$

[This is derived in most texts on partial differential equations.] The Legendre polynomials satisfy an analogous sequence of partial differential equation,

$$\frac{1}{\sin\theta}\frac{d}{d\theta}\left(\sin\theta\frac{d}{d\theta}P_m\right)+m(m+1)P_m=0. \tag{71}$$

To determine the individual radial factors, it is appropriate to define corresponding Green's functions $G_m(r,r')$ by the relations

$$\left[\frac{1}{r^2}\frac{d}{dr}\left(r^2\frac{d}{dr}\right)+k^2-\frac{m(m+1)}{r^2}\right]G_m(r,r')$$
$$=-\frac{\delta(r-r')}{4\pi r^2},\quad m=0,1,..., \tag{72a}$$

$$G_m=O(r^m),\quad r\to 0, \tag{72b}$$

$$\frac{d}{dr}G_m=ik\eta G_m,\quad r=a. \tag{72c}$$

Expressions for such Green's functions are derivable using the methodology explained in the preceding sections of this paper, the result being

$$G_m(r,r')=\frac{k}{4\pi}\left[\frac{j_m(kr_<)}{j_m'(ka)-i\eta j_m(ka)}\right]$$
$$\times\{[n_m'(ka)-i\eta n_m(ka)]j_m(kr_>)$$
$$-[j_m'(ka)-i\eta j_m(ka)]n_m(kr_>)\} \tag{73}$$

and is similar to what was found in the previous example.

Combining the differential equations for ϕ_m and G_m and integrating over the range $0<r<a$ yields the jump condition

$$-\frac{1}{4\pi}\phi_m(r')=\lim_{\epsilon\to 0}\left\{r^2\left(G_m\frac{d}{dr}\phi_m-\phi_m\frac{d}{dr}G_m\right)\Bigg|_{r=\delta-\epsilon}^{r=\delta+\epsilon}\right\}$$
$$=\delta^2 G_m(\delta,r')\frac{d}{dr}\phi_m\Bigg|_{r=\delta-\epsilon}^{r=\delta+\epsilon}, \tag{74}$$

when the behaviors of ϕ_m, G_m at $r=0$, a are taken into account.

In the application of Eq. (74), one notes that near the point source the specification

$$\phi_m=\frac{ikQ}{4\pi}(2m+1)j_m(kr_<)h_m^{(1)}(kr_>) \tag{75}$$

is implied by Eq. (67): thus Eq. (74) yields

$$\frac{d}{dr}\phi_m\Bigg|_{r=\delta-0}^{r=\delta+0}=\frac{iQk^2}{4\pi}(2m+1)[h_m^{(1)\prime}(ka)j_m(k\delta)$$
$$-h_m^{(1)}(k\delta)j_m'(k\delta)]$$
$$=-\frac{Qk^2}{4\pi}(2m+1)[j_m(k\delta)n_m'(ka)$$
$$-j_m'(k\delta)n_m(k\delta)]$$
$$=-\frac{Q}{4\pi\delta^2}(2m+1). \tag{76}$$

This in turn yields the result

$$\phi_m(r)=\frac{kQ}{4\pi}(2m+1)\left[\frac{j_m(k\delta)}{j_m'(ka)-i\eta j_m(ka)}\right]$$
$$\times\{[n_m'(ka)-i\eta n_m(ka)]j_m(kr)$$
$$+[i\eta j_m(ka)-j_m'(ka)]n_m(kr)\}. \tag{77}$$

The overall velocity potential is consequently given, for $r>\delta$, by

$$\chi(r,\theta)=\sum_{m=0}^{\infty}\phi_m(r)P_m(\cos\theta)$$
$$=\frac{kQ}{4\pi}\sum_{m=0}^{\infty}(2m+1)\left[\frac{j_m(k\delta)}{j_m'(ka)-i\eta j_m(ka)}\right]$$
$$\times\{[n_m'(ka)-i\eta n_m(ka)]j_m(kr)$$
$$-[j_m'(ka)-i\eta j_m(ka)]n_m(kr)\}P_m(\cos\theta). \tag{78}$$

The analogous version for $r<\delta$ is similarly obtainable from Eq. (77).

F. Line source on the cylinder axis

As a final example of the foregoing Green's function approach, let it be supposed that a time-periodic line source is situated on the axis of a cylindrical cavity whose plane faces ($z=0,H$) are rigid. The curved surface ($\rho=a$, $0<z<H$) is characterized by an admittance parameter η. The line source is characterized by a volume velocity $Q(z)$ per unit length that depends on the axial coordinate z. Then the velocity potential $\phi(\rho,z)$ within the cavity obeys the system of equations

$$\left(\frac{\partial^2}{\partial\rho^2}+\frac{1}{\rho}\frac{\partial}{\partial\rho}+\frac{\partial^2}{\partial z^2}+k^2\right)\phi=-Q(z)\frac{\delta(\rho)}{2\pi\rho}, \tag{79a}$$

$$\frac{\partial\phi}{\partial\rho}=ik\eta\phi,\quad \rho=a,\quad 0<z<H, \tag{79b}$$

$$\frac{\partial\phi}{\partial z}=0,\quad z=0,\quad z=H,\quad 0\leqslant\rho<a. \tag{79c}$$

To determine the velocity potential, one introduces the expansion

$$\phi(\rho,z)=\sum_{m=0}^{\infty}\phi_m(\rho)\cos\frac{m\pi z}{H}, \tag{80}$$

and expands the source function in an analolgous Fourier series. It is subsequently found that the individual coefficient functions $\phi_m(\rho)$ are solutions of

$$\left[\frac{1}{\rho}\frac{d}{d\rho}\left(\rho\frac{d}{d\rho}\right)+k^2-\left(\frac{m\pi}{H}\right)^2\right]\phi_m(\rho)=-\frac{2}{H}Q_m\frac{\delta(\rho)}{2\pi\rho}, \tag{81}$$

where

$$Q_m=\int_0^H Q(z)\cos\frac{m\pi z}{H}dz. \tag{82}$$

These continue to satisfy the admittance boundary condition

$$\frac{d}{d\rho}\phi_m=ik\eta\phi_m, \quad \rho=a. \tag{83}$$

These equations hold for $m=0,1,...$

To solve Eq. (81) with the boundary condition (83), one defines a Green's function $G_m(\rho,\rho')$ such that

$$\left[\frac{1}{\rho}\frac{d}{d\rho}\left(\rho\frac{d}{d\rho}\right)+k^2-\left(\frac{m\pi}{H}\right)^2\right]G_m(\rho,\rho')=-\frac{\delta(\rho-\rho')}{2\pi\rho}, \tag{84a}$$

$$G_m(0,\rho') \quad \text{finite}, \tag{84b}$$

$$\frac{d}{d\rho}G_m=ik\eta G_m, \quad \rho=a. \tag{84c}$$

In a manner similar to that of the preceding examples, one concludes that this Green's function is expressible in the form

$$\begin{aligned}G_m(\rho,\rho')=&\frac{1}{4i}\left[\frac{J_0(\alpha_m\rho_<)}{\alpha_m J_1(\alpha_m a)+ik\eta J_0(\alpha_m a)}\right]\\&\times\{[ik\eta H_0^{(1)}(\alpha_m a)+\alpha_m H_1^{(1)}\\&\times(\alpha_m a)]J_0(\alpha_m\rho_>)-[ik\eta J_0(\alpha_m a)\\&+\alpha_m J_1(\alpha_m a)]H_0^{(1)}(\alpha_m\rho_>)\},\end{aligned} \tag{85}$$

where J_0, J_1 denote zero, first-order Bessel functions, and

$$H_0^{(1)}(z)=J_0(z)+iN_0(z), \quad H_1^{(1)}(z)=J_1(z)+iN_1(z) \tag{86}$$

are the corresponding order Hankel functions.

The parameter in Eq. (85)

$$\alpha_m=[k^2-(m\pi/H)^2]^{1/2} \tag{87}$$

assumes positive real or imaginary values according as

$$k>\frac{n\pi}{H} \text{ or } k<\frac{m\pi}{H}. \tag{88}$$

When the first inequality holds, the Hankel functions of Eq. (85) can be replaced by (i times) the like Neumann functions and the Green's function representation becomes (for $k>m\pi/H$)

$$\begin{aligned}G_m(\rho,\rho')=&\frac{1}{4}\left[\frac{J_0(\alpha_m\rho_<)}{\alpha_m J_1(\alpha_m a)+ik\eta J_0(\alpha_m a)}\right]\\&\times\{[ik\eta N_0^{(1)}(\alpha_m a)+\alpha_m N_1^{(1)}\\&\times(\alpha_m a)]J_0(\alpha_m\rho_>)-[ik\eta J_0(\alpha_m a)\\&+\alpha_m J_1(\alpha_m a)]N_0^{(1)}(\alpha_m\rho_>)\}.\end{aligned} \tag{89}$$

When the second inequality in Eq. (88) holds, the Bessel and Hankel functions are replaced by another quartet of cylinder functions, in accordance with the relations

$$J_0(iz)=I_0(z), \quad J_1(iz)=iI_1(z), \tag{90a}$$

$$H_0^{(1)}(iz)=\frac{2}{\pi i}K_0(z), \quad H_1^{(1)}(iz)=-\frac{1}{\pi}K_1(z), \tag{90b}$$

and the corresponding version of Eq. (85) becomes (for $k<m\pi/H$)

$$\begin{aligned}G_m(\rho,\rho')=&\frac{1}{4i}\left[\frac{I_0(\beta_m\alpha_<)}{\beta_m I_1(\alpha_m a)+ik\eta I_0(\beta_m a)}\right]\\&\times\{[\beta_m K_1(\beta_m a)+ik\eta K_0(\beta_m a)]I_0(\beta_m\rho_>)\\&+[\beta_m I_1(\beta_m a)-ik\eta I_0(\beta_m a)]\\&\times K_0^{(1)}(\beta_m\rho_>)\},\end{aligned} \tag{91}$$

with

$$\alpha_m=i\beta_m, \quad \beta_m^2=(m\pi/H)^2-k^2>0. \tag{92}$$

It follows from Eqs. (81) and (84a) jointly that

$$G_m\rho\frac{d}{d\rho}\phi_m-\phi_m\rho\frac{d}{d\rho}G_m=\frac{\phi_m(\rho')}{2\pi}. \tag{93}$$

This equation with the aid of Eq. (81) leads to the inner boundary condition

$$\lim_{\rho\to 0}\rho\frac{d}{d\rho}\phi_m=-\frac{Q_m}{\pi H}. \tag{94}$$

After examination of the behaviors of ϕ_m, G_m in the respective limits $\rho\to 0$, a, one determines that the the coefficient functions $\phi_m(\rho)$ of Eq. (80) are related to the Green's functions G_m by the relation

$$\phi_m(\rho)=\frac{2}{H}Q_m G_m(0,\rho), \quad m=0,1,.... \tag{95}$$

IV. POWER CALCULATIONS

A significant measure pertaining to the source excited cavity field, namely the time averaged rate at which energy is absorbed at the surface, can be determined once the velocity potential is known.

For harmonically time varying states the average power absorbed at the surface S of a cavity with specific admittance η is expressed by

$$P_{\text{abs}}=\frac{\rho\omega}{2}\text{Im}\int_S\phi^*\frac{\partial\phi}{\partial n}dS=\frac{\rho\omega}{2}\text{Im}\int_S ik\eta|\phi|^2\,dS, \tag{96}$$

where ρ is the mass density of the fluid within the cavity.

For simplicity, the admittance parameter η is taken to be real in the examples below. The passive nature of the surface requires that it be positive.

A. Source at the center of a sphere

For the previously considered example of a monopole source at the center of a spherical cavity with radius a, the expression above yields

$$P_{\text{abs}}=\frac{\rho\omega k}{2}\,\eta[4\pi a^2]|\phi(a)|^2 \tag{97}$$

with the assumption (stated above) that the parameter η has a real and uniform value. Substituting for $\phi(a)$ from Eq. (34b) yields

$$P_{\text{abs}}=\frac{1}{8\pi}\left[\frac{\rho c\,\eta k^4 a^2 Q^2}{(ka\cos ka-\sin ka)^2+(ka\,\eta\sin ka)^2}\right]. \tag{98}$$

To gauge the magnitude of this result, it is appropriate to compare it to the power output from the identical source in free space, namely

$$P_0=\frac{1}{8\pi}\rho c k^2 Q^2. \tag{99}$$

The relative power output is consequently seen to be

$$\frac{P_{\text{abs}}}{P_0}=\frac{\eta(ka)^2}{(ka\cos ka-\sin ka)^2+(ka\,\eta\sin ka)^2}. \tag{100}$$

This is the same in essence as a previous result given by Waterhouse (1963).

B. Oscillating spherical surface inside the cavity

In the case of a source featuring a uniform radial velocity over a spherical surface of radius a, as relation (41) details, the result in Eq. (47b) implies that

$$P_{\text{abs}}=\frac{1}{8\pi}\,\frac{\rho c\,\eta k^4 a^2 Q^2}{|\Delta|^2}, \tag{101}$$

where the complex quantity Δ is defined by Eq. (46). The previously derived result Eq. (98) follows from this when $\delta\to 0$, because

$$\Delta\to\sin ka-ka\cos a+ika\,\eta\sin ka,\quad \delta\to 0. \tag{102}$$

C. Off-center source within a sphere

For an off-center source within a spherical cavity the velocity potential at the cavity outer surface can be deduced from Eq. (78) and from the Wronskian relation

$$j_m(z)n_m'(z)-j_m'(z)n_m(z)=\frac{1}{z^2}. \tag{103}$$

The derived field at the surface is consequently

$$\chi(a,\theta)=\frac{kQ}{4\pi}\,\frac{1}{(ka)^2}\sum_{m=0}^{\infty}(2m+1)\times\frac{j_m(k\delta)}{j_m'(ka)-i\,\eta j_m(ka)}P_m(\cos\theta). \tag{104}$$

From this, in turn, one determines that the rate of energy absorption is

$$\begin{aligned}P_{\text{abs}}&=\frac{\rho\omega k}{2}\,\eta\int_0^{\pi}|\chi(a,\theta)|^2(2\pi a^2)\sin\theta\,d\theta\\&=\frac{1}{8\pi}\,\frac{\rho c\,\eta k^2 Q^2}{(ka)^2}\sum_{m=0}^{\infty}(2m+1)\times\frac{j_m^2(k\delta)}{[j_m'(ka)]^2+[\eta j_m(ka)]^2}.\end{aligned} \tag{105}$$

The derivation makes use of the orthogonality relation for Legendre polynomials

$$\int_0^{\pi}\sin\theta P_m(\cos\theta)P_n(\cos\theta)d\theta=\frac{2}{2m+1}\,\delta_{mn}. \tag{106}$$

The normalized version of the above result is

$$\frac{P_{\text{abs}}}{P_0}=\frac{\eta}{(ka)^2}\sum_{m=0}^{\infty}(2m+1)\,\frac{j_m^2(k\delta)}{(j_m'(ka))^2+(\eta j_m(ka))^2}. \tag{107}$$

If the source is allowed to approach the center of the sphere, one expects the result for a monopole at the center to result. In this regard, one notes that Eq. (107) assumes, in the limit $k\delta\to 0$, the form

$$\begin{aligned}\frac{P_{\text{abs}}}{P_0}&=\frac{\eta}{(ka)^2}\,\frac{1}{[j_1(ka)]^2+[\eta j_0(ka)]^2}\\&=\frac{\eta(ka)^2}{(ka\cos ka-\sin ka)^2+(\eta ka\sin ka)^2}\end{aligned} \tag{108}$$

which agrees with Eq. (100).

D. Dipole at the sphere center

The velocity potential for a dipole at the center of the sphere, as given by Eq. (63), reduces at the outer boundary of the cavity to

$$\phi(a)\cos\theta=\frac{Q}{4\pi a^2}\,\frac{\cos\theta}{j_1'(ka)-i\,\eta j_1(ka)}. \tag{109}$$

Consequently, the corresponding rate at which energy is absorbed at the surface equals

$$\begin{aligned}P_{\text{abs}}&=\frac{1}{2}\rho\omega k\,\eta[2\pi a^2]|\phi(a)|^2\int_0^{\pi}\cos^2\theta\sin\theta\,d\theta\\&=\frac{\rho c\,\eta}{24\pi}\,\frac{k^2Q^2}{a^2}\,\frac{1}{[j_1'(ka)]^2+[\eta j_1(ka)]^2}.\end{aligned} \tag{110}$$

This can be compared to the power output by the same dipole in free space, such being

$$P_0=\frac{\rho c k^4}{24\pi}Q^2. \tag{111}$$

The corresponding ratio of these two powers is

$$\frac{P_{\text{abs}}}{P_0}=\frac{\eta}{(ka)^2}\,\frac{1}{(j_1'(ka))^2+(\eta j_1(ka))^2}. \tag{112}$$

E. Line source at the center of a cylinder

As regards a cylindrical cavity with a nonuniform source distribution along its axis, the time rate of energy absorption at the curved surface can be determined from the defining expression

$$P_{\rm abs}=\frac{1}{2}(\rho\omega k\eta)2\pi a\int_0^H|\phi(a,z)|^2\,dz. \tag{113}$$

The appropriate insertion for the velocity potential is

$$\phi(a,z)=\sum_{m=0}^{\infty}\frac{2}{H}Q_mG_m(0,a)\cos\frac{m\pi z}{H}, \tag{114}$$

where the Green's function factors are found from Eqs. (89) and (91). Thus introducing the symbol $[x]$ to denote the integer closest in value to x, but yet which is smaller than x, it follows that

$$\begin{aligned}P_{\rm abs}&=2\pi\rho c\,\eta\frac{ak^2}{H}\sum_{m=0}^{\infty}Q_m^2|G_m(0,a)|^2\\&=\frac{1}{2\pi}\rho c\,\eta\frac{k^2}{aH}\left\{\sum_{m=0}^{[kH/\pi]}\frac{Q_m^2}{[\alpha_mJ_1(\alpha_ma)]^2+[\eta J_0(\alpha_ma)]^2}\right.\\&\quad\left.+\sum_{[kH/\pi]+1}^{\infty}\frac{Q_m^2}{[\beta_mI_1(\beta_ma)]^2+[\eta J_0(\beta_ma)]^2}\right\}.\end{aligned} \tag{115}$$

While this appears somewhat cumbersome, one anticipates a rapid convergence in the latter sum when

$$\beta_ma=[(m\pi/H)^2-k^2]^{1/2}a\gg 1. \tag{116}$$

ACKNOWLEDGMENT

I am indebted to Prof. Allan Pierce for substantial help in organizing this account.

Bowman, J. J., Senior, T. B. A., and Uslenghi, P. L. E. (**1987**). *Electromagnetic and Acoustic Scattering by Simple Shapes*, revised printing of 1969 edition (Hemisphere, New York), pp. 115, 117, 124, 126, 355, 369.

Chen, P.-T. (**1996**). ''Variational formulation of interior cavity frequencies for spheroidal bodies,'' J. Acoust. Soc. Am. **100**, 2980–2988.

DiNapoli, F. R., and Deavenport, R. L. (**1980**). ''Theoretical and numerical Green's function field solution in a plane multilayered medium,'' J. Acoust. Soc. Am. **67**, 92–105.

Easwaran, V., and Craggs, A. (**1996**). ''Transient response of lightly damped rooms: A finite element approach,'' J. Acoust. Soc. Am. **99**, 108–113.

Eisenhart, L. P. (**1934**). ''Separable systems of Staekel,'' Ann. Math. **35**, 284–305.

Franzoni, L. P., and Labrozzi, D. S. (**1999**). ''A study of damping effects on spatial distribution and level of reverberant sound in a rectangular acoustic cavity,'' J. Acoust. Soc. Am. **106**, 802–815.

Haskell, N. A. (**1951**). ''Asymptotic approximation for the normal modes in sound channel wave propagation,'' J. Appl. Phys. **22**, 157–168.

Kang, S. W., and Moo, J. (**2000**). ''Eigenmode analysis of arbitrarily shaped two-dimensional cavities by the method of point-matching,'' J. Acoust. Soc. Am. **107**, 1153–1160.

Kim, Y. Y., and Kim, D. K. (**1999**). ''Applications of waveguide-type base functions for the eigenproblems of two-dimensional cavities,'' J. Acoust. Soc. Am. **106**, 1704–1711.

Kokkarakis, G. C., and Roumeliotis, J. A. (**1999**). ''Acoustic eigenfrequencies in a spheroidal cavity with a concentric penetrable sphere,'' J. Acoust. Soc. Am. **105**, 1539–1547.

Lobkis, O. I., and Weaver, R. L. (**2000**). ''Complex modal statistics in a reverberant dissipative body,'' J. Acoust. Soc. Am. **108**, 1480–1485.

Mathews, J., and Walker, R. L. (**1970**). *Mathematical Methods of Physics*, 2nd ed., first edition published in 1964 (Benjamin, Menlo Park), pp. 270–275.

Missaoui, J., and Cheng, L. (**1997**). ''A combined integro-modal approach for predicting acoustic properties of irregular-shaped cavities,'' J. Acoust. Soc. Am. **101**, 3313–3321.

Morse, P. M., and Feshbach, H. (**1953**). *Method of Theoretical Physics*, Vol. 1 (McGraw-Hill, New York), pp. 655–666.

Morse, P. M., and Ingard, K. U. (**1988**). *Theoretical Acoustics* (Princeton University Press, Princeton), pp. 554–564.

Pekeris, C. L. (**1946**). ''Theory of propagation of sound in a half-space of variable sound velocity under conditions of formation of a shadow zone,'' J. Acoust. Soc. Am. **18**, 295–315.

Pierce, A. D. (**1981**). *Acoustics, An Introduction to its Physical Principles and Applications* (McGraw-Hill, New York), pp. 288–291.

Rayleigh, J. W. S. (**1945**). *The Theory of Sound*, Vol. 1, revised second edition, first edition published 1877 (Dover, New York), pp. xxxiii, 195–196.

Schaffner, A. (**1999**). ''Accurate estimate of the mean sound pressure level in enclosures,'' J. Acoust. Soc. Am. **106**, 823–827.

Sumbatyan, M. A., Pompei, A., and Rigano, M. A. (**2000**). ''New explicit solutions in acoustics of closed spaces on the basis of divergent series,'' J. Acoust. Soc. Am. **107**, 709–713.

Waterhouse, R. V. (**1963**). ''Radiation impedance of a source near reflectors,'' J. Acoust. Soc. Am. **35**, 1144–1151.

A staggered-grid finite-difference method with perfectly matched layers for poroelastic wave equations

Yan Qing Zeng and Qing Huo Liu[a)]
Department of Electrical and Computer Engineering, Duke University, Durham, North Carolina 27708

(Received 1 November 2000; accepted for publication 3 March 2001)

A particle velocity-strain, finite-difference (FD) method with a perfectly matched layer (PML) absorbing boundary condition is developed for the simulation of elastic wave propagation in multidimensional heterogeneous poroelastic media. Instead of the widely used second-order differential equations, a first-order hyperbolic leap-frog system is obtained from Biot's equations. To achieve a high accuracy, the first-order hyperbolic system is discretized on a staggered grid both in time and space. The perfectly matched layer is used at the computational edge to absorb the outgoing waves. The performance of the PML is investigated by calculating the reflection from the boundary. The numerical method is validated by analytical solutions. This FD algorithm is used to study the interaction of elastic waves with a buried land mine. Three cases are simulated for a mine-like object buried in ''sand,'' in purely dry ''sand'' and in ''mud.'' The results show that the wave responses are significantly different in these cases. The target can be detected by using acoustic measurements after processing.
[DOI: 10.1121/1.1369783]

PACS numbers: 43.20.Bi, 43.20.Fn, 43.20.Gp [ANN]

I. INTRODUCTION

Simulation of elastic waves propagating in fluid-saturated porous media is of great importance to geophysical exploration, reservoir engineering, and military applications.

With the increasing difficulty of exploring natural resources and the growing realization that hydrocarbon reservoirs are more heterogeneous and complex than assumed in the past, it is desirable to characterize the subsurface materials as fluid-saturated porous media than perfectly elastic single phase materials.

In military applications, simulation of waves in porous media is important for underwater acoustics. More recently, acoustic waves are used for land mine detection. For plastic land mines, acoustic waves provide a much better measurement than the traditional electromagnetic induction method. Although the soil can be approximated as a single phase elastic material, it is more accurate to treat soil as two phase composite materials consisting of granular solid and pore fluid.

Simulation of wave propagation in porous, fluid-saturated media requires the analytical or numerical solution of Biot's equations.[1–3] For a heterogeneous, complex model, in general it is not possible to find analytical solutions to Biot's equations. Numerical methods have to be used to obtain these solutions. Finite-difference (FD) algorithms have been developed to simulate wave propagation in poroacoustic media,[4] and in homogeneous poroelastic media.[5] A centered-grid FD scheme has also been developed for heterogeneous poroelastic media.[6] In this article, a velocity-strain, finite-difference method is developed in a staggered grid for heterogeneous poroelastic media. In this method, Biot's equations[3] are reformulated into first-order equations to arrive at a leap-frog system in a staggered grid both in time and space domains. Numerical solutions have been validated by analytical solutions.

In order to simulate an unbounded medium, an absorbing boundary condition (ABC) must be implemented to truncate the computational domain in numerical algorithms. There are many kinds of ABCs developed for numerical simulation of wave propagation. Cerjan *et al.*[7] introduced a simple damping taper to the boundaries to attenuate the outgoing waves. Since this lossy layer is not perfectly matched to the interior region, however, it requires a substantial number of layers for the taper to be effective. Clayton and Engquist[8] (CE) use the paraxial approximation to the wave equation to make the boundary transparent to outgoing waves. The CE ABC can lead to instability when the Poisson ratio is greater than 2.[9] Since Berenger[10] proposed the highly effective perfectly matched layer (PML) as an absorbing boundary condition for electromagnetic waves, the PML has been widely used for finite-difference and finite-element methods. Chew and Liu[11,12] first proposed the PML for elastic waves in solids, and proved the zero reflections from PML to the regular elastic medium. Hastings *et al.*[13] have independently implemented the PML ABC for two-dimensional problems by using potentials. The PML has also been extended to model acoustic waves and electromagnetic waves in lossy media.[14] The PML has been applied to the second-order Biot's equation for fluid-saturated poroelastic media,[15] which requires a complicated convolution. In this article, as the PML is developed for the first-order system, incorporation of PML becomes much simpler. The effectiveness of this ABC is confirmed by examining the reflection from the boundary.

By using this numerical method, interaction of elastic waves with a buried plastic minelike object is investigated. Three cases are simulated for a plastic minelike object buried

a)Electronic mail: qhliu@ee.duke.edu

in ''sand,'' in purely dry ''sand'' and in ''mud.'' The results show that the wave responses are significantly different in these cases. After processing, the target can be detected by using surface acoustic measurements.

II. FORMULATION

A. The governing equations

The propagation of acoustic waves in porous and fluid-saturated media is different from that in single phase elastic media. In addition to the regular P waves and S waves in solid elastic media, a slow P wave which results from the relative motion between solid frame and fluid may be present in porous media. Thus the pattern of energy dissipation in porous media is different from that in solid elastic media. Based on continuum mechanics and macroscopic constitutive relationship, Biot[1–3] developed a theory of wave motion in a porous elastic solid saturated with a viscous compressible fluid. Biot's theory was confirmed by Burridge and Keller[16] based on the dynamic equations which govern the behavior of medium on a microscopic scale. Plona[17] also confirmed Biot's theory through experiments.

In an isotropic, heterogeneous porous elastic medium, the parameters describing the physical properties of the medium are as follows:

- μ shear modulus of dry porous matrix
- λ_c Lame constant of saturated matrix
- ϕ porosity
- η viscosity
- κ permeability
- ρ the overall density of the saturated medium determined by $\rho_f\phi+(1-\phi)\rho_s$
- ρ_s density of solid material
- ρ_f density of fluid
- a tortuosity of the matrix
- K_s bulk modulus of the solid
- K_f bulk modulus of the fluid
- K_b bulk modulus of the dry porous frame

The macroscopic displacements and strains are defined as

- u_i ith component of displacements of solid particle
- U_i ith component of displacements of fluid particle
- w_i ith component of relative displacement, $w_i=\phi(U_i-u_i)$
- e_{il} il component of strain tensor in porous medium, $e_{il}=[((\partial u_l/\partial x_i)+(\partial u_i/\partial x_l))/2]$
- e $e=\Sigma_{i=1,2,3}e_{ii}$
- ξ dilatation for the relative motion, $\xi=-\Sigma_{i=1,2,3}(\partial w_i/x_i)$

For a three-dimensional isotropic, heterogeneous and porous elastic medium, wave propagation is governed by Biot's equations:[3]

$$2\sum_l \frac{\partial}{\partial x_1}(\mu e_{i1})+\frac{\partial}{\partial x_i}(\lambda_c e-\alpha M\xi)=\frac{\partial^2}{\partial t^2}(\rho u_i+\rho_f w_i), \tag{1}$$

$$\frac{\partial}{\partial x_i}(\alpha Me-M\xi)=\frac{\partial^2}{\partial t^2}(\rho_f u_i+mw_i)+\frac{\eta}{\kappa}\frac{\partial w_i}{\partial t}, \tag{2}$$

where $m=a\rho_f/\phi$ and

$$M=\frac{1}{\phi/K_f+(\alpha-\phi)/K_s}, \quad \alpha=1-\frac{K_b}{K_s}.$$

Let $\mathbf{v^s}$ be the velocity of the solid particle, and $\mathbf{v^f}$ be the velocity of the pore fluid relative to the solid frame. Then the second-order equations (1) and (2) can rearranged as the first-order equations

$$(m\rho-\rho_f^2)\frac{\partial v_i^s}{\partial t}=2m\sum_l \frac{\partial}{\partial x_l}(\mu e_{il})+m\frac{\partial}{\partial x_i}(\lambda_c e-\alpha M\xi)-\rho_f\frac{\partial}{\partial x_i}(\alpha Me-M\xi)+\rho_f\frac{\eta}{\kappa}v_i^f, \tag{3}$$

$$(m\rho-\rho_f^2)\frac{\partial v_i^f}{\partial t}=\rho\frac{\partial}{\partial x_i}(\alpha Me-M\xi)-\rho\frac{\eta}{\kappa}v_i^f-2\rho_f\sum_l \frac{\partial}{\partial x_l}(\mu e_{il})-\rho_f\frac{\partial}{\partial x_i}\times(\lambda_c e-\alpha M\xi). \tag{4}$$

The time derivatives of strains e_{il} and ξ can be expressed as

$$\frac{\partial e_{il}}{\partial t}=[(\partial v_l^s/\partial x_i+\partial v_i^s/\partial x_l)/2], \tag{5}$$

$$\frac{\partial \xi}{\partial t}=-\nabla\cdot\mathbf{v^f}. \tag{6}$$

In the explicit first-order finite-difference schemes, Eqs. (3)–(6) consist of a leap-frog system for the strain field e_{il}, ξ and velocity field $\mathbf{v^s}$ and $\mathbf{v^f}$. With proper absorbing boundary conditions, these equations can be solved numerically for the wave field in an unbounded medium.

Equations (3)–(6) predict the existence of three different waves in fluid-saturated poroelastic media: a shear wave and two compressional waves with a faster and a slower propagation velocities.

B. Equations for the PML absorbing boundary condition

In this article, the perfectly matched layer (PML) will be used to truncate the unbounded medium, absorbing all outgoing waves. The artificial absorptive medium is introduced in the regular medium by modifying Eqs. (3)–(6) with complex coordinates.[12,13,15] In the frequency domain (where a time-harmonic factor $e^{-j\omega t}$ is implied and $j=\sqrt{-1}$), a complex coordinate variable is chosen as

$$\tilde{x}_i=\int_0^{x_i} e_i(x_i')dx_i', \tag{7}$$

$$e_i=a_i+j\frac{\omega_i}{\omega} \quad (i=1,2,3), \tag{8}$$

where $a_i \geqslant 1$ is a scaling factor, and $\omega_i \geqslant 0$ is an attenuation factor. The operator $\partial/\partial x_i$ can be expressed in terms of the regular coordinate,

$$\frac{\partial}{\partial \tilde{x}_i} = \frac{1}{e_i}\frac{\partial}{\partial x_i}. \tag{9}$$

The PML formulation is to replace x_i in (3)–(6) by the corresponding complex coordinate $\tilde{x}_i$. In a PML region, the real part a_i is a scaling factor, and the imaginary part ω_i represents a loss in the PML. In a regular non-PML region, $a_i = 1$ and $\omega_i = 0$.

In order to simplify the PML equations, the field variables are split as follows:

$$v_i^s = \sum_{k=1}^{3} v_i^{s(k)}, \quad v_i^f = \sum_{k=1}^{3} v_i^{f(k)},$$

where $v_i^{s(k)}$ and $v_i^{f(k)}$ represent the split field variables containing space derivative $\partial/\partial x_k$ only. For example, Eq. (3) for $i=1$ can be split into the following three equations,

$$(m\rho - \rho_f^2)\frac{\partial v_1^{s(1)}}{\partial t} = 2m\frac{\partial}{\partial x_1}(\mu e_{11}) + m\frac{\partial}{\partial x_1}(\lambda_c e - \alpha M \xi) - \rho_f \frac{\partial}{\partial x_1}(\alpha M e - M\xi),$$

$$(m\rho - \rho_f^2)\frac{\partial v_1^{s(2)}}{\partial t} = 2m\frac{\partial}{\partial x_2}(\mu e_{12}) + \rho_f \frac{\eta}{\kappa} v_1^f,$$

$$(m\rho - \rho_f^2)\frac{\partial v_1^{s(3)}}{\partial t} = 2m\frac{\partial}{\partial x_3}(\mu e_{13}).$$

The diagonal strain components e_{ii} need not be split. However, other strain components have to be split as $e_{il} = \Sigma_{k=1}^{3} e_{il}^{(k)}$ for $i \neq l$, and $\xi = \Sigma_{k=1}^{3} \xi^{(k)}$. For example, from (5) we have

$$\frac{\partial e_{ii}}{\partial t} = \frac{\partial v_i^s}{\partial x_i},$$

$$e_{12} = e_{12}^{(1)} + e_{12}^{(2)},$$

$$\frac{\partial e_{12}^{(1)}}{\partial t} = \frac{1}{2}\frac{\partial v_2^s}{\partial x_1}, \quad \frac{\partial e_{12}^{(2)}}{\partial t} = \frac{1}{2}\frac{\partial v_1^s}{\partial x_2},$$

$$\xi = \xi^{(1)} + \xi^{(2)} + \xi^{(3)},$$

$$\frac{\partial \xi^{(1)}}{\partial t} = -\frac{\partial v_1^f}{\partial x_1},$$

$$\frac{\partial \xi^{(2)}}{\partial t} = -\frac{\partial v_2^f}{\partial x_2}, \quad \frac{\partial \xi^{(3)}}{\partial t} = -\frac{\partial v_3^f}{\partial x_3}.$$

In frequency domain PML formulation, after x_i is replaced by $\tilde{x}_i$, equations for v_1^s, for example, can be rewritten as

$$(m\rho - \rho_f^2)(-j\omega)\left(1 + j\frac{\omega_{x_1}}{\omega}\right)v_1^{s(1)} = 2m\frac{\partial}{\partial x_1}(\mu e_{11}) + m\frac{\partial}{\partial x_1}(\lambda_c e - \alpha M \xi) - \rho_f \frac{\partial}{\partial x_1}(\alpha M e - M\xi),$$

$$(m\rho - \rho_f^2)(-j\omega)\left(1 + j\frac{\omega_{x_1}}{\omega}\right)v_1^{s(2)} = 2m\frac{\partial}{\partial x_2}(\mu e_{12}) + \left(1 + j\frac{\omega_1}{\omega}\right)\rho_f \frac{\eta}{\kappa} v_1^f,$$

$$(m\rho - \rho_f^2)(-j\omega)\left(1 + j\frac{\omega_1}{\omega}\right)v_1^{s(3)} = 2m\frac{\partial}{\partial x_3}(\mu e_{13}).$$

By taking the inverse Fourier transform, the above equations yield the time-domain PML equations,

$$(m\rho - \rho_f^2)\left(\frac{\partial v_1^{s(1)}}{\partial t} + \omega_1 v_1^{s(1)}\right) = 2m\frac{\partial}{\partial x_1}(\mu e_{11}) + m\frac{\partial}{\partial x_1}(\lambda_c e - \alpha M \xi) - \rho_f \frac{\partial}{\partial x_1}(\alpha M e - M\xi), \tag{10}$$

$$(m\rho - \rho_f^2)\left(\frac{\partial v_1^{s(2)}}{\partial t} + \omega_1 v_1^{s(2)}\right) = 2m\frac{\partial}{\partial x_2}(\mu e_{12}) + \rho_f \frac{\eta}{\kappa}\left(v_1^f + \omega_2 \int_{-\infty}^{t} v_1^f d\tau\right), \tag{11}$$

$$(m\rho - \rho_f^2)\left(\frac{\partial v_1^{s(3)}}{\partial t} + \omega_1 v_1^{s(3)}\right) = 2m\frac{\partial}{\partial x_3}(\mu e_{13}), \tag{12}$$

$$\frac{\partial e_{11}}{\partial t} = \frac{\partial v_1}{\partial x_1} - \omega_1 e_{11}, \tag{13}$$

$$\frac{\partial e_{12}^{(1)}}{\partial t} = \frac{1}{2}\frac{\partial v_2^s}{\partial x_1} - \omega_1 e_{12}^{(1)}, \tag{14}$$

$$\frac{\partial e_{12}^{(2)}}{\partial t} = \frac{1}{2}\frac{\partial v_1^s}{\partial x_2} - \omega_2 e_{12}^{(2)}, \tag{15}$$

$$\frac{\partial \xi^{(1)}}{\partial t} = -\frac{\partial v_1^f}{\partial x_1} - \omega_1 \xi^{(1)}, \tag{16}$$

$$\frac{\partial \xi^{(2)}}{\partial t} = -\frac{\partial v_2^f}{\partial x_2} - \omega_2 \xi^{(2)}, \tag{17}$$

$$\frac{\partial \xi^{(3)}}{\partial t} = -\frac{\partial v_3^f}{\partial x_3} - \omega_3 \xi^{(3)}. \tag{18}$$

Similar equations can be obtained in the same way for other components v_2^s, v_3^s, v_1^f, v_2^f, v_3^f, and e_{13}, e_{23}. Within the PML region, Eqs. (3) and (4) are split into 18 equations for 3D. Equation (5) is split into nine equations and Eq. (6) is split into three equations. So the total number of the equa-

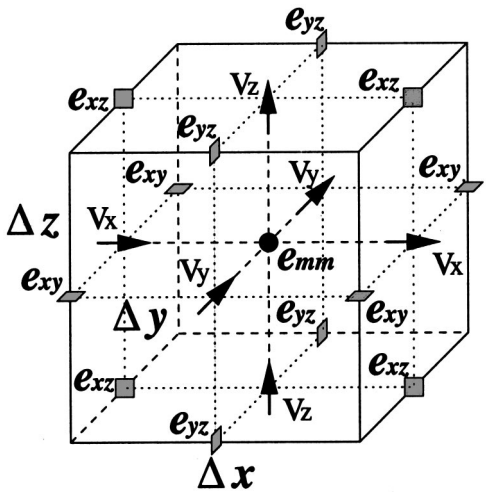

FIG. 1. The relative locations of field components in a unit cell of staggered grid.

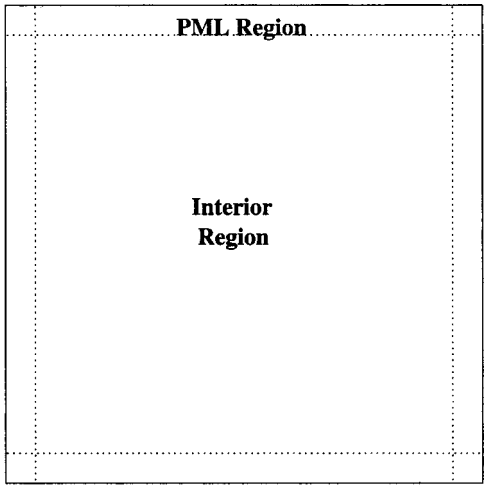

FIG. 2. Computational domain with an interior region and a PML boundary region.

tions is 30 for the PML region, compared to 13 for the regular interior region. Thus, the memory requirement within the PML region is about two and half times that required by a regular medium for three-dimensional problems. This extra memory requirement in the PML region is offset by the effectiveness of PML in absorbing the outgoing waves.

C. Finite-difference implementation

The governing equations for the PML absorbing boundary condition, such as Eqs. (10)–(18), are first-order partial differential equations for particle velocity and strain. They can be solved with different numerical methods. For the evaluation of seismic and acoustic responses of specific models, the accuracy and convenience of the numerical method are of primary concern. The finite-difference method is widely used in wave modeling because of its flexibility and accuracy. For the first-order, leap-frog system of Eqs. (3)–(6) and (10)–(18), the explicit finite-difference method is used on a staggered grid.

To implement a 3-D finite-difference solution to the equations with the PML, the material parameters and unknown field components are discretized on a regular 3-D grid at the intervals Δx_1, Δx_2 and Δx_3. The time domain is also discretized with time step Δt. There are two discretization schemes to approximate the first-order derivatives, i.e., the centered grid and the staggered grid. Because the centered-grid operator to perform first derivatives is less accurate than the staggered grid operator,[18] a staggered grid is used in this article. For the FD implementation of Biot's equations on a staggered grid in Fig. 1, the velocity field components are located at the cell's face centers, while material parameters and normal strains are located at the center of the cell, and shear strains are located the at six edge centers. Strain field is computed at $n\Delta t$ and velocity field is computed at $(n+\frac{1}{2})\Delta t$. This staggered grid is similar to that for elastic waves in a solid.[19,20]

With this discretization, the leap-frog system can be written in a time-stepping form. In order to make the layout of the formulas simple, the governing equations with PML boundary conditions can be generalized as the first-order differential equation. For examples, (11), (13) and (16) can be rewritten as

$$\frac{\partial v_1^{s(2)}}{\partial t}+c_0 v_1^{s(2)}=c_1\int_{-\infty}^{t} v_1^f d\tau + c_2\left[2m\frac{\partial}{\partial x_2}(\mu e_{12})+\rho_f\frac{\eta}{\kappa}(v_1^f)\right], \tag{19}$$

$$\frac{\partial e_{11}}{\partial t}+\omega_1 e_{11}=\frac{\partial v_2^s}{\partial x_1}, \tag{20}$$

$$\frac{\partial \xi^{(1)}}{\partial t}+\omega_1 \xi^{(1)}=-\frac{\partial v_1^f}{\partial x_1}, \tag{21}$$

where c_0, c_1 and c_2 space-dependent coefficients. The corresponding time-stepping equations can then be written as

$$v_1^{s(2)}[j_1,j_2,j_3,(n+\tfrac{1}{2})]=f_1 v_1^{s(2)}[j_1,j_2,j_3,(n-\tfrac{1}{2})] + f_2 R_1, \tag{22}$$

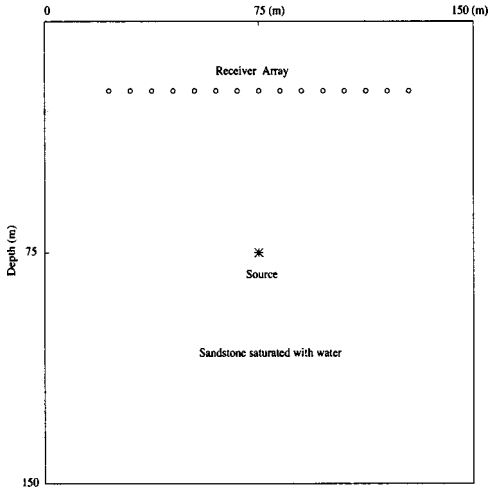

FIG. 3. A physical model showing source and receiver geometry used to generate seismograms. Receivers are 7.5 m apart.

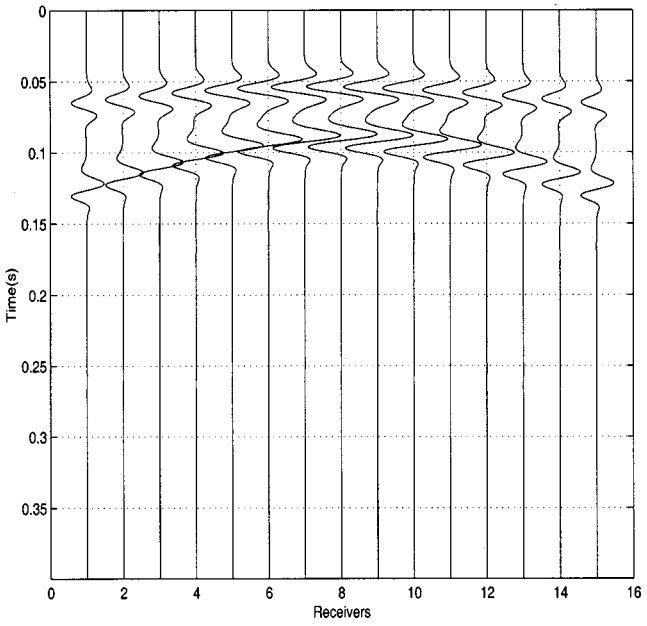

FIG. 4. Vertical velocity components waveforms of the model in Fig. 3.

$$e_{11}[j_1,j_2,j_3,(n+1)]=g_1 e_{11}[j_1,j_2,j_3,n]+g_2 R_2, \quad (23)$$

$$\xi^{(1)}[j_1,j_2,j_3,(n+1)]=-g_1\xi^{(1)}[j_1,j_2,j_3,n]-g_2 R_3, \quad (24)$$

$$f_1=\frac{c_0/2-1/\Delta t}{1/\Delta t+c_0/2}, \quad f_2=\frac{1}{1/\Delta t+c_0/2},$$

$$g_1=\frac{\omega_1/2-1/\Delta t}{1/\Delta t+\omega_1/2}, \quad g_2=\frac{1}{1/\Delta t+\omega_1/2},$$

where R_1, R_2 and R_3 are the right-hand sides of Eqs. (19), (20) and (21) respectively. It should be noted that the material parameters in the above equations must be properly averaged in order to arrive at a higher accuracy.[19] In order to incorporate the PML boundary condition, the computational domain is divided into a PML region and an interior region, as shown in Fig. 2. The absorption of outgoing waves is achieved by the PML region, which consists of several cells of mathematically defined materials with a quadratically tapered ω_i profile to increase the attenuation toward the outer boundary. In this article, ω_i of the PML region is chosen as

$$\omega_i(j_i)=\frac{(M-1/2-j_i)^2}{(M-1/2)^2}\omega_{i,\max}, \quad (25)$$

where $\omega_{i,\max}$ is the value at the center of the cell at the outermost boundary. At the outer boundary, the velocity components and shear strain are forced to be zero. For convenience, $\omega_{i,\max}$ can be expressed in terms of dominant frequency and a normalized coefficient a_0. Then Eq. (25) becomes

$$\omega_i=\begin{cases}2\pi a_0 f_0 (l_{x_i}/L_{\mathrm{PML}})^2, & \text{inside PML},\\ 0, & \text{outside PML},\end{cases} \quad (26)$$

where f_0 is the dominant frequency of the source, L_{PML} is the thickness of the PML region, and l_{x_i} is the distance from the interface between the interior region and the PML region.

III. NUMERICAL RESULTS

The finite-difference algorithm on a staggered grid has a higher accuracy than on a centered grid. Thus, the PML region can be made thinner with a staggered grid with a better absorption than with a centered grid. In this article, the length of the PML region is chosen to be 10 cells. The FD algorithm is illustrated by its two-dimensional implementation.

In the following numerical results, a pure P-wave source is used to excite the seismic wave field. The source time function is the first derivative of a Gaussian function

$$S(t)=(t-t_0)e^{-\pi^2 f_0^2 (t-t_0)^2},$$

where f_0 is the predetermined dominant frequency, and t_0 the time shift.

Unless otherwise stated, a bulk source is used in the following examples. The source energy is partitioned linearly between the solid and the fluid phases with factors

$$W_f=\phi, \quad W_s=(1-\phi), \quad W_r=\phi|W_f-W_s|,$$

where W_f is the weighting factor for the fluid motion, W_s is for the solid motion and W_r is for the relative motion between solid frame and pore fluid.

A. PML performance

The effectiveness of the absorbing boundary condition is an essential factor for the successful numerical simulation. A good absorbing boundary condition has the characteristics of effective absorption of outgoing waves without requiring a large memory. In this article, the performance of the PML is investigated on a homogeneous, fluid-saturated poroelastic

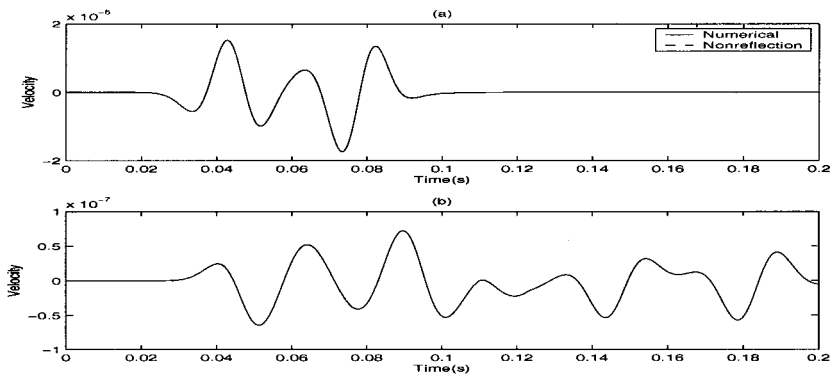

FIG. 5. (a) Comparison of numerical solution at a location 5 cells away from the PML boundary in the model in Fig. 3 with a reference solution. (b) The difference between these two solutions.

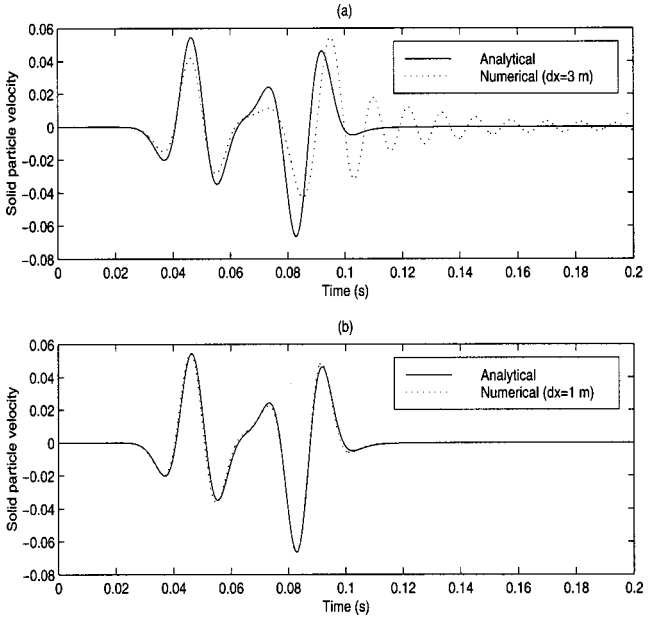

FIG. 6. Comparison of analytical and numerical solutions for the vertical velocity component in the solid for (a) $\Delta x=3$ m and (b) $\Delta x=1$ m.

medium by comparing numerical solutions of PML model with reference solutions that do not have reflections. The optimized a_0 can be obtained by examining the attenuation of the wave field in the PML region.

The homogeneous model for the PML performance test is a sandstone fully saturated with water having the properties of $\rho_s=2650$ kg/m^3, $\rho_f=1040$ kg/m^3, and porosity $\phi=0.3$. This model has the wave properties $v_{\text{fast}}=2365.7$ m/s for fast P wave, $v_{\text{slow}}=776.95$ m/s for slow P wave and $v_{\text{shear}}=960.5$ m/s for shear wave. The geometry of the physical model with receivers and source is shown in Fig. 3.

Figure 4 shows the numerical results of vertical velocity in solid from the model with the PML boundary condition. With the PML region, the reflections are eliminated from the seismograms. Another advantage of the PML absorbing boundary condition is its stability. For this particular model, $v_{\text{fast}}/v_{\text{shear}}=2.46$, which will cause an instability problem for the CE boundary condition.[10]

In order to quantify the reflections from the PML boundary, the reflection coefficient in dB is calculated for a location 5 cells away from PML interface in this model. The reflection was obtained by comparing the numerical results from the model with the PML boundary to those from a much larger model with the Dirichlet boundary in which reflections have not arrived within the time window of interest. Figure 5(a) shows these two results together, while Fig. 5(b) shows the difference. The PML result and the reference are almost indistinguishable at the signal scale. Compared to incident signal, the reflection is about 50 dB down.

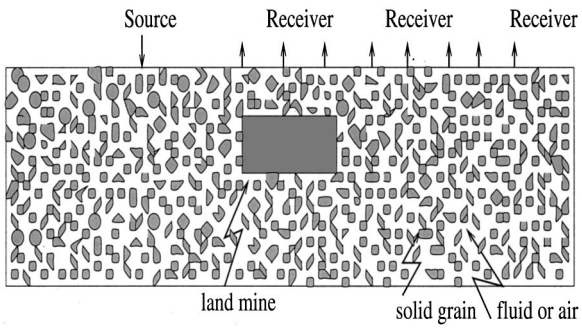

FIG. 7. Geometry of the model of a buried minelike object.

TABLE I. Properties of sand and mud (from Ref. 21).

	Sand	Mud
Porosity	0.4	0.6
Density (kg/m^3)	1990	1660
Structure factor	1.8	1.9
Permeability (m^2)	3×10^{-11}	3×10^{-13}
Bulk modulus (Pa)	4×10^7	1×107
Shear modulus (Pa)	2.2×10^7	6×10^6

B. Validation of numerical results

An analytical solution for the particle velocity field in a homogeneous, fluid-saturated poroelastic medium subject to a point source in 3-D space or a line source in 2-D space can be derived.[6] The particle velocity is obtained in a closed form via potential functions.

For Biot's equations, it is convenient to solve for the particle velocity through potential functions. The velocity of particles and body force at source can be expressed in terms of potentials as

$$\mathbf{u}=\nabla\psi_s+\nabla\times\Psi_s,$$

$$\mathbf{U}=\nabla\psi_f+\nabla\times\Psi_f,$$

$$\mathbf{f}=\nabla\Phi+\nabla\times\Psi,$$

where $\nabla\cdot\Psi_f=0$, $\nabla\cdot\Psi_s=0$ and $\nabla\cdot\Psi=0$ and describe the rotational potentials, while ψ_s, ψ_f and Φ describe the dilatational potentials. If the source is purely dilatational, then its rotational component disappears. In the time domain, for a purely P-wave point source and ideal nonviscous fluid, the potential can be expressed as

$$\psi_s(r,t)=\frac{\alpha s(t-r/V_f)+\beta s(t-r/V_s)}{4\pi r},$$

$$\psi_s(r,t)=\frac{\alpha A_f s(t-r/V_f)+\beta A_s s(t-r/V_s)}{4\pi r},$$

where r is the distance and $s(t)$ is the source time function. A_f and A_s represent the ratios between the solid and fluid motion for the fast P wave and the slow P wave. The coefficients α and β are determined by the regularity conditions. V_f and V_s are the velocities of the fast P wave and the slow P wave, respectively.

In two dimensions, for a pure P-wave line source along the y axis, the solution can be obtained by integrating the point source solution in the y direction. In the $x-z$ plane, the dilatational potentials are

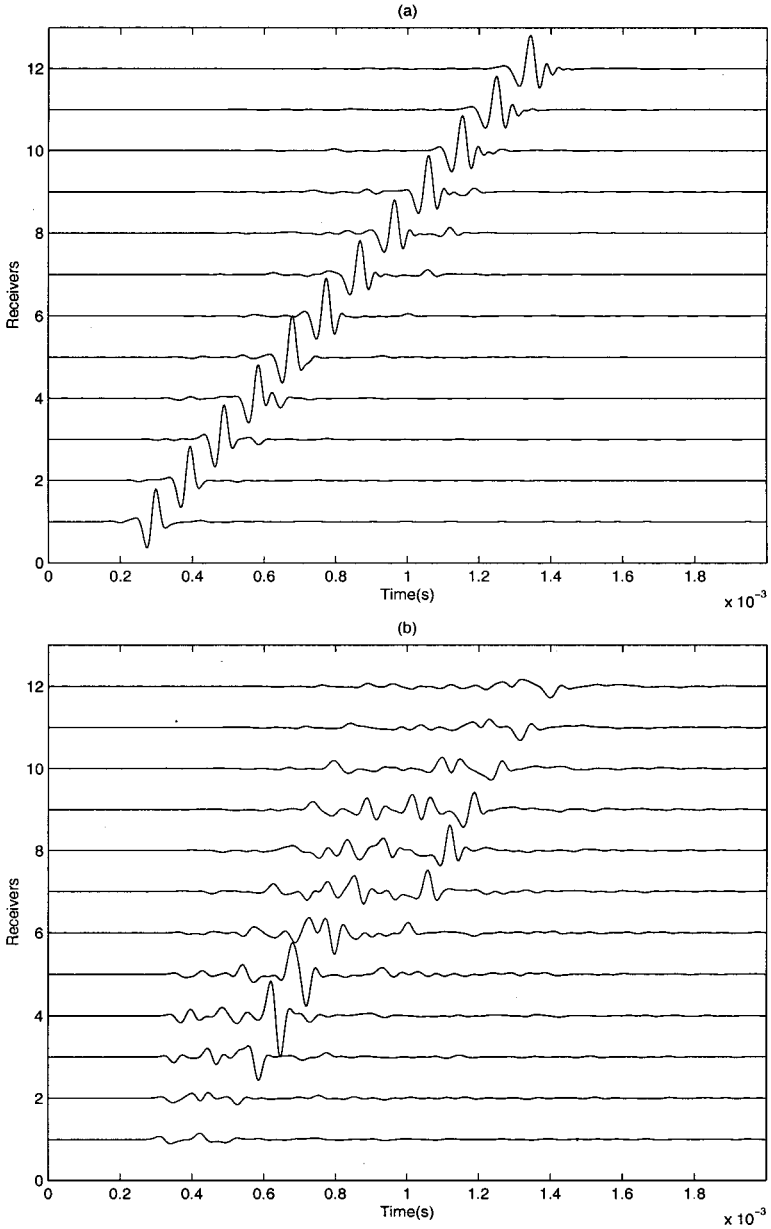

FIG. 8. Seismograms of the vertical particle velocity on the surface for a plastic minelike object in a ''dry sand'' model. (a) The total field. (b) The scattered field.

$$\psi_s(x,z,t)=\frac{\alpha \mathrm{H}(t-r/V_f)}{2\pi}\int_{r/V_f}^{t}\frac{s(t-\tau)}{\sqrt{\tau^2-r^2/V_f^2}}\,d\tau + \frac{\beta \mathrm{H}(t-r/V_s)}{2\pi}\int_{r/V_s}^{t}\frac{s(t-\tau)}{\sqrt{\tau^2-r^2/V_s^2}}\,d\tau,$$

$$\psi_f(x,z,t)=\frac{\alpha A_f \mathrm{H}(t-r/V_f)}{2\pi}\int_{r/V_f}^{t}\frac{s(t-\tau)}{\sqrt{\tau^2-r^2/V_f^2}}\,d\tau + \frac{\beta A_s \mathrm{H}(t-r/V_s)}{2\pi}\int_{r/V_s}^{t}\frac{s(t-\tau)}{\sqrt{\tau^2-r^2/V_s^2}}\,d\tau,$$

where H( ) is the Heaviside step function and $r=\sqrt{x^2+z^2}$. Once the potential functions are available, the velocity can be easily obtained by taking the gradient of potential functions.

The validation of the numerical method can be done by comparing the numerical results with the above analytical solution. A homogeneous model whose parameters are the same as the previous model is considered. A P-wave line source of the first derivative Gaussian time function with $f_0=40$ Hz is located at (0,0). Then the solution at (30 m,30 m) is calculated numerically and analytically. The numerical solutions for two different grid spacings are displayed with an analytical solution in Fig. 6. The oscillatory tails and disagreement in Fig. 6(a) for a coarser grid are caused by the dispersion of the slow P wave. When the grid spacing is decreased, the numerical solutions agree well with the analytical solution in Fig. 6(b).

C. Applications

This algorithm can be used to characterize a reservoir in a large scale as well as to investigate soil property in a small scale. In this section, this method is used to model a plastic minelike object that is difficult to detect with the more conventional electromagnetic induction sensors (i.e., metal de-

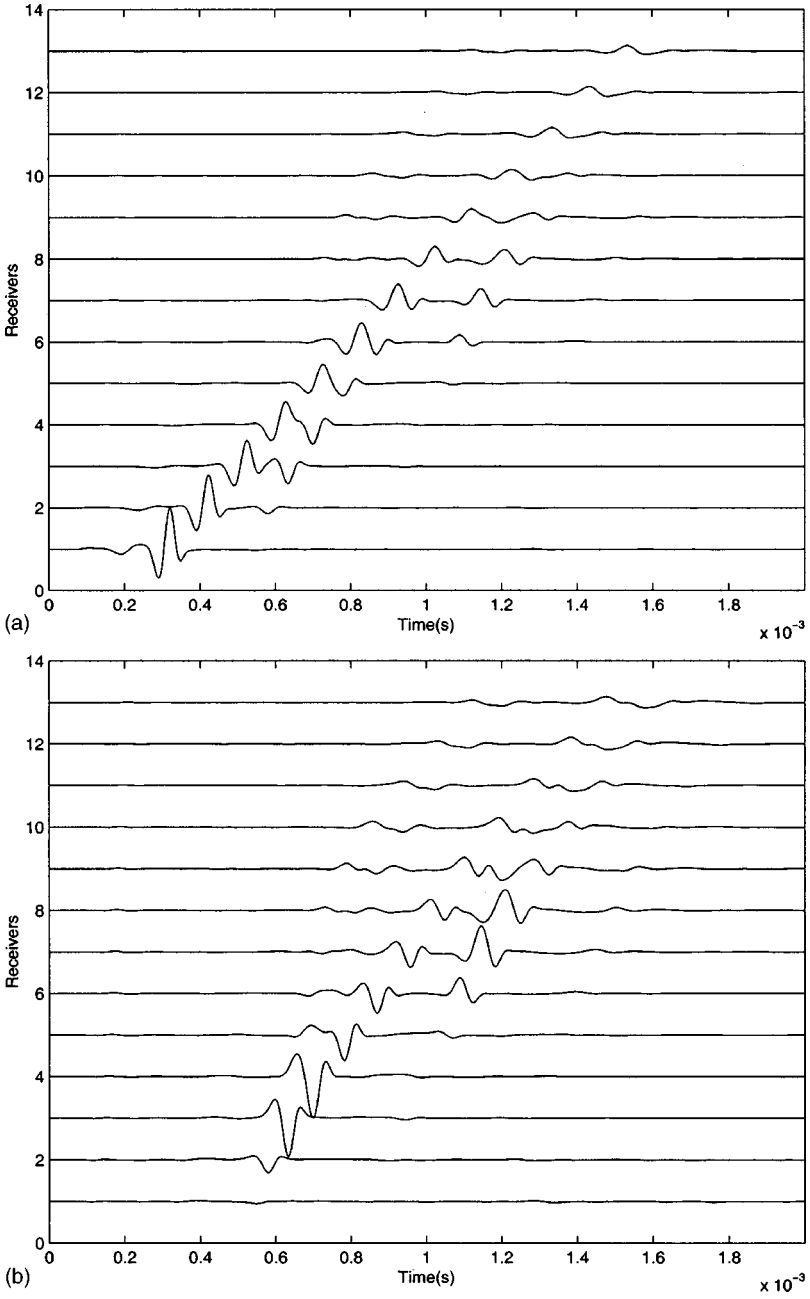

FIG. 9. Same as Fig. 8 except for the ''sand'' model.

tectors). The geometry of the model of a buried object is shown in Fig. 7.

For the plastic minelike object, the parameters are chosen as $\rho = 1330$ kg/M^3, S-wave velocity $v_{\text{shear}} = 417$ m/s and P-wave velocity $v_p = 1060$ m/s. The material in the ground may be considered as a two-phase composite material consisting of granular solid and pore fluid. The nature of this composite varies with environment, geographic location, and with depth below the surface of ground. Three different types of soil—dry ''sand,'' ''sand'' and ''mud''—are used. The first is similar to a coarse sand deposit saturated with air. The second is similar to a coarse sand deposit saturated with water. The third is similar to a fine clay mixture or mud. The elastic properties of these materials are listed next and in Table I.

Grain and fluid properties	$K_s = 3.6 \times 10^{10}$ Pa
	$K_f = 2.0 \times 10^9$ Pa
	$\rho_s = 2650$ kg/m^3
	$\rho_f = 1000$ kg/m^3
Viscosity	$\eta = 1.0 \times 10^{-3}$ Mks
Sound speed of fluid	$C_0 = 1414$ m/s

A vertical dipole line source with the first derivative of Gaussian pulse with center frequency of 15 kHz is located on the free surface. The receivers are uniformly distributed on the free surface at a distance 2 to 14.5 cm from the source. The plastic minelike object is buried in the ground with its upper edge 2 cm beneath the surface of the ground. The space step is chosen such that there are 15 grid points per minimum wavelength. The time step is chosen according to the stability condition. Because the minimum wave velocity is different, these three models have a different grid size and number of cells. The computational domain contains 600 $\times$160 cells for the ''dry sand'' model, 400$\times$100 cells for the

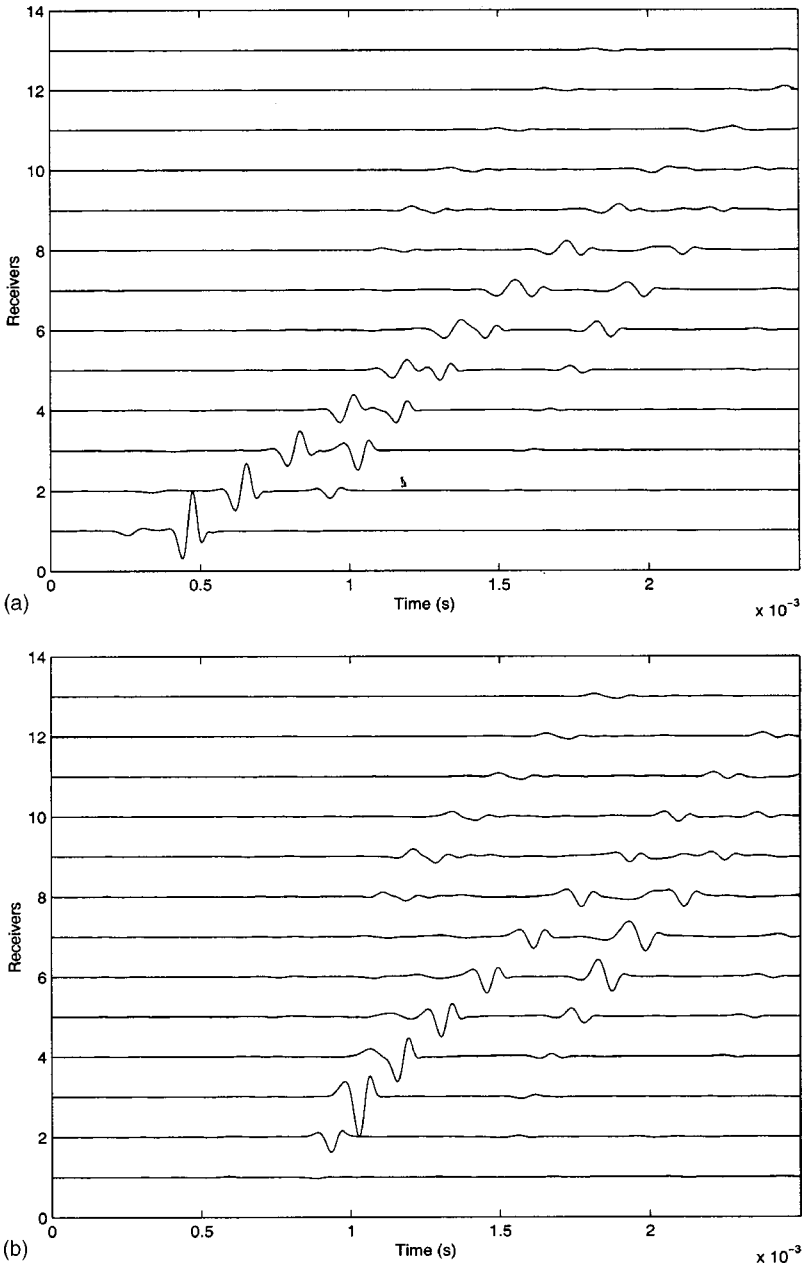

FIG. 10. Same as Fig. 8 except for the ''mud'' model.

''sand'' model, and 600×160 for the ''mud'' model, including a PML region with a thickness of 10 cells.

The numerical simulations of the soil with plastic mine-like objects were carried out to examine the effects of the plastic object on the wave field and investigate the possibility of the detection of a plastic object in the ground by using acoustic method. Figure 8(a) shows the synthetic seismograms of the vertical velocity of solid particle at the surface for the dry sand model. Here, the vertical velocity is plotted as a function of time and vertically offset by the distance from the source. The wave speed is indicated by the slope of the traveling waves in the figure. Clearly, the Rayleigh surface wave dominates the wave field. In the scattered field in Fig. 8(b) (obtained by subtracting the background field from the total field), the reflected shear wave dominates the wave field. Figures 9(a) and (b) show the total field and scattered field for the ''sand'' model. In the total field, a strong Rayleigh surface which has lower speed than the shear wave is present. The reflected shear wave can be seen clearly just behind the surface wave on the first several traces. Because it has a higher speed, it surpasses the surface wave at far offsets. In this figure, the reflected shear wave dominates other waves. Figures 10(a) and (b) show the total and scattered fields respectively for the ''mud'' model. The results are very similar to those of the ''sand'' model except that the speeds of surface waves and shear waves are much lower.

IV. CONCLUSION

A particle velocity-strain, finite-difference method combined with the perfectly matched layer (PML) has been formulated in three dimensions for the simulation of seismic waves propagating in porous media. The performance of the PML boundary in two dimensions has been studied on a

homogeneous model by calculating the reflection from the boundary. The analytical solution to Biot's equations is used to validate the numerical algorithm. The results show that the first-order, leap-frog, staggered-grid scheme has a higher accuracy than the second-order, centered-grid finite-difference scheme. Even with only a 10-cell PML region, the reflection is much less than that of second-order centered-grid scheme with 20-cell PML. The results also show the scheme is stable even if the ratio of the fast P-wave velocity to shear wave velocity is greater than 2.

This numerical method has been used to investigate the interaction of elastic waves with a buried minelike object. Three cases have been investigated: a plastic object buried in purely dry ''sand,'' in ''sand,'' and in '' mud.'' The results show that the wave responses are substantially different for different backgrounds.

[1] M. A. Biot, ''Theory of propagation of elastic waves in a fluid-saturated porous solid. 1. Low-frequency range,'' J. Acoust. Soc. Am. **28**, 168–178 (1956).

[2] M. A. Biot, ''Theory of propagation of elastic waves in a fluid-saturated porous solid. 2. Higher-frequency range,'' J. Acoust. Soc. Am. **28**, 179–191 (1956).

[3] M. A. Biot, ''Mechanics deformation and acoustic propagation in porous media,'' J. Appl. Phys. **33**, 1482–1498 (1962).

[4] S. Hassanzadeh, ''Acoustic modeling in fluid saturated porous media,'' Geophysics **56**, 424–435 (1991).

[5] X. Zhu and G. A. McMechan, ''Finite-difference modeling of the seismic response of fluid saturated, porous, elastic media using Biot theory,'' Geophysics **56**, 328–339 (1991).

[6] N. Dai, A. Vafidis, and E. R. Kanasewich, ''Wave propagation in heterogeneous, porous media: A velocity-stress, finite-difference method,'' Geophysics **60**, 327–340 (1995).

[7] C. Cerjan, D. Kosloff, R. Kosloff, and M. Reshef, ''A non-reflecting boundary condition for discrete acoustic and elastic wave equations,'' Geophysics **50**, 705–708 (1985).

[8] R. Clayton and B. Engquist, ''Absorbing boundary conditions for acoustic and elastic wave equations,'' Bull. Seismol. Soc. Am. **67**, 1529–1540 (1977).

[9] K. D. Mahrer, ''An empirical study of instability and improvement of absorbing boundary conditions for elastic wave equation,'' Geophysics **51**, 1499–1501 (1986).

[10] J. P. Berenger, ''A perfectly matched layer for the absorption of electromagnetic waves,'' J. Comput. Phys. **114**, 185–200 (1994).

[11] W. C. Chew and Q. H. Liu, ''Perfectly matched layers for elastodynamics: A new absorbing boundary condition,'' J. Comput. Acoust. **4**, 72–79 (1996).

[12] Q. H. Liu, ''Perfectly matched layers for elastic waves in cylindrical and spherical coordinates,'' J. Acoust. Soc. Am. **105**, 2075–2084 (1999).

[13] F. D. Hastings, J. B. Schneider, and S. L. Broschat, ''Application of the perfectly matched layer (PML) absorbing boundary condition to elastic wave propagation,'' J. Acoust. Soc. Am. **100**, 3061–3069 (1996).

[14] Q. H. Liu and J. Tao, ''The perfectly matched layer for acoustic waves in absorptive media,'' J. Acoust. Soc. Am. **102**, 2072–2082 (1997).

[15] Y. Q. Zeng, J. He, and Q. H. Liu, ''The application of the perfectly matched layer in numerical modeling of wave propagation in poroelastic media,'' Research Report, Duke University (1999).

[16] R. Burridge and J. B. Keller, ''Poroelasticity equations derived from microstructure,'' J. Acoust. Soc. Am. **70**, 1140–1146 (1981).

[17] J. Plona, ''Observation of the second bulk compressional wave in a porous medium at ultrasonic frequencies,'' Appl. Phys. Lett. **36**, 259–261 (1980).

[18] G. Kneib and C. Kerner, ''Accurate and efficient seismic modeling in random media,'' Geophysics **58**, 576–588 (1993).

[19] Q. H. Liu, F. Daube, C. Randall, E. Schoen, H. Liu, and P. Lee, ''A 3D finite difference simulation of sonic logging,'' J. Acoust. Soc. Am. **100**, 72–79 (1996).

[20] Q. H. Liu, ''Some current trends in numerical methods for transient acoustic and elastic waves in multidimensional inhomogeneous media,'' Current Topics Acoustical Research **2**, 31–42 (1998).

[21] J. I. Dunlop, ''Propagation of acoustic waves in marine sediments, a review,'' Exploration Geophysics **19**, 513–535 (1988).

Pulse propagation in randomly fluctuating media

Dalcio K. Dacol[a)]
Naval Research Laboratory, Washington, DC 20375-5350

(Received 12 October 2000; revised 26 March 2001; accepted 28 March 2001)

Pulse propagation in a weakly and randomly inhomogeneous medium is studied using a time-domain progressive wave equation. An eikonal-like approximated solution to the wave equation derived from the path integral representation is used to obtain the time-dependent statistics of pulses propagating through this random medium. This approach yields both a simple way of producing simulations of time series as well as their statistical properties.
[DOI: 10.1121/1.1373448]

PACS numbers: 43.20.Bi, 43.20.Fn, 43.20.Lv [ANN]

I. INTRODUCTION

Pulse propagation in inhomogeneous and random media is a phenomena of much interest in applied sciences such as ocean acoustics and atmospheric optics. Much of the theoretical work done in wave propagation in random media (see review in Ref. 1) consists of analysis in the frequency domain, that is, studies of the Helmholtz equation rather than the time-domain wave equation. The reason for this is that this problem can be treated as a scattering problem and there are powerful techniques to study wave scattering in the frequency domain while time-domain formulations are notoriously more difficult to use and obtain results. Fourier synthesis must then be used to find out the implications for pulse propagation of the results obtained by single frequency methods. Recently (see Ref. 2) an approach for treating wave propagation in random media in a space–time framework was proposed using a time-domain progressive wave equation derived a few years ago by McDonald and Kuperman[3] from the wave equation. This equation is the equivalent in the space–time formulation of the well-known parabolic (or paraxial) wave equation in the space-frequency formulation[4,5] and mathematically similar to the time-dependent Schrödinger equation. The parabolic equation in the frequency domain has been extensively used to discuss wave propagation in random media; an important example of its use can be found in Ref. 6. In the present article a previously developed (see Ref. 2) path integral representation for the solution of the time-domain progressive wave equation is applied to study pulse propagation in randomly fluctuating media. This approach allows us to use our knowledge about time-dependent wave propagation in homogeneous media to approximately evaluate the path integrals and obtain analytical expressions for the moments of the propagating pulse in a weakly and randomly inhomogeneous medium. Besides obtaining expressions for the various statistical moments, the approach discussed in this article also yields a simple algorithm for producing simulations of pulse propagation in such media. Thus time series at a point detector are computed using this method and their behavior can then be related to the hypothesized properties of the medium.

[a)]Electronic mail: dacol@nrl.navy.mil

II. THE TIME-DOMAIN PROGRESSIVE WAVE EQUATION

In this section the time-domain progressive wave equation, derived in Ref. 3, is introduced and its application to pulse propagation discussed. The time-domain progressive wave equation is an approximate, first order in the time derivative, version of the usual wave equation:

$$\nabla^2 P - \frac{1}{c^2}\partial_t^2 P = -S. \tag{1}$$

In this equation P is the acoustic pressure and c is the sound speed in the medium. In the following discussion it is assumed that the sound speed can be split into a large homogeneous part, c_0, and a small inhomogeneous part $c_1(\mathbf{r},t)$, that is, $c=c_0+c_1(\mathbf{r},t)$ with $1 \gg |c_1(\mathbf{r},t)/c_0|$. This assumption implies that the wave fronts move through the medium with speed very close to c_0. Thus it is expected that in a reference frame that moves along the direction of propagation with speed c_0 the acoustic pressure will vary slowly with time. This observation plus the weak inhomogeneity assumption are the basic ingredients in obtaining the progressive wave equation.

In the following discussion the x axis is directed along a line that goes through the source and the observation point. Along this direction the position of the wave front is, approximately, $x \approx c_0 t$. In Ref. 2 the following equation is found to be a very good approximation to the wave equation along the propagation direction (the x axis) and for $c_0 t \gg r_\perp$ where $\mathbf{r}_\perp$ is a position vector in the plane perpendicular to the propagation direction (the $y-z$ plane):

$$i\partial_t \phi = H(\mathbf{r}, -i\nabla, t)\phi - \frac{ic_0}{2}S, \tag{2}$$

with

$$H(\mathbf{r},\mathbf{p},t) = c(\mathbf{r},t)p_x + \frac{c_0}{2}p_\perp^2 \frac{1}{p_x}, \tag{3}$$

and with P being related to ϕ through

$$P(\mathbf{r},t) = \int_{-\infty}^{x} dx'\, \phi(x',y,z,t). \tag{4}$$

In Eq. (4), $p_x = -i\partial_x$ and $p_\perp^2 = -\nabla_\perp^2 = -\partial_y^2 - \partial_z^2$.

At this point it is convenient to introduce a propagator for Eq. (2). The propagator is the solution $\phi(\mathbf{r},t|\mathbf{r}',t')$ of the time-domain progressive wave equation, Eq. (2), with $S=0$ such that

$$\phi(\mathbf{r},t'|\mathbf{r}',t')=\delta(\mathbf{r}-\mathbf{r}'). \tag{5}$$

The propagator has the following two useful properties for $t\geqslant t'$,

$$\phi(\mathbf{r},t)=\int d\mathbf{r}'\ \phi(\mathbf{r},t|\mathbf{r}',t')\phi(\mathbf{r}',t'), \tag{6}$$

i.e., a solution at time t can be obtained from the solution at time t' if one knows the propagator, and

$$\phi(\mathbf{r},t)=-\frac{c_0}{2}\int d\mathbf{r}'\int_{-\infty}^{t}dt'\ \phi(\mathbf{r},t|\mathbf{r}',t')S(\mathbf{r}',t'), \tag{7}$$

that is, knowing the propagator one can construct the solution of the time-domain progressive wave equation for an arbitrary source function $S(\mathbf{r},t)$.

III. PULSE PROPAGATION IN A WEAKLY INHOMOGENEOUS MEDIUM

In the previously cited work, Ref. 2, the similarity between the equation for the propagator $\phi(\mathbf{r},t|\mathbf{r}',t')$ and the time-dependent Schrödinger equation leads to a Feynman path integral representation for the propagator:

$$\phi(\mathbf{r},t|\mathbf{r}',t')=\int \mathcal{D}\mathbf{q}p_x\mathcal{D}p_x e^{i\int_{t'}^{t}dt''p_x(t'')[\dot{q}_x(t'')+(1/2c_0)\dot{q}_\perp^2(t'')-\mathbf{c}(\mathbf{q}(t''),t'')]}, \tag{8}$$

In Eq. (8), as usual in Feynman path integrals (see Ref. 7), the position path $\mathbf{q}(t'')$ is constrained such that $\mathbf{q}(t')=\mathbf{r}'$ and $\mathbf{q}(t)=\mathbf{r}$ while the x-component of the momentum (or, as it is appropriate for classical wave propagation, the wave vector) path is not constrained, that is, $p_x(t')$ and $p_x(t'')$ are also integration variables.

It was argued in that work that in the case of weak inhomogeneities the direct path connecting $\mathbf{r}'$ and $\mathbf{r}$,

$$\mathbf{q}(t'')=\mathbf{R}(t'')\equiv\mathbf{r}'+(\mathbf{r}-\mathbf{r}')\frac{t''-t'}{t-t'}, \tag{9}$$

is dominant in the path integral. Thus a good approximation for the path integral in this case is obtained by replacing the path variables in $c(\mathbf{q}(t''),t'')$ by the direct path $\mathbf{R}(t'')$. This yields the following approximated expression for the propagator:

$$\phi(\mathbf{r},t|\mathbf{r}',t')=-\frac{1}{2\pi c_0(t-t')}\delta'\left(x-x'+\frac{(\mathbf{r}-\mathbf{r}')_\perp^2}{2c_0(t-t')}-c_0(t-t')-\int_{t'}^{t}dt''\,c_1(\mathbf{R}(t''),t'')\right), \tag{10}$$

where $\delta'(u)=\partial_u\delta(u)$. Thus for the Green function of the Helmholtz equation, that is, for the pressure due to an impulsive point source, one obtains (with $t>t'$ and $x>x'$)

$$G(\mathbf{r},t|\mathbf{r}',t')=\frac{1}{4\pi(t-t')}\delta\left(x-x'+\frac{(\mathbf{r}-\mathbf{r}')_\perp^2}{2c_0(t-t')}-c_0(t-t')-\int_{t'}^{t}dt''\,c_1(\mathbf{R}(t''),t'')\right), \tag{11}$$

Thus, for example, the pressure field due to an impulsive point source at $\mathbf{r}=0$ and turned on at $t=0$ is

$$P(\mathbf{r},t)=\frac{1}{4\pi t}\delta\left(x+\frac{\mathbf{r}_\perp^2}{2c_0t}-c_0t-\int_0^t dt'\,c_1(\mathbf{R}(t'),t')\right). \tag{12}$$

Of course, in the above equation $\mathbf{R}(t')=(t'/t)\mathbf{r}$.

At this point it is interesting to compare the above result with what one would obtain using a standard perturbation approach to solve Eq. (2). This equation can be rewritten in terms of the pressure:

$$\partial_t\partial_x P(\mathbf{r},t)=-(c_0+c_1(\mathbf{r},t))\partial_x^2P(\mathbf{r},t)-\frac{c_0}{2}\nabla_\perp^2P(\mathbf{r},t). \tag{13}$$

In the absence of fluctuations, that is, for $c_1(\mathbf{r},t)=0$, the solution of Eq. (13) is

$$P_0(\mathbf{r},t)=\frac{1}{4\pi t}\delta(F_0(\mathbf{r},t)),\quad F_0(\mathbf{r},t)=x+\frac{\mathbf{r}_\perp^2}{2c_0t}-c_0t. \tag{14}$$

Thus the unperturbed wave front is characterized by the surface

$$F_0(\mathbf{r},t)=x+\frac{\mathbf{r}_\perp^2}{2c_0t}-c_0t=0. \tag{15}$$

The equation that determines the characteristic surface $F(\mathbf{r},t)=0$ for Eq. (13) is (see Ref. 8 for a discussion of characteristic surfaces)

$$(\partial_tF)(\partial_xF)+(c_0+c_1(\mathbf{r},t))(\partial_xF)^2+\frac{c_0}{2}(\nabla_\perp F)^2=0. \tag{16}$$

The standard perturbation technique to obtain a ''retarded potential'' type of solution for Eq. (13) is to assume that

$$P(\mathbf{r},t)=\frac{1}{4\pi t}\delta(F(\mathbf{r},t)), \tag{17}$$

and

$$F(\mathbf{r},t)=F_0(\mathbf{r},t)+\Psi(\mathbf{r},t), \tag{18}$$

where $\Psi(\mathbf{r},t)$ is to be determined perturbatively from Eq. (16). Inserting the above *ansatz* for $F(\mathbf{r},t)$ into Eq. (16) one finds

$$\partial_t\Psi+c_1(\mathbf{r},t)-\frac{\mathbf{r}_\perp^2}{2c_0t^2}\partial_x\Psi+\frac{1}{t}\mathbf{r}_\perp\cdot\nabla_\perp\Psi=0. \tag{19}$$

One wants to determine the characteristic function perturbation $\Psi(\mathbf{r},t)$ in the neighborhood of the observation point when the wave front arrives there, that is, for $x\approx c_0t$ and for $c_0t\gg r_\perp$ as discussed before in Sec. I. Thus the last two terms

in Eq. (19) can be neglected and one obtains the following equation for $\Psi(\mathbf{r},t)$:

$$\partial_t \Psi + c_1(\mathbf{r},t) = 0. \tag{20}$$

Thus one has, by integrating Eq. (20) with respect to time,

$$\Psi(\mathbf{r},t) = -\int_0^t dt''\, c_1(\mathbf{r},t'). \tag{21}$$

Therefore, standard perturbation techniques lead to the following ''retarded potential'' type of solution for Eq. (2) in the case of an impulsive point source at $\mathbf{r}=0$ and turned on at $t=0$:

$$P(\mathbf{r},t)_{\text{pert}} = \frac{1}{4\pi t}\,\delta\left(x + \frac{\mathbf{r}_\perp^2}{2c_0 t} - c_0 t - \int_0^t dt'\, c_1(\mathbf{r},t') \right). \tag{22}$$

Comparing the expressions for the correction to the unperturbed characteristic surface function obtained from the perturbative approach and from the path integral not only shows the difference in their underlying physical assumptions, but also indicates why the path integral expression is preferable. The perturbative approach yields $\Psi(\mathbf{r},t)_{\text{pert}} = -\int_0^t dt'\, c_1(\mathbf{r},t')$ and the path integral method yields $\Psi(\mathbf{r},t)_{\text{path}} = -\int_0^t dt'\, c_1(\mathbf{r}(t'/t),t')$. The perturbation result $\Psi(\mathbf{r},t)_{\text{pert}}$ states that the distortions of the wave front (with respect to what it would be in the absence of inhomogeneities) observed at point $\mathbf{r}$ and time t are caused by an accumulation of sound propagation speed fluctuations at the observation point $\mathbf{r}$ during the time interval t. The Feynman path integral result $\Psi(\mathbf{r},t)_{\text{path}}$ recognizes that the wave front has traversed the space between the source and the observation point accumulating distortions due to the fluctuations in the sound propagation speed along the path between source and receiver. This difference is more clearly illustrated in the case in which the inhomogenities in the sound propagation speed are only position dependent. In this case $\Psi(\mathbf{r},t)_{\text{pert}} = -c_1(\mathbf{r})t$, that is, only the inhomogeneity at the observation point contributes to the wave front distortion. The path integral result in this case is $\Psi(\mathbf{r},t)_{\text{path}} = -\int_0^t dt'\, c_1(\mathbf{r}(t'/t))$ and it takes into account all the inhomogeneities along a straight line from the source to the observation point. Thus the path integral estimation of the wave front distortions is more faithful to the physics of wave propagation which is one of the reasons for using the Feynman path integral representation of the solution of the progressive wave equation. This path integral representation of the solution also allows one to explore higher order corrections in a fairly straightforward way. It can also be used to analyze the moments of the acoustic field averaged over the propagation speed fluctuations.

Now, the progressive equation is a good approximation for the wave equation in the region where

$$x - x' + \frac{(\mathbf{r}-\mathbf{r}')_\perp^2}{2c_0(t-t')} - c_0(t-t') \approx |\mathbf{r}-\mathbf{r}'| - c_0(t-t'). \tag{23}$$

Using the above near equality in the expression for the Green function one obtains the approximation that will be used to study pulse propagation in weakly inhomogeneous media:

$$G(\mathbf{r},t|\mathbf{r}',t') = \frac{1}{4\pi(t-t')}\,\delta\left(|\mathbf{r}-\mathbf{r}'| - c_0(t-t') - \int_{t'}^t dt'\, c_1(\mathbf{R}(t''),t'') \right). \tag{24}$$

Thus, for a pulse generated by a point source of the form $S(\mathbf{r},t) = \delta(\mathbf{r}) f(t)$, where $f(t)$ is the pulse shape function, one has the following expression for the pressure field $[P(\mathbf{r},t) = \int d\mathbf{r}' \int dt'\, G(\mathbf{r},t|\mathbf{r}',t') S(\mathbf{r}',t')]$:

$$P(\mathbf{r},t) = \int_{-\infty}^t dt'\, f(t')\,\frac{1}{4\pi(t-t')}\,\delta\left(r - c_0(t-t') - \int_{t'}^t dt''\, c_1(\mathbf{R}(t''),t'') \right). \tag{25}$$

By parametrizing the time delay, $t-t'$, with propagation speeds through the change of variables $v = r/(t-t')$, one obtains an expression for the pulse as an average over propagation speeds of pulse shape functions with different arrival times:

$$P(\mathbf{r},t) = \frac{1}{4\pi r}\int_0^\infty dv\, f\left(t - \frac{r}{v} \right)\delta(v - c_0 - V(\mathbf{r},t,v)), \tag{26}$$

where

$$V(\mathbf{r},t,v) = \frac{v}{r}\int_{t-(r/v)}^t dt'\, c_1\left(\left(1 - (t-t')\frac{v}{r} \right)\mathbf{r}, t' \right). \tag{27}$$

Let the argument of the delta function in Eq. (26) be $g(v)$, that is, $g(v) = v - c_0 - V(\mathbf{r},t,v)$. With v_0 such that $g(v_0) = 0$ the acoustic field can be evaluated yielding

$$P(\mathbf{r},t) = \frac{1}{4\pi r}\,\frac{1}{|1 - \partial V/\partial v|_{v=v_0}|}\,\theta(v_0) f\left(t - \frac{r}{v_0} \right), \tag{28}$$

where $\theta(v_0)$ is the step function [$\theta(v_0) = 0$ if $v_0 < 0$ and $\theta(v_0) = 1$ if $v_0 > 0$] and notice that $v_0 = v_0(\mathbf{r},t)$. Thus the pulse propagates with a variable effective propagation speed. If the equation $g(v_0) = 0$ has multiple solutions, then on the right-hand side of Eq. (28) one must sum over all the solutions. As it will be shown in the next section, for the weak fluctuation case, where the approximations made to obtain the above equation should be valid, a unique solution to $g(v_0) = 0$ can be obtained perturbatively.

IV. NUMERICAL SIMULATION OF THE TIME SERIES

The effective propagation speed obtained in Sec. III, $v_0(\mathbf{r},t)$, can be approximately expressed in terms of c_1:

$$v_0(\mathbf{r},t) \approx c_0 + \frac{V(\mathbf{r},t,c_0)}{1 - \partial V/\partial v|_{v=c_0}}. \tag{29}$$

Equation (27) can be rewritten as

$$V(\mathbf{r},t,v) = \int_0^1 d\mu\, c_1\left(\mu\mathbf{r}, t - (1-\mu)\frac{r}{v} \right), \tag{30}$$

and so one gets

$$\frac{\partial V}{\partial v}(\mathbf{r},t,v)=\frac{r}{v^2}\int_0^1 d\mu(1-\mu)\partial_t c_1\left(\mu\mathbf{r},t-(1-\mu)\frac{r}{v}\right). \tag{31}$$

Both $V(\mathbf{r},t,c_0)$ and $(\partial V/\partial v)(\mathbf{r},t,c_0)$ are random processes and if the statistical properties of $c_1(\mathbf{r},t)$ are known then their statistical properties are also known since they both are simple linear functionals of $c_1(\mathbf{r},t)$.

The pressure field $P(\mathbf{r},t)$ according to Eq. (28) is an explicit function of $V(\mathbf{r},t,c_0)$ and $(\partial V/\partial v)(\mathbf{r},t,c_0)$, thus it is straightforward to generate numerical simulations of the pressure field in this random medium if one assumes that $c_1(\mathbf{r},t)$ is a Gaussian random process. For simplicity only the case of the time series at a point $\mathbf{r}$, that is, $P(\mathbf{r},t)$ for fixed $\mathbf{r}$, will be discussed in this section.

To obtain the desired time series one must produce a simulation of the Gaussian stochastic processes $S_1(t)=V(\mathbf{r},t,c_0)$ and $S_2(t)=(\partial V/\partial v)(\mathbf{r},t,c_0)$. Those processes have zero mean and are correlated such that $\langle S_i(t_1)S_j(t_2)\rangle=C_{ij}(t_1-t_2)$ with $\langle\cdots\rangle$ indicating an ensemble average over the sound speed fluctuations. To generate time sequences of the two-dimensional vector process $\mathbf{S}(t)$ one needs the conditional probability $p(\mathbf{U_2},t_2|\mathbf{U_1},t_1)$, that is, the probability that $\mathbf{S}(t_2)$ assumes the value $\mathbf{U_2}$ given that $\mathbf{S}(t_1)$ is known to have the value $\mathbf{U_1}$. One finds that

$$p(\mathbf{U_2},t_2|\mathbf{U_1},t_1)=\frac{1}{2\pi\sqrt{\mathrm{Det}(K)}}e^{-(1/2)\mathbf{W}\cdot K^{-1}\cdot\mathbf{W}}, \tag{32}$$

where

$$K_{ij}(t_1-t_2)=C_{ij}(0)-[C(t_2-t_1)C(0)^{-1}C(t_1-t_2)]_{ij}, \tag{33}$$

and

$$\mathbf{W}=\mathbf{U_2}-\mathbf{U_1}\cdot C(0)^{-1}C(t_1-t_2). \tag{34}$$

From Eq. (32) one sees that $\mathbf{W}$ is a Gaussian random vector with correlated components such that $\langle W_iW_j\rangle=K_{ij}$.

Thus, in order to generate a sample sequence of values for $\mathbf{S}(t)$ one initially generates a Gaussian random vector $\mathbf{U_1}$ with correlated components such that $\langle U_{1i}U_{1j}\rangle=C_{ij}(0)$. This provides the initial value of the sequence $\mathbf{S}(t)$. The next value is obtained by first generating another Gaussian random vector $\mathbf{W}$ with correlated components such that $\langle W_iW_j\rangle=K_{ij}$, then the next value is, according to Eq. (32),

$$\mathbf{U_2}=\mathbf{W}+\mathbf{U_1}\cdot C(0)^{-1}C(t_1-t_2). \tag{35}$$

That is, $\mathbf{U_1}$ is the sample value of $\mathbf{S}(t)$ at $t=t_1$ and $\mathbf{U_2}$ is the sample value of $\mathbf{S}(t)$ at $t=t_2$. The next sample value is obtained by setting $\mathbf{U_1}=\mathbf{U_2}$ and using Eq. (35) to get the third value in the sequence. Iterating this procedure one obtains a sample time series for $\mathbf{S}(t)$ and for the pressure field $P(\mathbf{r},t)$ by using Eq. (28).

For the example discussed in this section the fluctuation correlation function was chosen to be a simple function, namely $\rho(r,t)=\rho_0 e^{(-r/L)-(t/T)}$, where ρ_0 is the strength of the sound speed fluctuations, and L and T are, respectively, the correlation length and time of those fluctuations. The fluctuation strength was chosen so that $\rho_0/c_0^2=10^{-4}$. The pulse shape function used was $f(t)=e^{-t^2/2\tau^2}\cos(\omega_0 t)$. The parameters were chosen so that $\omega_0/2\pi=300$ Hz and $\omega_0\tau=2\pi$. For c_0 the value used was typical of sound speed in water, that is, $c_0=1500$ m/s. The time series was computed for a point detector at a range of 1500 m from the source.

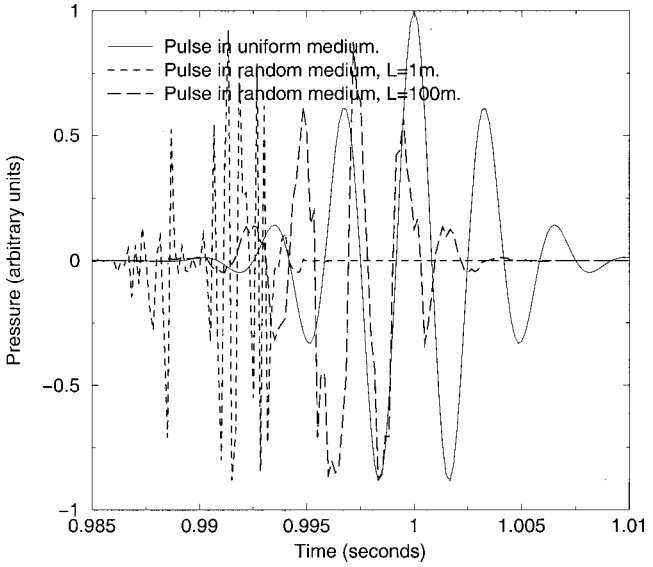

FIG. 1. Pressure as a function of time for both uniform and random media.

Two examples of the resulting time series are presented in Fig. 1. The continuous line representing the received pulse in the absence of fluctuations was included for comparison purposes. The two other time series correspond to two distinct samples of the fluctuations with distinct environmental parameters. In one case, represented by the dashed line, the correlation length of the fluctuations was 1 m while in the other example, represented by a dotted line, the correlation length was 100 m, in both cases the correlation time was 10 s. Otherwise, both examples were computed in exact the same manner.

For those two sample time series in Fig. 1 the main effect of the random fluctuations was to make the pulse arrive earlier than in the absence of fluctuations. This is not a general feature. Different simulations, involving the same parameters but a different sequence of the uniformly distributed random numbers used to generate the Gaussian random vectors, can yield pulses that arrive later than they would arrive in the absence of fluctuations, for example. Basically the reason for this is that any finite sequence of Gaussian random numbers is going to have a preponderance of either positive or negative values, even if, on average, the total number of positive and negative values should be the same. This is the mathematical expression of the implicit assumption that fluctuations of the propagation speed $c(\mathbf{r},t)$ can make c larger or smaller than the background speed c_0. Thus one can invoke Fermat's extremum path argument here. If along the shortest path the fluctuations $c_1(\mathbf{r},t)$ happen to be preponderantly negative, thus reducing the effective propagation speed along this path, the pulse wil be delayed compared to a similar pulse propagating in the absence of propagation speed fluctuations. Similarly if the fluctuations happen to be predominantly positive, thus increasing the effective

propagation speed along such path, the pulse will arrive earlier than a comparable pulse propagating in the undisturbed background medium.

The other major feature noticed in the examples in Fig. 1 is the degradation of pulse coherence and increased pulse spreading as the fluctuation correlation length decreases. This is a general feature which is intuitively expected and verified by many such simulations that were carried out by the author but not shown here. Decreasing the fluctuation correlation length or the fluctuation correlation time leads to increased pulse spreading and loss of coherence. As either the fluctuation correlation length or fluctuation correlation time decreases, the pulse propagates over an environment that is more inhomogeneous as the fluctuations at two separated points will be more likely to be more disparate in sign and magnitude than when the correlation length and time are longer.

The more extensive simulations carried out by the author indicate that the random pulses are, to a very good approximation, Gaussian with zero mean.

V. PULSE STATISTICS IN A RANDOMLY FLUCTUATING MEDIUM

In this section statistical properties of a pulse propagating through a random medium will be evaluated analytically in the weak inhomogeneity approximation assuming the sound speed fluctuations to be Gaussian. It is convenient to start from the expression for the pulse as an average over propagation speeds of pulse shape functions with different arrival times determined by the propagation speeds as given in Eq. (26).

Thus, for the n-point correlation function one has

$$\begin{aligned}\langle P(\mathbf{r_1},t_1)\cdots P(\mathbf{r_n},t_n)\rangle &= \int_0^\infty \frac{dv_1}{4\pi r_1} f\left(t_1-\frac{r_1}{v_1}\right)\cdots\int_0^\infty \frac{dv_n}{4\pi r_n} f\left(t_n-\frac{r_n}{v_n}\right)\\ &\times \frac{1}{\sqrt{(2\pi)^n \mathrm{Det}(M)}} e^{-(1/2)\Sigma_{j,k=1}^n M_{jk}^{-1}(v_j-c_0)(v_k-c_0)}, \quad (36)\end{aligned}$$

where

$$M_{jk}=\langle V(\mathbf{r}_j,t_j,v_j)V(\mathbf{r}_k,t_k,v_k)\rangle. \quad (37)$$

One should notice here that the distribution of the propagation speeds, v, is almost Gaussian but not quite so due to the dependence of the sound speed fluctuation covariance matrix, M, on the propagation speeds.

The simplest approximation that allows one to evaluate the above integral order by order for the pulse shape function previously discussed, and for a few other simple functions too, starts with a change of variables, $v_j=c_0e^{\sigma_j x_j}$ where $\sigma_j^2=1/c_0^2\langle V(\mathbf{r_j},t_j,c_0)^2\rangle$. It is also convenient to introduce the Fourier transform of $f(t_j-r_j/v_j)$,

$$\begin{aligned}f\left(t_j-\frac{r_j}{v_j}\right) &= \int_{-\infty}^\infty \frac{d\omega_j}{2\pi} F(\omega_j)\\ &\times \exp -i\omega_j\left(t_j-\frac{r_j}{c_0}+\frac{r_j}{c_0}(1-e^{-\sigma_j x_j})\right). \quad (38)\end{aligned}$$

$$\begin{aligned}\langle P(\mathbf{r_1},t_1)\cdots P(\mathbf{r_n},t_n)\rangle &= \int_{-\infty}^\infty \frac{d\omega_1}{2\pi}\frac{F(\omega_1)}{4\pi r_1} e^{-i\omega_1[t_1-(r_j/c_0)]}\cdots\\ &\times \int_{-\infty}^\infty \frac{d\omega_n}{2\pi}\frac{F(\omega_n)}{4\pi r_n} e^{-i\omega_n[t_n-(r_n/c_0)]}\\ &\times K\left(\omega_1\frac{r_1}{c_0},\ldots,\omega_n\frac{r_n}{c_0}\right), \quad (39)\end{aligned}$$

where

$$\begin{aligned}K(\alpha_1,\ldots,\alpha_n) &= \int_{-\infty}^\infty dx_1\cdots\int_{-\infty}^\infty dx_n \frac{c_0^n}{\sqrt{(2n)^n \mathrm{Det}(M)}}\\ &\times\exp\left[\sum_{j=1}^n [\sigma_j x_j - i\alpha_j(1-e^{-\sigma_j x_j})]\right.\\ &\left.-\frac{c_0^2}{2}\sum_{j,k=1}^n M_{jk}^{-1}(e^{\sigma_j x_j}-1)(e^{\sigma_k x_k}-1)\right]. \quad (40)\end{aligned}$$

Now, the approximation $e^{\pm\sigma_j x_j}\approx 1\pm\sigma_j x_j$ will be used in the above integral. Also one should notice that

$$\begin{aligned}\frac{1}{\sqrt{\mathrm{Det}(M(\mathbf{x}))}} &= e^{-(1/2)Tr[\ln(M(x))]}\\ &\approx \frac{1}{\sqrt{\mathrm{Det}(M(\mathbf{0}))}}\\ &\times e^{-(1/2)Tr[\Sigma_{j=1}^n x_j Tr[M^{-1}(\mathbf{0})(\partial/\partial x_j)M(\mathbf{0})]}. \quad (41)\end{aligned}$$

Using the above approximations one reduces $K(\alpha_1,\ldots,\alpha_n)$ to a multi-dimensional Gaussian integral which, upon evaluation, yields

$$\begin{aligned}K(\alpha_1,\ldots,\alpha_n) &= \exp\left[-\frac{c_0^2}{2}\sum_{j,k=1}^n (\alpha_j+i\beta_j)\right.\\ &\left.\times(\alpha_k+i\beta_k)M_{jk}^{-1}\big|_{v_j=v_k=c_0}\right], \quad (42)\end{aligned}$$

where

$$\beta_j = 1-c_0\sum_{k=1}^n M_{j,k}^{-1}\frac{\partial}{\partial v_j}M_{k,j}\big|_{v_j=v_k=c_0}. \quad (43)$$

One finds that the analytic results are in good agreement with the averages and other statistics computed from the numerical simulations and allow one to interpret those as will be discussed in the next section. Obviously the numerical simulation also allows for studying pulse statistics for pulse shapes for which, even with the above-mentioned simplifying approximations, analytical results cannot be obtained.

VI. CONCLUSION

In this work pulse propagation through a weakly inhomogeneous medium was studied in a explicit time-dependent approach instead of the traditional frequency domain analy-

sis. The formalism used was the analog in the time domain of the parabolic approximation that has been successfully used in the frequency domain approaches to wave propagation in random medium. The advantages of a time-domain approach go beyond the obvious one of being able to study the propagation of very broadband pulses. It also takes advantage of the fact that our intuition about the physics of wave phenomena is much better when dealing with such phenomena in space and in time rather than in the more abstract frequency and position approach. Finally, such a framework allows for straightforward incorporation of time-dependent propagation speed fluctuations.

The combination of numerical simulation and analytical approximations permitted a thorough analysis of pulse statistics. It was found that numerically the pulse tend to effectively obey Gaussian statistics even though formally it would seem otherwise. This corresponds to nearly saturated propagation in a regime where full saturation is not expected. By formally it is meant by inspection of the analytically calculated moments and correlation functions. However, numerical evaluation of those formulas matches the conclusions of the computer simulations.

This conclusion depends on a complex interaction of pulse characteristics and the fluctuation scales and traveled range. Short pulses exposed to a highly fluctuating propagation speed field between source and receiver will be more randomized than longer pulses. Center frequency and bandwidth also come into play. What is surprising is that ''Gaussianization'' occurs even when there are only about ten fluctuation correlation lengths in range provided that the pulse length is very short compared with range. In signal processing the number of samples available for analysis from a detected signal is estimated by the product of detection time and frequency bandwidth; the larger this product the larger the number of samples that can be extracted from the received time series. One could think that some product of the fluctuation correlation length times the wave-number bandwidth of the pulse could yield a ''Gaussianization'' criterion. But even in this relatively simple situation one has three different length scales playing a role. Thus for ''Gaussianization'' one must have the pulse length (which is inversely related to the frequency bandwidth) much greater than the fluctuation correlation length and the traveled range much greater than the pulse length. While ''Gaussianization'' is a consequence of the central limit theorem, the way this plays out for random fields is much more subtle than in the case of discrete random numbers.

Finally, a few words about possible extensions of this work. The more obvious one is the inclusion of higher-order corrections in the path integral formulation. Another interesting extension is the incorporation of boundaries. A promising approach here involves obtaining the equivalent of Eq. (2) for the case where the background medium has position-varying sound speed and density. Boundaries could then be simulated as regions of rapid transition between sharply different values of those quantities. Such extensions are currently being studied by the author.

ACKNOWLEDGMENTS

This work was supported by the U.S. Naval Research Laboratory and the Office of Naval Research.

[1] A. Ishimaru, *Wave Propagation and Scattering in Random Media* (Academic, New York, 1978).
[2] D. K. Dacol, ''Path integral solution of the time-domain progressive wave equation and wave propagation in random media,'' Waves Random Media **4**, 117 (1994).
[3] B. E. McDonald and W. A. Kuperman, ''Time-domain formulation for pulse propagation including non-linear behavior at a caustic,'' J. Acoust. Soc. Am. **81**, 1406 (1987).
[4] M. A. Leontovich and V. A. Fock, ''Solution of the problem of propagation of electromagnetic waves along the Earth's surface by the parabolic equation method,'' J. Phys. USSR **10**, 13 (1946).
[5] F. D. Tappert, ''The parabolic approximation method,'' in *Wave Propagation and Underwater Acoustics*, edited by J. B. Keller and J. S. Papadakis, Lecture Notes in Physics, Vol. 70 (Springer-Verlag, New York, 1977).
[6] R. Dashen, ''Path integrals for waves in random media,'' J. Math. Phys. **20**, 894 (1979).
[7] R. P. Feynman and A. R. Hibbs, *Quantum Mechanics and Path Integrals* (McGraw-Hill, New York, 1965).
[8] G. B. Whitham, *Linear and Nonlinear Waves* (Wiley, New York, 1974).

Multiple scattering in a reflecting cavity: Application to fish counting in a tank

Julien De Rosny and Philippe Roux[a)]
Laboratoire Ondes et Acoustique, ESPCI, Université Paris VII, 10 rue Vauquelin, 75005 Paris, France

(Received 21 August 2000; revised 6 February 2001; accepted 6 March 2001)

Classical fisheries acoustics techniques are useless in the presence of multiple scattering or reflecting boundaries. A general technique is developed that provides the number and the scattering strength of scatterers in motion placed inside a highly reflecting cavity. This approach is based on multiple scattering theory. The idea is to measure the average effect of the scatterers on the acoustic echoes of the cavity interfaces. This leads to the measure of the scattering mean free path, a typical length that characterizes the scattering strength of the cloud of scatterers. Numerical results are shown to agree with a simple theoretical analysis. Experiments are performed with fish in a tank at two different scales: ultrasonic frequency (400 kHz) in a 1.4-1 beaker with 1-cm-long fish as well as fisheries acoustics frequency (12.8 kHz) in a 30-m^3 tank with 35-cm-long fish. These results have interesting applications to fish target strength measurement and fish counting in aquaculture. [DOI: 10.1121/1.1369101]

PACS numbers: 43.20.El, 43.30.Gv, 43.80.Ev [DLB]

I. INTRODUCTION

Most fish act as strong acoustic reflectors because of their gas-filled swim bladder. During the past 30 years, acoustical measurement of fish abundance has been widely developed, and acoustic devices range now from classical single-beam sonar systems to direction-sensing arrays.[1,2] Acoustic estimation of fish abundance (called echo integration) is based on single scattering theory which assumes that the expected energy of the received echoes is proportional to the number of fish insonified.[3] However, in the presence of boundaries or multiple scattering, this assumption is not valid and echo integration leads to incorrect estimates of fish biomass.[4] In this work, we are interested in the worst case: how to measure the density of a multiple scattering medium inside a highly reflecting cavity? In parallel with numerical and theoretical approaches, we will show that the experimental results have a direct and simple application to fish counting in a tank.

We consider first the general problem of a set of scatterers randomly distributed in a closed cavity. The particularity of the system lies in the fact that the scatterers are continuously moving, whereas the cavity boundaries are motionless. In order to measure the density of scatterers, we must solve the following double problem: first, we have to sort the scatterer echoes from the cavity echoes; second, we wish to count the number of scatterers even if this number is too large to resolve each scatterer separately. If a pulsed source is placed in a closed cavity without scatterers, the backscattered signal is made of multiple echoes due to the reflections of the incident field on the cavity boundaries. In other words, the cavity disperses in time the acoustic energy of the initial pulse. If scatterers are present in the cavity, the backscattered acoustic field is now composed of two parts: the wave field that has interacted at least once with one scatterer and the wave field that has propagated inside the cavity as if there was no scatterer. Using a ray picture of acoustic propagation, the first family is made of rays that have been reflected at least once by one scatterer, whereas the second family corresponds to rays that have been reflected by the cavity interfaces only. For a given backscattered signal, it is obvious that the two families of echoes are not distinguishable. On the other hand, between two successive shots the scatterers move slightly, which allows us to separate the wave field due to the scatterers from the wave field due to the cavity: the echoes that have interacted with scatterers arrive at different times from one shot to another, whereas echoes from the cavity boundaries remain unchanged. If we average the backscattered field over many shots, echoes from the scatterers are attenuated due to destructive interference and the average signal looks like the backscattered signal of the cavity without scatterer. However, the amplitude of these averaged echoes is not the same as the amplitude of the echoes obtained without scatterer in the cavity. Indeed, even if there is no trace of scatterer in the average field, the scatterers were present in the cavity at each shot. The amplitude of an average echo is then proportional to the probability that one ray propagates inside the cavity without any reflection on the scatterers. Of course, the longer the ray path (there can be many reflections on the cavity boundaries), the smaller the probability and the smaller the average amplitude. The aim of this work is then to measure this probability and, with the help of multiple scattering theory, to link the average amplitude of the backscattered field to the density of scatterers inside the cavity.

Another way to understand acoustic propagation inside the cavity+scatterers system is to apply the method of images to the cavity interfaces. For simplicity, we suppose that the cavity is a 2D square in which scatterers are randomly distributed (Fig. 1).

We consider one particular ray that has interacted sev-

a)Author to whom correspondence should be addressed. Electronic mail: philippe.roux@espci.fr

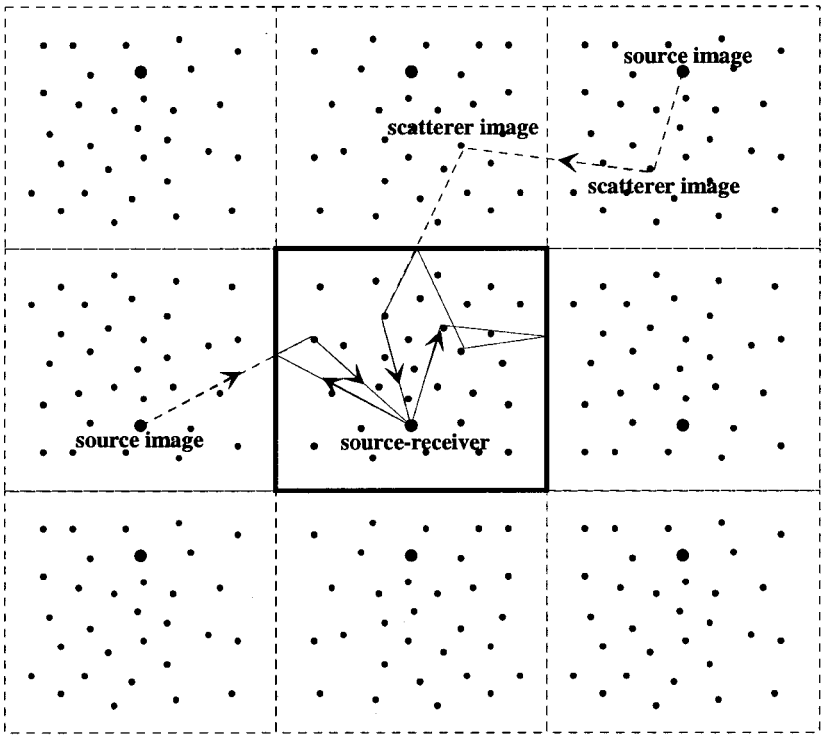

FIG. 1. Representation of two ray paths in a square cavity (full lines) and their analog in a medium without interface (dashed lines) using the method of images.

eral times with the scatterers and the cavity interfaces. From the actual ray path inside the cavity, we define a conjugated image path in free space (Fig. 1). This image path links the image of the source to the actual receiver with reflections on the image of the scatterers. Acoustic propagation inside the cavity is then equivalent to acoustic propagation in a medium without interface between a set of source images and the actual receiver through a set of scatterers images. The cavity+scatterers system is thus equivalent to a sources+scatterers system with no interface. Between two shots, the scatterers move in the cavity and the cavity boundaries are motionless, which means that, in the equivalent medium, the scatterers' images move compared to the motionless source images. The backscattered signal in the cavity can then be interpreted as the transmitted signal obtained at the actual receiver from the source images. Each image of the source simultaneously emits the same signal as the signal emitted by the actual source inside the cavity at time $t=0$. Then, the longest paths inside the cavity correspond to the furthest source images of the equivalent medium and to the latest echo arrivals. The interest of this representation lies in the fact that multiple scattering theory can be applied in free space between a source and a receiver through a cloud of scatterers.[5] For a large number of realizations of a set of scatterers, the coherent intensity I_c is classically defined as the intensity of the average field and the total intensity I_t as the average incoherent intensity.[6] The coherent and incoherent intensity follow the equations

$$I_t(L)=I_0\exp(-L/l_a), \tag{1}$$

$$I_c(L)=I_0\exp(-L/l_a)\exp(-L/l_s), \tag{2}$$

where L is the length of the path between the source and the receiver through the scatterers, l_s is the scattering mean free path which characterizes the elastic scattering strength of the medium, l_a is the absorption mean free path which takes into account both dissipation in the medium and the inelastic scattering strength of the scatterers, and I_0 is the field intensity. In the cavity+scatterers system, the quantity we are interested in is the ratio between the coherent and the incoherent intensity

$$\frac{I_c}{I_t}(L)=\exp(-L/l_s) \tag{3}$$

This ratio only depends on the elastic scattering strength of the scatterers whatever the attenuation in the medium. Transposed in the equivalent medium with the method of images, Eq. (3) can be written by changing from a space variable to a time variable

$$\frac{I_c}{I_t}(t)=\exp(-t/\tau_s), \tag{4}$$

where $\tau_s=l_s/c$, c is the sound speed in the medium, and t is the arrival time of the coherent echo between each source image and the actual receiver in the cavity. Actually, the exponential decrease corresponds to the probability that one cavity echo is scattered by the set of scatterers at time t. Thus, measuring the ratio between the coherent and the incoherent intensity leads to the measurement of l_s, the elastic scattering mean free path. As long as the density of scatterers is not too high, we have the classical relation[7]

$$l_s=\frac{1}{n\sigma_s}, \tag{5}$$

where n is the density of scatterers and σ_s the elastic scattering cross section of the scatterers. If we know σ_s, the measurement of l_s gives the density of scatterers n. On the other hand, knowing the density of scatterers n, the measurement of l_s gives the scattering cross section σ_s. We will

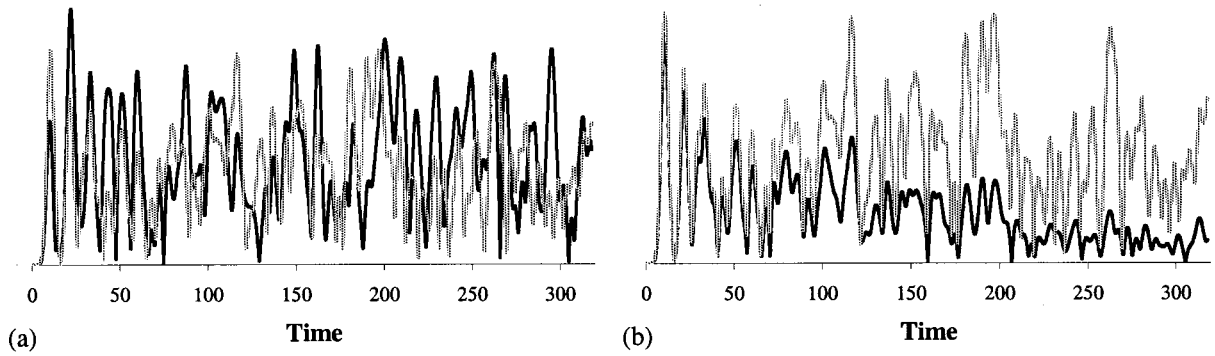

FIG. 2. (a) Envelope of the signal received after one shot on one receiver in the cavity in the presence of 200 scatterers $h(t)$ (bold line) and without scatterers ref(t) (light line); (b) Envelope of the average signal received after 1000 shots on one receiver in the cavity in the presence of scatterers $\langle h(t)\rangle$ (bold line) and without scatterers ref(t) (light line). Time scale corresponds to the number of periods of the acoustic signal.

show in the following that, for the particular case of fish in a tank, a simple double measurement allows us to get both n and σ_s.

After this Introduction, the paper is divided into four parts. Section I deals with a numerical simulation whose application is twofold: we present first an estimator of the scattering mean free path from a set of computed backscattered time series. Second, we use the simulation to study the robustness of the estimator as a function of the parameters of the cavity+scatterers system in a noiseless environment. In Sec. II, we develop a theoretical approach which confirms and generalizes the previous numerical results. We introduce also another estimator of the scattering mean free path based on the correlation between successive shots. In Sec. III, we first compare the robustness of the two estimators with regard to experimental configurations. We report then experimental results at two different scales: in a 25-m^3 tank with 35-cm-long fish at 10-kHz frequency and in a 1.4-l beaker with 1-cm-long fish at 400-kHz frequency. Finally, we discuss applications of this new technique to aquaculture in Sec. IV.

II. NUMERICAL SIMULATION

In this part, we describe acoustic propagation in a 2D cavity+scatterers system with a finite difference simulation. The goal is to closely model the experimental configuration in a noiseless environment while varying some parameters of the system. In particular, we will show how to measure the scattering mean free path from a set of backscattered signals.

For convenience, the cavity is a square but the results do not depend on the cavity shape. We sample space with a $\lambda/5$ grid spacing (λ is the central wavelength) on a $40\lambda\times40\lambda$ grid. The emitted signal is a Gaussian pulse with a 20% bandwidth around the central frequency F. Time is sampled at a $8\times F$ frequency ($\lambda=c/F=cT$). The finite difference simulation is a second-order algorithm. Grid spacing and sampling frequency are a compromise between an accurate numerical result and a reasonable run time. In other words, a $\lambda/5$ grid spacing is not enough to avoid anisotropy and numerical dispersion, but numerical results are good enough to understand the physical insight involved in the problem. We use Dirichlet conditions on the cavity interfaces (i.e., perfect reflection). We define scatterers as grid points whose acoustical impedance is different from the acoustical impedance of the medium. At each shot, K identical scatterers are randomly placed in the cavity. This means that the acoustic wave propagates in a frozen medium from one realization to another. After emission from a point source, the scattered signal is recorded on one or several receivers. Figure 2(a) shows both the received signal in the absence of scatterers ref(t) and the received signal $h(t)$ after one shot in the presence of scatterers. The signal envelopes of course look different, but the average intensity is constant because, in both cases, the acoustic wave propagates in a lossless medium. Figure 2(b) represents the reference signal ref(t) without scatters and the field averaged on 1000 shots $\langle h(t)\rangle$ in the presence of scatterers. As expected, we observe that the scatterers' echoes have vanished in the average field $\langle h(t)\rangle$. Thus, the two signals ref(t) and $\langle h(t)\rangle$ are composed of the same echoes but the amplitude of the average field decreases with time.

We get another perspective on the same phenomenon by considering intensity. For a signal $h(t)$, we define here the instantaneous intensity $h^2(t)$ as the square of the envelope of $h(t)$. Figure 3(a) shows both the intensity of the average field (or coherent intensity) $\langle h(t)\rangle^2$ and the field intensity averaged on 1000 shots $\langle h(t)^2\rangle$ (or incoherent intensity). The decreasing of the coherent intensity observed on $\langle h(t)\rangle^2$ confirms that energy is transferred from cavity echoes to scatterer echoes as time increases. Figure 3(b) is the same as Fig. 3(a) in the presence of absorption. Of course, we observe now that the incoherent intensity $\langle h(t)^2\rangle$ decreases with time but the coherent intensity $\langle h(t)\rangle^2$ still decreases faster. Finally, Fig. 4 shows in a logarithmic scale the ratio $R(t)$ between the coherent intensity $\langle h(t)\rangle^2$ and the incoherent intensity $\langle h(t)^2\rangle$ with or without absorption, respectively. The two curves follow the same slope, which is proportional to the scattering mean free path of the set of scatterers. As stated above [Eq. (4)], this can be written as

$$R(t)=\frac{\langle h(t)\rangle^2}{\langle h^2(t)\rangle}\approx\exp\left(-\frac{tc}{l_s}\right), \tag{6}$$

where c is the sound speed in the medium. Note that the second equality of Eq. (6) is valid only if $\langle h(t)\rangle^2\neq0$. $\langle h(t)\rangle^2=0$ physically means that there is no cavity echo at time t. For example, this occurs in Fig. 4 for $t\sim50\,\mathrm{T}$ and

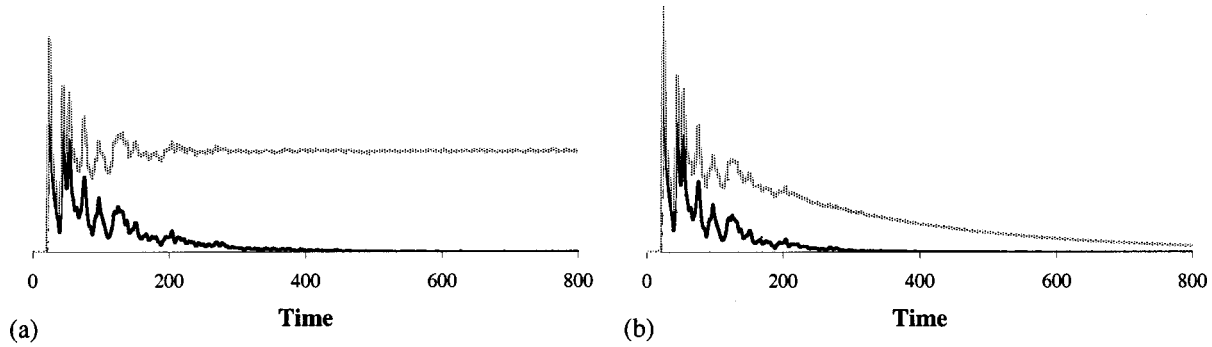

FIG. 3. Comparison between the instantaneous incoherent intensity $\langle h(t)^2 \rangle$ (light line) and the instantaneous coherent intensity $\langle h(t) \rangle^2$ (bold line) for 1000 shots in a squared cavity with 200 scatterers (a) without attenuation; (b) in the presence of absorption (0.017 dB/λ). In each case, the intensity is averaged over 29 receiver positions. Time scale corresponds to the number of periods of the acoustic signal.

$10 \log_{10}(R(t))$ is then not defined. This confirms that we measure the scattering mean free path as an effect of the scatterers *on the cavity echoes*.

Thus, this numerical experiment shows how to extract information about the scattering strength of scatterers placed in a highly reflecting cavity. The solution is to measure the scattering effect as an averaged attenuation $R(t)$ on the amplitude of the successive echoes of the cavity. We have shown that $R(t)$ does not depend on absorption in the medium. Similarly, this result does not depend on attenuation at the cavity interfaces.

Finally, we test the accuracy of the numerical measurement of the scattering mean free path. We choose a density of scatterers $n=0.20$ scatterers/λ^2. We compute numerically with the same simulation the scattering cross section σ_s using one scatterer surrounded by receivers in free space ($\sigma_s = 5.05 \times 10^{-2} \lambda$). From the data represented in Fig. 4, we find $l_{\text{numerical}} = 97\lambda$ to be compared to $l_{\text{theoretical}} = 1/n\sigma_s = 99\lambda$.

The accuracy of the results depends on two different types of average. The first is an average over realizations of the scatterers. This is the basic principle of this work. We average the backscattered field from N shots to make the echoes from the scatterers vanish and to record the amplitude of the cavity echoes in the presence of scatterers. However, if there is no cavity echo at time t or if the cavity echo amplitude is too small, the variance of the estimator $R_N(t) = \langle h(t) \rangle_N^2 / \langle h^2(t) \rangle_N$ becomes important (we define here $\langle \cdots \rangle_N$ as an average over N scatterer realizations). That is why we introduce a second average over the source–receiver positions. When the source–receiver position is changed, then the time arrivals of cavity echoes are changed. In other words, if no cavity echo arrived at time t for a source–receiver in r_0, you may expect one at time t for a source-receiver in r_1. Then, the estimator

$$R_{N,M}(t) = \left[\frac{\langle h(t) \rangle_N^2}{\langle h^2(t) \rangle_N} \right]_M \tag{7}$$

is more robust (we define here $[]_M$ as an average over M source–receiver positions). For example, the fluctuations observed on $R_{N,5}(t)$ for 5 source–receiver positions are more important than the fluctuations observed on $R_{N,29}(t)$ for 29 different source–receiver positions (see Figs. 4 and 5). Another way to artificially increase M, or more generally to increase the robustness of $R(t)$, is to work either with a wideband transducer, an omnidirectional transducer, or in an ergodic cavity. The first solution leads to a larger number of modes excited inside the cavity and thus to a larger number of cavity echoes received at time t. In an ergodic cavity or

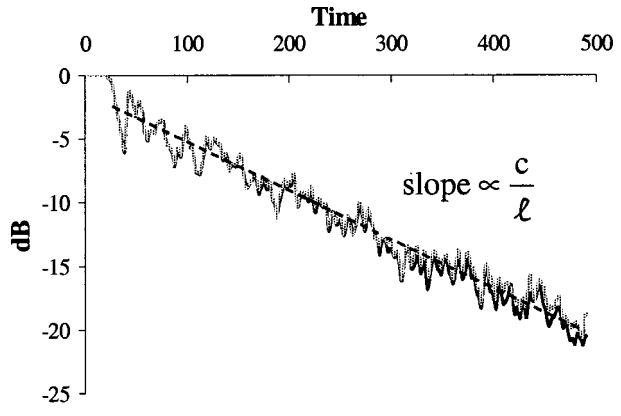

FIG. 4. Representation on a logarithmic scale of the ratio $R(t)$ without attenuation (bold line) and in the presence of absorption (clear line) for 200 scatterers and 1000 shots in a cavity. The dashed line corresponds to the average slope. In each case, the ratio $R(t)$ is averaged over 29 receiver positions. Time scale corresponds to the number of periods of the acoustic signal.

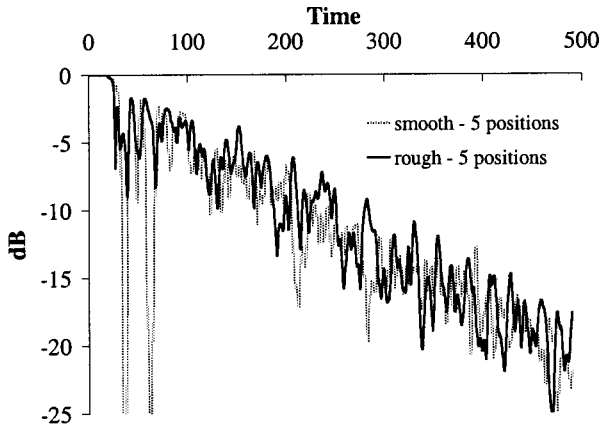

FIG. 5. Representation in a logarithmic scale of the ratio $R_{600,5}(t)$ for 200 scatterers in a smooth cavity (dashed line) and in a rough cavity (bold line). By definition, the ratio $R_{600,5}(t)$ is averaged over 5 receiver positions. Time scale corresponds to the number of periods T of the acoustic signal.

with an omnidirectional transducer, acoustic energy is spread rapidly in the whole cavity, which leads to the same consequences (Fig. 5).

III. THEORETICAL APPROACH

In this part, we verify theoretically the numerical results obtained in Sec. I. More particularly, we show that two different estimators allow us to get the scattering mean free path. One is based, as defined above, on the ratio of the coherent intensity on the incoherent intensity. The other is given by the measure of the average correlation between successive shots. We first recall the two types of average introduced above: the first one $\langle \cdots \rangle_N$ is an average over N realizations obtained by repeatedly illuminating on a randomly distributed set of scatterers. The second one $[\cdots]_M$ is an average on M different source–receiver positions in the cavity for a given realization.

For each shot, we now define the backscattered field at the source $h^i(t)$ in the presence of scatterers as

$$h^i(t) = \tilde{h}(t) + h_r^i(t), \tag{8}$$

where i refers to the realization number, $\tilde{h}(t)$ is the average field obtained for an infinite number of shots, and $h_r^i(t)$ is the residual field that depends on the scatterers' positions from one shot to another. We then write two equations based on energy conservation and multiple scattering theory. Energy conservation leads to

$$[h^{i^2}(t)]_\infty = [\tilde{h}^2(t) + h_r^{i^2}(t)]_\infty = I_0 \exp\left(-\frac{t}{\tau_a}\right), \tag{9}$$

where τ_a corresponds to the characteristic absorption time of the cavity+scatterers system which takes into account acoustic loss in water, on the cavity interfaces as well as acoustic attenuation due to scatterers' inelasticity. I_0 is the total energy transmitted from the source in the cavity. $[]_\infty$ means that we average over an infinite number of source–receiver positions. Equation (9) is based on the assumption that scatterer echoes and cavity echoes are uncorrelated, i.e., $[\tilde{h}(t) h_r^i(t)]_\infty \equiv 0$. On the other hand, multiple scattering theory applied to the scatterers+cavity system implies

$$[\tilde{h}^2(t)]_\infty = I_0 \exp\left(-t\left(\frac{1}{\tau_a} + \frac{1}{\tau_s}\right)\right), \tag{10}$$

where $\tau_s = l_s/c$ and l_s is the elastic scattering mean free path. Equation (10) states that the coherent intensity through a cloud of scatterers exponentially decreases as a function of the length of the path through the scattering medium. We now define

$$\langle h^i(t) \rangle_N = \frac{1}{N} \sum_{i=1}^{N} h^i(t)$$

and

$$\langle h^{i^2}(t) \rangle_N = \frac{1}{N} \sum_{i=1}^{N} h^{i^2}(t).$$

From Eqs. (8), (9), and (10), we show in Appendix A that

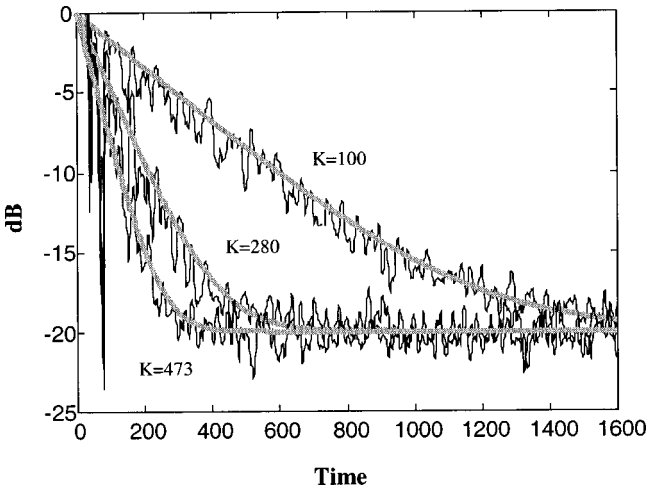

FIG. 6. Comparison on a logarithmic scale between numerical and theoretical results. Numerical $R_{N,M}(t)$ is plotted in black lines for a number K of scatterers, $N=100$ realizations, and $M=15$ receiver positions. Gray lines corresponds to the theoretical $R_{N,\infty}(t)$. Time scale corresponds to the number of periods T of the acoustic signal.

$$R_{N,\infty}(t) = \left[\frac{\langle h^i(t) \rangle_N^2}{\langle h^{i^2}(t) \rangle_N}\right]_\infty = \exp\left(-\frac{t}{\tau_s}\right) + \frac{1}{N}\left(1 - \exp\left(-\frac{t}{\tau_s}\right)\right). \tag{11}$$

The first exponential in Eq. (11) corresponds to the attenuation due to the scattering effect of the scatterers. For a given shot i, the contribution of the average field $\tilde{h}(t)$ to the total field $h^i(t)$ becomes very small as time increases. The second term in Eq. (11) represents then the variance of N random variables $h_r^i(t)$, $i \in [1,N]$.

We now compare this theoretical result to numerical experiments. Figure 6 presents theoretical and numerical results obtained for three different sets of scatterers. Keeping the same scattering cross section σ_s, we first vary the density n of scatterers, thus varying the scattering mean free path $l_s = 1/n\sigma_s$. The estimator $R_{N,M}(t)$ is numerically measured from $N=100$ signals and $M=15$ source–receiver positions. In Fig. 7, we use the same scatterers and the same density (thus keeping l_s constant), but we vary the number N of realizations. In both Figs. 6 and 7, the agreement between theory and numerical results is excellent.

Finally, we present another estimator $S(t)$ which allows us to get the scattering mean free path in a different way. $S(t)$ is based on the average correlation of successive backscattered signals. For each shot $i \in [1,N]$, we consider once again the decomposition of the backscattered field $h^i(t) = \tilde{h}(t) + h_r^i(t)$. We expect $h_r^i(t)$ to change from one shot to another. Measuring $\tilde{h}^2(t)$ is necessary to get the scattering mean free path. With this in mind, instead of measuring the average field on N realizations, we now measure the average correlation between two successive shots. Starting from Eqs. (9) and (10), we show in Appendix B that

$$S_{N,\infty}(t) = \left[\frac{\langle h^i(t) h^{i+1}(t) \rangle_N}{\langle h^{i^2}(t) \rangle_N}\right]_\infty = \exp\left(-\frac{t}{\tau_s}\right), \tag{12}$$

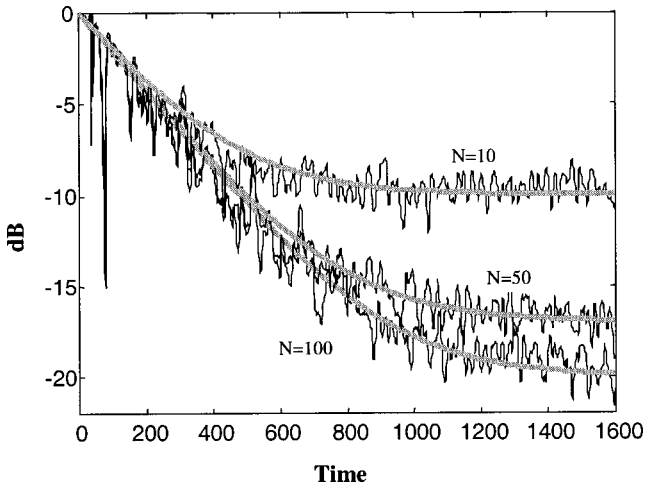

FIG. 7. Comparison on a logarithmic scale between numerical and theoretical results. Numerical $R_{N,M}(t)$ is plotted in black lines for a number $K=100$ of scatterers, N realizations, and $M=15$ receiver positions. Gray lines corresponds to the theoretical $R_{N,\infty}(t)$. Time scale corresponds to the number of periods of the acoustic signal.

where

$$\langle h^i(t)h^{i+1}(t)\rangle_N=\frac{1}{N}\sum_{i=1}^{N} h^i(t)h^{i+1}(t).$$

Equation (12) is valid if $\lfloor h_r^i(t)h_r^{i+1}(t)\rfloor_\infty \equiv 0$, which means that we wait until the scatterer' echoes become uncorrelated between two successive shots. In other words, we wait until the scatterers have sufficiently moved. We represent in Fig. 8 the results obtained for $S_{N,M}(t)$ and $R_{N,M}(t)$ on the same numerical acquisitions. It is important to notice that $S_{N,\infty}(t)$ does not depend on N. On the other hand, $S_{N,M}(t)$ depends on M, meaning that the plateau observed in Fig. 8 for $S_{N,M}(t)$ depends altogether on the number of source–receiver positions, the frequency bandwidth of the emitted signal, and the ergodicity of the cavity.

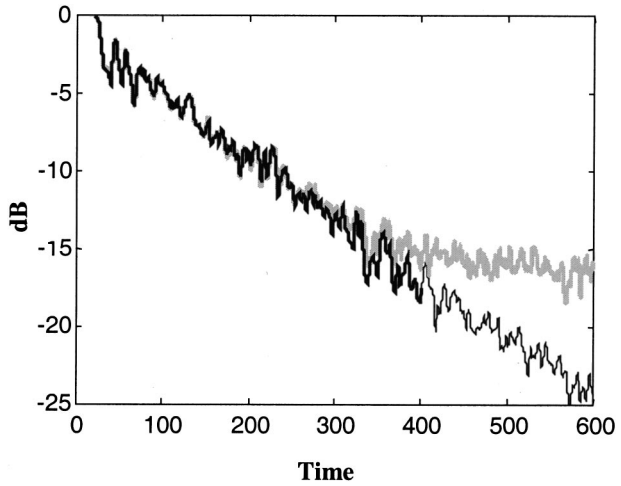

FIG. 8. Comparison in a logarithmic scale between $R_{N,M}(t)$ (black line) and $S_{N,M}(t)$ (gray line) obtained on the same numerical acquisitions: $N=600$, $M=26$, 200 scatterers in a rough cavity. Time scale corresponds to the number of periods of the acoustic signal.

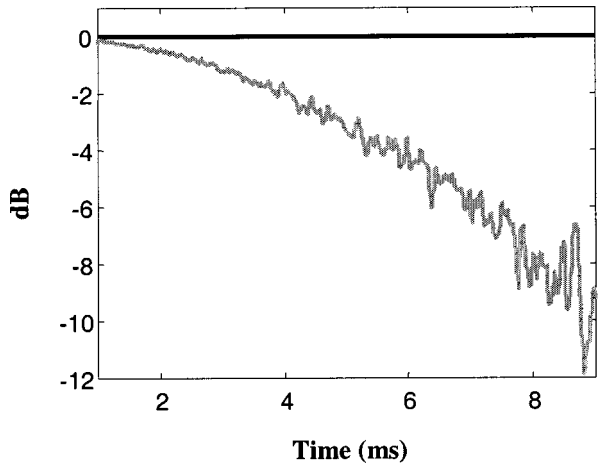

FIG. 9. Experimental comparison in a logarithmic scale between $S_N(t)$ (black line) and $R_N(t)$ (gray line) for $N=400$ shots in a 1.4-1 beaker without fish. Expected result is $10\log_{10}(S_N(t))=10\log_{10}(R_N(t))=0$.

We show in the next section on experimental results the important advantage of the new estimator $S_{N,M}(t)$ compared to $R_{N,M}(t)$.

IV. EXPERIMENTAL RESULTS

In this section, we present experimental results where the scatterers are fish and the cavity is a tank. Experiments are performed at two different scales. We first work with ultrasound at a 400-kHz central frequency transducer (wavelength $\lambda\sim 3.8$ mm) in a 1.8-liter beaker with 1-cm-long zebra fish. The second scale is a more typical scale in aquaculture. We carry out experiments in a 30-m^3 tank with a 12.8-kHz central frequency transducer on 35-cm-long striped bass. The advantage of working at a large scale is that one approaches potential applications. The advantage of working at an ultrasonic scale lies in the ease with which experiments are performed. It is then much simpler to vary all the parameters of the system such as the number of fish, the volume of the beaker, or the position of the source. For this reason, we first focus attention on the ultrasonic experimental results.

The first experiments determine the choice of the estimator we will use to measure the scattering mean free path. To this goal, we place a 400-kHz transducer in a 1.4-1 cylindrical beaker. The transducer works as a source and a receiver. No fish are present in the beaker. After emission of a high-amplitude pulsed signal, we receive long reverberation echoes that last on the order of 8 ms: an 8-ms signal corresponds approximately to a 12-m propagation length, which is very large compared to the typical size of the beaker (on the order of 15 cm). We record a number N of successive impulse responses with which we compute the estimators $R_{N,1}(t)=R_N(t)$ and $S_{N,1}(t)=S_N(t)$. Of course, without fish, all the echoes are due to reflections on the glass beaker and on the water–air interface. Shot after shot, every signal should be the same and we should get $10\log_{10}(S_N(t))=10\log_{10}(R_N(t))=0$. In practice it is not the case, as shown in Fig. 9. As time increases, we observe that $S_N(t)$ is remarkably stable: we have $10\log_{10}(S_N(t))=-0.01$ dB at $t=8$ ms. On the other hand, we see a decrease of the estimator $R_N(t)$ which seems to be biased in this experimental

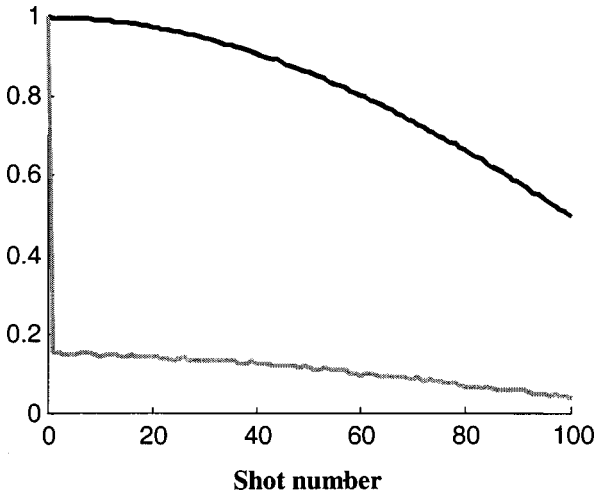

FIG. 10. Correlation coefficient of a selected time window of the back scattered signal as a function of the shot number: without fish (black line) and in the presence of 20 fish in the beaker (gray line). Shot rate is 1 shot/s. The selected time window starts at $t_m = 3$ ms after the beginning of the back scattered signal and lasts 100 μs.

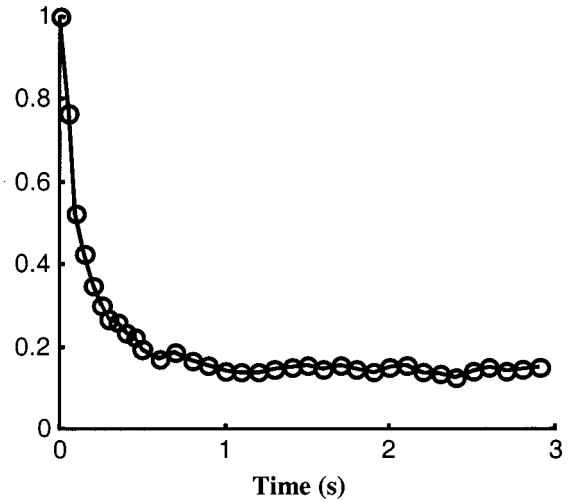

FIG. 11. Correlation coefficient of a selected time window of the back scattered signal as a function of time. There are 20 fish in the beaker. Shot rate is 20 shots/s. The selected time window starts at $t_m = 3$ ms after the beginning of the back scattered signal and lasts 100 μs.

configuration. $R_N(t)$ is based on the recording of N successive time series, which lasts a few minutes. During an $N = 400$ shots experiments lasting 400 s (1 shot/s), we observe temperature variations inside the beaker due to dissipation in the beaker and/or a changing environment in the laboratory. This temperature change $\Delta T \sim 0.2\,^{\circ}\mathrm{C}$ implies a sound velocity change which induces a delay Δt in the time arrivals of the beaker echoes. For instance, for $\Delta c \approx \Delta T \times (\partial c/\partial T)|_T \approx 1$ m/s and if $t_m = 4$ ms is the time arrival of a given echo, we get $\Delta t/T_0 \approx (t_m/T_0)(\Delta c/c) = 1$, where $T_0 = 1/(400 \times 10^3)$ s is the period of the acoustic wave. This means that the echoes become progressively delayed as temperature increases and that the average on the successive shots then turns out to be a destructive average. As a consequence, the use of $R_N(t)$ requires a good stability of the cavity echoes from the beginning to the end of the experiment. $S_N(t)$ is much less sensitive to such slow variations because it is only based on correlation of backscattered signals on successive recordings.

Figure 10 represents the correlation coefficient of a given time window of the signal as a function of shot number. Without fish, we observe the progressive effect of temperature variation on the correlation coefficient. The correlation starts from a plateau equal to 1 for the first seconds but is already under 0.9 after 40 s, corresponding to 40 shots. With fish, the problem is different. $S_N(t)$ is based on the assumption that fish echoes are uncorrelated from one shot to another. Figure 10 shows that a 1 shot/s rate is enough to verify this condition. The value of the correlation after 1 s corresponds then to the correlation coefficient of cavity echoes only and thus to the average value of $S_N(t)$ in the considered time window. Last, we observe once again a slow decrease of the correlation due to temperature effects on cavity echoes. In Fig. 11, we use a short rate of 20 shots/s to measure the decorrelation time of fish echoes. In other words, Fig. 11 is a zoom of the gray curve in Fig. 10 between 0 and 3 s. For ten fish and a 100-μs time window after $t_m = 3$ ms, the decorrelation time is around 0.2 s. In the following, we use the estimator $S_N(t)$ with a 1 shot/s rate to experimentally measure the scattering mean free path.

In this paragraph, we study the effects of ripples that may be generated by fish or wind at the water–air interface on the measure of the scattering mean free path. Of course, it is difficult to reproduce in a beaker wind-driven disturbances that occur in a large tank. However, in order to obtain qualitative results, we perform the following experiment: we measure $S_N(t)$ with $N = 100$ shots in a 1.4-1 beaker in the absence of fish while creating surface waves at the water–air interface. Experimental results are presented in Fig. 12. The two upper curves correspond to two experiments in which the water–air interface is similarly hit by a needle every two

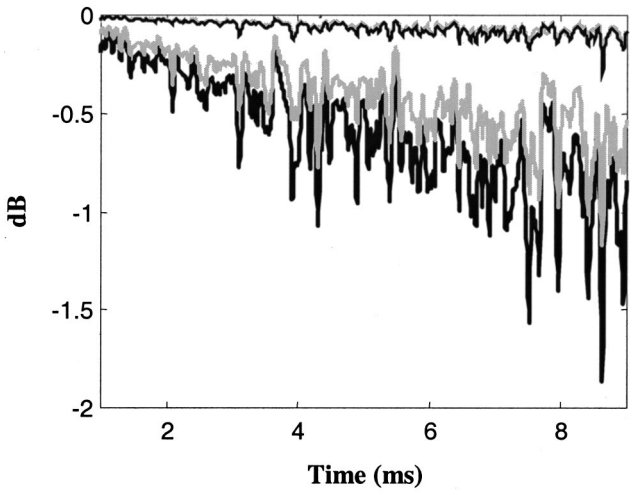

FIG. 12. Experimental measurement of $S_N(t)$ for $N = 100$ shots at 400 kHz in a 1.4-1 beaker without fish in the presence of surface disturbances at the water–air interface. Results are presented in a dB scale. The two upper curves (thin gray and black lines) correspond to two experiments performed with small-amplitude surface disturbances. The equivalent scattering cross section is $\sigma_s = 2.4\ \mathrm{mm}^2$. The two lower curves (full gray and black lines) correspond to two experiments with high-amplitude surface disturbances. The equivalent scattering cross section is $\sigma_s \sim 26\ \mathrm{mm}^2$.

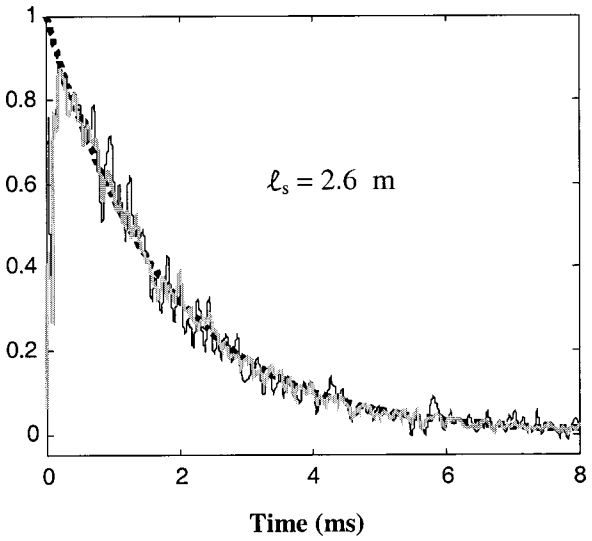

FIG. 13. Experimental measurement of $S_{N,M}(t)$ for $N=100$ and $M=1$ (black line) or $M=5$ (gray line). $S_{N,5}(t)$ looks smoother than $S_{N,1}(t)$. The experiment is performed at 400 kHz with 40 fish in a 1.4-1 beaker. The dotted line corresponds to the theoretical $S_{N,\infty}(t)$. From the theoretical fit, we get $l_s=2.6$ m.

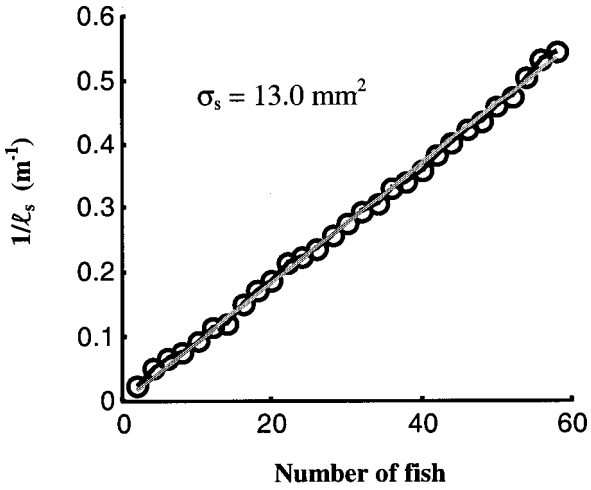

FIG. 14. Experimental measurement of $1/l_s$ as a function of the number of fish. Experiments are performed with $N=200$ shots and $M=1$ source–receiver positions. The slope of the curve is proportional to the fishes' average scattering cross section. We find $\sigma_s=13.0\,\mathrm{mm}^2$ with a 3% standard deviation.

shots. This would reproduce on the water–air interface the behavior of very active fish, for example during fish feeding. Results are very close from one experiment to the other. The two lower curves correspond to two experiments in which the surface is continuously hit by the same needle. The amplitude of surface waves, though difficult to measure in the beaker, seems much larger in this case. For example, this would reproduce strong wind-driven disturbances at the water–air interface. Results are comparable from one experiment to the other. In the absence of fish in the beaker, an ideal experiment gives $10\log_{10}(S_N(t))=0$ (cf. Fig. 9). Fluctuations at the surface induce a slow decrease of $S_N(t)$ as if scatterers were present in the cavity. In the case of small surface disturbances like the one that could be generated during fish feeding by the fish themselves, we obtain $l_s=586$ m. This corresponds to the scattering mean free path obtained with one fish whose scattering cross section is 2.4 mm^2. This scattering cross section is small compared to the scattering cross section of one zebra fish at 400 kHz ($\sigma_s=13.0$ mm^2, see Fig. 14). In the case of surface waves equivalent to strong wind-driven disturbances, we obtain $l_s\sim 54$ m. This corresponds to the scattering mean free path obtained with two zebra fish in the beaker ($\sigma_s\sim 26\,\mathrm{mm}^2=2\times 13\,\mathrm{mm}^2$). These results show that surface agitation may affect the measure of the scattering cross section of scatterers present inside the cavity. The relevant parameters are both the root-mean-square height of surface disturbances with respect to the acoustic wavelength and the area of the water–air interface compared to the total area of the cavity.

The next set of experiments focuses on the study of the parameters of the beaker+fish system at an ultrasonic scale. In particular, we study the influence of the beaker volume, the number of fish, and the source–receiver positions on the measurement of the scattering mean free path. Figure 13 represents the estimator $S_{N,M}(t)$ for $N=100$, and $M=1$ or $M=5$ source–receiver positions, respectively. The experiment is performed with $K=40$ fish in a 1.4-1 beaker. It confirms the average effect observed previously with numerical experiments. The standard deviation of the estimated scattering mean free path l_s is around 3%. Figure 14 shows the influence of the number of fish on the scattering mean free path. Experiments are performed here with $N=200$ shots and $M=1$ source–receiver positions. These results validate the definition of the scattering mean free path in a diluted medium $l_s=1/n\sigma_s$. Knowing the density of scatterers, the measure of l_s leads to a very accurate measure of the scattering cross section (Fig. 14). Finally, Fig. 15 shows that the measure of the scattering cross section does not depend on the volume of the beaker.

We complete this section by reporting a set of experiments conducted at a scale close to fisheries acoustics standards. We worked with an omnidirectional 12.8-kHz transducer in a 30-m^3 tank on 35-cm-long striped bass. Two experiments were performed with $K=161$ and $K=211$ fish, respectively. Results are presented in Fig. 16. Once again,

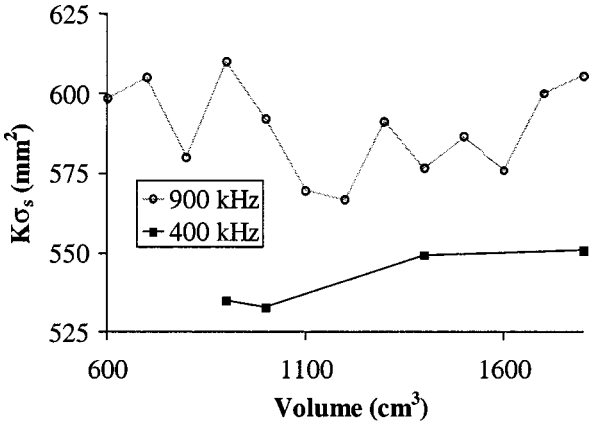

FIG. 15. Experimental measurement of $K\sigma_s$ ($K=40$ fish) at two different frequencies as a function of the beaker volume. Experiments are performed with $N=200$ shots and $M=1$ source–receiver position. Standard deviation is less than 5%. Results show that the measure of σ_s does not depend on the beaker volume.

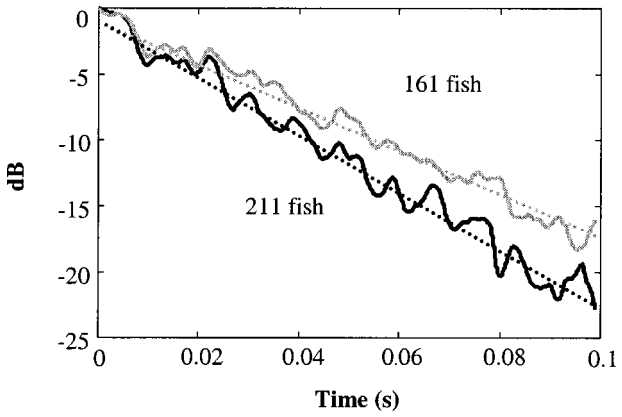

FIG. 16. Experimental measurement of $S_{N,M}(t)$ (plotted here on a logarithmic scale) for $N=1000$ shots and $M=5$ source–receiver positions. Experiments are performed at 12.8 kHz in a 30-m^3 tank on 35-cm-long fish. Dashed lines correspond to the average slopes.

the behavior of the estimator $S_{N,M}(t)$ is in agreement with the previous theoretical and numerical predictions. The fish density being known, we obtain an average value of the fish scattering cross section. For the two different values of the number K of fish, we find the same target strength TS, which confirms the consistency of the experimental results. We have $\mathrm{TS}=10\log_{10}(\sigma_s/4\pi)\approx-35\,\mathrm{dB}$. Considering the fish swim bladder as an air-filled sphere, we get $\sigma_s=4\pi R^2$ with $R\sim 3.8\,\mathrm{cm}$, which is in agreement with the fish size.

In summary, these experiments performed at different scales with small fish in a beaker or large fish in a tank validate theoretical predictions. Moreover, we see in the next section that they lead to interesting applications in fisheries acoustics.

V. DISCUSSION

This last section is threefold: first, we describe potential applications of this method to fisheries acoustics. The second part is devoted to experimentalists who would like to reproduce these experiments. To this regard, we try to define some optimal experimental configurations. Last, we extend this work to multiple scattering in a fish school in the ocean.

The main point of this work is the measure of the scattering mean free path of a set of scatterers placed inside a reflecting cavity. The measure of the scattering mean free path $l_s=1/n\sigma_s$ leads to the measure of the scattering cross section of the scatterers if the scatterer density is known. This is of particular interest in fisheries acoustics, where a great amount of time is spent on scattering cross-section measurement.[8] Of course, this measure does not correspond to standards such as the dorsal or the lateral scattering cross section used classically in fisheries acoustics. However, this technique combines three advantages: it is simple and low cost (it just requires one transducer and an acquisition channel), it is fast (one obtains an accurate scattering cross section with $N\sim 200$ shots, which lasts a few minutes), and it provides a reference measurement, the total scattering cross section, which does not depend on the angle of incidence of the acoustic wave, on the anisotropy of the fish backscatter function, or on the fish behavior in the tank. In future work, it would then be of great interest to apply this technique to study the influence of physical and biological parameters on the scattering cross section: depth, water temperature, or salinity, but also amount of food in the fish stomach or fish sexual maturation. The measurement could either be done on one fish (in a small tank) or on a given number of fish with the same characteristics (then, we measure the average scattering cross section of the fish).

TABLE I. Experimental results obtained performing fish counting at 400 kHz in a 1.4-1 beaker. Experiments are performed with $N=200$ shots and $M=1$ source–receiver position.

Number of fish	25	18	13	7	4
Results of fish-counting experiments	25.7	18.7	14	8.2	4.7

The other application of the scattering mean free path measurement concerns aquaculture and, more particularly, fish counting in a tank. Fish counting is a two-stage experiment. Actually, measuring the fish density via the scattering mean free path requires the knowledge of the scattering cross section. To this end, we propose a first experiment with a given number of fish in a small tank that will be used as a test tank. Knowing the fish density n, we measure the scattering mean free path l_s and thus the scattering cross section σ_s. Then, we place the transducer in the tank that is to be sampled and from which came the fish placed in the test tank. We assume that all fish in the tank have approximately the same characteristics, which is usually true in aquaculture. The previously measured σ_s is then a good approximation of the average σ_s for all fish in the tank. The new measure of l_s provides the fish density n and thus the number of fish in the tank. Following this double-step procedure, we perform several fish-counting experiments in a 1.4-1 beaker at 400 kHz. Table I summarizes the results. The accuracy of the measurements is remarkable, taking into account that fish size distribution is quite heterogeneous.

Concerning the experimental setup, its main advantage relies on the simplicity of the electronics. It is made of one transducer, a waveform generator, a power amplifier, and an acquisition channel. We have shown that the accuracy of the measure of the scattering mean free path is improved by an average over the transducer positions. Because this is not always practical in a tank, we suggest the use of an omnidirectional and/or wide band transducer. Then, the optimal configuration is obtained when the scattering mean free path l_s is on the order of 5 times the characteristic length of the tank $L(l_s\sim 5L)$. This means that after ten round trips inside the cavity, we would get

$$10\log_{10}\left(S\left(t=\frac{20L}{c}\right)\right)=10\log_{10}(\exp(-4))\approx-17.5\,\mathrm{dB}. \tag{13}$$

In this case, we expect to measure on a long time scale a linear decrease of the estimator $S(t)$ from 0 dB down to nearly -20 dB. This configuration should provide an accurate value of the average slope of $S(t)$ on a logarithmic scale. In practice, the parameters that need to be adjusted are the tank volume, the number of scatterers, and the central fre-

quency of the transducer. The relationship between frequency and scattering cross section is rather complex. A good choice is to use a central wavelength comparable to the typical size of the scatterers (the length of the swim bladder for fish, for instance). Then, concerning the application to fish counting, where a double measurement in two tanks is required, it may be of interest to work with a similar mean free path in the two tanks. In this case, a constant mean free path means a constant density. For instance, if the fish density corresponds to 5000 fish in a 40-m^3 tank, one could first work with 50 fish in a 400-liter test tank to measure the average scattering cross section of the fish.

Finally, we consider application to fisheries acoustics: is there multiple scattering in fish schools in the ocean? In multiple scattering theory, the scattering mean free path l_s is classically used as the typical length scale for multiple scattering: multiple scattering cannot be neglected as soon as $L > l_s$, where L is the width of the scattering medium. This criterion is valid when the scattering cross section of the scatterers is isotropic. In the case of anisotropic scatterers, such as fish, the scattering mean free path has to be replaced by the transport mean free path l^*, which is, in general, at most the double of the scattering mean free path l_s ($l_s \leqslant l^* \leqslant 2l_s$). With 35-cm-long striped bass in a tank, we experimentally got $l_s \sim 25$ m at a 12.8-kHz frequency for an $n \sim 7$ fish/m^3 density. According to Eq. (3), we would get $l_s \sim 5$ m with a 35-fish/m^3 density. This means that multiple scattering should not be neglected for a 35-cm-long striped bass school with a density $n \sim 35$fish/m^3 and whose width $L > 10$ m. These conditions seem to be easy to obtain in the ocean. This point is interesting because presence of multiple scattering may then lead to bias in fish biomass assessment usually performed under a strong, single scattering approximation.

ACKNOWLEDGMENTS

This work is born from a collaboration between the Marine Physical Laboratory, Scripps Institution of Oceanography, UC San Diego, and the Laboratoire Ondes et Acoustique, ESPCI, Paris. Fish experiments at 12.8 kHz have been performed in San Diego with the help of Jules Jaffe, Gerald D'Spain, Dan Sternlicht, Richard Harriss, and Fernando Simonet. A special thank you to Stephen Mitchell, from Kent Sea Tech Corporation (San Diego), who graciously lent us more than 200 striped bass, and to Frederic Rosa, from the Ecole Normale Superieure (Paris), who gave us zebra fish. Finally, nothing would have been done without William A. Kuperman's encouragement. This work was partly done while P.R. was at Marine Physical Laboratory, Scripps Institution of Oceanography, UCSD, San Diego, CA.

APPENDIX A:

We wish to get an analytic formula for

$$R_{N,\infty}(t) = \left[\frac{\langle h^i(t) \rangle_N^2}{\langle h^{i^2}(t) \rangle_N} \right]_\infty . \tag{A1}$$

We start from Eqs. (8), (9), and (10)

$$h^i(t) = \tilde{h}(t) + h_r^i(t), \tag{8}$$

$$[h^{i^2}(t)]_\infty = [\tilde{h}^2(t) + h_r^{i^2}(t)]_\infty = I_0 \exp\left(-\frac{t}{\tau_a} \right), \tag{9}$$

$$[\tilde{h}^2(t)]_\infty = I_0 \exp\left(-t\left(\frac{1}{\tau_a} + \frac{1}{\tau_s} \right) \right). \tag{10}$$

We have

$$\langle h^i(t) \rangle_N^2 = \left(\frac{1}{N} \sum_{i=1}^{N} h^i(t) \right)^2 = \frac{1}{N^2} \sum_{i=1}^{N} h^{i^2}(t) + \frac{1}{N^2} \sum_{i}^{N} \sum_{j \neq i}^{N} h^i(t) h^j(t). \tag{A2}$$

Using Eq. (8) and averaging over source–receiver positions, we obtain

$$[\langle h^i(t) \rangle_N^2]_\infty = \frac{1}{N^2} \sum_{i=1}^{N} [h^{i^2}(t)]_\infty + \frac{1}{N^2} \sum_{i}^{N} \sum_{j \neq i}^{N} [\tilde{h}^2(t) + h_r^i(t) h_r^j(t) + \tilde{h}(t) h_r^i(t) + \tilde{h}(t) h_r^j(t)]_\infty \tag{A3}$$

We assume then that

$$\lfloor \tilde{h}(t) h_r^i(t) \rfloor_\infty = \lfloor h_r^j(t) h_r^i(t) \rfloor_\infty \equiv 0. \tag{A4}$$

This physically means, first, that echoes from the scatterers are uncorrelated from one shot to another, and second, that scatterers echoes and cavity echoes are also uncorrelated. It follows:

$$[\langle h^i(t) \rangle_N^2]_\infty = \frac{1}{N} [h^{i^2}(t)]_\infty + \frac{1}{N^2} N(N-1) [\tilde{h}^2(t)]_\infty . \tag{A5}$$

Using Eqs. (9) and (10), we get

$$[\langle h^i(t) \rangle_N^2]_\infty = \frac{1}{N} I_0 \exp(-t/\tau_a)(1 + (N-1) \times \exp(-t/\tau_s)). \tag{A6}$$

Concerning the denominator of $R_{N,\infty}(t)$, we have

$$[\langle h^{i^2}(t) \rangle_N]_\infty = \frac{1}{N} \sum_{i=1}^{N} [h^{i^2}(t)]_\infty = I_0 \exp(-t/\tau_a). \tag{A7}$$

From Eqs. (A6) and (A7), we finally obtain

$$R_{N,\infty}(t) = \left[\frac{\langle h^i(t) \rangle_N^2}{\langle h^{i^2}(t) \rangle_N} \right]_\infty = \exp\left(-\frac{t}{\tau_s} \right) + \frac{1}{N} \left(1 - \exp\left(-\frac{t}{\tau_s} \right) \right). \tag{11}$$

APPENDIX B:

We wish to get an analytic formula for

$$S_{N,\infty}(t) = \left[\frac{\langle h^i(t) h^{i+1}(t) \rangle_N}{\langle h^{i^2}(t) \rangle_N} \right]_\infty . \tag{B1}$$

Once again, we start from Eqs. (8), (9), and (10). We have

$$\langle h^i(t)h^{i+1}(t)\rangle_N=\frac{1}{N}\sum_{i=1}^{N} h^i(t)h^{i+1}(t). \tag{B2}$$

Using Eq. (8) and averaging over source–receiver positions, we obtain

$$[\langle h^i(t)h^{i+1}(t)\rangle_N]_\infty=\frac{1}{N}\sum_{i=1}^{N}[\tilde{h}^2(t)]_\infty+\frac{1}{N}\sum_{i}^{N}[h_r^i(t)h_r^{i+1}(t) + \tilde{h}(t)h_r^i(t)+\tilde{h}(t)h_r^{i+1}(t)]_\infty. \tag{B3}$$

As in Appendix A, we assume that

$$\lfloor\tilde{h}(t)h_r^i(t)\rfloor_\infty=\lfloor h_r^i(t)h_r^{i+1}(t)\rfloor_\infty\equiv 0. \tag{B4}$$

It follows, using Eq. (10):

$$[\langle h^i(t)h^{i+1}(t)\rangle_N]_\infty=I_0\exp\left(-1\left(\frac{1}{\tau_a}+\frac{1}{\tau_s}\right)\right). \tag{B5}$$

From Eqs. (9) and (B5), we finally obtain

$$S_{N,\infty}(t)=\left[\frac{\langle h^i(t)h^{i+1}(t)\rangle_N}{\langle h^{i^2}(t)\rangle_N}\right]_\infty=\exp\left(-\frac{t}{\tau_s}\right). \tag{12}$$

[1] D. N. Mac Lennan, ''Acoustical measurement of fish abundance,'' J. Acoust. Soc. Am. **87**, 1–15 (1990).

[2] E. J. Simmonds, S. T. Forbes, and P. J. Stevens, ''Design, construction and testing of a multi-beam transducer for *in situ* target strength measurement,'' FAO Fish. Rep. 300, pp. 18–26, 1984.

[3] K. G. Foote, ''Linearity of fisheries acoustics, with addition theorems,'' J. Acoust. Soc. Am. **73**, 1932–1940 (1983).

[4] T. K. Stanton, ''Multiple scattering with applications to fish-echo processing,'' J. Acoust. Soc. Am. **73**, 1164–1169 (1983).

[5] A. Ishimaru, *Wave Propagation and Scattering in Random Media* (Academic, New York, 1978), Vols. I and II.

[6] *New Aspects of Electromagnetic and Acoustic Wave Diffusion*, edited by the POAN research group, Springer Tracts in Modern Physics, Vol. 144 (Springer, Berlin, 1998).

[7] P. Sheng, *Introduction to Wave Scattering, Localization, and Mesoscopic Phenomena* (Academic, San Diego, 1995).

[8] K. G. Foote, ''Summary of methods for determining fish target strength at ultrasonic frequencies,'' ICES J. Mar. Sci. **46**, 211–217 (1991).

Reflectance properties of two-dimensional sonic band-gap crystals

L. Sanchis[a] and F. Cervera
Centro Tecnológico de Ondas, Unidad Asociada de Investigación (CSIC), Edificio de Institutos II, Universidad Politécnica de Valencia, Avenida de los Naranjos s/n, 46022 Valencia, Spain

J. Sánchez-Dehesa[b]
Departamento de Física Teórica de la Materia Condensada, Facultad de Ciencias (C-V), Universidad Autónoma de Madrid, 28049 Madrid, Spain

J. V. Sánchez-Pérez, C. Rubio, and R. Martínez-Sala
Centro Tecnológico de Ondas, Unidad Asociada de Investigación (CSIC), Edificio de Institutos II, Universidad Politécnica de Valencia, Avenida de los Naranjos s/n, 46022 Valencia, Spain

(Received 23 August 2000; accepted for publication 12 March 2001)

An analysis of the reflectance of sonic band-gap crystals consisting of square arrays of rigid cylinders in air is presented. The standing wave formed in front of the structures is studied both experimentally and theoretically. Experiments have been performed with a mobile robotized microphone that obtains pressure maps on the plane perpendicular to the axes of the cylinders. Enhancements of the standing wave ratio (SWR) are observed in frequency regions where attenuation bands appear in zero-order transmission experiments. Also, the SWR presents oscillations that can be related to the finite dimension of the structure (Fabry–Perot effect). Both features are well described by calculations based on a double-scattering approach. © *2001 Acoustical Society of America.* [DOI: 10.1121/1.1369784]

PACS numbers: 43.20.Fn, 43.20.Ks, 43.20.Ye [ANN]

I. INTRODUCTION

The existence of frequency regions where the propagation of electromagnetic waves is forbidden was predicted in certain structures having a periodic modulation of the dielectric function.[1,2] The structures that exhibit such behavior are called photonic-band-gap (PBG) materials. The underlying theory has been applied to other types of waves like sound or elastic waves and the corresponding structures are called sonic-band-gap (SBG) or elastic-band-gap (EBG) materials. Great theoretical effort has been put into the study of these kinds of waves.[3–6] Most of the works calculated the acoustic band structure of infinite crystal using the plane-wave expansion method. Recently, other approaches based on a variational method[7] and a Korringa–Khon–Rostoker method[8] have been developed. On the other hand, finite systems have been studied by the transfer-matrix method[9] and multiple-scattering theory.[10] In this work we use multiple-scattering theory to study our finite samples. In our approach each scatterer is characterized by its scattered pressure, which links the diffracted pressure field to the incoming one. Our procedure is a simplified version of the one employed in Ref. 11, which uses a rigorous multiple-scattering theory to study light scattering by dielectric cylinders. We will see that this simplified approach, which takes up to double-scattering events, reproduces the experiments fairly well.

Most experimental work on SBG structures reports zero-order attenuation spectra.[7,12,13] A recent paper by Torres *et al.*[14] shows nice pictures of Bloch waves on a liquid having wave velocity modulation. In the same spirit we have developed an experimental setup which permits the measurement of pressure patterns in the plane where the two-dimensional arrays of scatterers are deployed.

Making use of both theoretical and experimental tools, our goal in this work is to study the reflectance properties of SBG crystals formed by two-dimensional arrays of rigid rods in air. Those properties will be inferred from the study of the partial standing wave formed in front of the SBG structure. As we discuss below, the method of pressure measurement effectively detects a full standing wave whose standing wave ratio (SWR) allows the characterization of some features in the acoustic band structure. Also, the comparison with our model based on a multiple-scattering approach facilitates such analysis.

II. THEORETICAL APPROACH

A. Sound scattering by an ensemble of rigid cylinders in single-scattering approach

Let us first compute the scattering of a sound plane wave, with frequency ω, by a cylinder of radius R_0 placed at the origin of coordinates. The incident wave travels in a direction perpendicular to the cylinder's axis (i.e., along the positive X axis) and impinges on a cylinder infinite along the Z axis. If we assume a temporal dependence $e^{-i\omega t}$, the wave can be expressed as

$$P^{\text{incid}} = e^{ikx} = e^{ikr\cos\theta} = \sum_{s=-\infty}^{s=\infty} i^s J_s(kr) e^{is\theta}, \tag{1}$$

where k is the wave number ($k=2\pi/\lambda$) and J_s is the Bessel function of the first kind and order s. The scattered wave takes the form

[a]Electronic mail: lsanchis@fis.upv.es
[b]Electronic mail: jose.sanchezdehesa@uam.es

$$P^{\text{scatt}} = \sum_{s=-\infty}^{s=\infty} A_s H_s(kr) e^{is\theta}, \tag{2}$$

where H_s is the Hankel function of the first kind and order s with the superscript (1) omitted for simplicity; $H_s(z) = J_s(z) + iY_s(z)$, $Y_s(z)$ is the Bessel function of the second kind and order s. The coefficients A_s are calculated by applying the boundary condition on the cylinder's surface.

If we assume a rigid cylinder, the radial velocity of the air particles at the surface must be zero. This velocity is generated by the combination of the plane wave and the scattered wave. Since the velocity is proportional to the pressure gradient, this boundary condition is

$$\frac{\partial}{\partial r}[P^{\text{inc}} + P^{\text{scatt}}]_{r=R_0} = 0. \tag{3}$$

After an easy calculation, the coefficients are

$$A_s = \frac{-i^s (J_{s-1}(kR_0) - J_{s+1}(kR_0))}{(H_{s-1}(kR_0) - H_{s+1}(kR_0))}. \tag{4}$$

The total pressure at any point on the XY plane is the sum of the scattered wave and the incident wave

$$P = P^{\text{inc}} + P^{\text{scatt}}. \tag{5}$$

Now, if we consider that the wave is scattered not by a single cylinder but by an ensemble, a scattered wave is generated on every cylinder and, therefore, to obtain the net pressure we have to add the waves of all cylinders at any point of the XY plane. This is a single-scattered approach since it involves the scattered pressure originated in each cylinder by just the incident wave arriving on it. Let us assume that the jth cylinder is placed at the point (x_j, y_j); so, if we take the phase origin at $x=0$, when the plane wave reaches this cylinder its phase will be kx_j, and the corresponding scattered pressure at this point must be the same as the one calculated above multiplied by the phase factor $\exp(ikx_j)$

$$P_j^{\text{scatt}} = e^{ikx_j} \sum_{s=-\infty}^{s=\infty} A_s H_s(kr_j) e^{is\theta_j}. \tag{6}$$

Therefore, the total pressure at the point (x, y) takes the form

$$\begin{aligned} P(x,y) &= P^{\text{inc}} + \sum_{j=1}^{N} P_j^{\text{scatt}} \\ &= e^{ikx} + \sum_{j=1}^{N} e^{ikx_j} \sum_{s=-\infty}^{s=\infty} A_s H_s(kr_j) e^{is\theta_j}, \end{aligned} \tag{7}$$

N being the number of cylinders ($j = 1, \ldots, N$).

We must keep in mind that this pressure field is related to the system of coordinates of each cylinder j

$$\begin{aligned} r_j &= \sqrt{(x-x_j)^2 + (y-y_j)^2}, \\ \theta_j &= \arcsin((y-y_j)/r_j). \end{aligned} \tag{8}$$

This approach usually works well in systems where the scatterers are distant enough from each other; in other words, when the fraction of volume occupied by the cylinders is small.

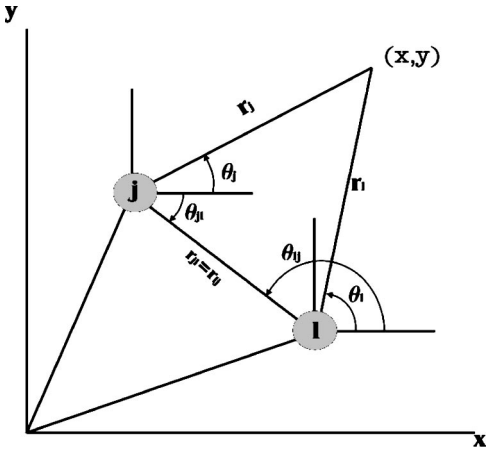

FIG. 1. Notation used for a change of coordinate system between cylinder jth and lth. They are placed at the points (x_j, y_j) and (x_l, y_l).

B Sound scattering by an ensemble of cylinders with double-scattering term

Now, consider cylinder jth and lth shown in Fig. 1. As we mentioned before, the field generated by the plane wave on the jth cylinder is

$$P_j = e^{ikx_j} \sum_{s=-\infty}^{s=\infty} A_s H_s(kr_j) e^{is\theta_j}. \tag{9}$$

Using Graf's formula[15] for the Hankel function, we can express the term $H_s(kr_j)e^{is\theta_j}$ in the lth coordinate system

$$H_s(kr_j)e^{is\theta_j} = \sum_{q=-\infty}^{q=\infty} e^{[i(s-q)\theta_{lj}]} H_{q-s}(kr_{lj}) J_q(kr_l) e^{iq\theta_l}. \tag{10}$$

The pressure scattered by the jth cylinder in the system of coordinates of the lth cylinder is

$$P_{jl} = \sum_{s=-\infty}^{s=\infty} A_s e^{ikx_j} \sum_{q=-\infty}^{q=\infty} e^{[i(s-q)\theta_{lj}]} H_{q-s}(kr_{lj}) J_q(kr_l) e^{iq\theta_l}. \tag{11}$$

The field generated at the lth cylinder produced by the wave scattered by the jth cylinder can be written in the following form:

$$PP_{jl} = \sum_{s=-\infty}^{s=\infty} A_{jls} H_s(kr_l) e^{is\theta_l}. \tag{12}$$

If we apply the boundary condition on the lth cylinder

$$\frac{\partial}{\partial r_l}[P_{jl} + PP_{jl}]_{r_l=R_o} = 0, \tag{13}$$

$$\begin{aligned} \frac{\partial}{\partial r_l} \Bigg[& \sum_{s=-\infty}^{s=\infty} A_s e^{ikx_j} \sum_{q=-\infty}^{q=\infty} e^{[i(s-q)\theta_{lj}]} H_{q-s}(kr_{lj}) J_q(kr_l) e^{iq\theta_l} \\ & + \sum_{s=-\infty}^{s=\infty} A_{jls} H_s(kr_l) e^{is\theta_l} \Bigg]_{r_l=R_o} = 0. \end{aligned} \tag{14}$$

Making use of the relations between the partial derivatives of the Bessel and Hankel functions, the last equation takes the form

$$A_s e^{ikx_j} \sum_{q=-\infty}^{q=\infty} e^{[i(s-q)\theta_{lj}]} H_{q-s}(kr_{lj})(J_{q-1}(kR_o) - J_{q+1}(kR_o)) e^{iq\theta_l} + A_{jls}(H_{s-1}(kR_o) - H_{s+1}(kR_o)) e^{is\theta_l} = 0. \tag{15}$$

Now it is possible to find the coefficients A_{jls}

$$A_{jls} = \frac{A_s e^{ikx_j} \Sigma_{q=-\infty}^{q=\infty} e^{[i(s-q)\theta_{lj}]} H_{q-s}(kr_{lj})(J_{q+1}(kR_0) - J_{q-1}(kR_0))}{(H_{s-1}(kR_0) - H_{s+1}(kR_0))} e^{i(q-s)\theta_l}. \tag{16}$$

We can repeat the same process, but this time the *l*th cylinder is the one that induces the scattered wave on the *j*th. In this case the coefficients are

$$A_{ljs} = \frac{A_s e^{ikx_l} \Sigma_{q=-\infty}^{q=\infty} e^{[i(s-q)\theta_{jl}]} H_{q-s}(kr_{jl})(J_{q+1}(kR_0) - J_{q-1}(kR_0))}{(H_{s-1}(kR_0) - H_{s+1}(kR_0))} e^{i(q-s)\theta_j}. \tag{17}$$

It is clear that $j=l$ makes no sense regarding the coefficients A_{ljs}. Therefore, the coefficients can be cast in the following form:

$$A_{ljs} = (1-\delta_{lj}) \frac{A_s e^{ikx_l} \Sigma_{q=-\infty}^{q=\infty} e^{[i(s-q)\theta_{jl}]} H_{q-s}(kr_{jl})(J_{q+1}(kR_0) - J_{q-1}(kR_0))}{(H_{s-1}(kR_0) - H_{s+1}(kR_0))} e^{i(q-s)\theta_j}, \tag{18}$$

where δ_{lj} is the Kronecker delta ($\delta_{lj}=1$ if $l=j$ and $\delta_{lj}=0$ if $l \neq j$). The pressure induced on the *j*th cylinder by the *l*th is

$$PP_{lj} = \sum_{s=-\infty}^{s=\infty} A_{ljs} H_s(kr_j) e^{is\theta_j}. \tag{19}$$

So, the pressure field produced by a finite number of cylinders, *N*, due to the double-scattering process is

$$PP^{\text{scatt}} = \sum_{l=1}^{N} \sum_{j=1}^{N} \sum_{s=-\infty}^{s=\infty} A_{ljs} H_s(kr_j) e^{is\theta_j}. \tag{20}$$

This is the multiple-scatter term employed in our calculation.

Finally, the pressure at any point (x, y) will be the sum of all contributions

$$\begin{aligned} P(x,y) &= P^{\text{inc}} + P^{\text{scatt}} + PP^{\text{scatt}} \\ &= e^{ikx} + \sum_{j=1}^{N} e^{ikx_j} \sum_{s=-\infty}^{s=\infty} A_s H_s(kr_j) e^{is\theta_j} \\ &\quad + \sum_{l=1}^{N} \sum_{j=1}^{N} \sum_{s=-\infty}^{s=\infty} A_{ljs} H_s(kr_j) e^{is\theta_j}. \end{aligned} \tag{21}$$

Notice that the summations over *j* and *l* permit the analysis of any arrangement of cylinders, either ordered or disordered. Here, we are concerned with ordered structures.

Let us stress that our approach cuts the expansion procedure of Twersky[16] after the double-scattering term. Our simplified approach is justified by the agreement with experimental results as described below.

III. EXPERIMENTS

The experiments have been performed in an anechoic chamber of $8 \times 6 \times 3$-m^3 size. As a sound source we used a speaker placed at the focus of a parabolic reflector. The reflector is employed to collimate the beam. Nevertheless, the distance between the source and sample is not enough to produce full plane-wave fronts when the sound reaches the sample.

With the aim of obtaining pressure maps on the plane perpendicular to the cylinder's axis, we have developed a computer-controlled automatic positioning system (called robot for short) capable of sweeping the microphone through a grid of measuring points located in a plane. The movement along each *X*- or *Y*-axis is accomplished by means of steeper motors with a maximum resolution of 0.25 mm per step. The maximum length of each axis is 1800 mm. Nevertheless, larger distances can be explored by hand relocation of the whole frame of the robot. Sound-pressure measurements are automatically taken by means of a B&K 2144 frequency analyzer controlled by a computer through a general purpose interface bus (GPIB) interface. At each grid point the microphone samples the sound with a sampling frequency of 15 kHz. Afterwards the analyzer makes the fast Fourier transform (FFT) of such data and produces the corresponding pressure spectrum with a resolution of 8Hz. Frequencies below 6.4 kHz are well described in the spectra. A total of 256 spectra has been taken to generate an averaged spectrum, which is the one finally assigned to that grid point. The total measuring time in one point is 10 s. As a result we obtain at each point, and for a given frequency, the root-mean-squared (rms) pressure, $P_{\text{rms}}(x,y)$. In order to put it in decibels we used a reference pressure $P_{\text{ref}} \equiv 20$ μPa; in other words, $L_{\text{exp}}(x,y) = 20 \log_{10}(P_{\text{rms}}(x,y)/P_{\text{ref}})$. The total time employed to elaborate a pressure map with 400 grid points, like the ones shown here, is about 7 h.

Our SBG crystals are built up by hanging cylindrical rods on a frame which has the crystal symmetry. Here, we have studied square arrays of hollow aluminum rods of $R_0 = 2$ cm radius put in a square lattice with 11 cm of lattice constant, *a*. The fraction of volume occupied by the cylinders *f* is quite small: $f = \pi R_0^2/a^2 = 0.104$. It has been shown previously[17] that this structure does not possess a full acoustic band gap.

In Fig. 2 we show the two samples under study. They were constructed along the *X* axis, the incident sound direction, in order to represent the two high-symmetry directions in the Brillouin zone; i.e., the ΓX direction [Fig. 2(a)] and

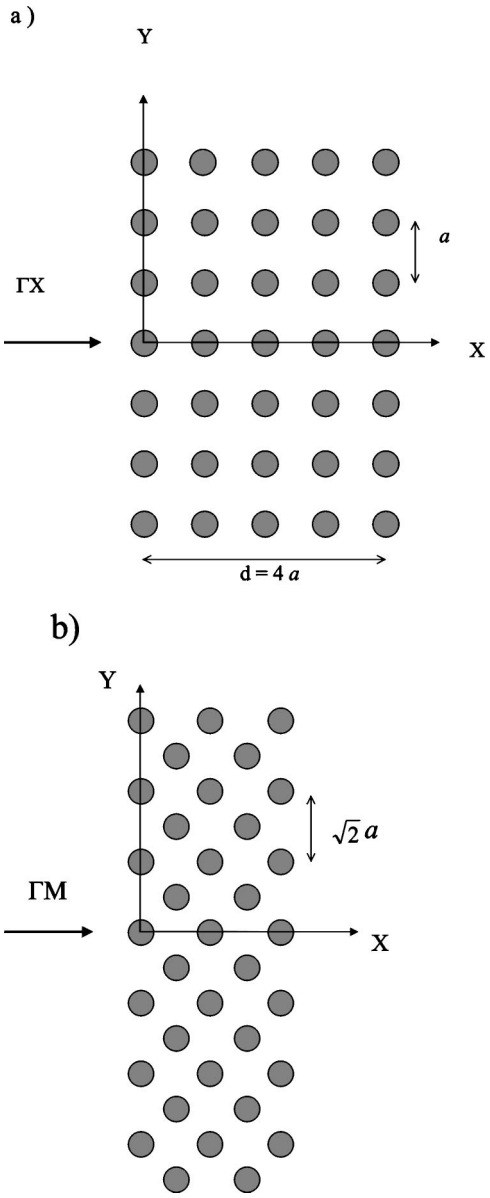

FIG. 2. (a) Geometry of the sample used to study the scattering of sound waves incident along the Γ*X* direction. (b) Sample employed to study sound waves along the Γ*M* direction. The incident direction is always from left to right in the figures.

Γ*M* direction [Fig. 2(b)], respectively. Both structures have five rows of cylinders so as to have short computational times, and to make for an easier comparison. We choose them as test materials to study their properties in reflectance by using our experimental setup.

IV. RESULTS AND DISCUSSION

The structures under study have been analyzed previously by using zero-order transmission experiments, and the following results were obtained: (1) along the Γ*X* direction an attenuation band appears[18] in the frequency region (1260–1750 Hz); (2) along the Γ*M* direction the attenuation band measured covers the region (1900–2500 Hz). When compared to the acoustic band structure calculated by a variational method one finds that attenuation along Γ*X* is fairly well explained by the gap existing at the region (1204–1764 Hz). On the contrary, along the Γ*M* no gap was found in the band calculation. The origin of the attenuation along this direction is twofold. One is the existence of one deaf band;[7] i.e., a band that is not coupled with the incident sound for reasons of symmetry. The other is the possible energy transfer to Bragg waves of higher order when the sound leaves the sample. In what follows we will see how these effects are shown in our experiments and by our multiple scattering calculation. First, we analyze pressure maps. Afterwards, the study of the standing wave observed in front of the structure will give us further confirmation of the SBG crystal properties inferred from the transmission experiments.

A. Pressure maps

The pressure, $P(x,y)$, has been calculated by our double-scattering approach (see Sec. II) at different frequencies. The sums to the orders of Hankel functions, *s* or *q*, have been truncated to five terms. This truncation is justified due to the fast decreasing of the coefficient's modulus. Thus, for example, at 2720 Hz, $|A_0|/|A_3| \approx 140$. On the other hand, to reduce the computational time the double-scattering term, Eq. (20), is calculated by using just first-neighbors interaction; i.e., $A_{ljs}=0$ if $r_{lj} > \sqrt{2}a$.

To compare with experiments we define a theoretical RMS-pressure, $P^2_{\text{theo}}(x,y)=\frac{1}{2}PP^*=\frac{1}{2}|P(x,y)|^2$, which is the average squared pressure at each point.

Therefore, the pressure in decibels is

$$L_{\text{theo}}(x,y)=20\ \log_{10}(|P(x,y)|/\alpha), \tag{22}$$

where α is an adjustable parameter that takes into account that the incident pressure is not unity in the experiments. In particular, we will present here results for two relevant frequencies; both are in regions where attenuation bands are observed.

Figure 3 shows the calculated pressure pattern at 1600 Hz for the sample constructed along the Γ*X* direction [see Fig. 2(a)]. It can be observed how the pressure decreases as the wave penetrates inside the structure. This behavior is well explained by the fact that the frequency is inside the existing acoustic gap along this direction. Both low transmission and high reflectance are observed along the incident direction, as is shown in Fig. 3. On the other hand, Fig. 4 plots the map obtained at 2540 Hz for the sample constructed along the Γ*M* direction. In comparison with the previous result, we now notice how the pressure takes nonzero values at angles tilted with respect to the incident direction and in the lateral sides of the structure. In this case the attenuation measured in the forward direction is due to an energy transfer to other directions; i.e., other than the collinear between source and microphone.

In Fig. 5 we compare pressure maps calculated and measured for the same sample and at the same frequency as in Fig. 3. The area represented in front of the structure is $x \in [-0.985\text{ m}, -0.485\text{ m}]$, $y \in [-0.160\text{ m}, 0.160\text{ m}]$. This plot shows that both experiment and theory display periodic high- and low-pressure levels, which clearly define standing waves that are in good qualitative agreement.

Figure 6 compares the measured values (squares) with the predictions of the model inside the region (−0.985 m,

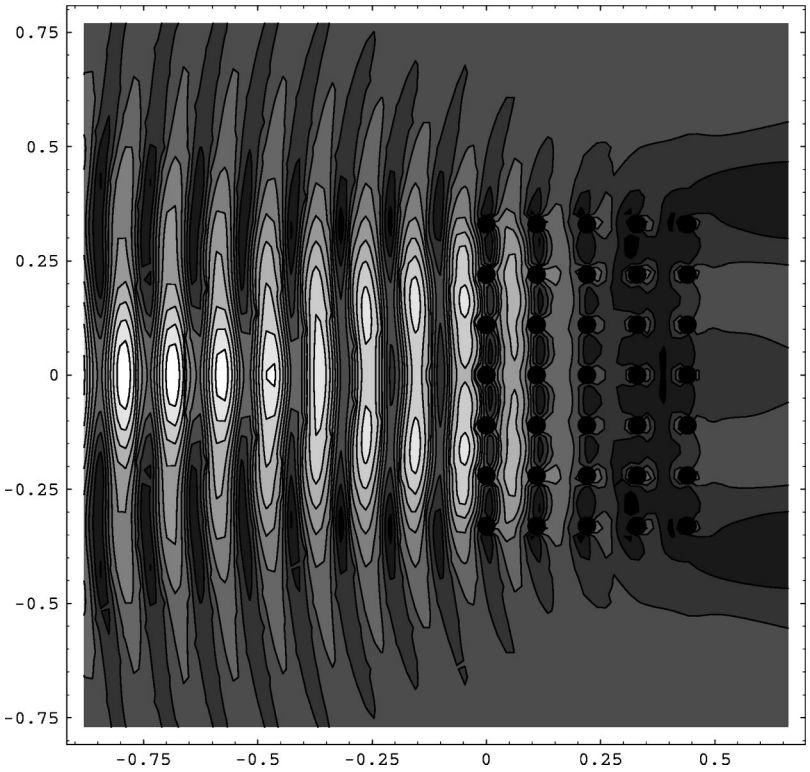

FIG. 3. Double-scattering calculation of the mean-square pressure pattern at 1600 Hz for the sample along the ΓX direction [see Fig. 2(a)].

-0.485 m) along the X axis. The continuous line represents the function $L_{\text{theo}}(x,y=0)$ in Eq. (22) with $\alpha=0.004$. We fitted the theoretical curve so that experimental maxima and minima were always above and below, respectively, the calculated ones. An improved fitting could have been done if our calculations had taken into account the fact that the incident sound probably does not have a plane-wave front when it reaches the structures. This effect will be discussed further in the next subsection.

B. Standing wave ratio

If we consider that an incident sound wave with unit pressure amplitude impinges on the SBG crystal, it will be

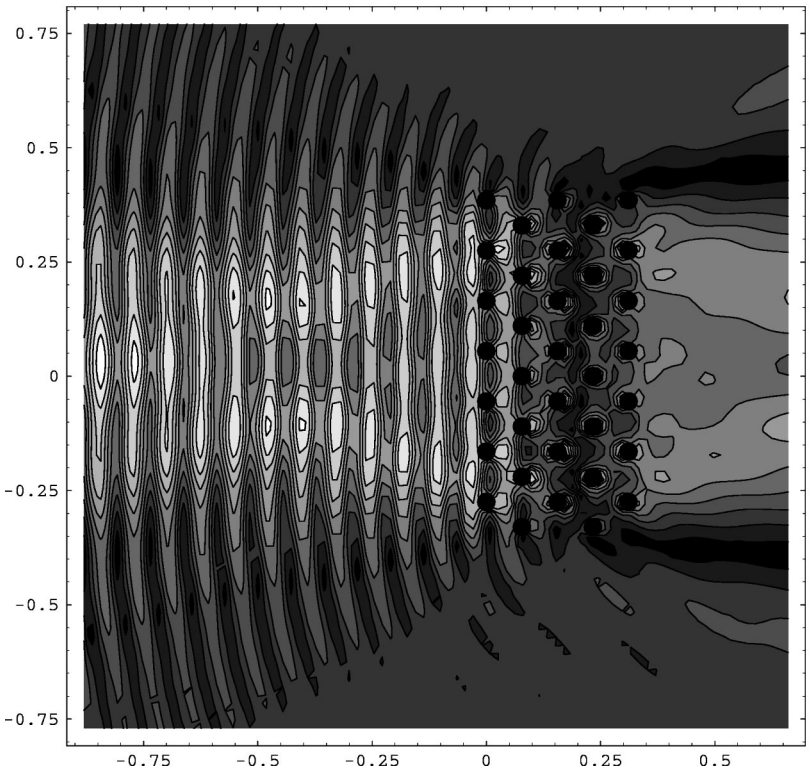

FIG. 4. Double-scattering calculation of the mean-square pressure pattern at 2540 Hz for the sample along the ΓM direction [see Fig. 2(b)].

a)

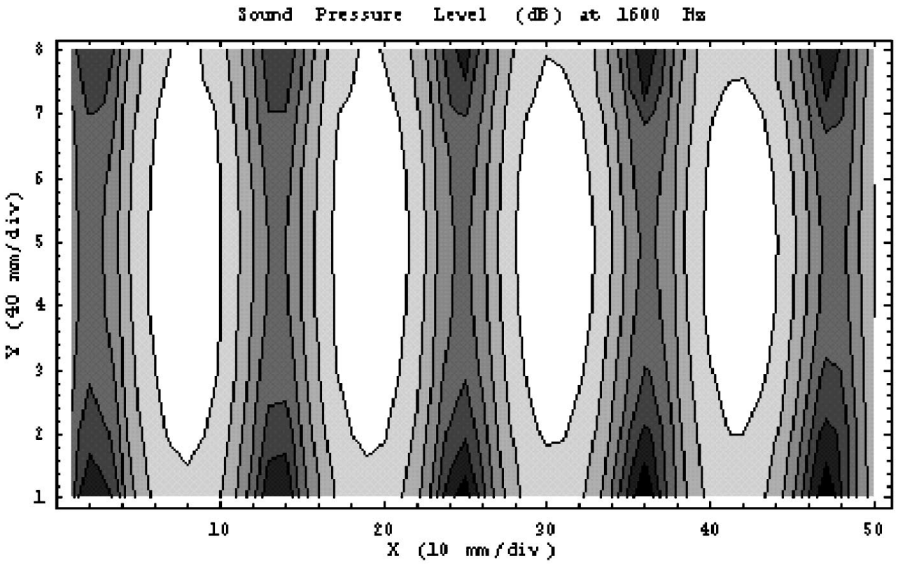

b)

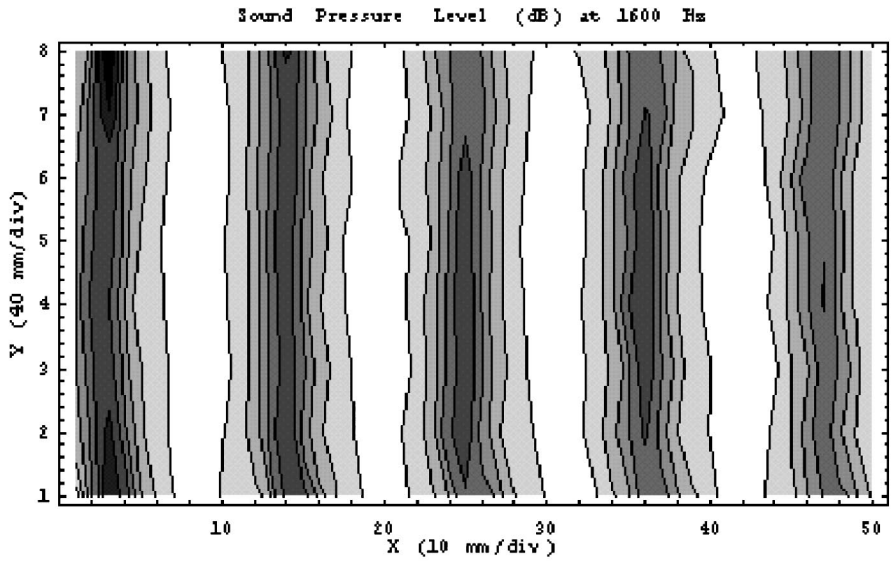

FIG. 5. Comparison between the mean-square pressure levels calculated (a) and measured (b) for the sample along the ΓX direction at 1600 Hz. The area represented in front of the sample is $(-0.985\ \text{m}, -0.485\ \text{m}) \times (-0.160\ \text{m}, 0.160\ \text{m})$, along the x- and y-axis, respectively. The scale numbered the grid points employed in the plot.

partially reflected. The net pressure in front of the crystal is the superposition of the incident and reflected wave

$$\cos(kx-\omega t)+R\ \cos(-kx-\omega t) = A(x)\cos(-\omega t-\varphi(x)), \tag{23}$$

where R is the reflection coefficient, $\varphi(x)$ is a phase angle which is of no concern here, and $A(x) = \sqrt{1+2R\ \cos 2kx+R^2}$. Only for $R=\pm 1$ is a full standing wave formed. For the general case $R\neq\pm 1$ the sum of the incoming traveling wave and the reflected wave is a partial standing wave. If we explore the wave with a microphone, as we have done, we are, in fact, measuring its mean square pressure, $\overline{P^2}$. In other words, we are measuring $A(x)$, which ranges (if $R>0$) from a maximum value $(1+R)$ at antinode positions $kx=0+n\pi$, to a minimum value $(1-R)$ at node position $kx=\pi/2+n\pi$. The standing wave ratio is defined by[19]

$$\frac{\overline{P^2}_{\max}}{\overline{P^2}_{\min}}=\frac{(1+R)^2}{(1-R)^2}=\text{SWR}^2. \tag{24}$$

Experimentally, to obtain the SWR it is better to work in terms of rms-pressures

$$\begin{aligned}\text{SWR}_{\text{exp}} &= L_{P\max}-L_{P\min}\\ &= 10\ \log_{10}(P_{\max}/P_{\text{ref}})^2-10\ \log_{10}(P_{\min}/P_{\text{ref}})^2\\ &= 20\ \log_{10}(P_{\max}/P_{\min}).\end{aligned} \tag{25}$$

In this equation $L_{P\min}$ and $L_{P\max}$ are the rms-pressure levels measured in decibels, P_{ref} is an arbitrary value (see Sec. III), and $P_{\max}$ and $P_{\min}$ are the maximum and minimum values of

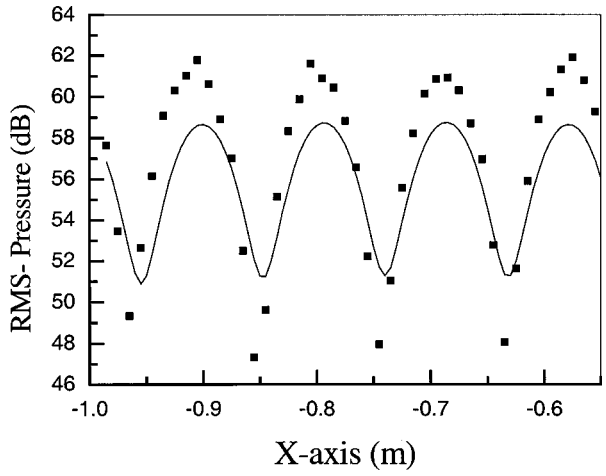

FIG. 6. Comparison between the effective pressures measured (symbols) and calculated (solid line) for the sample constructed along the ΓX direction at 1600 Hz. The data represented are in the region (-0.985 m, -0.485 m) along the x axis.

the root time-averaged pressures, respectively.

With regards to theoretical calculation, the SWR can be calculated using the following formula:

$$\mathrm{SWR}_{\mathrm{theo}} = 20\ \log_{10}(|P_{\max}|/|P_{\min}|). \tag{26}$$

Figures 7 and 8 show the SWRs along the two high-symmetry directions: ΓX and ΓM, respectively. The thick solid lines represent the measurements, while dotted lines define the calculations using the theory described in Sec. II. On the other hand, to evaluate the effect associated with a possible nonplanar wavefront, a phase mismatch between the cylinders in the planes perpendicular to the incident wave has been introduced in the model: the phase factors are considered to have the form $e^{ik|\mathbf{R}_{\mathrm{source}}-\mathbf{r}_j|}$ instead of $\exp(ikx_j)$, where $\mathbf{r}_j=(x_j,\ y_j)$ is the position vector of the cylinder j, and $\mathbf{R}_{\mathrm{source}}$ is the position of a line source at a distance L in front of the sample; $\mathbf{R}_{\mathrm{source}}=(-L,0)$. The thin solid lines in Figs. 7 and 8 represent the calculations for this cylindrical wavefront with a fitted value $L=10a$.

When the sound wave impinges the structure along the ΓX direction (see Fig. 7), the SWR measured (thick solid line) show an enhancement in the very same frequency region where the first gap appears in the acoustic band structure. The lack of states available to sound transmission produces a large reflectance R and, consequently, explains the SWR increasing. With regard to the oscillations observed, they are related to the resonances associated with the finite thickness of the SBG crystal (Fabry–Perot resonances). The frequency of these resonances is determined by $kd=m\pi$, $m=1,2,\ldots$, $d=4a=0.44$ m being the thickness of the sample constructed along this direction [see Fig. 2(a)]. From the oscillation period, $\Delta\omega$, it would be possible to obtain the sound velocity inside the sonic crystal (SC), c_{SC}, through the formula $c_{\mathrm{SC}}=\Delta\omega d/\pi$. Nevertheless, since the period measured changes with frequency (its values are in the range 222–355 Hz), a frequency-dependent sound velocity must be considered instead. The study of this magnitude, which impinges on the broad problem of homogenization, requires the analysis of more structures and detailed calculations on their corresponding acoustic bands for comparison. Such a task is beyond the scope of this work. The comparison with the SWR resulting from our double-scattering model is qualitatively good, although both calculations (i.e., plane and cylindrical wavefronts, respectively) define the gap shifted with respect to the measurements and the band structure calculation. This disagreement mainly comes from the fact that we didn't include all the multiple-scattering terms as they are in the acoustic band calculation. Furthermore, the result for the case of a cylindrical wavefront predicts a smaller gap.

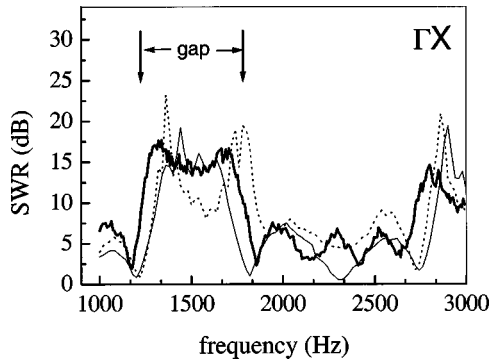

FIG. 7. Frequency dependence of the standing wave ratio (SWR) (in dB) measured (thick solid line) and calculated for the sample along the ΓX direction. The dotted line represents the calculated results for an incoming sound plane wave. The thin solid line shows the corresponding ones calculated with an incident sound with a cylindrical shape (see the text).

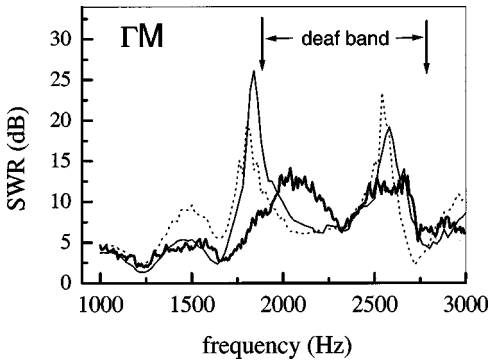

FIG. 8. Frequency dependence of the SWR (in dB) measured (thick solid line) and calculated for the structure along the ΓM direction. The dotted line represents the calculated results for an incoming sound plane wave. The thin solid line shows the corresponding ones calculated with an incident sound with a cylindrical shape (see the text).

When the sound is incident along the ΓM direction (see Fig. 8) we notice an SWR enhancement in the region (1800–2700 Hz), though no gap appears in the acoustic band structure calculated along this direction. Now, the origin of large SWR values is associated with the existence of a deaf band that goes from 1878 Hz up to 2798 Hz. This band, ideally uncoupled, weakly couples with the exciting sound and produces large reflectance values. The multiple-scattering calculations are also in qualitatively good agreement and reproduce most of the features observed. Again, the theoretical frequencies at which the SWR enhances are shifted (now to lower frequencies) compared to the experimental ones and to the ones deduced from band structure. Regarding the Fabry–Perot oscillations, its period is now larger since the slab thickness is smaller, $d=4a/\sqrt{2}=0.31$ m. These oscilla-

tions are well reproduced by our models. In fact, we observe that the results with the cylindrical wavefront give a better account of the SWR amplitude. This effect leads us to conclude that phase mismatch plays a role and has to be included in improved models based on the multiple-scattering approaches.

V. SUMMARY

In this work we have studied the standing wave formed in front of a SBG crystal when a sound wave impinges on it. The crystals analyzed consist of two-dimensional arrays of rigid cylinders in air. Experiments were conducted in an free-echo chamber by using a new experimental setup based on a computer-controlled automatic positioning system which is able to obtain the effective pressure pattern on the plane perpendicular to the cylinder axis. On the other hand, we have used a theoretical approach based on a multiple-scattering algorithm, which takes into account up to double-scattering events. The comparison between theory and experiments has allowed us to obtain intrinsic properties of the SBG crystal. In particular, we have shown that gaps and uncoupled bands can be characterized in the SWR of the standing wave. Moreover, the finite thickness of our SBG structures along the sound propagation direction produces Fabry–Perot-type resonances that were detected as oscillations in the SWR.

ACKNOWLEDGMENTS

This work has been supported by the Comisión Interministerial de Ciencia y Tecnología of Spain, Contract No. MAT00-1670-C04. We thank F. Meseguer for his continuous support. Also, we thank D. Caballero, R. Llopis, and D. López for their comments and suggestions. We acknowledge the computational help provided by the Centro de Computación Científica at the Universidad Autonoma de Madrid.

[1] E. Yablonovitch, ''Inhibited spontaneous emission in solid state physics and electronics,'' Phys. Rev. Lett. **58**, 2059–2062 (1987).
[2] S. John, ''Strong localization of photons in certain disordered structures,'' Phys. Rev. Lett. **58**, 2486–2489 (1987).
[3] L. Flax, L. R. Dragonette, and H. Uberall, ''Theory of elastic resonance excitation by sound scattering,'' J. Acoust. Soc. Am. **63**, 723–731 (1978).
[4] M. M. Sigalas and E. N. Economou, ''Elastic and acoustic band structure,'' J. Sound Vib. **158**, 377–382 (1992).
[5] M. S. Kushwaha, P. Halevi, L. Dobrzynski, and B. Djafrari-Rouhani, ''Acoustic band structure of periodic elastic composites,'' Phys. Rev. Lett. **71**, 2022–2025 (1993).
[6] E. N. Economou and M. Sigalas, ''Classical wave propagation in periodic structures,'' Phys. Rev. B **48**, 13434–13438 (1993).
[7] J. V. Sánchez-Pérez, D. Caballero, R. Martínez-Sala, C. Rubio, J. Sánchez-Dehesa, F. Meseguer, J. Llinares, and F. Gálvez, ''Sound attenuation by a two-dimensional array of rigid cylinders,'' Phys. Rev. Lett. **80**, 5325–5328 (1998).
[8] M. Kafesaki and E. N. Economou, ''Multiple scattering theory for 3D periodic acoustic composites,'' Phys. Rev. B **60**, 11993–11999 (1999).
[9] M. M. Sigalas and N. Economou, ''Attenuation of multiple scattered sound,'' Europhys. Lett. **36**, 241–246 (1996).
[10] Zhen Ye, ''Acoustic localization in bubbly liquid media,'' Phys. Rev. Lett. **80**, 3503–3506 (1998).
[11] D. Felbacq, G. Tayeb, and D. Maystre, ''Scattering by a random set of parallel cylinders,'' J. Opt. Soc. Am. A **11**, 2526–2538 (1994).
[12] F. R. Montero de Espinosa, E. Jiménez, and M. Torres, ''Ultrasonic band gap in a periodic two-dimensional composite,'' Phys. Rev. Lett. **80**, 1208–1211 (1998).
[13] W. M. Robertson and W. F. Rudy, III, ''Measurement of acoustic stop bands in two-dimensional periodic scattering arrays,'' J. Acoust. Soc. Am. **104**, 694–699 (1998).
[14] M. Torres, J. P. Adrados, and F. R. Montero de Espinosa, ''Visualizacion of Bloch waves and domain walls,'' Nature (London) **398**, 114–115 (1999).
[15] E. T. Wittaker and G. N. Watson, *A Course of Modern Analysis* (Cambridge University Press, Cambridge, 1965), p. 429.
[16] V. Twersky, ''On scattering of waves by random distributors,'' J. Math. Phys. **3**, 700–715 (1962).
[17] See Fig. 4 in Ref. 7.
[18] See Fig. 1 in Ref. 7.
[19] D. H. Towne, *Wave Phenomena* (Dover, New York, 1988), pp. 49–51.

Acoustically coupled gas bubbles in fluids: Time-domain phenomena

Christopher Feuillade[a)]
Naval Research Laboratory, Stennis Space Center, Mississippi 39529-5004

(Received 26 May 2000; revised 12 February 2001; accepted 6 March 2001)

In previous work [C. Feuillade, J. Acoust. Soc. Am. **98**, 1178–1190 (1995)] a coupled oscillator formalism was introduced for describing collective resonances, scattering, and superresonances, of multiple gas bubbles in a fluid. Subsequently, time-domain investigations of the impulse response of coupled systems have disclosed the exact conditions which determine whether the ensemble scattering behavior should be described using: either (a), a multiple scattering; or (b), a self-consistent methodology. The determining factor is the *Q* of the individual scatterers, and their typical spatial separations in the medium. For highly damped or sparse systems, e.g., scattering from loose schools of swimbladder fish, or from a gassy seabed containing entrained bubbles, the multiple scatter counting approach should be applicable. For more strongly coupled systems, e.g., a dense cloud of resonating bubbles in the water column, energy exchange may be due primarily to radiative cycling rather than scattering, in which case a self-consistent approach is indicated. The result has implications for both volume and bottom scattering applications. © *2001 Acoustical Society of America.* [DOI: 10.1121/1.1369102]

PACS numbers: 43.20.Fn, 43.20.Px, 43.20.Ks, 43.30.Jx [ANN]

I. INTRODUCTION

The collective acoustic behavior of multiple gas bubbles in water, and other fluids, continues to be a topic of critical importance and interest. For example, in seawater, the presence of dense clouds of air bubbles can have a strong effect on the passage of sound which impacts propagation, attenuation, scattering, and reverberation, phenomena.[1] Bubbles in the water column are generated by several factors, including entrainment due to the action of breaking waves, cavitation from ship propellers, or even the biological action of microorganisms. Another cause of ''bubbles'' might be the presence of fish. A fish swimbladder is a type of gas bubble (albeit highly damped), and the presence of large dense schools of swimbladder-bearing fish can have an effect on the propagation of sound similar to that of bubble clouds.[2] There has also been great interest recently in the acoustic properties of bubbles entrained in gassy seabed sediments, and the effects they have on bottom scattering and propagation (e.g., see the paper by Gardner,[3] which also contains a helpful list of references).

It has been recognized for a long time[4,5] that scattering from gas bubbles in fluids is closely linked to the propagation of sound, and plays a critical role in determining acoustic attenuation and dispersion in the medium. Attempts to incorporate interactions between bubbles, in order to produce an improved scattering description, have frequently used a multiple scattering methodology, which seeks to more accurately represent the scattering process by adding higher-order interactions (i.e., second order, where the field interacts with two bubbles before returning to the receiver, and third order, where it interacts three times, etc.) as a series of perturbation corrections to the primary first-order scatter (the direct return from the individual bubbles). However, while this approach embodies an intuitively appealing picture of the scattering problem, it also entails a number of serious obstacles. First, for very strong scatterers (e.g., resonating bubbles) in close proximity to each other, the perturbation terms may become large enough to cause the series to diverge. In this case, the method cannot be used. Second, even though the series may still converge, it is frequently not clear how many orders of perturbation are needed to provide a sufficiently accurate prediction of the true scattering level. Third, after the first- and second-order corrections, the bookkeeping needed to correctly count all of the interactions becomes formidable when many scatterers are involved. Recently, attempts have been made to overcome this third problem in extended media by developing sophisticated scattering schemes.[6,7]

The problems associated with the multiple scattering approach just described may be significantly ameliorated by using a self-consistent methodology, which *defines* the total field incident on any bubble as the sum of the external field plus the scattered fields from all the other bubbles, where these other bubbles are considered to have *already experienced* all of the interactions which affect them. Because the interactions between bubbles then implicitly contain, by definition, all orders of multiple scattering, the self-consistent approach: (a) is not limited to weak scatterers; (b) accurately predicts the true level of scattering after many interactions; and (c), greatly simplifies counting of the scattering processes. A formalism which utilizes this methodology has been developed to provide a description of multiple scattering effects in fish schools.[8]

While scattering is essentially a time-domain phenomenon, theories of scattering from multiple bubbles in water have predominantly used time-independent descriptions. This is unfortunate, because there are critical aspects of this scattering problem which become evident only in the time

a)Electronic mail: cf@nrlssc.navy.mil

domain. The aim of this present paper is to decrease this deficiency by specifically investigating the transient behavior of multiply interacting bubbles. In so doing, a number of the fundamental physical features of the phenomenon are revealed.

First, it is seen that the acoustic interaction between gas bubbles is best understood in terms of the classical theory of coupled resonators. The self-consistent methodology applied to bubbles implicitly adopts this picture, and consequently gives the most complete physical description. Second, with this understanding, it is possible to differentiate between the multiple scattering and self-consistent approaches to the interaction problem in a completely new way. It is seen that, by imposing a multiple scattering paradigm on the interaction between the bubbles, discretely separated scattering events are implicitly incorporated as the means by which energy is exchanged. The self-consistent methodology, conversely, is capable of characterizing the system more comprehensively: either (as before) as an interaction between multiple scatterers, or else as an interaction between strongly coupled resonators wherein the energy exchange is primarily due to radiative cycling rather than scattering. Third, the work described here indicates the limitations of the multiple scattering approach and its point of failure, and also shows how the number of perturbation terms necessary to determine the true scattering level depends on the properties of the individual bubbles and their spacings. The restrictions on the usage and implementation of the multiple scattering approach which are identified here are clearly extendable to the general case of large ensembles of bubbles, and circumscribe the applicability of this approach to practical problems.

While much of the discussion in this paper is concerned with the behavior of air bubbles in water, this is intended to be only a representative case. The formalism developed has applicability to the general problem of the interactions of multiple gas bubbles entrained in a fluid.

Section II of this paper gives brief outlines of the Minnaert/Devin theory of a single bubble, Twersky's two methods for multiple scattering, and the coupled equation method. Section III develops the time-domain solutions to the coupled equations and describes the solutions in the multiple scattering and strong coupling regimes. Section IV gives a summary of conclusions.

II. TIME-INDEPENDENT THEORY FOR ONE AND TWO BUBBLES

A. One bubble: the Minnaert/Devin theory

Anderson's fluid sphere scattering model[9,10] offers a physically accurate method for describing acoustic scattering from a single spherical air bubble in water. This analysis shows that the monopole (or ''breathing mode'') resonance of air bubbles is a salient feature which dominates the scattering response. The ''dipole'' mode, which is the resonance effect next in sequence in the frequency spectrum, is very much smaller in amplitude than the monopole mode, and its modal frequency is ~33 times higher. These features render the dipole mode negligible, for most practical purposes, when considering the effects of air bubbles on sound propagation in water. This also applies to subsequent higher-order modes.

The predominant influence of the monopole resonance on acoustic scattering from air bubbles in water has led to the common usage of an alternative theory, which was first introduced by Minnaert[11] and given an excellent development and explanation by Devin,[12] to describe this phenomenon. In the monopole resonance frequency region and below, it can be shown to be practically equivalent to the Anderson theory. The monopole response is identified as the solution of a second-order ''mass-spring'' differential equation as follows:

$$m\ddot{v} + b\dot{v} + \kappa v = -Pe^{i\omega t}. \tag{1}$$

In this equation, the variable v (called the ''differential'' volume) is the difference between the instantaneous and equilibrium ($=4\pi a^3/3$) volumes of a bubble of radius a. The coefficient $m(=\rho/4\pi a)$ is termed the inertial ''mass'' of the bubble, where ρ is the density of water. The quantity $\kappa(=3\gamma P_A/4\pi a^3)$ is the ''adiabatic stiffness,'' where γ is the gas constant and P_A is the ambient water pressure. The coefficient b describes the damping of the bubble motion, while P and ω represent the amplitude and frequency, respectively, of the external pressure field applied to the bubble (P is preceded by a minus sign since a decrease in pressure results in an increase in the bubble volume).

If a harmonic quasi-steady-state solution of (1) of the form $v=\overline{v}e^{i\omega t}$ is assumed, substitution yields the individual bubble resonance response function

$$\overline{v} = \frac{-P}{\kappa - \omega^2 m + i\omega b} = \frac{-P/\omega^2 m}{\left[\dfrac{\omega_0^2}{\omega^2} - 1\right] + i\dfrac{b}{m\omega}}, \tag{2}$$

where $\omega_0(=\sqrt{\kappa/m}=(1/a)\sqrt{3\gamma P_A/\rho})$ is Minnaert's resonance frequency. If $k_0=\omega_0/c$ is the propagation wave number at resonance, then for an air bubble at atmospheric pressure in water ($c=1500$ m/s) the value of $k_0 a \approx 0.0136$, making the wavelength at resonance several hundred times greater than the bubble radius. The imaginary component $(b/m\omega)$ in the denominator of (2) can be identified with a bubble damping parameter δ_B comprising radiative, thermal, and viscous terms

$$b/m\omega = \delta_B = \delta_r + \delta_t + \delta_v\,. \tag{3}$$

Air bubbles in water are typically lightly (or ''under'') damped. At the resonance frequency the ''quality factor'' $Q=m\omega_0/b=1/\delta_B(\omega_0)$ may be defined. The acoustic field reradiated by the bubble is given by[13]

$$p(r,t) = \frac{\rho e^{-ikr}}{4\pi r}\ddot{v} = \frac{-\rho\omega^2}{4\pi r}\overline{v}e^{i(\omega t - kr)} = fP\frac{e^{i(\omega t - kr)}}{r}, \tag{4}$$

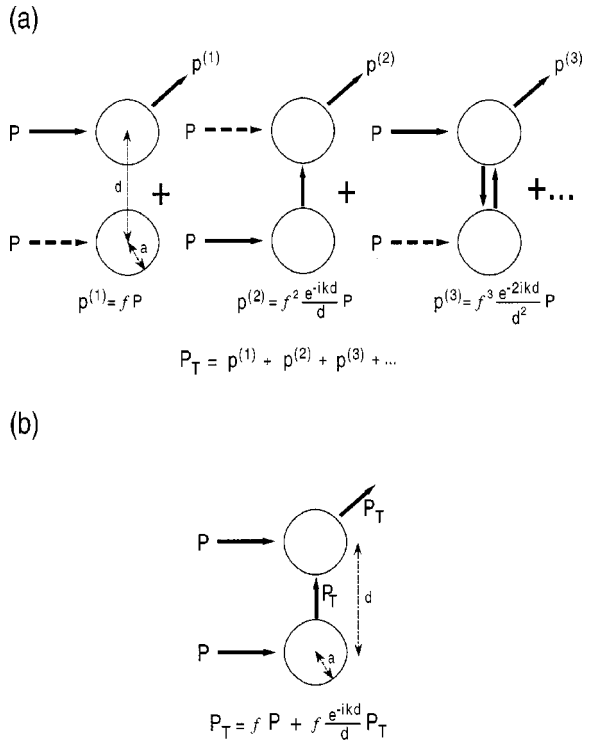

FIG. 1. Twersky's two approaches for enumerating multiple scattering. (a) The ''scatter-counting'' approach. The total scattered field from either bubble is written as the sum of an infinite power series, in which each term represents a specific order of multiple scattering, i.e., $P_T = p_1 + p_2 + p_3 + \cdots$, and the multiplying factor in the series, i.e., fe^{-ikd}/d [see Eq. (6)], represents scattering and propagation from one bubble to the other and is derived from Eq. (4). (b) The ''self-consistent'' approach. The total scattered field from either bubble is written as the sum of two parts: (1) the scattering of the external field; and (2), the scattering of the total scattered field from the second bubble. When $d/a > Q$ the two methods give formally identical results.

where

$$f = \frac{a}{\left[\frac{\omega_0^2}{\omega^2} - 1\right] + i\delta_B} \tag{5}$$

is the ''scattering amplitude.''

B. Two bubbles: The Twersky method

What effect do multiple scattering processes have on the total field scattered from air bubbles in water? A seminal analysis of multiple scattering was presented by Twersky,[14] who identified two different methodologies for evaluating the scattered field. Kapodistrias and Dahl[15] have recently experimentally investigated some of his predictions for multiple bubble scattering.

1. The multiple scatter ''counting'' approach

The first method Twersky described is schematically depicted in Fig. 1(a). For two identical bubble scatterers, the total field is determined by calculating the aggregate of a series of perturbation terms representing successive scattering events at the two bubbles. Thus, writing $p_T(r,t) = fP_T e^{i(\omega t - kr)}/r$, and using (4), yields

$$P_T = fP\left[1 + f\frac{e^{-ikd}}{d} + f^2\frac{e^{-2ikd}}{d^2} + \cdots\right], \tag{6}$$

where $d(>2a)$ is the distance separating the bubbles. This approach only leads to a physically meaningful determination of the scattered field when $|fe^{-ikd}/d| < 1$; otherwise, the power series on the right-hand side of (6) does not converge. The maximum value of $|f|(=a/\delta_B)$ occurs when $\omega = \omega_0$, and this leads to an equivalent condition, i.e., $d/a > 1/\delta_B \approx Q$. This indicates a minimum bubble spacing restriction for successful implementation of the approach for resonating bubbles. In order for the power series to converge, either the damping δ_B must be high enough to result in a low value of Q, or the spacing d must be sufficiently large, or both.

2. The ''self-consistent'' approach

The restrictions inherent in the multiple scattering procedure just described may be avoided by using the second approach discussed by Twersky, which implements the so-called ''self-consistent'' methodology. This is exemplified in Fig. 1(b). The amplitude P_T of the total field scattered from either of the identical bubbles is evaluated by adding together terms arising from just two events. The first term represents scattering of the external field. The second represents rescattering of the field incident on the bubble due to scattering from its partner. This time, however, the coefficient of the second term is *defined* as the total field amplitude P_T scattered from the partner. Thus, the self-consistent equation for P_T may be written.

$$P_T = fP + f\frac{e^{-ikd}}{d}P_T, \tag{7}$$

which, after rearrangement, yields

$$P_T = \frac{fP}{1 - f\frac{e^{-ikd}}{d}}. \tag{8}$$

If $|fe^{-ikd}/d| < 1$, a binomial expansion of (8) recovers (6), indicating that the multiple scattering and self-consistent approaches produce identical results. While this establishes an important connection between the two procedures, one of the purposes of this present work is to demonstrate that the two methods should not be mistaken as simply alternative formulations of the same phenomenon. Neither should the self-consistent methodology be viewed merely as a convenient technique for extending the multiple scattering solution into the region where the power series diverges. Instead, it will be shown that for multiple strongly interacting air bubbles in water, there is a critical physical distinction between the two approaches.

C. Two bubbles: The coupled-resonator method

In a previous paper,[16] the interaction between two ensonified air bubbles in water, with different m, b, κ, etc., was described by a pair of coupled differential equations, each similar to (1), i.e.,

$$m_1\ddot{v}_1+b_1\dot{v}_1+\kappa_1 v_1=-P_1e^{i(\omega t+\phi_1)}-\frac{\rho e^{-ikd}}{4\pi d}\ddot{v}_2, \quad (9)$$

$$m_2\ddot{v}_2+b_2\dot{v}_2+\kappa_2 v_2=-P_2e^{i(\omega t+\phi_1)}-\frac{\rho e^{-ikd}}{4\pi d}\ddot{v}_1. \quad (10)$$

The second term on the right-hand side of (9) and (10) is the radiative coupling to the other bubble, derived from (4); and v_1 and v_2 are defined *to include the effects of all radiative interactions*, so these equations give a completely self-consistent description of the system. Since the coupling is proportional to the second derivatives of v_1, v_2, the mechanical system represented is equivalent to two electrical circuits coupled through a mutual inductance (Ref. 17, pp. 103–105).

For two identical bubbles (i.e., $v_1=v_2=v$, $b_1=b_2=b$, etc.) the equations may be solved by adding and subtracting to obtain two uncoupled equations for $v_+=\frac{1}{2}(v_1+v_2)$ and $v_-=\frac{1}{2}(v_1-v_2)$ (Ref. 17, pp. 96–98)

$$\left[m+\frac{\rho e^{-ikd}}{4\pi d}\right]\ddot{v}_+ + b\dot{v}_+ + \kappa v_+ = -\tfrac{1}{2}[P_1e^{i\phi_1}+P_2e^{i\phi_2}]e^{i\omega t}, \quad (11)$$

$$\left[m-\frac{\rho e^{-ikd}}{4\pi d}\right]\ddot{v}_- + b\dot{v}_- + \kappa v_- = -\tfrac{1}{2}[P_1e^{i\phi_1}-P_2e^{i\phi_2}]e^{i\omega t}. \quad (12)$$

The quantities v_+ and v_- represent normal modes of the system: v_+ describes the motion in which the two bubbles oscillate in phase; v_- describes the bubbles oscillating in antiphase. Any collective oscillation of the system driven by an external field can be expanded as some linear superposition of these modes.

Equations (11) and (12) are identical in form to Devin's Eq. (1). Assuming harmonic solutions yields coupled bubble resonance response functions

$$\overline{v}_\pm=\frac{-\frac{1}{2}(P_1e^{i\phi_1}\pm P_2e^{i\phi_2})}{\kappa-\omega^2\left[m\pm\frac{\rho e^{-ikd}}{4\pi d}\right]+i\omega b}=\frac{-\frac{1}{2}(P_1e^{i\phi_1}\pm P_2e^{i\phi_2})}{\kappa-\omega^2 m_\pm+i\omega b_\pm}, \quad (13)$$

where e^{-ikd} has been separated into real and imaginary parts to give

$$m_\pm=m\pm\frac{\rho\cos kd}{4\pi d}, \quad (14)$$

$$b_\pm=b\pm\frac{\omega\rho\sin kd}{4\pi d}. \quad (15)$$

Applying (4) to (13), in particular, gives the radiated field amplitude corresponding to v_+ as

$$p_+(r,t)=\frac{-\rho\omega^2}{4\pi r}\overline{v}_+ e^{i(\omega t-kr)}=\frac{f}{1-f\frac{e^{-ikd}}{d}}\left(\frac{P_1e^{i\phi_1}+P_2e^{i\phi_2}}{2}\right)\frac{e^{i(\omega t-kr)}}{r}. \quad (16)$$

Comparing (16) with (8) shows that the Twersky self-consistent calculation discussed earlier incorporates radiation from the ''+'' mode. However, depending on the external field amplitudes and phases, the ''−'' mode may also be excited. It is this latter mode which gives rise to the superresonance phenomenon described by Tolstoy,[18] as Ref. 16 makes clear.

The ''+'' and ''−'' modes resonate at frequencies different from each other and from a single bubble. Manipulating the denominator of (13) gives

$$\omega_{0\pm}=\frac{\omega_0}{\sqrt{1\pm\left(\frac{a}{d}\right)\cos\frac{\omega_{0\pm}d}{c}}}, \quad (17)$$

which can be solved by recursion. In Fig. 2(a), $\omega_{0\pm}/\omega_0$ is plotted as a function of bubble separation, together with data from the experiments of Lauer,[19] who measured the resonance frequencies of air bubbles in water adjacent to rigid and free boundaries. A bubble next to a rigid wall creates a positive acoustic image of itself with which it oscillates in phase. The combined behavior of the bubble and image is equivalent to the ''+'' mode. A bubble next to a free surface creates a negative acoustic image with which it oscillates in antiphase, and their combined behavior forms the ''−'' mode. Lauer used quite large bubbles with resonance frequencies ranging from 1515 to 2330 Hz. Following Devin,[12] the corresponding values of $Q(\approx 30-33)$ can be estimated for these bubbles. In Fig. 2(a), the bubble separation is scaled in bubble radii, and the evident agreement between data and theory indicates the validity of the self-consistent methodology, which correctly predicts the resonance frequencies $\omega_{0\pm}$ for $d/a < Q$ [when the multiple scattering approach, as Eq. (6) indicates, would be inapplicable].

Just as $\omega_{0\pm}$ varies for the ''+'' and ''−'' modes due to the radiative interactions between the bubbles, so do their damping rates. If the damping of the individual bubbles is purely radiative then, from (3), $\delta_B=\delta_r(=ka)$, where $k=\omega/c$. Thermal and viscous damping increases the value of δ_B. Let us assume that the total damping may be represented by $\delta_B=\delta_r(1+\alpha)=ka(1+\alpha)$, where $\alpha[=(\delta_t+\delta_v)/\delta_r\geqslant 0]$ is a phenomenological parameter representing incremental damping due to nonradiative effects. It may then be shown, from the denominator of (13), that

$$\frac{\delta_\pm}{\delta_B}=\frac{1\pm\frac{1}{1+\alpha}\frac{\sin kd}{kd}}{1\pm\frac{a}{d}\cos kd}. \quad (18)$$

For very small d, δ_-/δ_B approaches 0, which is one of the features of superresonances (see Ref. 16). In Fig. 2(b),

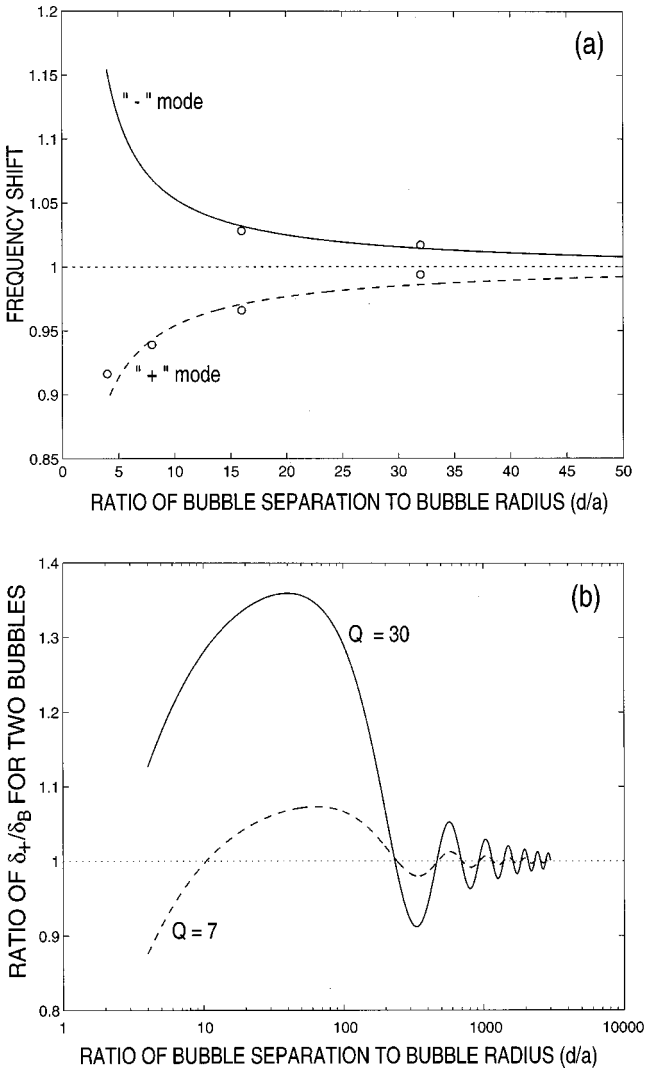

FIG. 2. Frequency shifts and damping of two identical coupled bubbles. (a) Radiative coupling between bubbles leads to shifts in the resonance frequency for the ''+'' and ''−'' modes. The ratios ω_{0+}/ω_0 and ω_{0-}/ω_0 are plotted as a function of the bubble separation scaled in numbers of bubble radii. The points denoted ''o'' are experimental results from Lauer's work (Ref. 19). The dotted line (ratio=1) corresponds to the unshifted single bubble frequency. (b) The ratio δ_+/δ_B at the ''+'' mode resonance frequency (ω_{0+}) is plotted as a function of bubble separation, using a logarithmic scale, for two values of Q. The cyclic variation with separation occurs because the phase of the scattered field from one bubble alternately assists and retards the damping of the other as the distance between them changes. The dotted line (ratio=1) corresponds to the single-bubble damping.

δ_+/δ_B is plotted at the resonance frequency of the ''+'' mode (i.e., $k=k_{0+}=\omega_{0+}/c$) as a function of bubble separation, for two values of $Q=1/k_0a(1+\alpha)$. The modal damping varies with the bubble separation, due to cycling at the spatial frequency k_{0+}. When two bubbles are close together the damping is often, but not always, greater than that of a single bubble.

III. TIME-DOMAIN THEORY FOR COUPLED BUBBLES

The primary interest of this work is to develop a physical understanding of the time-dependent behavior of multiple gas bubbles in fluids which are coupled together by their mutually scattered, or reradiated, fields. The time response of an acoustic system to an external field can be represented as the convolution of the impulse response of the system with the time signature of the source drive. Investigations of the time evolution of multiple bubbles are therefore facilitated by determining the impulse response for the coupled system. The impulse response also represents a particularly appropriate method for studying the effects of multiple interactions between bubbles because its behavior is predominantly governed by processes in the resonance region where these interactions have their most significant effects.

The dominant central region of the bubble resonance spectrum represented by (2) is typically narrow for air bubbles in water. Over this region the variation in b is small, and this parameter may, for present purposes, be assumed frequency independent. The impulse response $G(t)$ of a single bubble may then be found from (1), with a delta function replacing the original source term on the right-hand side, i.e.,

$$m\ddot{G}+b\dot{G}+\kappa G=-\delta(t), \tag{19}$$

where $\delta(\cdot)$ denotes the Dirac delta function. It is convenient to solve this equation entirely in the Fourier transform domain. Thus, if we obtain $g(\omega)=\int_{-\infty}^{\infty}G(t)e^{-i\omega t}\,dt$, and similarly transform $\dot{G}$ and $\ddot{G}$ using the derivative theorem for Fourier transforms (Ref. 20, pp. 117–118), a few simple manipulations yield

$$g(\omega)=\frac{-1}{\kappa-\omega^2m+i\omega b}\equiv\frac{-f}{ma\omega^2}, \tag{20}$$

where the second equivalence has been derived by inspection from (5). A simple expression for $G(t)$ may then be found by performing the inverse Fourier transform of (20), i.e.,

$$G(t)=-\frac{e^{-\alpha t}\sin\Omega t}{m\Omega},\quad (t\geqslant 0) \tag{21}$$

where $\alpha=b/2m$; $\Omega=\sqrt{\omega_0^2-\alpha^2}$, and b is evaluated at ω_0. This expression (representing a sinusoid decaying in time) describes the ''ringing'' response of the bubble as it reacts to the impulse. The value of α can be related, via Q, to the resonance halfwidth. Since $Q=m\omega_0/b=\omega_0/(2\Delta\omega_{1/2})$, where $2\Delta\omega_{1/2}$ is the halfwidth of the resonance, then $\alpha=b/2m=\omega_0/2Q=\Delta\omega_{1/2}$. This indicates that the exponential time decay of $G(t)$ is characterized by a damping parameter equal to the semi-halfwidth of the resonance. The frequency of the sinusoid can also be rewritten $\Omega=\sqrt{\omega_0^2-(\Delta\omega_{1/2})^2}$. Typically $\omega_0\gg\Delta\omega_{1/2}$, so $\Omega\approx\omega_0-(\Delta\omega_{1/2}/2\omega_0)\Delta\omega_{1/2}$, i.e., the ringing frequency lies well within the central spectral range of the original bubble resonance. For the smaller microbubbles found in the ocean, $Q\sim 7$, in which case the difference between Ω and ω_0 is found to be $<0.5\%$, so $\Omega\approx\omega_0$. When Q is greater than this, the difference between Ω and ω_0 is even smaller.

Like b in (19), the coupling factor (i.e., $\rho e^{-ikd}/4\pi d$) appearing on the right-hand side of Eqs. (9) and (10) typically varies little over the central peak of the bubble resonance spectrum, and may be assumed practically frequency independent. The impulse response of two radiatively

coupled bubbles may then be determined in a similar manner to (19), by modifying Eqs. (9) and (10) so that the driving terms on the right-hand side are replaced by delta functions. If the bubbles are identical (i.e., $\kappa_1=\kappa_2=\kappa$, $m_1=m_2=m$, $b_1=b_2=b$), we have

$$m\ddot{G}_1+b\dot{G}_1+\kappa G_1=-\delta(t-t_1)-\frac{\rho e^{-ikd}}{4\pi d}\ddot{G}_2, \tag{22}$$

$$m\ddot{G}_2+b\dot{G}_2+\kappa G_2=-\delta(t-t_2)-\frac{\rho e^{-ikd}}{4\pi d}\ddot{G}_1, \tag{23}$$

where the inclusion of t_1 and t_2 allows for a difference in the time of excitation of the two bubbles. Transformation to the Fourier transform domain yields two simultaneous algebraic equations, for $g_1(\omega)$ and $g_2(\omega)$. If $t_1=t_2=0$, so that both bubbles are excited at the same time, solution of these equations yields

$$\begin{aligned} g_1(\omega)=g_2(\omega)=g_+(\omega) &= \frac{-1}{(\kappa-\omega^2m+i\omega b)-\dfrac{\omega^2\rho e^{-ikd}}{4\pi d}} \\ &= g(\omega)\left[\frac{1}{1-f\dfrac{e^{-ikd}}{d}}\right], \end{aligned} \tag{24}$$

where $g_+=\frac{1}{2}(g_1+g_2)$; and f,$g(\omega)$ are related by (20) above. Recalling that we are still in the Fourier transform domain, Eq. (24) [which may be instructively compared with (8)] indicates that the impulse response for either of the coupled bubbles is the convolution of the impulse response for a single *un*coupled bubble with the time domain response of the interaction between the bubbles, whose Fourier transform is given by $[1-f(e^{-ikd}/d)]^{-1}$.

A. The multiple scattering regime

What information can be obtained by studying the properties of the bubble interaction transfer function represented in (24)? Let us first examine the case where $|fe^{-ikd}/d|<1$, so that the term in brackets may be expanded in a binomial series to give

$$\begin{aligned} g_+(\omega) &= g(\omega)\left[1+f\frac{e^{-ikd}}{d}+f^2\frac{e^{-2ikd}}{d^2}+\cdots\right] \\ &= g(\omega)\sum_{n=0}^{\infty} f^n\frac{e^{-inkd}}{d^n}. \end{aligned} \tag{25}$$

The factor f^n (i.e., representing powers of the scattering function f) appearing in (25) strongly suggests that each individual term in the summation represents a specific order of multiple scattering between the two bubbles. This may be explicitly shown by considering the inverse Fourier transform of the individual terms. Thus, denoting the nth term of $g_+(\omega)$ in (25) as $g_+^{(n)}(\omega)$, we can write

$$\begin{aligned} \int_{-\infty}^{\infty} g_+^{(n)}(\omega)\,e^{i\omega t}\,d\omega &= \int_{-\infty}^{\infty} g(\omega)\,\frac{f^n}{d^n}\,e^{i\omega(t-[nd/c])}d\omega \\ &= G_+^{(n)}\left(t-\frac{nd}{c}\right), \end{aligned} \tag{26}$$

where ω/c has been substituted for k, and the ''shift'' theorem for Fourier transforms (Ref. 20, pp. 104–107) has been used to show that the inverse Fourier transform of $g_+^{(n)}(\omega)$ represents a time function which is *delayed* by $t=nd/c$. Now, d/c is exactly the time it takes sound to propagate between the two bubbles and, bearing this in mind, inspection of (25) shows that, while the first term in the summation [i.e., $g(\omega)$ (at $t=0$)] indicates the original uncoupled scattering response of a single bubble, the higher-order terms in the series correspond to time functions delayed by $t=d/c$, $t=2d/c$, $t=3d/c,\ldots$, $t=nd/c$, etc., after the single bubble impulse response, and may be uniquely identified with successive rescattering events at the bubble sites as sound travels back and forth between them.

What can be learned from (25) about the actions of the successive rescattering processes, and their contributions to the final level of scattering from the two-bubble system? We have already seen, in Fig. 2(b), that damping can vary with the bubble separation. This effect should give rise to an associated variation in the scattered energy from the coupled system. The effects of the successive rescattering events may be studied by forming partial sums of the power series for $g_+(\omega)$ in (25), i.e., by calculating $\mathcal{P}_N[g_+(\omega)]=g(\omega)\Sigma_{n=0}^{N} f^n(e^{-inkd}/d^n)$. By Rayleigh's energy theorem for Fourier transforms (Ref. 20, pp. 112–113), the energy in the scattered time signal, up to and including the Nth rescattering, is then given by

$$\mathcal{E}_N=\int_{-\infty}^{\infty}|\mathcal{P}_N[g_+(\omega)]|^2d\omega. \tag{27}$$

In Fig. 3(a) the scattered energy for the impulse response of a system of two identical bubbles, each with $Q=30$ (i.e., a value of Q approaching that of the rather large bubbles used in Lauer's experiments[19]), is plotted as a function of the number of scatters [i.e., $N+1=$number of *re*scatters$+1$, since $N=0$ corresponds to the uncoupled scattering response]. The integral in (27) was evaluated numerically. The scattered energy $\mathcal{E}_N$ is scaled to the energy for an uncoupled bubble $\mathcal{E}_0$, and the number of scatters is plotted on a logarithmic scale.

Results are shown in Fig. 3(a) for four different values of d/a. When $d/a=300$ (solid line), the calculation indicates that the output scattered energy of the system [i.e., $\mathcal{E}_\infty$, which may be inferred by estimating asymptotes for the curves in Fig. 3(a)] is increased by multiple scattering. The increase ($\sim$ 7%–8%) is affected primarily by the first rescatter, while later rescatters have an essentially negligible effect. In contrast, when $d/a=100$ (dashed line), the overall effect of multiple scattering is to *reduce* the scattered energy of the system. The first rescatter reduces the energy by about 24%, while the second rescatter increases it again slightly, and subsequent rescatters after this have a small effect. What is the reason for these alternations in output energy? The

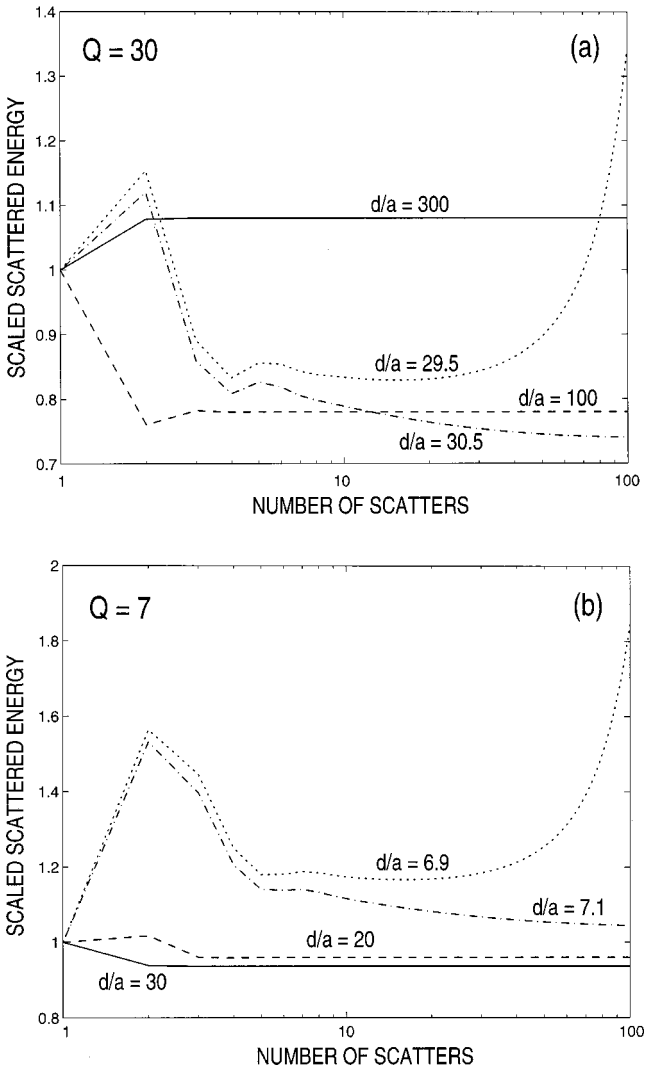

FIG. 3. Scattered energy from a coupled two-bubble system. The cumulative scattered energy is scaled against the energy for an uncoupled system (i.e., from one scatter), and plotted as a function of the number of scatters. [The scattered energy values for the discrete scattering increments are connected together by lines (solid, dashed, etc.) in order to accent the overall variation, and avoid the clutter of overlapping symbols due to the logarithmic scale.] The asymptotic value for many scatters is inversely proportional to the value of δ_+/δ_B [see Fig. 2(b)] for the same combination of d/a and Q: (a) $Q=30$; (b) $Q=7$.

explanation is indicated by Fig. 2(b), which shows that, at the resonance frequency of the ''+'' mode [i.e., ω_{0+}, see the discussion following (18)], multiple scattering may lead to $\delta_+/\delta_B<1$ or $\delta_+/\delta_B>1$ depending on the spacing and damping of the bubbles. Now, the impulse response of two identical bubbles coupled in the ''+'' mode should be similar to the decaying sinusoid for a single bubble represented by (21), but with a ringing frequency close to the downshifted resonance frequency ω_{0+}. It can be readily shown that the integrated energy of the impulse response of such an oscillatory system is inversely proportional to the damping. We should therefore expect the output energy $\mathcal{E}_\infty$ from the coupled system to vary with the bubble spacing, but in an *inverse manner* from δ_+/δ_B (evaluated at ω_{0+}). This is indeed observed: Detailed comparison of Figs. 2(b) and 3(a) shows that the asymptotic value of the scattered energy, reached after 100 scattering events [see Fig. 3(a)], approaches the value of δ_B/δ_+ [i.e., the inverse of δ_+/δ_B, derived from Fig. 2(b)] for corresponding values of d/a and Q.

The dot-dash line in Fig. 3(a) shows the variation in scattered energy when $d/a=30.5$. Since $d/a>Q(=30)$, the power series in (25) should still converge, which it does, although quite slowly. The first rescatter increases the energy by ~12%, but the second markedly reduces it again to a level ~15% below $\mathcal{E}_0$. Further rescatters cause the level to oscillate slightly, and then gradually approach the asymptotic limit of ~25% below $\mathcal{E}_0$ [cf. δ_B/δ_+, as inferred from Fig. 2(b)]. The dotted line in Fig. 3(a) shows the variation in scattered energy when $d/a=29.5$. Since $d/a<Q$, the power series in (25) should diverge. We see that the first few rescatters have effects similar to those seen when $d/a=30.5$. In this case, however, the energy does not approach an asymptotic limit, but eventually exhibits strongly divergent and unphysical behavior. The results for $d/a=30.5$ and $d/a=29.5$ in Fig. 3(a) illustrate the limitations of using a perturbation method to predict the effects of multiple scattering in bubbles. First, the power series may not converge. Second, even if the series does converge, great care must be taken to ensure that sufficient terms are included to correctly determine the final output scattering level (i.e., a level asymptotically close to $\mathcal{E}_\infty$), because the predicted level can fluctuate strongly from one scattering event to the next.

This second issue is emphasized more strongly in Fig. 3(b), which shows the scattered energy for a system of two identical bubbles with $Q=7$ (i.e., a value typical of the much smaller microbubbles found in bubble clouds and plumes near the ocean surface[12,21]). In this case, when $d/a\sim Q$, the first few rescatters can give rise to energy fluctuations of more than 50%. However, the asymptote predicted when $d/a=7.1$ indicates that the final change in energy due to multiple scattering remains much smaller [cf. Fig. 2(b)]. Figure 3(b) again shows that, when $d/a<Q$, the power series diverges. Subsequent calculations of this type [results not shown in Fig. 3(a) or (b)] demonstrated that, if the value of d/a is reduced much further below Q, the power series diverges more rapidly, and the partial sum over the first few terms increases catastrophically.

B. The strong coupling regime

Let us now consider the general case where $|fe^{-ikd}/d|>1$, so that (24) cannot be expanded in a binomial series. What is the physical implication of the impulse response in this case? Is the divergent power series merely a mathematical artifact, or does it signify a substantively different physical process?

To answer these questions, first rewrite (24) in a form similar to (20), i.e.,

$$g_+(\omega)=\frac{-1}{(\kappa-\omega^2 m+i\omega b)-\dfrac{\omega^2\rho e^{-ikd}}{4\pi d}}$$

$$=\frac{-1}{\kappa-\omega^2 m_++i\omega b_+} \tag{28}$$

[and also see Eqs. (13), (14), and (15)]. Both m_+ and b_+ are slowly varying within the dominant central spectral region of the bubble resonance. Assuming they are constant, and performing the inverse Fourier transform, yields [cf. (21)]: $G_+(t) = -e^{\alpha_+ t}\sin(\Omega_+ t)/(m_+\Omega_+)$ for the impulse response of the coupled system, where $\alpha_+ = b_+/2m_+$, and b_+, m_+ are evaluated at ω_0; $\Omega_+ = \sqrt{\omega_{0+}^2 - \alpha_+^2}$; and ω_{0+} is given by (17). The frequency Ω_+ is less than Ω (the value for a single bubble), having been downshifted as a result of the interactions between the bubbles.

It is instructive to study the magnitude of the frequency shift $\Omega - \Omega_+ \approx \omega_0 - \omega_{0+}$ [cf. discussion following (21)] as a function of d/a. Since it is always the case that $d/a > 1$, Eq. (17) for ω_{0+} can be expanded by using the binomial theorem, i.e.,

$$\omega_{0+} = \omega_0\left[1 - \frac{a}{2d}\cos\frac{\omega_{0+}d}{c} + \frac{3a^2}{8d^2}\cos^2\frac{\omega_{0+}d}{c} - \cdots\right]. \tag{29}$$

If $d/a > 4$, which is approximately the smallest bubble separation where the monopole approximation has been experimentally justified,[19,22,23] an error $< 2.5\%$ is incurred by truncating the expansion in (29) after the first order in (a/d) and writing

$$\omega_0 - \omega_{0+} \approx \frac{\omega_0 a}{2d}\cos\frac{\omega_{0+}d}{c}. \tag{30}$$

The condition for divergence of the power series for multiple scattering, i.e., $d/a < Q$, can now be reexpressed in the following way:

$$\frac{d}{a}\left\{ = \frac{\omega_0\cos\dfrac{\omega_{0+}d}{c}}{2(\omega_0 - \omega_{0+})}\right\} < Q\left\{ = \frac{\omega_0}{2\Delta\omega_{1/2}}\right\}, \tag{31}$$

which yields:

$$\omega_0 - \omega_{0+} > \Delta\omega_{1/2}\cos\frac{\omega_{0+}d}{c}. \tag{32}$$

For the cases under consideration, $0.54 \leqslant \cos(\omega_{0+}d/c) \leqslant 1$. Equation (32) is an important result, because it indicates that the impulse response of the coupled bubble system cannot be represented by a power series when the center frequency of the corresponding downshifted resonance peak lies outside the central spectral range of the original resonance. This makes good sense, since the spectral range of the scattering function f spans only the original resonance, and forming the aggregate of an infinite series of terms containing powers of f, as in (25), will not supply the spectral information required for $G_+(t)$, which lies outside this range when (32) applies.

There is, however, another interpretation of condition (32), which may be discerned when the time response of the two bubble system is such that they oscillate with different phases, i.e., when the motion is a combination of both ''+'' and ''−'' modes. Obviously, there are innumerable ways in which such motion could be generated. For the purposes of this discussion, let us consider the time response of the system when an external impulse is applied to only one of the bubbles, which then reradiates sound and interacts with the second bubble. This may be achieved, for example, by eliminating the delta function in (23), and then solving the coupled equations (22) and (23) to determine $G_1(t)$ and $G_2(t)$. These solutions, which may be obtained straightforwardly using the methods and assumptions already discussed, are

$$\begin{aligned}
G_1(t) &= [C_-(t) + C_+(t)]\cos\left(\frac{\Omega_- - \Omega_+}{2}t\right)\sin\left(\frac{\Omega_- + \Omega_+}{2}t\right) \\
&\quad + [C_-(t) - C_+(t)]\sin\left(\frac{\Omega_- - \Omega_+}{2}t\right)\cos\left(\frac{\Omega_- + \Omega_+}{2}t\right) \\
&\approx [C_-(t) + C_+(t)]\cos\left(\frac{\omega_{0-} - \omega_{0+}}{2}t\right)\sin\omega_0 t \\
&\quad + [C_-(t) - C_+(t)]\sin\left(\frac{\omega_{0-} - \omega_{0+}}{2}t\right)\cos\omega_0 t\,; \qquad (33)
\end{aligned}$$

$$\begin{aligned}
G_2(t) &= -[C_-(t) + C_+(t)]\sin\left(\frac{\Omega_- - \Omega_+}{2}t\right)\cos\left(\frac{\Omega_- + \Omega_+}{2}t\right) \\
&\quad - [C_-(t) - C_+(t)]\cos\left(\frac{\Omega_- - \Omega_+}{2}t\right)\sin\left(\frac{\Omega_- + \Omega_+}{2}t\right) \\
&\approx -[C_-(t) + C_+(t)]\sin\left(\frac{\omega_{0-} - \omega_{0+}}{2}t\right)\cos\omega_0 t \\
&\quad - [C_-(t) - C_+(t)]\cos\left(\frac{\omega_{0-} - \omega_{0+}}{2}t\right)\sin\omega_0(t)\,, \qquad (34)
\end{aligned}$$

where $C_-(t) = -e^{-\alpha_- t}/(2m_-\Omega_-)$; $\alpha_- = b_-/2m_-$, and b_-, m_- are evaluated at ω_0; $\Omega_- = \sqrt{\omega_{0-}^2 - \alpha_-^2}$; ω_{0-} is given by (17); and $C_+(t) = -e^{-\alpha_+ t}/(2m_+\Omega_+)$.

Examination of these equations shows that each of the terms in (33) and (34) contains three parts. First, a coefficient which incorporates amplitude and exponential time decay components. Second, an oscillatory feature which varies at about the resonance frequency ω_0 of the single-bubble resonance. Third, another oscillation which varies at a much slower frequency (approximately equal to half the difference between the frequencies of the ''+'' and ''−'' modes) and serves to modulate the envelope of the overall response. Examination also shows that G_1 and G_2 are in quadrature. The phases of both the ω_0 and $(\omega_{0-} - \omega_{0+})/2$ oscillations in G_2 lag behind their counterparts in G_1 by 90 deg.

The phenomenon represented by (33) and (34) closely resembles behavior which is observed in a well-known problem of classical mechanics, i.e., the combined motion of two coupled pendulums (Ref. 17, pp. 103–105). Bubble 1 is set into motion by an external impulse, while bubble 2 initially remains at rest. Bubble 1 begins to oscillate, radiates sound, and bubble 2 begins to move by responding to the radiated field from bubble 1. The oscillation amplitude of bubble 2 increases by absorbing energy from bubble 1, whose amplitude correspondingly decreases. The amplitude of bubble 1

reaches a minimum at exactly the same time as the amplitude of bubble 2 reaches a maximum. As time goes on the process reverses, and the energy is transferred back to bubble 1. Energy continues to be transferred back and forth between the bubbles while, at the same time, their oscillations are damped by radiation of sound outside the system and other loss mechanisms. The cyclical variation of the amplitudes G_1 and G_2 is represented by the slower of the oscillatory terms in Eqs. (33) and (34), and is thus characterized by the frequency $(\omega_{0-}-\omega_{0+})/2$.

Modifying the procedure which led through Eq. (29) to Eq. (30), we can show, to the same order of approximation, that $(\omega_{0-}-\omega_{0+})/2 \approx \omega_0-\omega_{0+} \approx (\omega_0 a/2d)\cos(\omega_{0+} d/c)$, and then rewrite condition (32) as

$$\frac{\omega_{0-}-\omega_{0+}}{2} > \Delta\omega_{1/2} \cos\frac{\omega_{0+} d}{c}. \tag{35}$$

Recognizing that the exchange of energy back and forth between the bubbles is driven (or ''induced'') by the radiative coupling between them, and is inversely proportional to the distance separating them, now leads to a second, and more physically intuitive, interpretation of the equivalent inequality conditions (32) and (35). When the two bubbles are far apart the coupling is weak, and the rate of energy exchange due to cycling is less than the rate of energy loss which each bubble experiences as a result of its individual damping mechanisms. In this case, the time variation of the scattering amplitude of each bubble is predominantly determined by its damping parameter α [$=\Delta\omega_{1/2}$, see (21) and the following discussion] rather than the cycling frequency, so that $\Delta\omega_{1/2} > (\omega_{0-}-\omega_{0+})/2$. The interaction between the two bubbles can be treated as a perturbation of their individual motions, and characterized as a *multiple scattering* process whose magnitude may be determined via a power series expansion [*viz.*, (25)].

When the coupling is strong, however, so that the rate of energy exchange due to cycling is greater than the rate of individual energy loss due to damping, i.e., $\Delta\omega_{1/2} < (\omega_{0-}-\omega_{0+})/2$, the perturbation picture is no longer valid. The energy ''stored'' in the coupling is so great that it dominates the behavior of the two bubbles, which can then no longer be individually resolved insofar as the scattering process is concerned. In this case, a fully coupled self-consistent description is strongly indicated if the behavior of the ensemble is to be accurately determined.

We can now see that the multiple scattering and self-consistent approaches to describing acoustic interactions between the two air bubbles should not be viewed as alternative ways of looking at the same phenomenon. Due to the strongly resonant character of bubbles, they actually represent distinct physical pictures. The multiple scattering approach imposes a paradigm which implicitly incorporates discretely separated scattering events as the primary means of energy exchange. The self-consistent methodology, conversely, while capable of characterizing the system as an interaction between multiple scatterers, can also describe it as an interaction between stongly coupled resonators wherein the energy exchange is primarily due to radiative cycling rather than scattering. Only when $|fe^{-ikd}/d|<1$ are the two approaches formally equivalent.

C. More than two bubbles

What effects would the introduction of additional bubbles into the ensemble have on the conclusions of the foregoing discussion? In my previous paper,[16] I also considered the case of three identical bubbles placed at the apices of an equilateral triangle, and mutually separated by a distance d. In this case, three self-consistent coupled differential equations may be written to describe the behavior of the system [cf. Eqs. (9) and (10)]. Just as the equations for the two-bubble case can be combined to give uncoupled equations for v_+ and v_-, a similar procedure can be adopted for the three-bubble system using the following combinations of v_1, v_2, and v_3: $v_A=1/\sqrt{3}(v_1+v_2+v_3)$, $v_B=1/\sqrt{2}(v_1-v_2)$; $v_C=1/\sqrt{6}(v_1+v_2-2v_3)$, where the square-root factors are normalizing constants. In particular, the differential equation for v_A describes motion (cf. v_+ in the two-bubble case) in which all of the three bubbles oscillate in phase. Transforming to the Fourier transform domain, and solving for the corresponding impulse response, yields

$$g_A(\omega) = \frac{-1}{(\kappa-\omega^2 m+i\omega b)-\dfrac{2\omega^2\rho e^{-ikd}}{4\pi d}} = g(\omega)\left[\frac{1}{1-2f\dfrac{e^{-ikd}}{d}}\right]. \tag{36}$$

This expression may be expanded in a binomial series (to achieve a perturbation expansion for the multiple scattering interactions) if $|2fe^{-ikd}/d|<1$. Substituting the maximum value of $|f|$ $(=a/\delta_B)$ yields the convergence condition $d/a > 2/\delta_B \approx 2Q$ [cf. the discussion following Eq. (6)]. The introduction of the third bubble has the effect of making the convergence condition more restrictive than when there were just two bubbles, i.e., the bubbles now have to be *twice as far apart* from each other than before (for the same Q) in order for a multiple scatter counting approach to be applicable. As further bubbles are added to the system it can be shown, by setting up larger sets of coupled differential equations and solving them in an equivalent manner, that the convergence condition becomes progressively more restrictive.

While these phenomena have been discussed in terms of ensembles of identical bubbles, which rarely occur in nature, they should nevertheless circumscribe the applicability of the multiple scattering approach to practical problems involving extended media containing many strong, and closely spaced, scatterers.

IV. CONCLUSIONS

The multiple interactions of air bubbles in water have been studied in the time domain and show that the acoustic phenomena are best understood in terms of the classical theory of coupled resonators. The self-consistent methodol-

ogy for enumerating the interactions implicitly adopts this picture, gives the most complete physical description, and makes it possible to differentiate between the multiple scattering and self-consistent approaches to the interaction problem in a completely new way. It is seen that, by imposing a multiple scattering paradigm on the interaction between the bubbles, discretely separated scattering events are implicitly incorporated as the means by which energy is exchanged. The self-consistent methodology, conversely, is capable of characterizing the system more comprehensively: either (as before) as an interaction between multiple scatterers; or else as an interaction between strongly coupled resonators wherein the energy exchange is primarily due to radiative cycling rather than scattering. The work described here indicates the limitations of the multiple scattering approach for systems of strongly interacting bubbles, particularly in the resonance region, and its point of failure, and also shows how the number of perturbation terms necessary to determine the true scattering level depends on the properties of the individual bubbles and their spacings.

ACKNOWLEDGMENTS

The author would like to thank G. E. Ioup for helpful discussions concerning the theory of the Fourier transform; and J. C. Novarini and P. M. Jordan for carefully reading and commenting upon the manuscript. This work was supported by the Office of Naval Research with technical management provided by the Naval Research Laboratory, PE 61153N.

[1] See, for example, the following papers: P. H. Dahl, ''Bubble clouds and their transport within the surf zone as measured with a distributed array of upward-looking sonars,'' J. Acoust. Soc. Am. **109**, 133–142 (2001); J. W. Caruthers, S. J. Stanic, P. A. Elmore, and R. R. Goodman, ''Acoustic attenuation in very shallow water due to the presence of bubbles in rip currents,'' *ibid.* **106**, 617–625 (1999); P. H. Dahl and W. J. Plant, ''The variability of high-frequency acoustic backscatter from the region near the sea surface,'' *ibid.* **101**, 2596–2602 (1997); A. Prosperetti, N. Q. Lu, and H. S. Kim, ''Active and passive acoustic behavior of bubble clouds at the ocean's surface,'' *ibid.* **93**, 3117–3127 (1993); D. M. Farmer and S. Vagle, ''Waveguide propagation of ambient sound in the ocean-surface bubble layer,'' *ibid.* **86**, 1897–1908 (1989).

[2] P. A. Ching and D. E. Weston, ''Wideband studies of shallow-water acoustic attenuation due to fish,'' J. Sound Vib. **18**, 499–510 (1971).

[3] T. N. Gardner, ''An acoustic study of soils that model seabed sediments containing gas bubbles,'' J. Acoust. Soc. Am. **107**, 163–176 (2000).

[4] L. L. Foldy, ''The multiple scattering of waves. I. General theory of isotropic scattering by randomly distributed scatterers,'' Phys. Rev. **67**, 107–119 (1945).

[5] E. L. Carstensen and L. L. Foldy, ''Propagation of sound through a liquid containing bubbles,'' J. Acoust. Soc. Am. **19**, 481–501 (1947).

[6] Z. Ye and L. Ding, ''Acoustic dispersion and attenuation relations in bubbly mixture,'' J. Acoust. Soc. Am. **98**, 1629–1636 (1995).

[7] F. S. Henyey, ''Corrections to Foldy's effective medium theory for propagation in bubble clouds and other collections of very small scatterers,'' J. Acoust. Soc. Am. **105**, 2149–2154 (1999).

[8] C. Feuillade, R. W. Nero, and R. H. Love, ''A low frequency acoustic scattering model for small schools of fish,'' J. Acoust. Soc. Am. **99**, 196–208 (1996).

[9] V. C. Anderson, ''Sound scattering from a fluid sphere,'' J. Acoust. Soc. Am. **22**, 426–431 (1950).

[10] C. Feuillade and C. S. Clay, ''Anderson (1950) revisited,'' J. Acoust. Soc. Am. **106**, 553–564 (1999).

[11] M. Minnaert, ''On musical air-bubbles and the sounds of running water,'' Philos. Mag. **16**, 235–248 (1933).

[12] C. Devin, ''Survey of thermal, radiation, and viscous damping of pulsating air bubbles in water,'' J. Acoust. Soc. Am. **31**, 1654–1667 (1959).

[13] H. Lamb, *Hydrodynamics*, 6th ed. (Dover, New York, 1945), Sec. 56.

[14] V. Twersky, ''Multiple scattering of waves and optical phenomena,'' J. Opt. Soc. Am. **52**, 145–171 (1962).

[15] G. Kapodistrias and P. H. Dahl, ''Effects of interaction between two bubble scatterers,'' J. Acoust. Soc. Am. **107**, 3006–3017 (2000).

[16] C. Feuillade, ''Scattering from collective modes of air bubbles in water and the physical mechanism of superresonances,'' J. Acoust. Soc. Am. **98**, 1178–1190 (1995).

[17] T. D. Rossing and N. H. Fletcher, *Principles of Vibration and Sound* (Springer, New York, 1995).

[18] I. Tolstoy, ''Superresonant systems of scatterers. I,'' J. Acoust. Soc. Am. **80**, 282–294 (1986).

[19] H. Lauer, ''Über die thermische dampfung von blasen verschiedener gase in wasser,'' Acustica, Akust. Beih. **1**, AB12–AB24 (1951).

[20] R. N. Bracewell, *The Fourier Transform and its Applications*, 2nd ed. revised (McGraw-Hill, New York, 1986).

[21] E. C. Monahan, ''Occurrence and evolution of acoustically relevant subsurface bubble plumes and their associated, remotely monitorable, surface whitecaps,'' in *Natural Physical Sources of Underwater Sound*, edited by B. R. Kerman (Kluwer Academic, Dordrecht, Netherlands, 1993), pp. 503–516.

[22] M. Strasberg, ''The pulsation frequency of non-spherical gas bubbles in liquids,'' J. Acoust. Soc. Am. **25**, 536–537 (1953).

[23] Z. Ye and C. Feuillade, ''Sound scattering by an air bubble near a plane sea surface,'' J. Acoust. Soc. Am. **102**, 798–805 (1997).

Time reversal for a single spherical scatterer

David H. Chambers
Lawrence Livermore National Laboratory, P.O. Box 808, L-154, Livermore, California 94551

A. K. Gautesen
Department of Mathematics, 136 Wilhelm Hall, Iowa State University, Ames, Iowa 50011

(Received 11 December 2000; accepted for publication 3 March 2001)

We show that the time reversal operator for a planar time reversal mirror (TRM) can have up to four distinct eigenvalues with a small spherical acoustic scatterer. Each eigenstate represents a resonance between the TRM and an induced scattering moment of the sphere. Their amplitude distributions on the TRM are orthogonal superpositions of the radiation patterns from a monopole and up to three orthogonal dipoles. The induced monopole moment is associated with the compressibility contrast between the sphere and the medium, while the dipole moments are associated with density contrast. The number of eigenstates is related to the number of orthogonal orientations of each induced multipole. For hard spheres (glass, metals) the contribution of the monopole moment to the eigenvalues is much greater than that of the dipole moments, leading to a single dominant eigenvalue. The other eigenvalues are much smaller, making it unlikely multiple eigenvalues could have been observed in previous experiments using hard materials. However, for soft materials such as wood, plastic, or air bubbles the eigenvalues are comparable in magnitude and should be observable. The presence of multiple eigenstates breaks the one-to-one correspondence between eigenstates and distinguishable scatterers discussed previously by Prada and Fink [Wave Motion **20**, 151–163 (1994)]. However, eigenfunctions from separate scatterers would have different phases for their eigenfunctions, potentially restoring the ability to distinguish separate scatterers. Since relative magnitudes of the eigenvalues for a single scatterer are governed by the ratio of the compressibility contrast to the density contrast, measurement of the eigenvalue spectrum would provide information on the composition of the scatterer.
[DOI: 10.1121/1.1368404]

PACS numbers: 43.20.Fn, 43.60.Pt [ANN]

I. INTRODUCTION

Time reversal is a technique that focuses waves onto a source or scatterer by emitting a time-reversed version of the received wave field measured at several points in space. It exploits the invariance of the wave equation for lossless media to changes in the sign of the time variable. This invariance has been apparent since the initial development of the wave equation. In 1965 Parvulescu and Clay demonstrated the technique between pairs of receivers in the ocean.[1] However, a practical acoustic system that can measure a wave field at multiple points, time reverse the signals, and then send them back towards their origin has only recently been developed. Since the first results from a time-reversing array system by Fink *et al.*[2] in 1989, time reversal has become a subject of great interest both experimentally and theoretically (see Refs. 3 and 4 for recent reviews). Much of this interest has centered on the ability of time reversal systems to focus wave energy through complicated inhomogeneous media.

In the presence of multiple scatterers, the time reversal procedure has typically been used to focus on the strongest scatterer in the volume. Using an operator formalism to describe the time reversal process, Prada *et al.*[5–7] in a series of papers showed that the eigenvalues of the time reversal (TR) operator corresponded one-to-one with distinct scatterers in the volume. Furthermore, the eigenvalues were naturally ordered according to the strength of the scatterers, with the largest eigenvalue corresponding to the strongest scatterer. The eigenfunctions of the TR operator specified the amplitude and phase distributions across the array that focused on their respective scatterers. An experimental procedure (D.O.R.T method) based on the singular value decomposition of the TR operator was employed to focus sequentially on individual scatterers in a water tank. Prada's proof of the one-to-one correspondence between TR eigenvalues and scatterers assumes that the scatterers are pointlike (spherically symmetric scattered amplitude) and well separated (negligible multiple scattering). The first assumption requires the scatterers to be small, less than a wavelength in size, and have densities matched to the acoustic medium. Small scatterers whose densities are different from the host medium will scatter acoustic energy in a preferential direction (see Ref. 8).

In this article we extend Prada's analysis of the acoustic TR operator to small (pointlike) scatterers with arbitrary densities. We show that even for the case of a single spherical scatterer, the TR operator can have up to four distinct nonzero eigenvalues. One eigenvalue, typically the largest in magnitude, is associated with the spherically symmetric part of the scattered amplitude (monopole moment). The other three eigenvalues are associated with the directional part of the scattered amplitude (dipole moment) and vanish when the scatterer material density approaches the density of the medium. These results are obtained from an analysis of a planar time reversal mirror (TRM)[9] and a single small spherical scatterer. We derive an explicit expression for the TR operator in the second section and determine the eigen-

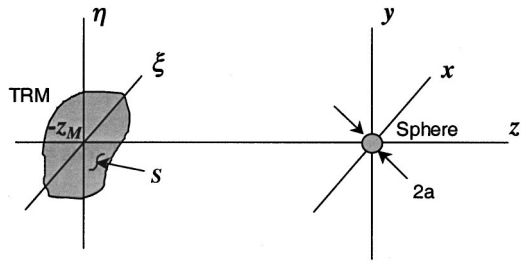

FIG. 1. Geometry of time reversal mirror (TRM) and sphere.

value problem that gives the eigenvalues and eigenfunctions. In the next section we calculate the analytic solution for the case of a TRM symmetric about the *x* and *y* axes. We determine bounds for the relative amplitudes of the eigenvalues and discuss the variation with different materials. We show that the first eigenvalue dominates for the hard, dense materials such as those investigated experimentally by Prada,[5–7] making it unlikely that other eigenvalues could be observed. We evaluate the eigenvalues for the specific examples of a circular and narrow rectangular TRM in the fourth section. The latter approximates a linear array. The eigenvalues for other examples, including an elliptical TRM, are given in Appendix A. Finally, we repeat the eigenvalue analysis for TRMs composed of discrete array elements in Appendix B.

II. DEVELOPMENT OF THE TR OPERATOR

Consider a planar time reversal mirror at a distance z_M from a sphere of radius a at the origin of our coordinate system (Fig. 1). The TRM is finite in extent but otherwise of arbitrary shape and size. We will assume that the distance z_M is much greater than the wavelength λ of the acoustic field and the sphere radius a is much less than a wavelength. Following Cassereau and Fink,[9] we model the TRM in transmission as a region in an infinite, rigid baffle where the distribution of normal velocity $U_M(\xi,\eta,\omega)$ is specified, ξ and η are the *x* and *y* coordinates of a point on the TRM. In reception the TRM measures the pressure field $P_M(\xi,\eta,\omega)$ incident on the mirror surface. This configuration follows models of real transducers.[10] In actual practice the normal velocity is a pulse, but for analytical convenience we will consider the case of single frequency ω and omit explicit references to frequency unless otherwise required for clarity. The TRM then becomes equivalent to a phase conjugate mirror (PCM)[11,13] and results for an actual pulse and TRM can be obtained by Fourier synthesis.

We start by calculating the pressure field at a given point of the mirror that is scattered back from the sphere when it is irradiated by the TRM. The pressure field emitted from an arbitrary velocity distribution on the mirror is[12]

$$p(x)=-\frac{i\rho\omega}{2\pi}\int_S U_M(\xi,\eta)\frac{e^{ikr_M}}{r_M}dS, \tag{1}$$

where $r_M=\sqrt{z_M^2+(x-\xi)^2+(y-\eta)^2}$, $k=\omega/c$, ρ is the density, and c is the sound speed in the medium. The sphere scatters this field in all directions, including back towards the TRM. Since $z_M \gg \lambda$ and $a \ll \lambda$ the incident field on the sphere can be considered as a superposition of plane waves, each emitted from an element $dS=d\xi d\eta$ on the TRM. Using the expression for the scattered field from a small sphere illuminated by a unit amplitude plane wave,[8]

$$P_a(x)=\frac{1}{3}k^2a^3\left(\frac{\kappa_s-\kappa}{\kappa}-3\frac{\rho_s-\rho}{2\rho_s+\rho}\cos\theta\right)\frac{e^{ikr}}{r}, \tag{2}$$

the received pressure at position (ξ',η') on the TRM is

$$P_M(\xi',\eta')=-\frac{i\rho c}{6\pi}k^3a^3\frac{e^{ikr_M'}}{r_M'}\int_S U_M(\xi,\eta)\times\left(\frac{\kappa_s-\kappa}{\kappa}-3\frac{\rho_s-\rho}{2\rho_s+\rho}\cos\theta\right)\frac{e^{ikr_M}}{r_M}dS. \tag{3}$$

In the above expression, r_M is the distance between the sphere and element dS, r_M' is the distance to the point $\boldsymbol{\xi}'=(\xi',\eta',-z_M)$, cos θ is the angle between the vectors $\boldsymbol{\xi}=(\xi,\eta,-z_M)$ and $\boldsymbol{\xi}'$, κ and κ_s are the compressibilities of the medium and sphere, and ρ_s is the density of the sphere. Note that the sign of the density contrast term is opposite to that in Ref. 8 because $\boldsymbol{\xi}$ is directed opposite to the propagation direction of the plane wave from *dS*.

To complete the description of the time reversal operator we imagine the TRM to be composed of a distribution of transducers which convert input voltages $E(\xi,\eta,\omega)$ to normal velocity $U_M(\xi,\eta,\omega)$ on transmit and pressure $P_M(\xi',\eta',\omega)$ to output voltages $R(\xi',\eta',\omega)$ on receive. Time reversal is applied to the output voltage to generate the next input voltage. Following Prada and Fink,[5] we assume linear relationships between voltages and acoustic field quantities,

$$U_M(\xi,\eta,\omega)=cA_e(\omega)E(\xi,\eta,\omega),$$

$$R(\xi,\eta,\omega)=A_r(\omega)P_M(\xi,\eta,\omega)/\rho c^2.$$

The final expression relating the output voltage to the input voltage is obtained by combining these relationships with Eq. (3):

$$R(\xi',\eta',\omega)=\int_S K_s(\boldsymbol{\xi}',\boldsymbol{\xi},\omega)E(\xi,\eta,\omega)\,dS\equiv K_s\circ E. \tag{4}$$

(The circle operator is used instead of the asterisk to distinguish the integral operator here from convolution.) This integral operator is the continuous version of Prada's time reversal operator for a finite array. The *scattering kernel* $K_s(\boldsymbol{\xi}',\boldsymbol{\xi},\omega)$ is given by

$$K_s(\boldsymbol{\xi}',\boldsymbol{\xi},\omega)=-\frac{i}{6\pi}A_r(\omega)A_e(\omega)(ka)^3\times\left(\alpha-\beta\frac{\boldsymbol{\xi}'\cdot\boldsymbol{\xi}}{r_M'r_M}\right)\frac{e^{ik(r_M'+r_M)}}{r_M'r_M}, \tag{5}$$

where $\alpha=(\kappa_s-\kappa)/\kappa$, $\beta=3(\rho_s-\rho)/(2\rho_s+\rho)$, and the cosine is replaced with the equivalent vector dot product.

Time reversal is an iterative procedure in which the nth input voltage E_n is determined by time reversing the previous output voltage, i.e., $E_n=R_{n-1}^*$. In the frequency domain, time reversal is equivalent to applying the complex conjugate assuming the voltages are real.[11,13] Applying time reversal iteratively to a given input E_0 using (4), we generate the sequence

$$
\begin{aligned}
&R_0 = K_s \circ E_0 \\
&E_1 = R_0^* = K_s^* \circ E_0^*, \quad R_1 = K_s \circ E_1, \\
&\vdots \\
&E_{2m} = (K_s^* \circ K_s)^m \circ E_0, \quad R_{2m} = K_s \circ E_{2m} \\
&E_{2m+1} = (K_s^* \circ K_s)^m \circ K_s^* \circ E_0, \quad R_{2m+1} = K_s \circ E_{2m+1}.
\end{aligned} \tag{6}
$$

This sequence is the same as that derived by Prada and Fink[5] for a discrete array. It eventually converges to an eigenfunction (or linear combination of eigenfunctions for degenerate eigenvalues) of the time reversal kernel $K_s^* \circ K_s$. Subsequent applications of the operator produce the original input multiplied by an eigenvalue of the operator. For a general input E_0, the sequence converges to the eigenfunction(s) associated with the largest eigenvalue.

III. ANALYSIS OF THE TR OPERATOR

The convergence of the time reversal process is governed by the eigenvalues of the time reversal operator. These are determined from solutions of the eigenvalue problem

$$
(K_s^* \circ K_s) \circ \Phi = \mu_{\mathrm{TR}}^2 \Phi. \tag{7}
$$

The kernel $(K_s^* \circ K_s)$ is Hermitian, which implies that its eigenvalues are real and the eigenvectors are orthogonal. We can reduce the number of extraneous factors by defining

$$
\phi(\xi,\eta) = \Phi(\xi,\eta) e^{ikr_M}, \quad \mu^2 = \frac{36\pi^2}{(ka)^6} \frac{\mu_{\mathrm{TR}}^2}{|A_e A_r|^2}.
$$

The eigenvalue problem becomes

$$
(K \circ K) \circ \phi = \mu^2 \phi, \tag{8}
$$

with the *reduced scattering kernel* $K(\boldsymbol{\xi}', \boldsymbol{\xi})$,

$$
K(\boldsymbol{\xi}', \boldsymbol{\xi}) = \frac{1}{r_M' r_M} \left(\alpha - \beta \frac{\boldsymbol{\xi}' \cdot \boldsymbol{\xi}}{r_M' r_M} \right). \tag{9}
$$

It is simpler to solve the equivalent eigenvalue problem

$$
\mu \phi(\xi', \eta') = \int_S \frac{1}{r_M' r_M} \left(\alpha - \beta \frac{\boldsymbol{\xi}' \cdot \boldsymbol{\xi}}{r_M' r_M} \right) \phi(\xi,\eta)\, dS, \tag{10}
$$

where μ is real due to the symmetry of the kernel. Note that we have removed the phase distribution of the eigenfunction by our definition of ϕ. The reduced eigenvalue problem then determines only the amplitude distribution of the TRM for an eigenstate. Thus all the eigenstates of the TR operator for a single scatterer share the same phase structure, i.e., they all focus on the scatterer but with different amplitude distributions.

Equation (10) is the fundamental eigenvalue problem that determines the properties of the time reversal operator. It is a Fredholm integral equation of the second kind with a real, symmetric, separable kernel composed of four terms. There can be up to four distinct real eigenvalues with four orthogonal eigenfunctions, each representing an amplitude distribution of the TRM that focuses on the sphere. The orthogonality relation for the eigenfunctions is

$$
\int_S \phi_m(\xi,\eta)\, \phi_n(\xi,\eta)\, dS \propto \delta_{mn}.
$$

Iteration of the time reversal process will generally converge to the eigenfunction associated with the largest eigenvalue. However, if the contribution from this eigenfunction were removed using an orthogonalization process such as Gram–Schmidt, time reversal would converge to the eigenfunction associated with the next largest eigenvalue. This procedure could be repeated four times to identify the four eigenfunctions in descending order of their eigenvalue magnitudes. Each term in the kernel is linearly independent, with one term associated with compressibility contrast (monopole) and the other three terms associated with density contrast (dipoles). The eigenfunctions are orthogonal combinations of these terms. If the density contrast vanishes, the time reversal operator will have only one eigenstate, which is the case previously investigated by Prada for multiple point scatterers.[5–7] In the presence of multiple scatterers, one can no longer assume each eigenstate of the time reversal operator identifies a different scatterer since several eigenstates are associated with each scatterer. Thus breaking the spherical symmetry of the scattering amplitude for a given scatterer produces multiple eigenstates of the TR operator.

The integral equation (10) can be reduced to an ordinary matrix eigenvalue problem using the property that the eigenfunctions $\phi(\xi, \eta)$ are linear combinations of the separable functions in the kernel. We write the kernel in the form

$$
K(\boldsymbol{\xi}, \boldsymbol{\xi}') = \alpha w_1(\boldsymbol{\xi}) w_1(\boldsymbol{\xi}') - \beta \sum_{j=2}^{4} w_j(\boldsymbol{\xi}) w_j(\boldsymbol{\xi}'), \tag{11}
$$

and the eigenfunctions as $\phi(\xi,\eta) = \Sigma_{j=1}^4 \hat{\phi}_j w_j(\boldsymbol{\xi})$. The functions $w_j(\boldsymbol{\xi})$ are

$$
\begin{aligned}
&w_1(\boldsymbol{\xi}) = \frac{1}{r_M}, \quad w_2(\boldsymbol{\xi}) = \frac{z_M}{r_M^2}, \\
&w_3(\boldsymbol{\xi}) = \frac{\eta}{r_M^2}, \quad w_4(\boldsymbol{\xi}) = \frac{\xi}{r_M^2}.
\end{aligned} \tag{12}
$$

The eigenvalue problem reduces to the system

$$
\begin{aligned}
&\alpha \sum_{n=1}^{4} W_{1n} \hat{\phi}_n = \mu \hat{\phi}_1, \\
&-\beta \sum_{n=1}^{4} W_{mn} \hat{\phi}_n = \mu \hat{\phi}_m, \quad m = 2,3,4,
\end{aligned} \tag{13}
$$

where $W_{mn} = \int_s w_m(\boldsymbol{\xi}) w_n(\boldsymbol{\xi})\, dS$ is the symmetric reduced scattering matrix.

If the TRM is symmetric around the ξ and η axes, all the off-diagonal terms of W_{mn} vanish except for W_{12} (and W_{21}). These are

$$
\begin{aligned}
&W_{11} = \int_S \frac{dS}{r_M^2}, \quad W_{12} = z_M \int_S \frac{dS}{r_M^3}, \quad W_{22} = z_M^2 \int_S \frac{dS}{r_M^4}, \\
&W_{33} = \int_S \frac{\eta^2 dS}{r_M^4}, \quad W_{44} = \int_S \frac{\xi^2 dS}{r_M^4}.
\end{aligned}
$$

TABLE I. Compressibility and density ratios relative to water for common materials.

Material	α	β	β/α
Brass	83	1.3	0.016
Copper	98	1.3	0.013
Steel	130	1.2	0.0092
Glass	31	0.70	0.023
Hard rubber	1.8	0.25	0.14
Soft rubber	−0.53	−0.052	0.098
Cork	−0.97	−1.5	0.65
Oak	4.1	−0.34	−0.83
Pine	1.4	−0.87	−0.62
Air	−1.0	−3.0	3.0

The characteristic equation for the eigenvalues is then

$$(\mu+\beta W_{33})(\mu+\beta W_{44})(\mu^2-(\alpha W_{11}-\beta W_{22})\mu - \alpha\beta(W_{11}W_{22}-W_{12}^2))=0, \tag{14}$$

with solutions

$$\mu_m=\frac{\alpha}{2}\left(W_{11}-\frac{\beta}{\alpha}W_{22}\right) \times\left[1-(-1)^m\sqrt{1+\frac{4\beta}{\alpha}\frac{W_{11}W_{22}-W_{12}^2}{(W_{11}-\beta W_{22}/\alpha)^2}}\right], \quad m=1,2, \tag{15}$$

$$\mu_3=-\beta W_{33}, \quad \mu_4=-\beta W_{44}.$$

We have $W_{12}^2\leqslant W_{11}W_{22}$ from the Schwartz inequality, which guarantees that for $\beta/\alpha\geqslant 0$ the quantity under the radical is non-negative and the eigenvalues are real. When $\beta/\alpha<0$ the quantity under the radical can be written as

$$\frac{(W_{11}+\beta W_{22}/\alpha)^2-4\beta W_{12}^2/\alpha}{(W_{11}-\beta W_{22}/\alpha)^2},$$

which is also non-negative, so that the eigenvalues are always real, as expected. Note also that the denominator of the term in the radical of Eq. (15) is identical to the prefactor so that the eigenvalue is always finite if all the W_{mn} are finite. The numbering of the eigenvalues was chosen so that μ_1 is the only nonvanishing eigenvalue when $\beta\to 0$.

From the form of the eigenvalues it is clear that the relative magnitudes between the first eigenvalue and the others depend on the ratio β/α, which can assume any positive or negative value. Since multiple eigenvalues have yet to be observed, we will investigate their relative magnitudes as a function of β/α. Table I shows values of α and β for various materials relative to water calculated from data found in the text by Kinsler *et al.*[14] The ratio β/α ranges from around 0.01 for hard materials (metal and glass) to nearly 1.0 for soft woods. The maximum value of 3.0 for air represents time reversal with a single small bubble. In Prada *et al.*'s experiments[5–7] no evidence of multiple eigenfunctions for single scatters was reported, which is consistent with the values of β/α for the scatterer materials used in her measurements. To determine conditions where other eigenvalues become important, we will calculate the magnitudes of the ratios of the other eigenvalues to μ_1.

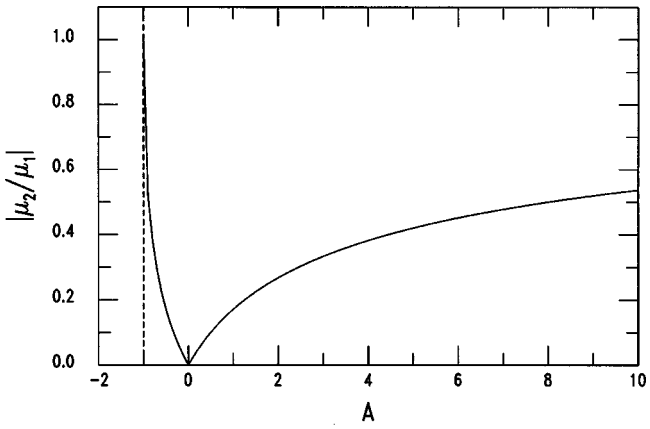

FIG. 2. Ratio of second to first eigenvalue as a function of A. See text for definition of A. Dashed vertical line at $A=-1$ is shown for reference.

The ratio between μ_2 and μ_1 is

$$\left|\frac{\mu_2}{\mu_1}\right|=\frac{|1-\sqrt{1+A}|}{1+\sqrt{1+A}}, \quad A=\frac{4\beta}{\alpha}\frac{W_{11}W_{22}-W_{12}^2}{(W_{11}-\beta W_{22}/\alpha)^2}. \tag{16}$$

Note that A ranges from a minimum of $-1+W_{12}^2/(W_{11}W_{22})$ at $\beta/\alpha=-W_{11}/W_{22}$ to a maximum of ∞ at $\beta/\alpha=W_{11}/W_{22}$. A plot of $|\mu_2/\mu_1|$ as a function of A (Fig. 2) shows that this ratio never exceeds 1. It achieves its maximum when $A\to\infty$ at $\beta/\alpha=W_{11}/W_{22}$. When $|\beta/\alpha|\ll 1$, the ratio simplifies to

$$\left|\frac{\mu_2}{\mu_1}\right|\sim\left|\frac{\beta}{\alpha}\right|\frac{W_{11}W_{22}-W_{12}^2}{W_{11}^2}. \tag{17}$$

Thus we would expect μ_2 to be $\sim$100 times smaller than μ_1 for a hard sphere.

We now consider the ratio between μ_3, μ_4, and μ_1, which we combine in the following ratio:

$$\left|\frac{\mu_{3,4}}{\mu_1}\right|=2\left|\frac{\beta}{\alpha}\right|\frac{W_{33,44}}{|W_{11}-\beta W_{22}/\alpha|(1+\sqrt{1+A})}. \tag{18}$$

This also attains a maximum when $\beta/\alpha=W_{11}/W_{22}$, giving a strict upper bound for all β/α of

$$\left|\frac{\mu_{3,4}}{\mu_1}\right|\leqslant\frac{W_{33,44}}{W_{22}\sqrt{1-(W_{12}^2/W_{11}W_{22})}}. \tag{19}$$

From this bound we see that this ratio can be greater than 1 depending on the relative values of the matrix elements W_{mn}. For $|\beta/\alpha|\ll 1$, the ratio becomes

$$\left|\frac{\mu_{3,4}}{\mu_1}\right|\sim\left|\frac{\beta}{\alpha}\right|\frac{W_{33,44}}{W_{11}}. \tag{20}$$

Unless the ratio of W_{mn} factors is unusually large, we expect the eigenvalues μ_3 and μ_4 to also be $\sim$100 times smaller than μ_1 for a hard scatterer. These estimates of the relative magnitudes of the eigenvalues imply that detection of multiple eigenvalues would be difficult with hard scatterers. However, they should be observable for soft scatterers.

It is instructive to consider the limits of the eigenvalues for very small and very large TRMs. If the dimensions of the TRM are much less than z_M, the integrals for W_{mn} can be estimated using the mean value theorem. The largest eigenvalue in magnitude becomes

$$\mu_1 \sim (\alpha-\beta)\frac{\Delta S}{z_M^2}, \quad \beta \neq \alpha, \tag{21}$$

where $\Delta S(\ll z_M^2)$ is the area of the TRM. The magnitudes of the other eigenvalues are much smaller than $|\mu_1|$ unless $\beta=\alpha$. We investigate this latter case in the examples in Sec. IV. If the TRM is large compared with z_M, the domain of integration for W_{mn} becomes infinite. W_{11}, W_{33}, and W_{44} diverge logarithmically causing μ_1, μ_3, and μ_4 to diverge.

The eigenfunctions for the symmetric TRM are

$$\phi_m(\boldsymbol{\xi}) = \frac{1}{r_M}\left[\alpha W_{12} + (\mu_m - \alpha W_{11})\frac{z_M}{r_M}\right], \quad m=1,2,$$
$$\phi_3(\boldsymbol{\xi}) = \frac{\eta}{r_M^2}, \quad \phi_4(\boldsymbol{\xi}) = \frac{\xi}{r_M^2}. \tag{22}$$

Two eigenfunctions, ϕ_3 and ϕ_4, are antisymmetric around the η and ξ axes, respectively, while the other two eigenfunctions are axisymmetric. In the limit $\beta \to 0$ there is only one nonzero eigenvalue, $\mu_1 = \alpha W_{11}$, and one axisymmetric eigenfunction, $\phi_1(\boldsymbol{\xi}) = \alpha W_{12}/r_M$. The functional forms of the eigenfunctions can be interpreted as the intersection of monopole and dipole radiation patterns centered at the sphere with the plane of the TRM. The first two eigenfunctions, ϕ_1 and ϕ_2, are superpositions of a spherical radiation pattern associated with the compressibility contrast and a dipole radiation pattern oriented along the z axis associated with the density contrast. The last two eigenfunctions, ϕ_3 and ϕ_4, are produced by the intersection of the TRM with dipole radiation patterns aligned with the y and x axes, respectively. If we calculate the radiated pressure field associated with each eigenfunction using Eq. (1), we find that the pressure gradient at the sphere position is aligned with the dipole axis. Thus the eigenfunctions represent different resonant modes of acoustic excitation and scattering between the TRM and the scatterer.

The normalization of the eigenvalues and eigenfunctions used to obtain the final eigenvalue problem [Eq. (10)] largely eliminates the dependence on frequency. Any variation of the reduced eigenvalues and eigenstates with frequency would be due to frequency dependence of the compressibility ratio α. If this is constant over the frequency range of interest, then the amplitude distributions of the eigenfunctions will not vary with frequency. The phase distributions will vary linearly, and the measured eigenvalues μ_{TR}^2 will increase with the sixth power of frequency, assuming the system response $A_e A_r$ is constant over the frequency range of interest.

IV. EXAMPLES

For a circular TRM with radius R the nonzero elements of the TR reduced matrix are

$$W_{11} = -2\pi \ln\chi, \quad W_{12} = 2\pi(1-\chi),$$
$$W_{22} = \pi(1-\chi^2), \quad W_{33} = W_{44} = -\pi\left[\ln\chi + \tfrac{1}{2}(1-\chi^2)\right], \tag{23}$$
$$\chi = \frac{1}{\sqrt{1+R^2/z_M^2}},$$

and the eigenvalues are

$$\mu_m = -\alpha\pi\left[\ln\chi + \frac{\beta}{2\alpha}(1-\chi^2)\right] \times\left\{1-(-1)^m\sqrt{1-\frac{2\beta}{\alpha}\frac{(1-\chi^2)\ln\chi + 2(1-\chi)^2}{[\ln\chi+\beta(1-\chi^2)/2\alpha]^2}}\right\}, \quad m=1,2,$$
$$\mu_3 = \mu_4 = \pi\beta\left[\ln\chi + \tfrac{1}{2}(1-\chi^2)\right]. \tag{24}$$

The parameter χ ranges from zero for an infinite TRM to one for a pointlike TRM. As noted before, the denominator of the term in the radical is identical to the prefactor so that the eigenvalue is always finite.

If the radius is much smaller than the distance to the sphere, the eigenvalues become

$$\mu_1 \sim \pi(\alpha-\beta)\frac{R^2}{z_M^2}, \quad \mu_2 \sim -\frac{\pi}{48}\frac{\alpha\beta}{\alpha-\beta}\frac{R^6}{z_M^6},$$
$$\mu_3 = \mu_4 \sim -\frac{\pi\beta}{4}\frac{R^4}{z_M^4}, \tag{25}$$

for $|1-\beta/\alpha| \gg R^2/z_M^2$. The expression for μ_1 agrees with our previous calculation for a small TRM [Eq. (21)] with $\Delta S = \pi R^2$. When $\beta=\alpha$, the first two eigenvalues become

$$\mu_{1,2} \sim \frac{\pi}{4}\frac{\alpha R^4}{z_M^4}\left(1 \pm \frac{2}{\sqrt{3}}\right), \tag{26}$$

and all eigenvalues are comparable in size. In the limit of large radius, the eigenvalues μ_1, μ_3, and μ_4 diverge logarithmically, as expected.

Figure 3 shows the variation of the eigenvalues with aperture size and β/α. The radius values were chosen to span the region between the small aperture asymptotic limit and the large aperture limit. The behavior of the eigenvalues in Fig. 3(a) is typical for small β/α values. Each eigenvalue increases monotonically with aperture size. The overall size of $|\mu_3|$ scales with β/α and happens to be between $|\mu_1|$ and $|\mu_2|$ for $\beta/\alpha = 0.3$. When $\beta/\alpha = 1.0$ [Fig. 3(b)], all three eigenvalues have the same small aperture asymptotic behavior. Finally, for $\beta/\alpha = 3.0$ [Fig. 3(c)], the eigenvalue associated with transverse sphere oscillations $|\mu_3|$ exceeds $|\mu_1|$ for radii greater than $2z_M$. We would expect $|\mu_3|$ to continue to grow relative to $|\mu_1|$ for larger values of β/α.

A second specific case of interest is a rectangular slit along the ξ axis, length L, and width $2h, h \ll L$. We evaluate the integrals for the TR reduced matrix in the limit of h/L small:

$$W_{11} = \frac{4h}{z_M}\psi, \quad W_{12} = \frac{4h}{z_M}\frac{\sigma}{\sqrt{1+\sigma^2}}, \quad W_{22} = \frac{2h}{z_M}\psi(1+\chi),$$

$$W_{33}=\frac{2}{3}\left(\frac{h}{z_M}\right)^3\psi(1+\chi),\quad W_{44}=\frac{2h}{z_M}\psi(1-\chi), \tag{27}$$

$$\sigma=L/2z_M,\quad \psi=\arctan(\sigma),\quad \chi=\frac{\sigma/\psi}{1+\sigma^2}.$$

The eigenvalues are

$$\mu_n=\frac{2\alpha h}{z_M}\psi(1-\beta(1+\chi)/2\alpha)\times\left[1-(-1)^m\sqrt{1+\frac{2\beta}{\alpha}\frac{1+\chi(1-2\sigma/\psi)}{\alpha(1-\beta(1+\chi)/2\alpha)^2}}\right],\quad m=1,2, \tag{28}$$

$$\mu_3=O(h^3/z_M^3),\quad \mu_4=-\frac{2\beta h}{z_M}\psi(1-\chi).$$

This case approximates the configuration of a linear TRM. Note again that the prefactor cancels the denominator of the term under the radical so that the eigenvalue is always finite.

If the slit length is small compared with the distance to the sphere, the eigenvalues reduce to

$$\mu_1\sim\frac{2hL}{z_M^2}(\alpha-\beta),\quad \mu_2\sim-\frac{hL^5}{360z_M^6}\frac{\alpha\beta}{\alpha-\beta},\quad \mu_4\sim-\frac{hL^3}{6z_M^4}\beta, \tag{29}$$

for $|1-\alpha/\beta|\gg(L/z_M)^2$. When $\beta=\alpha$ the first two eigenvalues become

$$\mu_{1,2}\sim\alpha\frac{hL^3}{12z_M^4}\left(1\pm\frac{3}{\sqrt{5}}\right). \tag{30}$$

This behavior of the eigenvalues is similar to the circular TRM case. In the limit of an infinitely long slit, the eigenvalues approach finite values:

$$\mu_{1,2}\sim\frac{\pi h}{2z_M}(2\alpha-\beta)\times\left[1\pm\left|\frac{2\alpha+\beta}{2\alpha-\beta}\right|\sqrt{1-\frac{64\alpha\beta}{\pi^2(2\alpha+\beta)^2}}\right],\quad \mu_4\sim-\frac{\pi\beta h}{z_M}. \tag{31}$$

Figure 4 shows the variation of the eigenvalues with slit length L and β/α. These behave qualitatively like those for the circular aperture. The main difference is that they approach a constant for large L rather than diverge. The point where $|\mu_3|$ exceeds $|\mu_l|$ for $\beta/\alpha=3.0$ is now $L>5z_M$, more than twice the value for the circular aperture. Thus for the case of time reversal on a small bubble ($\beta/\alpha=3.0$), we would not expect the eigenstate associated with transverse oscillations to dominate unless the standoff distance to the bubble is less than a fifth of the slit length.

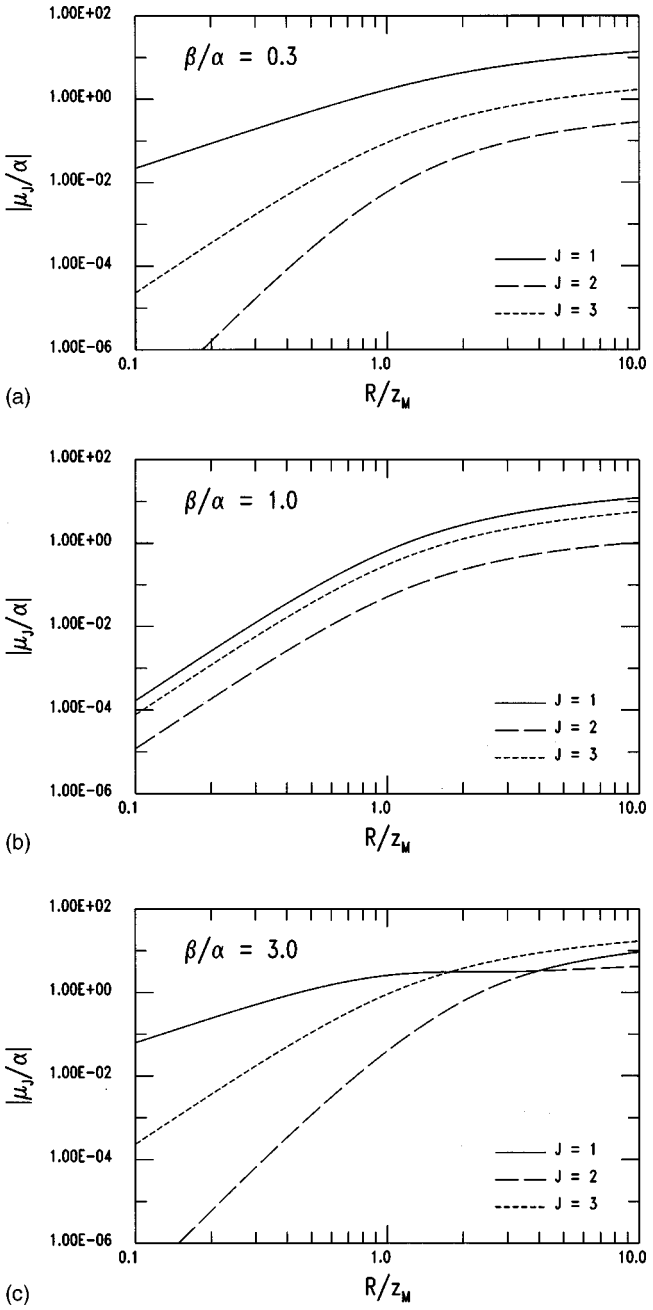

FIG. 3. Eigenvalues $|\mu_1/\alpha|$, $|\mu_2/\alpha|$, and $|\mu_3/\alpha|$ for a circular aperture with $\beta/\alpha=0.3$ (a), $\beta/\alpha=1.0$ (b), and $\beta/\alpha=3.0$ (c).

In Appendix A we show the expressions for the nonzero TR matrix elements for other symmetric TRMs, including an elliptical TRM. Appendix B repeats the analysis for a TRM composed of discrete array elements.

V. SUMMARY

We have shown that the acoustic time reversal operator can have up to four orthogonal eigenstates for a single small spherical scatterer. Each eigenstate represents a resonance between the TRM and an induced multipole scattering moment of the sphere. The amplitude distributions of the eigenstates on the TRM are orthogonal superpositions of the radiation patterns from the induced multipole moments. For a small spherical scatterer (size less than a wavelength), only

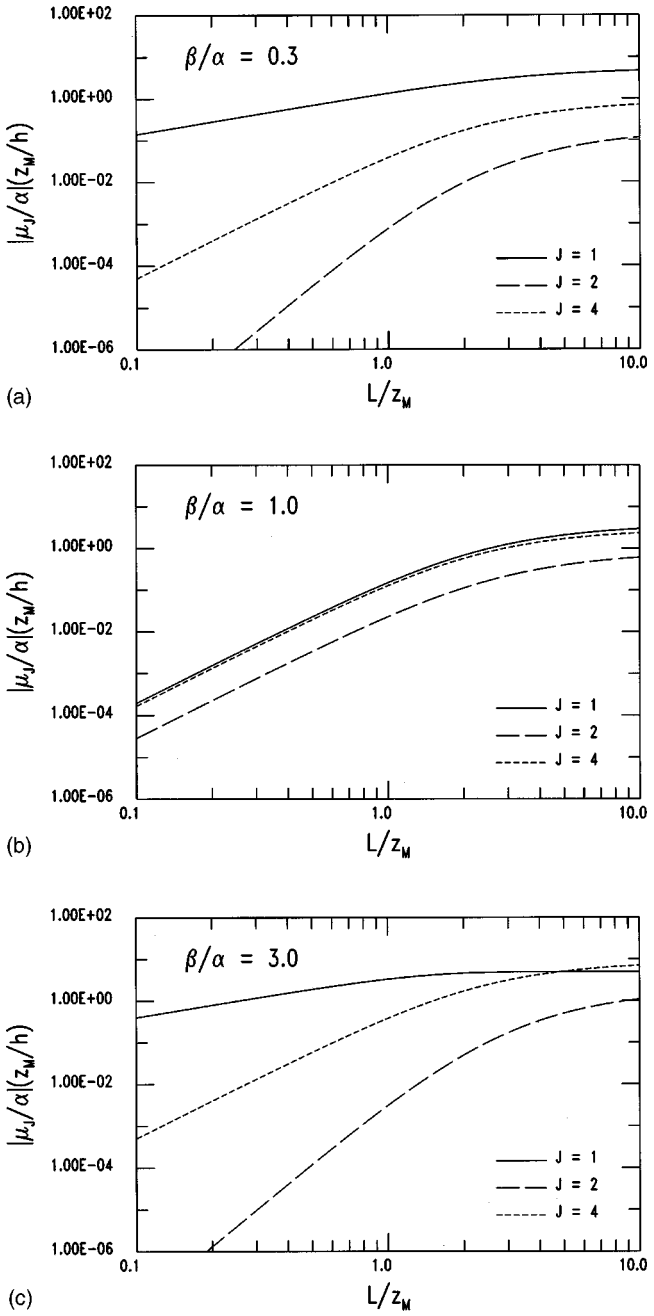

FIG. 4. Eigenvalues $|\mu_1/\alpha|$, $|\mu_2/\alpha|$, and $|\mu_4/\alpha|$ for a slit with $\beta/\alpha = 0.3$ (a), $\beta/\alpha = 1.0$ (b), and $\beta/\alpha = 3.0$ (c). Eigenvalues have been normalized by h/z_M.

monopole and dipole moments are induced. Higher-order moments could be induced on larger scatters. The monopole moment is associated with the compressibility contrast while dipole moments are associated with the density contrast. The maximum number of eigenstates for a single scatterer is equal to the total number of orthogonal orientations of each induced multipole. The spectrum of eigenvalues depends on both the geometry and the relative contribution of compressibility contrast and density contrast to the amplitude of the induced moments. For hard scatterers (metal, glass), the first eigenvalue can be 100 times larger than the other eigenvalues. For soft scatterers (wood, plastic, air bubbles) the eigenvalues can have comparable magnitudes and would be more easily observed.

The variation of the eigenfunctions and eigenvalues with frequency is governed by the size of the scatterer and the variation of compressibility contrast with frequency. The eigenfunctions vary only when the compressibility contrast changes with frequency. The eigenvalues are proportional to the scatterer cross section, which is known for a sphere and could be scaled out. The frequency variation of the rescaled eigenvalues is governed by the compressibility contrast.

The presence of multiple eigenstates breaks the correspondence between eigenstates and distinguishable scatterers. For the case of N small spheres we could have up to $4N$ separate eigenfunctions. However, the TRM phase distributions of the four eigenstates are identical for each sphere. It may then be possible to distinguish between different scatterers based on the phase structure of the eigenstates. In addition, information about the relative compressibility and density of a scatterer is contained in the spectrum of eigenvalues, which, if measurable, provides information about the composition of the scatterer.

ACKNOWLEDGMENTS

The authors would like to thank James Berryman and James Candy for stimulating discussions and their suggestions in the preparation of this manuscript. This work was performed under the auspices of the U.S. Department of Energy by the University of California, Lawrence Livermore National Laboratory under Contract No. W-7405-ENG-48.

APPENDIX A: ADDITIONAL EXAMPLES

Suppose the boundary of the TRM can be expressed as a single-valued function $R(\xi,\eta)=z_M f(\theta)$, $0\leqslant\theta<2\pi$. Then the elements of the TR reduced matrix can be expressed as integrals over θ:

$$W_{11}=\int_0^{2\pi}\ln\chi(\theta)\,d\theta,\quad W_{12}=\int_0^{2\pi}\left(1-\frac{1}{\chi(\theta)}\right)d\theta,$$

$$W_{13}=\int_0^{2\pi}\sin\theta\left(\operatorname{arcsinh}(f(\theta))-\frac{f(\theta)}{\chi(\theta)}\right)d\theta,$$

$$W_{14}=\int_0^{2\pi}\cos\theta\left(\operatorname{arcsinh}(f(\theta))-\frac{f(\theta)}{\chi(\theta)}\right)d\theta,$$

$$W_{22}=\frac{1}{2}\int_0^{2\pi}\left(1-\frac{1}{\chi^2(\theta)}\right)d\theta,$$

$$W_{23}=\frac{1}{2}\int_0^{2\pi}\sin\theta\left(\arctan(f(\theta))-\frac{f(\theta)}{\chi^2(\theta)}\right)d\theta,$$

$$W_{24}=\frac{1}{2}\int_0^{2\pi}\cos\theta\left(\arctan(f(\theta))-\frac{f(\theta)}{\chi^2(\theta)}\right)d\theta,$$

$$W_{33}=\int_0^{2\pi}\sin^2\theta\left[\ln(\chi(\theta))-\frac{1}{2}\left(1-\frac{1}{\chi^2(\theta)}\right)\right]d\theta,$$

$$W_{34}=\int_0^{2\pi}\sin\theta\cos\theta\left[\ln(\chi(\theta))-\frac{1}{2}\left(1-\frac{1}{\chi^2(\theta)}\right)\right]d\theta,$$

$$W_{44}=\int_0^{2\pi}\cos^2\theta\left[\ln(\chi(\theta))-\frac{1}{2}\left(1-\frac{1}{\chi^2(\theta)}\right)\right]d\theta,$$

$$\chi(\theta)=\sqrt{1+f^2(\theta)}.$$

For the specific case of an ellipse, $x^2/a^2+y^2/b^2=1, a\geqslant b$, the nonzero elements of the TR reduced matrix are

$$W_{11}=2\pi\ln\left(\frac{aR_b+bR_a}{z_M(a+b)}\right),$$

$$W_{12}=2\pi\left[1-\frac{2bz_M}{\pi aR_a}\boldsymbol{\pi}\left(\frac{\pi}{2},1-\frac{b^2}{a^2},\frac{\sqrt{a^2-b^2}}{R_a}\right)\right],$$

$$W_{22}=\frac{\pi ab}{R_aR_b},$$

$$W_{33}=\pi\ln\left(\frac{aR_b+bR_a}{z_m(a+b)}\right)-\frac{\pi ab}{aR_b+bR_a}\times\left[\frac{(a-b)(ab+R_aR_b-z_M^2)}{(a+b)(aR_b+bR_a)}+\frac{b}{R_a}\right],$$

$$W_{44}=\pi\ln\left(\frac{aR_b+bR_a}{z_M(a+b)}\right)+\frac{\pi ab}{aR_b+bR_a}\times\left[\frac{(a-b)(ab+R_aR_b-z_M^2)}{(a+b)(aR_b+bR_a)}-\frac{a}{R_a}\right],$$

where $R_a=\sqrt{a^2+z_M^2}$, $R_b=\sqrt{b^2+z_M^2}$, and $\boldsymbol{\pi}$ is the complete elliptic integral of the third kind,

$$\boldsymbol{\pi}\left(\frac{\pi}{2},s,t\right)=\int_0^{\pi/2}\frac{dx}{(1-s\sin^2x)\sqrt{1-t^2\sin^2x}}.$$

APPENDIX B: DISCRETE TRMs

Here we derive the equivalent results for a TRM composed of discrete point elements. To convert the continuous TRM to the discrete case, we can represent the normal velocity distribution as a weighted sum of Dirac delta functions in two dimensions,

$$U_M(\xi,\eta)=\sum_{j=1}^{N}u_jS_j\delta(\xi-\xi_j)\delta(\eta-\eta_j), \tag{B1}$$

where S_j is the area and u_j the normal velocity of the jth element. Substituting this into Eq. (3) we obtain the following expression for the pressure force $P_j=S_jP(\xi_j,\eta_j)$ on the jth element:

$$P_j=-\frac{i\rho c}{6\pi}(ka)^3S_j\frac{e^{ikr_j}}{r_j}\sum_{l=1}^{N}u_lS_l\left(\alpha-\beta\frac{\boldsymbol{\xi}_j\cdot\boldsymbol{\xi}_l}{r_jr_l}\right)\frac{e^{ikr_l}}{r_l}, \tag{B2}$$

where $\xi_j=(\xi_j,\eta_j,-z_M)$ and $r_j=\sqrt{z_M^2+\eta_j^2+\xi_j^2}$.

The conversion to input and output voltages proceeds as before, so we obtain

$$R_j=\sum_{l=1}^{N}K_{jl}^SE_l,$$

$$K_{jl}^S=-\frac{i}{6\pi}A_r(\omega)A_e(\omega)(ka)^3S_jS_l\left(\alpha-\beta\frac{\boldsymbol{\xi}_j\cdot\boldsymbol{\xi}_l}{r_jr_l}\right)\times\frac{e^{ik(r_j+r_l)}}{r_jr_l}. \tag{B3}$$

The integral operator is now a linear transformation of the input voltages with a Hermitian matrix K_{jl}^S that Prada and Fink identify as the transfer matrix.[5] The sum in (B3) is over the total number of elements in a general planar (or linear) array.

The iterative time reversal procedure is the same as before with the integral operation ($\circ$) replaced by a summation. The reduction to the final eigenvalue problem proceeds as before, leading to the following discrete form of Eq. (10):

$$\mu\phi_j=\sum_{l=1}^{N}\left[\frac{\sqrt{S_jS_l}}{r_jr_l}\left(\alpha-\beta\frac{\boldsymbol{\xi}_j\cdot\boldsymbol{\xi}_l}{r_jr_l}\right)\right]\phi_l. \tag{B4}$$

This is the fundamental equation for the eigenvectors and eigenvalues for a discrete TRM. There are four real eigenvalues with four orthogonal eigenvectors in general. The quantity in square brackets is the *reduced transfer matrix* K_{jl}. This matrix is real, symmetric, and can be represented as a sum of four terms:

$$K_{jl}=\alpha w_j^{(1)}w_l^{(1)}-\beta\sum_{m=2}^{4}w_j^{(m)}w_l^{(m)}, \tag{B5}$$

where

$$w_j^{(1)}=\frac{\sqrt{S_j}}{r_j},\quad w_j^{(2)}=\frac{z_M\sqrt{S_j}}{r_j^2},$$
$$w_j^{(3)}=\frac{\eta_j\sqrt{S_j}}{r_j^2},\quad w_j^{(4)}=\frac{\xi_j\sqrt{S_j}}{r_j^2}. \tag{B6}$$

The eigenvectors can be expressed as a combination of the four w vectors:

$$\phi_j=\sum_{n=1}^{4}\chi_nw_j^{(n)},$$

which reduces the N by N system to a 4 by 4 eigenvalue problem:

$$\alpha\sum_{n=1}^{4}W_{1n}\chi_n=\mu\chi_1,$$

$$-\beta\sum_{n=1}^{4}W_{mn}\chi_n=\mu\chi_m,\quad m=2,3,4, \tag{B7}$$

$$W_{mn}=\sum_{j=1}^{N}w_j^{(m)}w_j^{(n)}.$$

If the array is symmetrical around the ξ and η axes, all of the off-diagonal terms vanish except for W_{12} (and W_{21}). The characteristic equation is given by Eq. (14) and the eigenvalues are

$$\mu_m=\frac{\alpha}{2}\left(W_{11}-\frac{\beta}{\alpha}W_{22}\right)\times\left[1-(-1)^m\sqrt{1+\frac{4\beta}{\alpha}\frac{W_{11}W_{22}-W_{12}^2}{(W_{11}-\alpha W_{22}/\beta)^2}}\right],\quad m=1,2,$$
$$\mu_3=-\beta W_{33},\quad \mu_4=-\beta W_{44}. \tag{B8}$$

repeated here for completeness. The orthogonal eigenvectors can be calculated explicitly and are given by

$$\phi_j^{(n)}=\frac{\sqrt{S_j}}{r_j}\left[\alpha W_{12}+(\mu_n-\alpha W_{11})\frac{z_M}{r_j}\right],\quad n=1,2,$$
$$\phi_j^{(3)}=\frac{\eta_j\sqrt{S_j}}{r_j^2},\quad \phi_j^{(4)}=\frac{\xi_j\sqrt{S_j}}{r_j^2}. \tag{B9}$$

The general properties of the eigenvalues and eigenvectors are the same as for the continuous case.

As an example, consider a linear array parallel to the x axis, with its midpoint at the intersection with the z axis. The sphere is then located normal to the array at a distance z_M on the z axis. The nonzero elements of the W matrix are

$$W_{11}=\sum_{j=1}^{N}\frac{S_j}{r_j^2},\quad W_{12}=\sum_{j=1}^{N}\frac{z_M S_j}{r_j^3},\quad W_{22}=\sum_{j=1}^{N}\frac{z_M^2 S_j}{r_j^4},$$
$$W_{33}=\sum_{j=1}^{N}\frac{\eta_j^2 S_j}{r_j^4},\quad W_{44}=\sum_{j=1}^{N}\frac{\xi_j^2 S_j}{r_j^4}.$$

These cannot be evaluated in closed form even when the element areas S_j are identical. However, they can be approximated with integrals if N is large, the spacing is small, and $S_j\leqslant h\Delta x$ for all j, where h is the element width and Δx is an upper bound to the element spacing. In the limit that $N\to\infty$, $\Delta x\to 0$, $N\Delta x=L$, the sums converge to the same integrals used to obtain the matrix elements in Eq. (27).

[1] A. Parvulescu and C. S. Clay, ''Reproducibility of Signal Transmissions in the Ocean,'' Radio Electron. Eng. **29**, 223–228 (1965).
[2] M. Fink, C. Prada, F. Wu, and D. Cassereau, ''Self focusing in inhomogeneous media with ''time reversal'' acoustic mirrors,'' Proc. IEEE Ultrason. Symp. (1989), Vol. 2, pp. 681–686.
[3] M. Fink, D. Cassereau, A. Derode, C. Prada, P. Roux, M. Tanter, J-L. Thomas, and F. Wu, ''Time-reversed acoustics,'' Rep. Prog. Phys. **63**, 1933–1995 (2000).
[4] M. Fink and C. Prada, ''Acoustic time-reversal mirrors,'' Inverse Probl. **17**, R1–R38 (2001).
[5] C. Prada and M. Fink, ''Eigenstates of the time reversal operator: A solution to selective focusing in multiple-target media,'' Wave Motion **20**, 151–163 (1994).
[6] C. Prada, J-L. Thomas, and M. Fink, ''The iterative time reversal process: Analysis of the convergence,'' J. Acoust. Soc. Am. **97**, 62–71 (1995).
[7] C. Prada, S. Manneville, D. Spoliansky, and M. Fink, ''Decomposition of the time reversal operator: Detection and selective focusing on two scatterers,'' J. Acoust. Soc. Am. **99**, 2067–2076 (1996).
[8] P. M. Morse and K. U. Ingard, *Theoretical Acoustics* (Princeton U. P., Princeton, NJ, 1968).
[9] D. Cassereau and M. Fink, ''Focusing with plane time-reversal mirrors: An efficient alternative to closed cavities,'' J. Acoust. Soc. Am. **94**, 2373–2386 (1993).
[10] G. Harris, ''Review of transient field theory for a baffled planar piston,'' J. Acoust. Soc. Am. **70**, 10–20 (1981).
[11] M. Fink, ''Time reversal of ultrasonics fields—Part I: Basic principles,'' IEEE Trans. Ultrason. Ferroelectr. Freq. Control **39**(5), 555–566 (1992).
[12] G. Harris, ''Transient field of a baffled planar piston having an arbitrary vibration amplitude distribution,'' J. Acoust. Soc. Am. **70**, 186–204 (1981).
[13] D. R. Jackson and D. R. Dowling, ''Phase conjugation in underwater acoustics,'' J. Acoust. Soc. Am. **89**, 171–181 (1991).
[14] L. E. Kinsler, A. R. Frey, A. B. Coppens, and J. V. Sanders, *Fundamentals of Acoustics* (Wiley, New York, 1982).

The surface motion due to a line force or dislocation within an anisotropic elastic half-space

Kuang-Chong Wu[a)]
Institute of Applied Mechanics, National Taiwan University, Taipei 106, Taiwan

(Received 9 December 2000; accepted for publication 14 March 2001)

An explicit solution of the surface displacements due to a line force or a line dislocation within an anisotropic half-space is presented. The surface displacements are derived from the solution corresponding to a suddenly applied surface line force using the reciprocal theorem. The solution is in a closed form for isotropic media. For anisotropic solids, only an eigenvalue problem needs to be solved numerically for a given time and position to calculate the surface response. Numerical results are given for silicon. © *2001 Acoustical Society of America.* [DOI: 10.1121/1.1371765]

PACS numbers: 43.20.Gp [ANN]

I. INTRODUCTION

The propagation and reflection of waves in an elastic half-space is of practical importance in the field of seismology and nondestructive testing. Lamb (1904) was the first to consider the generation of elastic waves by the application of a surface impulsive line or point force on the surface of an isotropic half-space. He also gave the formal solutions for a buried force as integrals that were later studied by Nakano (1925) and Lapwood (1949), among others.

The two-dimensional Lamb's problem for a transversely isotropic half-space subjected to a surface line force has been studied by Kraut (1963) using Cagniard's technique. The treatment has been extended to general anisotropic materials by Burridge (1971). Payton (1983) has obtained an explicit closed form solution for the surface displacements for transversely isotropic media. The interior response was calculated for a half-space of cubic symmetry by Mourad *et al.* (1996). Maznev and Every (1997) employed the Fourier transform to show a functional equivalence for surface response between the time and Fourier domain. Recently, Wu (2000) has used a formulation that does not require integral transform to derive explicit solution for the displacement fields. The formulation is an extension of Stroh's formalism for two-dimensional anisotropic elastostatics as well as for steady-state motion (Stroh, 1958, 1962).

Willis (1973) has obtained the formal solution to the three-dimensional Lamb's problem with a surface point force for a general anisotropic continuum using Fourier and Radon transforms. Wang and Achenbach (1996) have developed a method based on Radon transform to derive new expressions for the displacements. Mourad and Deschamps (1995) have used the Cagniard de Hoop method to compute the interior response for half-spaces of cubic and hexagonal symmetries, and the same problem has been treated by Tewary and Fortunko (1996) using a delta-function representation. Every *et al.* (1997, 1998) have established integral expressions for the surface and interior displacement response in a general anisotropic medium using the Fourier transform.

All of the aforementioned works on anisotropic half-spaces are for surface loading. There appear to be few results for internal sources. Payton (1983) has obtained a closed form expression for the epicenter displacement due to a buried point force in a transversely isotropic half-space. Spies (1997) has given the solution in the Fourier transform domain for a point force in a general anisotropic half-space. In addition to buried forces, which may be considered as traction discontinuities, dislocations, which give rise to displacement discontinuities, are another form of internal sources. Dislocations are often used to model earthquake sources. The problem of buried line dislocations seem to have received little attention insofar as explicit solutions are concerned.

In this paper an explicit solution is provided for the surface displacements due to an impulsive line force or a line dislocation within a general anisotropic half-space. Eringen and Suhubi (1975) showed that the surface displacements caused by a buried line force and the solution corresponding to a surface line force for the whole region are intimately related by the reciprocal theorem. This relation is applied here to derive the surface displacements induced by the internal sources from the existing solution of a surface line force given by Wu (2000). Although the dislocation may also be represented by equivalent distributions of double-couples on the slip surface (Burridge and Knopoff, 1964), it is considered here as a separate source so that the force and the dislocation can be treated simultaneously. The solution is in a closed form for isotropic media. For anisotropic solids, only an eigenvalue problem needs to be solved numerically for a given time and position to calculate the surface response.

II. BASIC EQUATIONS

For two-dimensional deformation in which the Cartesian components of the stress σ_{ij} and the displacement u_i, $i,j=1,2,3$, are independent of x_3, the general dynamic self-similar solution may be represented as (Wu, 2000)

$$\frac{\partial \mathbf{u}(x_1,x_2,t)}{\partial t} = -2\,\mathrm{Re}\left\{ \mathbf{A}(\omega)\left\langle \omega_* \frac{\partial \omega_*}{\partial x_1} \right\rangle \mathbf{f}(\omega) \right\}, \qquad (1)$$

a)Electronic mail: wukc@spring.iam.ntu.edu.tw

$$\mathbf{t}_2(x_1,x_2,t)=2\,\mathrm{Re}\left\{\mathbf{B}(\omega)\left\langle\frac{\partial\omega_*}{\partial x_1}\right\rangle\mathbf{f}(\omega)\right\},\tag{2}$$

where Re stands for ''the real part of''

$$\mathbf{t}_2=(\sigma_{12},\sigma_{22},\sigma_{32})^{\mathrm{T}},$$

$$\mathbf{A}(\omega)=[\mathbf{a}_1(\omega_1),\mathbf{a}_2(\omega_2),\mathbf{a}_3(\omega_3)],$$

$$\mathbf{B}(\omega)=[\mathbf{b}_1(\omega_1),\mathbf{b}_2(\omega_2),\mathbf{b}_3(\omega_3)],$$

$$\mathbf{f}(\omega)=[f_1(\omega_1),f_2(\omega_2),f_3(\omega_3)]^{\mathrm{T}},$$

and

$$\omega_k t=x_1+p_k(\omega_k)x_2,\tag{3}$$

$$\frac{\partial\omega_k}{\partial x_1}=\frac{1}{t-p_k'(\omega_k)x_2},\tag{4}$$

with prime denoting differentiation with respect to the argument. Note that $\partial\omega_k/\partial x_1$ is denoted as $1/\Delta_k'$ in Wu (2000). In Eqs. (1) and (2) $\langle h_*\rangle=\mathrm{diag}[h_1,h_2,h_3]$ represents a diagonal matrix. The scalar $p_k(\omega)$ and the vector $\mathbf{a}_k(\omega)$ are, respectively, the eigenvalue and eigenvector of the following eigenvalue problem

$$[\mathbf{Q}+p(\mathbf{R}+\mathbf{R}^{\mathrm{T}})+p^2\mathbf{T}-\rho\omega^2\mathbf{I}]\mathbf{a}(\omega)=\mathbf{0},\tag{5}$$

where ρ is the density and the matrices $\mathbf{Q}$, $\mathbf{R}$, and $\mathbf{T}$ are related to the elastic constants C_{ijks} by

$$Q_{ik}=C_{i1k1},\quad R_{ik}=C_{i1k2},\quad T_{ik}=C_{i2k2}.$$

The vector $\mathbf{b}_k(\omega)$ is given by

$$\mathbf{b}_k(\omega)=(\mathbf{R}^{\mathrm{T}}+p_k(\omega)\mathbf{T})\mathbf{a}_k(\omega).\tag{6}$$

For $x_2>0$, the eigenvalue $p_k(\omega)$, $k=1,2,3$, is selected such that the imaginary part is positive when it is complex and $p_k'(\omega)>0$ when real.

For a line force $\mathbf{F}^*=\mathbf{F}_0^*\,\delta(x_1-\xi_1)H(t)$ applied on the surface of the half-space $x_2>0$, where δ is the Dirac delta function and H is the unit step function. The analytic function $\mathbf{f}(\omega)$ is given as (Wu, 2000)

$$\mathbf{f}(\omega)=\frac{1}{2\pi i}\left\langle\frac{1}{\omega_*}\right\rangle\sum_{k=1}^{3}\mathbf{I}_k\mathbf{B}^{-1}(\omega_k)\mathbf{F}_0^*,\tag{7}$$

where $\mathbf{I}_k=\mathbf{e}_k\mathbf{e}_k^{\mathrm{T}}$, $\mathbf{e}_k$ being the unit vector in the x_k direction, $\mathbf{B}(\omega_k)=[\mathbf{b}_1(\omega_k),\mathbf{b}_2(\omega_k),\mathbf{b}_3(\omega_k)]$, and $\omega_k(x_1,x_2,t;\xi_1)$ is determined by

$$\omega_k t=x_1-\xi_1+p_k(\omega_k)x_2.\tag{8}$$

The corresponding solution of $\partial\mathbf{u}^*/\partial t$ and $\mathbf{t}_2^*$ may be expressed as

$$\frac{\partial\mathbf{u}^*(x_1,x_2,t;\xi_1)}{\partial t}=\mathbf{V}(x_1,x_2,t;\xi_1)\mathbf{F}_0^*,\tag{9}$$

$$\mathbf{t}_2^*(x_1,x_2,t;\xi_1)=\mathbf{T}(x_1,x_2,t;\xi_1)\mathbf{F}_0^*,\tag{10}$$

where

$$\mathbf{V}(x_1,x_2,t;\xi_1)=-\frac{1}{\pi}\mathrm{Im}\left\{\mathbf{A}(\omega)\left\langle\frac{\partial\omega_*}{\partial x_1}\right\rangle\sum_{k=1}^{3}\mathbf{I}_k\mathbf{B}^{-1}(\omega_k)\right\},\tag{11}$$

$$\mathbf{T}(x_1,x_2,t;\xi_1)=\frac{1}{\pi}\mathrm{Im}\left\{\mathbf{B}(\omega)\left\langle\frac{1}{\omega_*}\frac{\partial\omega_*}{\partial x_1}\right\rangle\sum_{k=1}^{3}\mathbf{I}_k\mathbf{B}^{-1}(\omega_k)\right\}\tag{12}$$

and Im denotes ''the imaginary part of.''

III. SURFACE DISPLACEMENTS DUE TO BURIED SOURCES

Let a line force $\mathbf{F}=\mathbf{F}_0\,\delta(x_1-\eta_1)\,\delta(x_2-\eta_2)\,\delta(t)$ and a line dislocation $\Delta\mathbf{u}=\boldsymbol{\beta}_0 H(\eta_1-x_1)\,\delta(x_2-\eta_2)\,\delta(t)$ be present in the half-space $x_2>0$, where $\mathbf{F}_0$ and $\boldsymbol{\beta}_0$ are constant vectors. The resulting displacement is denoted by $\mathbf{u}(x_1,x_2,t;\eta_1,\eta_2)$. Application of the reciprocal theorem to the present problem and the surface force problem discussed in the preceding section leads to

$$(\mathbf{F}_0^*)^{\mathrm{T}}\int_0^t\mathbf{u}(\xi_1,\tau;\eta_1,\eta_2)\,d\tau$$

$$=\mathbf{u}^*(\eta_1,\eta_2,t;\xi_1)^{\mathrm{T}}\mathbf{F}_0+\int_{-\infty}^{\eta_1}\mathbf{t}_2^*(x_1,\eta_2,t;\xi_1)^{\mathrm{T}}dx_1\boldsymbol{\beta}_0,$$

or by taking the time derivative

$$(\mathbf{F}_0^*)^{\mathrm{T}}\mathbf{u}(\xi_1,t;\eta_1,\eta_2)=\frac{\partial\mathbf{u}^*(\eta_1,\eta_2,t;\xi_1)^{\mathrm{T}}}{\partial t}\mathbf{F}_0+\frac{\partial}{\partial t}\int_{-\infty}^{\eta_1}\mathbf{t}_2^*(x_1,\eta_2,t;\xi_1)^{\mathrm{T}}dx_1\boldsymbol{\beta}_0.\tag{13}$$

Substitution of Eqs. (9) and (10) into Eq. (13) yields

$$(\mathbf{F}_0^*)^{\mathrm{T}}\mathbf{u}(\xi_1,t;\eta_1,\eta_2)=(\mathbf{F}_0^*)^{\mathrm{T}}\mathbf{V}(\eta_1,\eta_2,t;\xi_1)^{\mathrm{T}}\mathbf{F}_0+(\mathbf{F}_0^*)^{\mathrm{T}}\frac{\partial}{\partial t}\int_{-\infty}^{\eta_1}\mathbf{T}(x_1,\eta_2,t;\xi_1)^{\mathrm{T}}dx_1\boldsymbol{\beta}_0.\tag{14}$$

Since $\mathbf{F}_0^*$ is arbitrary, we have

$$\mathbf{u}(\xi_1,t;\eta_1,\eta_2)=\mathbf{G}_F(\xi_1,t;\eta_1,\eta_2)\mathbf{F}_0+\mathbf{G}_b(\xi_1,t;\eta_1,\eta_2)\boldsymbol{\beta}_0,\tag{15}$$

where

$$\mathbf{G}_F(\xi_1,t;\eta_1,\eta_2)=\mathbf{V}(\eta_1,\eta_2,t;\xi_1)^{\mathrm{T}},\tag{16}$$

$$\mathbf{G}_b(\xi_1,t;\eta_1,\eta_2)=\frac{\partial}{\partial t}\int_{-\infty}^{\eta_1}\mathbf{T}(x_1,\eta_2,t;\xi_1)^{\mathrm{T}}dx_1.\tag{17}$$

The matrix $\mathbf{G}_b$ can be further simplified by writing $\mathbf{T}(x_1,\eta_2,t;\xi_1)$ as

$$\mathbf{T}(x_1,\eta_2,t;\xi_1)=\frac{1}{\pi}\mathrm{Im}\left\{\sum_{k=1}^{3}\frac{1}{\omega_k}\frac{\partial\omega_k}{\partial x_1}\mathbf{b}_k(\omega_k)\mathbf{e}_k^{\mathrm{T}}\mathbf{B}^{-1}(\omega_k)\right\}$$

so that

$$\int_{-\infty}^{\eta_1}\mathbf{T}(x_1,\eta_2,t;\xi_1)dx_1$$

$$=\frac{1}{\pi}\mathrm{Im}\left\{\sum_{k=1}^{3}\int_{-\infty}^{\hat{\omega}_k}\frac{1}{\omega_k}\mathbf{b}_k(\omega_k)\mathbf{e}_k^{\mathrm{T}}\mathbf{B}^{-1}(\omega_k)d\omega_k\right\}, \tag{18}$$

where $\hat{\omega}_k=\omega_k(\eta_1,\eta_2,t;\xi_1)$. The time derivative of Eq. (18) is thus given by

$$\frac{\partial}{\partial t}\int_{-\infty}^{\eta_1}\mathbf{T}(x_1,\eta_2,t;\xi_1)dx_1$$

$$=-\frac{1}{\pi}\mathrm{Im}\left\{\sum_{k=1}^{3}\frac{\partial\hat{\omega}_k}{\partial\eta_1}\mathbf{b}_k(\hat{\omega}_k)\mathbf{e}_k^{\mathrm{T}}\mathbf{B}^{-1}(\hat{\omega}_k)\right\}$$

$$=-\frac{1}{\pi}\mathrm{Im}\left\{\mathbf{B}(\hat{\omega})\left\langle\frac{\partial\hat{\omega}_*}{\partial\eta_1}\right\rangle\sum_{k=1}^{3}\mathbf{I}_k\mathbf{B}^{-1}(\hat{\omega}_k)\right\}, \tag{19}$$

where the relation

$$\frac{\partial\hat{\omega}_k}{\partial t}=-\hat{\omega}_k\frac{\partial\hat{\omega}_k}{\partial\eta_1}, \tag{20}$$

has been used (Wu, 2000). Substituting Eqs. (11) and (19) into Eq. (15), we have

$$\mathbf{G}_F(\xi_1,t;\eta_1,\eta_2)$$

$$=-\frac{1}{\pi}\mathrm{Im}\left\{\sum_{k=1}^{3}\mathbf{B}^{-1}(\hat{\omega}_k)^{\mathrm{T}}\mathbf{I}_k\left\langle\frac{\partial\hat{\omega}_*}{\partial\eta_1}\right\rangle\mathbf{A}^{\mathrm{T}}(\hat{\omega})\right\}, \tag{21}$$

$$\mathbf{G}_b(\xi_1,t;\eta_1,\eta_2)$$

$$=-\frac{1}{\pi}\mathrm{Im}\left\{\sum_{k=1}^{3}\mathbf{B}^{-1}(\hat{\omega}_k)^{\mathrm{T}}\mathbf{I}_k\left\langle\frac{\partial\hat{\omega}_*}{\partial\eta_1}\right\rangle\mathbf{B}^{\mathrm{T}}(\hat{\omega})\right\}. \tag{22}$$

IV. ISOTROPIC MEDIA

For isotropic media under plane strain deformation, the eigenvalues $p_1(\omega)$ and $p_2(\omega)$ of Eq. (5) can be easily obtained as

$$p_k(\omega)=\sqrt{(\omega/c_k)^2-1},\quad k=1,2, \tag{23}$$

where c_1 and c_2 are, respectively, the P wave and S wave speeds. The corresponding eigenvectors $\mathbf{a}_1(\omega)$ and $\mathbf{a}_2(\omega)$ may be taken as

$$\mathbf{a}_1(\omega)=\begin{pmatrix}1\\ p_1(\omega)\end{pmatrix},\quad \mathbf{a}_2(\omega)=\begin{pmatrix}-p_2(\omega)\\ 1\end{pmatrix}. \tag{24}$$

The vectors $\mathbf{b}_1(\omega)$ and $\mathbf{b}_2(\omega)$ defined by Eq. (6) are

$$\mathbf{b}_1(\omega)=\rho c_2^2\begin{pmatrix}2p_1(\omega)\\ p_2^2(\omega)-1\end{pmatrix},\quad \mathbf{b}_2(\omega)=\rho c_2^2\begin{pmatrix}1-p_2^2(\omega)\\ 2p_2(\omega)\end{pmatrix}. \tag{25}$$

The variables $\hat{\omega}_k$ as determined by substituting Eq. (23) into Eq. (8) and replacing x_1 and x_2, respectively, with η_1 and η_2 are

$$\hat{\omega}_k=\frac{y_1+iy_2\sqrt{1-(y/c_k)^2}}{1-(y_2/c_k)^2}, \tag{26}$$

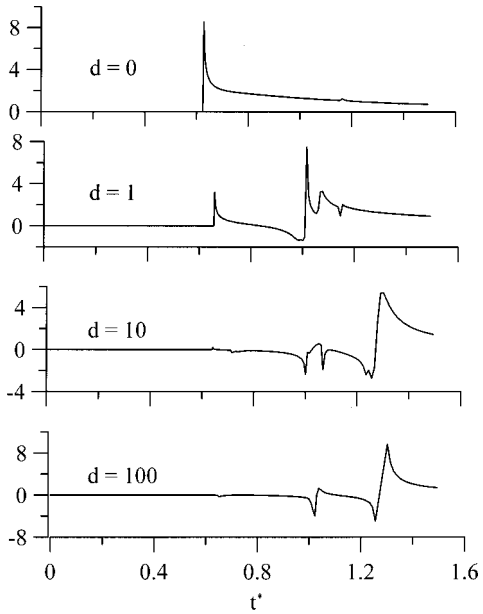

FIG. 1. Dimensionless vertical displacement due to the line force in silicon.

for $y<c_k$ and

$$\hat{\omega}_k=\frac{y_1+\mathrm{sign}(y_1)y_2\sqrt{(y/c_k)^2-1}}{1-(y_2/c_k)^2}, \tag{27}$$

for $y>c_k$ and $y_2<c_k$, where $y_1=(\eta_1-\xi_1)/t$, $y_2=\eta_2/t$ and $y=\sqrt{y_1^2+y_2^2}$. With Eqs. (23) and (26), $\partial\hat{\omega}_k/\partial\eta_1$ may be expressed as

$$\frac{\partial\hat{\omega}_k}{\partial\eta_1}=\frac{p_k(\hat{\omega}_k)c_k}{\sqrt{r^2-c_k^2t^2}}, \tag{28}$$

where $r=yt$. The explicit expressions for $\mathbf{G}_F$ and $\mathbf{G}_b$ for isotropic media are thus given by

$$\mathbf{G}_F(\xi_1,t;\eta_1,\eta_2)=-\frac{1}{\pi\rho c_2^2}\mathrm{Im}\{\mathbf{J}_1(\hat{\omega}_1)+\mathbf{J}_2(\hat{\omega}_2)\}, \tag{29}$$

$$\mathbf{G}_b(\xi_1,t;\eta_1,\eta_2)=-\frac{1}{\pi}\mathrm{Im}\{\mathbf{K}_1(\hat{\omega}_1)+\mathbf{K}_2(\hat{\omega}_2)\}, \tag{30}$$

where

$$\mathbf{J}_1(\hat{\omega}_1)=\frac{c_1p_1}{R\sqrt{r^2-c_1^2t^2}}\begin{pmatrix}2p_2 & 2p_2p_1\\ p_2^2-1 & (p_2^2-1)p_1\end{pmatrix},$$

$$\mathbf{J}_2(\hat{\omega}_2)=\frac{c_2p_2}{R\sqrt{r^2-c_2^2t^2}}\begin{pmatrix}-(1-p_2^2)p_2 & 1-p_2^2\\ -2p_2p_1 & 2p_1\end{pmatrix},$$

$$\mathbf{K}_1(\hat{\omega}_1)=\frac{c_1p_1}{R\sqrt{r^2-c_1^2t^2}}\begin{pmatrix}4p_2p_1 & 2p_2(p_2^2-1)\\ 2p_1(p_2^2-1) & (p_2^2-1)^2\end{pmatrix},$$

$$\mathbf{K}_2(\hat{\omega}_2)=\frac{c_2p_2}{R\sqrt{r^2-c_2^2t^2}}\begin{pmatrix}(1-p_2^2)^2 & 2p_2(1-p_2^2)\\ 2p_1(1-p_2^2) & 4p_2p_1\end{pmatrix},$$

and

$$R(\omega)=|\mathbf{B}(\omega)|=4p_1(\omega)p_2(\omega)+(1-p_2^2(\omega))^2.$$

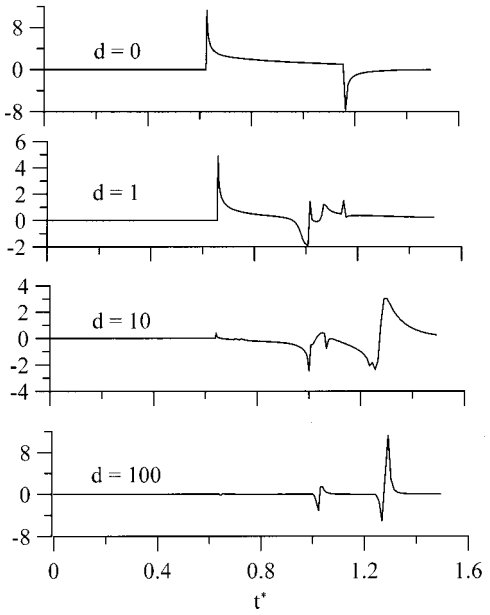

FIG. 2. Dimensionless vertical displacement due to the line dislocation in silicon.

The expression for $\mathbf{G}_F$ has been checked to agree with that given in Eringen and Suhubi (1975, pp. 671–672). The result of $\mathbf{G}_b$ appears to be new.

V. NUMERICAL RESULTS

In this section, the histories of the vertical surface displacement due to a buried vertical force $\mathbf{F}_0 = F_0\mathbf{e}_2$ or an edge dislocation with $\boldsymbol{\beta}_0 = b_0\mathbf{e}_1$ at various distances from the epicenter are presented. The results are expressed in terms of the dimensionless displacement v defined as

$$v(d,t^*) = \frac{\pi\rho c_0 r u_2}{F_0},$$

for the line force and

$$v(d,t^*) = \frac{\pi r u_2}{c_0 b_0},$$

for the line dislocation, where $t^* = tc_0/r$, $d = (\xi_1 - \eta_1)/\eta_2$, $c_0 = \sqrt{C_{44}/\rho}$ and C_{ij} is the contracted notation for the elastic constants. The material considered was silicon with the elastic constants: $C_{11} = 165$ Gpa, $C_{12} = 63$ Gpa, and $C_{44} = 79$ Gpa. The (x_1, x_3) plane is on the (111) surface and the x_1-axis is along the $[1\bar{1}0]$ direction. The calculations were performed for receivers located at $d = 0$, 1, 10, and 100.

Figures 1 and 2 show the dimensionless displacement due to the force and the dislocation, respectively. There are three bulk waves- a quasi-*P* (*qP*) and two quasi-*S* (*qS*1 and *qS*2) waves. The arrival times of the bulk wave vary with the incident angles. Furthermore, the refracted *qP* waves due to the *qS*1 and *qS*2 waves and the refracted *qS*1 waves due to *qS*2 waves occur. For $d = 10$ and 100 the emergence of the Rayleigh wave is evident. Note that the surface wave speed c_R is determined by $|\mathbf{B}(c_R)| = 0$ (Barnett and Lothe, 1974). In general, after the arrival of the last wave the displacements due to the dislocation decay to zero more rapidly than those due to the force.

VI. CONCLUSION

Explicit expressions for the surface displacements due to a line force and dislocation in a general anisotropic half-space have been derived from the solution of a surface line force using reciprocal theorem. For isotropic media, a closed form solution is obtained. For anisotropic media, the expressions can be evaluated simply by solving an eigenvalue problem.

ACKNOWLEDGMENT

The research was supported by the National Science Council of Taiwan under Grant No. NSC 89-2212-E-007.

Barnett, D. M., and Lothe, J. (**1974**). ''Consideration of the existence of surface wave (Rayleigh wave) solutions in anisotropic elastic crystals,'' J. Phys. F: Met. Phys. **4**, 671–686.

Burridge, R., and Knopoff, L. (**1964**). ''Body force equivalents for seismic dislocations,'' Bull. Seismol. Soc. Am. **54**, 1875–1888.

Burridge, R. (**1971**). ''Lamb's problem for an anisotropic half-space,'' Quart. J. Mech. Appl. Math. **24**, 81–98.

Eringen, A. C., and Suhubi, E. S. (**1975**). *Elastodynamics, Vol. 2* (Academic, New York), pp. 600–644.

Every, A. G., Kim, K. Y., and Maznev, A. A. (**1997**). ''The elastodynamic response of a semi-infinite anisotropic solid to sudden surface loading,'' J. Acoust. Soc. Am. **102**, 1346–1355.

Every, A. G., Kim, K. Y., and Maznev, A. A. (**1998**). ''Surface dynamic response functions of anisotropic solids,'' Ultrasonics **36**, 349–353.

Lamb, H. (**1904**). ''On the propagation of tremors over the surface of an elastic solid,'' Philos. Trans. R. Soc. London, Ser. A **203**, 1–42.

Lapwood, E. R. (**1949**). ''The disturbance due to a line source in a semi-infinite elastic medium,'' Philos. Trans. R. Soc. London, Ser. A **242**, 63–100.

Kraut, E. A. (**1963**). ''Advances in the theory of elastic wave propagation,'' Rev. Geophys. **1**, 401–448.

Maznev, A. A., and Every, A. G. (**1997**). ''Time-domain dynamic surface response of an anisotropic elastic solid to an impulsive line force,'' Int. J. Eng. Sci. **35**, 321–327.

Mourad, A., and Deschamps, M. (**1995**). ''Lamb's problem for an anisotropic half-space studied by the Cagniard de Hoop method,'' J. Acoust. Soc. Am. **97**, 3194–3197.

Mourad, A., Deschamps, M., and Castagnede, B. (**1996**). ''Acoustic waves generated by a transient line source in an anisotropic half-space,'' Acustica **82**, 839–851.

Nakano, H. (**1925**). ''On Rayleigh waves,'' Jpn. J. Astron. Geophys. **2**, 233–326.

Payton, R. G. (**1983**). *Elastic Wave Propagation in Transversely Isotropic Media* (Martinus Nijhoff, The Hague).

Spies, M. (**1997**). ''Green's tensor function for Lamb's problem: The general anisotropic case,'' J. Acoust. Soc. Am. **102**, 2438–2441.

Stroh, A. N. (**1958**). ''Dislocations and cracks in anisotropic elasticity,'' Philos. Mag. **3**, 625–646.

Stroh, A. N. (**1962**). ''Steady state problems in anisotropic elasticity,'' J. Math. Phys. **41**, 77–103.

Tewary, V. K., and Fortunko, C. M. (**1996**). ''Surface waves in three-dimensional half-space tetragonal solids,'' J. Acoust. Soc. Am. **100**, 86–88.

Wang, C.-Y., and Achenbach, J. D. (**1996**). ''Lamb's problem for solid of general anisotropy,'' Wave Motion **24**, 227–242.

Willis, J. R. (**1973**). ''Self-similar problems in elastodynamics,'' Philos. Trans. R. Soc. London, Ser. A **443**, 435–491.

Wu, K.-C. (**2000**). ''Extension of Stroh's formalism to self-similar problems in two-dimensional elastodynamics,'' Proc. R. Soc. London, Ser. A **456**, 869–890.

Modeling elastic wave forward propagation and reflection using the complex screen method

Xiao-Bi Xie and Ru-Shan Wu
Institute of Geophysics and Planetary Physics, University of California, Santa Cruz, California 95064

(Received 18 January 2000; revised 24 February 2001; accepted 27 February 2001)

Formulation for calculating forward propagation and reflection in a 3D elastic structure based on the complex-screen method is given in this paper. The calculation of reflections is formulated based on the local Born approximation. When using a small angle approximation, the backscattering operator reduces to a screen operator which is similar to the forward screen propagator. Combining the forward propagator and backscattering operator together, the new method can properly handle the multiple forward scattering and single backscattering in a 3D heterogeneous model. Using a dual-domain technique, the new method is highly efficient in CPU time and memory savings. For models where reverberation and resonance scattering can be neglected, this method provides a fast and accurate algorithm. Synthetic seismograms for two-dimensional elastic models are calculated with this method and compared with those generated by the finite-difference method. The results show that the method works well for small to medium scattering angles and medium velocity contrasts. © *2001 Acoustical Society of America.* [DOI: 10.1121/1.1367248]

PACS numbers: 43.20.Gp, 43.20.Bi [ANN]

I. INTRODUCTION

Fast modeling methods and algorithms in complex heterogeneous media, especially for 3D media, are crucial to the application of seismic methods in complex structures including the development of interpretation, imaging and inversion methods. Finite-difference and finite-element algorithms are very flexible. In principle, they can be applied to arbitrarily heterogeneous medium. However, they are very time consuming. High-frequency asymptotic methods, such as ray based methods (e.g., Červený, 1981; Červený and Klimes, 1984; Chapman, 1985), provide high computation efficiency for smooth 3D models. However, they fail to deal with complicated 3D volume heterogeneities. Frequency-dependent and wave related phenomena in complex media cannot be correctly modeled by the ray methods. Born scattering formulation (Gubernatis *et al.*, 1977; Wu and Aki, 1985), ray-Born (Beydoun and Mendes, 1989; Coates and Chapman, 1990), or generalized Born scattering methods (Coates and Chapman, 1991) can model small volume complex heterogeneities in a smooth background. However, they are not capable of modeling long distance propagation in complex media. It is necessary to develop intermediate modeling methods functioning between the full wave equation methods and the high-frequency asymptotic methods.

The phase screen method, or split step Fourier method (e.g., Flatté and Tappert, 1975; Tappert, 1977; Thomson and Chapman, 1983), has been used to calculate the one-way forward propagation for acoustic waves. Recently, the method has also been used to deal with elastic waves. To generalize a scalar wave case to vector elastic waves, the center part is the coupling between *P*- and *S*-waves. Fisk and McCartor (1991) derived coupling terms using a projection method. Their method has some problems for some limiting cases. Wu (1994) derived these terms based on formal scattering theory of elastic waves. Wild and Hudson (1998) used another approach, the geometrical derivation, and reached similar results. The screen method has also been used as back propagators for seismic wave migration in either acoustic or elastic media (e.g., Stoffa *et al.*, 1990; Wu and Xie, 1994; Huang *et al.*, 1999). Generally speaking, these methods give better imaging quality compared with the ray based Kirchhoff method. The generalized screen methods are based on the one-way wave equation that neglects backscattered waves, but correctly handles all the forward multiple-scattering effects, e.g., focusing/defocusing, diffraction, interference, and conversion between different wave types. For media where the resonance scattering or reverberations caused by heterogeneities can be neglected, the reflections will be dominated by single backscatterings. In this case, the screen method can also be adopted to calculate reflections. Wu and Huang (1995) tested the method for acoustic reflections. Wu (1996) discussed approximations for forward and backward scatterings of different wave types. Xie and Wu (1996) tested the screen approximation for modeling elastic wave reflections.

In this study, the complex-screen method is extended to deal with both forward propagation and reflection of elastic waves. The current formulation is based on a small angle approximation of the one-way wave equation and the local Born approximation using the perturbation theory. Under the small angle approximation, backscattering can also be formulated into a screen operator which is similar to the screen propagator. The interaction between the incident wave field and the heterogeneities gives both forward and backward scattered waves. The forward scattered waves, together with the primary wave, construct the transmitted waves. The backscattered waves give the reflections by the structure. With an iterative method, it can correctly handle multiple forward scattering and single backscattering. By using a dual-domain operation, it retains the advantages of the original screen method, i.e., high-efficiency in computation speed and tremendous memory savings. Numerical results show

that this is a very promising method in modeling primary reflections from complicated large scale 3D elastic structures.

In the following sections, we first present the formulation. Then numerical examples are conducted to test the method. For a two-dimensional test model, the results from the screen method are compared with that from the full wave finite-difference method.

II. EXPRESSIONS FOR FORWARD AND BACKWARD SCATTERED WAVE FIELDS

We start from the equation of motion for displacement $\mathbf{u}$ in a linear elastic medium (Aki and Richards, 1980):

$$-\rho(\mathbf{x})\omega^2\mathbf{u}(\mathbf{x})=\nabla\cdot[\tfrac{1}{2}\mathbf{c}(\mathbf{x}):(\nabla\mathbf{u}(\mathbf{x})+\mathbf{u}(\mathbf{x})\nabla)], \tag{1}$$

where $\mathbf{u}$ is the displacement, $\mathbf{c}$ is the elastic constant tensor, ρ is density, $\mathbf{u}\nabla$ is the transpose of $\nabla\mathbf{u}$ and ''$:$'' is for double scalar product, i.e., $(\mathbf{ab}):(\mathbf{cd})=(\mathbf{b}\cdot\mathbf{c})(\mathbf{a}\cdot\mathbf{d})$. If elastic parameters and the wave field can be decomposed into

$$\rho(\mathbf{x})=\rho_0+\delta\rho(\mathbf{x}),$$

$$\mathbf{c}(\mathbf{x})=\mathbf{c}_0+\delta\mathbf{c}(\mathbf{x}),$$

$$\mathbf{u}(\mathbf{x})=\mathbf{u}_0(\mathbf{x})+\mathbf{U}(\mathbf{x}),$$

where ρ_0 and $\mathbf{c}_0$ are density and elastic parameters for the background medium, $\delta\rho(\mathbf{x})$ and $\delta\mathbf{c}(\mathbf{x})$ are the corresponding perturbations, $\mathbf{u}_0(\mathbf{x})$ and $\mathbf{U}(\mathbf{x})$ are the incident field and the scattered field, then Eq. (1) can be rewritten as

$$-\rho_0\omega^2\mathbf{U}(\mathbf{x})-\nabla\cdot[\tfrac{1}{2}\mathbf{c}_0:(\nabla\mathbf{U}(\mathbf{x})+\mathbf{U}(\mathbf{x})\nabla)]=\mathbf{F}(\mathbf{x}), \tag{2}$$

where

$$\mathbf{F}(\mathbf{x})=\omega^2\delta\mathbf{c}(\mathbf{x})\mathbf{u}(\mathbf{x})+\nabla\cdot[\tfrac{1}{2}\delta\mathbf{c}(\mathbf{x}):(\nabla\mathbf{u}(\mathbf{x})+\mathbf{u}(\mathbf{x})\nabla)] \tag{3}$$

is the equivalent body force due to scattering. The scattered field can be expressed as

$$\mathbf{U}(\mathbf{x})=\int_{V'}dv'\,\mathbf{G}(\mathbf{x};\mathbf{x}')\mathbf{F}(\mathbf{x}'), \tag{4}$$

where $\mathbf{G}$ is the Green's function in the background medium. We will consider a special case where an incident wave $\mathbf{u}_0(\mathbf{x})$ interacts with a heterogeneous thin slab which is perpendicular to the main propagation direction. Figure 1 shows the primary incident waves and various types of secondary waves generated by the scattering process. If the slab is thin enough, the local Born approximation can be adopted within the slab. The wave field $\mathbf{u}(\mathbf{x})$ in Eq. (3) can be replaced by the incident field $\mathbf{u}_0(\mathbf{x})$. Let $\hat{\mathbf{e}}_z$ be the unit vector along the main propagation direction, and $\mathbf{x}_T=x\hat{\mathbf{e}}_x+y\hat{\mathbf{e}}_y$ be a position vector in the transverse plane. The slab is between z_0 and z_1, with a thickness of $\Delta z=z_1-z_0$. The scattered field from the slab can be expressed as

$$\mathbf{U}(\mathbf{x})=\int_{z_0}^{z_1}dz'\int\int d\mathbf{x}_T'\mathbf{G}(\mathbf{x}_T,z;\mathbf{x}_T',z')\mathbf{F}_0(\mathbf{x}_T',z'), \tag{5}$$

where $\mathbf{F}_0(\mathbf{x})$ is Eq. (3) with $\mathbf{u}(\mathbf{x})$ replaced by $\mathbf{u}_0(\mathbf{x})$.

The incident field $\mathbf{u}_0(\mathbf{x})$ can be decomposed into a superposition of plane *P*- and *S*-waves:

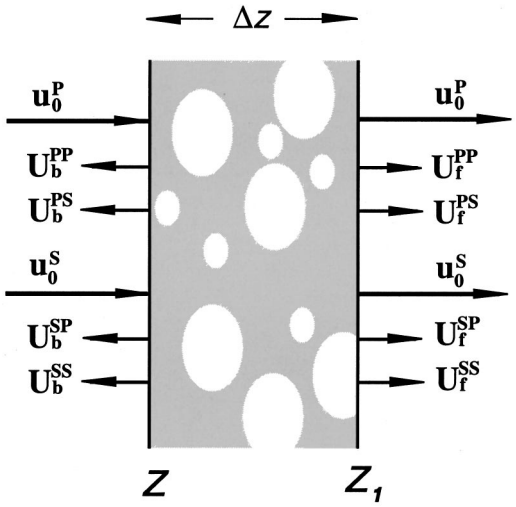

FIG. 1. A sketch showing the primary waves and various scattering waves generated when an incident wave interacts with an inhomogeneous thin slab. For details see text.

$$\mathbf{u}_0(\mathbf{x}_T,z)=\frac{1}{4\pi^2}\int d\mathbf{K}_T[\mathbf{u}_0^P(\mathbf{K}_T,z)+\mathbf{u}_0^S(\mathbf{K}_T,z)]e^{i\mathbf{K}_T\cdot\mathbf{x}_T}, \tag{6}$$

where $\mathbf{K}_T$ is the incident transverse wave number of plane waves and superscripts *P* and *S* denote *P*- and *S*-waves. The forward propagated field is composed of primary wave and forward scattered *P*- and *S*-waves. At z_1, it can be expressed as

$$\mathbf{u}_f(\mathbf{x}_T,z_1)=\frac{1}{4\pi^2}\int d\mathbf{K}_T'[\mathbf{u}_f^P(\mathbf{K}_T',z_1)+\mathbf{u}_f^S(\mathbf{K}_T',z_1)]e^{i\mathbf{K}_T'\cdot\mathbf{x}_T}, \tag{7}$$

where

$$\mathbf{u}_f^P(\mathbf{K}_T',z_1)=e^{i\gamma_\alpha'|z_1-z_0|}[\mathbf{u}_0^P(\mathbf{K}_T',z_0)+\mathbf{U}_f^{PP}(\mathbf{K}_T',z_0)+\mathbf{U}_f^{SP}(\mathbf{K}_T',z_0)], \tag{8}$$

$$\mathbf{u}_f^S(\mathbf{K}_T',z_1)=e^{i\gamma_\beta'|z_1-z_0|}[\mathbf{u}_0^S(\mathbf{K}_T',z_0)+\mathbf{U}_f^{SS}(\mathbf{K}_T',z_0)+\mathbf{U}_f^{PS}(\mathbf{K}_T',z_0)], \tag{9}$$

where $\mathbf{K}_T'$ is the transverse wave number of scattered waves, $\gamma_\alpha=(k_\alpha^2-K_T^2)^{1/2}$ and $\gamma_\beta=(k_\beta^2-K_T^2)^{1/2}$ are longitudinal components of *P*- and *S*-wave numbers in the background media, and $k_\alpha=\omega/\alpha$ and $k_\beta=\omega/\beta$ are *P*- and *S*-wave numbers, α and β are *P*- and *S*-wave velocities. Phase advance operators $e^{i\gamma_\alpha'|z_1-z_0|}$ and $e^{i\gamma_\beta'|z_1-z_0|}$ propagate the incident and scattered fields from z_0 to z_1. The reflected wave is composed of backscattered *P*- and *S*-waves. At z_0, the reflected wave can be expressed as

$$\mathbf{u}_b(\mathbf{x}_T,z_0)=\frac{1}{4\pi^2}\int d\mathbf{K}_T'[\mathbf{u}_b^P(\mathbf{K}_T',z_0)+\mathbf{u}_b^S(\mathbf{K}_T',z_0)]e^{i\mathbf{K}_T'\cdot\mathbf{x}_T}, \tag{10}$$

where

$$\mathbf{u}_b^P(\mathbf{K}_T',z_0)=\mathbf{U}_b^{PP}(\mathbf{K}_T',z_0)+\mathbf{U}_b^{SP}(\mathbf{K}_T',z_0), \tag{11}$$

$$\mathbf{u}_b^S(\mathbf{K}_T',z_0)=\mathbf{U}_b^{PS}(\mathbf{K}_T',z_0)+\mathbf{U}_b^{SS}(\mathbf{K}_T',z_0). \tag{12}$$

In above equations, **U** denotes scattered waves. The subscripts *f* and *b* denote forward and backward scatterings, respectively. Superscripts *PP*, *PS*, *SP* and *SS* indicate the scattering between different wave types as shown in Fig. 1. For isotropic elastic medium, the scattered fields for both forward and backward scatterings can be derived from Eq. (5) (Wu, 1994):

$$\mathbf{U}^{PP}(\mathbf{K}_T',\mathbf{K}_T)=\frac{i}{2\gamma_\alpha'}k_\alpha^2u_0^P\hat{k}_\alpha'\left\{(\hat{k}_\alpha\cdot\hat{k}_\alpha')\frac{\delta\rho(\tilde{\mathbf{k}})}{\rho_0}-\frac{\delta\lambda(\tilde{\mathbf{k}})}{\lambda_0+2\mu_0}-(\hat{k}_\alpha\cdot\hat{k}_\alpha')^2\frac{2\,\delta\mu(\tilde{\mathbf{k}})}{\lambda_0+2\mu_0}\right\}, \tag{13}$$

$$\mathbf{U}^{PS}(\mathbf{K}_T',\mathbf{K}_T)=\frac{i}{2\gamma_\beta'}k_\beta^2u_0^P[\hat{k}_\alpha-\hat{k}_\beta'(\hat{k}_\alpha\cdot\hat{k}_\beta')]\left\{\frac{\delta\rho(\tilde{\mathbf{k}})}{\rho_0}-2\frac{\beta_0}{\alpha_0}(\hat{k}_\alpha\cdot\hat{k}_\beta')\frac{\delta\mu(\tilde{\mathbf{k}})}{\mu_0}\right\}, \tag{14}$$

$$\mathbf{U}^{SP}(\mathbf{K}_T',\mathbf{K}_T)=\frac{i}{2\gamma_\alpha'}k_\alpha^2(\mathbf{u}_0^S\cdot\hat{k}_\alpha')\hat{k}_\alpha'\left\{\frac{\delta\rho(\tilde{\mathbf{k}})}{\rho_0}-2\frac{\beta_0}{\alpha_0}(\hat{k}_\beta\cdot\hat{k}_\alpha')\frac{\delta\mu(\tilde{\mathbf{k}})}{\mu_0}\right\}, \tag{15}$$

$$\mathbf{U}^{SS}(\mathbf{K}_T',\mathbf{K}_T)=\frac{i}{2\gamma_\beta'}k_\beta^2\left\{[\mathbf{u}_0^S-\hat{k}_\beta'(\mathbf{u}_0^S\cdot\hat{k}_\beta')]\frac{\delta\rho(\tilde{\mathbf{k}})}{\rho_0}-[(\hat{k}_\beta\cdot\hat{k}_\beta')[\mathbf{u}_0^S-\hat{k}_\beta'(\mathbf{u}_0^S\cdot\hat{k}_\beta')]+(\mathbf{u}_0^S\cdot\hat{k}_\alpha')\times(\hat{k}_\beta-\hat{k}_\beta'(\hat{k}_\beta\cdot\hat{k}_\beta'))]\frac{\delta\mu(\tilde{\mathbf{k}})}{\mu_0}\right\}, \tag{16}$$

where $u_0^P=|\mathbf{u}_0^P(\mathbf{K}_T)|$ and $\mathbf{u}_0^S=\mathbf{u}_0^S(\mathbf{K}_T)$, $\delta\rho(\mathbf{k})$, $\delta\lambda(\mathbf{k})$ and $\delta\mu(\mathbf{k})$ are three-dimensional Fourier transforms of medium perturbations, wave numbers without primes are for incident waves and with primes are for scattered waves, $\tilde{\mathbf{k}}=\mathbf{k}'-\mathbf{k}$ is the exchange wave number with $\mathbf{k}$ and $\mathbf{k}'$ as the incident and scattering wave numbers, respectively, $\hat{k}_\alpha$ and $\hat{k}_\beta$ are unit wave number vectors for *P*- and *S*-waves, and

$$\begin{aligned}&\mathbf{k}_\alpha=\mathbf{K}_T+\gamma_\alpha\hat{\mathbf{e}}_z, \quad \mathbf{k}_\beta=\mathbf{K}_T+\gamma_\beta\hat{\mathbf{e}}_z,\\ &\mathbf{k}_\alpha'=\mathbf{K}_T'\pm\gamma_\alpha'\hat{\mathbf{e}}_z, \quad \mathbf{k}_\beta'=\mathbf{K}_T'\pm\gamma_\beta'\hat{\mathbf{e}}_z,\end{aligned} \tag{17}$$

where the + or − sign depends on whether it is forward or backward scattering, and $\hat{\mathbf{e}}_z$ is the unit vector in the *z*-direction. The longitudinal coordinate z_0 has been temporarily omitted from these equations.

Equations (13)–(16) give scattered fields of different wave types. They are scattered plane waves with transverse wave number $\mathbf{K}_T'$ generated by the plane incident wave with transverse wave number $\mathbf{K}_T$. The total scattered plane wave is the integration of contributions from all incident plane waves,

$$\mathbf{U}(\mathbf{K}_T',z_0)=\frac{1}{4\pi^2}\int d\mathbf{K}_T\mathbf{U}(\mathbf{K}_T',\mathbf{K}_T,z_0). \tag{18}$$

In principle, Eqs. (7)–(18) provide all equations needed for calculating wave fields $\mathbf{u}_f(\mathbf{x}_T,z_1)$ and $\mathbf{u}_b(\mathbf{x}_T,z_0)$. However, from these equations we can see that scattered waves composed of contributions from all $\mathbf{K}_T'$ which are coupled with all incident $\mathbf{K}_T$. For a general three-dimensional velocity model, both of them are two-dimensional and the $\mathbf{U}(\mathbf{K}_T',\mathbf{K}_T)$ is a four-dimensional matrix. The calculations of these matrix operations are very time consuming. To obtain a highly efficient algorithm, we introduce a small angle approximation to the formulation.

III. SMALL ANGLE APPROXIMATION

Under the small angle approximation, γ_α and γ_α' can be approximated by k_α, and γ_β and γ_β' by k_β. The exchange wave numbers for forward and backward scattered fields can be simplified. For forward scattering

$$\begin{aligned}&\mathbf{k}_\alpha'-\mathbf{k}_\alpha\approx\mathbf{K}_T'-\mathbf{K}_T+0\hat{\mathbf{e}}_z,\\ &\mathbf{k}_\beta'-\mathbf{k}_\alpha\approx\mathbf{K}_T'-\mathbf{K}_T+(k_\beta-k_\alpha)\hat{\mathbf{e}}_z,\\ &\mathbf{k}_\alpha'-\mathbf{k}_\beta\approx\mathbf{K}_T'-\mathbf{K}_T+(k_\alpha-k_\beta)\hat{\mathbf{e}}_z,\\ &\mathbf{k}_\beta'-\mathbf{k}_\beta\approx\mathbf{K}_T'-\mathbf{K}_T+0\hat{\mathbf{e}}_z.\end{aligned} \tag{19}$$

For backward scattering

$$\begin{aligned}&\mathbf{k}_\alpha'-\mathbf{k}_\alpha\approx\mathbf{K}_T'-\mathbf{K}_T-2k_\alpha\hat{\mathbf{e}}_z,\\ &\mathbf{k}_\beta'-\mathbf{k}_\alpha\approx\mathbf{K}_T'-\mathbf{K}_T-(k_\beta+k_\alpha)\hat{\mathbf{e}}_z,\\ &\mathbf{k}_\alpha'-\mathbf{k}_\beta\approx\mathbf{K}_T'-\mathbf{K}_T-(k_\alpha+k_\beta)\hat{\mathbf{e}}_z,\\ &\mathbf{k}_\beta'-\mathbf{k}_\beta\approx\mathbf{K}_T'-\mathbf{K}_T-2k_\beta\hat{\mathbf{e}}_z.\end{aligned} \tag{20}$$

The three-dimensional Fourier transforms of the perturbations $\delta\rho(\mathbf{k})$, $\delta\lambda(\mathbf{k})$ and $\delta\mu(\mathbf{k})$ can also be simplified. Taking the density perturbation for back scattering as an example,

$$\delta\rho(\mathbf{k}_\alpha'-\mathbf{k}_\alpha)=\int_0^{\Delta z}dz\,e^{i(\gamma_\alpha'+\gamma_\alpha)z}\int\int d\mathbf{x}_T\times\delta\rho(\mathbf{x}_T,z-z_0)e^{-i(\mathbf{K}_T'-\mathbf{K}_T)\cdot\mathbf{x}_T}. \tag{21}$$

If the slab is thin enough, the variation of $\delta\rho(\mathbf{x}_T,z)$ along the *z*-direction will be small, the integral can be approximated as

$$\delta\rho(\mathbf{k}_\alpha'-\mathbf{k}_\alpha)\approx\Delta z\,\delta\rho(\mathbf{K}_T'-\mathbf{K}_T,z_0)\,\eta_b^{PP}, \tag{22}$$

where

$$\eta_b^{PP}=\frac{1}{i2k_\alpha\Delta z}(e^{i2k_\alpha\Delta z}-1)=\mathrm{sinc}(k_\alpha\Delta z)e^{ik_\alpha\Delta z}, \tag{23}$$

and $\mathrm{sinc}(z)=\sin(z)/z$. In the above equations, the original three-dimensional Fourier transform has been decomposed into a 2D Fourier transform and a 1D Fourier transform. $\delta\rho(\mathbf{K}_T,z_0)$ is a 2D Fourier transform of $\delta\rho(\mathbf{x}_T,z)$ averaged over an interval between z_0 and z_1, η_b^{PP} is the 1D Fourier transform of a boxcar function since the medium variation in *z* direction has been neglected due to the screen assumption. For simplicity, z_0 is omitted in the following equations. Similarly, for forward scatterings of different wave types we have

$$\delta\rho(\mathbf{k}'_\alpha-\mathbf{k}_\alpha)\approx\Delta z\,\delta\rho(\mathbf{K}'_T-\mathbf{K}_T)\,\eta_f^{PP},$$
$$\delta\rho(\mathbf{k}'_\beta-\mathbf{k}_\alpha)\approx\Delta z\,\delta\rho(\mathbf{K}'_T-\mathbf{K}_T)\,\eta_f^{PS},$$
$$\delta\rho(\mathbf{k}'_\alpha-\mathbf{k}_\beta)\approx\Delta z\,\delta\rho(\mathbf{K}'_T-\mathbf{K}_T)\,\eta_f^{SP},$$
$$\delta\rho(\mathbf{k}'_\beta-\mathbf{k}_\beta)\approx\Delta z\,\delta\rho(\mathbf{K}'_T-\mathbf{K}_T)\,\eta_f^{SS}, \tag{24}$$

and for backward scatterings of different wave types

$$\delta\rho(\mathbf{k}'_\alpha-\mathbf{k}_\alpha)\approx\Delta z\,\delta\rho(\mathbf{K}'_T-\mathbf{K}_T)\,\eta_b^{PP},$$
$$\delta\rho(\mathbf{k}'_\beta-\mathbf{k}_\alpha)\approx\Delta z\,\delta\rho(\mathbf{K}'_T-\mathbf{K}_T)\,\eta_b^{PS},$$
$$\delta\rho(\mathbf{k}'_\alpha-\mathbf{k}_\beta)\approx\Delta z\,\delta\rho(\mathbf{K}'_T-\mathbf{K}_T)\,\eta_b^{SP},$$
$$\delta\rho(\mathbf{k}'_\beta-\mathbf{k}_\beta)\approx\Delta z\,\delta\rho(\mathbf{K}'_T-\mathbf{K}_T)\,\eta_b^{SS}. \tag{25}$$

The modulation factors are

$$\eta_f^{PP}=1,$$
$$\eta_f^{PS}=\mathrm{sinc}[(k_\beta-k_\alpha)\Delta z/2]e^{-i(k_\beta-k_\alpha)\Delta z/2},$$
$$\eta_f^{SP}=\eta_f^{*PS},$$
$$\eta_f^{SS}=1, \tag{26}$$
$$\eta_b^{PP}=\mathrm{sinc}(k_\alpha\Delta z)e^{ik_\alpha\Delta z},$$
$$\eta_b^{PS}=\mathrm{sinc}[(k_\beta+k_\alpha)\Delta z/2]e^{i(k_\beta+k_\alpha)\Delta z/2},$$
$$\eta_b^{SP}=\eta_b^{PS},$$
$$\eta_b^{SS}=\mathrm{sinc}(k_\beta\Delta z)e^{ik_\beta\Delta z}, \tag{27}$$

where η^* is the complex conjugate of η. Similar expressions can be derived for the elastic constants λ and μ.

Note that under small angle approximation, $(\hat{k}_\alpha\cdot\hat{k}'_\alpha)$, $(\hat{k}_\beta\cdot\hat{k}'_\beta)$, $(\hat{k}_\beta\cdot\hat{k}'_\alpha)$ and $(\hat{k}_\alpha\cdot\hat{k}'_\beta)$ approach $+1$ for forward and -1 for backward scatterings, respectively. Substituting Eqs. (24)–(27) into Eqs. (13)–(16), for forward scatterings we have

$$\mathbf{U}_f^{PP}(\mathbf{K}'_T,\mathbf{K}_T)=-ik_\alpha\Delta z\hat{k}'_\alpha u_0^P(\mathbf{K}_T)\frac{\delta\alpha(\tilde{\mathbf{K}}_T)}{\alpha_0}\eta_f^{PP}, \tag{28}$$

$$\mathbf{U}_f^{PS}(\mathbf{K}'_T,\mathbf{K}_T)=-ik_\beta\Delta z u_0^P(\mathbf{K}_T)[\hat{k}_\alpha-\hat{k}'_\beta(\hat{k}_\alpha\cdot\hat{k}'_\beta)]\times\left[\frac{\delta\beta(\tilde{\mathbf{K}}_T)}{\beta_0}+\left(\frac{\beta_0}{\alpha_0}-\frac{1}{2}\right)\frac{\delta\mu(\tilde{\mathbf{K}}_T)}{\mu_0}\right]\eta_f^{PS}, \tag{29}$$

$$\mathbf{U}_f^{SP}(\mathbf{K}'_T,\mathbf{K}_T)=-ik_\alpha\Delta z(\mathbf{u}_0^S(\mathbf{K}_T)\cdot\hat{k}'_\alpha)\hat{k}'_\alpha\times\left[\frac{\delta\beta(\tilde{\mathbf{K}}_T)}{\beta_0}+\left(\frac{\beta_0}{\alpha_0}-\frac{1}{2}\right)\frac{\delta\mu(\tilde{\mathbf{K}}_T)}{\mu_0}\right]\eta_f^{SP}, \tag{30}$$

$$\mathbf{U}_f^{SS}(\mathbf{K}'_T,\mathbf{K}_T)=-ik_\beta\Delta z[\mathbf{u}_0^S(\mathbf{K}_T)-\hat{k}'_\beta(\mathbf{u}_0^S(\mathbf{K}_T)\cdot\hat{k}'_\beta)]\times\frac{\delta\beta(\tilde{\mathbf{K}}_T)}{\beta_0}\eta_f^{SS}, \tag{31}$$

and for backward scatterings, we have

$$\mathbf{U}_b^{PP}(\mathbf{K}'_T,\mathbf{K}_T)=-ik_\alpha\Delta z\hat{k}'_\alpha u_0^P(\mathbf{K}_T)\times\left[\frac{\delta\rho(\tilde{\mathbf{K}}_T)}{\rho_0}+\frac{\delta\alpha(\tilde{\mathbf{K}}_T)}{\alpha_0}\right]\eta_b^{PP}$$
$$=-ik_\alpha\Delta z\hat{k}'_\alpha u_0^P(\mathbf{K}_T)\frac{\delta Z_\alpha(\tilde{\mathbf{K}}_T)}{Z_{\alpha0}}\eta_b^{PP}, \tag{32}$$

$$\mathbf{U}_b^{PS}(\mathbf{K}'_T,\mathbf{K}_T)=-ik_\beta\Delta z u_0^P(\mathbf{K}_T)[\hat{k}_\alpha-\hat{k}'_\beta(\hat{k}_\alpha\cdot\hat{k}'_\beta)]\times\left[\frac{\delta\beta(\tilde{\mathbf{K}}_T)}{\beta_0}-\left(\frac{\beta_0}{\alpha_0}+\frac{1}{2}\right)\frac{\delta\mu(\tilde{\mathbf{K}}_T)}{\mu_0}\right]\eta_b^{PS}$$
$$=ik_\beta\Delta z u_0^P(\mathbf{K}_T)[\hat{k}_\alpha-\hat{k}'_\beta(\hat{k}_\alpha\cdot\hat{k}'_\beta)]\times\left[\frac{\delta Z_\beta(\tilde{\mathbf{K}}_T)}{Z_{\beta0}}+\left(\frac{\beta_0}{\alpha_0}-\frac{1}{2}\right)\frac{\delta\mu(\tilde{\mathbf{K}}_T)}{\mu_0}\right]\eta_b^{PS}, \tag{33}$$

$$\mathbf{U}_b^{SP}(\mathbf{K}'_T,\mathbf{K}_T)=-ik_\alpha\Delta z(\mathbf{u}_0^S(\mathbf{K}_T)\cdot\hat{k}'_\alpha)\hat{k}'_\alpha\times\left[\frac{\delta\beta(\tilde{\mathbf{K}}_T)}{\beta_0}-\left(\frac{\beta_0}{\alpha_0}+\frac{1}{2}\right)\frac{\delta\mu(\tilde{\mathbf{K}}_T)}{\mu_0}\right]\eta_b^{SP}$$
$$=ik_\alpha\Delta z(\mathbf{u}_0^S(\mathbf{K}_T)\cdot\hat{k}'_\alpha)\hat{k}'_\alpha\times\left[\frac{\delta Z_\beta(\tilde{\mathbf{K}}_T)}{Z_{\beta0}}+\left(\frac{\beta_0}{\alpha_0}-\frac{1}{2}\right)\frac{\delta\mu(\tilde{\mathbf{K}}_T)}{\mu_0}\right]\eta_b^{SP}, \tag{34}$$

$$\mathbf{U}_b^{SS}(\mathbf{K}'_T,\mathbf{K}_T)=ik_\beta\Delta z[\mathbf{u}_0^S(\mathbf{K}_T)-\hat{k}'_\beta(\mathbf{u}_0^S(\mathbf{K}_T)\cdot\hat{k}'_\beta)]\times\left[\frac{\delta\rho(\tilde{\mathbf{K}}_T)}{\rho_0}+\frac{\delta\beta(\tilde{\mathbf{K}}_T)}{\beta_0}\right]\eta_b^{SS}$$
$$=ik_\beta\Delta z[\mathbf{u}_0^S(\mathbf{K}_T)-\hat{k}'_\beta(\mathbf{u}_0^S(\mathbf{K}_T)\cdot\hat{k}'_\beta)]\times\frac{\delta Z_\beta(\tilde{\mathbf{K}}_T)}{Z_{\beta0}}\eta_b^{SS}. \tag{35}$$

In Eqs. (28)–(35), $\tilde{\mathbf{K}}_T=\mathbf{K}'_T-\mathbf{K}_T$ is the exchange transverse wave number, $\delta\alpha(\mathbf{K}_T)$ and $\delta\beta(\mathbf{K}_T)$ are transverse spectra of *P*- and *S*-wave velocity perturbations, $\delta Z_\alpha(\mathbf{K}_T)$ and $\delta Z_\beta(\mathbf{K}_T)$ are transverse spectra of *P*- and *S*-wave impedance perturbations, respectively. Equations (28) and (32) show that the forward scattered *P*-*P* wave is proportional to the *P*-wave velocity perturbation, while the backward scattered *P*-*P* wave depends on the *P*-wave impedance perturbation, consistent with the scattering theory. A similar situation is true for *S*-*S* scattering as can be seen from Eqs. (31) and (35). The quantity $(\beta_0/\alpha_0-1/2)$ is usually small, and as can be seen from Eqs. (29) and (30), the forward converted waves $\mathbf{U}_f^{PS}$ and $\mathbf{U}_f^{SP}$ are basically controlled by the *S*-wave velocity perturbation. Similarly, from Eqs. (33) and (34), the backward converted waves $\mathbf{U}_b^{PS}$ and $\mathbf{U}_b^{SP}$ are controlled by *S*-wave impedance perturbation. The forward and backward scattered waves reveal different characteristics of the medium, since they are controlled by different medium parameters.

The total scattered plane wave is the integration of contributions from scattering of all incident plane waves. For example, for *P*-*P* forward scattering we have

$$\mathbf{U}_f^{PP}(\mathbf{K}_T',z_0)=\frac{1}{4\pi^2}\int d\mathbf{K}_T\mathbf{U}_f^{PP}(\mathbf{K}_T',\mathbf{K}_T,z_0).$$

From Eq. (28) we can see that the above equation is a convolution between the incident wave and medium parameter in the transverse wave number domain. A more efficient calculation is to transfer the wave number domain convolution into a spatial domain multiplication using the fast Fourier transform. Thus

$$\mathbf{U}_f^{PP}(\mathbf{K}_T',z_0)=-ik_\alpha\Delta z\hat{k}_\alpha'\eta_f^{PP}\int\int d\mathbf{x}_f'e^{-i\mathbf{K}_T'\cdot\mathbf{x}_T'}\times u_0^P(\mathbf{x}_T',z_0)\frac{\delta\alpha(\mathbf{x}_T')}{\alpha_0},\tag{36}$$

where $\delta\alpha(\mathbf{x}_T)$ is $\delta\alpha(\mathbf{x}_T,z)$ averaged over the interval between z_0 and z_1. Similarly, dual-domain formulas for other wave types can be obtained as

$$\mathbf{U}_f^{PS}(\mathbf{K}_T',z_0)=-ik_\beta\Delta z\,\eta_f^{PS}\hat{k}_\beta'\times\left\{\hat{k}_\beta'\times\int\int d\mathbf{x}_T'e^{-i\mathbf{K}_T'\cdot\mathbf{x}_T'}\times\mathbf{u}_0^P(\mathbf{x}_T',z_0)\left[\left(\frac{\beta_0}{\alpha_0}-\frac{1}{2}\right)\frac{\delta\rho(\mathbf{x}_T')}{\rho_0}+2\left(\frac{\beta_0}{\alpha_0}\right)\frac{\delta\beta(\mathbf{x}_T')}{\beta_0}\right]\right\},\tag{37}$$

$$\mathbf{U}_f^{SP}(\mathbf{K}_T',z_0)=-ik_\alpha\Delta z\,\eta_f^{SP}\hat{k}_\alpha'\left\{\hat{k}_\alpha'\cdot\int\int d\mathbf{x}_T'e^{-i\mathbf{K}_T'\cdot\mathbf{x}_T'}\times\mathbf{u}_0^S(\mathbf{x}_T',z_0)\left[\left(\frac{\beta_0}{\alpha_0}-\frac{1}{2}\right)\frac{\delta\rho(\mathbf{x}_T')}{\rho_0}+2\left(\frac{\beta_0}{\alpha_0}\right)\frac{\delta\beta(\mathbf{x}_T')}{\beta_0}\right]\right\},\tag{38}$$

$$\mathbf{U}_f^{SS}(\mathbf{K}_T',z_0)=-ik_\beta\Delta z\,\eta_f^{SS}\hat{k}_\beta'\times\left\{\hat{k}_\beta'\int\int d\mathbf{x}_T'\times e^{-i\mathbf{K}_T'\cdot\mathbf{x}_T'}\mathbf{u}_0^S(\mathbf{x}_T',z_0)\frac{\delta\beta(\mathbf{x}_T')}{\beta_0}\right\},\tag{39}$$

$$\mathbf{U}_b^{PP}(\mathbf{K}_T',z_0)=-ik_\alpha\Delta z\hat{k}_\alpha'\eta_b^{PP}\int\int d\mathbf{x}_T'e^{-i\mathbf{K}_T'\cdot\mathbf{x}_T'}\times u_0^P(\mathbf{x}_T',z_0)\frac{\delta Z_\alpha(\mathbf{x}_T')}{Z_{\alpha0}},\tag{40}$$

$$\mathbf{U}_b^{PS}(\mathbf{K}_T',z_0)=ik_\beta\Delta z\,\eta_b^{PS}\hat{k}_\beta'\times\left\{\hat{k}_\beta'\times\int\int d\mathbf{x}_T'e^{-i\mathbf{K}_T'\cdot\mathbf{x}_T'}\times\mathbf{u}_0^P(\mathbf{x}_T',z_0)\left[\left(\frac{\beta_0}{\alpha_0}+\frac{1}{2}\right)\frac{\delta\rho(\mathbf{x}_T')}{\rho_0}+2\left(\frac{\beta_0}{\alpha_0}\right)\frac{\delta\beta(\mathbf{x}_T')}{\beta_0}\right]\right\},\tag{41}$$

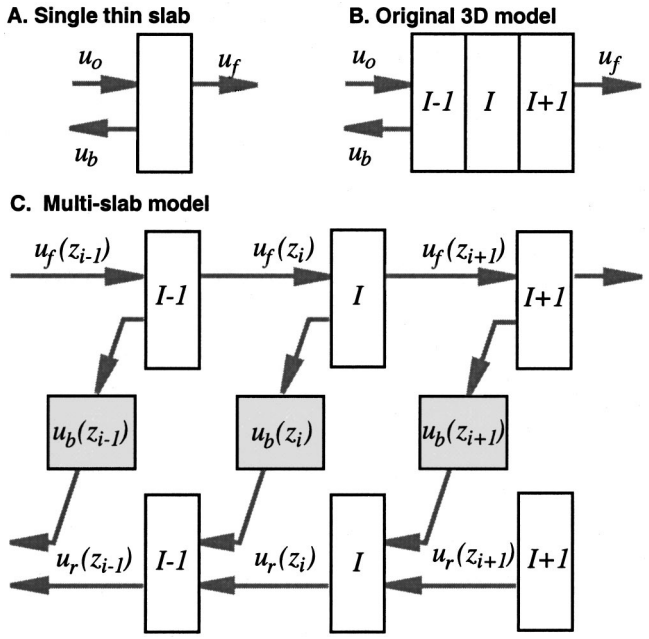

FIG. 2. A sketch of the multiscreen method. For details see text.

$$\mathbf{U}_b^{SP}(\mathbf{K}_T',z_0)=ik_\alpha\Delta z\,\eta_b^{SP}\hat{k}_\alpha'\left\{\hat{k}_\alpha'\cdot\int\int d\mathbf{x}_T'e^{-i\mathbf{K}_T'\cdot\mathbf{x}_T'}\times\mathbf{u}_0^S(\mathbf{x}_T',z_0)\left[\left(\frac{\beta_0}{\alpha_0}+\frac{1}{2}\right)\frac{\delta\rho(\mathbf{x}_T')}{\rho_0}+2\left(\frac{\beta_0}{\alpha_0}\right)\frac{\delta\beta(\mathbf{x}_T')}{\beta_0}\right]\right\},\tag{42}$$

$$\mathbf{U}_b^{SS}(\mathbf{K}_T',z_0)=ik_\beta\Delta z\,\eta_b^{SS}\hat{k}_\beta'\times\left\{\hat{k}_\beta'\times\int\int d\mathbf{x}_T'e^{-i\mathbf{K}_T'\cdot\mathbf{x}_T'}\times\mathbf{u}_0^S(\mathbf{x}_T',z_0)\frac{\delta Z_\beta(\mathbf{x}_T')}{Z_{\beta0}}\right\}.\tag{43}$$

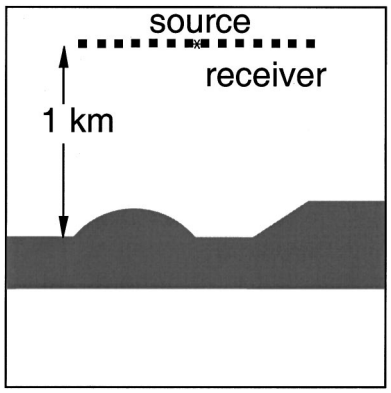

FIG. 3. Two-dimensional model used to compare the results from the screen approximation method and finite-difference method. The model is a 2D profile from the French model (French, 1974). The parameters for the background medium are $V_P=3.6$ km/s, $V_S=2.08$ km/s and $\rho=2.2$ g/cm^3. The intermediate layer has a -20% perturbation for both *P*- and *S*-wave velocities.

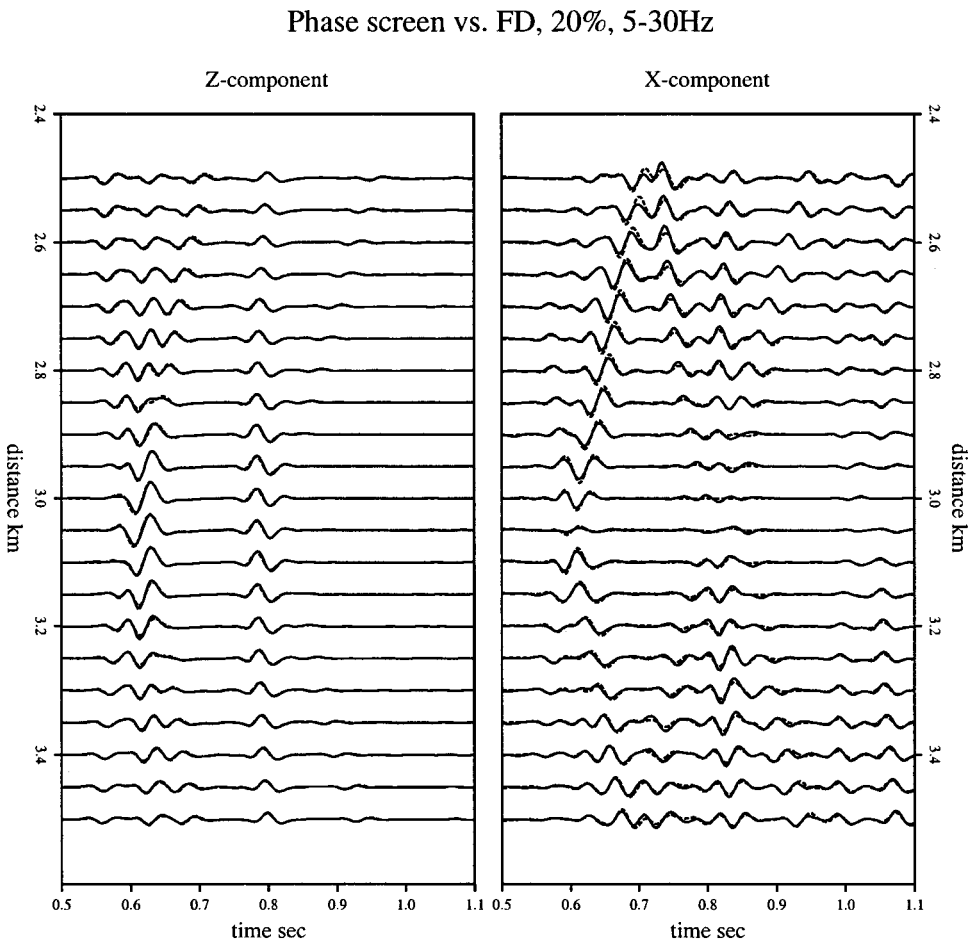

FIG. 4. Comparison of synthetic seismograms calculated by different methods. The solid lines are from the screen method and the dashed lines are from the finite-difference method. The results show general agreement between the two methods in both amplitude and arrival times.

The spatial domain operation of medium-wave interactions are multiplications which are very efficient. The scattered field $\mathbf{U}(\mathbf{K}_T',z)$ from Eqs. (36)–(43) is then substituted into Eqs. (7)–(12) to calculate forward and reflected fields. The propagation of plane waves passing through the homogeneous background medium is conducted in wave number domain by Eqs. (8) and (9). In wave number domain, the propagation operator involves only a phase advance, which is also an efficient operation. Note the difference between Eqs. (13)–(16) and Eqs. (28)–(35). The former involves complicated calculations and the medium-wave interactions are not local, while the later involves simple convolutions in the transverse wave number domain, which results from the small angle approximation and greatly simplifies the calculation.

In summary, the wave propagation through a thin slab is decomposed into a series of highly efficient steps. The model parameters are separated into two parts, the background parameters and the perturbations. The interaction with the perturbations in the spatial domain gives the scattered waves. The propagation through the background medium is in the wave number domain. The calculations in both domains are local and very efficient. The forward and inverse fast Fourier transforms switch the wave field between the two domains.

IV. ITERATIVE PROCEDURE AND NUMERICAL EXAMPLES

Figure 2 is a sketch showing how to calculate the interaction between incident wave and a 3D heterogeneous model with an iterative method. First, the 3D model is divided into a series of thin slabs [Fig. 2(B)]. The Ith slab is between z_i and z_{i+1}. The last section provides us with the formulas for calculating the interaction between the incident wave and a single thin slab [Fig. 2(A)]. With these equations we can calculate the transmitted field $u_f(z_{i+1})$ and the backscattered field $u_b(z_i)$ from the incident wave $u_f(z_i)$. The transmitted field is used as the input for the next slab and in this way the forward propagated field in the entire model can be obtained. The backscattered field are stored temporarily. After finishing the forward propagation, the backscattered fields are retrieved and once again propagated using the one-way propagator. The reflected fields $u_r(z)$ in the entire model are calculated [Fig. 2(C)]. In this way, all the multiple forward scatterings and single backscatterings (MFSB) can be taken into account.

Numerical simulations are conducted to test the accuracy and efficiency of this method. The model is a 2D cut from the French model (French, 1974). Figure 3 shows the velocity structure of this model. The parameters of the background medium are $V_P=3.6$ km/s, $V_S=2.08$ km/s, and $\rho=2.2$ g/cm^3. The intermediate layer has a -20% perturbation for both *P*- and *S*-wave velocities. The *P*-wave source and receivers are located 1 km above the upper interface. With this source–receiver configuration, the observed signals are basically reflections from the structure. The synthetic seismograms are calculated using the elastic complex-screen method presented in this study and a finite-difference

method. The later is a fourth order elastic wave finite-difference code (Xie and Yao, 1988; Xie and Lay, 1994). Free surface effects and primary arrivals have been properly removed from these results. The synthetic seismograms are compared in Fig. 4. Solid lines are from the complex-screen method and the dashed lines are from the finite-difference method. For the *z*-component, there are mainly *P*-waves. The waves arriving between 0.5 and 0.7 s are *P-P* reflections from different parts of the upper interface. Several arrivals can be identified. The second group of waves is relatively simple. They are *P*-to-*P* reflections from the lower plane interface. Due to the complexity of the upper interface, both *P-P* and *P-S* reflections from this interface are rather complicated. They are composed of reflections from the flat and curved sections, and diffractions from the sharp corner. The later is a challenge for ray-based methods. The transverse components of the synthetics are composed of *P-S* reflections from both interfaces, as well as some *P*-waves. Generally speaking, the agreement between the two methods is very good.

V. CONCLUSIONS

The elastic complex-screen method is based on the one-way wave equation, local Born approximation and small angle approximation. It provides an efficient way for calculating both forward and backward scattered waves. This method calculates both forward propagating waves and primary reflections for complicated models. As an example, synthetic seismograms for a 2D elastic model are calculated with this method. The results are compared with those of a finite-difference method. For small to medium scattering angles and medium velocity contrast, the method is well in agreement with the finite-difference method. For wide scattering angles, there are errors in synthetic seismograms. Further investigations show that the errors result from the small angle approximation to the scattering radiation pattern (Wu and Wu, 1998) and phase delay under wide angle and large velocity perturbation (Ristow and Ruhl, 1994; Xie and Wu, 1998). Wide angle accuracy should be further improved in future studies.

ACKNOWLEDGMENTS

This research is supported by the Office of Naval Research under Grant No. N00014-95-1-0093. The facility support from the W. M. Keck Foundation is also acknowledged. Contribution No. 437 of the IGPP, University of California, Santa Cruz.

Aki, K., and Richards, P. G. (**1980**). *Quantitative Seismology: Theory and Methods*, Vol. 1 (W. H. Freeman, New York), pp. 9–36.

Beydoun, W. B., and Mendes, M. (**1989**). ''Elastic ray-Born l_2-migration/inversion,'' Geophys. J. Int. **97**, 151–160.

Červený, V. (**1981**). ''Seismic wave fields in structurally complicated media (Ray and Gaussian beam approaches),'' Lecture Notes, Rijksuniversiteit Utrecht, Vening-Meinesz Laboratory, Utrecht.

Červený, V., and Klimeš, L. (**1984**). ''Synthetic body wave seismograms for three-dimensional laterally varying media,'' Geophys. J. Int. **79**, 119–133.

Chapman, C. H. (**1985**). ''Ray theory and its extensions: WKBJ and Maslov seismograms,'' J. Geophys. **58**, 27–43.

Coates, R. T., and Chapman, C. H. (**1990**). ''Ray perturbation theory and the Born approximation,'' Geophys. J. Int. **100**, 379–392.

Coates, R. T., and Chapman, C. H. (**1991**). ''Generalized Born scattering of elastic waves in 3-D media,'' Geophys. J. Int. **107**, 231–263.

Fisk, M. D., and McCartor, G. D. (**1991**). ''The phase screen method for vector elastic waves,'' J. Geophys. Res. **96**, 5985–6010.

Flatté, S. M., and Tappert, F. D. (**1975**). ''Calculation of the effect of internal waves on oceanic sound transmission,'' J. Acoust. Soc. Am. **58**, 1151–1159.

French, W. S. (**1974**). ''Two-dimensional and three-dimensional migration of model-experiment reflection profiles,'' Geophysics **39**, 265–277.

Gubernatis, J. E., Domany, E., Krumhansl, J. A., and Huberman, M. (**1977**). ''The Born approximation in the theory of the scattering of elastic waves by flaws,'' J. Appl. Phys. **48**, 2812–2819.

Huang, L. J., Fehler, M. C., and Wu, R. S. (**1999**). ''Extended local Born Fourier migration method,'' Geophysics **64**, 1524–1534.

Ristow, D., and Ruhl, T. (**1994**). ''Fourier finite-difference migration,'' Geophysics **59**, 1882–1893.

Stoffa, P. L., Fokkema, J. T., Freire, R. M. D., and Kessinger, W. P. (**1990**). ''Split-step Fourier migration,'' Geophysics **55**, 410–421.

Tappert, F. D. (**1977**). ''The parabolic equation method,'' in *Wave Propagation and Underwater Acoustics*, edited by Keller and Papadakis (Springer, New York), pp. 224–287.

Thomson, D. J., and Chapman, N. R. (**1983**). ''A wide-angle split-step algorithm for the parabolic equation,'' J. Acoust. Soc. Am. **74**, 1848–1854.

Wild, J., and Hudson, J. A. (**1998**). ''A geometrical approach to the elastic complex screen,'' J. Geophys. Res. **103**, 707–726.

Wu, R. S. (**1994**). ''Wide-angle elastic wave one-way propagation in heterogeneous media and an elastic wave complex-screen method,'' J. Geophys. Res. **99**, 751–766.

Wu, R. S. (**1996**). ''Synthetic seismograms in heterogeneous media by one-return approximation,'' Pure Appl. Geophys. **148**, 155–173.

Wu, R. S., and Aki, K. (**1985**). ''Scattering characteristics of waves by an elastic heterogeneity,'' Geophysics **50**, 582–595.

Wu, R. S., and Huang, L. J. (**1995**). ''Reflected wave modeling in heterogeneous acoustic media using the De Wolf approximation,'' in *Mathematical Methods in Geophysical Imaging III*, SPIE Proceedings Series **2571**, 176–193.

Wu, R. S., and Xie, X. B. (**1994**). ''Multi-screen backpropagator for fast 3D elastic prestack migration,'' in *Mathematical Methods in Geophysical Imaging II*, SPIE Proceedings Series **2301**, 181–193.

Wu, X., and Wu, R. S. (**1998**). ''An improvement to complex screen method for modeling elastic wave reflections,'' Expanded abstracts, SEG 68th Annual Meeting, pp. 1941–1944.

Xie, X. B., and Lay, T. (**1994**). ''The excitation of Lg waves by explosions: A finite-difference investigation,'' Bull. Seismol. Soc. Am. **84**, 324–342.

Xie, X. B., and Wu, R. S. (**1996**). ''3D elastic wave modeling using the complex screen method,'' Expanded abstracts, SEG 66th Annual Meeting, pp. 1247–1250.

Xie, X. B., and Wu, R. S. (**1998**). ''Improve the wide angle accuracy of screen method under large contrast,'' Expanded abstracts, SEG 68th Annual Meeting, pp. 1811–1814.

Xie, X. B., and Yao, Z. X. (**1988**). ''*P-SV* wave responses for a point source in two-dimensional heterogeneous media, finite-difference method,'' Chinese J. Geophys. **31**, 473–493.

Mode counts in an aluminum foam

Oleg I. Lobkis and Richard L. Weaver[a)]
Theoretical and Applied Mechanics, University of Illinois, 104 South Wright Street, Urbana, Illinois 61801

(Received 6 November 2000; revised 22 March 2001; accepted 26 March 2001)

Measurements of the ultrasonic modal density of a disordered elastic frame, a 20 pore-per-inch open-celled aluminum foam, are reported. While the material is dissipative, with a Q only around 700, sufficiently careful signal processing has allowed reliable counts of the modes up through a few hundred, corresponding to wavelengths comparable to the strut lengths. The modal density is found to be essentially constant over this range, and to bear no resemblance to theoretical estimates based on long-wavelength effective moduli. © *2001 Acoustical Society of America.*
[DOI: 10.1121/1.1372914]

PACS numbers: 43.20.Ks, 43.35.Yb [ANN]

I. INTRODUCTION

The work reported here concerns the use of ultrasonics in the 10–150 kHz range in a 20 pore-per-inch open-celled aluminum foam. The material is termed Duocel and is manufactured by ERG Aerospace in Oakland, California (web site: http://www.ergaerospace.com). It is available in a range of pore sizes (between 5 and 40 ppi) and porosities (50%–97%). A sample is shown in Fig. 1. The structure is nominally isotropic and consists of short struts of lengths of the order of 1 mm and widths of the order of one quarter the lengths, joined at three-strut junctions. Theoretical and experimental analyses of their static elastic and plastic properties do exist. See, for example, the paper on mechanics of cellular solids by Ashby.[1]

The history of ultrasonics in such materials is limited. While there has been some interest in biot-wave acoustics of immersed metal foams and in fluid-borne acoustic emission from immersed foams under destructive testing,[2] and in acoustic losses due to the many fluid/solid interfaces, the work reported here is like that in Ref. 3, and is concerned with the acoustics borne entirely by the solid structure. Because the wavelengths are comparable to or longer than the strut lengths, this material might best be conceptualized as a disordered structural frame.

Ultrasonic characterization of materials with strong heterogeneity like these foams cannot be carried out using conventional techniques; no coherent signal can be unambiguously propagated across the samples. Ultrasonic testing must proceed in nonconventional ways. Possibilities include measurements of diffusivity and absorption, as described elsewhere.[3] Another possibility is measurement of modal density.

This work consists of two parts. First, a measurement of effective long-wavelength properties is undertaken by means of low-frequency vibrations. An effective Young's modulus is found that is not dissimilar to that predicted by Ashby.[1] Then, a higher-frequency ultrasonic pulse–echo technique, a kind of transient resonant ultrasonic spectroscopy,[4] is conducted, and the spectral peaks of the resulting transients observed and counted. Finally, we compare the counts with various theoretical considerations.

II. EFFECTIVE BULK PROPERTIES

Our sample is described by the manufacturer as having 20 pores-per-inch, i.e., strut lengths of about 1.2 mm, and to be composed of ordinary aluminum alloy. Strut diameters varied considerably, between 0.25 and 0.75 mm within a single specimen. We have measured the mass density of bar ($1.25\,\text{cm}\times 1.25\,\text{cm}\times 20.0\,\text{cm}$) and plate ($0.62\times 30.0\times 30.0$ cm) samples and compared them to the known densities of bulk aluminum and determined both samples to be $p=7.1\%$ aluminum by volume. Standard estimates that such materials have elastic moduli less than that of the parent bulk material by a factor of the square of p (Ref. 1) lead to a conclusion that the effective (long-wavelength) elastic wave speeds should be less than those of aluminum by a factor of $\sqrt{p}=0.27$.

We have measured the fundamental clamped-free frequencies of bending vibrations of these bar and plate samples by Fourier analyzing the air-borne acoustic signal generated by such vibrations. Varying the length and the orientation of the sample, allows consistency to be ascertained, and an effective Young's modulus found. The actual quantity measured is the ''bar-wave speed,'' equal to the square root of the ratio of the Young's modulus to mass density. A value of $0.698\pm 0.023\,\text{mm}/\mu\text{s}$ was found. The value is rather less than that expected $[pE_{\text{aluminum}}/\rho_{\text{aluminum}}]^{1/2}=1.37\,\text{mm}/\mu\text{s}$, but the difference may be ascribed to oversimplifications in the theory. For example, examination of the material clearly shows the struts to be thinner in their centers than at their ends, thus diminishing the effective stiffness. It also shows the joints to have excess material, material that contributes inertia to the effective properties, but little stiffness. The material manufacturer has provided data on static moduli for samples, of volume fractions 4.9% and 8.7% with 10 pore-per-inch pore density, data that correspond to bar-wave speeds of approximately 0.67 and 0.58 mm/μs. These numbers are similar to our measurements. The discrepancy with the idealized theory[1] is, therefore, not serious.

a)Electronic mail: r-weaver@uiuc.edu

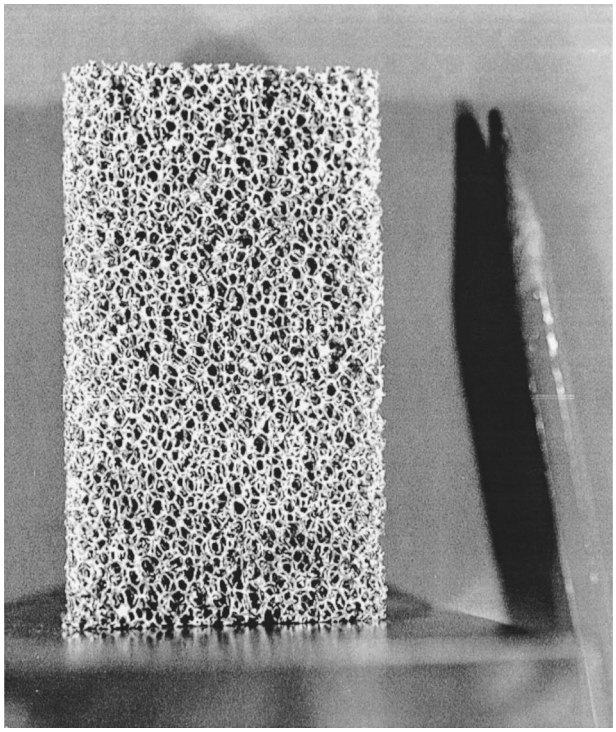

FIG. 1. The material investigated is a 20 pore-per-inch open-celled aluminum foam, of 92.9% porosity.

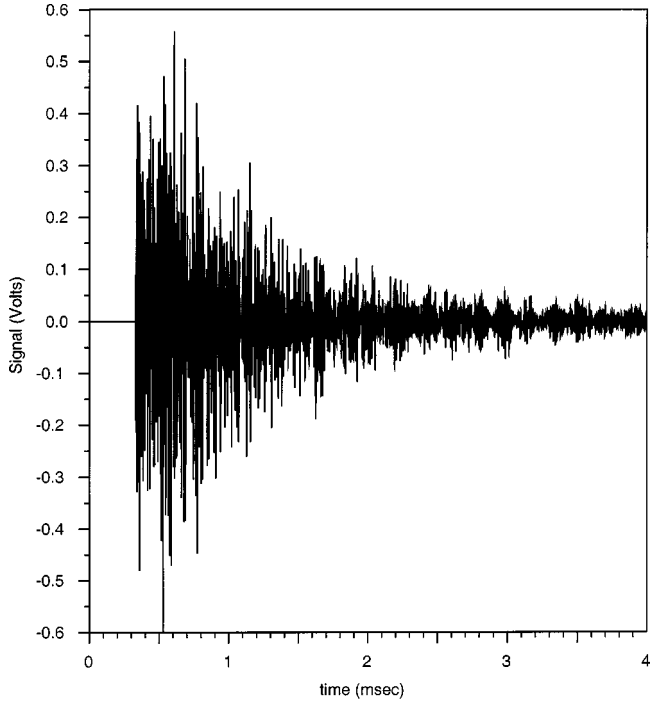

FIG. 2. The first few milliseconds of a typical waveform after repetition averaging.

III. MODE COUNT

To obtain ultrasonic properties, two small, $6.35\times6.35\times12.7$ and $6.35\times12.7\times12.7$ mm, samples were excited by transient pulses from a piezoelectric ultrasonic *pin* transducer (diameter ~1.2 mm) applied without liquid couplant to judiciously chosen joints or struts. The pulses were provided by a standard ultrasonic pulser/receiver and consisted of a single negative-going spike of a few hundred volts, and a duration a few tens of ns. The *pin* transducers used have complicated spectra. They have weak sensitivity at low frequency and spectra which vary erratically over their nominal range to 1 MHz, but the variations are smooth on the fine scale of modal spacings and modal widths (1 kHz) and they do not complicate analysis of spectral peaks. While some tests were done with a receiver distinct from the source, good acoustic contacts were difficult to secure on such small samples, and it was usually found simpler to attempt only one at a time; therefore, most tests were done with a single transducer in pulse/echo mode. The circuit is described in Ref. 5. The circuit employs a magnetic reed relay to completely isolate the receiver circuitry from the source circuitry, but due to its slow switching, it does not allow the first 0.4 ms of the waveform to be recorded. That early part of the signal is, however, not needed in the present application. The resulting transient ultrasonic signals were low-pass filtered at 240 kHz and digitized at 2.5 MSa/s. They were repetition-averaged (repetition rate 3 Hz) about 200 times to improve the signal-to-noise ratios (by 23 dB).[6] The resulting signals then had useful durations of many milliseconds. A representative waveform is shown in Fig. 2.

The manufacturer's data on static responses at large strains suggest that this material has substantial nonlinearity, though it is difficult to quantify reliably. In any case, and as is common in diffuse field ultrasonics, we test for nonlinearity by repeating our measurements with lower source pulse energy. While this does degrade the signal-to-noise ratios, any consequent variation of other spectral details would indicate nonlinearity. We have yet to see any such sign of nonlinearity. Strain amplitudes, estimated as below 10^{-6}, are unlikely to generate nonlinearities in aluminum alloys.

The specimens were supported in a variety of ways. The simplest was merely to place them on a large wooden block, with size and dissipation sufficient to assure that any acoustic energy that leaked from the sample into the block would not revisit the sample, thus guaranteeing that that support contributes only dissipation without affecting the number of modes. The near-rigid constraint that the wood supplies to the few asperities in contact with the wood will, at most, tend to slightly increase the frequencies of the modes by a small amount. The transducer itself plays a similar role, providing a nearly rigid constraint to the sample; furthermore, any acoustic energy that does enter the transducer is absorbed in a few microseconds within the transducer, long before it can reenter the sample. The samples were also supported by a web of threads, or by suspending the sample between two transducers and relying on friction for stability. Variation of the supports did not lead to variations in the recovered modal density, but did lead to variations in the dissipation rate, variations in the widths of the spectral peaks, and consequent variations in the difficulty with which the often overlapping peaks could be resolved. The least dissipation was obtained by gluing (cyano-acrylate) the transducer to the sample, omitting all other supports, and conducting the test in a vacuum. In all cases, the dissipation was approximately pro-

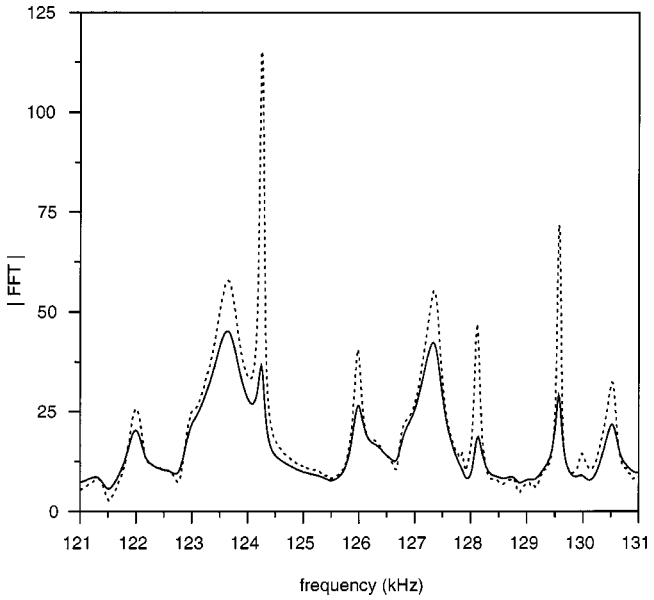

FIG. 3. A short section of the FFT of the signal. The dashed line shows the same signal after a compensation effected by multiplying the time-domain waveform by $\exp(+0.61t/\text{ms})$.

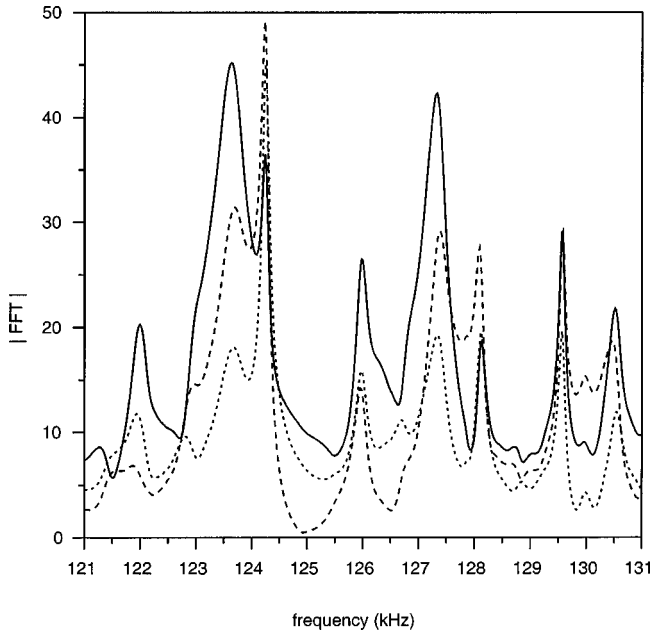

FIG. 4. The spectra for three different amounts of temporal truncation. The solid curve is identical to the solid curve of Fig. 3, with the 0.4 ms truncation imposed by the reed-relay circuit. The dashed and dotted curves are the spectra after additional artificial truncations of 0.8 and 1.2 ms.

portional to frequency, with a mean Q between 500 and 1000, and substantial fluctuation from mode to mode.

Regardless of the support scheme, dissipation was, in all cases, sufficiently strong to cause significant overlap among resonances, and indicate a need for some nonstandard signal processing in order to unambiguously locate the peaks. The solid line of Fig. 3 shows a short section of the spectrum [absolute value of the fast Fourier transform (FFT)] of the smaller sample. A few of the expected Lorentzian-shaped peaks are quite apparent; in addition, there are several features that are less easily identified as resonances, perhaps being the result of the overlap of two or more wide Lorentzians. In order to resolve these peaks, the spectra were ''compensated'' by attempting to remove the dissipation. We multiplied time-domain waveforms (waveforms obtained by inverse Fourier transforming short bands of the spectrum of the original signal) by a compensation factor $\exp(\gamma t)$, where γ was chosen to be slightly less than the width of the narrowest peak in the frequency band of interest. Upon re-Fourier transforming, the effect is to narrow all peaks by an amount γ. This was repeated for every frequency band of interest. If all modes in a narrow band of interest have equal widths, and if noise levels are low enough, this can, in principle, resolve otherwise strongly overlapping peaks. The dashed curve of Fig. 3 shows the effect of such a compensation. It is clear that many of the peaks that were barely discernable originally are now resolved.

In another scheme to resolve peaks in the spectrum, the early parts of the original waveform were deleted before Fourier analysis. This, in principle, removes the more highly damped modes. The peaks associated with weak modes of long duration, but less total energy, are thereby enhanced relative to those of strongly excited and strongly damped other modes. The effect of such a process is illustrated in Fig. 4. The three curves of Fig. 4 are the spectra of a transient waveform for three different amounts of temporal truncation. The solid curve is identical to the solid curve of Fig. 3, with the 0.4 ms truncation imposed by the reed-relay circuit. The dashed and dotted curves are the spectra after additional artificial truncations of 0.8 and 1.2 ms. There are peaks apparent in the dashed and dotted curves that are missing, or sometimes merely less obvious, in the original.

These two methods for aiding in the discernment of resonance peaks in signals obtained from individual positions of source and receiver are not sufficient for finding all modes. Such compensations allow only the resolution of the peaks of the spectrum of the signal obtained from an individual position of source and receiver. A mode that has a node at the position of the transducer(s) will not contribute a peak to that spectrum. In order to avoid missing such modes, the sample was restudied with new positions for the transducer. The spectra for two distinct positions, as compensated by $2\gamma = 0.61/\text{ms}$, are shown in Fig. 5. Comparison with Figs. 3 and 4 shows that many modes are unchanged, but many modes have very different amplitudes, and that many modes have slightly different resonant frequencies. The former effect is largely due to the mode being sampled at a different point. The latter effect is not unexpected; the near-rigid constraint provided by the transducer and/or support has been moved. A random variation in the frequency is the consequence, by an amount that depends on the details of the mode shape. The shifts in resonant frequency were generally small enough that peaks from each position of the transducers could be unambiguously paired. Comparison also indicates a few peaks that are not present in the spectra of both positions; quite commonly, a peak is found in the spectrum from one position that cannot be found in another. Such a peak is, nevertheless, counted as a natural frequency of the structure, even if it appears at only a few transducer positions.

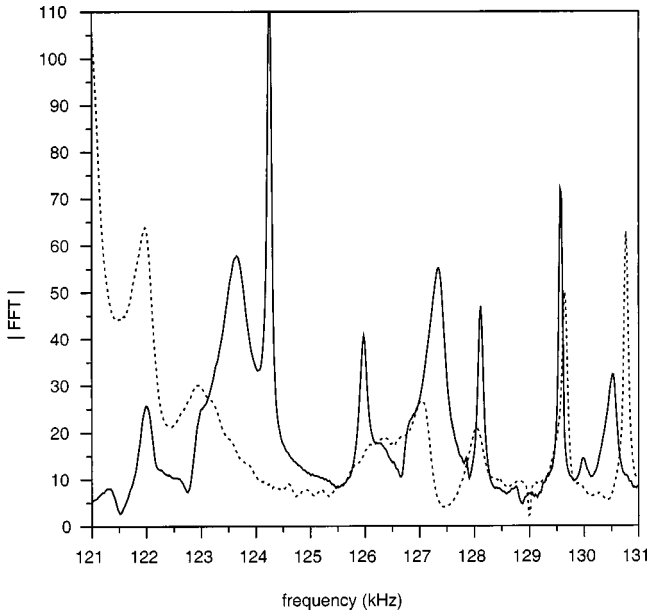

FIG. 5. The compensated spectra from two different positions of transducer. Note that each spectrum has peaks that are present in the other, and peaks which are weak or barely discernable in the other.

Figures 6(a) and (b) show the mode count as determined by these processes. The several, lower valued, curves correspond to counts conducted from individual transducer positions and support schemes. The upper curve represents the composite mode count, including all peaks found. There is a potential for some inaccuracy here, as it was occasionally unclear as to whether a peak has moved, or merely strengthened, when it shows up at one transducer position but not another. In almost all cases, however, the count is unambiguous.

For each sample, there were six distinct waveforms processed, one from each of six different transducer positions and support structures. Each waveform revealed about half of all the peaks ultimately ascribed to the sample. A composite mode count based on two distinct waveforms found about 75% of all the modes, one based on any three waveforms found close to 90% of them. These numbers, and the apparent exponential convergence, are consistent with the expectation that each waveform independently and randomly samples the system's modes. Correspondingly, there is good reason to think that the process of studying six waveforms has converged and the final composite mode count is very close to the actual mode count. In any case, the individual mode counts from individual positions of transducer and supports provide a rigorous and safe lower bound (at about 2 modes/kHz/cm^3) on the specimen mode counts, a lower bound which is itself greatly different from expectations.

The count fails at around 150 kHz in the small sample, and at about 100 kHz in the larger sample, in each case failing when the modal overlap reaches about 3.0 and the peaks can no longer be distinguished, even by means of the compensations discussed above. That the mode count in the larger (double-volume) sample is approximately twice that of the smaller sample is also a sign of consistency. In both cases, the mode count is about 3.9 modes per kHz per cm^3.

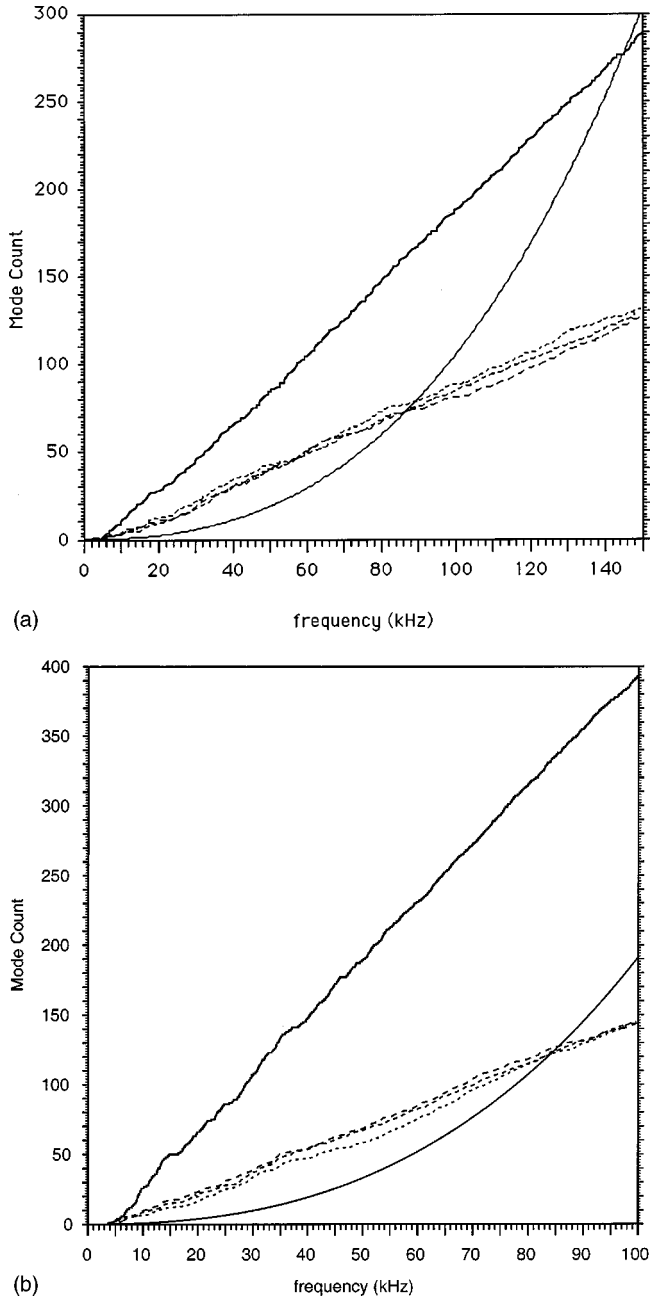

FIG. 6. (a) The mode count for the smaller of the two samples. The three dashed lines represent the mode count for three (of the total of eight, six of which were used to construct the composite mode count) distinct positions of the transducer. The dark solid line is the composite mode count and includes modes that were not apparent at individual transducer positions. The lighter solid curve is the theoretical mode count, based on the effective homogeneous continuum moduli. (b) The mode count for the larger of the two samples.

IV. DISCUSSION

One of the most striking features in these counts is that the modal density, the slope of the count, is independent of frequency. This is in contrast to the modal density of conventional three-dimensional bulk materials in which the modal density is quadratic in frequency. The elastic wave Weyl formula for the mode count in an isotropic material is

$$N(f)=(4\pi/3)f^3V[2/c_e^3+1/c_d^3]+\sigma f^2 S/c_e^2+O(fL/c_e), \quad (1)$$

where V is the sample volume, S is its surface area, L is the length of the sample edge, c_e and c_d are the (effective) equivoluminal and dilatational wave speeds, and σ is a dimensionless modulus ratio, depending on Poisson ratio, that takes a value of $19\pi/24$ at $\nu=0.333$. Such formulas have been widely discussed.[7,8]

One expects such a formula to apply in the present circumstances in the event that the wavelengths are long compared to the microstructure, where the material should be able to be modeled as an effective homogeneous isotropic elastic continuum. One therefore substitutes, for the respective two samples, $V=512$ and 1024 mm^3, $S=403$ and 645 mm^2, and $L=102$ and 127 mm. After taking the previously measured $c_{\mathrm{Bar}}=0.698\,\mathrm{mm}/\mu\mathrm{s}$, and guessing at a Poisson ratio of 0.33, one obtains $c_d=0.855$ and $c_e=0.427$. Except for the outright guess about the Poisson ratio, this should be a sound model at sufficiently long wavelengths where the structure can be considered an effective homogeneous continuum.

Figures 6(a) and (b) also show these predictions, Eq. (1), for the mode count of conventional bulk materials with those properties: $0.000\,117\,1f^3+0.007\,41f^2+O(0.3f)$, and $0.000\,058\,9f^3+0.004\,63f^2+O(0.24f)$, where f is in kHz. The predictions are in striking disagreement with the observations. While the total count of modes up to 100 kHz is within a factor of 2 of agreeing, the theoretical count at lower frequencies [where it was argued that Eq. (1) should be most reliable since effective property shear wavelengths at 40 kHz are about 10 mm, and thus greater than the microscale] is utterly incorrect. Up to 40 kHz, for example, theory predicts a total of $19+O(12)$ modes in the larger sample, yet about 150 were observed. A better informed estimate for the foam's Poisson ratio does not improve the correspondence. Indications from the manufacturer's data suggest that the foam's Poisson ratio is actually somewhere in the range $\{-0.5, -1.0\}$. The corresponding correction to the above formulas increases the estimate for c_e, and decreases the predicted modal density.

The linearity in the observed mode count, $N\propto f$, leads one to speculate that a better model, at least for modal density, might be that of a long wire. If the sample, largely composed as it is of struts, were conceptualized as a long circular rod of constant small radius and length l, then the mode count would be approximately linear. In the limit that the rod diameter is small compared to a wavelength of structural waves, wave propagation is well described by torsional waves (with speed in aluminum of $c_{\mathrm{equivoluminal}}=3\,\mathrm{mm}/\mu\mathrm{s}$, by extensional waves with speed $c_{\mathrm{Bar}}=5.15$, and by two dispersive bending waves. By writing N as a sum of the contributions from each wave (each kl/π, where k is the corresponding wave number), we obtain

$$\frac{1}{V}\frac{\partial N}{\partial f}=\frac{1}{V}\frac{\partial}{\partial f}\left[\frac{2f}{c_e}l+\frac{2f}{c_{\mathrm{Bar}}}l+4l\sqrt{\frac{f}{\pi c_{\mathrm{Bar}}\,a}}\right]. \tag{2}$$

This model does not precisely match observations, as it predicts a modal density that slowly decreases with frequency, whereas we observed a constant modal density. But, it does give numbers that are in closer accord to those observed. If we choose $a=0.25$ mm, comparable to the average strut radius, and choose a length consistent with the known total mass: $l=Vp/\pi a^2$, then the above quantity becomes identical for each sample, and equal to

$$\frac{2p}{\pi a^2}\left[\frac{1}{c_e}+\frac{1}{c_{\mathrm{Bar}}}+\frac{1}{\sqrt{\pi f c_{\mathrm{Bar}}\,a}}\right]. \tag{3}$$

This is $0.374+1.47/\sqrt{f_{100}}$ modes per kHz per cm^3, where f_{100} is the frequency in units of 100 kHz. This number is dominated by the third term (the bending wave contribution) and is 1.84 at 100 kHz, and 2.70 at 40 kHz. The frequency dependence in Eq. (3) is different from that which is observed, but the magnitude is comparable to the observation of 3.9. A slightly smaller choice for mean strut radius a would bring these numbers closer to the observation. It would not, however, ameliorate the discrepancy in frequency dependence. The model, therefore, has little to recommend it, aside from its being substantially better than that provided by Eq. (1). One-dimensional (1D) structural waves have wavelengths, at frequencies of 10–20 kHz, which are $[\pi c_{\mathrm{Bar\ aluminum}}a/f]^{1/2}\approx 14-10$ mm, or $c_e/f=200$ mm, or $c_d/f=400$ mm, considerably longer than the strut lengths. That 1D waves of such long wavelengths would be relevant for wires with so much cross linking seems unlikely, but we are at a loss for any other model.

We conclude that the modes of this foam are not those of an effective homogeneous elastic continuum, even at frequencies of 10–20 kHz where the effective medium wavelengths are 40–20 mm or more, and much greater than the microscale. An attempt at a description in terms of bending waves in the microscale struts is slightly better, but still fails to fully account for the observations.

We close with one final observation. The summary mode count curves of Figs. 6(a) and (b) show fluctuations, especially strong in the larger sample. The short band gap between 14.7 and 16.4 kHz there is particularly striking. Similar gaps occur at other frequencies. These fluctuations are in excess of those predicted by Random matrix theory (RMT).[7,8] RMT predicts a degree of level repulsion and spectral rigidity in the spectra of generic systems, a regularity that has been well corroborated in experiments. While the observed spectra do show some sign of level repulsion, with very few successive eigenfrequencies closer than one third the mean spacing, these spectra do not have the longer-range spectral rigidity of the RMT. The RMT probability of finding a gap of width at least $m=7$ average mode spacings somewhere in a sequence of 400 modes is only $400\exp(-m^2)=2\times10^{-19}$. And, yet, the mode counts of Figs. 6(a) and (b) show several gaps of that or similar size. Accordingly, we take the observed fluctuations as evidence that the microstructure has sufficient periodicity, or at least a dominant characteristic length scale, which manifests in the mode count. That there is such a characteristic length scale is apparent in Fig. 1. Whether or not that apparent periodicity is responsible for the band gaps remains to be determined.

V. CONCLUSION

Ultrasonic characterization of materials with this kind of strong heterogeneity must proceed in nonconventional ways.

Here, we have reported a measurement of the material's modal density. The modal density has been found to be much larger than anticipated. Furthermore, it is essentially independent of frequency in this range, a result that is also unanticipated.

ACKNOWLEDGMENTS

This work has been supported by the National Science Foundation through Grant Nos. 9701142 and 9988645. The samples were provided by ERG Materials and Aerospace Corporation.

[1] M. F. Ashby, ''The mechanical properties of cellular solids,'' Metall. Trans. A **14**, 1755–1769 (1983).

[2] Q. Ji, L. H. Le, L. J. Filipow, and S. A. Jackson, ''Ultrasonic wave propagation in water-saturated aluminum foams,'' Ultrasonics **36**, 759–765 (1998); L. C. Krysac and J. D. Maynard, ''Detailed observation of the complete fracture process of brittle carbon foams,'' J. Acoust. Soc. Am. **98**, 2875 (1995).

[3] R. L. Weaver, ''Ultrasonics in an aluminum foam,'' Ultrasonics **36**, 435–442 (1998).

[4] A. Migliori and J. L. Sarrao, *Resonant Ultrasound Spectroscopy* (Wiley, New York, 1997).

[5] R. L. Weaver and O. I. Lobkis, ''Enhanced backscattering and modal echo of reverberant elastic waves,'' Phys. Rev. Lett. **84**, 4942–4945 (2000).

[6] Repetition averaging is a standard well-understood method in ultrasonics, in general, and diffuse field ultrasonics, in particular (see, e.g., Refs. 3 and 5). It may be used whenever the source is reproducible and the stability of the waveform can be relied on. Temperature drifts, sample and transducer movements, or couplant flow and evaporation can affect the waveform and degrade the quality of the repetition averaging. But, such effects are readily detected by the presence of changes in the waveform that may take place over periods of the order of minutes.

[7] A good discussion of the Weyl series for scalar waves may be found in the book by M. C. Gutzwiller, *Chaos in Classical and Quantum Systems* (Springer, Berlin, 1990), p. 258. The form for elastic waves in isotropic media is discussed by R. Weaver, ''Spectral statistics in elastodynamics,'' J. Acoust. Soc. Am. **85**, 1005–1013 (1989).

[8] M. L. Mehta, *Random Matrices* (Academic, Boston, MA, 1990); T. A. Brody, J. Flores, J. B. French, P. A. Mello, A. Pandey, and S. S. M. Wong, ''Random matrix physics: Spectrum and strength fluctuations,'' Rev. Mod. Phys. **53**, 385–478 (1981); C. Ellegaard, T. Guhr, K. Lindemann, J. Nygård, and M. Oxborrow, ''Symmetry breaking and spectral statistics of acoustic resonances in quartz blocks,'' Phys. Rev. Lett. **77**, 4918–4921 (1996).

Acoustic nonlinearity of cracks partially filled with liquid: Cubic approximation

V. E. Nazarov[a)]
Institute of Applied Physics, 46 Uljanov Street, Nizhny Novgorod 603600, Russia

(Received 5 January 1999; revised 15 February 2001; accepted 1 March 2001)

The theoretical investigation of mechanisms of the acoustic nonlinearity (elastic and inelastic) of cracks partially filled with an ideal and viscous liquid and associated with the nonlinear dependence of the capillary and viscous pressure in the liquid on the distance between the crack surfaces and the velocity of the change of this distance is proposed. The nonlinear (in cubic approximation) equations of the state of these cracks is obtained, and its parameters are defined. It is shown that the presence of the viscous liquid may lead to the considerable increase of the acoustic nonlinearity of such cracks in comparison with cracks filled with the ideal liquid. © *2001 Acoustical Society of America.* [DOI: 10.1121/1.1369096]

PACS numbers: 43.25.−x [MAB]

LIST OF SYMBOLS

R	the radius of a crack
R_0	the radius of a circle limiting a liquid on the surface of the crack
σ_{nn}	the normal stress to the surfaces of the crack
σ_0	the original the positive normal stress
$U_z(r)$	the normal displacements of crack surfaces
r	the radial coordinate in the crack plane
V_0	the elliptic crack volume
E and ν_0	Young modulus and Poission ratio of a solid,
ΔV_0	the change of elliptic crack volume
D	the distance between surfaces of the plane-parallel cavity
ΔV_1	the change of the volume of the plane-parallel cavity
$2d$	the effective change of the distance between the surfaces of the plane-parallel cavity
K	$=3\pi E/8(1-\nu_0^2)R$ is the effective coefficient of the cavity elasticity
σ_0	$=\pi KD/2$ is the effective tensile stress
ω	frequency
Ω_c	the resonance frequency of monopole oscillations of the elliptical cavity
Ω_s	the resonance frequency of monopole oscillations plane-parallel of the cavity
C_t	velocity of the shear wave in a solid
b	the volume of the liquid
α	the coefficient of the liquid surface tension
ϑ	the contact angle
H	$=D+2d_0$ is the equilibrium distance between the surfaces of the cavity when it is filled with liquid
$2d_0$	the equilibrium change of the distance between the cavity surface
$\tilde{H}$	$=H+2d$ is the intersurfaces distance of the cavity
μ_0	$=b/\pi R^2 H=(R_0/R)^2$ is the original surface of the liquid concentration in the cavity
a	$=[2\alpha/\rho g]^{1/2}$ is the capillary constant
ρ	the density of the liquid
g	the acceleration of gravity
K_0, g, and q	coefficients of linear and nonlinear (quadratic and cubic) elasticity of the crack, partially filled with liquid
$P(r,d,\dot{d})$	the pressure of the viscous liquid
$P_1(d)$ and $P_2(r,\dot{d})$	the capillary and the viscous pressure in the viscous liquid
$\dot{d}$	the velocity of the cavity surface
V_z and V_r	z and r components of the liquid velocity
Re	$=\dot{d}H/\nu$ is the Reynolds number
ν	the kinematic viscosity of the liquid
ω	the frequency of acoustic perturbations
ω^*	$=\nu/H^2$
η	$=\nu\rho$ the dynamic liquid viscosity
$\xi(z,r\simeq R_0,d)$	the perturbation of the meniscus of the viscous liquid
$S(\tilde{H})$	the square of the meniscus of the viscous liquid
β	the coefficient of linear dissipative
γ and δ	coefficients of nonlinear dissipative

a)Electronic mail: nazarov@hydro.appl.sci-nnov.ru

I. INTRODUCTION

One of the urgent problems in nonlinear acoustics is searching for media with strong nonlinearity, defining the media nonlinearity mechanisms, creating physical models, and constructing equations of state for these media. The strong acoustic nonlinearity of such media is caused by their inherent micro-structure associated with different micro-inclusions (or defects), for instance, gas bubbles in a liquid, grains, dislocations, cracks and cavities in a solid, etc. In acoustics such media are usually called micro-inhomogeneous.[1–5] Investigation of nonlinear interactions of acoustic waves in micro-inhomogeneous media is of interest because of the prospects to realize nonlinear methods of diagnostics and nondestructive testing. To a considerable extent this is caused by the fact that nonlinear properties of media are more sensitive to the presence of defects than linear ones.

By now, the nonlinear elasticity models and mechanisms of the polycrystals,[6,7] the liquids containing gas bubbles,[8] porous waterlike materials,[9,10] granular,[11,12] and solids, containing ''dry'' and partially filled with liquid cracks[13–15] have been elaborated in detail. In the series of works, on the basis of experimental results and the phenomenological approach, the non-analytical equations of state were obtained for the solids (metals and rocks), which have elastic power nonlinearity with a fractional exponent,[16–19] and dissipative (inelastic)[19–22] and hysteretic[2,18,23,24] nonlinearities. In Ref. 3 the generalized rheological model of the micro-inhomogeneous media was proposed in the frames of which the common criterion of increase of the elastic nonlinearity was obtained. It was shown in this work that the cause of strong nonlinearity of such media is the presence of a small quantity of relatively soft nonlinear inclusions in the media.

In the present article, the theoretical investigation of the acoustic (elastic and inelastic) nonlinearity of cracks partially filled with liquid, caused by the capillary and the viscous pressure in a liquid, is carried out.[15–17] (The defects of this type are characteristic of rock massives in their natural bedding. These defects especially manifest themselves due to the increase of the tectonic stresses.[25–27]) Here the behavior of one such crack under the action of variable (oscillatory) stress will be described. In this article, the nonlinear (in cubic approximation) equations of state for cracks, partially filled with an ideal and viscous liquid, will be obtained.

II. THE MODEL OF THE CRACK AND BASIC ASSUMPTIONS

We shall search for the nonlinear equations of state of the crack with the liquid in the following approximations.

(1) The crack, being a narrow cavity formed in an ideal elastic solid, occupies an area limited by a circle with radius R.
(2) The crack is partially filled with ideal or viscous incompressible liquid in such a way that the liquid connects both crack surfaces inside the circle with radius $R_0 < R$ whose center coincides with the crack center. There is gas under low enough pressure in the crack volume free of the liquid, therefore we may neglect its elasticity.
(3) The ideal liquid does not possess the property of adhesion (i.e., it does not stick) to surfaces of the crack and the line of three-phase contact (gas–liquid–solid) can move (or slide) on the surface of the crack due to its small oscillations.[28] The viscous (i.e., real) liquid has the property of adhesion to the crack surfaces and the line of three-phase contact (gas–liquid–solid) is fastened to the surface of crack and cannot move (or slide) on the surface of the crack at its small oscillations.[28]
(4) The distance between the crack surfaces and its volume change under the action of normal stress σ_{nn}.

To get the equations of state [i.e., the dependence $\sigma_{nn} = \sigma_{nn}(d)$, where $2d$ is the change of the distance between the crack surfaces] for one crack partially filled with the ideal or viscous liquid, we shall consider the behavior of the narrow elliptic crack without liquid under the action of the static positive normal stress σ_0. In cylindric coordinates with the origin in the crack center, the normal displacements of its surfaces are defined by the equation[29]

$$U_z(r) = 4(1-\nu_0^2)(R^2-r^2)^{1/2}\sigma_0/nE \ll R,$$

the crack volume being equal to

$$V_0 = 16(1-\nu_0^2)R^3\sigma_0/3E, \tag{1}$$

where E and ν_0 are Young modulus and Poisson ratio of a solid without cracks, and r is the radial coordinate in the crack plane.

It is seen from expression (1) that the change of the elliptic crack volume is a linear function of the stress σ_{nn} at $\sigma_0 + \sigma_{nn} > 0$:

$$\Delta V_0 = 16(1-\nu_0^2)R^3\sigma_{nn}/3E. \tag{2}$$

To simplify the calculations we shall consider below a round narrow cavity (similar to such a crack) with radius R and plane-parallel surfaces, the distance between which equals D $(D \ll R)$. The change of the volume of such a cavity due to the stress σ_{nn} is

$$\Delta V_1 = 2\pi R^2 d(\sigma_{nn}), \tag{3}$$

where $2d(\sigma_{nn})$ is the effective change of the distance between the surfaces of the similar cavity.

From the equality of the change of the volumes of the elliptic crack and the narrow plane-parallel cavity equivalent to it defined by expressions (2) and (3), we obtain

$$\sigma_{nn} = Kd, \tag{4}$$

where $K = 3\pi E/8(1-\nu_0^2)R$ is the effective coefficient of the cavity elasticity. This relation is the equation of the state of a narrow cavity, which is equivalent to the elliptic crack and is under the action of the effective tensile stress $\sigma_0 = \pi KD/2$. It is necessary to note that Eq. (4) describes the behavior of such a cavity in quasistatic approximation only, i.e., in the frequency range $\omega \ll \Omega_c$, where Ω_c is the resonance frequency of ''monopole'' oscillations (along the z axis) of the cavity. It is very difficult to obtain the correct expression for Ω_c, however, we can take that the elliptical cavity resonance frequency Ω_c is approximately equal to the resonance frequency Ω_s of the spherical cavity of the same radius R, i.e.,

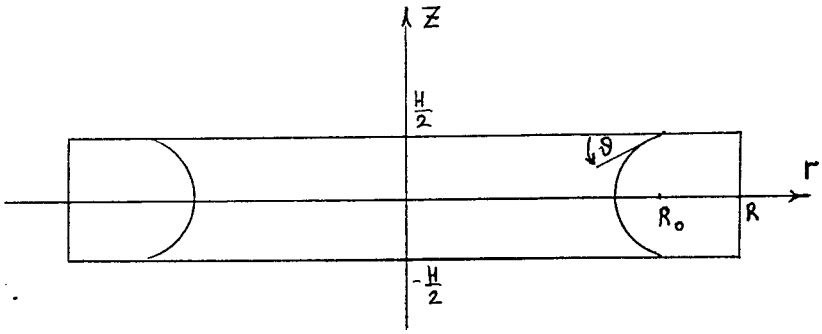

FIG. 1. The scheme of the narrow plane-parallel cavity partially filled with the liquid.

$\Omega_c \sim \Omega_s = (C_t/R)[2/(1-\nu_0)]^{1/2}$, where C_t is the velocity of the shear wave in solid.[1] In this connection, the obtained below equations of state for the cracks with ideal and viscous liquids will be correct in the frequency range $\omega \ll \Omega_s$.

III. THE EQUILIBRIUM (OR THE STATIC) STATE OF THE CRACK, PARTIALLY FILLED WITH IDEAL OR VISCOUS LIQUID

Let this cavity be filled partially with the ideal or viscous incompressible liquid of a volume b in such a way that the liquid connects both cavity surfaces inside the circle with radius $R_0 < R$ and $D \ll R_0$ (Fig. 1). Because of the surface tension the liquid pressure will differ from the pressure in the gas cavity by the value[28,30,31]

$$\Delta P = 2\alpha \cos\vartheta/H, \tag{5}$$

where α is the coefficient of the liquid surface tension, ϑ is the contact angle, $H = D + 2d_0$ is the equilibrium distance between the surfaces of the cavity when it is filled with liquid, and $2d_0$ is the equilibrium change of the distance between the cavity surfaces, caused by the liquid capillary pressure, $H \ll R_0 \cos\vartheta$.

In this case the cavity equilibrium state will be defined by the following equation (we neglect the gas pressure):

$$\pi R^2 K d_0 + 2\alpha b \cos\vartheta/(D+2d_0)^2 = 0,$$

or

$$K d_0 + 2\alpha\mu_0 \cos\vartheta/H = 0, \tag{6}$$

where $\mu_0 = b/\pi R^2 H = (R_0/R)^2$ is the equilibrium surface of the liquid concentration in the cavity.

It follows from Eqs. (6) that

$$2d_0 = -D(1-[1-16\alpha b \cos\vartheta/\pi R^2 HKD^2]^{1/2})/2,$$
$$H = D(1+[1-16\alpha\mu_0 \cos\vartheta/KD^2]^{1/2})/2, \tag{7}$$

i.e., the presence of the liquid in the cavity changes the initial distance D between its surfaces, thus for the nonwetting liquid ($\pi/2 < \vartheta \leqslant \pi$) the cavity widens, and for the wetting liquid ($\vartheta < \pi/2$) it compresses. It follows also from this expressions that the equilibrium state of the cavity takes place under the condition $H > 16\alpha b \cos\vartheta/\pi R^2 KD^2$ or $(16\alpha\mu_0 \cos\vartheta/KD^2) < 1$. However, we note that the equilibrium distance between the cavity surfaces cannot be less than the value $H^* = b/\pi R^2$ for the wetting liquid. At $H = H^*$ the cavity will be completely filled with the liquid ($\mu_0 = 1$), and the nonlinearity of the cavity will be equal to zero. In this connection we shall suppose further that $H > H^*$, $16\alpha\mu_0 \cos\vartheta/KD^2 < 1$, and $\mu_0 < 1$.

For the narrow cavity ($H \ll a$, where $a = [2\alpha/\rho g]^{1/2}$ is capillary constant, ρ is the density of the liquid, and g is the acceleration of gravity), the profile of the undisturbed (i.e., equilibrium) meniscus is a part of the circle with radius $R_m = H/2\cos\vartheta$,[28,30,31] therefore in the assumed cylindric coordinates its form is defined by the equation

$$U_r(z,H,\vartheta) = R_0 + (Htg\,\vartheta/2) - [(H/2\cos\vartheta)^2 - z^2]^{1/2}. \tag{8}$$

Generally speaking, the previously described equilibrium state of the crack with the liquid is correct both for the ideal and the viscous liquids. However, the motion of those liquids will be different at crack oscillations due to the difference of their adhesion to surfaces.

IV. THE EQUATION OF STATE FOR THE PARTIALLY IDEAL-LIQUID-FILLED CRACK

Let us consider the behavior of a crack with ideal liquid under the action of external variable stress σ_{nn}. In this case the liquid meniscus form is a part of a circle (because the contact angle does not change[28,30,31]), and the distance $\tilde{H}$ between crack surfaces will vary by a magnitude $2d$ ($\tilde{H} = H + 2d$), so that the equation

$$\dot{P}_z = \pi R^2 \sigma_{nn} - \pi R^2 K(d+d_0) + 2\pi \int_0^{\tilde{R}} P(r,d,\dot{d}) r\, dr \tag{9}$$

will be realized, where P_z is the z-component of the impulse of the liquid locating in the crack in the layer from $z=0$ to $z = \tilde{H}/2$; $P(r,d,\dot{d})$ is the liquid pressure; $\dot{d}$ is the velocity the crack surface motion, and $\tilde{R} = R_0(H/\tilde{H})^{1/2}$ is the circle radius (or of three-phase contact line) on the crack surface limiting liquid.

To determine the impulse P_z and the pressure $P(r,d,\dot{d})$ we solve the problem on the oscillation motion of the ideal liquid in the crack, the distance $\tilde{H}$ between whose surfaces changes under the action of the dynamic stress σ_{nn}. In cylindric coordinates with the origin in the center of the cavity, the liquid motion is axially symmetric and, basically radial because of the cavity narrowness; and $V_z \ll V_r$, $\partial V_r/\partial r \ll \partial V_r/\partial z$, $P = P(r,t)$, where V_z and V_r are z and r components of the liquid velocity. At small oscillations of the crack ($|2d| \ll H$) the motion of liquid is potential and is determined by the linear equations of hydrodynamics:[31]

$$\partial V_r/\partial t = -(1/\rho)\partial P/\partial r, \tag{10}$$

$$(1/r)\partial(rV_r)/\partial r + \partial V_z/\partial z = 0, \tag{11}$$

with the nonlinear boundary conditions, which admit that the liquid is sliding on the surfaces of the crack:

$$V_z(z = \pm\tilde{H}/2) = \pm\dot{d}, \tag{12}$$

$$P(r = \tilde{R}, d) = P_1(d), \tag{13}$$

where $P_1(d) = -2\alpha\cos\vartheta/\tilde{H}$ is the capillary pressure in liquid. The solution of these equations has the following form:

$$V_z(z) = 2\dot{d}z/\tilde{H}, \quad V_r(r) = -\dot{d}r/\tilde{H}, \tag{14}$$

$$P_z = \pi\rho\tilde{R}^2\int_0^{\tilde{H}/2} V_z(z)\,dz = \pi\rho R_0^2 H\dot{d}/4, \tag{15}$$

$$P(r) = -2\alpha\cos\vartheta/\tilde{H} + \rho(r^2 - \tilde{R}^2)(\ddot{d}\tilde{H} - 2\dot{d}^2)/2\tilde{H}^2. \tag{16}$$

Substituting Eqs. (14)–(16) in (9) and taking into account (6), we obtain the equation of state of the crack, partially filled with ideal liquid:

$$\sigma_{nn} = Kd - 8\alpha\mu_0\cos\vartheta d(H+d)/H(H+2d)^2 + \rho\mu_0 H\ddot{d}/4 + \rho\mu_0^2 R^2 H^2(H\ddot{d} + 2d\ddot{d} - 2\dot{d}^2)/4(H+2d)^4. \tag{17}$$

This equation is nonlinear because of nonlinear dependencies of pressure in liquid and instant surfaces concentration $\mu = \mu_0 H/\tilde{H}$ on the distance between the surfaces of the cavity $\tilde{H}$.

From Eq. (17) we can obtain the expression for the resonance frequency linear oscillation of such a crack:

$$\Omega_0 = \left(\frac{4K_0 HR^2}{\rho R_0^4}\right)^{1/2}, \tag{18}$$

where K_0 is the coefficient of linear elasticity of the crack, determined by the expression $K_0 = K - 8\alpha\mu_0\cos\vartheta/H^2 > 0$. It should be noted here that for the steady state of the cavity with an ideal liquid (with respect to a small perturbation of d) the condition $K_0 > 0$, or $18\alpha\mu_0\cos\vartheta/KD^2 < 1$, should be fulfilled. This condition is more rigid in the comparison with the inequality $16\alpha\mu\cos\vartheta/KD^2 < 1$, which was obtained earlier [after Eq. (7)].

It follows from expression (18) that for the crack with parameters $R = 1$ cm, $R_0 = 0.7$ cm, $E = 5\times10^{11}$ g/cm·s^{-2}, $v_0 = 0.25$, $\rho = 1$ g/cm^3, $\alpha = 73$ g/s^2, $\vartheta = 0$, $H = 10^{-4}$ cm we have $\Omega_0 \simeq 3\times10^4$ Hz.

In quasistatic approximation ($\omega \ll \Omega_0$) from (17) we obtain the equation with cubic nonlinearity:

$$\sigma_{nn} = K_0 d - gd^2 - qd^3, \tag{19}$$

where g and q are coefficients of nonlinear (quadratic and cubic) elasticity of the crack, partially filled with ideal liquid:

$$g = -24\alpha\mu_0\cos\vartheta/H^3, \quad q = 64\alpha\mu_0\cos\vartheta/H^4. \tag{20}$$

V. THE EQUATION OF STATE FOR THE PARTIALLY VISCOUS LIQUID-FILLED CRACK

Now let this cavity be partially filled with the viscous incompressible liquid of the same volume b. As we noted earlier, the equilibrium state of the viscous liquid in the cavity does not differ from the state of the ideal liquid; the distinction takes place only if they move. The basic difference of the behavior of the ideal and viscous liquids in the cavity is that when the flow of the ideal liquid in the narrow cavity is oscillatory, the contact angle does not change, the form of the meniscus is a part of a circle, and the surfaces concentration of liquid changes. In the case of the viscous liquid oscillatory flow, because of its adhesion to the crack surfaces, the surface concentration of the liquid will not change, and the meniscus form will not be circular.

When such a cavity is affected by the external small variable stress σ_{nn} (such that the meniscus oscillations are also small) the distance $\tilde{H}(\tilde{H} = H + 2d)$ between its surfaces changes by the value $2d \ll H$, thus the relation is fulfilled:

$$\dot{P}_z = \pi R^2\dot{\sigma}_{nn} - \pi R^2 K(\dot{d} + \dot{d}_0) + 2\pi\int_0^{R_0} P(r,d,\dot{d})r\,dr, \tag{21}$$

where $P(r,d,\dot{d}) = P_1(d) + P_2(r,\dot{d})$, $P_1(d)$ and $P_2(r,\dot{d})$ are the capillary and viscous pressures in the liquid, and $\dot{d}$ is the velocity of the cavity surface.

To define the pressure $P(r,d,\dot{d})$ we solve the problem on the oscillatory motion of the viscous liquid in the cavity, the distance $\tilde{H}$ between these surfaces changes also under the action of the variable stress σ_{nn}. (The solution of the analogous linear problem without taking into account the capillary pressure is given in Ref. 31.) In cylindric coordinates at small Reynolds number ($\mathrm{Re} = \dot{d}H/\nu \ll 1$) the liquid motion in the narrow cavity is described also by linear equations of hydrodynamics:[31]

$$\partial V_r/\partial t = -(1/\rho)\partial P/\partial r + \nu\partial^2 V_r/\partial z^2, \tag{22}$$

$$(1/r)\partial(rV_r)/\partial r + \partial V_z/\partial z = 0, \tag{23}$$

with nonlinear boundary conditions, which do not admit that the liquid slides on the surfaces of the crack:

$$V_r(z = \pm\tilde{H}/2) = 0, \tag{24}$$

$$V_z(z = \pm\tilde{H}/2) = \pm\dot{d}, \tag{25}$$

$$P(r = R_0, t) = P_1(d), \tag{26}$$

where ν is the kinematic viscosity of the liquid.

For the acoustic perturbations in the frequency range $\omega \ll \omega^* = \nu/H^2$, the flow of the liquid in the cavity will be stationary and we can neglect the term $\partial V_r/\partial t$ in Eq. (22).[31] We will neglect also the inertial term $\dot{P}_z \sim V_z$ in Eq. (21). In this case the solution of Eqs. (22)–(26) has the form

$$V_r(z,r,\dot{d}) = \frac{6r\dot{d}}{\tilde{H}^3}\cdot(z^2 - \tilde{H}^2/4), \tag{27}$$

$$V_z(z,\dot{d}) = -\frac{4\dot{d}z}{\tilde{H}^3}\cdot(z^2-3\tilde{H}^2/4), \tag{28}$$

$$P(r,d,\dot{d}) = \frac{6\eta\dot{d}}{\tilde{H}^3}\cdot(r^2-R_0^2)+P_1(d), \tag{29}$$

where $\eta=\nu\rho$ is the dynamic liquid viscosity. [In the linear approximation without taking into account the capillary pressure of the liquid, the expression (29) coincides with the analogous one which was obtained in Ref. 31.] [For the narrow cavity the frequency ω^* is high enough. For example, for the cavity with water ($\vartheta=0$, $\nu=10^{-2}\,\mathrm{cm}^2/\mathrm{s}$) at $H=10^{-4}\,\mathrm{cm}$ $\omega^*\simeq 10^6\,\mathrm{Hz}$ is obtained. The exact solution of Eq. (22) based on Fourier's transform[29] has shown that $\omega^*\simeq 10\nu/H^2$.]

As it was mentioned earlier the viscous liquid oscillatory flow in the cavity leads to the vibration of the meniscus, and its form will be defined by the equation

$$\tilde{U}_r(z,\tilde{H},\vartheta) = U_r(z,\tilde{H},\vartheta)+\xi(z,r\simeq R_0,d), \tag{30}$$

where $U_r(z,\tilde{H},\vartheta)$ is determined by Eq. (8) in which, however, the constant value H should be replaced by the variable $\tilde{H}=H+2d$, and $\xi(z,r\simeq R_0,d)$ is the perturbation of the meniscus of the liquid which is found from the equation

$$d\xi/dt = \partial\xi/\partial t+(V_r\partial\xi/\partial r+V_z\partial\xi/\partial z)=V_r(z,r\simeq R_0,\dot{d}). \tag{31}$$

By using Eqs. (8) and (30) we can find the square $S(\tilde{H})$ of the meniscus of the viscous liquid locating in the cavity, and, by the change of this square, the capillary pressure $P_1(d)$:[28,30,31]

$$S(\tilde{H}) = 4\pi\int_0^{\tilde{H}/2}\tilde{U}_r(z,\tilde{H},\vartheta) \times(1+[\partial\tilde{U}_r(z,\tilde{H},\vartheta)/\partial z]^2)^{1/2}\,dz, \tag{32}$$

$$P_1(d) = -(\alpha/\pi R_0^2)\cdot\frac{\partial S(\tilde{H})}{\partial\tilde{H}}. \tag{33}$$

It follows from these equations that for the description of the cubic elastic nonlinearity of the crack, partially filled with the viscous liquid, Eq. (31) should be solved with the accuracy to the terms proportional to d^4. However, if the conditions $R_0\gg(Htg\,\vartheta)/2$ and $R_0(\pi/2-\vartheta)\gg H/2$ are fulfilled, for the description of the elastic nonlinearity of such a crack in the expression for the perturbation of the meniscus form, it is enough to take into account the linear (on d) term, which has the form

$$\xi(z,r\simeq R_0,d) = 6R_0(d/H)((z/H)^2-\tfrac{1}{4}). \tag{34}$$

From Eqs. (8), (30), (32), and (34) we find the square $S(\tilde{H})$ of the meniscus of the viscous liquid which is in the cavity:

$$S(\tilde{H}) = 2\pi R_0 H(\pi/2-\vartheta)/\cos\vartheta+(4\pi R_0^2\cos\vartheta/H)d +(9\pi R_0^3/4H^3)F_1(\vartheta)d^2 -(216\pi R_0^4/35H^5)F_2(\vartheta)d^3 +(81\pi R_0^5/16H^7)F_3(\vartheta)d^4, \tag{35}$$

where

$$F_1(\vartheta) = ((\pi/2-\vartheta)+(\sin 2\vartheta+\sin 4\vartheta)/4 -(\tfrac{1}{12})\sin 6\vartheta)/\cos^3\vartheta,$$

$$F_2(\vartheta) = \cos\vartheta(7-10\cos^2\vartheta+\tfrac{35}{9}\cos^4\vartheta),$$

$$F_3(\vartheta) = (3(\pi/2-\vartheta)+\sin 4\vartheta-(\tfrac{1}{8})\sin 8\vartheta -(\tfrac{6}{5})\sin^5 2\vartheta)/\cos^5\vartheta.$$

The plots of functions $F=F_1(\vartheta)$ $(i=1,2,3)$ are shown in Fig. 2. Here we note that the function $F_1=F_1(\vartheta)$ is positive at all contact angles, but the functions $F_i=F_{2,3}(\vartheta)$ may have positive or negative signs according to the contact angle ϑ, and $F_2(\vartheta)=0$ at $\vartheta=\pi/2$, and $F_3(\vartheta)=0$ at $\vartheta\simeq\pi/2\pm\pi/6$.

Substituting the expression (35) in Eq. (33) we find the capillary pressure in the liquid locating in the cavity:

$$P_1(d) = -\alpha(2\cos\vartheta/H+(9R_0/4H^3)F_1(\vartheta)d -(324R_0^2/35H^5)F_2(\vartheta)d^2 +(81R_0^5/16H^7)F_3(\vartheta)d^3). \tag{36}$$

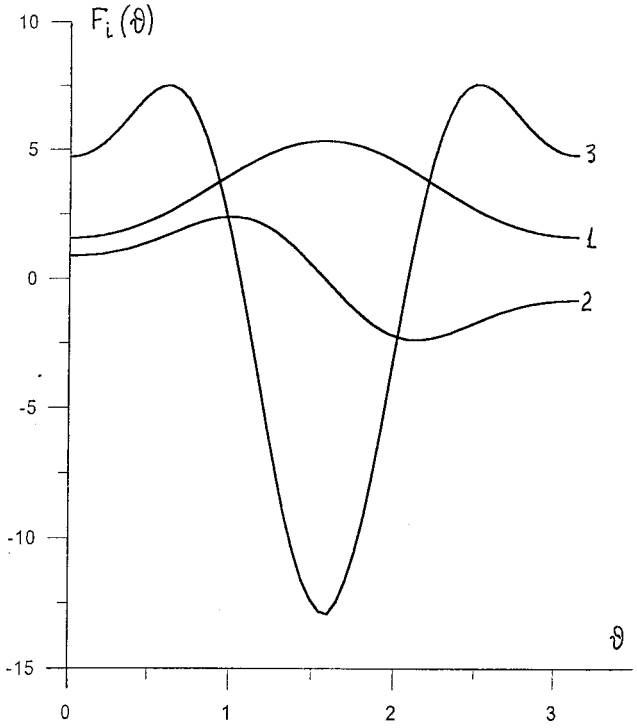

FIG. 2. The diagrams of functions $F=F_i(\vartheta)$, $i=1,2,3$.

Finally, from Eqs. (6), (21) and (35) we yield the nonlinear equation of the state of the crack partially filled with the viscous liquid:

$$\sigma_{nn}=K_0 d-gd^2-qd^3+\beta\dot{d}-\gamma d\dot{d}+\delta d^2\dot{d}, \tag{37}$$

where

$$\begin{aligned} K_0&=K+(9\alpha\mu_0 R_0/4H^3)F_1(\vartheta)>0,\\ g&=324\alpha\mu_0 R_0^2 F_2(\vartheta)/35H^5,\\ q&=-81\alpha\mu_0 R_0^3 F_3(\vartheta)/8H^7,\\ \beta&=3\mu_0\eta R_0^2/H^3,\quad \gamma=18\mu_0\eta R_0^2/H^4,\\ \delta&=72\mu_0\eta R_0^2/H^5. \end{aligned} \tag{38}$$

The obtained equation is nonlinear with respect to both the change of the distance between the crack surfaces and the velocity of the change of this distance. The terms $K_0 d$, gd^2, and qd^3 describe the linear and nonlinear (quadratic and cubic) elasticity of the crack, which is due to the surface tension of the liquid, and the terms $\beta\dot{d}$, $\gamma d\dot{d}$, and $\delta d^2\dot{d}$ describe the linear dissipation and the dissipative nonlinearity, which is due to the viscosity.

VI. DISCUSSION OF THE RESULTS

It is interesting to compare the equations of state (19) and (37) for the cracks with the ideal and the viscous liquids. It is seen from Eqs. (20) and (38) that it is impossible to obtain the equation of the crack state with the ideal liquid from the equation of the crack state with the viscous liquid, assuming in the latter that $\eta=0$. This is because (although the dissipative terms disappear in this case) the boundary conditions for these liquids on the crack surfaces remain different, due to their different adhesion properties. [For the transition from the viscous (i.e., real) liquid to the ideal one, besides the condition $\eta=0$, it is also necessary to put that the liquid has no property of adhesion to the solid. It will lead to the cancellation of the boundary condition (24).] The difference in boundary conditions for $V_r(z=\pm\tilde{H}/2)$ leads to the different behaviors of the meniscus of the ideal and the viscous liquids at the fluctuation of the distance between the crack surfaces and, as a consequence, to the difference, in the coefficients of the linear and nonlinear crack elasticities. It is seen from the first Eq. (38) that, in the comparison of the crack with the ideal liquid, the crack with the viscous liquid is stable with respect to a small number of d perturbations when only the conditions are fulfilled [so long as $F_1(\vartheta)>0$ at any angles contact ϑ], which ensures its being partially filled with liquid ($16\alpha\mu_0\cos\vartheta/KD^2<1$, $\mu_0<1$ and $H>H^*$). It also follows from expressions (20) and (37) that the relations of quadratic and cubic coefficients of the nonlinear elasticity for cracks with the viscous and ideal liquids are determined by the expressions

$$M_2=-(27R_0^2/70H^2)\cdot F_2(\vartheta)/\cos\vartheta, \tag{39}$$

$$M_3=-(81R_0^3/512H^3)\cdot F_3(\vartheta)/\cos\vartheta. \tag{40}$$

We obtain from these expressions for the completely wetting liquids at $R_0/H=10^4$ the relation $M_2\simeq-10^8$ and $M_3\simeq-10^{12}$.

It is interesting to compare also the elastic and inelastic crack nonlinearity with the viscous liquid. It follows from Eq. (37) that there are two ranges of frequencies ω of the acoustic perturbations, determined by the expressions

$$\omega<\Omega_2=|g/\gamma|=18\alpha|F_2(\vartheta)|/35\eta H, \tag{41}$$

$$\omega<\Omega_3=|q/\delta|=9\alpha R_0|F_3(\vartheta)|/64\eta H^2, \tag{42}$$

in which, accordingly, the quadratic (cubic) elastic nonlinearity predominates over the quadratic (cubic) inelastic nonlinearity. Calculations show that for cracks with water ($\vartheta=0$, $\alpha=73\,\mathrm{g/s^2}$, $\eta=10^{-2}\,\mathrm{g/s\cdot cm}$) at $H=10^{-2}$ cm, $R_0=1$ cm the frequencies Ω_2 and Ω_3 are of about 10^6 Hz and 5×10^7 Hz, correspondingly. This, however, does not mean that at the description of nonlinear wave processes in this or that frequency range, one may neglect the first nonlinearity in favor of the second one and vise versa, so far as different types of nonlinearities determine different nonlinear effects.

VII. CONCLUSION

The mechanisms of the acoustic (elastic and inelastic) nonlinearity of cracks partially filled with the ideal and viscous liquids, associated with the nonlinear dependence of the capillary and viscous pressure in liquids on the change of the distance between crack surfaces and the velocity of the change of this distance, are described. For such cracks nonlinear (in cubic approximation) equations of state are obtained and it is shown that the presence of the viscous liquid may lead to considerable increase of the acoustic nonlinearity of such cracks in comparison with cracks filled with an ideal liquid. We note also that the same mechanism of the acoustic nonlinearity may manifest itself in other medium: contact micro-inhomogeneous media containing liquid and gas, and in water-saturated porous and grain media. The obtained equations (19) and (37) can be used further for the derivation of the nonlinear equation of the state of solids containing a great number of cracks partially filled with the viscous liquid.

ACKNOWLEDGMENTS

The work was supported by the Russian Fund of Fundamental Research (Grant Nos. N01-05-64417 and N00-05-64252) and International Science-Technology Center (Grant No. N1369).

[1] M. I. Isakovich, *General Acoustics* (Nauka, Moscow, 1973) (in Russian).
[2] V. E. Nazarov, L. A. Ostrovsky, I. A. Soustova, and A. M. Sutin, ''Nonlinear acoustics of micro-inhomogeneous media,'' Phys. Earth Planet. Inter. **50**, 65–73 (1988).
[3] V. Y. Zaitsev, ''A model of anomalous elastic nonlinearity of micro-inhomogeneous media,'' Acoust. Lett. **19**(9), 171–174 (1996).
[4] V. Y. Zaitsev and V. E. Nazarov, ''On the frequency-independent acoustic *Q*-factor of micro-inhomogeneous solids,'' Acoust. Lett. **21**(1), 11–15 (1997).
[5] V. E. Gusev, W. Lauriks, and J. Thoen, ''Dispersion of nonlinearity, and absorption of sound in micro-inhomogeneous materials,'' J. Acoust. Soc. Am. **103**, 3216–3226 (1998).

[6] A. Granato and K. Lucke, ''Theory of mechanical damping due to dislocation,'' J. Appl. Phys. **27**(5), 583–593 (1956).
[7] A. Granato and K. Lucke, ''String model of dislocations and dislocation absorption,'' in *Physical Acoustics. Principles and Methods*, edited by W. Mason, Vol. 4, p. A, ''Applications to quantum and solid state physics'' (Academic, New York, 1966).
[8] Y. A. Kobelev and L. A. Ostrovsky, ''Models of gas-liquid mixture as the nonlinear dispersion medium,'' in *Nonlinear Acoustics* (IAP Academiya Nauk SSSR, Gorky, 1990), pp. 143–160 (in Russian).
[9] L. A. Ostrovsky, ''Nonlinear acoustics of slightly compressible porous media,'' Sov. Phys. Acoust. **34**, 908–913 (1988).
[10] L. A. Ostrovsky, ''Nonlinear properties of elastic medium with cylindrical nonlinearity,'' Sov. Phys. Acoust. **35**, 490–494 (1989).
[11] I. Y. Belyaeva, V. Yu. Zaitsev, and L. A. Ostrovsky, ''Nonlinear acoustoelastic properties of grainy media,'' Akust. Zh. **39**, 25–32 (1993).
[12] A. N. Norris and D. L. Johnson, ''Nonlinear elasticity of granular media,'' J. Appl. Mech. **64**, 39–49 (1997).
[13] V. E. Nazarov and A. M. Sutin ''Nonlinear elastic constants of solids with cracks,'' J. Acoust. Soc. Am. **102**, 3349–3354 (1997).
[14] V. E. Nazarov, ''A capillary mechanism of the acoustic nonlinearity of solids with partially liquid-filled cracks,'' Acoust. Lett. **20**(3), 50–53 (1996).
[15] V. E. Nazarov, ''Acoustic nonlinearity of cracks partially filled with viscous liquid,'' Acoust. Lett. **22**(4), 71–75 (1998).
[16] V. E. Nazarov and S. V. Zimenkov, ''Sound-by-sound modulation in metallic resonators,'' Acoust. Lett. **16**, 198–201 (1993).
[17] V. E. Nazarov, ''Nonlinear sound by sound damping in metals,'' Akust. Zh. **37**, 1177–1182 (1991).
[18] V. E. Nazarov and A. B. Kolpakov, ''Experimental investigations of nonlinear acoustic phenomena in polycrystalline zinc,'' J. Acoust. Soc. Am. **107**, 1915–1921 (2000).
[19] V. E. Nazarov, ''Sound damping by sound in metals,'' Acoust. Lett. **15**, 22–25 (1991).
[20] S. V. Zimenkov and V. E. Nazarov, ''Dissipative acoustic nonlinearity of copper,'' Phys. Met. Metallogr. **3**, 242–244 (1992).
[21] V. E. Nazarov, ''Sound damping by sound in metals,'' in *Advances in Nonlinear Acoustics*, edited by H. Hobaek, 13th ISNA (Bergen, Norway, 1993), pp. 508–512.
[22] S. V. Zimenkov and V. E. Nazarov, ''Nonlinear acoustic effects in rock samples,'' Izvestiya Russian Acad. Sci., Phys. Solid Earth **29**(1), 12–18 (1993).
[23] K. E-A. Van Den Abeele, P. A. Johnson, R. A. Guyer, and K. R. McCall, ''On the quasi-analytic treatment of hysteretic nonlinear response in elastic wave propagation,'' J. Acoust. Soc. Am. **101**, 1885–1898 (1997).
[24] V. Gusev, C. Glorieux, W. Lauriks, and J. Thoen, ''Nonlinear bulk and surface shear acoustic waves in materials with hysteretic and endpoint memory,'' Phys. Lett. A **232**, 77–86 (1997).
[25] A. Nur, ''Dilatancy, pore fluids, and premonitory variations of t_s/t_p travel times,'' Bull. Seismol. Soc. Am. **62**, 1217–1222 (1972).
[26] R. J. O'Connell and B. Budiansky, ''Seismic velocities in dry and saturated cracked solids,'' J. Geophys. Res. **79**(35), 5412–5426 (1974).
[27] W. F. Murphy, W. K. Winkler, and R. L. Kleinberg, ''Acoustic relaxation in sedimentary rocks: Dependence on grain contacts and saturation,'' Geophysics **51**(3), 757–766 (1986).
[28] A. W. Adamson, *Physical Chemistry of Surfaces* (Wiley–Interscience, New York, 1976).
[29] I. Sneddon, *Fourier Transforms* (McGraw-Hill, New York, 1951).
[30] D. V. Sivukhin, *General Course of Physics. Thermodynamics and Molecular Physics* (Nauka, Moscow, 1979) (in Russian).
[31] L. D. Landau, E. M. Lifshiz, *Gidrodynamika* (Nauka, Moscow, 1986) (in Russian).

Weak nonlinear propagation of sound in a finite exponential horn

Philippe Béquin
Laboratoire d'Acoustique de l'Université du Maine–CNRS UMR 6613, Université du Maine, Avenue Olivier Messiaen, 72085 Le Mans Cedex 9, France

Christopher L. Morfey
Institute of Sound and Vibration Research, University of Southampton, Southampton SO17 1BJ, England

(Received 7 September 1999; accepted for publication 15 February 2001)

This article presents an approximate solution for weak nonlinear standing waves in the interior of an exponential acoustic horn. An analytical approach is chosen assuming one-dimensional plane-wave propagation in a lossless fluid within an exponential horn. The model developed for the propagation of finite-amplitude waves includes linear reflections at the throat and at the mouth of the horn, and neglects boundary layer effects. Starting from the one-dimensional continuity and momentum equations and an isentropic pressure–density relation in Eulerian coordinates, a perturbation analysis is used to obtain a hierarchy of wave equations with nonlinear source terms. Green's theorem is used to obtain a formal solution of the inhomogeneous equation which takes into account linear reflections at the ends of the horn, and the solution is applied to the nonlinear horn problem to yield the acoustic pressure for each order, first in the frequency and then in the time domain. In order to validate the model, an experimental setup for measuring fundamental and second harmonic pressures inside the horn has been developed. For an imposed throat fundamental level, good agreement is obtained between predicted and measured levels (fundamental and second harmonic) at the mouth of the horn. [DOI: 10.1121/1.1362688]

PACS numbers: 43.25.Cb, 43.25.Gf, 43.20.Bi, 43.20.Mv [MFH]

I. INTRODUCTION

A. Motivation for the present study

The high electroacoustic efficiency of horn/driver systems coupled with a relatively large radiating area makes them suitable for the production of high sound pressure levels with good directivity characteristics. This is important when horns are used in public address systems, where propagation over large distances may be required, and is the main reason for their widespread use in this application. In order to produce high far-field levels, high acoustic pressure levels must be present at the throat of the horn and particularly in the horn driver. It is clear that linear modeling of the driver and the horn is likely to fail at high drive levels. The various studies of nonlinearity in electroacoustic drive units have been summarized in the papers of Sherman and Butler.[1,2] For horn loudspeakers, the modeling of driver nonlinearities has been discussed by Klippel[3,4] and Schurer *et al.*[5] Nonlinearity of the compression driver falls outside the scope of the present article, which is concerned rather with transmission within the horn and the inevitable nonlinear distortion which is introduced, at high sound pressure levels, when the linear Webster equation breaks down.

Although the literature concerning one-dimensional nonlinear propagation and shock waves is quite extensive (Whitham,[6] Bjørnø,[7] Rudenko and Soluyan,[8] Pierce,[9] Crighton *et al.*,[10] Makarov and Ochmann,[11–13] Hamilton and Blackstock[14]) there are very few publications concerning the transmission of finite-amplitude waves in horns with standing waves included. The purpose of the present work is to set up a benchmark analytical solution for weakly nonlinear transmission in an exponential horn, taking explicit account of axial standing waves. An analysis will be developed for the exponential horn which permits an explicit Green function solution; adaptation to other horn geometries is then possible via a numerical method based on exponential elements. The motivation for seeking a solution for weakly nonlinear waves is the value of such a solution as nontrivial benchmark for numerical methods. As a check on the analytical solution, we have compared some of the predictions with measurements, reported at the end of the article.

B. Summary of background literature

Acoustic horns have been in use for thousands of years, but the development of theoretical models started relatively recently with a paper published in 1919 by Webster.[15] Webster derived an equation for modeling one-dimensional plane-wave propagation in horns, often called the Webster horn equation, actually due to Lagrange (see Ref. 16). In 1994, Post and Hixson[17] surveyed the horn literature and concluded that only minor improvements to Webster's horn model have been made in the past 80 years. A more sophisticated mathematical model has not been practicable because of the corresponding increase in difficulty of solution. The useful contributions that various researchers have made to Webster's original model equation are (i) choosing the appropriate size of mouth for the one-dimensional horn representation, and (ii) defining the rate of wavefront area expansion more accurately than by means of the plane-wave model (Holland *et al.*[18]). Moreover, despite the significant progress, noted by Klippel,[19] that has been made in the last decade

towards applying modern numerical techniques to the analysis of three-dimensional sound fields in acoustic horns, the assumption has always been that the amplitude of the disturbance is small and the sound propagation is linear.[17,20,21]

We therefore follow earlier investigators in seeking an extension of Webster's one-dimensional approach to finite amplitudes, but without excluding axial standing waves. A literature survey on nonlinear wave propagation in horns reveals that simple formulas for estimating the nonlinear distortion of purely progressive waves in an exponential horn were developed in the 1930s (Rocard,[22,23] Goldstein and McLachlan,[24] Thuras *et al.*[25]). More recently, Zamorski[26,27] gave progressive-wave expressions based on perturbation theory for Bessel, conical, and hyperbolic horns. However, outgoing waves arriving at the mouth of a finite horn are partially reflected by the discontinuity in geometry, and the resulting system of standing waves cannot be analyzed as a simple superposition of traveling waves because of nonlinearity.

Recently, Chester[28] has investigated the disturbances produced in a gas-filled tube of varying cross section by the oscillations of a piston at one end, when the tube is rigidly terminated at the other end and the piston oscillates at near-resonant frequencies. The main purpose of his investigation was to consider the influence of area variation on the basic solution obtained earlier[29] for a tube of uniform cross section. Within a band of excitation frequencies around each resonant frequency, shock waves appear in the solution; outside this interval the oscillations are continuous, but not purely sinusoidal. More recently, Il'inskii *et al.*[30] have presented a one-dimensional mathematical model and a numerical code for the analysis of acoustic standing waves of very high amplitude in rigid closed axisymmetric resonators. The model equation is derived from the fundamental gas dynamics equations for an ideal gas. Total nonlinearity of the gas and gas dynamic equations, volume attenuation due to viscosity, and dependence of the cavity radius on the axial coordinate are included in the model equation. The model equation is solved numerically in the frequency domain and the results presented for different resonators agree well with measurements. The theoretical and numerical results obtained by Chester and Il'inskii *et al.* cannot be directly used in our case because the boundary conditions at the open end are not so well defined as for the rigid termination.

Some recent papers published since 1995 claim to be able to describe nonlinear distortion in horns when reflections are present. Klippel[3,4,19] has developed an acoustic transmission line model to describe finite-amplitude sound in horns and ducts with reflection (only for the fundamental), by using conical 1-D elements. Each element is represented by a linear four-pole plus a nonlinear source of volume velocity, derived from the nonlinear wave equation in Lagrangian coordinates. Unfortunately no comparison of this model with measurements is reported. In a separate study, Holland and Morfey[31] have proposed a semi-numerical model for nonlinear sound transmission in finite-length horns. This model is a synthesis of linear propagation in the frequency domain (Webster's equation) and nonlinear distortion in the time domain; the two algorithms are applied sequentially to convert the acoustic variables on the mouth side of an exponential element into the corresponding variables on the throat side, and are linked by Fourier transforms. The model takes account of standing waves and their finite-amplitude interaction, but the nonlinear part of the calculation treats the standing waves as plane and is therefore accurate only at frequencies well above cutoff in the horn. A further disadvantage relative to the present article is that the calculation proceeds from the mouth to the throat. The authors compared their model with measurements inside a horn that was sinusoidally driven at a number of frequencies. Given the amplitude and phase of each harmonic measured at the horn mouth, the model was used to predict the corresponding harmonic levels at the throat. This was done for sound pressure levels (fundamental frequency component) at the throat of 140, 150, and 160 dB $re\ 20\ \mu$ Pa. The predicted harmonic levels at the throat compared reasonably well with the few measurements available, up to the second harmonic.

A one-dimensional model by Czerwinski *et al.*[32] introduces some additional approximations that simplify the calculation relative to Ref. 31. Specifically, nonlinear distortion is confined in Ref. 32 to the forward wave (traveling from throat to mouth). Distortion of the forward waveform is estimated at each point x along the horn from the ''excess wavespeed'' $\beta u_{\mathrm{lin}}(x,t)$. Here $u_{\mathrm{lin}}(x,t)$ is the forward-wave particle velocity given by linear theory, and β is the nonlinearity parameter $(\gamma+1)/2$. Distortion of the forward wave due to the particle velocity and excess sound speed in the backward wave is treated as a second-order effect that can be neglected.

Czerwinski *et al.*[32] have tested their model experimentally. They find reasonable agreement between the measured and predicted total harmonic distortion (THD) at the horn mouth, for sinusoidal input signals between 1 and 3 kHz (horn cutoff=700 Hz) and throat levels of 137, 147, and 157 dB. The highest measured THD is around 2% (at 157 dB).

Further work is needed to establish the range of validity of the approximate models in Refs. 31 and 32. The present work offers a benchmark against which these ''excess wavespeed'' models can be tested; in particular, it is the only analytical model available for calculating finite-amplitude transmission in horns down to the horn cutoff frequency and below, where the propagation is dispersive and the excess wavespeed concept breaks down.

C. Structure of the article

In Sec. II the finite-amplitude wave equations associated with the fundamental and higher-harmonic pressure fields are deduced for a sinusoidally driven exponential horn. Taking into account linear boundary conditions, Sec. III gives the solution of this boundary-value problem. Section IV deals with particular solutions of the pressure (fundamental and second harmonic) when a simple harmonic driving source is applied to the throat of the horn. In Secs. V and VI, experimental results are collected and compared with theoretical ones. Section VII gives conclusions and makes recommendations for further work. In the Appendix, the lumped-element model used to represent the impedance of the driver output is explained.

II. EQUATIONS FOR NONLINEAR HORN ACOUSTICS

In this section, a finite-amplitude plane wave equation is developed for one-dimensional standing waves in a horn. All dissipative processes are neglected.

A. Equations of fluid motion

The following equations apply to an inviscid, nonconducting fluid, and are therefore appropriate only for sufficiently weak nonlinearity that no shocks appear in the horn (in contrast to the model of Chester[28,29] and Il'inskii *et al.*[30]). They are based on a one-dimensional approximation (slowly varying area, rigid walls). Symbols ∂_t, ∂_x denote partial derivatives with respect to t and x, respectively.

Mass conservation: $$S\partial_t R + \partial_x[RVS] = 0. \tag{1}$$

Momentum conservation: $$R[\partial_t V + V\partial_x V] + \partial_x P = 0. \tag{2}$$

Isentropic compression: $P = f(R)$; for ideal gas,

$$\frac{P}{P_0} = \left(\frac{R}{\rho_0}\right)^{\gamma}. \tag{3}$$

Here $V(x,t)$ and $S(x)$ are respectively the particle velocity and the area, and $R(x,t)$ and $P(x,t)$ denote the total instantaneous density and the pressure of the fluid. In what follows, we model the air as an ideal gas with constant specific-heat ratio γ.

No analytical solution of the complete set of Eqs. (1)–(3) is available for an open horn. However, a perturbation analysis allows us to find some approximate solutions for finite amplitude waves.

B. Perturbation analysis

The perturbation analysis, leading to a first-order, linearized, approximation and to higher-order approximations, is based on the following procedure. The physical quantities are written in the form of an asymptotic series, giving

$$\begin{aligned} R(x,t) &= \rho_0 + \rho_1 + \rho_2 + \cdots + \rho_n + \cdots, \\ V(x,t) &= 0 + v_1 + v_2 + \cdots + v_n + \cdots, \\ P(x,t) &= P_0 + p_1 + p_2 + \cdots + p_n + \cdots. \end{aligned} \tag{4}$$

Here P_0 and ρ_0 correspond to the stationary undisturbed fluid; ρ_1, v_1, and p_1 are the first-order (linear) approximation; ρ_2, v_2, and p_2 are the second-order correction to ρ_1, v_1, and p_1, and so on. We expect to find

$$\begin{aligned} &\rho_2 \sim \rho_1^2, \quad \rho_3 \sim \rho_1^3, \quad \rho_n \sim \rho_1^n; \\ &v_2 \sim v_1^2, \quad v_3 \sim v_1^3, \quad v_n \sim v_1^n; \\ &p_2 \sim p_1^2, \quad p_3 \sim p_1^3, \quad p_n \sim p_1^n. \end{aligned} \tag{5}$$

With this composite form of the dependent variables, we obtain by substitution in Eqs. (1) and (2) the following first-order set of equations:

$$S\partial_t \rho_1 + \rho_0 \partial_x[v_1 S] = 0, \quad \rho_0 \partial_t v_1 + \partial_x p_1 = 0. \tag{6}$$

Analogously, the second-order set of equations may be written

$$\begin{aligned} &S\partial_t \rho_2 + \rho_0 \partial_x[v_2 S] = -\partial_x[\rho_1 v_1 S], \\ &\rho_0 \partial_t v_2 + \partial_x p_2 = -\rho_0 v_1 \partial_x v_1 - \rho_1 \partial_t v_1. \end{aligned} \tag{7}$$

In the same manner, we can also apply the composite form of the dependent variables to Eq. (3). We obtain the following pressure-density relations:

$$\begin{aligned} &p_1 = c_0^2 \rho_1, \quad c_0^2 = \frac{\gamma P_0}{\rho_0}, \\ &p_2 = c_0^2 \rho_2 + \frac{\gamma - 1}{2\rho_0 c_0^2} p_1^2. \end{aligned} \tag{8}$$

C. Differential equations

If we now differentiate the first of Eqs. (6) with respect to t, differentiate the second equation with respect to x, and use the pressure-density relations (8), then a combination of the two resulting equations gives the first-order equation of propagation

$$\partial_{xx}^2 p_1 + (\partial_x \ln S)(\partial_x p_1) - \frac{1}{c_0^2}\partial_{tt}^2 p_1 = 0. \tag{9}$$

In a similar manner, combining the set of Eqs. (7) with the relations (8) yields a second-order equation of propagation:

$$\begin{aligned} &\partial_{xx}^2 p_2 + (\partial_x \ln S)(\partial_x p_2) - \frac{1}{c_0^2}\partial_{tt}^2 p_2 \\ &\quad = -v_1\left[\rho_0 \partial_x v_1 - \frac{1}{c_0^2}\partial_t p_1\right](\partial_x \ln S) \\ &\qquad - \frac{1}{c_0^2}\left\{\frac{\gamma - 1}{\rho_0 c_0^2}\partial_t[p_1 \partial_t p_1] - \partial_x[v_1 \partial_t v_1]\right\} \\ &\qquad - \rho_0 \partial_x[v_1 \partial_x v_1]. \end{aligned} \tag{10}$$

The second-order pressure is governed by a linear partial-differential equation with an inhomogeneous term acting as a source. It is interesting to see from Eqs. (9) and (10) that both wave equations have a similar form for the left-hand side. The terms on the right-hand side of Eq. (10) depend on the pressure p_1 and the velocity v_1. Neglecting the nonlinear phenomena in Eq. (10) leads to Webster's equation.[15]

The perturbation analysis has been pursued up to third order. However, detailed results are confined in this article to the second-order approximation.

III. SOLUTION PROCEDURE

The present study is concerned with a horn possessing an exponential area profile defined as

$$S(x) = S_0 e^{mx}, \tag{11}$$

where m is the flare constant of the horn.

A. Wave equations

The wave equations (9) and (10) for the pressure p_i of the ith order can be rewritten as

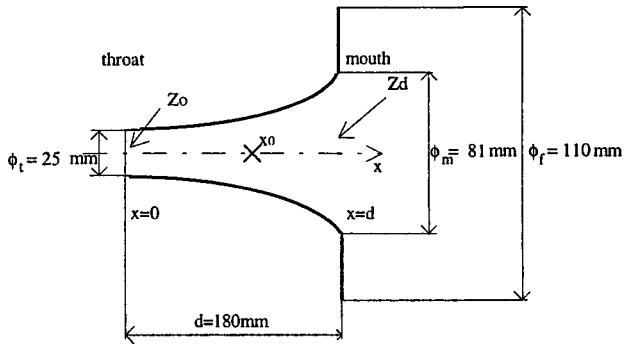

FIG. 1. Schematic representation of an axisymmetric exponential horn constructed for experiments. Z_0 and Z_d are the acoustic impedances and x_0 is the source point position. Material: fiberglass; Dimensions: throat diameter: 25 mm, mouth diameter: 81 mm, flange diameter: 110 mm, axial length: 180 mm, wall thickness: 10 mm, flare-rate: 13.06 m^{-1}. Cutoff frequency: 360 Hz.

$$\left[\partial_{xx}^2 + m\partial_x - \frac{1}{c_0^2}\partial_{tt}^2\right] p_i(x,t) = \Lambda_i(x,t), \quad i = 1,2,..., \tag{12}$$

with the source terms

$$\begin{aligned}
&\Lambda_1(x,t) = 0,\\
&\Lambda_2(x,t) = -\rho_0 v_1\left[\partial_x v_1 - \frac{1}{\rho_0 c_0^2}\partial_t p_1\right] m\\
&\qquad - \frac{1}{c_0^2}\left\{\frac{\gamma-1}{\rho_0 c_0^2}\partial_t[p_1\partial_t p_1] - \partial_x[v_1\partial_t p_1]\right\}\\
&\qquad - \rho_0\partial_x[v_1\partial_t v_1].
\end{aligned} \tag{13}$$

The formal solution of the above inhomogeneous equations can be obtained from a convolution of the right-hand side of Eq. (12) with the appropriate Green function.

B. Boundary conditions

We shall solve the generalized wave equation (Webster equation), Eq. (12), in the one-dimensional domain between the horn throat ($x=0$) and the horn mouth ($x=d$) (see Fig. 1). It will be necessary to take into account reflections by imposing appropriate boundary conditions at each end. We shall adopt linear boundary conditions in the form of specific acoustic impedances $Z=p/v$; thus Z_0 is the throat impedance and Z_d is the mouth impedance.

Use of a linear impedance at the horn mouth is justified on the grounds that mouth levels in a horn are much lower than levels at the throat. At the throat, in order to calculate the second-harmonic pressure field excited in the horn by the nonlinear virtual sources, we shall adopt a linear modeling of the driver with an output acoustic impedance Z_{a0} (see the Appendix).

A formal solution of the wave equation (12) can be obtained by using Green's theorem. The Green function associated with the linear wave operator can be derived by solving the following Helmholtz equation,

$$\left[\partial_{xx}^2 + m\partial_x + \left(\frac{2\pi\nu}{c_0}\right)^2\right] \mathrm{G}(x,x_0) = -\delta(x-x_0), \tag{14}$$

where $\delta(x-x_0)$ is the Dirac delta function; with impedance boundary conditions at each end of the horn:

$$\text{throat } (x=0): \quad \left[-\partial_x + jk\frac{\rho_0 c_0}{Z_0}\right]\mathrm{G}(0,x_0) = 0; \tag{15}$$

$$\text{mouth } (x=d): \quad \left[\partial_x + jk\frac{\rho_0 c_0}{Z_d}\right]\mathrm{G}(d,x_0) = 0. \tag{16}$$

Here ν and k are respectively the frequency and the acoustic wave number $2\pi\nu/c_0$. $\mathrm{G}(x,x_0)$ is the Green function which represents the pressure response at x due to point forcing at x_0.

C. Green function

The Green function solution of this boundary-value problem can be obtained analytically.[33] After some calculations we obtain

$$\begin{aligned}
\mathrm{G}(x,x_0) = &-\frac{e^{-(m/2)[x-x_0]}}{\Gamma\sin[\Gamma d + \alpha_0 + \alpha_d]}\\
&\times\begin{cases}\cos[\Gamma x_0 + \alpha_0]\cos[\Gamma(x-d) - \alpha_d], & x_0 < x,\\ \cos[\Gamma(x_0-d) - \alpha_d]\cos[\Gamma x + \alpha_0], & x_0 > x,\end{cases}
\end{aligned} \tag{17}$$

where d is the length of the horn, x_0 is the source point location (Fig. 1), and Γ is the horn wave number defined by

$$\Gamma(k) = \mp j\sqrt{(m/2)^2 - k^2}, \quad k \gtrless 0. \tag{18}$$

The cutoff frequency of the horn is the frequency for which $\Gamma=0$; it is given by $\nu_c = (k_c/2\pi)c_0$ with $k_c = |m|/2$. Acoustic waves go from evanescent to propagating at this frequency.

With knowledge of the acoustic impedances $Z_0(k)$ and $Z_d(k)$, the quantities $\alpha_0(k)$ and $\alpha_d(k)$ of the Green function can be found from the relations

$$\begin{aligned}
\tan[\alpha_0(k)] &= -\frac{m/2 + jk\,\rho_0 c_0/Z_0(k)}{\Gamma(k)},\\
\tan[\alpha_d(k)] &= -\frac{jk\,\rho_0 c_0/Z_d(k) - m/2}{\Gamma(k)},
\end{aligned} \tag{19}$$

where $\Gamma(k)$ is defined by the relations (18).

The Green function (17) is not defined at the cutoff frequency ($k_c = |m|/2$; $\Gamma=0$). A special Green function is calculated for this frequency and is given by

$$\mathrm{G}_c(x,x_0) = -\frac{1}{d}e^{-(m/2)|x-x_0|}\frac{[x_0\beta_0 + 2/m][(x-d)\beta_d + 2/m]}{\beta_0\beta_d - (2/md)(\beta_0 - \beta_d)}, \quad x > x_0, \tag{20}$$

with (x,x_0) interchanged when $x<x_0$. The dimensionless admittance parameters β_0 and β_d are defined as $(1 + j\,\rho_0 c_0/Z_0)$ and $(1 - j\,\rho_0 c_0/Z_d)$, respectively.

IV. SOLUTION OF BOUNDARY-VALUE PROBLEM

In the horn, a primary sound source with an output acoustic impedance Z_{a0} (see the Appendix) is placed at the throat ($x=0$). For single-frequency excitation at frequency ν_0, the right side of the wave equation (12) can be expressed as

$$\Lambda_1(x,t)=Q_0\delta(x)\sin(2\pi\nu_0 t), \tag{21}$$

whose Fourier transform with respect to time is

$$\Lambda_1(x,\nu)=\int_{-\infty}^{+\infty}\Lambda_1(x,t)e^{-2j\pi\nu t}\,dt$$

$$=\delta(x)\frac{Q_0}{2j}[\delta(\nu-\nu_0)-\delta(\nu+\nu_0)]. \tag{22}$$

A. First-order acoustic pressure

The first-order acoustic pressure in the frequency domain is given by

$$p_i(x,\nu)=-\int_0^d \mathrm{G}(x,x_0)\Lambda_i(x_0,\nu)\,dx_0 \quad \text{with} \quad i=1, \tag{23}$$

where d is the axial length of the horn and $\mathrm{G}(x,x_0)$ is the Green function [Eq. (17)]. If the excitation frequency ν_0 is equal to the cutoff frequency ν_c, the Green function G given by Eq. (20) must be used.

After some calculation, p_1 is deduced to be

$$p_1(x,\nu)=\Phi(x,\nu)\frac{1}{2j}[\delta(\nu-\nu_0)-\delta(\nu+\nu_0)],$$

where

$$\Phi(x,\nu)=p_0 e^{-(m/2)x}\frac{\cos[\Gamma(x-d)-\alpha_d]}{\cos[\Gamma d+\alpha_d]}. \tag{24}$$

The acoustic pressure depends on only one adjustable parameter, p_0, which is the first-order pressure at the throat. From a practical point of view, the pressure value at the throat is easier to obtain by measurement than the velocity value.

The expression for the first-order pressure in the time domain can be easily calculated using the fact that the real part and the imaginary part of the radiation impedance are an even and an odd function, respectively.

In Eq. (24), the complex quantity α_d depends on the impedance Z_d [see Eq. (19)] which can be written as $Z_d(\nu)=R_d(\nu)+jX_d(\nu)$ where $R_d(\nu)$ and $X_d(\nu)$ are respectively the real and the imaginary parts of $Z_d(\nu)$. The real part $R_d(\nu)$ of the radiation impedance is an even function whereas the imaginary part $X_d(\nu)$ is an odd function. From this observation Z_d has the property $Z(-\nu_0)=Z^*(\nu_0)$, and it follows that

$$\alpha_d(-\nu_0)=\alpha_d^*(\nu_0). \tag{25}$$

Thus $\Phi(x,-\nu_0)=\Phi^*(x,\nu_0)$, where Z^*, α_d^*, and Φ^* are respectively the complex conjugates of Z, α_d, and Φ.

The inverse Fourier transform $p_1(x,t)=\int_{-\infty}^{+\infty}p_1(x,\nu)e^{+2j\pi\nu t}\,d\nu$ and the relationship between Φ and Φ^* are finally used to calculate the acoustic pressure in the time domain, corresponding to pressure $p_0\sin(2\pi\nu_0 t)$ at the throat. The first-order acoustic pressure at x, generated by an acoustic source placed at $x=0$, can be written as

$$p_1(x,t)=\Re e[\Phi(x,\nu_0)]\sin(2\pi\nu_0 t)$$

$$+\Im m[\Phi(x,\nu_0)]\cos(2\pi\nu_0 t), \tag{26}$$

where $\Re e[\Phi(x,\nu_0)]$ and $\Im m[\Phi(x,\nu_0)]$ are respectively the real and the imaginary parts of the function Φ [Eq. (24)].

This equation reveals how a plane wave at the throat of a horn transforms as it propagates linearly along the horn.

B. Second-order pressure in frequency domain

We proceed to find an expression for the second-order pressure. Frequency-domain versions of Eqs. (6) and (24) are substituted into the Fourier transform of Eq. (12) and use is made of the relation $\Phi(x,-\nu_0)=\Phi^*(x,\nu_0)$, to give an expression for the source term Λ_2 in which terms of equal frequency are combined:

$$\Lambda_2(x,\nu)=\frac{-1}{2}\frac{1}{\rho_0 c_0^2}\left\{+\left(\frac{[m+\partial_x]\{(\partial_x\Phi^*)(\partial_{xx}^2\Phi)+(\partial_x\Phi)(\partial_{xx}^2\Phi^*)\}}{k_0^2}-[m+\partial_x](\Phi\partial_x\Phi^*+\Phi^*\partial_x\Phi)\right)\frac{\delta(\nu)}{2}\right.$$

$$+\left(\frac{[m+\partial_x](\partial_x\Phi)(\partial_{xx}^2\Phi)}{k_0^2}-[m+\partial_x](\Phi\partial_x\Phi)+2(\gamma-1)k_0^2\Phi^2\right)\frac{\delta(\nu-2\nu_0)}{2}$$

$$\left.+\left(\frac{[m+\partial_x](\partial_x\Phi^*)(\partial_{xx}^2\Phi^*)}{k_0^2}-[m+\partial_x](\Phi^*\partial_x\Phi^*)+2(\gamma-1)k_0^2\Phi^{*2}\right)\frac{\delta(\nu+2\nu_0)}{2}\right\}. \tag{27}$$

Note that the response frequency ν is distinguished from the excitation frequency ν_0, both here and in what follows.

From the expression for Φ [Eq. (24)], the complex conjugate Φ^* is obtained and the partial derivatives (Φ, $\partial_x\Phi$ and $\partial_{xx}^2\Phi$) are calculated. The wave equation for the pressure p_2 finally becomes

$$\partial_{xx}^2 p_2 + m\partial_x p_2 + k^2 p_2 = \Lambda_2(x,\nu_0) = -e^{-mx}\left\{\Lambda_2'(x,\nu_0)\,\delta(\nu) + [\Lambda_2''(x,\nu_0)]\frac{\delta(\nu-2\nu_0)}{2} + [\Lambda_2''(x,\nu_0)]^*\frac{\delta(\nu+2\nu_0)}{2}\right\}. \quad (28)$$

The weighting factors Λ_2' and Λ_2'' are dependent upon both the excitation frequency ν_0 and the position x, and can be expressed as

$$\Lambda_2'(x,\nu_0) = C_0'[C_1\cos(\theta_0+\theta_0^*) - C_2\sin(\theta_0+\theta_0^*)],$$
$$\Lambda_2''(x,\nu_0) = C_0[(C_1+C_3)\cos 2\theta_0 - C_2\sin 2\theta_0 + C_3], \quad (29)$$

with

$$C_0' = \left(\frac{p_0^2}{\cos[\Gamma_0 d+\alpha_{d0}]\cos[\Gamma_0 d+\alpha_{d0}]^*}\right)\frac{k_0^2}{\rho_0 c_0^2}$$
$$C_0 = \left(\frac{p_0}{\cos[\Gamma_0 d+\alpha_{d0}]}\right)^2\frac{k_0^2}{\rho_0 c_0^2};$$
$$C_1 = \left[1-\left(\frac{m}{2k_0}\right)^2\right]\left[1-2\left(\frac{m}{2k_0}\right)^2\right]$$
$$C_2 = 2\left(\frac{m}{2k_0}\right)\left[1-\left(\frac{m}{2k_0}\right)^2\right]^{3/2}$$
$$C_3 = \frac{\gamma-1}{2} \quad (30)$$

and

$$\theta_0(x,\nu_0) = \Gamma_0(x-d) - \alpha_{d0} \quad \text{with} \quad \begin{cases} \theta_0+\theta_0^* = -2\Re e[\alpha_{d0}] & \text{for } k_0 < \dfrac{m}{2}, \\ \theta_0+\theta_0^* = 2\Re e[\Gamma_0(x-d)-\alpha_{d0}] & \text{for } k_0 > \dfrac{m}{2}. \end{cases} \quad (31)$$

Note that $\Gamma_0 = \Gamma(\nu)|_{\nu=\nu_0}$ and $\alpha_{d0} = \alpha_d(\nu)|_{\nu=\nu_0}$, with Γ and α_d respectively defined by Eqs. (18) and (19). Only the quantities θ_0, θ_0^*, and C_0 are complex and depend on the impedance Z_d (through the quantity α_{d0}). C_0', $(\theta_0+\theta_0^*)$, and thus Λ_2' are real.

The right-hand side of the wave equation for p_2 [Eq. (28)] contains terms of frequency zero and $\pm 2\nu_0$. The second-order pressure p_2 in the frequency domain follows from Eqs. (23) and (17):

$$p_2(x,\nu,\nu_0) = \tfrac{1}{2}\{A_0(x,\nu,\nu_0)\,\delta(\nu) + A_2^+(x,\nu,\nu_0)\,\delta(\nu-2\nu_0) + A_2^-(x,\nu,\nu_0)\,\delta(\nu+2\nu_0)\}, \quad (32)$$

where the quantities A_0, A_2^+ and A_2^- are discussed next.

1. Mean pressure field

At a given value of excitation frequency ν_0, the time-average contribution $(\nu=0)$ to p_2 at point x inside the horn is given by

$$\begin{aligned} A_0(x,\nu=0,\nu_0) &= -e^{-(m/2)x}\left\{+\frac{\cos[\Gamma(x-d)-\alpha_d]}{\Gamma\sin[\Gamma d+\alpha_0+\alpha_d]}\int_0^x \Lambda_2'(x_0,\nu_0)\cos[\Gamma x_0+\alpha_0]e^{-(m/2)x_0}\,dx_0\right. \\ &\quad \left. + \frac{\cos[\Gamma x+\alpha_0]}{\Gamma\sin[\Gamma d+\alpha_0+\alpha_d]}\int_x^d \Lambda_2'(x_0,\nu_0)\cos[\Gamma(x_0-d)-\alpha_d]e^{-(m/2)x_0}\,dx_0\right\} \\ &= -\frac{C_0'}{2}e^{-(m/2)x}\left\{+\frac{\cos[\Gamma(x-d)-\alpha_d]}{\Gamma\sin[\Gamma d+\alpha_0+\alpha_d]}[F_u(C;\kappa_+;\Gamma_+)+F_u(C;\kappa_-;\Gamma_-)]_{x_0=0}^{x_0=x}\right. \\ &\quad \left. + \frac{\cos[\Gamma x+\alpha_0]}{\Gamma\sin[\Gamma d+\alpha_0+\alpha_d]}[F_u(C;\beta_+;\Gamma_+)+F_u(C;\beta_-;\Gamma_-)]_{x_0=x}^{x_0=d}\right\}, \end{aligned} \quad (33)$$

with

$$F_u(C;X_\pm;\Gamma_\pm) = e^{-(m/2)x_0}\frac{-(m/2)[C\cos X_\pm - C_2\sin X_\pm] + \Gamma_\pm[C\sin X_\pm + C_2\cos X_\pm]}{\Gamma_\pm^2 + (m/2)^2}. \quad (34)$$

Here the function $F_u(C;X_\pm;\Gamma_\pm)$ depends on the quantities κ_+, β_+, κ_-, β_-, Γ_-, Γ_+ and C which can be written as

$$\begin{aligned}
&\kappa_\pm(x_0,\nu,\nu_0)=[\Gamma x_0+\alpha_0]\pm[\theta_0(x_0,\nu_0)+\theta_0^*(x_0,\nu_0)],\\
&\beta_\pm(x_0,\nu,\nu_0)=\theta(x_0,\nu)\pm[\theta_0(x_0,\nu_0)+\theta_0^*(x_0,\nu_0)],\\
&\Gamma_\pm(\nu,\nu_0)=\Gamma\pm[\Gamma_0+\Gamma_0^*],\quad C=C_1.
\end{aligned}\tag{35}$$

For C_1, see Eq. (30). Also, recall Eq. (31):

$$\begin{aligned}
&\theta(x_0,\nu)=\Gamma(x_0-d)-\alpha_d,\\
&\theta_0(x_0,\nu_0)=\theta(x_0,\nu)|_{\nu=\nu_0}=\Gamma_0(x_0-d)-\alpha_{d0}.
\end{aligned}\tag{36}$$

2. Fluctuating pressure field

At a given value of excitation frequency ν_0, the fluctuating contribution ($\nu=2\nu_0$) to p_2 at point x inside the horn is given by

$$\begin{aligned}
A_2^+(x,\nu=2\nu_0,\nu_0)=&-e^{-(m/2)x}\Bigg\{+\frac{\cos[\Gamma(x-d)-\alpha_d]}{\Gamma\sin[\Gamma d+\alpha_0+\alpha_d]}\int_0^x\Lambda_2''(x_0,\nu_0)\cos[\Gamma x_0+\alpha_0]e^{-(m/2)x_0}\,dx_0\\
&+\frac{\cos[\Gamma x+\alpha_0]}{\Gamma\sin[\Gamma d+\alpha_0+\alpha_d]}\int_x^d\Lambda_2''(x_0,\nu_0)\cos[\Gamma(x_0-d)-\alpha_d]e^{-(m/2)x_0}\,dx_0\Bigg\}\\
=&-\frac{C_0}{2}e^{-(m/2)x}\Bigg\{+\frac{\cos[\Gamma(x-d)-\alpha_d]}{\Gamma\sin[\Gamma d+\alpha_0+\alpha_d]}[F_u(C;K_+;\Gamma_+)+F_u(C;K_-;\Gamma_-)+F_v(\Gamma x_0+\alpha_0)]_{x_0=0}^{x_0=x}\\
&+\frac{\cos[\Gamma x+\alpha_0]}{\Gamma\sin[\Gamma d+\alpha_0+\alpha_d]}[F_u(C;B_+;\Gamma_+)+F_u(C;B_-;\Gamma_-)+F_v(\Gamma(x_0-d)-\alpha_d)]_{x_0=x}^{x_0=d}\Bigg\},
\end{aligned}\tag{37}$$

where the function $F_u(C;X_\pm;\Gamma_\pm)$ is defined by Eq. (34). Here this function depends on the quantities K_+, B_+, K_-, B_-, Γ_-, Γ_+ and C which can be written as

$$\begin{aligned}
&K_\pm(x_0,\nu,\nu_0)=[\Gamma x_0+\alpha_d]\pm 2\theta_0(x_0,\nu_0),\\
&B_\pm(x_0,\nu,\nu_0)=\theta(x_0,\nu)\pm 2\theta_0(x_0,\nu_0),\\
&\Gamma_\pm(\nu,\nu_0)=\Gamma\pm 2\Gamma_0,\\
&C=C_1+C_3.
\end{aligned}\tag{38}$$

The function $F_v(Y)$, where Y is equal to $\Gamma x_0+\alpha_0$ or to $\theta(x_0,\nu)=\Gamma(x_0-d)-\alpha_d$, is defined by

$$F_v(Y)=e^{-(m/2)x_0}\,\frac{2C_3}{k^2}\,[\Gamma\sin Y-(m/2)\cos Y].\tag{39}$$

Finally, the fluctuating contribution ($\nu=-2\nu_0$) to p_2 is given by

$$A_2^-(x,-2\nu_0,\nu_0)=[A_2^+(x,2\nu_0,\nu_0)]^*.\tag{40}$$

In the final expression for p_2 [Eq. (32) associated with Eqs. (37) and (40)], terms which come from the Green function have a ν frequency dependence, whereas the weighting quantities $\Lambda_2'(x_0,\nu_0)$ and $\Lambda_2''(x_0,\nu_0)$ are independent of ν. Note that the choice of the Green function depends on the value of the excitation frequency ν_0. If ν_0 is one-half of the cutoff frequency of the horn ν_c, the source term involves $2\nu_0$ equal to ν_c, and the Green function defined by Eq. (20) must be used.

V. EXPERIMENTAL RESULTS

An exponential horn with a flange was constructed for testing (see Fig. 1). In choosing the appropriate dimensions of the horn to be tested, several factors were considered. The overall length and mouth diameter, and the frequency range of operation, were chosen to be compatible with the driver available. The experimental setup is shown in Fig. 2. A small hole to take the microphone was drilled in the horn at each end, to permit measurement of the sound field at the throat and the mouth.

The compression driver used is an 8 Ω, 25 mm exit diameter driver, manufactured by FANE (model MD 2151). The compression driver consists of a titanium diaphragm which is forced to oscillate by the force produced when a current is passed through the voice-coil suspended in the field of a permanent magnet [see the Appendix and Table I]. In front of the diaphragm there is a phase correction plug to eliminate radial standing waves inside the circular compression chamber[34] and to prevent dips in the sound pressure response due to interfering sound waves traveling different

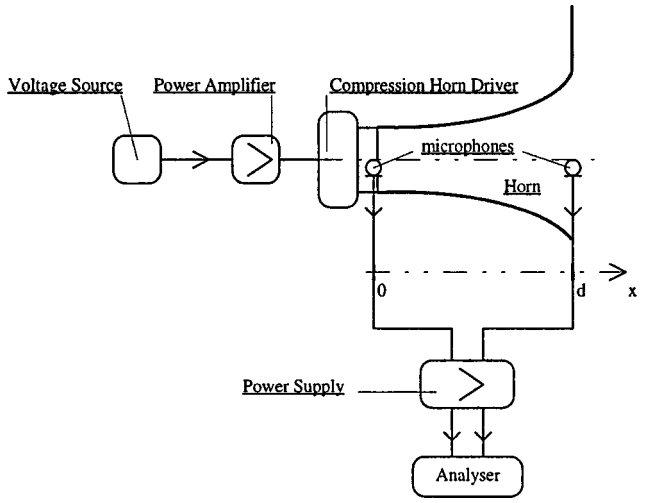

FIG. 2. Experimental setup used for the measurement of the pressure in the horn.

TABLE I. Estimated values of the compression driver elements.

Force factor: Bl	9.3 (N/A)
Electrical resistance of voice coil: R_e	8.5 (Ω)
Electrical inductance of voice coil: L_e	17×10^{-6} (H)
Mechanical resistance: R_d	0.6 (kg/s)
Mass of diaphragm: M_d	2×10^{-3} (kg)
Mechanical compliance of suspension: C_d	16×10^{-6} (m/N)
Diaphragm area: S_d	3×10^{-3} (m^2)
Throat area: S_t	4.91×10^{-4} (m^2)
Acoustical compliance of air in front volume: C_f	1×10^{-11} (m^5/N)
Acoustical resistance of phase plug: R_p	890 (N s/m^5)
Acoustical inductance of phase plug: L_p	35 (N s^2/m^5)
Mechanical radiation impedance at horn throat: Z_{horn}	$-$(kg s^{-1})

paths. However, this correction plug introduces a thin air film between the diaphragm and the plug itself. When high pressures occur in the compression driver, this air film will introduce nonlinearities caused by the adiabatic behavior of air (see Refs. 4 and 5). Indicative information about nonlinear distortion of the compression driver used without horn is now given. The very near field pressure from this compression driver was observed to have harmonic distortion at least 40 dB below the fundamental (maintained at 130 dB SPL) over the range of frequencies from 1.2 to 4 kHz, at least 20 dB below the fundamental over the range 600 Hz to 1.2 kHz, and at least 10 dB below the fundamental over the range 300 to 600 Hz.

Two Brüel and Kjær $\frac{1}{4}$-in. condenser microphones were used in this experimental work, a B&K microphone type 4136 at the throat (3% distortion limit, at 100 Hz, of at least 172 dB SPL) and a B&K microphone type 4135 at the mouth (3% distortion limit, at 100 Hz, of at least 164 dB). The microphones had been calibrated in amplitude, and their phase difference over the given frequency range has been estimated as less than 5 degrees. The microphones were connected to a B&K microphone power supply type 2807. The electrical signals from the microphone were measured (amplitude and phase) using a Hewlett Packard 35665A Dynamic Signal Analyser.

The horn/compression driver system and the microphones were placed in an anechoic chamber. All the other apparatus (power amplifiers, analyser and voltage source) was placed outside the anechoic chamber.

At the throat the impedance Z_0 is derived from a lumped-element equivalent circuit for the physical model of the compression driver (see the Appendix, Fig. A2). The end of the flanged horn is open and radiates into a free field; the mouth impedance is approximated by a semi-empirical impedance given by Dalmont *et al.*[35] This expression combines the reflection coefficient of an open pipe with an additional term which takes into account effects of reflections from the edge of the flange. Owing to the complicated form of the impedance Z_d, the formula is not reproduced here.

VI. DISCUSSION

Figures 3 and 4 show the mouth fundamental pressure response. The data show good agreement with the linear theoretical predictions [Eq. (26), Sec. IV]. The cause of the slight discrepancy between predicted and measured results at low frequencies (<500 Hz) may be the nonlinear behavior of the compression driver (discussed in Sec. V).

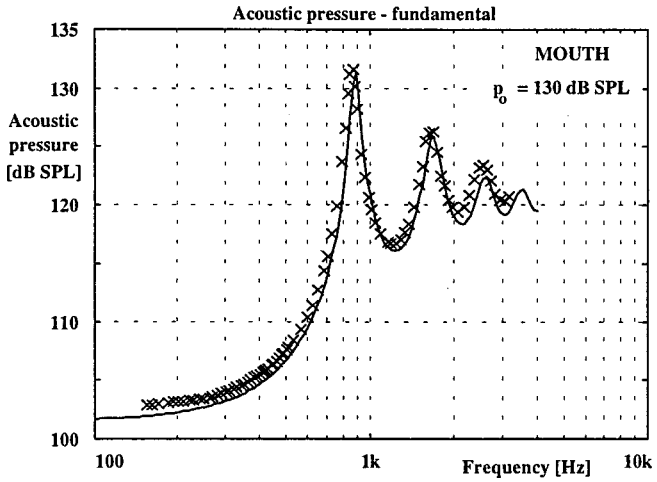

FIG. 3. Sound pressure level at the horn mouth of the fundamental (relative to the reference pressure $p_r=2\times10^{-5}$ Pa) versus the excitation frequency (ν_0) for a fixed level of 130 dB SPL at the throat. ($\times\times\times$) experimental results, (———) theoretical predictions [Eq. (24)]. The voltage level applied to the compression chamber is adjusted in order to maintain the pressure level constant at the throat. The model parameter p_0 in Eqs. (24) and (26) corresponds to 130 dB SPL at the throat.

Figures 5(a) and 6(a) display the throat second harmonic pressure response. Above $\nu_0\approx700$ Hz, the agreement between measured and predicted data is good, but not nearly as good as for the mouth second harmonic pressure response (discussed in the next paragraph). Below $\nu_0\approx700$ Hz the lack of agreement could be mainly due to nonlinear behavior of the compression driver (discussed in Sec. V).

Figures 5(b) and 6(b) show the mouth second harmonic pressure response. Nonlinearity predicted by the model is characterized by increasing distortion with increasing frequency (6 dB/oct). This phenomenon can be seen for frequencies above 1 kHz. In this frequency region good agree-

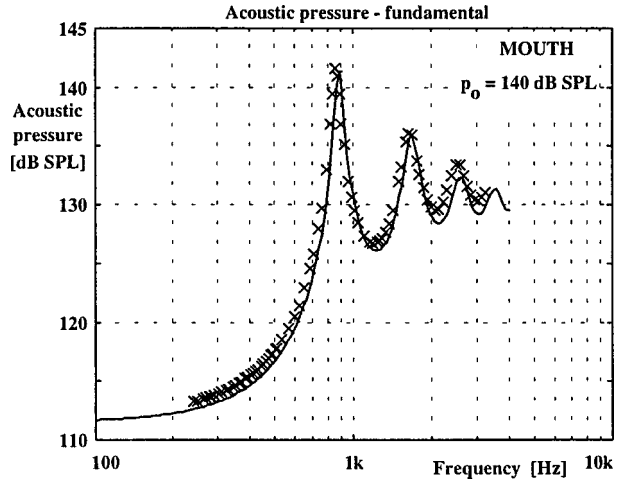

FIG. 4. Sound pressure level at the horn mouth of the fundamental (relative to the reference pressure $p_r=2\times10^{-5}$ Pa) versus the excitation frequency (ν_0) for a fixed level of 140 dB SPL at the throat. ($\times\times\times$) experimental results, (———) theoretical predictions [Eq. (24)]. The voltage level applied to the compression chamber is adjusted in order to maintain the pressure level constant at the throat. The model parameter p_0 in Eq. (24) corresponds to 140 dB SPL at the throat.

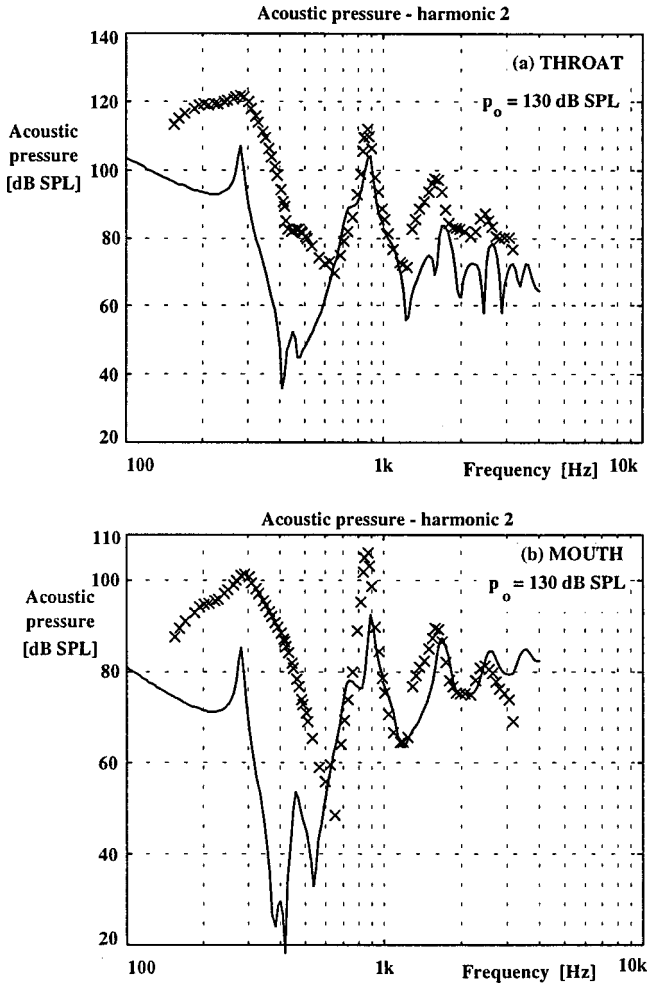

FIG. 5. Sound pressure level of the second harmonic (relative to the reference pressure $p_r = 2\times10^{-5}$ Pa) versus the excitation frequency (ν_0) for a fixed level of 130 dB SPL at the throat. ($\times\times\times$) experimental results, (———) theoretical predictions [Eq. (32)]. The model parameter $p_0 = p_1(x=0,\nu_0)$ corresponds to 130 dB SPL at the throat. Acoustic pressure: (a) at the throat and (b) at the mouth.

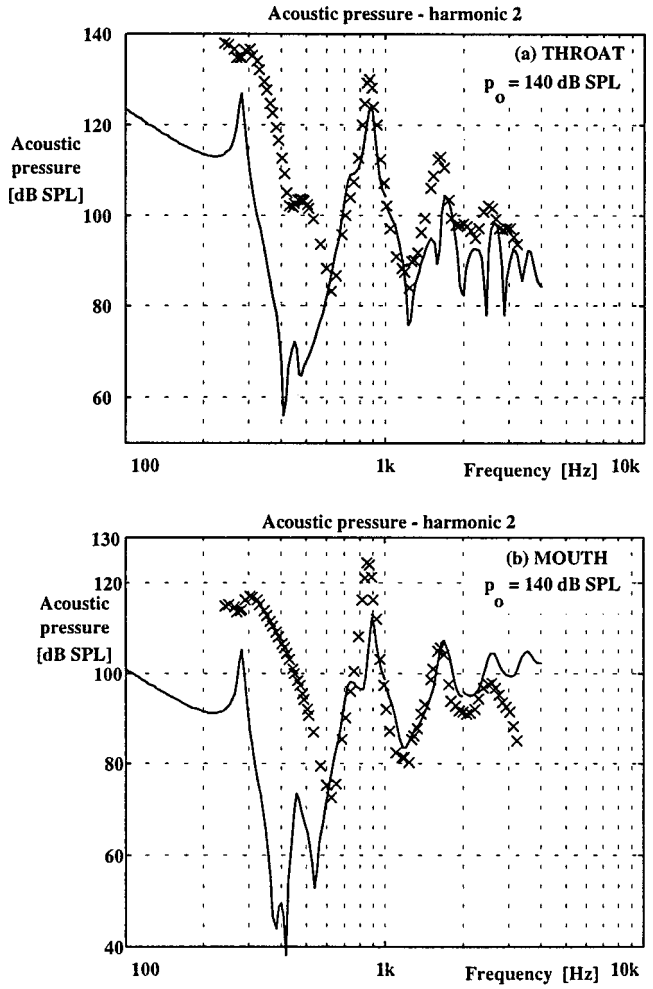

FIG. 6. Sound pressure level of the second harmonic (relative to the reference pressure $p_r = 2\times10^{-5}$ Pa) versus the excitation frequency (ν_0) for a fixed level of 140 dB SPL at the throat. ($\times\times\times$) Experimental results, (———) theoretical predictions [Eq. (32)]. The model parameter $p_0 = p_1(x=0,\nu_0)$ corresponds to 140 dB SPL at the throat. Acoustic pressure: (a) at the throat and (b) at the mouth.

ment exists between the measured and predicted [Eq. (34), Sec. IV] second harmonic mouth levels.

The amplitude of the mouth measured peak at $\nu_0 \approx 900$ Hz is greater than predicted; the cause of this difference is not clear, but could be associated with the lack of precision in the predicted radiation impedance.

It can be seen from the experimental results [Figs. 5(b) and 6(b)] that a drop in the second harmonic mouth level appears after 3 kHz. This behavior is not predicted by the plane-wave model developed in Sec. IV. The plane-wave limitation is valid only when the wavelength of the sound transmitted is much longer than the mouth diameter of the horn ($\lambda \gg \phi = 81$ mm), in other words when the frequency of the wave is much smaller than $c_0/\phi \approx 4$ kHz. This point may indicate the limitations of the model for prediction of the second harmonic at high frequencies.

Below $\nu_0 \approx 900$ Hz the agreement between measured and predicted [Eqs. (32) and (37), Sec. IV] second harmonic mouth results is not so good. The nonlinear behavior of the compression driver is responsible for this difference. Note that we have observed[36] good agreement between the predicted second harmonic mouth levels and the experimental results obtained by Holland and Morfey[31] with the same horn but excited by a powerful compression driver having a weak harmonic distortion ($\approx$1%) over the frequency range.

VII. SUMMARY AND CONCLUSIONS

Nonlinear axial standing waves in the interior of an acoustic horn have been investigated theoretically and experimentally. The propagation of finite-amplitude waves is modeled by a perturbation expansion, applied to a one-dimensional lossless propagation model with rigid-wall boundary conditions; thus wall boundary layer effects are neglected. Specific results are presented for an exponential horn driven by a sinusoidal velocity at the throat plane, with linear reflections included at the mouth. By limiting the expansion to second-order terms, it is possible to find frequency and time domain expressions for both the fundamental and second harmonic pressure, as a function of position along the horn.

In order to validate the model, an experimental setup was developed for measuring the fundamental (ν_0) and sec-

ond harmonic ($2\nu_0$) response of a sinusoidally excited horn. As might be expected in view of the weak nonlinearity, the fundamental component at the mouth of the horn shows good agreement between measured and predicted levels, for imposed throat levels [sound pressure p_0] of 130 and 140 dB *re* 20 μPa and a range of driving frequencies ν_0 from 200 Hz to 3 kHz.

Quite good agreement is also found at the mouth between predicted and measured second harmonic levels above $\nu_0 = 700$ Hz. However, in the low-frequency range 200–700 Hz, the comparison is poor. This lack of agreement below 700 Hz is believed to be caused by compression driver distortion producing excessive second harmonic at the throat. If this is the case, better agreement could be obtained by using an appropriate driver with low compression ratio.

Further work is recommended in two areas:

(i) a more detailed controlled experiment, in which harmonic amplitudes and phases of the pressure response are measured at various points along a horn when it is driven at various amplitudes, and

(ii) development of a generalized calculation scheme in which the present model is applied to successive exponential elements, thus permitting distortion level predictions for arbitrary horn profiles.

ACKNOWLEDGMENTS

This work was supported by the Engineering and Physical Sciences Research Council (U.K.). The authors thank Dr. Keith Holland for helpful discussions during different stages of this project, and Brian Edwards for his technical advice. We further wish to thank Dr. Mark Hamilton and the anonymous reviewers for their comments and suggestions on an earlier version of this manuscript.

APPENDIX: OUTPUT DRIVER IMPEDANCE Z_0

The driver is modeled in the ordinary way,[37,38] as a mass-spring-dashpot system driven by a coil of length l in a magnet gap with induction B (see the simplified physical model shown in Fig. A1). The diaphragm is assumed to act as a piston with a mass M_d and an area S_d. The mechanical compliance C_d is related to the suspension stiffness. Compliances C_b and C_f take into account the effective spring constant of the gas in the back and the front enclosures, respectively. It is assumed that the enclosures are small

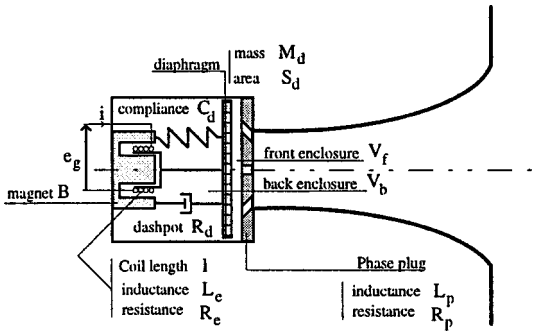

FIG. A1. Simplified physical model of compression driver.

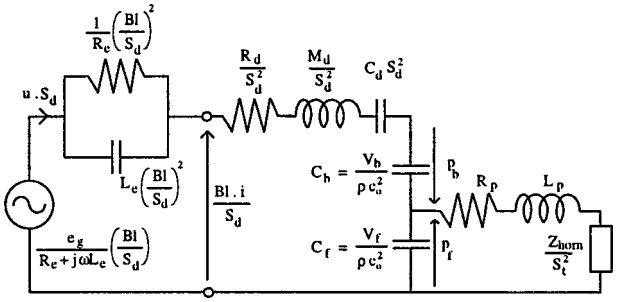

FIG. A2. Lumped-element equivalent circuit for the physical model in the acoustic impedance domain. u is the velocity of diaphragm.

enough that wave effects in the enclosures can be neglected at the low frequencies of interest. Effect of the phase plug is modeled with a mass term L_p and a loss term R_p. Nonlinearities caused by the adiabatic behavior of air in the front enclosure, between the diaphragm and the phase plug, are not taken into account in this study.

A lumped-element equivalent circuit for the physical model of the compression driver is shown in Fig. A2. All elements have been brought into the acoustic impedance domain and their estimated values are listed in Table I. The output driver impedance Z_{a0} at the throat is derived from this circuit and expressed as

$$Z_{a0} = \frac{Z_f (Z_b + Z_{\mathrm{dia}})}{Z_f + Z_b + Z_{\mathrm{dia}}} + Z_p , \tag{A1}$$

with

$$\begin{aligned} &Z_f = \frac{1}{j\omega C_f}, \quad Z_b = \frac{1}{j\omega C_b}, \\ &Z_{\mathrm{dia}} = \frac{1}{S_d^2}\left\{ R_d + j\omega M_d + \frac{1}{j\omega C_d} \right\}, \\ &Z_p = R_p + j\omega L_p . \end{aligned} \tag{A2}$$

[1] C. H. Sherman and J. L. Butler, ''Analysis of harmonic distortion in electroacoustic transducers,'' J. Acoust. Soc. Am. **98**, 1596–1611 (1995).
[2] C. H. Sherman, J. L. Butler, and A. L. Butler, ''Analysis of harmonic distortion in electroacoustic transducers under indirect drive conditions,'' J. Acoust. Soc. Am. **101**, 297–314 (1997).
[3] W. Klippel, ''Modeling the nonlinearities in horn loudspeakers,'' J. Audio Eng. Soc. **44**(6), 470–480 (1996).
[4] W. Klippel, ''Nonlinear system identification for horn loudspeakers,'' J. Audio Eng. Soc. **44**(10), 811–820 (1996).
[5] H. Schurer, A. P. Berkhoff, C. H. Slump, and O. E. Herrmann, ''Modeling and compensation of nonlinear distortion in horn loudspeakers,'' J. Audio Eng. Soc. **43**(7/8), 592–598 (1995).
[6] G. B. Whitham, *Linear and Nonlinear Waves* (Wiley-Interscience, New York, 1974), pp. 143–208.
[7] L. Bjørnø, *Acoustics and Vibration Progress* (Chapman and Hall, London, 1976), Vol. 2, pp. 102–198.
[8] O. V. Rudenko and S. I. Soluyan, *Theoretical Foundations of Nonlinear Acoustics* (Studies in Soviet Science, Consultants Bureau, Plenum, New York, 1977), pp. 1–77.
[9] A. D. Pierce, *Acoustics. An Introduction to its Physical Principles and Applications* (Acoustical Society of America, New York, 1991), pp. 566–617.
[10] D. G. Crighton, A. P. Dowling, J. E. Ffowcs Williams, M. Heckl, and F. G. Leppington, *Modern Methods in Analytical Acoustics* (Springer-Verlag, London, 1992), pp. 648–670.
[11] S. Makarov and M. Ochmann, ''Nonlinear and thermoviscous phenomena, Part I,'' Acustica **82**(4), 579–606 (1996).

[12] S. Makarov and M. Ochmann, ''Nonlinear and thermoviscous phenomena, Part II,'' Acustica **83**(2), 197–222 (1997).
[13] S. Makarov and M. Ochmann, ''Nonlinear and thermoviscous phenomena, Part III,'' Acustica **83**(5), 827–846 (1997).
[14] M. F. Hamilton and D. T. Blackstock (eds.), *Nonlinear Acoustics* (Academic, San Diego, 1998).
[15] A. G. Webster, ''Acoustical impedance, and the theory of horns and of the phonograph,'' Proc. Natl. Acad. Sci. USA **5**, 275–282 (1919).
[16] E. Eisner, ''Complete solution of the Webster horn equation,'' J. Acoust. Soc. Am. **41**, 1126–1146 (1967).
[17] J. T. Post and E. L. Hixson, ''A modeling and measurement study of acoustic horns,'' Report of the Electroacoustics Research Laboratory—Department of Electrical and Computer Engineering—The University of Texas at Austin (1994).
[18] K. R. Holland, F. J. Fahy, and C. L. Morfey, ''Prediction and measurement of the one-parameter behaviour of horns,'' J. Audio Eng. Soc. **39**(5), 315–337 (1991).
[19] W. Klippel, ''Nonlinear wave propagation in horns and ducts,'' J. Acoust. Soc. Am. **98**, 431–436 (1995).
[20] V. Pagneux, N. Amir, and J. Kergomard, ''A study of wave propagation in varying cross-section waveguides by modal decomposition. Part I. Theory and validation,'' J. Acoust. Soc. Am. **100**, 2034–2048 (1996).
[21] N. Amir, V. Pagneux, and J. Kergomard, ''A study of wave propagation in varying cross-section waveguides by modal decomposition. Part II. Results,'' J. Acoust. Soc. Am. **101**, 2504–2517 (1997).
[22] Y. Rocard, ''Sur la propagation des ondes sonores d'amplitude finie,'' C. R. Hebd. Seances Acad. Sci. **196**, 161–164 (1933) (ISSN: 0001-4036, OCLC: 1124612).
[23] Y. Rocard, *Théories Mécaniques* (Hermann & Cie, Paris, 1935), Vol. II, pp. 5–39.
[24] S. Goldstein and N. W. McLachlan, ''Sound waves of finite amplitude in an exponential horn,'' J. Acoust. Soc. Am. **6**, 275–278 (1935).
[25] A. L. Thuras, R. T. Jenkins, and H. T. O'Neil, ''Extraneous frequencies generated in air carrying intense sound waves,'' J. Acoust. Soc. Am. **6**, 173–180 (1935).
[26] T. Zamorski, ''Waves with finite amplitude in Bessel horns,'' Arch. Acoust. **15**(3–4), 531–540 (1990).
[27] T. Zamorski, ''Propagation of sound waves of finite amplitude in a horn at frequencies below the cut-off frequency,'' Arch. Acoust. **22**(4), 411–421 (1997).
[28] W. Chester, ''Nonlinear resonant oscillations of a gas in a tube of varying cross-section,'' Proc. R. Soc. London, Ser. A **444**, 591–604 (1994).
[29] W. Chester, ''Resonant oscillations in closed tubes,'' J. Fluid Mech. **18**, 44–64 (1964).
[30] Y. A. Il'inskii, B. Lipkens, T. S. Lucas, T. W. Van Doren, and E. A. Zabolotskaya, ''Nonlinear standing waves in an acoustical resonator,'' J. Acoust. Soc. Am. **104**(5), 2664–2674 (1998).
[31] K. R. Holland and C. L. Morfey, ''A model of nonlinear wave propagation in horns,'' J. Audio Eng. Soc. **44**(7/8), 569–580 (1996).
[32] E. Czerwinski, A. Voishvillo, S. Alexandrov, and A. Terekhov, ''A model of nonlinear wave propagation in horns,'' J. Audio Eng. Soc. **47**(6), 427–446 (1999).
[33] P. M. Morse and H. Feshbach, *Methods of Theoretical Physics* (McGraw–Hill, New York, 1953), pp. 523–530.
[34] B. H. Smith, ''An investigation of the air chamber of horn type loudspeaker,'' J. Acoust. Soc. Am. **25**, 305–312 (1953).
[35] J.-P. Dalmont, C. J. Nederveen, and N. Joly, ''Radiation impedance of tubes with different flanges: numerical and experimental investigations,'' J. Sound Vib. (accepted).
[36] P. Béquin, ''The investigation of nonlinear sound propagation in acoustic horns,'' ISVR internal report (1995).
[37] L. L. Beranek, *Acoustics* (American Institute of Physics, New York, 1988), pp. 183–207, 259–284.
[38] M. Rossi, *Electroacoustique—traité d'électricité de l'école polytechnique fédérale de Lausanne* (Presses polytechniques romandes, 1986), Vol. XXI, pp. 283–367.

Numerical model for nonlinear standing waves and weak shocks in thermoviscous fluids

Christian Vanhille[a)]
E.S.C.E.T. Universidad Rey Juan Carlos, Tulipán, s/n. 28933 Móstoles, Madrid, Spain

Cleofé Campos-Pozuelo[b)]
Instituto de Acústica (C.S.I.C.), Serrano, 144, 28006 Madrid, Spain

(Received 1 November 1999; accepted for publication 15 February 2001)

Nonlinear standing waves in a one-dimensional tube are studied numerically by using a finite-difference algorithm. The numerical code models the acoustic field in resonators for homogeneous, thermoviscous fluids. Calculations are performed exclusively in the time domain, and all harmonic components are obtained by one resolution. The fully nonlinear differential equation is written in Lagrangian coordinates. It is solved without truncation. Effects of absorption are included. Displacement and pressure wave forms are calculated at different locations and results are shown for different excitation levels and tube lengths. Amplitude distributions along the resonator axis for every harmonic component are also evaluated. Simulations are performed for amplitudes ranging from linear to strongly nonlinear and weak shock. A very good concordance with classic experimental and analytical results is obtained.
[DOI: 10.1121/1.1366318]

PACS numbers: 43.25.Gf [MFH]

I. INTRODUCTION

High-intensity applications of acoustic energy in industrial processing are based on nonlinear effects produced by finite-amplitude pressure variations. Resonant chambers are usually used in real applications since high pressures can be reached. Therefore knowledge of the nonlinear pressure distribution inside resonant cavities is essential for the development of practical systems. This paper deals with a simulation code to model finite-amplitude standing waves in thermoviscous fluids.

Classic works on analytical approximations of nonlinear progressive waves are found in the literature.[1] There are several reviews on the development of nonlinear acoustics,[2–4] and the main contributions in this field were compiled and edited by Beyer in 1984.[2] Analytical or experimental studies of the propagation of plane, cylindrical, and spherical finite-amplitude waves as well as one-dimensional standing waves have been reported in the literature.[5–12]

Several computational methods for progressive waves have been developed in the frequency and time domains. A recent review by Ginsberg and Hamilton is given in Ref. 13. The time-domain algorithms for modeling finite-amplitude propagating pulses which use the finite-difference method[14–17] and a frequency-domain algorithm for modeling three-dimensional propagation of acoustic waves of finite but moderate amplitude[18] should be noted especially.

Far fewer numerical algorithms for the solution of one-dimensional standing waves have been reported in the literature. Ilinskii *et al.*[19] describe a frequency-domain numerical algorithm to solve a nonlinear wave equation in terms of the velocity potential. Some publications can be found in the time domain.[20,21] They treat a nonlinear resonance problem in an acoustic chamber by using existing numerical methods.

In this work a new finite-difference numerical algorithm for modeling one-dimensional standing waves of finite amplitude is described. The differential equation of motion is obtained from the conservation laws and the Tait–Kirkwood isentropic equation of state without truncation. Lagrangian coordinates are used. The numerical algorithm works in the time domain: The whole wave form is then obtained by only one solution. The transient phase is completely modeled and any time function can be used as excitation. The simulation code is able to simulate waves of infinitesimal amplitude, finite but moderate amplitude, and strongly nonlinear waves, including weak shock.[22] Stability and convergence of the algorithm do not impose restrictions on physical parameters. The only limitation of applicability of the model comes from the consideration of an isentropic state equation. We then have to consider small dissipation effects and isentropic evolution of the fluid.[23] A criterion giving the limits of theoretical applicability of the model is obtained. This depends on the level of the wave and on the duration of the study (the number of periods for a given frequency).

II. FUNDAMENTAL EQUATIONS

In this study we consider nonlinear standing waves in a homogeneous thermoviscous fluid. In order to obtain a one-dimensional nonlinear wave equation, the equation of state and equations expressing the conservation of mass and momentum are considered.[1] The isentropic state equation of Tait–Kirkwood is used (see Chap. 2 in Ref. 13 and Ref. 24)

$$\frac{p+\Pi}{p_0+\Pi}=\left(\frac{\rho}{\rho_0}\right)^{\chi}, \tag{1}$$

a)Electronic mail: c.vanhille@escet.urjc.es
b)Electronic mail: ccampos@ia.cetef.csic.es

where p is the pressure, ρ is the density of the fluid, p_0 is the ambient pressure, ρ_0 is the ambient density, and Π and χ are characteristic constants of the fluid. This state equation reduces to the ideal-gas state equation for $\Pi=0$ and $\chi=\gamma$, where γ is the specific heat ratio. Note that in Eq. (1) there is no connection in general between the index χ and the specific heat ratio of the fluid. Equation (1) is also valid for seawater.[24]

From the state equation and the mass-conservation and momentum-conservation equations written in Lagrangian coordinates, the derivation of the following fully nonlinear wave equation can be carried out:

$$\rho_0 \frac{\partial^2 u}{\partial t^2} = \chi(p_0+\Pi) \frac{1}{\left(1+\frac{\partial u}{\partial x}\right)^{\chi+1}} \frac{\partial^2 u}{\partial x^2} + \rho_0 \nu b \frac{\partial^3 u}{\partial t \partial x^2}, \tag{2}$$

where u is the displacement and ν is the kinematic shear viscosity of the fluid. The parameter

$$b = \frac{\eta'}{\eta} + \frac{4}{3} + \frac{\kappa}{\eta}\left(\frac{1}{c_v} - \frac{1}{c_p}\right)$$

is the so-called viscosity number,[1,4,25] where η is the shear viscosity, η' is the dilatational viscosity, c_v is the specific heat at constant volume, c_p is the specific heat at constant pressure, and κ is the thermal conductivity. It corresponds to the assumption of weak nonlinearity and small dissipation. t and x are, respectively, the time and one-dimensional spatial coordinates.

In nonlinear acoustics, fluids are often characterized and described by the two parameters

$$A = \rho_0 \left(\frac{\partial p}{\partial \rho}\right)_{S,\rho=\rho_0}, \quad B = \rho_0^2 \left(\frac{\partial^2 p}{\partial \rho^2}\right)_{S,\rho=\rho_0},$$

where S is the entropy. From Eq. (1) we can easily obtain

$$A = (p_0+\Pi)\chi, \quad B = (p_0+\Pi)\chi(\chi-1). \tag{3}$$

The parameter A is sufficient to describe the linear acoustic behavior of the fluid and B is necessary for the knowledge of its nonlinear characteristics. Values of B/A are given in the literature for common fluids (see Chap. 2 in Ref. 13). On the other hand, if the nonlinear acoustic behavior of the fluid is known, parameters A and B can be deduced and the state equation of the fluid can then be exactly written.

The code incorporates a calculation of the acoustic pressure wave form and distribution. The following expression, deduced from Eq. (1) and the mass conservation in Lagrangian coordinates, is used:

$$p+\Pi = \frac{p_0+\Pi}{\left(1+\frac{\partial u}{\partial x}\right)^{\chi}}. \tag{4}$$

We consider standing waves in a rigid-walled tube of length L excited at one of its ends by a harmonic source of amplitude u_0 and pulsation $\omega=2\pi f$, where f is the excitation frequency. The following boundary conditions are applied:

$$\begin{aligned} &x=0, \quad u(0,t)=u_0 \sin(\omega t), \\ &x=L, \quad u(L,t)=0. \end{aligned} \tag{5}$$

The fluid is assumed to be at complete rest at $t=0$, i.e., particle displacement and velocity are null at $t=0$. The following initial conditions are employed:

$$t=0 \begin{cases} u(x,0)=0 \\ \dfrac{\partial u(x,0)}{\partial t}=0, \quad \forall x \neq 0 \end{cases}. \tag{6}$$

An important nondimensional parameter exists: the acoustic Mach number,

$$M = ku = 2\pi \frac{f}{c_0} u = \frac{\omega}{c_0} u = 2\pi \frac{u}{\lambda}, \tag{7}$$

$c_0=(\chi(p_0+\Pi)/\rho_0)^{1/2}$ is the low-amplitude velocity of sound, $k=\omega/c_0$ is the wave number, and $\lambda=c_0/f$ is the wavelength. The order of M points out the importance of the nonlinear behavior of the wave. The acoustic Mach number on the sound source is $M_0=ku_0=2\pi(f/c_0)u_0=(\omega/c_0)u_0=2\pi(u_0/\lambda)$.

The fundamental equations that we have considered are valid for small attenuation and isentropic waves.[3] It indicates that the increase of entropy $\Delta S \ll 1$ and thus the anisentropic state equation of Tait–Kirwood

$$\frac{p+\Pi}{p_0+\Pi} = \left(\frac{\rho}{\rho_0}\right)^{\chi} \exp\left(\frac{\Delta S}{c_v}\right) \tag{8}$$

yields to Eq. (1).[13] However entropy is produced at the shock front and accumulated everywhere in the tube as time goes by (twice a period). This fact clearly indicates that a short time of study limits the production of entropy. The entropy produced at the shock front is of $O(M^3)$,

$$\Delta S = \frac{\beta c_0^2}{6T_0} M^3, \tag{9}$$

where $\beta=1+(\chi-1)/2$ is the coefficient of nonlinearity and T_0 is the ambient absolute-temperature of the fluid.[12,25] Throughout NP periods the variation of entropy is $\Delta S = O(2\mathrm{NP}\,M^3)$. The increase of entropy and, therefore, the validity of the isentropic equation depend on M and NP. If $O(2\mathrm{NP}\,M^3) \ll 1$ the isentropic equation and our model are valid. At fixed M, an applicability criterion is established,

$$\mathrm{NP} \ll \frac{1}{2M^3}. \tag{10}$$

Table I shows this limiting value for some values of M. It should be noted that the transient phase is much shorter when using large M_0 and NP is fixed to enable us to observe

TABLE I. Model applicability criterion. Limiting value of the number of periods for some M. $L=\lambda/2$.

M	Criterion	Comments
0.01	$\mathrm{NP} \ll 5\times10^5$	Always verified
0.05	$\mathrm{NP} \ll 4\times10^3$	Always verified
0.1	$\mathrm{NP} \ll 5\times10^2$	Always verified
0.5	$\mathrm{NP} \ll 4$	Never verified

the establishment of the standing wave. The use of the criterion assures the success of the modeling. However some other authors have published works at high M by considering an isentropic state equation and good results have been obtained by comparing with experimental data.

III. NUMERICAL FORMULATION

In this section, the numerical scheme is described. This is a finite-difference algorithm.[26–28] A new numerical technique is used to find the solution $u(x,t)$ of the nonlinear problem. Once u is calculated, the pressure p is obtained by Eq. (4).

A time-domain numerical approach based on a new finite-difference algorithm is developed to solve the fully nonlinear wave equation, without truncation. The complete solution is carried out in the time domain, i.e., all the harmonic components are obtained by only one solution and, therefore, computation time is saved. In the differential equation the dissipation effects of the fluid factorize a third-order partial derivative. Since the fluid is at complete rest at the outset, the transient phase is completely modeled. The model can support any small attenuation parameters without any stability or convergence problem, and cases from linear to strongly nonlinear behavior can be studied.

Dimensionless variables are introduced into the partial differential equation, and boundary and initial conditions. Spatial and temporal variation scales are then coherent for any kind of tube length or frequency. To this purpose, two dimensionless variables are created,

$$X=\frac{x}{L}, \quad T=\omega t. \tag{11}$$

Therefore, partial derivatives are

$$\frac{\partial u}{\partial u}=\frac{1}{L}\frac{\partial u}{\partial X}, \quad \frac{\partial u}{\partial t}=\omega\frac{\partial u}{\partial T}, \tag{12}$$

$$\frac{\partial u}{\partial x}=\frac{1}{L^2}\frac{\partial^2 u}{\partial X^2}, \quad \frac{\partial^2 u}{\partial t^2}=\omega^2\frac{\partial^2 u}{\partial T^2}, \quad \frac{\partial^3 u}{\partial x^2\partial t}=\frac{\omega}{L^2}\frac{\partial^3 u}{\partial X^2\partial T}.$$

Thus wave equation (2) is

$$\frac{\partial^2 u}{\partial T^2}-\frac{\nu b}{\omega L^2}\frac{\partial^3 u}{\partial X^2\partial T}=\frac{c_0^2}{\omega^2 L^2}\left(1+\frac{1}{L}\frac{\partial u}{\partial X}\right)^{-\chi-1}\frac{\partial^2 u}{\partial X^2}. \tag{13}$$

The acoustic pressure [Eq. (4)] is

$$p+\Pi=\frac{\rho_0 c_0^2}{\chi}\left(\frac{1}{1+\frac{1}{L}\frac{\partial u}{\partial X}}\right)^{\chi}. \tag{14}$$

The boundary and initial conditions [Eqs. (5) and (6)] are

$$X=0, \quad u(0,T)=u_0\sin(T),$$

$$X=1, \quad u(1,T)=0, \tag{15}$$

$$T=0\begin{cases} u(X,0)=0 \\ \dfrac{\partial u(X,0)}{\partial T}=0, \quad \forall X\neq 0. \end{cases}$$

The $X-T$ plane is divided into sets of equal rectangles of sides $\delta X=h=1/(\mathrm{NPS}-1)$ and $\delta T=\tau$. The discretization of X is $X_m=(m-1)h$ $(m=1\cdots\mathrm{NPS})$ and the discretization of T is $T_n=(n-1)\tau$ $(n=1\cdots\mathrm{NP}T)$. The variable X varies from 0 to 1 and the variable T from 0 to 2πNP where NP represents the number of periods. We denote by $u_{m,n}$ (respectively, $p_{m,n}$) the displacement (respectively, pressure) at the node (X_m,T_n) of the plane.

The absorption term factorizes a third-order partial derivative solved by a finite-difference scheme with a leading error of high order. This scheme is a multi-time-step, implicit, six-point scheme of order $O(\tau^2+h^2)$. This technique is obtained by approximation of displacements up to the fifth order.

The approximations employed for the derivatives appearing in Eq. (13) are

$$\left.\frac{\partial^3 u}{\partial X^2\partial T}\right|_{m,n}=\frac{(u_{m-1}-2u_m+u_{m+1})_{n+1}+(-u_{m-1}+2u_m-u_{m+1})_{n-1}}{2h^2\tau}+O(\tau^2+h^2), \tag{16}$$

$$\left.\frac{\partial^2 u}{\partial X^2}\right|_{m,n}=\frac{(u_{m-1}-2u_m+u_{m+1})_n}{h^2}+O(h^2), \quad \left.\frac{\partial^2 u}{\partial T^2}\right|_{m,n}=\frac{u_{m,n+1}-2u_{m,n}+u_{m,n-1}}{\tau^2}+O(\tau^2), \tag{17}$$

$$\left.\frac{\partial u}{\partial X}\right|_{m,n}=\frac{-u_{m-1,n}+u_{m,n}}{h}+O(h). \tag{18}$$

The generation of results about consistency, stability, and convergence of the nonlinear scheme is a very difficult task and we can only obtain results for a corresponding linearized scheme and use a safety factor when carrying out a

nonlinear simulation.[28] Therefore, we consider the term

$$\left(1+\frac{1}{L}\frac{\partial u}{\partial X}\right)^{-\chi-1}=C_{\mathrm{loc}}$$

as a constant in a local sense. We are then able to estimate consistency, stability, and convergence of the linearized scheme. An exhaustive study of consistency, stability, and convergence of an equivalent linear scheme is reported in Ref. 29. However the ''nonlinear term'' is not constant here but depends upon the solution itself. The study of Ref. 29 enables us to monitor a nonlinear calculation by taking, however, considerable caution since it corresponds to a local linearization of the equation. Nevertheless, experience indicates that the results are satisfactory.

The spatial step h is an input to the numerical code. τ is evaluated from the h value by using

$$\tau=\frac{-\nu b\pi}{c_0\lambda}+\pi\sqrt{\frac{(\nu b)^2}{c_0^2\lambda^2}+h^2}. \tag{19}$$

This value assures the stability and convergence of the linear corresponding scheme,[29] and thus, as seen before, of the nonlinear finite-difference scheme.

Since the numerical scheme is implicit, a linear system of $(\mathrm{NPS}-2)$ equations with $(\mathrm{NPS}-2)$ unknown values has to be solved at each time step. The solution of the system is carried out by the Gauss method.[30] The computational code is written in FORTRAN 77 and uses double precision real numbers. Pressure is evaluated from displacement values through a classic progressive finite-difference scheme.

The place to reserve for storage on disk is the following $(113*\mathrm{NP}T*\mathrm{NPS})/(1024^2)$ Mbytes. This place includes two files (for displacement and pressure) written in columns which make postprocessing easier.

IV. RESULTS

The numerical algorithm developed to model nonlinear standing waves has been applied to different cases. Results are shown in this section. All the results are for air-filled rigid-walled tubes. The density $\rho_0=1.29\,\mathrm{kg/m^3}$ and the specific heat ratio $\gamma=1.4$ are used in all the calculations. For all the representations, the convergence of the numerical scheme is obtained by selecting a suitable number of spatial points. The attenuation values are given for the excitation frequency. We use the parameter α defined by

$$\alpha=\alpha_{\mathrm{bulk}}+\alpha_{\mathrm{wall}}, \tag{20}$$

where

$$\alpha_{\mathrm{bulk}}=\frac{\omega^2\nu b}{2c_0^3},$$

$$\alpha_{\mathrm{wall}}=2^{-3/2}\left(\frac{\omega\eta}{\rho_0 c_0^2}\right)^{1/2}\left[1+\frac{\gamma-1}{\mathrm{Pr}^{1/2}}\right]\frac{\mathrm{per}}{\mathrm{ar}},$$

$$\mathrm{Pr}=\frac{\eta c_p}{\kappa}$$

is the Prandtl number, per is the perimeter of the tube, and ar is the cross-sectional area of the tube.[25]

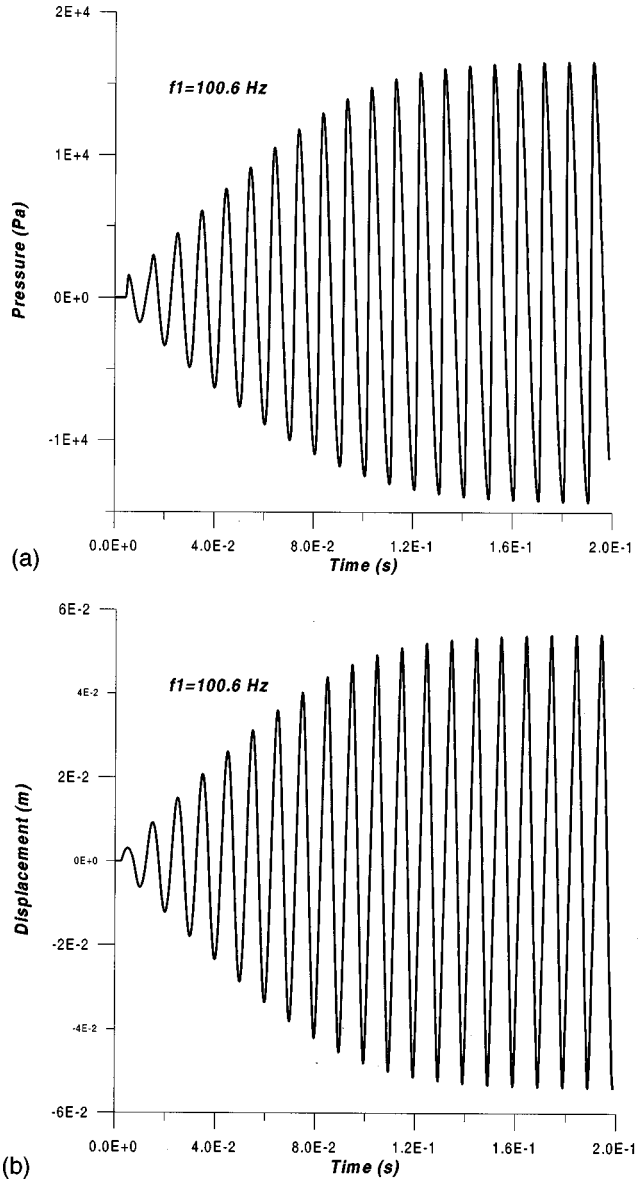

FIG. 1. Standing wave establishment at the fundamental frequency $f_1=100.6$ Hz. $L=\lambda/2$ and $M_0=0.0059$. (a) Pressure at the reflector. (b) Displacement at the center of the tube.

We now test the performance of our model by comparing with the results obtained experimentally by Saenger and Hudson,[10] Cruikshank, Jr.,[9] and analytically by Chester.[7] Thus, we consider a 0.048-m-diam tube of length $L=1.70\,\mathrm{m}$; $c_0=342.39\,\mathrm{m/s}$. The fundamental frequency is $f_1=100.6\,\mathrm{Hz}$ for which $M_0=0.0059$ is considered. Figure 1 shows the standing wave establishment from the complete rest at f_1 for the pressure at the reflector and for the displacement at the center of the tube. Figure 2 shows the finite-amplitude pressure waves and periodic shocks observed at the closed end of the tube for frequencies around f_1. We see that at $f=100.7\,\mathrm{Hz}$ the shock strength (peak to peak) is 30 940 Pa (183.79 dB, $M=0.1$). The experimental value is 28 798 Pa (183.17 dB).[10] A very good accuracy is then obtained. The small difference between the two results can be due to the evaluation of the parameters c_0 (calculated from L and f_1), and especially α (approximated using theoretical values of the parameters at ambient temperature); a small

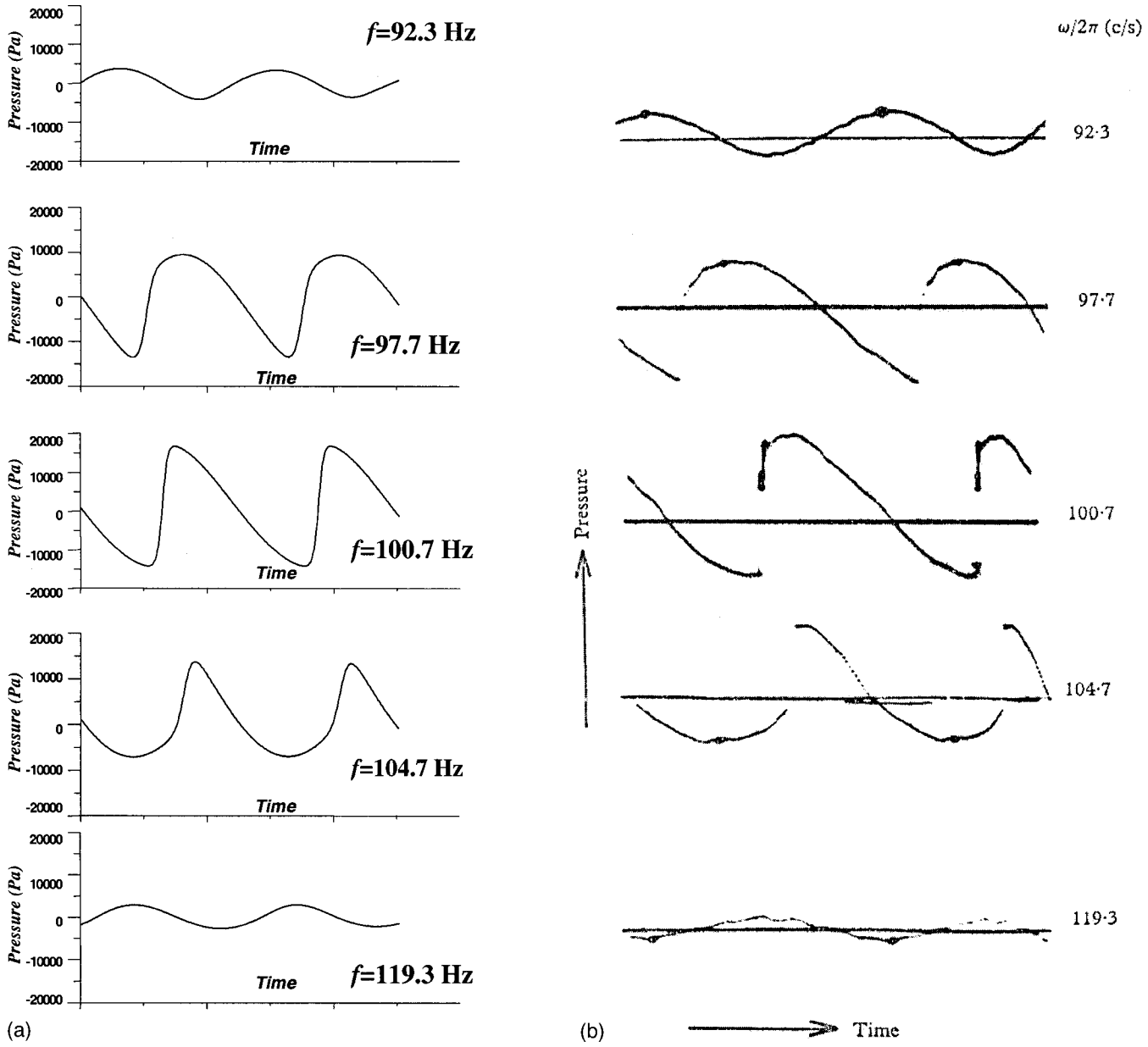

FIG. 2. Finite-amplitude pressure waves and periodic shocks observed at the closed end of the tube for frequencies near the fundamental frequency $f_1 = 100.6$ Hz. $L = \lambda/2$ and $M_0 = 0.0059$. (a) Calculations using the simulation code. (b) Experimental results from Saenger *et al.* (Ref. 10).

deviation of the value α can generate differences of the same order as those that have been obtained. The wave shapes (Fig. 2) are very similar to the one shown in Refs. 10, 9, and 7. This example demonstrates the very good concordance between our results and experimental or analytical results. Thus, our model is qualitatively and quantitatively validated in the case of high acoustic Mach number waves. Some computational data are now given: 20 periods are analyzed, 101 space points and 4924 time points are used for discretization, CPU time is about 16 minutes (Pentium II MMx 300 MHz, RAM: 64 MB).

At f_1 we now study the evolution of the finite-amplitude wave when ranging M_0 from a linear case up to a very nonlinear wave. As we have seen in Sec. II, our model is still valid when employing high displacement values at the piston throughout a relatively small number of periods: NP ranges, respectively, from 75 to 3 periods. Figure 3 shows the variation of the pressure amplitude at the reflector versus excitation. The nonexistence of saturation (in the sense of no dependence on source amplitude and in the applicability limits of the model) in the resonant oscillation in the cylindrical closed tube of length $\lambda/2$ is evident here. The behavior of the pressure amplitude seems to act like the square root of u_0 in the $\lambda/2$-length tube. This result is in concordance with Temkin's theory.[12] However, as seen in Sec. II, a limit of applicability of our model could exist. For instance, in the strongest nonlinear case shown in Fig. 3, the isentropic condition limits the number of periods to $NP \ll 3$. The data would indicate that our model is not valid in this case. However other authors consider an isentropic state equation for such orders of M.[19]

Figure 4 shows the steady state pressure amplitude as a function of time and space at f_1. Examples are shown for a linear case (A) and the strongly nonlinear case corresponding

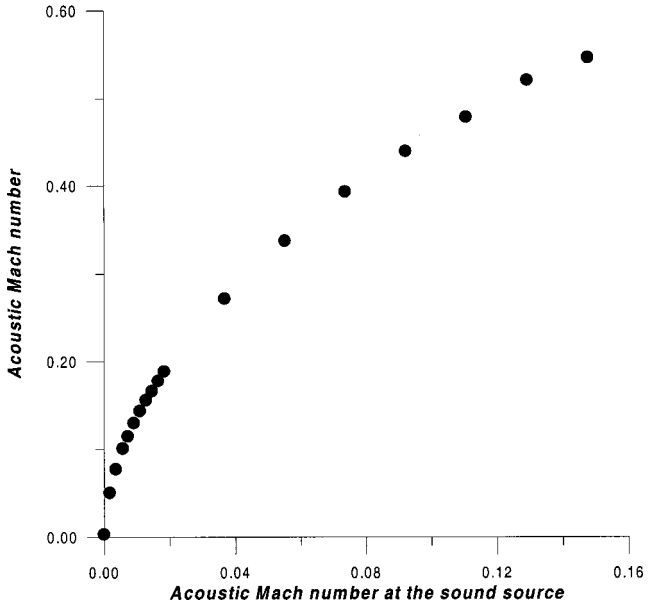

FIG. 3. Variation of the pressure amplitude at the reflector versus excitation at the fundamental frequency $f_1 = 100.6$ Hz. $L = \lambda/2$.

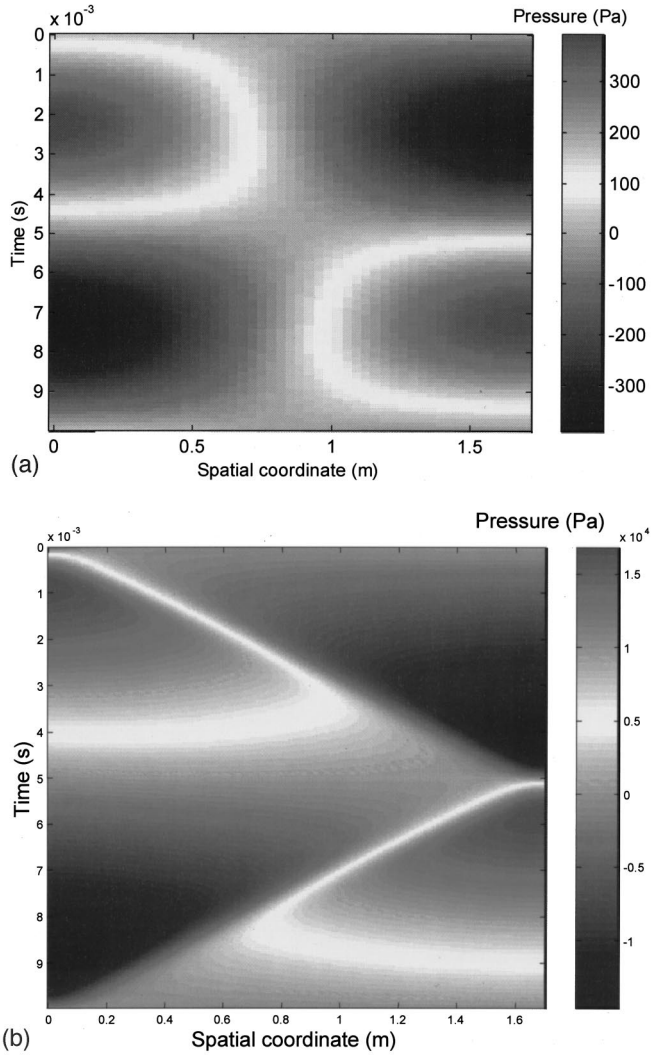

FIG. 4. Steady state pressure amplitude as a function of time and space at the fundamental frequency $f_1 = 100.6$ Hz. $L = \lambda/2$. (a) Linear, (b) $M_0 = 0.0059$.

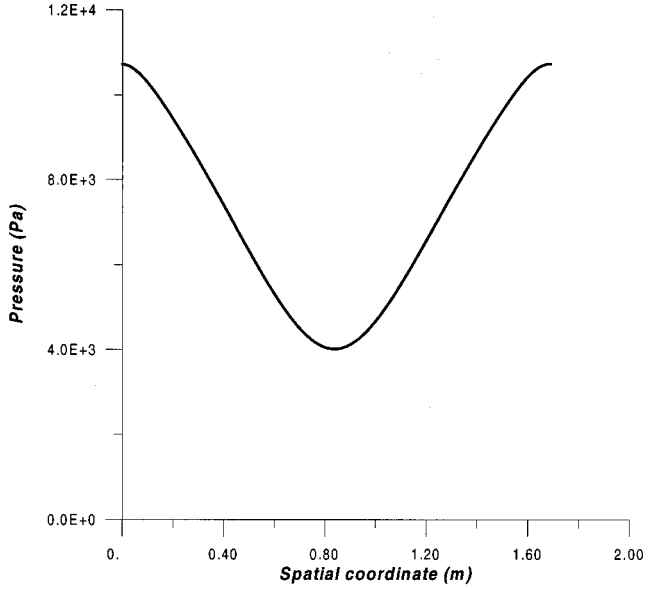

FIG. 5. Efficient pressure distribution at the fundamental frequency $f_1 = 100.6$ Hz. $L = \lambda/2$ and $M_0 = 0.0059$.

to the anterior experimental comparison (B, $M = 0.1$). Figure 4 shows a space–time diagram where color represents the value of the pressure. We see that the wave is distorted when M_0 increases and the changes become more abrupt in both time and space. We also observe an asymmetry between rarefaction and compression zones in the time as in the space in the nonlinear case. For the linear case (infinitesimal amplitudes) we see the well-known half cosine distribution with a node at the center of the tube. When the wave becomes of finite amplitude we find that, throughout a period, the pressure nulls vary within a zone that takes almost all the tube. This result indicates that even if we have a standing wave, when nonlinear terms are considered, there is not a real node for the pressure. It changes during a period. It is a ''quasi-standing'' wave. In fact, we observe that the pressure wave

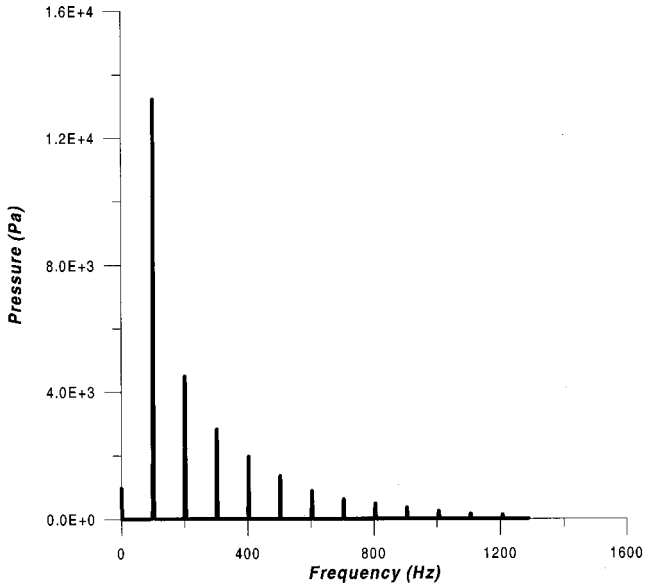

FIG. 6. Fast Fourier transform of the pressure signal at the fundamental frequency $f_1 = 100.6$ Hz at the reflector. $L = \lambda/2$ and $M_0 = 0.0059$.

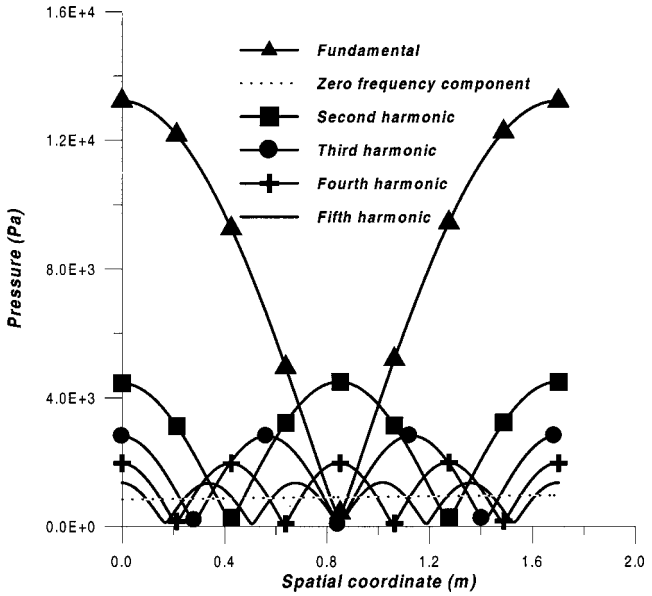

FIG. 7. Distribution of harmonic components of pressure at the fundamental frequency $f_1 = 100.6$ Hz. $L = \lambda/2$ and $M_0 = 0.0059$.

TABLE II. Comparison between M and $\sqrt{M_0}$ for some M_0 at the fundamental frequency $f_1 = 100.6$ Hz. $L = \lambda/2$.

$\sqrt{M_0}$	0.007	0.04	0.06	0.08	0.09	0.1	0.11	0.12	0.13
M	0.003	0.05	0.08	0.1	0.11	0.13	0.14	0.17	0.18
$\sqrt{M_0}$	0.14	0.19	0.24	0.27	0.31	0.33	0.36	0.38	
M	0.19	0.27	0.34	0.4	0.44	0.48	0.52	0.55	

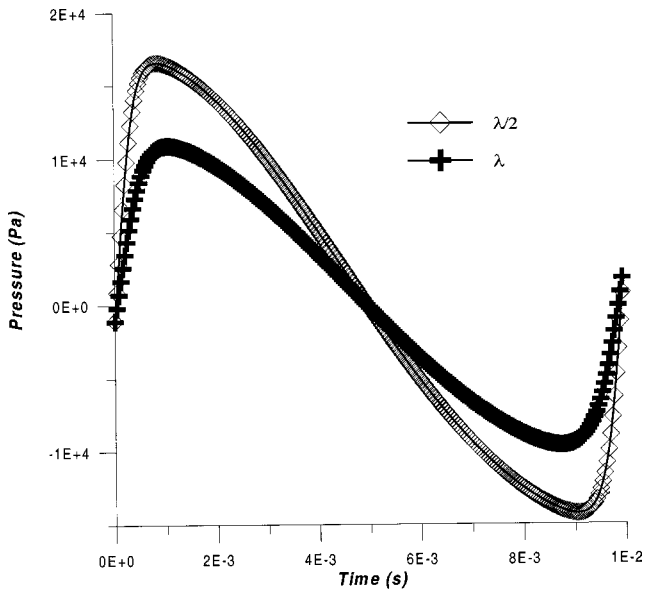

FIG. 8. Pressure wave shapes at the reflector for a $\lambda/2$ and a λ length tubes. $f = 100.6$ Hz. $M_0 = 0.0059$.

TABLE III. Decreasing factor obtained for some M_0 when the tube length doubles. $f = 100.6$ Hz.

M_0	0.002	0.006	0.009	0.018	0.037
Decreasing factor	0.62	0.67	0.68	0.68	0.68

has formed a shock. This shock front propagates from the emitter to the reflector (from $t = 0$ to 0.5 times a period) and vice versa (from $t = 0.5$ to 1 times a period). Even, when considering another time scale, greater than a period, we have standing rms pressure values everywhere in the cavity, as shown in Fig. 5.

The fast Fourier transform of the pressure signal is presented in Fig. 6 at f_1 in the nonlinear case (B). Since it is a ''quasistanding'' wave the harmonic distortion depends on the spatial position. We have chosen the point of maximum amplitude, i.e., the reflector of the tube. In the same configuration, Fig. 7 shows the pressure distribution for harmonic components. The amplitude distribution observed for every frequency ($n\omega_1$, where n is an integer number and $\omega_1 = 2\pi f_1$) presents a cosine shape with spatial periodicity $n\omega_1/c_0$. It should be noted that all the odd harmonics are at a maximum at the center of the tube.

Table II shows a comparison between M and $\sqrt{M_0}$ when ranging M_0 as before. We observe a linear dependence between M and $\sqrt{M_0}$ up to the limit of applicability of our model. This result confirms our result about the nonexistence of saturation of the wave in a cylindrical tube of length $\lambda/2$ as seen before. The proportionality factor between M and $\sqrt{M_0}$ is about 1.5 for the investigated cases. This result is coherent with the one shown in Fig. 3 and with the results obtained by Chester,[7] Temkin,[12] and Yano.[21]

Figure 8 shows results for the $\lambda/2$-length tube at $f_1 = 100.6$ Hz compared to a λ-length tube excited at its second resonance frequency 100.6 Hz, for $M_0 = 0.0059$. We compare the pressure wave shapes at the reflector. The strong nonlinear dissipation is the major phenomena and the wave amplitudes are not so different. We observe that the harmonic distortion is bigger when increasing the length of the tube. An investigation about the variation of the wave amplitude with respect to the length of the tube is made. Table III shows the decreasing factor obtained for some M_0 when the tube-length doubles. We see that very good agreement (4% error) with Chester's criterion[7] is obtained for a range of M_0 greater than the order 0.01.

V. CONCLUSIONS

A new numerical algorithm for the simulation of nonlinear standing waves has been presented. The fully nonlinear wave equation including dissipation effects solved numerically without any truncation is written in Lagrangian coordinates and use is made of the Tait–Kirkwood isentropic state equation. The algorithm works in the time domain; the whole wave shape is then obtained by only one solution and the transient phase is completely modeled. The code has been used to simulate standing waves from linear up to strongly nonlinear cases. The numerical algorithm has been successfully compared to classic experimental and analytical results. Strongly nonlinear waves have illustrated the capacity of the numerical method to model the behavior of the shock included in the wave.

[1] R. T. Beyer, ''Nonlinear acoustics,'' in *Physical Acoustics*, edited by W. P. Mason (Academic, New York, 1965), Vol. II, Pt. B, pp. 231–332.
[2] R. T. Beyer, *Nonlinear Acoustics in Fluids*, Benchmark Papers in Acous-

tics Series (Van Nostrand Reinhold, New York, 1984).
[3] L. Bjorno, ''Nonlinear Acoustics,'' in *Acoustics and Vibration Progress*, edited by R. W. B. Stephens and H. G. Leventhall (Chapman and Hall, London, 1976), Vol. 2, pp. 101–198.
[4] O. V. Rudenko and S. I. Soluyan, *Theoretical Foundations of Nonlinear Acoustics* (Consultants Bureau, New York, 1977).
[5] E. Fubini-Ghiron, ''Anomalies in the propagation of an acoustic wave of larger amplitude,'' Alta Freq. **4**, 532–581 (1935). English version by R. T. Beyer in Ref. 2.
[6] D. T. Blackstock, ''On plane, spherical, and cylindrical sound waves of finite amplitude in lossless fluids,'' J. Acoust. Soc. Am. **36**, 217–219 (1964).
[7] W. Chester, ''Resonant oscillations in closed tubes,'' J. Fluid Mech. **18**, 44–64 (1964).
[8] A. B. Coppens and J. V. Sanders, ''Finite-amplitude standing waves in rigid-walled tubes,'' J. Acoust. Soc. Am. **43**, 516–529 (1968).
[9] D. B. Cruikshank, Jr., ''Experimental investigation of finite-amplitude acoustic oscillations in a closed tube,'' J. Acoust. Soc. Am. **52**, 1024–1036 (1972).
[10] R. A. Saenger and G. E. Hudson, ''Periodic shock waves in resonating gas columns,'' J. Acoust. Soc. Am. **32**, 961–970 (1960).
[11] C. C. Lawrenson, B. Lipkens, T. S. Lucas, D. K. Perkins, and T. W. Van Doren, ''Measurements of macrosonic standing waves in oscillating closed cavities,'' J. Acoust. Soc. Am. **104**, 623–636 (1998).
[12] S. Temkin, ''Propagating and standing sawtooth waves,'' J. Acoust. Soc. Am. **45**, 224–227 (1969).
[13] *Nonlinear Acoustics*, edited by M. F. Hamilton and D. T. Blackstock (Academic, New York, 1998).
[14] R. O. Cleveland, M. F. Hamilton, and D. T. Blackstock, ''Time-domain modeling of finite-amplitude sound in relaxing fluids,'' J. Acoust. Soc. Am. **99**, 3312–3318 (1996).
[15] B. E. McDonald and W. A. Kuperman, ''Time domain formulation for pulse propagation including nonlinear behavior at a caustic,'' J. Acoust. Soc. Am. **81**, 1406–1417 (1987).
[16] Y.-S. Lee and M. F. Hamilton, ''Time-domain modeling of pulsed finite-amplitude sound beams,'' J. Acoust. Soc. Am. **97**, 906–917 (1995).
[17] Y. Inoue and T. Yano, ''Propagation of strongly nonlinear plane waves,'' J. Acoust. Soc. Am. **94**, 1632–1642 (1993).
[18] C. Campos-Pozuelo, B. Dubus, and J. A. Gallego-Juárez, ''Finite-element analysis of the nonlinear propagation of high intensity acoustic waves,'' J. Acoust. Soc. Am. **106**, 91–101 (1999).
[19] Y. A. Ilinskii, B. Lipkens, T. S. Lucas, T. W. Van Doren, and E. A. Zabolotskaya, ''Nonlinear standing waves in an acoustical resonator,'' J. Acoust. Soc. Am. **104**, 2664–2674 (1998).
[20] C. P. Lee and T. G. Wang, ''Nonlinear resonance and viscous dissipation in an acoustic chamber,'' J. Acoust. Soc. Am. **92**, 2195–2206 (1992).
[21] T. Yano, ''Turbulent acoustic streaming excited by resonant gas oscillation with periodic shock waves in a closed tube,'' J. Acoust. Soc. Am. **106**, L7–L12 (1999).
[22] C. Vanhille and C. Campos-Pozuelo, ''A time-domain numerical algorithm for the analysis of nonlinear standing acoustic waves,'' *Nonlinear Acoustics at the Turn of the Millenium*, Proceedings of the 15th International Symposium on Nonlinear Acoustics, edited by W. Lauterborn and T. Kurz (American Institute of Physics, Melville, New York, 2000), pp. 177–180.
[23] L. D. Landau and E. M. Lifshitz, *Fluid Mechanics* (Butterworth–Heinemann, Oxford, 1987).
[24] D. A. Sullivan, ''Historical review of real-fluid isentropic flow models,'' Trans. ASME, J. Fluids Eng. **103**, 258–267 (1981).
[25] A. D. Pierce, *Acoustics* (Acoustical Society of America, New York, 1989).
[26] G. D. Smith, *Numerical Solution of Partial Differential Equations, Finite Difference Methods*, 3rd ed. (Clarendon, Oxford, 1985).
[27] W. E. Milne, *Numerical Solution of Differential Equations* (Dover, New York, 1970).
[28] L. Lapidus and G. F. Pinder, *Numerical Solution of Partial Differential Equations in Science and Engineering* (Wiley-Interscience, New York, 1999).
[29] C. Vanhille and C. Campos-Pozuelo, ''A high-order finite-difference algorithm for the analysis of standing acoustic waves of finite but moderate amplitude,'' J. Comput. Phys. **165**, 334–353 (2000).
[30] D. M. Young and R. T. Gregory, *A Survey of Numerical Mathematics* (Dover, New York, 1988), Vol. II.

Time-reversed sound beams of finite amplitude

Kevin B. Cunningham[a] and Mark F. Hamilton[b]
Department of Mechanical Engineering, The University of Texas at Austin, Austin, Texas 78712-1063

Andrew P. Brysev and Leonid M. Krutyansky
Wave Research Center, General Physics Institute, Russian Academy of Sciences, 38 Vavilov Street, Moscow 119991, Russia

(Received 22 May 2000; accepted for publication 20 February 2001)

Numerical simulations based on the nonlinear parabolic wave equation are used to investigate time reversal of sound beams radiated by unfocused and focused sources. Emphasis is placed on nonlinear propagation distortion in the time-reversed beam, and specifically its effect on field reconstruction. Distortion of this kind, due to amplification during time reversal, has been observed in recent experiments [A. P. Brysev *et al.*, Acoust. Phys. **44**, 641–650 (1998)]. Effects of diffraction introduced by time-reversal mirrors with finite apertures are also considered. It is shown that even in the presence of shock formation, the ability of time reversal to retarget most of the energy on the source or focal region of the incident beam is quite robust. © *2001 Acoustical Society of America.*
[DOI: 10.1121/1.1368405]

PACS numbers: 43.25.Jh [FD]

I. INTRODUCTION

Time reversal refers to the process in which a wave field is reversed in time and reradiated back in the direction from which it emanated. A principal advantage of time reversal is the ability to retarget energy on a source or scattering site in an inhomogeneous or reverberant medium. Devices that perform such functions are referred to as time-reversal mirrors. For arbitrary acoustic waveforms, time reversal requires separate storage, delay, and reradiation of signals at each element of a transducer array.[1,2]

Phase conjugation refers to methods for performing time reversal at a single frequency and normally without the need for transducer arrays. Phase conjugation was developed first in optics (a review is given, e.g., in the book by Zel'dovich *et al.*[3]) and subsequently introduced in acoustics by Bunkin *et al.*[4] The most effective physical mechanisms for acoustic phase conjugation involve parametric modulation of the sound speed in solids through application of electromagnetic fields.[5–8] These and other methods of acoustic phase conjugation are reviewed by Brysev *et al.*[6] and Ohno *et al.*[7]

In principle, perfect reproduction of the incident field by the time-reversed field may be accomplished when the following conditions are met: the mirror is a surface that encloses the source of radiation; the medium is lossless; and inhomogeneous properties of the medium do not vary with time. Although nonlinear propagation does not, by itself, prevent exact field reproduction, it does when amplification is introduced during time reversal, or when shocks are formed and therefore losses occur in either the incident or time-reversed fields.

The main purpose of the present article is to investigate consequences of removing the restriction that the time-reversed field is sufficiently weak that its propagation is accurately described by linear theory. This interest is motivated by recent experiments in which phase conjugation of sound beams introduces sufficient amplification that the reradiated wave field is finite amplitude and distorts as it propagates. Phase conjugation in these experiments was accomplished via parametric interaction of the incident sound beam, after transmission into a magnetostrictive ferrite, with an alternating magnetic field.[6] The incident sound fields were ultrasonic beams radiated by unfocused[9] and focused[10] sources. In Ref. 10, comparisons of measured harmonic generation in the conjugate beam with computations obtained from the algorithm used below demonstrate clearly the finite-amplitude behavior of the conjugate beam. Acoustic microscopy experiments have been reported in which images obtained with the second harmonic generated in the conjugate beam show enhancement over images constructed from the fundamental component.[11]

The present investigation is based on numerical simulations which account for nonlinear distortion, thermoviscous absorption, and diffraction of both the incident and time-reversed sound beams. Practical realizations of time-reversal mirrors normally have finite apertures that do not capture the entire incident field. Diffraction introduced by a finite mirror aperture can substantially degrade reproduction of the incident field by the time-reversed field, and this effect, too, is considered. Incident beams radiated from both unfocused and focused sources are investigated. Inhomogeneity of the medium is not taken into account at this time. The results presented below are discussed in greater detail in the master's thesis of one of the authors.[12]

II. MODEL

Nonlinear propagation of an axisymmetric sound beam in a thermoviscous fluid may be described by the KZK equation:[13]

[a]Present address: Medical Physics Department, St. Thomas' Hospital, London SE1 7EH, United Kingdom.
[b]Electronic mail: hamilton@mail.utexas.edu

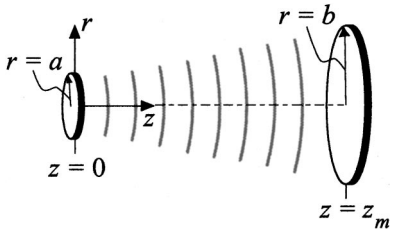

FIG. 1. Geometry, with source at $z=0$ and time-reversal mirror at $z=z_m$.

$$\frac{\partial^2 p}{\partial z\,\partial t'}=\frac{c_0}{2}\left(\frac{\partial^2 p}{\partial r^2}+\frac{1}{r}\frac{\partial p}{\partial r}\right)+\frac{\delta}{2c_0^3}\frac{\partial^3 p}{\partial t'^3}+\frac{\beta}{2\rho_0 c_0^3}\frac{\partial^2 p^2}{\partial t'^2}, \tag{1}$$

where $p(r,z,t)$ is the sound pressure, z is the axis of the beam, r is distance from the z axis, $t'=t-z/c_0$ is retarded time, c_0 is the sound speed, δ is the diffusivity of sound for a thermoviscous fluid, ρ_0 is the ambient density, and β is the coefficient of nonlinearity. Two types of sources are considered, unfocused and focused circular pistons of radius a that radiate at angular frequency ω in the plane $z=0$. The boundary condition for the unfocused piston is taken to be

$$p(r,0,t)=p_0 H(a-r)\sin\omega t, \tag{2}$$

where p_0 is the sound pressure amplitude and H is the Heaviside unit step function. The boundary condition for the focused piston is

$$p(r,0,t)=p_0 H(a-r)\sin(\omega t+kr^2/2d), \tag{3}$$

where d is the focal length and $k=\omega/c_0$ is the wave number.

The geometry for the time reversal is shown in Fig. 1. A circular time-reversal mirror of radius b is centered on the axis of the incident beam in the plane $z=z_m$. Time reversal corresponds to replacing t by $-t$. The finite radius of the mirror is taken into account by truncating the time-reversed field at $r=b$. The boundary condition in the plane $z=z_m$ is thus

$$p_{\rm rev}(r,z_m,t)=KH(b-r)p_{\rm inc}(r,z_m,-t), \tag{4}$$

where K is an arbitrary amplification factor associated with the time-reversal procedure, and the notations ''inc'' and ''rev'' refer to the incident and time-reversed fields, respectively. Following time reversal, propagation of the beam is modeled once again with Eq. (1), and in terms of the same retarded time $t'=t-z/c_0$. Solutions are thus presented as though the incident beam, traveling to the right in Fig. 1, continues to travel to the right following time reversal. This unfolded geometry is convenient not only for computational purposes, but also for graphical presentation.

Numerical solutions of Eq. (1) for the incident beams satisfying Eqs. (2) and (3), and for the resulting time-reversed beams satisfying Eq. (4), were obtained using the algorithm described in Ref. 14 and with the modifications described in Ref. 15.

Use of Eq. (1) to model the incident and time-reversed fields in the vicinity of the mirror is based on the assumption that their mutual nonlinear interaction may be ignored. We justify this assumption in two ways. First, in conventional operation of time-reversal (and phase-conjugation) devices, the entire pulse is captured by the device, reversed, and reradiated into the fluid. Under normal circumstances, the incident and time-reversed fields do not overlap in the fluid, and it is propagation in the fluid alone that we model in the present work. Second, even if overlap does occur in the fluid, counterpropagating waves couple very weakly with each other. Any nonlinear interaction arising from the overlap may be ignored in comparison with the much stronger effects of self-interaction that give rise to cumulative nonlinear distortion and shock formation. Although we simulate continuous radiation in the present article, which suggests continuous overlap of counterpropagating waves between the source and mirror, tone bursts of finite pulse length are used in practice. The region of overlap is thus at most the pulse length itself, which further reduces the relative effects of mutual interaction. In previous reflection experiments with finite-amplitude sound beams, where comparisons made with calculations based on Eq. (1) show good agreement,[16] nonlinear effects due to mutual interaction of the counterpropagating incident and reflected beams were not observable.

To facilitate interpretation of the graphical results, the following convention is employed. The incident and time-reversed fields are plotted in terms of a dimensionless pressure P that is defined in such a way that $P_{\rm inc}=P_{\rm rev}$ at $z=z_m$:

$$P=p/p_0, \quad \text{incident field}, \tag{5}$$

$$=p/Kp_0, \quad \text{time-reversed field}, \tag{6}$$

i.e., the amplification K is factored out of the time-reversed pressure field. The purpose of this choice is to make it easier to assess whether time-reversal accurately reproduces the spatial structure of the incident field in the presence of nonlinearity and diffraction. Dimensionless coordinates are also introduced:

$$\sigma=z/z_0, \quad \rho=r/a, \quad \tau=\omega t', \tag{7}$$

where $z_0=ka^2/2$ is the Rayleigh distance, $\sigma_m=z_m/z_0$ indicates distance to the mirror, and $\rho_m=b/a$ indicates the radius of the mirror.

The following sets of dimensionless parameters are useful for characterizing the absorption of the fluid, the amplitude of the time-reversed field, and the focusing gain of the source. For the unfocused source we employ the parameters

$$A=\alpha z_0, \quad N=z_0/\overline{z}, \tag{8}$$

where $\alpha=\delta\omega^2/2c_0^3$ is the absorption coefficient at frequency ω, and $\overline{z}=\rho_0 c_0^3/\beta\omega K p_0$ the plane-wave shock formation distance for a wave with initial amplitude Kp_0 in a lossless fluid. The parameters for the focused source are

$$A_f=\alpha d, \quad N_f=d/\overline{z}, \quad G=z_0/d, \tag{9}$$

where G is the focusing gain. The parameters A, A_f, and G apply to computations for both the incident and time-reversed fields, but except for one preliminary example (Fig. 2), the parameters N and N_f apply only to the time-reversed field. In all examples following Fig. 2, nonlinearity is assumed to be negligible prior to time reversal, and computations of the incident field were performed with the last term in Eq. (1) set to zero. When there is no nonlinearity, which is

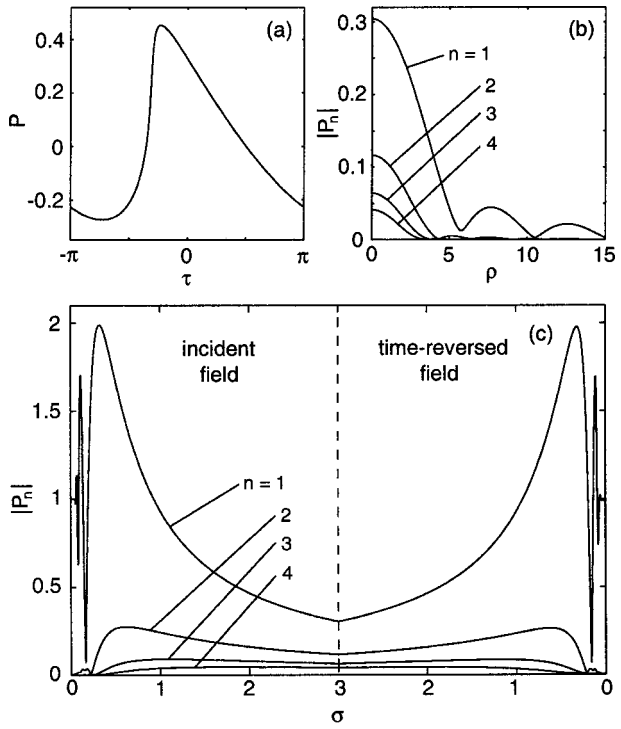

FIG. 2. Nonlinear propagation of both incident and time-reversed fields, with no shock formation, no absorption ($A=0$), no amplification at mirror ($K=1$), and $\sigma_m=3$. (a) Axial waveform at mirror; (b) harmonic beam patterns at mirror; and (c) harmonic propagation curves along the axis.

equivalent to setting $\beta=0$, there is no need for parameters such as N and N_f.

Numerical values selected for the parameters in Eqs. (8) and (9) are associated with experiments performed recently with both unfocused[9] and focused[10] incident sound beams in water at megahertz frequencies. In these experiments the amplitude of the incident beam was sufficiently weak that nonlinear effects were insignificant over the propagation path between the source and the phase conjugator.

III. SIMULATIONS

A. Unfocused incident beams

Our aim in the present article is to consider time reversal of incident beams that are essentially unaffected by nonlinearity. However, we begin with an example demonstrating that under restricted circumstances, nonlinear distortion of the incident beam does not affect the ability of time reversal to reproduce the incident field. The first restriction is that there are no losses, and therefore shock formation is prohibited. The second is that the time-reversal mirror is of infinite extent, and therefore it has no edges that may introduce secondary diffraction effects. The third is that the mirror introduces neither amplification nor attenuation.

For this demonstration we consider an unfocused beam and thus take the source condition to be Eq. (2), with $A=0$ to suppress absorption. A mirror for which $\rho_m=\infty$ and $K=1$ is located at $\sigma_m=3$. The nonlinearity parameter is selected to be $N=0.4$ for both the incident and time-reversed fields. The results are presented in Fig. 2. Figure 2(a) shows the axial waveform at $\sigma=\sigma_m^-$ (i.e., immediately before time reversal), which demonstrates that for this value of N the waveform, although significantly distorted by nonlinearity, has not formed a shock. The beam profiles of the first four harmonics (with $n=1$ designating the source frequency) in the plane $\sigma=\sigma_m$ are shown in Fig. 2(b). Figure 2(c) shows the amplitudes of the first four harmonics along the axis of the beam. Following time reversal at $\sigma=3$ the waveform undistorts, and the behavior of the harmonic propagation curves reverses. The harmonics $n>1$ transfer energy back to the spectral component at the source frequency as the time waveform undistorts back to its original sinusoidal shape in the image source plane. For this scenario it is seen that the time-reversed field does indeed reproduce the incident field, despite strong waveform distortion. We note that the coordinate σ in the right half of Fig. 2(c), *and in all subsequent figures*, designates distance from the image source plane in the time-reversed field.

In the remaining simulations it is assumed that the amplitude of the incident beam is sufficiently weak that its propagation may be described by linear theory, and therefore the values of N and N_f apply only to the time-reversed fields. The nonlinearity of interest to follow thus arises in the time-reversed field as a result of amplification at the mirror. Also of interest is the effect of the finite radius of the mirror.

We first consider only the effect of diffraction introduced by the finite radius of the mirror. We thus disregard absorption and nonlinearity for both the incident and time-reversed fields, such that $A=N=0$. The mirror is located at $\sigma_m=3.5$, and results for $5\leqslant\rho_m\leqslant40$ are presented in Fig. 3. Axial propagation curves are shown in the left column ($\rho=0$), beam profiles in the (image) source plane in the right column ($\sigma=0$). For $\rho_m=40$ the finite radius of the conjugator has a negligible effect on the time-reversed field, and the axial field (left column) is virtually the mirror image of the incident field (not shown). However, the corresponding beam profile in the source plane (right column) is not a perfect replica of the step function $H(1-\rho)$ prescribed by Eq. (2). Two factors contribute to this discrepancy. One is that Eq. (1), which is based on the parabolic approximation, does not account for evanescent waves associated with the high spatial frequencies of the source step function. The other is the inability of the numerical algorithm to follow the rapid phase variations in the vicinity of a source with high spatial frequency content. The discrepancy disappears as smoother source functions are considered. As ρ_m decreases, diffraction oscillations in the axial propagation curves become more substantial, and the beam profiles in the source plane tend toward far-field directivities associated with scattering of a plane wave from a circular disk of radius $r=b$.

Diffraction introduced by the finite radius of a time-reversal mirror can thus be very pronounced and must often be included in simulations of experiments.[9,10] We henceforth concentrate on mirrors of infinite radius ($\rho_m=\infty$) in order to emphasize nonlinear effects in the time-reversed field.

Time reversal of a small-signal sound beam for which $A=0.035$ and with the mirror located at $\sigma_m=3.5$ is simulated in Fig. 4. The parameters correspond, for example, to a source of radius $a=2$ mm radiating in water at frequency $f=5.5$ MHz and thus having Rayleigh distance $z_0=4.7$ cm,

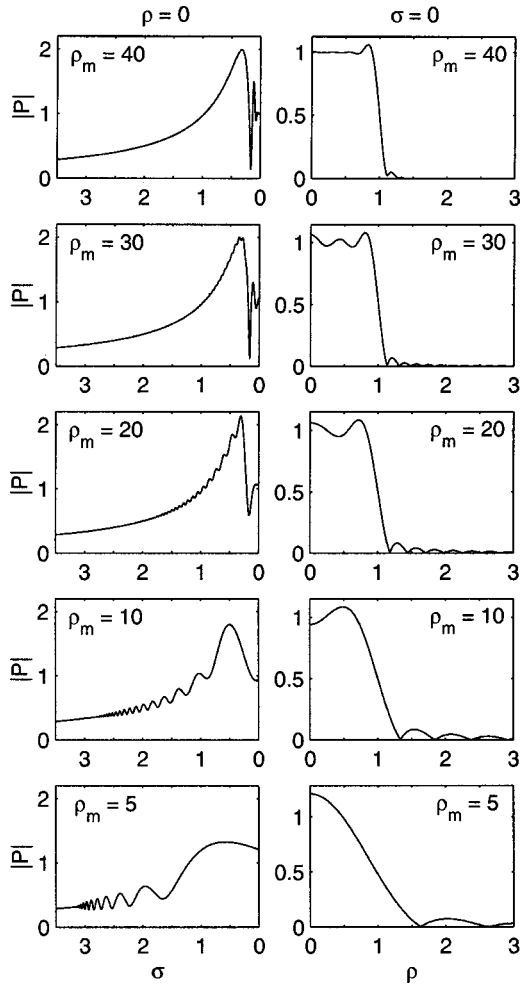

FIG. 3. Effect of variation in radius of the time-reversal mirror for $A=N=0$ and $\sigma_m=3.5$. Left column—axial propagation curves. Right column—beam profiles in the image source plane.

with the mirror at distance $z_m=16$ cm. These conditions are similar to those in experiments conducted by Brysev *et al.*[9] The nonlinearity parameter of the time-reversed field spans the range $0\leqslant N\leqslant 4$, where increasing N may be interpreted as increasing the amplification K associated with time reversal, with the source pressure p_0 held constant.

Axial propagation curves for the dimensionless rms pressure P_{rms} are presented in Fig. 4(a) (the incident field is not displayed). For $N\leqslant 1$ the deviation from linear theory (dashed line) is negligible. For $N>1$, because of losses due to shock formation, the propagation curves deviate significantly from linear theory. Beam profiles in the (image) source plane at $\sigma=0$ are shown in Fig. 4(b). For $N\leqslant 1$ the profiles are in reasonable agreement with the source condition $H(1-\rho)$ (the discrepancy in the dashed line for $N=0$, discussed earlier, notwithstanding). For $N>1$, increasing nonlinearity results in decreasing quality of the profile in the source plane, in comparison with the original step function. Beam profiles of individual harmonics in the source plane are presented in Fig. 5.

Axial waveforms at $\sigma=1$ and $\sigma=\pi^{-1}$ are presented in the left and right columns, respectively, of Fig. 6. The plane $\sigma=\pi^{-1}$ is significant because it is the location of the local maximum observed in the propagation curves in Fig. 4(a),

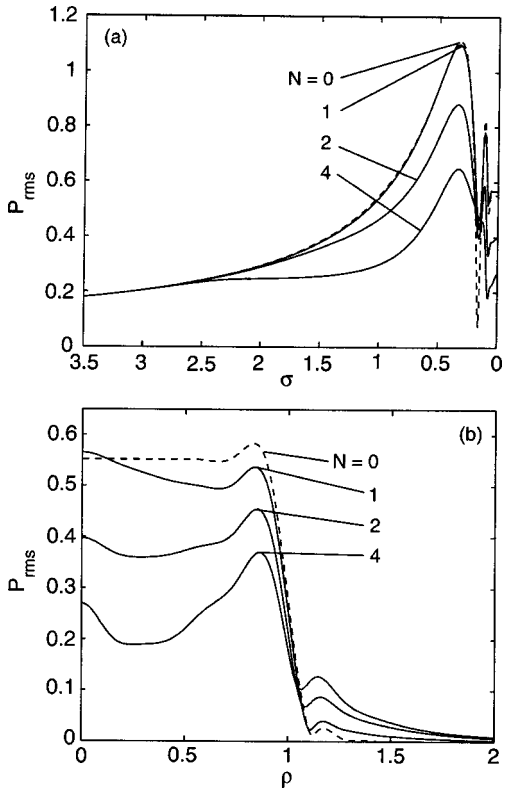

FIG. 4. Effect of nonlinearity on the time-reversed field for $A=0.035$ and $\sigma_m=3.5$. (a) Axial propagation curves and (b) beam profiles in the image source plane.

where waveform distortion may be expected to be greatest. Distortion increases from $\sigma=\sigma_m$ to $\sigma=\pi^{-1}$ as the field converges and thus increases in amplitude toward the source plane [recall that the sound propagates from left to right in Fig. 4(a)]. In the region $0\leqslant\sigma\leqslant\pi^{-1}$, the rapid variations in amplitude and phase disrupt coherence of the harmonics in the waveform, and the shocks are generally dispersed. Figure 6 reveals that very strong waveform distortion is achieved for $N>1$. Shock formation is essentially absent for $N<1$, which corresponds to the reasonably accurate reconstruction of the incident field that is observed in Fig. 4.

Insofar as a principal application of time reversal is to retarget energy, it is helpful to introduce a measure of this property. A useful quality factor is the fraction of total energy in the time-reversed field that is retargeted on a given surface, normalized by the fraction of the total energy in the incident field that passed through the same surface. Such a measure was introduced previously by Zel'dovich *et al.*[3] In a similar manner we thus define the following quality factor for the axisymmetric geometry under consideration:

$$Q=\frac{W_{\mathrm{rev}}(\hat{\rho})/W_{\mathrm{rev}}(\infty)}{W_{\mathrm{inc}}(\hat{\rho})/W_{\mathrm{inc}}(\infty)}, \tag{10}$$

where W is dimensionless power defined by

$$W(\hat{\rho})=\int_0^{\hat{\rho}} P_{\mathrm{rms}}^2\,\rho\,d\rho, \tag{11}$$

and the target area is taken to be a circle of (dimensionless) radius $\hat{\rho}$. By this definition, even in the presence of absorption $(A\neq 0)$ and amplification by the mirror $(K\neq 1)$, if

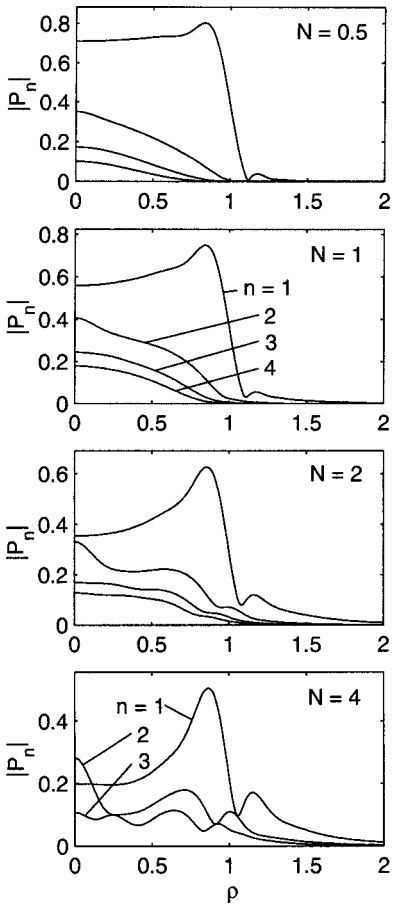

FIG. 5. Harmonic beam profiles in the image source plane, for the same parameters as in Fig. 4.

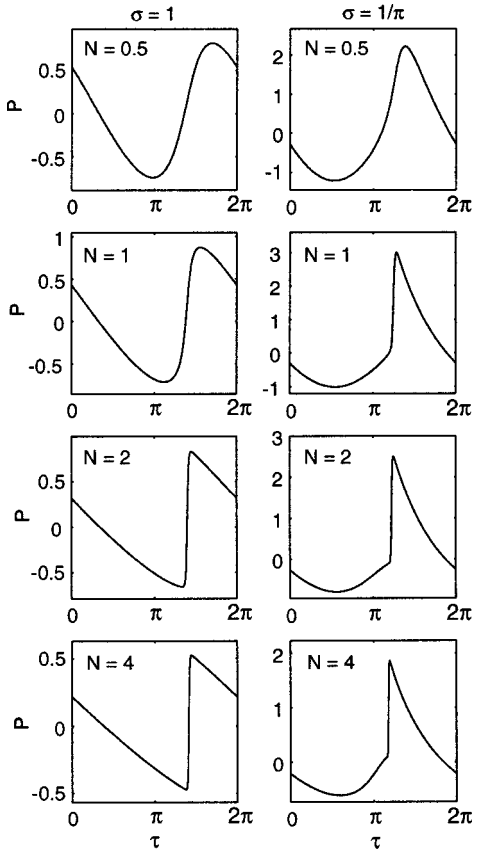

FIG. 6. Waveforms on the axis of the time-reversed field corresponding to Fig. 4, at $\sigma=1$ (left column) and $\sigma=\pi^{-1}$ (right column).

propagation of both the incident and time-reversed fields is linear ($N=0$), and if the mirror is infinite in extent ($\rho_m=\infty$), the result obtained is $Q=1$. For $N\neq 0$ and $\rho_m\neq\infty$, the value of Q is expected to deviate from unity. Generally, the extent to which Q is less than unity indicates the degree to which retargeting of the time-reversed field is less effective. As shown later in this work, nonlinearity can also result in values of Q that are slightly in excess of unity. Note also that whereas Eq. (10) describes the fraction of energy that is retargeted on a given surface, it does not account for how well the structure of the incident field is reproduced by the time-reversed field within the perimeter of this surface. The definition in Eq. (10) is nevertheless adequate for our purposes.

For the case at hand, an unfocused source, it is convenient to take the target surface to be the uniform circular source itself, for which $\hat{\rho}=1$ in Eqs. (10) and (11), and $W_{\mathrm{inc}}(\hat{\rho})/W_{\mathrm{inc}}(\infty)=1$. Figure 7(a) shows the dependence of Q on N for the conditions in Figs. 4–6. The result $Q=1$ is not obtained in the linear case, $N=0$, because of the discrepancy associated with reconstruction of an ideal step function, as discussed earlier. Instead, we find that 98% of the energy in the time-reversed field is retargeted on the source for this case, because the discrepancy accounts for approximately 2% of the energy spilling over into the region outside the source [this is the spillover indicated by the dashed line in Fig. 4(b)]. The value $Q=0.98$ thus serves as the baseline for linear theory, and the effect of increasing N is clearly observed in Fig. 7(a). For $N<1$, virtually all available energy is retargeted on the source. For $N>1$, Q decreases almost linearly with N. The trend continues up to $N=8$, the highest value considered [not shown in Fig. 7(a)]. For $N=4$, despite

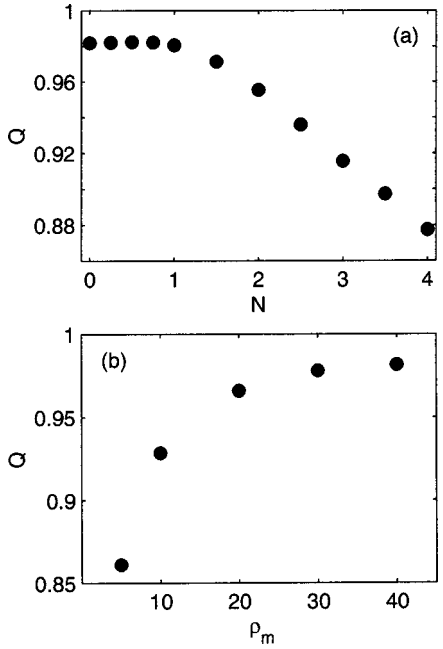

FIG. 7. Quality factor for the time-reversed field corresponding to (a) Fig. 5 and (b) right column of Fig. 3.

the strong distortion of the beam profile observed in Fig. 4(b) as a result of the advanced shock formation observed in Fig. 6, only 10% of the energy in the time-reversed field misses the source.

The quality factor also quantifies the adverse effect associated with finite mirror radius. Specifically, Fig. 7(b) corresponds to the right column in Fig. 3, where beam patterns are shown in the source plane for $A=N=0$. For the maximum value $\rho_m=40$ we have $Q=0.98$ in Fig. 7(b), which is the same value as in Fig. 7(a) for $N=0$. It is seen that for the geometry under consideration, Q decreases rapidly for $\rho_m \lesssim 20$. This transition point may be understood in terms of the far-field amplitude distribution of the incident beam for constant σ:

$$D(\rho)=\frac{J_1(2\rho/\sigma)}{\rho/\sigma}, \tag{12}$$

where J_1 is the Bessel function of the first kind. The values $\rho_m=20$ and $\sigma_m=3.5$ yield $2\rho_m/\sigma_m=11.4$, which is just above the third zero of the Bessel function. Therefore, the plateau region in Fig. 7(b), $Q\gtrsim 0.95$, requires that the mirror encompass at least the first two sidelobes of the incident beam.

B. Focused incident beams

Here the source condition is taken to be Eq. (3). Focused sources are considered because reconstruction of the focal region via time reversal bears comparison with localization

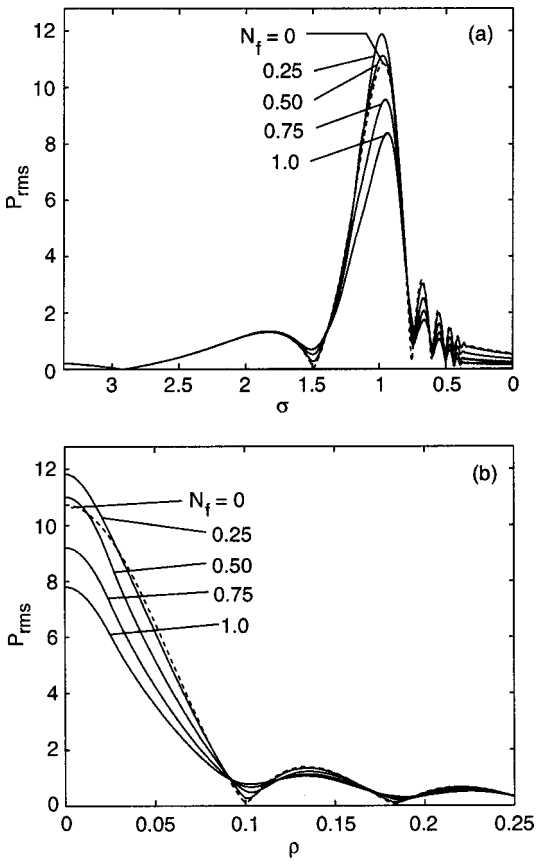

FIG. 8. Effect of nonlinearity on the time-reversed field for a focused incident beam with $G=19$, $A_f=0.04$, and $\sigma_m=3.5$. (a) Axial propagation curves and (b) beam profiles in the image focal plane.

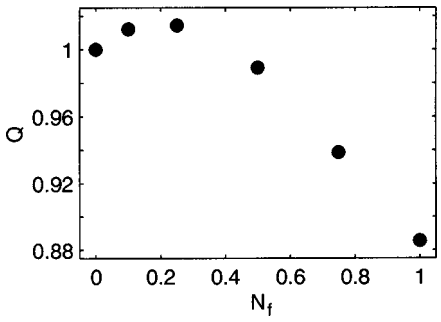

FIG. 9. Quality factor for the time-reversed field corresponding to Fig. 8(b).

of energy on small scattering sites, and it is also relevant to acoustic microscopy. Figure 8 displays rms pressures in the time-reversed field (a) along the axis and (b) in the focal plane for absorption $A_f=0.04$, focusing gain $G=19$, and mirror located at $\sigma_m=3.5$ with $\rho_m=\infty$. These parameters correspond to those of the experiments reported by Brysev *et al.*,[10] who used a source of radius $a=7.5$ mm and focal length $d=39$ mm radiating in water at frequency $f=6.23$ MHz, with the mirror at distance $z_m=131$ mm. Values of the nonlinearity parameter are varied from $N_f=0$ (linear) to $N_f=1$ (substantial shock formation). As in Sec. III A, small-signal propagation of the incident beam is assumed. The slight increase in relative rms pressure at the focus for small N_f, particularly $N_f=0.25$, is due to the slightly higher effective focusing gain of the harmonics generated in the prefocal region. With further increase in N_f, finite-amplitude absorption reduces the relative amplitude at the focus, and consequently the effective beamwidth at the focus is increased.

The effectiveness of retargeting energy in the focal plane as a function of N_f, with all other parameters the same as in Fig. 8, is indicated by the quality factor Q in Fig. 9. The target area is chosen to be the circle in the focal plane corresponding to the first null in the beam pattern predicted by linear theory, such that $\hat{\rho}=3.83/2G=0.10$ and $W_{\rm inc}(\hat{\rho})/W_{\rm inc}(\infty)=0.84$. For $N_f=0$ we obtain $Q=1$; the discrepancy $Q<1$ encountered for $N=0$ in Fig. 7(a) is not

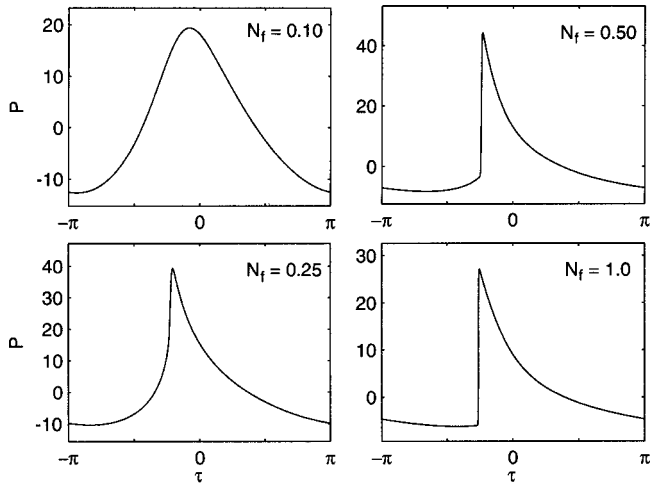

FIG. 10. Waveforms at the focus of the time-reversed field corresponding to Fig. 8.

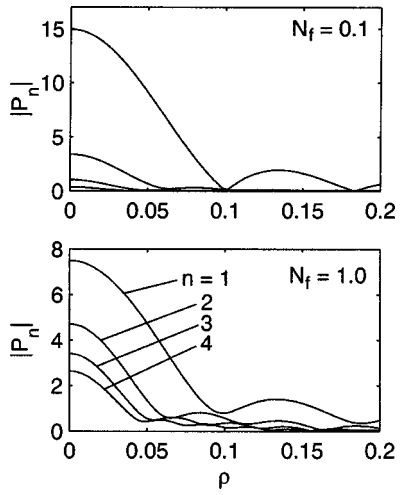

FIG. 11. Harmonic beam profiles in the image focal plane, for the same parameters as in Fig. 8.

observable in Fig. 9 because of the smoothness of the beam profile in the focal plane. For $N_f \simeq 0.2$ the quality factor exceeds unity by 1%–2%, because of the nonlinear enhancement of focusing discussed in relation to Fig. 8. The quality of retargeting deteriorates rapidly for $N_f \gtrsim 0.5$. Indeed, the waveforms shown in Fig. 10 reveal that shock formation is prominent at the focus for $N_f \gtrsim 0.5$. The corresponding harmonic profiles in the focal region are shown in Fig. 11.

IV. CONCLUSION

Provided shock formation does not occur, it was found that nonlinear propagation effects in the time-reversed beam do not significantly degrade reproduction of the incident field. If shock formation does occur, further increase in amplification by the time-reversal mirror causes significant deterioration in the quality of field reproduction. Nevertheless, even in the presence of shock formation, the ability of time reversal to retarget most of the energy on the source or focal region of the incident beam is found to be remarkably robust. A potentially greater influence on accurate reproduction of the incident field is the finite dimension of the aperture of the time-reversal mirror.

ACKNOWLEDGMENTS

This work was supported by the U.S. Office of Naval Research, the U.S. Civilian Research and Development Foundation for the Independent States of the Former Soviet Union, and the Russian Foundation for Basic Research. The authors appreciate the comments made by each of the reviewers.

[1] D. R. Jackson and D. R. Dowling, ''Phase conjugation in underwater acoustics,'' J. Acoust. Soc. Am. **89**, 171–181 (1991).
[2] M. Fink, ''Time reversal of ultrasonic fields—Part I: Basic principles,'' IEEE Trans. Ultrason. Ferroelectr. Freq. Control **39**, 555–566 (1992).
[3] B. Y. Zel'dovich, N. F. Pilipetsky, and V. V. Shkunov, *Principles of Phase Conjugation* (Springer-Verlag, Berlin, 1985).
[4] F. V. Bunkin, D. V. Vlasov, and Yu. A. Kravstov, ''Problem of reversal of an acoustic wavefront and amplification of the reversed wave,'' Sov. J. Quantum Electron. **11**, 687–688 (1981).
[5] A. P. Brysev, F. V. Bunkin, D. V. Vlasov, L. M. Krutianskii, V. L. Preobrazhenskii, and A. D. Stakhovskii, ''Parametric phase conjugation of an ultrasonic wave in a ferrite,'' Sov. Phys. Acoust. **34**, 642–643 (1988).
[6] A. P. Brysev, L. M. Krutyanskii, and V. L. Preobrazhenskii, ''Wave phase conjugation of ultrasonic beams,'' Phys. Usp. **41**, 793–805 (1998).
[7] M. Ohno, K. Yamamoto, A. Kokubo, K. Sakai, and K. Takagi, ''Acoustic phase conjugation by nonlinear piezoelectricity. I. Principle and basic experiments,'' J. Acoust. Soc. Am. **106**, 1330–1338 (1999).
[8] K. Yamamoto, M. Ohno, A. Kokubo, K. Sakai, and K. Takagi, ''Acoustic phase conjugation by nonlinear piezoelectricity. II. Visualization and application to imaging systems,'' J. Acoust. Soc. Am. **106**, 1339–1345 (1999).
[9] A. P. Brysev, F. V. Bunkin, M. F. Hamilton, L. M. Krutyanskii, K. B. Cunningham, V. L. Preobrazhenskii, Yu. V. Pyl'nov, A. D. Stakhovskii, and S. J. Younghouse, ''Nonlinear propagation of a quasi-plane conjugate ultrasonic beam,'' Acoust. Phys. **44**, 641–650 (1998).
[10] A. P. Brysev, L. M. Krutyansky, V. L. Preobrazhensky, Yu. V. Pylnov, K. B. Cunningham, and M. F. Hamilton, ''Nonlinear propagation of phase-conjugate focused sound beams in water,'' in *Nonlinear Acoustics at the Turn of the Millennium, ISNA 15*, edited by W. Lauterborn and T. Kurz (AIP, New York, 2000), pp. 183–186.
[11] Yu. Pyl'nov, P. Pernod, and V. Preobrazhensky, ''Acoustic imaging by second harmonic of phase conjugate wave in inhomogeneous medium,'' Appl. Phys. Lett. **78**, 553–555 (2001).
[12] K. B. Cunningham, ''Numerical simulation of time-reversed sound beams of finite amplitude,'' Master's thesis, The University of Texas at Austin, 1999.
[13] M. F. Hamilton and C. L. Morfey, ''Model equations,'' in *Nonlinear Acoustics*, edited by M. F. Hamilton and D. T. Blackstock (Academic, Boston, 1998), Chap. 3.
[14] Y.-S. Lee and M. F. Hamilton, ''Time-domain modeling of pulsed finite-amplitude sound beams,'' J. Acoust. Soc. Am. **97**, 906–917 (1995).
[15] S. J. Younghouse, ''Acoustic streaming at high Reynolds numbers produced by focused sound beams with shocks in real fluids,'' Master's thesis, The University of Texas at Austin, 1998.
[16] M. A. Averkiou, ''Experimental investigation of propagation and reflection phenomena in finite amplitude sound beams,'' Doctoral dissertation, The University of Texas at Austin, 1994.

Blast noise propagation above a snow cover

Donald G. Albert[a)]
U.S. Army Cold Regions Research and Engineering Laboratory (USACRREL), 72 Lyme Road, Hanover, New Hampshire 03755

Lars R. Hole[b)]
Norwegian Defence Construction Service, FBT/S, Oslo mil/Akerhus, 0015 Oslo, Norway

(Received 9 October 1998; revised 9 January 2001; accepted 8 February 2001)

A porous medium model of a snow cover, rather than a viscoelastic treatment, has been used to simulate measured, horizontally traveling acoustic waveform propagation above a dry snow cover 11–20 cm thick. The waveforms were produced by explosions of 1-kg charges at propagation distances of 100 to 1400 m. These waveforms, with a peak frequency around 30 Hz, show pulse broadening effects similar to those previously seen for higher-frequency waves over shorter propagation distances. A rigid-ice-frame porous medium (''rigid-porous'') impedance model, which includes the effect of the pores within the snow but ignores any induced motion of the ice particles, is shown to produce much better agreement with the measured waveforms compared with a viscoelastic solid treatment of the snow cover. From the acoustic waveform modeling, the predicted average snow cover depth of 18 cm and effective flow resistivities of 16–31 kPa s m^{-2} agree with snow pit observations and with previous acoustic measurements over snow. For propagation in the upwind direction, the pulse broadening caused by the snow cover interaction is lessened, but the overall amplitude decay is greater because of refraction of the blast waves. [DOI: 10.1121/1.1360240]

PACS numbers: 43.28.En, 43.28.Fp, 43.50.Pn, 43.50.Vt [LCS]

I. INTRODUCTION

Military training activities and firing ranges can produce loud sounds that cause significant annoyance to civilian populations. To minimize this annoyance, noise prediction models are often used to schedule military activities during periods when atmospheric and other environmental conditions are favorable. However, a better understanding of environmental effects on sound propagation and predictive models capable of including these effects are still needed.

A series of blast noise measurements has been conducted in Norway to investigate the effects of forest vegetation, micro-meteorological conditions, and winter ground conditions, and their temporal variations, on the propagation of low-frequency impulse noise. The goal of these measurements was to elucidate these environmental effects and to provide data suitable for validating more realistic propagation models.[1] In an earlier analysis of some of the Norwegian experimental data, Hole[2] used a Fast Field Program[3] with a viscoelastic ground to predict pulses for propagation distances up to 1400 m. Predictions of overpressure amplitudes correlated well with experimental data in strongly upward and downward refracting atmospheres when a wet, slushy snow surface was present. However, the predicted amplitudes and waveforms did not agree with the measured results when a dry snow cover was present. In this paper, we analyze a subset of these measurements to examine the effect of a snow cover on the blast waves. Our purpose here is to determine whether a rigid-porous model of the snow can predict the measured waveforms better than does the viscoelastic model.

Many authors have predicted blast overpressure as a function of distance from the source,[4,5] but there have been fewer predictions of the entire waveform.[6–9] Albert and Orcutt[10] compared predictions and measured waveforms for short range propagation above a snow cover, and showed that the rigid-frame porous model of Attenborough[11] (and its low-frequency approximation) gave good agreement with the large waveform changes that were observed. Subsequently, the Attenborough model has been applied[12] to similar measurement data in an inversion process to find the snow parameters that control the acoustic effects of the snow cover. This paper applies Attenborough's ''rigid-porous'' ground impedance model to predict waveforms at much longer distances and lower frequencies than were previously examined.

In the next section, we describe the measurements and the experimental data. This is followed by a brief outline of the theory of acoustic pulse propagation above a rigid-porous medium and the waveform inversion method used to determine the snow parameters. The results of these theoretical calculations are compared with the measurements, and conclusions are presented in the following sections.

II. FIELD EXPERIMENT

A. Description of site

Acoustic measurements were obtained on 22 February 1995 in an open field of pastureland at a site about 200 km north of Oslo, Norway. Two measurement locations near the north and south ends of the field were instrumented with microphones. C4 explosive charges were detonated at vari-

[a)]Electronic mail: dalbert@crrel.usace.army.mil
[b)]Now at: Norwegian Defense Research Establishment (NDRE), P.O. Box 25, N-2027 Kjeller, Norway; electronic mail: lrh@ffi.no

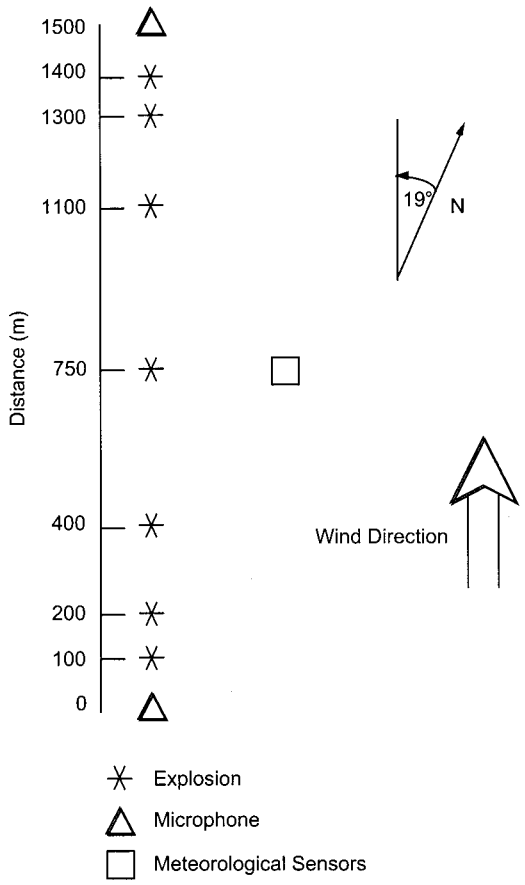

FIG. 1. Plan view of the experimental layout. The orientation of the sensor line is 341° true. Detonation height was 2 m, and the acoustic waveforms were recorded using surface microphones at the 0 (south, or upwind) and 1500 m (north, or downwind) locations.

ous distances between these measurement locations and digitally recorded (Fig. 1). The field was virtually flat, with a dry snow cover about 0.1 to 0.2 m deep. Below the snow, there was a frozen crust of soil, 0.5 m thick, which had very high compressional wave speeds (around 3000 $\mathrm{m\,s^{-1}}$),[13] and a density of 2100 $\mathrm{kg\,m^{-3}}$. Apart from this thin frozen layer, conditions were *superseismic*; i.e., air pressure waves traveled faster than seismic compressional body waves, which had a typical speed of 300 $\mathrm{m\,s^{-1}}$. Below the frozen soil crust, the soil density was around 1600 $\mathrm{kg\,m^{-3}}$.

B. Meteorological and snow conditions

Meteorological measurements were carried out using tower-mounted instruments and a tethered balloon.[14] During the acoustic measurements, the average wind speed at 10 m above ground was around 5 $\mathrm{m\,s^{-1}}$, blowing approximately from the south toward the north, so the south location recorded waveforms that had propagated upwind, while the north location recorded waveforms that had propagated downwind. The air temperature was around 0 °C. The atmospheric sound velocity profile was almost constant with time and height during the acoustic measurements. However, because of the influence of the wind, the value of the sound velocity was 326 $\mathrm{m\,s^{-1}}$ in the upwind direction (toward the south) and 336 $\mathrm{m\,s^{-1}}$ in the downwind direction (toward the north) in Fig. 1. Figure 2 shows the meteorological conditions during the acoustic measurements. Even though the wind profiles are almost constant with height, the wind shear close to the ground (which is not visible in Fig. 2) caused a difference in propagation conditions for the two directions studied. This will be described in Sec. IV.

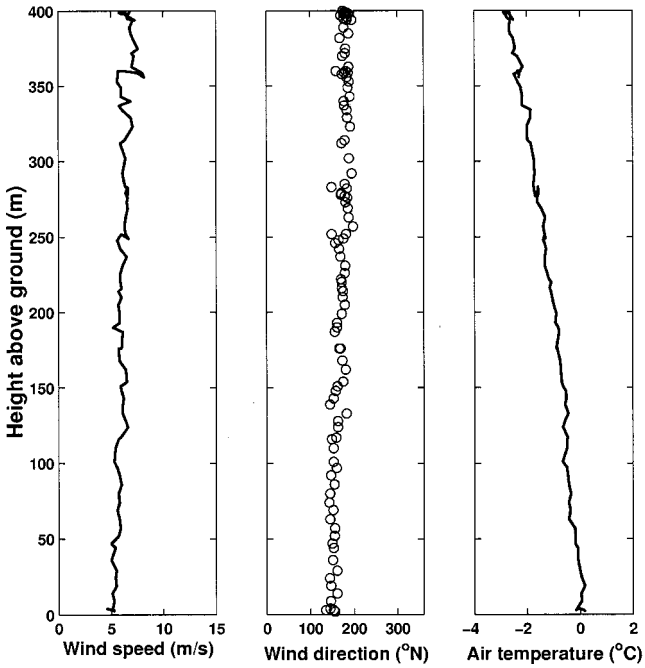

FIG. 2. Meteorological conditions during the blast noise measurements, 22 February 1252–1308 UTC, measured by Tethersonde (Ref. 19). The wind speed was approximately 4–5 $\mathrm{m\,s^{-1}}$ during the tests, and always blowing approximately from the south along the detonation line.

Observations were made in two snow pits, concurrent with the blast noise measurements.[15,16] The total snow cover thicknesses in the two pits were 18 and 16 cm. A hard snow layer just above the ground surface was overlain by an ice crust, and topped by a layer of newly fallen, partially broken precipitation grains. The top layer was 5–6 cm thick, with small grain sizes between 0.5 and 1 mm and a relatively low density of 125 $\mathrm{kg\,m^{-3}}$. Beneath this layer was a permeable ice crust 1 cm thick. The lowest snow layer was 9–10 cm thick with a density of 300–350 $\mathrm{kg\,m^{-3}}$. The grain size in this layer ranged from 1 to 4 mm, with rounded clusters and mixed faceted grain types, indicating that some metamorphosis was occurring. Beneath the snow and just above the soil surface was a discontinuous ice layer at the bottom 1–2 cm thick. Snow cover depths measured at other locations in the field on the day of the blast tests ranged from 11 to 20.5 cm, with most values between 14 and 16 cm.

C. Acoustical measurements

The Department of Applied Acoustics, University of Salford, England, carried out the acoustical measurements. We analyze only the acoustical data recorded using microphones placed at the snow surface. Table I contains a description of acoustical instrumentation used at both locations. (While the original data were recorded with a 20-kHz bandwidth, the data analysis discussed later was conducted after reducing the sampling rate to 2 kHz.) The reader is referred

TABLE I. Acoustical instrumentation for each measurement location. Only one channel, at 0 m height, was used in this paper.

Microphones	4 B&K, 4147
Preamplifiers	4 B&K, 2639
Recorders	SONY PC 204 4-channel DAT
Analyzers	2 Oni Sokki
Bandwidth	0.6–20 000 Hz
Microphone heights	0, 2, 4, and 8 m

to papers in the Inter-noise'96 proceedings[1,17–21] and in a special issue of the Noise Control Engineering Journal for further details on all these measurements.[14,15,22–24]

The experimental geometry is presented in Fig. 1. One kg charges of C4 explosive[2,25,26] were detonated 2 m above the surface along a line between the two acoustic measurement stations, which were 1500 m apart. The blast waveforms for the downwind and upwind locations are shown in Fig. 3. For both recording locations, the duration of the waveforms increases as the propagation distance increases, and the peak amplitude decreases with distance. The amplitude decay is caused in part by spherical spreading of the blast wave front, and in part by environmental effects, as will be discussed below. The measured pulses have a broad frequency content from about 10 to 100 Hz. For the source, the central frequency for the 1-kg C4 detonations used here is around 30 Hz, compared to a peak frequency of around 200 Hz for the blank pistol shots used in previous measurements.[10,12] For the snow surface present during these measurements, we observed that the highest frequencies were quickly attenuated as the blast waves propagated.

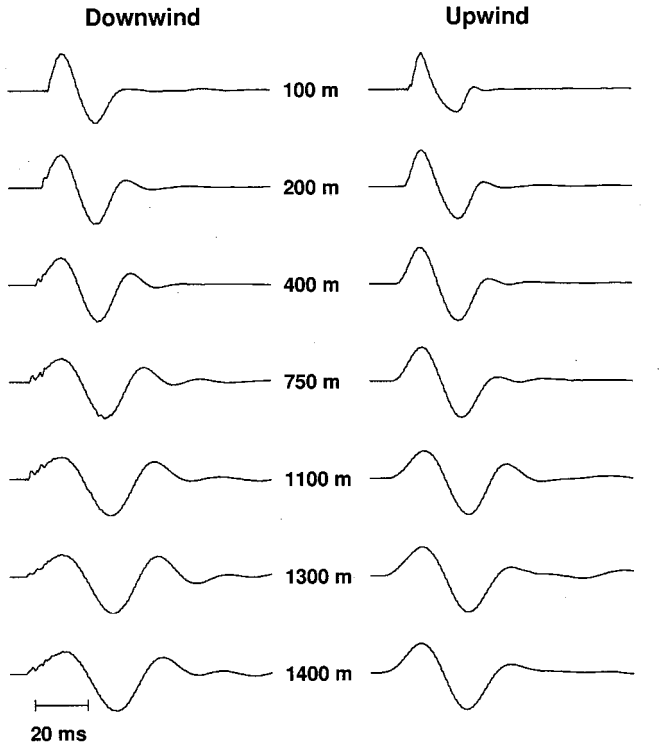

FIG. 3. Normalized blast waveforms experimentally observed by surface microphones for 1-kg explosive charges detonated 2 m above the surface. Although the propagation distances are the same for both observation locations, the waveforms recorded at the downwind location are longer than those measured at the upwind location.

The waveforms recorded at the downwind (north) location last longer than those recorded at the upwind (south) location, and they also exhibit small irregularities in their early portions that do not appear in the upwind location waveforms. Except for the shortest propagation distance (100 m), the north location waveforms also have higher peak pressure amplitudes than those at the south location. These differences with respect to propagation direction will be discussed below.

III. THEORY

A. Pulse waveform for a rigid-porous medium and homogeneous atmosphere

Although a method of calculating pulse shapes based on an empirical model of ground impedance[27] has been developed [6–8,28] and works well for grass-covered ground, we have included a more complicated, but physically based, model of ground impedance in our calculations to give better agreement with observed measurements for snow.[10] This model gives increased accuracy at low frequencies compared to the empirical model. We briefly outline the procedure for calculating theoretical acoustic pulse waveforms from a known (or assumed) surface. For a monofrequency source (with frequency ω) in the air and a receiver on the surface, the acoustic pressure P at a slant distance r away from the source is given by

$$\frac{P}{P_0}=\frac{e^{ikr}}{r}(1+Q)e^{-i\omega t}, \tag{1}$$

where P_0 is a reference source pressure, k is the wave number in air, and Q is the image source strength representing the effect of the ground. At high frequencies ($kr \gg 1$), Q can be written as[29–33]

$$Q=R_P+(1-R_P)F(w), \tag{2}$$

where R_P is the plane wave reflection coefficient, F is the boundary loss factor, and w is a numerical distance, all of which depend on the specific impedance $Z(\omega)$ of the ground. By determining the image source strength Q_n at the nth frequency f_n, the corresponding response amplitude $\hat{P}_n$ can be written as:

$$\hat{P}_n=\frac{P_0}{4\pi r}S_nW_n(1+Q_n)e^{i2\pi f_n r/c}, \quad n=0,1,2,...N-1, \tag{3}$$

where S_n and W_n represent the source and instrument effects at the nth frequency and c is the speed of sound in air. An inverse FFT,

$$P_m=\frac{1}{N}\sum_{n=0}^{N-1}\hat{P}_n e^{-i2\pi mn/N}, \quad m=0,1,2,...N-1, \tag{4}$$

is used to construct theoretical pulse waveforms in the time domain. An explicitly layered model of the ground must be used to represent thin snow covers[34] using (omitting the frequency subscripts)

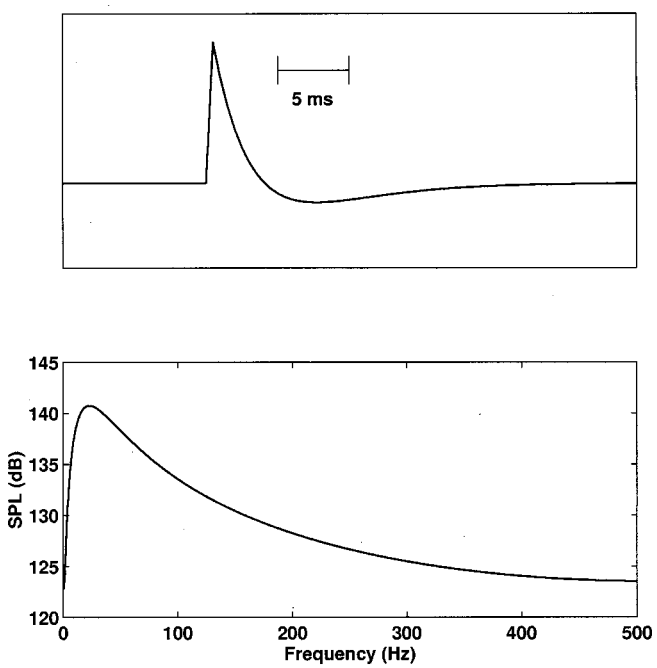

FIG. 4. Assumed source waveform (a) and its power spectrum (b) used in the theoretical calculations.

$$Z = Z_2 \frac{Z_3 - iZ_2 \tan k_2 d}{Z_2 - iZ_3 \tan k_2 d}, \tag{5}$$

where d is the snow layer thickness, k_2 is the wave number in the snow layer, and Z_2 and Z_3 are the impedances of the snow layer and substratum, respectively.[35]

The acoustic behavior of the soil or snow is specified by the impedance Z_2 and wave number k_2, which are used in Eqs. (5) and (2) to find the theoretical waveform. We use Attenborough's four-parameter model of ground impedance[11] to calculate these parameters. The four input parameters are the effective flow resistivity σ, the porosity Ω, the pore shape factor ratio s_f, and the grain shape factor n'. The snow depth d and the substrate properties are also required in a layered model.

An exponentially decaying source pulse $S(t)$ of the form

$$S(t) = P^+(1 - t/t_+)e^{-t/t_+} \tag{6}$$

is used as the starting waveform in all of the blast wave calculations. In Eq. (6), P^+ is the positive peak overpressure, t the time, and t_+ the duration of the positive overpressure. This pulse shape is sometimes known as a Friedlander waveform, and has been previously used in blast wave calculations[25,36,37] and in the ANSI standard blast noise estimation method.[38] Values of $P^+ = 55\,\text{kPa}$ and $t_+ = 3.6\,\text{ms}$ were selected to represent the blast wave produced by a 1-kg charge of C4 at a distance of 5 m,[25] and all calculations began with this source pulse. The waveform and spectrum of the source are shown in Fig. 4.

B. Inversion technique

The acoustic pulse calculation method discussed in the previous section can be used to calculate the pulse shape for a C4 blast if the geometry (source and receiver heights and propagation distance) and ground properties (parameters needed for Attenborough's rigid-porous ground impedance model) are known. The calculation method assumes that the atmosphere is homogeneous. The method can also be used in a waveform inversion procedure to estimate the unknown ground parameters that produce a measured waveform. In this procedure, the geometry and some of the ground parameters (discussed below) are known and are fixed at a constant value in the inversion calculations. Pulses are calculated using Eqs. (1)–(6) using assumed starting values of the unknown parameters, and the calculated waveforms are directly compared with the observed waveforms.[12] The unknown parameters are varied in a systematic way using an iterative search procedure[39] until good agreement is obtained.

For our rigid-porous medium calculations, the grain shape factor n' was set to 0.5, corresponding to spherical grains, and the porosity $\Omega = 0.70$ was determined from the measured average density, 275 kg m^{-3}, of the entire snow cover. We fixed the pore shape factor ratio s_f at 0.8 for dry snow.[12] Parameters for the frozen soil[12] beneath the snow were fixed at $\sigma = 3000\,\text{kPa s m}^{-2}$, $\Omega = 0.27$, $s_f = 0.73$, and $n' = 0.5$. Only the effective flow resistivity σ of the snow and the snow depth d were varied in the inversion procedure.

Waveform inversion to determine the snow parameters was performed independently for each source–receiver distance. We compared calculated and observed pulses using time-aligned, normalized waveforms.

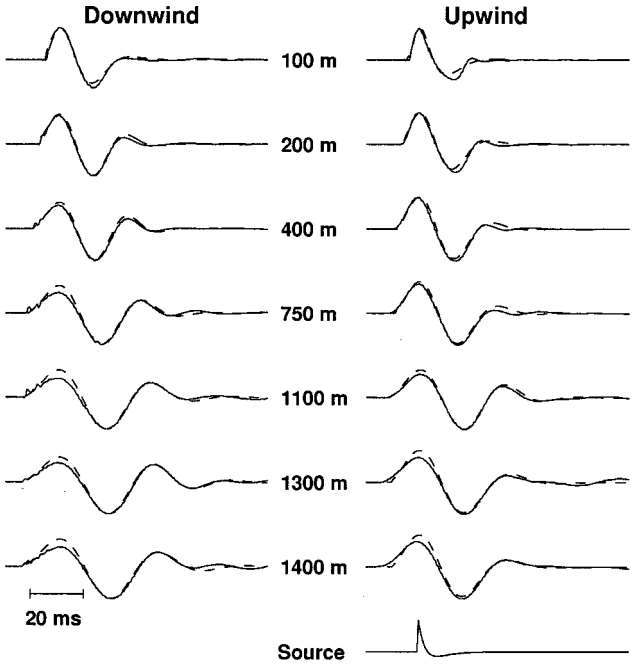

FIG. 5. Observed (solid line) and predicted (dashed line) waveforms at the snow surface, made using the rigid-porous medium model, for the downwind and upwind measurement locations. The source waveform used to calculate the predicted waveforms appears at the bottom of the figure.

IV. RESULTS

The measured and automatically calculated waveforms are compared in Fig. 5, and the snow parameters determined from the inversion procedure are listed in Table II. In general

TABLE II. Waveform inversion results.

	Downwind location		Upwind location	
Range (m)	Effective flow resistivity (σ) kPa s m^{-2}	Snow depth (cm)	Effective flow resistivity (σ) kPa s m^{-2}	Snow depth (cm)
100	21	25	57	19
200	16	21	34	19
400	20	17	37	17
750	28	18	51	15
1100	29	18	37	15
1300	24	17	58	15
1400	31	18	72	14

there is good agreement, and the theoretical waveforms match the measured waveform shapes and time duration. These calculations show that a model with a rigid-porous ground surface and a homogeneous atmosphere is sufficient to explain the waveform elongation in the measured data.

Figure 6 compares the experimentally measured waveform for the downwind measurement location with the rigid-porous snow cover calculations of this paper and with a Fast Field Program (FFP) calculation, assuming a viscoelastic ground surface, that did not take the dry snow cover into account.[2] The propagation distance was 1300 m. The improvement in the modeling accuracy using the porous treatment of the snow is clear from this figure. Previous modeling calculations[2,40] have shown that no selection of parameters for a viscoelastic model will be able to produce the correct amount of waveform broadening shown by the measured data.

The snow cover depths determined by the theoretical

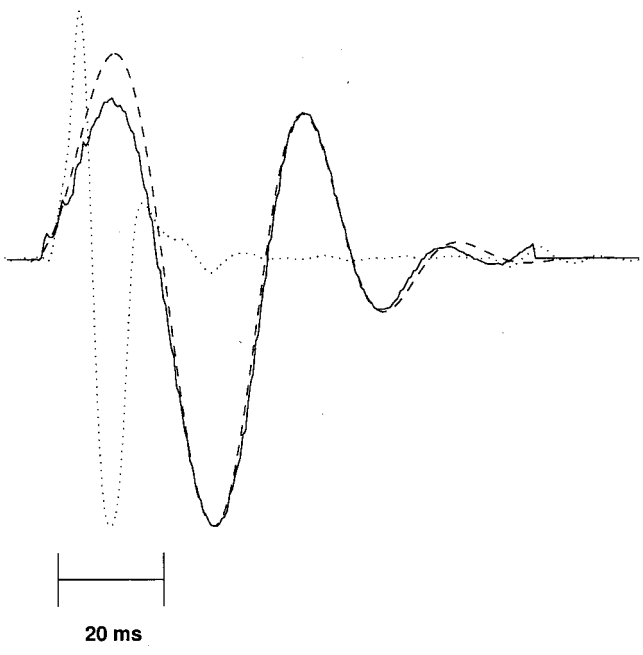

FIG. 6. Comparison of the experimental waveform (solid line) at downwind (north) measurement location, 1300 m from the source with a Fast Field Program (FFP) calculation using a viscoelastic ground (dashed line, same result as in Fig. 9 in Hole, Ref. 2), and with the rigid-porous medium calculations of this paper (dotted line). All waveforms have been normalized.

waveform inversions have an average value of 18 ± 3 cm, in agreement with the measured snow depths of 16 and 18 cm at two widely spaced snow pits. The effective flow resistivities derived from the inversion are nearly constant for the north downwind location, ranging between 16 and 31 kPa s m^{-2}. For the upwind location, the values are higher, 34–72 kPa s m^{-2}, and they seem to fluctuate randomly with distance.

These results can be explained by the effects of the snow cover and the wind. For the downwind location, the blast waves tended to be refracted downward causing them to interact strongly with the porous snow. While the refraction by the wind tends to increase the wave amplitude, compared with the case of a homogeneous atmosphere, the interaction with the snow decreased the amplitude and elongated the waveform. This pulse broadening leads to a low effective flow resistivity in the inversion process. The inversion results are constant with increasing propagation distance, as expected from the fairly uniform snow cover.

The pulse broadening observed at the upwind location was less than at the downwind location, so the effective flow resistivities determined by the waveform inversion procedure are higher. Here, the propagation was upwind, so that the waves tended to be refracted upward, away from the snow surface. Although these waves interacted less with the snow cover, they have lower peak pressure amplitudes because some of the energy that was refracted upward never reaches the microphone on the ground. The amplitudes, and the inversion parameters, fluctuate more than for the downwind waveforms because they are strongly affected by slight fluctuations in the wind. The waveform and amplitude changes in this case are caused by both the wind-generated refraction and by snow cover interaction.

Single frequency Fast Field Program calculations presented in Fig. 7 demonstrate the effect of the wind shear close to the ground. A viscoelastic ground surface with a compressional wave velocity of 1500 m s^{-1}, shear wave velocity of 1000 m s^{-1}, and density of 2000 kg m^{-3} was used in the calculations. The refractive effect of the wind shear for a speed of 5 m s^{-1} at 10 m height above the ground (Fig. 2) was modeled first by setting the sound velocity in the calculations to 331 m s^{-1} at the ground. Then the sound velocity was smoothly varied to values of 336 m s^{-1} for the downwind case and 326 m s^{-1} for the upwind case.

The solid lines in Fig. 7 show the calculated difference in transmission loss between the upwind and downwind directions at 30, 50, and 100 Hz, and clearly demonstrate the expected wind effect at these low frequencies. The circles in Fig. 7 show the measured differences in the peak amplitudes for the blast wave pulses. These measured (broadband) differences are similar to the calculated values at 30 Hz corresponding to the peak pulse frequencies. This figure shows that the differences between the measured amplitudes in the upwind and downwind directions can be attributed to the wind effects.

The effective flow resistivities, 16–31 kPa s m^{-2}, determined for the snow cover for downwind propagation agree with values determined from most previous pulse measurements on seasonal snow.[12,15,21]

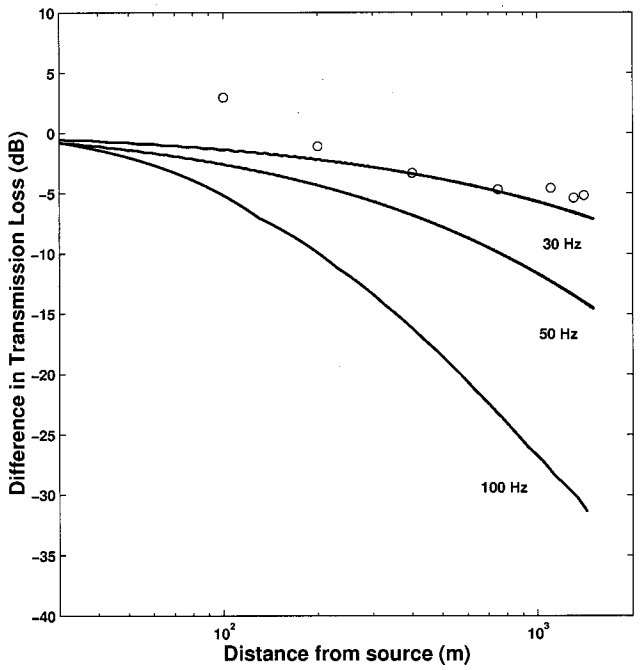

FIG. 7. Measured and calculated amplitude differences between upwind and downwind propagation directions. The measured differences in peak amplitudes are shown by circles. The theoretical differences (solid lines) were calculated using a single frequency FFP with a viscoelastic ground surface and a wind speed of 5 m s^{-1} at 10 m height.

Impedance tube measurements[41] done the day after the blast measurements gave relatively high values for the effective flow resistivity of 59–69 kPa s m^{-2}. However, rain had fallen on the snow after the blast noise measurements, and the warm air temperature overnight may have caused substantial changes in the snow structure by the time the impedance tube measurements were conducted.

Note that in both the downwind and upwind cases, the waveform inversion method uses a homogeneous atmosphere and therefore attributes all of the observed waveform shape changes to the snow cover properties only. There is no difference in the actual snow cover properties in the upwind and downwind directions, and the true flow resistivity should be nearly uniform. The differences in the effective flow resistivity values determined by this procedure arise from ignoring all of the atmospheric effects in the waveform inversion calculations.

V. SUMMARY AND CONCLUDING REMARKS

Blast waves propagating in the upwind and downwind directions above a dry snow cover exhibit pulse broadening caused by wave interaction with the snow cover. By modeling the effect of the snow cover using a rigid-frame porous medium model, the predicted pulse shapes are in much better agreement with experimental results than are previously published calculations using a Fast Field Program with a viscoelastic ground surface that did not take the dry snow cover into account. These results indicate that a porous boundary condition is required for correctly modeled sound propagation over snow.

Note added in proof: A database of the experimental measurements from the Norwegian trials is available from the second author. Additional analysis of the Norwegian data appears in Ref. 42.

ACKNOWLEDGMENTS

We thank Robert L. Guice at ARA, USA, for organizing acoustic and seismic data; Geoffrey Kerry at University of Salford, U.K., for providing the measured acoustic data; Amir M. Kaynia and Christian Madshus at NGI, Norway, for determining the seismic properties of the test site; and Steve Arcone and Mark Moran, CRREL, for technical reviews. The field experiment was initiated and managed by Arnfinn Jenssen at NDCS, Norway. We especially thank the anonymous reviewers and the Associate Editor, Lou Sutherland, for many constructive and helpful comments. This work was funded by the Norwegian Defense Construction Service and the Directorate of Research and Development, U.S. Army Corps of Engineers.

[1] G. Kerry, ''An overview of the long range impulse sound propagation measurements made in Norway,'' Inter-noise 96, Liverpool, UK, 583–588 (1996).
[2] L. R. Hole, ''An experimental and theoretical study on propagation of acoustic pulses in a strongly refracting atmosphere,'' Appl. Acoust. **53**, 583–588 (1997).
[3] H. Schmidt, *SAFARI: Seismo-acoustic fast field algorithm for range-independent environments. User's guide*, Report SR-113 (SACLANTCEN, 1987).
[4] J. W. Reed, *BLASTO, a PC program for predicting positive phase overpressure at distance from an explosion* (JWR Inc., Albuquerque, NM, n.d.).
[5] G. Kerry, D. J. Saunders, and A. Sills, ''The use of meteorological profiles to predict the peak sound pressure level at distance from small explosions,'' J. Acoust. Soc. Am. **81**, 888–896 (1987).
[6] R. Raspet, J. Ezell, and H. E. Bass, ''Additional comments on and erratum for 'Effect of finite ground impedance on the propagation of acoustic pulses' [J. Acoust. Soc. Am. **74**, 267–274 (1983)];'' J. Acoust. Soc. Am. **77**, 1955–1958 (1985).
[7] R. Raspet, H. E. Bass, and J. Ezell, ''Effect of finite ground impedance on the propagation of acoustic pulses,'' J. Acoust. Soc. Am. **74**, 267–274 (1983).
[8] C. G. Don and A. J. Cramond, ''Impulse propagation in a neutral atmosphere,'' J. Acoust. Soc. Am. **81**, 1341–1349 (1987).
[9] I. P. Chunchuzov, G. A. Bush, and S. N. Kulichov, ''On acoustical impulse propagation in a moving inhomogeneous atmospheric layer,'' J. Acoust. Soc. Am. **88**, 455–461 (1990).
[10] D. G. Albert and J. A. Orcutt, ''Acoustic pulse propagation above grassland and snow: Comparison of theoretical and experimental waveforms,'' J. Acoust. Soc. Am. **87**, 93–100 (1990).
[11] K. Attenborough, ''Acoustical impedance models for outdoor ground surfaces,'' J. Sound Vib. **99**, 521–544 (1985).
[12] D. G. Albert, ''Acoustic waveform inversion with application to seasonal snow covers,'' J. Acoust. Soc. Am. **109**, 91–101 (2001).
[13] A. M. Kaynia and C. Madshus, *Blast propagation through forest-NOR 95/1 tests*, NGI report 515137-4 (Norwegian Geotechnical Institute, Oslo, Norway, 1995).
[14] L. R. Hole, Y. Gjessing, and T. de Lange, ''Meteorological measurements and conditions during Norwegian trials,'' Noise Control Eng. J. **46**, 199–207 (1998).
[15] D. G. Albert, ''Snow cover properties from impulsive noise propagation measurements,'' Noise Control Eng. J. **46**, 208–214 (1998).
[16] S. Bakkehøi, *Snow classification during tests at Haslemoen, February 1995*, NGI Report 51537-4 (Norwegian Geotechnical Institute, Oslo, Norway, 1995).
[17] R. Guice and A. Jenssen, ''Impulse noise measurements in a forest during summer and winter—An overview of measurements,'' Inter-Noise 96, Liverpool, UK, 2589–2594 (1996).

[18] M. Trimpop and K.-W. Hirsch, ''On the advantage of relational data structures and client/server applications for shooting noise data using ODBC, SQL and OLE standards,'' Internoise 96, Liverpool, UK, 549–554 (1996).
[19] L. R. Hole, Y. Gjessing, and T. de Lange, ''Meteorological measurements during Norwegian Trials,'' Inter-noise 96, Liverpool, UK, 605–610 (1996).
[20] C. Madshus and A. M. Kanyia, ''Ground response to propagating airblast,'' Inter-Noise 96, Liverpool, UK, 1433–1438 (1996).
[21] D. G. Albert, ''Snow cover effects on impulsive noise propagation in a forest,'' Inter-Noise 96, Liverpool, UK, 663–668 (1996).
[22] K.-W. Hirsch, ''On the influence of local ground reflections on sound levels from distant blasts at large distances,'' Noise Control Eng. J. **46**, 215–226 (1998).
[23] R. L. Guice, L. R. Hole, A. Jenssen, and G. Kerry, ''Impulsive noise measurements in a forest during summer and winter conditions,'' Noise Control Eng. J. **46**, 185–189 (1998).
[24] C. Madshus and A. M. Kaynia, ''Measurement and interpretation of ground response to airblast,'' Noise Control Eng. J. **46**, 191–198 (1998).
[25] L. Kennedy, S. Hikida, and R. Ekler, *Overpressure and dynamic pressure waveforms for small C4 charge detonations*, Report No. SSS-DFR-94-14507 (Maxwell S-Cubed Division, Albuquerque, NM, 1994).
[26] R. Ford, D. J. Saunders, and G. Kerry, ''The acoustic pressure waveform from small unconfined charges of plastic explosive,'' J. Acoust. Soc. Am. **94**, 408–417 (1993).
[27] M. E. Delaney and E. N. Bazley, ''Acoustical properties of fibrous absorbent materials,'' Appl. Acoust. **3**, 105–116 (1970).
[28] A. J. Cramond and C. G. Don, ''Reflection of impulses as a method of determining acoustic impedance,'' J. Acoust. Soc. Am. **75**, 382–389 (1984).
[29] K. Attenborough, S. I. Hayek, and J. M. Lawther, ''Propagation of sound above a porous half-space,'' J. Acoust. Soc. Am. **68**, 1493–1501 (1980).
[30] K. U. Ingard, ''On the reflection of a spherical wave from an infinite plane,'' J. Acoust. Soc. Am. **23**, 329–335 (1951).
[31] I. Rudnick, ''Propagation of an acoustic wave along a boundary,'' J. Acoust. Soc. Am. **19**, 348–356 (1947).
[32] C. I. Chessell, ''Propagation of noise along a finite impedance boundary,'' J. Acoust. Soc. Am. **62**, 825–834 (1977).
[33] C. F. Chien and W. W. Soroka, ''Sound propagation along an impedance plane,'' J. Sound Vib. **43**, 9–20 (1975).
[34] J. Nicolas, J.-L. Berry, and G. A. Daigle, ''Propagation of sound above a finite layer of snow,'' J. Acoust. Soc. Am. **77**, 67–73 (1985).
[35] L. M. Brekhovskikh, *Waves in Layered Media*, 2nd ed. (Academic, New York, 1980).
[36] W. E. Baker, *Explosions in Air* (University of Texas Press, Austin, 1973), p. 268.
[37] M. J. Crocker and L. C. Sutherland, ''Instrumentation requirements for measurement of sonic boom and blast waves—A theoretical study,'' J. Sound Vib. **7**, 351–370 (1968).
[38] ANSI, ''Estimating airblast characteristics for single point explosions in air, with a guide to evaluation of atmospheric propagation and effects'' (American National Standards Institute, New York, 1983), p. vi+25.
[39] W. H. Press, B. P. Flannery, S. A. Teukolsky, and W. T. Vetterling, *Numerical Recipes: The Art of Scientific Computing* (Cambridge University Press, New York, 1986).
[40] D. G. Albert, *Attenuation of outdoor sound propagation levels by a snow cover*, CRREL Report 93-20 (USA CRREL, Hanover, NH, 1993).
[41] S. Storeheier, *A preliminary investigation on the acoustic characterization of snow at the Haslemoen site*, Report 40-NO950182 (Sintef Delab, Trondheim, Norway, 1995).
[42] H. Dong, A. M. Kaynia, C. Madshus, and J. M. Hovem, ''Sound propagation over layered poroelastic ground using a finite-difference model,'' J. Acoust. Soc. Am. **108**, 494–502 (2000).

Acoustic sounding of wind velocity profiles in a stratified moving atmosphere

Vladimir E. Ostashev
NOAA/Environmental Technology Laboratory, 325 Broadway, Boulder, Colorado 80305
and Physics Department, New Mexico State University, Las Cruces, New Mexico 88003-8001

Thomas M. Georges and Steven F. Clifford
NOAA/Environmental Technology Laboratory, 325 Broadway, Boulder, Colorado 80305

George H. Goedecke
Physics Department, New Mexico State University, Las Cruces, New Mexico 88003-8001

(Received 18 April 2000; revised 3 March 2001; accepted 21 March 2001)

The paper deals with analytical and numerical studies of the effects of atmospheric stratification on acoustic remote sensing of wind velocity profiles by sodars. Both bistatic and monostatic schemes are considered. Formulas for the Doppler shift of an acoustic echo signal scattered by atmospheric turbulence advected with the mean wind in a stratified moving atmosphere are derived. Numerical studies of these formulas show that errors in retrieving wind velocity can be of the order of 1 m/s if atmospheric stratification is ignored. Formulas for the height at which wind velocity is retrieved are also derived. Approaches are proposed which allow one to take into account the effects of atmospheric stratification when restoring the wind velocity profile from measured values of the Doppler shift and the time interval of acoustic impulse propagation from a sodar to the scattering volume and back to the ground.
[DOI: 10.1121/1.1371975]

PACS numbers: 43.28.Fp, 43.20.Bi, 43.20.Fn [LCS]

I. INTRODUCTION

Since their invention in the 1960's, sodars have been widely used for acoustic remote sensing of the atmosphere.[1–3] Sodars allow one to measure the Doppler shift $\Delta\omega$ of the sound wave scattered by turbulence advected with the mean wind, the time interval Δt of sound propagation from a sodar to the scattering volume and back to the ground, and the intensity of the acoustic echo signal scattered by atmospheric turbulence, which is proportional to the sound-scattering cross section σ. The first two measured quantities enable one to retrieve a vertical profile of the wind velocity vector $\mathbf{v}(z)$. Here, z is the height above the ground. The second and third measured quantities enable one to retrieve vertical profiles of the structure parameters of temperature and wind velocity fluctuations, $C_T^2(z)$ and $C_v^2(z)$. This remote sensing of $\mathbf{v}$, C_T^2, and C_v^2 can be affected by the refraction of sound waves due to atmospheric stratification, i.e., due to vertical profiles of the adiabatic sound speed $c(z)$ and wind velocity vector $\mathbf{v}(z)$. The present paper focuses on the effects of atmospheric stratification on remote sensing of vertical profiles of wind velocity.

Georges and Clifford[4] were the first to study these effects in detail. They formulated the main steps employed in this study: derivation of a formula for the Doppler shift $\Delta\omega$ of a sound wave scattered at the height z_V by atmospheric turbulence; rewriting the formula for the source–receiver height; retrieving wind velocity vector $\mathbf{v}$ from measured values of $\Delta\omega$; and estimation of z_V in a stratified moving atmosphere. Most of the subsequent research in this field[3,5–10] has been influenced by Ref. 4. For example, Refs. 5 and 7–10 employ formulas for $\Delta\omega$ obtained in Ref. 4 to study the effects of sound refraction on monostatic and bistatic sounding of $\mathbf{v}$. In Ref. 6, formulas for $\Delta\omega$ are derived anew, however, by an approach suggested in Ref. 4. The effects of sound refraction on systematic errors in retrieving wind velocity and the paths of the emitted and scattered sound waves in a stratified moving atmosphere were studied in Refs. 11 and 12, respectively.

Atmospheric stratification can also cause ''off-axis'' arrival of a sound impulse scattered by turbulence at an emitting–receiving antenna in the monostatic scheme. The intensity of such a signal was studied in Ref. 13. Furthermore, measurements of the arrival angle of the scattered impulse and time interval Δt of impulse propagation can provide information about the integral characteristics of vertical profiles of wind velocity and temperature.[4,14–16]

Results obtained in Refs. 17 and 18 showed that the sound-scattering cross section σ in bistatic and monostatic schemes of acoustic sounding of the atmosphere can be significantly affected by vertical profiles of $c(z)$ and $\mathbf{v}(z)$. Therefore, remote sensing of C_T^2 and C_v^2 can also be significantly affected by atmospheric stratification. For example, it was shown[18] that for moderate to strong wind conditions, the direct retrieval of C_T^2 from the echo signal measured by monostatic sodar may not be possible or may lead to significant errors.

Studies of the effects of atmospheric stratification on acoustic remote sensing of wind velocity profiles essentially employ theories of sound propagation in moving media. These theories are summarized in Ref. 19. The objective of the present paper is to use these theories and approaches developed in Refs. 17 and 18 to study the effects of atmo-

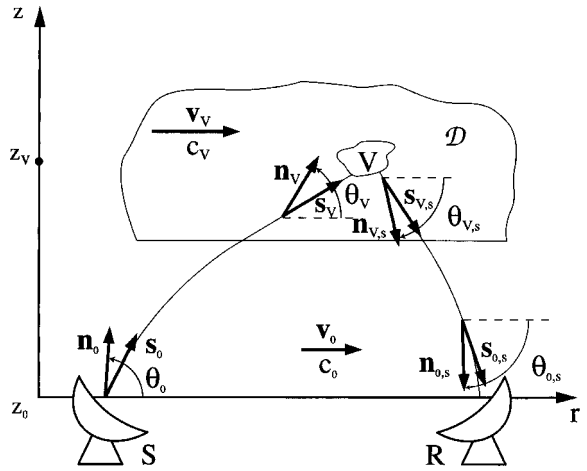

FIG. 1. Geometry of the problem. S is the source, R is the receiver, and V is the scattering volume. Vectors **s** with different indexes are the unit vectors in the direction of the ray paths of the emitted and scattered waves near the source, scattering volume, and receiver. Vectors **n** with different indexes are unit vectors normal to the wavefront of these waves.

spheric stratification on acoustic remote sensing of vertical profiles of the wind velocity vector and to reconsider some of the results obtained previously.

The paper is organized as follows. The geometry of acoustic sounding in a stratified moving atmosphere is described in Sec. II. This geometry is basically the same as in Refs. 17 and 18. However, these references deal with the sound-scattering cross section, while the present paper considers remote sensing of wind velocity profiles. Section III deals with a bistatic scheme of acoustic sounding. In this section, a formula for the Doppler shift $\Delta\omega$ of a sound wave scattered by the turbulence advected with the mean wind is derived, errors in retrieving wind velocity vector **v** due to ignoring atmospheric stratification are discussed, an approach for retrieving **v** in a stratified moving atmosphere is proposed, and a formula for the height z_V at which **v** is retrieved is obtained. The same issues, but for the case of monostatic sounding, are considered in Sec. IV. In Sec. V, the results obtained are summarized.

II. GEOMETRY OF THE PROBLEM

The geometry of the problem is shown in Fig. 1, which is the same as Fig. 1 in Ref. 17. The z axis of the Cartesian coordinate system $\mathbf{R}=(x,y,z)$ is directed upward, and $\mathbf{r}=(x,y)$ are the horizontal coordinates. The source S and receiver R are located at the height z_0 above the ground (z_0 might be zero). Both the source and receiver are sodars. The source emits a monochromatic sound wave. The sound field emitted by the source can be expressed as a Fourier integral of plane waves. These plane waves radiate in a cone formed by a radiation pattern of the source, are bent by refraction, and are scattered by atmospheric turbulence within the scattering volume V. The scattered waves are further refracted. The receiver R receives scattered waves which propagate into a cone of the receiver's radiation pattern. Most sodars have narrow radiation patterns of about $5-7°$. Therefore, we will calculate the Doppler shift for the plane wave which is emitted in the direction of the axis of the source's radiation pattern and for the scattered wave which is received in the direction of the axis of the receiver's radiation pattern. The refracted ray paths of these waves are shown in Fig. 1. Other pairs of emitted and received plane waves that reach different parts of the scattering volume have slightly different Doppler shift. This results in Doppler broadening of the received signal (e.g., Ref. 20). For sufficiently narrow radiation patterns of source and receiver, the Doppler broadening is less than the Doppler shift. In what follows, we will ignore Doppler broadening and consider only the average Doppler shift.

The plane wave emitted by the source propagates in the direction of the unit vector $\mathbf{s}_0$ (shown in Fig. 1) which is tangential to the ray path of this wave. The unit vector $\mathbf{n}_0$ is normal to the wavefront of the emitted wave and does not coincide with $\mathbf{s}_0$ if the wind velocity at the sodar's height is not zero. It is convenient to express $\mathbf{n}_0$ in the following form: $\mathbf{n}_0=(\mathbf{e}_0\cos\theta_0,\sin\theta_0)$, where $\mathbf{e}_0\cos\theta_0$ and $\sin\theta_0$ are, respectively, the horizontal and vertical components of the vector $\mathbf{n}_0$. Furthermore, θ_0 is the grazing angle of $\mathbf{n}_0$, and $\mathbf{e}_0$ is a horizontal unit vector in the azimuthal direction of $\mathbf{n}_0$.

We assume that the atmosphere is horizontally stratified; i.e., the mean adiabatic sound speed $c(z)$ and the mean wind velocity vector $\mathbf{v}(z)=(\mathbf{u}(z),w(z))$ depend only on z. Here, **u** and w are the horizontal and vertical components of **v**. The values of c and **v** at the height z_0 are denoted by c_0 and $\mathbf{v}_0=(\mathbf{u}_0,w_0)$, and their values at the height z_V of the center of the scattering volume V are denoted by c_V and $\mathbf{v}_V=(\mathbf{u}_V,w_V)$.

The scattering volume V is formed as an intersection of the radiation patterns of the source and receiver. We assume that atmospheric turbulence is moving with the mean wind velocity $\mathbf{v}_V$ through the fixed scattering volume V. This causes the frequency of the scattered wave to be different from that of the emitted wave.

We also assume that the vertical scale of the scattering volume V and the sound wavelength λ are less than the vertical scale of variations in $c(z)$ and $\mathbf{v}(z)$. This allows us to introduce the region $\mathcal{D}$ which includes V, where $c(z)$ and $\mathbf{v}(z)$ can be considered constant and equal to c_V and $\mathbf{v}_V$. In $\mathcal{D}$, the unit vector normal to the wavefront of the emitted wave and the unit vector tangential to the ray path of this wave are denoted by $\mathbf{n}_V=(\mathbf{e}_V\cos\theta_V,\sin\theta_V)$ and $\mathbf{s}_V$, and those of the scattered wave are denoted by $\mathbf{n}_{V,s}=(\mathbf{e}_{V,s}\cos\theta_{V,s},-\sin\theta_{V,s})$ and $\mathbf{s}_{V,s}$; near the receiver, the latter two unit vectors are denoted by $\mathbf{n}_{0,s}=(\mathbf{e}_{0,s}\cos\theta_{0,s},-\sin\theta_{0,s})$ and $\mathbf{s}_{0,s}$. Here, $\mathbf{e}_V$, $\mathbf{e}_{V,s}$, and $\mathbf{e}_{0,s}$ are the unit vectors in the horizontal directions of the vectors $\mathbf{n}_V$, $\mathbf{n}_{V,s}$, and $\mathbf{n}_{0,s}$, respectively. Furthermore, θ_V, $\theta_{V,s}$, and $\theta_{0,s}$ are the grazing angles of the latter three vectors.

Figure 1 illustrates these quantities in a bistatic scheme of acoustic sounding of the atmosphere. For monostatic sounding, a receiver is combined with a source. One can easily imagine this geometry if in Fig. 1 the source and receiver are located at one place. In this case, the ray paths of the emitted and scattered waves do not coincide if there is wind shear.

III. BISTATIC SOUNDING

A. Doppler shift

Let ω_0 and $\mathbf{k}_0 = k_0 \mathbf{n}_0$ be the frequency and the wave vector, respectively, of the emitted plane wave propagating in the direction of the axis of the source's radiation pattern at the source's height. In the ground-fixed coordinate system K, the sound pressure of this plane wave in region $\mathcal{D}$ can be written as

$$p(\mathbf{R},t) = A_V \exp(-i\omega_0 t + i\mathbf{k}_V \cdot \mathbf{R}). \tag{1}$$

Here, $\mathbf{k}_V = k_V \mathbf{n}_V$ is the wave vector in region $\mathcal{D}$, which is different from $\mathbf{k}_0$ due to refraction, and A_V is the complex amplitude of the emitted sound wave at the boundary of this region. (The exact values of A_V and the amplitude of the scattered wave are not needed in derivation of a formula for the Doppler shift.) In Eq. (1), ω_0 and $\mathbf{k}_V$ are related by the dispersion equation (e.g., Ref. 19)

$$\omega_0 = k_V c_V + \mathbf{k}_V \cdot \mathbf{v}_V. \tag{2}$$

In the coordinate system K' moving with the mean wind velocity $\mathbf{v}_V$, the position vector $\mathbf{R}' = (x', y', z')$ is related to $\mathbf{R}$ by the Galilean transformation

$$\mathbf{R} = \mathbf{R}' + \mathbf{v}_V t. \tag{3}$$

Substituting $\mathbf{R}$ from this formula into Eq. (1), one obtains an expression for the sound pressure of the emitted wave in the coordinate system K' and in the region $\mathcal{D}$

$$p(\mathbf{R}',t) = A_V \exp(-i\omega' t + i\mathbf{k}_V \cdot \mathbf{R}'), \tag{4}$$

where $\omega' = \omega_0 - \mathbf{k}_V \cdot \mathbf{v}_V$.

Since we assume that atmospheric turbulence is advected with the mean wind, temperature inhomogeneities are not moving within the scattering volume V in the coordinate system K'. The mean velocity of wind velocity fluctuations is also zero in V and K'. However, due to variance of wind velocity fluctuations, there is still some turbulence motion within the scattering volume in the coordinate system K'. This motion results in Doppler broadening of the spectrum of the scattered sound wave. We will ignore this broadening because it is usually less than the Doppler shift. Thus, when considering only the Doppler shift in the frequency of the scattered wave, we can assume that within the scattering volume V and in the coordinate system K', atmospheric turbulence is at rest. Because of this assumption, the frequency of the scattered wave in K' is the same as that of the emitted wave, given by Eq. (4).

Let $\mathbf{k}_{V,s} = k_{V,s} \mathbf{n}_{V,s}$ be the wave vector of the scattered wave in region $\mathcal{D}$. Then, the sound pressure of this wave in K' can be written as

$$p_s(\mathbf{R}',t) = A_s \exp(-i\omega' t + i\mathbf{k}_{V,s} \cdot \mathbf{R}'). \tag{5}$$

Here, A_s is the complex amplitude of the scattered wave. In Eq. (5), we use the Galilean transformation (3) to express $\mathbf{R}'$ in terms of $\mathbf{R}$. As a result, we obtain the sound pressure of the scattered wave in the coordinate system K and in the region $\mathcal{D}$

$$p_s(\mathbf{R},t) = A_s \exp(-i\omega_s t + i\mathbf{k}_{V,s} \cdot \mathbf{R}). \tag{6}$$

Here, $\omega_s = \omega' + \mathbf{k}_{V,s} \cdot \mathbf{v}_V$ is the frequency of the scattered sound wave. The dispersion equation for the scattered wave given by Eq. (6) can be written as

$$\omega_s = k_{V,s} c_V + \mathbf{k}_{V,s} \cdot \mathbf{v}_V. \tag{7}$$

Near the receiver, the frequency and the wave vector of the scattered wave are ω_s and $\mathbf{k}_{0,s} = k_{0,s} \mathbf{n}_{0,s}$, respectively. Substituting the value of ω' into the equation $\omega_s = \omega' + \mathbf{k}_{V,s} \cdot \mathbf{v}_V$, one obtains a formula for the frequency recorded by the receiver

$$\omega_s = \omega_0 + (\mathbf{k}_{V,s} - \mathbf{k}_V) \cdot \mathbf{v}_V. \tag{8}$$

This equation is also derived in Ref. 21. Our derivation of Eq. (8) is somewhat different from that in Ref. 21 and gives us a relationship between $\mathbf{k}_V$ and ω_0 and a relationship between $\mathbf{k}_{V,s}$ and ω_s; see Eqs. (2) and (7), respectively. Another approach for deriving a formula for ω_s was used in Ref. 4. Equation (5) from this reference coincides with Eq. (8) to order v/c but differs from this equation by terms of order $(v/c)^2$. The reason for this difference is explained in the Appendix. Note that Eq. (5) from Ref. 4 and its consequences were used in papers[5,7–10] for studies of the effects of atmospheric stratification on acoustic remote sensing of wind velocity.

In order to derive a formula for the Doppler shift, the wave vectors $\mathbf{k}_{V,s}$ and $\mathbf{k}_V$ in Eq. (8) should be expressed in terms of the frequencies ω_s and ω_0, respectively. Subtracting Eq. (2) from Eq. (7) and taking into account Eq. (8), one finds that $k_V = k_{V,s}$. Therefore, Eq. (8) can be written as $\Delta\omega = k_V(\mathbf{n}_{V,s} - \mathbf{n}_V) \cdot \mathbf{v}_V$. It can be shown from Eq. (2) that $k_V = \omega_0/(c_V + \mathbf{n}_V \cdot \mathbf{v}_V)$. Substituting this value of k_V into the formula for $\Delta\omega$, one obtains the following formula for the Doppler shift in acoustic sounding of the atmosphere:

$$\frac{\Delta\omega}{\omega_0} = \frac{(\mathbf{n}_{V,s} - \mathbf{n}_V) \cdot \mathbf{v}_V / c_V}{1 + \mathbf{n}_V \cdot \mathbf{v}_V / c_V}. \tag{9}$$

Multiplying both sides of this formula by $1 + \mathbf{n}_V \cdot \mathbf{v}_V / c_V$ and taking into account that $\Delta\omega = \omega_s - \omega_0$, one obtains another form of a formula for the Doppler shift

$$\Delta\omega = (\omega_0 \mathbf{n}_{V,s} - \omega_s \mathbf{n}_V) \cdot \mathbf{v}_V / c_V. \tag{10}$$

This formula coincides with Eq. (5.47) from Ref. 19, where it was derived by a different approach. That approach employs a general formula for the Doppler effect in an inhomogeneous moving medium [see Eq. (5.43) from Ref. 19] and a concept that moving turbulence can first be considered as a receiver of the emitted wave, and then as a source for the scattered wave. This general formula for the Doppler effect was also considered elsewhere.[22,23] Furthermore, note that a formula for the Doppler shift in acoustic sounding of the atmosphere obtained in Ref. 11 [see Eq. (13) from that reference] contains terms proportional to $\int_{z_0}^{z_V} \mathbf{v}(z)\,dz$, while Eqs. (9) and (10) do not contain such terms.

B. Doppler shift as observed near the ground

Equations (9) and (10) contain the unit vectors $\mathbf{n}_V$ and $\mathbf{n}_{V,s}$, which are determined near the scattering volume V. It

is desirable to express these vectors in terms of the unit vectors $\mathbf{n}_0$ and $\mathbf{n}_{0,s}$, which are determined near the source and receiver and can be measured experimentally.

In Eq. (9), we replace the vectors $\mathbf{n}_V$, $\mathbf{n}_{V,s}$, and $\mathbf{v}_V$ by $\mathbf{n}_V=(\mathbf{e}_V\cos\theta_V,\sin\theta_V)$, $\mathbf{n}_{V,s}=(\mathbf{e}_{V,s}\cos\theta_{V,s},-\sin\theta_{V,s})$, and $\mathbf{v}_V=(\mathbf{u}_V,w_V)$, respectively. Also, we denote $N=c_0/c_V$, where N is the refractive index in a motionless atmosphere at the height z_V. Finally, we take into account that $\mathbf{e}_V=\mathbf{e}_0$, and $\mathbf{e}_{V,s}=\mathbf{e}_{0,s}$ (see, e.g., Refs. 17 and 19). Then, Eq. (9) can be written as

$$\frac{\Delta\omega}{\omega_0}=\frac{(\mathbf{e}_{0,s}\cdot\mathbf{u}_V/c_0)\cos\theta_{V,s}-(\mathbf{e}_0\cdot\mathbf{u}_V/c_0)\cos\theta_V-\beta(\sin\theta_{V,s}+\sin\theta_V)}{1/N+(\mathbf{e}_0\cdot\mathbf{u}_V/c_0)\cos\theta_V+\beta\sin\theta_V}, \tag{11}$$

where $\beta=w_V/c_0$ is the vertical Mach number at the height z_V. Using results obtained in Ref. 17, we express θ_V and $\theta_{V,s}$ in terms of θ_0 and $\theta_{0,s}$, respectively

$$\cos\theta_V=\frac{\cos\theta_0}{N}\,\frac{1-M+N\beta\sqrt{(1-M)^2-(N^{-2}-\beta^2)\cos^2\theta_0}}{(1-M)^2+\beta^2\cos^2\theta_0}, \tag{12}$$

and

$$\cos\theta_{V,s}=\frac{\cos\theta_{0,s}}{N}\,\frac{1-M_s-N\beta\sqrt{(1-M_s)^2-(N^{-2}-\beta^2)\cos^2\theta_{0,s}}}{(1-M_s)^2+\beta^2\cos^2\theta_{0,s}}. \tag{13}$$

Here, $M=(\mathbf{e}_0\cdot(\mathbf{u}_V-\mathbf{u}_0)/c_0)\cos\theta_0$, and $M_s=(\mathbf{e}_{0,s}\cdot(\mathbf{u}_V-\mathbf{u}_0)/c_0)\cos\theta_{0,s}$. In Eqs. (12), (13), and below, it is assumed that the vertical component of velocity at the height z_0 is zero.

Equations (11)–(13) express $\Delta\omega$ in terms of $\mathbf{v}_V$ and c_V and quantities $\mathbf{u}_0$, c_0, $\cos\theta_0$, $\cos\theta_{0,s}$, $\mathbf{e}_0$, and $\mathbf{e}_{0,s}$ that can be measured near the source and the receiver. These equations are valid to any order in v/c. If c_V is known, and $\Delta\omega$ is measured experimentally, Eqs. (11)–(13) can, in principle, be used to retrieve the value of $\mathbf{v}_V$.

However, these equations are rather involved. Therefore, it is worthwhile to obtain a simpler, approximate formula for $\Delta\omega$ and a simpler approach for retrieving $\mathbf{v}_V$. In order to do these, we introduce a parameter $\epsilon=\max(v/c_0,|\tilde{c}|/c_0)$, where $\tilde{c}=c-c_0$ is the deviation of the adiabatic sound speed from its value at the height z_0. In the atmosphere up to 1–2 km, ϵ is always a small parameter. It follows from Eqs. (12) and (13) that

$$\cos\theta_V=[1-(N-1)+M+\beta\sin\theta_0]\cos\theta_0+O(\epsilon^2), \tag{14}$$

and

$$\cos\theta_{V,s}=[1-(N-1)+M_s-\beta\sin\theta_{0,s}]\cos\theta_{0,s}+O(\epsilon^2). \tag{15}$$

Substituting these values of θ_V and $\theta_{V,s}$ into Eq. (11) and neglecting terms of order ϵ^3, one obtains the desired, approximate formula for the Doppler shift

$$\frac{\Delta\omega}{\omega_0}=(\mathbf{n}_{0,s}-\mathbf{n}_0)\cdot\mathbf{v}_V/c_0+(\Delta v_V)_b/c_0+O(\epsilon^3), \tag{16}$$

where $(\Delta v_V)_b$ is given by

$$\begin{aligned}(\Delta v_V)_b=c_0\Big\{&\tilde{M}_s(M_s-\tilde{M})+\tilde{M}(\tilde{M}-M)+\beta\Big[-(N-1)\\&\times\left(\frac{1}{\sin\theta_0}+\frac{1}{\sin\theta_{0,s}}\right)+(\tilde{M}-\tilde{M}_s)\\&\times(\sin\theta_0+\sin\theta_{0,s})+M_s\frac{\cos^2\theta_{0,s}}{\sin\theta_{0,s}}+M\frac{\cos^2\theta_0}{\sin\theta_0}\Big]\\&+\beta^2(\sin\theta_0+\sin\theta_{0,s})\sin\theta_{0,s}\Big\}.\end{aligned} \tag{17}$$

Here, $\tilde{M}=(\mathbf{e}_0\cdot\mathbf{u}_V/c_0)\cos\theta_0$, and $\tilde{M}_s=(\mathbf{e}_{0,s}\cdot\mathbf{u}_V/c_0)\cos\theta_{0,s}$. Note that $\tilde{M}=M$, and $\tilde{M}_s=M_s$ if $\mathbf{u}_0=0$. The first term on the right-hand side of Eq. (16) can be written as

$$\begin{aligned}(\mathbf{n}_{0,s}-\mathbf{n}_0)\cdot\mathbf{v}_V/c_0=&(\mathbf{e}_{0,s}\cdot\mathbf{u}_V/c_0)\cos\theta_{0,s}-(\mathbf{e}_0\cdot\mathbf{u}_V/c_0)\cos\theta_0\\&-\beta(\sin\theta_0+\sin\theta_{0,s}).\end{aligned} \tag{18}$$

This term is proportional to v and is of order ϵ. The second term on the right-hand side of Eq. (16), $(\Delta v_V)_b/c_0$, is a sum of all terms proportional to ϵ^2. This term is ignored in a standard technique for retrieving a vertical profile of the wind velocity vector.

In the standard technique, the Doppler shift $\Delta\omega$ and the time interval Δt of the echo signal propagation from the source to the scattering volume and from the scattering volume to the receiver are measured for different values of the unit vectors $\mathbf{n}_0$ and $\mathbf{n}_{0,s}$. Then, the value of the wind velocity vector is retrieved from a formula for the Doppler shift where terms of order ϵ^2 are ignored (e.g., Ref. 15)

$$\frac{\Delta\omega}{\omega_0}=(\mathbf{n}_{0,s}-\mathbf{n}_0)\cdot\mathbf{v}_V^{(0)}/c_0. \tag{19}$$

Here, the superscript (0) at $\mathbf{v}_V$ indicates that terms of order ϵ^2 are ignored. The retrieved value of $\mathbf{v}_V^{(0)}$ is the value of the wind velocity vector at the height z_V of the scattering vol-

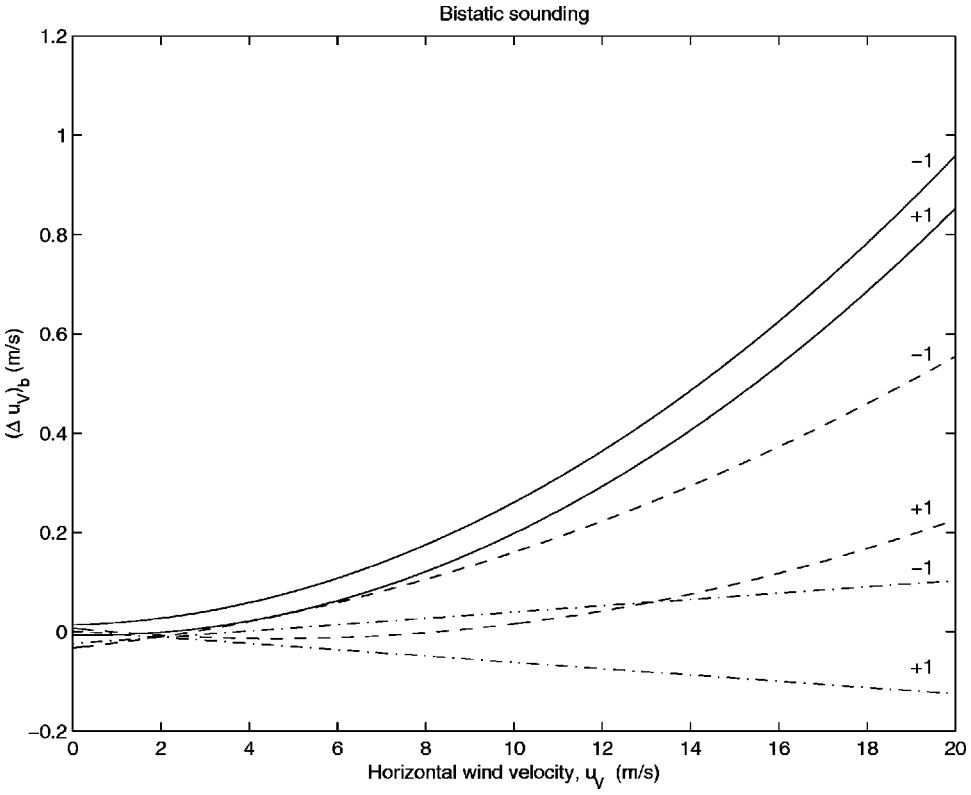

FIG. 2. Error $(\Delta u_V)_b$ in measuring horizontal wind velocity versus the value of this velocity u_V for bistatic sounding. Solid lines correspond to the case $\theta_0=90°$ and $\theta_{0,s}=40°$; dashed lines to $\theta_0=45°$ and $\theta_{0,s}=70°$; and dash-dotted lines to $\theta_0=60°$ and $\theta_{0,s}=90°$. The value of vertical wind velocity w_V in m/s is indicated above the lines.

ume. This height can be found by using the measured values of Δt. If sound refraction is ignored, the height of the scattering volume is

$$z_V^{(0)}=z_0+\frac{c_0\ \Delta t}{1/\sin\theta_0+1/\sin\theta_{0,s}}+O(\epsilon). \tag{20}$$

Here, the superscript (0) at z_V indicates that terms of order ϵ are ignored. Thus, in the standard technique, the use of Eqs. (19) and (20) allows one to retrieve the vertical profile $\mathbf{v}_V^{(0)}(z_V^{(0)})$.

Equation (16) is a more accurate formula for the Doppler shift than Eq. (19). Subtracting Eq. (19) from Eq. (16), one obtains

$$(\Delta v_V)_b=(\mathbf{n}_{0,s}-\mathbf{n}_0)\cdot(\mathbf{v}_V^{(0)}-\mathbf{v}_V). \tag{21}$$

It follows from this formula that $(\Delta v_V)_b$ can be interpreted as an error in retrieving the wind velocity component in the direction of the vector $(\mathbf{n}_{0,s}-\mathbf{n}_0)$ due to the omission of terms of order ϵ^2. It also follows from Eq. (21) that $\mathbf{v}_V=\mathbf{v}_V^{(0)}+\mathbf{b}$, where $b\sim O(\epsilon^2)$. We substitute this formula for $\mathbf{v}_V$ into Eq. (17). In the resulting equation, terms containing the vector $\mathbf{b}$ are of order ϵ^3 or ϵ^4 and can be ignored. Thus, in Eq. (17), $\mathbf{v}_V$ can be replaced by $\mathbf{v}_V^{(0)}$ to order ϵ^2, i.e., to the same order to which Eq. (16) is derived.

C. Analysis

Let us numerically study an error in retrieving $\mathbf{v}_V$ due to the omission of terms of order ϵ^2. We shall assume that $\mathbf{u}_0=0$. Furthermore, we assume that the vectors $\mathbf{u}_V$, $\mathbf{e}_0$, and $\mathbf{e}_{0,s}$ lie in one vertical plane, and that $\mathbf{e}_0\cdot\mathbf{u}_V=u_V$, and $\mathbf{e}_{0,s}\cdot\mathbf{u}_V=u_V$. Finally, let $c_0=340$ m/s, and $c_V=339$ m/s.

For the considered case and with the use of Eq. (18), Eq. (16) can be written as

$$\frac{\Delta\omega}{\omega_0}=\frac{1}{c_0}[u_V(\cos\theta_{0,s}-\cos\theta_0)-w_V(\sin\theta_{0,s}+\sin\theta_0)+(\Delta u_V)_b)]+O(\epsilon^3). \tag{22}$$

Suppose that w_V is known. Also, let us factor out the term $(\cos\theta_{0,s}-\cos\theta_0)$ from the square brackets in Eq. (22). Then, the third term in the square brackets of the equation obtained, which we denote as $(\Delta u_V)_b$, is equal to $(\Delta u_V)_b=(\Delta v_V)_b/(\cos\theta_{0,s}-\cos\theta_0)$. This term can be interpreted as an error in measuring u_V if terms of order ϵ^2 are ignored.

The dependence of $(\Delta u_V)_b$ on u_V, calculated with the use of Eq. (17), is shown in Fig. 2 for three pairs of the values of the grazing angles of the emitted and scattered waves: $\theta_0=90°$ and $\theta_{0,s}=40°$ (solid lines); $\theta_0=45°$ and $\theta_{0,s}=70°$ (dashed lines); and $\theta_0=60°$ and $\theta_{0,s}=90°$ (dash-dotted lines). For each pair of the grazing angles, $(\Delta u_V)_b$ is calculated for the case when the vertical wind velocity $w_V=1$ m/s and for the case when $w_V=-1$ m/s. These cases are marked by numbers $+1$ or -1 above the lines.

Instrumentation error and accuracy in measuring horizontal and vertical components of wind velocity vector by sodars can be as low as 0.1–0.3 m/s.[3,6,11,24] It follows from Fig. 2 that for the first two pairs of the grazing angles of the emitted and scattered waves, which correspond to the solid and dashed lines $(\Delta u_V)_b$ can be greater than 0.1–0.3 m/s. In this case, the term $(\Delta v_V)_b$ on the right-hand side of Eq. (16) should be taken into account when retrieving the wind velocity vector $\mathbf{v}_V$. This can be done by the following approach, which is similar to that proposed in Ref. 4. First, we use the standard technique for retrieving the wind velocity

vector $\mathbf{v}_V^{(0)}$. Then, the obtained value of $\mathbf{v}_V^{(0)}$ is used to calculate $(\Delta v_V)_b$, as explained at the end of the previous subsection. (We assume that the value of c_V is known.) Finally, the value of $\mathbf{v}_V$ is retrieved by using Eq. (16) where $\Delta\omega$ and $(\Delta v_V)_b$ are known. This approach allows us to account for terms of order ϵ^2 when retrieving $\mathbf{v}_V$.

The described approach for retrieving $\mathbf{v}_V$ is straightforward and easy to employ. However, it should be noted that for two geometries of bistatic acoustic sounding, the term $(\Delta v_V)_b$ is small and might be ignored. For the first geometry, $\theta_{0,s}=90°$, and for the second, $\mathbf{e}_{0,s}\cos\theta_{0,s}=\mathbf{e}_0\cos\theta_0$. For both geometries, the first term on the right-hand side of Eq. (17) vanishes. The second term is also zero if $\mathbf{u}_0=0$. The other terms on the right-hand side of Eq. (17) are proportional to the vertical Mach number β and are rather small, since in the atmosphere $w\ll u$ almost always. Thus, for the two geometries, the term $(\Delta v_V)_b$ can be rather small. For example, the dash-dotted lines in Fig. 2, corresponding to the case $\theta_{0,s}=90°$, show that an error in retrieving u_V is less than or of the order of 0.1 m/s.

The case $\mathbf{e}_{0,s}\cos\theta_{0,s}=\mathbf{e}_0\cos\theta_0$ also allows us to measure the vertical component of velocity, w_V, more accurately. Indeed, in this case, the first term on the right-hand side of Eq. (16) is equal to $-\beta(\sin\theta_0+\sin\theta_{0,s})$. [This is clearly seen from Eq. (18).] Furthermore, for this case $(\Delta v_V)_b\sim\beta\epsilon$, provided that $\mathbf{u}_0=0$. Therefore, the first term on the right-hand side of Eq. (16), $-\beta(\sin\theta_0+\sin\theta_{0,s})$, is much greater than $(\Delta v_V)_b$. This enables one to reliably retrieve β.

We have also numerically studied the effects of values of c_V on the $(\Delta v_V)_b$. The results obtained show that if c_V varies from ±1 to ±3 m/s, the value of $(\Delta v_V)_b$ remains practically unchanged.

D. Height of the scattering volume

In acoustic sounding of wind velocity $\mathbf{v}_V$, one also needs to retrieve the height z_V at which $\mathbf{v}_V$ is measured. In this subsection, we derive a formula for z_V which accounts for sound refraction due to atmospheric stratification.

Let Ψ be the eikonal of a sound wave in a stratified moving atmosphere. It follows from Ref. 19 [see Eq. (3.59) from this reference] that

$$\Psi=\Psi^{(0)}+\frac{\omega}{k^{(0)}}\int_{z_1}^{z_2}\frac{(\omega-\mathbf{a}\cdot\mathbf{u})c-w\chi^{\pm}}{(c^2-w^2)\chi^{\pm}}\,dz. \tag{23}$$

Here, z_1 and z_2 are initial and final heights of the ray path, $\Psi^{(0)}$ is the value of the eikonal at the beginning of the ray path (i.e., at $z=z_1$), ω is the frequency of a sound wave, $k^{(0)}$ is a reference value of the wave number, $\mathbf{a}$ is the horizontal component of the wave vector (the vector $\mathbf{a}$ remains constant as a plane sound wave propagates in a stratified atmosphere), and $\chi^{\pm}$ is given by

$$\chi^{\pm}=\pm\sqrt{(\omega-\mathbf{a}\cdot\mathbf{u})^2-(c^2-w^2)a^2}. \tag{24}$$

The plus sign in this equation corresponds to a wave propagating upward, and the minus sign corresponds to a wave propagating downward.

The time interval Δt_{12} of sound propagation from the height z_1 to the height z_2 is related to Ψ by (see Ref. 19, Sec. 3.3.2)

$$\Delta t_{12}=(\Psi-\Psi^{(0)})/c^{(0)}, \tag{25}$$

where $c^{(0)}$ is the reference value of the adiabatic sound speed.

We now use Eqs. (23), (24), and (25) to obtain the time interval Δt_0 of sound propagation from the source to the scattering volume for the geometry in Fig. 1. For this case in these equations, ω should be replaced by the frequency of the emitted wave ω_0; $k^{(0)}$ by k_0; $c^{(0)}$ by c_0; z_1 by z_0; z_2 by z_V; $\chi^{\pm}$ by χ^{+}; and $\mathbf{a}$ by $\mathbf{a}_0$, where $\mathbf{a}_0$ is the horizontal component of the vector $\mathbf{k}_0$. Also, ω_0 is replaced by its value from the dispersion equation at the source's height: $\omega_0=k_0c_0+\mathbf{a}_0\cdot\mathbf{u}_0$. As a result, we have

$$\Delta t_0=\frac{k_0c_0+\mathbf{a}_0\cdot\mathbf{u}_0}{k_0c_0}\int_{z_0}^{z_V}\frac{(k_0c_0-\mathbf{a}_0\cdot(\mathbf{u}-\mathbf{u}_0))c-w\chi^{+}}{(c^2-w^2)\chi^{+}}\,dz. \tag{26}$$

We divide the numerator and denominator of the integrand in this equation by k_0c. We also take into account a relationship: $\mathbf{a}_0/k_0=\mathbf{e}_0\cos\theta_0$. [This relationship can be obtained by equating two representations of the vector $\mathbf{n}_0$: $\mathbf{n}_0=(\mathbf{e}_0\cos\theta_0,\sin\theta_0)$ and $\mathbf{n}_0=(\mathbf{a}_0/k_0,q_0/k_0)$, where q_0 is the vertical component of the wave vector $\mathbf{k}_0$.] As a result, one obtains the following formula for Δt_0:

$$\Delta t_0=[1+(\mathbf{e}_0\cdot\mathbf{u}_0/c_0)\cos\theta_0]\times\int_{z_0}^{z_V}\frac{c_0-\mathbf{e}_0\cdot(\mathbf{u}-\mathbf{u}_0)\cos\theta_0-wQ_0}{(c^2-w^2)Q_0}\,dz, \tag{27}$$

where $Q_0=\chi^{+}/(k_0c)$ is given by

$$Q_0=\sqrt{\left(\frac{c_0}{c}-\frac{\mathbf{e}_0\cdot(\mathbf{u}-\mathbf{u}_0)}{c}\cos\theta_0\right)^2-\left(1-\frac{w^2}{c^2}\right)\cos^2\theta_0}. \tag{28}$$

Analogously, we obtain the time interval Δt_s of sound propagation from the scattering volume to the receiver. For this case in Eqs. (23), (24), and (25), ω should be replaced by ω_s; $k^{(0)}$ by $k_{0,s}$; $c^{(0)}$ by c_0; z_1 by z_V; z_2 by z_0; $\chi^{\pm}$ by χ^{-}; and $\mathbf{a}$ by $\mathbf{a}_{0,s}$, where $\mathbf{a}_{0,s}$ is the horizontal component of the vector $\mathbf{k}_{0,s}$. Also we replace ω_s by its value from the dispersion equation for the scattered wave at the receiver's height: $\omega_s=k_{0,s}c_0+\mathbf{a}_{0,s}\cdot\mathbf{u}_0$. Finally, we use the relationship: $\mathbf{a}_{0,s}/k_{0,s}=\mathbf{e}_{0,s}\cos\theta_{0,s}$, which can be obtained from: $\mathbf{n}_{0,s}=(\mathbf{e}_{0,s}\cos\theta_{0,s},-\sin\theta_{0,s})=(\mathbf{a}_{0,s}/k_{0,s},q_{0,s}/k_{0,s})$, where $q_{0,s}$ is the vertical component of $\mathbf{k}_{0,s}$. As a result, we have

$$\Delta t_s=[1+(\mathbf{e}_{0,s}\cdot\mathbf{u}_0/c_0)\cos\theta_{0,s}]\times\int_{z_0}^{z_V}\frac{c_0-\mathbf{e}_{0,s}\cdot(\mathbf{u}+\mathbf{u}_0)\cos\theta_{0,s}+wQ_{0,s}}{(c^2-w^2)Q_{0,s}}\,dz, \tag{29}$$

where $Q_{0,s}$ is given by

$$Q_{0,s} = \sqrt{\left(\frac{c_0}{c} - \frac{\mathbf{e}_{0,s}\cdot(\mathbf{u}-\mathbf{u}_0)}{c}\cos\theta_{0,s}\right)^2 - \left(1-\frac{w^2}{c^2}\right)\cos^2\theta_{0,s}}. \tag{30}$$

The total time interval Δt of sound propagation from the source to the receiver is

$$\Delta t = \Delta t_0 + \Delta t_s. \tag{31}$$

Substitution of Δt_0 and Δt_s from Eqs. (27) and (29) into Eq. (31) results in an integral equation for z_V. In principle, this integral equation can be solved numerically for z_V.

However, this approach is rather involved. It is worthwhile to obtain an approximate solution for z_V where terms of order ϵ are retained. Developing Δt_0 and Q_0 in series in ϵ and substituting the obtained value of Q_0 into Eq. (27), one obtains

$$\Delta t_0 = \frac{z_V - z_0}{c_0\sin\theta_0}\left[1 - \frac{\mathbf{e}_0\cdot\mathbf{u}_0}{c_0}\ \frac{\cos\theta_0\cos(2\theta_0)}{\sin^2\theta_0} - \xi\sin\theta_0 + \eta\frac{\cos(2\theta_0)}{\sin^2\theta_0} + \mathbf{e}_0\cdot\mathbf{m}\ \frac{\cos^3\theta_0}{\sin^2\theta_0}\right] + O(\epsilon^2). \tag{32}$$

Here, η, ξ, and $\mathbf{m}$ are the mean values of $\tilde{c}$, w, and $\mathbf{u}$ between z_0 and z_V

$$\eta = \frac{1}{z_V - z_0}\int_{z_0}^{z_V}\frac{\tilde{c}(z)}{c_0}dz, \quad \xi = \frac{1}{z_V - z_0}\int_{z_0}^{z_V}\frac{w(z)}{c_0}dz, \quad \mathbf{m} = \frac{1}{z_V - z_0}\int_{z_0}^{z_V}\frac{\mathbf{u}(z)}{c_0}dz. \tag{33}$$

In Eq. (33), z_V and $\mathbf{v}(z)$ can be approximately replaced by $z_V^{(0)}$, and $\mathbf{v}^{(0)}(z_V^{(0)})$. This approximation ignores terms of order ϵ^2, which are neglected on the right-hand side of Eq. (32). The values of η, ξ, and $\mathbf{m}$ after these substitutions are denoted as $\eta^{(0)}$, $\xi^{(0)}$, and $\mathbf{m}^{(0)}$

$$\eta^{(0)} = \frac{1}{z_V^{(0)} - z_0}\int_{z_0}^{z_V^{(0)}}\frac{\tilde{c}}{c_0}dz, \quad \xi^{(0)} = \frac{1}{z_V^{(0)} - z_0}\int_{z_0}^{z_V^{(0)}}\frac{w^{(0)}}{c_0}dz, \quad \mathbf{m}^{(0)} = \frac{1}{z_V^{(0)} - z_0}\int_{z_0}^{z_V^{(0)}}\frac{\mathbf{u}^{(0)}}{c_0}dz. \tag{34}$$

Analogously, developing Δt_s and $Q_{0,s}$ in series in ϵ, one obtains

$$\Delta t_s = \frac{z_V - z_0}{c_0\sin\theta_{0,s}}\left[1 - \frac{\mathbf{e}_{0,s}\cdot\mathbf{u}_0}{c_0}\ \frac{\cos\theta_{0,s}\cos(2\theta_{0,s})}{\sin^2\theta_{0,s}} + \xi\sin\theta_{0,s} + \eta\frac{\cos(2\theta_{0,s})}{\sin^2\theta_{0,s}} + \mathbf{e}_{0,s}\cdot\mathbf{m}\ \frac{\cos^3\theta_{0,s}}{\sin^2\theta_{0,s}}\right] + O(\epsilon^2). \tag{35}$$

In this equation, η, ξ, and $\mathbf{m}$ can also be replaced by $\eta^{(0)}$, $\xi^{(0)}$, and $\mathbf{m}^{(0)}$.

We now substitute the obtained values of Δt_0 and Δt_s given by Eqs. (32) and (35) into Eq. (31). Furthermore, we replace η, ξ, and $\mathbf{m}$ by $\eta^{(0)}$, $\xi^{(0)}$, and $\mathbf{m}^{(0)}$, respectively. Solving the resulting equation for z_V yields

$$z_V = z_0 + \frac{c_0\ \Delta t}{1/\sin\theta_0 + 1/\sin\theta_{0,s}} + (\Delta z_V)_b + O(\epsilon^2). \tag{36}$$

Here, $(\Delta z_V)_b$ is a sum of all terms proportional to ϵ

$$(\Delta z_V)_b = \frac{c_0\ \Delta t}{(1/\sin\theta_0 + 1/\sin\theta_{0,s})^2}\left[\frac{\mathbf{u}_0}{c_0}\cdot\left(\mathbf{e}_0\frac{\cos\theta_0\cos(2\theta_0)}{\sin^3\theta_0} + \mathbf{e}_{0,s}\frac{\cos\theta_{0,s}\cos(2\theta_{0,s})}{\sin^3\theta_{0,s}}\right) - \eta^{(0)}\left(\frac{\cos(2\theta_0)}{\sin^3\theta_0} + \frac{\cos(2\theta_{0,s})}{\sin^3\theta_{0,s}}\right) - \mathbf{m}^{(0)}\cdot(\mathbf{e}_0\cot^3\theta_0 + \mathbf{e}_{0,s}\cot^3\theta_{0,s})\right]. \tag{37}$$

If $(\Delta z_V)_b$ is ignored, Eq. (36) coincides with Eq. (20), which is used in the standard technique of acoustic sounding to retrieve the height z_V at which wind velocity is measured. Equations (36) and (37) allow us to more accurately calculate z_V by accounting for sound refraction in a stratified moving atmosphere. To calculate $(\Delta z_V)_b$, one needs to know $\mathbf{v}_V^{(0)}(z_V^{(0)})$ (which can be retrieved by the standard technique), Δt and $c(z)$. Note that a formula for $(\Delta z_V)_b$ was also derived in Ref. 12 [see Eq. (14) from that reference]. This formula for $(\Delta z_V)_b$ is expressed in terms of parameters which differ from those in Eq. (37), and contains not only terms of order ϵ, but also higher order terms in ϵ.

Let $\mathbf{m}^{(0)}$ be parallel to $\mathbf{e}_0 = \mathbf{e}_{0,s}$, $c(z) = c_0 = 340$ m/s, $\theta_0 = \theta_{0,s} = 45°$, $z_V^{(0)} = 600$ m, $u_0 = 0$, $u_V = 18$ m/s, and wind velocity be linearly increasing with height. Then, it can be shown from Eq. (37) that $(\Delta z_V)_b = -11.2$ m.

IV. MONOSTATIC SOUNDING

The principal difference of monostatic sounding from bistatic is that the values of $\theta_{0,s}$ and $\mathbf{e}_{0,s}$, determining the direction of propagation of the scattered wave near the receiver which is combined with the source, are no longer independent from θ_0 and $\mathbf{e}_0$. Indeed, if there is no wind shear in the atmosphere, the ray path of the scattered wave is the same as that of the emitted wave, and the following equalities hold: $\theta_{0,s} = \theta_0$, and $\mathbf{e}_{0,s} = -\mathbf{e}_0$. In the presence of wind shear, the ray paths of the emitted and scattered waves do not coincide, and $\theta_{0,s}$ and $\mathbf{e}_{0,s}$ can be expressed in terms of θ_0, $\mathbf{e}_0$, and vertical profiles $c(z)$ and $\mathbf{v}(z)$. Therefore, in the theory of monostatic sounding, one needs first to find $\theta_{0,s}$ and $\mathbf{e}_{0,s}$. Then, $\theta_{0,s}$ and $\mathbf{e}_{0,s}$ should be substituted into Eqs. (11), (16), and (36) for the Doppler shift $\Delta\omega$ and the height z_V. This results in formulas for $\Delta\omega$ and z_V for monostatic sounding, which are presented below.

A. Formulas for $\theta_{0,s}$ and $\mathbf{e}_{0,s}$

In order to find $\theta_{0,s}$ and $\mathbf{e}_{0,s}$, one can write an equation for the horizontal displacement $\mathbf{r}_0$ of the ray path of the emitted wave from a sodar to the scattering volume and an

equation for the horizontal displacement $\mathbf{r}_s$ of the scattered wave from the scattering volume to the sodar. Equating $\mathbf{r}_0$ and $-\mathbf{r}_s$ yields the following equation:

$$\int_{z_0}^{z_V}\left\{\mathbf{e}_0\cos\theta_0+\frac{\left[\frac{c_0}{c}-\frac{\mathbf{e}_0\cdot(\mathbf{u}-\mathbf{u}_0)}{c}\cos\theta_0-\frac{wQ_0}{c}\right]\frac{\mathbf{u}}{c}}{1-w^2/c^2}\right\}\frac{dz}{Q_0}$$

$$=-\int_{z_0}^{z_V}\left\{\mathbf{e}_{0,s}\cos\theta_{0,s}+\frac{\left[\frac{c_0}{c}-\frac{\mathbf{e}_{0,s}\cdot(\mathbf{u}-\mathbf{u}_0)}{c}\cos\theta_{0,s}+\frac{wQ_{0,s}}{c}\right]\frac{\mathbf{u}}{c}}{1-w^2/c^2}\right\}\frac{dz}{Q_{0,s}}. \tag{38}$$

A detailed derivation of Eq. (38) is given elsewhere.[18] This equation is valid to any order in v/c_0. Equation (38) can be numerically solved for $\theta_{0,s}$ and $\mathbf{e}_{0,s}$ if θ_0, $\mathbf{e}_0$, $c(z)$, and $\mathbf{v}(z)$ are known. Then, Eqs. (11)–(13) allow us to calculate the Doppler shift $\Delta\omega$ to any order in v/c_0.

It is worthwhile to obtain an approximate solution of Eq. (38) by making use of the small parameter ϵ. Let us decompose the integrands on the left- and right-hand side of Eq. (38) into the series in ϵ. Retaining terms of order ϵ, we obtain

$$\frac{\mathbf{e}_0\cos\theta_0}{\sin\theta_0}+\frac{\mathbf{m}}{\sin\theta_0}+\frac{\mathbf{e}_0[\mathbf{e}_0\cdot(\mathbf{m}-\mathbf{u}_0/c_0)]\cos^2\theta_0}{\sin^3\theta_0}+\frac{\mathbf{e}_0\eta\cos\theta_0}{\sin^3\theta_0}$$

$$=-\frac{\mathbf{e}_{0,s}\cos\theta_{0,s}}{\sin\theta_{0,s}}-\frac{\mathbf{m}}{\sin\theta_{0,s}}-\frac{\mathbf{e}_{0,s}[\mathbf{e}_{0,s}\cdot(\mathbf{m}-\mathbf{u}_0/c_0)]\cos^2\theta_{0,s}}{\sin^3\theta_{0,s}}-\frac{\mathbf{e}_{0,s}\eta\cos\theta_{0,s}}{\sin^3\theta_{0,s}}+O(\epsilon^2). \tag{39}$$

It can be shown from Eq. (39) that

$$\cos\theta_{0,s}=\cos\theta_0+O(v/c),\quad \mathbf{e}_{0,s}=-\mathbf{e}_0+O(v/c). \tag{40}$$

These relationships allow us to replace $\theta_{0,s}$, and $\mathbf{e}_{0,s}$ by θ_0 and $-\mathbf{e}_0$ in the second, third, and fourth terms on the right-hand side of Eq. (39), to order $O(\epsilon^2)$. The resulting equation can be written as

$$\frac{\mathbf{e}_{0,s}\cos\theta_{0,s}}{\sin\theta_{0,s}}=-\frac{\mathbf{e}_0\cos\theta_0}{\sin\theta_0}-\frac{2\mathbf{m}}{\sin\theta_0}-\frac{2\mathbf{e}_0[\mathbf{e}_0\cdot(\mathbf{m}-\mathbf{u}_0/c_0)]\cos^2\theta_0}{\sin^3\theta_0}+O(\epsilon^2). \tag{41}$$

Squaring both sides of Eq. (41) and solving this equation for $\cos\theta_{0,s}$, yields

$$\cos\theta_{0,s}=\cos\theta_0+2\mathbf{e}_0\cdot\mathbf{m}-2(\mathbf{e}_0\cdot\mathbf{u}_0/c_0)\cos^2\theta_0+O(\epsilon^2). \tag{42}$$

Substituting the value of $\cos\theta_{0,s}$ given by this equation into Eq. (41), one obtains

$$\mathbf{e}_{0,s}=-\mathbf{e}_0+(2/\cos\theta_0)[\mathbf{e}_0(\mathbf{e}_0\cdot\mathbf{m})-\mathbf{m}]+O(\epsilon^2)\quad . \tag{43}$$

Thus, Eqs. (42) and (43) give us approximate analytical formulas for the grazing angle $\theta_{0,s}$ and the unit vector $\mathbf{e}_{0,s}$ which determine the direction of propagation of the scattered wave near the sodar. For the particular case $w=0$ and $\mathbf{u}_0=0$, these equations were presented without derivation elsewhere.[18]

B. Formula for Doppler shift

Using Eq. (40), it can be shown that $M_s=-M+O(v/c)$, and $\tilde{M}_s=-\tilde{M}+O(v/c)$. We substitute these relationships and Eqs. (42) and (43) into Eq. (16) for the Doppler shift $\Delta\omega$. Retaining terms of order ϵ and ϵ^2, we obtain a desired, approximate formula for the Doppler shift

$$\frac{\Delta\omega}{2\omega_0}=-\mathbf{n}_0\cdot\mathbf{v}_V/c_0+(\Delta v_V)_m/c_0+O(\epsilon^3). \tag{44}$$

Here, $(\Delta v_V)_m$ is a sum of terms of order ϵ^2

$$(\Delta v_V)_m=c_0\left[\tilde{M}^2-\frac{\mathbf{m}\cdot\mathbf{u}_V}{c_0}+\frac{\mathbf{e}_0\cdot\mathbf{u}_0}{c_0}\tilde{M}\cos\theta_0+\beta\left(-\frac{N-1}{\sin\theta_0}+2\tilde{M}\sin\theta_0+\mathbf{e}_0\cdot\mathbf{m}\cot\theta_0-\frac{\mathbf{e}_0\cdot\mathbf{u}_0}{c_0}\cot\theta_0\cos^2\theta_0\right)+\beta^2\sin^2\theta_0\right]. \tag{45}$$

Equation (44) coincides with Eq. (21) from Ref. 5 to order v/c but differs from this equation to terms of order ϵ^2. This difference can be explained by the fact that Eq. (21) from Ref. 5 was derived from Eq. (5) in Ref. 4 which differs from Eq. (8) to terms of order ϵ^2. A formula for the Doppler shift that is used in the standard technique of retrieving the wind velocity vector ignores the term $(\Delta v_V)_m$ in Eq. (44)

$$\frac{\Delta\omega}{2\omega_0}=-\mathbf{n}_0\cdot\mathbf{v}_V^{(0)}/c_0. \tag{46}$$

Here, the vector $\mathbf{v}_V^{(0)}$ has the same physical meaning as that in Sec. III. In the standard technique, the height of the scattering volume $z_V^{(0)}$ is given by Eq. (20), where $\theta_{0,s}=\theta_0$.

Subtracting Eqs. (44) and (46), one obtains $(\Delta v_V)_m=-\mathbf{n}_0\cdot(\mathbf{v}_V^{(0)}-\mathbf{v}_V)$. It follows from this equation that $(\Delta v_V)_m$ can be interpreted as an error in retrieving the wind velocity component in the direction of the vector $-\mathbf{n}_0$ due to omitting terms of order ϵ^2. It also follows from this equation that $\mathbf{v}_V=\mathbf{v}_V^{(0)}+O(\epsilon^2)$. As in Sec. III, this relationship allows us to replace $\mathbf{v}_V$ and $\mathbf{m}$ in Eq. (45) by $\mathbf{v}_V^{(0)}$ and $\mathbf{m}^{(0)}$.

Let us numerically study the error in retrieving the wind velocity vector due to omitting terms of order ϵ^2. We assume that the vectors $\mathbf{e}_0$, $\mathbf{u}_V$, and $\mathbf{m}$ lie in one vertical plane; $\mathbf{e}_0\cdot\mathbf{u}_V=u_V$, $\mathbf{e}_0\cdot\mathbf{m}=m$, and $\mathbf{m}\cdot\mathbf{u}_V=mu_V$; the horizontal wind velocity $u(z)$ varies linearly from z_0 to z_V; $\mathbf{u}_0=0$; $c_0=340$ m/s; and $c_V=339$ m/s. For the considered case, Eq. (44) can be written as

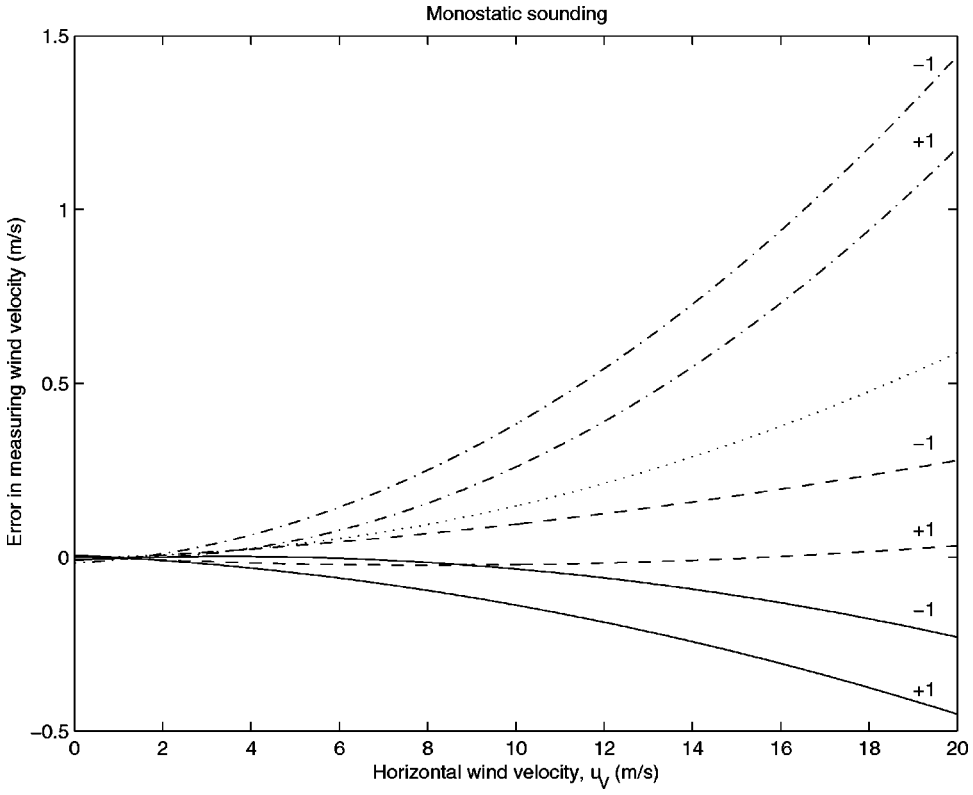

FIG. 3. Error in measuring wind velocity versus the value of the horizontal wind velocity u_V for monostatic sounding. Solid, dashed, and dash-dotted lines are the errors $(\Delta u_V)_m$ in retrieving the horizontal wind velocity for the cases $\theta_0=30°$, $\theta_0=50°$, and $\theta_0=70°$, respectively. The value of the vertical wind velocity in m/s is indicated above the lines. The dotted line is the error in retrieving the vertical wind velocity for $w_V=0.3$ m/s.

$$\frac{\Delta\omega}{2\omega_0}=-\frac{1}{c_0}[u_V\cos\theta_0+w_V\sin\theta_0-(\Delta v_V)_m]+O(\epsilon^3). \tag{47}$$

In this equation, factor out $\cos\theta_0$ from the square brackets. Then, the third term in the square brackets, $-(\Delta v_V)_m/\cos\theta_0$, which we denote as $(\Delta u_V)_m$, can be interpreted as the error in retrieving the horizontal wind velocity due to omitting terms of order ϵ^2. This term is plotted in Fig. 3 versus the horizontal wind velocity u_V for different values of the grazing angle of the emitted wave: $\theta_0=30°$ (solid lines); $\theta_0=50°$ (dashed lines); and $\theta_0=70°$ (dash-dotted lines). The numbers $+1$ and -1 above the lines indicate the value of w_V in m/s. It follows from Fig. 3 that $(\Delta u_V)_m$ can be greater than instrumentation error in measuring the wind velocity.

Thus, when retrieving the wind velocity vector, it is desirable to take into account the term $(\Delta v_V)_m$ in Eq. (44). This can be done by the same approach as in Sec. III.

Vertically pointed sodars can be used to measure w_V. In this case in Eq. (47), $\theta_0=90°$, the term proportional to u_V vanishes, and $(\Delta v_V)_m$ can be interpreted as an error in measuring w_V due to omitting terms of order ϵ^2. The dotted line in Fig. 3 shows $(\Delta v_V)_m$ vs u_V for $w_V=0.3$ m/s. It is clearly seen that the error in retrieving the vertical wind velocity can become greater than the value of w_V. However, the error in retrieving w_V can be significantly decreased if in Eq. (44), the term $(\Delta v_V)_m$ is accounted for as described in Sec. III. Note that although Refs. 7 and 8 used approximate formulas for the Doppler shift, they came up with a similar conclusion that measurements of vertical wind velocity by vertically pointed monostatic sodars can be significantly affected by wind shear.

C. Height of the scattering volume

Substituting the values of $\theta_{0,s}$ and $\mathbf{e}_{0,s}$ given by Eqs. (42) and (43) into Eqs. (36) and (37), we obtain the following formula for the height of the scattering volume:

$$z_V=z_0+(1/2)c_0\Delta t\sin\theta_0+(\Delta z_V)_m+O(\epsilon^2). \tag{48}$$

Here, $(\Delta z_V)_m$ is a sum of all terms proportional to ϵ

$$(\Delta z_V)_m=(1/2)c_0\Delta t\left(\frac{\mathbf{e}_0\cdot\mathbf{u}_0}{c_0}\,\frac{\cos^3\theta_0}{\sin\theta_0}-\mathbf{e}_0\cdot\mathbf{m}^{(0)}\cot\theta_0-\eta^{(0)}\frac{\cos(2\theta_0)}{\sin\theta_0}\right). \tag{49}$$

Note that a sum of the first two terms on the right-hand side of Eq. (48) is equal to $z_V^{(0)}$. Equations (48) and (49) allow us to calculate $(\Delta z_V)_m$ provided that $c(z)$ is known, Δt is measured, and $\mathbf{v}_V^{(0)}(z_V^{(0)})$ is retrieved by the standard technique.

The effects of atmospheric stratification on the height z_V of sound scattering were also studied in Refs. 6 and 12. In the first of these references, a formula for the refraction correction Δz to this height was derived, see Eq. (17) from Ref. 6. This formula is expressed in terms of the time interval Δt_0 of sound propagation from a sodar to the scattering volume and, therefore, is different from Eq. (49) of the present paper, which is written in terms of Δt. Note that Δt_0 cannot be measured experimentally, while Δt can. Combining Eq. (17) for Δz from Ref. 6 with the preceding equation for Δt_0, one obtains a formula which coincides with Eq. (32) from the present paper if $\mathbf{u_0}=0$. In Ref. 12 a formula for $(\Delta z_V)_m$ was derived [see Eqs. (10) and (8) from that reference]. It is mentioned in Ref. 12 that this formula coincides with the corresponding formula from Ref. 6 if $\mathbf{u_0}=0$. However, we

were not able to obtain such a coincidence. Also, it is not clear whether $\cos\alpha$ in Eq. (8) and $\tan\alpha$ in Eq. (10) from Ref. 12 are in the denominators or numerators of the corresponding terms. If they are in the numerators, the formula for $(\Delta z_V)_m$ in Ref. 12 coincides with Eq. (49) from the present paper.

V. CONCLUSIONS

The theory of bistatic and monostatic acoustic sounding of a vertical profile of the wind velocity vector in a stratified moving atmosphere is developed. The theory is based on results presented in Refs. 17–19 and uses main steps suggested in Ref. 4. Equations (11), (16), and (44) for the Doppler shift $\Delta\omega$ and Eq. (36) for the height z_V at which the wind velocity is measured are new results obtained in the present paper.

For the case of bistatic sounding, a formula (9) for the Doppler shift $\Delta\omega$ of the scattered wave at the height z_V of the scattering volume is derived. Then, this formula is rewritten in terms of quantities that can be measured at source and receiver; see Eqs. (11)–(13). Finally, the latter formula for $\Delta\omega$ is simplified by accounting only for leading terms due to sound refraction caused by atmospheric stratification. The resulting formula (16) for the Doppler shift $\Delta\omega$ is used to study the effects of atmospheric stratification on retrieving the wind velocity vector $\mathbf{v}_V$ from the measured values of $\Delta\omega$. Atmospheric stratification is usually ignored in such retrievals. It is shown that the errors in retrieving $\mathbf{v}_V$ due to ignoring effects of atmospheric stratification can be of order of 1 m/s and can be greater than instrumentation error in retrieving $\mathbf{v}_V$. Specific geometries of bistatic sounding are revealed for which the effects of atmospheric stratification on remote sensing of horizontal and vertical components of wind velocity are relatively small. Equation (36) for the height z_V at which $\mathbf{v}_V$ is measured is derived, which accounts for sound refraction in a stratified moving atmosphere. Approaches are proposed which take into account the effects of atmospheric stratification when retrieving $\mathbf{v}_V$ and z_V from the measured values of the Doppler shift and the time interval of impulse propagation in the bistatic scheme.

The theory of monostatic sounding of $\mathbf{v}_V(z_V)$ in a stratified moving atmosphere is developed analogously to that of bistatic sounding. Equation (44) for the Doppler shift in monostatic sounding of the atmosphere takes into account leading terms due to atmospheric stratification. Ignoring these terms may result in errors of more than 1 m/s in retrieving the horizontal wind velocity. Equation (48) gives the height z_V of the scattering volume in a stratified moving atmosphere.

ACKNOWLEDGMENTS

This material is partly based upon work that was supported by NRC-ETL Research Associateship and the U.S. Army Research Office under Contract Number DAAG55-98-1-0463.

APPENDIX: COMPARISON OF EQ. (8) WITH EQ. (5) FROM REF. 4

In Ref. 4, a formula for the Doppler shift is written in the following form:

$$\Delta\omega = -\frac{\partial}{\partial t}\int_{P(t)} \mathbf{k}\cdot\mathbf{s}\ \ d\zeta. \tag{A1}$$

Here, the integration is over the time-dependent ray path $P(t)$ which is a sum of a path from the source to a point turbulent eddy moving with the velocity $\mathbf{v}_V$ within the scattering volume V and a path from this eddy to the receiver (see Fig. 1 from Ref. 4). The eddy scatters the sound wave emitted by the source. In Eq. (A1), $\mathbf{k}$ and $\mathbf{s}$ depend on time t since the eddy is moving. In Ref. 4, $\mathbf{k}$ and $\mathbf{s}$ were approximately assumed to be independent of t for the case when c and $\mathbf{v}$ do not depend on time. As a result of this assumption, the following formula for the Doppler shift was obtained [see Eq. (5) from Ref. 4]:

$$\Delta\omega = (\mathbf{k}_{V,s}\cdot\mathbf{s}_{V,s})(\mathbf{v}_V\cdot\mathbf{s}_{V,s}) - (\mathbf{k}_V\cdot\mathbf{s}_V)(\mathbf{v}_V\cdot\mathbf{s}_V). \tag{A2}$$

This formula differs from Eq. (8). To show this difference, in Eq. (A2), we use the relationships $\mathbf{s}_V = (\mathbf{n}_V + \mathbf{v}_V/c)/|\mathbf{n}_V + \mathbf{v}_V/c|$ and $\mathbf{s}_{V,s} = (\mathbf{n}_{V,s} + \mathbf{v}_V/c)/|\mathbf{n}_{V,s} + \mathbf{v}_V/c|$, and develop the right-hand side in series in v_V/c. Keeping the first two terms in this series yields

$$\omega_s = \omega_0 + (\mathbf{k}_{V,s} - \mathbf{k}_V)\cdot\mathbf{v}_V + k_{V,s}[v^2/c - (\mathbf{n}_{V,s}\cdot\mathbf{v})^2/c] - k_V[v^2/c - (\mathbf{n}_V\cdot\mathbf{v})^2/c]. \tag{A3}$$

The first two terms on the right-hand side of this equation coincide with those in Eq. (8). However, Eq. (A3) contains terms of order v_V^2/c^2 which are not present in Eq. (8).

To illustrate the role of these terms, let us introduce the angle α_1 between $\mathbf{k}_V$ and $\mathbf{v}_V$ and the angle α_2 between $\mathbf{k}_{V,s}$ and $\mathbf{v}_V$. Then, it follows from Eq. (9) that to order v_V^2/c^2

$$\frac{\Delta\omega}{\omega_0} = (\cos\alpha_2 - \cos\alpha_1)\frac{v_V}{c_V} - (\cos\alpha_2 - \cos\alpha_1)\cos\alpha_1\frac{v_V^2}{c_V^2}. \tag{A4}$$

On the other hand, starting from Eq. (A2), the following formula for $\Delta\omega$ was derived in Ref. 4 [see Eq. (12) from this reference]:

$$\frac{\Delta\omega}{\omega_0} = (\cos\alpha_2 - \cos\alpha_1)\frac{v_V}{c_V} - 2(\cos^2\alpha_2 - \cos^2\alpha_1)\frac{v_V^2}{c_V^2}. \tag{A5}$$

Comparison between Eqs. (A4) and (A5) shows that they are equivalent to order v_V/c_V; however, they differ by terms of order v_V^2/c_V^2. Reference 23 also indicates that a formula for the Doppler shift obtained in Ref. 4 is an approximate formula.

Note that Eq. (A1) is a correct formula for the Doppler shift. Starting from this equation and taking into account that $\mathbf{k}$ and $\mathbf{s}$ depend on t, we derived a formula for the frequency of the scattered wave ω_s which coincides with Eq. (8). The derivation is not presented here for brevity.

[1] E. H. Brown and F. F. Hall, ''Advances in atmospheric acoustics,'' Rev. Geophys. Space Phys. **16**, 47–110 (1978).
[2] S. P. Singal, ''Acoustic sounding stability studies,'' in *Encyclopedia of Environment Control Technology. Vol. 2: Air Pollution Control* (Gulf, Houston, 1989), pp. 1003–1061.
[3] J. Fortuna and E. Kozaczka, ''Review of acoustical methods for probing the atmospheric boundary layer,'' Arch. Acoust. **14**, 453–510 (1992).
[4] T. M. Georges and S. F. Clifford, ''Acoustic sounding in a refracting atmosphere,'' J. Acoust. Soc. Am. **52**(2), 1397–1405 (1972).
[5] T. M. Georges and S. F. Clifford, ''Estimating refractive effects in acoustic sounding,'' J. Acoust. Soc. Am. **55**, 934–936 (1974).
[6] A. Spizzichino, ''Discussion of the operating conditions of a Doppler sodar,'' J. Geophys. Res. **79**, 5585–5591 (1974).
[7] P. D. Phillips, H. Richner, and W. Nater, ''Layer model for assessing acoustic refraction effects in echosounding,'' J. Acoust. Soc. Am. **62**, 277–285 (1977).
[8] S. A. Leelananda and T. Mathews, ''A method of correcting wind profiles, obtained using Doppler acoustic sounder, for refraction effects,'' in *Proceedings of the International Symposium Acoustic Remote Sensing of the Atmosphere and Ocean* (University of Calgary, Calgary, Alberta, Canada, 1981).
[9] A. Schomburg and D. Englich, ''Analysis of the effect of acoustic refraction on Doppler measurements caused by wind and temperature,'' in *Proceedings of the 9th Symposium on Acoustic Remote Sensing of the Atmosphere and Oceans* (Vienna, Austria, 1998).
[10] A. Schomburg, ''Schallstreuung in der atmosphärischen Grenzschicht,'' Ph.D. dissertation, Universität Oldenburg, Germany (1998).
[11] A. Ya. Bogushevich and N. P. Krasnenko, ''Effect of atmospheric wind shear on the accuracy of Doppler sodar measurements,'' Izv., Acad. Sci., USSR, Atmos. Oceanic Phys. **23**, 536–541 (1987).
[12] A. Ya. Bogushevich and N. P. Krasnenko, ''Influence of the refraction on geometry of acoustic sounding of the atmosphere,'' Atmos. Oceanic Opt. **7**, 680–689 (1994).
[13] V. M. Bovsheverov and G. A. Karyukin, ''Influence of wind on the accuracy of determination of the temperature structure parameter by acoustic sounding,'' Izv., Acad. Sci., USSR, Atmos. Oceanic Phys. **17**, 151–153 (1981).
[14] A. R. Mahoney, L. G. McAllister, and J. R. Pollard, ''The remote sensing of wind velocity in the lower troposphere using an acoustic sounder,'' Boundary-Layer Meteorol. **4**, 155–167 (1973).
[15] G. Peters, C. Wamser, and H. Hinzpeter, ''Acoustic doppler and angle of arrival wind detection and comparison with direct measurements at a 300m Mast,'' J. Appl. Meteorol. **17**, 1171–1178 (1978).
[16] A. Ya. Bogushevich and N. P. Krasnenko, ''Influence of refraction effects on the information content of bistatic systems for acoustic sounding of the atmosphere,'' Izv., Acad. Sci., USSR, Atmos. Oceanic Phys. **20**, 286–290 (1984).
[17] V. E. Ostashev, G. H. Goedecke, R. Wood, H. Auvermann, and S. F. Clifford, ''Sound scattering cross section in a stratified moving atmosphere,'' J. Acoust. Soc. Am. **105**, 3115–3125 (1999).
[18] V. E. Ostashev and D. K. Wilson, ''Relative contributions from temperature and wind velocity fluctuations to the statistical moments of a sound field in a turbulent atmosphere,'' Acust. Acta Acust. **86**(2), 260–268 (2000).
[19] V. E. Ostashev, *Acoustics in Moving Inhomogeneous Media* (E & FN SPON, An Imprint of Thompson Professional, London, 1997).
[20] G. H. Goedecke, R. C. Wood, H. J. Auvermann, V. E. Ostashev, D. I. Havelock, and C. Ting, ''Spectral broadening of sound scattered by advecting atmospheric turbulence,'' J. Acoust. Soc. Am. **109**, 1923–1934 (2001).
[21] A. D. Pierce, *Acoustics—An Introduction to its Physical Principles and Applications* (McGraw-Hill, New York, 1989).
[22] A. Ya. Bogushevich, ''Derivation of formula for the Doppler effect in geometrical acoustics of inhomogeneous moving media,'' Acoust. Phys. **40**, 794–797 (1994).
[23] A. Ya. Bogushevich, ''To an analysis of the acoustic Doppler effect in a three-dimensional inhomogeneous moving medium,'' Atmos. Oceanic Opt. **12**, 301–308 (1999).
[24] M. A. Kallistratova and A. I. Kon, *Radioacoustic Sounding of the Atmosphere* [in Russian] (Nauka, Moscow, 1985).

On the stability of long-range sound propagation through a structured ocean

Michael A. Wolfson[a] and Steven Tomsovic
Department of Physics, Washington State University, Pullman, Washington 99164-2814

(Received 16 February 2000; revised 27 November 2000; accepted 5 February 2001)

Several acoustic experiments show a surprising degree of stability in wave fronts propagating over multi-megameter ranges through the ocean's sound channel despite the presence of random-like, sound-speed fluctuations. Previous works have pointed out the existence of chaos in simplified ray models incorporating structure inspired by the true ocean environment. A ''predictability horizon'' has been introduced beyond which stable wavefronts cease to exist and point-wise, detailed comparisons between even the most sophisticated models and experiment may be limited for fundamental reasons. By applying one of the simplified models it is found that, for finite ranges, the fluctuations of the ray stabilities are very broad and consistent with log-normal densities. A fraction of the ray density retains a much more stable character than the typical ray. This may be one of several possible mechanisms leading to greater than anticipated sound-field stability. The log-normal ray stability density may underlie the recent, experimentally determined, log-normal density of wave-field intensities [Colosi *et al.*, J. Acoust. Soc. Am. **105**, 3202–3218 (1999)].
 [DOI: 10.1121/1.1362685]

PACS numbers: 43.30.Cq, 43.30.Ft, 43.30.Pc [SAC-B]

I. INTRODUCTION

There is a great deal of experimental and theoretical interest in long-range, low-frequency acoustic pulse propagation through the deep ocean's sound channel. It has been investigated as a problem of wave propagation in random media (WPRM),[1,2] and as a basis for tomography.[3,4] Recent results from the Acoustic Engineering Test (AET) as part of the Acoustic Thermometry of Ocean Climate (ATOC) project can be found in Colosi *et al.*[5] and Worcester *et al.*[6] One of the main challenges in analyzing and understanding long-range acoustic propagation is in dealing with difficulties arising from the ocean environment's tendency to generate multiple, weak, small-angle (forward) scattering.[7] At sufficiently long ranges of propagation, the multiple scattering should effectively randomize an acoustic pulse so that it is very difficult to deduce much information. However, several long-range experiments have found a great deal of stability in the earlier portions of the received wavefronts in spite of the fluctuations inherent in the ocean environment.[8,9,4] In addition, it has been found that wave-field intensity fluctuations at long range are consistent with a log-normal density[5] which would be reminiscent of earlier work in optics on WPRM,[10] except that this earlier work was for the short-range (weak focusing) regime.

In the past 10–15 years, simplified models inspired by the ocean environment have been shown to possess chaotic ray limits.[11–13] Essentially simultaneously, there has been enormous progress in the understanding of chaotic systems.[14] Some of the most familiar emerging concepts are simpler for bounded systems and are not easily applicable to open, scattering systems as we have here. However, there is an important tool which does straightforwardly generalize for our purposes the stability analysis of the rays. Stability matrices can be constructed as a function of range for each ray [14]. Their properties, such as the stability exponents, reveal the basic character of the rays, and are at the foundation of the findings reported in this paper.

There are several intriguing questions that arise from comparing the theoretical results to date regarding chaotic acoustic ray dynamics in the ocean and the high amount of stability observed in the data. The most general question concerns how an acoustic pulse—which at multi-megameter ranges extends to nearly 10 s in time and 2 km in depth—loses its coherence from multiple forward scattering through interaction with internal waves and mesoscale energetics. Because refraction is adequate to explain the scattering physics,[15] the ray limit should suffice for understanding long-range propagation. Some manifestations of the underlying chaotic dynamics should be observed.

It has been suggested that there exists a ''predictability horizon'' at the range of propagation defined by the scale over which chaotic dynamics develops.[16] Beyond this range, the wave fields should appear as random superpositions of many plane waves,[17,18] which would imply that acoustic field intensity fluctuations are exponentially distributed.[19,20] Several problems crop up beyond the predictability horizon. It becomes increasingly difficult to get numerically calculated rays to converge to true rays of the system. Worse, semiclassical approximations (i.e., wavefront reconstructions) from the rays might fail for fundamental reasons related to the breakdown of stationary phase approximations, but one should recognize that more optimistic viewpoints exist on this issue.[21–23] Whether or not this is true, it is currently not known to what extent tomographic inversions fail for any system beyond its predictability horizon where eigenrays are proliferating exponentially fast with increasing range. In order to begin addressing these and related issues, we focus on

[a]Electronic mail: mwolfson@wsu.edu

the ''forward propagation problem'' by performing a statistical analysis that should be much less sensitive to the difficulties engendered by the predictability horizon.

In fact, justifications for statistical laws derived by invoking stochastic or ergodic postulates are often ultimately founded on the presence of fully developed chaos; see for example, Ref. 24. Systems that once were approached by stochastic methods have more recently begun to be regarded from the perspective of dynamical systems. The two approaches mostly give consistent results, but there are important distinctions. Stochastic ray modeling is the traditional approach to the geometric limit of the problem of WPRM.[25] This nondeterministic treatment leads one to pessimistic conclusions regarding the overall stability expected in an ocean acoustic pulse at sufficiently long range.[16] By carefully defining the Lyapunov exponent, it turns out to be roughly half the value reported in Ref. 16. The scales relevant to the ocean are such that this factor of 2 increase in an important length scale might prove to be significant. Also, for this problem the validity of the stochastic or ergodic assumptions deserves to be critically examined. It is not obvious that a dynamical systems perspective would lead to similar pessimistic conclusions as does the stochastic ray theory. For example, the predictability horizon concept that has grown out of the chaotic dynamics point of view does not necessarily lead to a sudden transition—regular behavior at short ranges, completely stochastic just beyond—and remnants of stability that violate assumptions of stochasticity could persist well into the horizon's initial onset. We anticipate several features of deterministic dynamics playing an interconnected role in this regard, but we focus on the importance of only one, *intermittent-like dynamics*. Intermittency is a common feature for nonintegrable dynamical systems.[26,27] For the ray acoustics problem, intermittent-like behavior is evident through the appearance of rays which persist in remaining relatively insensitive to their initial conditions (also environment) for remarkably long ranges, as measured on the inverse scale of the mean Lyapunov exponent. It might then be expected that the existence of intermittent-like dynamics might allow linear-based tomographic inversions based on acoustic ray models to be suitable to greater ranges than previously anticipated.

One objective of this article is to illustrate the existence of intermittent-like dynamics in the generic long-range ocean acoustics problem. This is a direct consequence of the wide variability in the eigenvalues of the stability matrix which is defined in Sec. III A. We demonstrate that the magnitude of its largest eigenvalue follows a log-normal distribution, and that the stability exponent follows a Gaussian distribution. Importantly, there is preliminary evidence suggesting that these distributions are robust, i.e., that they would be found in much more realistic, sophisticated ocean models, where sound-speed fluctuations due to internal waves are superposed on a background sound-speed field which acts as a slowly varying waveguide in range.[28] To be more explicit, if one knows the probability density of the stability exponents, then one can determine the expected measure of intermittent-like rays that will persist out to the reception range. It follows that these rays will not require extremely precise numerical interpolation schemes for quantities such as the gradient of the potential.

The model upon which we rely in this paper is admittedly extremely simplified. However, it is not the model that is of concern; it is whether or not general features of simplified WPRM models carry over to the ocean itself. If we are careful enough, the simplifications that we accept remove nonessential complications for uncovering the general physical features of interest, and no more. A follow-up study to this one is underway which uses a more realistic ocean sound-speed model. It is important for confirming the applicability of our results to long-range ocean acoustics experiments.

The organization is as follows: in Sec. II, we introduce and motivate a simple model leading to a one-degree-of-freedom, nonautonomous Hamiltonian dynamical system for the rays. This is followed by a discussion of the analysis methods which are most critical for our study. They are based on the stability matrix and its well-known properties. Section IV examines the fluctuation behavior of the stability exponents giving their densities as a function of range. The proportion of intermittent-like rays is deduced and compared with the numerical results of the model. We finish with a discussion and conclusions.

II. FROM WAVE EQUATION TO RAY MODEL

We briefly outline the assumptions and approximations leading to the highly idealized ray model used in this paper. The primary physics we are concerned about involves refraction of acoustic energy due to volume inhomogeneities in the ocean sound speed. We assume that interactions of the acoustic energy with both the surface and sub-bottom are negligible. For multi-megameter ranges of propagation in midlatitude, deep ocean environments, a significant amount of acoustic energy is received that satisfies this assumption.[3] As alluded to above, the necessary assumptions leading to the primary results are that: (i) the linear, one-way Helmholtz wave equation is valid (the important point here is that backscattering is negligible), and (ii) the spatial scales of the sound-speed field are long compared to the acoustic wavelength so that ray theory is justified. A detailed derivation is readily available.[29] We point out *a priori* that the coordinate system is three-dimensional Cartesian $\mathbf{x}=(r,y,z)$, with r the range from the source, y the transverse or cross-range coordinate, and z the depth from the surface. Thus, earth curvature effects are neglected.

The fundamental starting point is the linear acoustic wave equation[7]

$$\frac{1}{c^2}\frac{\partial^2\psi(\mathbf{x};t)}{\partial t^2}=\nabla^2\psi(\mathbf{x};t), \tag{1}$$

where $\psi(\mathbf{x};t)$ is the complex scalar wave function whose real part denotes the acoustic pressure. The sound-speed field c can be taken as a function of space $\mathbf{x}$ only whereby it has been assumed that the time scales for the propagation of the acoustic wave function are small compared to the time scales associated with the evolution of the sound-speed field. For nondispersive sources, the acoustic group and phase speeds

are equivalent, and one can linearly transform Eq. (1) from time to frequency, arriving at a Helmholtz equation with the magnitude of the wave vector defined as $k=2\pi f/c$, where f is the continuous wave source frequency. Attenuation effects can of course be incorporated by modifying k to be a complex quantity, but since we are interested in: (1) acoustic energy that interacts negligibly with the ocean bottom, and (2) typical sources operating at frequencies with minimal volume attenuation (with center frequencies of about 100 Hz[6]), ignoring attenuation effects seems reasonable. Also, one can similarly derive a reduced wave equation which includes variations in density, but we ignore this effect because it is known to be important predominantly with acoustic energy that interacts with the ocean sub-bottom, which is not considered herein.

The next assumption (which is quite a reasonable one) is that the strength of the sound-speed fluctuations, whatever the physical process that produces it is small. This allows one to neglect backscattered acoustic energy, and admits the one-way Helmholtz wave equation, whereby one assumes a primary direction of propagation along the range. The so-called ''standard parabolic approximation'' is invoked next. This allows one to derive a linear partial differential wave equation of parabolic type for the complex envelope of ψ. The principal assumption is that this envelope wave function evolves slowly on the scale of the acoustic wavelength. There are many *flavors* of parabolic approximations that have varying degrees of phase errors in the complex wave function ψ as compared to the one-way Helmholtz equation,[30] but we choose to use the standard parabolic approximation, which takes the form

$$-\frac{i}{k_0}\frac{\partial\phi(y,z;r)}{\partial r}=\frac{1}{2k_0^2}\nabla_\perp^2\phi(y,z;r)+V(y,z;r)\phi(y,z;r), \tag{2}$$

where the transverse Laplacian is represented by $\nabla_\perp^2=\partial_y^2+\partial_z^2$, and the variable r is the range (propagation variable), but plays an exact analogous role to time in the Schrödinger equation of quantum mechanics. The parameter $k_0=2\pi f/c_0$ represents the reference wave number, and depends on the choice of a reference sound speed c_0, which we take to be 1.5 km/s. The potential, $V(y,z;r)$, is related to the sound-speed fluctuations as

$$V(y,z;r)=\frac{1}{2}\left[\left(\frac{c_0}{c(y,z;r)}\right)^2-1\right]\sim\frac{\delta c(y,z;r)}{c_0}, \tag{3}$$

where the sound-speed variations away from an average profile has been expressed as $c(y,z;r)=c_0+\delta c(y,z;r)$. The sound-speed fluctuations refract the rays and lead to chaos in a deterministic, mathematically defined sense. Under the parabolic approximation, the basic problem maps precisely onto problems of quantum chaos.[31] The fields of long-range acoustic propagation in the ocean and quantum chaos thus have the opportunity for cross fertilization.

Because the instability does not critically depend on having multiple degrees of freedom, we make a significant, practical simplification in the model of ignoring the depth degree of freedom (z); see Ref. 16 for a more detailed discussion of the model presented here. The system could be thought of as lying in the plane of the sound-channel axis, but this is really just the generic problem of WPRM (see, for example, Ref. 2). The gain in simplicity more than compensates for the loss of realism at this point as long as the main physical phenomena carry over to more realistic models. As was mentioned in the Introduction, preliminary evidence for our main results has been found in recent calculations incorporating a much more realistic model.[28]

The magnitude of the wave vector k is large enough that, for the purposes of this study, we can focus on the ray limit. The rays can be generated by a system of Hamilton's equations

$$\frac{dy}{dr}=\frac{\partial H(y,p;r)}{\partial p},\quad \frac{dp}{dr}=-\frac{\partial H(y,p;r)}{\partial y}, \tag{4}$$

where y and p are the phase space variables cross range (position) and horizontal slowness (momentum), respectively. The independent variable r denotes range. Correspondence with Eq. (2) necessitates that the Hamiltonian is explicitly

$$H=\frac{p^2}{2}+V(y;r). \tag{5}$$

The physical meaning of momentum is $p=\tan\theta$, where θ represents the angle a ray subtends in cross range about the range axis.

The state of the ocean is constantly changing, and its exact state is unknown. A statistical ansatz is thus fruitful for making assertions concerning its ''typical'' state. Assuming isotropy in the sound-speed fluctuations in range and cross range, the potential is taken to be a realization of a zero-mean, stationary, random function with a single correlation length scale L. The standard deviation is denoted by $\epsilon=c_0^{-1}\langle\delta c^2\rangle^{1/2}$, where $\langle\delta c^2\rangle^{1/2}$ is the root-mean-square fluctuation of the sound speed about c_0. Typical values for underwater acoustics are $\epsilon=O(10^{-3})$, and $L=O(100)$ km, but both ϵ and L vary plus or minus an order of magnitude depending on which ocean structure is considered and the geographic location. For purposes of studying a fully defined, deterministic dynamical system, we complete the description of V by defining its correlation function to be Gaussian

$$\langle V(y;r)V(y+\delta y;r+\delta r)\rangle=\epsilon^2\exp[-(\delta y^2+\delta r^2)/L^2]. \tag{6}$$

We exploit this single scale throughout the rest of this article by transforming space variables as $r\to r/L$ and $y\to y/L$, so the physical dimensions will always be in units of L. One should envision the potential as being deterministic, even though it is selected from an ensemble of realizations. This implies that the potential is to be considered a highly complicated (albeit smooth and fixed) function of both y and r. To provide some idea of the character of this potential, contours of sound-speed fluctuations based on a typical region of $V(y;r)$ are shown contoured in Fig. 1. The boundary conditions are taken as open in y, but numerically y is treated as periodic, with the ray coordinate unfolded *a posteriori* to simulate the open boundary condition. A variety of initial conditions is possible with the restriction that the initial momentum is always kept small enough that the parabolic approximation is valid all along the rays. The rays deriving

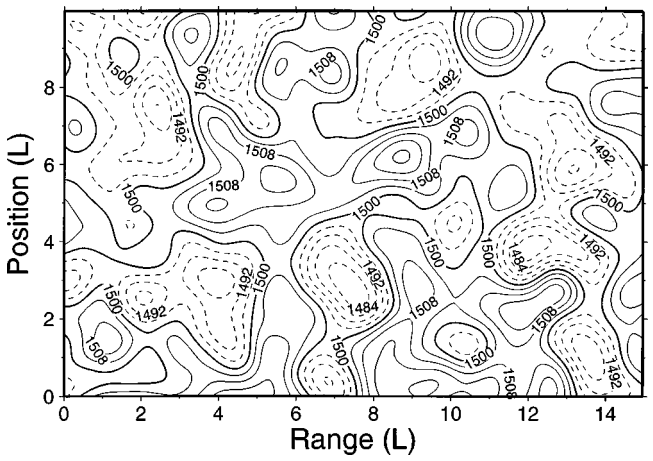

FIG. 1. A portion of a realization of $V(y;r)$ whose full domain is 20 $\times$320 L in y and r respectively. The realization is constructed by the method described in Ref. 16. Contours are labeled in units of sound speed (m/s). The heavy solid contour line indicates the reference sound speed of 1500 m/s. The normalized root-mean-square fluctuations is $\epsilon=5\times10^{-3}$.

from two such initial conditions are plotted in Fig. 2, which shows their phase space portraits (position, momentum). In the absence of a varying potential, the solutions to the equations of motion are $p(r)=p_0$, $y(r)=p_0r+y_0$. In this figure, rays would trace out vertical lines except in the case $p_0=0$, in which rays would show up as points $(y(r),p(r))=(y_0,0)$. With the potential included, the rays trace out a random-walk-like motion with some drift as they move further away from the $p=0$ line.

III. ANALYSIS METHODS

The standard analysis of ray stability in the theory of dynamical systems begins with the stability matrix [14]. From here, it is possible to calculate whether a ray is stable or unstable, what its Lyapunov exponent is, and for the unstable ray, determine the orientations of the associated stable and unstable manifolds that characterize the exponential sensitivity to initial conditions. All of our results and conclusions are based on the behavior of the stability matrices of the rays in the model introduced in the previous section. The stability matrix is a strictly local analysis in range about some particular reference trajectory. It may be stable at one range, yet for a greater range be unstable. There is no restriction that various portions of its full history cannot have completely different stability properties. In fact, one expects the portions to be almost entirely uncorrelated.[24]

Often, research done in chaotic dynamics uses either time (range)-independent or periodic Hamiltonians, and the stability matrix is investigated about periodic orbits. The Hamiltonian of Eq. (5) is aperiodic, and as many others have done before, we slightly generalize those treatments by considering arbitrary, aperiodic rays.

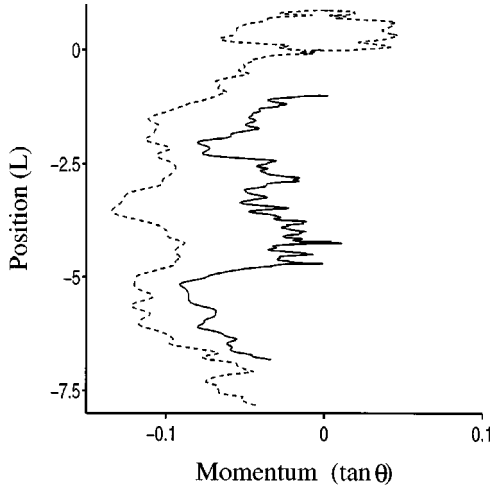

FIG. 2. Two distinct ray trajectories which have traveled through the sound-speed field characterized in Fig. 1 are shown out to the range of 160 L. The trajectory which starts at zero position and zero momentum (dashed line) is highly unstable, and the trajectory which starts at unit position and zero momentum (solid line) is stable.

A. Stability matrix

The stability matrix for a ray describes the behavior of other rays that remain within its infinitesimal neighborhood, $\{\delta y,\delta p\}$, for all ranges. It is derived by linearizing the dynamics locally; see Ref. 32 for more details. At the range r, one has

$$\begin{pmatrix}\delta p_r\\ \delta y_r\end{pmatrix}=M\begin{pmatrix}\delta p_0\\ \delta y_0\end{pmatrix}, \tag{7}$$

with the stability matrix being given by the partial derivatives

$$M=\begin{pmatrix}m_{11} & m_{12}\\ m_{21} & m_{22}\end{pmatrix}=\begin{pmatrix}\left.\frac{\partial p_r}{\partial p_0}\right|_{y_0} & \left.\frac{\partial p_r}{\partial y_0}\right|_{p_0}\\ \left.\frac{\partial y_r}{\partial p_0}\right|_{y_0} & \left.\frac{\partial y_r}{\partial y_0}\right|_{p_0}\end{pmatrix}. \tag{8}$$

The multidimensional generalizations are immediate. The m_{21} matrix element is well known for its appearance in the prefactor of the standard time (range) Green's function of the parabolic equation; it therefore gives directly information on wave amplitudes.

The evolution of M is governed by

$$\frac{d}{dr}M=KM, \tag{9}$$

with the initial condition $M(r=0)$ being the identity matrix, and

$$K=\begin{pmatrix}-\frac{\partial^2 H}{\partial y\,\partial p} & -\frac{\partial^2 H}{\partial y^2}\\ \frac{\partial^2 H}{\partial p^2} & \frac{\partial^2 H}{\partial y\,\partial p}\end{pmatrix}\Rightarrow\begin{pmatrix}0 & -\frac{\partial^2 V}{\partial y^2}\\ 1 & 0\end{pmatrix}. \tag{10}$$

The latter form is the simplification relevant for Hamiltonians of the so-called mechanical type as in Eq. (5). Since Eq. (9) represents linear, coupled, first-order differential equations, the elements of M can be numerically calculated as a function of range simultaneously with the calculation of its reference ray using identical numerical techniques, e.g., variable step, fourth-order Runge–Kutta.

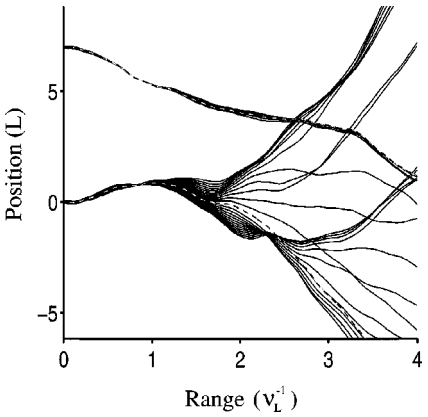

FIG. 3. Two bundles of rays surrounding the stable and unstable rays of Fig. 2 (dashed lines). For the unstable bundle, 12 rays on each side of the reference ray were chosen, each initially with zero momentum and uniformly sampling the initial position over a 0.1-L window about the reference ray. The stable bundle used only two rays on each side of the reference ray, but used the same initial condition domain as for the unstable bundle; this bundle's position is translated to 7 L. Note the range scale is in units of the inverse Lyapunov exponent ν_L^{-1}, defined in Eq. (12), and for the potential characterized in Fig. 1, is approximately 42.94 L.

B. Stability and Lyapunov exponents

The stability matrix has several important properties. It can be viewed as generating a linear, canonical transformation, and therefore its determinant is equal to unity. It is diagonalized by a linear, similarity transformation

$$\Lambda = LML^{-1} \Rightarrow \begin{pmatrix} \lambda & 0 \\ 0 & \lambda^{-1} \end{pmatrix}, \tag{11}$$

where the last form applies specifically to the case of a single degree of freedom. Here, the second eigenvalue must be the inverse of the first in order for $\det[M]=1$. The diagonalizing similarity transformation leaves the sum of the diagonal elements (trace), $\mathrm{Tr}(M)$, invariant. It is then clear that $\mathrm{Tr}(M)$ is real, and three distinct cases may arise. The first is $|\mathrm{Tr}(M)|<2$ which is linked to stable motion, and it is then customary to denote $\lambda=\exp(i\theta r)$. The second case is $|\mathrm{Tr}(M)|=2$, and it is often called marginally stable because it is the boundary case between stable and unstable motion. The third case represents unstable motion, and is characterized by $|\mathrm{Tr}(M)|>2$. In Fig. 2, a typically stable ray is represented by the solid line, and a typically highly unstable ray is represented by the dashed line. Their distinctions are not immediately obvious.

The evolution of neighboring rays about a ray that has $|\mathrm{Tr}(M)|<2$ satisfied from the source to the reception range will undergo only rotations in phase space, and subsets of phase space of finite measure where this behavior dominates the dynamics is precisely where intermittent-like rays reside. Figure 3 illustrates this characteristic behavior by showing a group of stable rays winding about each other as they propagate. The dashed ray in the group is the stable ray of Fig. 2. They perform their ''random walks,'' yet remain winding about each other. For the purposes of this paper, we make a slightly generalized definition of intermittent-like rays as being all those for which $|\mathrm{Tr}(M)|$ remains sufficiently small over the range of propagation, i.e., not far from 2.

For unstable motion, it is customary to denote $\lambda=\pm\exp(\nu r)$, where ν is positive and real. The neighboring rays move hyperbolically relative to each other. We add a collection of unstable (chaotic) rays to Fig. 3 to illustrate the distinction between neighboring groups of stable and unstable rays. The dashed ray is the highly unstable ray from Fig. 2. The rays were selected to span the same-size initial neighborhood as the stable group, yet they fan out and become completely independent. For the unstable case one can introduce a definition for the Lyapunov exponent as

$$\nu_L \equiv \lim_{r\to\infty} \frac{\ln(|\mathrm{Tr}(M)|)}{r}. \tag{12}$$

Note that there is no ensemble averaging implied in the definition of ν_L. None of the theory presented thus far prevents it from taking on a distinct value for each ray for each realization of the random potential. In Sec. IV, the value of ν_L will be shown to be independent of the particular ray, and the particular realization of the potential as well. It thus defines a unique length scale, ν_L^{-1}, which is used from Fig. 3 onward wherever the range variable is involved.

For unstable motion $|\lambda|$ tends to be very large, leaving λ^{-1} negligible. With little inaccuracy, $\mathrm{Tr}(M)=\lambda+\lambda^{-1}\approx\lambda$, even for finite ranges. One then deduces a stability exponent ν from $\mathrm{Tr}(M)$ as

$$\nu = \frac{\ln|\mathrm{Tr}(M)|}{r}. \tag{13}$$

Thus, ν depends on the particular ray and varies with range, whereas the Lyapunov exponent has no range dependence by definition.

For any fixed range, an ensemble of ν can be created by considering various initial conditions [by exploiting the isotropic and stationary properties of $V(y;r)$], and different realizations of $V(y;r)$. The resulting statistical densities of $|\mathrm{Tr}(M)|$, $\rho_{|\mathrm{Tr}(M)|}(x)$, and similarly ν, $\rho_\nu(x)$, are the main objects of concern; the two densities are directly tied to each other. The cumulative probability distribution is given as

$$F_\nu(x) = \int_{-\infty}^{x} dx'\, \rho_\nu(x'), \tag{14}$$

which provides a useful tool for numerically studying the behavior of $\rho_\nu(x)$. It also has the utility of directly giving the proportion of nearly stable rays up to some argument set to a maximum instability criterium, $\nu=x$.

We denote the mean and variance, respectively, as

$$\begin{aligned} \nu_0 &= \langle \nu \rangle = \int dx\, x \rho_\nu(x), \\ \sigma_\nu^2 &= \langle (\nu-\nu_0)^2 \rangle = \int dx (x-\nu_0)^2 \rho_\nu(x), \end{aligned} \tag{15}$$

where the brackets $\langle\,\rangle$ denote ensemble averaging over the initial phase space variables (y_0,p_0). For any real γ, ensemble averages of powers of $|\mathrm{Tr}(M)|$ are expressed as

$$\langle |\mathrm{Tr}(M)|^\gamma \rangle = \langle \exp(\gamma\nu r) \rangle = \int dx \exp(\gamma x r) \rho_\nu(x). \tag{16}$$

Note that this equation does not immediately apply to wave amplitude statistics which require ensemble averaging over the final position; this will be discussed in a future work.

To continue the theoretical development, it is useful to introduce a slightly modified stability exponent, $\overline{\nu}$

$$\overline{\nu} \equiv \frac{\ln\langle |\mathrm{Tr}(M)|^2 \rangle}{2r}. \tag{17}$$

Clearly, $\overline{\nu}$ is necessarily greater than ν_0 because of the important distinction of ensemble averaging before taking the natural logarithm as opposed to the inverse order and the root-mean-square fluctuation contributions. It is shown in the next section that the Lyapunov exponent becomes $\nu_L = \lim_{r\to\infty} \nu_0$, and not $\lim_{r\to\infty} \overline{\nu}$, which surprisingly remains greater than ν_L. Near a parameter regime motivated by the ocean, we find numerically that analytical estimates of ν_L being equal to $\overline{\nu}$ are roughly double their actual values.

C. Stochastic analysis results

An analytic estimate of $\overline{\nu}$ can be derived from previous analytic results based on a stochastic analysis which involves a strong Markovian assumption.[16,33,34] It was verified in Ref. 16 that, in the context of the present acoustic ray model, the stochastic analysis predictions for $\overline{\nu}$ (actually gn', see the text ahead) matched to a high degree of precision with numerical tests. In fact, no statistically significant deviations were observed. Thus, although the stochastic system is not strictly mathematically equivalent to the deterministic dynamics, we accept the applicability of those specific results at sufficiently long ranges (defining this range scale is admittedly not as trivial to determine for the general ocean acoustics scenario as it is for the idealized problem). We begin with

$$\langle [\mathrm{Tr}(M)]^2 \rangle = \langle m_{11}^2 \rangle + \langle m_{22}^2 \rangle + 2\langle m_{11} m_{22} \rangle. \tag{18}$$

By appealing to stochastic integration techniques,[35–37] it has been shown that in the small-ϵ, large-r limit that[16,33,34]

$$\langle m_{22}^2 \rangle = \tfrac{1}{3}\exp(2\nu' r), \tag{19}$$

where

$$\nu' \approx \left(\frac{1}{2}\int_0^\infty d\xi \left\langle \left.\frac{\partial^2 V(y;r-\xi)}{\partial y^2}\right|_{\substack{y=y_0\\p=p_0}} \left.\frac{\partial^2 V(y;r)}{\partial y^2}\right|_{\substack{y=y_0\\p=p_0}} \right\rangle \right)^{1/3} = (3\sqrt{\pi})^{1/3}\epsilon^{2/3} \tag{20}$$

(in dimensional units $\nu' = (3\sqrt{\pi})^{1/3}\epsilon^{2/3}/L$). The last result of Eq. (20) is for the specific example of a Gaussian single-scale potential of Eq. (6). The first result of Eq. (20) is more general, but requires numerical confirmation for models with greater realism, and will also depend on the ray's initial conditions for models with a nonuniform background sound-speed field.

By symmetry considerations of the stochastic equations, $\langle m_{11}^2 \rangle = \langle m_{22}^2 \rangle$. It is also deduced that $\langle m_{11} m_{22} \rangle$ can, at most, grow on the same scale. Defining a correlation coefficient

$$\mu = \frac{\langle m_{11} m_{22} \rangle}{\langle m_{22}^2 \rangle}, \tag{21}$$

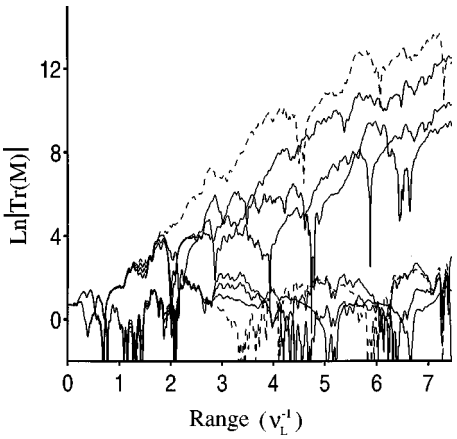

FIG. 4. The stability, $\ln|\mathrm{Tr}(M)|$, for the reference rays of Fig. 2 (dashed), and 3 of their neighboring rays initially with zero momentum and initial position shifted 0.008, 0.016, and 0.024 L away from the reference rays.

where $|\mu| \leqslant 1$, it follows that

$$\langle [\mathrm{Tr}(M)]^2 \rangle = \tfrac{2}{3}(1+\mu)\exp(2\nu' r). \tag{22}$$

Then, by using the definition of Eq. (17), one obtains

$$\overline{\nu} = \nu' + \frac{1}{2r}\ln\left[\frac{2}{3}(1+\mu)\right]. \tag{23}$$

Note that the second term disappears if μ equals 1/2; i.e., $\langle m_{11} m_{22} \rangle = \langle m_{22}^2 \rangle/2$. We give its value numerically in the next section. In that case, $\overline{\nu} = \nu'$ at finite range, and we have an analytic estimate for $\overline{\nu}$ (which has not been derived previously to our knowledge). It is also worth remarking that ν' is not the Lyapunov exponent itself (just as $\overline{\nu}$ is not), but rather only an upper bound. By analogy with the behavior of $\overline{\nu}$ stated at the end of the last subsection, ν' will turn out to be about numerically double the actual ν_L.

IV. FLUCTUATIONS

The ocean is not infinite in extent, and so the distribution of the stability exponents, ν (or $|\mathrm{Tr}(M)|$) at a specified range r, is more directly relevant to the ocean acoustics problem than the Lyapunov exponent, ν_L [or $\exp(\nu_L r)$]. In order to visualize the magnitude of the fluctuations we are discussing, Fig. 4 displays the $\ln|\mathrm{Tr}(M)|$ for eight of the rays from Fig. 3 as a function of range out to $7.5\nu_L^{-1}$. By the right end of the figure, for any fixed range one ray might have a $|\mathrm{Tr}(M)| = e^{13}$, and another one might have $|\mathrm{Tr}(M)| = e^0$. At $7.5\nu_L^{-1}$, there exist fluctuations in the stabilities of at least six orders of magnitude which are characteristic of broad-tailed densities.

To characterize the fluctuations more quantitatively, we consider the cumulative densities for ν and $|\mathrm{Tr}(M)|$. An initial working hypothesis might be to check whether at some long, fixed range, a diagonal element of M, say m_{ii}, is distributed as a Gaussian random variable across the ensemble of $V(y;r)$ and derive the implied cumulative densities from there. However, there ought to be an identifiable mechanism for a central limit theorem (CLT) to be operating with respect to m_{ii}. From Eq. (9), one can deduce that M can be decomposed into a product of shorter-range stability matri-

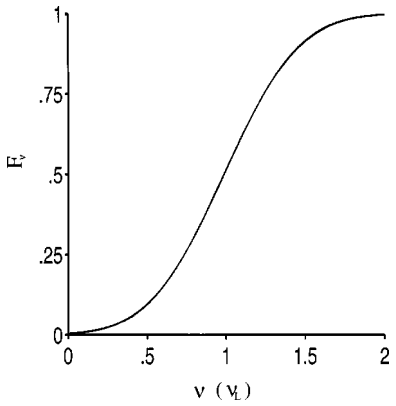

FIG. 5. Plot of the cumulative density for ν at the range of $7.5\nu_L^{-1}$. The measured cumulative density is computed from five realizations of sound-speed fields characterized in Fig. 1 ($\epsilon=5\times10^{-3}$). It incorporates 20 000 rays per realization whose initial conditions uniformly sample 20 L in position and have zero initial momentum. Superposed is the cumulative density associated with the Gaussian density for ν [see Eq. (26)] using a value of $\nu_0=0.0232$ (which is our best estimate for ν_L derived from the same simulations) and $\overline{\nu}=\nu'$ [see Eq. (20)]. Note the scale for ν has been normalized by ν_L.

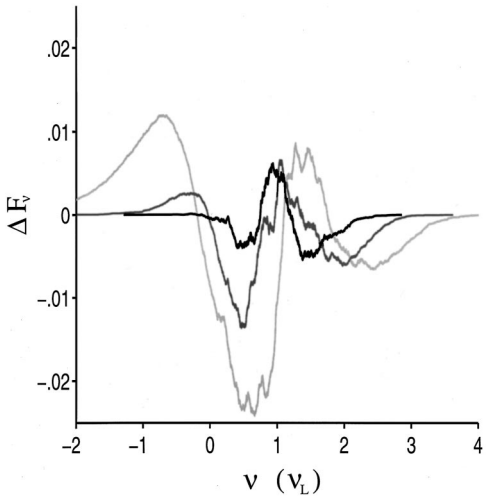

FIG. 6. Plot of difference between analytical and measured cumulative densities for ν at the ranges of 1.87 (light gray), 3.75 (medium gray), and 7.5 (black) ν_L^{-1}. The measured cumulative densities are taken from the same simulations that produce Fig. 5. The values of the free parameters ν_0 and $\overline{\nu}$ were adjusted within their simulated standard deviations to minimize the maximum difference for each range shown. Note the scale for ν has been normalized by ν_L.

ces. For very large r, consider a range Δr which is short compared to the final range r, yet long compared with ν_L^{-1}. Let $N\Delta r=r$ where N is large. Then, it follows that the stability matrix is given by the left-ordered product

$$M=\prod_{l=1}^{N} M_l, \tag{24}$$

where M_l is the stability matrix for the range $l\Delta r$ to the range $(l-1)\Delta r$. To a great degree of accuracy the set of M_l should behave independently with the only correlations being among the matrix elements necessary for maintaining unit determinant. The stability matrix should have the statistical properties of an ensemble of products of uncorrelated, random matrices.

If there exists a limiting form for a distribution at long-range r, one would expect the same form (with different parameters, i.e., mean, variance) at $r/2$. In other words, the limiting form would have to be invariant under the matrix multiplication process. Denoting $m_{l,ij}$ as the matrix elements of M_l, for the $N=2$ case, we have

$$m_{11}=m_{2,11}m_{1,11}+m_{2,12}m_{1,21}. \tag{25}$$

If the $m_{l,ij}$ behave as independent, random Gaussian variables, then m_{11} could not be Gaussian because of the product form. The applicability of a CLT results from an additive process involving random variables. Instead, we anticipate something closer to a log-normal density because the log of a product of random variables acts like a sum of random variables. It should be mentioned here that this concept has been in use in many problems involving statistical physics.[24]

To test whether $|\mathrm{Tr}(M)|$ is log-normally distributed, we calculate 100 000 rays through five realizations of $V(y;r)$ to $7.5\nu_L^{-1}(320L)$ (a reasonable upper bound for global acoustic propagation) for values of $\epsilon=2\times10^{-3}$, 3×10^{-3}, and 5×10^{-3}. If $|\mathrm{Tr}(M)|$ is distributed log-normally, then ν is distributed in a Gaussian manner by definition. In Fig. 5, we plot the cumulative density for ν. The corresponding analytic Gaussian form is superposed. It is impossible to distinguish the numerical results from the Gaussian form from this plot. A similar plot for $|\mathrm{Tr}(M)|$ carries little new information, and is not pictured in this paper, though we have verified its excellent consistency with a log-normal density as well. By plotting the differences between the numerical and analytical curves for three different ranges, we see in Fig. 6 that the consistency with a Gaussian density is excellent, and that as range increases the consistency of $\rho_\nu(x)$ with a Gaussian density improves. Note the small scale of the deviations. We have verified that they are roughly of the order of expected sample size errors for the curve at maximum range.

There are several relationships implied by the log-normal density that are straightforward to test. First, if we denote the variance of ν as σ_ν^2, then a relationship between $\overline{\nu}$ and ν_0 can be derived. With

$$\rho_\nu(x)=\frac{1}{\sqrt{2\pi\sigma_\nu^2}}\exp\left[-\frac{(x-\nu_0)^2}{2\sigma_\nu^2}\right],$$

$$\overline{\nu}=\frac{1}{2r}\ln\langle e^{2\nu r}\rangle=\frac{1}{2r}\ln\left(\frac{1}{\sqrt{2\pi\sigma_\nu^2}}\int_{-\infty}^{\infty}dx\exp(2xr)\times\exp\left[-\frac{(x-\nu_0)^2}{2\sigma_\nu^2}\right]\right)=r\sigma_\nu^2+\nu_0. \tag{26}$$

Inverting this last relation for σ_ν^2, one obtains

$$\sigma_\nu^2=\frac{\overline{\nu}-\nu_0}{r}. \tag{27}$$

Both exponents $\overline{\nu},\nu_0$ were defined [see Eqs. (13), (15), (17)] to be independent of r to leading order; see the upper panel of Fig. 7 where $\overline{\nu},\nu_0$ are plotted as a function of range. The stochastic approximation for ν' also given matches precisely the value of $\overline{\nu}$ implying that $\mu=1/2$. From numerical simu-

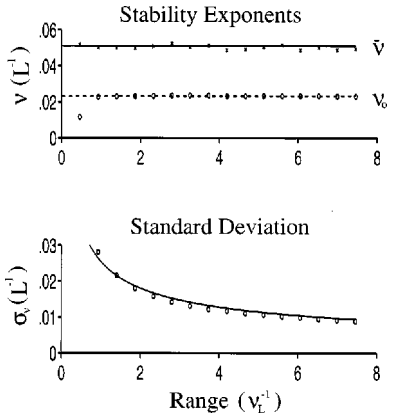

FIG. 7. Upper panel: The range dependence of $\overline{\nu}$ derived from simulations (x's) with the solid line indicating the analytical value (=0.0510) determined by Eq. (20). Also shown is the range dependence of ν_0 derived from simulations (o's) with the dashed line indicating our best estimate of $\langle \nu_0 \rangle = 0.0232$ derived by taking the mean of the ν_0 values at ranges beyond $2\nu_L^{-1}$. Lower panel: The standard deviation of ν as a function of range derived from simulations (o's), and the analytical estimate (solid line) from Eq. (27) using the value $\langle \nu_0 \rangle$ for ν_0 (as described in the upper panel) and Eq. (20) for $\overline{\nu}$.

lations, it turns out that μ is 0.466, but this number is poorly determined due to sample size errors. There is no discernible r dependence in either $\overline{\nu}$ or ν_0 beyond the scale at which the stochastic approximation begins to work for $\overline{\nu}$. They maintain a rather constant ratio of 2.20 among themselves. The log-normal $|\mathrm{Tr}(M)|$ density thus implies that the standard deviation of $\rho_\nu(x)$ approaches zero as $r^{-1/2}$. Again there is excellent consistency; see the lower panel of Fig. 7 where σ_ν is plotted versus $[(\overline{\nu}-\nu_0)/r]^{1/2}$. Thus, in the limit of $r \to \infty$, $\rho_\nu(x)$ goes to a δ density; all ν converge to the single value ν_0. This value would also have to be the Lyapunov exponent from the definition in Eq. (12), and the Lyapunov exponent would be a constant for all trajectories independent of the specific realization of the potential or the initial conditions. It appears that the approach of ν_0 to ν_L is so rapid as to warrant replacing ν_0 with ν_L in all the formulas of this section. In fact, the lower panel of Fig. 7 actually incorporates our best value for ν_L and not ν_0 as a function of range.

A consequence of the log-normal density for $|\mathrm{Tr}(M)|$ is that the density of $|\mathrm{Tr}(M)|^\gamma$ for any real γ must also be log-normally distributed. This follows from the fact that $\gamma\nu$ would be Gaussian distributed with mean $\gamma\nu_0$ and variance $\gamma^2\sigma_\nu^2$, and $\gamma\nu = \ln|\mathrm{Tr}(M)|^\gamma/r$. Thus, γ enters as a linear scale factor in the parameters that define the log-normal density. It is given by

$$\rho_{|\mathrm{Tr}(M)|^\gamma}(x) = \sqrt{\frac{1}{2\pi r(\overline{\nu}-\nu_0)}}\,\frac{1}{|\gamma|x} \times \exp\left[\frac{-(\ln(x)/\gamma-\nu_0 r)^2}{2r(\overline{\nu}-\nu_0)}\right], \quad x \geqslant 0. \tag{28}$$

Straightforward integration gives

$$\langle |\mathrm{Tr}(M)|^\gamma \rangle = \exp([\gamma\nu_0 + \gamma^2(\overline{\nu}-\nu_0)/2]r) \tag{29}$$

for its ensemble averaged value. Note that the $\gamma=2$ case for which the stochastic theory was worked out is the only one independent of ν_0, and thus also ν_L in the large-r limit. Using Eq. (29), a variety of estimates for the Lyapunov exponent can be constructed. For example, for r large enough

$$\nu_L \approx \frac{2}{r}\ln\langle |\mathrm{Tr}(M)| \rangle - \frac{1}{2r}\ln\langle |\mathrm{Tr}(M)|^2 \rangle, \tag{30}$$

as given in Ref. 24. Another example would be

$$\nu_L \approx \frac{1}{r}\ln\langle |\mathrm{Tr}(M)|^2 \rangle - \frac{1}{4r}\ln\langle |\mathrm{Tr}(M)|^4 \rangle, \tag{31}$$

etc.

Another interesting, rather curious consequence of the constant ratio of $\overline{\nu}$ to ν_0 is that $\overline{\nu}$ does not approach ν_L in the $r \to \infty$ limit, even though $\rho_\nu(x) \to \delta(x-\nu_0)$. Care must be taken to perform the noncommuting operations of taking the infinite range limit and ensemble averaging in the correct order. Furthermore, the variation of $|\mathrm{Tr}(M)|$ grows without bound as a function of range r, in spite of the fact that all the trajectories possess equal stability exponents in the limit $r \to \infty$. From Eq. (29), it follows that

$$\sigma^2_{|\mathrm{Tr}(M)|} = e^{\overline{\nu}r}(e^{\overline{\nu}r} - e^{\nu_0 r}) \sim e^{2\overline{\nu}r}, \tag{32}$$

where the last form applies in the large-r limit, even though σ_ν^2 is approaching zero.

Finally, we point out that a log-normal density has long tails and, as already noted, allows for many orders of magnitude fluctuations in $|\mathrm{Tr}(M)|$. To return to the issue of intermittent-like rays, at any range, all rays whose corresponding $|\mathrm{Tr}(M)|$ are less than some $O(1)$ constant can be considered as intermittent-like. Values of e or e^2 could be taken as criteria, for example. The equivalent criteria expressed for the maximum of ν would be $O(r^{-1})$. In the present model the proportion of intermittent-like rays approaches zero as $r \to \infty$, but for finite range the proportion of intermittent rays up to some maximum value $|\mathrm{Tr}(M)| = x$ is given by the cumulative density

$$F_{|\mathrm{Tr}(M)|}(x) = F_\nu\left(\frac{\ln(x)}{r}\right) = \frac{1}{2}\left(1 + \mathrm{erf}\left[\frac{\ln(x)-\nu_0 r}{\sqrt{2r(\overline{\nu}-\nu_0)}}\right]\right), \tag{33}$$

where erf(z) is the error function of argument z. With the replacement of ν_0 by ν_L, this gives a very interesting, nontrivial connection between the Lyapunov exponent (ν_L), $\overline{\nu}$, and the proportion of intermittent rays as a function of range. The validity of this expression is verified in Fig. 8. The behavior is just as predicted. The small deviations seen may be indicative of some slight non-log-normal behavior in the lower tail, or it may just be due to our not using best-fit values of $\overline{\nu}$ and ν_0. For long ranges, the proportion of intermittent-like rays decreases exponentially as $a_0 r^{1/2} \times \exp(-b_0 r)$, where a_0 and b_0 can be deduced from the asymptotic properties of the error function, and this behavior is independent of the precise criterion used for the maximum desired $|\mathrm{Tr}(M)|$. As can be seen in Fig. 8, 10% of the initial ray density remains stable or nearly stable out to ranges of order $5\nu_L^{-1}$. This 10% of the initial acoustic energy is then only linearly sensitive to the fluctuating sound-speed field, and since this energy remains in coherent bundles (see Fig. 3), it will be expected to have a longer time coherence over repeated experiments as the environment evolves. Perform-

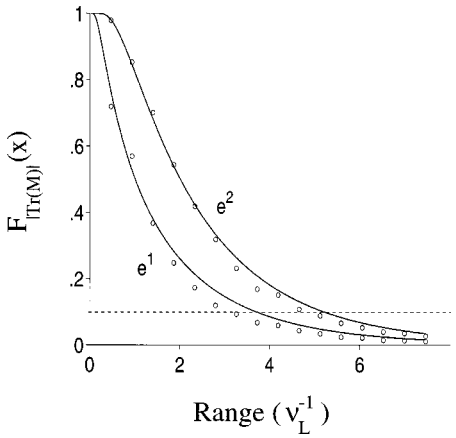

FIG. 8. The range dependence of the cumulative distribution for $|\mathrm{Tr}(M)|$ evaluated at e^1 and e^2. The measured values (o's) are derived from simulations (see the caption of Fig. 5) and the theoretical curves (solid) are derived from Eq. (33) using the values of $\overline{\nu}$ and ν_0 indicated in Fig. 7. The horizontal dashed line at $F_{|\mathrm{Tr}(M)|}=0.1$ indicates the range at which 10% of the ray density remains nearly stable.

ing repeated experiments and applying coherent averaging as a filter to pick up this energy, one can imaging being able to use this apportionment of the initial acoustic pulse for acoustic tomography.

V. DISCUSSION AND SUMMARY

Long-range, low-frequency sound propagation in the ocean has been previously investigated both as a problem of wave propagation through a random medium, and as a basis for tomography. Several outstanding quandaries remain that our results only begin to address: (i) in the early arriving portion of a wavefront, there seems to be more coherence and stability than would be expected from an analysis based on stochastic ray techniques common to the subject of WPRM; we note that recent analytical studies of the coupling of acoustic modes suggest that this early arriving energy should be stable,[38] which supports our findings; (ii) one expects that in moving from the weak focusing to strong focusing regimes (roughly speaking, from short range to long range), there should be a transition from log-normally distributed wave-field intensities to exponentially-distributed ones. Data analyses suggest that the log-normal densities extend well beyond the weak focusing regime, and the crossover is not understood theoretically; and (iii) related to the first item, given the presence of more stability than seems consistent with theoretical modeling, how valid are the underlying assumptions of tomographic inversions performed at long ranges?

Complete solutions to these problems are well beyond the scope of this paper. Nevertheless, we believe that our results form one cornerstone for their eventual resolution. As the ocean acoustic problem mainly involves refraction, and is in a wavelength regime that should be extremely well-suited to semiclassical analysis, we have focused our attention exclusively on a simple ray model inspired by the ocean. Our approach is from a dynamical systems perspective as opposed to a stochastic ray method. It has the advantage of being a more fundamental starting point in the sense that a system's dynamics may determine where a stochastic ray method is appropriate, whereas a stochastic ray method just presupposes a certain randomness that may or may not actually exist in the system's dynamics.

Our main concern is the ray stability properties that govern wave-field amplitudes in semiclassical approximations. A follow-up study is underway to address the phases (classical actions and geometric indices), correlations among ray properties, and robustness, i.e., the generality and applicability of our results to the ocean. The stability matrix is our key analysis tool because it contains all the necessary information about how stable or unstable each ray is. The distribution of stabilities reflects on statistical properties arising in the study of WPRM, whereas the existence or lack thereof of stable rays impacts tomographic inversion. We also note that studying the stability matrix has the utility of providing additional strong checks on one's numerical integration techniques. Its determinant must remain unity.

We have carefully introduced several stability exponents depending upon whether ensemble averaging is taken before or after the logarithm (or at all), and whether the range is finite or the infinite range limit is taken. We have related them to the absolute value of the trace of the stability matrix, which we have found to fluctuate to a high degree of consistency with a log-normal density; note that this also applies to the absolute value of individual matrix elements of the stability matrix. We have given a heuristic argument for this distribution, and are not aware of any known analytic derivations of this result.

An important consequence follows from the appearance of log-normally distributed stabilities, or equivalently Gaussian densities in the stability exponents (the logarithmic variables). As shown in Sec. IV [see Eq. (28)], any power of the stability matrix trace, or individual matrix elements, is also distributed log-normally. Thus, each individual contribution of an eigenray to the semiclassical approximation of the Green's function has a magnitude fluctuating as a log-normal density. Further study is underway to determine theoretically the crossover from log-normal wave-field intensity distributions characteristic of the weak focusing limit to exponential densities in the strong focusing limit. It is tempting to extrapolate our results to compute statistically relevant quantities such as the scintillation index (normalized variance of intensity) by using Eq. (29). Although one can immediately deduce that the normalized variance of intensity due to a single ray contribution grows exponentially with range with an e-folding scale of $(\overline{\nu}-\nu_0)$, one cannot infer anything about the scintillation index in the region where multipathing is important since the phase of each contributing ray must be incorporated into the calculation. Also, our work assumes one is at or beyond the regime of strong focusing. This is confirmed in the upper panel of Fig. 7, where ν_0 is seen to converge at the range $O(\nu_L^{-1})$. Since the strong Markov assumption is valid for this problem, this range can be shown to be of the order where strong focusing occurs. Thus, it is erroneous to compute the scintillation index from our work in the weak focusing regime $(r \ll \nu_L^{-1})$, where only one ray contributes to the intensity distribution.

All rays in the model possess identical Lyapunov expo-

nents, and the finite-range, mean stability exponent, ν_0, converges rapidly to it (see the upper panel of Fig. 7). This follows from the finite-range stability exponent acting as a Gaussian random variable with a standard deviation shrinking with range as $r^{-1/2}$. This is also a consequence of the log-normal density, and not the single scale nature of the sound-speed fluctuations *per se*. This behavior may be rather general (as general as the log-normal behavior), and it would be interesting to verify it in more realistic models. It is quite unlike the $\epsilon^{2/3}$-scaling law for the stability exponents, which should only apply to a model with a single correlation scale in range for the sound-speed fluctuations.

The log-normal distribution has very broad tails. One typically observes stability matrix traces that fluctuate many orders of magnitude at a given range. Long after the appearance of highly unstable rays as a function of range, some stable or nearly stable rays will still be present. Their proportion decays essentially exponentially with range where the parameters are uniquely fixed by the Lyapunov exponent and the related stability exponent $\overline{\nu}$. However, they may be topographically invertible, and relatively speaking, more important than their proportion would suggest. We have pointed out the distinctiveness of their behavior relative to unstable rays such as the way they twist about each other, and hang together as they propagate. Their collective properties appear to be highly correlated.

The $r^{-1/2}$ behavior of the standard deviation of the stability exponent leads to a paradoxical situation in which all the rays possess a unique Lyapunov exponent, yet the exponentiated quantity, the matrix elements, or trace of the stability matrix possess a divergent variance as the range approaches infinity. This illustrates dramatically the differences arising when noncommuting operations, i.e., ensemble averaging, taking the logarithm, and taking the infinite range limit, are interchanged. It is the stability matrix elements which are relevant to semiclassical approximations. So, the individual terms in a summation over eigenrays will vary infinitely in their relative importance.

ACKNOWLEDGMENTS

We gratefully acknowledge helpful discussions with M. G. Brown, F. D. Tappert, J. A. Colosi, and financial support from the Office of Naval Research.

[1] J. A. Colosi, A. B. Baggeroer, T. G. Birdsall, C. Clark, B. D. Cornuelle, D. Costa, B. D. Dushaw, M. Dzieciuch, A. M. G. Forbes, B. M. Howe, D. Menemenlis, J. A. Mercer, K. Metzger, W. Munk, R. C. Spindel, P. F. Worcester, and C. Wunsch, ''A review of recent results on ocean acoustic wave propagation in random media: Basin scales,'' IEEE J. Ocean Eng. **24**, 138–155 (1999).

[2] B. J. Uscinski, *Wave Propagation and Scattering in Random Media* (Academic, New York, 1978), Vol. 2.

[3] W. Munk, P. Worcester, and C. Wuncsh, *Ocean Acoustic Tomography* (Cambridge University Press, Cambridge, England, 1995).

[4] A. B. Baggeroer, T. G. Birdsall, C. Clark, J. A. Colosi, B. D. Cornuelle, D. Costa, B. D. Dushaw, M. Dzieciuch, A. M. G. Forbes, C. Hill, B. M. Howe, J. Marshall, D. Menemenlis, J. A. Mercer, K. Metzger, W. Munk, R. C. Spindel, D. Stammer, P. F. Worcester, and C. Wunsch, ''Ocean climate change: Comparison of acoustic tomography, satellite altimetry, and modeling,'' Science **281**, 1327–1332 (1998).

[5] J. A. Colosi, E. K. Sheer, S. M. Flatté, B. D. Cornuelle, M. A. Dzieciuch, W. H. Munk, P. F. Worcester, B. M. Howe, J. A. Mercer, R. C. Spindel, K. M. Metzger, T. G. Birdsall, and A. B. Baggeroer, ''Comparisons of measured and predicted acoustic fluctuations for a 3250-km propagation experiment in the eastern North Pacific Ocean,'' J. Acoust. Soc. Am. **105**, 3202–3218 (1999).

[6] P. F. Worcester, B. D. Cornuelle, M. A. Dzieciuch, W. H. Munk, B. M. Howe, J. A. Mercer, R. C. Spindel, J. A. Colosi, K. Metzger, T. G. Birdsall, and A. B. Baggeroer, ''A test of basin-scale acoustic thermometry using a large-aperture vertical array at 3250-km range in the eastern North Pacific Ocean,'' J. Acoust. Soc. Am. **105**, 3185–3201 (1999).

[7] S. M. Flatté, R. Dashen, W. H. Munk, and F. Zachariasen, *Sound Transmission through a Fluctuating Ocean* (Cambridge University Press, Cambridge, England, 1979).

[8] J. A. Colosi, S. M. Flatté, and C. Bracher, ''Internal-wave effects on 1000-km oceanic acoustic pulse propagation: Simulation and comparison with experiment,'' J. Acoust. Soc. Am. **96**, 452–468 (1994).

[9] J. L. Spiesberger, E. Terray, and K. Prada, ''Successful ray modeling of acoustic multipaths over a 3000-km section in the Pacific,'' J. Acoust. Soc. Am. **95**, 3654–3657 (1994).

[10] V. I. Tatarskii, *Wave Propagation in a Turbulent Medium* (McGraw-Hill, New York, 1961).

[11] D. R. Palmer, M. G. Brown, F. D. Tappert, and H. F. Bezdek, ''Classical chaos in nonseparable wave propagation problems,'' Geophys. Res. Lett. **15**, 569–572 (1988).

[12] K. B. Smith, M. G. Brown, and F. D. Tappert, ''Ray chaos in underwater acoustics,'' J. Acoust. Soc. Am. **91**, 1939–1949 (1992).

[13] K. B. Smith, M. G. Brown, and F. D. Tappert, ''Acoustic ray chaos induced by mesoscale ocean structure,'' J. Acoust. Soc. Am. **91**, 1950–1959 (1992).

[14] E. Ott, *Chaos in Dynamical Systems* (Cambridge University Press, Cambridge, England, 1993).

[15] J. Simmen, S. M. Flatté, and G. Wang, ''Wave front folding, chaos, and diffraction for sound propagation through ocean internal waves,'' J. Acoust. Soc. Am. **102**, 239–255 (1997).

[16] M. A. Wolfson and F. D. Tappert, ''Study of horizontal multipaths and ray chaos due to ocean mesoscale structure,'' J. Acoust. Soc. Am. **107**, 154–162 (2000).

[17] M. V. Berry, ''Semi-classical mechanics in phase space: a study of Wigner's function,'' Philos. Trans. R. Soc. London, Ser. A **287**, 237–271 (1977).

[18] M. V. Berry, ''Regular and irregular semiclassical wave functions,'' J. Phys. A **10**, 2083–2091 (1977).

[19] V. I. Shishov, ''Theory of wave propagation in random media,'' Izv. Vyssh. Uchebn. Zaved., Radiofiz. **11**, 866–875 (1968).

[20] R. Dashen, ''Path integrals for waves in random media,'' J. Math. Phys. **20**, 894–920 (1979).

[21] S. Tomsovic and E. J. Heller, ''Long-time semiclassical dynamics of chaos: The stadium billiard,'' Phys. Rev. E **47**, 282–299 (1993).

[22] M.-A. Sepúlveda, S. Tomsovic, and E. J. Heller, ''Semiclassical propagation: How long can it last?,'' Phys. Rev. Lett. **69**, 402–405 (1992).

[23] M. G. Brown and M. A. Wolfson, ''A numerical investigation of semiclassical breakdown in the presence of ray chaos'' (in preparation).

[24] A. Crisanti, G. Paladin, and A. Vulpiani, *Products of Random Matrices in Statistical Physics* (Springer, Berlin, 1993).

[25] L. A. Chernov, *Wave Propagation in a Random Medium* (McGraw-Hill, New York, 1960).

[26] A. B. Zisook, ''Intermittency in area-preserving mappings,'' Phys. Rev. A **25**(4), 2289–2292 (1982).

[27] P. Bergé, Y. Pomeau, and C. Vidal, *Order Within Chaos* (Hermann, Paris, 1984).

[28] J. A. Colosi, private communication (2000). Calculations were performed using AET climatology measurements of mesoscale energetics, and with a Garrett–Munk internal wave spectrum.

[29] F. D. Tappert, ''The parabolic approximation method,'' in *Wave Propagation and Underwater Acoustics*, Lecture Notes in Physics, Vol. 70, edited by J. B. Keller and J. S. Papadakis (Springer, New York, 1977), Chap. V, pp. 224–287.

[30] F. D. Tappert and M. G. Brown, ''Asymptotic phase errors in parabolic approximations to the one-way Helmholtz equation,'' J. Acoust. Soc. Am. **99**, 1405–1413 (1996).

[31] E. J. Heller and S. Tomsovic, ''Postmodern quantum mechanics,'' Phys. Today **46**, 38–46 (1993).

[32] E. J. Heller, ''Wave packet dynamics and quantum chaology,'' in *Chaos and Quantum Physics*, edited by M.-J. Giannoni, A. Voros, and J. Zinn-

Justin, Les Houches, Session LII (Elsevier Science, Amsterdam, 1991), Course IX, pp. 549–663.
[33] A. N. Malakhov, S. N. Molodtsov, and A. I. Saichev, ''To the hypothesis of a logarithmically normal distribution law of amplitude fluctuations of a light wave propagating in a randomly, inhomogeneous medium,'' Radiophys. Quantum Electron. **20**, 169–176 (1977).
[34] V. A. Kulkarny and B. S. White, ''Focusing of waves in turbulent inhomogeneous media,'' Phys. Fluids **25**, 1770–1784 (1982).
[35] G. C. Papanicolau and W. Kohler, ''Asymptotic theory of mixing stochastic ordinary differential equations,'' Commun. Pure Appl. Math. **27**, 641–668 (1974).
[36] D. A. Dawson and G. C. Papanicolau, ''A random wave process,'' Appl. Math. Optim. **12**, 97–114 (1984).
[37] R. L. Stratanovich, *Topics in the Theory of Random Noise* (Gordon and Breach, New York, 1963), Vol. 1.
[38] A. L. Virovlyansky, ''Comment on 'Mode coupling by internal waves for multimegameter acoustic propagation in the ocean' [J. Acoust. Soc. Am. **100**, 3607–3620 (1996)],'' J. Acoust. Soc. Am. **106**, 1174–1176 (1999).

Three-dimensional elasticity model for a decoupling coating on a rectangular plate immersed in a heavy fluid

A. Berry[a] and O. Foin
G.A.U.S., Department of Mechanical Engineering, University of Sherbrooke, Quebec J1K 2R1, Canada

J. P. Szabo
Defence Research Establishment Atlantic, P.O. Box 1012, Dartmouth, Nova Scotia B2Y 3Z7, Canada

(Received 29 April 2000; revised 19 March 2001; accepted 25 March 2001)

This paper presents an analysis of the vibroacoustic response of a finite, simply supported rectangular plate covered by a layer of decoupling material and immersed in a heavy fluid. An exact formulation using the three-dimensional theory of elasticity for the decoupling material is derived for this problem, thereby extending previous studies that were limited to infinite plates. The paper details the constitutive equations of the problem and the analytical method of solution. Numerical results show that shear waves in the decoupling material generally have little influence on the sound radiation in the heavy fluid. Comparisons with a locally reacting model of the decoupling material and with the simple model of House [Proc. I.O.A. **13**(3), 166–173 (1991)] are also presented. [DOI: 10.1121/1.1372224]

PACS numbers: 43.30.Jx, 43.40.Dx, 43.40.Tm [CBB]

I. INTRODUCTION

The addition of a decoupling (or compliant) material on a resonant structure is a common way to reduce the sound radiated by a structure immersed in water. The aim of this treatment is to isolate the fluid from the vibrations of the resonant structure. The decoupling material should have a low stiffness in comparison to the elastic material forming the base structure to support thickness deformation induced by the action of the dynamic pressure in the fluid. This deformation leads to the decoupling of the motions of the base structure and of the fluid in contact with the decoupling layer.

A simple description of a compliant coating is the locally reacting model, which assumes that the decoupling material behaves as evenly distributed massless springs on the plate. This model is able to account for the transverse strain of the decoupling layer. It is called ''locally reacting'' because the thickness deformation of the layer at a given position depends on the surface acoustic pressure at this position only. Many previous studied have used the locally reacting model to describe the vibroacoustics of an infinite structure covered by a compliant material and immersed in water (Crigthon, 1979; Maidanik *et al.*, 1968, 1974, 1984). Other studies have also applied the locally reacting model to a finite, piston-like base structure (Sandman *et al.*, 1995), or a rectangular, elastic plate (Foin *et al.*, 2000) covered by a decoupling material. Such locally reacting models remain limited by their inherent incapability to capture complex propagation of elastic waves in the decoupling material.

In order to accurately model the dynamics of a decoupling material, the three-dimensional theory of elasticity is required. This theory ensures that complex, three-dimensional deformations of the decoupling layer are properly accounted for. Ko (1997) and Keltie (1998) have considered the three-dimensional theory of elasticity for base plate–decoupling layer systems of infinite dimensions. Laulagnet *et al.* (1991, 1994) have also used the three-dimensional elasticity to predict the sound radiated from a thin, simply supported cylindrical shell covered by a thin compliant coating. In their work, asymptotic expressions of the three-dimensional elasticity were considered, based on thin coating approximations. On the other hand, House (1991) presented a very simple model of the transmission loss for an infinite panel covered by a decoupling layer and radiating into water. In this model, a closed-form solution of the sound transmission loss is obtained under the assumption that the base panel and decoupling material behave as fluid-like media.

In this paper, a rigorous analytical formulation of the sound radiation from a finite bending plate covered by a decoupling material and immersed in a heavy fluid is investigated. The formulation uses the three-dimensional theory of elasticity for the decoupling material, thereby extending previous work of Ko (1997) and Keltie (1998) to a system of finite dimensions. Also, the base plate in this work is treated as a bending plate. An analytical solution of the dynamic and acoustic response is derived for the finite system with simply supported boundary conditions. Section II of the paper presents the exact, constitutive equations of the problem and the method of solution. Section III presents some numerical results on the influence of shear waves as compared to extensional waves in the decoupling material, comparisons with a locally reacting model of the decoupling material, and with the model of House (1991).

II. ANALYSIS

A. Propagation of waves in an elastic solid

In this paper, as in previous work (Ko, 1997; Keltie, 1998), the decoupling material is treated as a three-dimensional, linear, homogeneous, elastic solid. Although

[a]Electronic mail: alain.berry@gme.usherb.ca

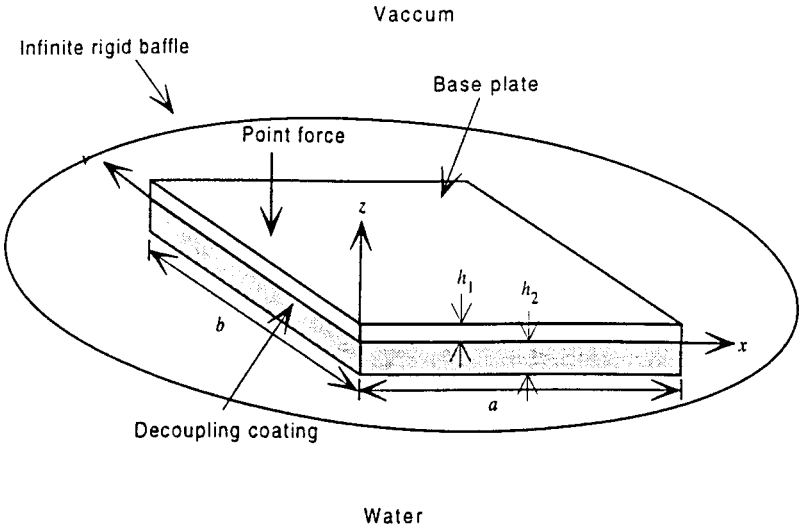

FIG. 1. Schematics of the system.

the use of a *poroelastic* analysis may more adequately describe the air-voided elastomeric decoupling materials considered here than a purely *elastic* analysis, this option was not pursued. This section recalls the basic theory to describe the propagation of waves in an elastic, isotropic, and homogeneous solid. The following results are borrowed from Kolsky (1963), Achenbach (1973), and Davis (1988).

In general, the elastic displacement $\mathbf{u}=(u_x,u_y,u_z)$ in the solid can be written in the form

$$\mathbf{u}=\boldsymbol{\nabla}\phi+\nabla\times\boldsymbol{\psi}, \tag{1}$$

where the first term $\mathbf{u}_L=\boldsymbol{\nabla}\phi$ corresponds to a longitudinal (or compressional) wave, and the second term $\mathbf{u}_T=\nabla\times\boldsymbol{\psi}$ corresponds to a transverse (or shear) wave. These two types of waves can be expressed as a function of a scalar potential ϕ and a vector potential $\boldsymbol{\psi}=(\psi_x,\psi_y,\psi_z)$. The scalar potential is governed by the wave equation

$$\nabla^2\phi-\frac{\rho}{\lambda+2\mu}\frac{\partial^2\phi}{\partial t^2}=0, \tag{2}$$

where the longitudinal wave speed is $c_L=([\lambda+2\mu]/\rho)^{1/2}$, ρ is the mass density of the solid, and λ, μ are the Lamé coefficients. On the other hand, the potential vector is governed by the wave equation

$$\nabla^2\boldsymbol{\psi}-\frac{\rho}{\mu}\frac{\partial^2\boldsymbol{\psi}}{\partial t^2}=0, \tag{3}$$

where the shear wave speed is $c_T=(\mu/\rho)^{1/2}$.

Since the three components of the displacement u_x, u_y, u_z depend on four potential components ϕ, ψ_x, ψ_y, ψ_z, it is necessary to specify an additional relation between the potentials. Achenbach (1973) assumes an additional relation of the form

$$\nabla\cdot\boldsymbol{\psi}=\frac{\partial\psi_x}{\partial x}+\frac{\partial\psi_y}{\partial y}+\frac{\partial\psi_z}{\partial z}=0. \tag{4}$$

In addition to the above equations, boundary conditions on the surface of the elastic domain need to be specified in order to completely solve the scalar potential and potential vector. These boundary conditions are presented hereafter for the system considered in this study.

B. Constitutive equations of the vibroacoustic problem

The structure under study is a rectangular (dimensions *a*, *b*), simply supported bending plate covered by a decoupling coating and immersed in water. The outer (''wet'') surface of the coating is inserted in an infinite rigid baffle. The excitation is a point force exerted on the base plate or an acoustic plane wave (Fig. 1). The base plate is described with the classical Love–Kirchhoff theory for bending motion, whereas the previous equations of three-dimensional elasticity is used for the decoupling coating. The model thus accounts for compressional (longitudinal) waves and shear (transverse) waves in the decoupling material. The main difference between the locally reacting model previously presented in Foin *et al.* (2000) lies in the fact that the locally reacting model only accounts for thickness deformation of the coating, whereas the 3D model accounts for all types of deformations. To our knowledge, all previous modelling of decoupling coatings using the three-dimensional theory of elasticity considered only infinite geometry; in this work, the three-dimensional theory of elasticity is extended to a finite plate.

1. Dynamics of the base plate

The equation of motion of the base plate is

$$\rho_1 h_1\frac{\partial^2 w}{\partial t^2}+D_1\nabla^4 w=-f(x,y)-\sigma_z(x,y,0), \tag{5}$$

where ρ_1 is the density and h_1 is the thickness of the plate, w is the transverse displacement, $f(x,y)$ is the external force per unit area acting on the plate and $\sigma_z(x,y,0)$ is the normal stress exerted by the coating on the plate. Also, $D_1=(E_1h_1^3)/[12(1-\nu_1^2)]$ is the bending stiffness of the plate, where E_1, and ν_1 are the Young's modulus and the Poisson's ratio of the plate, respectively. The fluid loading on the free side of the base plate is neglected in the dynamics of the base plate. The boundary conditions at the edges of the plate (simply supported boundary conditions) are

$$
\begin{aligned}
&w=0 \quad \text{at } x=0,\ x=a,\ y=0,\ y=b,\\
&\frac{\partial^2 w}{\partial y^2}=0 \quad \text{at } x=0,\ x=a,\\
&\frac{\partial^2 w}{\partial x^2}=0 \quad \text{at } y=0,\ y=b.
\end{aligned} \tag{6}
$$

2. Dynamics of the coating

Extensional and shear waves in the decoupling material are governed by Eqs. (1)–(4). The boundary conditions at the plate/coating interface ($z=0$) are

$$
\begin{aligned}
&w(x,y)=u_z(x,y,0),\\
&\frac{h_1}{2}\frac{\partial w(x,y)}{\partial x}=u_z(x,y,0),\\
&\frac{h_1}{2}\frac{\partial w(x,y)}{\partial y}=u_y(x,y,0).
\end{aligned} \tag{7}
$$

These boundary conditions express the continuity of the displacement between the plate and the coating in all three directions. The boundary conditions on the lateral sides of the coating are

$$
\begin{aligned}
&u_z=0 \quad \text{at } x=0,\ x=a,\ y=0,\ y=b,\\
&u_r=0 \quad \text{at } y=0,\ y=b,\\
&u_y=0 \quad \text{at } x=0,\ x=a,\\
&\sigma_x=0 \quad \text{at } x=0,\ x=a,\ y=0,\ y=b,\\
&\sigma_y=0 \quad \text{at } x=0,\ x=a,\ y=0,\ y=b,\\
&\sigma_{xz}=0 \quad \text{at } y=0,\ y=b,\\
&\sigma_{yz}=0 \quad \text{at } x=0,\ x=a,
\end{aligned} \tag{8}
$$

where σ_x, σ_y, σ_{xz}, σ_{yz} are stress components. The above boundary conditions physically mean that the lateral sides of the coating are fixed in the z direction and in the tangential direction, but are free to move along the direction normal to the side. These boundary conditions will allow the scalar potential ϕ and the potential vector $\boldsymbol{\psi}$ to be simply expressed in terms of trigonometric functions, as will be shown later.

3. Fluid equations

The fluid is treated here as compressible and nonviscous. The acoustic pressure p in the fluid is therefore governed by the wave equation

$$
\nabla^2 p-\frac{1}{c_0^2}\frac{\partial^2 p}{\partial t^2}=0, \tag{9}
$$

where c_0 is the sound speed. At the fluid–coating interface the continuity of normal mechanical and acoustic velocities leads to

$$
\left.\frac{\partial^2 u_z}{\partial t^2}\right|_{z=-h_2}=\left.\frac{1}{\rho_0}\frac{\partial p}{\partial z}\right|_{z=-h_2}, \tag{10}
$$

where ρ_0 is the density of the fluid. Since the fluid cannot withstand tangential stress, no continuity conditions are imposed to tangential displacements at the fluid–coating interface. In the following, a time-harmonic dependence of the form $e^{j\omega t}$ is assumed. From the Kirchhoff–Helmholtz theorem, the acoustic pressure in the fluid half-space is related to the normal displacement at the coating surface by the Rayleigh integral

$$
\begin{aligned}
p(x,y,z)=-\rho_0\omega^2\int_S\int u_z(x',y',-h_2)\\
\times G(x,y,z/x',y',-h_2)\,dx'\,dy',
\end{aligned} \tag{11}
$$

where G is the acoustic Green's function that satisfies a Neumann's condition at $z=-h_2$

$$
G=\frac{e^{-jk_0((x-x')^2+(y-y')^2+(z+h_2)^2)^{1/2}}}{2\pi((x-x')^2+(y-y')^2+(z+h_2)^2)^{1/2}}, \tag{12}
$$

and $k_0=\omega/c_0$. The boundary conditions at the coating/fluid interface ($z=-h_2$) are

$$
\begin{aligned}
&\sigma_z(x,y,-h_2)=-p(x,y,-h_2),\\
&\sigma_{xz}(x,y,-h_2)=0,\\
&\sigma_{yz}(x,y,-h_2)=0.
\end{aligned} \tag{13}
$$

These equations express the stress continuity at the coating/fluid interface: since the fluid is nonviscous, the tangential stress is zero on the coating surface; moreover, the normal stress is equal to the surface acoustic pressure $-p(x,y,-h_2)$.

The problem is entirely defined by Eqs. (1)–(8) and (11)–(13). In the following, a solution is derived for the four unknown variables w, ϕ, ψ_x, ψ_y [ψ_z is ultimately expressed in terms of ψ_x, ψ_y using Eq. (4)].

C. Solving the problem

Equation (6) allows the displacement of the base plate w to be written in terms of trigonometric functions

$$
w(x,y)=\sum_{m=1}^{\infty}\sum_{n=1}^{\infty} a_{mm}W_{mn}(x,y), \tag{14}
$$

where $W_{mn}(x,y)=\sin(m\pi x/a)\sin(n\pi y/b)$ are the eigenfunctions of a simply supported plate *in vacuo*. The scalar potential and potential vector can also be written in terms of similar trigonometric functions

$$
\phi(x,y,z)=\sum_{p=1}^{\infty}\sum_{q=1}^{\infty}\phi_{pq}(z)W_{pq}(x,y). \tag{15a}
$$

$$
\begin{aligned}
\psi_x(x,y,z)&=\sum_{p=1}^{\infty}\sum_{q=0}^{\infty}\psi_{x,pq}(z)\sin\left(\frac{p\pi x}{a}\right)\cos\left(\frac{q\pi y}{b}\right)\\
\psi_y(x,y,z)&=\sum_{p=0}^{\infty}\sum_{q=1}^{\infty}\psi_{y,pq}(z)\cos\left(\frac{p\pi x}{a}\right)\sin\left(\frac{q\pi y}{b}\right)
\end{aligned} \tag{15b}
$$

The choice of such combinations of sine and cosine functions in Eqs. (15a) and (15b) will later be justified by the boundary conditions of Eq. (8). Substituting Eqs. (15a) and (15b) into Eqs. (2) and (3) results in the following second-order differential equations:

$$
\left[\frac{\omega^2}{c_L^2}-\left(\frac{p\pi}{a}\right)^2-\left(\frac{q\pi}{b}\right)^2\right]\phi_{pq}(z)+\frac{\partial^2\phi_{pq}(z)}{\partial z^2}=0. \tag{16a}
$$

$$\left[\frac{\omega^2}{c_T^2}-\left(\frac{p\pi}{a}\right)^2-\left(\frac{q\pi}{b}\right)^2\right]\psi_{x,pq}(z)+\frac{\partial^2\psi_{x,pq}(z)}{\partial z^2}=0$$

$$\left[\frac{\omega^2}{c_T^2}-\left(\frac{p\pi}{a}\right)^2-\left(\frac{q\pi}{b}\right)^2\right]\psi_{y,pq}(z)+\frac{\partial^2\psi_{y,pq}(z)}{\partial z^2}=0. \tag{16b}$$

The general solutions can be written in the form

$$\phi_{pq}(z)=b_{pq}\cos(\alpha_{pq}z)+c_{pq}\sin(\alpha_{pq}z) \tag{17a}$$

$$\begin{aligned}\psi_{x,pq}(z)&=d_{pq}\cos(\beta_{pq}z)+e_{pq}\sin(\beta_{pq}z)\\ \psi_{y,pq}(z)&=f_{pq}\cos(\beta_{pq}z)+g_{pq}\sin(\beta_{pq}z),\end{aligned} \tag{17b}$$

where b_{pq}, c_{pq}, d_{pq}, e_{pq}, f_{pq}, and g_{pq} are unknown coefficients related to the longitudinal wave and the shear wave in the decoupling layer and α_{pq} and β_{pq} are defined by

$$\alpha_{pq}=\left(\frac{\omega^2}{(c_L)^2}-\left(\frac{p\pi}{a}\right)^2-\left(\frac{q\pi}{b}\right)^2\right)^{1/2},$$

$$\beta_{pq}=\left(\frac{\omega^2}{(c_T)^2}-\left(\frac{p\pi}{a}\right)^2-\left(\frac{q\pi}{b}\right)^2\right)^{1/2},$$

which are complex quantities in general.

The three displacements u_x, u_y, u_z, and the six stress components σ_x, σ_y, σ_z, σ_{xy}, σ_{xz}, σ_{yz} in the decoupling layer can later be expressed as a function of the potentials ϕ and $\boldsymbol{\psi}$. Ultimately, the displacements and stresses depend on the six series of unknown coefficients b_{pq}, c_{pq}, d_{pq}, e_{pq}, f_{pq}, and g_{pq}, as detailed in what follows. Equation (1) allows the displacement in the x, y, and z directions to be written

$$u_x(x,y,z)=\frac{\partial\phi}{\partial x}+\frac{\partial\psi_z}{\partial y}-\frac{\partial\psi_y}{\partial z}, \tag{18a}$$

$$u_y(x,y,z)=\frac{\partial\phi}{\partial y}-\frac{\partial\psi_z}{\partial x}+\frac{\partial\psi_x}{\partial z}, \tag{18b}$$

$$u_z(x,y,z)=\frac{\partial\phi}{\partial z}+\frac{\partial\psi_y}{\partial x}-\frac{\partial\psi_x}{\partial y}. \tag{18c}$$

Using Eq. (15), this leads to

$$u_x(x,y,z)=\sum_{p=0}^{\infty}\sum_{q=1}^{\infty}\cos\left(\frac{p\pi x}{a}\right)\sin\left(\frac{q\pi y}{b}\right)u_{x,pq}(z), \tag{19a}$$

$$u_y(x,y,z)=\sum_{p=1}^{\infty}\sum_{q=0}^{\infty}\sin\left(\frac{p\pi x}{a}\right)\cos\left(\frac{q\pi y}{b}\right)u_{y,pq}(z), \tag{19b}$$

$$u_z(x,y,z)=\sum_{p=1}^{\infty}\sum_{q=0}^{\infty}\sin\left(\frac{p\pi x}{a}\right)\sin\left(\frac{q\pi y}{b}\right)u_{z,pq}(z), \tag{19c}$$

where $u_{x,pq}$, $u_{y,pq}$, and $u_{z,pq}$ are defined by

$$u_{x,pq}(z)=\frac{p\pi}{a}\phi_{pq}(z)-\frac{q\pi}{b}\psi_{z,pq}(z)-\frac{\partial\psi_{y,pq}(z)}{\partial z}, \tag{20a}$$

$$u_{y,pq}(z)=\frac{q\pi}{b}\phi_{pq}(z)+\frac{p\pi}{a}\psi_{z,pq}(z)+\frac{\partial\psi_{x,pq}(z)}{\partial z}, \tag{20b}$$

$$u_{z,pq}(z)=\frac{\partial\phi_{pq}(z)}{\partial z}-\frac{p\pi}{a}\psi_{y,pq}(z)+\frac{q\pi}{b}\psi_{x,pq}(z). \tag{20c}$$

It can be noted that u_x, u_y, and u_z in Eqs. (19a)–(19c) automatically satisfy the first three boundary conditions in Eq. (8).

The stress components in the coating are also derived from the displacements using the relations of linear elasticity. The stress components are defined by

$$\sigma_x=(\lambda_2+2\mu_2)\frac{\partial u_x}{\partial x}+\lambda_2\frac{\partial u_y}{\partial y}+\lambda_2\frac{\partial u_z}{\partial z}, \tag{21a}$$

$$\sigma_y=\lambda_2\frac{\partial u_x}{\partial x}+(\lambda_2+2\mu_2)\frac{\partial u_y}{\partial y}+\lambda_2\frac{\partial u_z}{\partial z}, \tag{21b}$$

$$\sigma_z=\lambda_2\frac{\partial u_x}{\partial x}+\lambda_2\frac{\partial u_y}{\partial y}+(\lambda_2+2\mu_2)\frac{\partial u_z}{\partial z}, \tag{21c}$$

$$\sigma_{xy}=\mu_2\left(\frac{\partial u_x}{\partial y}+\frac{\partial u_y}{\partial x}\right), \tag{21d}$$

$$\sigma_{xz}=\mu_2\left(\frac{\partial u_x}{\partial z}+\frac{\partial u_z}{\partial x}\right), \tag{21e}$$

$$\sigma_{yz}=\mu_2\left(\frac{\partial u_y}{\partial z}+\frac{\partial u_z}{\partial x}\right), \tag{21f}$$

where λ_2, μ_2 are the Lamé coefficients of the coating. Using Eq. (19), this leads to

$$\sigma_x(x,y,z)=\sum_{p=1}^{\infty}\sum_{q=1}^{\infty}\sin\left(\frac{p\pi x}{a}\right)\sin\left(\frac{q\pi y}{b}\right)\sigma_{x,pq}(z), \tag{22a}$$

$$\sigma_y(x,y,z)=\sum_{p=1}^{\infty}\sum_{q=1}^{\infty}\sin\left(\frac{p\pi x}{a}\right)\sin\left(\frac{q\pi y}{b}\right)\sigma_{y,pq}(z), \tag{22b}$$

$$\sigma_z(x,y,z)=\sum_{p=1}^{\infty}\sum_{q=1}^{\infty}\sin\left(\frac{p\pi x}{a}\right)\sin\left(\frac{q\pi y}{b}\right)\sigma_{z,pq}(z), \tag{22c}$$

$$\sigma_{xy}(x,y,z)=\sum_{p=0}^{\infty}\sum_{q=0}^{\infty}\cos\left(\frac{p\pi x}{a}\right)\cos\left(\frac{q\pi y}{b}\right)\sigma_{xy,pq}(z), \tag{22d}$$

$$\sigma_{xz}(x,y,z)=\sum_{p=0}^{\infty}\sum_{q=1}^{\infty}\cos\left(\frac{p\pi x}{a}\right)\sin\left(\frac{q\pi y}{b}\right)\sigma_{xz,pq}(z), \tag{22e}$$

$$\sigma_{yz}(x,y,z)=\sum_{p=1}^{\infty}\sum_{q=0}^{\infty}\sin\left(\frac{p\pi x}{a}\right)\cos\left(\frac{q\pi y}{b}\right)\sigma_{yz,pq}(z), \tag{22f}$$

where

$$\sigma_{x,pq}(z) = -\frac{p\pi}{a}(\lambda_2+2\mu_2)u_{x,pq}(z) - \frac{q\pi}{b}\lambda_2 u_{y,pq}(z) + \lambda_2\frac{\partial u_{z,pq}(z)}{\partial z}, \tag{23a}$$

$$\sigma_{y,pq}(z) = -\frac{p\pi}{a}\lambda_2 u_{x,pq}(z) - \frac{q\pi}{b}(\lambda_2+2\mu_2)u_{y,pq}(z) + \lambda_2\frac{\partial u_{z,pq}(z)}{\partial z}, \tag{23b}$$

$$\sigma_{z,pq}(z) = -\frac{p\pi}{a}\lambda_2 u_{x,pq}(z) - \frac{q\pi}{b}\lambda_2 u_{y,pq}(z) + (\lambda_2+2\mu_2)\frac{\partial u_{z,pq}(z)}{\partial z}, \tag{23c}$$

$$\sigma_{xy,pq}(z) = \mu_2\frac{q\pi}{b}u_{x,pq}(z) + \mu_2\frac{p\pi}{a}u_{y,pq}(z), \tag{23d}$$

$$\sigma_{xz,pq}(z) = \mu_2\frac{\partial u_{x,pq}(z)}{\partial z} + \mu_2\frac{p\pi}{a}u_{z,pq}(z), \tag{23e}$$

$$\sigma_{yz,pq}(z) = \mu_2\frac{\partial u_{y,pq}(z)}{\partial z} + \mu_2\frac{q\pi}{b}u_{z,pq}(z). \tag{23f}$$

Again, the stress components σ_x, σ_y, σ_{xz}, σ_{yz} in Eqs. (22a)–(22f) automatically satisfy the last four boundary conditions in Eq. (8).

The final step is to write the constitutive equations of the problem in terms of the series of unknown coefficients a_{mn}, b_{pq}, c_{pq}, d_{pq}, e_{pq}, f_{pq}, and g_{pq}. Using the orthogonality of the eigenfunctions $W_{mn}(x,y)$, the dynamics of the base plate Eq. (5) can be written

$$\rho_1 h_1(\omega_{mn}^2-\omega^2)a_{mn}N_{mn} = -\int_0^a\int_0^b f(x,y)W_{mn}(x,y)\,dx\,dy - \int_0^a\int_0^b \sigma_z(x,y,0)W_{mn}(x,y)\,dx\,dy, \tag{24}$$

where the natural angular frequencies of the base plate *in vacuo* are defined by

$$\omega_{mn} = \sqrt{\frac{D_1}{\rho_1 h_1}}\left(\left(\frac{m\pi}{a}\right)^2+\left(\frac{n\pi}{b}\right)^2\right)$$

and

$$N_{mn} = \int_0^a\int_0^b W_{mn}^2(x,y)\,dx\,dy = \frac{ab}{4}.$$

The other equations are provided by the plate/coating and coating/fluid interface conditions. The boundary conditions Eq. (7) become

$$\sum_{m=1}^{\infty}\sum_{n=1}^{\infty} a_{mn}W_{mn}(x,y) = \sum_{p=1}^{\infty}\sum_{q=1}^{\infty} u_{z,pq}(0)W_{pq}(x,y) \quad \forall x,y, \tag{25a}$$

$$\frac{h_1}{2}\sum_{m=1}^{\infty}\sum_{n=1}^{\infty} a_{mn}\frac{m\pi}{a}\cos\left(\frac{m\pi x}{a}\right)\sin\left(\frac{n\pi y}{b}\right) = \sum_{p=0}^{\infty}\sum_{q=1}^{\infty} u_{x,pq}(0)\cos\left(\frac{m\pi x}{a}\right)\sin\left(\frac{n\pi y}{b}\right) \quad \forall x,y, \tag{25b}$$

$$\frac{h_1}{2}\sum_{m=1}^{\infty}\sum_{n=1}^{\infty} a_{mn}\frac{n\pi}{b}\sin\left(\frac{m\pi x}{a}\right)\cos\left(\frac{n\pi y}{b}\right) = \sum_{p=1}^{\infty}\sum_{q=0}^{\infty} u_{y,pq}(0)\sin\left(\frac{m\pi x}{a}\right)\cos\left(\frac{n\pi y}{b}\right) \quad \forall x,y, \tag{25c}$$

which leads to

$$a_{mn} = u_{z,mn}(0), \tag{26a}$$

$$\frac{h_1}{2}\frac{m\pi}{a}a_{mn} = u_{x,mn}(0) \quad \text{if } m>0, \qquad u_{x,mn}(0) = 0 \quad \text{if } m=0. \tag{26b}$$

$$\frac{h_1}{2}\frac{n\pi}{b}a_{mn} = u_{y,mn}(0) \quad \text{if } n>0, \qquad u_{y,mn}(0) = 0 \quad \text{if } n=0. \tag{26c}$$

From Eqs. (22c), (11), and (19c), the first plate/coating interface condition in Eq. (13) takes the form

$$\sum_{p=1}^{\infty}\sum_{q=1}^{\infty}\sigma_{z,pq}(-h_2)W_{pq}(x,y) = \rho_0\omega^2\int_0^a\int_0^b\sum_{m=1}^{\infty}\sum_{n=1}^{\infty} u_{z,mn}(-h_2)W_{mn}(x,y) \times G(x,y,-h_2/x',y',-h2)dx'\,dy'. \tag{27}$$

The orthogonality of $W_{mn}(x,y)$ is used to simplify the above relation

$$N_{pq}\sigma_{z,pq}(-h_2) = j\omega\sum_{m=1}^{\infty}\sum_{n=1}^{\infty} u_{z,mn}(-h_2)Z_{mnpq}, \tag{28}$$

where Z_{mnpq} are the radiation impedance terms defined by

$$Z_{mnpq} = j\rho_0\omega\int_0^a\int_0^b\int_0^a\int_0^b W_{mn}(x',y') \times G(x,y,-h_2,x',y',-h_2)W_{pq}(x,y)\,dx\,dy\,dx'\,dy'. \tag{29}$$

It is noted that these radiation impedance terms take the same form as in the analysis of the sound radiation from a simply supported bending plate; therefore, they can be computed using the usual techniques described in Nelisse *et al.* (1996) and Sandman (1975).

The last two plate/coating interface conditions in Eq. (13) can be written in the form

$$\sigma_{xz,pq}(-h_2)=0 \quad \forall p,q,$$
$$\sigma_{yz,pq}(-h_2)=0 \quad \forall p,q. \tag{30}$$

Equations (24), (26a), (26b), (26c), (28) and (38) form the equations of the problem in terms of the unknown coefficients a_{mn}, b_{pq}, c_{pq}, d_{pq}, e_{pq}, f_{pq}, and g_{pq}. Solving the corresponding linear system allows the unknown coefficients of the problem to be obtained, and ultimately the various vibroacoustic indicators to be derived.

D. Vibroacoustic indicators

In this section global vibroacoustic indicators are derived from the previous theoretical analysis. The vibroacoustic indicators are the mean square velocity of the base structure, the mean square velocity of the outer surface of the decoupling layer, the sound power radiated by the system in the heavy fluid, and the acoustic insertion loss.

1. Mean square vibration velocities

The mean square velocity of the base plate is defined by

$$\langle V_1^2\rangle = \frac{\omega^2}{2ab}\int_0^a\int_0^b w(x,y)w^*(x,y)dx\,dy$$
$$= \frac{\omega^2}{8}\sum_{m=1}^{\infty}\sum_{n=1}^{\infty}|a_{mn}|^2. \tag{31}$$

The transverse mean square velocity of the outer surface of the decoupling layer is

$$\langle V_2^2\rangle = \frac{\omega^2}{2ab}\int_0^a\int_0^b u_z(x,y,-h_2)u_z^*(x,y,-h_2)dx\,dy$$
$$= \frac{\omega^2}{8}\sum_{p=1}^{\infty}\sum_{q=1}^{\infty}|u_{z,pq}(-h_2)|^2. \tag{32}$$

The mean square velocity ratio is representative of the effectiveness of the decoupling material; it is expressed as the ratio of the mean square velocity of the base plate to the mean square velocity of the outer surface of the decoupling layer

$$V_R = \frac{\langle V_1^2\rangle}{\langle V_2^2\rangle}. \tag{33}$$

2. Sound radiation in the heavy fluid

The sound power radiated by the system in the heavy fluid is given by

$$W = \frac{1}{2}\mathrm{Re}\left[\int_0^a\int_0^b p(x,y,-h_2)(-j\omega)u_z^*(x,y,-h_2)dx\,dy\right]$$
$$= \frac{\omega^2}{2}\sum_{mnpq}u_{z,pq}(-h_2)\mathrm{Re}[Z_{mnpq}]u_{z,mn}^*(-h_2). \tag{34}$$

The acoustic insertion loss is defined by the ratio of the radiated power with the decoupling material to the radiated power W_0 of the base structure without the decoupling material

$$IL = \frac{W}{W_0}. \tag{35}$$

III. NUMERICAL RESULTS

A. Comparison with the model of House (1991)

House (1991) developed a very simple model to describe the sound radiation of an *infinite* base structure immersed in air on one side and covered by a decoupling coating which radiates sound in water on the other side. The excitation in his model is a *normal* acoustic plane wave acting on the base structure (air side). Each structural component (i.e., the base plate and the coating) is described by an equivalent fluid model and is characterized by its density and longitudinal wave velocity. House calculated the transmission loss of this system, defined by

$$\mathrm{TL} = 10\log_{10}\left(\frac{A_1}{A_4}\right), \tag{36}$$

where A_1 is the magnitude of the incident acoustic wave and A_4 is the magnitude of the transmitted acoustic wave in water. He derived the following expression of the transmission loss:

$$\mathrm{TL}_4 = 20\log_{10}\left[\left[\cos(k_2l_2)\cos(k_3l_3)\left(1+\frac{z_1}{z_4}\right)\right.\right.$$
$$-\sin(k_2l_2)\sin(k_3l_3)\left(\frac{z_2}{z_3}+\frac{z_1z_3}{z_2z_4}\right)$$
$$+j\cos(k_2l_2)\sin(k_3l_3)\left(\frac{z_1}{z_3}+\frac{z_3}{z_4}\right)$$
$$\left.\left.+j\sin(k_2l_2)\cos(k_3l_3)\left(\frac{z_1}{z_2}+\frac{z_2}{z_4}\right)\right]\right]. \tag{37}$$

The notations of House are used in Eq. (37) and throughout this section. Subscripts 1, 2, 3, and 4 are devoted to air, the base structure, the coating, and water, respectively. Also, z_i is the acoustic impedance ($z_i=\rho_i c_i$) of the medium i ($i=1,...,4$), ρ_i is the density, c_i is the wave velocity, k_i is the acoustic wave number $k_i=\omega/c_i$, l_2 and l_3 are the thicknesses of the base plate and the coating, respectively. The indicator used by House to quantify the decoupling effect is the insertion loss, defined by the difference between the transmission loss without coating and the transmission loss with the coating

$$IL = \mathrm{TL}_3 - \mathrm{TL}_4, \tag{38}$$

where TL_3 is the transmission loss without coating [obtained from Eq. (37) by taking $l_3=0$].

Figures 2 and 3 show comparisons between the model of House and the present approach for a base plate made of steel ($\rho_2=7850\,\mathrm{kg/m^3}$, $E_2=210(1+0.005j)$ GPa, $\nu_2=0.3$, corresponding to a longitudinal wave velocity $c_2=6000$ m/s in the model of House) with dimensions a=b=0.6 m and thickness $h_2=9$ mm. In the context of the present study, a *normal* acoustic plane wave excitation is represented in Eq.

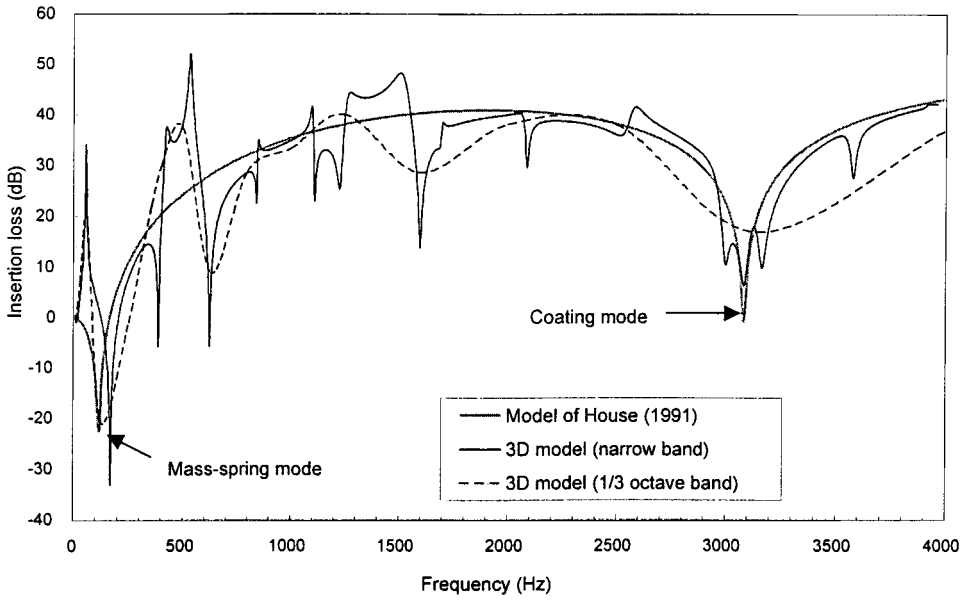

FIG. 2. Comparison of the insertion loss obtained with the model of House and with the three-dimensional model; excitation: normal acoustic wave; coating properties: $E_3=10^5$ Pa, $c_3=61.6$ m/s, $h_3=0.01$ m, $\nu_3=0.45$, $\rho_3=100$ kg/m^3, $\eta_3=0.01$.

(5) by a uniform force per unit area, $f(x,y)=2p_0$, where p_0 is the amplitude of the incident plane wave; a blocked pressure approximation is therefore invoked in order to express the surface pressure on the base plate to the amplitude of the incident wave. The decoupling layer has a thickness $h_3=0.01$ m, with $\nu_3=0.45$, $\rho_3=100$ kg/m^3, and a loss factor $\eta_3=0.01$. In Fig. 2 the Young's modulus of the coating is $E_3=10^5$ Pa ($c_3=61.6$ m/s) and in Fig. 3, $E_3=10^3$ Pa ($c_3=6.16$ m/s). The incident acoustic wave propagates in air ($c_1=340$ m/s, $\rho_1=1.2$ kg/m^3), the transmitted wave propagates in water ($c_4=1460$ m/s, $\rho_4=1000$ kg/m^3). The results of the three-dimensional model have been computed both in narrow-frequency bands and in one-third-octave bands. The first dip in the model of House corresponds to a frequency range in which the insertion loss is negative and can be interpreted as the mass-spring mode of the base structure/coating system. If the base plate is approximated by a lumped mass (with surface mass $\rho_2 h_2$) and the coating by a distribution of linear transverse springs (characterized by a stiffness per unit area L_3/h_3), the natural frequency of the mass-spring mode is given by the following formula:

$$F_r=\frac{1}{2\pi}\sqrt{\frac{L_3}{\rho_2 h_2 h_3}}, \tag{39}$$

where L_3 is the plate modulus of the coating (expressed in terms of the Lamé constants by: $L_3=\lambda_3+2\mu_3$). In the case of Fig. 2, Eq. (39) gives a value of 116 Hz, whereas the dip in the model of House is found to be around 120 Hz. Figure 2 shows that the three-dimensional elasticity model also predicts a negative insertion loss at a frequency close to the mass-spring resonance in the model of House (strictly, the mass-spring mode does not exist in the three-dimensional model because the boundary conditions of the base plate prevent rigid body motion of the plate). In Fig. 2, the subsequent dip observed in the model of House around 3 kHz corresponds to a thickness coating mode, i.e., a standing wave in the thickness of the coating. The coating modes are determined by the thickness of the coating and the longitudinal wave velocity in the coating. In an approximate way, the coating modes correspond to situations where the longitudinal wavelength in the coating γ, satisfies the relation

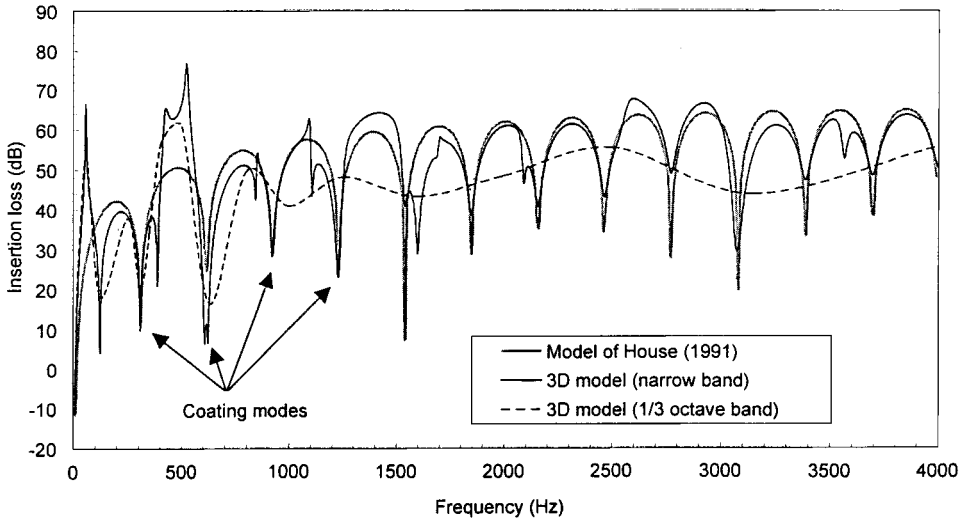

FIG. 3. Comparison of the insertion loss obtained with the model of House and with the three-dimensional model; excitation: normal acoustic wave; coating properties: $E_3=10^3$ Pa, $c_3=6.16$ m/s, $h_3=0.01$ m, $\nu_3=0.45$, $\rho_3=100$ kg/m^3, $\eta_3=0.01$.

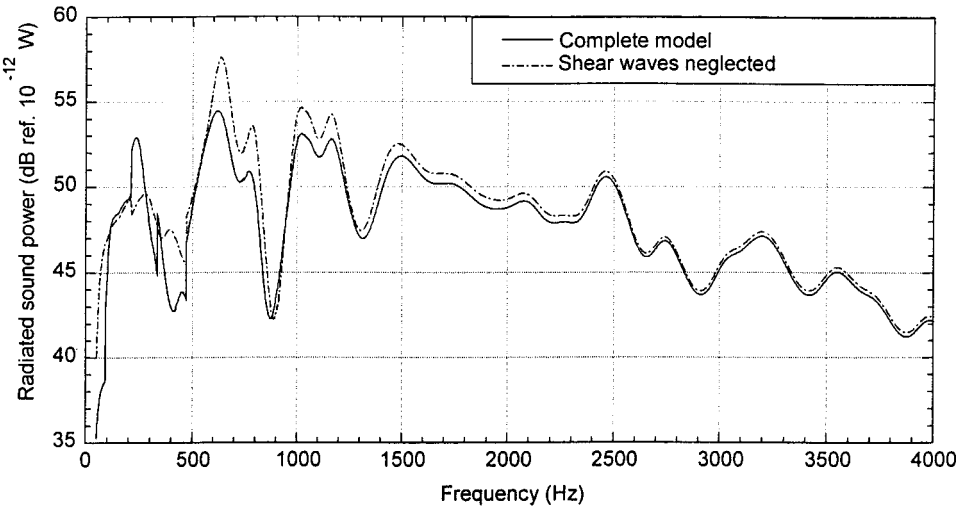

FIG. 4. Sound power radiated by the system calculated with the three-dimensional model, influence of the shear waves; coating properties: $h_2 = 0.05$ m, $\rho_2 = 600$ kg/m^3, $E_2 = 7.2 \times 10^6$ Pa, $\eta_2 = 0.65$, $\nu_2 = 0.38$.

$$\gamma = \frac{2h}{n}, \quad n = 1,...,\infty, \tag{40}$$

where h is the thickness of the coating. Hence, the natural frequencies of the coating modes are given by

$$f_n = \frac{nc_L}{2h}, \quad n = 1,...,\infty, \tag{41}$$

where c_L is the longitudinal wave velocity in the coating. In Fig. 3 (softer coating material), most of the dips in the model of House correspond to such coating modes. Figures 2 and 3 show that the three-dimensional model accurately predicts the coating modes observed in the simplified model of House. It is noted that the one-third-octave band results in the case of Fig. 3 do not reveal the coating modes because the frequency bands of integration are too large.

B. Relative influence of longitudinal and shear wave components

This section investigates the influence of the shear wave component in the three-dimensional elasticity model of the decoupling material. Earlier work (Ko, 1997) concluded that shear waves in the coating generally have little influence on the sound radiation from the system. Neglecting shear waves in the formulation implies that only the scalar potential ϕ accounting for longitudinal waves is considered in the equation of motion of the coating. The potential vector $\boldsymbol{\psi}$ accounting for the shear waves in the material is neglected. This approximation allows the unknown coefficients of the problem to be reduced to a_{mn}, b_{pq}, and c_{pq} only, and the governing equations reduce to Eqs. (24), (26a) and (28). Thus, Eqs. (26b), (26c) and (30) are not considered in this simplified model. Disregarding Eqs. (26b) and (26c) physically implies that the continuity of the tangential displacement u_x and u_y between the base plate and the coating is no longer enforced, while disregarding Eq. (30) means that the nullity of the tangential stresses σ_{xz} and σ_{yz} is not enforced at the coating/fluid interface. These simplifications therefore may violate some of the physics involved in the problem.

In the following numerical results a steel plate [$\rho_1 = 7850$ kg/m^3, $E_1 = 210(1 + 0.005j)$ GPa, $\nu_1 = 0.3$] of dimensions a=b=0.6 m, thickness $h_1 = 9$ mm is considered. The acoustic medium is water ($c_0 = 1460$ m/s, $\rho_0 = 1000$ kg/m^3). A point force is applied on the base plate at $x = y = 0.06$ m from a plate corner. Figures 4 and 5 show comparisons between the complete model and the simplified model (neglecting shear waves) in terms of the radiated sound power in the frequency range 0–4 kHz, for two dif-

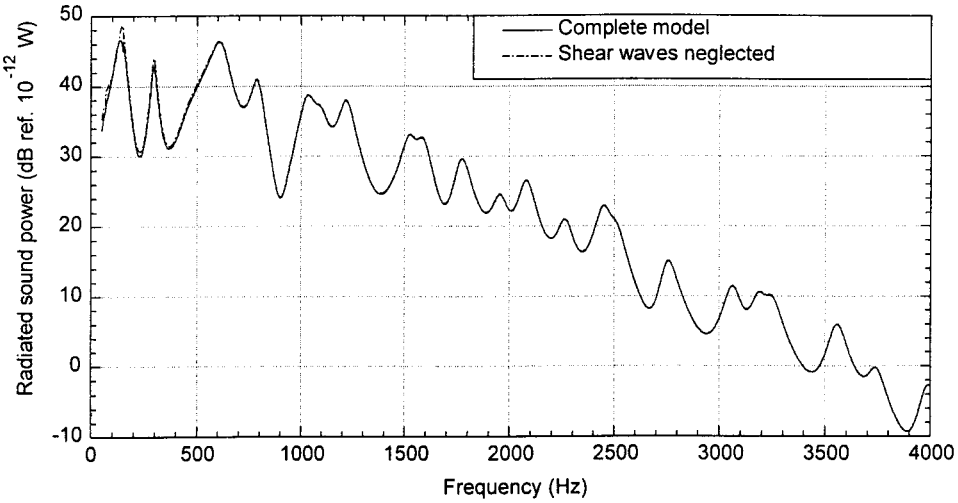

FIG. 5. Sound power radiated by the system calculated with the three-dimensional model, influence of the shear waves; coating properties: $h_2 = 0.05$ m, $\rho_2 = 600$ kg/m^3, $E_2 = 7.2 \times 10^5$ Pa, $\eta_2 = 0.65$, $\nu_2 = 0.38$.

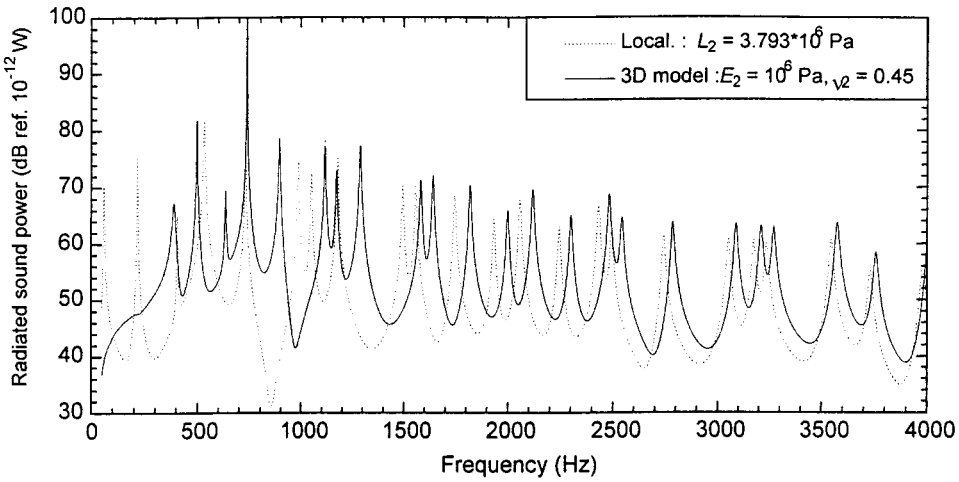

FIG. 6. Sound power radiated by the system, comparison between the locally reacting model and the 3D model; coating properties $h_2=10$ mm, $\rho_2=100$ kg/m^3, $E_2=10^6$ Pa, $\nu_2=0.45$ (corresponding to a plate modulus $L_2=3.793\times10^6$ Pa), loss factor $\eta_2=0.01$. Only longitudinal waves are accounted for in the 3D model.

ferent coating materials with thickness $h_2=0.05$ m. The decoupling materials in Figs. 4 and 5 correspond to typical highly damped ($\eta_2=0.65$), medium density foams ($\rho_2=600$ kg/m^3); a relatively rigid material is considered in Fig. 4 ($E_2=7.2\times10^6$ Pa), whereas a softer material is assumed in Fig. 5 ($E_2=7.2\times10^5$ Pa). The series in Eqs. (14) and (15) have been truncated to 8 terms in each direction x,y; this guarantees that the series include all *in vacuo* modes of the base plate in the frequency range 0–4 kHz. It was verified that increasing the number of terms does not change the results in this frequency range. The numerical results show that the influence of shear waves is limited to low frequency and relatively stiff decoupling materials. The conclusion that shear waves in the coating have little influence on the sound radiation is consistent with previous studies in the literature (Ko, 1997). In most of the following numerical results, only longitudinal waves are accounted for in the 3D model.

C. Comparison with a locally reacting model

In this section the three-dimensional elasticity model of the decoupling material is compared to a simplified, locally reacting model previously published by the authors (Foin *et al.*, 2000). In this simplified model, the decoupling material is described by a distribution of massless linear springs acting in the transverse direction; the decoupling material is therefore subject to thickness deformation only, instead of three-dimensional deformation. Also, the locally reacting model assumes a zero mass of the decoupling material, while the density is taken into account in the three-dimensional model. In the following results, only the longitudinal waves in the coating are accounted for in the three-dimensional elasticity model. The base plate properties, point force excitation, and fluid property are similar to the previous section.

In the three-dimensional theory of elasticity the transverse stress in the coating σ_z is related to the transverse strain ε_z by the relation:

$$\sigma_z=(\lambda_2+2\mu_2)\varepsilon_z=(B_2+\tfrac{4}{3}\mu_2)\varepsilon_z, \tag{42}$$

where λ_2 and μ_2 are the Lamé coefficients and B_2 is the bulk modulus of the coating. The term $L_2=\lambda_2+2\mu_2$ is referred to as the plate modulus. In the locally reacting model only the transverse stress and transverse strain are considered in the decoupling material. Hence, the stress–strain relation in the decoupling material should be expressed by Eq. (42). Applying Eq. (42) to a locally reacting, massless decoupling layer on a base plate results in:

$$P(x,y,-h_2)=L_2\left(\frac{w_2(x,y)-w_1(x,y)}{h_2}\right), \tag{43}$$

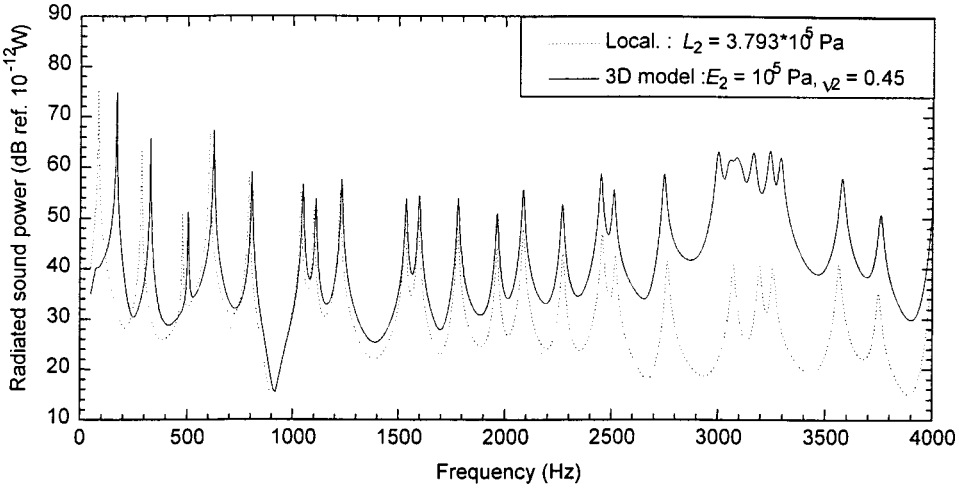

FIG. 7. Sound power radiated by the system, comparison between the locally reacting model and the 3D model; coating properties $h_2=10$ mm, $\rho_2=100$ kg/m^3, $E_2=10^5$ Pa, $\nu_2=0.45$ (corresponding to a plate modulus $L_2=3.793\times10^5$ Pa), loss factor $\eta_2=0.01$. Only longitudinal waves are accounted for in the 3D model.

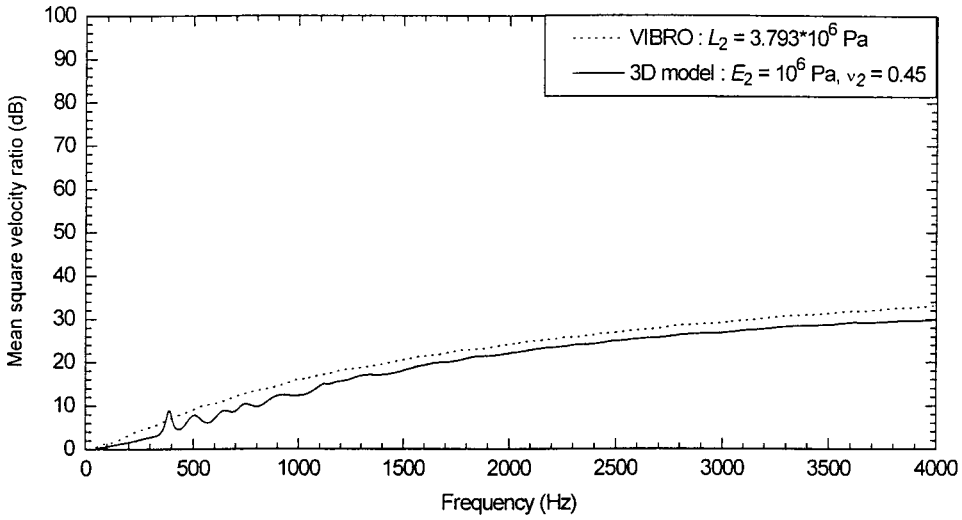

FIG. 8. Mean square velocity ratio; coating properties $h_2=10$ mm, $\rho_2=100$ kg/m^3, $E_2=10^6$ Pa, $\nu_2=0.45$ (corresponding to a plate modulus $L_2=3.793\times10^6$ Pa), loss factor $\eta_2=0.01$. Only longitudinal waves are accounted for in the 3D model.

where $P(x,y,-h_2)$ is the acoustic pressure on the coating surface; w_2 and w_1 are the transverse displacements of the coating surface and of the base structure, respectively. Equation (43) shows that the *plate* modulus should be considered to represent the stiffness of the decoupling material in the locally reacting model. The relation $L_2=\lambda_2+2\mu_2$ thus dictates a relation between the plate modulus used to describe the coating stiffness in the locally reacting model, and the corresponding Young's modulus and Poisson's ratio used in the three-dimensional model.

Figure 6 shows the sound power radiated from the system into water for the following coating properties: $h_2=10$ mm, $\rho_2=100$ kg/m^3, $E_2=10^6$ Pa, $\nu_2=0.45$ (corresponding to a plate modulus $L_2=3.793\times10^6$ Pa in the locally reacting model); a loss factor $\eta_2=0.01$ is considered in the coating (meaning that a complex Young's modulus $\tilde{E}_2=10^6(1+0.01j)$ is considered). The one-dimensional, locally reacting model and the three-dimensional model are in reasonable agreement, especially in high frequency. In low frequency, the resonances predicted by the three-dimensional model are shifted to higher frequency as compared to the locally reacting model; this may be attributed to more rigid boundary conditions of the decoupling layer in the three-dimensional model (for example, the edges of the decoupling layer are constrained to have a zero transverse displacement, which is not the case in the locally reacting model). Figure 7 shows numerical results for the following coating properties: $h_2=10$ mm, $\rho_2=100$ kg/m^3, $E_2=10^5$ Pa, $\nu_2=0.45$ (corresponding to a plate modulus $L_2=3.793\times10^5$ Pa in the locally reacting model); a loss factor $\eta_2=0.01$ is considered in the coating. These properties correspond to a softer material, as compared to Fig. 6. The low-frequency results obtained with the two models are comparable. However, there is a high-frequency (starting at 1.5 kHz) deviation of the models; specifically, the three-dimensional model predicts a significant amplification phenomenon around 3 kHz, which is due to a coating resonance (mode in the thickness dimension of the coating). Such thickness modes in the coating cannot be predicted by the locally reacting model because of the massless assumption of the coating. As a result, the three-dimensional elasticity model predicts an acoustic amplification in the frequency range of the thickness mode.

In this section the mean square velocity ratio [Eq. (33)] is compared for both models. The mean square velocity ratio gives an indication of the vibration isolation provided by the decoupling layer; moreover, it was found in Foin *et al.* (2000) that this ratio is also an appropriate indicator of the noise reduction provided by the coating. In the following

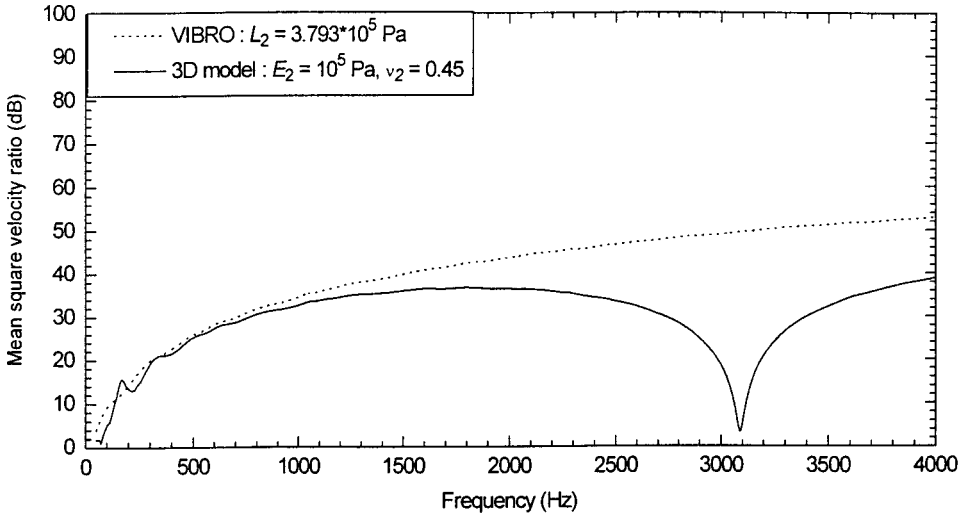

FIG. 9. Mean square velocity ratio; coating properties $h_2=10$ mm, $\rho_2=100$ kg/m^3, $E_2=10^5$ Pa, $\nu_2=0.45$ (corresponding to a plate modulus $L_2=3.793\times10^5$ Pa), loss factor $\eta_2=0.01$. Only longitudinal waves are accounted for in the 3D model.

results, only the longitudinal waves in the coating are accounted for in the three-dimensional elasticity model. The base plate properties, point force excitation, and fluid property are similar to the previous sections. Figure 8 shows the mean square velocity ratio for coating properties similar to those of Fig. 6. In this case, a good agreement is obtained between the three-dimensional model and the locally reacting model. Figure 9 is for the case of a softer decoupling material, with properties similar to those of Fig. 7. The three-dimensional model shows a small vibration isolation in the region corresponding to the first thickness mode of the coating. The coating modes are determined by Eq. (41). The locally reacting model cannot predict such modes because of the massless assumption used for the coating ($c_L = \infty$), and therefore overestimates the isolation provided by the coating in the frequency region corresponding to thickness modes in the coating.

IV. CONCLUSIONS

An exact analysis of the vibroacoustic response of a finite, simply supported rectangular plate covered by a layer of decoupling material and immersed in a heavy fluid has been presented. The three-dimensional theory of elasticity was used along with appropriate boundary conditions for the decoupling material, thereby extending previous studies which were limited to infinite plates and coating systems. Such a model is therefore more complete than the locally reacting model previously investigated by the authors. The following general conclusions can be drawn from the numerical results obtained:

(i) The very simple model of House was found to be in good agreement with the three-dimensional model in terms of the acoustic insertion loss of the coating layer.

(ii) Shear wave components in the decoupling material usually have little influence on the sound radiation in a heavy fluid, as compared to longitudinal wave components.

(iii) A good agreement was found between the locally reacting model and the three-dimensional model in the case of relatively stiff, lightly damped, and low mass density coating materials. However, dynamic effects in the decoupling material such as coating modes are revealed by the three-dimensional model; these effects translate into a poor noise reduction provided by the coating.

Achenbach, J. D. (**1973**). *Wave Propagation in Elastic Solids* (North-Holland, Amsterdam).

Crigthon, D. G. (**1979**). ''Aspects of the reflexion and free wave properties of a composite panel under fluid loading,'' J. Sound Vib. **64**(4), 467–474.

Davis, J. L. (**1988**). *Wave Propagation in Solids and Fluids* (Springer, Berlin).

Foin, O., Berry, A., and Szabo, J. (**2000**). ''Acoustic radiation from an elastic baffled rectangular plate covered by a decoupling coating and immersed in a heavy acoustic fluid,'' J. Acoust. Soc. Am. **107**, 2501–2510.

House, J. R. C. (**1991**). ''Considerations for underwater decoupling treatment,'' Proc. I.O.A. **13**(3), 166–173.

Keltie, R. F. (**1998**). ''Signal response of elastically coated plates,'' J. Acoust. Soc. Am. **103**, 1855–1863.

Ko, S. H. (**1997**). ''Reduction of structure-borne noise using an air-voided elastomer,'' J. Acoust. Soc. Am. **101**, 3306–3312.

Kolsky, H. (**1963**). *Stress Waves in Solids* (Dover, New York).

Laulagnet, B., and Guyader, J. L. (**1991**). ''Sound radiation from finite cylindrical shell covered with a compliant layer,'' Trans. ASME, J. Vib. Acoust. **113**, 267–272.

Laulagnet, B., and Guyader, J. L. (**1994**). ''Sound radiation from finite cylindrical coated shells, by means of asymptotic expansion of three-dimensional equations for coating,'' J. Acoust. Soc. Am. **96**, 277–286.

Maidanik, G., and Reader, W. T. (**1968**). ''Filtering action of a blanket dome,'' J. Acoust. Soc. Am. **44**, 497–502.

Maidanik, G., and Tucker, J. (**1974**). ''Acoustic properties of coated panels immersed in fluid media,'' J. Sound Vib. **34**(4), 519–550.

Maidanik, G. (**1984**). ''Modification caused by compliant layers and blankets in the pressure field induced on a boundary,'' Trans. ASME, J. Vib., Acoust., Stress, Reliab. Des. **106**, 369–375.

Nelisse, H., Beslin, O., and Nicolas, J. (**1996**). ''Fluid–structure coupling for an unbaffled elastic panel immersed in a diffuse field,'' J. Sound Vib. **198**(4), 485–506.

Sandman, B. E. (**1975**). ''Motion of a three-layered elastic-viscoelastic plate under fluid loading,'' J. Acoust. Soc. Am. **57**, 1097–1107.

Sandman, B. E., and Boisvert, J. E. (**1995**). ''Simplified structural acoustic characterization of external compliant coatings on submerged surfaces,'' NUWC Division Newport Technical Digest, June, pp. 65–71.

A modal Pritchard approximation for computing array element mutual impedance

C. L. Scandrett
Department of Mathematics, Naval Postgraduate School, Monterey, California 93943

J. L. Day
Office of Naval Intelligence, ONI-11, Washington, D.C. 20395-5720

S. R. Baker
Department of Physics, Naval Postgraduate School, Monterey, California 93943

(Received 9 June 2000; revised 15 January 2001; accepted for publication 17 January 2001)

An investigation into the applicability and accuracy of Pritchard's approximation for closely packed transducer arrays is undertaken. A new, ''modal'' Pritchard approximation is developed, based upon normal modes of the acoustic medium, and is tested for arrays of acoustically hard spheres to ascertain its accuracy in determining the mutual acoustic radiation impedance between array elements. For $ka \approx 1$, it is found that the modal Pritchard approximation works quite well in approximating the mutual radiation impedance of a two-element array, even for relatively close spacing; but for arrays of three or more scatterers in close proximity the approximation may have relatively large errors. The effect of neglecting inter-element scattering is analyzed for the monopole-to-monopole scattering of various configurations of a three-element array and a sixteen-element double line array. [DOI: 10.1121/1.1354985]

PACS numbers: 43.30.Jx, 43.30.Yj [ANN]

I. THEORETICAL BACKGROUND

The so-called Pritchard[1] and ''generalized Pritchard'' methods[2] are popular techniques used to approximate the acoustic interactions between elements in an underwater acoustic array. Origins of the method can be traced back to an asymptotic analysis for small spherical scatterers in an acoustic medium performed by Karnovsky,[3] who in turn references (as does Pritchard in his paper) earlier work done (including baffled pistons) by Rayleigh in 1903.[4]

In Pritchard's paper, the approximation is based upon an analytical treatment of acoustic interactions in an array of baffled circular pistons loaded by a semi-infinite fluid medium. Extensions to more general arrays are possible, however, if the following three criteria are met:

- The mutual impedance between any two elements of the array can be considered without regard to other array elements in the construction of a global impedance matrix for the entire array.
- The dimensions of an array element (in our case, the sphere radius a) are small relative to the acoustic wavelength [$(ka)^2 \ll 1$, where $k = \omega/c$ is the wave number of the time harmonic problem and c is the acoustic wave speed].
- The ratio of array element dimension to inter-element distances (d) is small ($a/d \ll 1$).

While it is true that if the second and third conditions are met, so must the first, the method is often applied when the latter two conditions are not strictly satisfied, with very good results. This is most likely due to the first condition being met. In Pritchard's paper the first of these approximations is exactly satisfied, since his array elements are coplanar with the baffle. When the assigned velocity of all but one of the pistons vanishes, the remainder of the array becomes essentially part of the baffle, and the exact mutual radiation impedance between it and any of the remaining array elements can be found analytically without regard to the other array elements, because there is no scattering.

The Pritchard approximation for the mutual radiation impedance between two array elements (for example, pistons 1 and 2) can be formulated mathematically as follows: A series representation of the mutual acoustic radiation impedance between the two pistons to leading order for small ka and small a/d is:

$$Z_{12} \approx R_{22}\left[\frac{\sin kd}{kd} + i\,\frac{\cos kd}{kd}\right] = R_{22} h_0^{(2)}(kd), \tag{1}$$

in which Z_{12} is the mutual radiation impedance seen by piston 1 due to a radiated pressure from piston 2, $h_0^{(2)}$ is the zeroth order spherical Hankel function of the second kind (an $e^{i\omega t}$ time dependence is used throughout), and R_{22} is the real (resistive) part of the self-radiation impedance of piston 2. Pritchard demonstrated that the above approximation is quite accurate in comparisons with exact calculations over a range of center-to-center distances between pistons in the baffled array.

Benthien[2] reported on extensions of Pritchard's method to other types of arrays. In particular, Benthien found excellent agreement in comparing a Pritchard approximation to experimental as well as numerically determined results based on the boundary element technique CHIEF,[5] for a three-element array of flextensional transducers. In Benthien's methodology, the mutual radiation impedances between ar-

ray elements are found by numerically determining the free-field self-radiation impedance of a single array element (Z_{self}). This uses the code CHIEF.[6] The resulting matrix is then used to obtain the mutual radiation impedance of that array element on a second (identical) array element by multiplying the self-radiation resistance matrix (R_{self}) by $h_0^{(2)} \times (kd)$ where d is the distance between the two array elements.

A more complicated and perhaps more accurate calculation would apply a Pritchard-type approximation on a *finite element* by *finite element* basis rather than from *array element* to *array element*, but is not done for two reasons. One reason is that the calculations involved in finding the mutual radiation impedance between finite elements for a large array would be greatly increased. A second reason is based on the underlying assumption of the Pritchard approximation itself, namely that $a \ll d$ where a is a characteristic length of the array element. This implies that finite element to finite element spacing between two array elements whose center to center spacing is d would be very nearly d as $d \pm a \approx d$.

In the Benthien formulation, the mutual radiation impedance matrix so constructed is applied to the velocity degrees of freedom (one for each surface finite element facet) for each element of the array to produce a pressure forcing function on each of the array element fluid-loaded surfaces. One can then solve for the unknown values of the velocities by matrix inversion techniques. Following Benthien, one could also normalize the matrix equations utilizing the *in vacuo* eigenvectors of the mass/stiffness finite element matrices of the array element prior to solving the system.

The work of Blottman *et al.*[7] should be mentioned. These authors numerically determined the mutual radiation impedance between a two-element array of transducers wherein the *in vacuo* normal modes of the transducers were used as degrees of freedom of the system. In this regard, Blottman's work resembles that of Benthien's ''normalization.'' Unlike the work of Benthien, it is assumed that intermode (cross-) coupling of the self-radiation impedance for a single transducer is negligible (i.e., *in vacuo* normal modes do not couple when heavy fluid loading is applied). *Modal* mutual impedances between array elements are found by employing a boundary element technique (EQI/ATILA)[8–10] which (unlike a Pritchard approximation) numerically accounts for scattering effects to all orders. While the work by Blottman *et al.* would appear to have little to do with the Pritchard approximation, the idea of applying a ''modal'' mutual radiation impedance is of interest. In particular, this report considers the possibility of a modal Pritchard approximation which might improve upon the Pritchard approximations currently in use.

II. THE MUTUAL RADIATION IMPEDANCE MATRIX AND THE PRITCHARD APPROXIMATION

Given a fluid-loaded array of M elements/transducers, and that the total pressure on array element n is represented by P_n, its value can be formally written in terms of the mutual and self-radiation impedances, and the prescribed normal surface velocities on each of the array elements (V_m for array element m), by the sum

$$P_n = \sum_{m=1}^{M} Z_{nm} V_m . \tag{2}$$

These pressures can in turn be used in conjunction with surface velocities to calculate pressures at arbitrary field points in the acoustic medium.

Crucial to Pritchard's method is an accurate representation of the self-radiation impedance of an array element since it is the basis for determination of all mutual radiation impedances imposed by that element on other elements in the array (it is used to find the Z_{nm} along that row of the global impedance matrix). If the self-radiation impedance is approximated by the *free-field* radiation impedance for the array element, the effect of inter-element array backscattering is necessarily neglected. Backscatter might, however, be taken into account at some level. At one extreme, one could numerically find the self-radiation impedance of a single element which accounts for all scattering between array elements, but that would be tantamount to solving the full array problem numerically, precluding the need for a Pritchard approximation altogether. (Incidentally, this is exactly what Pritchard was able to do for his baffled array.) A second alternative, neglects all backscattering except what is between those two array elements for which the mutual radiation impedance is being found. For a two-body array, this and the former methods of finding the self-radiation impedance are equivalent. A difficulty with this latter technique is that the self-radiation impedance expression used in a Pritchard approximation for each array element would depend on the geometry (distance and orientation) between it and each member of the array. Calculations would then have to be done on every combination of two-element arrays possible in the full array, leading to a considerable amount of work for ''large'' arrays.

If the free-field self-radiation impedance *is* used in the Pritchard approximation, and the velocity on the surface of each array element is known, the field pressure at any point in the acoustic medium can be found by a simple superposition of the radiated pressures resulting from each of the array elements. The surface pressure on the nth array element can be expressed as the sum of its self-radiated pressure ($Z_{nn}V_n$), plus contributions of radiated pressures from all other array elements, through the mutual radiation impedance matrix. Pritchard's approximation essentially substitutes the contribution to the radiation impedance from the mth array element on the nth element by a point source with amplitude equal to the resistive part of the mth array element's self-radiation impedance. This can be written as

$$P_n = \sum_{m=1}^{M} Z_{nm} V_m \approx Z_{nn_{\text{free}}} V_n + \sum_{m=1, m\neq n}^{M} R_{mm} h_0^{(2)}(kd_{nm}) V_m, \tag{3}$$

where M is the number of elements in the array, and d_{nm} is the distance between array elements n and m.

To gauge the accuracy of the Pritchard approximation an exact form of the mutual radiation impedance between elements of an array is needed which is more general than the ''flat'' array considered by Pritchard in his original work. An analytical form for the mutual radiation impedance between two acoustically hard spheres is given by New and Eisler[11] which employs a Green's function analysis coupled with spherical addition formulas.[12] Self- and mutual acoustic radiation impedances between the spheres are found and are represented by infinite series involving spherical Bessel functions and spherical harmonics. Results are then given over a range of center-to-center distances for cases in which one or both of the spheres are oscillating in a monopole fashion.

The surface radiation impedance used by New and Eisler is based on the definition[13,14]

$$Z_{r_j} = \frac{1}{V_j V_j^*} \int \int p(\overline{r_j}) v^*(\overline{r_j}) ds_j, \tag{4}$$

where $p(\overline{r})$ and $v(\overline{r})$ are, respectively, the pressure and normal velocity on the surface (s_j), and where $v(\overline{r})$ is further defined as $v(\overline{r}) = V\beta(\overline{r})$ in which V is an amplitude applied to the spatially varying function $\beta(\overline{r})$. (The asterisks refer to complex conjugates.)

It is a simple matter to find values for the self- and mutual radiation impedance for the two-element array analyzed in New and Eisler's work since the two spheres are identical. For this array, the total radiation impedance seen by sphere 1 is:

$$Z_{r_1} = Z_{11} + \frac{V_2}{V_1} Z_{12}. \tag{5}$$

The scaled radiation impedance seen by sphere 1 when both spheres have identical velocities, is given by the sum $Z_{11} + Z_{12}$, while Z_{11} is found by calculating the radiation impedance seen by sphere 1 while assigning a zero velocity on sphere 2. To find the mutual radiation impedance between sphere 2 and sphere 1 (Z_{12}), the difference between these two radiation impedances is taken $(Z_{r_1}|_{V_1=V_2=1} - Z_{r_1}|_{V_1=1,V_2=0})$. (Equivalently, Z_{12} could be found by determining the pressure on sphere 1 when $V_1=0$ and $V_2=1$.)

In reporting their results, New and Eisler make the following observation regarding the two-sphere array and the radiation impedance seen by sphere 1 (Z_{r_1}):

> ...the contribution of the mutual term Z_{12} is certainly significant. However, the primary contribution to the deviation of Z_{r_1} from the free-field value is *not* scattering, but merely a consequence of the added pressure field from sphere number 2. One can conclude, therefore, that, in the transition region $(ka_1 \approx ka_2 \approx 1)$, the effects of scattering on the radiation impedance of one spherical transducer in the presence of a second spherical transducer are barely significant, even for close spacings.

This would appear to validate a ''Pritchard'' type approximation for an array of spheres, up to and including $ka \approx 1$, and small inter-array element spacings.

In our analysis, spherical harmonic functions and the spherical addition formula are used to find an appropriate ''modal'' Pritchard approximation based upon **normal modes of the acoustic medium**. Our work explores the nature of this approximation with comparisons to exact solutions found by a T-matrix formalism,[15] in which scattering effects between array elements are fully taken into account.

III. DERIVATION OF THE MODAL PRITCHARD APPROXIMATION

The time harmonic radiated or scattered pressure field is represented in terms of outgoing spherical Hankel functions applied to the set of spherical harmonics. For a single radiator/scatterer with a local coordinate system written with the index ''j,'' the functional form of the pressure field (p_j) is written

$$p_j(r_j, \theta_j, \phi_j) = \sum_{n=0}^{N} \sum_{m=-n}^{n} A_{mn}^j h_n(kr_j) \Omega_n^m(\theta_j, \phi_j), \tag{6}$$

where

$$\Omega_n^m(\theta, \phi) = P_n^m(\cos\theta) e^{im\phi}$$

are spherical harmonic functions.

Representation of a single outgoing spherical wave using the spherical addition formula is given by[12]

$$h_n(kr_2)\Omega_n^m(\theta_2, \phi_2) = \sum_{\nu=0}^{\infty} \sum_{\mu=-\nu}^{\nu} \sum_{\substack{p=|n-\nu| \\ p \geq |m-\mu|}}^{n+\nu}{}' a(\nu, p, n, \mu, m) j_\nu(kr_{1_<}) \times h_p(kr_{1_>}) \Omega_p^{\mu+m}(\theta_{12}, \phi_{12}) \Omega_\nu^\mu(\theta_1, \phi_1) \tag{7}$$

(the prime on the summation over p indicates jumps of 2 in the sum) (r_1, θ_1, ϕ_1) = spherical coordinates relative to system 1, (r_2, θ_2, ϕ_2) = spherical coordinates relative to system 2, $(r_{12}, \theta_{12}, \phi_{12})$ = origin of system 2 relative to 1, $r_{1_>} = \max\{r_2, r_{12}\}$, $r_{1_<} = \min\{r_2, r_{12}\}$ and where the coefficients $a(\ldots)$ are related to the Wigner 3-j symbols used in quantum mechanics.

Derivation of the modal Pritchard approximation begins with a description of a two-element array. Spheres have a common radius a, and velocities specified on spheres 1 and 2 are given by individual normal modes:

$$V_1 = \frac{i}{\omega\rho} \left.\frac{\partial p}{\partial r}\right|_{r_1=a} = V_{n_1}^{m_1} \Omega_{n_1}^{m_1}(\theta_1, \phi_1) \tag{8}$$

$$V_2 = \frac{i}{\omega\rho} \left.\frac{\partial p}{\partial r}\right|_{r_2=a} = V_{n_2}^{m_2} \Omega_{n_2}^{m_2}(\theta_2, \phi_2). \tag{9}$$

Letting

$$\overline{\Omega}_n^m = \Omega_n^m(\theta_{12}, \phi_{12})$$

and noting that

$$\Omega_n^m(\pi - \phi_{12}, \pi - \phi_{12}) = (-1)^{n+m} \overline{\Omega}_n^m,$$

the pressure from sphere 2 translated to sphere 1 coordinates (with $r_1 < r_{12}$) is given by:

$$p_2^1=\sum_{t_2=0}^{\infty}\sum_{s_2=-t_2}^{t_2}A_{s_2t_2}^2\Bigg\{\sum_{\nu_1=0}^{\infty}\sum_{\mu_1=-\nu_1}^{\nu_1}j_{\nu_1}(kr_1)\times\sum_{\substack{\sigma_1=|t_2-\nu_1|\\ \sigma_1\geqslant|s_2-\mu_1|}}^{t_2+\nu_1}{}'\ a(\nu_1,\sigma_1,t_2,\mu_1,s_2)\times h_{\sigma_1}(kd)\Omega_{\nu_1}^{\mu_1}(\theta_1,\phi_1)\overline{\Omega}_{\sigma_1}^{\sigma_2-\mu_1}\Bigg\}. \tag{10}$$

Similarly, the pressure from sphere 1 translated to sphere 2 coordinates is

$$p_1^2=\sum_{t_1=0}^{\infty}\sum_{s_1=-t_1}^{t_1}A_{s_1t_1}^1\Bigg\{\sum_{\nu_2=0}^{\infty}\sum_{\mu_2=-\nu_2}^{\nu_2}j_{\nu_2}(kr_2)\times\sum_{\substack{\sigma_2=|t_1-\nu_2|\\ \sigma_2\geqslant|s_1-\mu_2|}}^{t_1+\nu_2}{}'\ a(\nu_2,\sigma_2,t_1,\mu_2,s_1)h_{\sigma_2}(kd)\times\Omega_{\nu_2}^{\mu_2}(\theta_2,\phi_2)\overline{\Omega}_{\sigma_2}^{s_1-\mu_2}(-1)^{\sigma_2+s_1-\mu_2}\Bigg\}. \tag{11}$$

Upon application of the boundary conditions:

$$\frac{i}{\omega\rho}\frac{\partial}{\partial r}[p_1+p_2^1]|_{r_1=a}=V_{n_1}^{m_1}\Omega_{n_1}^{m_1}(\theta_1,\phi_1), \tag{12}$$

$$\frac{i}{\omega\rho}\frac{\partial}{\partial r}[p_2+p_1^2]|_{r_2=a}=V_{n_2}^{m_2}\Omega_{n_2}^{m_2}(\theta_2,\phi_2), \tag{13}$$

and formally applying normal modes with division by derivatives of Hankel functions applied at *ka* leads to the system of equations

$$\begin{aligned}\frac{-i\rho cV_{n_1}^{m_1}}{h_{n_1}'(ka)}\delta_{mm_1}\delta_{nn_1}&=A_{mn}^1\delta_{mm_1}\delta_{nn_1}+\frac{j_{n_1}'(ka)}{h_{h_1}'(ka)}\sum_{t_2=0}^{\infty}\sum_{s_2=-t_2}^{t_2}A_{s_2t_2}^2\times\Bigg[\sum_{\substack{\sigma_1=|t_2-n_1|\\ \sigma_1\geqslant|s_2-m_1|}}^{t_2+n_1}{}'\ a(n_1,\sigma_1,t_2,m_1,s_2)h_{\sigma_1}(kd)\overline{\Omega}_{\sigma_1}^{s_2-m_1}\Bigg]\\ &\times\frac{-i\rho cV_{n_2}^{m_2}}{h_{n_2}'(ka)}\delta_{mm_2}\delta_{nn_2}\\ &=A_{mn}^2\delta_{mm_2}\delta_{nn_2}+\frac{j_{n_2}'(ka)}{h_{n_2}'(ka)}\sum_{t_1=0}^{\infty}\sum_{s_1=-t_1}^{t_1}A_{s_1t_1}^1\times\Bigg[\sum_{\substack{\sigma_2=|t_1-n_2|\\ \sigma_2\geqslant|s_1-m_2|}}^{t_1+n_2}{}'\ a(n_2,\sigma_2,t_1,m_2,s_1)\times h_{\sigma_2}(kd)\overline{\Omega}_{\sigma_2}^{s_1-m_2}(-1)^{\sigma_2+s_1-m_2}\Bigg].\end{aligned}$$

(The δ_{ij} terms above are Kronecker delta functions which are one when $i=j$ and zero otherwise.)

Truncating the series, letting

$$B_{mn}^1=\frac{-i\rho cV_{n_1}^{m_1}}{h_{n_1}'(ka)}\delta_{mm_1}\delta_{nn_1},\quad B_{mn}^2=\frac{-i\rho cV_{n_2}^{m_2}}{h_{n_2}'(ka)}\delta_{mm_2}\delta_{nn_2}, \tag{14}$$

and rewriting these equations in matrix form (e.g., $\mathbf{A}^1=[A_{00}^1,A_{-11}^1,A_{10}^1,A_{11}^1,A_{-22}^1,\cdots]^T$)

$$\begin{bmatrix}I & K_{12}\\ K_{21} & I\end{bmatrix}\begin{bmatrix}\mathbf{A}^1\\ \mathbf{A}^2\end{bmatrix}=\begin{bmatrix}\mathbf{B}_1\\ \mathbf{B}^2\end{bmatrix}, \tag{15}$$

where the $[(s_1,t_1),(s_2,t_2)]$ entry of the K_{12} matrix is

$$K_{12}((s_1,t_1),(s_2,t_2))=\frac{j_{s_1}'(ka)}{h_{s_1}'(ka)}\sum_{\substack{\sigma_1=|t_2-t_1\\ \sigma_1\geqslant|s_2-s_1|}}^{t_2+t_1}{}'\ a(t_1,\sigma_1,t_2,s_1,s_2)h_{\sigma_1}(kd)\overline{\Omega}_{\sigma_1}^{s_2-s_1}, \tag{16}$$

and the $[(s_2,t_2),(s_1,t_1)]$ entry of the K_{21} is

$$K_{21}((s_2,t_2),(s_1,t_1))=\frac{j_{s_2}'(ka)}{h_{s_2}'(ka)}\sum_{\substack{\sigma_2=|t_1-t_2|\\ \sigma_2\geqslant|s_1-s_2|}}^{t_1+t_2}{}'\ a(t_2,\sigma_2,t_1,s_2,s_1)\times h_{\sigma_2}(kd)\overline{\Omega}_{\sigma_2}^{s_1-s_2}(-1)^{\sigma_2+s_1-s_2}. \tag{17}$$

Solution of the above matrix equation for the unknown amplitudes provides an ''exact'' answer to the array problem, and is equivalent to the solution found by employing the T-matrix formalism of Scandrett and Baker.[16]

For $ka\ll 1$ asymptotic forms for the ratio of the spherical Bessel functions are[17]

$$\frac{j_n'(ka)}{h_n'(ka)}\sim\begin{cases}O[(ka)^3] & \text{for } n=0 \text{ or } 1\\ O[(ka)^{2n+1}] & \text{for } n\geqslant 2\end{cases}\quad \text{as } ka\to 0. \tag{18}$$

Therefore the magnitude of the matrix entries K_{12} and K_{21} are of order $(ka)^3$, and an approximate inverse to the matrix can be found which is accurate to order $(ka)^6$

$$\begin{bmatrix}I & K_{12}\\ K_{21} & I\end{bmatrix}^{-1}=\left\{\begin{bmatrix}I & 0\\ 0 & I\end{bmatrix}+\begin{bmatrix}0 & K_{12}\\ K_{21} & 0\end{bmatrix}\right\}^{-1}=\begin{bmatrix}I & -K_{12}\\ -K_{21} & I\end{bmatrix}+O[(ka)^6] \tag{19}$$

and an explicit calculation for the unknown scattering amplitudes is possible:

$$\mathbf{A}^1\approx\mathbf{B}^1-K_{12}\mathbf{B}^2\ \text{ and }\ \mathbf{A}^2\approx\mathbf{B}^2-K_{21}\mathbf{B}^1.$$

To obtain the radiation impedance component on the (n_1,m_1) mode of sphere 1 given that sphere 2 is radiating in

the (n_2,m_2) mode, the pressure amplitudes are substituted into the radiation impedance integral formula, and all terms of order $(ka)^6$ or higher are neglected. One is left with the expression:

$$Z_{r_1}=\frac{-i\rho c}{V_{n_1}^{m_1}}\int\int_{s_1}\|\Omega_{n_1}^{m_1}(\theta_1,\phi_1)\|^2\,ds_1\Bigg\{\frac{h_{n_1}(ka)}{h'_{n_1}(ka)}V_{n_1}^{m_1}$$
$$-\delta_{n_10}\frac{j_{n_1}(ka)}{h'_{n_1}(ka)}V_{n_1}^{m_1}\Bigg[\frac{j'_0(ka)}{h'_0(ka)}[h_0(kd)]^2+3\cos(2\theta_{12})$$
$$\times\frac{j'_1(ka)}{h'_1(ka)}[h_1(kd)]^2\Bigg]\frac{-iH(4-n_1-n_2)}{(ka)^2h'_{n_1}(ka)h'_{n_2}(ka)}V_{n_2}^{m_2}$$
$$\times\sum_{\substack{\sigma=|n_2-n_1|\\ \sigma\geqslant|m_2-m_1|}}^{n_2+n_1\prime}a(n_1,\sigma,n_2,m_1,m_2)$$
$$\times h_\sigma(kd)\bar{\Omega}_\sigma^{m_2-m_1}\Bigg\}+O[(ka)^6],\tag{20}$$

where $H(4-n_1-n_2)$ is a Heaviside function which is zero for $n_1+n_2\geqslant 4$ and equals one otherwise.

The middle term in the above expression is the sole contribution to scattering from one sphere to the other, and is present only when one of the spheres is radiating with a nonzero amplitude in the monopole mode (at least to $O[(ka)^6]$). The two parts of this term result from monopole and dipole backscatter from sphere 2 which affect the amplitude of the *scattered* monopole pressure amplitude on sphere 1. The backscatter terms are to leading order $(ka)^5$, and if neglected, one obtains an approximation for the radiation impedance to $O[(ka)^5]$ which completely neglects all scattering effects, and is consistent with using the free-field radiation impedance for the self-radiation impedance, as outlined in the previous section:

$$Z_{r_1}\approx\frac{-i\rho c}{V_{n_1}^{m_1}}\int\int_{s_1}\|\Omega_{n_1}^{m_1}(\theta_1,\phi_1)\|^2\,ds_1$$
$$\times\Bigg\{\frac{h_{n_1}(ka)}{h'_{n_1}(ka)}V_{n_1}^{m_1}\frac{-iH(3-n_1-n_2)}{(ka)^2h'_{n_1}(ka)h'_{n_2}(ka)}V_{n_2}^{m_2}$$
$$\times\sum_{\substack{\sigma=|n_2-n_1|\\ \sigma\geqslant|m_2-m_1|}}^{n_2+n_1\prime}a(n_1,\sigma,n_2,m_1,m_2)h_\sigma(kd)\bar{\Omega}_\sigma^{m_2-m_1}\Bigg\}.\tag{21}$$

The first term which is multiplied by $V_{n_1}^{m_1}$ is the self-radiation impedance

$$Z_{11}\approx-i\rho c\int\int_{s_1}\|\Omega_{n_1}^{m_1}(\theta_1,\phi_1)\|^2\,ds_1\frac{h_{n_1}(ka)}{h'_{n_1}(ka)}\tag{22}$$

and equals the free-field radiation impedance of sphere 1. The summation term multiplying $V_{n_2}^{m_2}$ is the mutual radiation impedance of sphere 2 on sphere 1, and can be thought of as an approximation to the *translation* of the *radiated pressure* from sphere 2 onto sphere 1:

$$Z_{12(n_2,m_2)\to(n_1,m_1)}$$
$$\approx-i\rho c\int\int_{s_1}\|\Omega_{n_1}^{m_1}(\theta_1,\phi_1)\|^2\,ds_1\frac{-iH(3-n_1-n_2)}{(ka)^2h'_{n_1}(ka)h'_{n_2}(ka)}$$
$$\times\sum_{\substack{\sigma=|n_2-n_1|\\ \sigma\geqslant|m_2-m_1|}}^{n_2+n_1\prime}a(n_1,\sigma,n_2,m_1,m_2)h_\sigma(kd)\bar{\Omega}_\sigma^{m_2-m_1}.\tag{23}$$

The matrix form for the non-neglected terms in the modal Pritchard approximation to the mutual radiation impedance is:

$$\begin{bmatrix}
Z_{(00)(00)} & Z_{(00)(1-1)} & Z_{(00)(10)} & Z_{(00)(11)} & Z_{(00)(2-2)} & Z_{(00)(2-1)} & Z_{(00)(20)} & Z_{(00)(21)} & Z_{(00)(22)} & 0 & \cdots\\
Z_{(1-1)(00)} & Z_{(1-1)(1-1)} & Z_{(1-1)(10)} & Z_{(1-1)(11)} & 0 & 0 & 0 & 0 & 0 & 0 & \cdots\\
Z_{(10)(00)} & Z_{(10)(1-1)} & Z_{(10)(10)} & Z_{(10)(11)} & 0 & 0 & 0 & 0 & 0 & 0 & \cdots\\
Z_{(11)(00)} & Z_{(11)(1-1)} & Z_{(11)(10)} & Z_{(11)(11)} & 0 & 0 & 0 & 0 & 0 & 0 & \cdots\\
Z_{(2-2)(00)} & 0 & 0 & 0 & 0 & 0 & 0 & 0 & 0 & 0 & \cdots\\
Z_{(2-1)(00)} & 0 & 0 & 0 & 0 & 0 & 0 & 0 & 0 & 0 & \cdots\\
Z_{(20)(00)} & 0 & 0 & 0 & 0 & 0 & 0 & 0 & 0 & 0 & \cdots\\
Z_{(21)(00)} & 0 & 0 & 0 & 0 & 0 & 0 & 0 & 0 & 0 & \cdots\\
Z_{(22)(00)} & 0 & 0 & 0 & 0 & 0 & 0 & 0 & 0 & 0 & \cdots\\
0 & 0 & 0 & 0 & 0 & 0 & 0 & 0 & 0 & 0 & \cdots\\
\vdots & \vdots & \vdots & \vdots & \vdots & \vdots & \vdots & \vdots & \vdots & \vdots & \ddots
\end{bmatrix}.$$

It is interesting to compare the real part of the self-impedance to the amplitude of the mutual impedance in the special case that both spheres are radiating identically ($\mathbf{B}^1=\mathbf{B}^2$ or $n_1=n_2=n$ and $m_1=m_2=m$). In this case, the real part of $Z_{11}=R_{11}$ becomes

$$R_{11}\approx\rho c\int_{s_1}\int\|\Omega_{n_1}^{m_1}(\theta_1,\phi_1)\|^2\,ds_1\,\mathrm{Im}\left\{\frac{h_{n_1}(ka)}{h'_{n_1}(ka)}\right\}$$

$$=-\rho c\int_{s_1}\int\|\Omega_{n_1}^{m_1}(\theta_1,\phi_1)\|^2\,ds_1\frac{1}{(ka)^2\|h'_{n_1}(ka)\|^2}$$

$$\approx\frac{(ka)^{2n+2}}{[(n+1)(1)(3)\cdots(2n-1)]^2}\rho c\times\int_{s_1}\int\|\Omega_{n_1}^{m_1}(\theta_1,\phi_1)\|^2\,ds_1, \tag{24}$$

while Z_{12} has the asymptotic form

$$Z_{12}\approx\frac{(ka)^{2n+2}}{[(n+1)(1)(3)\cdots(2n-1)]^2}\rho c\times\int_{s_1}\int\|\Omega_{n_1}^{m_1}(\theta_1,\phi_1)\|^2\,ds_1 H(3-2n)\times\sum_{\sigma=0}^{2n}{}'\ a(n,\sigma,n,m,m)h_\sigma(kd)\overline{\Omega}_\sigma^0. \tag{25}$$

When only the first term in the series for Z_{12} [the $\sigma=0$ case which results in an $h_0(kd)$ term] is kept, the ''standard'' Pritchard approximation results. In this instance note that $a(n,0,n,m,m)=1$ for all $n\geqslant 0$ and $-n\leqslant m\leqslant n$. The remaining terms in the series have an angular dependence which affects the amplitude of Z_{12} as the relative angles between array elements vary. Such an angular dependence is *not* built into the standard Pritchard approximation—only the relative *distance* between elements as expressed by the factor $h_0(kd)$ is present.

IV. RESULTS

A. Two-body interactions

In this section several graphs will be displayed in an effort to demonstrate the modal Pritchard approximation given above. The first set of numerical experiments involves the New and Eisler problem of an array of two, identical, acoustically hard spheres separated by a distance d. Each sphere has radius $a=1/2$, and is assigned a modal velocity in such a way that the mutual radiation impedance can be found.

Besides the modal Pritchard method, there are two other approximations displayed. The results labeled ''Pritchard's method'' and ''Simplified Pritchard'' are found as follows. For the ''Pritchard method,'' an ''exact'' value for R_{11}, which includes all backscattering, is used in the approximation, while the ''simplified Pritchard'' employs only the *free-field* values of the self-radiation resistance term R_{11}, and therefore neglects backscatter.

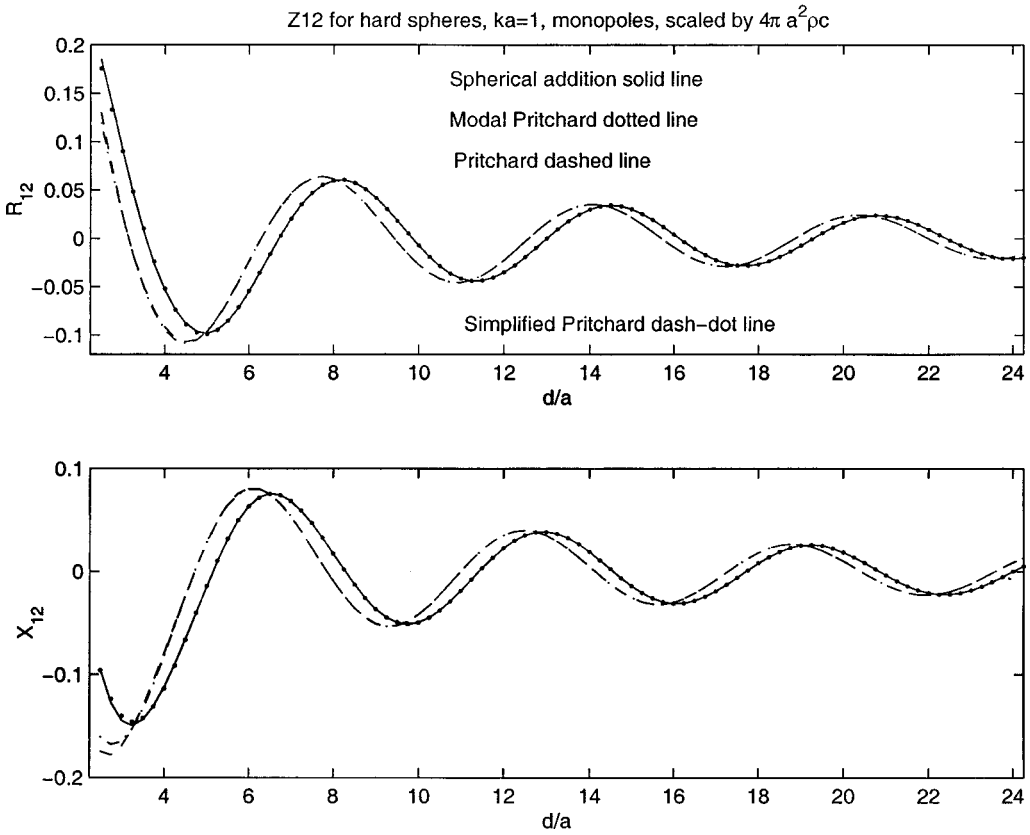

FIG. 1. Monopole-to-monopole two-body interaction.

The first series of graphs display the monopole-to-monopole (Fig. 1), axially symmetric dipole-to-dipole (Fig. 2), and axially symmetric quadrupole-to-quadrupole (Fig. 3), mutual radiation impedances for the two spheres which are aligned with the z axis. The final graph of quadrupole-to-quadrupole is included only to show the accuracy of the modal Pritchard approximation even through the quadrupole term, in spite of the fact that this term is of order $(ka)^6$ in the expansion for small ka of the mutual radiation impedance and therefore would be neglected in an application of the derived modal Pritchard approximation.

It would appear from Fig. 1 that backscattering effects in the R_{11} determination are negligible by comparing results of the ''simplified Pritchard'' and ''Pritchard'' methods. Additionally, the ''modal Pritchard'' curve seems to very closely match the ''exact'' spherical addition formula curve which includes all scattering effects. The results of the monopole-to-monopole mutual radiation impedance highlight what appears to be a phase shift between the ''modal'' and ''simplified'' Pritchard methods. A comparison between the Pritchard approximation and the exact solution can be analytically performed by comparing the simplified Pritchard formula with the modal Pritchard formula. The formulas for the modal and simplified Pritchard approximations (scaled by $4\pi a^2\rho c$) as a function of the distance between spheres (d) follow.

Modal Pritchard monopole to monopole:

$$Z_{(00)(00)}=h_0(kd)\frac{-1}{[kah_0'(ka)]^2},$$

Simplified Pritchard monopole to monopole:

$$Z_{(00)(00)}=h_0(kd)\mathrm{Re}\left[\frac{-ih_0(ka)}{h_0'(ka)}\right].$$

Taking the ratio of these two expressions, one has

$$\frac{h_0(kd)\dfrac{-1}{[kah_0'(ka)]^2}}{h_0(kd)\mathrm{Re}\left[\dfrac{-ih_0(ka)}{h_0'(ka)}\right]}=-\frac{j_0'(ka)+iy_0'(ka)}{j_0'(ka)-iy_0'(ka)}$$

$$\approx 1+\frac{2i}{3}(ka)^3 \quad \text{as} \quad ka\to 0.$$

One can also see from the above expression that the amplitude of the ratio is one with a constant phase shift. When $ka=1$, this phase shift is about 24.6 deg, which is what is seen in the monopole-to-monopole figure above.

For the dipole-to-dipole case (Fig. 2), the relative position of the spheres introduces an angular dependence in the mutual radiation impedance predicted by the modal Pritchard approximation which is not present in the simplified Pritchard approximation. As in the monopole-to-monopole case, one finds that the simplified Pritchard approximation is essentially equivalent to the Pritchard method which accounts for backscattering, but to compare with the exact and/or modal Pritchard approximation, the results must be magnified by a factor of 3. To see where the factor of 3 comes from, one can again compare the (scaled) modal and simplified Pritchard approximations

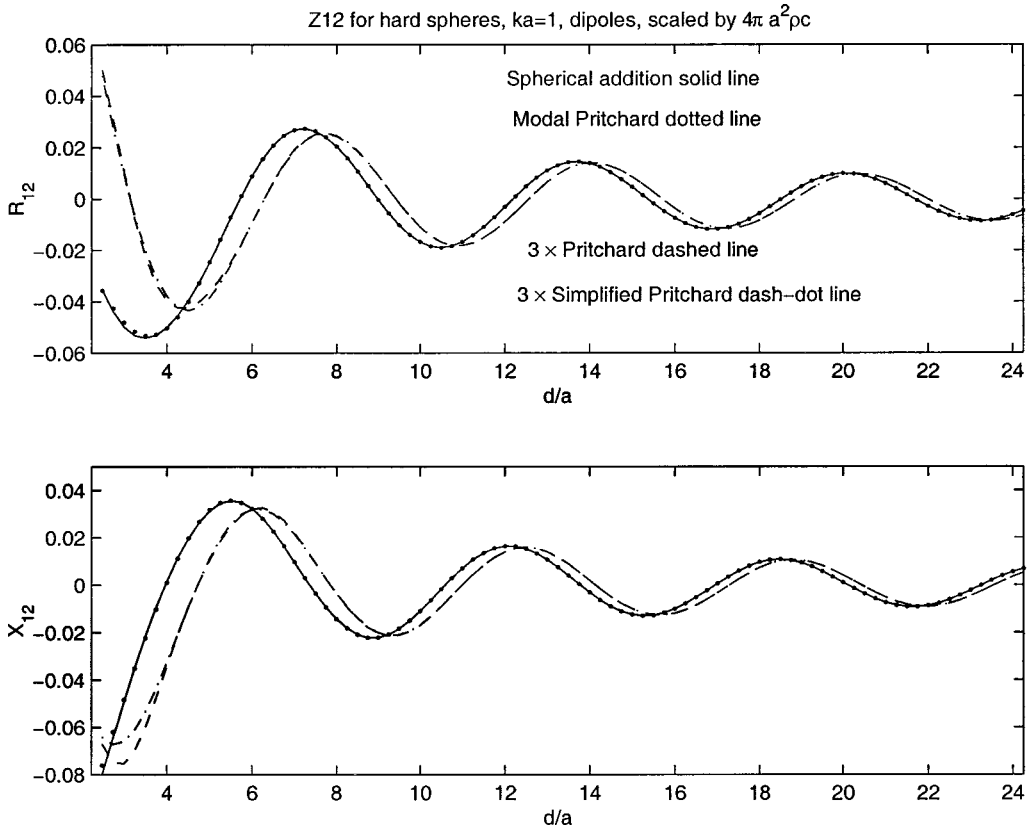

FIG. 2. Dipole-to-dipole two-body interaction.

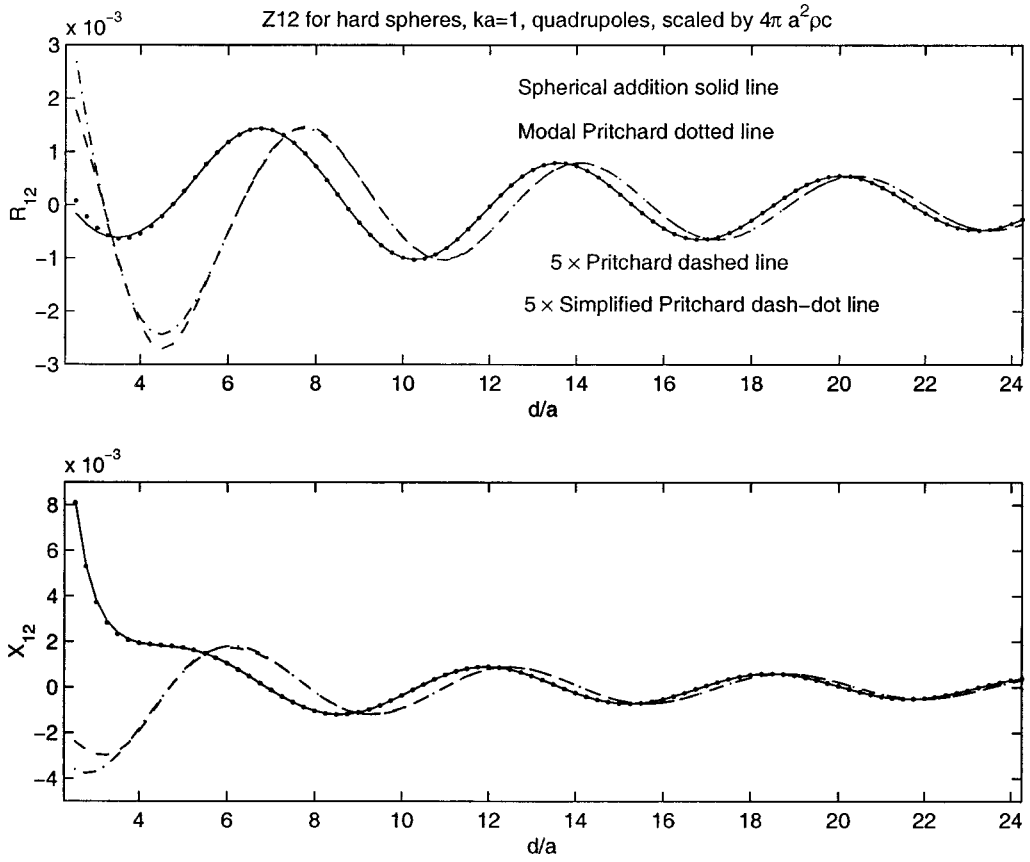

FIG. 3. Quadrupole-to-quadrupole two-body interaction.

Model Pritchard dipole to dipole:

$$Z_{(10)(10)}=\frac{-1}{3[kah_1'(ka)]^2}\{h_0(kd)-2h_2(kd)\times\Omega_2^0(\theta_{12},\phi_{12})\},$$

Simplified Pritchard dipole to dipole:

$$Z_{(10)(10)}=\frac{h_0(kd)}{3}\mathrm{Re}\left[\frac{-ih_1(ka)}{h_1'(ka)}\right].$$

If one assumes $kd\gg 1$, the approximation $h_2(kd)\approx -h_0(kd)$ can be made, and with the fact that $\Omega_2^0(\theta_{12})=[1+3\cos(2\theta_{12})]/4$, the ratio of the two expressions can be written:

$$\frac{h_0(kd)-\dfrac{3[1+\cos(2\theta_{12})]/2}{[kah_1'(ka)]^2}}{h_0(kd)\mathrm{Re}\left[\dfrac{-ih_1(ka)}{h_1'(ka)}\right]}$$

$$=-\frac{3[1+\cos(2\theta_{12})]}{2}\left\{\frac{j_1'(ka)+iy_1'(ka)}{j_1'(ka)-iy_1'(ka)}\right\}$$

$$\approx\frac{3[1+\cos(2\theta_{12})]}{2}+O[(ka)^3]\quad\text{as}\quad ka\to 0.$$

In addition to the phase shift embodied by the ratio of the spherical Hankel functions, one sees an amplitude variation with respect to the angle θ_{12} between the spheres (in this instance, the axis of the dipole aligns with the z axis from which the angle θ_{12} is measured). For the geometry considered in the graph, the angle $\theta_{12}=0$, leading to a factor of 3 needed to bring the Pritchard approximation in accord with the analytic solution. The amplitude and phase shift are unfortunately not the only differences between the solutions. For small distances d the approximation used for $h_2(kd)$ is no longer valid, and this can be readily seen in the graph of the dipole-to-dipole mutual radiation for small values of d/a.

Figure 3 shows the axially symmetric quadrupole-to-quadrupole mutual radiation impedances of the various Pritchard approximations along with the spherical addition result. The modal Pritchard result would actually be zero if we neglected all terms of order ka^5 since quadrupole-to-quadrupole radiation is of higher order. This graph is only included to show the continued success of the approximation embodied by the formula derived in the previous section for Z_{12}. Note also that the magnitude of these quadrupole impedances are an order of magnitude less significant than the dipole terms.

B. Three-body interactions

One might hope that the modal Pritchard method works well even for situations in which there are more than two elements in a given array. This would indeed be true if ''third party'' scattering were negligible. Third party is meant to imply single or multiple scattering of an incident pressure from one array element to another (thereby affecting the mutual radiation impedance between the two), by way of scattering from a third obstacle or array element. This is an

important effect when considering closely packed arrays of transducers. If one considers only two-element arrays in the production of mutual radiation impedances between array elements, such scattering effects are necessarily neglected.

The most elementary, and perhaps most enlightening, cases to consider are three-element arrays, in which one of the elements acts solely as an acoustically hard obstacle, and is moved around relative to the remaining two, which are fixed. For such an array, one can anticipate the negligible effects of the third array element when it is far from the two active elements, and one can quantify the effect it has on the mutual radiation impedance when it is moved to the near field. Because the two active array elements are fixed in space, the modal Pritchard approximation (and for that matter all of the Pritchard approximations), produce constant mutual radiation impedances between the two elements, regardless of the positioning of the third. Because of its accuracy in the two-element array problem, only the modal Pritchard approximation will be compared with the spherical addition results to see how important third party scattering is in the determination of mutual radiation impedances.

In the first test case, the two active array elements (numbered elements 1 and 3) are aligned to the z axis, and are at a constant center-to-center distance of $\lambda/2$, which for $ka=1$ implies a separation of $\pi/2$. The third element (element number 2) of the array starts at a distance of $\lambda/4$ away from the axis of the array, halfway between the two active array elements. It then moves axially away from the two active array elements. Figure 4 plots the comparison of the monopole-to-monopole mutual radiation impedance of sphere 3 on sphere 1.

Notice that there is a sizeable difference in the resistance and reactance terms of the mutual radiation impedance when sphere number 2 is in close proximity to the radiating spheres. In fact, in the third graph of the above series, the relative error of the *magnitude* of the mutual radiation impedance

$$\text{percent error} = 100 \times \frac{\|Z_{13}\|_{\text{modal Pritchard}} - \|Z_{13}\|_{\text{spherical addition}}}{|Z_{13}\|_{\text{spherical addition}}}$$

shows relative errors as great as 15%.

The deviations of the mutual radiation impedance amplitudes can be explained by a relatively simple argument (see Fig. 5). Depending on the total distance from sphere 3 to 2 to 1, the scattered pressure is either in phase (when Z_{13} is at a maximum), or out of phase, with the direct pressure from sphere 3 to sphere 1. This occurs when the total scattered distance from sphere 3 to 2 to 1 is an integral multiple of the acoustic wavelength. This may seem counterintuitive since the scattering sphere is acoustically hard, but can be explained by a simple argument involving monopole radiators and the spherical addition formula. Considering only the monopole terms, the sum of the directly incident and once scattered monopole pressures is given by the formula

$$Aj_0(ka)\left\{h_0(kd_{13}) - \frac{j_{0'}(ka)}{h_{0'}(ka)}[h_0(kd_{12})]^2\right\},$$

where d_{13} is the distance between spheres 1 and 3, d_{12} is the distance between spheres 1 and 2 (and also the distance between spheres 2 and 3), and A is the amplitude of the monopole pressure radiated from sphere 3. The value of d_{12} can be represented in terms of sphere 2's distance from the z axis (D) by $d_{12}=\sqrt{(\lambda/4)^2+D^2}$. In the figure above, the amplitude of the above factor for $A=1$ is produced, and to a large degree explains the variation seen in the amplitude of the mutual radiation impedance term (Z_{13}) found in Fig. 5.

A second three-element array is also considered, in which the active elements are the same as before, but in which the scattering element moves in an elliptical path around the two active elements in such a way that the two active elements are the foci of the ellipse. In this case, the scattering distance from sphere 3 to 2 to 1 has the constant value $3\lambda/2$. In terms of the preceding three-body graph, the point which would intersect the elliptical path occurs when $D/a \approx 4.44$, or when the relative error in Z_{13} is at its maximum value (corresponding to the Pritchard approximation being greater than the spherical addition result). Figure 6 graphs the resistance and reactance as well as the relative error in the amplitude of Z_{13} for angles 0 to 180 deg. At 0 deg, the center values for spheres 1, 2, and 3 are, respectively, 0, λ, and $\lambda/2$, while at 180 deg, the z values of these spheres is 0, $-\lambda/2$, and $\lambda/2$.

In this instance the variation due to scattering is nearly uniform, with maximum deviations occurring at the poles and perpendicular to the ''active'' array axis. Unlike the previous three-body case, monopole scattering alone does not explain the variation of the amplitude of Z_{13}. Figure 7 shows the result of limiting the number of terms retained in the spherical addition formulation to monopole only, monopole and dipole only, and monopole, dipole, and quadrupole terms. The graph illustrates that the monopole-to-dipole back-to-monopole scattering is the primary reason for the deviations seen in the amplitude of the Z_{13} term (the monopole-monopole-monopole and monopole-quadrupole-monopole terms are nearly constant throughout the range of angles). Note also that the result of keeping only through the quadrupole terms very nearly matches the result of keeping harmonics up through order 6.

C. Double line array of hard spheres

As a final example, consider a double line array of hard spheres which are spaced $\lambda/2$ apart along the lines, and which has the spacing $\lambda/4$ between the two lines. The double line of spheres is parallel with the z axis. Figure 8 is a graphic of the array, with the numbering of the spheres starting at the bottom left, and ending with the sixteenth element at the top right.

In Fig. 9, the source level (in dB) of the array given that each sphere is oscillating in a breathing mode with surface velocity one is shown. The spherical addition result is compared to the modal Pritchard calculation, and as can be seen, the modal Pritchard approximation does quite well, with a maximum error of about 2 dB at broadside. The far field results are scaled by the far field amplitude of a single oscil-

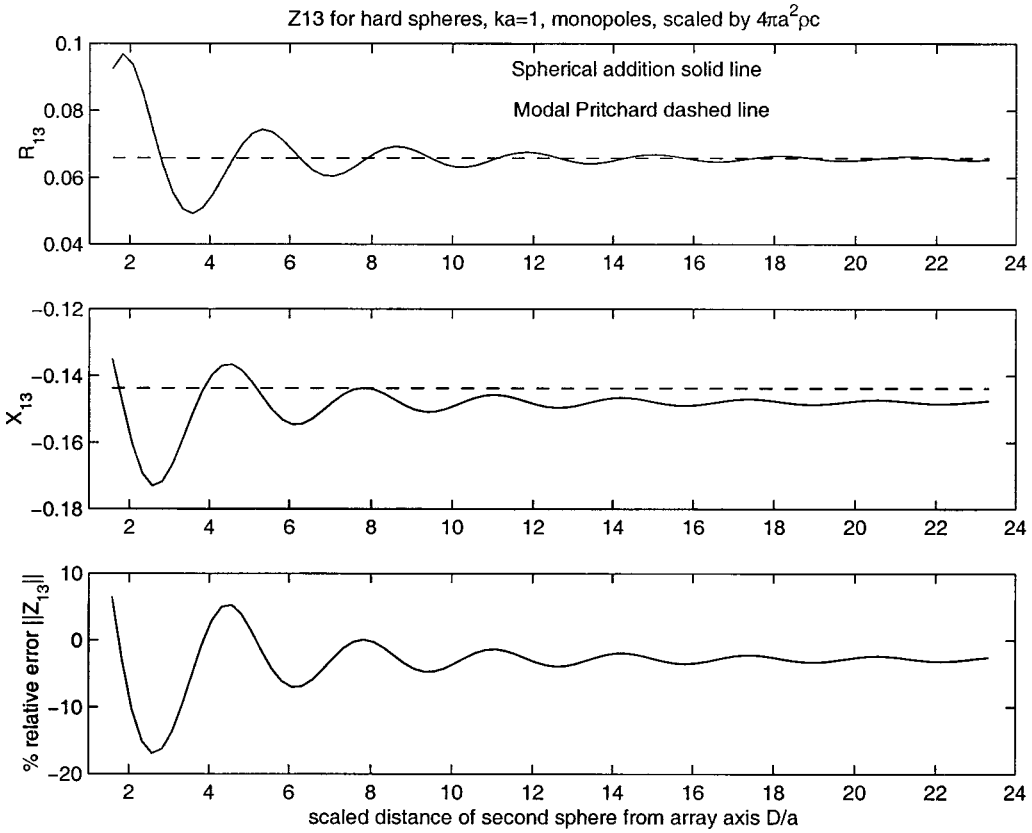

FIG. 4. Monopole-to-monopole three-body interaction. Normal distance of one sphere from the center point of the remaining two spheres varies.

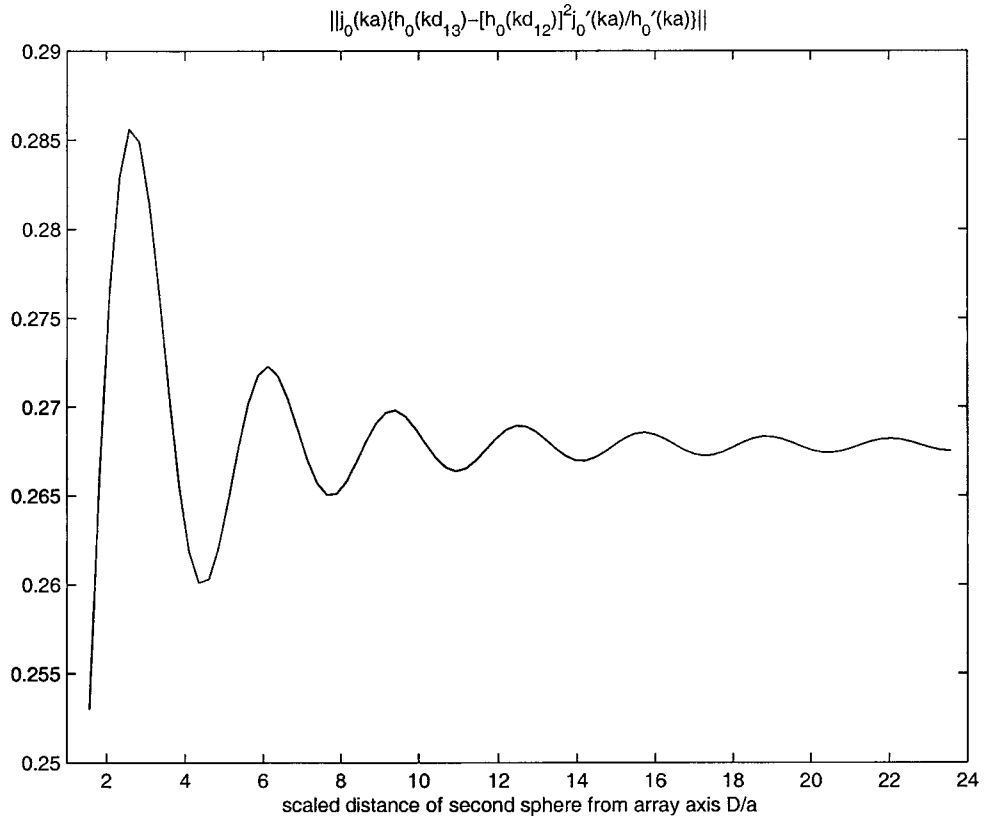

FIG. 5. Variation of the mutual radiation impedance for the three-body problem. Array geometry is the same as for Fig. 4.

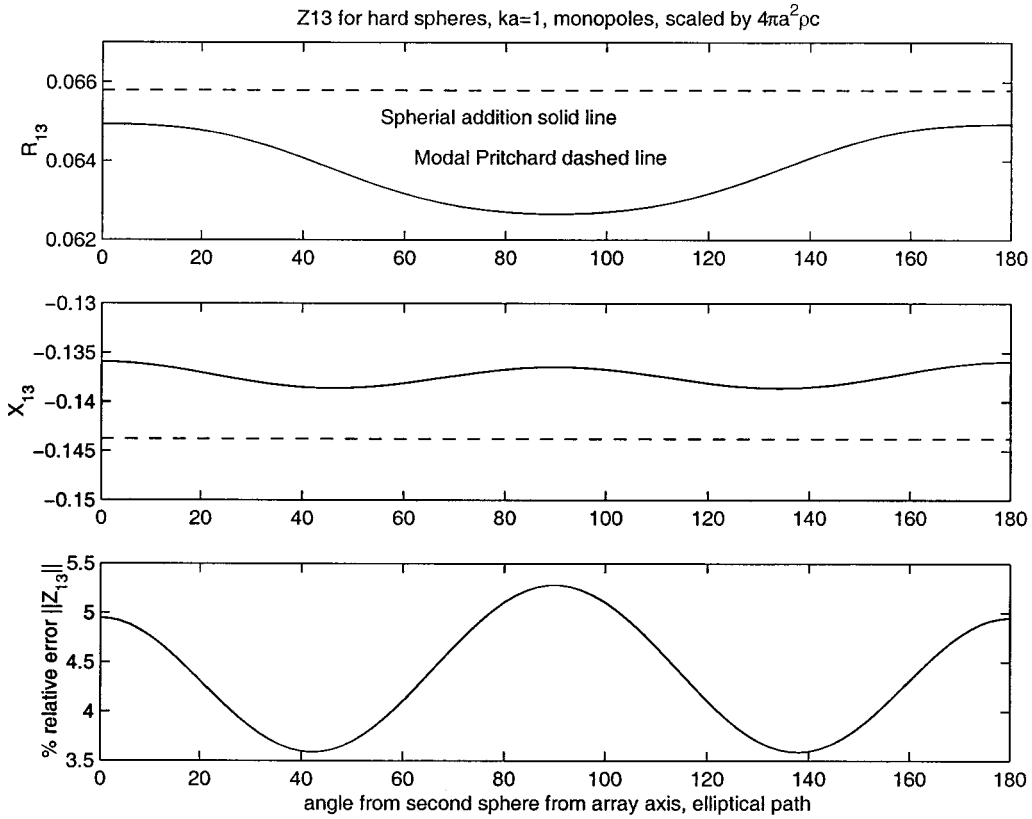

FIG. 6. Monopole-to-monopole three-body interaction. Distance of one sphere from the center point of the remaining two spheres remains constant as the position varies.

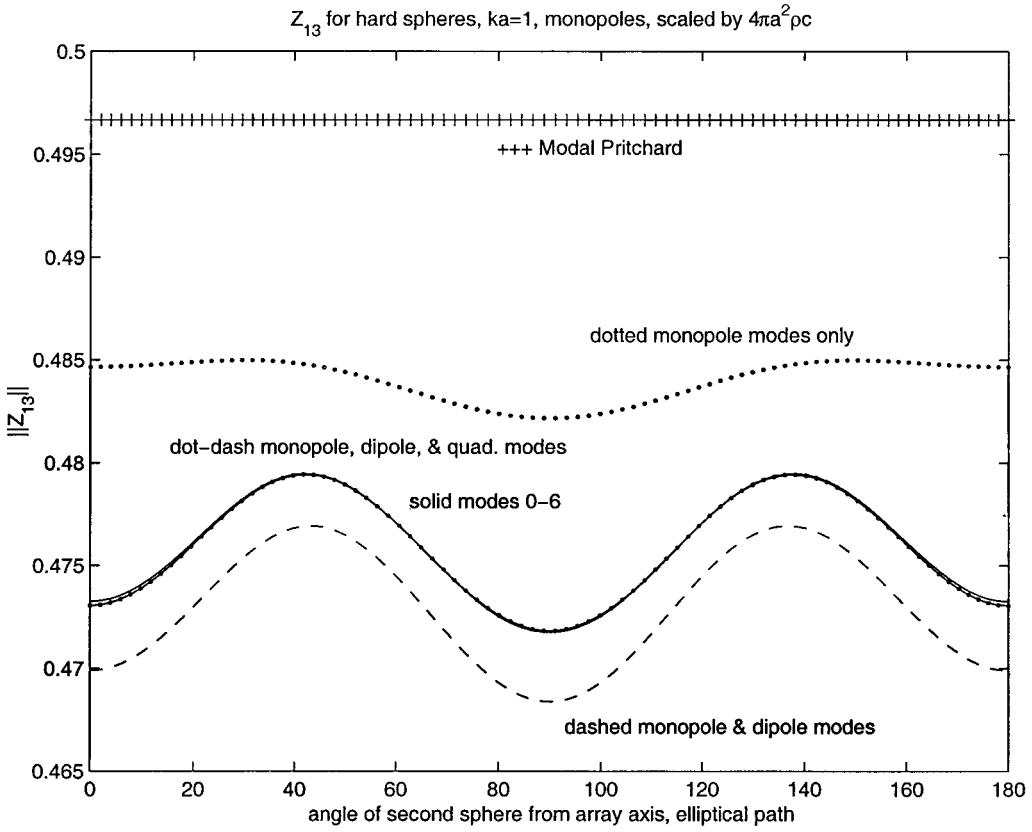

FIG. 7. The geometry is the same as Fig. 6. The varies number of harmonics kept in the mutual radiation impedance.

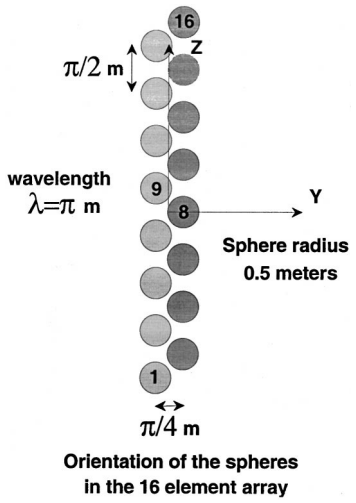

FIG. 8. Double line array geometry.

lating sphere. Figure 10 shows the magnitude of the far field pressure, scaled by that of a single radiating sphere.

It is possible for this array to compare the self- and mutual radiation impedances for the monopole terms without too much difficulty. In Figs. 11 and 12, the self-radiation impedance of each of the array elements is given, using both the modal Pritchard approximation and the full spherical addition results. Recall that the modal Pritchard approximation result neglects third party scattering *and* backscattering. In the first graph of the self-radiation impedance (Fig. 11) one can see that there is nearly a uniform 15% relative error for all but the spheres found at the extremities of the array. The reason for the variation from the modal Pritchard curve is because of backscatter not being taken into account, and that, at array elements 1 and 16, the backscatter is less than that for any of the remaining array elements. The second graph (Fig. 12) shows, on an element-by-element basis, the total mutual radiation on each sphere due to the radiation of pressure from all other array elements. Essentially, it is the sum of the off-diagonal elements in the monopole impedance matrix of the array in any given row, e.g., for array element i, this value is essentially

$$p_{\mathrm{rad}}^{\mathrm{mutual}} = \sum_{j=1, j\neq i}^{16} Z_{ij}$$

since all array elements have identical (monopole excited) velocities of one.

V. CONCLUSIONS AND RECOMMENDATIONS

Results presented would indicate that improvements can be made to existing methodology in array modeling. In particular, for low frequency active array calculations with close array spacing, it would appear that the spherical addition formula should be used to incorporate inter-element scattering. It would appear, however, that the number of harmonics needed is only through the quadrupole term for accuracy up to a level of $(ka)^6$, and so if a T-matrix algorithm is adopted, a total of 81 matrix elements should properly characterize the array problem.

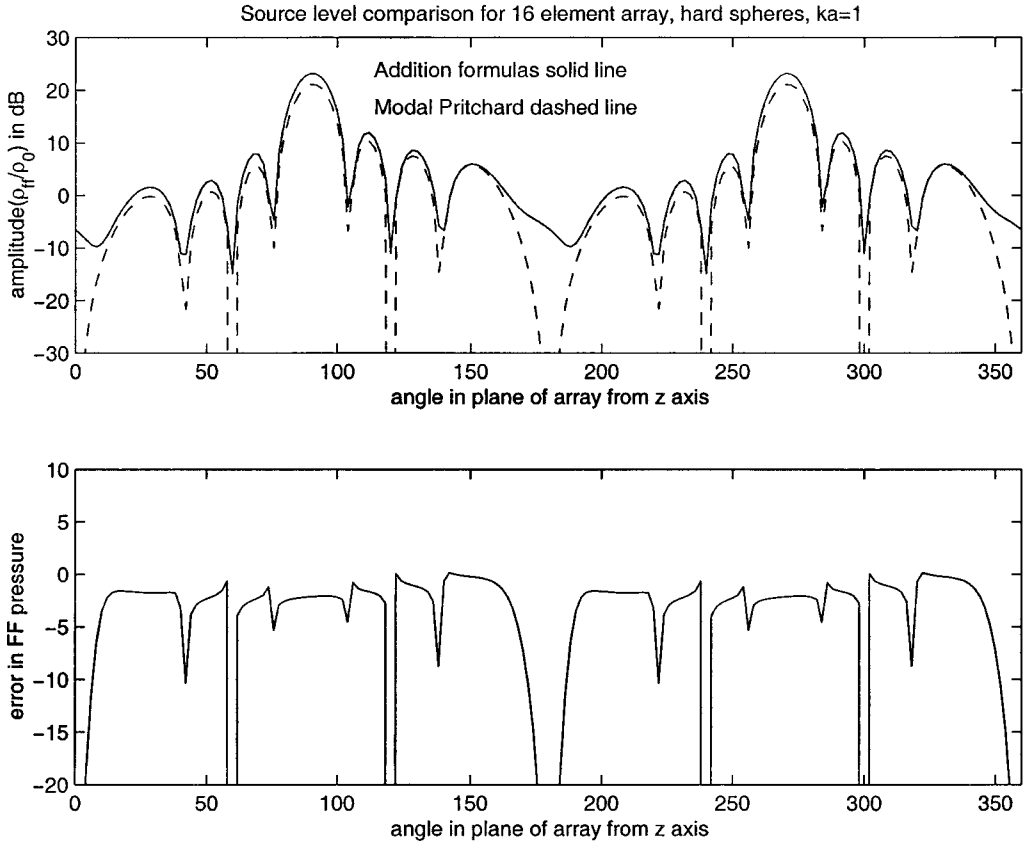

FIG. 9. Double line array source level in dB.

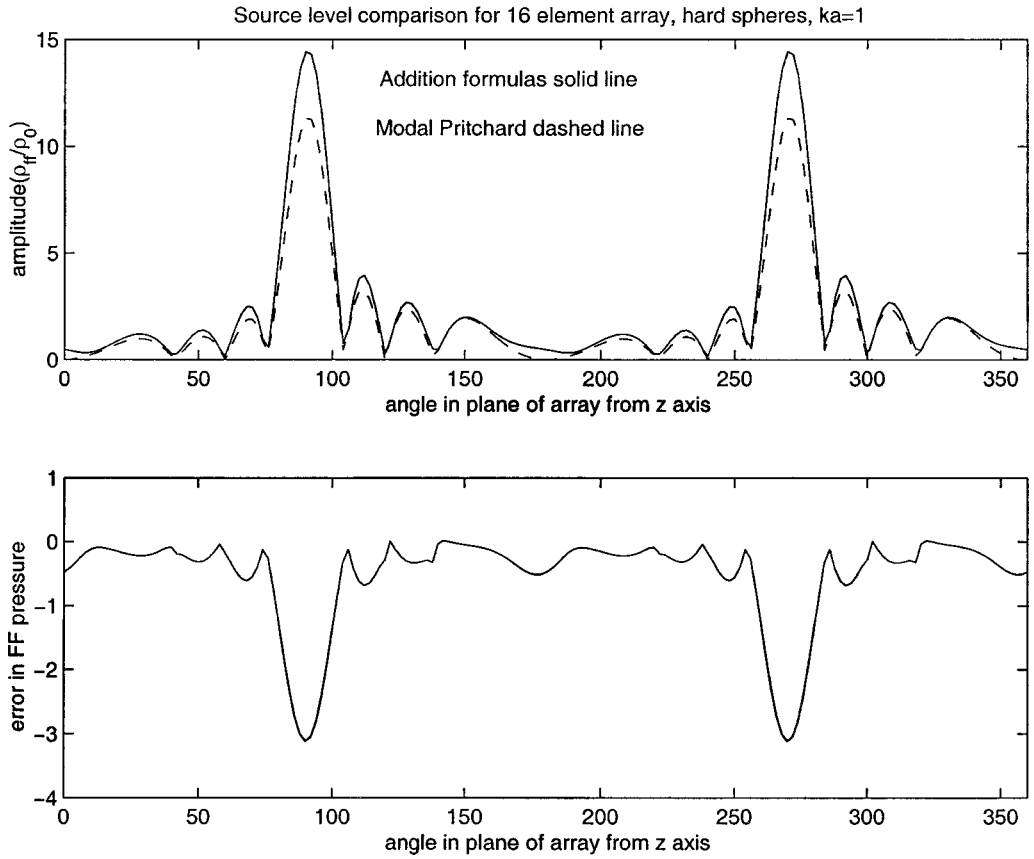

FIG. 10. Double line array source level scaled by a single radiating sphere.

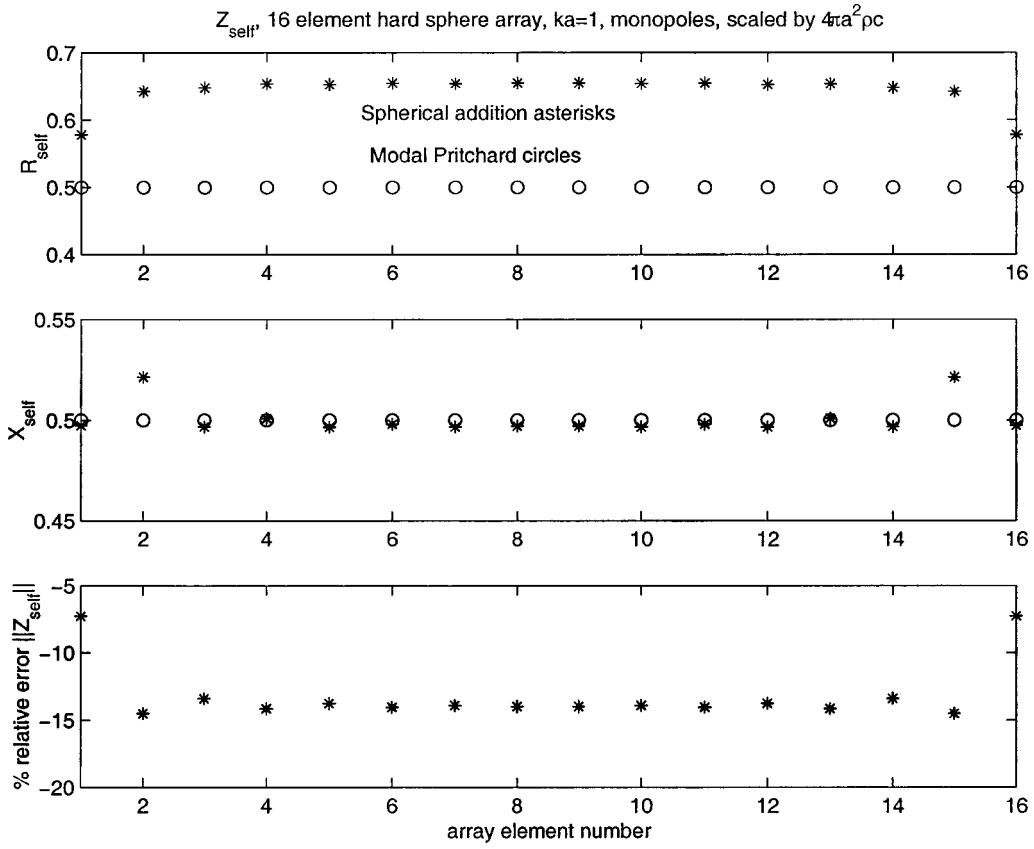

FIG. 11. Double line array. Element by element self-radiation.

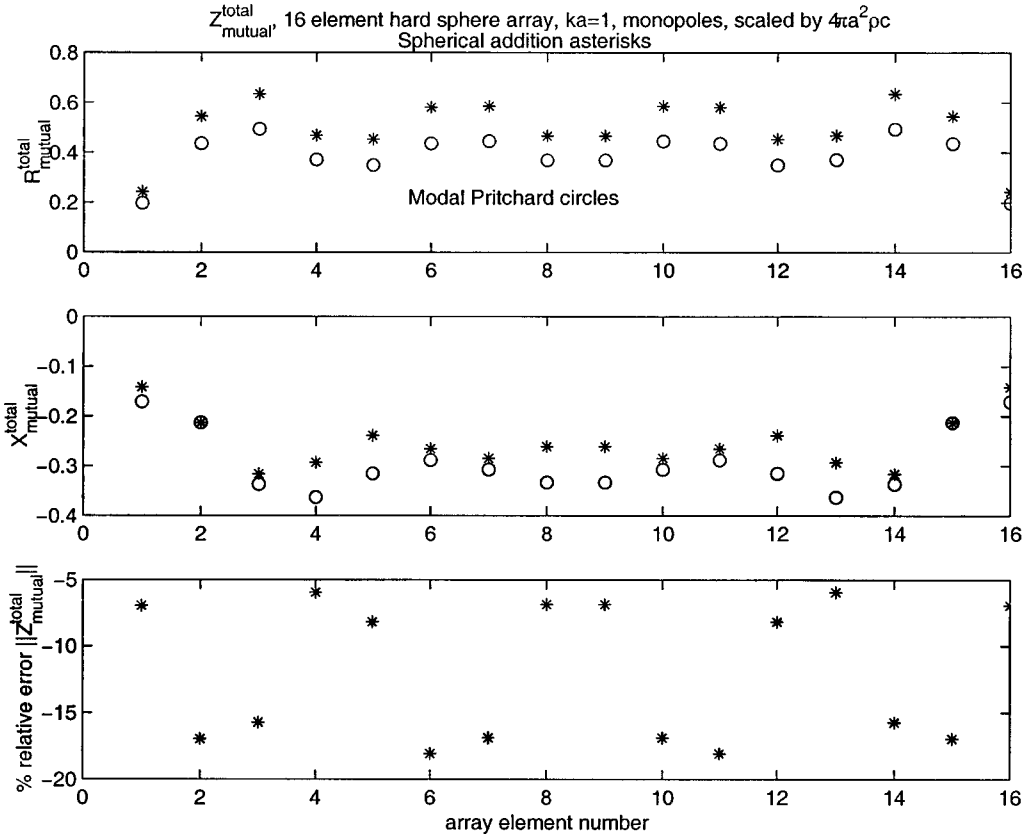

FIG. 12. Double line array. Element-by-element *total* mutual radiation.

Great accuracy has been achieved by using a Pritchard approximation to model the mutual radiation impedance between array elements for several of the reasons discussed. Improvement would seem to be possible, however, by adopting a modal-type Pritchard approximation. There are still limitations to the methodology, however, which should be addressed in an actual application, such as the need to model third party scattering. The manner in which such a modal approximation might be incorporated into a finite element code is as follows.

The finite element code must be used to determine the self-radiation impedance of a given array element. Almost any boundary element code would do, for example, EQI or CHIEF, but it must couple to the finite element code of the array element. Given nodal values of the normal surface velocity $(\mathbf{V}_j)$ (or $i\omega\times$the normal surface displacement), and the free-field self-impedance radiation matrix, the *nodal* pressure vector $(\mathbf{P}_j)$ on the jth array element is given by

$$(\mathbf{P}_j)_{\text{nodal}} = Z_{jj}\mathbf{V}_j . \tag{26}$$

The nodal pressure values must be converted to modal pressure amplitudes which can be used by the spherical addition formula for translations to other array elements. First introduce an intermediate matrix (A) of spherical Hankel/spherical harmonic functions evaluated at the surface nodes of the jth array element (r_s, θ_s, and ϕ_s)

$$A_{s,(n,m)} = h_n^{(2)}(kr_s)\Omega_n^m(\theta_s,\phi_s). \tag{27}$$

The size of this matrix is $M\times K$ where M is the number of surface nodes, and K is the number of harmonics (9 if only harmonics through the quadrupole term are used). The equation to be solved is

$$(\mathbf{P})_{\text{nodes}} = A(\mathbf{P})_{\text{modes}} . \tag{28}$$

The least squares solution to this problem is found by solving the normal equations, resulting in

$$(\mathbf{P})_{\text{modes}} = \underbrace{(A^H A)^{-1}A^H}_{C}(\mathbf{P})_{\text{nodes}} , \tag{29}$$

where A^H is the Hermitian conjugate of A, and C is the sought after translation matrix from nodal pressures to modal pressures.

Now with the modal radiated pressures, the addition formula can be used to determine the nodal pressures resulting from the modal radiated pressures through an application of a truncated spherical addition formula. The translation from array element j to array element i's nodal coordinates r_t, θ_t, and ϕ_t is given by

$$(\mathbf{P}_i)_t^{\text{nodal}} = \left\{ \sum_{l_1,m_1}^{K} (\mathbf{P}_j)_{l_1,m_1}^{\text{modal}} \sum_{l_2,m_2}^{K} H(3-l_1-l_2) j_{l_2}(kr_t) \right.$$
$$\times \Omega_{l_2}^{m_2}(\theta_t,\phi_t) \sum_{\substack{\sigma=|l_2-l_1| \\ \sigma\geqslant|m_2-m_1|}}^{l_2+l_1}{}' a(l_1,\sigma,l_2,m_1,m_2)$$
$$\left. \times h_\sigma(kd)\overline{\Omega}_\sigma^{m_2-m_1} \right\}, \tag{30}$$

where d is the distance between the ith and jth array element, and $H(\,)$ is the Heaviside function. Introducing the

matrix G which is $M \times K$ (assuming the ith array element also has M surface nodes) it is given by

$$G_{t,(l_1,m_1)} = \sum_{l_2,m_2}^{K} H(3-l_1-l_2) j_{l_2}(kr_t) \Omega_{l_2}^{m_2}(\theta_t,\phi_t) \times \sum_{\substack{\sigma=|l_2-l_1| \\ \sigma \geqslant |m_2-m_1|}}^{l_2+l_1}{}' a(l_1,\sigma,l_2,m_1,m_2) \times h_\sigma(kd) \bar{\Omega}_\sigma^{m_2-m_1}. \quad (31)$$

Combining the three matrices into a modal approximation for the mutual radiation impedance leads to

$$Z_{ij} \approx G_{ik} C_{kj} Z_{jj}, \quad (32)$$

which corresponds to the modal Pritchard approximation used in this report, and which should be compared to the standard Pritchard approximation given by

$$Z_{ij} \approx \mathrm{Re}(Z_{jj}) h_0(kd_{ij}).$$

ACKNOWLEDGMENT

This work was carried out under Contract No. N0001499WR30167 from the Sensors, Sources, and Arrays division of the Office of Naval Research.

[1] R. L. Pritchard, ''Mutual acoustic impedance between radiators in an infinite rigid plane,'' J. Acoust. Soc. Am. **32**, 730–737 (1960).
[2] G. W. Benthien, *Power Transducers for Sonics and Ultrasonics: Proceedings of the International Workshop, Toulon, France, June 12–13, 1990* (Springer-Verlag, New York, 1991), pp. 109–124.
[3] M. L. Karnovsky, ''Interaction acoustical impedance of spherical radiators and resonators,'' C. R. Acad. Sci. URSS **32**, 40–43 (1941).
[4] J. W. Rayleigh, Philos. Mag. **6**, 301–302 (1903).
[5] H. A. Schenck, ''Improved integral formulations for acoustic radiation problems,'' J. Acoust. Soc. Am. **44**, 41–58 (1968).
[6] G. W. Benthien, D. Barach, and D. Gillette, CHIEF *User's Manual, rev. 1*, September, 1988.
[7] J. B. Blottman, ''Close-packed acoustic array element interaction phenomenon,'' NUWC-NPT Report 10,686, December 2, 1996.
[8] J. C. Bebus, J. N. Decarpigny, A. Lavie, and B. Hamonic, ''Modeling of the acoustic interaction in a Class IV flextensional transducer array'' (in French), convention DRET No. C89.34.093.00.0470.75.01 (1991).
[9] J. N. Decarpigny, ''Application de la méthode des éléments finis à l'étude de transducteurs piézoélectriques,'' Thése de Doctorat d'Etat, Université des Sciences et Techniques de Lille (1984).
[10] A. Lavie, ''Modélisation due rayonnement ou de la diffraction acoustique par un méthode mixte équations intégrales-champ nul,'' Thése de Doctorat, Université des Sciences et Techniques de Lille (1989).
[11] R. New and T. J. Eisler, ''Acoustic radiation from multiple spheres,'' J. Sound Vib. **22**, 1–17 (1972).
[12] B. J. King and A. L. Van Buren, ''A general addition theorem for spheroidal wave functions,'' SIAM (Soc. Ind. Appl. Math.) J. Math. Anal. **4**, 149–160 (1973).
[13] C. H. Sherman, ''Analysis of acoustic interactions in transducer arrays,'' IEEE Trans. Sonics Ultrason. **SU-13**, 9–15 (1966).
[14] L. L. Foldy, ''Theory of passive linear electroacoustic transducers with fixed velocity distribution,'' J. Acoust. Soc. Am. **21**, 595–604 (1949).
[15] C. L. Scandrett and D. R. Canright, ''Acoustic interactions in arrays of spherical elastic shells,'' J. Acoust. Soc. Am. **90**, 589–595 (1991).
[16] C. L. Scandrett and S. R. Baker, ''T-matrix approach to array modeling,'' Technical Report NPS-UW-98-001, Naval Postgraduate School, Monterey, CA (1998).
[17] M. Abramowitz and I. Stegun, *Handbook of Mathematical Functions* (Dover, New York, 1972), p. 437.

A multifrequency scintillation method for ocean flow measurement

I. Fuks, M. Charnotskii, and K. Naugolnykh
Environmental Technology Laboratory, University of Colorado, CIRES/NOAA, 325 Broadway, Boulder, Colorado 80305

(Received 29 March 2000; revised 8 January 2001; accepted 2 March 2001)

The transverse flow of inhomogeneous fluid produces fluctuation of the acoustic signal passing through it. The coherence of frequency-spaced signal fluctuation is related to the advection of the inhomogeneous medium through the sound path, thus providing a basis for the current velocity measurement. This method can be considered to be the ''frequency-domain'' version of the conventional scintillation approach to the current velocity registration based on the measurement of the signal correlation transmitted from the source to the two separated in space receivers (space-domain scintillation) [S. Clifford and D. Farmer, J. Acoust. Soc. Am. **74**, 1826–1832 (1983)]. The sensitivity of the method depends on the features of the ocean fine structure, which is determined mainly by the internal waves and turbulence. To estimate the sensitivity of the multifrequency method of transverse current probing, the coherence function of two signals propagating through a frozen and moving internal wave field and through the turbulence is considered. The application of the multifrequency signal allows estimation of the fine-structure parameters as well as the current velocity. © *2001 Acoustical Society of America.*
[DOI: 10.1121/1.1369099]

PACS numbers: 43.30.Pc, 43.30.Re [DLB]

I. INTRODUCTION

Different features of acoustic signals such as ray travel time, amplitude, angle of ray arrival, mode group velocity, and carrier phase are integral functionals of the oceanic sound speed and currents fields. The variation of sound signal parameters can be used to solve the inverse problem of the sound-speed field and current velocity acoustic measurements.[1] A longitudinal current component can be estimated from differential travel-time measurements.

Another possible acoustic scheme would measure currents transverse to the acoustic path by using the correlation of acoustic scintillations recorded at transversely spaced receivers—a technique that has been suggested for ocean current measurements in Refs. 2–4 and was based on the seminal work Ref. 5, in which such types of microwave scintillation transport in a turbulent atmosphere were discovered experimentally. The essence of the technique lies in the interpretation of the combined spatial and temporal variability of forward-propagated sound. A sound signal passing through the ocean fine structure is modulated, producing an irregular pattern of amplitude and travel-time variation at the receivers. These variations evolve as the intervening medium changes. Under the assumption that the fluctuations in the medium are produced mainly by the advection of a ''frozen'' fine-structure field (Taylor's model of turbulence), evolution of the signal pattern can be directly linked to the motion of the medium. This allows determination of the transverse component of the current by measurements of the time lag between the signal variations at two closely spaced receivers. In general, the coherence of sound received by different hydrophones (separated in space, time, or frequency) in the ocean is a useful measure of the behavior of the intervening fluid medium.[6] Correspondingly, another version of the scintillation method is based on the use of a multifrequency signal. This method can be considered a ''frequency-domain'' version of the conventional scintillation approach to the current velocity registration based on the measurement of the signal correlation transmitted from the source to the two separated receivers (space-domain scintillation).[2–4] The transverse flow of inhomogeneous fluid produces fluctuation of the acoustic signal passing through it. These fluctuations vary with the cw signal frequency change due to variations of the Fresnel zone size and diffraction angles. Subsequently, the fluctuations of amplitude and phase of frequency-spaced signals are coherent at the low fluctuation frequency and noncoherent at the high-frequency band. The measurement of the cutoff frequency allows determination of the transverse current velocity. The feasibility of this technique was confirmed in Refs. 7–10, for wind velocity measurement in a turbulent atmosphere. A detailed description of the theoretical approach to this problem, comparison of theoretical results with experimental data, and references can be found in Ref. 11. Further progress in this field has been connected with investigation of coherence radiowave fluctuations at a millimeter radiowave band, where absorption as well as directivity of transmitter and receiver antennas becomes very important (see, for example, Refs. 12–15).

In all the above-mentioned papers the fine structure of refractive index fluctuations was assumed to be caused only by turbulence and was described by the isotropic Kolmogorov–Obukhov spectrum, and temporal variations were caused only by ''frozen'' transportation of inhomogeneities. In the present paper, along with the turbulent refractive index fluctuations (isotropic as well as anisotropic), we consider underwater sound scattering and refraction by moving internal waves with a given dispersion law, where refractive index fluctuations can be described by the Garret–Munk spectrum.[16] The cutoff frequency of the coherence function

of two cw frequency-separated signals is considered a quantitative indicator of transverse current velocity. The application of the multifrequency signal allows, in addition to the current velocity, estimation of the fine-structure parameters, as noted previously by Flatté.[17] Indeed, Flatté mentioned that the internal wave spectrum features could be obtained by using correlations between two acoustic propagating waves with separate carrier frequencies. The sensitivity of the transverse current measurement depends on features of the ocean fine structure determined mainly by internal waves and turbulence. We show that the value of the cutoff frequency is almost independent of the particular form of refractive index inhomogeneity spectrum and is determined mainly by the transverse flow velocity (which is assumed to be constant everywhere in the scattering volume), whereas the shape of the coherence function depends on the spatial power spectrum of inhomogeneities.

In the present paper we analyze the feasibility of multifrequency current probing by examining statistical characteristics of acoustical signals. To emphasize the essence of this approach the Rytov smooth perturbation method is used, which is generally applied in the case of unsaturated fluctuations.[18,19] Multifrequency probing of the fine structure parameters is also discussed.[20]

Section II presents general equations and statistical models. In Sec. III we discuss the most common, frozen inhomogeneities case. Section IV presents a simple analytical theory of corrections associated with internal waves, and in Sec. V we develop a more complicated theory of multifrequency measurements in the presence of both current and internal waves.

II. GENERAL EQUATIONS

Consider the propagation through the random medium of the two cw waves of different frequencies $\omega_{1,2}$

$$\varphi_n = e^{\psi_n(t) - i\omega_n t}, \tag{1}$$

Here, φ_n is the pressure or velocity potential, Ψ_n is the complex phase, $n=1,2$, where

$$\Psi_n(t) = \chi_n(t) + iS_n(t). \tag{2}$$

$\chi_n(t)$ and $S_n(t)$ are the log amplitude and the phase of the signal, respectively.

In the framework of the smooth perturbation method, the fluctuations of the complex phase of the signal at the distance L from the source are[21]

$$\Psi_n(t) = \frac{k_n^2 L}{2\pi} \int_0^L \frac{dx}{x(L-x)} \int \int_{-\infty}^{\infty} dy\, dz \mu(x,y,z,t) \times \exp\left\{ \frac{ik_n L(y^2+z^2)}{2x(L-x)} \right\}; \tag{3}$$

here $k_n = \omega_n / c$ is the wave number, c is the sound velocity, and $\mu(x,y,z,t)$ are the refraction index fluctuations. The sound waves are thought to propagate along the x axis, which is a horizontal line connected to a point sound source ($x=0$) and a nondirectional receiver ($x=L$), and the axis z directs vertically. The relative coherence of the signals can be characterized by the cross-correlation function and its Fourier transform, i.e., the cross spectrum.

The cross spectrum of the log-amplitude temporal fluctuations is

$$W_\chi^{(n,m)}(\nu) = \frac{1}{2\pi} \int_{-\infty}^{\infty} e^{i\nu\tau} \langle \chi_n(t) \chi_m(t+\tau) \rangle d\tau, \tag{4}$$

and the cross spectrum $W_S^{(n,m)}(\nu)$ for the phase temporal fluctuations $S_n(t)$ and $S_m(t)$ can be introduced by a similar equation. If $m=n$, this equation gives the power spectrum of log-amplitude (or phase) fluctuations on a given carrier frequency ω_n. The cross- and power spectra defined in such a way depend upon the spectrum of the refraction index $\mu(\mathbf{R},t)$ inhomogeneities in the medium that can be characterized by the spatial-temporal power spectrum density

$$\tilde{\Phi}_\mu(\mathbf{q},\nu) = \frac{1}{(2\pi)^4} \int B_\mu(\boldsymbol{\rho},\tau) \exp[i(\nu\tau - \mathbf{q}\boldsymbol{\rho})] d^3\rho\, d\tau, \tag{5}$$

where 4D integration in the infinite limits is implied, and $B_\mu(\boldsymbol{\rho},\tau)$ is the spatial-temporal autocorrelation function of the refractive index fluctuations

$$B_\mu(\boldsymbol{\rho},\tau) = \langle \mu(\mathbf{R},t) \mu(\mathbf{R}+\boldsymbol{\rho}, t+\tau) \rangle. \tag{6}$$

Here, the brackets $\langle \cdots \rangle$ denote the statistical averaging, and the spatial statistical homogeneity on a vector variable $\mathbf{R}=(x,y,z)$ and temporal stationarity of refractive index fluctuations $\mu(\mathbf{R},t)$ are implied.

If the spatial-temporal fluctuations of the refractive index $\mu(\mathbf{R},t)$ are the result of turbulence or internal wave propagation in the presence of a regular medium flow with a current velocity $\mathbf{U}$, then the spatial-temporal power spectrum density of the refractive index fluctuations $\Phi_\mu(\mathbf{q},\nu)$ can be represented in the form (see, for example Ref. 22)

$$\tilde{\Phi}_\mu(\mathbf{q},\nu) = \tfrac{1}{2}\Phi_\mu(\mathbf{q}) \{ \delta[\nu - \Omega_I(\mathbf{q}) - \mathbf{qU}] + \delta[\nu + \Omega_I(\mathbf{q}) - \mathbf{qU}] \}, \tag{7}$$

where $\Omega_I(\mathbf{q})$ is a dispersion law for internal waves

$$\Omega_I(\mathbf{q}) = \left[\frac{N^2(q_y^2+q_x^2) + \omega_i^2 q_z^2}{q_x^2+q_y^2+q_z^2} \right]^{1/2}. \tag{8}$$

Hence, N and ω_i are the buoyancy (Brunt–Väisälä) and the inertial frequency, correspondingly. If the current flow does not have a vertical component ($U_z=0$), then the cross spectra for the phase $W_S^{(n,m)}(\nu)$ and log amplitude $W_\chi^{(n,m)}(\nu)$ temporal fluctuations can be expressed as follows:

$$W_{\chi,S}^{(n,m)}(\nu) = \frac{\pi k^2}{2(1-\Omega^2)} \int_0^L dx \int \int_{-\infty}^{\infty} dq_y\, dq_z \times \Phi_\mu(0,q_y,q_z) \{ \delta[\nu - \Omega_I(0,q_y,q_z) - uq_y] + \delta[\nu + \Omega_I(0,q_y,q_z) - uq_y] \} \times \left\{ \cos\left[x(L-x) \frac{q_\perp^2}{kL} \Omega \right] \mp \cos\left[x(L-x) \frac{q_\perp^2}{kL} \right] \right\}. \tag{9}$$

Here, the upper sign $(-)$ corresponds to the log-amplitude $W_{\chi}^{(n,m)}(\nu)$ spectrum, and the lower one $(+)$ corresponds to the phase $W_S^{(n,m)}(\nu)$ spectrum, $q_{\perp}^2 = q_y^2 + q_x^2$, u is the projection of current velocity $\mathbf{U}$ on the axis Oy, Ω is the relative frequency spacing, and k is the median sound wave number

$$\Omega = \frac{\omega_2 - \omega_1}{\omega_2 + \omega_1}, \quad k = \frac{2k_1k_2}{k_1 + k_2}. \tag{10}$$

Here and below we assume, without losing generality, that $\omega_2 \geqslant \omega_1$, and hence $\Omega \geqslant 0$. In the following sections, we will consider an application of Eq. (9) for particular cases of medium motion and spatial power spectra of refractive index fluctuations.

III. "FROZEN" INHOMOGENEITIES ($\Omega_I = 0$) TRANSFERRING BY A CONSTANT CURRENT

In the limiting case of "frozen" (stable) inhomogeneities moving in a horizontal plane with a constant velocity $\mathbf{U}$, we can neglect the term $\Omega_I(\mathbf{q})$ compared with $\mathbf{qU}$ in Eq. (7), and then carry out the integration over q_y in (9) due to the delta function $\delta(\nu - uq_y)$. In this case, introducing the characteristic frequency $\nu_0 = u\sqrt{k/L}$ (it is inverse to the travel time across Fresnel zone $\sqrt{L/k}$ by homogeneities traveling with transversal velocity u), we obtain from (9)

$$W_{\chi,S}^{(n,m)}(\nu) = \frac{2\pi k^3}{1-\Omega^2} \cdot \frac{F}{\nu_0}[\hat{Q}(F,\Omega) \mp \hat{Q}(F,1)], \tag{11}$$

and

$$\hat{Q}(F,\Omega) = \int_0^1 d\zeta \int_0^{\infty} d\eta\, \Phi_{\mu}\left(O, F\sqrt{\frac{k}{L}}, \eta F\sqrt{\frac{k}{L}}\right) \times \cos[\zeta(1-\zeta)(1+\eta^2)\Omega F^2], \tag{12}$$

where the new dimensionless (normalized) fluctuation frequency $F = \nu/\nu_0$ is introduced, and the variable of integration q_z in (9) is replaced by η according to the relation $q_z = \eta F\sqrt{k/L}$. If the refractive index fluctuations are caused by the internal waves we can use the empirical spatial power spectrum $\Phi_{\mu}(q_x, q_y, q_z)$ suggested by Gurret and Munk[16] with some modifications presented by Desaubies.[23]

$$\Phi_{\mu}(q_x, q_y, q_z) = \frac{4}{\pi^3}\langle\mu^2\rangle\varepsilon(1-\varepsilon^2)^{3/2}\frac{q|q_z|q_z^*}{(q^2+\varepsilon^2 q_z^2)^2[q^2+q_z^2+q_z^{*2}]}, \tag{13}$$

where $q = \sqrt{q_x^2 + q_y^2}$ is the horizontal wave number of an internal wave, $\langle\mu^2\rangle$ is the mean square index of refraction fluctuations, $\varepsilon = \omega_i/N$, and $q_z^* = Nt\sqrt{1-\varepsilon^2}$ is the characteristic vertical wave number of the internal wave, where t is an empirical parameter which takes values in the interval $(1-2)(cpm/Hz)$ and can be considered as an inverse characteristic vertical velocity of an internal wave motion.

Substituting (13) in (11) and (12), we obtain

$$W_{\chi,S}^{(n,m)}(\nu) = D\frac{k}{\nu_0(1-\Omega^2)F}[\hat{Y}(F,\Omega) \mp \hat{Y}(F,1)], \tag{14}$$

and

$$\hat{Y}(F,\Omega) = \int_0^1 d\zeta \int_0^{\infty} \frac{\cos[\zeta(1-\zeta)(1+x)\Omega F^2]}{(1+\varepsilon^2 x)^2[(1+x)F^2 + p^2(1-\varepsilon^2)]}\, dx, \tag{15}$$

where $D = 4\langle\mu^2\rangle\varepsilon(1-\varepsilon^2)^2L^2Nt/\pi^2$, and the variable of integration η was changed by $x = \eta^2$. Substituting these equations into the definition of the coherence function $\Gamma_{x,S}^{(1,2)}(\nu)$ of log-amplitude or phase fluctuations on the carrier frequencies ω_1 and ω_2,

$$\Gamma_{\chi,S}^{(1,2)}(\nu) = \frac{W_{\chi,S}^{(1,2)}(\nu)}{[W_{\chi,S}^{(1,1)}(\nu) \cdot W_{\chi,S}^{(2,2)}(\nu)]^{1/2}}, \tag{16}$$

we obtain

$$\Gamma_{\chi,S}^{(1,2)}(\nu) = \frac{\hat{Y}(F,\Omega) \mp \hat{Y}(F,1)}{[\hat{Y}(F,0) \mp \hat{Y}(F,1+\Omega)]^{1/2}[\hat{Y}(F,0) \mp \hat{Y}(F,1-\Omega)]^{1/2}}. \tag{17}$$

The oscillation of the coherence functions $\Gamma_{\chi,S}^{(1,2)}(\nu)$ is determined by the term $\cos[\xi(1-\xi)(1+\eta^2)F^2\Omega]$ of the integrand in (15). The structure of the cosine argument indicates that the pronounced oscillation takes place if

$$\Omega F^2 \approx 1. \tag{18}$$

Therefore, the estimate for the cutoff frequency $F_c \equiv \nu_c/\nu_0$ is

$$F_c \approx 1/\sqrt{\Omega}. \tag{19}$$

Later, we will see that this conclusion is supported by the numerical calculation.

If the main cause of the refractive index fluctuations is the turbulence (due, for example, to the current flow), but not the internal waves, we can use the Obukhov–Kolmogorov spatial power spectrum, instead of (13)

$$\Phi_{\mu}(q, q_z) = 0.033C_{\mu}^2(q^2 + q_z^2)^{-11/6}; \tag{20}$$

here, C_{μ}^2 is the structure constant of the turbulence field. Equations (11) and (12) for this case take the form

$$W_{\chi,S}^{(n,m)}(\nu) = 0.21\frac{C_{\mu}^2 k^{7/6}L^{11/6}}{\nu_0(1-\Omega^2)F^{8/3}}[\hat{X}(F^2\Omega) \mp \hat{X}(F^2)], \tag{21}$$

and

$$\hat{X}(x) = \int_0^1 d\zeta \int_0^{\infty} \frac{d\eta}{(1+\eta^2)^{11/6}} \cos[\zeta(1-\zeta)(1+\eta^2)x]. \tag{22}$$

Substituting these equations into (16), we obtain the coherence functions $\Gamma_{\chi,S}^{(1,2)}(\nu)$ for log-amplitude and phase fluctuations of frequency separated signals in the form

$$\Gamma_{\chi,S}^{(1,2)}(\nu) = \frac{\hat{X}(F^2\Omega) \mp \hat{X}(F^2)}{[\hat{X}(0) \mp \hat{X}[F^2(1+\Omega)]]^{1/2}[\hat{X}(0) \mp \hat{X}[F^2(1-\Omega)]]^{1/2}}. \tag{23}$$

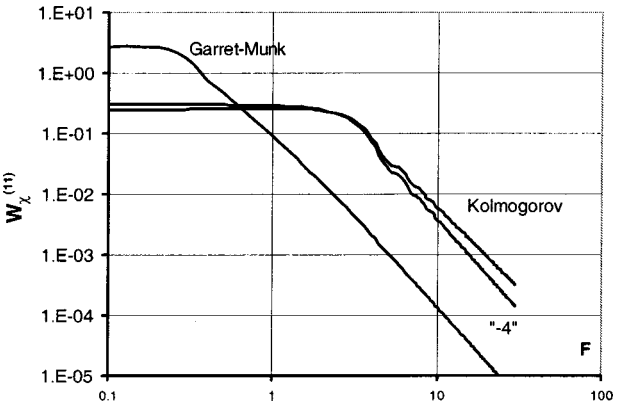

FIG. 1. Temporal power spectra (normalized on the unitary variance) of log-amplitude fluctuations of cw sound signal propagating in a medium with refractive index inhomogeneities [described by Garret–Munk ($\varepsilon=0.04$, $p=1.7$), Kolmogorov, and fourth power ''-4'' decreasing spatial power spectra] ''frozen'' in a current flow with a constant velocity.

In Fig. 1, the temporal power spectra of log-amplitude fluctuations $W_\chi^{(1,1)}(\nu)$, corresponding to the Garret–Munk (13) and Kolmogorov (20) spatial power spectra of refractive index fluctuations [Eqs. (14) and (21), correspondingly], are presented as functions of the dimensionless frequency F. For comparison, the result of power spectra $W_\chi^{(1,1)}(\nu)$ computations for isotropic refractive index fluctuations described by the power spectrum similar to (20) but decreasing as a fourth power of spatial wave number [i.e., as $\sim(q^2+q_z^2)^{-2}$] is also represented in Fig. 1. It is seen that besides the monotonous decreasing at high frequencies [as $F^{-8/3}$ for Kolmogorov turbulent spectrum (20) and as F^{-3} for the spatial spectrum introduced above which decreases as a fourth power of spatial wave number], these power spectra oscillate at frequencies near $F\simeq 1$.

The origin of these oscillations is very close to that described in Ref. 24 for waves scattered by a moving rough surface. In both cases, the wave-field amplitude and phase fluctuations on frequency ν are caused by the moving inhomogeneities (of refractive index here and surface roughness in Ref. 24) with the characteristic length

$$l_F \approx \frac{u}{\nu}=\frac{1}{F}\sqrt{\frac{L}{k}}. \tag{24}$$

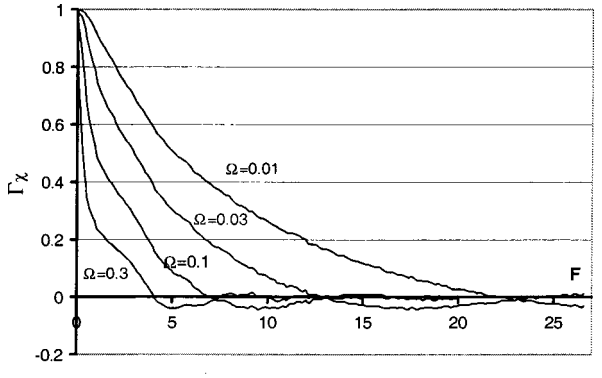

FIG. 2. The coherence functions of log-amplitude fluctuations of cw signals with different frequency separation Ω, propagating through the medium with Garret–Munk spatial power spectra of refractive index inhomogeneities ($\varepsilon=0.04$, $p=1.7$).

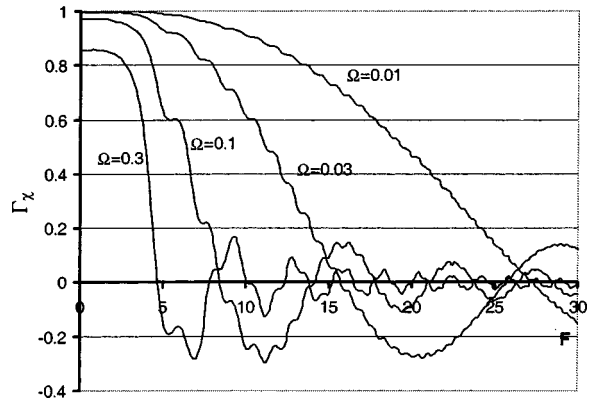

FIG. 3. The same as in Fig. 2, but for the Kolmogorov spatial power spectra.

The angular width ϑ of the scattering diagram on these inhomogeneities could be estimated as $\vartheta\simeq(kl_F)^{-1}$, and the path length difference ΔR_F of scattered waves that interfere in the observation point is equal approximately to

$$\Delta R_F \approx L(1-\cos\vartheta)\approx \frac{L}{2}(kl_F)^{-2}. \tag{25}$$

The frequencies F_n of the spectrum oscillations correspond to the interference of scattered waves with the path length difference equal to an integer number of wavelength, i.e., $k\Delta R_F=2n\pi$ ($n=0,1,2,...$), which implies that $F_n^2=4\pi n$.

In Figs. 2 and 3 the coherence functions $\Gamma_\chi^{(1,2)}(\nu)$ of log-amplitude fluctuations, given by (17) and (23), are plotted as functions of F for several frequency separations Ω. It is seen that slow ($F\ll 1$) signal variations are strongly correlated [$\Gamma_\chi^{(1,2)}(\nu)\simeq 1$] for a carrier frequency separation, small enough $\Omega\ll 1$. With the fluctuation frequency F increasing, the coherence $\Gamma_x^{(1,2)}(\nu)$ diminishes abruptly at frequency $F_c\sim\Omega^{-1/2}$. In Fig. 4, the coherence function (23) is plotted as a function of $F\sqrt{\Omega}$. We found that the relation $F_c=C_1\Omega^{-1/2}$ [with $C_1\simeq 2.7$ for F_c corresponding to the first zero of $\Gamma_\chi^{(1,2)}(\nu)$] has a high validity.

To estimate the dimensional cutoff frequency $\nu_c=\nu_0 F_c$, we consider, for example, sound with frequency 30 kHz ($k=125$ rad/m), propagating distance $L=2$ km, and

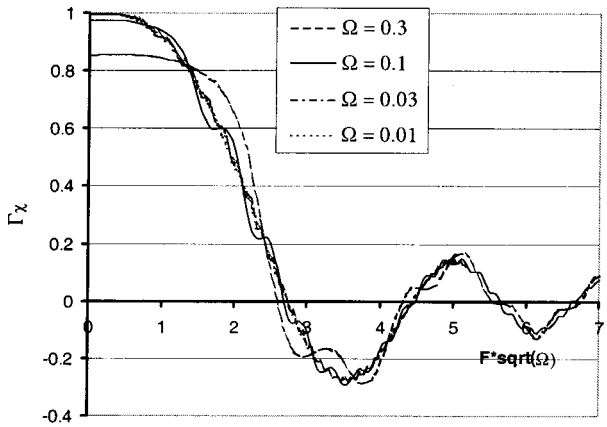

FIG. 4. The same as in Fig. 3, but as a function of modified frequency $F\sqrt{\Omega}$.

current velocity $u=10$ cm/s. The characteristic frequency is $\nu_0=2.5\cdot 10^{-2}s^{-1}$, and cutoff frequency is $\nu_c=C_1\nu_0\Omega^{-1/2}\simeq 0.2$ rad/s.

It is possible to give a simple qualitative interpretation to this result based on the following speculations (see Refs. 10 and 25). It was shown above that the fluctuations with the frequency F appear as a result of interference of waves that arrive at the observation point with a path difference $\Delta R_F \sim L(kl_F)^{-2}\sim F^2/k$. The changes of carrier frequency ω lead to the shift of this interference pattern, and if this shift proves to be large enough, the fluctuations on two different carrier frequencies ω_1 and ω_2 become noncorrelated. To destroy the interference pattern, it is enough to change the wave number $k=\omega/c$ on the value Δk, found from the equation $\Delta k\Delta R_F \simeq 1$, from which it is easy to obtain the relation $\Omega F_c^2 \simeq$const, which in its turn leads to the above-mentioned results of numerical simulation (see Figs. 2 and 3).

On the other hand, this result means that the decorrelation of amplitude (and phase) fluctuations at a given fluctuation frequency F occurs when the difference of Fresnel zone areas $\Delta S=L/k_1-L/k_2=2L\Omega/k$ for two carrier frequencies ω_1 and ω_2 becomes equal to the area of one inhomogeneity $\Delta s=l_F^2$, where l_F is given by (24). Namely, from equation $\Delta S\simeq\Delta s$ the relation $\Omega F_c^2\simeq 1$ follows which is in agreement with the numerical and analytical results obtained above.

From Figs. 2 and 3 it follows that along with these long periodic oscillations of coherence function [the sequence of frequencies F_{cn} where $\Gamma_\chi^{(1,2)}(\nu)$ becomes zero is given by approximate relation $\Omega F_{cn}^2\simeq n\pi$ for $\Omega\ll 1$], there exist short periodic oscillations with the above-mentioned periods $F_n \simeq 2\sqrt{n\pi}$. These oscillations are seen very clearly for the Kolmogorov spectrum of spatial inhomogeneities in Figs. 3 and 4, but are almost invisible for the Garret–Munk internal wave spectrum in Fig. 2. Very likely the main reason for this difference is the very high degree of anisotropy of the Garret–Munk spatial spectrum given by (13) for $\varepsilon\ll 1$. To confirm this statement, we considered the model anisotropic spatial spectrum (see, for example, Ref. 26)

$$\Phi_{\alpha\mu}(q,q_z)=0.033\alpha C_{\mu\perp}^2(q^2+\alpha^2q_z^2)^{-11/6}, \tag{26}$$

where α is the anisotropy coefficient (the ratio of vertical length of inhomogeneities to their horizontal scale), and $C_{\mu\perp}^2$ is the structure constant of refractive index fluctuations in the horizontal plane ($C_{\mu z}^2=\alpha^{-2/3}C_{\mu\perp}^2$ is the structure constant of refractive index fluctuations in the vertical direction). When $\alpha=1$, this spectrum becomes the Kolmogorov isotropic spectrum (20). The computation results for $\Gamma_\chi^{(1,2)},(\nu)$ with $\Omega=0.1$ and spectrum (26), are presented in Fig. 5 as functions of dimensionless frequency $F=\nu/\nu_0$. It is easy to see that the cutoff frequencies F_{cn} [where $\Gamma_\chi^{(1,2)}(\nu)$ becomes zero] do not depend on the anisotropy parameter α, but the width of coherence function in the interval $F_{c1}>F>0$ strongly depends on α: for very anisotropic inhomogeneities (small α corresponds to ''pancake'' inhomogeneities), the coherence function decreases much faster with increasing frequency than for isotropic inhomogeneities ($\alpha=1$). The same principle relates to the amplitude of coherence function $\Gamma_\chi^{(1,2)}$ oscillations with the long periods $F_{cn}\simeq\sqrt{n\pi/\Omega}$ as well as with the short ones $F_n\simeq 2\sqrt{n\pi}$: the more anisotropy (the less α), the smaller the amplitude of these oscillations. The refractive index inhomogeneities described by the Garret–Munk spectrum are very anisotropic (parameter $\varepsilon=0.04$ plays the role of anisotropy parameter α in this case); therefore, the short period oscillations of log-amplitude power spectrum fluctuations $W_\chi^{(1,1)}$ are invisible in Fig. 1 (because of the logarithmic scale on the ordinate axis) and are very small in coherence function $\Gamma_\chi^{(1,2)}$ plots shown in Fig. 2. The amplitude of long-periodic oscillations of $\Gamma_\chi^{(1,2)}$ in Fig. 2 also is much less than the coherence function oscillations represented in Fig. 3 for the isotropic Kolmogorov spatial power spectrum. It is worth mentioning that the periods of these long-periodic oscillations do not depend on the spatial power spectrum type (Garret–Munk or Kolmogorov) or on the anisotropy parameter α (ε for the Garret–Munk spectrum): their periods are completely determined by the current flow velocity and signal frequency separation Ω.

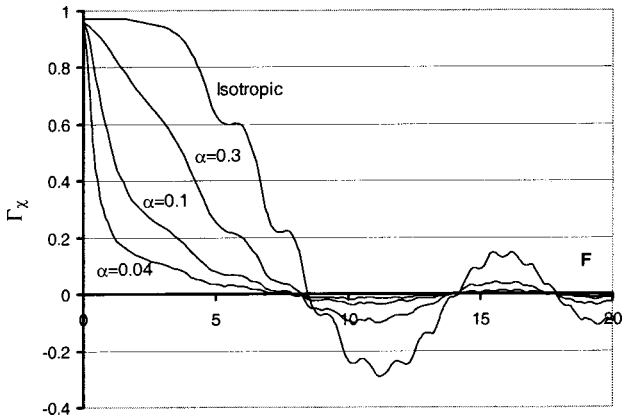

FIG. 5. The coherence functions of log-amplitude fluctuations of cw signals with frequency separation $\Omega=0.1$, propagating through the medium with anisotropic spatial power spectra (26) of refractive index inhomogeneities (with different anisotropy parameters α) frozen in a current flow with a constant velocity.

IV. CORRECTIONS FOR INTERNAL WAVES

If the current velocity u is low enough, we cannot neglect the term Ω_I in a dispersion equation presented in (9) by arguments of δ functions

$$\nu=uq_y\pm\Omega_I(0,q_y,q_x). \tag{27}$$

Neglecting the inertial frequency ω_i in the dispersion law (8), we can represent this equation in the form

$$q_y=\frac{\nu}{u}\pm\frac{Nq_y}{u\sqrt{q_y^2+q_z^2}}. \tag{28}$$

Considering the second term on the right-hand side of (28) as a small correction to the dispersion equation solution $q_y=\nu/u$ which was used in the previous section, we obtain the following expression for q_y:

$$q_y=\frac{\nu}{u}\left[1\pm\frac{N}{\nu\sqrt{1+(uq_z/\nu)^2}}\right]. \tag{29}$$

Using this solution of a dispersion equation for the integral over q_y in (9), we obtain the first term in the braces in (9) in a form similar to (12) with the following substitution:

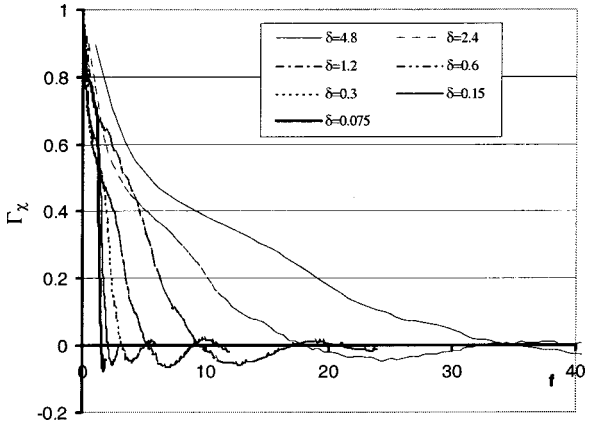

FIG. 6. The coherence functions of log-amplitude fluctuations of cw signals with frequency separation $\Omega=0.1$, propagating through the medium with Garret–Munk spatial power spectra of refractive index inhomogeneities ($\varepsilon=0.04$, $p=1.7$) and a different ratio $\delta=v_0/N$ of the transferring current frequency $v_0=uk/L$ to the Brunt–Väisälä frequency N.

$$\Omega F^2(1+\eta^2)\Rightarrow\Omega F^2\left(1+\eta^2\pm\frac{2}{\delta F\sqrt{1+\eta^2}}\right), \tag{30}$$

where $\delta=\nu_0/N$. The evaluation of coherence cutoff frequency F_c can be found from a rough estimation of trigonometric function period oscillation in (12) and (15) with the argument changing according to (30). This is equivalent to equating the right-hand side of (30) to a constant of the unity order. The solution of the corresponding equation has the form

$$F_c\approx\frac{1}{\sqrt{\Omega}}+O\left(\frac{N}{\nu_0}\right). \tag{31}$$

This approximate solution is valid if the correction to the qualitative result (19) obtained in the previous section ($F_c\simeq 1/\sqrt{\Omega}$) is small enough; i.e., if the following inequality holds:

$$\frac{N}{\nu_0}\sqrt{\Omega}\ll 1. \tag{32}$$

Taking into account that the dimensionless frequency F_c is related to the cutoff frequency ν_c by the relation $F_c=\nu_c/\nu_0$, we obtain the estimation

$$\nu_c=C_1u\sqrt{\frac{k}{L\Omega}}+C_2N, \tag{33}$$

where C_1 and C_2 are order of unity constants. As was shown in the previous section from computation results represented in Figs. 4, 5, and 6, $C_1\simeq 2.7$ if we define the cutoff frequency F_c as the first zero of coherence functions $\Gamma_\chi^{(1,2)}$. From the last equation, it follows that measurement of the coherence cutoff frequency ν_c allows us to estimate the current velocity u

$$u=u_0+\Delta u, \tag{34}$$

where

$$u_0=C_1\nu_c\sqrt{\frac{L\Omega}{k}} \tag{35}$$

is the ''zero-order'' estimation of current frequency, and

$$\Delta u\approx N\sqrt{\frac{L\Omega}{k}} \tag{36}$$

is the absolute value of the current measuring error. It follows from the last equations that the relative precision of current velocity measurement is equal to the ratio of Brunt–Väisälä frequency N to the coherence cutoff frequency ν_c

$$\frac{\Delta u}{u_0}\approx\frac{N}{\nu_c}.$$

Consider, for example, the transverse current probing at a distance of $L=2$ km. Let the current velocity be $u=10$ cm/s. The appropriate sound wave frequency is $\omega/2\pi=1$ kHz, so $k=4.25$ rad/m. Then, $\nu_0=u\sqrt{k/L}=4.6\cdot 10^{-3}\,\mathrm{s}^{-1}$, and the frequency cutoff $\nu_c=\nu_0(2.7/\sqrt{\Omega})=4\cdot 10^{-2}\,\mathrm{s}^{-1}$ for $\Omega=0.1$. The Brunt–Väisälä frequency N is of the order of 10^{-3}–10^{-4} Hz; therefore, the relative accuracy of the current velocity estimation due to the internal wave movement is $\Delta u/u_0\sim 2.5\cdot 10^{-2}$.

V. INTERNAL WAVES AND CURRENT SUPERPOSITION

In more general case, when propagating internal waves ($\Omega_I\neq 0$) are superimposed by the constant current flow ($U\neq 0$), integration in (9) can be transformed (because the δ function is in the integrand) to the integration along the contours at the plane of spatial frequencies, similar to Ref. 22. In the case under consideration it is possible to complete the integration over variable q_z in (9) in an explicit form using the following solution:

$$q_z^0=q_y\left[\frac{N^2-(\nu-q_yu)^2}{(\nu-q_yu)^2-\omega_i^2}\right]^{1/2} \tag{37}$$

of equations $\nu\pm\Omega_I(0,q_y,q_z)-uq_y=0$. Shifting to the new dimensionless variables of integration in (9), $\xi=x/L$, $y=q_y\sqrt{L/k}$, and using the notation

$$\delta=\frac{\nu_0}{N}=\frac{u}{N}\sqrt{\frac{k}{L}}, \tag{38}$$

we obtain from (9) an equation similar to (11)

$$W_{\chi,S}^{(n,m)}(\nu)=\frac{2\pi k^3(1-\varepsilon^2)}{N(1-\Omega^2)}[Q(f,\Omega)\mp Q(f,1)], \tag{39}$$

with the following expression for function $Q(f,\Omega)$:

$$Q(f,\Omega)=\int_0^1 d\zeta\int_C dy\left|\frac{y(f-\delta y)}{[1-(f-\delta y)^2]^{1/2}[(f-\delta y)^2-\varepsilon^2]^{3/2}}\right|\times\Phi_\mu\left\{0,y\sqrt{\frac{k}{L}},y\sqrt{\frac{k}{L}}\left[\frac{1-(f-\delta y)^2}{(f-\delta y)^2-\varepsilon^2}\right]^{1/2}\right\}\times\cos\left[\zeta(1-\zeta)\frac{(1-\varepsilon^2)\Omega}{(f-\delta y)^2-\varepsilon^2}y^2\right], \tag{40}$$

where the nondimensional normalized fluctuation frequency $f=\nu/N$ is introduced (which relates to the frequency F used above by the obvious equation $f=\delta\cdot F$), and integration over dy is carried out on two line segments

$$\int_C \cdots dy \equiv \int_{(f-1)/\delta}^{(f-\varepsilon)/\delta} \cdots dy + \int_{(f+\varepsilon)/\delta}^{(f+1)/\delta} \cdots dy. \tag{41}$$

It is easy to see that in the limiting case of $u=0$ (and, consequently, $\delta=0$), the integral limits in (41) tend to $\pm\infty$ depending on the normalized frequency value f. For $f \geqslant 0$, the second integral in (41) disappears when $\delta \to 0$, and the first one has the finite (nonzero) limit only for $1 \geqslant f \geqslant \varepsilon$ (which corresponds to the frequency band $N \geqslant \nu \geqslant \omega_i$).

After substitution in (40) of Eq. (13) for $\Phi_\mu(q,q_z)$, we obtain the final expressions for co- and cross spectra of log-amplitude and phase fluctuations in the general case ($\Omega_I \neq 0$, $u \neq 0$)

$$W_{\chi,S}^{(n,m)}(\nu) = B \frac{k}{2(1-\Omega^2)} [G(f,p,\delta,\Omega) \mp G(f,p,\delta,\Omega)], \tag{42}$$

and

$$G(f,p,\delta,\Omega) = \left(\int_{(f-1)/\delta}^{(f-\varepsilon)/\delta} + \int_{(f+\varepsilon)/\delta}^{(f+1)/\delta} \right) dy \times \frac{(f-\delta y)^2 - \varepsilon^2}{|y||f-\delta y|^3 \{y^2 + p^2[(f-\delta y)^2 - \varepsilon]\}} \times \int_0^1 d\zeta \cos\left[\zeta(1-\zeta) \frac{y^2(1-\varepsilon^2)}{(f-\delta y)^2 - \varepsilon^2} \Omega \right], \tag{43}$$

where the following notations are introduced:

$$B = \frac{16}{\pi^2} \langle \mu^2 \rangle \varepsilon t L^2, \quad p = N\tau_0, \tag{44}$$

and $\tau_0 = t\sqrt{L/k}$ is the internal wave travel time across the Fresnel zone $\sqrt{L/k}$ with velocity $1/t$. Using these equations in definition (16), we obtain the following result for the coherence functions:

$$\Gamma_{\chi,S}^{(1,2)}(\nu) = (1-\Omega^2)^{-1/2} [G(f,p,\delta,\Omega) \mp G(f,p,\delta,\Omega)] \times [G(f,p_1,\delta_1,0) \mp G(f,p_1,\delta_1,1)]^{-1/2} \times [G(f,p_2,\delta_2,0) \mp G(f,p_2,\delta_2,1)]^{1/2}, \tag{45}$$

where $p_{1,2} = p\sqrt{1 \pm \Omega}$, and $\delta_{1,2} = \delta/\sqrt{1 \pm \Omega}$.

The calculation results for $\Gamma_\chi^{(1,2)}(\nu)$, given by (45), are presented in Fig. 6 as functions of normalized frequency f for different values of δ and for the following set of parameters: $\varepsilon = 0.04$, $p = 1.7$, $\Omega = 0.1$. The limiting case $\delta \ll 1$, as follows from definition (38), corresponds to the very slow current flow u, when the power spectra W of field fluctuations are proportional to f^{-3}, concentrated at the frequency interval $1 \geqslant f \geqslant \varepsilon$, and are equal to zero outside of this interval. The coherence functions Γ inside this interval is independent on frequency f.

When the current velocity u increases, and current travel time $\sqrt{L/k}/u$ across the Fresnel zone becomes comparable with the period of internal waves $1/N$, the power spectra of field fluctuations are broadening, and the coherence of fluctuations of two cw frequency separated signals stretches to the frequency $f_c \simeq \delta/\sqrt{\Omega}$. It follows from (38) that the cutoff frequency f_c is proportional to the current velocity u and, consequently, can be the tool of its measurement.

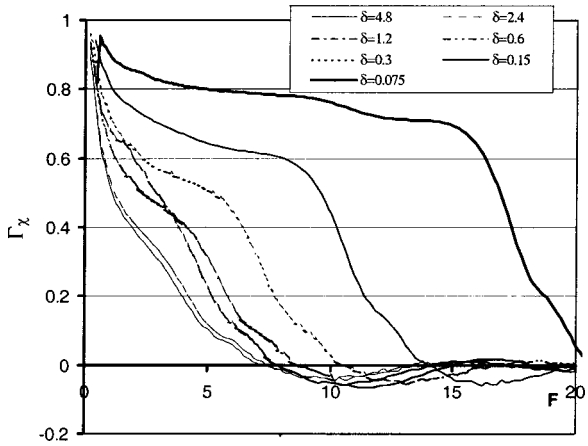

FIG. 7. The same plots as in Fig. 6, as functions of the fluctuation frequency $F = f/\delta$.

The same results as in Fig. 6 are represented in Fig. 7 as functions of dimensionless frequency $F = \nu/\nu_0 = f/\delta$. It is seen that for large-enough values of δ (when fluctuation spectrum is determined mostly by the current flow but not the internal waves), cutoff frequency F_c tends to the value that does not depend on δ. According to the results obtained in Sec. IV, for $\delta \gg 1$, the cutoff frequency probing F_c is determined entirely by the cw frequency separation Ω.

VI. DISCUSSION AND CONCLUSION

The transverse flow of inhomogeneous fluid produces fluctuations of the acoustic signal passing through it. These fluctuations vary with the cw signal frequency change due to variation of the Fresnel zone size and diffraction angles. Similarly, the fluctuations of amplitude and phase of frequency-spaced signals are coherent at the low fluctuation frequency and noncoherent at the high-frequency band. The coherence function behavior depends upon the flow velocity at the given fine structure of the flow. The measurement of the cutoff frequency allows determination of the transverse current velocity. The application of the multifrequency signal allows, in addition to the current velocity, estimation of the fine-structure parameters.

In comparison with the spatial-temporal scintillation method,[2] the multifrequency (frequency-temporal) method suggested in this paper has at least two essential advantages: (a) only one receiver is needed in contrast to several (at least two) which are needed for the spatial-temporal scintillation method; (b) the data obtained relate to parameters of a single propagation path, whereas space separated receivers measure signal parameter fluctuations along several propagation paths.

We estimated the sensitivity of the proposed technique to internal waves and turbulence under the following simplifying assumptions:

(a) Parameters of refractive index spatial spectra (N, ω_i) and $\langle \mu^2 \rangle$ for the Garret–Munk spectrum, and C_μ^2 for the Obukhov–Kolmogorov spectrum are assumed to be

constants everywhere in the region of sound propagation. In the real ocean all these parameters are functions of depth and range. The above assumption requires that these parameters do not change substantially, at least in the Fresnel zone. Since the transverse linear size of the Fresnel zone is proportional to $\sim\sqrt{L/k}$, it indicates that the theory presented above fails for long distances and low frequencies.

(b) The regular refraction effects have not been taken into account; only the refractive index fluctuations are considered, assuming that the mean value of the refraction index does not depend on space coordinates.

(c) The results obtained are not applicable either to waveguide underwater sound propagation (described by eigenmodes propagation) or to multipass sound propagation with interference of two or more rays in the observation point.

(d) There is no reflection from the ocean bottom or sea surface.

(e) The results are not valid for strong or ''saturated'' fluctuations, and the sound wave amplitude fluctuations are assumed to be small enough: for Rytov smooth perturbation method applicability the normalized variance of intensity σ_I must be less than 0.3 (see, for example, Ref. 27 and references cited therein). If we assume that the boundary between Rytov and strong fluctuation regimes is roughly given by an equation $\sigma_I=1$, then the following inequalities must hold (see, for example, Ref. 18):

$$\Phi^2=\gamma\Lambda<1, \quad \text{for } \Lambda>1, \qquad \Lambda\Phi^2=\gamma\Lambda^2<1, \quad \text{for } \Lambda<1, \tag{46}$$

where $\Lambda=L/kL_v^2$ is the diffraction parameter, L_v is the transverse correlation scale of the index of refraction fluctuations, $\gamma=k^3\langle\mu^2\rangle L_pL_v^2$ is the scattering strength (see Ref. 28), L_p is the integral range scale of the index of refraction fluctuations, and $\Phi^2=k^2\langle\mu^2\rangle L_pL$ is the variance of phase fluctuations in the far (wave or diffraction) field $\Lambda\gg1$ (the opposite limiting case $\Lambda\ll1$ corresponds to the geometrical optics limit). For values typical for midocean Atlantic or Pacific internal waves from Ref. 28: $\langle\mu^2\rangle L_p=1.7\cdot10^{-5}$ m, $L_v=147$ m, and sound speed $c=1480$ m/s, (46) takes the form

$$\frac{\omega}{2\pi}[\text{kHz}]\cdot\sqrt{L[\text{km}]}<1.8, \quad \text{for } \Lambda>1, \qquad \frac{\omega}{2\pi}[\text{kHz}]\cdot(L[\text{km}])^2<3\cdot10^2, \quad \text{for } \Lambda<1. \tag{47}$$

These inequalities give the limits of frequency ω and range L where the multiple scattering processes do not affect the total variance of acoustic field amplitude.

As to restriction ''b,'' it is necessary to make some additional remarks. Since we considered sound wave scattering not only by turbulence but also by internal waves, there must be stratification and hence there will be a depth-dependent sound speed, and the ray paths will necessarily be curved. Strictly speaking, all results presented in our paper relate only to the straight-line propagation paths, because the starting equation (3) concerns only this particular case. But, we believe that the results obtained have a wider field of validity, including in particular, slightly curved ray paths. Integrals (15) and (40) along the propagation path include only the running distance between two rays, which are necessary to compose a second moment of the field, but not the shape of the actual rays. In our approach this distance is a linear function of dimensionless distance ξ. This is not exact for curved rays, of course, but since the typical distance between the two rays is of the order of Fresnel zone $\sqrt{L/k}$, the error associated with it will be small as long as ray curvature changes are small at the depth change of the order of $\sqrt{L/k}$.

In fact, in a plane stratified medium, the rays bend only in the vertical plane xz, whereas the flow $\mathbf{U}$ is considered to be the horizontal ($U_z=0$). The variation of wavefront curvature leads to changes of the ray tube cross section as compared to the straight-line propagation, which in turn causes the propagating wave amplitude and intensity modulation [in addition to their fluctuations caused by scattering by refractive index inhomogeneities $\mu(x,y,z)$]. The corresponding modification of the Rytov approximation for sound wave propagation along the curved rays was suggested in Ref. 29, where it was shown that the agreement between experimental data of amplitude fluctuations and the theoretical results became essentially better if ray curvature was taken into account. As for the temporal power spectrum frequency dependence, it is not affected by rays bending in the vertical plane. These fluctuations arise because of inhomogeneities traveling in transverse horizontal direction (in the model of the ''frozen'' transfer), where the wavefront curvature ($1/L$) and the Fresnel zone transverse size ($\sqrt{L/k}$) are the same as in a homogeneous nonstratified medium. In particular, it easy to see that the characteristic frequency of amplitude fluctuations $\nu_0=u\sqrt{k/L}$ is equal to the inverse time of crossing the Fresnel zone, remains the same, and is not sensitive to the ray curvature in the vertical plane. We assume here that the current velocity $\mathbf{U}$ is great enough, so it is the main reason for temporal field fluctuations. This allows us to neglect the effect of vertical advection of short vertical wavelength internal waves (and fine-structure turbulence) by the dominant long wave length internal waves, considered in Ref. 30.

Sensitivity of the proposed multifrequency method is limited by the cospectrum variations due to the internal wave field. In the open ocean using low carrier frequencies at long propagation paths, it is possible to determine not only the current velocity, but also path-averaged parameters p and t of the internal wave power spectrum. Using a high-frequency sound signals one can determine current velocity and the parameters of the turbulent spectra of homogeneities in straits and channels.

In the present paper, the majority of theoretical results for log-amplitude and phase fluctuation spectra and their coherence functions were derived simultaneously: the corresponding expressions for log-amplitude and phase fluctuation functions differ only by the signs plus or minus signs in the starting equation (9), as well as in the resulting ones (17),

(23), and (45). As for the numerical results of computing, only log-amplitude fluctuation spectra and coherence functions are represented; additional data can be obtained by the analyses of the phase fluctuation coherence functions as well as mutual phase-amplitude coherence functions. Our attention has been drawn to the fact that ray curvature as well as vertical advection of fine short-scaled inhomogeneities by internal waves affect mainly the log-amplitude fluctuations rather than phase fluctuations, as was noted in Ref. 30. Multiple scattering causes a similar effect: as was shown in Ref. 19, the power spectra of phase fluctuations agree with Rytov method results (see Fig. 15 in Ref. 19) even for strong amplitude fluctuations, when multiple scattering plays the major role in forming the signal fluctuations. We believe that since coherence functions of phase and amplitude fluctuations are ratios of corresponding power spectra, they will not be affected by ray curvature and multiple scattering processes that are as strong as the power spectra are. This means that the weak scattering result obtained above in the framework of the Rytov method for phase (travel-time) fluctuations appears to be valid over a much broader frequency band and longer ranges than for log-amplitude fluctuations.

In conclusion, we emphasize that all the above results are based on the well-known general expression (3) for the complex phase fluctuations in the Rytov smooth perturbation method. In this paper we consider only the second statistical moments of acoustic field fluctuations, and do not consider either higher statistical moments, or probability distribution functions (PDF). According to the generally accepted first principles (in particular, the central limit theorem), the PDF of the intensity (square amplitude) fluctuations must be log normal for weak fluctuations and exponential for strong ones. The detailed investigation of PDF transition from the first limiting case to the second one can be found in Ref. 28, where the multiple scattering process was modeled as a consecutive diffraction on the set of phase screens representing the 3D medium with refractive index fluctuations.

ACKNOWLEDGMENTS

This work was supported by the joint NOAA/DOD—Advanced Sensor Application Program and partially supported by the European Commission Environment and Climate Program, Grant No. ENV4-CT97-0463 and NATO Linkage Grant (E.NVIR.LG960352)528 (96) LVdC). We are grateful to Dr. R. Hill and Dr. V. Zavorotny for the useful suggestions, and to two anonymous reviewers for their valuable comments.

[1] W. H. Munk, P. Worcester, and C. Wunch, *Ocean Acoustic Tomography* (Cambridge University Press, Cambridge, 1995), p. 115.
[2] S. Clifford and D. Farmer, ''Ocean flow measurement using acoustical scintillation,'' J. Acoust. Soc. Am. **74**, 1826–1832 (1983).
[3] D. M. Farmer and S. F. Clifford, ''Space-time acoustic scintillation analysis: A new technique for probing ocean flows,'' IEEE J. Ocean Eng. **OE-11**(1), 42–50 (1986).
[4] D. M. Farmer and G. B. Crawford, ''Remote sensing of ocean flows by spatial filtering of acoustic scintillations: Observations,'' J. Acoust. Soc. Am. **90**, 1582–1591 (1991).
[5] R. W. Lee and A. T. Waterman, Jr., ''Space correlations of 35-GHz transmissions over a 28-km path,'' Radio Sci. **3**(2), 135–139 (1968).
[6] R. Esswein and S. Flatté, ''Calculation of the phase-structure function density from oceanic internal waves,'' J. Acoust. Soc. Am. **70**, 1387–1396 (1981).
[7] H. B. Janes, M. S. Thompson, Jr., D. Smith, and A. W. Kirpatrick, ''Comparison of simultaneous line-of-sight signals at 9.6 and 34.5 GHz,'' IEEE Trans. Antennas Propag. **AP-18**(4), 447–451 (1970).
[8] A. Ishimaru, ''Temporal frequency spectra of multifrequency waves in turbulent atmosphere,'' IEEE Trans. Antennas Propag. **AP-20**(1), 10–19 (1972).
[9] P. A. Mandics, J. C. Harp, R. W. Lee, and A. T. Waterman, Jr., ''Multifrequency coherency of short-term fluctuations of line-of-sight signals—electromagnetic and acoustic,'' Radio Sci. **9**(8,9), 723–731 (1974).
[10] I. M. Fuks, ''Coherence function of the fluctuations of frequency spaced signals propagating through the randomly inhomogeneous medium,'' Radiotekh. Elektron. (Moscow) **20**(3), 515–524 (1975) [Radio Eng. Electron. Phys. **20**(3), 46 (1975)].
[11] A. Ishimaru, *Wave Propagation and Scattering in Random Media* (Academic, New York, 1978), Vol. 2, Chap. 19, pp. 396– 399.
[12] K. L. Ho, R. S. Cole, and N. D. Mavrokoukoulakis, ''The effect of wind velocity on the amplitude scintillations of millimeter radio waves,'' J. Atmos. Terr. Phys. **40**(140), 443–448 (1978).
[13] A. D. Sarma *et al.*, ''Theoretical and experimental investigation of millimeter wave phase fluctuations in an absorbtion region,'' Int. J. Infrared Millim. Waves **7**(6), 785–793 (1986).
[14] A. D. Sarma and M. H. J. Herben, ''Theoretical investigation of differential phase fluctuations between two coherent radio signals,'' AEÜ- Arch. Electr. Communic. **44**(6), 444–447 (1990).
[15] G. L. Siqueira and R. S. Cole, ''Temporal-frequency spectra for plane and spherical waves in a millimetric wave absorption band,'' IEEE Trans. Antennas Propag. **AP-39**(2), 229–235 (1991).
[16] C. Garret and W. Munk, ''Space-time scales of internal waves: A progress report,'' J. Geophys. Res. **80**, 291–297 (1975).
[17] S. M. Flatté, ''Sound transmission through internal waves, including internal-wave tomography,'' *Proceedings of the Symposium in Honor of Walter Munk's 65th Birthday* (Scripps Institution of Oceanography, La Jolla, CA, 1983).
[18] S. M. Flatté, R. Dashen, W. H. Munk, K. M. Watson, and F. Zachariasen, *Sound Transmission through a Fluctuating Ocean*, edited by S. M. Flatté (Cambridge University Press, New York, 1979).
[19] T. E. Ewart and S. A. Reynolds, ''The mid-ocean acoustic transmission experiment, MATE,'' J. Acoust. Soc. Am. **75**, 785–802 (1984).
[20] I. Fuks, K. Naugolnykh, and M. Charnotskii, ''Multifrequency scintillation method for ocean flow measurement,'' J. Acoust. Soc. Am. **106**, 2119 (1999).
[21] V. Tatarskii, *The Effect of the Turbulent Atmosphere on Wave Propagation* (Israel Program for Scientific Translation: Jerusalem, Israel, 1971), Chap. 3, pp. 218–225.
[22] I. V. Chashei, ''On the temporal power spectra of scintillations by propagating through a moving random medium with wave turbulence,'' Waves Random Media **3**, 19–26 (1995).
[23] Y. Desaubies, ''On the scattering of sound by internal waves in the ocean,'' J. Acoust. Soc. Am. **64**, 1460–1468 (1978).
[24] F. G. Bass and I. M. Fuks, *Wave Scattering from Statistically Rough Surfaces* (Pergamon, New York, 1979), Chap. 5, pp. 174–184.
[25] I. M. Fuks, ''Correlation of the fluctuations of frequency-spaced signals in a randomly inhomogeneous medium,'' Radiophys. Quantum Electron. **27**(7), 1272–76 (1974).
[26] V. Freilikher and I. Fuks, ''Influence of refractive index fluctuations on the attenuation of the field in a tropospheric duct,'' Radiophys. Quantum Electron. **24**(4), 281–286 (1981).
[27] T. F. Duda, ''Modeling weak fluctuations of undersea telemetry signals,'' IEEE J. Ocean Eng. **16**(1), 3–11 (1991).
[28] T. E. Ewart, ''A model of the intensity probability distribution for waves propagating in random media,'' J. Acoust. Soc. Am. **86**, 1490–1498 (1989).
[29] W. H. Munk and F. Zachariasen, ''Sound propagation through a fluctuating stratified ocean: Theory and observation,'' J. Acoust. Soc. Am. **59**, 818–838 (1976).
[30] S. M. Flatté, R. Leung, and S. Y. Lee, ''Frequency spectra of acoustic fluctuations caused by oceanic internal waves and other fine structure,'' J. Acoust. Soc. Am. **68**, 1773–1779 (1980).

Stationary velocity and pressure gradients in a thermoacoustic stack

Roger Waxler[a)]
Graduate Program in Acoustics, Penn State University, University Park, Pennsylvania 16802

(Received 19 May 2000; revised 12 February 2001; accepted 21 February 2001)

The second-order time-averaged acoustics of a viscous, thermally conducting gas between closely spaced parallel plates is studied. The acoustic disturbance is studied by expanding the equations of fluid dynamics and heat transfer to second order in Mach number. The undisturbed state is allowed to have a nonzero temperature gradient. A set of coupled equations for the time-averaged pressure gradient, velocity, and temperature are obtained and solved. Particular attention is paid to the relation between the time-averaged mass flux and pressure gradient. An explicit expression is obtained relating the time-averaged pressure drop across a thermoacoustic stack to the time-averaged mass flux through the stack. © *2001 Acoustical Society of America.*
[DOI: 10.1121/1.1370358]

PACS numbers: 43.35.Ud, 43.25.Nm, 43.25.Qp [SGK]

I. INTRODUCTION

Rott's treatment of the theoretical acoustics of a viscous, thermally conducting gas in a narrow pipe with a mean-temperature gradient imposed along the axis of the pipe[1] has become the basis for the modeling of thermoacoustic engines.[2,3] By making the standard acoustic expansion in powers of Mach number of the equations of fluid dynamics Rott used his solution of the linearized problem to estimate the second-order contribution to the time-averaged temperature gradient normal to the walls of the pipe. This allowed him to estimate the time-averaged power flux which arises at second order. It is this power flux which is exploited in thermoacoustic engines.

There are several time-averaged quantities which are zero in the linear approximation, but can become nonzero at second order. These include, in addition to the power flux and temperature gradients, velocity, pressure gradients, and mass flux. These effects are all coupled to each other and it has become apparent that a nonzero mass flux can significantly degrade the performance of an engine.[4,5]

In Fig. 1, the geometry to be considered in this paper is depicted: a stack of parallel plates in a duct or resonator. The mean temperatures to the left and to the right of the stack, T_L and T_R, respectively, are not necessarily equal so that there may be a mean-temperature gradient in the stack along the duct's axis. Two distinct mechanisms have been identified through which time-averaged mass flux induced by the presence of the stack can degrade performance.[6] These are depicted in Fig. 1. There can be a net mass flow through the duct itself, mixing gas of one temperature from one side of the stack with gas of another temperature on the other side of the stack. In addition, there can be flow which is concentrated in the neighborhood of the stack. Mass can flow out of one of the channels formed by a pair of parallel plates and back into another, again mixing gas of different mean temperatures.

Two distinct types of devices can be identified (see Fig. 2) depending on the topology of the branch in which the stack is found. In one type, the stack is located in a loop. For these devices mass flux through the duct can be a serious problem and techniques to control it are being developed.[4,5] In the other type, the stack is located in a dead end so that mass conservation prevents mass flux through the duct. For these devices only the latter form of mass flux, out one channel and in another, is possible. Such behavior has been observed,[7] but it is not yet clear how much of an effect it has on performance.

A prerequisite to the understanding of both types of time-averaged mass flux in a thermoacoustic stack is an understanding of the same phenomena in one channel of the stack, between a single pair of parallel plates. Developing a theory for and estimating the time-averaged velocity and pressure produced by sound at constant mean temperature is a classical problem. The time-averaged velocity induced by standing waves in ducts was first considered by Lord Rayleigh (see Sec. 352 of Ref. 8). An extension of Rayleigh's theory to traveling waves in ducts was first considered by Eckart.[9] In all these cases the ducts considered are wide compared to both the thermal and viscous penetration depths but are narrow compared to an acoustic wavelength. Recent reviews can be found in Refs. 10 and 11.

For applications to thermoacoustics one must allow the stack to have a mean-temperature gradient along the duct axis. Further, the spacing between the parallel plates in the stack is typically comparable to the thermal or viscous penetration depths. The classical theory has been extended by Rott to include sound in ducts in which there is a mean-temperature gradient,[12] however, Rott works in the boundary-layer approximation which is valid when the ducts considered are wide compared to both the thermal and viscous penetration depths. In the calculations presented here, the problem is solved for arbitrary imposed temperature gradient, arbitrary boundary conditions, and a range of plate

[a)]Current address: National Center for Physical Acoustics, University of Mississippi, University, MS 38677; electronic mail: rwax@olemiss.edu

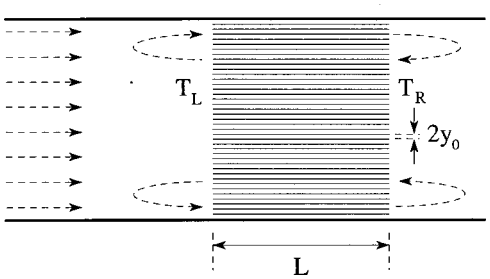

FIG. 1. Time-averaged mass flux through a stack.

separations which interpolates between the boundary-layer approximation and the limit in which the plates touch.

The conclusions of the classical theory differ, depending on whether the sound field has traveling- or standing-wave phasing. In a traveling wave (see Ref. 13), the density and velocity fluctuations are in phase with each other. When the velocity in the direction of propagation is greatest, the density is greatest as well, and when the velocity is greatest opposite to the direction of propagation, the density is least. Thus, in an acoustic cycle, more mass is moved in the direction of propagation than opposite to the direction of propagation. This leads to a time-averaged mass flux. The only way this mass flux can be canceled is by the flow which would result from a small opposing pressure gradient.

In a standing wave (the mathematical argument behind this physical picture goes back to Lord Rayleigh[8]), the density and velocity fluctuations are out of phase with each other so that the acoustic pumping of mass found in traveling waves does not occur. However, in a standing wave, the velocity is in phase with its gradient. At a given point, faster-moving gas is advected in one direction during one half of the acoustic cycle while slower-moving gas is advected in the opposite direction during the other half of the acoustic cycle. This leads to a time-averaged acceleration. The pressure associated with this acceleration is known as the acoustic-Bernoulli effect.

Near a boundary, in the thermoviscous boundary layer, phase gets distorted (again, this goes back to Lord Rayleigh[8]). There is never pure-standing- or traveling-wave phasing. All of the fluctuating quantities have components in phase with each other. Thus, in the boundary layer there is both acoustic mass pumping as well as acoustic-Bernoulli pressure. A thermoacoustic stack, where the boundary layer fills the channels between the plates, can be a significant source of mass flux.

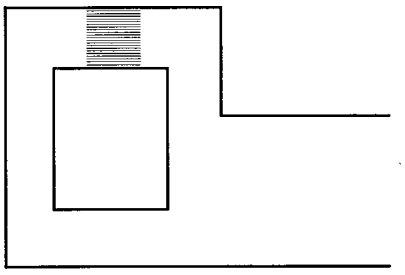

A stack in a loop.

A stack in a dead end.

FIG. 2. Two distinct duct topologies: a stack in a loop or a stack in a dead end.

The design of Stirling cycle acoustic devices often incorporates an element similar to a thermoacoustic stack know as a regenerator.[6] The chief distinction between regenerators and stacks is that regenerators tend to be more like a porous medium, consisting of extremely narrow, smaller than the viscous penetration depth, tortuous paths. It was noted by Gedeon[14] that in a regenerator the time-averaged mass flux is proportional to the acoustic intensity. These ideas apply equally well to the straight channels of a thermoacoustic stack. Swift, Gardner, and Backhaus,[4] expanding on ideas of Gedeon,[14] produced an estimate for the time-averaged pressure gradient needed for there to be no mass flux. They arrive at this estimate by arguing that the pressure gradient should be sufficient to produce enough flow (assuming Poiseille flow[15]) to cancel the time-averaged mass flux produced by the acoustic field. They estimate the mass flux produced by the acoustic field by computing the time average of the product of density and velocity in the acoustic approximation, ignoring the acoustic-Bernoulli effect.

In this paper, the complete set of time-averaged second-order equations is solved for parallel plates. The approximations made are valid as long as the plate spacing is not too much greater than the thermal penetration depth. For wider plate spacings the flow is expected to be turbulent.[6] In particular, the entire range of interest for thermoacoustic engines, from plate spacings of several thermal penetration depths down to zero, is accessible. New results include expressions for the time-averaged velocity as well as for the relation between pressure gradient and mass flux. It is shown that the results of Swift, Gardner, and Backhaus [see Eq. (19) of Ref. 4] are valid in this parallel-plate geometry only when the plate spacing is much less than the viscous penetration depth. For larger plate spacings the acoustic-Bernoulli effect becomes important.

It should be emphasized that the calculations are done in a single channel. While this is a prerequisite for understanding mass flux through a stack, conclusions can be drawn only in the case in which the behavior in each channel is identical. In particular, the component of the mass flux which only involves circulation out one channel and in another will not be specifically addressed in this paper. This effect, due presumably to thermal convection or to inhomogeneities either in the construction of the stack or in the time-averaged pressure field which develops outside the stack in the resonator, will require additional investigation.

II. GENERAL FORMULATION OF THE PROBLEM

Consider a stack of parallel plates located somewhere in a gas-filled duct or resonator. The spacing between plates is $2y_0$, the length of the stack is L, and the width is large enough that one can assume that variables are constant in the

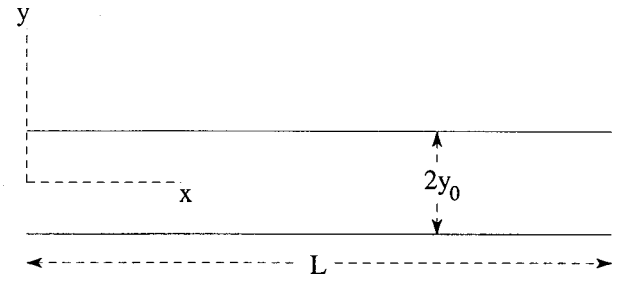

FIG. 3. Single channel in the stack with the coordinate system used for calculations.

direction perpendicular to the page. The calculations are done in a single channel between a pair of plates as depicted in Fig. 3. The axis perpendicular to the plates is the y axis. $y=0$ is chosen to be the midpoint between the two adjacent plates. The axis parallel to the plates is the x axis. $x=0$ is chosen to be the beginning of the stack on the left.

The gas is described by the density ρ, entropy S, pressure P, temperature T, and local velocity $\mathbf{v}$. The equation of state of the gas is taken to be the ideal gas relation

$$\rho=\frac{P}{RT}. \tag{1}$$

Here, R is the universal gas constant. Assuming that the specific heat per unit mass at constant pressure c_p is constant, the entropy is given by

$$S=c_p \ln T - R \ln P + \text{const.} \tag{2}$$

These thermodynamic equations are supplemented by the three conservation laws:[15] conservation of mass is expressed by the equation of continuity

$$\frac{\partial \rho}{\partial t}+\nabla\cdot(\rho\mathbf{v})=0, \tag{3}$$

conservation of momentum by the Navier–Stokes equation

$$\rho\left(\frac{\partial}{\partial t}+\mathbf{v}\cdot\nabla\right)\mathbf{v}=-\nabla P+\eta\nabla(\nabla\cdot\mathbf{v})-\mu\nabla\times(\nabla\times\mathbf{v}), \tag{4}$$

where $\eta=\mu_B+\frac{4}{3}\mu$, μ is the shear viscosity, and μ_B is the bulk viscosity, and conservation of energy by the equation of heat transfer

$$\rho T\left(\frac{\partial}{\partial t}+\mathbf{v}\cdot\nabla\right)S=\kappa\nabla^2 T+\frac{\mu}{2}\sum_{jk}\left(\frac{\partial v_j}{\partial x_k}+\frac{\partial v_k}{\partial x_j}-\frac{2}{3}\delta_{jk}\nabla\cdot\mathbf{v}\right)^2 + \mu_B(\nabla\cdot\mathbf{v})^2, \tag{5}$$

where κ is the thermal conductivity of the gas and δ_{jk}, 0 if $j\neq k$ and 1 if $j=k$, is the Kronecker delta. Variations in the viscosities and the thermal conductivity are ignored.

In addition to the conservation laws there are boundary conditions. At gas/solid interfaces the gas velocity is zero, $\mathbf{v}(x,y_0)=0$. The solid portion of the stack is assumed to be rigid and to have large thermal conductivity compared to the gas. Thus, gas/solid interfaces are taken to be isothermal $T(x,y_0,t)=T_0$, where T_0 is the temperature in the absence of the acoustic disturbance. Along the center of the pore, $y=0$, symmetry dictates that $(\partial T/\partial y)|_{y=0}=0$, $(\partial P/\partial y)|_{y=0}=0$, $(\partial v_x/\partial y)|_{y=0}=0$, and $v_y(x,0)=0$. Boundary conditions at the open ends of the pores, $x=0$ and $x=L$, will be treated as unknown in this paper and will be discussed further as the analysis develops.

The steady-state response to driving the system at frequency $\omega/2\pi$ is to be estimated. The analysis will be restricted to a region far enough from the ends of the stack to ignore entrance effects. Thus, the analysis to be presented is applicable inside the stack for distances much greater than both y_0 and the displacement amplitude $|v_x(x,y,t)|/\omega$ from the ends. Near the ends of the stack it is expected that nonperturbative effects become important.[16]

In the gas there are several length scales. Let P_0 be the pressure in the absence of the acoustic disturbance. Then, one has the viscous penetration depth

$$\delta_\mu=\sqrt{\frac{2\mu RT_0}{\omega P_0}}, \tag{6}$$

the thermal penetration depth

$$\delta_\kappa=\sqrt{\frac{2\kappa(\gamma-1)T_0}{\gamma\omega P_0}}, \tag{7}$$

the stack spacing y_0, the stack length L, and the wavelength

$$\lambda=\frac{2\pi\sqrt{\gamma RT_0}}{\omega}.$$

Here, γ is the ratio of specific heats $\gamma=c_p/c_V$, c_V is the specific heat per unit mass at constant density. It is assumed that δ_μ, δ_κ, and y_0 are all of comparable magnitude and δ_κ will be used to denote the scale of all three. Accordingly, it is assumed that $\delta_\kappa \ll \lambda$. Further, both y_0 and the displacement amplitude $|v_x(x,y,t)|/\omega$ are taken to be small compared to L.

Once entrance effects are negligible one expects that $\partial/\partial x \sim 1/\lambda$, that $\partial/\partial y \sim 1/\delta_\kappa$ and that the velocity in the y direction, v_y, is of order δ_κ/λ smaller than the velocity in the x direction, v_x. Keeping only leading terms in δ_κ the Navier–Stokes equation is approximated by

$$\rho\left(\frac{\partial}{\partial t}+\mathbf{v}\cdot\nabla\right)\mathbf{v}=-\nabla P+\begin{pmatrix}\mu\dfrac{\partial^2}{\partial y^2} & 0\\ (\eta-\mu)\dfrac{\partial^2}{\partial x\partial y} & \eta\dfrac{\partial^2}{\partial y^2}\end{pmatrix}\mathbf{v}. \tag{8}$$

Similarly, the heat equation becomes

$$\rho T\left(\frac{\partial}{\partial t}+\mathbf{v}\cdot\nabla\right)S=\kappa\frac{\partial^2 T}{\partial y^2}+\mu\left(\frac{\partial v_x}{\partial y}\right)^2. \tag{9}$$

The continuity equation is unchanged since $\partial v_y/\partial y$ is of the same order of magnitude as $\partial v_x/\partial x$.

Note that the y component of the Navier–Stokes equation is of order δ_κ/λ relative to the x component. Thus, $\partial P/\partial y$ is of order δ_κ/λ relative to $\partial P/\partial x$ so that, in this approximation,

$$\frac{\partial P}{\partial y}=0.$$

The usual acoustic perturbation expansion in powers of Mach number is made. Let

$$T=T_0+T_1+T_2+\cdots, \quad P=P_0+P_1+P_2+\cdots,$$

$$\rho=\rho_0+\rho_1+\rho_2+\cdots, \quad S=S_0+S_1+S_2+\cdots,$$

$$\mathbf{v}=\mathbf{v}_0+\mathbf{v}_1+\mathbf{v}_2+\cdots.$$

Here, the subscript j indicates jth order in Mach number. The zeroth-order state to be considered has $\mathbf{v}_0=0$, P_0 constant and T_0 time independent, so that at zeroth order one has

$$\nabla^2 T_0=0. \tag{10}$$

Note that both

$$\rho_0=\frac{P_0}{RT_0},$$

and

$$S_0=c_p \ln T_0 - R \ln P_0 + \text{const.},$$

are constant in time, but vary spatially through the variations in T_0. Further, $\partial T_0/\partial y=0$. It follows that T_0 is a linear function of x and is independent of y,

$$T_0(x)=T_0(0)+\frac{T_0(L)-T_0(0)}{L}x. \tag{11}$$

Note that the derivative of T_0 with respect to x is constant:

$$T_0'(x)=\frac{T_0(L)-T_0(0)}{L}.$$

The first-order equations have been solved by Rott.[1–3] Introduce the amplitudes T_A, P_A, and $\mathbf{v}_A$ by setting

$$T_1(t,x,y)=\mathrm{Re}\, T_A(x,y)e^{i\omega t},$$

$$P_1(t,x,y)=\mathrm{Re}\, P_A(x,y)e^{i\omega t},$$

$$\mathbf{v}_1(t,x,y)=\mathrm{Re}\, \mathbf{v}_A(x,y)e^{i\omega t}.$$

Introducing the Prandtl number

$$\sigma=\frac{\delta_\mu^2}{\delta_\kappa^2},$$

and, using Swift's notation,[2]

$$f_\mu=\frac{\tanh\dfrac{1+i}{\delta_\mu}y_0}{\dfrac{1+i}{\delta_\mu}y_0},$$

and

$$f_\kappa=\frac{\tanh\dfrac{1+i}{\delta_\kappa}y_0}{\dfrac{1+i}{\delta_\kappa}y_0},$$

one has

$$P_A(x,y)=p(x), \tag{12}$$

$$v_{Ax}=\frac{1}{i\omega\rho_0}\left[-1+\frac{\cosh\dfrac{1+i}{\delta_\mu}y}{\cosh\dfrac{1+i}{\delta_\mu}y_0}\right]\frac{dp}{dx}, \tag{13}$$

and

$$\frac{T_A}{T_0}=\frac{\gamma-1}{\gamma}\frac{p}{P_0}-\frac{T_0'}{\omega^2\rho_0 T_0}\frac{dp}{dx}-\frac{\sigma}{1-\sigma}\times\frac{T_0'}{\omega^2\rho_0 T_0}\frac{dp}{dx}\frac{\cosh\dfrac{1+i}{\delta_\mu}y}{\cosh\dfrac{1+i}{\delta_\mu}y_0}+\left(-\frac{\gamma-1}{\gamma}\frac{p}{P_0}+\frac{T_0'}{\omega^2\rho_0 T_0}\frac{1}{1-\sigma}\frac{dp}{dx}\right)\frac{\cosh\dfrac{1+i}{\delta_\kappa}y}{\cosh\dfrac{1+i}{\delta_\kappa}y_0}. \tag{14}$$

S_1 and ρ_1 can be found from (1) and (2),

$$\frac{\rho_1}{\rho_0}=\frac{P_1}{P_0}-\frac{T_1}{T_0}, \tag{15}$$

and

$$\frac{S_1}{R}=\frac{\gamma}{\gamma-1}\frac{T_1}{T_0}-\frac{P_1}{P_0}. \tag{16}$$

The pressure amplitude $p(x)$ satisfies Rott's equation

$$\left[(1-f_\mu)\frac{d^2}{dx^2}+\frac{T_0'}{T_0}\left(1-\frac{1}{2}\delta_\mu\frac{\partial f_\mu}{\partial\delta_\mu}-\frac{f_\kappa-\sigma f_\mu}{(1-\sigma)}\right)\frac{d}{dx}+\frac{\omega^2}{c^2}(1+(\gamma-1)f_\kappa)\right]p=0, \tag{17}$$

which must be solved numerically.

It will be necessary to have v_{1y}, even though it is order δ_κ/λ smaller than v_{1x}, since derivatives $\partial v_{1y}/\partial y$ will arise at second order. It follows from the linearized equation of continuity that

$$v_{Ay}=-\int_0^y\left(i\omega\frac{P_A}{P_0}-i\omega\frac{T_A}{T_0}+T_0\frac{\partial}{\partial x}\frac{1}{T_0}v_{Ax}\right)dy', \tag{18}$$

which becomes, on substituting (12), (13), and (14) in (18) and using (17),[1]

$$v_{Ay}=\frac{1}{i\omega\rho_0}\left(\frac{d^2p}{dx^2}+\frac{1+\sigma}{2(1-\sigma)}\frac{T_0'}{T_0}\frac{dp}{dx}\right)\times\left(\frac{1}{\frac{1+i}{\delta_\mu}}\frac{\sinh\frac{1+i}{\delta_\mu}y}{\cosh\frac{1+i}{\delta_\mu}y_0}-f_\mu y\right)+\frac{T_0'}{2i\omega\rho_0T_0}\frac{dp}{dx}\times\left(\frac{1+i}{\delta_\mu}y_0^2f_\mu\frac{\sinh\frac{1+i}{\delta_\mu}y}{\cosh\frac{1+i}{\delta_\mu}y_0}-\frac{y\cosh\frac{1+i}{\delta_\mu}y}{\cosh\frac{1+i}{\delta_\mu}y_0}+\frac{y}{\cosh^2\frac{1+i}{\delta_\mu}y_0}\right)-\frac{i\omega(\gamma-1)}{\gamma P_0}\times\left(p-\frac{c_pT_0'}{\omega^2(1-\sigma)}\frac{dp}{dx}\right)\left(\frac{1}{\frac{1+i}{\delta_\kappa}}\frac{\sinh\frac{1+i}{\delta_\kappa}y}{\cosh\frac{1+i}{\delta_\kappa}y_0}-f_\kappa y\right). \tag{19}$$

We are interested in the time-independent parts of the second-order variables T_2, P_2, and $\mathbf{v}_2$. A convenient way to extract time-independent parts is to use the time average

$$\langle f\rangle=\lim_{\tau\to\infty}\frac{1}{\tau}\int_0^\tau f(t)dt.$$

Note that $\langle T_1\rangle=\langle P_1\rangle=\langle\mathbf{v}_1\rangle=\langle\rho_1\rangle=\langle S_1\rangle=0$. Introduce the notation $\mathbf{u}_2=\langle\mathbf{v}_2\rangle$, $p_2=\langle P_2\rangle$, and $t_2=\langle T_2\rangle$ for the second-order time-averaged velocity, pressure, and temperature fields, respectively.

Time averaging the equations of motion and expanding to second order, one obtains a set of coupled linear equations for $\mathbf{u}_2$, p_2, and t_2. The second-order time-averaged equation of continuity is

$$\nabla\cdot(\rho_0\mathbf{u}_2+\langle\rho_1\mathbf{v}_1\rangle)=0. \tag{20}$$

The x component of the second-order time-averaged Navier–Stokes equation is

$$\frac{dp_2}{dx}=\mu\frac{\partial^2u_{2x}}{\partial y^2}-\rho_0\langle(\mathbf{v}_1\cdot\nabla)v_{1x}\rangle-\left\langle\rho_1\frac{\partial v_{1x}}{\partial t}\right\rangle. \tag{21}$$

The y component of the second-order time-averaged Navier–Stokes equation will not be considered. If needed, u_{2y} can be determined by integrating the second-order continuity equation with respect to y. Finally, the second-order time-averaged heat-conduction equation is

$$\kappa\frac{\partial^2t_2}{\partial y^2}=\frac{P_0}{R}(\mathbf{u}_2\cdot\nabla S_0+\langle\mathbf{v}_1\cdot\nabla S_1\rangle)+\frac{1}{R}\left\langle P_1\left(\frac{\partial S_1}{\partial t}+(\nabla S_0)\cdot\mathbf{v}_1\right)\right\rangle-\mu\left\langle\left(\frac{\partial v_{1x}}{\partial y}\right)^2\right\rangle. \tag{22}$$

III. SOLUTION OF THE SECOND-ORDER TIME-AVERAGED EQUATIONS

Note that Eqs. (20) and (21) do not depend on t_2. Thus, one can first solve for u_{2x} and p_2 and then solve for t_2.

Integrate (20) over y from 0 to y_0 and note that

$$\int_0^{y_0}\frac{\partial}{\partial y}(\rho_0u_{2y}+\langle\rho_1v_{1y}\rangle)dy=(\rho_0u_{2y}+\langle\rho_1v_{1y}\rangle)\big|_{y=0}^{y=y_0}=0,$$

since u_{2y} and v_{1y} are both 0 when $y=y_0$ and are both odd, and thus 0 when $y=0$. Thus,

$$\frac{\partial}{\partial x}\int_0^{y_0}(\rho_0u_{2x}+\langle\rho_1v_{1x}\rangle)dy=0,$$

so that

$$\int_0^{y_0}(\rho_0u_{2x}+\langle\rho_1v_{1x}\rangle)dy=\tfrac{1}{2}\dot{M}, \tag{23}$$

for some constant $\dot{M}$. Given that the second-order time-averaged mass-flux density through the pore is given by

$$\dot{\mathbf{m}}_2=\rho_0\mathbf{u}_2+\langle\rho_1\mathbf{v}_1\rangle, \tag{24}$$

one sees that $\dot{M}$ times the width of the stack is the total time-averaged mass flux through the pore.

Using the linearized equation of continuity, it follows that for any function $f(t,x)$

$$(\mathbf{v}_1\cdot\nabla)f=\nabla\cdot(\mathbf{v}_1f)-f\nabla\cdot\mathbf{v}_1=\nabla\cdot(\mathbf{v}_1f)+\frac{1}{\rho_0}\frac{\partial\rho_1}{\partial t}f-\mathbf{v}_1\cdot\frac{\nabla T_0}{T_0}f.$$

Further, $\langle\partial f/\partial t\rangle=\langle f(\partial f/\partial t)\rangle=\langle f(\partial g/\partial t)+g(\partial f/\partial t)\rangle=0$. Using these identities and the linearized Navier–Stokes equation, the second-order time-averaged Navier–Stokes Eq. (21) can be manipulated into the form

$$\mu\frac{\partial^2u_{2x}}{\partial y^2}=\frac{dp_2}{dx}+\rho_0T_0\nabla\cdot\frac{\langle\mathbf{v}_1v_{1x}\rangle}{T_0}. \tag{25}$$

Since p_2 is constant in y this equation can be solved immediately, yielding

$$u_{2x}=\frac{y^2-y_0^2}{2\mu}\frac{dp_2}{dx}+\frac{\rho_0}{\mu}\int_{-y_0}^{y}\int_0^{y'}T_0\nabla\cdot\left(\frac{\langle\mathbf{v}_1v_{1x}\rangle}{T_0}\right)dy''dy'=\frac{y^2-y_0^2}{2\mu}\frac{dp_2}{dx}+\frac{\rho_0}{\mu}T_0\frac{\partial}{\partial x}\left[\frac{1}{T_0}\times\int_{-y_0}^{y}\int_0^{y'}\langle v_{1x}v_{1x}\rangle dy''dy'\right]+\frac{\rho_0}{\mu}\int_{-y_0}^{y}\langle v_{1y}v_{1x}\rangle dy'. \tag{26}$$

In this last equation, the integrands in the double integrals are evaluated at y'' while the integrand in the single integral is evaluated at y'. The limits of integration insure that the solution satisfies the boundary conditions $u_{2x}(\pm y_0)=0$.

Substituting (26) in (23) yields the following equation for dp_2/dx:

$$\frac{dp_2}{dx} = -\frac{3\mu}{2\rho_0 y_0^3}\dot{M} + \frac{3\mu}{y_0^3}\int_0^{y_0}\left\langle \frac{\rho_1}{\rho_0} v_{1x}\right\rangle dy + \frac{3\rho_0}{y_0^3}\int_0^{y_0}\int_{-y_0}^{y}\int_0^{y'} T_0 \nabla\cdot\frac{\langle \mathbf{v}_1 v_{1x}\rangle}{T_0} dy'' dy' dy, \tag{27}$$

with the integrand in the second integral evaluated at y''. Substituting this last equation back into (26) gives u_{2x}.

Finally, rather than solving (22), the heat flux into the stack walls, $-\kappa(\partial t_2/\partial y)|_{y=y_0}$, is considered. This quantity was originally calculated by Rott[1–3] ignoring the effect of time-averaged mass flux. In the steady state, once the temperature gradient has developed and the temperature of the stack is no longer changing, conservation of energy shows that $-2\kappa(\partial t_2/\partial y)|_{y=y_0}$ is equal to the time-averaged power flux through the gas along the x axis. One finds (the $\dot{M}=0$ version of this result has been obtained by directly calculating the power flux in the Appendix to Ref. 2):

$$\kappa\left.\frac{\partial t_2}{\partial y}\right|_{y=y_0} = \int_0^{y_0}\left[\frac{P_0}{R}(\mathbf{u}_2\cdot\nabla S_0 + \langle v_1\cdot\nabla S_1\rangle) + \frac{1}{R}\left\langle P_1\left(\frac{\partial S_1}{\partial t} + (\nabla S_0)\cdot\mathbf{v}_1\right)\right\rangle - \mu\left\langle\left(\frac{\partial v_{1x}}{\partial y}\right)^2\right\rangle\right]dy = \frac{1}{2}c_p\dot{M}T_0' + c_p\frac{d}{dx}\int_0^{y_0}\rho_0\langle v_{1x}T_1\rangle dy. \tag{28}$$

The integrals in (26) and (27) are elementary: as functions of y, the integrands are products of hyperbolic functions. These integrations yield long and extremely cumbersome expressions which are not, in themselves, very informative. Further, the appropriate solution, p, of Rott's Eq. (17), as well as its derivatives p' and p'', must be obtained numerically. The results of these integrations will be plotted below after some general remarks.

It is to be emphasized that these solutions depend on only five free real parameters. Two complex parameters are needed as boundary conditions for Rott's equation. It suffices to specify any two independent linear combinations of $p(0)$, $p'(0)$, $p(L)$, and $p'(L)$. Once these two parameters are specified the linear solutions are uniquely determined. At second order there is only one free parameter, the real mass flux $\dot{M}$.

Let

$$V = u_{2x}|_{\dot{M}=0} + \left\langle\frac{\rho_1}{\rho_0}v_{1x}\right\rangle.$$

Using (26) and (27) the x component of the second-order time-averaged mass-flux density (24) can be written

$$\dot{m}_{2x} = \rho_0 u_{2x} + \langle\rho_1 v_{1x}\rangle = -\frac{3\dot{M}(y^2-y_0^2)}{4y_0^3} + \rho_0 V. \tag{29}$$

Using (23) one finds that

$$\int_0^{y_0} V(x,y)dy = 0.$$

Equation (29) separates the second-order mass flux into two terms. The term $[-3\dot{M}(y^2-y_0^2)]/4y_0^3$ has the classical form for viscous flow in a pipe.[15] The remaining term, $\rho_0 V$, is independent of $\dot{M}$ and does not contribute to the total mass transport.

Even if there is no total mass transport, so that $\dot{M}=0$, there is still nonzero mass flux representing circulation within the channel. V can be thought of as the associated volume flux. As will be seen below, the direction of V can change as y varies from one side of the channel to the other, mixing gas of different mean temperatures. This term cannot be avoided in this parallel-plate geometry. It should be emphasized, however, that the second-order power flux is given by (28) regardless of V. Any additional degradation of performance occurs at higher order in Mach number.

If the mass flux $\dot{M}$ is nonzero it should not be thought of as externally imposed flow. Rather, it develops in response to nonlinear effects in the pore as well as to externally imposed pressure differences. Note that the pressure difference across the stack, Δp_2, is given by

$$\Delta p_2 = p_2(L) - p_2(0) = -\frac{3\mu R[T_0(L)+T_0(0)]L}{4P_0 y_0^3}\dot{M} + \int_0^L \left.\frac{dp_2}{dx}\right|_{\dot{M}=0} dx, \tag{30}$$

with

$$\left.\frac{dp_2}{dx}\right|_{\dot{M}=0} = \frac{3\mu}{y_0^3}\int_0^{y_0}\left\langle\frac{\rho_1}{\rho_0}v_{1x}\right\rangle dy + \frac{3\rho_0}{y_0^3}\int_0^{y_0}\int_{-y_0}^{y}\int_0^{y'} T_0\nabla\cdot\frac{\langle\mathbf{v}_1 v_{1x}\rangle}{T_0}dy''dy'dy.$$

Thus, $\dot{M}$ is not simply the mass flux which would develop in response to a pressure difference Δp_2. In particular, if a time-averaged pressure difference across the pore cannot be maintained so that $p_2(L)=p_2(0)$, then there must be be a nonzero time-averaged mass flux

$$\dot{M}|_{\Delta p_2=0} = \frac{4P_0 y_0^3}{3\mu R[T_0(L)+T_0(0)]L}\int_0^L\left.\frac{dp_2}{dx}\right|_{\dot{M}=0} dx.$$

In this case, (29) shows that the mass flux is given by the term $\rho_0 V$ plus the Poiseille flow which would result from a pressure gradient $-(dp_2/dx)|_{\dot{M}=0}$. Conversely, if there is to be no net mass flux through the pore, then there must be a time-averaged pressure difference

$$\Delta p_2|_{\dot{M}=0} = \int_0^L\left.\frac{dp_2}{dx}\right|_{\dot{M}=0} dx, \tag{31}$$

across the pore.

As mentioned, the treatment in this paper is not general enough to describe the pressure gradients which develop near the pore openings. However, if the plates are much longer than the distance over which entrance effects persist then the relation between mass flux and pressure gradient is given by (27) over most of the stack. Thus, if the stack is long enough, then the relation between $\dot{M}$ and the time-averaged pressure difference is given by (30).

IV. TIME-AVERAGED PRESSURE DROP

As a consequence of (30), there is a linear relation between the total time-averaged mass flux $\dot{M}$ and the time-averaged pressure drop Δp_2. The slope in this linear relationship,

$$\frac{d\Delta p_2}{d\dot{M}} = -\frac{3\mu R[T_0(L)+T_0(0)]L}{4P_0 y_0^3},$$

is a simple function of the parameters and is the same slope that would result from an applied pressure drop in the absence of the acoustic disturbance. The intercept in this linear relation, $\Delta p_2|_{\dot{M}=0}$, is a quite complicated function of the parameters. Further, $\Delta p_2|_{\dot{M}=0}$ contains the nonlinear effects of the acoustic disturbance: in particular, in the absence of an acoustic disturbance $\Delta p_2|_{\dot{M}=0}=0$. Once $\Delta p_2|_{\dot{M}=0}$ is known, the relation between $\dot{M}$ and Δp_2 is also known.

It is thus necessary to compute $\Delta p_2|_{\dot{M}=0}$. As mentioned, the integrals in Eqs. (26) and (27) are all elementary, however, in addition to solutions of Rott's equation, the integral over x in (31) must be obtained numerically.

Before plotting the results of the numerical integrations, the small and large y_0 limits are discussed. Small y_0 asymptotics are developed first [see, also, Sec. 350, Eq. (29) of Ref. 8], treating the Prandtl number σ as an $\mathcal{O}(1)$ constant. For $y_0 \ll \delta_\kappa$, one then has

$$f_\mu = 1 - \frac{2}{3} i \frac{y_0^2}{\delta_\mu^2} + \mathcal{O}\left(\frac{y_0^4}{\delta_\mu^4}\right),$$

and

$$f_\kappa = 1 - \frac{2}{3} i \frac{y_0^2}{\delta_\kappa^2} + \mathcal{O}\left(\frac{y_0^4}{\delta_\kappa^4}\right).$$

Rott's equation becomes

$$\left[\frac{d^2}{dx^2} - i\frac{3}{2}\frac{\omega^2}{RT_0}\frac{\delta_\mu^2}{y_0^2} + \mathcal{O}\left(\frac{\delta_\mu}{y_0}\right)\right] p(x) = 0,$$

so that

$$p(x) \approx A e^{-(1+i)(\omega\sqrt{3}/2\sqrt{RT_0})(\delta_\mu/y_0)x} + B e^{(1+i)(\omega\sqrt{3}/2\sqrt{RT_0})(\delta_\mu/y_0)(x-L)}.$$

In particular, the acoustic pressure field becomes evanescent, only penetrating a distance on the order of $(\omega/\sqrt{RT_0})\times(\delta_\mu/y_0)$, that is, 2π divided by the isothermal wavelength times the ratio of viscous penetration depth to y_0. Further, if

$$\frac{\omega L}{\sqrt{RT_0}} \gg \frac{y_0}{\delta_\mu},$$

then one has

$$p(x) \approx p(0) e^{-(1+i)(\omega\sqrt{3}/2\sqrt{RT})(\delta_\mu/y_0)x} + p(L) e^{(1+i)(\omega\sqrt{3}/2\sqrt{RT_0})(\delta_\mu/y_0)(x-L)}. \quad (32)$$

Proceeding, assuming that the isothermal wavelength is $\mathcal{O}(1)$, and then noting that

$$\frac{d^n p}{dx^n} \sim \left(\frac{\omega}{\sqrt{RT_0}}\frac{\delta_\mu}{y_0}\right)^n p,$$

for v_{Ax} one has

$$v_{Ax} = \frac{1}{\omega\rho_0}\frac{(y^2-y_0^2)}{\delta_\mu^2}\frac{dp}{dx} + \mathcal{O}\left(\frac{p}{\rho_0 c}\frac{y_0^3}{\delta_\kappa^2}\right),$$

for T_A and ρ_A

$$\frac{T_A}{T_0} = \mathcal{O}\left(\frac{y_0}{\delta_\kappa}\right),$$

and

$$\frac{\rho_A}{\rho_0} = \frac{p}{P_0} + \mathcal{O}\left(\frac{y_0}{\delta_\kappa}\right),$$

and for v_{Ay}

$$v_{Ay} = \frac{1}{6\omega\rho_0}\frac{y(y^2-y_0^2)}{\delta_\mu^2}\frac{d^2p}{dx^2} + \mathcal{O}\left(\omega y_0 \frac{p}{P_0}\frac{y_0^2}{\delta_\kappa^2}\right).$$

Substituting these formulas into (27), one finds that

$$\left.\frac{dp_2}{dx}\right|_{\dot{M}=0} = -\frac{1}{2P_0}\mathrm{Re}\left(p^*\frac{dp}{dx}\right) + \mathcal{O}\left(\frac{p^2}{P_0}\frac{\omega}{\sqrt{RT_0}}\frac{y_0}{\delta_\kappa}\right).$$

Note that only the term with the time average $\langle \rho_1 v_{1x}\rangle$ contributes as $y_0 \downarrow 0$. Further, in this limit length scales are determined only by δ_μ. Even though $dp_2/dx|_{\dot{M}=0}$ diverges like δ_μ/y_0 as $y_0/\delta_\mu \downarrow 0$, the region over which $dp_2/dx|_{\dot{M}=0}$ is not negligible is of order y_0/δ_μ so that $\Delta p_2|_{\dot{M}=0}$ remains finite. One finds

$$\begin{aligned}\Delta p_2|_{\dot{M}=0} &= -\frac{1}{2P_0}\mathrm{Re}\int_0^L p^*\frac{dp}{dx}dx + \mathcal{O}\left(\frac{|p(0)|^2+|p(L)|^2}{P_0}\frac{y_0^2}{\delta_\kappa^2}\right)\\ &= -\frac{|p(L)|^2-|p(0)|^2}{4P_0} + \mathcal{O}\left(\frac{|p(0)|^2+|p(L)|^2}{P_0}\frac{y_0^2}{\delta_\kappa^2}\right). \quad (33)\end{aligned}$$

For $y_0 \gg \delta_\kappa$, one recovers the adiabatic limit: $f_\kappa \approx 0$ and $f_\mu \approx 0$. In this limit the solutions to Rott's equations are linear combinations of the Bessel functions $J_0(2\omega\sqrt{T_0(x)}/\sqrt{\gamma R T_0'})$ and $Y_0(2\omega\sqrt{T_0(x)}/\sqrt{\gamma R T_0'})$. Further, for $y_0 - |y| \gg \delta_\kappa, v_{Ay} \approx 0$,

$$v_{Ax} \approx \frac{i}{\omega\rho_0}\frac{dp}{dx},$$

$$\frac{T_A}{T_0} \approx \frac{\gamma-1}{\gamma}\frac{p}{P_0} - \frac{T_0'}{\omega^2 \rho_0 T_0}\frac{dp}{dx},$$

and

$$\frac{\rho_A}{\rho_0} \approx \frac{1}{\gamma}\frac{p}{P_0} + \frac{T_0'}{\omega^2 \rho_0 T_0}\frac{dp}{dx}.$$

Substituting these formulas into (27), one finds

$$\left.\frac{dp_2}{dx}\right|_{\dot{M}=0} = -\frac{R}{2\omega^2 P_0}\frac{d}{dx}\left(T_0\left|\frac{dp}{dx}\right|^2\right)\left[1+\mathcal{O}\left(\frac{\delta_\kappa}{y_0}\right)\right],$$

so that integrating and using the ideal gas law, one obtains [in agreement with the result previously obtained by Rott, Eq. (12) of Ref. 12 using the boundary-layer approximation]

$$\Delta p_2|_{\dot{M}=0} \approx -\frac{1}{2\omega^2\rho_0}\left|\frac{dp}{dx}\right|^2\Bigg|_{x=L}^{x=0} \approx -\frac{\rho_0}{2}|v_{Ax}|^2\Bigg|_{x=L}^{x=0}.$$

Note that, here, only the term containing the time average $\langle \mathbf{v}_1 v_{1x}\rangle$ contributes.

We now turn to the numerical solution for $y_0 \sim \delta_\kappa$. Boundary conditions are needed to produce a unique solution to Rott's equation. Consider the case in which the linear pressure amplitude is specified at either end of the pore. Thus, boundary conditions

$$p(0) = p_l P_0,$$

and

$$p(L) = p_r P_0,$$

are imposed. Here, p_l and p_r depend on the particular device. A simple way to satisfy these conditions is to produce two solutions of Rott's equation, labeled $p_\pm$, with $p_-(0)=1$, $p_-(L)=0$, and $p_+(0)=0$, $p_+(L)=1$. Then,

$$\frac{p}{P_0} = p_l p_- + p_r p_+ .$$

Inspection of (13), (14), and (18) shows that, using the formula $\langle f_g\rangle = \frac{1}{2}\mathrm{Re}\, f^* g$,

$$\frac{1}{P_0}\Delta p_2|_{\dot{M}=0} = \mathcal{P}_-|p_l|^2 + \mathcal{P}_+|p_r|^2 + 2\,\mathrm{Re}\,\mathcal{P}_c p_l^* p_r, \quad (34)$$

where $\mathcal{P}_\pm$ is given by

$$\mathcal{P}_\pm = \frac{1}{P_0}\Delta p_2|_{\dot{M}=0, p=p_\pm},$$

and introducing the notation

$$\Delta_{-+} = \frac{3\mu}{y_0^3}\int_0^{y_0}\left\langle \frac{\rho_1}{\rho_0}\Big|_{p=p_-} v_{1x}|_{p=p_+}\right\rangle dy + \frac{3\rho_0}{y_0^3} \times \int_0^{y_0}\int_{-y_0}^{y}\int_0^{y'} T_0\nabla\cdot\frac{\langle \mathbf{v}_1|_{p=p_-} v_{1x}|_{p=p_+}\rangle}{T_0}dy''dy'dy,$$

and

$$\Delta_{+-} = \frac{3\mu}{y_0^3}\int_0^{y_0}\left\langle \frac{\rho_1}{\rho_0}\Big|_{p=p_+} v_{1x}|_{p=p_-}\right\rangle dy + \frac{3\rho_0}{y_0^3} \times \int_0^{y_0}\int_{-y_0}^{y}\int_0^{y'} T_0\nabla\cdot\frac{\langle \mathbf{v}_1|_{p=p_+} v_{1x}|_{p=p_-}\rangle}{T_0}dy''dy'dy,$$

$\mathcal{P}_c$ is given by

$$\mathcal{P}_c = \frac{1}{4P_0}\int_0^L(\Delta_{-+}+\Delta_{+-}^*)dx.$$

Using the standard notation, $\langle \mathbf{v},\mathbf{w}\rangle = \mathbf{v}^*\cdot\mathbf{w}$, for the inner product of two complex vectors, Eq. (34) may be written

$$\frac{1}{P_0}\Delta p_2|_{\dot{M}=0} = \left\langle \begin{pmatrix} p_l \\ p_r\end{pmatrix}, \mathcal{P}\begin{pmatrix} p_l \\ p_r\end{pmatrix}\right\rangle,$$

with

$$\mathcal{P} = \begin{pmatrix} \mathcal{P}_- & \mathcal{P}_c \\ \mathcal{P}_c^* & \mathcal{P}_+\end{pmatrix}.$$

Note that $\mathcal{P}$ is a self-adjoint matrix. Its eigenvalues are

$$E_\pm = \tfrac{1}{2}(\mathcal{P}_- + \mathcal{P}_+ \pm \sqrt{(\mathcal{P}_- - \mathcal{P}_+)^2 + 4|\mathcal{P}_c|^2}),$$

and a convenient choice for the corresponding normalized eigenvectors is

$$A_- = \frac{1}{\sqrt{(\mathcal{P}_+ - E_+)^2 + |\mathcal{P}_c|^2}}\begin{pmatrix} \mathcal{P}_c \\ \mathcal{P}_+ - E_+\end{pmatrix},$$

and

$$A_+ = \frac{1}{\sqrt{(\mathcal{P}_+ - E_+)^2 + |\mathcal{P}_c|^2}}\begin{pmatrix} \mathcal{P}_+ - E_+ \\ \mathcal{P}_c^*\end{pmatrix}.$$

The vectors $A_\pm$ form an orthonormal basis for $\mathbf{C}^2$ so that, given p_l and p_r, one may write

$$\begin{pmatrix} p_l \\ p_r\end{pmatrix} = \alpha A_- + \beta A_+ ,$$

with

$$\alpha = \left\langle A_-, \begin{pmatrix} p_l \\ p_r\end{pmatrix}\right\rangle,$$

and

$$\beta = \left\langle A_+, \begin{pmatrix} p_l \\ p_r\end{pmatrix}\right\rangle.$$

It follows that

$$\frac{1}{P_0}\Delta p_2|_{\dot{M}=0} = |\alpha|^2 E_- + |\beta|^2 E_+ . \quad (35)$$

The eigenvalues $E_\pm$ and eigenvectors $A_\pm$ are plotted in Figs. 4, 5, and 6 as functions of $y_0/\delta_\kappa|_{x=L}$. The stack length is taken to be $0.05\lambda|_{x=L}$. With these dimensionless measures of y_0 and L it is not necessary to specify the frequency. Other than the Prandl number σ, the thermophysical parameters are those appropriate to dry air at room temperature: $\gamma = 1.4$ and $\kappa = 0.026\,24$ W/K/m. To display the interplay between thermal and viscous effects σ is allowed to vary. The right-side temperature is fixed at $T_0(L) = 290$ K.

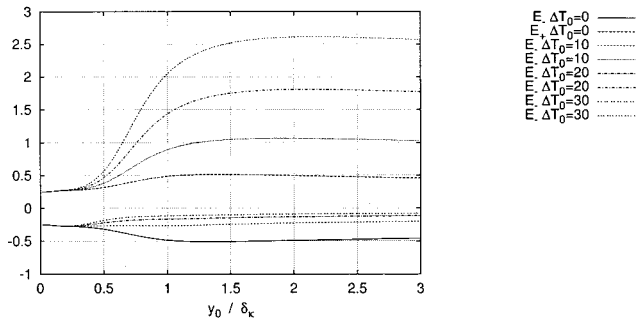

FIG. 4. Eigenvalues $E_{\pm}\times 10^{10}$ with $\sigma=0.7$; $\Delta T_0=0$, 10, 20, and 30 K; and $L=0.05\lambda|_{x=L}$.

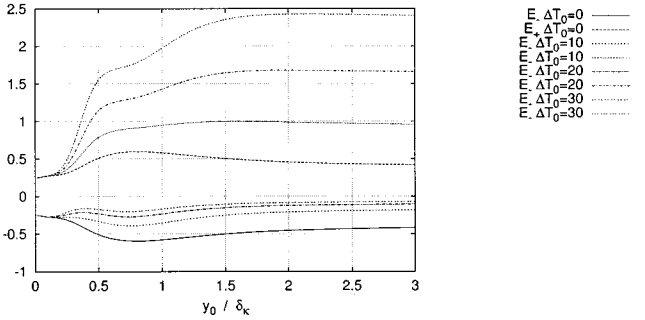

FIG. 5. Eigenvalues $E_{\pm}\times 10^{10}$, with $\sigma=0.2$; $\Delta T_0=0$, 10, 20, and 30 K; and $L=0.05\lambda|_{x=L}$.

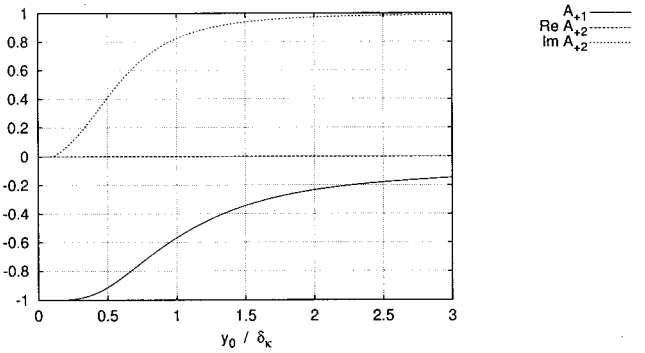

FIG. 6. Components of the eigenvectors $A_{\pm}$ with $\Delta T_0=0$ K, $\sigma=0.7$, and $L=0.05\lambda|_{x=L}$.

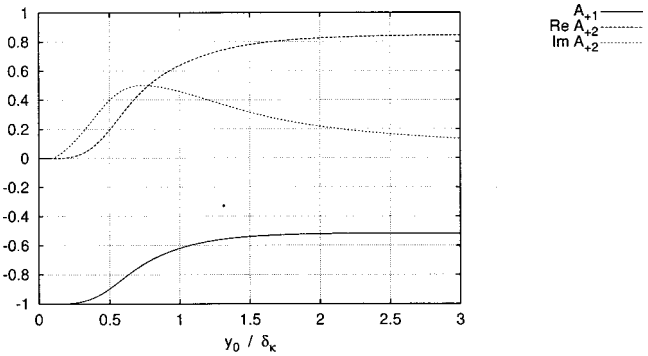

FIG. 7. Components of the eigenvectors $A_{\pm}$ with $\Delta T_0=20$ K, $\sigma=0.7$, and $L=0.05\lambda|_{x=L}$.

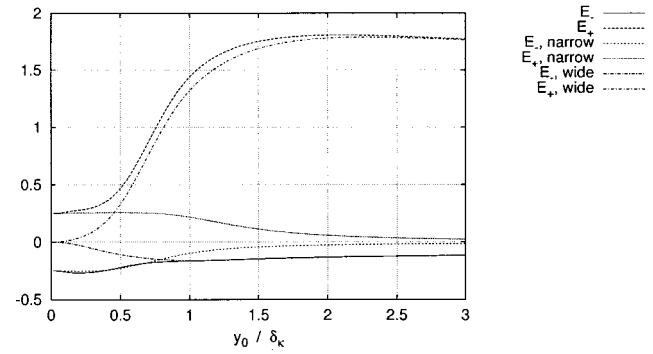

FIG. 8. Comparison of the exact eigenvalues $E_{\pm}\times 10^{10}$ to the narrow and wide approximations. $\Delta T_0=20$ K, $L=0.05\lambda|_{x=L}$, and $\sigma=0.7$.

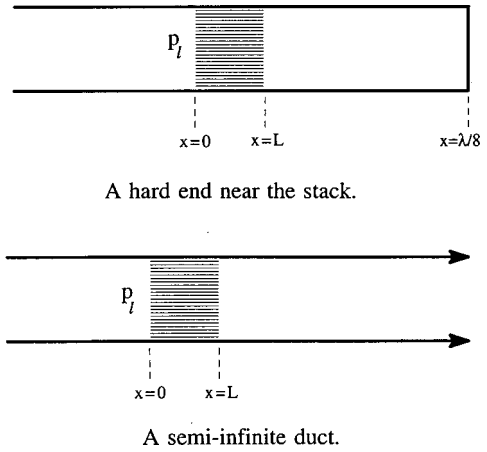

FIG. 9. Two model cases: a standing wave near a closed end and a traveling wave in a semi-infinite duct.

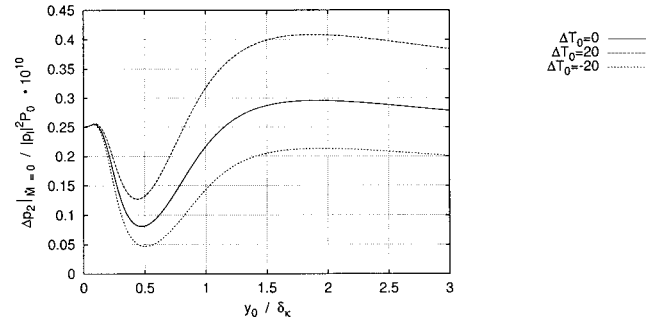

FIG. 10. Normalized pressure difference $\Delta p_2/|p_l|^2P_0|_{M=0}\times 10^{10}$ for the standing wave. $\Delta T_0=0$ K, $\Delta T_0=20$ K, $L=0.05\lambda|_{x=L}$, and $\sigma=0.7$.

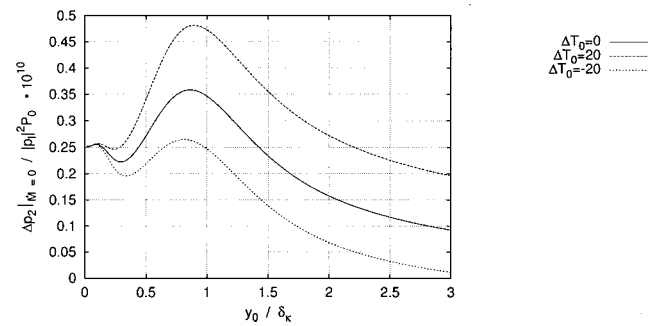

FIG. 11. Normalized pressure difference $\Delta p_2/|p_l|^2P_0|_{M=0}\times 10^{10}$ for the traveling wave. $\Delta T_0=0$ K, $\Delta T_0=20$ K, $L=0.05\lambda|_{x=L}$, and $\sigma=0.7$.

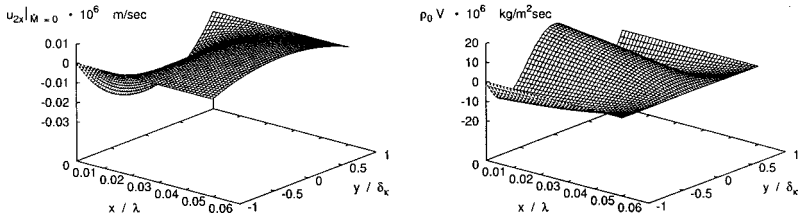

FIG. 12. Time-averaged velocity $u_{x2}|_{\dot{M}=0}\times 10^6$ and mass flux $\rho_0 V\times 10^6$ for the standing wave. $\Delta T_0 = -20$ K and $y_0/\delta_\kappa = 0.3$.

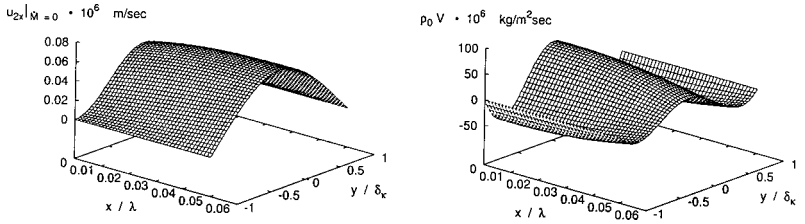

FIG. 13. Time-averaged velocity $u_{x2}|_{\dot{M}=0}\times 10^6$ and mass flux $\rho_0 V\times 10^6$ for the standing wave. $\Delta T_0 = -20$ K and $y_0/\delta_\kappa = 0.8$.

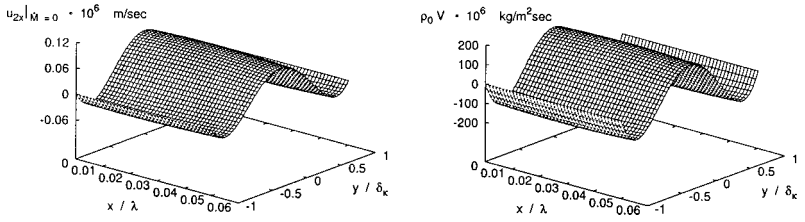

FIG. 14. Time-averaged velocity $u_{x2}|_{\dot{M}=0}\times 10^6$ and mass flux $\rho_0 V\times 10^6$ for the standing wave. $\Delta T_0 = -20$ K and $y_0/\delta_\kappa = 2.0$.

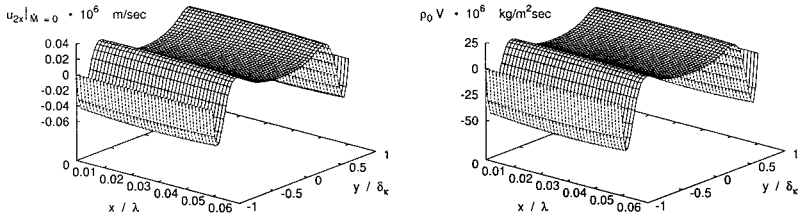

FIG. 15. Time-averaged velocity $u_{x2}|_{\dot{M}=0}\times 10^6$ and mass flux $\rho_0 V\times 10^6$ for the standing wave. $\Delta T_0 = -20$ K and $y_0/\delta_\kappa = 8.0$.

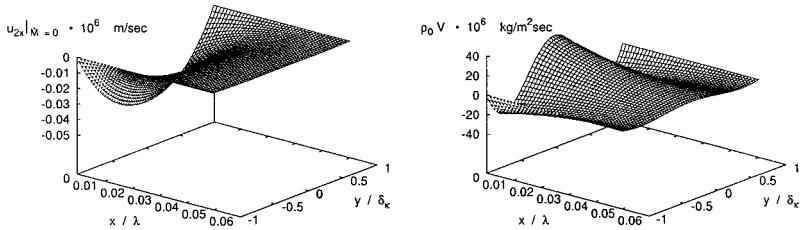

FIG. 16. Time-averaged velocity $u_{x2}|_{\dot{M}=0}\times 10^6$ and mass flux $\rho_0 V\times 10^6$ for the traveling wave. $\Delta T_0 = -20$ K and $y_0/\delta_\kappa = 0.3$.

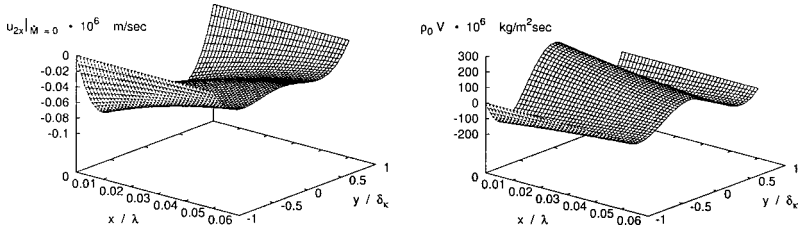

FIG. 17. Time-averaged velocity $u_{x2}|_{\dot{M}=0}\times 10^6$ and mass flux $\rho_0 V\times 10^6$ for the traveling wave. $\Delta T_0 = -20$ K and $y_0/\delta_\kappa = 0.8$.

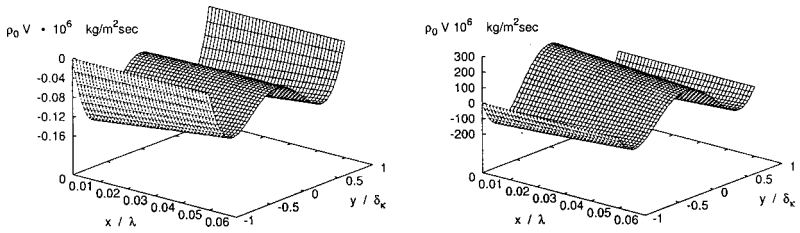

FIG. 18. Time-averaged velocity $u_{x2}|_{\dot{M}=0}\times 10^6$ and mass flux $\rho_0 V\times 10^6$ for the traveling wave. $\Delta T_0 = -20$ K and $y_0/\delta_\kappa = 2.0$.

In Fig. 4, the eigenvalues $E_\pm$ are plotted with $\sigma = 0.7$ and in Fig. 5 with $\sigma = 0.2$. The left-side temperature is allowed to vary. The values $T_0(0) = 290$ K, $T_0(0) = 280$ K, $T_0(0) = 270$ K, and $T_0(0) = 260$ K are taken. It is preferable to have some dimensionless measure of the temperature gradient. At any fixed x the ratio $\lambda(x)T_0'/T_0(x)$ is appropriate. Thus, a reasonable choice for a dimensionless parameter appears to be the average τ given by

$$\tau = \frac{1}{L}\int_0^L \frac{\lambda(x)}{T_0(x)} T_0' dx = 2\,\frac{\lambda(L)-\lambda(0)}{L}.$$

The values $T_0(0) = 290$ K, $T_0(0) = 280$ K, $T_0(0) = 270$ K, and $T_0(0) = 260$ K correspond to $\tau = 0$, $\tau = 0.695\,705$, $\tau = 1.403\,949$, and $\tau = 2.125\,434$, respectively.

Note that in general $E_- < 0$ while $E_+ > 0$. It follows from (35) that $\Delta p_2|_{\dot{M}=0}$ has neither a maximum nor a minimum. Thus, it can be tuned to particular values by appropriate choices of p_l and p_r. The structure that develops as σ decreases arises as the viscous and thermal penetration depths become different.

In Figs. 6 and 7, the components of the eigenvectors

$$A_\pm = \begin{pmatrix} A_{\pm 1} \\ A_{\pm 2} \end{pmatrix}$$

are plotted with $\sigma = 0.7$ and $L = 0.05\lambda|_{x=L}$, in Fig. 6 $\Delta T_0 = 0$ K while in Fig. 7 $\Delta T_0 = 20$ K. Note that $A_{-1} = -A_{+2}^*$ and $A_{-2} = A_{+1}$, so that it is only necessary to plot the components of A_+.

The term in $\Delta p_2|_{\dot{M}=0}$ which dominates for $y_0 \ll \delta_\mu$ is

$$(\Delta p_2|_{\dot{M}=0})_{\text{narrow}} = \frac{3\mu}{y_0^3}\int_0^L \int_0^{y_0} \left\langle \frac{\rho_1}{\rho_0} v_{1x} \right\rangle dy dx,$$

and the term which dominates for $y_0 \gg \delta_\mu$ is

$$(\Delta p_2|_{\dot{M}=0})_{\text{wide}} = \frac{3P_0}{R y_0^3}\int_0^L \int_0^{y_0} \int_{-y_0}^{y} \int_0^{y'} \nabla \cdot \frac{\langle \mathbf{v}_1 v_{1x}\rangle}{T_0} \times dy'' dy' dy dx.$$

The term $(\Delta p_2|_{\dot{M}=0})_{\text{narrow}}$ is the pressure difference that would cause enough steady flow to cancel the mass flux produced by $\langle \rho_1 v_{1x}\rangle$. This is the term retained by Swift, Gardner, and Backhaus.[4] The term $(\Delta p_2|_{\dot{M}=0})_{\text{wide}}$ is an additional pressure arising from nonlinear acoustic effects and is the contribution of the acoustic-Bernoulli effect.[10] In Fig. 8, the eigenvalues calculated by replacing $\Delta p_2|_{\dot{M}=0}$ by these approximate forms are compared with the exact eigenvalues. Again, $\sigma = 0.7$, $\Delta T_0 = 20$ K, and $L = 0.05\lambda|_{x=L}$. Note that in this parallel-plate geometry the acoustic-Bernoulli effect becomes important for y_0 greater than about $\frac{1}{2}\delta_\mu$.

V. TWO MODEL CASES

Finally, two model cases are considered. These are depicted schematically in Fig. 9. In both cases, the magnitude of the acoustic pressure field at the left entrance of the stack, $p_l P_0$, is held fixed as y_0 varies. Here, as before, $p_l = p(0)/P_0$ is dimensionless.

In the first case, a standing-wave device is modeled. The origin, $x = 0$, is placed at the left side of the stack. The boundary condition $p'(\lambda/8) = 0$ is imposed to the right of the stack. This is a common configuration for a standing-wave device.[2] To the right of the stack one has

$$p(x) = A\cos\left(\frac{\omega}{c_r}x - \frac{\pi}{4}\right),$$

for $x > L$. Here, c_r is the speed of sound to the right of the stack. The parameter A is chosen so the solution to Rott's equation, which matches to p and p' at L, has amplitude p_l at $x = 0$.

In the second case, it is assumed that to the right of the stack the duct continues indefinitely so that the acoustic pressure field is that of a rightward traveling wave. Accordingly,

$$p(x) = Ae^{-i(\omega/c_r)(x-L)},$$

for $x > L$. Again, A is chosen so that the solution to Rott's equation, which matches to p and p' at L, has amplitude p_l at $x = 0$.

In producing the plots in Figs. 10–19, the thermophysical parameters appropriate to dry air at room temperature are taken: $\gamma = 1.4$, $\sigma = 0.7$, and $\kappa = 0.026\,24$ W/K/m. The stack length is chosen to be $L = 0.05\lambda(L)$. First, the pressure difference is plotted for mean-temperature differences ΔT_0

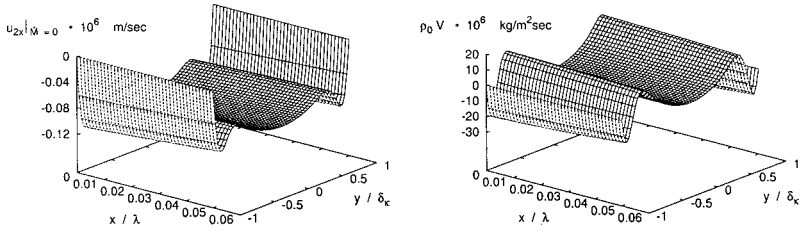

FIG. 19. Time-averaged velocity $u_{x2}|_{\dot{M}=0}\times 10^6$ and mass flux $\rho_0 V\times 10^6$ for the traveling wave. $\Delta T_0 = -20$ K and $y_0/\delta_\kappa = 8.0$.

$=0$ K, $\Delta T_0=20$ K, and $\Delta T_0=-20$ K. Again, dimensionless parameters are used so that it is not necessary to specify the frequency. In Fig. 10, the pressure difference in the standing-wave model is plotted and in Fig. 11, the pressure difference in the traveling-wave model is plotted.

Next, the time-averaged velocity at $\dot{M}=0, u_{2x}|_{\dot{M}=0}$, and the time-averaged mass flux at $\dot{M}=0, \dot{m}_{2x}|_{\dot{M}=0}=\rho_0 V$, are plotted as functions of $x/\lambda(L)$ and $y/\delta_\kappa|_{x=L}$ for several values of y_0. The values $y_0/\delta_\kappa|_{x=L}=0.3$, 0.8, 2.0, and 8.0 are taken. In the standing-wave example, since in such devices the higher temperature is typically closer to the pressure antinode,[2] $\Delta T_0=-20$ K is taken, while in the traveling-wave example $\Delta T_0=20$ K is taken. Figures 12–15 are for the standing-wave model while Figs. 16–19 are for the traveling-wave model.

Notice that the plots show several transitions as y_0/δ_κ increases. For $y_0/\delta_\kappa \ll \sigma$ the velocity is mostly towards the left, where the acoustic wave originates. This is the regime in which the acoustic-Bernoulli effect is unimportant. The mechanism discovered by Gedeon drives mass into the stack in the direction that acoustic intensity must flow, from the left to the right. In order that there be no mass flux, the velocity must drive the mass back to the left. As y_0/δ_κ increases a bit, the direction of the velocity changes as the acoustic-Bernoulli effect becomes important. For $y_0/\delta_\kappa \sim \sigma$, there is a transition as purely viscous effects give way to the effects of the thermoviscous boundary layer. As y_0/δ_κ increases, some boundary-layer flow develops and persists. For sufficiently large y_0/δ_κ, in addition to the boundary-layer flow, the parabolic profile in y, typical of low-Reynolds-number flow in a wide pipe, begins to emerge.

VI. CONCLUSIONS

The complete set of time-averaged second-order equations of fluid dynamics describing steady-state acoustic of a viscous, thermally conducting fluid between closely spaced parallel plates have been solved for $T_0' \neq 0$. Particular attention has been paid to the time-averaged velocity, pressure gradient, and mass flux. In the presence of an acoustic disturbance the linear relation between time-averaged mass flux and pressure gradient develops a nonzero constant term. The constant term can be interpreted as the pressure drop for which the total mass flux is zero.

For plate spacings large compared to the thermal and viscous penetration depths, known results for the time-averaged velocity and mass flux are recovered: one finds the parabolic profile characteristic of viscous flow superimposed on the boundary-layer flow familiar from Rayleigh streaming. For plate spacings small, compared to the viscous penetration depth, the estimates of Swift, Gardner, and Backhaus[4] are recovered. In the intermediate regime, where the plate spacing is comparable to the thermal penetration depth, the time-averaged velocity and pressure drop are plotted, both in the case in which the total mass flux is zero.

ACKNOWLEDGMENTS

It is a pleasure to be able to thank Anthony Atchley, Vic Sparrow, Robert Keolian, Steve Garrett, and Ray Wakeland for many comments and discussions.

[1] N. Rott, ''Thermoacoustics,'' Adv. Appl. Mech. **20**, 135–175 (1980).
[2] G. W. Swift, ''Thermoacoustic engines,'' J. Acoust. Soc. Am. **84**, 1145–1180 (1988).
[3] W. P. Arnott, H. E. Bass, and R. Raspet, ''General formulation of thermoacoustics for stacks having arbitrary-shaped pore cross section,'' J. Acoust. Soc. Am. **90**, 3228–3237 (1991).
[4] G. W. Swift, D. L. Gardner, and S. Backhaus, ''Acoustic recovery of lost power in pulse tube refrigerators,'' J. Acoust. Soc. Am. **105**, 711–724 (1999).
[5] S. Backhaus and G. W. Swift, ''A thermoacoustic-Stirling heat engine: Detailed study,'' J. Acoust. Soc. Am. **107**, 3148–3166 (2000).
[6] G. W. Swift, ''Thermoacoustics: A unifying perspective for some engines and refrigerators,'' (Draft available at http://www.lanl.gov/thermoacoustics/Book/index.html, 1999).
[7] D. F. Gaitan, A. Gopinath, and A. A. Atcheley, ''Experimental study of acoustic streaming and turbulence in a thermoacoustic stack,'' J. Acoust. Soc. Am. **96**, 3220 (1994).
[8] Lord Rayleigh, *Theory of Sound*, 2nd ed. (Dover, New York, 1945), Vol. II.
[9] C. Eckart, ''Vortices and streams caused by sound waves,'' Phys. Rev. **73**, 68–76 (1948).
[10] W. L. Nyborg, ''Acoustic streaming,'' in *Nonlinear Acoustics*, edited by M. F. Hamilton and D. T. Blackstock (Academic, San Diego, CA, 1998), pp. 207–231.
[11] T. G. Wang and C. P. Lee, ''Radiation pressure and acoustic levitation,'' *in Nonlinear Acoustics*, edited by Mark F. Hamilton and David T. Blackstock (Academic, San Diego, 1998), pp. 177–205.
[12] N. Rott, ''The influence of heat conduction on acoustic streaming,'' Z. Angew. Math. Phys. **25**, 417–421 (1974).
[13] B. T. Chu and R. E. Apfel, ''Acoustic radiation pressure produced by a beam of sound,'' J. Acoust. Soc. Am. **72**, 1673–1687 (1982).
[14] D. Gedeon, ''D. C. gas flows in Stirling and pulse-tube cryocoolers,'' in *Cryocoolers 9*, edited by R. G. Ross (Plenum, New York, 1997), pp. 385–392.
[15] L. D. Landau and E. M. Lifshitz, *Fluid Mechanics* (Pergamon, Oxford, U.K. 1984).
[16] N. Cao, J. R. Olson, G. W. Swift, and S. Chen, ''Energy flow density in a thermoacoustic couple,'' J. Acoust. Soc. Am. **99**, 3456–3464 (1996).

Development of panel loudspeaker system: Design, evaluation and enhancement

Mingsian R. Bai[a] and Talung Huang
Department of Mechanical Engineering, National Chiao-Tung University, 1001 TaHsueh Road, Hsin-Chu 300, Taiwan, Republic of China

(Received 10 July 2000; accepted for publication 13 March 2001)

Panel speakers are investigated in terms of structural vibration and acoustic radiation. A panel speaker primarily consists of a panel and an inertia exciter. Contrary to conventional speakers, flexural resonance is encouraged such that the panel vibrates as randomly as possible. Simulation tools are developed to facilitate system integration of panel speakers. In particular, electro-mechanical analogy, finite element analysis, and fast Fourier transform are employed to predict panel vibration and the acoustic radiation. Design procedures are also summarized. In order to compare the panel speakers with the conventional speakers, experimental investigations were undertaken to evaluate frequency response, directional response, sensitivity, efficiency, and harmonic distortion of both speakers. The results revealed that the panel speakers suffered from a problem of sensitivity and efficiency. To alleviate the problem, a woofer using electronic compensation based on H_2 model matching principle is utilized to supplement the bass response. As indicated in the result, significant improvement over the panel speaker alone was achieved by using the combined panel-woofer system.
[DOI: 10.1121/1.1371544]

PACS numbers: 43.38.Ja, 43.38.Ar [SLE]

I. INTRODUCTION

For decades, the design concept of conventional loudspeaker has been centered at the principle of rigid piston. The common practice is to make the diaphragm of the loudspeaker as light and stiff as possible such that the loudspeaker behaves as a rigid piston. Furthermore, the surface is generally made conical to further increase rigidity as well as on-axis sensitivity at low frequency. Although the technology is well established, conventional loudspeakers suffer from a problem: the sound generated by conventional loudspeakers becomes increasingly directional for high frequencies. This ''beaming'' effect results in the drop of sound power at the high frequency region. Consequently an audio system generally requires crossover circuits and multi-way loudspeakers to cover the audible frequency range, which makes the entire system unnecessarily large.

Panel speakers are based on a philosophy contradicting conventional design (Azima, 1998). A panel loudspeaker primarily consists of a panel and an inertia exciter (Fig. 1). The exciter is essentially a voice-coil driver with the coil attached to the panel. The magnet serves as a proof mass to produce inertia force. In lieu of a rigid diaphragm as used in conventional loudspeakers, flexible panels are employed as the primary sound radiators. Resonance of flexural motion is encouraged such that the panel vibrates as randomly as possible. The sound field produced by this type of *distributed mode loudspeaker* (DML) is very diffuse at high frequency. As claimed by the supporters of panel speakers, DML provide advantages over the conventional counterpart such as compactness, linear on-axis, attenuation, insensitivity to room conditions, bi-polar radiation, good linearity, and so forth (Azima, 1998). Of particular interest is that the DML has a less pronounced beaming problem at high frequencies than conventional loudspeakers, which bypass the need for crossover circuits and multi-way high frequency speakers. DML began to find applications in multimedia, notebook computers, mobile phones, high-fidelity audio systems, public addressing systems, projection screens, pictures, and decorations (Azima, 1998).

Although commercial panel speakers may have been around for more than a decade, only recently has this concept been subjected to scientific analysis devoted to electroacoustics design. In this paper, the operating principles of DML are investigated in terms of structural vibration and acoustic radiation. Simulation tools are developed prior to integration of a DML system. Specifically, electro-mechanical analogy is employed for modeling the panel-exciter system. Finite element analysis is used in the determination of aspect ratios of the panel and calculation of panel vibration. Two-dimensional fast Fourier transform (FFT) is utilized to predict the acoustic radiation. In order to compare DML with conventional loudspeakers, experiments were undertaken to evaluate frequency response, directional response, sensitivity, efficiency, and harmonic distortion of both speakers.

It was found in the comparison that the DML produced desirable omni-directional response, even at high frequency. Nevertheless, the DML suffered from the problem of poor sensitivity and efficiency. This price that DML have to pay is mainly due to the *hydrodynamic short circuit* of flexible panels vibrating below coincidence (Cremer and Heckl, 1988). To overcome the physical constraint, a woofer using electronic compensation based on the H_2 model matching principle is used to supplement the bass response. Electronic

[a]Electronic mail: msbai@cc.nctu.edu.tw

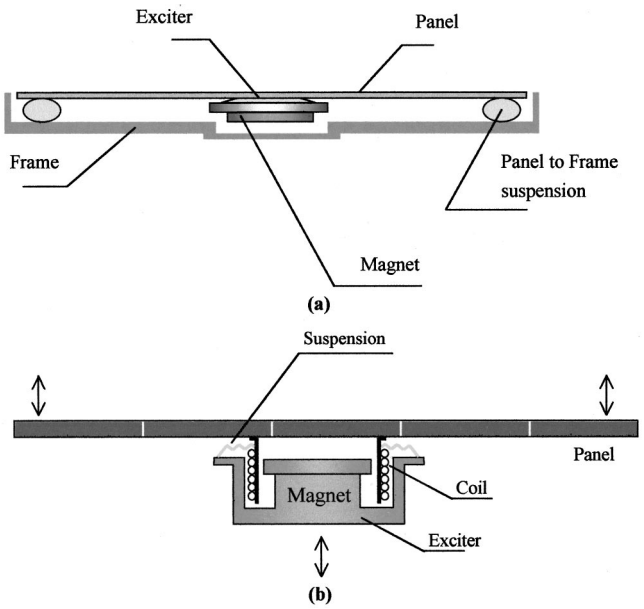

FIG. 1. Schematic of a DML. (a) The panel loudspeaker consisting of a panel and an exciter; (b) details of the intertia exciter.

compensation was realized by a digital signal processor (DSP). Experimental investigation showed that significant improvement of the combined system over the panel loudspeaker was achieved.

II. RATIONALES OF PANEL LOUDSPEAKERS

The operating principle of DML is based on acoustic radiation of modal bending waves. In contrast to conventional loudspeaker design, resonance of flexural motion is encouraged such that the panel will vibrate as randomly as possible. When excited, the flexible panel of a DML develops complex and dense vibration modes uniformly distributed over its entire surface and operating frequency range. The beaming effect of DML is generally not as pronounced as the coherent field of a rigid piston because the sound field radiated by a DML is very diffuse at high frequency. The panel of a DML can be modeled as a thin plate described by

$$d\nabla^4 w+\mu\frac{\partial^2 w}{\partial t^2}=0, \tag{1}$$

where w is the normal displacement, μ is mass per unit surface area,

$$\nabla^4=\left(\frac{\partial^2}{\partial x^2}+\frac{\partial^2}{\partial y^2}\right)^2$$

is the bi-harmonic operator, and

$$D=\frac{Eh^3}{12(1-\nu^2)} \tag{2}$$

is the bending stiffness per unit width of the plate (E, ν, and h are Young's modulus, Poisson ratio, and thickness, respectively). If there exists only a time-harmonic bending wave traveling in x-direction, Eq. (1) admits the general solution

$$w(x,t)=(C_1E^{-jk_bx}+C_2e^{jk_bx}+C_3e^{-k_bx}+C_4e^{k_bx})e^{j\omega t}, \tag{3}$$

where

$$k_b=\sqrt[4]{\omega^2\mu/D} \tag{4}$$

is called the free bending wave number, ω is angular frequency, and C_1, C_2, C_3, and C_4 are constants to be determined by boundary conditions. Note that the first two terms in Eq. (3) correspond to traveling components and the last two terms are evanescent components.

On the other hand, the sound pressure generated by the vibrating panel satisfies the linear wave equation

$$\nabla^2 p-\frac{1}{c^2}\frac{\partial^2 p}{\partial t^2}=0, \tag{5}$$

where p is sound pressure and c is sound speed. For time-harmonic field, this reduces to the Helmholtz equation

$$\nabla^2 p+k^2 p=0, \tag{6}$$

where $k=\omega/c$ is the wave number of sound wave.

The fundamental difference between a DML and a conventional loudspeaker lies in that the mechanical impedance of a point-excited infinite panel is a frequency-independent real constant (Morse and Ingard, 1986):

$$z_m=8\sqrt{D\mu}. \tag{7}$$

This property enables us to derive a constant driving-point velocity ν_c from a constant force f_e, which is approximately true for an electro-magnetic exciter driven by a constant current. In addition, it can be shown that the sound power W_R of a randomly vibrating panel is proportional to the time and space averaged square velocity $\langle\overline{\nu^2}\rangle$ which is also proportional to the driving-point velocity ν_c (Morse and Ingard, 1986). As a consequence, the panel would radiate constant sound power when driven by a constant force, i.e., $W_R \approx$ constant.

However, this is not the case for a conventional moving-coil loudspeaker. At the mass-controlled region, its cone acceleration is nearly constant with respect to frequency, i.e., the cone velocity is inversely proportional to frequency ($\nu_c \sim \omega^{-1}$). In the high frequency range ($ka \gg 1$), the radiation resistance R_R of a rigid piston is nearly constant (Beranek, 1996). Thus the sound power radiated by a conventional loudspeaker has the frequency dependence as

$$W_R=\tfrac{1}{2}R_R|\nu_c|^2\sim\omega^0\omega^{-2}=\omega^{-2}. \tag{8}$$

The radiation power drops as frequency increases (-20 dB/decade), even though the on-axis sound pressure remains constant. The main contributing factor to this power drop is the beaming effect resulting from the coherent phase motion of a rigid piston. In the case of a DML, the beaming effect would not be as pronounced because the sound field generated by the random panel vibration is ''quasi-diffuse.''

On the basis of panel velocity, the radiated sound pressure from the planar source can be calculated using the Rayleigh's integral (Kinsler *et al.*, 1982):

$$p(x,y,z)=-jk\rho_0 c\int_{-\infty}^{\infty}\int_{-\infty}^{\infty}\frac{e^{jkR}}{R}\nu(x_0,y_0)dx_0\,dy_0, \tag{9}$$

where ρ_0 is the density of air, (x,y,z) and $(x_0,y_0,0)$ are the field point and the source point, respectively, and R

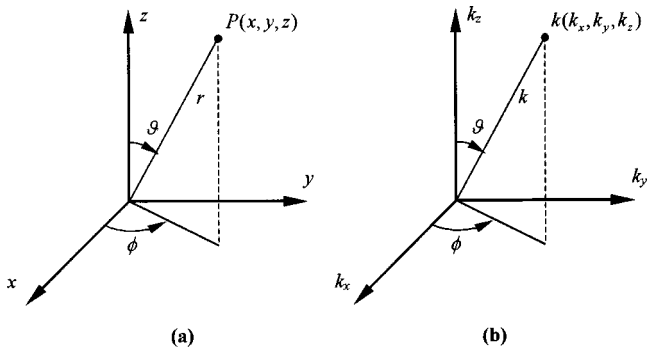

FIG. 2. Coordinate system for sound radiation analysis. (a) Spatial domain; (b) wave number domain.

$=\sqrt{(x-x_0)^2+(y-y_0)^2+(z-z_0)^2}$. In the far field, this integral can be rewritten as (Morse and Ingard, 1986)

$$p(x,y,z)\approx -jk\rho_0 c\frac{e^{jkr}}{r}V(k_x,k_y), \tag{10}$$

where $k_x=k\sin\vartheta\cos\phi$, $k_y=k\sin\vartheta\sin\phi$, $k_z=k\cos\vartheta$, $r=\sqrt{x^2+y^2+z^2}$, r, ϑ, and ϕ are spherical coordinates (Fig. 2), and $V(k_x,k_y)$ is the spatial Fourier transform of $\nu(x,y)$:

$$V(k_x,k_y)\equiv\int_{-\infty}^{\infty}\int_{-\infty}^{\infty}\nu(x,y)e^{-j(k_x x+k_y y)}\,dx\,dy. \tag{11}$$

Equation (10) implies that the far-field directivity of the source depends on the velocity spectrum on the wave number space. Only the propagating modes inside the radiation circle ($k_x^2+k_y^2\leq k^2$) contribute to the far-field radiation.

Classical theory of plate radiation has suggested a *hydrodynamic short circuit* phenomenon: a flexible infinite panel has no acoustic output at frequencies below the *coincidence frequency* (Cremer and Heckl, 1988)

$$\omega_c=c^2\sqrt{\frac{\mu}{D}} \tag{12}$$

at which the speed of sound matches the speed of bending wave in a panel. However, this is not true for a ''finite'' panel and it is possible to have sound radiation below coincidence due to the aperture effect. A finite panel can be described by an aperture function

$$a(x,y)=\begin{cases}1, & (x,y)\text{ inside aperture}\\ 0, & (x,y)\text{ outside aperture}\end{cases}. \tag{13}$$

By decomposing the flexural standing waves into traveling waves, the velocity distribution of the finite panel $\nu'(x,y)$ can be approximated in terms of the velocity distribution of an infinite panel $\nu(x,y)$,

$$\nu'(x,y)=\nu(x,y)a(x,y). \tag{14}$$

In wave number space, this amounts to

$$V'(k_x,k_y)=V(k_x,k_y)*A(k_x,k_y), \tag{15}$$

where ''*'' denotes convolution. Hence the aperture effect results in leakage of the wave number spectrum such that the panel could have nonzero acoustic output into the far field below coincidence (Panzer and Harris, 1998a). For example, a one-dimensional surface velocity distribution $\nu(x)=\cos(k_b x)$ (expressed as a standing wave due to boundary effects) corresponds to the velocity spectra in wave number space and the radiation patterns shown in Fig. 3. Even though ideal hydrodynamic short circuit no longer exists in such case, the acoustic radiation at low frequency remains not as efficient as rigid pistons because of cancellations of volume velocity on the surface. In addition, it was pointed out by the reviewer that the presence of boundaries will cause only evanescent waves. The boundary effects are not considered in the above arguments in that the differences in the subsonic portion of the wave number spectra of the finite and infinite plate responses have no effect on the far-field radiation (Junger and Feit, 1986).

III. SYSTEM MODELING AND SIMULATION

Simulation tools were developed to facilitate the design and integration of DML. These tools encompass two aspects: electro-mechanical modeling and acoustic radiation prediction.

A. Electro-mechanical modeling

Electro-mechanical equivalent circuit technique is employed for modeling the panel-exciter system of a DML. The equivalent circuit (mobility analogy) of a DML system is shown in Fig. 4(a). Although the equivalent circuit in Fig. 4(a) is in the form of graphic language, it is entirely based on Newton's second law, Lorentz force, and Kirchhoff's circuit laws. The details of how this circuit is derived are tedious but standard in literature, e.g., text by Beranek (1996) and are thus omitted for brevity. In this figure, $Z_c=R_c+jX_c$ is the electrical impedance of voice coil. Bl is the motor constant of the voice coil. C_s and R_s are the compliance and damping, respectively, between the magnet and the panel. M_m is the mass of the magnet assembly. M_c is the mass of the voice coil. Z_m is the mechanical impedance of an infinite panel at the driving point. M_f is the mass of the frame. C_p and R_p are the compliance and damping of the suspension between the panel and frame. Note that the constant real driving point impedance of Eq. (7) for an infinite plate is used and radiation loading is neglected in the modeling. It has been pointed out by the reviewer that the force on the plate should be dependent on the impedance predicted by the finite element model. The ''coupled'' electrical-mechanical-acoustical systems should be solved simultaneously. For the present, this is somewhat impractical from the engineering standpoint. In this work, we are merely content with the frequency-independent impedance of an infinite plate. This is a reasonable simplification because only far-field radiation is of interest (so that evanescent waves due to boundary effects are negligible) and also the panel is much heavier than the diaphragms of cone speakers (so that acoustic loading is negligible).

The equivalent circuit can be simplified into a Thevenin circuit of Fig. 4(b), where V_s is the voltage source, Z_s is the source impedance reflected to the mechanical side, and Z_L is the mechanical impedance of the load including the panel and the exciter assembly. The force is determined with the attached driver assembly taken into account. In terms of the Laplace transform,

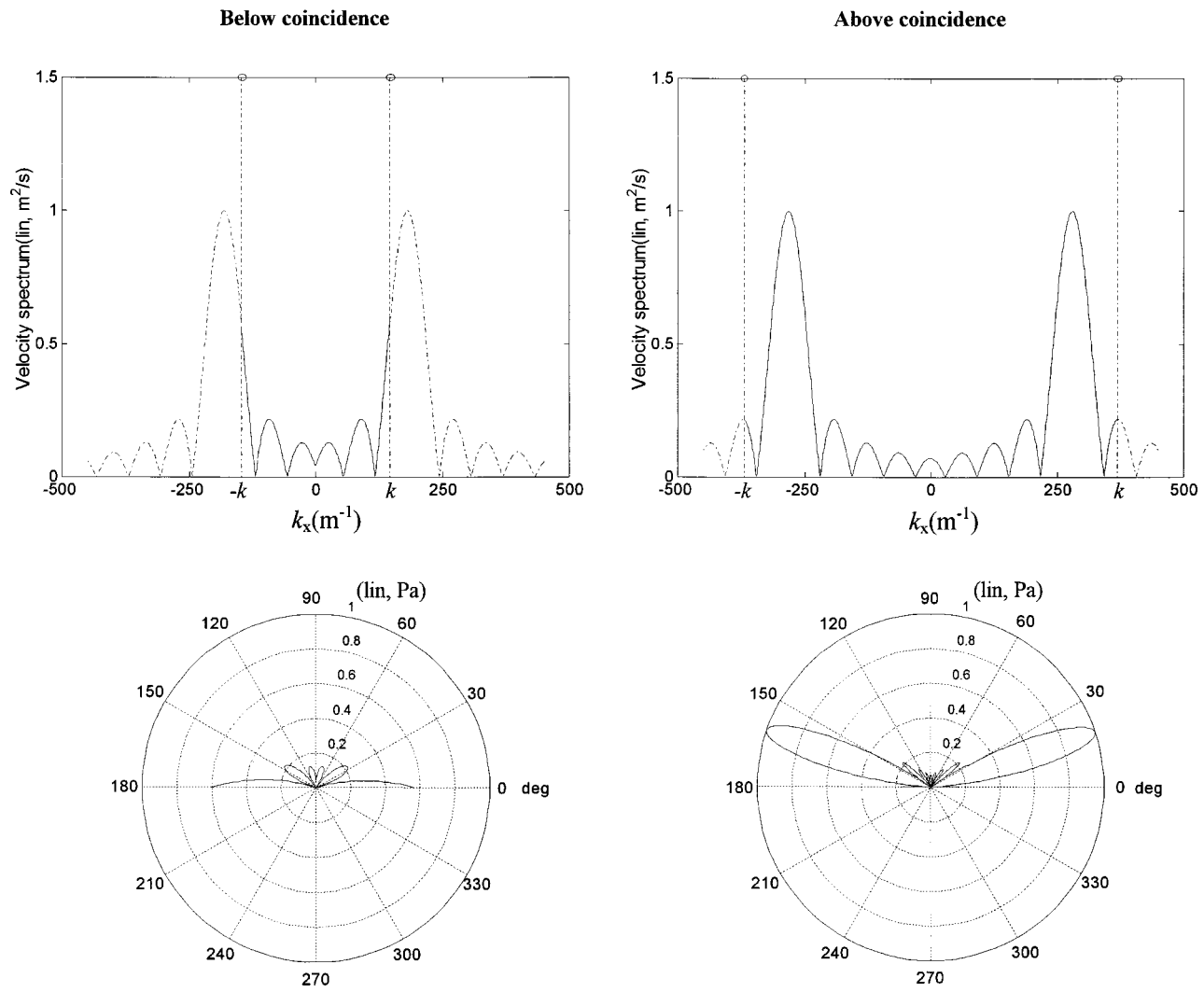

FIG. 3. Sound radiation of a vibrating panel with an aperture 0.2 m. The figures in the upper part are the velocity spectra in wave number domain, while the figures in the lower part are the polar radiation patterns. (a) Below coincidence ($f=8$ kHz, $k_b=180\ \mathrm{m}^{-1}$, $k=148\ \mathrm{m}^{-1}$); (b) above coincidence ($f=18$ kHz, $k_b=294\ \mathrm{m}^{-1}$, $k=368\ \mathrm{m}^{-1}$).

$$V_s(s)=\frac{N_1(s)}{D_1(s)}, \tag{16}$$

where

$$N_1(s)=Bl\cdot C_s\cdot Eg\cdot M_m s$$

and

$$\begin{aligned} D_1(s)=&C_sM_mM_cX_cs^3+(C_sM_mM_cR_c+C_sM_mR_sX_c\\ &+C_sM_cR_sX_c)s^2+(Bl^2C_sM_c+Bl^2C_sM_m\\ &+C_sM_mR_sR_c+C_sM_cR_sR_c+M_mX_c+M_cX_c)s\\ &+(M_m+M_c)R_c, \end{aligned} \tag{17}$$

$$Z_s(s)=\frac{N_2(s)}{D_2(s)},$$

where

$$\begin{aligned} N_2(s)=&C_sM_mX_cs^3+(C_sM_mR_c+X_c+C_sR_sX_c)s^2\\ &+(Bl^2C_s+C_sR_sR_c)s+R_c \end{aligned}$$

and

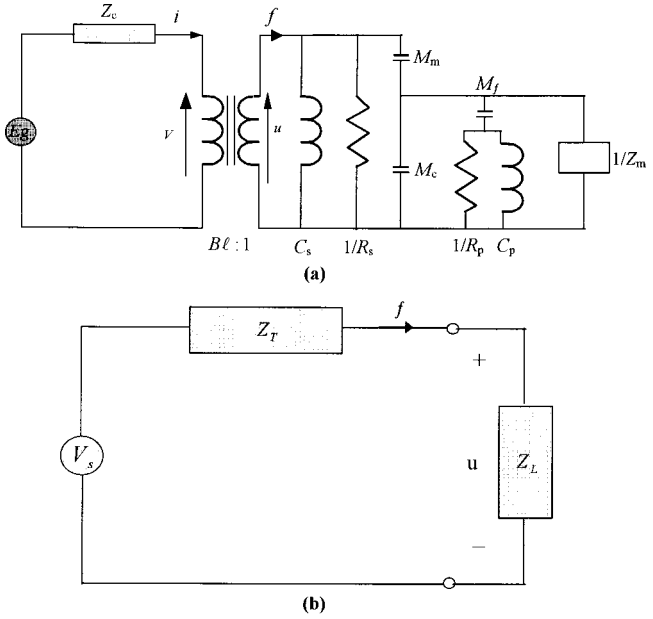

FIG. 4. Electro-mechanical analogy of a DML. (a) Equivalent circuit (mobility analogy); (b) simplified circuit. The symbols f and u in the figures denote, respectively, the force and the velocity of the panel.

TABLE I. Parameters of the panel and the exciter.

	Parameters
Panel	Bending stiffness $D=1.672\ \mathrm{N\cdot m}$
	Area density $\mu=0.492\ \mathrm{kg/m^2}$
	Dimension$=0.2\ \mathrm{m}\times0.112\ \mathrm{m}\times0.002\ \mathrm{m}$
	Poisson ratio $\nu=0.33$
	Mass of frame $M_f=0.06\ \mathrm{kg}$
	Panel mobility $Z_{mp}=7.255\ \mathrm{N\cdot s/m}$
	Damping of panel suspension $R_p=0\ \mathrm{N\cdot s/m}$
	Compliance of panel suspension $C_p=900\times10^{-6}\ \mathrm{m/N}$
Exciter	Impedance of voice coil $Z_c=4+j\omega\cdot32\times10^{-6}\ \Omega$
	Motor constant $Bl=1.54\ \mathrm{Wb/m}$
	Compliance of coil suspension $C_s=170\times10^{-6}\ \mathrm{m/N}$
	Damping of panel suspension $R_s=0.257\ \mathrm{N\cdot s/m}$
	Mass of magnet $M_m=37\times10^{-3}\ \mathrm{kg}$
	Mass of coil $M_c=0.35\times10^{-3}\ \mathrm{kg}$

$$
\begin{aligned}
D_2(s)=s[&C_sM_cM_mX_cs^3+(C_sM_mM_cR_c+C_sM_mR_sX_c\\
&+C_sM_cR_sX_c)s^2+(Bl^2C_sM_m+Bl^2C_sM_c\\
&+C_sM_mR_sR_c+C_sM_cR_sR_c+M_mX_c+M_cX_c)s\\
&+(M_m+M_c)R_c,\\
Z_L(s)=&\frac{1}{Z_{mp}(s)}.
\end{aligned}
\tag{18}
$$

Thus the power delivered to the load $Z_L(=R_L+jX_L)$ can be calculated as

$$
W_L=\frac{|V_s|^2R_L}{(R_s+R_L)^2+(X_s+X_L)^2}. \tag{19}
$$

In the work, a DML intended for multi-media application is examined. The parameters of the panel and exciter are listed in Table I. The simulation result of the exciter force f with a sinusoidal input of 1 V rms is shown in Fig. 5.

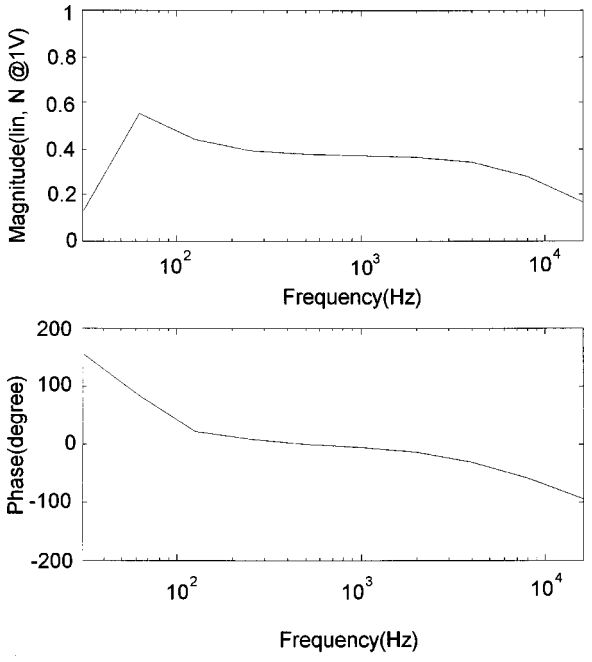

FIG. 5. Predicted force response of the exciter with 1 V rms electrical input.

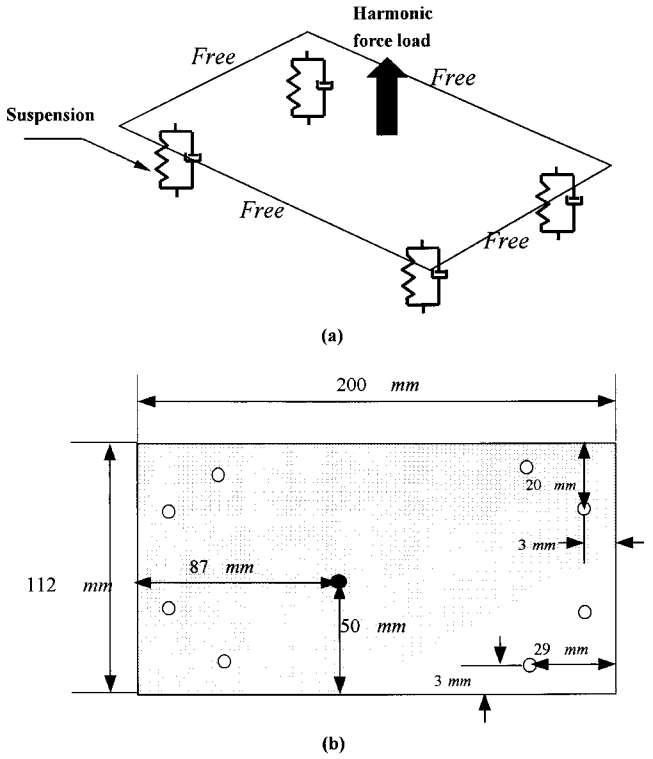

FIG. 6. Panel configuration for finite element analysis. (a) Panel driven by a harmonic concentrated force input. The panel is flexibly suspended with free boundaries; (b) dimensions of the panel and locations of the driving point (solid) and the suspensions (hollow).

B. Prediction of acoustic radiation

After the exciter force output f is determined, the surface velocity of the panel is calculated by the finite element method. A 200 mm$\times$112 mm rectangular polyurethane (PU) foam panel is examined. The locations of exciter and suspensions are shown in Fig. 6. From the finite element analysis, a sample surface velocity $v'(x,y)$ of the panel is shown in Fig. 7(a).

Having obtained surface velocity, one shall proceed with the calculation of far-field sound pressure $p(x,y,z)$ through the use of Eq. (10). In this step, two-dimensional FFT is employed to obtain the surface velocity spectrum $V'(k_x,k_y)$ in the wave number domain [Fig. 7(b)]. In this step, zero-padding (indicated in the figure) is used to improve resolution in the wave number space. The frequency response of the vibrating panel between the force input and sound pressure output at 1 m distance is calculated (Fig. 8). Combining the frequency response functions in Figs. 5 and 8 leads to the overall frequency response from the voltage input to the sound pressure output at 1 m distance (Fig. 9). In addition, directional response can also be calculated (Fig. 10). In some cases, the rms pressure within a band is required. This can be done by a straightforward integration:

$$
p_{\mathrm{rms}}=\left(\int_{f_1}^{f_2}|p(f)|^2\cdot G_{xx}\,df\right)^{1/2}, \tag{20}
$$

where f_1 and f_2 are the lower and the upper frequency limits, respectively, $p(f)$ is the frequency response between the voltage input and the sound pressure output, and G_{xx} is the power spectrum density of the input voltage.

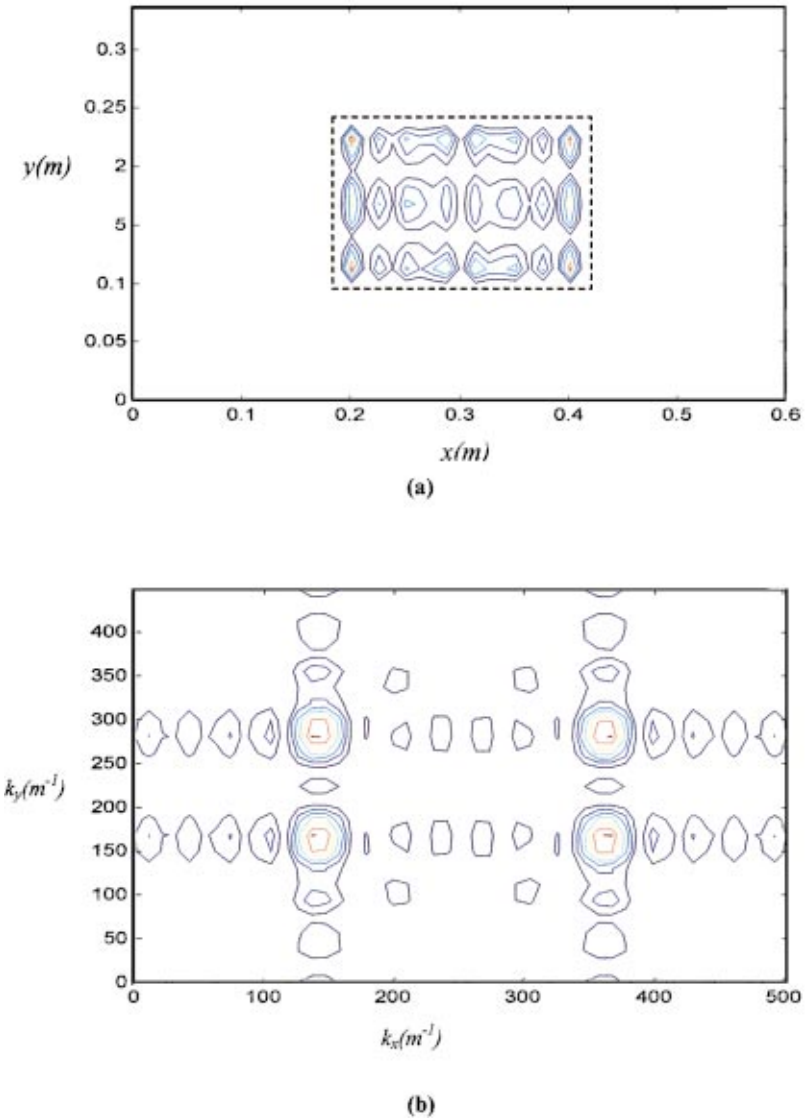

FIG. 7. Surface velocity of the panel excited by a 1 N harmonic (4 kHz) concentrated force. (a) Spatial domain; (b) wave number domain. Interior of the marked rectangle is the panel area; exterior of the marked rectangle is padded with zeros for improving resolution in the wave number space.

On the other hand, if sound power is of interest, the following formula can be utilized to calculate the power frequency response (Cremer and Heckl, 1988):

$$W(f)=\frac{\rho_0 ck}{8\pi^2}\int_{-k}^{k}\int_{-k}^{k}\frac{|V'(k_x,k_y)|^2}{\sqrt{k^2-k_x^2-k_y^2}}dk_x\,dk_y, \tag{21}$$

which entails again the surface velocity spectrum. A sample result of sound power is shown in Fig. 11. The total power within a band can be obtained from the following integration:

$$W_{\text{total}}=\int_{f_1}^{f_2}W(f)\cdot G_{xx}\,df. \tag{22}$$

IV. DESIGN PROCEDURE AND PERFORMANCE EVALUATION

A. Design procedures

The design procedures of DML are outlined as follows:

(1) Choose the area A of panel according to the specific application. In theory, a large area is preferable if efficiency is the major concern. In practice, however, the choice relies largely on packaging or artistic consideration for the application of interest. In our case, $A=0.0224\,\text{m}^2$, which is typical for multimedia or notebook applications.

(2) Choose D/μ ratio to achieve the fundamental frequency f_0 that is sufficiently low to produce reasonable low frequency response. The fundamental frequency of an isotropic vibrating plate can be approximated by (Leissa, 1993)

$$f_0\approx\frac{\pi}{A}\sqrt{\frac{D}{\mu}}. \tag{23}$$

In our case, $D/\mu=3.3984\,\text{N}\cdot\text{m}^3/\text{kg}$, $f_0=258\,\text{Hz}$, $\omega_c=64\,177\,\text{rad/s}$. Small D, or small μ, should be selected for a small panel.

(3) Minimize the panel mechanical impedance Z_m to achieve acceptable efficiency by choosing appropriate density ρ and Young's modulus E. Note that

$$Z_m=8\sqrt{D\mu}=16\frac{D}{\mu}\sqrt{3(1-\nu^2)\frac{\rho^3}{E}}. \tag{24}$$

For good acoustical efficiency, the chosen panel should be stiff (large E) and light (small ρ), e.g., composite and

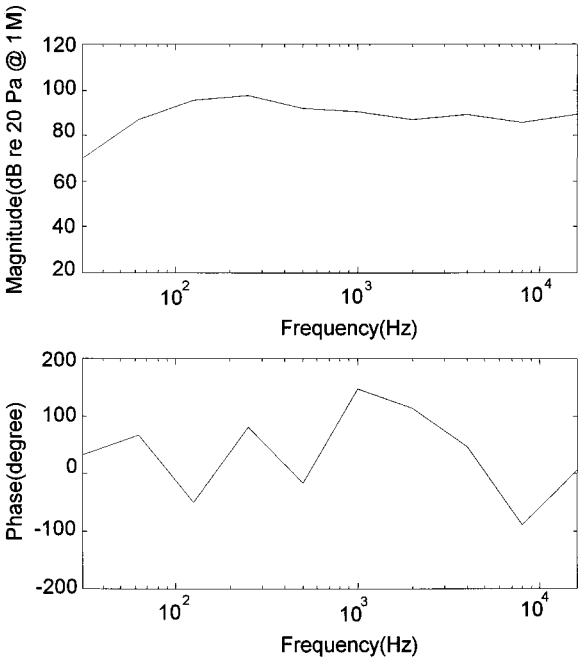

FIG. 8. Predicted frequency response of the vibrating panel between the force input and sound pressure output at 1 m on-axis distance.

honeycomb materials. Note that ρ is more critical than E in that Z_m is inversely proportional to $\sqrt{E/\rho^3}$.

(4) Choose the aspect ratio of the panel. As mentioned previously, flexural resonance is encouraged to excite as many as possible complex vibration modes in a panel. To this end, the vibration modes of panel are approximated by the product of two sets of ''beam'' modes along each side of the panel (Harris and Hawksford, 1997). For an Euler beam of length l, material constants D, μ, free at both ends, the resonance frequencies are

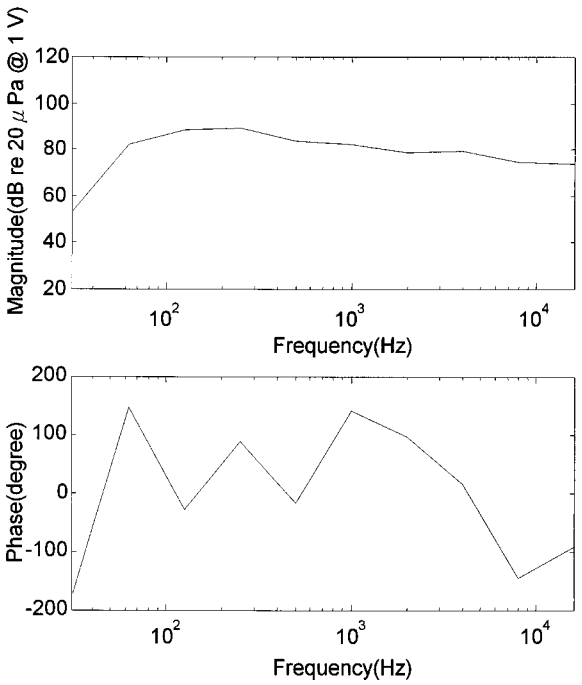

FIG. 9. Predicted overall frequency response of the DML between the voltage input and sound pressure output at 1 m on-axis distance.

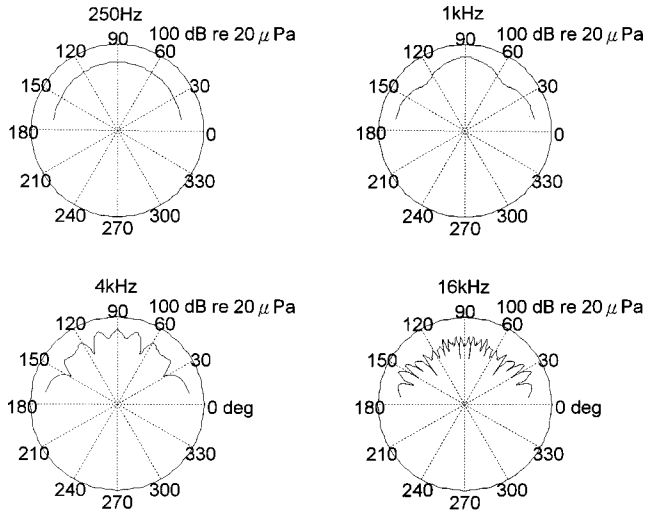

FIG. 10. Predicted directional response of the DML at 250, 1000, 4000, and 16 000 kHz for 1 W input.

$$\omega_i = \sqrt{\frac{\lambda_1^4 D}{\mu}}, \quad i = 1,2,3\cdots, \tag{25}$$

with

$$\lambda_i = \left(\frac{(2i-1)\pi}{2l}\right), \quad 1,2,3\cdots.$$

Complex vibration modes of a DML can be achieved by selecting an aspect ratio such that the beam modes along each side are best interleaved.

(5) Choose the driving point and suspension points of the panel. This can be done by a finite element based modal analysis. The driving point should be chosen at where the least nodal lines are, while the suspension points should be chosen at where the most nodal lines cross.

(6) Choose an exciter that matches the panel. A common practice is to choose a large Bl constant for ensuring sufficient output level. This is preferably achieved by using strong magnet rather than increasing the length of coil because the latter approach has an adverse effect of increasing resistance and inductance. Next, choose a

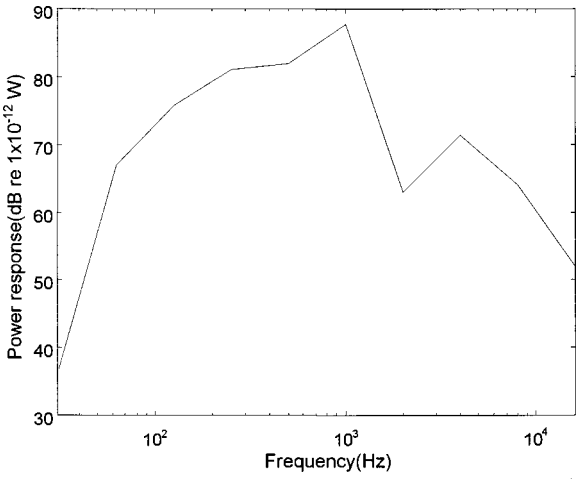

FIG. 11. Predicted sound power frequency response of the DML for 1 V rms electrical input.

large magnet mass M_m and a small coil mass M_c because the bandwidth is dependent of the ratio M_m/M_c (Panzer and Harris, 1998b).

(7) Calculate the response by the aforementioned simulation procedures. From the simulation, one can get an idea of the performance of a DML before it is practically implemented.

B. Performance evaluation

To compare the DML with the conventional loudspeaker, experimental investigations were undertaken. A conventional multimedia loudspeaker (4Ω, 2 W, 6 cm diameter) for a desktop computer was used in the comparison. The area ratio between the DML and the conventional speaker is approximately 8 to 1. Both speakers are embedded in a 1.5 m×2.0 m baffle. The enclosure of the multimedia speaker has been removed. The use of baffle is to meet the requirement of far-field calculation using Fourier transform, where rigid baffled planar sources are assumed. The performance indices to be measured are summarized as follows (Borwick, 1994).

1. Frequency response

The on-axis pressure responses at 1 m·W condition from the conventional speaker and the DML were measured in a semi-anechoic room such that the effect of room response can be minimized. Random noise band-limited to 16 kHz was used as the input. From the result of sound pressure spectral levels (Fig. 12), a significant gap (maximum 15 dB *re*: 20 μPa at 1 m·W) can be seen between the response levels.

2. Directional response

The microphone is positioned along a semi-circle at angles from 0° to 180° with 10° increments. Figure 13 shows the measured directional response of the DML versus the conventional speaker. Only data in half space are shown because both speakers are embedded in the baffle. The result indicates that DML yields an omni-directional response, even at high frequency (16 kHz). The conventional speaker does not show the kind of high frequency beaming because it is very small. If a larger DML were compared with a larger cone speaker, the contrast would be more apparent.

3. Sensitivity

The sensitivity of a speaker is defined as the free-field sound pressure level produced by 1 W electrical input, measured at the on-axis distance 1 m. In our case, a random noise input of 2 V rms (band-limited to 16 kHz) and nominal impedance of 4Ω in the coil was used. The measured sensitivities of the DML and the conventional speaker are 80.7 dB and 90.6 dB, respectively, *re*: 20 μPa over a 16 kHz band.

4. Efficiency

The efficiency of a speaker is defined as the ratio of the radiated acoustic power to the electrical power input. In the work, ISO 3745 was employed for measuring the sound power in the semi-anechoic room (ISO standard, 1977). The measured efficiencies of the DML and the conventional speaker are 0.039% and 0.089%, respectively. The result indicates the DML has a problem of sensitivity and efficiency in comparison with the conventional speaker. Poor radiation efficiency below coincidence frequency is a physical constraint of flexible panels.

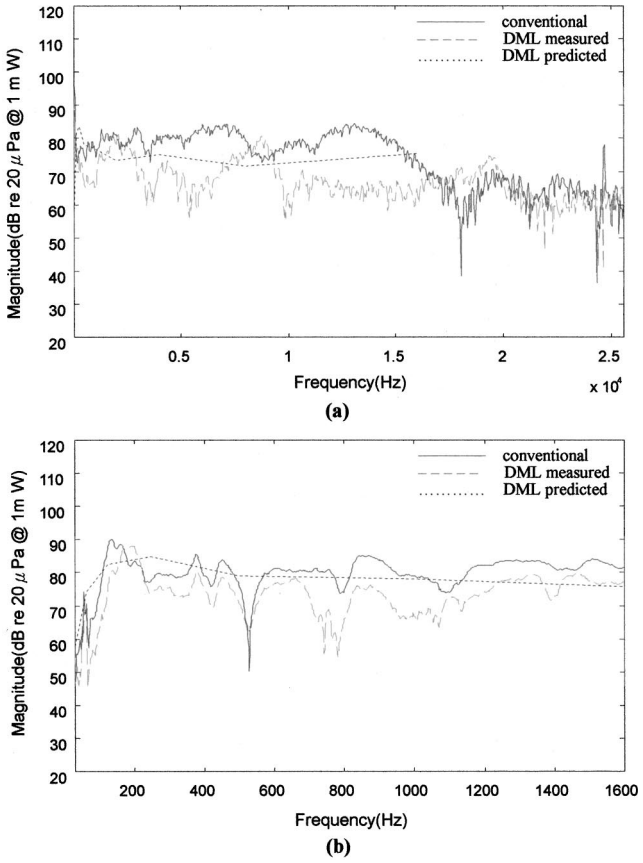

FIG. 12. The sound pressure spectral levels of the conventional speaker and the DML. The measurements are under 1 m·W condition. (a) Bandwidth = 25.6 kHz; (b) bandwidth = 1.6 kHz.

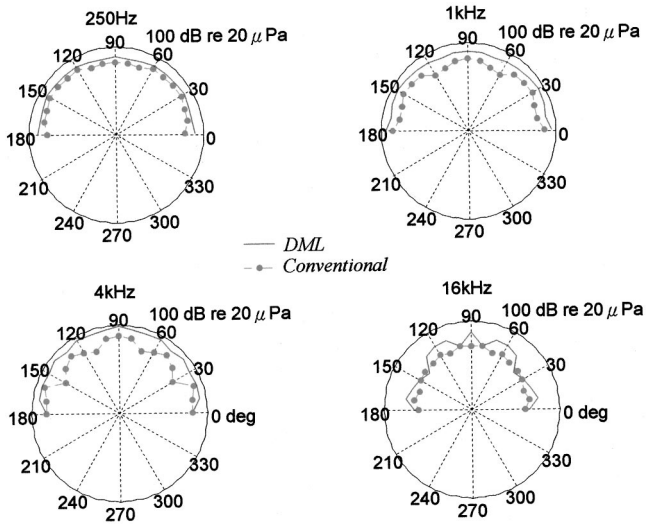

FIG. 13. Directional responses of the DML and the conventional speaker at 250, 1000, 4000, and 16 000 kHz, respectively. The radial scales are in dB with a full scale 100 dB *re*: 20 μPa.

TABLE II. Harmonic distortion of panel loudspeaker in comparison with conventional loudspeaker.

	250 Hz	1 kHz	4 kHz
Conventional speaker	1.96%	0.91%	1.02%
Panel speaker	3.25%	10.6%	12.6%

5. Harmonic distortion

Harmonic distortion represents the ratio of the rms distortion to the rms total signal. It can be calculated by measuring the rms total signal, using the same setup as for frequency response measurements and also that obtained when the driving frequency is filtered out. The harmonic distortions of the DML and the conventional loudspeaker measured with a 2 V rms and 1 W electrical input at three frequencies are summarized in Table II. The DML appears to have higher harmonic distortion than the conventional speaker does. A possible explanation is that the DML relies on resonant modes of the panel, where nonlinearity may arise due to an exceedingly large amplitude of motion at resonance.

V. SYSTEM ENHANCEMENT

The foregoing comparison between the DML and the conventional speaker reveals that the DML suffers from the problem of poor sensitivity and efficiency. In this work, a practical solution is adopted in an attempt to alleviate the problem. Such approach involves the use of an electronically compensated woofer to supplement the low frequency response.

The system consists of a woofer cascaded with a feedforward controller. The complete DML-woofer system is shown in Fig. 14(a). The design of the controller is based on a H_2 model matching idea. The system block diagram is shown in Fig. 14(b), where T_1 is the desired response model,

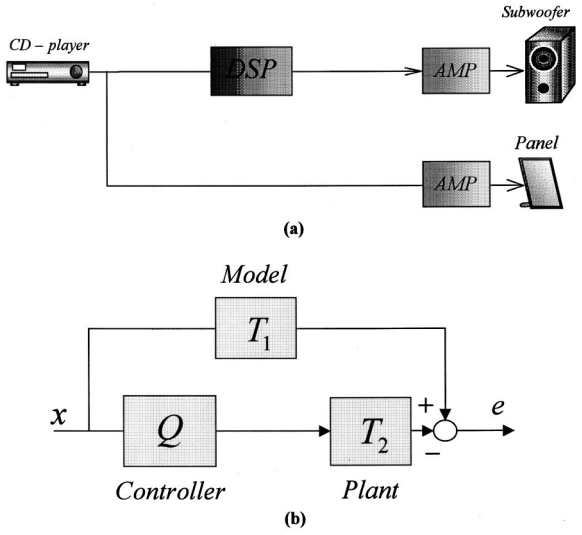

FIG. 14. The DML system enhanced by electronic compensation. (a) Integrated system of the DML and a woofer; (b) block diagram of the H_2 model matching method.

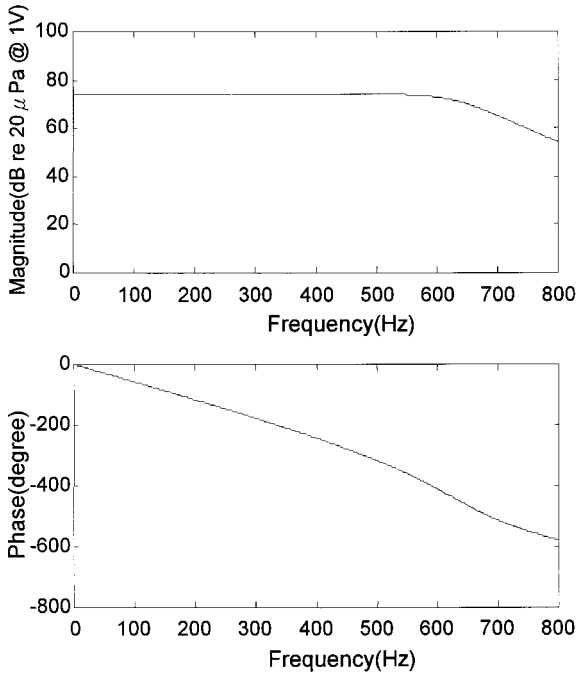

FIG. 15. Frequency response function of the desired model.

the plant T_2 is the woofer, and Q is the feedforward controller. In general, a low-pass filter with linear phase characteristics is selected as the model T_1, which is essentially similar to the low frequency crossover in conventional woofer design. The design problem is to find a proper and stable (denoted as RH^∞) transfer function Q such that the following cost function is minimized

$$J = \min_{Q \in RH^\infty} \|T_1 - T_2\|_2^2, \tag{26}$$

where ''$\|\ \|_2$'' denotes the 2-norm defined as

$$\|G(z)\|_2 \triangleq \left(\frac{1}{2\pi} \int_{-\pi}^{\pi} |G(e^{j\theta})|^2 \, d\theta \right)^{1/2}, \tag{27}$$

where z and θ are z-transform variable and digital frequency, respectively. It can be shown that the optimal solution of this problem is (Doyle *et al.*, 1992)

$$Q = T_{2m}^{-1} (T_{2a}^{-1} T_1)_s, \tag{28}$$

where T_{2m} is the minimum phase part of T_2, T_{a2} is an all pass function and the subscript s denotes the ''stable part.''

In the paper, a ninth-order low-pass filter with cutoff frequency 600 Hz is chosen as the model T_1 (Fig. 15). The frequency response of the plant is shown in Fig. 16. The plant model was found by MATLAB command *invfreqz* (Grace and Laub, 1992) and regenerated in the same plot. By using H_2 modal matching, the optimal controller is calculated, as shown in the frequency response of Fig. 17. The controller was then implemented on the platform of a floating-point DSP, TMS320C31, with a sampling rate of 2 kHz. Figure 18 compares the sound pressure frequency responses of the DML alone, the DML with woofer, and the DML with bass-enhanced woofer. The experimental result demonstrated the significant improvement of overall performance by using the woofer and electronic compensation.

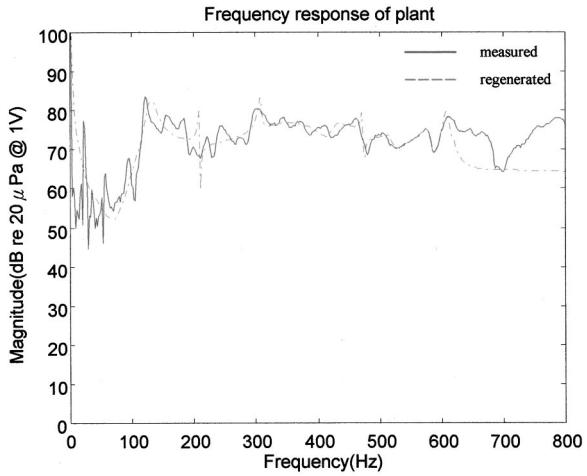

FIG. 16. Frequency response function of the plant. Solid line denotes the measured response and dash line the response regenerated from the curve fit model.

VI. CONCLUSIONS

In the paper, panel speakers were analyzed in terms of structural vibration and acoustic radiation. Simulation tools were developed to facilitate system integration of DML. The driving point impedance for an infinite plate is used and radiation loading is neglected in the modeling. Although this may be sufficient for the present study, a more sophisticated modeling approach dealing with the frequency dependent mechanical impedance and the associated radiation loading of a flexible finite plate should be developed in the future to improve the accuracy of response prediction.

In order to compare the DML with the conventional speaker, an objective evaluation regarding frequency response, directional response, sensitivity, efficiency, and harmonic distortion was undertaken. Experimental results revealed that the DML suffered from an inherent problem of sensitivity and efficiency. To alleviate the problem, electronic compensation based on the H_2 model matching principle was developed. The experimental result demonstrated the improvement of overall performance by using the woofer and electronic compensation. Alongside with the other advantages of DML, the enhanced efficiency should improve its practicality in applications where high audio quality is demanded.

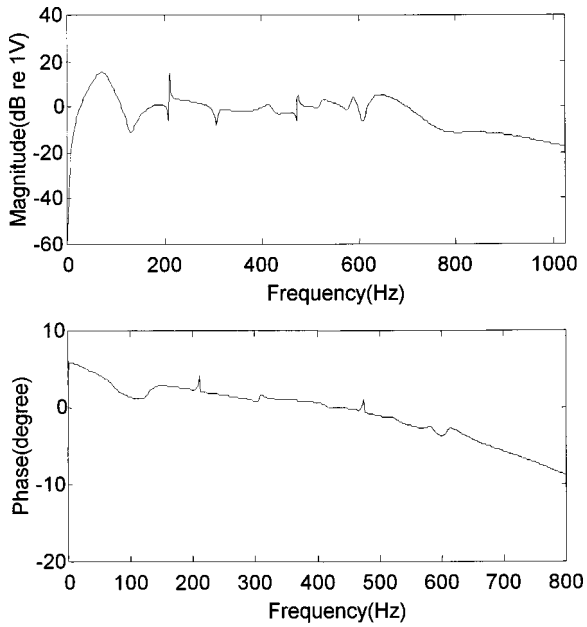

FIG. 17. Frequency response function of the H_2 feedforward controller.

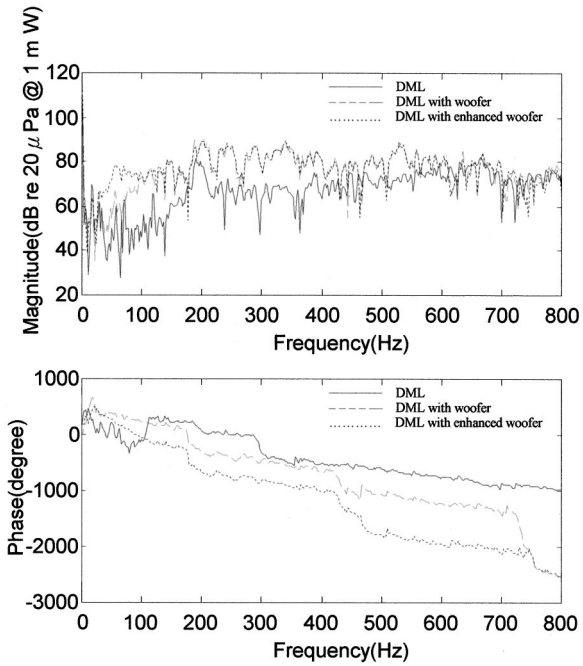

FIG. 18. Frequency response function of the DML system before and after enhancement: DML (solid line), DML with woofer (dash line), DML with enhanced woofer (dotted line). The measurements are under 1 m·W condition.

Although the compensated woofer proved to be a practical solution to the improvement of the overall efficiency, the bulky size of the woofer offsets somewhat the merits of DML. Furthermore, it should be noted that the efficiency problem of the DML alone has not been fundamentally changed in the present approach due to the physical constraint of flexible panels imposed by the sub-coincidence phenomenon. To further improve the efficiency of panel speakers, planar radiators without resort to the mechanism of flexural waves should be sought in the future. To summarize, the major limitations of the present work are: the use of impedance of infinite plate, the neglect of acoustic loading in circuit modeling, and the bass compensation by a conventional woofer. Research is currently on the way to circumvent these limitations.

ACKNOWLEDGMENTS

Special thanks are due to the illuminating discussions with New Transducers Limited, U.K. We also wish to thank Dr. William Thompson, Jr. of Applied Research Laboratory (ARL), Penn State University for lectures on acoustic transducers. The work was supported by the National Science Council (NSC) in Taiwan, Republic of China, under the Project No. NSC 89-2212-E009-057.

Azima, H. (**1998**). ''NXT Up against wall,'' *Audio Magazine*, September, pp. 34–41.
Beranek, L. L. (**1996**). *Acoustics* (Acoustical Society of America, Woodbury, NY).
Borwick, J. (**1994**). *Loudspeaker and Headphone Handbook* (Focal Press, Oxford, U.K.)
Cremer, L., and Heckl, M. (**1988**). *Structure-borne Sound* (Springer-Verlag, Berlin).
Doyle, J. C., Francis, B. A., and Tannenbaum, A. R. (**1992**). *Feedback Control Theory* (Macmillan, New York).
Grace, A., and Laub, A. J. (**1992**). MATLAB *Control System Toolbox* (Math Works, Natick, MA).
Harris, N., and Hawksford, M. O. (**1997**). ''The Distributed-Mode Loudspeaker (DML) as a Broadband Acoustic Radiator,'' The 103rd Convention of Audio Engineering Society Preprint, New York, September 1997, No. 4526 (D6).
ISO standard (**1977**). ''Basic Array of Microphone Positions in Free Field over a Reflecting Plane,'' ISO-3745-1977 (E).
Junger, M. C., and Feit, D. (**1986**). *Sound, Structures, and Their Interaction* (The MIT Press, Cambridge, MA).
Kinsler, L. E., Frey, A. R., Coppens, A. B., and Sanders, J. V. (**1982**). *Fundamentals of Acoustics* (Wiley, New York).
Leissa, A. (**1993**). *Vibration of Plates* (Acoustical Society of America, Woodbury, NY).
Morse, P. M., and Ingard, K. U. (**1986**). *Theoretical Acoustics* (Princeton University Press, Princeton, NJ).
Panzer, J. W., and Harris, N. (**1998a**). ''Distributed-Mode Loudspeaker Radiation Simulation,'' The 104th Convention of Audio Engineering Society Preprint, New York, No. 4783.
Panzer, J. W., and Harris, N. (**1998b**). ''Distributed Mode Loudspeaker Simulation Model,'' The 104th Convention of Audio Engineering Society Preprint, New York, No. 4739.

Time-domain analyses of acoustics–structure interactions for piezoelectric transducers

Sung Yi,[a] Shih Fu Ling, and Ming Ying
School of Mechanical and Production Engineering, Nanyang Technological University, Singapore, 639798, Republic of Singapore

(Received 21 December 1999; accepted for publication 10 July 2000)

Piezoelectric transducers coupled with a surrounding medium are analyzed in time domain using the coupled finite element and boundary element method. Three-dimensional solid elements are employed to model the piezoelectric transducer, while the surrounding medium is described by the boundary integral equation and the boundary of the medium is modeled by two-dimensional spatial elements. Verification studies were conducted to evaluate the accuracy and convergence of the present numerical algorithm and they show that the present numerical solutions agree well with the analytical ones. The influence of the surrounding medium on the acoustic field is studied. The interaction between the structure and surrounding medium affects the structure dynamic performances and acoustic pressure distributions significantly. However, in the present study we show that the radiation directivity is insignificantly influenced by the surrounding medium. [DOI: 10.1121/1.1310672]

PACS numbers: 43.40.At [PJR]

I. INTRODUCTION

Piezoelectric transducers play a paramount role in ultrasonic nondestructive testing systems, ultrasonic imaging and diagnostic equipment, and acoustic microscopy, which are increasingly employed in industrial, medical, and defense areas. There are many factors including characteristic dimensions, material properties, and surrounding medium properties influencing the performance of piezoelectric transducers. Optimal design of piezoelectric transducers is very important to improve their performance. Therefore, it is necessary to predict their structural and acoustic responses accurately.

Finite element analyses of piezoelectric transducers have received considerable attention in the last two decades. Allik *et al.*[1,2] developed the static and dynamic finite element formulations for piezoelectric structures considering piezoelectric–mechanic coupling. Kagawa and Yamabuchi[3] analyzed the axisymmetric vibrations of a piezoelectric circular rod of finite length in the frequency domain. A triangular ring element with linear interpolation functions was employed in the finite element formulations. Bugdayci and Bogy[4] analyzed the vibration characteristics of piezoelectric disks with a two-dimensional finite element method based on the plate theory. Lerch[5] computed the natural frequencies as well as the dynamic responses of piezoelectric transducers due to mechanical and electrical excitations. Challande[6] employed a finite element method to optimize ultrasonic transducers made of piezoelectric composites. Guo, Cawley, and Hitchings[7] used three-dimensional (3-D) finite element methods and modal analysis techniques to predict the vibration characteristics and electric impedance functions of piezoelectric disks. Similar works were also reported by Kagawa *et al.*[8] Hansen[9] set up a finite element model of the piezoelectric transducer consisting of two piezoelectric ceramic disks and two resonance rods. Yi *et al.*[10] also developed the finite element procedure to analyze piezoelectric polymer sensors and actuators.

In the previous studies,[1–9] the interaction between the structure and the surrounding medium was not considered. However, in order to predict the acoustic as well as structural responses of the transducer more accurately, the piezoelectric structure and the acoustic field should be solved simultaneously, as both of them influence each other. Smith, Hunt, and Barach[11] employed a finite element method to analyze an acoustically radiating transducer structure. Finite element methods were used to analyze structures and acoustic radiation loading on structures was modeled by approximating the surface Helmholtz integral equation formulation of acoustic radiation problems. Olson and Bathe[12] used acoustic and piezoelectric finite elements to model both acoustic field and piezoelectric structures. A special interface element was developed for the coupling of acoustic to piezoelectric finite elements. Consequently, they also developed an infinite element for an analysis of transient fluid–structure interactions for an infinite fluid region.[13] Friedrich *et al.*[14] analyzed a fluid–structure interaction for piezoelectric ultrasonic transducers using the finite element method. Chin *et al.*[15] proposed a hybrid finite element method to solve piezoelectric structures immersed in water.

Finite element methods are widely used to analyze complex structures, but are not well suited to handle an exterior fluid medium that is infinite in extent. On the other hand, boundary element methods are ideally suited to handle the exterior fluid problems since they replace the infinite domain problem by an integral equation over the boundary surface of the submerged structure. Therefore, the hybrid method of finite element and boundary element methods seems much more efficient for fluid–structure coupled problems.[15,16] However, most of the previous works[13–16,17] are focused on

[a]Author to whom correspondence should be addressed. Electronic mail: msyi@ntu.edu.sg

the frequency domain analysis and limited work has been reported in the area of the time–domain analysis of acoustics–piezoelectric structure coupled problems.

In the present study, the piezoelectric transducer coupled with the surrounding medium is studied in the time domain using the coupled finite element and boundary element method. The influence of the surrounding medium on the acoustic field is evaluated. The piezoelectric transducer is modeled by three-dimensional solid elements, while the surrounding medium is described by the boundary integral equation and the boundary of the medium is by two-dimensional spatial elements.

II. FORMULATIONS

A. Constitutive equations for piezoelectric materials

The constitutive relationships for linear piezoelectric materials can be described in the material coordinates as

$$\hat{\boldsymbol{\sigma}}=\hat{\mathbf{C}}\hat{\boldsymbol{\epsilon}}, \tag{1}$$

where

$$\hat{\mathbf{C}}=\begin{bmatrix}\mathbf{C} & \mathbf{e}^T\\ \mathbf{e} & -\mathbf{Z}\end{bmatrix},\quad \hat{\boldsymbol{\sigma}}=[\boldsymbol{\sigma}\quad \mathbf{D}]^T,\quad \hat{\boldsymbol{\epsilon}}=[\boldsymbol{\epsilon}\quad -\mathbf{E}]^T,$$

and

$$\boldsymbol{\sigma}=[\sigma_{11}\quad \sigma_{22}\quad \sigma_{33}\quad \tau_{12}\quad \tau_{23}\quad \tau_{13}]^T,$$

$$\mathbf{D}=[D_1\quad D_2\quad D_3]^T,$$

$$\boldsymbol{\epsilon}=[\epsilon_{11}\quad \epsilon_{22}\quad \epsilon_{33}\quad \gamma_{12}\quad \gamma_{23}\quad \gamma_{13}]^T,$$

$$\mathbf{E}=[E_1\quad E_2\quad E_3\quad]^T,$$

where $\boldsymbol{\sigma}$ is the vector of stresses, $\mathbf{D}$ is the vector of electric displacements, $\boldsymbol{\epsilon}$ is the vector of engineering strains, $\mathbf{E}$ is the vector of electric fields, $\mathbf{C}$ is the material stiffness matrix, $\mathbf{e}$ is the piezoelectric stress matrix, and $\mathbf{Z}$ is the dielectric constant matrix under the constant strain.

B. Finite element formulations of piezoelectric structures

The displacement field $\mathbf{u}$ within an element can be interpolated by their nodal displacements as

$$\mathbf{u}=\mathbf{N}_s\mathbf{q}^{(e)}, \tag{2}$$

where $\mathbf{q}^{(e)}$ is the vector of the nodal deformations and $\mathbf{N}_s$ is the element shape function matrix for mechanical deformation.

Consequently, the electric potential V within an element can be interpolated by the node electric potential as

$$V=\mathbf{N}_p\mathbf{V}^{(e)}, \tag{3}$$

where $\mathbf{V}^{(e)}$ is the vector of the nodal electric potential and $\mathbf{N}_p$ is the element shape function matrix for electric potential.

By differentiating Eqs. (2) and (3) with respect to x, y, z coordinates, the electrical and mechanical strain vectors can be expressed in terms of nodal displacements and electric potential as

$$\boldsymbol{\epsilon}=\mathbf{B}\mathbf{q}^{(e)} \tag{4}$$

and

$$\mathbf{E}=-\mathbf{B}_p\mathbf{V}^{(e)}. \tag{5}$$

Combining Eqs. (4) with (5) leads to

$$\hat{\boldsymbol{\epsilon}}=\hat{\mathbf{B}}\hat{\mathbf{q}}^{(e)}, \tag{6}$$

where

$$\hat{\mathbf{B}}=\begin{bmatrix}\mathbf{B} & \mathbf{0}\\ \mathbf{0} & \mathbf{B}_p\end{bmatrix},\quad \hat{\mathbf{q}}^{(e)}=\begin{bmatrix}\mathbf{q}^{(e)}\\ \mathbf{V}^{(e)}\end{bmatrix}.$$

The principle of virtual work for piezoelectric bodies is defined by

$$\int_{v^{(e)}}\delta\hat{\boldsymbol{\epsilon}}^T\hat{\boldsymbol{\sigma}}\,dv-\int_{v^{(e)}}\delta\mathbf{u}^T\mathbf{f}\,dv-\int_{\Gamma^{(e)}}[\,\delta\mathbf{u}^T\mathbf{t}+\delta V\,Q\,]d\Gamma=0, \tag{7}$$

in which δ denotes a small, arbitrary virtual variation, $\mathbf{f}$ is the vector of body force, $\mathbf{t}$ is the vector of boundary traction, Q is the surface charge, $v^{(e)}$ is volume of body, $\Gamma^{(e)}$ is the area on which boundary tractions and charge are prescribed, and the only body force is the inertial D'Alembert force defined by

$$\mathbf{f}=-\rho\ddot{\mathbf{u}}, \tag{8}$$

where ρ is the mass density.

By substituting Eqs. (2), (3), (4), and (5) into (7), the following finite element equilibrium equations are obtained for each element:

$$\hat{\mathbf{M}}^{(e)}\ddot{\hat{\mathbf{q}}}^{(e)}+\hat{\mathbf{K}}^{(e)}\hat{\mathbf{q}}^{(e)}=\hat{\mathbf{F}}^{(e)}, \tag{9}$$

where

$$\hat{\mathbf{M}}^{(e)}=\int_{v^{(e)}}\begin{bmatrix}\rho\mathbf{N}_s^T\mathbf{N}_s & 0\\ 0 & 0\end{bmatrix}dv,$$

$$\hat{\mathbf{K}}^{(e)}=\int_{v^{(e)}}\hat{\mathbf{B}}^T\hat{\mathbf{C}}\hat{\mathbf{B}}\,dv,$$

$$\hat{\mathbf{F}}^{(e)}=\int_{\Gamma^{(e)}}\begin{bmatrix}\mathbf{N}_s^T\mathbf{t}\\ \mathbf{N}_p^TQ\end{bmatrix}d\Gamma.$$

Subsequently, the finite element equation of the global system can be obtained by assembling element contributions over the entire domain,

$$\hat{\mathbf{M}}\ddot{\hat{\mathbf{q}}}+\hat{\mathbf{K}}\hat{\mathbf{q}}=\hat{\mathbf{F}}, \tag{10}$$

where $\hat{\mathbf{M}}$, $\hat{\mathbf{K}}$, and $\hat{\mathbf{F}}$ are the global mass matrix, stiffness matrix, and load vector, respectively.

C. Boundary element formulations

For three-dimensional acoustic problems, the governing equations for sound propagation in a medium can be described by a linear wave equation in Cartesian coordinate systems as

$$\nabla^2p(\mathbf{x},t)-\frac{1}{c^2}\frac{\partial^2p(\mathbf{x},t)}{\partial t^2}=0, \tag{11}$$

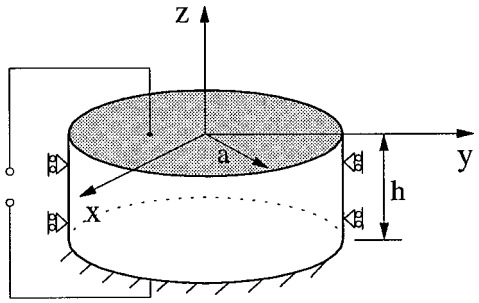

FIG. 1. Schematic of a piezoelectric transducer.

where ∇^2 is the Laplace operator, $p(\mathbf{x},t)$ represents the acoustic pressure in terms of the receiver position $\mathbf{x}$ and time t, and c is the speed of wave in the medium.

The weighted residual method is employed for an approximate solution over the domain. The residual within the time period from 0 to $+\infty$ can be weighted as follows:

$$\int_t \int_v \left[\nabla^2 p(\mathbf{x},t) - \frac{1}{c^2} \frac{\partial^2 p(\mathbf{x},t)}{\partial t^2} \right] p^* \, dv \, dt = 0, \tag{12}$$

where the fundamental solution for the three-dimensional domain is used as the weighted function,

$$p^* = \frac{\delta(t - t_{\mathrm{Ret}})}{4\pi R}, \tag{13}$$

where $R = |\mathbf{x} - \mathbf{x}_0|$ is the distance between the source point $\mathbf{x}$ and the receiver point $\mathbf{x}_0$, $t_{\mathrm{Ret}} = t_0 - R/c$ is the retarded time, and $\delta(t - t_{\mathrm{Ret}})$ is the Dirac delta function.

In general, the boundary integral equations for three-dimensional exterior and interior problems are derived as

$$\alpha(\mathbf{x}_0) p(\mathbf{x}_0, t_0) = - \int_S \frac{\rho_0}{R} \frac{\partial v_n(\mathbf{x}, t_{\mathrm{Ret}})}{\partial t} dS + \int_S \frac{\mathbf{Rn}}{R^3} \left[\frac{R}{c} \frac{\partial p(\mathbf{x}, t_{\mathrm{Ret}})}{\partial t} + p(\mathbf{x}, t_{\mathrm{Ret}}) \right] dS, \tag{14}$$

where $\mathbf{R} = \mathbf{x} - \mathbf{x}_0$, $\mathbf{n}$ is the normal vector of the boundary surface, $v_n(\mathbf{r}, t_{\mathrm{Ret}})$ is the normal particle velocity, and $\alpha(\mathbf{x}_0)$ is the solid angle subtended by the domain at point $\mathbf{x}_0$, i.e.,

$\alpha(\mathbf{x}_0) = 0$, outside the domain,

$\alpha(\mathbf{x}_0) = 4\pi$, inside the domain,

$\alpha(\mathbf{x}_0) = 2\pi$, on the smooth surface.

For the boundary element method, the boundary surface is discretized into several regions. The boundary integral equations for the acoustic pressure then become

$$\alpha(\mathbf{x}_0) p(\mathbf{x}_0, t_0) = - \sum_{j=1}^{m} \int_{S^j} \frac{\rho_0}{R^j} \frac{\partial v_n^j(\mathbf{x}, t_{\mathrm{Ret}})}{\partial t} dS + \sum_{j=1}^{m} \int_{S^j} \frac{\mathbf{R}^j \mathbf{n}^j}{R^{j^3}} \left[\frac{R^j}{c} \frac{\partial p^j(\mathbf{x}, t_{\mathrm{Ret}})}{\partial t} + p^j(\mathbf{x}, t_{\mathrm{Ret}}) \right] dS, \tag{15}$$

TABLE I. Material properties of PZT.

$E_{11} = E_{22}$ (N/m^2)	E_{33} (N/m^2)	$\nu_{12} = \nu_{23} = \nu_{31}$	ρ (kg/m^3)	
6.7×10^{10}	5.0×10^{10}	0.33	7800	
e_{31} (C/m^2)	e_{33} (C/m^2)	e_{15} (C/m^2)	Z_1 (F/m)	Z_3 (F/m)
-11.47	19.35	13.72	2.12×10^{-8}	2.03×10^{-8}

where the superscript j denotes the jth element and m is the total boundary element number.

The source point $\mathbf{x}$ is located at the boundary surface and can be interpolated by the nodal coordinates within an element. The distance from the source point to the receiver point can be interpolated by the interpolation functions $\mathbf{N}_a$ as

$$\mathbf{R}^j = \mathbf{N}_a \mathbf{x}^j - \mathbf{x}_0, \tag{16}$$

where

$$\mathbf{N}_a = [N_1 \quad N_2 \quad \cdots], \quad \mathbf{x}^j = [x_1^j \quad \mathbf{x}_2^j \quad \cdots]^T,$$

and the pressure distribution within an element can also be written as

$$p^j(\mathbf{x}, t_{\mathrm{Ret}}) = \mathbf{N}_a \mathbf{p}^j(t_{\mathrm{Ret}}), \tag{17}$$

where

$$\mathbf{p}^j(t_{\mathrm{Ret}}) = [p_1^j(t_{\mathrm{Ret}}) \quad p_2^j(t_{\mathrm{Ret}}) \quad \cdots]^T,$$

and $\mathbf{x}_i^j$ and $p_i^j(t_{\mathrm{Ret}})$ are the position vector and pressure at the ith node of the jth element, respectively. Similarly, the normal particle acceleration at the boundary surfaces can be interpolated as

$$\frac{\partial v_n^j(\mathbf{x}, t_{\mathrm{Ret}})}{\partial t} = \mathbf{N}_v \dot{\mathbf{v}}^j(t_{\mathrm{Ret}}), \tag{18}$$

where $\mathbf{N}_v$ is the interpolation function matrix and $\dot{\mathbf{v}}^j(t_{\mathrm{Ret}})$ is the nodal particle acceleration vector. If the interaction between structure and surrounding medium is considered, $\mathbf{N}_v$ and $\dot{\mathbf{v}}^j(t_{\mathrm{Ret}})$ depend on the element type used for both the structure and the medium since the normal particle acceleration continuity at the interface.

The nodal variables $p_i^j(t_{\mathrm{Ret}})$ and $\dot{v}^j(t_{\mathrm{Ret}})$ are the functions of the retarded time. Since the retarded time is not equal to an integer number of time step, the interpolation

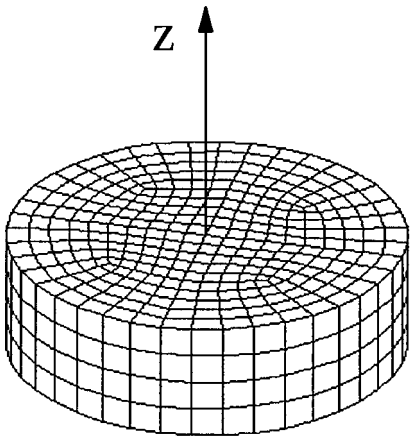

FIG. 2. Finite element and boundary element model for the piezoelectric transducer.

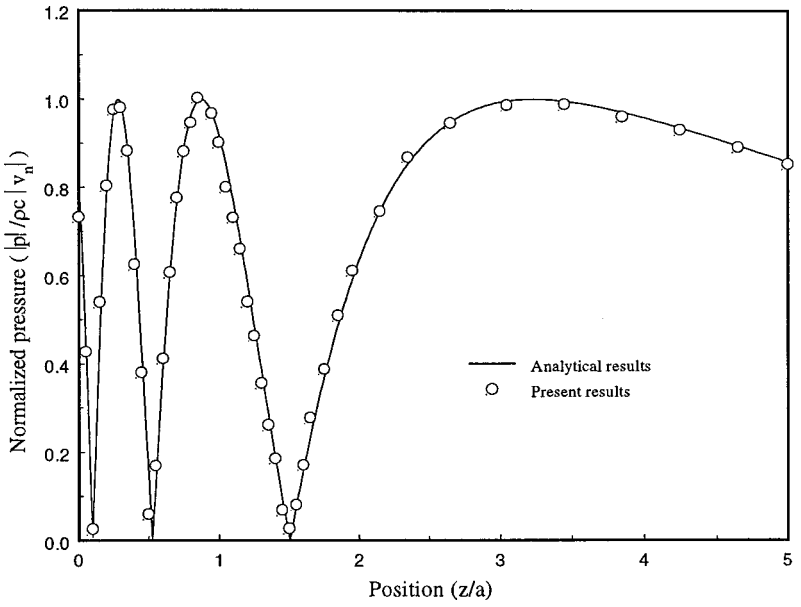

FIG. 3. Normalized acoustic pressure amplitudes along the normal direction with surrounding air.

between the adjacent nodal values is needed to obtain the values of the acoustic pressure and particle acceleration at the retarded time. The linear interpolation functions are employed for the time discretization of both the pressure and acceleration and the two adjacent time points t_l and t_{l+1} are defined as

$$t_l = l\,\Delta t, \quad t_{l+1} = (l+1)\Delta t, \tag{19}$$

where the time interval is Δt and l can be calculated as

$$l = \mathrm{INT}\left(\frac{t_{\mathrm{Ret}}}{\Delta t}\right),$$

where INT is an integer function. As a result, the nodal variables $p_i^j(t_{\mathrm{Ret}})$ and $\dot{\mathbf{v}}^j(t_{\mathrm{Ret}})$ at the retarded time can be expressed as

$$p_i^j(t_{\mathrm{Ret}}) = \sum_{k=l}^{l+1} p_i^j(t_k) T_k,$$

$$\frac{\partial p_i^j(t_{\mathrm{Ret}})}{\partial t} = \sum_{k=l}^{l+1} p_i^j(t_k) \frac{\partial T_k}{\partial t}, \tag{20}$$

$$\dot{\mathbf{v}}^j(t_{\mathrm{Ret}}) = \sum_{k=l}^{l+1} \dot{\mathbf{v}}^j(t_k) T_k,$$

where the linear temporal interpolation functions T_l and T_{l+1} are

$$T_l = \frac{t_{l+1} - t_{\mathrm{Ret}}}{\Delta t}, \quad T_{l+1} = \frac{t_{\mathrm{Ret}} - t_l}{\Delta t}.$$

In the discretized time domain, the boundary integral equation can be written as

$$\alpha(\mathbf{x}_0) p(\mathbf{x}_0, t_0) = -\sum_{j=1}^{m} \int_{S^j} \frac{\rho_0}{R^j} \mathbf{N}_v \sum_{k=l}^{l+1} \dot{\mathbf{v}}^j(t_k) T_k \, dS + \sum_{j=1}^{m} \int_{S^j} \frac{\mathbf{R}^j \mathbf{n}^j}{R^{j^3}} \mathbf{N}_a \sum_{k=l}^{l+1} \mathbf{p}^j(t_k) \times \left[\frac{R^j}{c} \frac{\partial T_k}{\partial t} + T_k\right] dS. \tag{21}$$

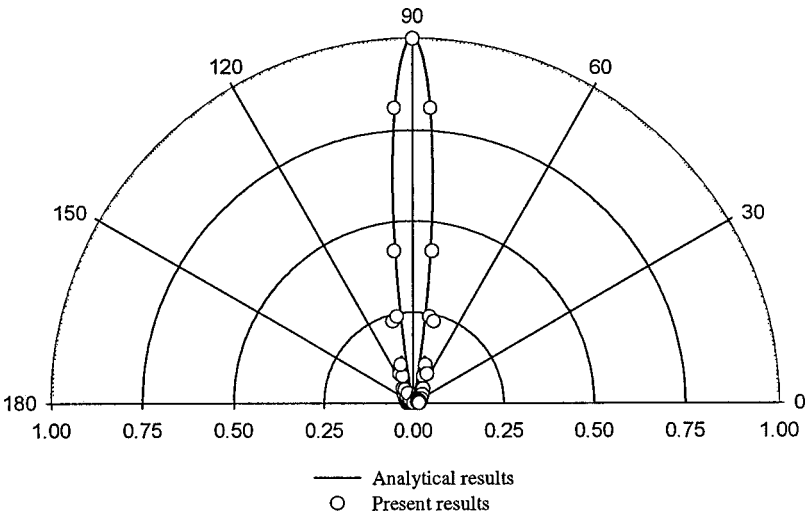

FIG. 4. Radiation directivity patterns with surrounding air.

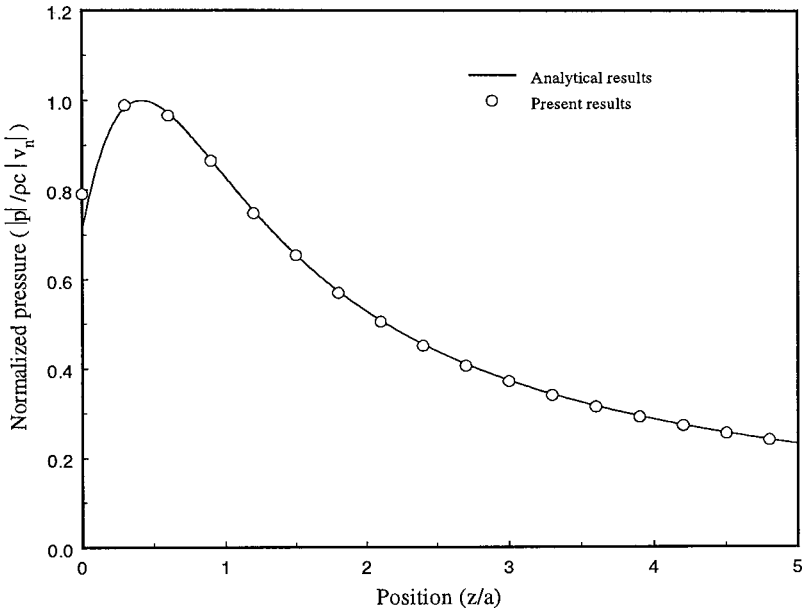

FIG. 5. Normalized acoustic pressure amplitudes along the normal direction with surrounding water.

If $\Delta t \geqslant R/c$, the right-hand side of Eq. (21) includes the unknown variables at the present time and Eq. (21) becomes implicit. Otherwise the right-hand side of Eq. (21) includes the previous solutions only and Eq. (21) becomes explicit. For both implicit or explicit equations, Eq. (21) can be rewritten in the matrix form as

$$\mathbf{A}_p \mathbf{p} = \mathbf{H} + \mathbf{A}_v \dot{\mathbf{v}}, \tag{22}$$

where $\mathbf{p}$ is the pressure vector of the nodes at the present time, $\dot{\mathbf{v}}$ is the acceleration vector of the nodes at the present time, and the vector $\mathbf{H}$ contains nodal variables at the previous time. For the explicit formulation, $\mathbf{A}_p$ and $\mathbf{A}_v$ are diagonal and zero matrices, respectively, while they are unsymmetric matrices for the implicit formulation. In the present study, the explicit method is used.

D. Acoustics–piezoelectric structure interaction

For acoustics–piezoelectric structure coupled problems, the only unknown boundary conditions for both the structure and the acoustic field are at acoustic–structure interfaces. In this case, the structural response and the acoustic field must be coupled together by ensuring that the normal particle acceleration and surface pressure are continuous on the interface surface.

The solid element is used for the analysis of piezoelectric structures. The acceleration field within an element can be interpolated by the nodal accelerations as

$$\ddot{\mathbf{u}} = \mathbf{N}_s \ddot{\mathbf{q}}^{(e)}. \tag{23}$$

When a solid element is coupled with the jth boundary element at one of its surfaces, i.e., $\xi = 1$ (the solid element has six surfaces at $\xi = \pm 1$, $\eta = \pm 1$, and $\xi = \pm 1$), to ensure the continuity conditions, the normal particle acceleration can be written in terms of the nodal accelerations of structures as

$$\dot{v}_n^j = (\mathbf{n}^T \mathbf{N}_s)_{\xi=1} \ddot{\mathbf{q}}^{(e)}. \tag{24}$$

From Eqs. (24) and (18), we obtain

$$\mathbf{N}_v = (\mathbf{n}^T \mathbf{N}_s)_{\xi=1} \tag{25}$$

and

$$\dot{\mathbf{v}}^j = \ddot{\mathbf{q}}^{(e)}. \tag{26}$$

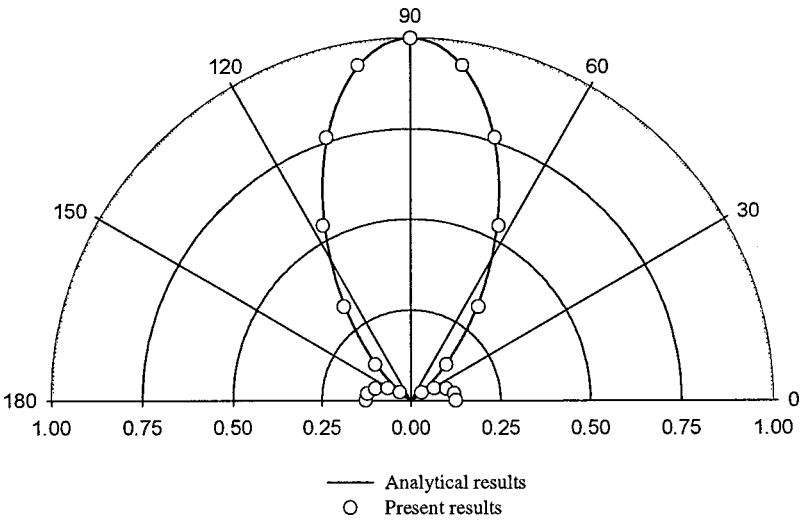

FIG. 6. Radiation directivity patterns with surrounding water.

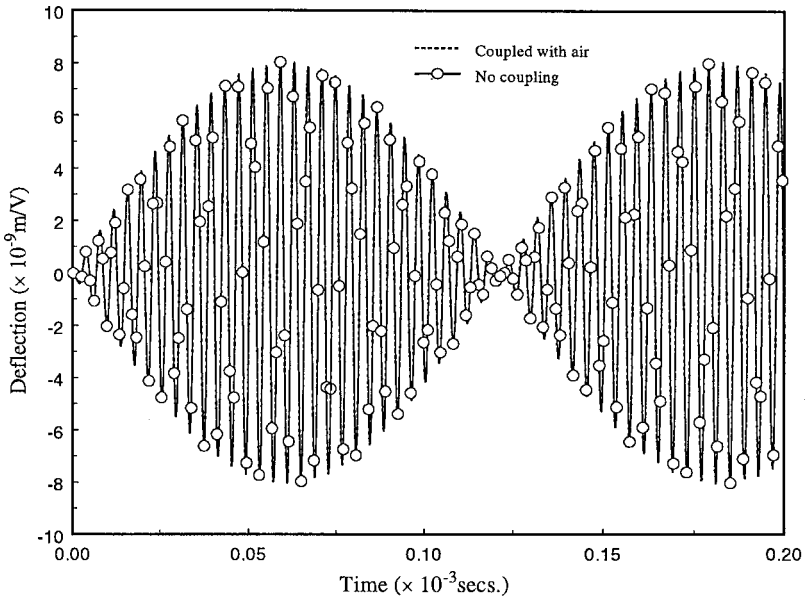

FIG. 7. Deflections of the piezoelectric transducer with surrounding air.

Subsequently, the global acceleration vector $\dot{\mathbf{v}}$ of the acoustic field can be defined as

$$\dot{\mathbf{v}} = \mathbf{T}_a \ddot{\mathbf{q}}, \tag{27}$$

where $\mathbf{T}_a$ is the variable transformation matrix between the entire elements used for the structure and the solid elements coupled with the boundary elements. Then Eq. (22) can be rewritten as

$$\mathbf{A}_p \mathbf{p} = \mathbf{H} + \mathbf{A}_v \mathbf{T}_a \ddot{\mathbf{q}}. \tag{28}$$

When the structure is subjected to the acoustic loading, the exterior loading vector $\hat{\mathbf{F}}$ in Eq. (10) becomes

$$\hat{\mathbf{F}} = \hat{\mathbf{F}}_s + \hat{\mathbf{F}}_a, \tag{29}$$

where $\hat{\mathbf{F}}_s$ is the loading vector due to applied traction and surface charge, and $\hat{\mathbf{F}}_a$ is the loading vector due to acoustic pressure $\mathbf{p}$ and can be expressed with the transformation matrix $\mathbf{L}$ as

$$\hat{\mathbf{F}}_a = \mathbf{L}\mathbf{p}. \tag{30}$$

The acoustic pressure can then be derived from Eq. (28) as

$$\mathbf{p} = \mathbf{A}_p^{-1}\mathbf{H} + \mathbf{A}_p^{-1}\mathbf{A}_v \mathbf{T}_a \ddot{\mathbf{q}}. \tag{31}$$

Substitution of Eqs. (29), (30), and (31) into (10) leads to

$$[\hat{\mathbf{M}} - \mathbf{L}\mathbf{A}_p^{-1}\mathbf{A}_v \mathbf{T}_a]\ddot{\hat{\mathbf{q}}} + \hat{\mathbf{K}}\hat{\mathbf{q}} = \hat{\mathbf{F}}_s + \mathbf{L}\mathbf{A}_p^{-1}\mathbf{H}. \tag{32}$$

The structural displacement and electrical potential can be found by solving Eq. (32) and then the velocity and the acceleration can be determined on the basis of the displacement field. Subsequently, the acoustic pressure can be calculated from the boundary integral equation.

The three-dimensional finite element and boundary element coupled program ACOUS–PIEZO has been developed based on the above formulation, which has four-node/eight-

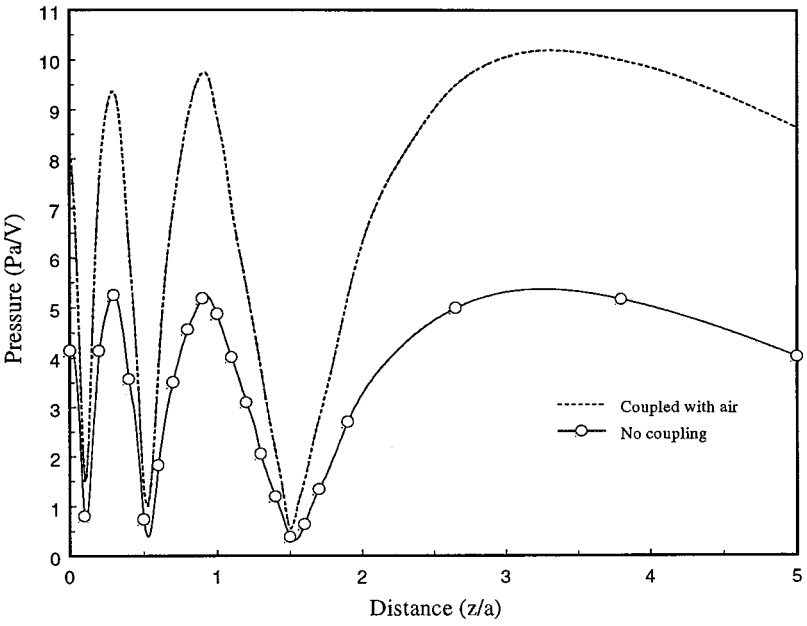

FIG. 8. Acoustic pressure amplitudes along the normal direction with surrounding air.

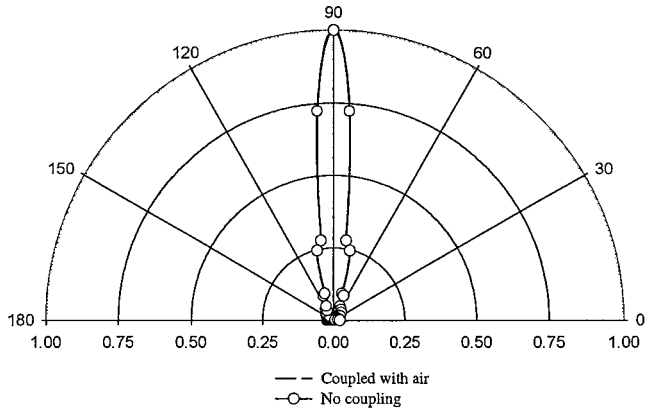

FIG. 9. Radiation directivity patterns of the piezoelectric transducer with surrounding air.

node isoparametric elements and eight-node/twenty-node isoparametric elements for acoustic field and piezoelectric structures.

III. RESULTS AND DISCUSSION

To demonstrate the influence of the surrounding medium, the simplified piezoelectric transducer shown in Fig. 1 is studied. The transducer is baffled in a half-infinite space. One end of the transducer is rigidly clamped and only longitudinal oscillation is considered. The reaction-free boundary condition is assumed for the infinite baffle. The radius a and thickness h are 4.5×10^{-3} m and 2.91×10^{-3} m, respectively. Each surface of the transducer is covered by one electrode. The polarized direction is along the longitudinal direction of the transducer. The material properties are listed in Table I. It is assumed that the acoustic reflection of the structure surfaces can be neglected, which leads to the Rayleigh integral

$$p(\mathbf{x}_0,t_0)=-\frac{\rho}{4\pi}\int_S\frac{1}{R}\frac{\partial v_n(\mathbf{x},t_{\mathrm{Ret}})}{\partial t}dS, \tag{33}$$

where ρ is the density of the medium. For the harmonic analysis, the amplitude of pressure on the symmetry axis with distance z from the center of the free surface normalized by the velocity amplitude can be derived as

$$\frac{|p|}{\rho c|v_n|}=\sin\left[\frac{k(z^2+a^2)^{1/2}-kz}{2}\right], \tag{34}$$

where the wave number $k=\omega/c$. Two surrounding mediums such as air and water are considered for the half-infinite space. The densities of air and water are taken as 1.2 K and 1000 K g/m^3, respectively, while the acoustic speed c of air and water are taken as 341 and 1500 m/s.

As shown in Fig. 2, the transducer is modeled by 1200 three-dimensional eight-node hexahedron elements with a total of 1605 nodes. The free surface is modeled by another 300 four-node spatial boundary elements. The time interval is taken as 0.1×10^{-6} s.

The structure coupled and without coupled with the surrounding medium is studied. For the coupled case, the acoustic pressure reflecting from the structure surfaces is considered and the acoustic pressure is also applied to the structure surfaces, while the without coupled case neglects the acoustic reflection and the acoustic pressure on the structure surfaces.

To compare with the results derived by the harmonic analysis with the Rayleigh integral, the transducer is forced to oscillate with constant frequency 250×10^3 Hz. The wave numbers for both air and water are 4606 and 1047 at the current frequency. The interaction between the structure and surrounding medium does not influence the structure dynamic performances. The analytical directivity patterns are obtained at the farfield, which means the radial distance R is much larger than a. For the present numerical analysis, R is taken as $5a$. Figures 3 and 4 show the acoustic pressure amplitudes along the normal direction and the corresponding directivity patterns with surrounding air, and Figs. 5 and 6 show the variables distributions with surrounding water. The good agreement between the results and the present results is

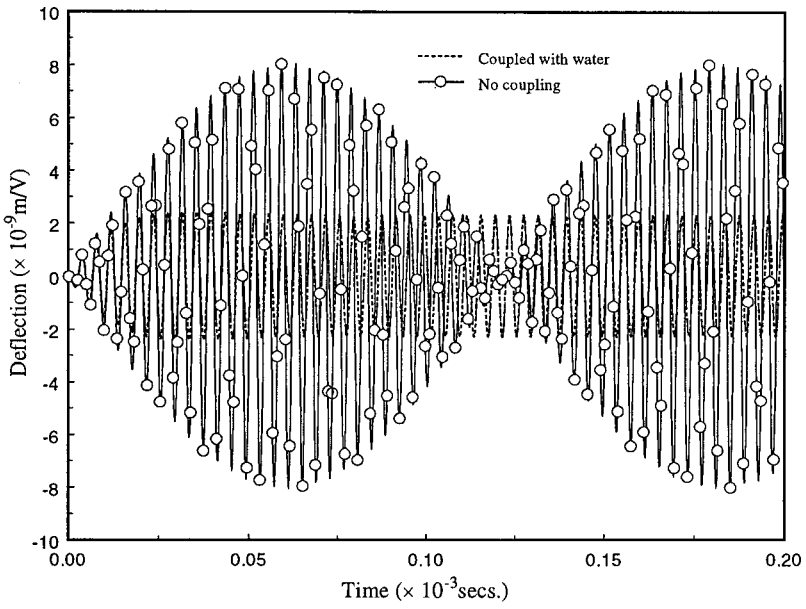

FIG. 10. Deflections of the piezoelectric transducer with surrounding water.

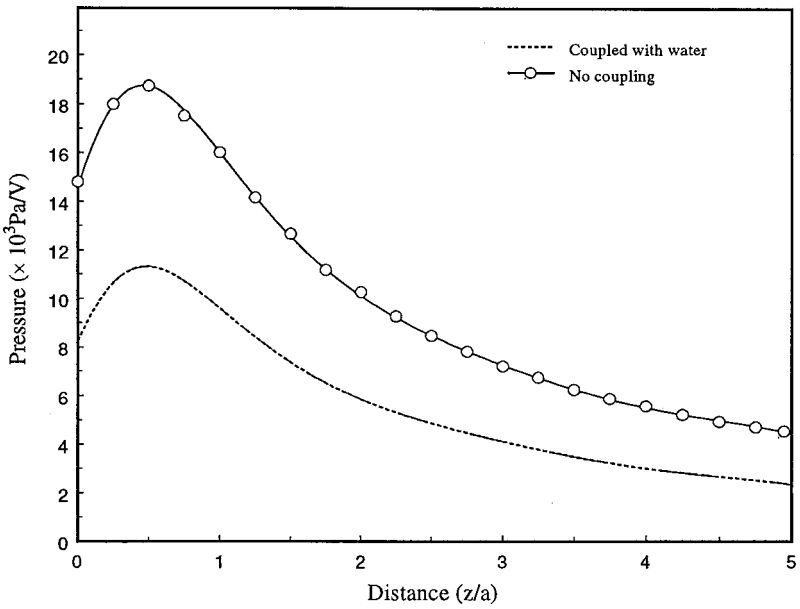

FIG. 11. Acoustic pressure amplitudes along the normal direction with surrounding water.

obtained. The acoustic reflection does not influence the acoustic pressure distribution and radiation directivity with the harmonic analysis for the current transducer.

Next, the electric exciting vibration problem with a transient analysis is considered. Input voltage is applied to the piezoelectric transducer surfaces and is taken as

$$\mathrm{Vol} = V_0 \sin(500 \times 10^3 \pi t) \quad (\mathrm{V}), \tag{35}$$

where $V_0 = 1.0$. The frequency of input voltage is chosen to be close to the first natural frequency of the transducer in order to generate large amplitudes of vibration. Initial displacement, velocity, and acceleration of the structure are zero. Figures 7, 8, and 9 show the deflection responses, the acoustic pressure distributions along the normal direction, and the radiation directivity patterns under the electric exciting with surrounding air.

The results show that the interaction between the structure and surrounding air does not influence structure dynamic responses and acoustic directivities for the current transducer, but it influences the acoustic pressure distributions. However, for the water, the interaction between the structure surface and surrounding water is very significant. Figures 10 and 11 show the deflection responses and acoustic pressure distributions along the normal dirction. Figure 12 also illustrates the radiation directivity patterns. The interaction between the structure and surrounding water does not influence the directivity. Comparing Figs. 9 and 12 with Figs. 4 and 6, it also can be found that the same radiation directivity can be derived from either harmonic or transient analyses.

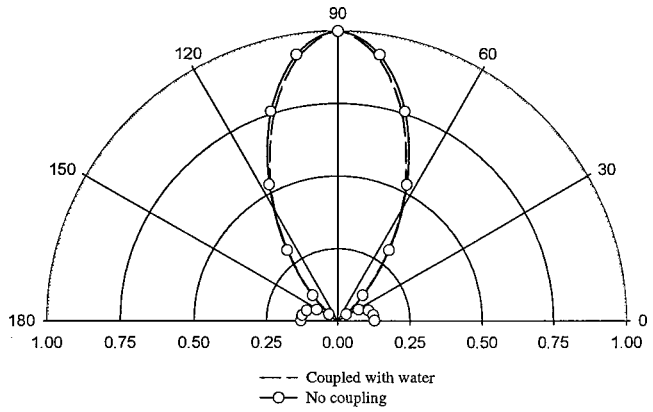

FIG. 12. Radiation directivity patterns of the piezoelectric transducer with surrounding water.

IV. CONCLUSIONS

Dynamic responses of piezoelectric transducers coupled with the surrounding medium are evaluated using the coupled finite element and boundary element method. The acoustics–structure interaction between the transducer and its surrounding medium is considered and the influence of the surrounding medium is studied. For the harmonic loading case, the influence of the medium on the acoustic field is negligible for the transducer with a given dimension. However, the results of the applied voltage loading case show that the interaction between the structure and surrounding medium influences the structure performances and acoustic distributions significantly. In the present study we demonstrate that the coupled finite element and boundary element method can be utilized for the accurate analysis of the structural and acoustic field of the transducer.

[1] H. Allik and T. J. R. Hughes, ''Finite element method for piezoelectric vibration,'' Int. J. Numer. Methods Eng. **2**, 151–157 (1970).
[2] H. Allik, K. M. Webman, and J. T. Hunt, ''Vibration response of sonar transducers using piezoelectric finite element,'' J. Acoust. Soc. Am. **56**, 1782–1791 (1974).
[3] Y. Kagawa and T. Yamabuchi, ''Finite element approach for a piezoelectric circular rod,'' IEEE Trans. Sonics Ultrason. **SU-23**, 379–385 (1976).
[4] N. Bugdayci and D. B. Bogy, ''A two dimensional theory for piezoelectric layers used in electromechanical transducers,'' Int. J. Solids Struct. **17**, 1159–1202 (1981).
[5] R. Lerch, ''Simulation of piezoelectric devices by two- and three-dimensional finite elements,'' IEEE Trans. Ultrason. Ferroelectr. Freq. Control **37**, 233–247 (1990).
[6] P. Challande, ''Optimizing ultrasonic transducers based on piezoelectric composites using a finite element method,'' IEEE Trans. Ultrason. Ferroelectr. Freq. Control **37**, 135–140 (1990).
[7] N. Guo, P. Cawley, and D. Hitchings, ''Finite element analysis of the

vibration characteristics of piezoelectric discs,'' J. Sound Vib. **159**, 115–138 (1992).
[8] Y. Kagawa, T. Tsuchiya, T. Kataoka, T. Yamabuchi, and T. Furukawa, ''Finite element simulation of dynamic responses of piezoelectric actuators,'' J. Sound Vib. **191**, 519–538 (1996).
[9] H. H. Hansen, ''Optimal design of an ultrasonic transducer,'' Struct. Opt. **14**, 150–157 (1997).
[10] S. Yi, S. F. Ling, M. Ying, H. H. Hilton, and J. R. Vinson, ''Finite element formulation of anisotropic coupled piezo-hygro-thermo-viscoelastic-dynamic problems,'' Int. J. Numer. Methods Eng. **45**, 1531–1546 (1999).
[11] R. R. Smith, J. T. Hunt, and D. Barach, ''Finite-element analysis of acoustically radiating structures with applications to sonar transducers,'' J. Acoust. Soc. Am. **54**, 1277–1288 (1973).
[12] L. G. Olson and K. J. Bathe, ''Analysis of fluid–structure interactions. A direct symmetric coupled formulation based on the fluid velocity potential,'' Comput. Struct. **21**, 21–32 (1985).
[13] L. G. Olson and K. J. Bathe, ''An infinite element for analysis of transient fluid–structure interactions,'' Eng. Comput. **2**, 319–328 (1985).
[14] W. Friedrich, R. Lerch, and P. Krammer, ''Analysis of fluid–structure interaction for piezoelectric ultrasonic transducers using the finite element method,'' *Ultrasonic International 89 Conference Proceedings*, 1989, pp. 430–435.
[15] L.-C. Chin, V. V. Varadan, and V. K. Varadan, ''Hybrid finite element formulation for periodic piezoelectric arrays subjected to fluid loading,'' Int. J. Numer. Methods Eng. **37**, 2987–3003 (1994).
[16] A. F. Seybert, T. W. Wu, and W. L. Li, ''Coupled FEM/BEM for fluid–structure interaction using Ritz vectors and eigenvectors,'' J. Vibr. Acoust. **115**, 152–158 (1993).
[17] C. Rajakumar and A. Ali, ''Boundary element-finite element coupled eigenanalysis of fluid–structure systems,'' Int. J. Numer. Methods Eng. **39**, 1625–1634 (1996).

Visualization of acoustic radiation from a vibrating bowling ball

Sean F. Wu, Nassif Rayess, and Xiang Zhao
Department of Mechanical Engineering, Wayne State University, Detroit, Michigan 48202

(Received 10 April 2000; revised 21 January 2001; accepted 8 February 2001)

This paper presents visualization of acoustic radiation from a vibrating bowling ball using the Helmholtz equation least squares (HELS) method. In conducting the experiments, the ball is excited by a vibration shaker using stationary random signals. The radiated acoustic pressures are measured using two microphones and taken as input to the HELS formulations. The reconstructed acoustic pressures on the bowling ball surface are compared with those measured at the same locations. Also shown are comparisons of the reconstructed and measured acoustic pressure spectra at various locations on the bowling ball surface. Results demonstrate that the accuracy of reconstruction based on measurements over a conformal surface is much higher than that over a finite planar surface. This is because the latter often extends beyond the near-field region, making the accuracy of measurements inconsistent. Nevertheless, satisfactory reconstruction of acoustic pressure fields over the entire bowling ball surface can still be obtained based on the measurements taken over a finite planar surface on one side of the source. In a similar manner, the normal component of the surface velocity is reconstructed. Once these acoustic quantities are determined, the time-averaged acoustic intensity is calculated. Also presented are the formulations for estimating *a priori* the numbers of expansion functions and measurements required by the HELS method and the guidelines for determining the reconstruction error and optimum measurement locations, given the overall dimensions of the source and the highest frequency of interest in reconstruction. [DOI: 10.1121/1.1361059]

PACS numbers: 43.40.Rj, 43.20.Rz, 43.50.Yw [CBB]

I. INTRODUCTION

Near-field acoustic holography (NAH) has been developed as a means for visualizing acoustic radiation from a vibrating object.[1–6] Over the past 2 decades many improvements on NAH have been made to extend it to an arbitrary surface and to enhance the efficiency and accuracy of reconstruction. The original NAH uses a plane wave expansion to represent the radiated acoustic field. The advantage of a planar NAH is that if the acoustic pressures over an infinite plane at $z=z_h$ can be measured continuously and exactly, the acoustic pressure and the normal component of the particle velocity anywhere including the source surface can be reconstructed with an infinite resolution. However, such a scenario cannot be realized because in practice the measurement area is always finite and the dynamic range of measurement devices is limited. Moreover, measurements and reconstruction of the acoustic field are confined to a planar surface, and the periphery of measurement aperture must be much larger than that of the source surface.[7] These shortcomings make the planar NAH suitable for a planar source, but not for an arbitrary surface.

To reconstruct acoustic radiation on the surface of an arbitrary object, one can utilize the Helmholtz integral theory that relates the field acoustic pressure to the acoustic quantities on the surface of the object.[8–13] While this integral formulation is advantageous for a general surface, it has several inherent drawbacks. The first one is the well-known nonuniqueness of solutions to the surface Helmholtz integral equation. This drawback can be overcome by the CHIEF method,[14] provided that the over-determined points are properly selected. The second drawback lies in the fact that the acoustic field is determined via a spatial discretization. In other words, the acoustic quantities are specified on certain discrete nodes and the measurements must be taken over a surface that completely encloses the source at once. For an arbitrary structure such as an engine vibrating in the low- to mid-frequency regime, the total number of discretized nodes on the surface can be very large, which necessitates taking a large number of measurements around the source. While one can use an iteration scheme[15,16] to select the optimal measurement locations that may lead to more accurate reconstruction and slightly reduce the overall number of measurements, the very process of this scheme can be very time consuming.

Recently, another technique known as the HELS method[17,18] was developed. In this method, the radiated acoustic pressure is expressed as an expansion of basis functions. The coefficients associated with these basis functions are determined by matching the assumed solution to the measured acoustic pressures. The errors incurred in this process are minimized by the least-squares method. Note that since the problem is often ill posed, it is critical to determine an optimal number of expansion functions, which depends on the signal to noise ratio (SNR), dynamic range of measurement devices, and standoff distances. The higher the SNR and dynamic range and the smaller the standoff distance, the larger the value of the optimum expansion number and the higher the accuracy of reconstruction.

The HELS method thus developed has been used to reconstruct acoustic radiation in both exterior[19] and interior[20] regions. One unique feature of this method is that it imposes no restrictions on the measurement locations. Moreover, the

measurement aperture can be set comparable to the reconstruction area and reconstruction on the source surface can be carried out on a piecewise basis, making the whole process flexible and versatile.

It must be pointed out that the principle (i.e., expansion theory) underlying the HELS method has been discussed extensively in the past. For example, it has been used to analyze directivity patterns,[21,22] far-field acoustic radiation based on near-field measurements,[23] sound radiation from a violin[24] and antenna,[25,26] noise source,[27] and near-field acoustic scanning.[28]

An alternative to the spherical expansions is a collocation method first presented by Frazer *et al.*[29] as a means for satisfying differential equations at discrete points with a series expansion, which satisfies boundary conditions exactly. Alternatively, one can write the acoustic pressure in terms of a series expansion that satisfies the Helmholtz equation, whose coefficients are determined by requiring the solutions to satisfy the boundary conditions at certain discrete points in the least-squares sense.[30] This finite-series expansion solution is discussed by Collatz[31] and used by Meggs[32] and Butler[33,34] to predict far-field radiation based on the near-field measurements.

Note that this boundary-collocation method is a variation of many related numerical techniques used to solve partial differential equations. These techniques are based on an assumed solution that satisfies the equation and/or boundary conditions exactly. The coefficients associated with this assumed solution can be determined using the least-squares, subdomain, collocation, or Galerkin's method, which are special cases of the general criterion that the weighted averages of the residual error must vanish. Each of these methods yields a different set of weighting functions.

All these techniques require the assumed solution to satisfy the boundary conditions at a number of points equal to that of the expansion coefficients. These unknown coefficients are then determined by taking a direct or pseudoinversion of the resulting matrix equation. Such an approach works for prediction of far-field acoustic radiation that can be described effectively by a few expansion functions. However, it cannot be used to reconstruct the acoustic field on the source surface. This is because the inverse acoustic radiation problem is ill posed. Hence any slight error in the input data may be so magnified in the inversion of the matrix that the reconstructed acoustic field can be completely distorted.

The main objective of the present paper is to demonstrate the effectiveness of the HELS method on reconstructing the acoustic field over the entire surface of a finite object, based on acoustic pressure measurements taken over a finite planar surface on one side. Also presented are guidelines for implementing the HELS method. In particular, formulations for estimating *a priori* the numbers of expansion functions and measurements, and procedures for determining the reconstruction error and optimum measurement locations are developed, given the overall dimensions of the source and the highest frequency of interest in reconstruction.

The test object is a typical bowling ball subject to random excitations via a vibration shaker. The acoustic pressures generated by this bowling ball are measured by a microphone and taken as the input to the HELS formulation. The reconstructed acoustic pressures and spectra are then compared with the values measured at the same locations. The normal component of the surface velocity can be reconstructed in a similar manner. Once these surface acoustic quantities are specified, the normal component of the time-averaged acoustic intensity can be calculated. In fact, the acoustic field in the entire exterior region can be visualized. Such a three-dimensional image can be very helpful in revealing the correlation between structural vibration and acoustic radiation.

II. THE HELS METHOD

In the HELS method the radiated acoustic pressure is expressed as a superposition of basis functions Ψ.[18] The coefficients associated with these basis functions C are obtained by matching the assumed solution to the measured acoustic pressures

$$\{\hat{p}(\vec{x}_m,\omega)\}_{M\times 1}=[\Psi]_{M\times J}\{C\}_{J\times 1}, \tag{1}$$

where $\hat{p}$ represents the complex amplitude of the acoustic pressure and $\vec{x}_m$, $m=1,2,...,M$, indicates measurement locations. If J expansion functions are used, then M measurements must be taken, where $M\geqslant J$. To minimize the errors incurred in this process, the least-squares method is used and the coefficients $\{C\}_{J\times 1}$ can be obtained by taking a pseudoinverse

$$\{C\}_{J\times 1}=([\Psi]^T_{M\times J}[\Psi]_{M\times J})^{-1}[\Psi]^T_{M\times J}\{\hat{p}(\vec{x}_m,\omega)\}_{M\times 1}. \tag{2}$$

Since the least-squares method always gives the best fit to the measured data, the accuracy of reconstruction at measurement locations increases monotonically with the number of expansion functions. On the other hand, the accuracy of reconstruction on the source surface increases with the number of expansion functions at first, and then deteriorates thereafter due to an inherent ill-conditioning difficulty. Therefore it is imperative to find an optimal number J_{op}, which can be accomplished either by minimizing the sum of $\|L\|^2$ errors in reconstruction through an iteration scheme[18] or using a constrained minimization through a quadratic programming technique.[35]

In general, the higher the signal to noise ratio (SNR) and the smaller the standoff distances, the larger the value of J_{op} and the higher the accuracy and the spatial resolution of reconstruction. In practice, however, the presence of measurement errors often limits the value of the optimum expansion number J_{op} to well within 100, thus yielding a small matrix in Eq. (2) and making the numerical computations extremely fast.

This small matrix equation is consistent with the result of an expansion theory, which indicates that the radiated acoustic field can often be described effectively by a finite number of expansion functions. As in the expansion theory, the low-order terms represent the far-field effect, while the high-order terms represent the near-field effect. The former is responsible for the acoustic radiation, while the latter is related to the complex acoustic near field. Therefore, one can use the HELS method to reconstruct acoustic radiation in the

far field by taking a few measurements in the field. The loss of the near-field effect in the measured data, equivalent to neglecting the high-order terms in the expansion, will have little impact on the accuracy of reconstruction, because the near-field effect decays exponentially with distance anyway. On the other hand, in reconstructing the acoustic field on the surface of a vibrating structure one must include the high-order terms and take more measurements at very close range in order to capture as much near-field information as possible.

Unlike the spherical expansion, the HELS formulation provides an approximate solution for the entire exterior region, with relatively higher accuracy of reconstruction outside the minimum sphere that encloses the source under consideration, and relatively lower accuracy inside. Moreover, one has complete freedom in selecting the measurement locations, can set a measurement aperture equal to the size of reconstruction, and carry out a piecewise reconstruction over the source surface. This is in contrast with the Helmholtz integral formulation-based NAH, which requires taking measurements over a control surface that completely encloses the source. The size of the matrix equation of the HELS method is also much less than that of the Helmholtz integral formulation, hence the former is computationally more efficient than the latter. However, the accuracy of reconstruction provided by the HELS method can be poor for an irregularly shaped surface. This is because the number of basis functions necessary for reproducing the acoustic field on a rough surface may be significantly increased, while the presence of measurement errors keeps the number of expansion functions down, thus lowering the accuracy of reconstruction.

III. IMPLEMENTATION OF THE HELS METHOD

For the HELS method to become a useful tool for engineers to reconstruct acoustic radiation, we must address the issues concerning its implementation. For example, it will be instructive to know: (1) how many expansion functions and measurements are needed; and (2) where the measurements should be taken. It is emphasized, however, that there are no definite answers to these questions for any given problem. This is because we are trying to reconstruct the acoustic field based on a finite number of acoustic pressure measurements that are incomplete and inaccurate. As a result, the problem becomes mathematically ill posed. Nonetheless, it is always helpful to have a guideline on these issues so as to better prepare for the data acquisition and post processing.

Assume that the source under consideration is of a finite extent, has a smooth surface, and is immersed in an unbounded fluid medium. Suppose that the average spatial dimension of the source is a and the maximum frequency of interest in reconstruction $f_{\max}$, so the highest dimensionless frequency is $(ka)_{\max}$.

The basis functions in Eq. (1) under spherical coordinates consist of the spherical Hankel functions and spherical harmonics. From the expansion theory we learn that if the source is contained in a sphere of radius a, the expansion solution will converge rapidly once the highest order in the Hankel function exceeds the value of $(ka)_{\max}$.[23] Let the highest order of the Hankel function be n. Then the total number of expansion functions J is given by $J=(n+1)^2$. Therefore it is reasonable to set an initial value of J as

$$J=[(ka)_{\max}+1]^2. \tag{3a}$$

For spherically symmetric radiation, the number of expansion functions can be reduced to

$$J=(ka)_{\max}+1, \tag{3b}$$

because the spherical harmonics reduce to those along the symmetry axis only. As mentioned before, the presence of errors in the measured data will cut the number of expansion functions down. Hence the value of J_{op} is always less than that given by Eq. (3).

Once the number of expansion terms is decided, we can then estimate the total number of measurements M needed to yield a satisfactory reconstruction. Since in this case the least-squares method is used, which gives the best fit of the assumed solution to the measured data, it is a good idea to take more measurements than the expansion functions. A recent study[36] shows that the most cost-effective choice of M is

$$M=\begin{cases} 1.4[(ka)_{\max}+1]^2, & \text{for general acoustic radiation,} \\ 1.4[(ka)_{\max}+1], & \text{for spherical symmetric cases.} \end{cases} \tag{4}$$

Moreover, the test results demonstrate that the best reconstruction can be obtained when the measurement points are randomly distributed over a conformal surface at a very close range to the source surface. However, such a measurement scheme is unrealistic in practice. A more realistic one is to take equidistant measurements over a conformal surface. If conformal measurements cannot be realized, then planar measurements (using either random or equidistant distributions) can be used, which can be facilitated by an x–y translator.

Once a measurement scheme is selected, the optimum measurement locations can be calculated using an effective independence procedure.[15,16] Since the locations having a negligibly small effective independence must be deleted, the number of optimum locations will be smaller than the initial value M.

Consider a set of measurements $N(N<M)$ containing errors $\{\varepsilon\}_{N\times 1}$ that are uncorrelated Gaussian random with variance σ^2 and zero mean. From Eq. (1), we can write

$$\{\hat{p}(\vec{x}_m,\omega)\}_{N\times 1}=[\Psi]_{N\times J}\{C\}_{J\times 1}+\{\varepsilon\}_{N\times 1}, \tag{5}$$

where $\{C\}_{J\times 1}$ can be obtained using a pseudoinverse or singular value decomposition (SVD),

$$\begin{aligned}\{C\}_{J\times 1}&=([\Psi]^T_{N\times J}[\Psi]_{N\times J})^{-1}[\Psi]^T_{N\times J}\{\hat{p}(\vec{x}_m,\omega)\}_{N\times 1}\\&=[\mathsf{W}]_{J\times J}[\Sigma_p^{-1}]_{J\times N}[\mathsf{U}]^T_{N\times N}\{\hat{p}(\vec{x}_m,\omega)\}_{N\times 1},\end{aligned} \tag{6}$$

where $[\Sigma_p^{-1}]$ represents a diagonal matrix that contains the inversion of singularities of $[\Psi]_{N\times J}$, $[\mathsf{U}]_{N\times N}$ is the matrix spanned by the first N-column vectors of $[\mathsf{U}]_{M\times M}$, $[\mathsf{U}]_{M\times M}[\mathsf{U}]^T_{M\times M}=[\mathsf{I}]$, and $[\mathsf{W}]_{J\times J}[\mathsf{W}]^T_{J\times J}=[\mathsf{I}]$.

Substituting Eq. (6) into (1) yields the reconstructed acoustic pressures

$$\{\tilde{\hat{p}}(\vec{x}_m,\omega)\}_{N\times 1}=[\Psi]_{N\times J}([\Psi]^T_{N\times J}[\Psi]_{N\times J})^{-1}\times[\Psi]^T_{N\times J}\{\hat{p}(\vec{x}_m,\omega)\}_{N\times 1}. \quad (7)$$

The measured acoustic pressures $\{\hat{p}(\vec{x}_m,\omega)\}_{N\times 1}$ on the right side of Eq. (7) are not error free. Substituting Eq. (5) into (7) then gives the reconstruction error

$$\{\tilde{\hat{p}}(\vec{x}_m,\omega)\}_{N\times 1}-\{\hat{p}(\vec{x}_m,\omega)\}_{N\times 1}=[E_f]_{N\times N}\{\varepsilon\}_{N\times 1}, \quad (8)$$

where $[E_f]_{N\times N}$ is known as the effective independence of the field pressure given by

$$[E_f]_{N\times N}=[\Psi]_{N\times J}([\Psi]^T_{N\times J}[\Psi]_{N\times J})^{-1}[\Psi]^T_{N\times J}. \quad (9)$$

Applying SVD to the right side of Eq. (9) then yields

$$[E_f]_{N\times N}=[\mathrm{U}]_{N\times N}[\Sigma_p]_{N\times J}[\mathrm{W}]^T_{J\times J}\times[\Sigma_p^{-1}]_{J\times N}[\mathrm{U}]^T_{N\times N}=[\mathrm{U}]_{N\times N}[\mathrm{U}]^T_{N\times N}, \quad (10)$$

where the ith diagonal element of $[E_f]_{N\times N}$ indicates the contribution of the ith measurement location to the linear independence of the matrix $[\Psi]_{N\times J}$.

Equation (10) enables one to minimize the error covariance matrix by eliminating the locations with the smallest effective independence values from a large measurement set M. Solutions to Eq. (10) can be facilitated by an iteration scheme. Note that the locations thus determined are not globally optimal, but merely optimal for a given set of measurements M.

IV. RECONSTRUCTION SCHEME

To test the robustness and effectiveness of the HELS method, we choose to confine all measurements to a finite planar surface on one side of the bowling ball. This is because in practice the size and area over which the radiated acoustic pressure signals can be measured are often restricted. Furthermore, the number of measurements cannot be too large in order to make the reconstruction process cost effective.

For comparison purpose, we also take measurements over a conformal surface around the ball and reconstruct the acoustic pressures on the surface. The acoustic pressure spectra at various locations of the ball surface are obtained by repeating this process over the frequency range of interest. The reconstructed acoustic pressure distributions and spectra are then compared with those measured at the same locations.

Having obtained the surface acoustic pressure, the normal component of the surface velocity $\hat{v}_n(\vec{x}_S,\omega)$ can be determined by the Euler's equation

$$\hat{v}_n(\vec{x}_S,\omega)=\frac{1}{i\omega\rho_0}\left\{\frac{\partial\psi}{\partial n}\right\}^T_{J\times 1}([\Psi]^T_{M\times J}[\Psi]_{M\times J})^{-1}\times[\Psi]^T_{M\times J}\{\hat{p}(\vec{x}_m,\omega)\}_{J\times 1}, \quad (11)$$

where ρ_0 is the fluid density and $\partial/\partial n$ represents a normal derivative, which in this case is equal to $\partial/\partial r$.

Once the surface acoustic pressure and the normal component of the surface velocity are specified, the time-averaged acoustic intensity can be calculated by

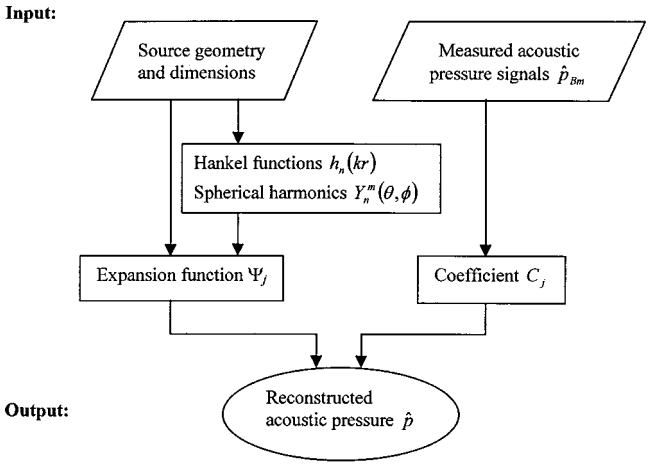

FIG. 1. Flow chart of the computer program for the HELS method.

$$I_{n,\mathrm{av}}(\vec{x}_S,\omega)=\tfrac{1}{2}\,\mathrm{Re}[\hat{p}(\vec{x},\omega)\,\hat{v}_n^*(\vec{x}_S,\omega)]. \quad (12)$$

Equation (12) enables one to visualize the entire acoustic energy flow from the surface of a vibrating object into the surrounding fluid medium. This three-dimensional image of acoustic radiation together with the normal component of surface velocity field can be very helpful in providing a better understanding of correlation between structural vibrations and sound radiation.

V. TEST SETUP

Figure 1 shows the flow chart of the computer program for the HELS method to reconstruct the radiated acoustic pressure field from a vibrating object. The input to the program includes the source geometry and dimensions, and the measured acoustic pressures. The former is used to generate the basis functions, while the latter is used to solve the coefficients associated with the basis functions.

Figure 2 illustrates the test setup for the bowling ball with a diameter 0.218 m. Experiments were conducted inside

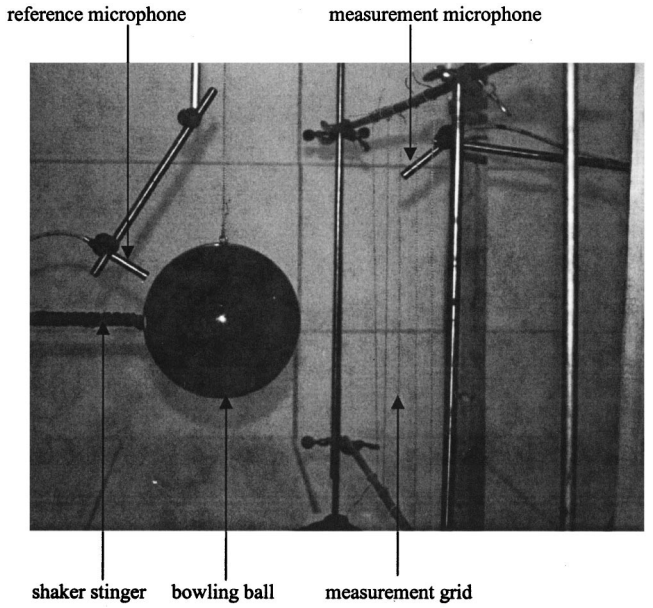

FIG. 2. Test setup for a vibrating bowling ball.

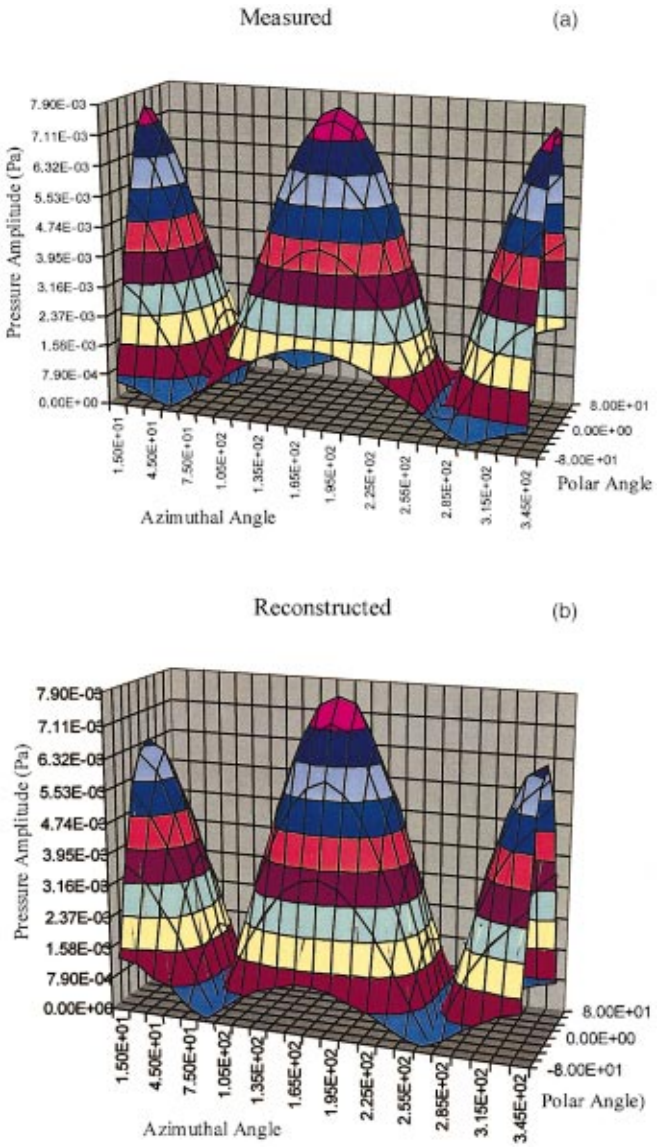

FIG. 3. Comparison of acoustic pressure distributions on the surface of the bowling ball at 232 Hz based on measurements over a planar surface: (a) measured; (b) reconstructed.

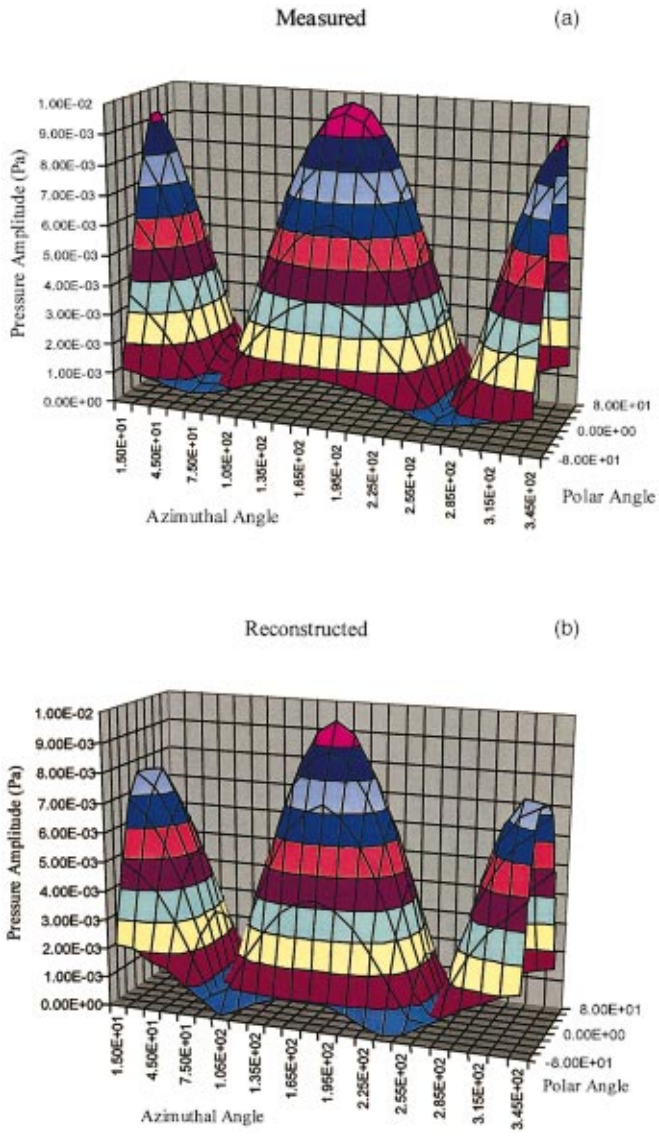

FIG. 4. Comparison of acoustic pressure distributions on the surface of the bowling ball at 360 Hz based on measurements over a planar surface: (a) measured; (b) reconstructed.

a large fully anechoic chamber in the Acoustics, Vibration, and Noise Control (AVNC) Laboratory at Wayne State University. The ball was hung from the top of a wooden frame through a string and was excited horizontally via a steel rod by the B&K Vibration Exciter type 4808 using stationary random signals. To minimize potential contamination of the input data by background noises from the shaker and the rod, an enclosure lined with sound absorptive materials inside was built around the shaker and the rod was wrapped by sound absorbing foam materials.

The acoustic pressure signals generated by the vibrating ball were measured by two B&K Prepolarized Free-field Microphones type 4188, one being fixed at a reference point located at 0.01 m behind the ball and the other moving in the field. The measured signals were analyzed by the B&K Dual Channel Signal Analyzer type 3550 and stored in an IBM PC with a Pentium Processor III 500 MHz.

Using the guidelines discussed in Sec. IV, we can estimate numbers of expansion functions and measurements. For example, given the diameter of the ball, $a=0.218$ m, and the highest frequency of interest in reconstruction, $f_{\max}=1000$ Hz, we obtain $(ka)_{\max}=4$. Hence we can set $J=(4+1)^2=25$ expansion functions and $M=1.4\times 25=35$ measurements over a conformal surface. In this study we choose an equidistant measurement scheme without further optimization using Eq. (10), because the iteration process was extremely time consuming.

Two sets of data were taken in this study. In the first set, the field microphone traversed over a planar surface in front of the bowling ball, while in the second set, the microphone scanned over a conformal surface at a constant radius. For validation purpose, the acoustic pressures on the ball surface were also measured.

The planar measurement surface was $0.4\times 0.4\,\mathrm{m}^2$ with an equal distance of 0.05 m between the neighboring points, thus resulting in 81 measurements over the entire plane. The shortest distance between the measurement plane and the bowling ball was 0.016 m. Also taken were 81 measurements

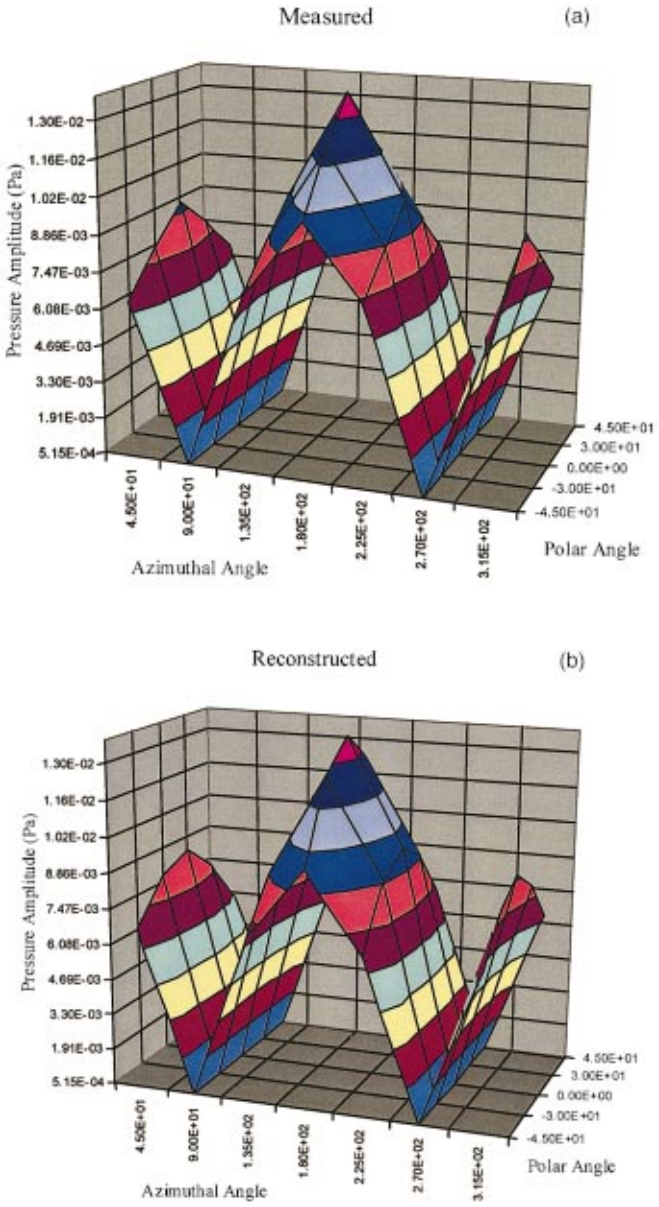

FIG. 5. Comparison of acoustic pressure distributions on the surface of the bowling ball at 200 Hz based on measurements over a conformal surface: (a) measured; (b) reconstructed.

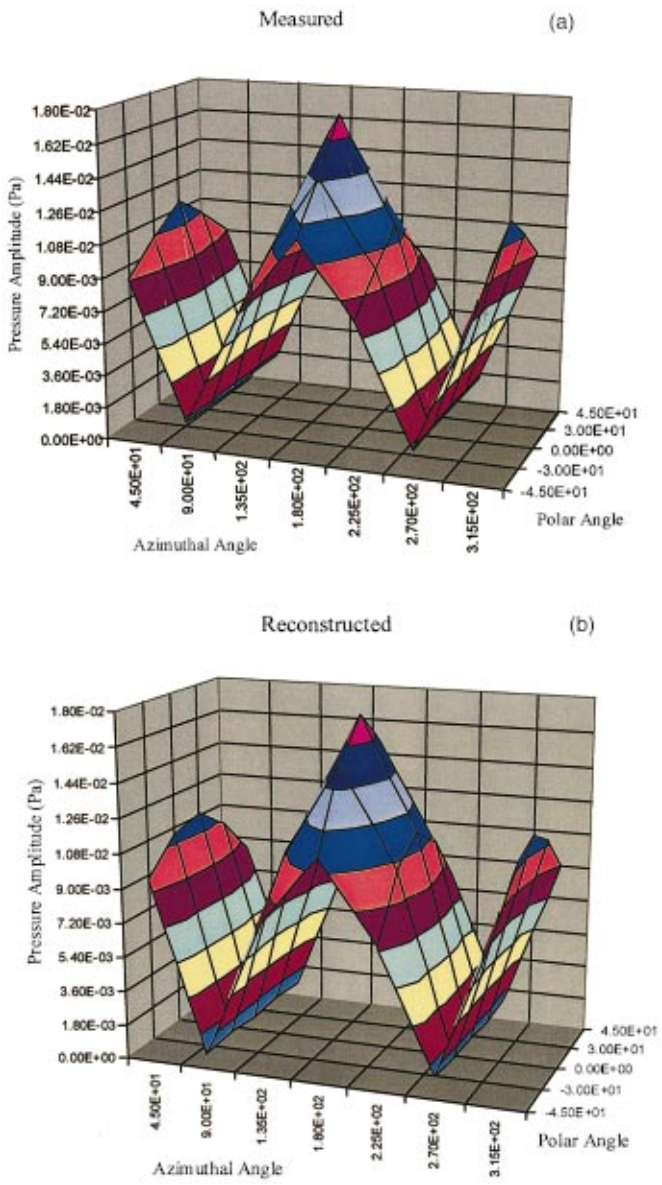

FIG. 6. Comparison of acoustic pressure distributions on the surface of the bowling ball at 400 Hz based on measurements over a conformal surface: (a) measured; (b) reconstructed.

uniformly distributed over the bowling ball surface with a 0.01 m clearance in the radial direction. These values were used for validation purpose. Hence the total number of measurements in this set of experiments became 162. Because of a lack of a microphone array, the measurements were taken by moving a microphone manually one location at a time. To eliminate possible errors caused by fluctuations in the signal level over the measurement time period, the transfer function instead of the acoustic pressure signal was measured with respect to the reference point.[19] Experimental results indicated that while the signal emitted from the source might fluctuate over time, the transfer function between any field and the reference points was relatively stable. Once all the transfer functions were collected, their values were multiplied by the acoustic pressure at the reference point, which was equivalent to measuring the acoustic pressures at 162 points simultaneously.

In the second set of experiments, 49 measurements were taken over a conformal surface at a clearance of 0.03 m in the radial direction. The number of measurements was slightly larger than the initial estimate of 35 in order to fit uniformly along the polar angles $\theta = \pm 45°$, $\pm 30°$, $\pm 15°$, and 0° (the ball was hung at $\theta = +90°$ and excited at the $\theta = 180°$) with the azmuthal angle varying from $\phi = 45°$, 90°, 135°, 180°, 225°, 270°, and 315° (the stinger was at $\phi = 0°$). Note that because of the presence of the reference microphone, stinger, hanging string, and their attachments, measurements of acoustic pressures in the regions beyond ($|\theta| > 45°$, $\phi < 45°$) and ($|\theta| > 45°$, $\phi > 315°$) were not taken.

For validation purpose, another 49 measurements were taken over the bowling ball surface with a 0.01 m clearance in the radial direction, thus yielding a total of 98 measurements. As in the first set of experiments, acoustic pressure signals were obtained by measuring the transfer functions

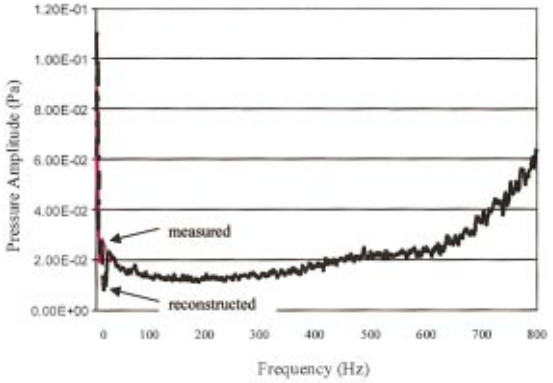

FIG. 7. Comparison of acoustic pressure spectra at ($\theta=0°$, $\phi=180°$) on the surface based on measurements over a conformal surface.

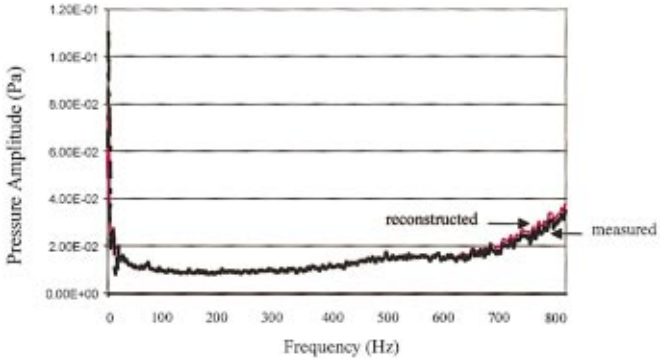

FIG. 8. Comparison of acoustic pressure spectra at ($\theta=45°$, $\phi=180°$) on the surface based on measurements over a conformal surface.

and then multiplying them by the acoustic pressure measured at the reference point to eliminate possible errors caused by fluctuations in the single level over a long period of time.

The field acoustic pressures thus obtained were used as input to reconstruct the surface acoustic pressure. This process was repeated from 1–800 Hz. The reconstructed acoustic pressure distributions at fixed frequencies and the spectra at various locations on the bowling ball surface were compared with those measured at the same frequencies and locations. Note that the reason for selecting this frequency range was to examine the reconstructed surface acoustic pressures at every single frequency since the B&K Signal Analyzer type 3550 could only display 800 discrete lines. For frequencies higher than 800 Hz, the zooming feature of the analyzer must be used.

In carrying out numerical computations, the number of expansion functions was optimized by minimizing the sum of $\|L\|^2$ errors with respect to the input data. The values of J_{op} may change with the input data and increase with the excitation frequency.

VI. RESULTS AND DISCUSSIONS

In this section, we display the reconstructed acoustic pressure distributions, pressure spectra, and intensity maps on the surface of a bowling ball subject to random excitations. For brevity, however, only representative results are shown in each case.

Figure 3 illustrates the comparison of the reconstructed and measured acoustic pressure distributions over the bowling ball surface at 232 Hz, based on the input data collected on a planar surface in front of the ball with $J_{\text{op}}=9$. Because of a small size of matrix Eq. (2), numerical computations are extremely fast.

Experimental results show that the accuracy of reconstruction is very high not only in the front, but also behind the ball. Similar comparison of the reconstructed and measured acoustic pressure distributions at 360 Hz is given in Fig. 4. Once again, the agreement between reconstructed and measured acoustic pressure is quite satisfactory. However, the amplitudes of the reconstructed acoustic pressures behind the bowling ball are found to be slightly lower than those of

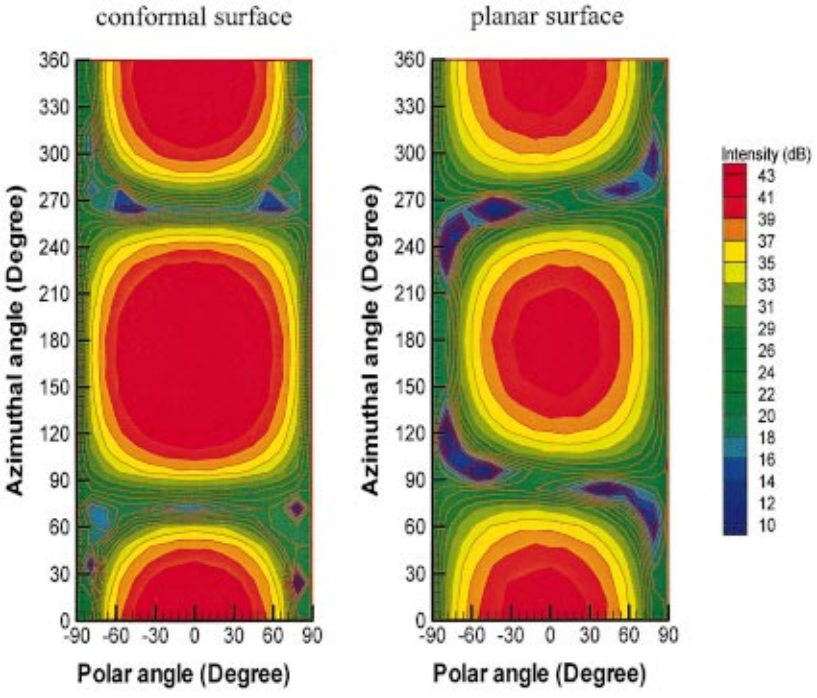

FIG. 9. Comparison of the reconstructed time-averaged acoustic intensity distributions on the bowling ball surface at 232 Hz.

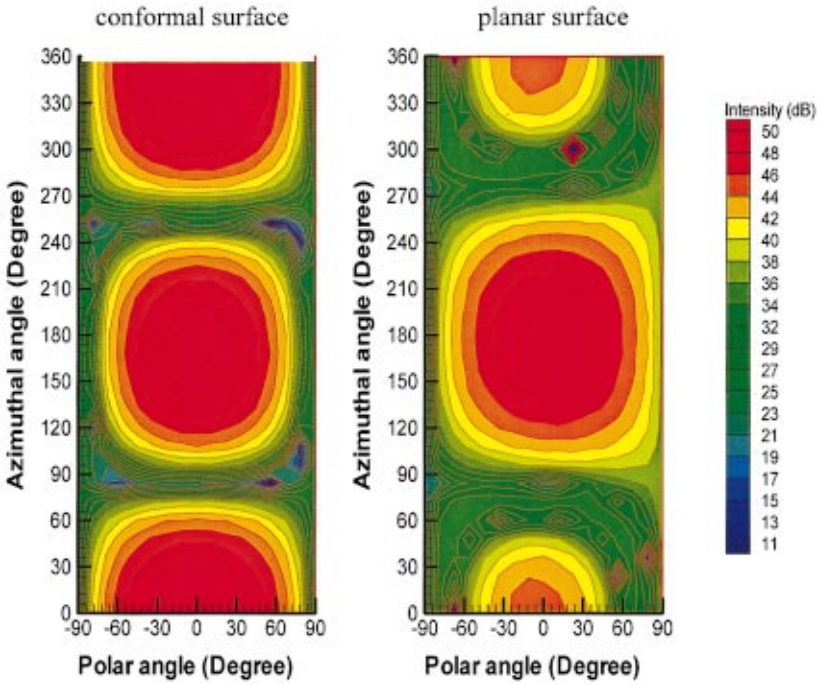

FIG. 10. Comparison of the reconstructed time-averaged acoustic intensity distributions on the bowling ball surface at 360 Hz.

the measured values. The discrepancy increases with the excitation frequency as expected. This is because the effect of acoustic diffraction becomes more and more pronounced as the frequency increases, which turns the region behind the ball into a shadow zone.

For comparison purpose, we also reconstruct acoustic pressures based on measurements taken over a conformal surface with $J_{op}=5$. Figures 5 and 6 illustrate the comparisons of the reconstructed and measured acoustic pressure distributions over the bowling ball surface at 200 and 400 Hz, respectively. Note that in the second set of experiments the numbers of the field and surface acoustic pressure measurements were less than those in the first set, respectively. As a result, the acoustic pressure distributions seem flat (see Figs. 5 and 6) as compared with those in Figs. 3 and 4. However, the reconstructed amplitudes of acoustic pressures agree extremely well with those of the measured data not only in the front, but also behind the bowling ball.

Results of these experiments demonstrate that the accuracy of reconstruction based on measurements over a conformal surface is much higher than that over a planar surface. This is not surprising because a planar surface picks up information primarily from the closest side of an object, while those from the behind are missed. Consequently, the input data from a planar measurement is incomplete. Moreover, a planar surface often extends beyond the near-field region, which makes the accuracy of input data inconsistent. Those limitations have an adverse impact on the accuracy of resulting reconstruction. However, measurements over a conformal surface are not easy to implement in engineering applications, while those over a planar surface are simple and can be facilitated by an x–y translator. Hence a preferred way is to take measurements over several small planar surfaces over a source at the closest possible distances.

The surface acoustic pressures were reconstructed one frequency at a time. This process was repeated from 1–800 Hz to generate the acoustic pressure spectra on the bowling ball surface. These spectra were then compared with the measured ones at the same locations. Experimental results demonstrate that satisfactory agreements were obtained in all cases. For brevity, however, we only demonstrate the results at $(\theta=0°,\ \phi=180°)$ and $(\theta=45°,\ \phi=180°)$. Note that the former corresponds to the location of a pressure peak because the ball is excited along the $(\theta=0°,\ \phi=180°)$ axis direction.

Figures 7 and 8 depict comparisons of the reconstructed and measured acoustic pressure spectra at these locations, based on the input data taken from a conformal measurement surface. Since these two spectra are so close together, it is very difficult to tell which is which. Only slight discrepancies are observed between the reconstructed and measured spectra at the location $(\theta=45°,\ \phi=180°)$ when the excitation frequency is above 700 Hz. Note that the measured acoustic pressure spectrum shows a rising trend from 0–800 Hz, even though the excitation is stationary random white with a relatively flat spectrum. This is expected because the amplitude of the acoustic pressure radiated from an oscillating sphere increases with the excitation frequency.

Once the surface acoustic pressure was specified, the normal component of the surface velocity was calculated using Eq. (11), and the normal component of the time-averaged acoustic intensity was determined using Eq. (12). This intensity map allowed for visualization of location and strength of the acoustic source and energy flow. Because of the lack of intensity measurements, we compare the reconstructed acoustic intensities based on the input data taken from a conformal surface and those taken from a planar surface. Since the accuracy of the reconstructed acoustic pressures for the former is so high, we consider the resulting acoustic intensity to be reliable.

Figures 9 and 10 depict the comparisons of the reconstructed time-averaged acoustic intensity maps on the bowl-

ing ball surface at 232 and 360 Hz based on the input data taken from a conformal and planar surfaces, respectively. These intensity distributions seem to be consistent with those of an oscillating sphere. Results show that the acoustic intensities reconstructed based on a conformal measurement surface are roughly the same both in the front and in the back of the bowling ball, whereas those based on a planar surface are higher in the front than in the back, as expected.

VII. CONCLUDING REMARKS

The acoustic fields radiated from a vibrating bowling ball are reconstructed successfully using the HELS method based on measurements taken over a finite planar surface on one side of the source. As a comparison, reconstruction is also conducted based on the input data taken over a conformal measurement surface. Results show that the accuracy of reconstruction based on measurements over a conformal surface is much higher than that over a planar surface. This is because a planar surface primarily picks up the information from the closest side of the source, whereas those from other sides are omitted. Moreover, a planar surface often extends beyond the near-field region, thus making the accuracy of input data inconsistent. The present study demonstrates that the HELS method can be extremely effective for a spherical surface. It allows for reconstruction of the radiated acoustic pressure field over the entire surface of a vibrating object based on measurements taken over a finite planar surface on one side. However, the accuracy of reconstruction may decrease at higher frequencies because of the diffraction effect.

ACKNOWLEDGMENTS

The authors would like to thank Mr. Martin G. Foulkes for his assistance in collecting acoustic pressure signals and in preparing some of the viewgraphs of this investigation. This work was supported by a grant from National Science Foundation, Grant No. CMS-9802847.

[1] E. G. Williams and J. D. Maynard, ''Holographic imaging without the wavelength resolution limit,'' Phys. Rev. Lett. **45**, 554–557 (1980).
[2] E. G. Williams, J. D. Maynard, and E. Skudrzyk, ''Sound source reconstructions using a microphone array,'' J. Acoust. Soc. Am. **68**, 340–344 (1980).
[3] J. D. Maynard and E. G. Williams, ''Nearfield holography, a new technique for noise radiation measurement,'' in *Proceedings of NOISE-CON 81*, edited by L. H. Royster *et al.* (Noise Control Foundation, New York, 1981), pp. 19–24.
[4] E. G. Williams, H. D. Dardy, and R. G. Fink, ''Nearfield acoustic holography using an underwater, automated scanner,'' J. Acoust. Soc. Am. **78**, 789–798 (1985).
[5] J. D. Maynard, E. G. Williams, and Y. Lee, ''Nearfield acoustic holography: I. Theory of generalized holography and the development of NAH,'' J. Acoust. Soc. Am. **78**, 1395–1413 (1985).
[6] W. A. Veronesi and J. D. Maynard, ''Nearfield acoustic holography (NAH): II. Holographic reconstruction algorithms and computer implementation,'' J. Acoust. Soc. Am. **81**, 1307–1322 (1987).
[7] E. Williams, *Fourier Acoustics: Sound Radiation and Nearfield Acoustical Holography* (Academic, San Diego, 1999), Chap. 2, pp. 15–81; Chap. 3, pp. 89–113.
[8] W. A. Veronesi and J. D. Maynard, ''Digital holographic reconstruction of sources with arbitrarily shaped surfaces,'' J. Acoust. Soc. Am. **85**, 588–598 (1989).
[9] G.-T. Kim and B.-T. Lee, ''3-D sound source reconstruction and field reproduction using the Helmholtz integral equation,'' J. Sound Vib. **136**, 245–261 (1990).
[10] M. R. Bai, ''Application of BEM (boundary element method)-based acoustic holography to radiation analysis of sound sources with arbitrarily shaped geometries,'' J. Acoust. Soc. Am. **92**, 533–549 (1992).
[11] B. K. Gardner and R. J. Bernhard, ''A noise source identification technique using an inverse Helmholtz integral equation method,'' Trans. ASME, J. Vib., Acoust., Stress, Reliab. Des. **110**, 84–90 (1988).
[12] J.-G. Ih and B.-K. Kim, ''Estimation of source strength of vibrating structures by using BEM and reciprocity,'' Proc. of Inter-Noise **93**, 1601–1604 (1993).
[13] B.-K. Kim and J.-G. Ih, ''Reconstruction of vibro-acoustic field of car panels using acoustic BEM,'' Proc. Inter-Noise **95**, 1341–1344 (1995).
[14] H. A. Schenck, ''Improved integral formulation for acoustic radiation problems,'' J. Acoust. Soc. Am. **44**, 41–58 (1968).
[15] B.-K. Kim and J.-G. Ih, ''On the reconstruction of the vibro-acoustic field over the surface enclosing an interior space using the boundary element method,'' J. Acoust. Soc. Am. **100**, 3003–3016 (1996).
[16] B.-K. Kim and J.-G. Ih, ''Design of an optimal wave-vector filter for enhancing the resolution of reconstructed source field by near-field acoustic holography (NAH),'' J. Acoust. Soc. Am. **107**, 3289–3297 (2000).
[17] Z. Wang and S. F. Wu, ''Helmholtz equation-least squares (HELS) method for reconstructing the acoustic pressure field,'' J. Acoust. Soc. Am. **102**, 2020–2032 (1997).
[18] S. F. Wu, ''On reconstruction of acoustic pressure fields by using HELS method,'' J. Acoust. Soc. Am. **107**, 2511–2522 (2000).
[19] N. E. Rayess and S. F. Wu, ''Experimental validation of the HELS method on reconstructing radiated acoustic pressures from complex vibrating structure,'' J. Acoust. Soc. Am. **107**, 2955–2964 (2000).
[20] S. F. Wu and J. Yu, ''Reconstructing interior acoustic pressure fields via Helmholtz equation least-squares (HELS) method,'' J. Acoust. Soc. Am. **104**, 2054–2060 (1998).
[21] J. Pachner, ''On the dependence of directivity patterns on the distance from the emitter,'' J. Acoust. Soc. Am. **28**, 86–90 (1956).
[22] J. Pachner, ''Investigation of scalar wave fields by means of instantaneous directivity patterns,'' J. Acoust. Soc. Am. **28**, 90–92 (1964).
[23] G. Weinreich and E. B. Arnold, ''Method for measuring acoustic radiation fields,'' J. Acoust. Soc. Am. **68**, 404–411 (1980).
[24] B. Weinreich, ''Sound hole sum rule and the dipole moment of the violin,'' J. Acoust. Soc. Am. **77**, 710–718 (1985).
[25] P. J. T. Filippi and J. Piraux, ''Noise sources modeling and identification,'' J. Sound Vib. **98**, 596–600 (1985).
[26] P. J. T. Pilippi, D. Habault, and J. Piraux, ''Noise sources modeling and intensimetry using antenna measurement and identification procedures,'' J. Sound Vib. **124**, 285–296 (1988).
[27] L. A. DeVries and J. S. Bolton, ''Acoustical holography in spherical coordinates for noise source identification,'' Proc. International Compressor Engineering Conference at Purdue University, West Lafayette, IN, July 1994, pp. 791–795.
[28] T. B. Hansen, ''Spherical expansions of time-domain acoustic fields: Application to near-field scanning,'' J. Acoust. Soc. Am. **98**, 1204–1215 (1995).
[29] R. A. Frazer, W. P. Jones, and S. W. Skan, ''Approximations to functions and to the solutions of differential equations,'' Rep. Memo No. 1799 (2913), British Aero. Res. Comm. , (1937).
[30] W. Williams, N. G. Parke, D. A. Moran, and C. H. Sherman, ''Acoustic radiation from a finite cylinder,'' J. Acoust. Soc. Am. **36**, 2316–2322 (1964).
[31] L. Collatz, *The Numerical Treatment of Differential Equations* (Springer, Berlin, 1960), pp. 409–413.
[32] W. J. Meggs, ''A practical method of predicting farfield acoustic pressure from measurements near the source,'' U.S.N. Marine Eng. Lab., Tech. Memo No. 442/65 (Nov. 1965).
[33] J. Butler, ''A series expansion method for the prediction of the farfield from nearfield measurements,'' Parke Math. Lab. Tech. Memo No. 1 (Dec. 1967).
[34] J. Butler, ''Solution of acoustical-radiation problems by boundary collocation,'' J. Acoust. Soc. Am. **48**, 325–336 (1970).
[35] B.-D. Lim and S. F. Wu, ''Determination of the optimal number of expansion terms in the HELS method,'' J. Acoust. Soc. Am. **108**, 2505 (2000).
[36] N. E. Rayess and S. F. Wu, ''Visualization of acoustic pressure radiation from a complex vibrating structure,'' J. Acoust. Soc. Am. **106**, 2293 (1999).

Experimental and numerical investigations of resonant vibration characteristics for piezoceramic plates

Chi-Hung Huang[a)]
Department of Mechanical Engineering, Ching Yun Institute of Technology, Chung-Li, Taiwan 320, Republic of China

Chien-Ching Ma[b)]
Department of Mechanical Engineering, National Taiwan University, Taipei, Taiwan 106, Republic of China

(Received 10 August 2000; accepted for publication 14 March 2001)

Electronic speckle pattern interferometry (ESPI) is a full field, non-contact technique for measuring the surface displacement of a structure subjected to static loading or, especially, to dynamic vibration. In this article we employ an optical system called the amplitude-fluctuation ESPI with out-of-plane and in-plane measurements to investigate the vibration characteristics of piezoceramic plates. Two different configurations of piezoceramic plates, namely the rectangular and the circular plates, are discussed in detail. As compared with the film recording and optical reconstruction procedures used for holographic interferometry, the interferometric fringes of AF-ESPI are produced instantly by a video recording system. Because the clear fringe patterns will be shown only at resonant frequencies, both the resonant frequencies and the corresponding mode shapes are obtained experimentally at the same time by the proposed AF-ESPI method. Excellent quality of the interferometric fringe patterns for both the in-plane and out-of-plane vibration mode shapes is demonstrated. The resonant frequencies of the piezoceramic plates are also measured by the conventional impedance analysis. From experimental results, we find that the out-of-plane vibration modes (type A) with lower resonant frequencies cannot be measured by the impedance analysis and only the in-plane vibration modes (type B) will be shown. However, both the out-of-plane (bending) and in-plane (extensional) vibration modes of piezoceramic plates are obtained by the AF-ESPI method. Finally, the numerical finite element calculations are also performed, and the results are compared with the experimental measurements. It is shown that the numerical calculations and the experimental results agree fairly well for both the resonant frequencies and the mode shapes. [DOI: 10.1121/1.1370359]

PACS numbers: 43.40.At, 43.40.Dx [CBB]

I. INTRODUCTION

Electronic speckle pattern interferometry (ESPI), which was first proposed by Butters and Leendertz[1] to investigate the out-of-plane vibration of disks, is a technique which uses a laser, CCD camera and digital processor to generate interferograms at the camera frame rate. This method has opened a new field of activity and been used in many engineering measurement problems involving the investigation of static and dynamic deformation and condition monitoring of machinery. Although different methods of holographic interferometry have been developed for vibration analysis,[2] the slow and cumbersome process of film development limits the application of holographic vibration analysis from the engineer's point of view. ESPI was developed by combining the techniques of holographic and speckle interferometry by employing an image hologram configuration and the method of double-exposure holography.

The most common light source for ESPI is a continuous wave (cw) laser because of the lower price and optical power requirement. When the cw source is employed, time-averaged interferometric fringes are produced for the harmonically vibrating object which offers a good observation of the vibration mode shape. The disadvantage of this time-averaged method is that the interferometric fringes represent the amplitude but not the phase of the vibration. To improve this shortcoming, the phase-modulation method, using the reference beam modulation technique, was developed by Løkberg and Hogmoen[3] to determine the relative phase of displacement. In addition to the methods previously mentioned, a number of variations for the principles based on the ESPI technique were proposed in many academic research and engineering applications. Creath *et al.*[4] developed the subtraction method to reduce the noise coming from the environment. The subtraction method differs from the time-averaged method in that the reference frame is first recorded before vibration and continuously subtracted from the incoming frames after vibration. Løkberg[5] indicated that in-plane vibration modes could be obtained by using an out-of-plane setup and tilting the specimen with a proper angle. Shellabear and Tyrer[6] extended the time-averaged ESPI to make three-dimensional vibration measurements. Doval *et al.*[7] proposed the additive stroboscopic TV-holography for out-of-plane vibration analysis, which exhibited an enhanced contrast with constant visibility fringes and dynamic phase shifting. Wang *et al.*[8] proposed the amplitude-fluctuation

[a)]Electronic mail: chhuang@cyit.edu.tw
[b)]Author to whom correspondence should be addressed. Electronic mail: cma@w3.me.ntu.edu.tw

ESPI method for out-of-plane vibration measurement to increase the visibility of the fringe pattern and to reduce the environmental noise simultaneously. In the AF-ESPI method, the reference frame is recorded in a vibrating state and subtracted from the incoming frames.

Since Pierre and Jacques Curie discovered the piezoelectric effect in 1880, there has been a large amount of research and applications addressed in later literatures (Berlincourt *et al.*,[9] Zelenka[10]). Piezoelectric transducers are widely used in electromechanical sensors, actuators, and nondestructive testing devices as well as electro-optic modulator. Piezoelectric effect is applied to many modern-engineering applications because it expresses the connection between the electrical and mechanical fields. Piezoelectricity describes the phenomenon in which the material generates electric charge when subjected to stress and, conversely, generates strain when the electric field is applied. Although the vibration characteristics of piezoelectric materials can be determined by the linear piezoelasticity, the Maxwell equation, and piezoelectric constitutive equations (Tiersten[11]), it is difficult to obtain analytical solutions even for a simple geometry.

In general, there are two numerical methods that are usually used to study the vibration problem of piezoelectric materials: one is the variational approximation method and the other is finite element analysis. Eer Nisse[12] applied the calculus of variation to the analysis of piezoelectric disks and compared the results to the experimental results obtained by Shaw.[13] Holland[14] used the Rayleigh–Ritz method to study the extensional modes of rectangular piezoelectric plates and classified them into four distinct symmetry types. Kunkel, Locke, and Pikeroen[15] studied the vibration modes of PZT-5H ceramics disks concerning the diameter-to-thickness (D/T) ratio ranging from 0.2 to 10. Due to the great flexibility and extensive applicability, the finite element method has become the alternative method to the analysis of piezoelectric material in various configurations. Guo, Cawley, and Hitchings[16] presented the results for PZT-5A piezoelectric disks with D/T of 20 and 10. There were five types of modes classified according to the mode shape characteristics and the physical interpretation was well clarified. In addition to variational and numerical methods, experimental techniques have been employed for investigation of vibration modes and natural frequencies of piezoelectric transducers. Shaw[13] used an optical interference technique in which a stroboscopically illuminated multiple beam was applied to measure the surface motion of thick barium titanate disks. However, only normal modes having symmetry with respect to the axis and to the central plane were observed. Chang[17] employed the dual-beam speckle interferometry to measure the in-plane vibration amplitude on the PZT surface. As the measured displacement spectrum reaches the local maximum under some driven voltages, the resonant frequencies of in-plane modes can be determined. Koyuncu[18] used ESPI with reference beam modulation to observe the vibration amplitudes and vibration modes of PZT-4 transducers in air and water. Oswin *et al.*[19] utilized ESPI to validate the finite element model of a flextensional transducer with an elliptical shape. Both in-plane and out-of plane vibrations were studied and discussed. Ma and Huang[20,21] used the AF-ESPI method to investigate the three-dimensional vibration of piezoelectric rectangular parallelepipeds and cylinders; both the resonant frequencies and mode shapes were presented.

The investigation of the vibration behavior for piezoelectric materials is a problem of great practical interest and the experimental measurement of resonant frequencies is generally performed by the impedance analysis. However, there are very few experimental results, especially for the full field measurement of mode shapes, available in the literature. In this article, both the optical method based on the amplitude-fluctuation ESPI (AF-ESPI) and an impedance analysis are employed to study experimentally the vibration characteristics for piezoceramic plates. The advantage of using the AF-ESPI method is that both resonant frequencies and the corresponding mode shapes can be obtained simultaneously from the experimental investigation. The fringe patterns shown in the experimental results correspond to the vibrating mode shapes. According to experimental results obtained in this study, the vibration modes of piezoceramic plates can be classified into two types, type A (out-of-plane) and type B (in-plane) modes. It is interesting to note that type A modes with lower resonant frequencies cannot be measured by the impedance analysis and the vibration mode shapes are similar to those of isotropic plates. To validate this conclusion, experimental results including the rectangular and circular piezoceramic plates are presented in this study. In addition to the AF-ESPI experimental technique, numerical computations based on a finite element package are presented and good agreements of resonant frequencies and mode shapes are found for both results.

II. THEORY OF AF-ESPI METHOD AND PIEZOELECTRICITY

A. Out-of-plane vibration

When the specimen vibrates periodically, the first image is recorded as a reference. The light intensity of this reference image detected by a charge-coupled device (CCD) camera can be expressed by the time-averaged method as

$$I_1=\frac{1}{\tau}\int_0^{\tau}\left\{I_A+I_B+2\sqrt{I_AI_B}\times\cos\left[\phi+\frac{2\pi}{\lambda}(1+\cos\theta)A\cos\omega t\right]\right\}dt, \tag{1}$$

where I_A=the object light intensity, I_B=the reference light intensity, τ=the CCD refresh time, ϕ=the phase difference between object and reference light, λ=the wavelength of laser, θ=the angle between object light and observation direction, A=the vibration amplitude, and ω=the angular frequency.

Let $\Gamma=(2\pi/\lambda)(1+\cos\theta)$ and $\tau=2m\pi/\omega$, where m is an integer. Then Eq. (1) can be written as

$$I_1=I_A+I_B+\frac{2\sqrt{I_AI_B}}{\tau}\int_0^{\tau}\cos(\phi+\Gamma A\cos\omega t)dt$$

$$=I_A+I_B+\frac{2\sqrt{I_AI_B}}{\tau}\mathrm{Re}\left\{e^{i\phi}\int_0^{\tau}\exp(i\Gamma A\cos\omega t)dt\right\},$$

where Re stands for the real part. Since $e^{iz\sin\alpha}=\Sigma_{-\infty}^{\infty}J_n(z)e^{in\alpha}$ (J_n is a Bessel function of the first kind of order n), hence we have

$$\mathrm{Re}\left\{e^{i\phi}\int_0^{\tau}\exp(i\Gamma A\cos\omega t)dt\right\}$$
$$=\mathrm{Re}\left\{e^{i\phi}\sum_{-\infty}^{\infty}J_n(\Gamma A)\int_0^{\tau}e^{in(\pi/2-\omega t)}dt\right\}$$
$$=\mathrm{Re}\left\{e^{i\phi}\sum_{-\infty}^{\infty}J_n(\Gamma A)e^{in\pi/2}\frac{(e^{-in\omega\tau}-1)}{-in\omega}\right\}.$$

However all the terms will be zero except $n=0$. Finally Eq. (1) can be expressed as

$$I_1=I_A+I_B+2\sqrt{I_AI_B}(\cos\phi)J_0(\Gamma A), \tag{2}$$

where J_0 is a zeroth order Bessel function of the first kind.

After image processing and rectifying, the intensity of the first image can be expressed as

$$I_1=I_A+I_B+2\sqrt{I_AI_B}|(\cos\phi)J_0(\Gamma A)|. \tag{3}$$

As the vibration of the specimen continues, we assume that the vibration amplitude changes from A to $A+\Delta A$ because of the electronic noise or instability of the apparatus. The light intensity of the second image can be represented as

$$I_2=\frac{1}{\tau}\int_0^{\tau}\{I_A+I_B+2\sqrt{I_AI_B}\cos[\phi+\Gamma(A+\Delta A)\cos\omega t]\}dt. \tag{4}$$

When the vibration amplitude variation ΔA is rather small, Eq. (4) can be expanded in Taylor series. By keeping the first two terms and neglecting the higher-order terms, we rewrite Eq. (4) as follows:

$$I_2=I_A+I_B+2\sqrt{I_AI_B}(\cos\phi)[1-\tfrac{1}{4}\Gamma^2(\Delta A)^2]J_0(\Gamma A). \tag{5}$$

By image processing and rectifying, I_2 can be similarly expressed as

$$I_2=I_A+I_B+2\sqrt{I_AI_B}|(\cos\phi)[1-\tfrac{1}{4}\Gamma^2(\Delta A)^2]J_0(\Gamma A)|. \tag{6}$$

When these two images (the first and second images) are subtracted by the image processing system, i.e., Eq. (3) is subtracted from Eq. (6), and are rectified, the resulting image intensity can be expressed as

$$I=I_2-I_1=\frac{\sqrt{I_AI_B}}{2}|(\cos\phi)\Gamma^2(\Delta A)^2J_0(\Gamma A)|. \tag{7}$$

B. In-plane vibration

Similar to the out-of-plane vibration case, the first and second image intensities, i.e., I_1 and I_2, for in-plane vibration are expressed as

$$I_1=I_A+I_B+2\sqrt{I_AI_B}|(\cos\phi)J_0(\Gamma' A')|, \tag{8}$$

$$I_2=I_A+I_B+2\sqrt{I_AI_B}|(\cos\phi)$$
$$\times[1-\tfrac{1}{4}\Gamma'^2(\Delta A')^2]J_0(\Gamma' A')|, \tag{9}$$

where $I_A=I_B=$the object light intensity, $A'=$the vibration amplitude of in-plane vibration, $\Gamma'=(2\pi/\lambda)(2\sin\theta')$, and $\theta'=$half of the angle between two illumination lights.

Subtracting Eq. (9) from Eq. (8) and rectifying by the image processing system, we can obtain the resulting image intensity as

$$I=I_2-I_1=\frac{\sqrt{I_AI_B}}{2}|(\cos\phi)\Gamma'^2(\Delta A')^2J_0(\Gamma' A')|. \tag{10}$$

From Eqs. (7) and (10), we find that the fringe patterns for both the out-of-plane and in-plane vibration obtained by AF-ESPI method are dominated by a zeroth-order Bessel function J_0. Ma and Huang[20] provided a detailed discussion of the AF-ESPI method. They also investigated the three-dimensional vibration of piezoelectric rectangular parallelepipeds by using the AF-ESPI method. Combining the out-of-plane with in-plane optical setups by the AF-ESPI method, we can construct completely the vibration characteristics of the piezoceramic plates, including resonant frequencies and mode shapes at the same time. This is different from the conventional impedance analysis, which has been used widely in determining only the resonant frequency for piezoelectric material.

C. Piezoelectricity

The vibration of piezoelectric material is electroelastic in nature, and it is necessary to include the coupled electrical field with the elastic behavior. In other words, the equation of linear elasticity is coupled to the charge equation of electrostatics using the piezoelectric constants. The system of equations that governs the behavior of the vibration characteristics of piezoelectric material was presented in detail by Tiersten.[11] The linear piezoelectric constitute equations are

$$\tau_{ij}=c_{ijkl}^{E}s_{kl}-e_{kij}E_k,\quad D_i=e_{ikl}s_{kl}+\epsilon_{ik}^{S}E_k, \tag{11}$$

where τ_{ij}, D_i, s_{kl}, and E_k represent the stress, electric displacement, strain, and electric field, respectively; and c_{ijkl}^{E}, e_{kij}, and ϵ_{ik}^{S} are the elastic, piezoelectric, and dielectric constants, respectively.

Because of the symmetry in general, the compressed matrix notation is introduced in place of the tensor notation. This matrix notation consists of replacing ij or kl by p or q, where i, j, k, and l take the values 1, 2, 3 and p and q take the values 1–6. By virtue of the transformation, we can make the identifications

$$c_{ijkl}^{E}\equiv c_{pq}^{E},\quad e_{ikl}\equiv e_{iq},\quad \tau_{ij}\equiv T_p, \tag{12}$$

and the constitutive equations (11) can be rewritten as

$$T_p=c_{pq}^{E}S_q-e_{kp}E_k,\quad D_i=e_{iq}S_q+\epsilon_{ik}^{S}E_k, \tag{13}$$

where $s_{kl}=S_q$ when $k=l$ and $q=1,2,3$ and $2s_{kl}=S_q$ when $k\neq l$ and $q=4,5,6$.

Because the polarized piezoelectric ceramics have the same symmetry as a hexagonal crystal in class $C_{6v}=6$ mm, it can be modeled as a transversely isotropic material. The elastic, piezoelectric, and dielectric constants are represented in matrix forms as

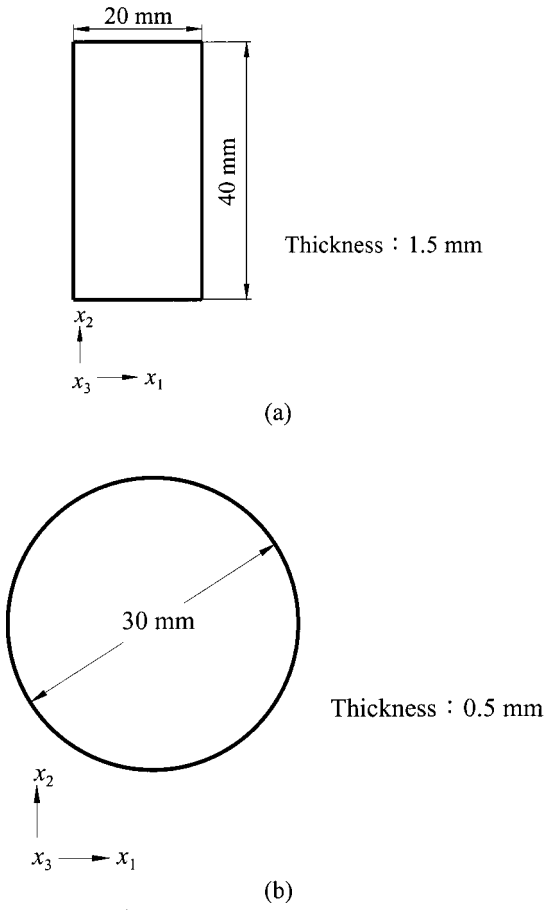

FIG. 1. Geometric dimensions of the (a) rectangular and (b) circular piezoceramic plates.

$$c_{ij}^E=\begin{bmatrix} c_{11}^E & c_{12}^E & c_{13}^E & 0 & 0 & 0 \\ c_{12}^E & c_{11}^E & c_{13}^E & 0 & 0 & 0 \\ c_{13}^E & c_{13}^E & c_{33}^E & 0 & 0 & 0 \\ 0 & 0 & 0 & c_{44}^E & 0 & 0 \\ 0 & 0 & 0 & 0 & c_{44}^E & 0 \\ 0 & 0 & 0 & 0 & 0 & \dfrac{c_{11}^E-c_{12}^E}{2} \end{bmatrix}, \tag{14}$$

$$e_{ip}=\begin{bmatrix} 0 & 0 & 0 & 0 & e_{15} & 0 \\ 0 & 0 & 0 & e_{15} & 0 & 0 \\ e_{31} & e_{31} & e_{33} & 0 & 0 & 0 \end{bmatrix}, \tag{15}$$

$$\epsilon_{ij}^S=\begin{bmatrix} \epsilon_{11}^S & 0 & 0 \\ 0 & \epsilon_{11}^S & 0 \\ 0 & 0 & \epsilon_{33}^S \end{bmatrix}, \tag{16}$$

and $c_{ij}^E=c_{ji}^E$.

III. EXPERIMENTAL RESULTS AND NUMERICAL ANALYSIS

The piezoelectric plates made of $Pb(Zr\cdot Ti)O_3$ ceramics are selected for experimental investigations and the modal number is PIC-151 (Germany Physik Instrument Company). There are two types of specimens as shown in Figs. 1(a) and (b), the rectangular and circular configurations, respectively, are considered in this study. The polarization axis is in the x_3 direction and two opposite faces (x_1–x_2 plane) of the specimen are completely coated with silver electrodes. The electroelastic properties of the test specimens PIC-151 are listed in Table I.

TABLE I. Material properties of the PIC-151 piezoceramic plate.

c_{11}^E (10^{10} N/m^2)	10.76
c_{33}^E	10.04
c_{12}^E	6.312
c_{13}^E	6.385
c_{44}^E	1.962
$c_{66}^E=(c_{11}^E-c_{12}^E)/2$	2.224
e_{31} (N/Vm)	−9.6
e_{33}	15.1
e_{15}	12.0
$\epsilon_{11}^S/\epsilon_0$	1110
$\epsilon_{33}^S/\epsilon_0$	852
ρ (kg/m^3)	7760
$\epsilon_0=8.85\times10^{-12}$ F/m	

The schematic layout of self-arranged time-averaged AF-ESPI optical systems, as shown in Figs. 2 and 3, are used to perform the out-of-plane and in-plane vibration measurements for resonant frequencies and corresponding mode shapes. A He–Ne laser with 30 mW and wavelength $\lambda=632.8$ nm is used as the coherent light source. We use a CCD camera (Pulnix Company) and a P360F (Dipix Technologies, Inc.) frame grabber with a digital signal processor onboard to record and process the images. As shown in Fig. 2 for the out-of-plane vibration measurement, the laser beam is divided into two parts, the object and reference beams, by a beamsplitter. The object beam travels to the specimen and then reflects to the CCD camera. The reference beam is directed to the CCD camera via a mirror and a reference plate. The plane of the CCD camera is chosen to coincide with the Cartesian coordinate x_1–x_2 plane and the x_3 axis is in the normal direction. The out-of-plane optical system used will measure the displacement component along the x_3 direction of the piezoceramic plates. For the in-plane measurement system as shown in Fig. 3, two laser beams with the same

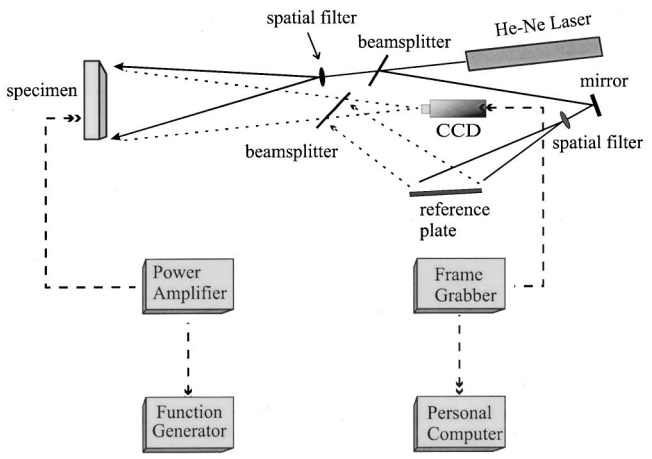

FIG. 2. Schematic diagram of AF-ESPI setup for the out-of-plane measurement.

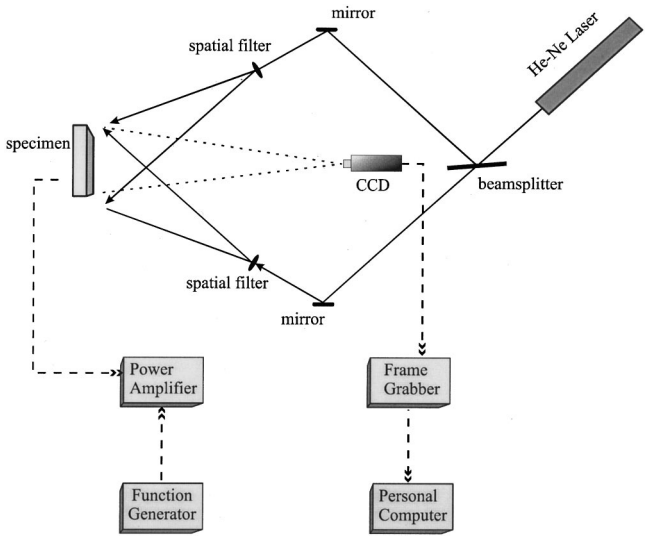

FIG. 3. Schematic diagram of AF-ESPI setup for the in-plane measurement.

optical path and light intensity are symmetrically incident to the specimen, and then reflect to the CCD camera. The in-plane setup will measure the displacement magnitude in the x_1 or x_2 direction. The CCD camera converts the intensity distribution of the interference pattern of the object into a corresponding video signal at 30 frames per second. The signal is electronically processed and final converted into an image on the video monitor. The interpretation of the fringe image is similar to the reading of a contour map. To achieve the sinusoidal output, a function generator HP33120A (Hewlett Packard) connected to a 4005 power amplifier (NF Electronic Instruments) is used.

The experimental procedure of the AF-ESPI technique is performed as follows. First, a reference image is taken after the piezoceramic plate is excited into vibration, then the second image is taken, and the reference image is subtracted by the image processing system. If the frequency of vibration is not the resonant frequency, only random distributed speckles are displayed and no fringe patterns will be shown. However, if the frequency of vibration is in the neighborhood of the resonant frequency, stationary distinct fringe patterns will be observed. Then the function generator is carefully and slowly turned; the number of fringes will increase and the fringe pattern will become clearer as the resonant frequency is approached. From the aforementioned experimental procedure, the resonant frequencies and the correspondent mode shapes can be determined at the same time.

Based on the experimental results obtained by using the AF-ESPI optical system, the resonant frequencies and correspondent mode shapes of the rectangular piezoceramic plate are classified into two types, named type A and B modes in this article. Comparing with type B modes, the resonant frequencies of type A modes are much lower than those of type B modes and the vibration mode shapes can be obtained only by the out-of-plane measurement. Hence we can conclude that the type A modes are the out-of-plane vibration modes (or bending modes) and the type B modes are the in-plane vibration modes (or extensional modes). In addition to the experimental measurement, numerical calculation is also performed by the commercially available software ABAQUS finite element package[22] in which 20-node three-dimensional solid piezoelectric elements (C3D20E) are selected to analyze the problem. Figure 4 shows the experimental and numerical results for the first three vibration mode shapes of type A. Owing to the geometric configuration of the rectangular piezoceramic plate, two in-plane vibration modes in the x_1 and x_2 directions are displayed in order to present the complete characteristics of the vibration behavior. Figure 5 shows the results for the first eight mode shapes of type B. Herein we indicate the phase of displacement in finite element results as a solid or dashed line, the solid lines are in the opposite direction to the dashed lines. The transition from solid lines to dashed lines corresponds to a zero displacement line, or a nodal line. The zeroth-order fringe, which is the brightest fringe on experimental results, represents the nodal lines of the vibrating piezoceramic plate at resonant frequencies. The rest of the fringes are contours of constant amplitudes of displacement, which can be quantitatively calculated by $J_0'(\Gamma A)=0$ [or $J_0'(\Gamma' A')=0$] according to Eq. (7) [or Eq. (10)] for out-of-plane (or in-plane) measurement. Since the sensitivity of the out-of-plane measurement will increase as θ decreases and the sensitivity of the in-plane measurement will increase as θ' increases, we choose $\theta=10$ degrees and $\theta'=60$ degrees for the experimental setup. The mode shapes obtained by experimental results can be checked by the nodal lines and fringe patterns with the numerical finite element calculations. Excellent agreements of the experimental measurement and numerical calculation are found for both the out-of-plane and in-plane vibration modes.

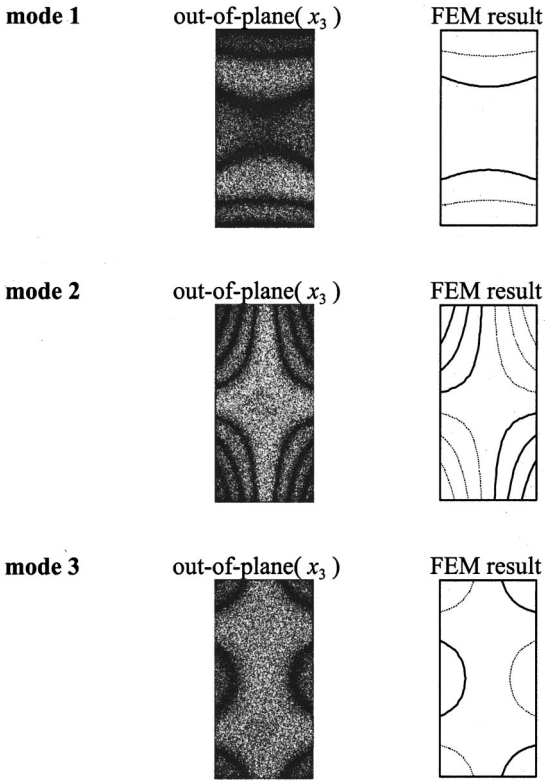

FIG. 4. Mode shapes of type A obtained by AF-ESPI and FEM for the rectangular piezoceramic plate.

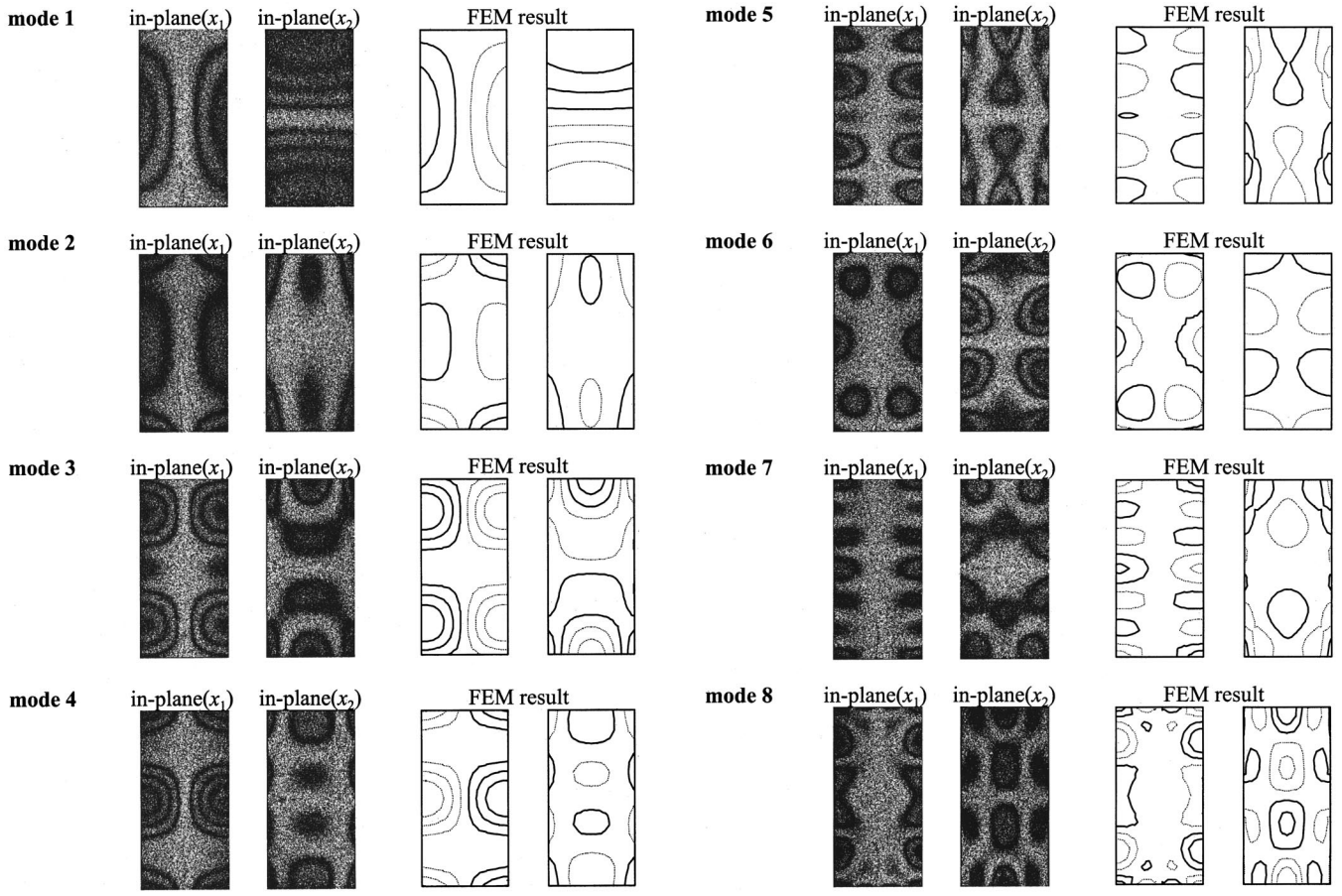

FIG. 5. Mode shapes of type B obtained by AF-ESPI and FEM for the rectangular piezoceramic plate.

Because the electrical impedance of the piezoceramic material drops to a local minimum when it vibrates at a resonant frequency, the resonant frequency can also be determined by an impedance analysis. Here it is carried out by using an HP4194A impedance/gain-phase analyzer (Hewlett Packard) and the impedance curve for the rectangular piezoceramic plate measured from HP4194A is shown in Fig. 6. The local minima appearing in the impedance curves correspond to resonance. Unexpectedly, we find that only the resonant frequencies of the type B modes are indicated in Fig. 6, i.e., those of the type A modes cannot be obtained by impedance analysis. This phenomenon can be explained by means of the characteristics of piezoelectricity. When the piezoelectric plate vibrates at a resonant frequency, the charge will greatly be induced on the electrode surfaces owing to the vibration deformation, named the direct piezoelectric effect, and the impedance will drop to a local minimum value. This is the reason that the resonant frequencies of piezoceramic plates can be determined by using the impedance analyzer. However, if the summation of the induced charge distributed over the electrode surfaces is zero, we are not able to find the large variation of impedance at the resonant frequency. Type A modes are just the situation mentioned earlier and we cannot obtain the resonant frequencies for these modes from the impedance curve shown in Fig. 6. Table II shows the first few resonant frequencies of the rectangular piezoceramic plate obtained by using the AF-ESPI, impedance analysis, and the FEM method. The discrepancy of resonant frequencies between AF-ESPI and impedance analysis for type B modes is smaller than that between AF-ESPI and FEM. However, the difference between the experimental measurement and FEM result may result from the determination of the material properties and the defects of the piezoceramic plate.

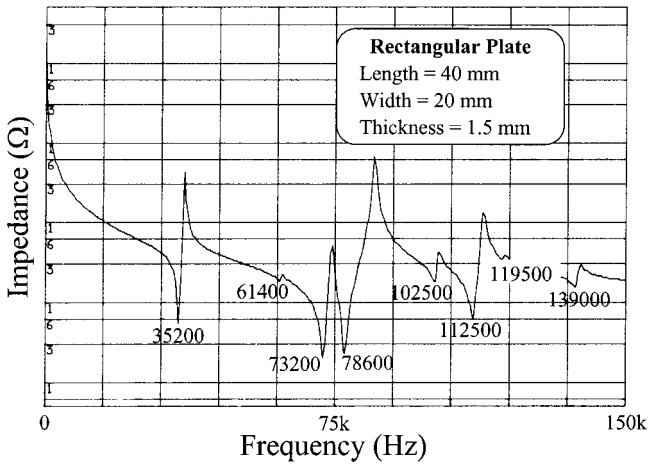

FIG. 6. Impedance variation curve of the rectangular piezoceramic plate.

By observing the mode shapes of type A for the rectangular piezoceramic plate, we find that the vibration modes are similar to that of the bending vibration for an isotropic plate. To validate the result obtained from the rectangular piezoceramic plate, a circular piezoceramic plate as shown in

TABLE II. Results of resonant frequencies obtained from AF-ESPI, impedance analysis and FEM for the rectangular piezoceramic plate.

Mode	AF-ESPI (Hz)	Impedance analysis (Hz)	FEM (Hz)
		Type A	
1	2940	⋯	2905
2	3270	⋯	3233
3	7320	⋯	7243
		Type B	
1	35 000	35 200	33 981
2	61 600	61400	59 785
3	73 100	73 200	70 729
4	78 600	78 600	76 113
5	102 200	102 250	99 154
6	112 500	112 500	108 866
7	119 700	119 500	116 663
8	139 100	139 000	134 810

Fig. 1(b) is also investigated. By performing the experimental procedure and numerical calculation as mentioned earlier, the first eight mode shapes for type A of the circular piezoceramic plate shown in Fig. 7 were obtained. Figure 8 shows the experimental and numerical results for the first two mode shapes of type B. The resonant frequencies of the circular piezoceramic plate obtained by AF-ESPI, impedance analysis, and FEM method are listed in Table III. The impedance variation curve for the circular piezoceramic plate is shown in Fig. 9 and the resonant frequencies of type A modes were again not to be found in the impedance curve.

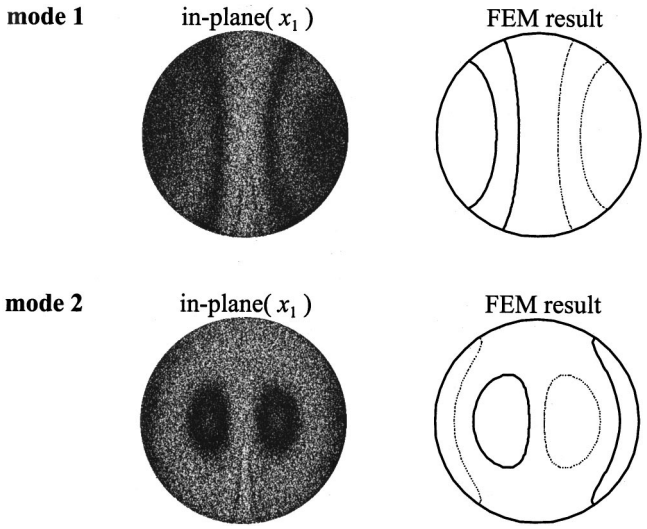

FIG. 8. Mode shapes of type B obtained by AF-ESPI and FEM for the circular piezoceramic plate.

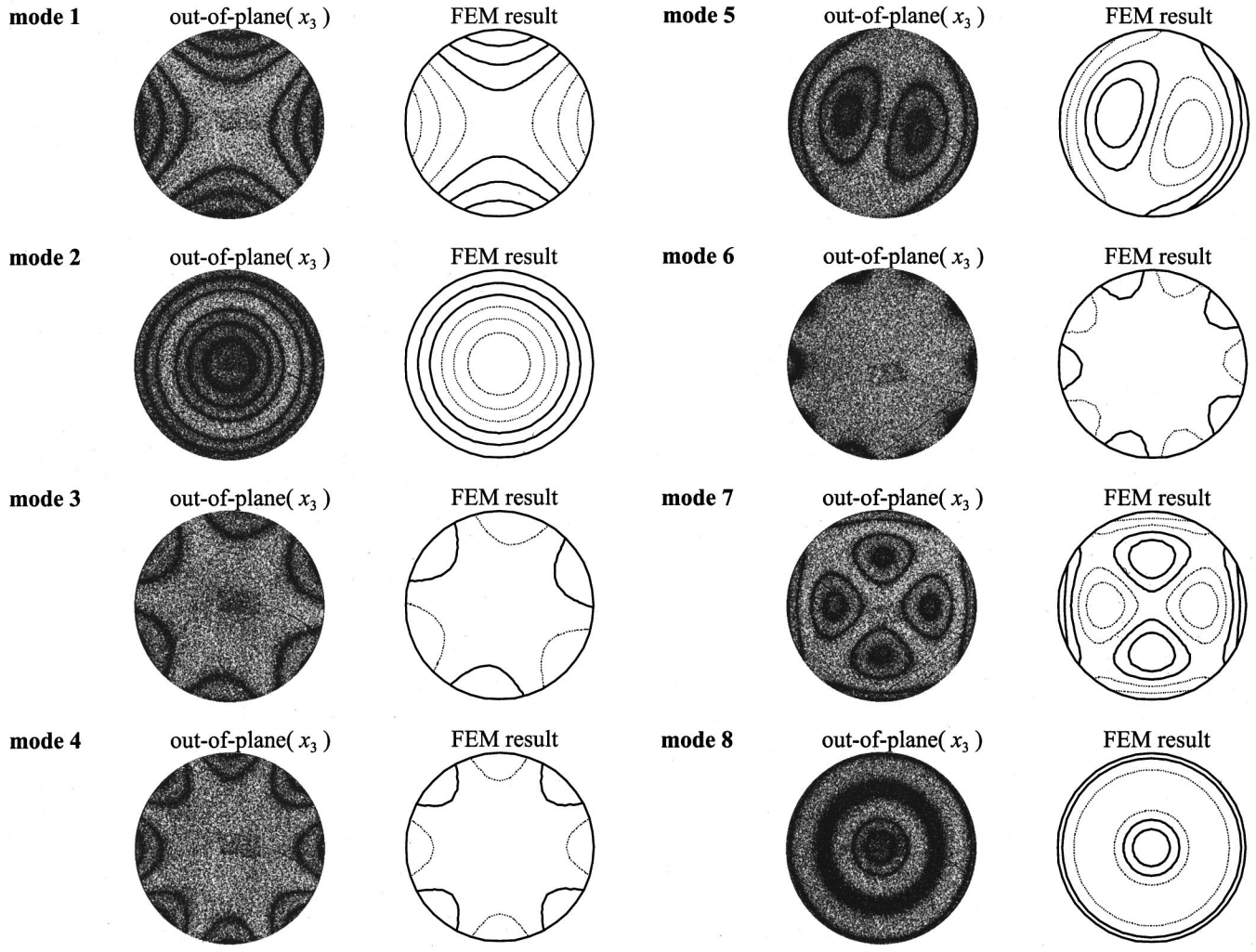

FIG. 7. Mode shapes of type A obtained by AF-ESPI and FEM for the circular piezoceramic plate.

TABLE III. Results of resonant frequencies obtained from AF-ESPI, impedance analysis and FEM for the circular piezoceramic plate.

Mode	AF-ESPI (Hz)	Impedance analysis (Hz)	FEM (Hz)
		Type A	
1	1687	···	1630
2	3406	···	3514
3	3928	···	3921
4	6940	···	7134
5	7470	···	7647
6	10 450	···	11 379
7	12 580	···	12 877
8	13 880	···	14 304
		Type B	
1	68 400	69 065	64 389
2	178 940	179 010	167 698

IV. CONCLUSIONS

Optical techniques have been shown to have certain advantages for vibration analysis and ESPI has been applied to many vibration problems. The advantages of the optical ESPI method include noncontact and full-field measurement, real-time observation, submicrometer sensitivity, and digital image processing among others. Unlike the film recording and optical reconstruction procedures used for holographic interferometry, the interferometric fringes of AF-ESPI are produced instantly by a video recording system.

It is known that the vibration characteristics of piezoelectric materials are important in many engineering applications. Most of the works for vibration analysis of piezoelectric plates published in the literature are analytical and numerical results. There are very few experimental results available for the full field configuration of mode shapes for vibrating plates. In this study, a self-arranged amplitude-fluctuation ESPI optical setup with good visibility and noise reduction has been established to simultaneously obtain the resonant frequencies and the corresponding mode shapes of vibrating piezoceramic plates. The resonant frequencies of piezoceramic plates are also determined by impedance analysis in this study. Both the rectangular and circular piezoceramic plates are investigated. Based on the experimental results obtained by AF-ESPI method, we have classified the vibration modes into two types, the out-of-plane (type A) and in-plane (type B) modes. However, all the resonant frequencies of type A modes cannot be measured by impedance analysis. Numerical calculations of resonant frequencies and mode shapes based on a finite element package are also performed and excellent agreement of the mode shapes obtained numerically with results obtained by AF-ESPI are found. The resonant frequencies of type B modes obtained by AF-ESPI are in good agreement with the impedance analysis but there is a slight difference if compared with finite element calculations. The results shown in this study demonstrate that the AF-ESPI method is applicable to many situations in vibration analysis for piezoceramic plates as long as the vibration amplitude reaches the sensitivity of the AF-ESPI method.

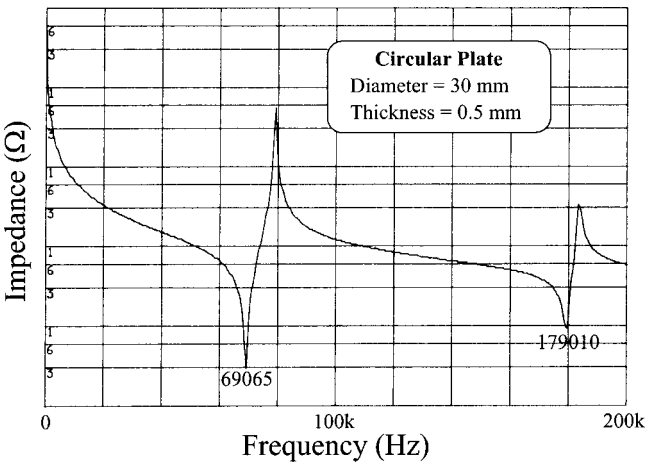

FIG. 9. Impedance variation curve of the circular piezoceramic plate.

ACKNOWLEDGMENTS

The authors gratefully acknowledge the financial support of this research by the National Science Council (Republic of China) under Grant No. NSC89-2212-E002-016.

[1] J. N. Butters and J. A. Leendertz, ''Speckle pattern and holographic technique in engineering metrology,'' Opt. Laser Technol. **31**(1), 26–30 (1971).
[2] P. K. Rastogi, *Holographic Interferometry* (Springer-Verlag, Germany, 1994).
[3] O. J. Løkberg and K. Hogmoen, ''Use of modulated reference wave in electronic speckle pattern interferometry,'' J. Phys. E **9**, 847–851 (1976).
[4] K. Creath and G. Å. Slettemoen, ''Vibration-observation techniques for digital speckle-pattern interferometry,'' J. Opt. Soc. Am. A **2**(10), 1629–1636 (1985).
[5] O. J. Løkberg, ''Mapping of in-plane vibration modes by electronic speckle pattern interferometry,'' Opt. Eng. **24**(2), 356–359 (1985).
[6] M. C. Shellebear and J. R. Tyrer, ''Application of ESPI to three-dimensional vibration measurement,'' Opt. Lasers Eng. **15**, 43–56 (1991).
[7] A. F. Doval, J. L. Fernández, M. Pérez-Amor, J. D. R. Valera, and J. D. C. Jones, ''Contrast enhanced and phase controlled stroboscopic additive fiber optic TV-holography for whole field out-of-plane vibration analysis,'' Opt. Lasers Eng. **25**, 323–342 (1996).
[8] W. C. Wang, C. H. Hwang, and S. Y. Lin, ''Vibration measurement by the time-averaged electronic speckle pattern interferometry methods,'' Appl. Opt. **35**(22), 4502–4509 (1996).
[9] D. A. Berlincourt, D. R. Curran, and H. Jaffe, ''Piezoelectric and piezomagnetic materials and their function in transducers,'' Phys. Acoust. **1**(A), 169–270 (1964).
[10] J. Zelenka, *Piezoelectric Resonators and Their Application* (Academia/Prague, Czechoslovakia, 1986).
[11] H. F. Tiersten, *Linear Piezoelectric Plate Vibration* (Plenum, New York, 1969).
[12] E. P. Eer Nisse, ''Variational method for electroelastic vibration analysis,'' IEEE Trans. Sonics Ultrason. **SU-14**(4), 153–160 (1967).
[13] E. A. G. Shaw, ''On the resonant vibrations of thick barium titanate disks,'' J. Acoust. Soc. Am. **28**, 38–50 (1956).
[14] R. Holland, ''Contour extensional resonant properties of rectangular piezoelectric plates,'' IEEE Trans. Sonics Ultrason. **SU-15**(2), 97–105 (1968).
[15] H. A. Kunkel, S. Locke, and B. Pikeroen, ''Finite-element analysis of vibrational modes in piezoelectric ceramics disks,'' IEEE Trans. Ultrason. Ferroelectr. Freq. Control **37**(4), 316–328 (1990).
[16] N. Guo, P. Cawley, and D. Hitchings, ''The finite element analysis of the vibration characteristics of piezoelectric discs,'' J. Sound Vib. **159**(1), 115–138 (1992).
[17] M. Chang, ''In-plane vibration displacement measurement using fiber-optical speckle interferometry,'' Precis. Eng. **16**(1), 36–41 (1994).
[18] B. Koyuncu, ''The investigation of high frequency vibration modes of PZT-4 transducers using ESPI techniques with reference beam modulation,'' Opt. Lasers Eng. **1**, 37–49 (1980).

[19] J. R. Oswin, P. L. Salter, F. M. Santoyo, and J. R. Tyrer, ''Electronic speckle pattern interferometric measurement of flextensional transducer vibration patterns: in air and water,'' J. Sound Vib. **172**(4), 433–448 (1994).
[20] C. C. Ma and C. H. Huang, ''The investigation of three-dimensional vibration for piezoelectric rectangular parallelepipeds by using the AF-ESPI method,'' IEEE Trans. Ultrason., Ferroelect., Freq. Contr. **48**(1), 142–153 (2001).
[21] C. H. Huang and C. C. Ma, ''Vibration characteristics for piezoelectric cylinders using amplitude-fluctuation electronic speckle pattern interferometry,'' AIAA J. **36**(12), 2262–2268 (1998).
[22] Hibbit, Karlsson, and Sorensen, Inc., *ABAQUS User's Manual, ver. 5.5* (Pawtucket, RI, 1995).

Transient response of an acoustic medium by an excited submerged spherical shell

U. Zakout
Ministry of Public Works, P.O. Box 5317, Gaza, Palestine

(Received 9 October 2000; revised 8 March 2001; accepted 10 March 2001)

An exact closed-form solution is obtained for the transient response of an acoustic fluid due to an excited submerged spherical shell. Step axisymmetric stress acting on the inner surface of the shell is expanded into modal Fourier components in which for each modal stress systematic exact expressions for modal radial displacement of the shell, fluid pressure, fluid particle velocity and displacement are presented. The superiority of the formulations herein is its applicability to any time and spatial distance in the fluid as well as on the shell. The formulation also does not require additional numerical computations associated with other methods. © *2001 Acoustical Society of America.* [DOI: 10.1121/1.1369104]

PACS numbers: 43.40.Ey [CBB]

I. INTRODUCTION

The transient response of a spherical elastic shell submerged in an infinite acoustic fluid has been the subject of interest for many years. Huang[1] and Huang *et al.*[2] derived exact closed form solutions for the modal radial deflections of the spherical shell to impinging plane and spherical stress waves of exponentially time-decaying functions with infinitely steep fronts. Using the mode method, they expanded the incident wave into modal components and applied Laplace transformation to the governing modal equations for the fluid wave and motion of the shell. Numerical results are presented for relative deflections and strains of the spherical shell obtained from the summation of the first eight modes. On the other hand, Lou and Klosner[3] derived expressions for modal transient response of spherical shell to concentrated impulse and Heaviside loads using the Laplace transform method. The disadvantage of this method is that the inversion integral of higher order modal displacements requires the treatment of branch points and poles. Geers[4] used finite element formulations of the doubly asymptotic approximations of fluid wave equation with shell's equations of motion to solve for free vibration and forced motion of the spherical shell in the acoustic fluid. However, the loss of accuracy of results at intermediate and late time of forced-response history still remains in the approach taken by Geers. Akkas[5,6] used the so-called residual potential method in order to solve for modal response of the spherical shell in acoustic fluid. In this method, the second order fluid wave equation is transformed into an equivalent first order equation. The modified first order wave equation is feasible for use with the two equations of the shell motion for obtaining modal deflections of the shell. Even though the equations used for solution are exact, the solution is obtained numerically. The numerical computation involves integration of time derivatives as well as integration of convolution terms. Akkas[7] obtained solutions at inner points in the fluid numerically by integration along radial and time coordinates of the transformed first order wave equation starting from the boundary of the shell to the point of interest in the fluid. The accuracy of results depends on time and radial distance increments used in the numerical implementation and it is uncertain if obtained results properly coincide with the realistic solution.

Tupholme[8] presented formulations for the problem in which excitation is provided by axisymmetrical small amplitude deformations of a spherical boundary. These formulations are expressed in terms of series and integrals of the Laplace transform of the wave velocity potential. He specialized the problem to the case in which movement is restricted to a cap of some angle. Unfortunately, several approximations are applied to obtain the flow only near the diffracted and edge wave fronts.

Zhang and Geers[12] solved for the transient response of an inviscid fluid-filled spherical shell submerged in an infinite acoustic medium to a plane wave. They obtained solutions numerically for the response of the sphere and the fluid at center and external surface of the sphere.

In the following we present exact closed-form and systematic formulations for the modal response of the shell as well as the surrounding fluid under the action of internal modal step stresses. Formulations are categorized into three groups. First, for breathing mode which corresponds to uniform, spherical symmetry of acting stress and hence response of the shell and the fluid. Second, for translational mode which corresponds to motion of the spherical shell as a rigid body in the medium. Last, for higher modes which correspond to excitation of the shell and the fluid without motion of the spherical shell in the fluid. The advantage of formulations appears clearly for nontranslational higher modes in which responses are obtained at inner points in the fluid and arbitrary times without an associated increase in numerical effort.

Solutions to incident step stresses are likely more useful than solutions to exponential decaying stresses used by Huang *et al.*[1,2] since the response to any time-history stress can be obtained from the response to step stress by the use of the Duhamel integral.

II. FORMULATION OF THE PROBLEM

A thin elastic spherical shell of radius a and thickness h is submerged in an infinite acoustic fluid as shown in Fig. 1.

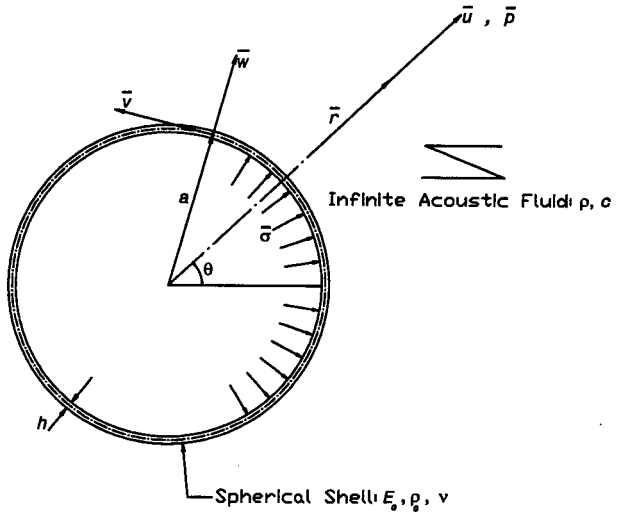

FIG. 1. Geometry of the problem.

The shell material has plate longitudinal wave velocity $c_0=[E/\rho_0(1-\nu^2)]^{1/2}$ where E, ρ_0, and ν are Young's modulus, mass density and Poisson's ratio of the shell. The acoustic fluid has mass density ρ and sound speed c.

The inner surface of the shell is subjected to axisymmetric, nontorsional stress $\bar{\sigma}$ at reference time $\bar{t}=0$. The shell and fluid responses are characterized by radial and meridional displacements $(\bar{w},\bar{v})$ of the shell, radial fluid particle displacement $\bar{u}$ and pressure $\bar{p}$ at radial distance $\bar{r}$ for the time history $\bar{t}$.

In the following all formulations are derived in terms of dimensionless components: $t=\bar{t}c/a$ for time, $r=\bar{r}/a$, $w=\bar{w}/a$, $v=\bar{v}/a$, and $u=\bar{u}/a$ for radial distance and displacement components, and $\sigma=\bar{\sigma}/\rho c^2$ and $p=\bar{p}/\rho c^2$ for acting stress on the shell and fluid pressure, respectively.

Using the mode method, the acting stress σ, radial and meridional displacements (w,v) for axisymmetric problem are expanded in terms of Fourier–Legendre series as follows:

$$\sigma(\theta,t)=\sum_{n=0}^{\infty}\sigma_n(t)P_n(\cos\theta), \tag{1}$$

$$w(\theta,t)=\sum_{n=0}^{\infty}w_n(t)P_n(\cos\theta), \tag{2}$$

$$v(\theta,t)=-\sum_{n=1}^{\infty}v_n(t)\frac{d}{d\theta}P_n(\cos\theta), \tag{3}$$

where P_n is the Legendre polynomial of order n. The equations of motion of the shell for the nth component in the Fourier–Legendre series are[9,12]

$$\ddot{w}_n+\lambda_n^{ww}w_n+\lambda_n^{wv}v_n=\mu p_n, \tag{4}$$

$$\lambda_n^{wv}w_n+n(n+1)\ddot{v}_n+\lambda_n^{vv}v_n=0, \tag{5}$$

where

$$\lambda_n^{ww}=[2(1+\nu)+n(n+1)\epsilon\xi_n]\gamma_0, \tag{6}$$

$$\lambda_n^{wv}=n(n+1)(1+\nu+\epsilon\xi_n)\gamma_0, \tag{7}$$

$$\lambda_n^{vv}=n(n+1)(1+\epsilon)\xi_n\gamma_0, \tag{8}$$

in which $\epsilon=(h/a)^2/12$, $\gamma_0=(c_0/c)^2$, and $\xi_n=n(n+1)-1+\nu$. Also, $\mu=(\rho/\rho_0)(a/h)$, and p_n is the modal net pressure acting radially outward on the shell and is given by

$$p_n=\sigma_n-p_n^e, \tag{9}$$

where σ_n is the modal stress acting on the inner surface of the shell outward and p_n^e is the modal pressure exerted by the enveloping fluid on the exterior surface of the shell inward. The pressure and particle velocity of acoustic fluid in an axisymmetric problem can be related by

$$p(r,t)=\dot{\phi}(r,t), \tag{10}$$

$$\dot{u}=-\frac{d\phi}{dr}(r,t), \tag{11}$$

where an overdot denotes differentiation with time. ϕ is the velocity potential of the fluid. If ϕ is expanded in terms of Fourier–Legendre series as

$$\phi=\phi(r,\theta,t)=\sum_{n=0}^{\infty}\phi_n(r,t)P_n(\cos\theta), \tag{12}$$

then the modal ϕ_n should satisfy the following modal wave equation:

$$\frac{d^2\phi_n}{dr^2}+\frac{2}{r}\frac{d\phi_n}{dr}-\frac{n(n+1)}{r^2}\phi_n=\ddot{\phi}_n. \tag{13}$$

Equation (13) has two independent variables t and r. By employing the Laplace transformation on (13), time derivatives are converted to algebraic quantities as follows:

$$r^2\frac{d^2\tilde{\phi}_n}{dr^2}+2r\frac{d\tilde{\phi}_n}{dr}-[n(n+1)+r^2s^2]\tilde{\phi}_n=0, \tag{14}$$

where s is the Laplace parameter. The exact solution of (14) for $\tilde{\phi}_n$ which is convergent at $r\to\infty$ is represented by[10,11]

$$\tilde{\phi}_n=C_n(s)\frac{e^{-sr}}{r^{n+1}}\sum_{k=0}^{n}g_k^n(rs)^{n-k}, \tag{15}$$

and its derivative with respect to r is

$$\frac{d\tilde{\phi}_n}{dr}=-C_n(s)\frac{se^{-sr}}{r^{n+1}}\times\left[\sum_{k=0}^{n}g_k^n(rs)^{n-k}+\sum_{k=0}^{n}(k+1)g_k^n(rs)^{n-k-1}\right], \tag{16}$$

where $C_n(s)$ is constant to be determined from boundary and compatibility conditions. g_n^k is given by[13]

$$g_k^n=\frac{(n+k)!}{2^k k!(n-k)!}. \tag{17}$$

The geometric compatibility at the outer surface requires that the velocity of the fluid particles $\dot{u}$ on the shell surface is

equal to radial velocity $\dot{w}$ of the shell. The Laplace transform of (11) yields the modal Fourier components

$$\left.\frac{d\tilde{\phi}_n}{dr}\right|_{r=1} = -s\tilde{w}_n. \tag{18}$$

Substituting (16) into (18) gives expression for C_n as

$$C_n = \frac{e^s}{\Sigma_{k=0}^n g_k^n s^{n-k} + \Sigma_{k=0}^n (k+1) g_k^n s^{n-k-1}} \tilde{w}_n. \tag{19}$$

Equation (19) is used to eliminate C_n in (15) and (16), and $\tilde{\phi}_n$ and $d\tilde{\phi}_n/dr$ are related to $\tilde{w}_n$. Modal stresses acting at the inner surface of shell are taken herein to be that of a step function, i.e., $\sigma_n(t) = \sigma_n H[t]$, where $H[t]$ is Heaviside function of time. By employing Laplace transformations to shell's equations of motion (4) and (5) and with modal external pressure on the shell $\tilde{p}_n^e = s\tilde{\phi}_n$, we obtain the following equation in matrix form:

$$\begin{bmatrix} A_{11}^n & A_{12}^n \\ A_{21}^n & A_{22}^n \end{bmatrix} \begin{Bmatrix} \tilde{w}_n \\ \tilde{v}_n \end{Bmatrix} = \mu\sigma_n \begin{Bmatrix} 1/s \\ 0 \end{Bmatrix}, \tag{20}$$

where

$$A_{11} = s^2 + \lambda_n^{ww} + \mu s^2 \frac{\Sigma_{k=0}^n g_k^n s^{n-k}}{\Sigma_{k=0}^n g_k^n s^{n-k+1} + \Sigma_{k=0}^n (k+1) g_k^n s^{n-k}}, \tag{21}$$

$$A_{12} = \lambda_n^{wv}, \tag{22}$$

$$A_{21} = \lambda_n^{wv}, \tag{23}$$

$$A_{22} = n(n+1)s^2 + \lambda_n^{vv}. \tag{24}$$

Equation (20) is solved for $\tilde{w}_n$ and $\tilde{v}_n$. When $\tilde{w}_n$ is substituted into (19), and C_n in turn is substituted into (15) and (16), we obtain solutions of $\tilde{\phi}_n$ and $d\tilde{\phi}_n/dr$ as functions of r and s. Hence, modal fluid particle pressure $\tilde{p}_n$ and displacement $\tilde{u}_n$ are obtained from (10) and (11). In the following we present formulations for three categories: breathing mode, translational mode, and lobar modes. Solution is completed by applying elementary Laplace inverses.

A. Breathing mode $n=0$

This mode corresponds to uniform stress $\sigma_0 H[t]$ acting on the internal surface of the shell. The response is spherical symmetrical and the meridional displacement v_0 vanishes. The problem reduces to the solution of one equation of motion in Eq. (4) along with wave equation in (13). Adopting the same solution strategy described above, we obtain the solution for shell displacement as

$$w_0 = \mu\sigma_0 \sum_{k=1}^{3} \frac{s_k + 1}{s_k[3s_k^2 + 2(1+\mu)s_k + \lambda_0^{ww}]} (e^{s_k t} - 1), \tag{25}$$

where s_k are three roots of

$$s_k^3 + (1+\mu)s_k^2 + \lambda_0^{ww} s_k + \lambda_0^{ww} = 0. \tag{26}$$

Fluid pressure at distance r and time t is given by

$$p_0 = -\frac{1}{r} \sum_{k=1}^{3} \left\{ \frac{s_k}{3s_k^2 + 2(1+\mu)s_k + \lambda_0^{ww}} e^{s_k[t-(r-1)]} \right\} \times \mu\sigma_0 H[t-(r-1)], \tag{27}$$

and the corresponding fluid particle displacement is

$$u_0 = \frac{1}{r^2} \sum_{k=1}^{3} \left\{ \frac{1 + rs_k}{s_k[3s_k^2 + 2(1+\mu)s_k + \lambda_0^{ww}]} [e^{s_k[t-(r-1)]} - 1] \right\} \times \mu\sigma_0 H[t-(r-1)]. \tag{28}$$

It is interesting to note that roots s_k are one negative real number and a pair of complex conjugate numbers with negative real part. The negative real parts of roots model contributions to the attenuation of the response with time and the complex parts model the oscillations of the response.

B. Translational mode $n=1$

This mode corresponds to the case that stress $\sigma = \sigma_1 \cos\theta H[t]$ acts on the internal surface of the shell. This mode is characterized by rigid body motion of the shell. The response at a particular point (r, θ) and time t is described by $w = w_1 \cos\theta$, $v = v_1 \cos\theta$, $u = u_1 \cos\theta$ and $p = p_1 \cos\theta$, for shell displacements, fluid particle displacement and pressure, respectively. Following the solution steps described above, the Laplace-transformed radial displacement $\tilde{w}_1$ is given by

$$\tilde{w}_1 = \frac{\Sigma_{i=0}^4 d_i s^{4-i}}{s^3 \Sigma_{i=0}^4 b_i s^{4-i}} \mu\sigma_1. \tag{29}$$

Hence, the shell displacement in time domain is given by

$$w_1 = \left[E_0 + E_1 t + \frac{E_2}{2} t^2 + \sum_{k=1}^{4} \frac{E_3 s_k^3 + E_4 s_k^2 + E_5 s_k + E_6}{4b_0 s_k^3 + 3b_1 s_k^2 + 2b_2 s_k + b_3} e^{s_k t} \right] \mu\sigma_1, \tag{30}$$

in which

$$E_2 = d_4/b_4, \tag{31}$$

$$E_1 = (d_3 - E_2 b_3)/b_4, \tag{32}$$

$$E_0 = (d_2 - E_1 b_3 - E_2 b_2)/b_4, \tag{33}$$

$$E_3 = -E_0 b_0, \tag{34}$$

$$E_4 = -E_0 b_1 - E_1 b_0, \tag{35}$$

$$E_5 = d_0 - E_0 b_2 - E_1 b_1 - E_2 b_0, \tag{36}$$

$$E_6 = d_1 - E_0 b_3 - E_1 b_2 - E_2 b_1, \tag{37}$$

where coefficients b_i and d_i are given by

$$b_0 = 2, \tag{38}$$

$$b_1 = 2(2+\mu), \tag{39}$$

$$b_2 = 2(\lambda_1^{ww} + \mu + 2) + \lambda_1^{vv}, \tag{40}$$

$$b_3 = 4\lambda_1^{ww} + (2+\mu)\lambda_1^{vv}, \tag{41}$$

$$b_4=4\lambda_1^{ww}+(\lambda_1^{ww}+\mu+2)\lambda_1^{vv}-(\lambda_1^{wv})^2 \tag{42}$$

and

$$d_0=2, \tag{43}$$

$$d_1=4, \tag{44}$$

$$d_2=4+\lambda_1^{vv}, \tag{45}$$

$$d_3=2\lambda_1^{vv}, \tag{46}$$

$$d_4=2\lambda_1^{vv}. \tag{47}$$

s_k in (29) are four roots of the polynomial

$$\sum_{i=0}^{4} b_i s_k^{4-i}=0. \tag{48}$$

The modal fluid pressure p_1 at coordinates (r,t) is given by

$$p_1=\frac{1}{r^2}\sum_{k=1}^{6}\left\{\frac{(rs_k+1)\Sigma_{i=0}^{4}d_i s_k^{4-i}}{s_k\Sigma_{i=0}^{5}(6-i)q_i s_k^{5-i}}[e^{s_k[t-(r-1)]}-1]\right\} \times\mu\sigma_1 H[t-(r-1)], \tag{49}$$

and the fluid particle displacement

$$u_1=\frac{1}{r^3}\sum_{k=1}^{6}\left\{\frac{(r^2s_k^2+2rs_k+2)\Sigma_{i=0}^{4}d_i s_k^{4-i}}{s_k^2\Sigma_{i=0}^{5}(6-i)q_i s_k^{5-i}} \times\left[\frac{1}{s_k}e^{s_k[t-(r-1)]}-\frac{1}{s_k}-[t-(r-1)]\right] -\frac{(rs_k+2)\Sigma_{i=0}^{4}d_i s_k^{4-i}}{s_k\Sigma_{i=0}^{5}(6-i)q_i s_k^{5-i}}\frac{1}{2}[t-(r-1)]^2\right\} \times\mu\sigma_1 H[t-(r-1)], \tag{50}$$

where coefficients q_i are defined by

$$q_0=2, \tag{51}$$

$$q_1=6+2\mu, \tag{52}$$

$$q_i=b_i+2b_{i-1}+2b_{i-2} \quad \text{for } i=2,3 \text{ and } 4, \tag{53}$$

$$q_5=16\lambda_1^{ww}+\lambda_1^{vv}(8+2\lambda_1^{ww}+4\mu)-2(\lambda_1^{wv})^2, \tag{54}$$

$$q_6=8\lambda_1^{ww}+2\lambda_1^{vv}(2+\lambda_1^{ww}+\mu)-2(\lambda_1^{wv})^2, \tag{55}$$

where b_i, $i=0-6$ are given in Eqs. (38)–(42) and s_k are the six roots of the polynomial

$$\sum_{k=0}^{6} q_i s_k^{6-i}=0. \tag{56}$$

It is noted from Eq. (30) that while exponent terms contribute to oscillation along with attenuation with time, quadratic and linear terms contribute to unbounded increase of radial shell displacement under the action of step stress. The same analogy applies to fluid particle displacement in Eq. (50).

C. Lobar nontranslational modes $n\geqslant 2$

These modes are characterized by excitation of the shell and fluid without changing the entire location of the shell. Equation (20) gives solution for $\tilde{w}_n$ in the following algebraic form:

$$\tilde{w}_n=\frac{\Sigma_{i=0}^{n+3}d_i s^{n+3-i}}{s\Sigma_{i=0}^{n+5}b_i s^{n+5-i}}\mu\sigma_n. \tag{57}$$

Laplace inverse of (57) gives the solution for shell radial displacement w_n,

$$w_n=\sum_{k=0}^{n+5}\left\{\frac{\Sigma_{i=0}^{n+3}d_i s_k^{n+3-i}}{s_k\Sigma_{i=0}^{n+5}(n+5-i)b_i s_k^{n+4-i}}[e^{s_k t}-1]\right\}\mu\sigma_n, \tag{58}$$

where s_k are $n+5$ roots of the polynomial

$$\sum_{i=0}^{n+5} b_i s_k^{n+5-i}=0. \tag{59}$$

Coefficients d_i in the numerator of (58) are given by

$$d_i=n(n+1)c_i \quad \text{for } i=0 \quad \text{and } 1, \tag{60}$$

$$d_i=n(n+1)c_i+\lambda_n^{vv}c_{i-2} \quad \text{for } i=2 \text{ to } n+1, \tag{61}$$

$$d_i=\lambda_n^{vv}c_{i-2} \quad \text{for } i=n+2 \quad \text{and } n+3, \tag{62}$$

in which coefficients c_i are given by

$$c_0=g_0^n, \tag{63}$$

$$c_i=g_i^n+ig_{i-1}^n \quad \text{for } i=1 \text{ to } n, \tag{64}$$

$$c_{n+1}=(n+1)g_n^n. \tag{65}$$

Coefficients b_i in the denominator of (57) are given by

$$b_i=n(n+1)a_i \quad \text{for } i=0 \quad \text{for } 1, \tag{66}$$

$$b_i=n(n+1)a_i+\lambda_n^{vv}a_{i-2} \quad \text{for } i=2 \text{ and } 3, \tag{67}$$

$$b_i=n(n+1)a_i+\lambda_n^{vv}a_{i-2}-(\lambda_n^{wv})^2c_{i-4} \quad \text{for } i=4 \text{ to } n+3, \tag{68}$$

$$b_i=\lambda_n^{vv}a_{i-2}-(\lambda_n^{wv})^2c_{i-4} \quad \text{for } i=n+4 \text{ to } n+5, \tag{69}$$

in which coefficients a_i are given by

$$a_0=c_0, \tag{70}$$

$$a_1=c_1+\mu g_0^n, \tag{71}$$

$$a_i=c_i+\lambda_n^{ww}c_{i-2}+\mu g_{i-1}^n \quad \text{for } i=2 \text{ to } n+1, \tag{72}$$

$$a_i=\lambda_n^{ww}c_{i-2} \quad \text{for } i=n+2 \text{ to } n+3. \tag{73}$$

Also, the Laplace-transformed velocity potential at radial distance r is given by

$$\tilde{\phi}_n(r,s)=\frac{e^{-s(r-1)}}{r^{n+1}}\frac{\Sigma_{i=0}^{n}g_i^n r^{n-i}s^{n-i}\Sigma_{i=0}^{n+3}d_i s^{n+3-i}}{\Sigma_{i=0}^{2n+6}q_i s^{2n+6-i}}\mu\sigma_n, \tag{74}$$

where coefficients q_i are given by the following relationships:

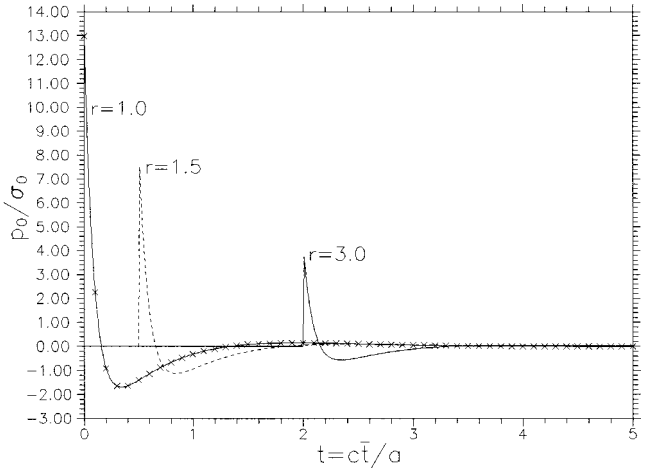

FIG. 2. Modal pressure for breathing mode $n=0$.

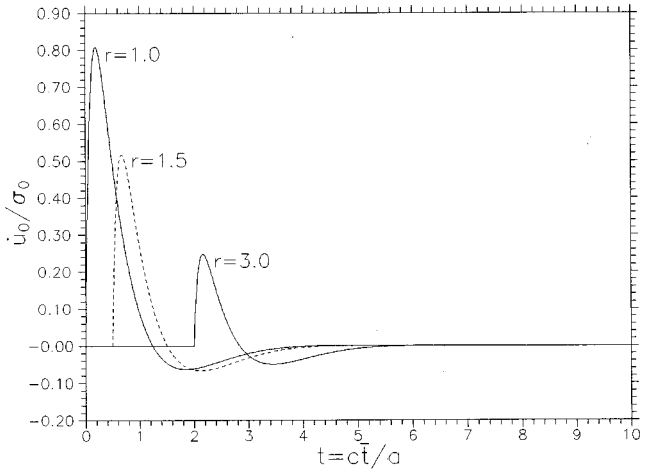

FIG. 3. Modal velocity for breathing mode $n=0$.

$$q_i=\sum_{j=0}^{i} c_j b_{i-j} \quad \text{for } i=0 \text{ to } n, \tag{75}$$

$$q_i=\sum_{j=0}^{n+1} c_k b_{i-j} \quad \text{for } i=n+1 \text{ to } n+5, \tag{76}$$

$$q_i=\sum_{j=i-n-5}^{n+1} c_j b_{i-j} \quad \text{for } i=n+6 \text{ to } 2n+6, \tag{77}$$

in which coefficients c_i and b_i are defined in Eqs. (63)–(65) and (66)–(69). The Laplace inverse of (74) gives the solution of ϕ_n in time domain, hence

$$\phi_n(r,t)=\frac{\mu\sigma_n}{r^{n+1}}\sum_{k=1}^{2n+6}\left\{\frac{\Sigma_{i=0}^{n} g_i^n r^{n-i} s_k^{n-i}\Sigma_{i=0}^{n+3} d_i s_k^{n+3-i}}{\Sigma_{i=0}^{2n+5}(2n+6-i)q_i s_k^{2n+5-i}} \times e^{s_k[t-(r-1)]}\right\} H[t-(r-1)], \tag{78}$$

where s_k are roots of polynomial

$$\sum_{i=0}^{2n+6} q_i s_k^{2n+6-i}=0. \tag{79}$$

The polynomial in (79) is the multiplication of polynomials in (59) and the following polynomial

$$\sum_{i=0}^{n+1} c_i s_k^{n+1-i}=0. \tag{80}$$

Hence, the roots of (79) can be taken as roots of polynomials in Eqs. (59) and (80). This reduces computational effort significantly. Given the velocity potential defined in (78) and the relationships in (10) and (11), we obtain solution for modal pressure, fluid particle velocity and displacement. So at distance r and time t, the modal fluid pressure is given by

$$p_n(r,t)=\frac{\mu\sigma_n}{r^{n+1}}\sum_{k=1}^{2n+6}\left\{ s_k\frac{\Sigma_{i=0}^{n} g_i^n r^{n-i} s_k^{n-i}\Sigma_{i=0}^{n+3} d_i s_k^{n+3-i}}{\Sigma_{i=0}^{2n+5}(2n+6-i)q_i s_k^{2n+5-i}} \times e^{s_k[t-(r-1)]}\right\} H[t-(r-1)], \tag{81}$$

and the modal fluid particle velocity $\dot{u}_n$ is given by

$$\dot{u}_n=\frac{\mu\sigma_n}{r^{n+2}}\sum_{k=1}^{2n+6}\left\{\frac{\Sigma_{i=0}^{n+3} d_i s_k^{n+3-i}}{\Sigma_{i=0}^{2n+5}(2n+6-i)q_i s_k^{2n+5-i}} \times\left[[n+1+rs_k]\sum_{i=0}^{n} g_i^n r^{n-i} s_k^{n-i} - \sum_{i=0}^{n-1}(n-i)g_i^n r^{n-i} s_k^{n-i}\right] e^{s_k[t-(r-1)]}\right\} \times H[t-(r-1)]. \tag{82}$$

By integrating the velocity with time and with the fact that initial displacement is zero, one obtains the displacement at distance r as

$$u_n=\frac{\mu\sigma_n}{r^{n+2}}\sum_{k=1}^{2n+6}\left\{\frac{\Sigma_{i=0}^{n+3} d_i s_k^{n+3-i}}{\Sigma_{i=0}^{2n+5}(2n+6-i)q_i s_k^{2n+6-i}} \times\left[[n+1+rs_k]\sum_{i=0}^{n} g_i^n r^{n-i} s_k^{n-i} - \sum_{i=0}^{n-1}(n-i)g_i^n r^{n-i} s_k^{n-i}\right][e^{s_k[t-(r-1)]}-e^{-(r-1)}]\right\} \times H[t-(r-1)]. \tag{83}$$

Coefficients d_i and q_i in the above equations are defined in (60)–(62) and (75)–(77).

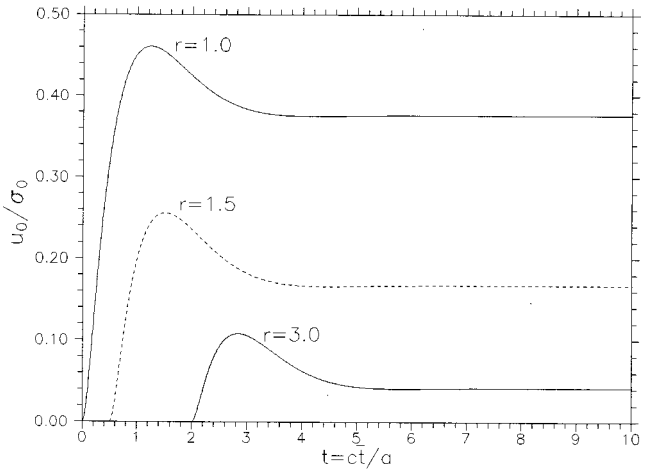

FIG. 4. Modal displacement for breathing mode $n=0$.

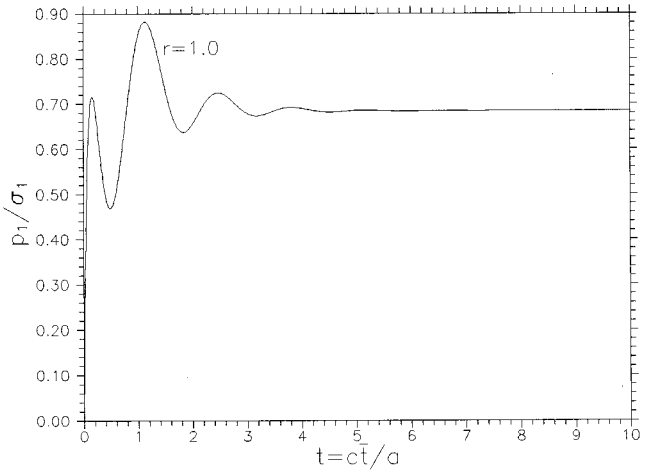

FIG. 5. Modal pressure for translational mode $n=1$.

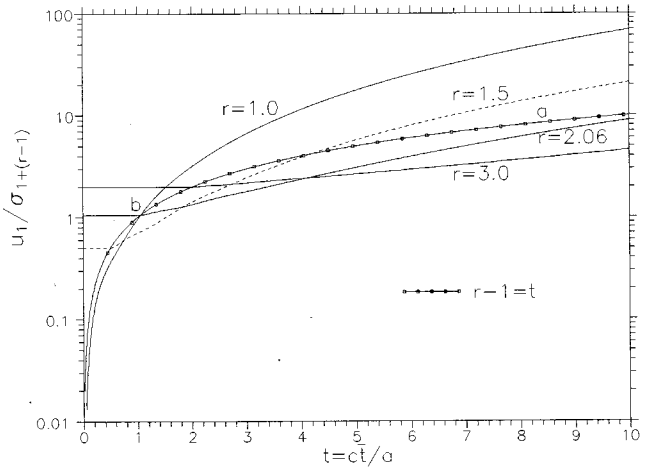

FIG. 6. Displacement of the shell and theoretical positions of fluid particles for translational mode $n=1$.

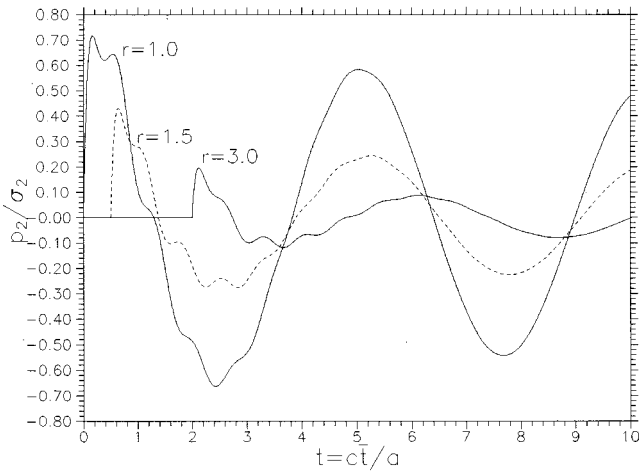

FIG. 7. Modal pressure for mode $n=2$.

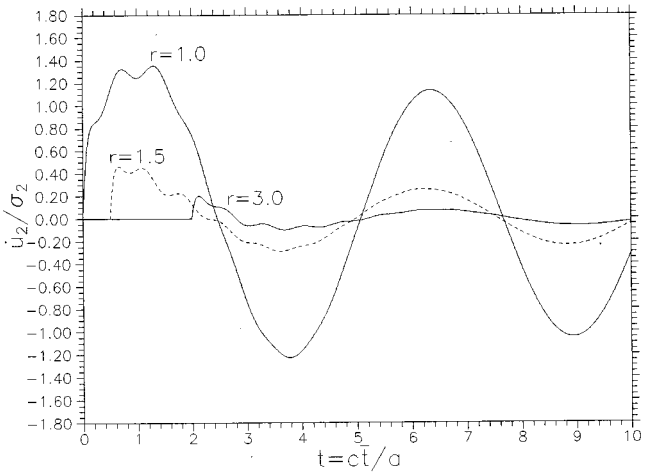

FIG. 8. Modal velocity for mode $n=2$.

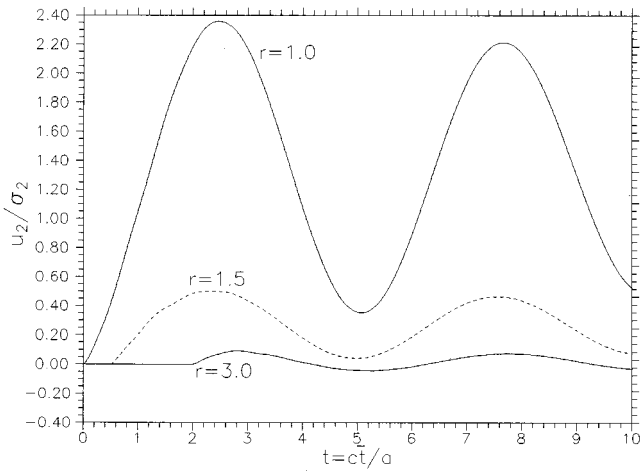

FIG. 9. Modal displacement for mode $n=2$.

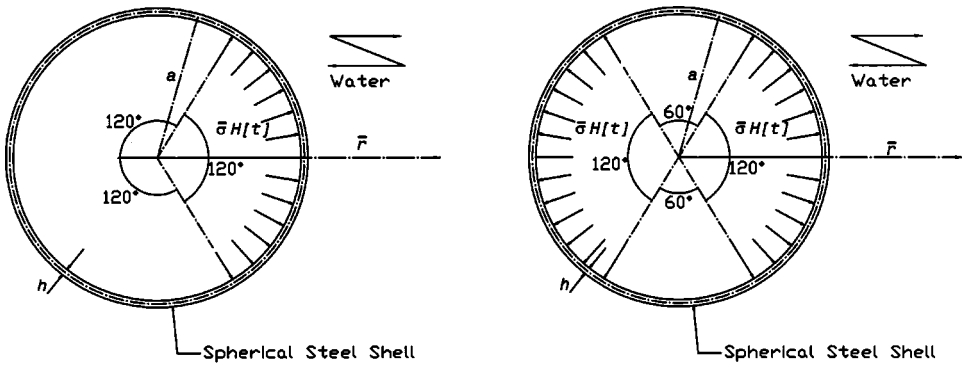

(a) Load Case (I) (b) Load Case (II)

FIG. 10. Description of two axisymmetric load cases.

It appears from Eqs. (81), (82), and (83) that exponent multipliers attributes to oscillation along with attenuation with time. This is because roots s_k are complex conjugate pairs with negative real parts.

III. NUMERICAL RESULTS

Computed transient response histories are presented for a steel spherical shell submerged in water and excited by radial axisymmetric modal step stresses on the internal surface of the shell as shown in Fig. 1. The thickness-to-radius ratio is $h/a=0.01$, the mass density ratio is $\rho_0/\rho=7.7$, sound-velocity ratio is $c_0/c=(13.8)^{(1/2)}$ and Poisson's ratio $\nu=0.25$. Figure 2 presents modal pressure for breathing mode. The pressure is characterized by a sudden jump at the instant of wave arrival followed by a rapid drop with negative excursion before the attenuation decreases to zero. Fluid particle velocity as shown in Fig. 3 increases rapidly to peak and then drops rapidly to negative excursion before it vanishes. As seen in Fig. 4 corresponding fluid particle displacement at the given point gradually increases from zero to the peak before damping to a hydrostatic asymptotic value. Figure 5 shows pressure at external shell surface for the translational mode. The time dependence shows vibration that reaches a peak value followed by lower amplitude vibration that approaches a hydrostatic value. Figure 6 shows the fluid particle motion on the shell surface as function of time at different spatial points in the fluid. Curve a:$t=r-1$ shows times at which waves presumably arrive at different points. It intersects the shell displacement curve ($r=1$) at point b:$r-1=t=1.06$. This means that points at $r<2.06$ are excited before the shell arrives whereas points $r>2.06$ are passed by the shell before fluid is first excited. For example, at $r=1.5$ the fluid is excited at $t=0.5$ up to $t\simeq 0.8$ when the shell arrives. On the other hand, at $r=3.0$ the shell passed by this point before the fluid was excited. Figures 7–9 present modal pressure, velocity and displacement histories for mode 2 at surface of the shell $r=1$, $r=1.5$, and $r=3.0$. It is noted that pressure and velocity histories at a given point increase rapidly at the time of wave arrival to the peak value with lower velocity. The response is then followed by oscillation around a stationary asymptotic value for late time. Each curve shows a smooth oscillation after one period. The displacement increases gradually to the peak value followed by slowly damped oscillation around an asymptotic hydrostatic value. The response histories for higher modes have similar shapes to Figs. 7–9 with increase of oscillation and slight decrease of amplitudes.

Now, we use the mode summation method to solve for the axisymmetric problems in Figs. 10(a) and (b). The modified Cesaro summation (CS) is used to give noticeable better convergence than the classical partial summation.[12] In Fig. 10(a), the spherical shell is subjected to radial stress $\sigma H[t]$ at $-\pi/3\leqslant\theta\leqslant\pi/3$. Figure 11 shows pressure at $\theta=0$ at the surface of the shell. The pressure jumps to peak followed by oscillation. As seen in Fig. 12, radial displacement of the shell at $\theta=0$ increases quadratically with time along with small reflections around the response history. This proves that translational mode $n=1$ governs the response and attributes to the quadratic increase of displacement. Reflections along the history are attributed by higher, lobar modes. The second load case is shown in Fig. 10(b) where stress $\sigma H[t]$ acts on $-\pi/3\leqslant\theta\leqslant\pi/3$ and $2\pi/3\leqslant\theta\leqslant-2\pi/3$. Due to the balance of stresses, the spherical shell will not translate with time. As seen in Fig. 13, the fluid particle pressure at a given point and $\theta=0$ jumps at the time of wave arrival to the peak and then drops rapidly, followed by a small negative excursion before oscillating around a stationary, zero-pressure late time asymptote. Finally, Fig. 14 shows that

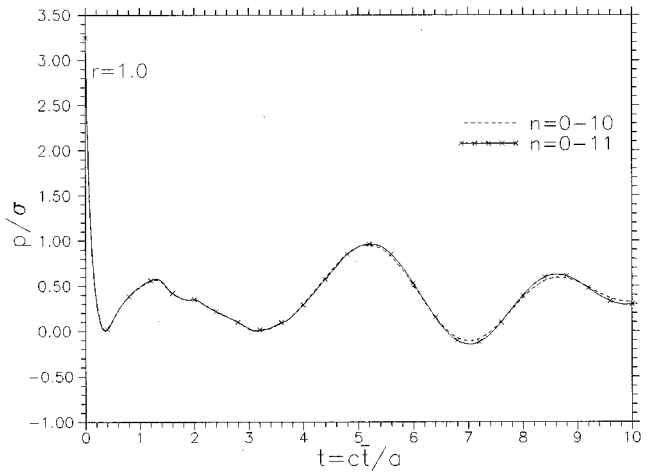

FIG. 11. Pressure at the external shell surface at $\theta=0$ for the first load case.

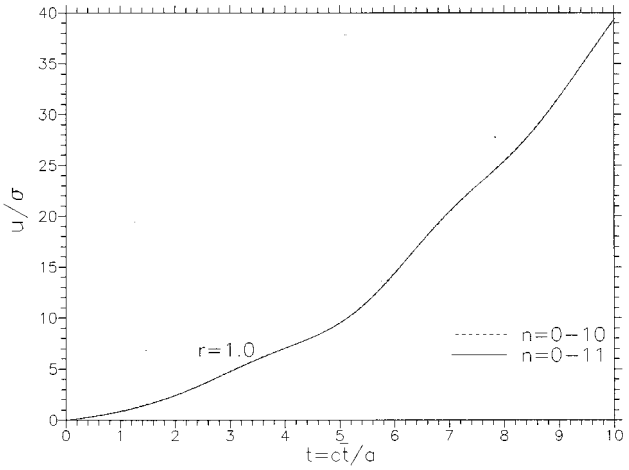

FIG. 12. Radial displacement of the shell at $\theta=0$ for the first load case.

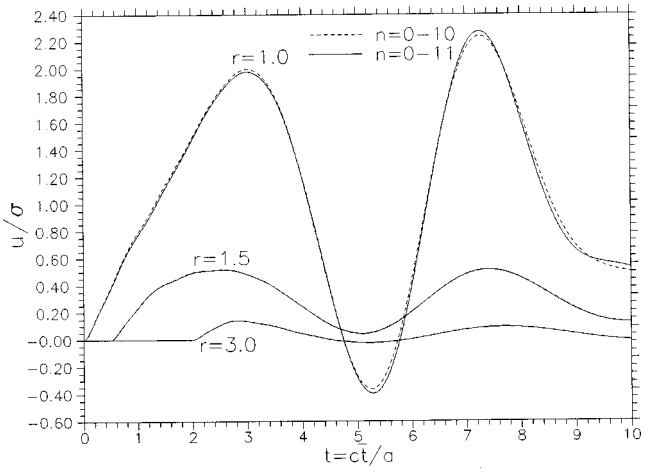

FIG. 14. Radial displacement at $\theta=0$ for the second load case.

fluid particle displacement increases gradually to the first peak and then oscillates about hydrostatic value.

IV. CONCLUSION

In this paper we presented an exact closed-form solution for modal response of acoustic fluid in terms of pressure, fluid particle velocity, and displacement caused by submerged spherical shell which is excited by internal modal stresses. By using the mode method with modified Cessaro summation, we obtain solution for axisymmetric problems. The exact systematic expressions are functions of radial distance, time, physical and mechanical properties of the shell and the fluid. The expressions are useful for obtaining solutions for the fluid as well as the shell. The numerical evaluations of these expressions are efficient compared with additional numerical computations or approximations used by other methods.

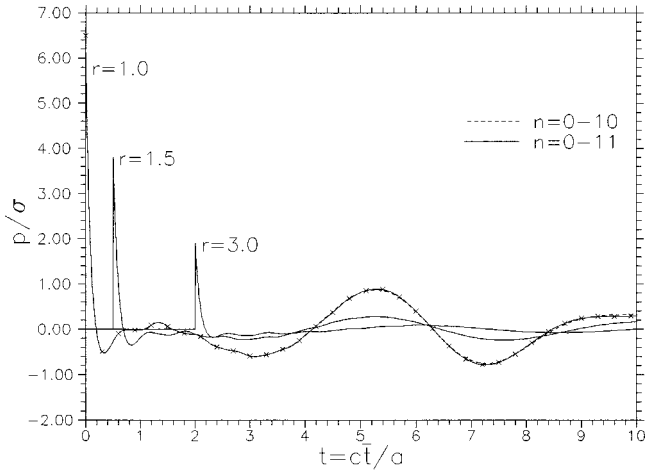

FIG. 13. Pressure at $\theta=0$ for the second load case.

The solutions presented in this paper can also be used to solve the problem in which a plane or spherical wave impinges a submerged spherical shell. In this case, the enveloping fluid response is obtained by superposition of modal responses to the incident and scattered waves. Modal responses to the scattered waves are obtained as described in this paper by influencing the modal components of the incident wave to the exterior surface of the sphere.

[1] H. Huang, ''Transient interaction of plane acoustic waves with a spherical elastic shell,'' J. Acoust. Soc. Am. **45**, 661–670 (1969).
[2] H. Huang, Y. P. Lu, and Y. F. Wang, ''Transient interaction of spherical acoustic waves and a spherical elastic shell,'' J. Appl. Mech. **38**, 71–74 (1971).
[3] Y. K. Lou and J. M. Klosner, ''Transient response of a point-excited submerged spherical shell,'' J. Appl. Mech. **40**, 1078–1084 (1973).
[4] T. L. Geers, ''Doubly asymptotic approximations for transient motions of submerged structures,'' J. Acoust. Soc. Am. **64**, 1500–1508 (1978).
[5] N. Akkas, ''Residual potential method in spherical coordinates and related approximations,'' Mech. Res. Commun. **6**, 257–262 (1979).
[6] N. Akkas and A. E. Engin, ''Transient response of a spherical shell in an acoustic medium-comparison of exact and approximate solutions,'' J. Sound Vib. **73**, 447–460 (1980).
[7] N. Akkas and F. Erdogan, ''The residual variable method applied to acoustic wave propagation from a spherical surface,'' J. Vibr. Acoust. **115**, 75–80 (1993).
[8] G. E. Tupholme, ''Generation of an axisymmetrical acoustic pulse by a deformable sphere,'' Proc. Cambridge Philos. Soc. **63**, 1285–1308 (1967).
[9] M. Junger and D. Feit, *Sound, Structures and Their Interactions* (MIT Press, Cambridge, MA, 1972).
[10] N. Akkas and U. Zakout, ''Transient response of an infinite elastic medium containing a spherical cavity with and without a shell embedment,'' Int. J. Eng. Sci. **35**, 89–112 (1997).
[11] U. Zakout, N. Akkas, and G. E. Tupholme, ''Transient response of an infinite elastic medium containing a spherical cavity subjected to torsion,'' J. Appl. Mech. **67**, 282–287 (2000).
[12] P. Zhang and T. L. Geers, ''Excitation of a fluid-filled, submerged spherical shell by a transient acoustic wave,'' J. Acoust. Soc. Am. **93**, 696–705 (1993).
[13] *Handbook of Mathematical Functions*, edited by M. Abramowitz and I. A. Stegun (Dover, New York, 1965).

The surface variational principle applied to an acoustic cavity

F. Franco[a)]
Dipartimento di Progettazione Aeronautica, Università di Napoli ''FEDERICO II,'' Via Claudio 21-80125 Napoli, Italy

K. A. Cunefare[b)]
The George W. Woodruff School of Mechanical Engineering, Georgia Institute of Technology, Atlanta, Georgia 30332-0405

(Received 30 August 1999; accepted for publication 9 March 2001)

This paper presents the development and application of the Surface Variational Principle (SVP) for the evaluation of axisymmetric interior acoustic domains. The interior form of the SVP is first developed in the same manner as the existing exterior form. Then, the surface pressure and normal velocity are represented with a Ritz expansion using basis functions that span the entire wetted surface of the object of interest. The resultant formulation is used to analyze the interior acoustic response of a harmonically forced, right circular elastic cylinder. This validation model was chosen as both the structural and acoustic responses can be solved analytically. Results are presented for two models: one with a length to radius ratio of 2.4, and another with a ratio of 12.3. The SVP is shown to well reproduce the analytical solution for this geometry, and displays the asymptotic convergence expected of its variational formulation. The SVP formulation developed here is not restricted to right-circular cylindrical geometries, and may, indeed, be readily applied to any axisymmetric body. © *2001 Acoustical Society of America.* [DOI: 10.1121/1.1369107]

PACS numbers: 43.40.Rj [CBB]

I. INTRODUCTION

The prediction of sound radiation from vibrating bodies is a recurrent problem of practical importance in engineering science. Analytical solutions for such problems are generally limited to analytical separable geometries. For objects with nonstandard shapes, a common approach consists of reformulating the problem as a boundary integral relation, using the Kirchhoff–Helmholtz integral theorem,[1] which enables one to express the acoustic field on and off the surface of the object as a definite integral over the surface of the object.

Systems that are not amenable to an analytical solution are usually modeled by discretization techniques in the form of boundary element methods (BEM) and/or finite element methods (FEM). The boundary element method is based on a boundary integral equation (BIE), such as the Kirchhoff–Helmholtz integral theorem. The integrand involves both the pressure and normal velocity on the surface. These two quantities are not independent: if the surface velocity is known, then the surface pressure can be determined. Applying the Kirchhoff–Helmholtz equation, it is possible to relate the surface pressure to the normal component of the surface velocity.

The finite element method has been used widely in structural dynamics problems for both the *in-vacuo* and fluid-loaded cases. The system matrices in FEM are banded (local connectivity), rather than full, and therefore it reduces the computer processing time and storage requirements as compared to BEM methods of the same degrees of freedom, especially for higher wave number ranges and slender bodies. The computation of full BEM system matrices is inherently more computationally expensive than an equivalently discretized FEM analysis, particularly so when using variational-based BEM methods as a consequence of the need to numerically evaluate double surface integrals.

The typical FEM or BEM implementation uses interpolating functions over patches of the surface to model the surface response, while the SVP formulation uses analytical representations of both the surface geometry and the response. An important corollary of the SVP approach is that it represents an independent formulation and method that may be used to validate other numerical methods (e.g., FEM and BEM models). Furthermore, the availability of an impedance matrix, describing the structural fluid interaction, allows for the ready analysis of radiated power sensitivity[2,3] for different structural models.

The surface variational principle (SVP) was introduced by Wu.[4] Over the ensuing years, a number of applications have been developed by using this approach for exterior acoustic fields, including both acoustic radiation and scattering.[5–15] The SVP has been developed as an alternative method to the FEM or BEM for modeling nonseparable geometries in the frequency domain. The implementations of the SVP to date have employed Ritz series expansions in which series of basis functions spanning the entire wetted surface represent surface pressure and velocity, in the manner of an analytical-type solution. Therefore, it is a different point of view from discretized methods. Even if the SVP does not represent an efficient approach in terms of computational efficiency and required memory, it has significant merit, in that (1) it provides a modeling technique that enables one to gain a physical understanding of fluid–structure interaction problems; (2) it provides an analytical-type solution whose convergence and error properties are predictable

[a)]Electronic mail: francof@unina.it
[b)]Electronic mail: ken.cunefare@me.gatech.edu

from its variational formulation; (3) the interior and exterior acoustic field can be modeled with the same basis functions (the scattered pressure problem, too). In fact, this latter consideration is the motivation for the work at hand. Prior work has demonstrated what is called the wavenumber-based SVP, where the basis functions incorporate structural wave numbers in their arguments,[8,16–18] and use the same set of basis functions for both the elastic structural response and the exterior acoustic response. If the wave number-based SVP can be extended to the interior problem, then it will be possible to formulate a fully coupled exterior–structural–interior axisymmetric implementation of the SVP employing a common set of basis functions to describe the exterior acoustics, the structural response, and the interior acoustics. Such an approach may provide an enhanced understanding of the mechanisms for structural acoustic coupling between exterior and interior sound fields. The work at hand is a step toward this goal: it focuses in the development and validation of the SVP for interior acoustic spaces, and its application to the analysis of the coupled interior acoustic response of an elastic cylinder. The fundamental novelty of the work at hand is the development of the interior form of the SVP, and the demonstration that there do not appear to be any fundamental roadblocks to its application. We wish to emphasize that our purpose here is to extend the SVP to address the coupled interior problem, not to take on the fully coupled exterior–structure–interior problem; such is the realm of future work.

In the following sections, we briefly present the development of the SVP for interior acoustic domains. We then detail the development of the wave number implementation of the SVP, and its integration into the analysis of the coupled structural acoustic modeling of elastic bodies. For validation purposes, we consider the acoustic response of an elastic right-circular cylinder. This geometry was selected as there are analytical solutions for both the elastic cylinder response as well as the acoustic response. Further, such a geometry is of interest in the engineering application (e.g., aircraft). We then compare the analytical solution for the chosen validation model to the results of numerical simulations obtained using the interior SVP. The convergence behavior of the SVP will also be briefly discussed.

II. INTERIOR FORM OF THE SURFACE VARIATIONAL PRINCIPLE

A derivation of the surface variational principle for interior acoustic domains is straightforward. As the interior domain derivation is not significantly different than the companion derivation for the exterior domain, we will omit the detailed development and state the end result. We will elucidate the essential difference between the interior and exterior formulations. The full measure of the derivation may be found in the literature.[4,5,8]

In brief, the surface variational principle states that the functional $J[p]$ is stationary to variation of the true surface pressure distribution $p(\xi)$ for the prescribed surface normal velocity distribution $V_n(\xi)$. The functional, $J[p]$ is expressed by a double integration over all pairs of points $\boldsymbol{\xi}$ and

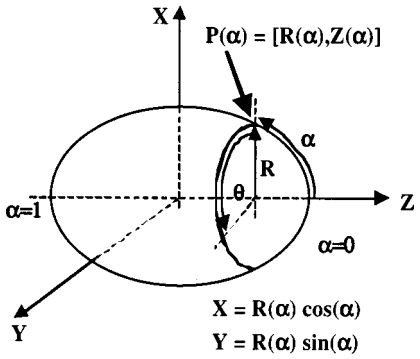

FIG. 1. Coordinate system for a body of revolution.

$\boldsymbol{\zeta}$ on the surface. For a fluid volume completely enclosed by a curved surface, the functional $J[p]$ is

$$
\begin{aligned}
J[p] = \frac{k^2}{2}\int\int \{\mathbf{n}(\xi)\cdot\mathbf{n}(\zeta)p(\xi)p(\zeta)G(\xi/\zeta)\}dS_\zeta\, dS_\xi \\
-\frac{1}{2}\int\int \{[\mathbf{n}(\xi)\cdot\boldsymbol{\nabla}_\xi p(\xi)] \\
\times[\mathbf{n}(\zeta)\cdot\boldsymbol{\nabla}_\zeta p(\zeta)]G(\xi/\zeta)\}dS_\zeta\, dS_\xi \\
-i\omega\rho\int\int p(\xi)V_n(\xi)[\mathbf{n}(\xi)\cdot\boldsymbol{\nabla}_\xi G(\xi/\zeta)]dS_\zeta\, dS_\xi \\
+2\pi i\omega\rho\int p(\xi)V_n(\xi)dS_\xi .
\end{aligned}
\tag{1}
$$

The sole difference between Eq. (1) for an interior domain and the companion expression for the exterior domain as derived by Wu and Ginsberg[8] is the sign of the last term. For the exterior version of the SVP, the sign of the last term is negative: all other terms are identical, and with identical interpretations. The sign difference arises when one brings a field point to the surface from the interior, rather than from the exterior.

The shape of the generating curve of an axisymmetric body may be described by the cylindrical coordinates $R(\alpha)$, $Z(\alpha)$ for points on the generating curve, as depicted in Fig. 1. The parameter α is a nondimensional coordinate on the generating curve for which $\alpha=0$ and $\alpha=1$ correspond to the ends of the shape generator. In this manner the positions of the surface points $\boldsymbol{\xi}$, $\boldsymbol{\zeta}$ are identified by $(\alpha,\ \theta)$ and $(\beta,\ \eta)$.

In the manner of a Ritz expansion, complex Fourier series are adopted to represent the azimuthal dependence of the surface pressure and normal velocity. Using nondimensional coefficients, these expansions are

$$
\begin{aligned}
P(\alpha,\theta) &= \frac{1}{2}\rho c^2 \sum_{m=-\infty}^{\infty} p^m(\alpha)\exp(im\theta), \\
V(\alpha,\theta) &= c\sum_{m=-\infty}^{\infty} V^m(\alpha)\exp(im\theta).
\end{aligned}
\tag{2}
$$

Time dependency of $e^{j\omega t}$ is assumed throughout this paper. The meridional dependency within Eq. (2) is represented by a Ritz series for each azimuthal harmonic of pressure and normal velocity as

$$P^m(\alpha)=\sum_{k=1}^{\infty} P_k^m \Psi_k^m(\alpha),$$
$$V^m(\alpha)=\sum_{k=1}^{\infty} V_k^m \Psi_k^m(\alpha), \tag{3}$$

where

$$\Psi_k^0=\cos[(k-1)\pi\alpha], \quad \text{for } m=0,$$
$$\Psi_k^m=\sin(k\pi\alpha), \quad \text{for } m\neq 0. \tag{4}$$

The basis function representation defined by Eqs. (3) and (4) has proven to be effective for analysis of exterior acoustic problems for axisymmetric bodies.[8,14] Further, this representation rather naturally may be interpreted as describing the response in terms of a discrete wave number spectrum,[14] hence, the wavenumber SVP. Finally, since the above basis functions are complete and satisfy the natural boundary conditions, we may expect this implementation of the SVP to be convergent,[19] and as has already been demonstrated for the exterior problem.[4,5,8]

Introducing the radius a as the reference length, the variational functional can be rewritten in terms of the azimuthal and meridian coordinates as

$$J[p]=\rho^2 c^4 a \sum_{m=-\infty}^{\infty} J^m, \tag{5}$$

where

$$J^m=\frac{\pi}{4}\int_0^1\int_0^1\{(k^2a^2R(\alpha)R'(\alpha)R(\beta)R'(\beta)-m^2Z'(\alpha)Z'(\beta))P^m(\alpha)P^{-m}(\beta)C^m(\alpha,\beta)+[k^2a^2R(\alpha)R(\beta)Z'(\alpha)Z'(\beta)$$
$$-m^2R'(\alpha)R'(\beta)P^m(\alpha)P^{-m}(\beta)-R(\alpha)R(\beta)P^m(\alpha)P'^{(-m)}(\beta)]D^m(\alpha,\beta)-m[R'(\alpha)R(\beta)P^m(\alpha)P^{-(-m)}(\beta)$$
$$+R(\alpha)R'(\beta)P^m(\alpha)P^{-m}(\beta)]E^m(\alpha,\beta)\}d\beta\,d\alpha-\frac{i\pi}{2}ka\int_0^1\int_0^1 P^{-m}(\alpha)V^m(\beta)F^m(\alpha,\beta)d\beta\,d\alpha$$
$$+i\pi^2 ka\int_0^1 R(\alpha)s'(\alpha)P^{-m}(\alpha)V^m(\alpha)d\alpha, \tag{6}$$

and where $s'(\alpha)=\sqrt{R'(\alpha)^2+Z'(\alpha)^2}$. In Eq. (6), the functions $C^m(\alpha,\beta)$, $D^m(\alpha,\beta)$, $E^m(\alpha,\beta)$, and $F^m(\alpha,\beta)$ are weighted integrals of the Green's function over all relative azimuthal positions:

$$C^m(\alpha,\beta)=\int_{-\pi}^{\pi}\frac{1}{r}\exp(ikar)\exp(im\chi)d\chi,$$
$$D^m(\alpha,\beta)=\int_{-\pi}^{\pi}\frac{1}{r}\exp(ikar)\exp(im\chi)\cos(\chi)d\chi$$
$$E^m(\alpha,\beta)=\int_{-\pi}^{\pi}\frac{1}{r}\exp(ikar)\exp(im\chi)\sin(\chi)d\chi, \tag{7}$$
$$F^m(\alpha,\beta)=R(\alpha)R(\beta)s'(\alpha)s'(\beta)\int_{-\pi}^{\pi}\left(\frac{\mathbf{n}(\xi)\cdot(\xi-\zeta)}{r^2}\right)$$
$$\times\left(\frac{ikar-1}{r}\right)\exp(ikar)\exp(im\chi)d\chi,$$

where χ is the azimuthal angle between two surface points, $\chi=\theta-\eta$.

Taking the variation of $J[p]$, and with the velocity coefficient fixed, then

$$\delta J=\sum_{m=-\infty}^{\infty}\sum_{k=1}^{\infty}\frac{\partial J}{\partial P_k^{-m}}\delta P_k^{-m}=0. \tag{8}$$

The derivatives in Eq. (8) for all k indices, at fixed m, lead to a system of linear algebraic equations for each azimuthal harmonic mode m,

$$[A^m]\{P^m\}=ika[B^m]^T\{V^m\}, \tag{9}$$

that can be expressed as

$$\{P^m\}=[Z\_\mathrm{SVP}^m]\{V^m\}. \tag{10}$$

where $[Z\_\mathrm{SVP}^m]$ identifies the SVP impedance matrix. The A and B matrices in Eq. (9) result from the double integration of Eq. (6) over the surface.

The numerical implementation of the above development will not be discussed here, as it is essentially no different than that which has already been documented for the equivalent exterior axisymmetric problem.[9,15] We do note that the evaluation of the integrals in Eqs. (6) and (7) make the SVP quite computationally expensive as compared to FEM or BEM methods.

III. ANALYTICAL SOLUTIONS

In order to assess the performance of the SVP, we will compare its results to the known analytical solution for the interior acoustic pressure response of a forced simply supported (or shear-diaphragm) right-circular cylinder. We could merely specify a boundary condition on the boundary of a right-circular cylindrical acoustic volume and analyze the response both analytically and with the SVP. However, as this work was developed to support fully coupled

exterior–structure–interior analyses, we consider the integration of the structural response into this validation analysis as appropriate.

As noted above, the analytical solution adopted as a reference in this work is that for a right-circular cylinder. The structural response of the cylinder is modeled using Donnel–Mushtari thin shell theory.[20] A set of assumed vibrational basis functions are used that satisfy simply supported boundary conditions for the ends of the cylinder. Therefore, the surface displacements are given by

$$
\begin{aligned}
u(x,\theta) &= \sum_{n=0}^{\infty}\sum_{m=0}^{\infty} U^c_{n,m}\cos\left(\frac{n\pi x}{L}\right)\cos(m\theta) \\
&\quad + \sum_{n=0}^{\infty}\sum_{m=1}^{\infty} U^s_{n,m}\cos\left(\frac{n\pi x}{L}\right)\sin(m\theta), \\
\nu(x,\theta) &= \sum_{n=0}^{\infty}\sum_{m=1}^{\infty} V^s_{n,m}\cos\left(\frac{n\pi x}{L}\right)\sin(m\theta) \\
&\quad - \sum_{n=0}^{\infty}\sum_{m=0}^{\infty} V^s_{n,m}\cos\left(\frac{n\pi x}{L}\right)\cos(m\theta), \\
w(x,\theta) &= \sum_{n=1}^{\infty}\sum_{m=0}^{\infty} W^c_{n,m}\sin\left(\frac{n\pi x}{L}\right)\cos(m\theta) \\
&\quad + \sum_{n=1}^{\infty}\sum_{m=1}^{\infty} W^s_{n,m}\sin\left(\frac{n\pi x}{L}\right)\sin(m\theta),
\end{aligned}
\tag{11}
$$

where u, ν, w are the axial, circumferential, and radial displacement while x,θ,r are the axial, azimuthal, and radial coordinates, as depicted in Fig. 2, and L is the cylinder length. Each mode amplitude can be determined by solving a linear algebraic system,[20]

$$
\begin{bmatrix} A_{11}+\Omega^2 & A_{12} & A_{13} \\ A_{21} & A_{22}+\Omega^2 & A_{23} \\ A_{31} & A_{32} & A_{33}+\Omega^2 \end{bmatrix} \cdot \begin{Bmatrix} U^i_{n,m} \\ V^i_{n,m} \\ W^i_{n,m} \end{Bmatrix} = \begin{Bmatrix} 0 \\ 0 \\ F^i_{n,m} \end{Bmatrix},
\tag{12}
$$

considering only radial excitations, where A_{ij} are the elements of the generalized stiffness matrix related to the n,mth structural mode and

$$
\Omega^2 = \frac{\rho_s a^2(1-\nu^2)\omega^2}{E},
\tag{13}
$$

with E Young's modulus, ρ_s material density, υ Poisson ratio, and ω the excitation frequency. In particular, the displacement components involved in the structural–acoustic interaction are

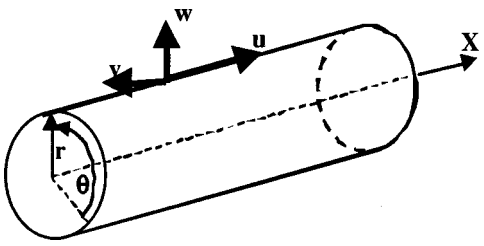

FIG. 2. Cylindrical shell and coordinate system.

$$
\begin{aligned}
W^i_{n,m} &= \frac{A_{11}\cdot A_{22} - A_{12}\cdot A_{21}}{\mathrm{DET}} F^i_{n,m}, \\
U^i_{n,m} &= \frac{A_{12}\cdot A_{23} - A_{22}\cdot A_{13}}{\mathrm{DET}} F^i_{n,m},
\end{aligned}
\tag{14}
$$

where

$$
\begin{aligned}
F^i_{n,m} &= \frac{\varepsilon_m a(1-\nu^2)}{L\pi E h}\int_0^{2\pi}\int_0^{L} f(x,\theta)\sin\left(\frac{n\pi x}{L}\right) \\
&\quad \times\cos\left(m\theta - \frac{i\pi}{2}\right) a\,dx\,d\theta \\
&\quad \text{with } \begin{cases} \varepsilon_m = 1, & \text{when } m=0, \\ \varepsilon_m = 2, & \text{when } m>0, \end{cases}
\end{aligned}
\tag{15}
$$

and h the shell thickness.

The analytical solution for the acoustic pressure field within the cylinder due to the radial displacement is[21,22]

$$
\begin{aligned}
p_{\mathrm{rad}}(x,\theta,r) &= \sum_{p=0}^{\infty}\sum_{q=0}^{\infty}\sum_{y=0}^{\infty}\sum_{i=0}^{1}\sum_{m=0}^{\infty} -j\omega A_{pqy} \\
&\quad \times \Psi^i_{pqy}(x,\theta,r)\Omega_{pqynm} W^i_{nm},
\end{aligned}
\tag{16}
$$

where

$$
A_{pqy} = \left(\frac{\omega\cdot\rho\cdot c^2}{V}\right)\left(\frac{1}{2\xi_{pqy}\omega^2_{pqy} - j(\omega^2_{pqy}-\omega^2)}\right),
\tag{17}
$$

V the cylinder volume, and

$$
\omega_{pqy} = c\sqrt{\left(\frac{p\pi}{L}\right)^2 + \left(\frac{k_{qy}}{a}\right)^2},
\tag{18}
$$

$$
\Psi^i_{pqy}(x,\theta,r) = \frac{\cos(p\pi x/L)\cos(q\theta - i\pi/2)J_q(k_{qy}r/a)}{\Delta^{1/2}_{pqy}}.
\tag{19}
$$

In Eq. (19), J_q is the Bessel function of order q, and k_{qy} are the solutions of $dJ_q(k_{qy})/dk_{qy}=0$, and

$$
\begin{aligned}
\Delta_{pqy} &= \left(\frac{2}{\varepsilon_p\varepsilon_q}\right)\left(1-\frac{q^2}{k_{qy}}\right)J^2_q(k_{qy}), \\
&\quad \text{with } \begin{cases} \varepsilon_p,\varepsilon_q = 1, & \text{when } p,q=0, \\ \varepsilon_p,\varepsilon_q = 2, & \text{when } p,q>0. \end{cases}
\end{aligned}
\tag{20}
$$

Finally,

$$
\Omega_{pqynm} = \int_0^{2\pi}\int_0^{L} \Psi^i_{pqy}(x,\theta,r)\Phi^i_{nm}(x,\theta)a\,dx\,d\theta,
\tag{21}
$$

and

$$
\Phi^i_{nm} = \varepsilon_m \sin\left(\frac{n\pi x}{L}\right)\cos\left(m\theta - \frac{i\pi}{2}\right).
\tag{22}
$$

Following the same approach as above, it is possible to determine the acoustic pressure of axial modes (i.e., those modes without dependency on azimuthal directions).

TABLE I. Model parameters, short cylinder, $L/a=2.4$.

Parameter	Symbol	Value and units
Length	L	6.0 m
Radius	a	2.5 m
Thickness	h	0.0012 m
Structural damping	η	0.01
Material density	ρs	2700 kg m^{-3}
Young's modulus	E	7.1 E +10 N m^{-2}
Speed of sound	c	343.0 m s^{-1}
Density of air	ρ	1.21 kg m^{-3}
Acoustic modal damping	ξ_{pqy}	0.0
Force excitation	F_0	100.0 N m^{-2}
ka range	$ka=\omega\cdot a/c$	0.0–4.6

IV. NUMERICAL RESULTS

We present in the following the results of numerical simulations intended to validate the SVP as applied to coupled structural acoustic interior analyses. We test the SVP for two cylinder configurations: one with a relatively low aspect ratio (the ratio of length to radius) and one with a higher aspect ratio. For both configurations we compare the SVP results against those obtained using the analytical formulation. In parallel with these simulations we also investigate the stability and convergence behavior of the SVP solution.

The first numerical validation considers the problem of a right-circular cylinder with aspect ratio (L/a) equal to 2.4 and having the characteristics defined in Table I. Further, we assume that the value of the amplitude of the axial displacement is constant across the span of the cylinder's endcaps (representing piston-like motion of the endcaps). We assume the shell to be excited by two equal, diametrically opposed normal forces at the midspan, such that the excitation function is

$$f(x,\theta)=F_0\delta\left(x-\frac{L}{2}\right)[\delta(\theta-0)+\delta(\theta-\pi)], \tag{23}$$

where δ represents the Dirac function.

The first step of the analysis consists of the identification of the required series length for the azimuthal and longitudinal indices for achieving convergence of the analytical solution for the surface displacement and acoustic pressure, Eqs. (11) and (16). Consideration of the analytical natural frequencies of the modeled cylindrical shell and the anticipated ka range lead to a longitudinal series length equal to 20 and an azimuthal series length equal to 50.

The same considerations for the acoustic volume indicate that only a few natural acoustic modes are present in the selected frequency range. However, since the coefficient Ω_{pqynm} in Eq. (16) couples the longitudinal and azimuthal structural and acoustic basis functions, it is necessary to maintain the same series lengths for both structural and acoustic solutions.

Turning now to the SVP analysis, the dependency of the analytical solutions on the series length was used as a basis for selecting the series lengths for the SVP analysis. For the azimuthal series, since the analytical and SVP series are identical in practice, the SVP series length was set to the same length as was used for the analytical analysis, that is, 50 terms. Since the meridional basis functions span from the center of one endcap along the surface of the shell all the way to the center of the opposite endcap, their geometric extent is greater than the longitudinal basis functions in the analytical solution. Therefore, more of these meridional functions are required to achieve an equivalent spatial resolution. Therefore, we used a series length of 30 terms for the meridional expansion. The meridional functions must reconstruct the velocity profile on the meridian length, which is the sum of the cylinder length plus the cylinder's endcap dimension. In fact, the meridian functions are also responsible for introducing the radial dependency of the acoustic pressure.

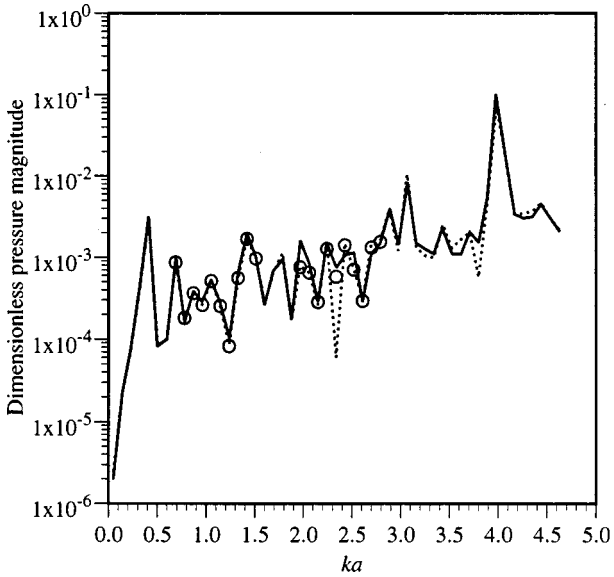

FIG. 3. Dimensionless pressure magnitude response versus wave number ka for SVP and analytical solutions; cylinder with $L/a=2.4$. —, analytical; ⋯, SVP with 30 meridional functions; ○, SVP with 45 meridional functions.

Figures 3 and 4 present the analytical solution and the SVP solution for the acoustic pressure magnitude and phase over the frequency range specified in Table I at an observation point at $x=L/2$, $\theta=0$, and $r=a$, and for the series lengths defined above. These figures demonstrate that the SVP solution for the pressure magnitude is in agreement with the analytical solution, whereas the phase solution shows some variation as compared to the analytical solution. The 180° phase error near $ka=1.2$ is due to the observation point at $L/2$ coinciding with a nodal line in the response. In such an instance, small computational errors lead to large phase errors. Figures 3 and 4 also include the results of individual SVP analyses using longer series lengths, which significantly improved the convergence, particularly with respect to phase. These analyses are discussed below.

Being variationally based, and with its complete orthogonal basis functions, the SVP solution should exhibit asymptotic convergence behavior: Increasing the number of the meridian functions should increase the quality of the solution.[19] To demonstrate convergence, as well as to improve the quality of the solution, we selected two frequency ranges for re-analysis at discrete values of ka: one already exhibiting a good convergence of the SVP (ka

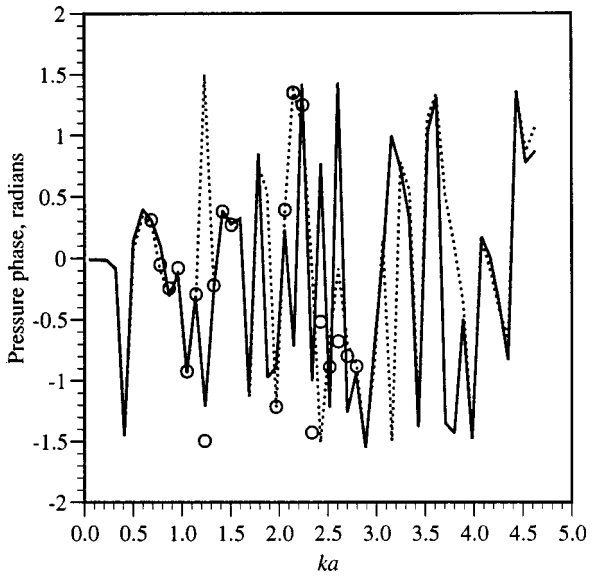

FIG. 4. Pressure phase response versus wave number ka for SVP and analytical solutions; cylinder with $L/a=2.4$. —, analytical; ···, SVP with 30 meridional functions; ○, SVP with 45 meridional functions.

$\in[0.69-1.42]$) and another, at higher frequency, exhibiting lesser convergence ($ka\in[1.97-2.79]$). The two frequency ranges were reanalyzed, increasing the number of meridional functions to 45, as compared to 30 in the original analysis. For the first frequency range ($ka\in[0.69-1.42]$) the intent was, also, to verify if the SVP solution was even stable (i.e., that it remained unchanged with an increasing number of basis functions) since the SVP solution had already converged to the analytical solution. For the first frequency range, as shown by the discrete data points in Figs. 3 and 4, the increased number of meridional functions does not introduce any numerical instability (that is, there is no evidence of the solution beginning to diverge). Moreover, the phase value for $ka=1.24$ now closer approximates the analytical value. For the second frequency range ($ka\in[1.97-2.79]$) the purpose was, simply, to achieve better values for the SVP results, in particular for $ka=2.336$ where there was the greatest discrepancy in the results for the 30 term analysis. With reference to the second frequency range, Figs. 3 and 4 show that by increasing the number of meridional functions, it is possible to achieve an improvement of the SVP solution, confirming one of its basic characteristics. These examples are not an absolute proof of convergence nor of stability. We have not analyzed cases with more than 45 meridional functions in an effort to find the limits of numerical stability, as the computational time is already daunting at 45 such functions.

Turning to the meridional solution, Figs. 5 and 6 present the acoustic pressure response as a function of the meridian coordinate α for two selected wave numbers. These figures demonstrate that at low frequency the SVP fits the analytical response very well, and as one would expect, the quality of the solution decreases with increasing wave number.

A subsequent analysis was performed to investigate the capability of the SVP approach in predicting the surface acoustic pressure on higher aspect ratio cylinders than considered above. A cylinder model was constructed with aspect

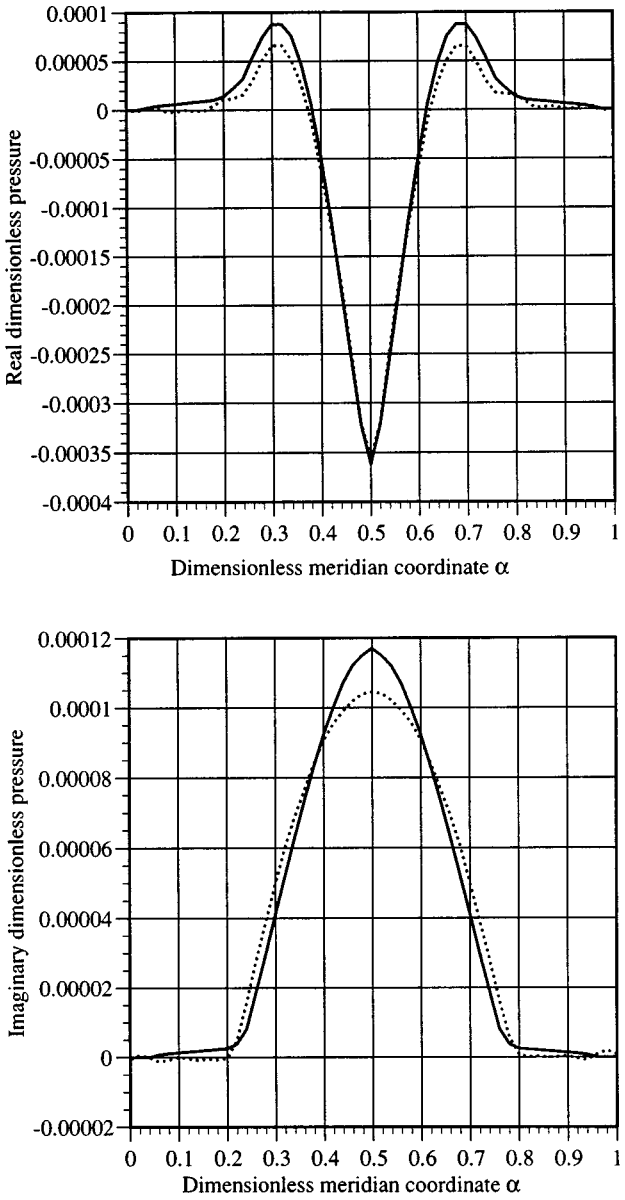

FIG. 5. Analytical and SVP dimensionless pressure response versus meridian coordinate α, $ka=0.87$; cylinder with $L/a=2.4$. —, analytical; ···, SVP.

ratio equal to 12.3, as detailed in Table II. The selected geometry corresponds to the dimension of a B.Ae.748 aircraft fuselage. The value of 12.3 for the aspect ratio represents an interesting test for the already mentioned problem of the number of meridian basis functions. Without repeating each step of the analysis reported for the low aspect ratio cylinder model, we note that (i) The analytical solution converges for the series lengths for the meridian, azimuthal, and radial expansions of, 25, 25, and 6, respectively; (ii) the radial dependency of the acoustic pressure is stronger than for the low aspect ratio cylinder; (iii) consequently, a series length of 30 for the SVP meridian basis functions permits us to analyze the response only up to $ka=2.4$; (iv) the acoustic response is dominated by the structural resonances over this frequency range (only a few acoustic modes are present in this range). Figures 7 and 8 present the pressure magnitude and phase response for an observation point located at $x=L/2$, $\theta=0$, $r=a$, and confirm the SVP capability in evaluating the

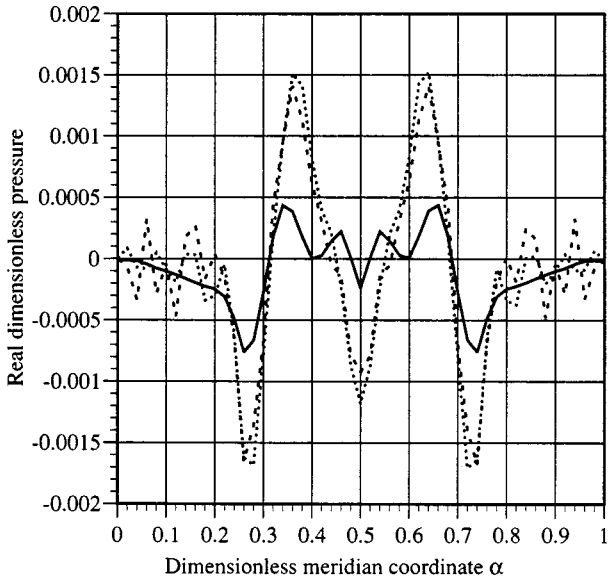

FIG. 6. Analytical and SVP dimensionless pressure response versus meridian coordinate α, $ka=2.70$; cylinder with $L/a=2.4$. —, analytical; ⋯, SVP with 30 meridional functions; ---, SVP with 45 meridional functions.

acoustic response for this slender cylinder model. Correct selection of the series length for the meridian functions is critical for agreement of the SVP solution with the analytical. At the moment, we have no *a priori* method of determining the required series lengths. However, unlike the FEM and BEM methods, where changing the model discretization requires the complete regeneration of the system matrices, for the SVP adding another basis function merely adds another row and column to the matrices. Consequently, it is rather straightforward to assess the adequacy of the solution by monitoring the convergence of the solution for increasing series lengths.

TABLE II. Model parameters, long cylinder, $L/a=12.3$. All other parameters are as in Table I.

Parameter	Symbol	Value and units
Length	L	16.0 m
Radius	a	1.3 m
ka range	$ka=\omega\cdot a/c$	0.0–2.4

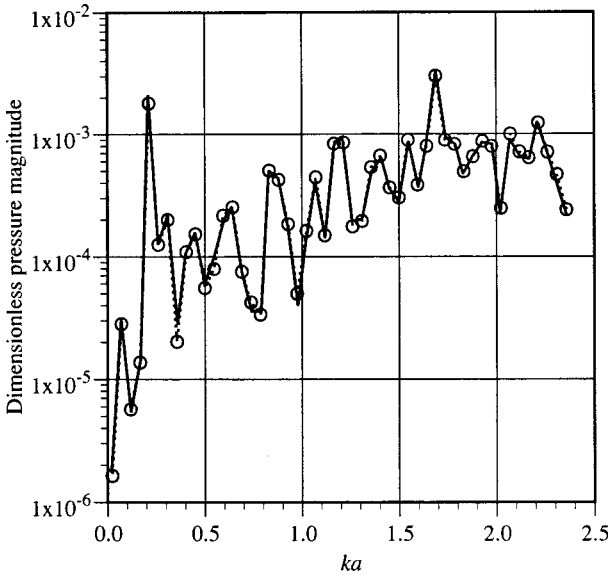

FIG. 7. Dimensionless pressure magnitude response versus wave number ka for SVP and analytical solutions, cylinder with $L/a=12.3$. —, analytical; ⋯○⋯, SVP.

V. CONCLUSIONS

The results presented in this paper demonstrate the suitability of the SVP for modeling interior acoustic fields for axisymmetric bodies. As with prior work for exterior acoustic problems, the approach demonstrated the characteristic asymptotic convergence of variational principal-based analysis tools with increasing numbers of basis functions. Hence, this provides a method for verifying solution accuracy.

The required computational effort for the SVP is a strong constraint against using it for industrial and/or large-scale applications. FEM and BEM methods have a clear

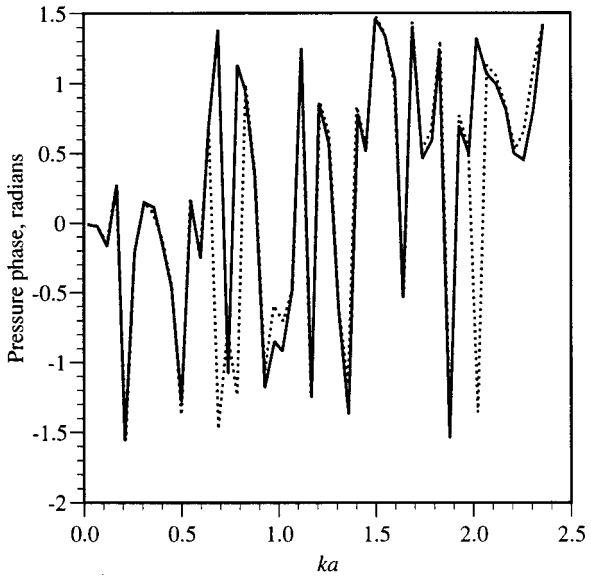

FIG. 8. Pressure phase response versus wave number ka for SVP and analytical solutions; cylinder with $L/a=12.3$. —, analytical; ⋯, SVP.

computational advantage over the SVP. Nonetheless, the SVP may be a better tool for elucidating physical understanding of coupling mechanisms between structures and fluids, as the SVP's basis functions span the entire surface, rather than individual elements. Further, the SVP represents an alternative formulation that may be used to independently assess the results from FEM and BEM solutions for axisymmetric bodies.

The work presented here represents a step toward the analysis of fully coupled problems using common basis functions for all three domains: the interior acoustic, exterior acoustics, and full fluid loaded shell.

ACKNOWLEDGMENTS

This paper contains some results obtained during a visiting research period at the Georgia Institute of Technology of the first author. A Fulbright grant, received in May 1996, made his permanence at Georgia Tech possible.

[1] A. D. Pierce, *Acoustics: An Introduction to its Physical Principles and Applications* (The Acoustical Society of America, Woodbury, NY, 1989).
[2] W. S. Shepard, Jr. and K. A. Cunefare, ''Sensitivity of structural acoustic response to attachment feature scales,'' J. Acoust. Soc. Am. **102**, 1612–1619 (1997).
[3] K. A. Cunefare and S. DeRosa, ''The sensitivity of structural acoustic response to attachment feature scale representation,'' J. Acoust. Soc. Am. **106**, 3384–3393 (1999).
[4] X.-F. Wu, ''Variational methods for prediction of acoustic radiation from vibrating bodies,'' Master's thesis, The Georgia Institute of Technology, 1984.
[5] X.-F. Wu, ''Variational principles for acoustic radiation and diffraction from underwater structures,'' Doctoral dissertation, The Georgia Institute of Technology, 1987.
[6] X.-F. Wu, A. D. Pierce, and J. H. Ginsberg, ''Variational method for computing acoustic pressure on vibrating bodies, applied to transversely oscillating disks,'' IEEE J. Ocean Eng. **12**, 412–418 (1987).
[7] X.-F. Wu, ''Faster calculations of sound radiation from vibrating cylinders using variational formulations,'' ASME J. Vib., Acoust., Stress, Reliab. Des. **111**, 101–107 (1989).
[8] K. Wu and J. H. Ginsberg, ''Progress in applying the surface variational principle to analyze acoustic radiation from slender elastic bodies,'' ASME 15th Biennial Conference on Mechanical Vibration and Noise, Boston, MA, October 1995.
[9] K. Wu, ''Extension of surface variational principle to nonsymmetric acoustic radiation and scattering problems,'' Doctoral dissertation, Georgia Institute of Technology, 1995.
[10] J. H. Ginsberg, A. D. Pierce, and X. F. Wu, ''A variational principle for sound radiation from vibrating bodies,'' Internal Report, GTADRL-86-101, Georgia Institute of Technology, 1986.
[11] J. H. Ginsberg and P.-T. Chen, ''Analysis using variational principles of the surface pressure and displacement along an axisymmetrically excited disk in a baffle,'' J. Acoust. Soc. Am. **88**, 548–559 (1990).
[12] J. H. Ginsberg and J. G. McDaniel, ''An acoustic variational principle and component mode synthesis applied to the analysis of acoustic radiation from a concentrically stiffened plate,'' ASME J. Vibr. Acoust. **113**, 401–408 (1991).
[13] J. H. Ginsberg and P. Chu, ''Asymmetric vibration of a heavy fluid-loaded circular plate using variational principles,'' J. Acoust. Soc. Am. **91**, 894–906 (1992).
[14] J. H. Ginsberg and K. Wu, ''Nonaxisymmetric acoustic radiation and scattering from rigid bodies of revolution using the surface variational principal,'' in Vol. NCA-17 *Acoustic Radiation and Wave Propagation*, edited by Sean F. Wu (American Society of Mechanical Engineers, 1994), pp. 93–104.
[15] P.-T. Chen and J. H. Ginsberg, ''Variational formulation of acoustic radiation from submerged spheroidal shells,'' J. Acoust. Soc. Am. **94**, 221–233 (1993).
[16] K. A. Cunefare, W. S. Shepard, and J. H. Ginsberg, ''Spectral techniques for assessing critical scales in models of fluid loaded structures,'' Proceedings of the 15th International Congress of Acoustics, Trondheim, Norway, June 1995, Vol. 4, pp. 405–408.
[17] K. A. Cunefare, W. S. Shepard, and J. H. Ginsberg, ''Methods for identifying critical elastic scales in structural-acoustic models,'' Proceedings of the ASME 15th Biennial Conference on Mechanical Vibration and Noise, DE Vol. 84-2, Boston, MA, October 1995, Vol 3—Part B, pp. 267–274.
[18] J. H. Ginsberg, K. A. Cunefare, and H. Pham, ''A spectral description of inertial effects in fluid-loaded plates,'' ASME J. Vibr. Acoust. **117**, 206–212 (1995).
[19] J. N. Reddy, *Applied Functional Analysis and Variational Methods in Engineering* (Krieger, Malabar, FL, 1991), p. 546.
[20] A. Leissa, *Vibration of Shells* (American Institute of Physics for the Acoustical Society of America, Woodbury, NY, 1993).
[21] D. R. Thomas, P. A. Nelson, and S. J. Elliot, ''Active control of the transmission of sound through a thin cylindrical shell, part I: the minimisation of vibration energy,'' J. Sound Vib. **167**, 91–111 (1993).
[22] D. R. Thomas, P. A. Nelson, and S. J. Elliott, ''Active control of the transmission of sound through a thin cylindrical shell, part II: the minimisation of acoustic potential energy,'' J. Sound Vib. **167**, 113–128 (1993).

A theoretical study of passive control of duct noise using panels of varying compliance

Lixi Huang
Department of Mechanical Engineering, The Hong Kong Polytechnic University, Kowloon, Hong Kong

(Received 8 June 1999; revised 25 October 2000; accepted 9 March 2001)

It is theoretically demonstrated that, in a duct, a substantial amount of sound energy can be transferred to flexural waves on a finite wall panel when the upstream portion of the panel is made to couple strongly with sound. The flexural wave then loses its energy either through radiating reflection sound waves or by internal friction. The effectiveness of the energy transfer and damping is greatly enhanced if the panel has a gradually decreasing *in vacuo* wave speed, which, in this study, is achieved by using a tapered membrane under tension. A high noise attenuation rate is possible with the usual viscoelastic materials such as rubber. The transmission loss has a broadband spectrum, and it offers an alternative to conventional duct lining where a smooth air passage is desired and nonacoustical considerations, such as chemical contamination or cost of operation maintenance, are important. Another advantage of the tapered panel is that, at very low frequencies, typically 5% of the first cut-on frequency of the duct, sound reflection occurs over the entire panel length. This supplements the inevitable drop in sound absorption coefficient, and a high transmission loss may still be obtained at very low frequencies. © *2001 Acoustical Society of America.* [DOI: 10.1121/1.1369108]

PACS numbers: 43.50.Gf, 43.20.Mv, 43.20.Tb [MRS]

I. INTRODUCTION

We are interested in devising a mechanism of broadband passive control of duct noise without using porous media such as glass wools or perforated metal sheets. Porous media have been the backbone of almost all dissipative noise abatement techniques (Beranek, 1992). When air is forced into the pores or cavities by sound, substantial viscous friction occurs between air and solid structures, typically fibrous and optimized to have the maximum surface contact area with air. The performance of a porous noise absorber is closely related to its ability to cause pressure loss to the mean flow. An air duct is often split into small channels with lined walls and the normalized flow resistance is usually over unity [Ingard (1994), p. 2-1]. If the flow speed is high, such lining may also cause extra noise. In addition, dusts get into pores easily and have to be cleaned periodically, which obviously contributes to the maintenance cost of building ventilation systems using porous linings. There are also places, such as operation theatres, where high hygienic requirement forbids the use of such materials. In fact, there are already public concerns of bacteria breading in the ventilation systems of ordinary commercial buildings equipped with central air conditioning systems. The use of porous material for noise or heat insulation purposes in the ventilation pipeworks is believed to contribute to an indoor air quality which is often worse than outdoors. The other problem of using porous or fibrous materials for sound absorption is that its performance degrades towards low frequencies, such as below 200 Hz.

To deal with the low-frequency noise and to avoid the disadvantages associated with the rough surfaces of porous materials, two types of membrane sound absorbers with smooth surfaces have been developed in the past. Ford and McCormick (1969) described an earlier type consisting of layers of thin membranes, such as 0.2 mm aluminum sheets, stacked at a certain distance from one another. They are used in broadcasting studios, concert halls, etc. Fuchs and his colleagues developed another type of membrane absorber (Ackermann *et al.*, 1988) in which a perforated thin plate is glued to an all-metal honeycomb structure forming an array of Helmholtz resonators. The device shows two resonance peaks relating to the Helmholtz resonance and the resonance of the cover plate, respectively. Another smooth cover sheet, typically of 0.1 mm aluminum, is then added in front of the perforated plate to protect the resonator from flow and dust. The separation distance is typically 1 mm. The result is an improved performance between the two resonance peaks. Membrane absorbers of this type has provided useful attenuation of low-frequency noise down to some 60 Hz when used in a papermill exhaust (Ackermann and Fuchs, 1989), but exact theoretical prediction proved rather difficult (Frommhold *et al.*, 1994). The main disadvantage of both types of membrane absorbers, however, is their narrow-bandedness typical of all resonator-type silencers. What is needed then is a nonresonator-type membrane absorber which will work for a broad frequency band. We propose to achieve this through transferring energy effectively from sound in air to the structural vibration by means of a strong fluid-structure coupling in the form of travelling waves.

The rationale behind introducing the strong air-structure coupling is that the attenuation of structural vibration could be made much higher than that resulted from the air-solid friction. Air-wall coupling has been a topic of investigation in the context of the so-called ''breakout noise'' from air-handling pipes (Cummings, 1994), but such coupling is unintended and the fraction of energy leaking is insignificant. If sound energy could be transferred to structure effectively, the expertise built in the field of vibration absorption and isolation will be readily deployed for noise absorption. The

question, then, is how could such energy transfer happen substantially and, if so, whether the damping coefficient required of the quick dissipation of structural energy is realistic? This study explores a theoretical model which yields encouraging answers to the above questions. The focus of this paper is on the characteristics of the fluid-structure coupling although the performance of such a potential noise absorption technique will also be briefly discussed. The present study is a development of the previous one on uniform panels (Huang, 1999), and the performance shown here represents a significant improvement in both sound reflection and dissipation.

We consider a finite, thin membrane under tension to form part of a duct wall. The panel has its own *in vacuo* wave speed, c_T^*, determined by its density and the tensile stress applied. Note that asterisk in the superscript signifies dimensional quantities which will be represented later by dimensionless ones of the same symbol without asterisk. The air-panel coupling is strong only when c_T^* is close to the isentropic speed of sound in free space, c_0^*, which is around 340 m/s at room temperature. Under such a condition, the structure may be regarded as being 'transparent' to sound. But at such speed structural waves will go a long way without significant damping, which is undesirable for the purpose of noise absorption. So a gradation of c_T^* is introduced to slow down the waves. We expect that the energy dissipation per unit distance will be increased to a level useful to noise absorption, which is confirmed in this study. We also found that the actual phase speed of the coupled wave, which is a function of the axial distance, $c^*(x^*)$, is somewhat less than c_T^* due to air inertia, but $c^*(x^*)$ follows the trend of $c_T^*(x^*)$ rather closely.

As a preliminary study, we tactically make the following assumptions or exclusions, some of which may well be important in practical terms.

The frequency of the incident wave is below the first cut-on frequency of the duct.

Bending stiffness if ignored even though membranes of moderate to high thickness are implied in numerical examples. It is hoped that, in future studies, means other than using tapered membrane may be found to achieve a certain distribution of $c_T^*(x)$.

The problem of possible flow-induced vibration is potentially the most serious one and is left to future studies.

The effect of the fluid loading on the external side of the panel serves to complicate the algebra and is excluded.

The last assumption may need further justification. It is noted that when the external air is not confined, it exhibits evanescent waves with an effect of added mass. Therefore it is not expected to impact on the qualitative results sought in this study. In real applications, however, the external air may be confined by a solid wall to form a cavity to prevent noise breakout. The fluid loading inside the cavity is expected to play a similar role as that of the internal loading and, for the special case of a cavity having a depth equal to the main duct height, the total loading on the panel is simply double that of the present model without external fluid. The exclusion of the external fluid will be better appreciated when further details are revealed for the complicated cross-modal interactions and many other physical ingredients already present in the current model.

II. FORMULATION OF NOISE-INDUCED VIBRATION

A. The theoretical model

We consider an infinite channel of height h^* fitted with a flexible strip of length L^* on the lower channel wall. We call this strip a panel although the theoretical configuration is two-dimensional in nature. Noise of low frequency comes from the left-hand side of the channel and causes the panel to vibrate. We first limit ourselves to frequencies below the first cut-on frequency of the channel, $c_0^*/2h^*$. The questions we ask are what proportion of sound energy is reflected, how much is transmitted to downstream, and how much is damped by the internal friction of the panel? The reflection and absorption coefficients of energy are denoted by β and α, respectively, while TL represents the transmission loss.

All variables are normalized using the length scale h^* and time scale h^*/c_0^*:

$$
\begin{aligned}
&x=\frac{x^*}{h^*}, \quad y=\frac{y^*}{h^*}, \quad t=\frac{c_0^* t^*}{h^*}, \quad c=\frac{c^*}{c_0^*},\\
&f=\frac{f^* h^*}{c_0^*}, \quad L=\frac{L^*}{h^*}, \quad k_0=\frac{\omega^* h^*}{c_0^*},\\
&\omega=2\pi\frac{f^*}{c_0^*/h^*}=k_0=2\pi f, \quad k=\frac{\omega}{c}, \quad \eta_0=\frac{\eta_0^*}{h^*},\\
&p=\frac{p^*}{\rho_0^*(c_0^*)^2}, \quad M=\frac{M^*}{\rho_0^* h^*}, \quad c_T=\frac{\sqrt{T^*/M^*}}{c_0^*},\\
&D=\frac{D^*}{\rho_0^* c_0^*}.
\end{aligned}
\tag{1}
$$

The dimensionless symbols are explained below. x and y are the Cartesian coordinates. L and η_0 are, respectively, the panel length and the amplitude of the local panel displacement. c is the phase speed of the coupled wave in panel and air, which may differ from the isentropic speed of sound in free space, i.e., $c \neq 1$. f is the dimensionless frequency, for which the first cut-on mode of a rigid wall duct has the value of 0.5. k is the wave number based on c. The dimensionless angular frequency ω defined here is equivalent to the dimensionless wave number (k_0) based on the speed of sound in free space. p is the general symbol for pressure perturbation. c_T is the *in vacuo* wave speed provided by the tensile force T^*. The panel has a dimensional mass per unit area M^* and damping D^*. The air has a mean density of ρ_0^*. M and D are, respectively, the dimensionless structure-to-air mass ratio (or simply mass henceforth) and the damping coefficient of the panel.

As shown in Fig. 1, the origin of the Cartesian coordinates, $x=y=0$, is located at the center of the panel which lies in the region of $|x|<L/2$. Both M and D may vary with x. The incident wave of unit amplitude is given as $p_i = \exp[i(\omega t - k_0 x)]$. The panel thickness distribution $b(x)$ is normalized by its mean, so that

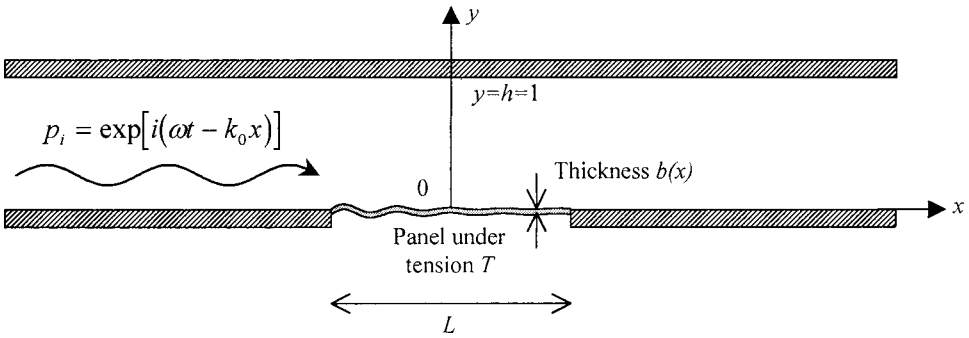

FIG. 1. The mathematical model of plane wave incident on a panel of nonuniform thickness. The panel has length L and is under tensile force T. The thickness distribution function $b(x)$ is normalized to have a mean value of unity.

$$L^{-1}\int_{-L/2}^{+L/2} b(x)dx = 1.$$

The local panel mass is written as

$$M(x) = M_0 b(x),$$

where M_0 is the mass averaged over the whole length. The dynamics of the panel vibration is governed by

$$M(x)\frac{\partial^2 \eta}{\partial t^2} + D(x)\frac{\partial \eta}{\partial t} + p_w - T\frac{\partial^2 \eta}{\partial x^2} = 0, \tag{2}$$

where p_w is the pressure perturbation on the inner side of the panel, the effect of fluid on the external surface being left to future studies as its inclusion at this moment may only serve to complicate the algebra. For instance, in real applications, the panel may be backed by an air cavity formed between the panel and a lower rigid wall to prevent the break-out noise. The cavity air pressure caused by the vibration of the panel is expected to have similar behavior to that inside the main duct. In the special case where the cavity has the same depth as the duct, the pressure loading p_w is simply doubled. If the depth is different, the algebra will become rather involved. Therefore the present study is based on an idealistic model of no external fluid. The structural damping $D(x)$ is estimated by its *in vacuo* dynamics. By specifying $p_w = 0$ and $\eta = \eta_0 \exp[i(\omega t - kx)]$ we have

$$-M\omega^2 + Di\omega + Tk^2 = 0.$$

The loss factor of a material, σ, is defined as the ratio of energy damping per radian to the maximum potential energy [cf. Ungar (1997)]

$$\sigma = \frac{\frac{1}{2}D\omega|\eta_0^2|}{\frac{1}{2}(Tk^2)|\eta_0^2|} = \frac{D\omega}{Tk^2}.$$

The wave number k here cannot be specified and for the tensioned membrane the issue of damping is in fact more complicated than that of bulk material (Berry, 1992). Since the present study is focused on other aspects of dynamics, we choose a simplistic model by substituting k with ω/c_T, so that

$$D = \frac{\sigma T k^2}{\omega}, \quad \frac{\sigma T \omega^2}{\omega c_T^2} = \sigma M \omega.$$

For metals, the loss factor σ is in the range of 10^{-4} to 10^{-3} and is independent of frequency of the audio range. For viscoelastic materials like natural rubber, σ is weakly dependent on frequency in the range of interest, such as from 100 Hz to 1 kHz. The value of σ for the natural rubber at 100 Hz is 0.2 at room temperature. Damping for other viscoelastic materials can be over unity, and effective damping for composite structures like sandwiched or shearing layers can be even higher. The typical value we choose in our examples will be 0.05.

B. Modal dynamics of the panel vibration

For harmonic excitation, the panel displacement may be replaced by its velocity as $\eta = V/i\omega$. Equation (2) may be rewritten as

$$\left(iM(x)\omega + D(x) - \frac{T}{i\omega}\frac{\partial^2}{\partial x^2}\right)V + p_w = 0. \tag{3}$$

In order to satisfy the structural boundary conditions of the panel, $V|_{x=\pm L/2} = 0$, we expand V in terms of sine-transform using a local dimensionless variable $\xi = ((x/L) + \frac{1}{2})$ which spans from 0 to 1 for the panel:

$$V = \sum_{j=1}^{\infty} V_j \sin j\pi\xi, \quad V_j = 2\int_0^1 V(\xi)\sin j\pi\xi \, d\xi.$$

V_j will be referred to as the coefficients of panel modes to avoid confusion with duct acoustic modes although $\sin j\pi\xi$ is certainly not the eigenfunctions of the tapered panel with or without fluid loading. The axial variations of the panel properties are expanded in terms of cosine-transform as follows:

$$M(x) = M_0\left(1 + \sum_{q=1}^{\infty} M_q \cos q\pi\xi\right),$$

$$D(x) = D_0\left(1 + \sum_{q=1}^{\infty} M_q \cos q\pi\xi\right),$$

where $D_0 = \sigma M_0 \omega$. Multiplying Eq. (3) by $2\sin j\pi\xi$ and integrating over the panel length lead to

$$\int_0^1 \left[i\omega M(\xi) + D(\xi) + \frac{T}{i\omega}\left(\frac{j\pi}{L}\right)^2\right]V(\xi)2\sin j\pi\xi d\xi + p_{wj} = 0,$$

where

$$p_{wj} = \int_0^1 p_w 2\sin j\pi\xi \, d\xi.$$

Substituting $V(\xi)$ by its sine expansion and $M(\xi), D(\xi)$ by their cosine expansions, and defining

$$\mathcal{L}_j = i\omega M_0 + D + \frac{T}{i\omega}\left(\frac{j\pi}{L}\right)^2,$$
$$S_q = (i\omega M_0 + D_0) M_q, \quad j,q = 1,2,3,\ldots, \tag{4}$$

we get

$$\mathcal{L}_j V_j + \sum_{q=1}^{\infty}\sum_{j'=1}^{N} V_{j'} \int_0^1 2S_q[\cos q\pi\xi \sin j'\pi\xi \times \sin j\pi\xi]d\xi + p_{wj} = 0$$

in which

$$\int_0^1 [\cos q\pi\xi \sin j'\pi\xi \sin j\pi\xi]d\xi = \tfrac{1}{4}[\delta_{j'(j+q)} + \delta_{j'(j-q)} - \delta_{j'(q-j)}],$$

and δ_{ij} is the delta function. So that

$$\mathcal{L}_j V_j + \frac{1}{2}\sum_{q=1}^{\infty} S_q(V_{j+q} - V_{j-q} - V_{q-j}) + p_{wj} = 0, \quad j = 1,2,3,\ldots,N. \tag{5}$$

The S_q series may be rewritten as

$$\sum_{q=1}^{\infty} S_q(V_{j+q} + V_{j-q} - V_{q-j}) = \sum_{n=1}^{N} Y_{jn}V_n, Y_{jn} = S_{n-j} + S_{j-n} - S_{j+n} \tag{6}$$

in which $S_{j\leqslant 0}$ should be assigned a value of zero.

The perturbation pressure on the wall (p_w) may be split into contributions from the incident wave and the radiation of its own. In terms of panel modes expansion,

$$p_{wj} = \sum_{n=1}^{N} V_n Z_{jn} + I_j, \tag{7}$$

where Z_{jn} is the radiation impedance on the jth panel mode induced by the vibration of the nth mode, which has been calculated in a previous study (Huang, 1999) and the result is given below in terms of summations over duct acoustic modes,

$$Z_{jn} = 2\int_0^1 p_n \sin j\pi\xi \, d\xi = L\sum_{m=0}^{\infty} c_m(2-\delta_{0m})\mathcal{I}_2(m,n,j), \tag{8}$$

where p_n is the radiation pressure of the nth mode, and

$$\mathcal{I}_2(m,n,j) = \frac{n\pi j\pi(e^{in\pi} - e^{-ik_mL})(e^{in\pi} + e^{ij\pi})}{[(k_mL)^2 - (n\pi)^2][(k_mL)^2 - (j\pi)^2]} - \frac{ik_mL\,\delta_{jn}}{(k_mL)^2 - (n\pi)^2}.$$

Here $c_m = [1-(m\pi/\omega)^2]^{-1/2}$ for cut-on modes, but $c_m = i|1-(m\pi/\omega)^2|^{-1/2}$ for cut-off modes, and $k_m = \omega/c_m$. Treatments for $\mathcal{I}_2$ (when it becomes 0/0-type) have also been given in (Huang, 1999). Note that it is necessary to take account of the cross-modal impedance, z_{jn}, $j \neq n$, since the panel dynamics are determined by the near-field pressure on the panel, which does not have the convenient orthogonal properties as far as the vibration modes are concerned.

I_j is the sine-transform of the incident wave:

$$I_j = 2\int_0^1 e^{-ik_0L(\xi-1/2)}\sin(j\pi\xi)d\xi = 2j\pi e^{ik_0L/2}\left[\frac{e^{i(-k_0L+j\pi)}-1}{(k_0L)^2-(j\pi)^2}\right], \tag{9}$$

where the term in square brackets becomes $(2ik_0L)^{-1}$ when $k_0L \to j\pi$.

Inserting Eqs. (6) and (7) into Eq. (5) we have

$$\mathcal{L}_j V_j + \sum_{n=1}^{\infty} Y_{jn}V_n + \sum_{n=1}^{\infty} Z_{jn}V_n = -I_j, \quad j = 1,2,3,\ldots,N,$$

for which the solution is written in the following matrix form:

$$[V_j] = -\mathcal{Z}^{-1}[I_j], \quad \mathcal{Z} = [Z_{jn}] + [Y_{jn}] + [\mathcal{L}_{jj}].$$

Here $[V_j]$ and $[I_j]$ are column vectors, $[\mathcal{L}_{jj}]$ is a diagonal matrix formed by structural constants $\mathcal{L}_j$ defined in Eq. (4).

C. Transmission loss and energetics of sound-panel coupling

The pressure perturbation induced by the wall oscillation was given by [Doak (1973), Eq. (123)] and is rewritten below in our notations and simplified for the two-dimensional configuration:

$$p(x,y,t) = \frac{1}{2}\sum_{m=0}^{\infty} c_m\psi_m(y)\int_{-L/2}^{+L/2}\psi_m(y')V(x',t) \times [H(x-x')e^{-i\omega(x-x')/c_m} + H(x'-x)e^{+i\omega(x-x')/c_m}]dx', \tag{10}$$

where H is the Heaviside function, $y' = 0$ is the coordinate of the panel, ψ_m is the channel modal function defined $\psi_m(y) = \sqrt{2-\delta_{0m}}\cos(m\pi y)$, and c_m is the complex modal wave speed defined earlier.

The sound waves transmitted downstream is the sum of incident wave and the downstream travelling wave radiated by the vibrating panel. For excitation frequencies below that of the first cut-on frequency of the channel, sound waves radiated downstream, $x > L/2$, may be calculated from Eq. (10),

$$\frac{p_+}{p_i} = \frac{L}{2}\sum_{j=1}^{\infty} V_j\int_0^1 \sin(j\pi\xi')e^{ik_0L(\xi'-1/2)}\,d\xi' = \frac{L}{2}\sum_{j=1}^{\infty} V_j j\pi e^{-ik_0L/2}\left[\frac{e^{i(k_0L-j\pi)}-1}{(k_0L)^2-(j\pi)^2}\right],$$

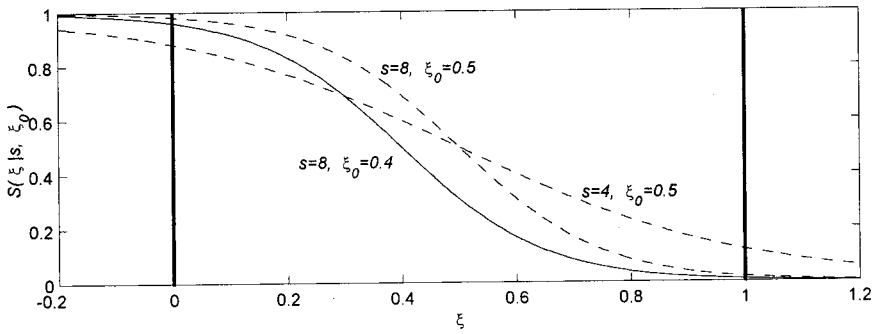

FIG. 2. Sigmoid curve used for *in vacuo* flexural wave speed prescription, $S(\xi|s,\xi_0)$, in which s controls the steepness in the mid-range of ξ and ξ_0 the center of symmetry. The solid curve with left-shift and moderately high steepness is the default shape used for later examples.

in which the square brackets takes the value of $i/2k_0L$ when $k_0L/\pi=j$. The transmission loss is found by

$$\mathrm{TL}=-20\log_{10}\left|\frac{p_i+p_+}{p_i}\right|.$$

Within the panel region, $|x|<L/2$, wave radiation from the panel is also split between left and right directions. The left-travelling wave is regarded as the local reflection wave,

$$p_-(x,t)=\frac{1}{2}e^{ik_0x}\int_x^{+L/2}V(x',t)e^{-ik_0x'}\,dx',$$

for which the time-mean intensity is calculated as

$$I_-\left(|x|<\frac{L}{2}\right)=\frac{1}{2}|p_-|^2=\frac{1}{8}\left|\int_x^{+L/2}V(x',t)e^{-ik_0x'}\,dx'\right|^2. \tag{11}$$

Once I_- is calculated, the intensity of the right-travelling wave, I_+, can also be found by taking a control volume from $x=x$ to $x=L/2$ and writing the energy flux conservation as follows:

$$I_+(x)+\int_x^{L/2}I_s\,dx=I_-+I_{+\mathrm{TE}},$$

$$I_+(x)=I_{+\mathrm{TE}}+I_--\int_x^{L/2}I_s\,dx,$$

where subscript TE means evaluation at the trailing edge $x=L/2$. Here

$$I_s=\tfrac{1}{2}\mathrm{Re}[p_w\hat{V}] \tag{12}$$

is the sound radiation intensity from the panel, and $\hat{V}$ is the conjugate of V. The time-mean energy damping I_d is found as

$$I_d=\tfrac{1}{2}\sigma M(x)\omega|V|^2 \tag{13}$$

and the energy balance between the incident, reflection, transmission waves and the damping is

$$\tfrac{1}{2}|p_i|^2=\tfrac{1}{2}|p_-|^2+\tfrac{1}{2}|p_i+p_+|^2+I_d,$$

which has been accurately validated in numerical implementations. Note that the reflection and damping coefficients are given by

$$\beta=\frac{|p_-|^2}{|p_i|^2},\quad \alpha=\frac{I_d}{\frac{1}{2}|p_i|^2}.$$

Also validated is the energy balance for the structure

$$\int_{-L/2}^{+L/2}(I_d+I_s)dx=0.$$

III. ANALYSES OF RESULTS

We choose long panels of length $L=50$ with moderate damping as the default setting for the purpose of understanding wave behaviors, but the noise abatement performance of shorter panels ($L=10$) will also be discussed towards the end. Two identical panels are installed on the two channel walls, which is equivalent to having one panel in a channel of width $h^*/2$, a fact which is conveniently used in numerical calculations. The following parameters will be regarded as the default values in examples and will not be described again in figure captions or text,

$$L=50,\quad M_0=10,\quad \sigma=0.05.$$

Tapering of membrane thickness $b(x)$ is specified via the local *in vacuo* wave speed defined as $c_T(x)=\sqrt{T/M(x)}$ and a sigmoid curve defined as

$$S(\xi|s,\xi_0)=\frac{1}{1+e^{s(\xi-\xi_0)}},$$

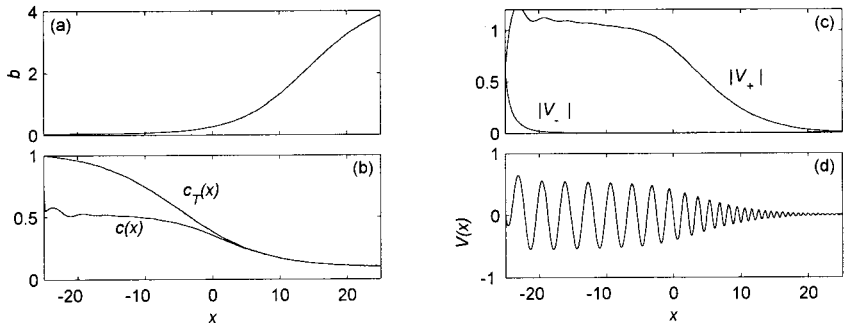

FIG. 3. The response of a tapered panel of default setting at frequency 0.15. $\alpha=0.095$, $\beta=0.905$, TL $=62.2$ dB.

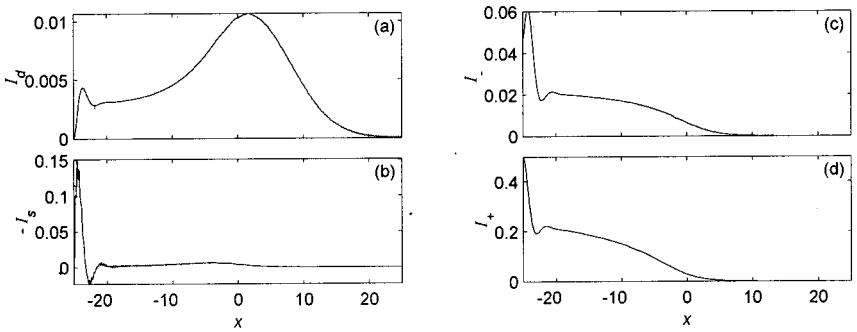

FIG. 4. Energetic analysis of the default tapered panel at frequency $f=0.15$. TL=62.2 dB.

$$c_T(\xi)=c_{T2}+\frac{S(\xi|s,\xi_0)-S(1|s,\xi_0)}{S(0|s,\xi_0)-S(1|s,\xi_0)}(c_{T1}-c_{T2}),$$

is adopted for easy manipulation of shapes as shown in Fig. 2. c_{T1} and c_{T2} are, respectively, the *in vacuo* wave speed at the upstream and downstream ends of the panel. The default values used in the calculations are

$$c_{T1}=1, \quad c_{T2}=0.1.$$

Parameter s controls the curve steepness in the middle region, and ξ_0 is the center position of the curve which controls the relative slope at the leading and trailing edges. The larger s is, the steeper the curve becomes in the middle region while the leading and trailing edges of the panel remain relatively smooth. Reducing ξ_0 has the effect of steepening the leading edge and flattening the trailing edge. The solid curve in Fig. 2 will be used as the default setting:

$$s=8, \quad \xi_0=0.4.$$

A. Fluid-structure interaction

Figures 3 and 4 show the solution for the panel of default setting at frequency $f=0.15$. Figure 3(a) shows the tapering curve $b(x)$ which is essentially $c_T^{-1/2}(x)$. The mass ratio at the leading and trailing edges are 0.388 and 38.8, respectively. The flexural wave $e^{i\omega t}V(x)$ is decomposed into waves travelling to the left, V_-, and right, V_+, by means of

$$e^{i\omega t}\sin j\pi\xi=[e^{i(\omega t+j\pi\xi)}-e^{i(\omega t-j\pi\xi)}]/2i$$

and the results are shown in Fig. 3(c). The actual local wave speed is calculated as $c(x)=\omega/k(x)$, where $k(x)$ is the local gradient of decreasing phase angle of $V_+(x)$. The result is shown in Fig. 3(b). $c(x)$ follows $c_T(x)$ very well at the downstream half of the panel but the deviation is large at the upstream half. The reason is that the upstream half of the panel is thin and the fluid loading dominates. A snapshot of the vibration is shown in Fig. 3(d) confirming the shortening of the wavelength. The reduction of $|V_+(x)|$ in general is caused by both damping and sound radiation.

The reflection coefficient of sound energy (α) is only 9.5% in this case, so the transmission loss of 62.2 dB is mainly contributed by the absorption in the form of flexural wave damping. The fact that the waves slow down should lead to a rising amplitude in V_+, but this is countered by the increase in panel mass and the removal of energy by damping. The full energy balance picture is shown in Fig. 4. Figure 4(a) gives the rate of energy damping per axial distance (I_d) defined by Eq. (13). The rate peaks somewhere in the middle of the panel due to the two competing factors. One is the increasing damping coefficient $D=\sigma M(x)\omega$, and the other is the decreasing vibration amplitude $|V(x)|$. Figure 4(b) gives the local energy influx from air to structure, $-I_s$, where I_s is the sound radiation power defined in Eq. (12). The energy balance for the panel means that the integral of curves in Figs. 4(a) and (b) should be equal, which is confirmed in the calculation with a numerical error less than 0.015%. The spike in Fig. 4(b) means that the sound energy is transferred to the panel mainly near the leading edge but the damping by panel friction takes place rather gradually. Figure 4(c) shows the distribution of intensity of left-travelling sound, $I_-(x)$, and its axial gradient reflects the local contribution towards sound reflection by the tapered panel. Starting from the trailing edge, I_- gathers strength and reaches about 0.02 near the leading edge, the slope being largest near the middle of the panel. Near the leading edge there is a distinct sharp rise in I_- representing the effect of scattering of incident wave. At $x=-L/2$, $I_-=0.047$ is the intensity of reflection sound further upstream which is somewhat lower than the peak of $I_-(x)$, indicating a destructive interference of reflection waves radiated over the panel length and the scattering by the leading edge. Figure 4(d) gives the intensity of the right-travelling sound, $I_+(x)$, which is the sum of the incident sound p_i and the panel radiation. The sharpest reduction of I_+ occurs near the leading edge where two events occur: (a) wave scattering by the leading edge, and (b) energy tansfer from sound to the panel, the latter being dominant in this case.

B. Comparison with uniform panel

We now compare the behavior of the typical tapered panel with that of a uniform panel and the results are listed in Table I. The uniform panel has the same mass of $M=10$, a damping coefficient of $\sigma=0.05$, and a tension of $T=0.39$ corresponding to the value of the *in vacuo* wave speed of

TABLE I. Comparison of tapered and uniform panels.

Panel	Tapered	Uniform	Tapered	Uniform
f	0.15	0.15	0.05	0.05
c_T	1→0.1	0.20	1→0.1	0.20
c	0.52→0.1	1.14	0.34→0.1	0.19
Reflection β (%)	9.5	0.3	20.2	44.1
Absorption α (%)	90.5	49.4	79.5	55.0
TL (dB)	62.2	3.0	25.0	20.5

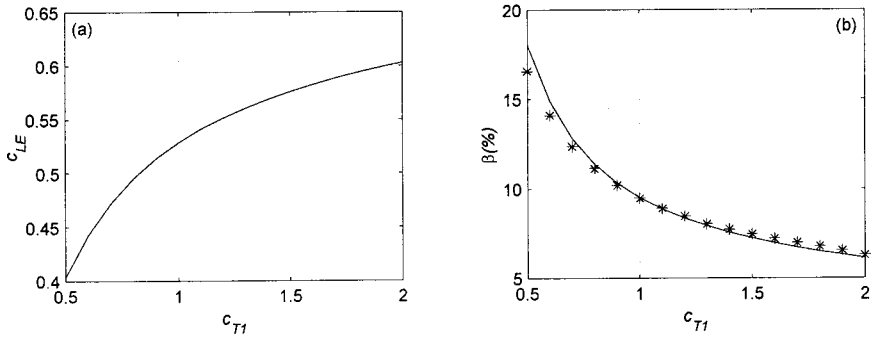

FIG. 5. Interface model for sound reflection. The panel parameters are those of default except c_{T1}. The frequency is 0.15. (a) is the variation of prevailing wave speed near the leading edge against c_{T1}, and (b) shows the agreement between the actual sound reflection coefficient β (shown as $*$) and that predicted by the interface model R_{int} (shown as the solid line).

$c_T=0.2$ We first calculate for the frequency of $f=0.15$ for which the results are listed at the second and third columns of Table I. For the tapered panel, the actual wave speed $c(x)$ varies from 0.52 at the leading edge towards 0.1 at the trailing edge, but for the uniform panel, the subsonic wave is dominated by the supersonic wave of speed 1.14; supersonic eigenvalue being identified in the previous study (Huang, 1999). Since the wave speed is very close to unity, very little reflection occurs. Damping takes away 49.4% of the sound energy, which is much lower than 90.5% on the tapered panel. This clearly demonstrates the utility of panel tapering. We then test a lower frequency of $f=0.05$ at which supersonic wave is avoided in the uniform panel. The results are shown at the last two columns of Table I. It is found that the tapered panel has a higher wave speed near the leading edge and the reflection is much lower than that of the uniform panel. But the much improved damping compensates for the overall performance in transmission loss. In fact the tapered panel has a TL of 25.0 dB while the uniform panel has 20.5 dB.

C. Modelling of the sound reflection

When using tapered panels, one wishes to maximize sound absorption coefficient α, but absorption cannot occur for sound reflected at the leading edge of the panel. In this section, we attempt to model the sound reflection coefficient β so that ways may be found to minimize it. As shown in the typical case of Fig. 3(b), the actual wave speed $c(x)$ is rather constant at the first one third of the panel length where the intensity of the upstream travelling sound, I_-, is significant. We model the sound reflection by the panel by replacing the panel with a hard wall and filling the whole downstream duct with another fluid with the density of air but a speed of sound equivalent to the prevailing flexural wave speed at the upstream portion of the panel denoted as c_{LE}. c_{LE} may be calculated by averaging the phase speed $c(x)$ over the first 25% of the panel length. For example, for the basic case shown in Fig. 3(b), c_{LE} is found to be 0.52. We call this interface model. The panel is finite but the damping used in the default setting is expected to eliminate substantial flexural wave reflection at the trailing edge, which provides some ground for optimism for the interface model. The reflection at such interface is

$$R_{\text{int}}=\left(\frac{1-c_{\text{LE}}}{1+c_{\text{LE}}}\right)^2.$$

For the default panel setting, $c_{\text{LE}}=0.52$ and $R_{\text{int}}=10.0\%$, comparing well with the actual result of $\beta=9.5\%$. We now vary the panel property by changing c_{T1} from 0.5 to 2.0 in order to change c_{LE} to validate the interface model. The result is shown in Fig. 5, which shows good agreement. Should c_{LE} reach unity, sound reflection might be eliminated.

Having identified the deviation of c_{LE} from unity [as shown in Fig. 5(a)] as the main source of sound reflection, we now focus on why $c_{\text{LE}}<c_{T1}$. The reason is that the air imposes virtual mass on the panel. For waves travelling to the right at constant speed c, the virtual mass may be found as

$$m_a=\frac{p}{i\omega V}=\frac{\coth k_a}{k_a},\quad k_a=\sqrt{\left(\frac{\omega}{c}\right)^2-\left(\frac{\omega}{c_0}\right)^2}$$

(Huang, 1999). When $c\to c_0=1$, $k_a\to 0$, $m_a\to\infty$. For $c<1$, lower frequency gives lower k_a, hence higher virtual mass. As $\omega\to 0$, $k_a\to 0$, $m_a\to\infty$, whatever the wave speed c. This analysis does not account for the fact that, near the leading edge, the panel experiences standing flexural waves,

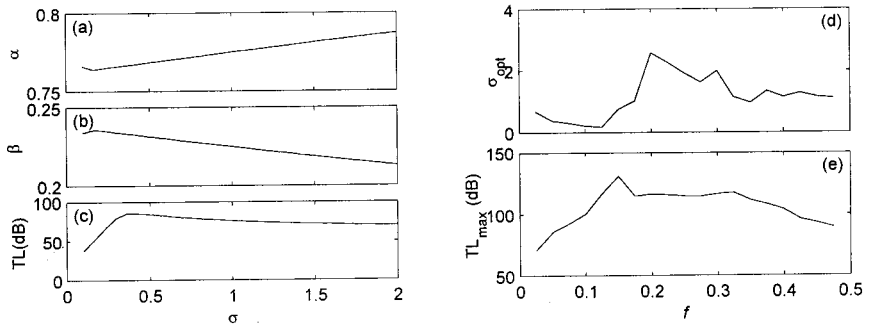

FIG. 6. Effect of damping parameter σ. (a) gives the sound absorption coefficient α, (b) gives the reflection coefficient β, and (c) shows the corresponding TL. All are calculated for $f=0.15$. (d) and (e) are the optimal damping coefficient σ and maximum TL, determined by the peak in (c), as a function of frequency.

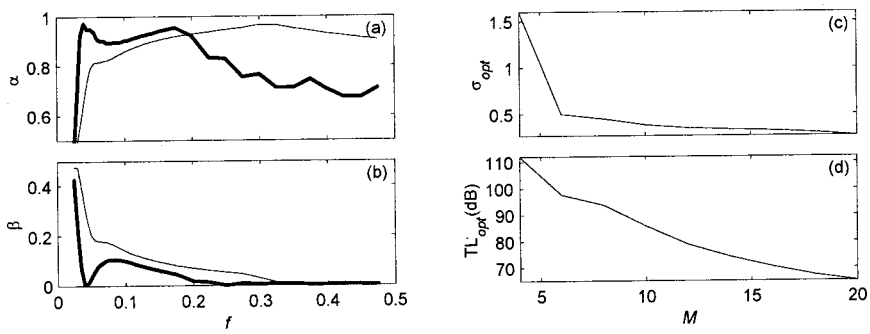

FIG. 7. Effect of mass on spectral performance and optimal damping. For (a) and (b) the thin solid lines are for the default panel of $M=10$, $\sigma=0.05$ while the thick one is for the heavy panel of $M=30$, $\sigma=0.05/3$. The loss factor σ is reduced so that the effective energy damping determined by $M\sigma$ is the same. For (c) and (d) the frequency is 0.05.

but the virtual mass factor could play an important role, especially where the panel is thin.

D. Optimal damping

For the moderate frequency of $f=0.15$, the variations of sound absorption and reflection coefficients with the material loss factor σ are shown in Figs. 6(a), (b), and (c) for the default panel setting. Damping reduces reflection β and increases absorption α over almost the whole range of σ shown above, but the total transmission loss has a peak at $\sigma=0.38$. The variation of the optimal loss factor (σ_{opt}) with frequency is shown in Fig. 6(d). Note that, for short panels, the curve of this relationship exhibits a highly oscillatory behavior. The maximum transmission loss achieved with the optimal loss factor is shown in Fig. 6(e).

E. The effects of mass and tension

The variation with panel mass M is studied by raising M while keeping $M\sigma$ constant since the latter determines the damping coefficient D. The results are shown in Figs. 7(a) and (b) covering the whole frequency range. The thick lines are for the heavier panel which has $M=30$. The heavier panel has less sound reflection over the whole frequency range. The reason is that the virtual mass that air imposes on the vibrating panel is relatively small and, as a result, the actual wave speed near the leading edge, c_{LE}, is closer to its *in vacuo* value c_{T1}. The absorption coefficient α increaseas at frequencies less than about 0.2 in the example but decreases at higher frequencies. The increase is related to the reduction in sound reflection but the decrease is associated with the lack of response from heavier panels at high frequencies. In Figs. 7(c) and (d) the effect of mass on the optimal loss factor σ_{opt} and the corresponding optimal transmission loss TL_{opt} are presented for the frequency of 0.05. The conclusion is that heavy panels cannot take advantage of higher damping.

The effects of tension are studied by increasing or decreasing the values of c_{T1} and c_{T2} proportionally so that the shape of $c_T(x)$ remains unchanged. Panels with higher tension are represented by thinner lines in Fig. 8. The thinnest line is for the case of $T=1.55$, $c_{T1}=2$, $c_{T2}=0.2$, while the thickest line is for the case of $T=0.097$, $c_{T1}=0.5$, $c_{T2}=0.05$. When the tension is increased, sound reflection reduces and absorption increases, although at very low frequency range there are considerable spectral oscillation, as expected. For panels with higher c_{T1}, the actual c_{LE} is closer to unity, hence less reflection. Notice that the increase in c_{T2} and $c_T(x)$ in general should not favor wave absorption, given the same amount of incident flexural waves, but the absorption coefficient is increased for panels with higher tension in this case. The reason is that the damping coefficient chosen for the default panel is high enough to absorb the increased amount of energy in the excited flexural waves.

F. Frictionless panels

Now we discuss cases where the finiteness of the panel plays an important role in sound reflection by considering frictionless panels. We first consider short panels of length $L=10$, and the distributions of left-travelling sound intensity, $I_-(x)$, are shown in Figs. 9(a) and (b). Figure 9(a) is for the frequency of $f=0.05$ and Figure 9(b) is for the frequency of 0.06. The oscillatory pattern of $I_-(x)$ is indicative of interference of sound waves reflected from different parts of the tapered panel. In the case of Fig. 9(a), the total intensity of the reflected sound at the leading edge is at the peak of the variation pattern, and β is 96.5%. In the case of Fig. 9(b), however, one can see values of I_- in excess of 0.5 (i.e.,

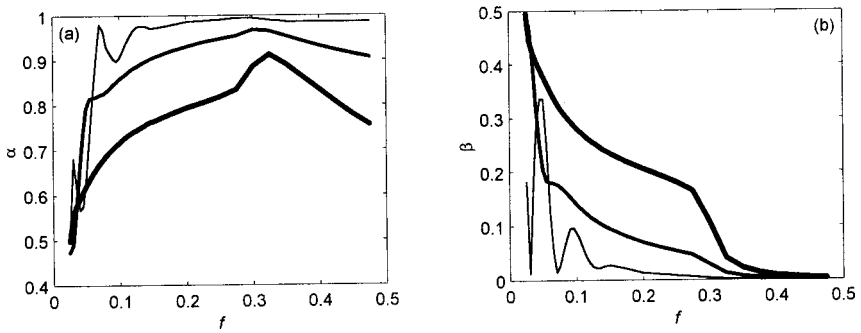

FIG. 8. Effect of tension on sound absorption coefficient α and reflection coefficient β. The panel properties are those of default except the thin line has tension four times the default value of $T=0.39$ (medium thickness line) while the thickest line has a quarter of the default tension.

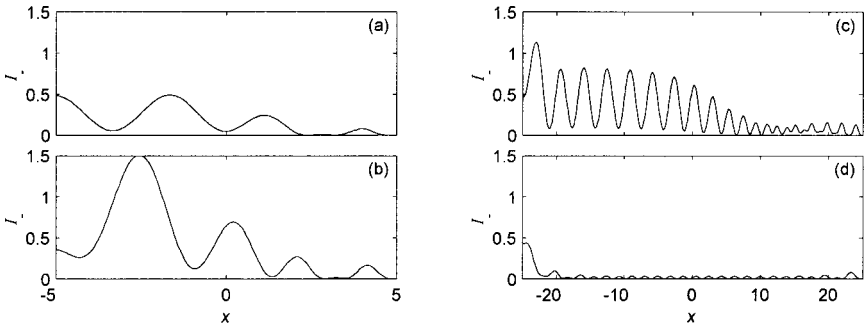

FIG. 9. Distributions of intensity of upstream travelling sound. The four cases are (a) $L=10$, $f=0.05$, $\beta=96.5\%$, (b) $L=10$, $f=0.06$, $\beta=71.0\%$, (c) $L=50$, $f=0.05$, $\beta=92.5\%$, (d) $L=50$, $f=0.05$, uniform panel of the same tension ($T=0.39$), $\beta=85.2\%$.

$\beta=1$) locally, but the total reflection is only 71.0% as the leading edge emerges near the bottom of the interference pattern. Figures 9(c) and (d) are for the default panel length of 50 and the frequencies are both 0.05. Figure 9(c) is for the tapered panel while Fig. 9(d) is for the uniform panel subject to the same tension as the tapered panel. The tapered panel has 92.5% sound reflection but the uniform panel has only 85.2%. The axial variation of $I_-(x)$ again suggests constructive and destructive interference of the reflection waves on the tapered panel. The lack of such varitaion on the uniform panel indicates that there is little reflection except around the leading edge. The prevailing wave speed near the leading edge (c_{LE}) is 0.33, 0.30, 0.33, and 0.52 for the four cases, and the corresponding reflection coefficients according to the interface model are 25%, 29%, 25%, 10%, respectively. The actual reflection in these cases are all much higher. This is because, on a frictionless panel, there is strong reflection of flexural waves by the trailing edge, $V_-(x)$, which radiates sound upstream very effectively.

The variation of wave reflection with the panel length is given in Fig. 10 for the frequency of $f=0.15$. The thick solid line is for the tapered panel, which shows a persistent performance when used as a noise reflector. The other two lines are for uniform panels with the same *in vacuo* wave speed of $c_T=0.20$, the solid line is for mass $M=10$, which is the same as the tapered panel, while the dashed line is for a light panel of $M=1$. The heavy uniform panel hardly reflects any sound except at a few discrete points, which is why we introduce the light one for comparison. The reflection is higher on the light uniform panel but passbands exist, which is typical of conventional reactive mufflers.

G. Performance of panel muffler

For the purpose of passive control of duct noise, $L=50$ is too long. $L=10$ would be more practical. One may always design smaller channels (smaller h^*) so the dimensional length $L^*=h^*L$ may be limited. But for the same panel material and thickness, the dimensionless mass parameter, $M=M^*/\rho_0^* h^*$, becomes higher and the dimensionless frequency $f=f^*h^*/c_0^*$ of interest will be shifted towards the lower range. Our task now is to design a muffler which would give high transmission loss over the whole frequency range of $f\in(0,0.5)$. We compare the performance of the following two panel settings, the first being similar to the default:

(1) $M=10$, $L=10$, $\sigma=0.05$, $c_{T1}=1$, $c_{T2}=0.1$;
(2) $M=10$, $L=10$, $\sigma=0.15$, $c_{T1}=2$, $c_{T2}=0.025$.

The second setting has a higher loss factor and a larger range of thickness tapering, the results are shown in thick lines in Fig. 11 in the form of one-third octave averaging starting from a dimensionless center frequency of 0.0275. In general the highly tapered and damped panel experiences more sound reflection and less absorption except at very low and high frequencies. The example shows that, by appropriate adjustment, it is possible to have a rather good performance over the whole frequency range of plane waves. The performance shown here is comparable to that of a typical lined duct, cf. Beranek (1992), which gives somewhere between 3 dB and 4 dB attenuation per unit distance h^* at the optimal frequency. At very low frequencies such as $f=0.0275$ (for a duct of 20 cm in height, $f^*=0.0275\times340/0.2=47$ Hz) lined ducts normally achieves some 0.6 dB per channel height using very resistive porous material, cf. Fig. 6.1.4 of Ingard (1994). Note that the latter is compiled for the single-sided duct lining, and the corresponding abscissa value of channel width/wavelength for the double lining channel should be $f/2=0.013\,75$. The TL reading of 0.3 dB is then doubled for the double lining. In our case the corresponding attenuation is 2 dB per h^*. This comparison means that a noise absorber

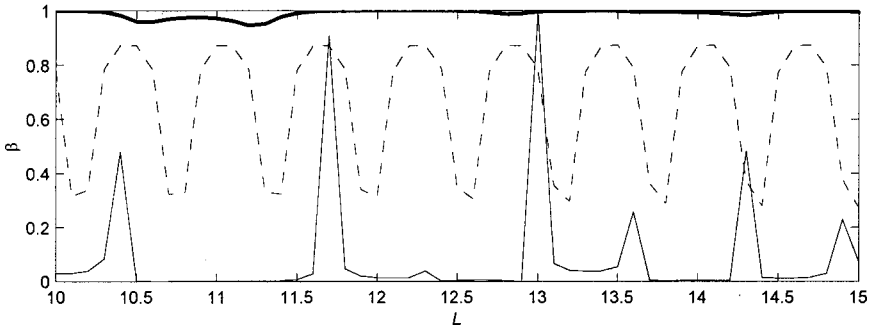

FIG. 10. Sound reflection on frictionless panels at frequency 0.15. The thick solid line is for the tapered panel showing near complete reflection for all length. The thin solid line is for the uniform panel of the same mass $M=10$ and tension. The dashed line is for much lighter uniform panels of $M=1$ and the same $c_T=0.2$.

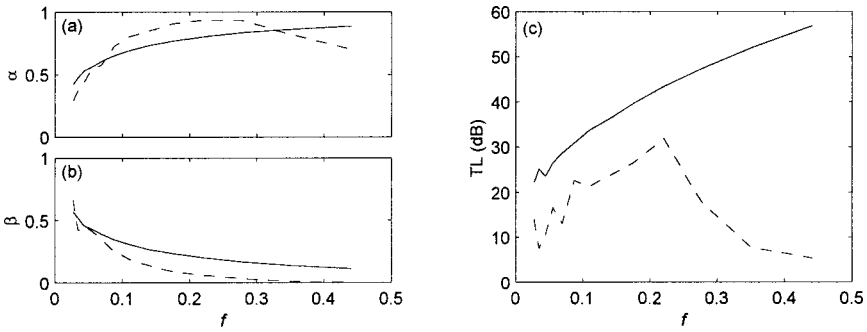

FIG. 11. Comparison of performance of panel muffler of length $L=10$ and $M=10$ in one-third octave band average starting from central frequency of 0.027 55. The thin lines have the default tapering setting of $c_{T1}=1$, $c_{T2}=0.1$, and $\sigma=0.05$, the thick lines are for $c_{T1}=2$, $c_{T2}=0.025$, $\sigma=0.15$.

made of tapered panel could achieve a transmission loss spectrum flatter than that of the conventional means.

IV. CONCLUDING REMARKS

If a flexible panel is to be used as a muffler for passive noise control in a duct, it is desirable to have low reflection and high absorption. For energy absorption to be effective, sound must first be transferred from air to the flexural waves in structure. The energy transfer takes place when sound couples strongly with the wall vibrations, but significant sound reflection occurs near the panel leading edge if the coupling is spatially abrupt. To suppress such reflection, the phase speed of the coupled wave must approach the isentropic speed of sound in free space. But a perfect match is difficult to achieve at low frequencies since air imposes high virtual mass on the vibrating panel whose actual wave speed differs from its *in vacuo* value. Typically, sound energy is pumped into the structure near the leading edge and it gets absorbed by the internal friction of the panel as it travels downstream. The distribution of the local phase speed can be made to follow closely a decreasing *in vacuo* wave speed $c_T(x)$, which should have a smooth profile to avoid significant sound reflection along the length. Damping of flexural wave energy is enhanced by the slowing down of the waves. It may be said that similar idea of using tapered structure for energy damping was attempted in vibration isolation (Ungar and Kurzweil, 1984). The use of sound absorption wedges in anechoic chambers is another example of the same philosophy. A high degree of sound absorption may be achieved this way and the transmission loss spectrum can be rather flat for the whole frequency range of the fundamental duct acoustic mode. Although there are many realistic factors excluded from our theoretical modelling, the fact that such a flat spectrum is possible at all with tapered wall panels is an encouraging sign worthy of further studies.

If the tapered panel has no damping, however, sound reflection occurs all along the panel length. There is strong interference of reflection sound waves radiated by different parts of the panel, but the overall sound reflection can be much higher than that on a uniform panel. In addition, passband is effectively removed and this phenomenon alone is potentially useful in designing reactive muffler using tapered panels. One of the potential advantages of such a muffler is that it does not change the duct passage area, which means zero extra pressure loss.

ACKNOWLEDGMENT

Funding support from the Research Grants Committee of the Hong Kong SAR and the Hong Kong Polytechnic University is gratefully acknowledged.

Ackermann, U., and Fuchs, H. V. (**1989**). ''Noise reduction in an exhaust stack of a papermill,'' Noise Control Eng. J. **33**, 57–60.

Ackermann, U., Fuchs, H. V., and Rambausek, N. (**1988**). ''Sound absorbers of a novel membrane construction,'' Appl. Acoust. **25**, 197–215.

Berry, B. S. (**1992**). ''Damping mechanisms in thin-layer materials,'' in *M3D: Mechanics and Mechanisms of Material Damping*, edited by V. K. Kinra and A. Wolfenden, ASTM STP 1169 (American Society for Testing and Materials, Philadelphia), pp. 28–44.

Beranek, L. L. (**1992**). *Noise and Vibration Control Engineering: Principles and Applications* (Wiley-Interscience, New York).

Cummings, A. (**1994**). ''Attenuation of sound in unlined ducts with flexible walls,'' J. Sound Vib. **174**, 433–450.

Doak, P. E. (**1973**). ''Excitation, transmission and radiation of sound from source distributions in hard-walled ducts of finite length (I): the effects of duct cross-section geometry and source distribution space-time pattern,'' J. Sound Vib. **31**, 1–72.

Ford, R. D., and McCormick, M. A. (**1969**). ''Panel sound absorbers,'' J. Sound Vib. **10**, 411–423.

Frommhold, W., Fuchs, H. V., and Sheng, S. (**1994**). ''Acoustic performance of membrane absorbers,'' J. Sound Vib. **170**, 621–636.

Huang, L. (**1999**). ''A theoretical study of duct noise control by flexible panels,'' J. Acoust. Soc. Am. **106**, 1801–1809.

Ingard, K. U. (**1994**). *Notes on Sound Absorption Technology* (Noise Control Foundation, New York).

Ungar, E. E. (**1997**). ''Vibration isolation and damping,'' *Handbook of Acoustics*, edited by M. J. Crocker (Wiley-Interscience, New York), Chap. 55.

Ungar, E. E., and Kurzweil, L. G. (**1984**). ''Structural damping potential of waveguide absorbers,'' in *Proceedings of Inter-Noise 84* (Noise Control Foundation, Poughkeepsie, New York, 1985), pp. 571–574.

A study of time-domain FXLMS algorithms with control output constraint

Xiaojun Qiu and Colin H. Hansen
Department of Mechanical Engineering, The University of Adelaide, South Australia 5005, Australia

(Received 14 July 2000; accepted for publication 28 February 2001)

A single input, single output active noise control system using the time-domain Filtered-X LMS algorithm with output constraint is investigated. The constraint on the output of the control filter is applied by three different methods: the leakage algorithm based on the transformation method using a penalty function; the re-scaling algorithm based on the active set method; and the simple practical (clipping) algorithm which just clips the output if a constraint is encountered. A comparison of the three algorithms shows that the re-scaling algorithm can usually work successfully under the constraint, while the leakage algorithm usually needs a large leakage coefficient to satisfy the constraint with a resulting performance loss. The clipping algorithm has potential problems both with the stability and convergence speed. © *2001 Acoustical Society of America.*
[DOI: 10.1121/1.1367247]

PACS numbers: 43.50.Ki [MRS]

I. INTRODUCTION

In some active noise and vibration control applications, the total power of the control signal or the amplitude of the individual control signal is limited, either because the system being controlled does not allow large injected power or the actuators used for control have limited driving capability. For example, when vibration actuators are used in aircraft to reduce the interior noise, an excessively large control power input to the aircraft body may reduce the fatigue life due to the spillover of the control energy.[1] Examples of constraints on the individual control signal amplitude can be found where smart foam (driven by an embedded PVDF element) or electrostrictive polymer film are used as acoustic sources for sound radiation control,[2,3] and where the piezoceramic patches are used to control power transformer noise by controlling the tank vibration.[4]

The filtered-X least mean square (FXLMS) algorithm is widely used for adapting the coefficients of a finite impulse response (FIR) filter for active noise control applications.[5–9] A common practical way to constrain the output amplitude is to use leakage during the updating of the control filter coefficients. This is a method based on using a penalty function, which transforms the constrained optimization problem into an unconstrained optimization problem by using Lagrange multipliers, leading to a very simple form which is effectively the same as the multiple error LMS algorithm with leakage.[10,11] Similar ideas were used for chemical plant process control, where an analysis of the robust stability of the quadratic dynamic matrix method with hard output constraints was given.[12]

The method of using leakage has several additional advantages in practical applications. For example, if a fixed point processor is used, leakage is also useful for reducing the accumulation of numerical error due to the finite-precision implementation.[7,11] For a multiple feedforward active control system, increasing the value of the leakage coefficient can always stabilize the control system at the expense of a degradation in the steady-state error reduction.[9] However, the method does not guarantee that the control output remains within any specified constraint and the selection of the value of the leakage coefficient can only be done using a trial and error procedure.

Many approaches have been put forward in the past for solving constrained optimization problems and they mostly fall into two categories: function modification followed by unconstrained optimization and direction modification without altering the function.[13–17] The first type of approach seeks to define a new function that has an unconstrained optimum at the same point as the optimum of the given constrained problem. Optimization of this new function then defines the required change in search direction. For the second type of approach, some methods attempt to follow a constraint while others try to rebound from the constraints and so continue the search in the feasible region.

The common method of using leakage in active noise control system belongs to the first category. The main advantage of it is that the constraints are virtually ignored; but there are serious disadvantages such as the true function might not be optimized and the constraints might be violated during optimization. A new method is proposed here for applying constraints to the FXLMS algorithm, which belongs to the second category of constrained optimization approaches and these are usually more efficient than the first type of approach. With the new method, the constraints are guaranteed not be violated during the optimization and the true function is optimized. The third method that is also discussed in the paper is a simple method that is often used in practical situations. Here this latter method is shown to have potential problems with stability and convergence speed.

In this paper, the three different methods are used to apply constraint to the control output in a single input, single output (SISO) active noise control system and the behavior of each is compared and discussed. Note that there is also an algorithm called the constraint filtered-X algorithm,[18] which uses modified residuals for the coefficient updating. This al-

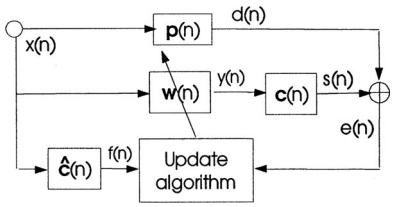

FIG. 1. Block diagram of a SISO adaptive feedforward active control system.

gorithm is not relevant to the control output amplitude constraint problem discussed here.

II. DESCRIPTION OF THE METHODS

A block diagram of the SISO adaptive feedforward control arrangement considered in the paper is shown in Fig. 1, where the primary disturbance $d(n)$ comes from the convolution of the reference signal $x(n)$ with the impulse response function of the physical structural/acoustic system $\mathbf{p}(n)$. The leakage algorithm comes from applying constraints by modifying the cost function that is to be minimized during adaptation.[6–10] For example, the cost function could be modified as

$$J(n)=e^2(n)+0.5\alpha\mathbf{w}^T(n)\mathbf{w}(n), \tag{1}$$

where $e(n)$ is the error signal and $\mathbf{w}(n)$ is the $(L\times 1)$ vector of control filter weights at time n:

$$\mathbf{w}(n)=[w_0(n)\, w_1(n)\, \ldots\, w_{L-1}(n)]^T. \tag{2}$$

Assuming that the cancellation path transfer function $\mathbf{c}(n)$ can be modeled in the time-domain as an M-order finite impulse response function (vector) $\hat{\mathbf{c}}(n)$ (it is time-varying in most practical situations; however, it is assumed to be constant here),

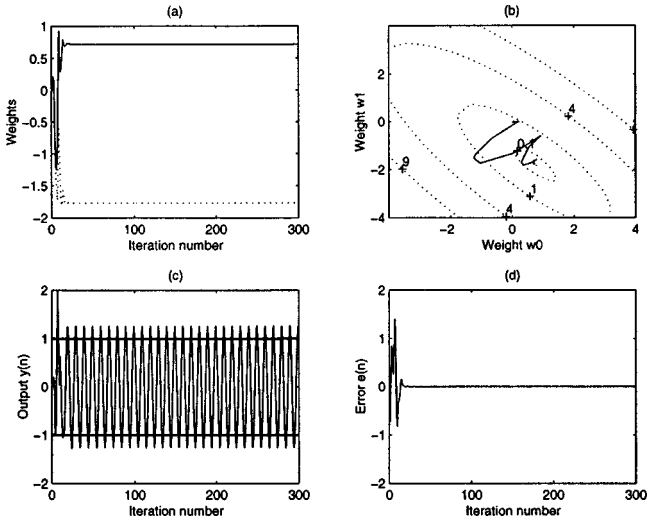

FIG. 2. Performance of the FXLMS algorithm (the leakage algorithm with $\alpha=0$, $\mu=0.5$): (a) variation of the control filter weights with iteration number, the dashed curve is for w_1 and the solid curve is for w_2; (b) convergence path of the control filter weights against contours of the mean square error $E\{e^2(n)\}$; (c) variation of the control filter output with iteration number; the thick lines show the constraints; (d) variation of the error signal with iteration number.

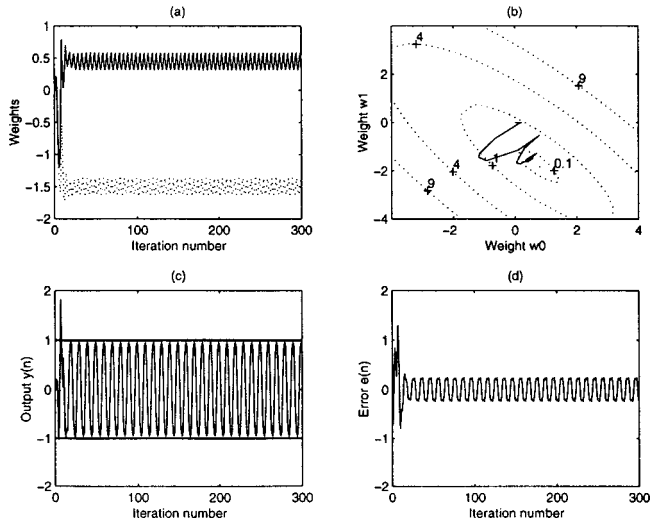

FIG. 3. Performance of the leakage algorithm with $\alpha=0.08$, $\mu=0.5$: (a) variation of the control filter weights with iteration number; the dashed curve is for w_1 and the solid curve is for w_2; (b) convergence path of the control filter weights against contours of the mean square error $E\{e^2(n)\}$; (c) variation of the control filter output with iteration number; the thick lines show the constraints; (d) variation of the error signal with iteration number.

$$\hat{\mathbf{c}}(n)=\mathbf{c}(n)=[c_0\, c_1\, \ldots\, c_{M-1}]^T \tag{3}$$

then the control signal at the location of the error sensor $s(n)$ can be expressed as the convolution of the control filter output vector $\mathbf{y}(n)$ and $\mathbf{c}(n)$

$$s(n)=\mathbf{y}^T(n)\mathbf{c}(n), \tag{4}$$

$$\mathbf{y}(n)=[y(n)\, y(n-1)\, \ldots\, y(n-M+1)]^T, \tag{5}$$

$$y(n)=[x(n)\, x(n-1)\, \ldots\, x(n-L+1)]^T\mathbf{w}(n). \tag{6}$$

The error signal $e(n)$ can then be given by the sum of the primary disturbance $d(n)$ and $s(n)$

$$e(n)=d(n)+s(n). \tag{7}$$

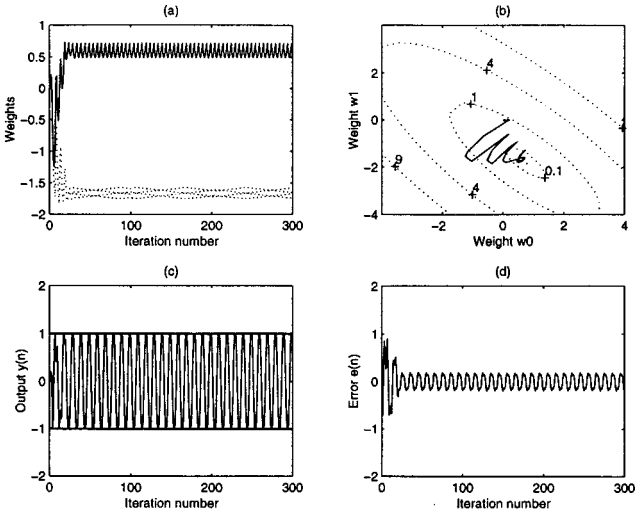

FIG. 4. Performance of the re-scaling algorithm with $\mu=0.5$: (a) variation of the control filter weights with iteration number; the dashed curve is for w_1 and the solid curve is for w_2; (b) convergence path of the control filter weights against contours of the mean square error $E\{e^2(n)\}$; (c) variation of the control filter output with iteration number; the thick lines show the constraints; (d) variation of the error signal with iteration number.

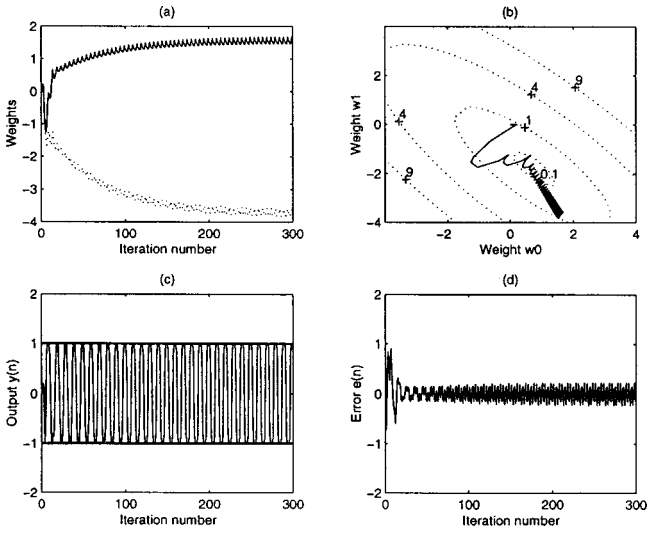

FIG. 5. Performance of the clipping algorithm with $\mu=0.5$: (a) variation of the control filter weights with iteration number; the dashed curve is for w_1 and the solid curve is for w_2; (b) convergence path of the control filter weights against contours of the mean square error $E\{e^2(n)\}$; (c) variation of the control filter output with iteration number; the thick lines show the constraints; (d) variation of the error signal with iteration number.

The resulting leaky FXLMS algorithm is expressed as

$$\mathbf{w}(n+1)=(1-\alpha\mu)\mathbf{w}(n)-2\mu e(n)\mathbf{f}(n), \tag{8}$$

where α is the leakage coefficient, μ is the convergence coefficient, and $\mathbf{f}(n)$ is called the filtered reference signal vector, which is obtained by filtering the reference signal $x(n)$ with $\hat{\mathbf{c}}(n)$:

$$\mathbf{f}(n)=[f(n)\,f(n-1)\,\ldots\,f(n-L+1)]^T, \tag{9}$$

$$f(n)=[x(n)\,x(n-1)\,\ldots\,x(n-M+1)]^T\hat{\mathbf{c}}(n). \tag{10}$$

The constraint equation is

$$|y(n)|<A_{\max}, \tag{11}$$

where $A_{\max}$ is a number (depending on bits of the digital to analog converter of the system) proportional to the maximal allowed voltage of the output.

The problem with the original FXLMS algorithm is that it sometimes fails to satisfy constraint equation (11) during updating. The addition of leakage in Eq. (8) remedies the problem by continual removal, or leakage, of a small value from the weights, which represents a compromise between biasing the control filter weights from the original optimum solution [where the cost function is $e^2(n)$] and bounding the control effort. Therefore the final performance of the control algorithm significantly depends on the value of the leakage coefficient and it is not guaranteed that the final solution will be within the constraint.

It is possible to increase the performance of the leakage algorithm by applying a time-varying leakage coefficient $\alpha(n)$, corresponding to the minimization of a time-varying cost function,[10,11] which, however, will not be discussed in the paper. The leakage algorithm discussed in the paper is confined to the normal adaptive algorithm with a constant leakage coefficient that is most commonly used in active noise control.

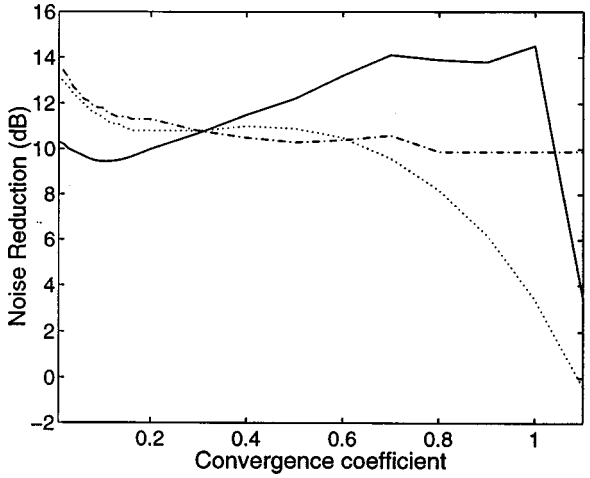

FIG. 6. Noise reduction of the three algorithms as a function of the convergence coefficient for a pure-tone disturbance (··· the leakage algorithm; —— the re-scaling algorithm; ·-·-·- the clipping algorithm).

An alternative way to solve this problem is to use the idea of the active set method (a gradient projection method focused on the solution of the Kuhn–Tucker equations), which is widely used in the field of the constrained optimization to solve the nonlinear programming problem.[13–17] The active set method is an iterative procedure that involves two phases: the first phase calculates a feasible point (a weight vector satisfies the constraint); the second phase generates an iterative sequence of feasible points that converge to the solution. The search direction for generating the sequence of feasibly points is calculated by projecting the gradient along the constraint boundary if the constraint is violated. Depending on the quadratic nature of the objective function and the strictly convex property of the constraint set, the algorithm should converge to the minimum under the constraints.[14] The

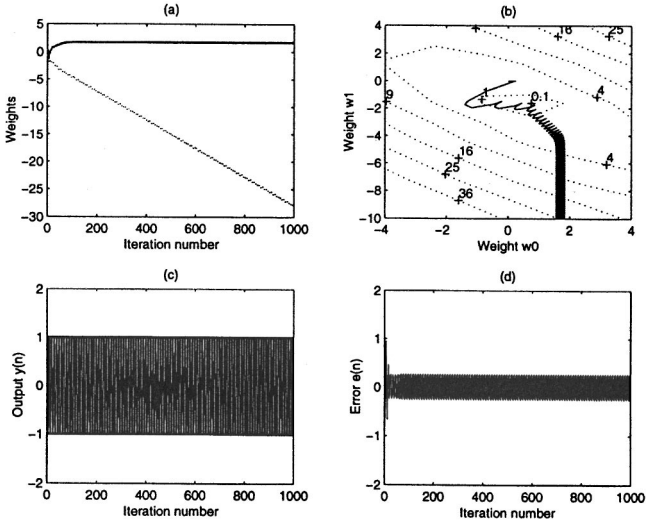

FIG. 7. Performance of the clipping algorithm with $\mu=0.5$, $d(n)=1.3\sin(2\pi f_0 n/f_s+5)$: (a) variation of the control filter weights with iteration number; the dashed curve is for w_1 and the solid curve is for w_2; (b) convergence path of the control filter weights against contours of the mean square error $E\{e^2(n)\}$; (c) variation of the control filter output with iteration number; the thick lines show the constraints; (d) variation of the error signal with iteration number.

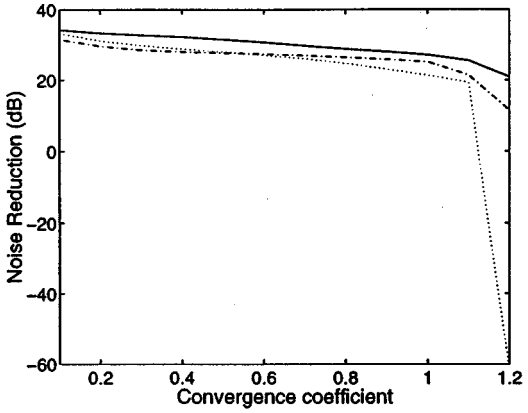

FIG. 8. Noise reduction of the three algorithms as a function of the convergence coefficient for a dual sine wave disturbance (··· the leakage algorithm; —— the re-scaling algorithm; ·-·-·- the clipping algorithm).

algorithm so obtained is called the rescaling algorithm in this paper and is given by

$$\mathbf{w}(n+1)=\mathbf{w}(n)-2\mu e(n)\mathbf{f}(n), \tag{12}$$

$$y(n+1)=[x(n+1)\,x(n)\,\ldots\,x(n-L+2)]^T\mathbf{w}(n+1), \tag{13}$$

if $(|y(n+1)|>A_{\max})$, then

$$\mathbf{w}(n+1)=\mathbf{w}(n+1)(A_{\max}/|y(n+1)|), \tag{14}$$

$$y(n+1)=y(n+1)(A_{\max}/|y(n+1)|). \tag{15}$$

The original FXLMS algorithm uses the estimated gradient $2e(n)\mathbf{f}(n)$ as the weight update vector, which, however, sometimes makes $|y(n)|$ greater than $A_{\max}$ after updating. The proposed algorithm remedies the problem by projecting the estimated gradient into the constraint set to obtain the new updated vector, which is simply obtained in Eq. (14) by re-scaling the control weight vector and control output after the updating. Note, a faster algorithm may exist by using the idea of the affine-scaling algorithm,[15] however, this is outside the scope of this paper.

The re-scaling algorithm is similar to the leakage algorithm in the sense of scaling the values of the filter weights when the output is too large. Actually, the leakage algorithm can be made to be equivalent to the re-scaling algorithm with some kind of specific selection of the noncontinuous time-varying leakage coefficient. For example, the leaky coefficient α is set to zero if the output is small and the leaky part, $(1-\alpha\mu)$ in Eq. (8), is set equal to $A_{\max}/|y(n+1)|$ if the output is greater than the maximal allowed amplitude.[10] However, the re-scaling algorithm originates from an idea that is completely different to the ''leaking'' mechanism that tends to increase the robustness of the system at the cost of the performance.

A method being used in many practical implementations (called the clipping algorithm in this paper) is given by

$$\mathbf{w}(n+1)=\mathbf{w}(n)-2\mu e(n)\mathbf{f}(n), \tag{16}$$

$$y(n+1)=[x(n+1)\,x(n)\,\ldots\,x(n-L+2)]^T\mathbf{w}(n+1), \tag{17}$$

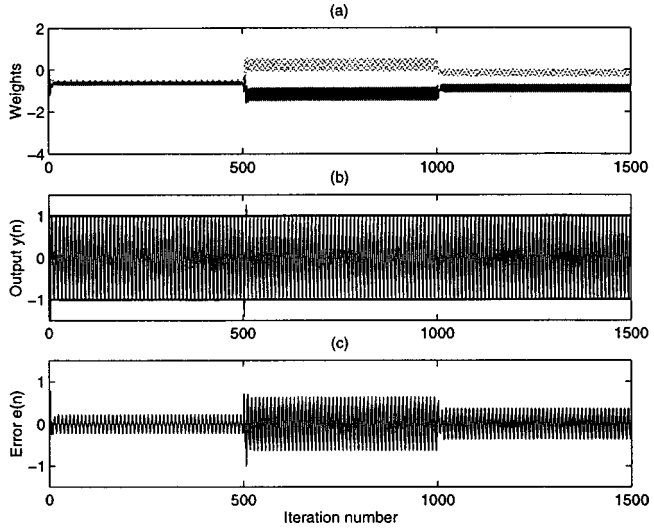

FIG. 9. Performance of the leakage algorithm with $\alpha=0.25$, $\mu=0.5$ for a SISO time-varying system with a pure-tone disturbance: (a) variation of the control filter weights with iteration number; the dashed curve is for w_1 and the solid curve is for w_2; (b) variation of the control filter output with iteration number; the thick lines show the constraints; (c) variation of the error signal with iteration number.

if $(|y(n+1)|>A_{\max})$, then

$$y(n+1)=y(n+1)(A_{\max}/|y(n+1)|). \tag{18}$$

The clipping algorithm is not derived from any kind of optimization theory. In fact, it is just a description of what normally happens in a real control system; for example, the saturation of the actuators, or the limitation of the maximum output of the controller. If the required control output is greater than the allowable upper limit, the easiest solution is to make the control output the same as the upper limit. Note that while this happens, the control output remains unchanged while the control weight vector is still updated. This

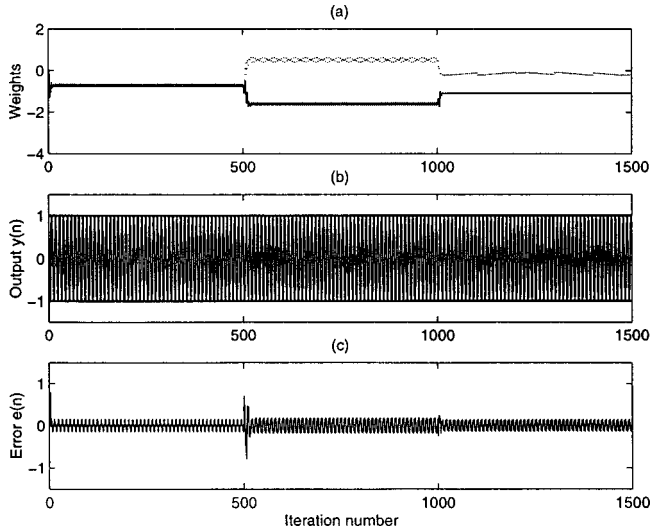

FIG. 10. Performance of the re-scaling algorithm with $\mu=0.5$ for a SISO time-varying system with a pure-tone disturbance: (a) variation of the control filter weights with iteration number; the dashed curve is for w_1 and the solid curve is for w_2; (b) variation of the control filter output with iteration number; the thick lines show the constraints; (c) variation of the error signal with iteration number.

causes potential problems to the controller, as is shown later. The difference between the clipping algorithm and the re-scaling algorithm is that the clipping algorithm just re-scales the output instead of re-scaling both the output and the control filter weights when a constraint is encountered. As can be seen in the text, the clipping Eq. (18) is the same as the re-scaling Eq. (15), but that Eq. (14) is not applied.

III. SIMULATIONS AND DISCUSSION

For the first simulation, the following definitions were used: the sampling frequency of the system $f_s=2000$ Hz, the frequency of the disturbance $f_0=200$ Hz, $A_{\max}=1.0$, $x(n)=\sin(2\pi f_0 n/f_s)$, $d(n)=1.2\sin(2\pi f_0 n/f_s+5)$, $\mathbf{c}(n)=[0.5\ 0.5]^T$, $\mu=0.5$. For clarity in presenting the results of the simulations, only two weights were used for the control filter, which started from $\mathbf{w}(0)=[0.0\ 0.0]^T$. Figures 2–5 show the results of the above algorithms. The noise reduction NR after convergence is 10.9 dB, 12.2 dB, and 10.4 dB for the leakage algorithm, the re-scaling algorithm, and the clipping algorithm, respectively. For the FXLMS algorithm, the noise reduction tends to be infinitely large in this ideal system. NR is defined as (where $E\{\ \}$ is the expected value)

$$\mathrm{NR}=10\log_{10}(E\{d^2(n)\}/E\{e^2(n)\}). \tag{19}$$

It can be seen from Fig. 2 that the FXLMS algorithm could successfully converge to the optimum and reduced the disturbance to almost zero. However, the control filter output constraint was violated as shown in Fig. 2(c). By a procedure of trial and error, the leakage coefficient α was selected as 0.08, which made the control filter output after convergence lie within the constraint. However, the control filter output still violated the constraint during the early adaptation period, as shown in Fig. 3(c). Also, as shown in Fig. 3(b), the convergence path could not achieve the optimum point (where the cost function is $E\{e^2(n)\}$ due to the leakage) although it probably converged to the optimum solution of the problem where the cost function is $E\{e^2(n)+0.5\alpha\mathbf{w}^T(n)\mathbf{w}(n)\}$. The noise reduction of the leakage algorithm with $\alpha=0.08$ is less than that of the re-scaling algorithm or the clipping algorithm. However, it is possible to increase the NR of the leakage algorithm after convergence by more careful selection of the leakage coefficient, α.

It can be seen from Figs. 4 and 5 that both the re-scaling algorithm and the clipping algorithm were able to reduce the error signal while at the same time maintain the constraint for the current setup. Although the noise reduction of the re-scaling method is higher than the clipping method for the current setup, there may be other setups for which the noise reduction of the clipping method is higher. One big difference between the two methods is that the re-scaling method seemed to stop convergence before it reached the optimum, while the clipping method continued going through the optimum point as seen from Figs. 4(b) and 5(b). The clipping algorithm tended to converge to control filter weights with larger absolute values. Another difference between the two algorithms can be seen from Figs. 4(d) and 5(d), where the clipping algorithm produced many high-frequency components in the residual error signal, which is caused by the simple crude clipping process. In this case, even though the original noise was reduced, the generated uncorrelated high-frequency components may increase the time-domain amplitude of the error signal, as can be seen in Fig. 5(d) after about iteration 30.

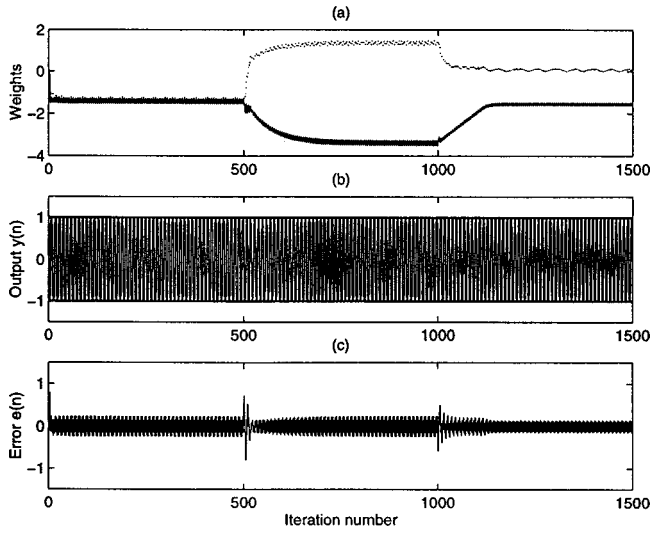

FIG. 11. Performance of the clipping algorithm with $\mu=0.5$ for a SISO time-varying system with a pure-tone disturbance: (a) variation of the control filter weights with iteration number; the dashed curve is for w_1 and the solid curve is for w_2; (b) variation of the control filter output with iteration number; the thick lines show the constraints; (c) variation of the error signal with iteration number.

Figure 6 shows the noise reduction of the three algorithms as a function of the convergence coefficient μ. For the leakage algorithm, the leakage coefficient was selected as $\alpha=0.08$. The convergence coefficient μ was selected from 0.01 to 1.1. This was obtained from a simulation where the FXLMS algorithm without leakage began to diverge when μ exceeded 0.8. Although a smaller μ may achieve better performance, it takes longer to converge. For all the NR calcu-

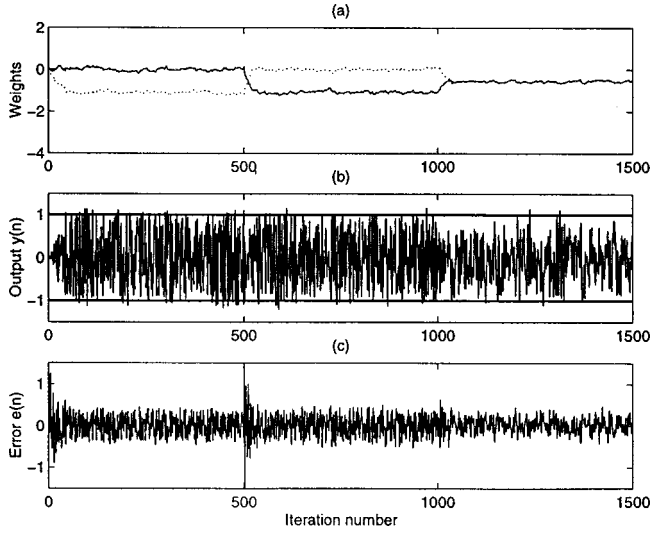

FIG. 12. Performance of the leakage algorithm with $\alpha=0.25$, $\mu=0.1$ for a SISO time-varying system with random noise disturbance: (a) variation of the control filter weights with iteration number; the dashed curve is for w_1 and the solid curve is for w_2; (b) variation of the control filter output with iteration number; the thick lines show the constraints; (c) variation of the error signal with iteration number.

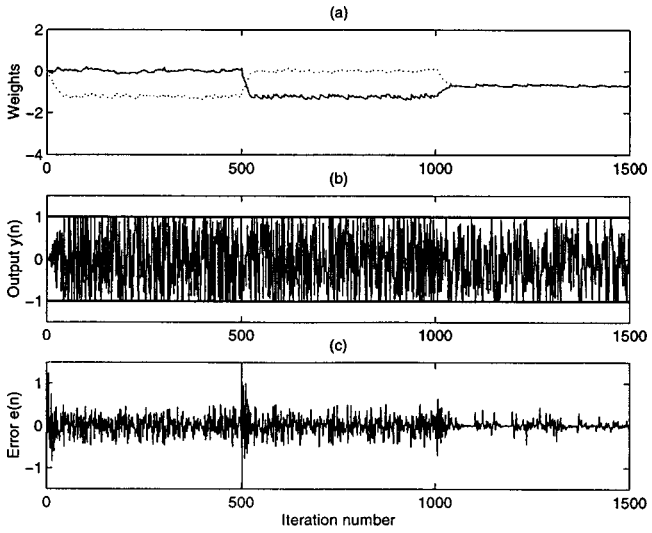

FIG. 13. Performance of the re-scaling algorithm with $\mu=0.1$ for a SISO time-varying system with random noise disturbance: (a) variation of the control filter weights with iteration number; the dashed curve is for w_1 and the solid curve is for w_2; (b) variation of the control filter output with iteration number; the thick lines show the constraints; (c) variation of the error signal with iteration number.

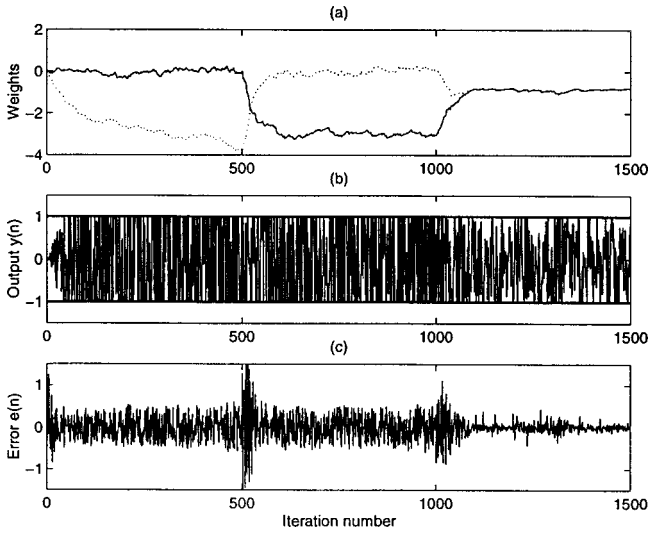

FIG. 14. Performance of the clipping algorithm with $\mu=0.1$ for a SISO time-varying system with random noise disturbance: (a) variation of the control filter weights with iteration number; the dashed curve is for w_1 and the solid curve is for w_2; (b) variation of the control filter output with iteration number; the thick lines show the constraints; (c) variation of the error signal with iteration number.

lations in Fig. 6, NR was obtained by the ratio of $E\{d^2(n)\}$ and $E\{e^2(n)\}$ after the algorithms converged. The curve of the standard FXLMS is still not included in Fig. 6 because the NR of it is very large (can be up to infinite for an ideal system if it can converge). Including it in the figure will make the trends of the other algorithms hard to observe.

It can be seen from Fig. 6 that the performance of each algorithm depends on the value of the convergence coefficient. A small μ results in slow convergence while a μ that is too large results in an unstable system. The introduction of leakage to the FXLMS algorithm increases the upper limit of the convergence coefficient μ for stable adaptation. For example, for the leakage algorithm with $\alpha=0.08$, the algorithm was still able to converge for $\mu=1.1$ although the constraint was violated sometimes in the adaptation. Normally the smaller the μ, the higher the NR achieved. However, the above conclusion is not always true for the NR of the re-scaling algorithm and clipping algorithm, as shown in Fig. 6, where some large μ achieved higher NR. The reason for this is due to the clipping effect, which will be discussed below.

The behavior of the clipping algorithm is interesting. It seems that the smaller the value of μ, the better the performance of the clipping algorithm after it converges. This can be explained by reference to Eqs. (16)–(18). If the control filter output is always less than $A_{\max}$, the clipping algorithm, the re-scaling algorithm, and the FXLMS algorithm without leakage are identical. They can achieve the same level of noise reduction at the same time. However, when the control filter output is greater than $A_{\max}$, the clipping algorithm just clips the output, which makes the control filter updating direction hard to predict as the control output is not linearly related to the control filter weights. Therefore, if a smaller μ is used, then after convergence, the weights may not move further away from the optimum point when the control output is larger than $A_{\max}$, and this results in a better control performance. However, the speed of convergence becomes slower.

The clipping algorithm has an inherent instability problem caused by the unpredictable direction of the control filter updating when a constant is encountered. Figure 7 shows an example, where all the other parameters were the same as the first simulation except that $d(n)=1.3\sin(2\pi f_0 n/f_s+5)$. As can be seen from Fig. 7, although the noise was still attenuated with an NR of 8.9 dB, one of the control filter weights, w_1, became increasingly more negative as the sample number increased. For a fixed-point processor, this causes fixed-point overflow, while for the floating-point processor, an unreasonably large absolute value of a filter weight causes the control filter to not adapt quickly when the disturbance changes.

The reason that the clipping algorithm still had a large NR with an unreasonably large absolute value of a filter weight is because a very large amplitude sine wave is still dominated by the fundamental frequency component after clipping. This is also part of the reason for the large NR achieved by the clipping algorithm and the re-scaling algorithm in Fig. 6, where the convergence coefficient μ is out of the region of stable adaptation ($\mu>0.8$). If the disturbance does not consist of pure tones, the clipping algorithm may not be able to achieve a large NR if the convergence coefficient is quite large or if a weight has an unreasonably large absolute value. Figure 8 shows the noise reduction achieved by the three algorithms as a function of the convergence coefficient for a two sine wave disturbance. For the simulation, $f_s=2000$ Hz, $f_0=200$ Hz, $A_{\max}=1.0$, $\mathbf{p}(n)=[0.6\ 0.6]^T$, $\mathbf{c}(n)=[1.0\ 0.0]^T$, and $x(n)=0.6\sin(2\pi f_0 n/f_s)+0.5\sin(4\pi f_0 n/f_s)$. As can be seen in Fig. 8, the NR achieved by the clipping algorithm is smaller than the re-scaling algorithm. If the primary disturbance is larger, the clipping algorithm might result in larger weights and even worse performance.

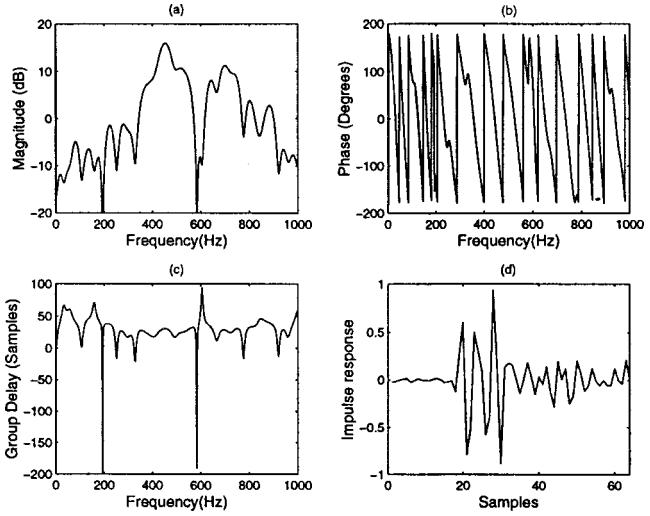

FIG. 15. The measured transfer function between a shaker on a transformer tank and a microphone: (a) magnitude response; (b) phase response; (c) group delay; (d) impulse response.

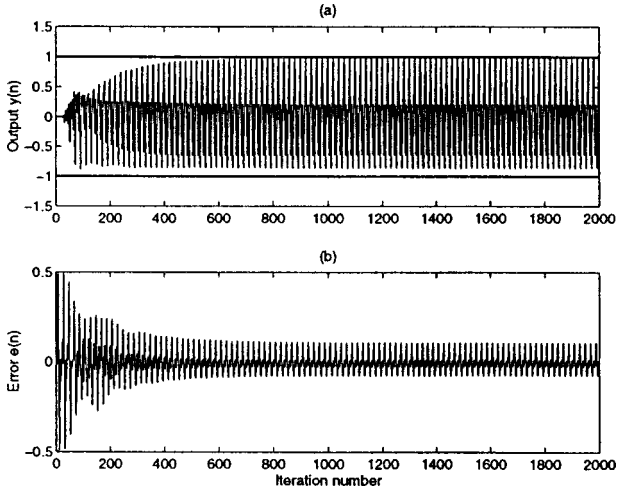

FIG. 16. Performance of the leakage algorithm with $\alpha=0.15$, $\mu=0.01$ for the transformer noise: (a) variation of the control filter output with iteration number; the thick lines show the constraints; (b) variation of the error signal with iteration number.

If the disturbance is so large that the control output cannot achieve the required amplitude, there always exists a certain level of residual error signal. As shown in Eqs. (8), (12), and (16), the amplitude of the update vector is decided by the product of the convergence coefficient μ and the amplitude of the error signal (the filtered reference signal is assumed fixed), so reducing the value of μ will reduce the swung amplitude of the control filter weights. This will usually increase the performance of the algorithm. This can also be seen in Fig. 8, where the smaller the μ, the higher the NR achieved for all three algorithms (remember small μ means slow adaptation).

Some short conclusions can be drawn from the above simulations. First, all three algorithms, the leakage algorithm, the re-scaling algorithm, and the clipping algorithm, are able to reduce the disturbance while at the same time maintain the output constraint. Second, it is normally true for all three algorithms that the smaller the convergence coefficient, the larger the noise reduction, and the slower the adaptation speed. Some exceptions exist for the re-scaling algorithm and the clipping algorithm where the disturbance is a pure tone, in which case a large convergence coefficient resulted in large noise reductions due to the nonlinear effect associated with clipping of a sine wave. Third, the leakage algorithm does not guarantee that the constraint will not be violated, even for a large leakage coefficient (the larger the leakage, the lower the noise reduction); the clipping algorithm sometimes has potential problems with stability and convergence speed due to the large absolute value of the control weights. The re-scaling algorithm seems to be a useful algorithm that can reduce the disturbance and maintain the output constraint at all times. It is also a stable algorithm provided that the convergence coefficient is within the stability constraint for the FXLMS algorithm.

Figures 9–14 further illustrate the behavior of the three algorithms. Figures 9–11 show results of simulations for a time-varying SISO system. During the simulation, the disturbance is a pure tone with a frequency of $f_0=200$ Hz, $f_s=2000$ Hz, $x(n)=\sin(2\pi f_0 n/f_s)$, and $\mathbf{c}(n)=[0.5\ 0.5]^T$. The primary disturbance is time-varying with $\mathbf{p}(n)=[0.0\ 1.2]^T$ for the first 500 samples, and then it is changed to $\mathbf{p}(n)=[1.2\ 0.0]^T$ for the second 500 samples and $\mathbf{p}(n)=[0.6\ 0.6]^T$ for the last 500 samples. The convergence coefficient is set to $\mu=0.5$. Figures 12–14 show results of simulations for a time-varying SISO system where the disturbance $x(n)$ is random noise uniformly distributed on the interval $(-1.0,1.0)$, and $\mathbf{c}(n)=[1.0\ 0.0]^T$. The primary disturbance is also time-varying with $\mathbf{p}(n)=[0.0\ 1.5]^T$ for the first 500 samples, and then changed to $\mathbf{p}(n)=[1.5\ 0.0]^T$ for the second 500 samples and $\mathbf{p}(n)=[0.75\ 0.75]^T$ for the last 500 samples. The convergence coefficient is set to $\mu=0.1$ for this case. For all the cases, the control weights started from $\mathbf{w}(0)=[0.0\ 0.0]^T$ and $A_{\max}=1.0$. Similar comments can again be made for Figs. 9–14. The leakage algorithm does not guarantee that the constraint will be satisfied (see the control output around sample 1, sample 500 and sample 1000 in Fig. 9, and many samples in Fig. 12). The leakage

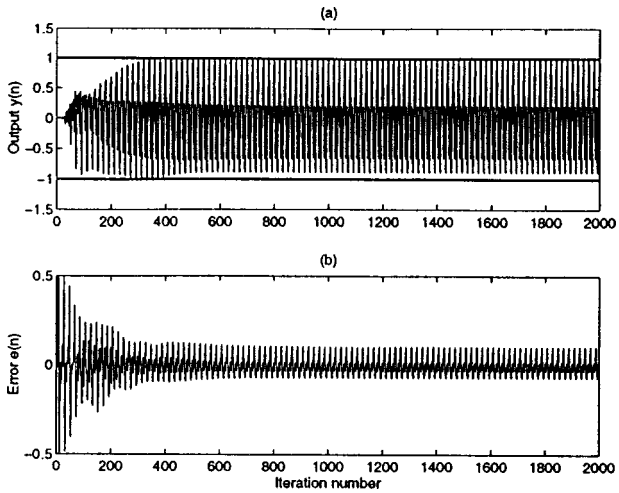

FIG. 17. Performance of the re-scaling algorithm with $\mu=0.01$ for the transformer noise: (a) variation of the control filter output with iteration number; the thick lines show the constraints; (b) variation of the error signal with iteration number.

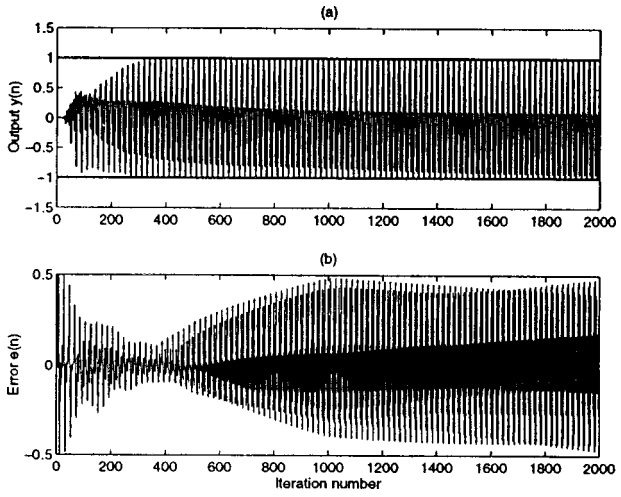

FIG. 18. Performance of the clipping algorithm with $\mu=0.01$ for the transformer noise: (a) variation of the control filter output with iteration number; the thick lines show the constraints; (b) variation of the error signal with iteration number.

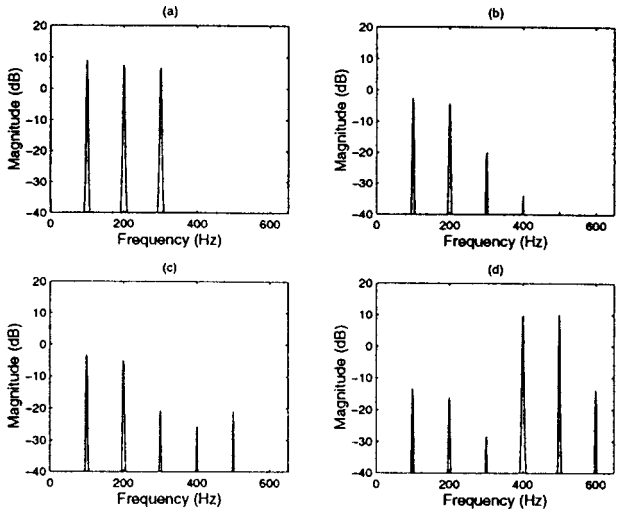

FIG. 19. Spectrum of the error signal for the transformer noise cancellation: (a) without control; (b) with the leakage algorithm; (c) with the re-scaling algorithm; (d) with the clipping algorithm.

coefficient α had to be selected as large as $\alpha=0.25$ so that the control output after convergence would seldom violate the constraint. However, this resulted in poor performance for the leakage algorithm. The clipping algorithm adapted a little slower than the other algorithms due to the large absolute value of the control filter weights. The re-scaling algorithm usually has the smallest residual error signal while satisfying the constraint at all times.

The last simulation used the complicated cancellation path transfer function measured between an inertial shaker attached to the tank of a power transformer and a microphone located about 2 m away from the transformer. The disturbance was the noise radiated by the transformer, which is dominated by 100 Hz, 200 Hz, and 300 Hz components, and was characterized by $d(n)=0.22\sin(2\pi f_0 n/f_s)-0.2\sin(4\pi f_0 n/f_s)+0.18\sin(6\pi f_0 n/f_s)$. The reference signal was $x(n)=\sin(2\pi f_0 n/f_s)+\sin(4\pi f_0 n/f_s)+\sin(6\pi f_0 n/f_s)$, where $f_0=100$ Hz, and the sampling frequency $f_s=2000$ Hz. The cancellation path transfer function was modeled by a 64 tap FIR filter and the length of the control filter was 16 taps. The constraint $A_{\max}$ was set equal to 1.0. Figure 15 shows the spectrum and the impulse response of the measured cancellation path transfer function. Figures 16–18 show the performance of the three algorithms. Figure 19 shows the spectrum of the error signal before and after the three algorithms converged.

It can be seen from Figs. 16–19 that all three algorithms are able to reduce the transformer noise to a certain level within the constraint (without the constraint, the FXLMS algorithm can reduce the noise to almost zero). The leakage coefficient for the leakage algorithm was chosen by trial and error and it did not guarantee that the constraint would be satisfied if the primary disturbance changed. In terms of the time-domain mean square error, the re-scaling method gave the best result with an NR of 13.6 dB, while for the leakage algorithm and the clipping algorithm, the NR was 13.0 dB and -1.4 dB, respectively. However, as can be seen in the frequency domain represented by Fig. 19, the clipping algorithm reduced the 100-Hz, 200-Hz, and 300-Hz components much more than the other two algorithms, but it significantly increases higher-frequency noise. It should be noted that the leakage algorithm and the re-scaling algorithm also introduce a small amount of high-frequency components, as can be seen in Fig. 19.

IV. CONCLUSIONS

A single input, single output active noise control system using a time-domain filtered-X LMS algorithm with output constraint was considered and three different methods were used to apply the constraint to the output of the control filter. These are the leakage algorithm based on the transformation method using a penalty function, the re-scaling algorithm based on the active set method, and the simple practical (clipping) algorithm which just clips the output if a constraint is encountered. Active control of a time-varying sinusoidal and random disturbance of a simple SISO system was simulated as well as simulation of the active control of transformer noise by using the measured cancellation path transfer function. The results show that the re-scaling algorithm works successfully under the output constraint, while the leakage algorithm usually has to use a large leakage coefficient to satisfy the constraint at the cost of performance loss. The clipping algorithm has potential problems both with the stability and convergence speed.

[1] R. H. Cabell and C. R. Fuller, ''A principal component algorithm for feedforward active noise and vibration control,'' J. Sound Vib. **227**, 159–181 (1999).
[2] C. Guigou and C. R. Fuller, ''Adaptive feedforward and feedback control methods for active/passive sound radiation control using smart foam,'' J. Acoust. Soc. Am. **104**, 226–231 (1998).
[3] R. Heydt, T. Kornbluh, R. Pelrine, and V. Mason, ''Design and performance of an electrostrictive polymer film acoustic actuator,'' J. Sound Vib. **215**, 297–311 (1998).
[4] K. Brungardt, J. Vierengel, and K. Weissman, ''Active structural acoustic control of noise from the power transformers,'' *Proc. Noise-Con 97*, 173–182 (Institute of Noise Control Engineering of the USA Inc., Washington, DC, 1997).
[5] B. Widrow and S. D. Stearns, *Adaptive Signal Processing* (Prentice-Hall, Englewood Cliffs, NJ, 1985).

[6] S. J. Elliott and P. A. Nelson, *Active Control of Sound* (Academic, New York, 1992), Chap. 12.
[7] S. M. Kuo and D. R. Morgan, *Active Noise Control Systems—Algorithms and DSP Implementations* (Wiley, New York, 1992), Chap. 3.
[8] C. H. Hansen and S. D. Snyder, *Active Control of Noise and Vibration* (E&FN SPON, London, UK, 1997), Chap. 6.
[9] S. J. Elliott and C. C. Boucher, ''Interaction between multiple feedforward active control system,'' IEEE Trans. Speech Audio Process. **2**, 521–530 (1994).
[10] S. J. Elliott and K. H. Baek, ''Effort constraints in adaptive feedforward control,'' IEEE Signal Process. Lett. **3**, 7–9 (1995).
[11] S. D. Snyder, ''Microprocessors for active control: Bigger is not always enough,'' *Proceedings of Active 99*, 45–63 (Institute of Noise Control Engineering of the USA Inc., Washington, DC, 1999).
[12] E. Zafiriou and A. L. Marchal, ''Robust stability of quadratic dynamic matrix method with hard output constraints,'' Technical research report TR91-2, Systems Research Center, University of Maryland (1991).
[13] R. Fletcher, *Practical Methods of Optimization, Vol. 2, Constrained Optimization* (Wiley, New York, 1981).
[14] P. E. Gill and W. Murray, *Numerical Methods for Constrained Optimization* (Academic, New York, 1974), p. 165.
[15] R. J. Vanderbei, *Linear Programming: Foundations and Extensions* (Kluwer Academic, Boston, 1997), p. 315.
[16] J. J. More and G. Toraldo, ''Algorithms for bound constrained quadratic programming problems,'' Numer. Math. **55**, 377–400 (1989).
[17] A. Dax, ''On computational aspects of bounded linear least squares problems,'' ACM Trans. Math. Softw. **17**, 64–73 (1991).
[18] I. S. Kim, H. S. Na, K. J. Kim, and Y. Park, ''Constraint filtered-X and filtered-U least-mean square algorithms for the active control of noise in ducts,'' J. Acoust. Soc. Am. **95**, 3379–3389 (1994).

Orthogonal acoustical factors of a sound field in a bamboo forest

Hiroyuki Sakai
Graduate School of Science and Technology, Kobe University, Rokkodai, Nada, Kobe 657-8501, Japan

Shozo Shibata
Faculty of Agriculture, Kyoto University, Kitashirakawa-Oiwake, Sakyo, Kyoto 606-8224, Japan

Yoichi Ando
Graduate School of Science and Technology, Kobe University, Rokkodai, Nada, Kobe 657-8501, Japan

(Received 13 September 2000; accepted for publication 18 January 2001)

To investigate the acoustical quality of a sound field in a bamboo forest, acoustical measurements were conducted to obtain orthogonal acoustical factors of the sound field. These results are compared with previous results for a sound field in an ordinary forest [H. Sakai, S. Sato, and Y. Ando, J. Acoust. Soc. Am. **104**, 1491–1497 (1998)]. The IACC, which is defined as a maximum value of the normalized interaural cross-correlation function between signals at the ears, was 0.07 (4 kHz) and 0.16 (2 kHz) at positions 20 and 40 m from the source, respectively. These values are much better than those in the previously investigated forest. The measured subsequent reverberation time T_{sub} was up to 1.5 s in the frequency range above 1 kHz at the position 40 m from the source. For certain music sources with higher frequency components, therefore, sound fields in a bamboo forest have excellent acoustic properties.
[DOI: 10.1121/1.1354988]

PACS numbers: 43.58.Gn, 43.55.Br [SLE]

I. INTRODUCTION

A number of acoustical measurements in outdoor fields involving a forest have been carried out (e.g., Eyring, 1946; Embleton, 1963; Price *et al.*, 1988). The reverberation time and the attenuation of the sound pressure level (SPL) as a function of distance in a forest were also reported (Huisman and Attenborough, 1991). In that study, sound attenuation was investigated in three forests in England under different atmospheric conditions of temperature, humidity, and sound speed. A prediction model that considered excess attenuation by the ground and multiple scattering by trees was used. However, it is quite difficult to estimate sound fields due to the complicated conditions of excess attenuation, multiple scattering effects, temperature, tree leaves, tree distributions, and so on, especially for the higher frequency range.

When a sound field is designed, both temporal and spatial factors must be simultaneously satisfied to achieve a total preference maximum (Ando, 1998). Recent results related to the acoustical quality of sound fields in a forest are briefly introduced here (Sakai *et al.*, 1998). In that paper, the temporal and spatial factors were analyzed and the results were compared with those in a concert hall. First, subsequent reverberation time T_{sub} (see the Appendix for the definition) became larger, mainly in the middle frequency range such as 500 Hz and 1 kHz of the 1/1 octave band center frequency and at measurement points far (40 m) from the sound source. Second, the decay level of reverberation in the forest kept its level after an initial decay as a result of multiple scattering from tree trunks although it normally decreases linearly in an enclosure. Such a decay curve shape is generally considered to be a specific characteristic of a sound field in the forest. Third, IACC, which is defined as a maximum value of the normalized interaural cross-correlation function between signals at the ears within its time duration $\tau = \pm 1$ ms, decreased at positions farther from the source. Finally, SPL relative to that at 5 m from the source decreased by about 12 dB for every doubling of distance, although in a free field it decreases in accordance with the inverse square law.

This paper describes acoustical characteristics in a bamboo forest obtained by using the same procedure for the previous measurements in the forest and in an enclosure. Bamboo is unique for its uniform diameter, hollow tube structure, and rigid surface. In the previous forest, the wavelength of the frequency band that was effective for T_{sub} and IACC, approximately matched the diameters of the tree trunks (0.6 m in average). Thus, a bamboo forest was selected in order to ensure the relationship between the effective frequency band and trunk diameter. In such a sound field, complicated conditions such as multiple scattering from tree trunks, excess attenuation by the ground, trunk distribution, and many atmospherical factors including temperature, humidity, and wind affect the sound field. Considering these factors, the sound field is difficult to simulate and the impulse responses are too complicated to calculate. At the present stage, therefore, the only effective approach is to use measured results.

From binaural impulse responses, orthogonal factors relating to the subjective preference theory of a sound field (SPL, T_{sub}, and IACC), and additional factors (A value, τ_{IACC}, and W_{IACC}) were calculated. Definitions of these factors are described in the Appendix. In this measurement, the initial time delay gap Δt_1 was not obtained because a strong reflection at the initial part of the impulse responses was not observed due to the effects of multiple scattering.

II. MEASUREMENTS

A. Site description

Acoustical measurements were conducted in part of the bamboo forest in Kyoto, Japan in June 1997. The bamboo is

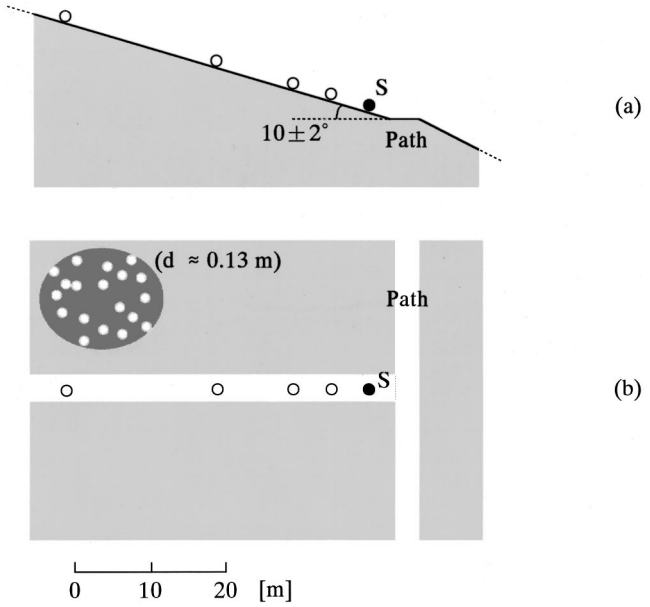

FIG. 1. The bamboo forest investigated. Locations of the sound source and receivers are indicated. Bamboo within the area was all around 0.13 m in diameter. (a) Cross section of the area for measurements; and (b) plan of the area for measurements.

a variety of *Phyllostachys pubescens*. The forest consists of randomly distributed trunks of bamboo. The density of bamboo in the area was about 50 trunks per 100 m^2. Although the tree diameters in the previously studied forest were almost random between 0.3 and 1.0 m, those in the bamboo forest were almost uniform with its diameter about 0.13 m. The height of bamboo around the area was about 8 m. The area had a space about 3 m wide in front of the source without any bamboo. The area in front of the sound source had a gentle slope as shown in Fig. 1(a). On the day when the measurements were conducted, there was no wind, and the temperature was between 25 and 27 degrees centigrade.

B. Procedure

The measuring procedure was exactly the same as for the previous measurements in the forest. Receiver positions for sites, 5, 10, 20, and 40 m from the sound source *S* were selected as shown in Fig. 1. The setup for measurements is illustrated in Fig. 2. An omnidirectional dodecahedron loudspeaker was used as a sound source with its height 1.5 m. As a receiver, a person with a tiny half-inch condenser microphone at each ear.

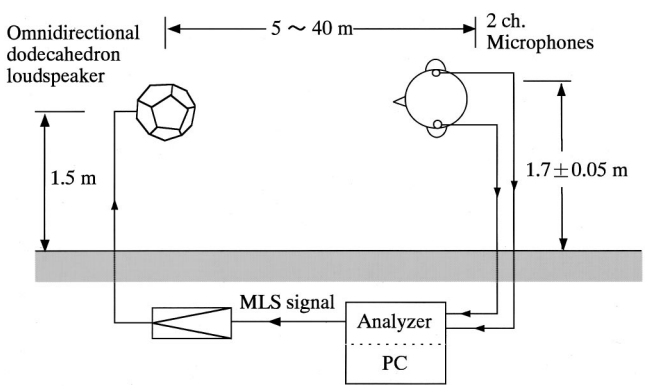

FIG. 2. Setup for acoustical measurements in the bamboo forest.

The maximum length sequence (MLS) (Alrutz, 1981; Alrutz and Schroeder, 1983; Borish and Angell, 1983) was used as a source signal. The signal was radiated from the dodecahedron loudspeaker with its A-weighted SPL 100 dB at 1 m from the source. In this measurement, sequence length was 2.7 s, the number of average was four, and sampling frequency was 48 kHz. Binaural impulse responses (h_l and h_r) at each receiving position were calculated using the Hadamard transform of signals at both ears. All acoustical factors, described in Sec. II C, were calculated from the binaural impulse responses.

C. Calculation

In order to compare the qualities of these sound fields, measurements were conducted to obtain the four orthogonal factors (Ando, 1998): (1) sound pressure level (SPL), (2) initial time delay gap (Δt_1), (3) subsequent reverberation time (T_{sub}), and (4) IACC. In addition, (5) total amplitude of reflections (A), (6) interaural time delay (τ_{IACC}), and (7) width of the interaural cross-correlation function (W_{IACC}) were calculated. Definitions and calculation procedures of the factors are given in the Appendix.

Results of SPL, T_{sub}, and IACC are obtained as values at 1/1 octave band center frequency between 125 Hz–4 kHz. A value, τ_{IACC}, and W_{IACC} are represented as values at A-weighted allpass band. The SPL at each receiving position was obtained relative to the reference point, 5 m from the source.

In these measurements, values for Δt_1 could not be identified in the bamboo forest except for a strong reflection from the ground, because of the weak scattered reflections from the trees. The Δt_1 as an orthogonal factor was defined as the time interval between a direct sound and the first reflection from a sidewall except for reflections from the ground. Hence, the first reflections coming from the ground were neglected in accordance with the definition.

III. MEASURED RESULTS

A. SPL and A

Initial parts (30 ms) of binaural-impulse responses at each position are indicated in Figs. 3(a)–(d). Well-balanced left and right impulse responses were obtained for all receiver positions. The physical factors described in the preceding section were calculated from these impulse responses.

Results for SPL relative to that at 5 m are shown in Fig. 4. The abscissa shows the distance from the source on a logarithmic scale. Decreases ranging from 15 to 30 dB for a doubling of distance from 5 to 10 m were observed in the bamboo forest, whereas the decrease given by the inverse square law (solid line) in a free field is 6 dB. At lower frequency ranges (125 and 250 Hz), interference effects are observed between the direct sound and the reflection from the ground. Namely, between 5 and 10 m, attenuation at 125 Hz was as small as 15.9 dB, but that at 250 Hz was as large

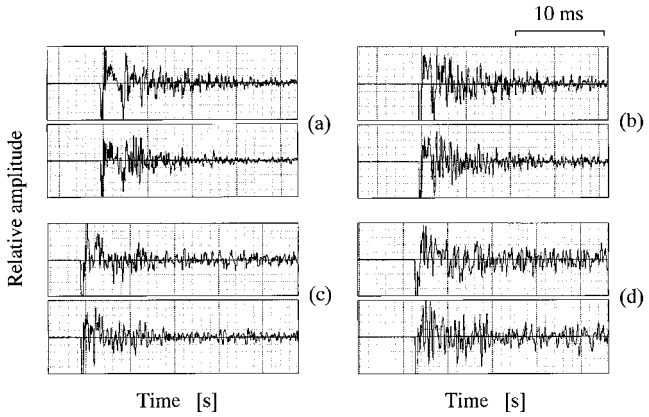

FIG. 3. Initial 30 ms of binaural-impulse responses at each measurement point. The vertical axis of each figure is normalized by the maximum amplitude of each impulse response. Top: impulse response at left ear. Bottom: impulse response at right ear. (a) 5 m; (b) 10 m; (c) 20 m; and (d) 40 m.

as 35.2 dB. On the other hand, at farther positions (10–40 m), the range of decrease was between 6 and 10 dB for a doubling of distance at all frequency bands.

Measured A values with those in the general forest and in the concert hall are shown in Fig. 5. Generally, A value increases with distance, because it represents the total amplitude of reflections in relation to the direct sound. In the bamboo forest, too, A increased with distance, corresponding to an apparent room radius (the position at $A=1$ with the same amplitudes for direct sound and reflections plus subsequent reverberation) of about 10 m from the source. A values in the bamboo forest are distributed between those in the general forest and in the hall. This means that there are many more reflection components in the bamboo forest than in the general forest.

B. T_{sub}

Decay curves of reverberation at 500 Hz and 1 kHz at each receiving position are shown in Fig. 6. Subsequent reverberation components were kept after an initial rapid decrease of 5–10 dB. This tendency is exactly the same as for previous results in the forest. In existing concert halls, decay curves decrease linearly as shown in Fig. 7 (for the Kirishima International Concert Hall, Japan as an example). Results for T_{sub} are shown in Fig. 8. T_{sub} increased with distance and frequency for both 5 and 10 m. For 20 and 40 m, T_{sub} became almost constant above 1 kHz or slightly decreased. T_{sub} had a maximum of 1.5 s at 1 kHz (40 m). Such a longer T_{sub} may be achieved due to multiple scattering effect from the bamboo trunks. For 125 Hz in particular, T_{sub} was as brief as 0.2–0.3 s, compared to those at other frequency ranges.

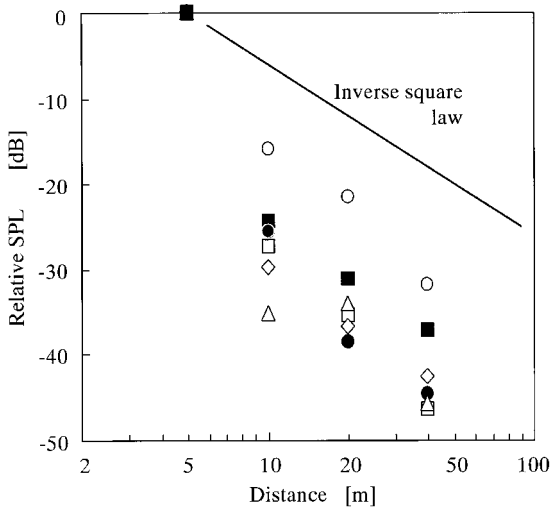

FIG. 4. SPL values relative to that at 5 m. The solid line shows the inverse square law. ○, 125 Hz; △, 250 Hz; ●, 500 Hz; □, 1 kHz; ■, 2 kHz; and ◇, 4 kHz.

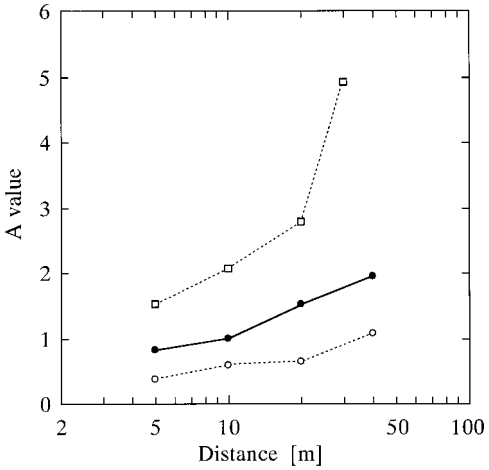

FIG. 5. Measured A values (all-pass band). ●, in the bamboo forest; ○, in the general forest (Kirishima Shrine, Japan); and □, in the concert hall (Kirishima International Concert Hall, Japan).

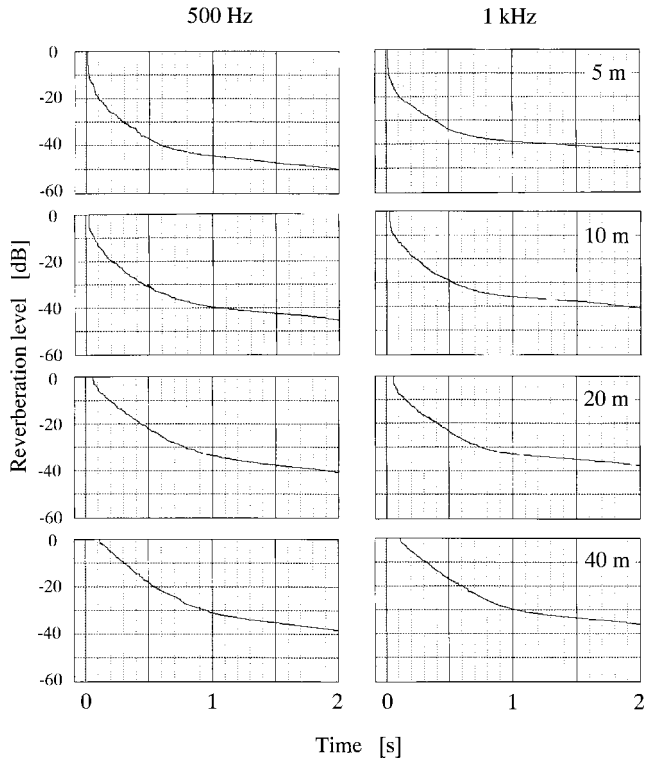

FIG. 6. Attenuation curves at each measurement point. Left and right columns represent results at 500 Hz and 1 kHz for each receiver position, respectively.

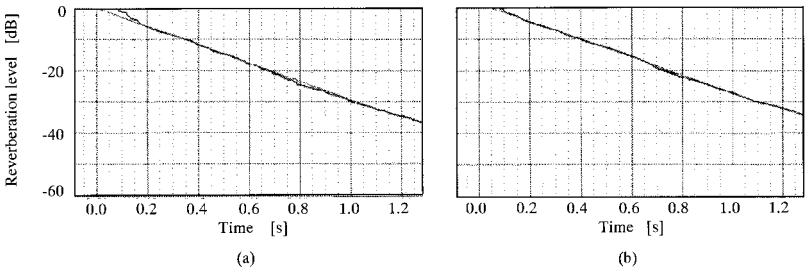

FIG. 7. Attenuation curves at 20 m from the sound source on the stage of Kirishima International Concert Hall (Sakai *et al.*, 1998). (a) 500 Hz; and (b) 1 kHz.

C. IACC, τ_{IACC}, and W_{IACC}

Results for IACC are shown in Fig. 9. In the higher frequency range, IACC became smaller and was 0.07 at 4 kHz at 20 m and 0.16 at 2 kHz at 40 m. These results are different from the results in the forest in which IACC was near 0.5 in the higher frequency range.

Interaural cross-correlation functions at each position are shown in Figs. 10(a)–(d). These functions are obtained at A-weighted allpass band. Results for τ_{IACC} and W_{IACC} are shown in Table I. Positive τ_{IACC} denote directional perception from the right side and negative values from the opposite side. The τ_{IACC} were obtained within ± 0.05 ms without exception. τ_{IACC} were between 0.02 and 0.05. Thus, the source should be perceived as being in front of the receiver for all receiver positions. The τ_{IACC} in the previous forest were also near zero as well as the results in the bamboo forest. Although we observed a tendency for W_{IACC} to increase with distance, there were some dips at 40 m. Above 20 m, W_{IACC} decreased. These values are smaller than the values in the general forest and the concert hall due to the dominance of higher frequency components compared with these sound fields.

IV. DISCUSSION

The SPL results showed a similar tendency to the previous results in the forest in terms of a decrease of 15–30 dB for doubling of the distance from 5 to 10 m, although SPL generally decreases by 6 dB for doubling of the distance in a free field. As there is no bamboo in front of the source, this was caused by excess attenuation by the ground (soil) and no reflections from above (e.g., from leaves or branches). For the bamboo forest, the rate of decrease was larger than in the case of the previous forest. This result is considered to be from excess attenuation from the ground (soil) over wider frequency ranges in the bamboo forest, although there was excess attenuation in the higher frequency range due to the path, which was made from asphalt, in the case of the previous forest (Embleton, 1996).

The maximum value of T_{sub} was shifted to the higher frequency range compared with the results in the previous forest, as shown in Fig. 11(a). Comparing the sound fields of bamboo and the forest, T_{sub} became maximum at 1 kHz or higher in the bamboo forest compared with 500 Hz in the forest. And although values of T_{sub} decreased above 500 Hz for the forest, T_{sub} kept constant with a large SPL decreasing above 1 kHz in the bamboo forest. The difference between sound fields in the bamboo and the previous forest cannot be explained easily. One reason is that the trunk diameter is constant (0.13 m) in the former whereas it ranges from 0.3 to 1.0 m in the latter. This raises the frequency range of reveberant components. This supports the hypothesis we had before the measurements.

T_{sub} itself was smaller than in the previous forest (1.6 s at the most). Thus, a bamboo forest is suitable for performances of relatively fast-tempo music. For example, the optimum T_{sub} is 1.2 s for music for which the effective duration of the autocorrelation function of the sound source τ_e is 50 ms, since the optimum T_{sub} is given by 23 times the τ_c (see Ando, 1998 for the definition of τ_e). Music with such a small value of τ_e includes chamber music. However, it is quite difficult to explain the phenomenon because of the complicated sound field, and there is no absorptive material in that specific frequency range. T_{sub} below 250 Hz was small due

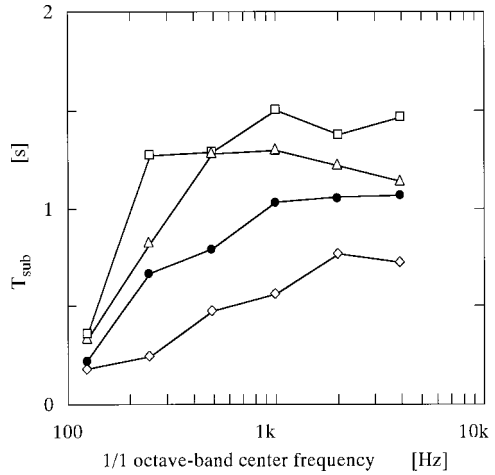

FIG. 8. Results for T_{sub}. ◇, 5 m; ●, 10 m; △, 20 m; and □, 40 m.

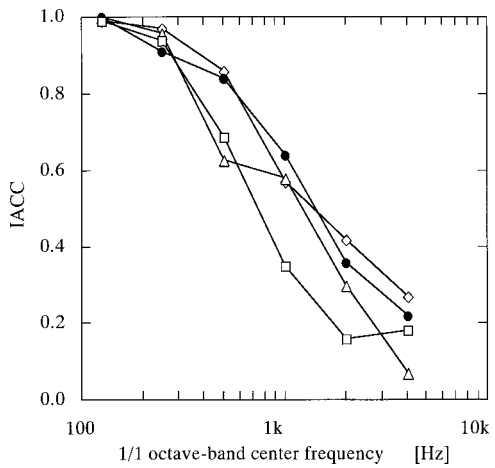

FIG. 9. Results for IACC. ◇, 5 m; ●, 10 m; △, 20 m; and □, 40 m.

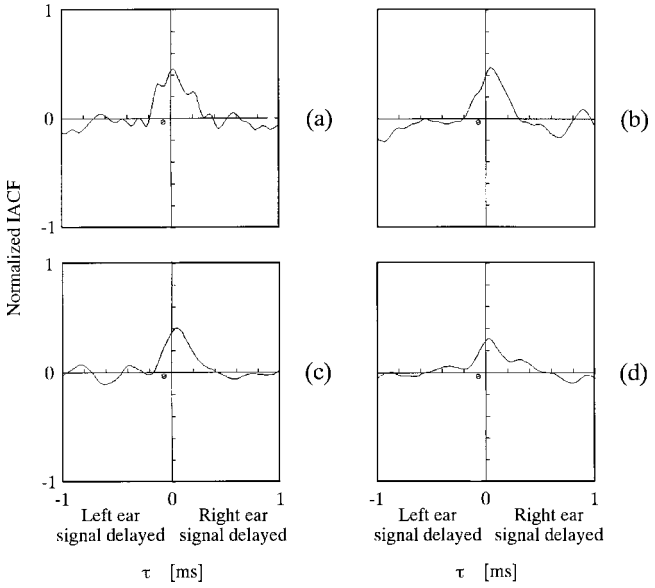

FIG. 10. Normalized interaural cross-correlation functions at each measurement point. (a) 5 m; (b) 10 m; (c) 20 m; and (d) 40 m.

to absorption by the air and bamboo leaves. At 20 m, T_{sub} was constant at around 1.3 s above 500 Hz. The τ_e obtained from these values was 53 ms. Thus, jazz music or a clarinet solo would be suitable for this sound field, but a cello or violin played at a slow tempo would not.

It is worth noting that in the higher frequency range, IACC was smaller than in the previous forest, as shown in Fig. 11(b). This may be caused by strong lateral reflections from the rigid surface of the bamboo. IACC generally becomes smaller if strong lateral reflection arrives at the ears. It is worth noting that IACC below 0.1 is the same as in a properly designed concert hall.

These results show that the sound field in a bamboo forest is suitable for listening to music. Thus, these measurements provide valuable and useful information for designing outdoor concert spaces using natural forests and concert halls having a number of columns. For Tsuyama Cultural Hall (Tsuyama, Japan), they were taken into account in computer simulations and measurements on a 1/10-scale model in the design phase. To avoid coloration in the lateral seat area near sidewalls in the hall, columns were designed along the walls and on the stage. Fifty-two hollow-wooden columns with its diameter 0.3 m were configured. Urethane foam was inserted in all columns to avoid resonance effect in this case. The effects found here can be achieved in any hall by using this knowledge. During the measuring phase after construction, it was clarified that columns on the stage and in the seating area improve IACC in front of the stage and in the lateral seat area, respectively (Suzumura *et al.*, 2000).

TABLE I. Results for τ_{IACC} and W_{IACC} for each receiver position.

Distance (m)	τ_{IACC} (ms)	W_{IACC} (ms)
5	0.02	0.061
10	0.04	0.074
20	0.05	0.098
40	0.03	0.068

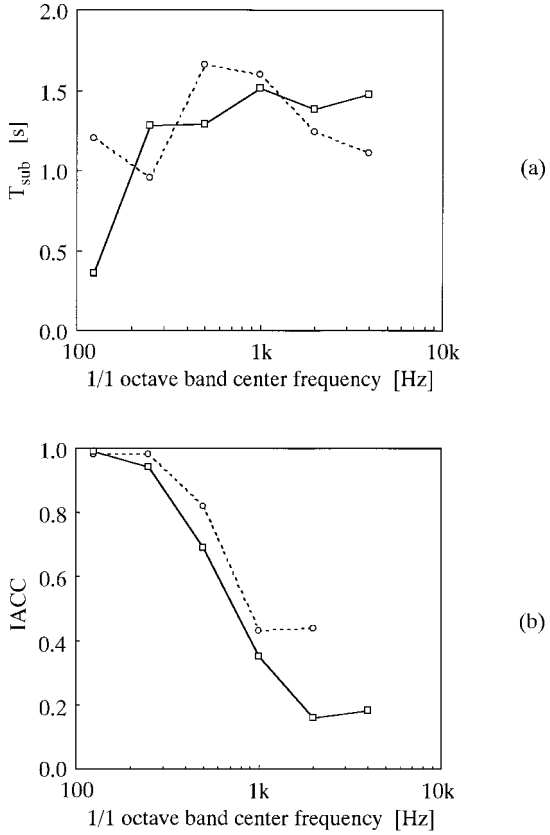

FIG. 11. Comparison between the bamboo forest and the previous forest. (a) T_{sub} at 40 m; and (b) IACC at 40 m. □, results for bamboo forest; and ○, results for previous forest (Sakai *et al.*, 1998).

V. CONCLUSION

It was clarified that the outdoor sound field in a bamboo forest has excellent acoustical properties. Like the sound field in the ordinary forest previously investigated, the specific sound field was determined, especially in terms of the factors T_{sub} and IACC. The tendency was found that the effect appears in higher frequency ranges (around 1 kHz) than in the sound field in an ordinary forest. T_{sub} was 1.5 s in the frequency range above 1 kHz at a position 40 m from the source. The effective frequency range for T_{sub} was above 1 kHz. It may be related to the diameter of the bamboo. IACC was as small as 0.07 (4 kHz) and 0.16 (2 kHz) at positions 20 and 40 m from the source. This is caused by the reflective surface of the bamboo.

ACKNOWLEDGMENTS

The authors thank Shigeo Hase, Dr. Shin-ichi Sato, and Kentaro Doge for their cooperation and assistance with the acoustical measurements in the bamboo forests.

APPENDIX: DEFINITIONS AND PROCEDURE FOR CALCULATING PHYSICAL FACTORS

The acoustical factors were calculated from binaural-impulse responses h_{jl} and h_{jr} (Osaki and Ando, 1983). The index j indicates the sampled elements of MLS with time interval σ $(j=0,1,2,...,L-1)$.

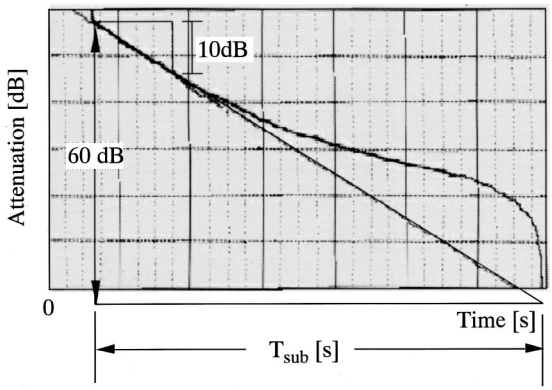

FIG. A1. Example of an attenuation curve of reverberation.

1. Relative SPL and total amplitude of reflections (A)

The relative SPL at a receiver position is obtained relative to that of the reference position. The SPL at each ear is given by the autocorrelation function $\Phi_{ll,rr}(\tau)$ at $\tau=0$ of the impulse responses $h_{jl,r}$

$$\Phi_{ll,jr}(0)=\sum_{j=0}^{L-1} h_{jl,r}^2. \tag{A1}$$

The relative SPL is defined by

$$SPL=10\log_{10}\frac{\sqrt{\Phi_{ll}(0)\Phi_{rr}(0)}}{\Phi^{\mathrm{ref}}(0)} \qquad \text{if } h_{jl,r}\neq 0, \tag{A2}$$

where

$$\Phi^{\mathrm{ref}}(0)=\sqrt{\Phi_{ll}^{\mathrm{ref}}(0)\Phi_{rr}^{\mathrm{ref}}(0)}. \tag{A3}$$

Here, $\Phi^{(\mathrm{ref})}(0)$ is the geometrical mean of the autocorrelation functions of binaural-impulse responses at $\tau=0$ at the reference position as indicated by Eq. (A3).

The value of total amplitude of reflections A is calculated from $h_{jl,r}$ as the energy ratio between the direct sound and early-plus-subsequent reverberation by

$$A=\sqrt{\frac{\Sigma_{\varepsilon+1}^{L}h_j^2}{\Sigma_1^{\varepsilon}h_j^2}}, \tag{A4}$$

where ε is the short delay time for the duration of direct sound. The value A is obtained by averaging for both ears.

2. Subsequent reverberation time (T_{sub})

The decay curve is obtained by squaring and integrating the impulse responses (Schroeder, 1965). The subsequent reverberation time T_{sub} is obtained by fitting the regression line of the curves for the initial 10 dB decay after the arrival of the direct sound. As the rapid attenuation of reverberation level is observed after arrival of a direct sound as shown in Fig. 6, start time for regression range is selected so as to avoid the initial rapid attenuation. Examples of the decay curves for this measurement are shown in Fig. A1. The results for T_{sub} are represented as an average value for both ears. The value of T_{sub} is defined by the time interval for 60 dB attenuation for this regression line.

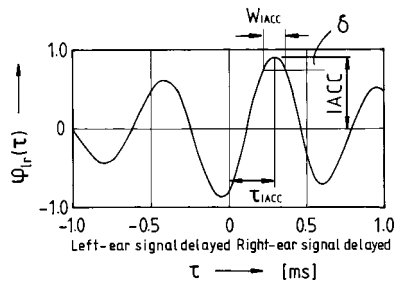

FIG. A2. Definitions of IACC, τ_{IACC}, and W_{IACC}. δ was determined as 0.1 (IACC) to analyze W_{IACC}.

3. Factors of the interaural cross-correlation function (IACC, τ_{IACC}, and W_{IACC})

The definitions of IACC, τ_{IACC}, and W_{IACC} as representative factors of interaural cross-correlation function are shown in Fig. A2. The normalized interaural cross-correlation function is given by

$$\phi_{lr}(j\sigma)=\frac{\Phi_{lr}(j\sigma)}{\sqrt{\Phi_{ll}(0)\Phi_{rr}(0)}}, \tag{A5}$$

where the values of $\Phi_{ll}(0)$ and $\Phi_{rr}(0)$ represent the autocorrelation functions ($\tau=0$) of impulse responses at both ears, respectively. The denominator means the geometrical mean of the sound energies arriving at the two ears. The $\Phi_{lr}(j\sigma)$ is the cross correlation of impulse responses at both ears. (1) The magnitude of interaural cross-correlation function is defined by

$$\mathrm{IACC}=|\phi_{l,r}(\tau)|_{\max}, \quad |\tau|\leqslant 1(\mathrm{ms}). \tag{A6}$$

This is a significant factor in determining the degree of subjective diffuseness as well as subjective preference in the sound field (Ando, 1983). It represents the degree of similarity in incident sound waves between both ears. (2) The interaural delay time, at which the IACC is determined as shown in Fig. A2, is denoted τ_{IACC}. When τ_{IACC} is zero, the frontal-sound-source image and a well-balanced-sound field may usually be perceived. (3) The width of the interaural cross-correlation function W_{IACC} is defined by the interval of delay time at a value 10% below the orthogonalized IACC as shown in Fig. A2. W_{IACC} is a significant factor related to the apparent source width (ASW). It is worth noting that ASW can be evaluated using IACC and W_{IACC} [Sato and Ando, 1999; Ando *et al.*, 1999a, 1999b].

Alrutz, H. (**1981**). ''Ein Neuer Algorithmus zur Auswertung von Messungen mit Pseudo-Rausch Signalen,'' Fortschritte der Akustik DAGA 81, Berlin, pp. 525–528.

Alrutz, H., and Schroeder, M. R. (**1983**). ''A fast Hadamard transform method for the evaluation of measurements using pseudorandom test signals,'' Proceedings of the 11th International Congress on Acoustics, Paris, Lyon-Toulouse, pp. 235–238.

Ando, Y. (**1983**). ''Calculation of subjective preference at each seat in a concert hall,'' J. Acoust. Soc. Am. **74**, 873–887.

Ando, Y. (**1998**). *Architectural Acoustics—Blending Sound Sources, Sound Fields, and Listeners* (AIP/Springer-Verlag, New York).

Ando, Y., Sakai, H., and Sato, S. (**1999a**). ''Fundamental subjective attributes of sound fields based on the model of auditory-brain system,'' in *Computational Acoustics in Architecture*, edited by J. J. Sondra (WIT Press, Southampton), Chap 4, pp. 63–99.

Ando, Y., Suzumura, Y., and Yamamoto, I. (**1999b**). ''Acoustic design of Tsuyama-Music-Cultural Hall based on the preference theory,'' Proceed-

ings of the 137th Meeting of the Acoustical Society of America, 2nd EAA, 25th DAGA, Berlin. [See also J. Acoust. Soc. Am. **105**, 927 (1999).]
Borish, J., and Angell, J. B. (**1983**). ''An efficient algorithm for measuring the impulse response using pseudorandom noise,'' J. Audio Eng. Soc. **31**, 478–488.
Embleton, T. F. W. (**1963**). ''Sound propagation in homogeneous deciduous and evergreen woods,'' J. Acoust. Soc. Am. **35**, 1119–1125.
Embleton, T. F. W. (**1996**). ''Tutorial on sound propagation outdoors,'' J. Acoust. Soc. Am. **100**, 31–48.
Eyring, C. F. (**1946**). ''Jungle acoustics,'' J. Acoust. Soc. Am. **18**, 257–270.
Huisman, W. H. T., and Attenborough, K. (**1991**). ''Reverberation and attenuation in a pine forest,'' J. Acoust. Soc. Am. **90**, 2664–2677.
Osaki, S., and Ando, Y. (**1983**). ''A fast method of analyzing the acoustical parameters for sound fields in existing auditoria,'' Proceedings of the 4th Comp. Environ. Eng. Build., Tokyo, pp. 441–445.
Price, M. A., Attenborough, K., and Heap, N. W. (**1988**). ''Sound attenuation through trees: measurements and models,'' J. Acoust. Soc. Am. **84**, 1836–1844.
Sakai, H., Sato, S., and Ando, Y. (**1998**). ''Orthogonal acoustical factors of sound fields in a forest compared with those in a concert hall,'' J. Acoust. Soc. Am. **104**, 1491–1497.
Sato, S., and Ando, Y. (**1999**). ''On the apparent source width (ASW) for bandpass noises related to the IACC and the width of the interaural cross-correlation function (W_{IACC}),'' Proceedings of the 137th Meeting of the Acoustical Society America, 2nd EAA, 25th DAGA, Berlin. [See also J. Acoust. Soc. Am. **105**, 1234 (1999).]
Schroeder, M. R. (**1965**). ''New method of measuring reverberation time,'' J. Acoust. Soc. Am. **37**, 409–412.
Suzumura, Y., Sakurai, M., Yamamoto, I., Iizuka, T., Oowaki, M., and Ando, Y. (**2000**). ''An evaluation of the effects of scattered reflections in a sound field,'' J. Sound Vib. **232**, 303–308.

Minimum entropy deconvolution of pulse-echo signals acquired from attenuative layered media

Tomas Olofsson and Tadeusz Stepinski[a)]
Signals and Systems Group, Department of Material Science, Uppsala University, Box 528, 751 20 Uppsala, Sweden

(Received 26 May 1999; revised 23 February 2001; accepted 23 March 2001)

In this article deconvolution of ultrasonic pulse-echo data acquired from attenuative layered media is considered. The problem is divided in two subproblems: treating the sparse reflection sequence caused by the layered structure of the media and treating the frequency-dependent attenuation. The first subproblem is solved by means of joint maximum *a posteriori* estimation of the assumed zero mean, white, nonstationary reflection sequence and its corresponding sequence of unknown standard deviations. This approach leads to an algorithm that seeks minimum entropy solutions for the reflection sequence and therefore the algorithm serves as a novel link between the classical Wiener filter and methods for sparse or minimum entropy deconvolution. The second subproblem is solved by introducing a new signal processing-oriented, linear discrete-time model for frequency-dependent attenuation in isotropic and homogeneous media. The deconvolution algorithm is tested using simulated data and its performance for real normal incidence pulse-echo data from a composite material is also demonstrated. The results show that the algorithm, in combination with the attenuation model, yields estimates that reveal the internal structure of the composite and, thus, simplify the interpretation of the ultrasonic data. [DOI: 10.1121/1.1373446]

PACS numbers: 43.60.Pt, 81.70.Cv, 43.20.Hq [JCB]

I. INTRODUCTION

The purpose of this article is twofold. The main purpose is to introduce a new deconvolution algorithm based on joint maximum *a posteriori* (MAP) estimation of a zero mean white Gaussian, nonstationary so-called reflection sequence and its corresponding sequence of standard deviations. As will be shown below, formulating the deconvolution problem in this manner leads to an algorithm that can be interpreted as a *sparse* or *minimum entropy* deconvolution algorithm, suitable for deconvolving pulse-echo data acquired from layered media. The novelty with the algorithm is that it puts the classical Wiener filter into the context of sparse deconvolution methods. The second purpose of the article is presenting a discrete-time model describing attenuation in pulse-echo measurements. The development of this attenuation model was necessitated by the application in mind, namely, the development of an algorithm suitable for deconvolving data obtained from normal incidence pulse-echo testing of layered attenuative composite materials.

The deconvolution problem is often encountered in, for instance, seismic exploration and nondestructive testing. The reflection sequence is estimated based on the measured data utilizing some prior knowledge of the reflection sequence and the measurement noise. A MAP estimate, derived under prior second-order stationary Gaussian assumptions concerning both these variables, takes the form of the non-causal Wiener filter.[1] If the true reflection sequence contains sparsely distributed spikes and the measurement system is relatively narrow band, the corresponding estimates of the amplitudes of spikes are usually underestimated and the estimated spikes are also masked by ringing. A number of amplitude probability density functions (pdf's) have been proposed as alternatives to the Gaussian aiming at better modeling the reflection sequence and thereby reducing the above-mentioned negative effects. Examples of such alternative models are the Bernoulli–Gaussian,[2–6] the generalized Gaussian,[7] and the mixed Gaussian models.[8]

As an alternative to the methods based on the above-mentioned statistical models, we propose in this article a new deconvolution algorithm that is based on joint MAP estimation of the reflection sequence and its standard deviation, under a Gaussian assumption but without restricting the sequence to be stationary. By using this approach sparse estimates can be obtained while still maintaining some of the computational advantages related to dealing with Gaussian distributions. The algorithm is best understood in a Bayesian perspective where the uncertainty of each sample in the reflection sequence is modeled by a Gaussian density and the uncertainty of the unknown standard deviations of each sample in this reflection sequence is modeled by a uniform distribution. Compared to the criterion associated with the noncausal Wiener filter, the criterion associated with the proposed algorithm contains an additional term which is proportional to the differential entropy of the reflection sequence. The algorithm can, therefore, be interpreted as a search for a minimum entropy realization of the reflection sequence within a class of otherwise equivalent realizations, in terms of matching to the measured data.

A simple discrete-time attenuation model is also presented in this article. We assume that the distortion of the propagating pulse, caused by traveling a distance z in an

a)Electronic mail: ts@signal.uu.se

attenuative medium, can be modeled using a linear time-invariant (LTI) system. Accordingly, a model of the pulse distortion associated with traveling a multiple of this distance, Lz, is obtained by serially connecting the above-mentioned LTI system L times. The impulse response of the serially connected LTI system is modeled as an L-time self-convolution of the impulse response of the LTI system associated with a material slice of thickness z.

Traditionally the impulse response describing the pulse distortion in dispersive media has been expressed in continuous time and obtained by means of frequency domain methods.[9–11] The approach here is to avoid many of the mathematical difficulties associated with continuous time models, such as generalized functions which are required when treating frequency power law attenuation,[11] and instead use simple heuristics to obtain a model directly in the discrete-time domain. By working in the time domain the causality issues are conveniently taken care of.

Although the attenuation model used in this article is determined by a single parameter, it enables for including several degrees of freedom in order to treat more complex situations. The model structure ensures that the amplitude of any frequency component is decreasing exponentially with depth. Similar signal-processing-oriented attenuation models were presented by Rasmussen[12] and Saffari *et al.*[13] However, the attenuation in the former model does not yield the above-mentioned exponential decrease.

The article begins with a section where the signal generation model is presented together with the statistical assumptions of the involved variables and a derivation of the estimation algorithm. In the subsequent section the algorithm is illustrated using simulated data. This is followed by a section where results obtained from real ultrasonic data are presented. Finally, some conclusions are presented.

II. THEORY

In this section we first present a signal generation model which we subsequently generalize to also include frequency-dependent attenuation. This is followed by a presentation of the statistical model assumptions of the involved variables. Finally, the MAP estimation algorithm is derived.

A. Signal model

To obtain a model suitable for treating thin layered objects we first consider the response from a planar reflector parallel to the surface of a planar transducer. Let the transducer impulse response, $h_T(t)$, be defined as

$$h_T(t) = h_{\text{exc}}(t) * h_{em}^b(t) * h_{em}^f(t), \tag{1}$$

where $h_{ea}^f(t)$ and $h_{ae}^b(t)$ are the transducer's electro-acoustical and acousto-electrical impulse responses, respectively. These impulse responses map the electrical excitation signal, $h_{\text{exc}}(t)$, to outgoing surface normal velocity waveform, and incoming instantaneous pressure to electrical output, respectively.

The response from the above-mentioned planar reflector can then be described using the convolutional model

$$h(t) = h_T(t) * r_c(t), \tag{2}$$

where $r_c(t)$ is the so-called radiation coupling function[14] associated with the transducer–reflector pair. The radiation coupling function depends on geometrical properties of the measurement setup such as the distance between the transducer and the reflector. When treating layered objects in the following the response $h(t)$ is conveniently used as an impulse response or a *prototype* response.

Now consider the normal incidence inspection of a relatively thin layered object. Furthermore, assume for the moment that the dispersion of the ultrasonic pulse, as it propagates forward to the subsequent layers, is negligible. Since the object is thin, the radiation coupling function associated with each layer will be approximately identical, except for a time shift and an amplitude scaling. A model of the received signal, $y(t)$, can then be written as

$$\begin{aligned} y(t) &\approx h_T(t) * \left(\sum_{m=1}^{M} a_m r_c(t - \Delta_m) \right) \\ &= h(t) * \left(\sum_{m=1}^{M} a_m \delta(t - \Delta_m) \right), \end{aligned} \tag{3}$$

where $\delta(t)$ is Dirac's delta function, Δ_m is the time delay associated with the mth received reflection, and a_m is the corresponding amplitude which depends on the reflection coefficient of the layer as well as the transmission losses at earlier boundaries.

Let T denote the sampling period and let $y(k)$ denote a discrete-time signal obtained by sampling the corresponding continuous signal $y(t)$ at time instants $0, T, 2T, \ldots, kT, \ldots$. The discrete-time and noise-corrupted version of Eq. (3) can then be written as

$$\begin{aligned} y(k) &= h(k) * \left(\sum_{m=1}^{M} a_m \delta(k - \Delta_m') \right) + e(k) \\ &= h(k) * x(k) + e(k), \end{aligned} \tag{4}$$

where $\delta(k)$ is the discrete-time Dirac pulse, or the *unit pulse*, and the integer Δ_m' expresses the delay Δ_m in number of samples. The reflection sequence, $x(k)$, is a sum of sharp pulses and is, thus, sparse. Note, however, that the expression in Eq. (4) is obtained under rather idealized conditions. For instance, layers are hardly perfectly planar and parallel. Moreover, scattering from material structures in between the layers will also contribute to $x(k)$. Therefore, in a realistic case the samples in $x(k)$ are typically nonzero between the pulses described by the sum in the parentheses in Eq. (4).

Regardless of the exact structure of $x(k)$, the right-hand side of Eq. (4) can be written in matrix form as

$$\mathbf{y} = \mathbf{H}\mathbf{x} + \mathbf{e}, \tag{5}$$

where bold, lower-case letters represent column vectors as, e.g, $\mathbf{y} = [y(0), y(1), \ldots, y(N-1)]^T$, and the $N \times N$ matrix $\mathbf{H}$ is a so-called convolution matrix or finite impulse response (FIR) matrix. The p,qth element in $\mathbf{H}$ is given by $\mathbf{H}_{p,q} = h(p-q)$.

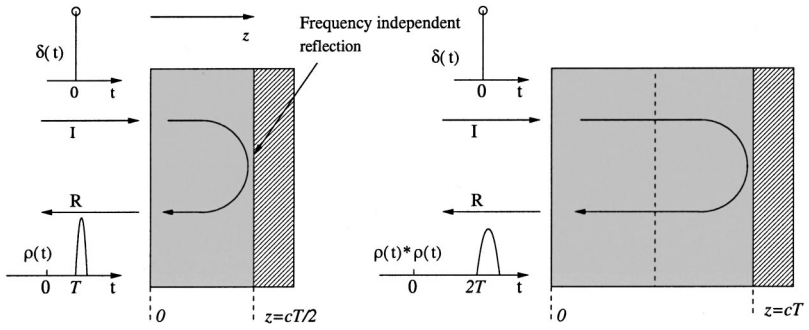

FIG. 1. A schematic illustration of the concept of attenuation impulse responses. At depth $z=0$ the incident (I) propagating pulse is the Dirac pulse, $\delta(\tau)$. After reflection (R) the pulse has been low-pass filtered due to attenuation and, thus, the received pulse, $\rho(\tau)$, has been elongated in time. Pulse propagation through a slice twice the thickness yields a received pulse that is $\rho_2(\tau)=\rho(\tau)*\rho(\tau)$.

B. A discrete-time attenuation model

Frequency-dependent attenuation causes a depth-dependent low-pass filtering of the reflected echo and this will violate the assumption of sharp pulses in $x(k)$ in Eq. (4) unless a model of the attenuation is included. To obtain such a model we consider a slice of an isotropic and homogeneous medium with thickness z. The slice is oriented normally to the pulse propagation direction. We assume that the medium acts on the interrogating wave as a LTI system which is described by its impulse response, $\rho_z(t)$, where t is the (continuous) time. Then, at depth z, the pulse wavelet of the interrogating (pressure) wave, $p_z(t)$, is governed by the relation

$$p_z(t)=\rho_z(t)*p_0(t), \tag{6}$$

where $p_0(t)$ is the pulse wavelet at $z=0$. Due to the homogeneity of the medium the pulse shape at a multiple of this depth, Lz, will then be governed by

$$\begin{aligned} p_{Lz}(t)&=\rho_z(t)*(\rho_z(t)*\cdots*(\rho_z(t)*p_0(t)))\\ &=\rho_z(t)*\rho_z(t)*\cdots*\rho_z(t)*p_0(t), \end{aligned} \tag{7}$$

where the convolution with kernel $\rho_z(t)$ is performed L times. Equation (7) is obtained by recursively applying Eq. (6) for each slice.

In Fig. 1 we illustrate schematically the pulse propagation, now for pulse-echo measurements. We assume that the normal incidence reflections at the planar boundaries indicated in Fig. 1 are frequency *independent*, meaning that a reflected pulse is simply an amplitude scaled version of the corresponding incident pulse. This implies that Eq. (7) can be used also to describe pulse-echo measurements with the modification $z\rightarrow 2z$ to account for the double path propagation, together with an amplitude scaling to account for the frequency-independent reflection, i.e.,

$$\begin{aligned} p^{pe}_{Lz}(t)&=r_{Lz}\rho_{2z}(t)*\rho_{2z}(t)*\cdots*\rho_{2z}(t)*p_0(t)*p_0*\delta(t-2z/c)\\ &=r_{Lz}\rho_{2Lz}(t)*\delta(t-2z/c), \end{aligned} \tag{8}$$

where r_{Lz} is the reflection coefficient of the reflecting layer at depth Lz and $\rho_{2Lz}(t)=\rho_{2z}(t)*\cdots*\rho_{2z}(t)$ and $\rho_{2z}=\rho_z(t)*\rho_z(t)$.

Specifically, we consider the slice thickness $z=cT/2$ which is the thickness that corresponds to a propagation delay of the sampling interval T. In Fig. 1 we let $\rho(t)$ denote the attenuation impulse response associated with this particular slice thickness.

Intuitively, since the slice is thin, the distortion of the propagating wave must be relatively small which implies that the impulse response of the system must be close to a Dirac pulse which has been delayed one sampling period. In the experiments presented here, $T=1/Fs=10\,\text{ns}$ and $c\approx 3000\,\text{m/s}$, which yields $z\approx 30\,\mu\text{m}$. For discrete-time signals this means $\rho(k)\approx\delta(k-1)$ where k is the time index. In this article we assume $\rho(k)$ to have the simple form

$$\rho(k)=\begin{cases} 0, & k=0,\\ 1-a, & k=1,\\ a, & k=2,\\ 0, & \text{otherwise}, \end{cases} \tag{9}$$

where $0<a\ll 1$. The form shown in Eq. (9) ensures, first, that there is no attenuation at angular frequency $\omega=0$ and, second, that $\rho(k)$ has the minimum phase property (when the inherent one sample delay has been removed). Note that $a=0$ yields $\rho(k)=\delta(k-1)$, i.e., a simple time delay with no pulse distortion and that $a>0$ ensure the frequency low-pass character of the linear transformation. Note also that $\rho(k)$ is not in any way restricted to have the simple one-parameter form given in Eq. (9) and, furthermore, an individual attenuation impulse response can be designated to each slice if found necessary.

Let $\rho_l(k)=\rho(k)*\cdots*\rho(k)$ denote the sampled *cumulative attenuation impulse response* (CAIR) corresponding to depth $z=lcT/2$. Then we can write the discrete-time attenuation model as

$$\mathbf{x}=\mathbf{A}\mathbf{r}, \tag{10}$$

where the $N\times N$ matrix $\mathbf{A}$ has elements $\mathbf{A}_{k,l}=\rho_l(k)$ and $\mathbf{r}$ is a hypothetical reflection sequence that would be observed if no attenuation was present in the medium. Combining the signal generation model in Eq. (5) with the attenuation model in Eq. (10) finally yields

$$\mathbf{y}=\mathbf{H}\mathbf{A}\mathbf{r}+\mathbf{e}=\mathbf{G}\mathbf{r}+\mathbf{e}, \tag{11}$$

where the matrix $\mathbf{G}=\mathbf{H}\mathbf{A}$ models the combined effects of the transducer impulse response, the radiation coupling function associated with the reflecting layers, as well as the frequency dependent attenuation. Note that attenuation caused by transmission losses due to frequency-independent reflections is not included in this model. This kind of attenuation does not change the shape of the propagating pulse wavelet, so the effects of this attenuation can instead be included in the scalar amplitudes in $\mathbf{r}$.

C. Statistical model assumptions

The measurement noise and the reflection sequence are assumed to be statistically independent and the measurement noise is assumed to be a stationary zero mean Gaussian sequence with covariance matrix (or autocorrelation matrix) $\mathbf{C_e}$. The reflection sequence is assumed to be zero mean Gaussian with uncorrelated components yielding a covariance matrix that is diagonal. This matrix is given by

$$\mathbf{C_r}=\begin{pmatrix} \sigma_{\mathbf{r}}^2(0) & & 0 \\ & \ddots & \\ 0 & & \sigma_{\mathbf{r}}^2(N-1) \end{pmatrix}, \tag{12}$$

where $\sigma_{\mathbf{r}}^2(n)$ is the (unknown) scalar variance of the nth component in $\mathbf{r}$.

We define $\mathbf{s_r}$ to be a column vector containing the standard deviations of the components in $\mathbf{r}$:

$$\mathbf{s_r}=[\sigma_{\mathbf{r}}(0),\sigma_{\mathbf{r}}(1),\ldots,\sigma_{\mathbf{r}}(N-1)]^T. \tag{13}$$

A relation between the energy in $\mathbf{y}$ and the components in $\mathbf{s_r}$ can be found by observing that

$$\begin{aligned}\mathcal{E}_{\mathbf{y}}&=E[\mathrm{tr}(\mathbf{y}\mathbf{y}^T)]=E[\mathrm{tr}((\mathbf{G}\mathbf{r}+\mathbf{e})(\mathbf{G}\mathbf{r}+\mathbf{e})^T)]\\ &=\sum_n \|(\mathbf{G})_n\|^2\sigma_{\mathbf{r}}^2(n)+N\sigma^2,\end{aligned} \tag{14}$$

where $\mathcal{E}_{\mathbf{y}}$ is the expected energy in signal $\mathbf{y}$, $\mathrm{tr}(\cdot)$ is the trace operator, which for a $N\times N$ matrix $\mathbf{A}$ is defined as the sum of the diagonal elements of $\mathbf{A}$, i.e., $\mathrm{tr}(\mathbf{A})=\Sigma_{n=1}^N(\mathbf{A})_{n,n}$. $\|(\mathbf{G})_n\|$ is the quadratic norm of the nth column in $\mathbf{G}$ and σ^2 is the variance of the components in $\mathbf{e}$. In Eq. (14) we have used the assumption that $\mathbf{r}$ and $\mathbf{e}$ are mutually uncorrelated. Instead of using the unknown expectation $\mathcal{E}_{\mathbf{y}}$, we below use the approximation

$$\mathcal{E}_{\mathbf{y}}\approx\hat{\mathcal{E}}_{\mathbf{y}}=\mathrm{tr}(\mathbf{y}\mathbf{y}^T). \tag{15}$$

Furthermore, the standard deviations in $\mathbf{s_r}$ are assumed to be limited below by a positive constant s_0, i.e.,

$$\sigma_{\mathbf{r}}(n)\geqslant s_0, \quad n=0,\ldots,N-1. \tag{16}$$

The constant s_0 can be seen as a user parameter that controls the sparsity of the estimates. The larger s_0, the less room is left for a single $\sigma_{\mathbf{r}}(n)$ to grow large because of the restriction of energy given in Eq. (14). On the other hand, as will be seen below, $s_0\to 0$ favors estimates which for some components $\hat{\sigma}_{\mathbf{r}}(n)\approx|\hat{r}(n)|\to 0$ and the estimates will, thus, become more sparse as s_0 decreases.

D. Joint MAP estimation of r and $\mathbf{s_r}$

The joint MAP estimate of $\mathbf{r}$ and $\mathbf{s}$, given the measured signal $\mathbf{y}$, is given by

$$\begin{aligned}[\hat{\mathbf{r}},\hat{\mathbf{s}}_{\mathbf{r}}]&=\arg\max_{\mathbf{r},\mathbf{s_r}} p(\mathbf{r},\mathbf{s_r}|\mathbf{y})=\arg\max_{\mathbf{r},\mathbf{s_r}} p(\mathbf{y}|\mathbf{r},\mathbf{s_r})p(\mathbf{r},\mathbf{s_r})\\ &=\arg\max_{\mathbf{r},\mathbf{s_r}} p(\mathbf{y}|\mathbf{r})p(\mathbf{r}|\mathbf{s_r})p(\mathbf{s_r}),\end{aligned} \tag{17}$$

where we have used Bayes' theorem and the chain rule for pdf's. Since all $\mathbf{s_r}$ are equally likely, $p(\mathbf{s_r})$ is assumed to be constant for all $\mathbf{s_r}$ and we obtain

$$[\hat{\mathbf{r}},\hat{\mathbf{s}}_{\mathbf{r}}]=\arg\max_{\mathbf{r},\mathbf{s_r}} p(\mathbf{y}|\mathbf{r})p(\mathbf{r}|\mathbf{s_r}), \tag{18}$$

under the constraint in Eqs. (14) and (16).

The conditional pdf $p(\mathbf{y}|\mathbf{r})$ is given by

$$p(\mathbf{y}|\mathbf{r})=\frac{1}{(2\pi)^{N/2}|\mathbf{C_e}|^{1/2}}e^{-(1/2)(\mathbf{y}-\mathbf{G}\mathbf{r})^T\mathbf{C_e}^{-1}(\mathbf{y}-\mathbf{G}\mathbf{r})}, \tag{19}$$

and $p(\mathbf{r}|\mathbf{s_r})$ is given by

$$\begin{aligned}p(\mathbf{r}|\mathbf{s_r})&=\frac{1}{(2\pi)^{N/2}|\mathbf{C_r}|^{1/2}}e^{-(1/2)\mathbf{r}^T\mathbf{C_r^{-1}}\mathbf{r}}\\ &=\frac{1}{(2\pi)^{N/2}\Pi_k\sigma_{\mathbf{r}}(k)}e^{-(1/2)\Sigma_k r^2(k)/\sigma_{\mathbf{r}}^2(k)},\end{aligned} \tag{20}$$

where $\mathbf{C_r}$ is given by Eqs. (13) and (12).

By taking the negative logarithm of the expression in Eq. (18) and excluding irrelevant terms we finally obtain the criterion function

$$\begin{aligned}J(\mathbf{r},\mathbf{s_r})&=\frac{1}{2}(\mathbf{y}-\mathbf{G}\mathbf{r})^T\mathbf{C_e}^{-1}(\mathbf{y}-\mathbf{G}\mathbf{r})+\frac{1}{2}\sum_{n=0}^{N-1}\frac{r^2(n)}{\sigma_{\mathbf{r}}^2(n)}\\ &\quad+\sum_{k=0}^{N-1}\ln\sigma_{\mathbf{r}}(k).\end{aligned} \tag{21}$$

The joint estimate $[\hat{\mathbf{r}},\hat{\mathbf{s}}_{\mathbf{r}}]$ is thus given by

$$[\hat{\mathbf{r}},\hat{\mathbf{s}}_{\mathbf{r}}]=\arg\max_{\mathbf{r},\mathbf{s_r}} J(\mathbf{r},\mathbf{s_r}), \tag{22}$$

under the constraints in Eqs. (14) and (16). We should note that if we exclude the third term in Eq. (21), we obtain the standard MAP criterion associated with the assumption of known covariance matrix[1] $\mathbf{C_r}$.

The structure of the criterion function in Eq. (21) suggests a block version of the iterative alternating variables optimization approach.[15] So, to minimize $J(\mathbf{r},\mathbf{s_r})$ we propose the following iterative algorithm. (As in all optimization problems, there are a number of possible optimization procedures that will also work. For instance, we could use a Lagrangian to treat the constraints in a formal correct way. The authors have found, however, that this simple scheme works nicely in the experiments tested so far.)

(1) Set $\hat{\mathbf{s}}_{\mathbf{r}}^{\mathbf{0}}=\sigma_0\mathbf{1}$ where $\mathbf{1}=[1,1,\ldots,1]^T$ is an $N\times 1$ vector and the constant $\sigma_0=(\mathcal{E}_{\mathbf{y}}-N\sigma^2)/\Sigma_n\|(\mathbf{G})_n\|^2$ fulfills the energy constraint in Eq. (14).
(2) Calculate $\hat{\mathbf{r}}^{\mathrm{it}+1}=\arg\max_{\mathbf{r}}J(\mathbf{r},\hat{\mathbf{s}}^{\mathrm{it}})$ for a fixed $\hat{\mathbf{s}}_{\mathbf{r}}^{\mathrm{it}}$.
(3) Calculate $\mathbf{z}_{\mathbf{r}}^{\mathrm{it}+1}=\arg\max_{\mathbf{s_r}}J(\hat{\mathbf{r}}^{\mathrm{it}+1},\mathbf{s_r})$.
(4) To obtain $\hat{\mathbf{s}}_{\mathbf{r}}^{\mathrm{it}+1}$, normalize $\mathbf{z}_{\mathbf{r}}^{\mathrm{it}+1}$ by meeting the constraints in Eqs. (14) and (16).
(5) Go to 2.

The superscript it is the iteration number and $\mathbf{z}_{\mathbf{r}}^{\mathrm{it}}=[z_{\mathbf{r}}^{\mathrm{it}}(0)\cdots z_{\mathbf{r}}^{\mathrm{it}}(N-1)]$ is a temporary variable.

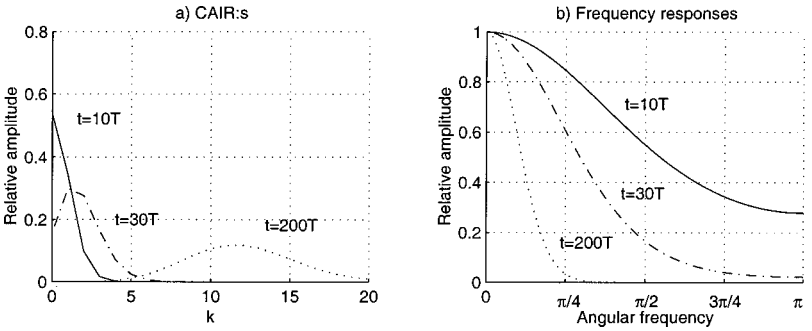

FIG. 2. (a) Cumulative attenuation impulse responses corresponding to depths $z=10cT/2$, $z=30cT/2$, and $z=200cT/2$. (b) Corresponding frequency responses (right). The attenuation model parameter was set to $a=0.06$.

Since the criterion function in Eq. (21) is quadratic in $\mathbf{r}$, the corresponding minimization problem (step 2 in the algorithm above) can be solved analytically. The solution is given by

$$\hat{\mathbf{r}}=(\mathbf{G}^T\mathbf{C}_\mathbf{e}^{-1}\mathbf{G}+\mathbf{C}_\mathbf{r}^{-1})^{-1}\mathbf{G}^T\mathbf{C}_\mathbf{e}^{-1}\mathbf{y}, \tag{23}$$

where $\mathbf{C}_\mathbf{r}$ is defined by the components in $\hat{\mathbf{s}}_\mathbf{r}^{\mathrm{it}}$, cf. Eqs. (12) and (13).

The minimization problem in step 3 is solved by equating the gradient $\partial J/\partial \mathbf{s}_\mathbf{r}$ to zero. The solution is given by

$$\sigma_\mathbf{r}(k)=|r(k)|, \quad \forall k. \tag{24}$$

To accomplish the normalization of $\mathbf{z}_\mathbf{r}^{\mathrm{it}+1}$ in step 4 we first observe that including Eq. (16) in Eq. (14) results in the condition

$$s_0^2\sum_{n|r^2(n)\leqslant s_0^2}\|(\mathbf{G})_n\|^2+\sum_{n|r^2(n)>s_0^2}\|(\mathbf{G})_n\|^2\sigma_\mathbf{r}^2(n)+N\sigma^2=\hat{\mathcal{E}}_\mathbf{y}, \tag{25}$$

which should be satisfied for the normalized standard deviations. Let $\sigma_\mathbf{r}(n)=Kz_\mathbf{r}(n)$ for $n|r^2(n)>s_0^2$ where K is a positive constant and let $\sigma_\mathbf{r}(n)=s_0$ for $n|r^2(n)\leqslant s_0^2$. Inserting this in Eq. (14) yields

$$K=\frac{\sqrt{\hat{\mathcal{E}}_\mathbf{y}-N\sigma^2-s_0^2\Sigma_{n|r^2(n)\leqslant s_0^2}\|(\mathbf{G})_n\|^2}}{\Sigma_{n|r^2(n)>s_0^2}\|(\mathbf{G})_n\|^2 z_\mathbf{r}^2(n)}. \tag{26}$$

It is interesting to note that apart from the quadratic expressions found in standard MAP estimation under stationary Gaussian assumptions, we find in Eq. (21) a term that is proportional to *differential entropy* of independent Gaussian variables,[16] namely $\Sigma_k \ln\sigma_\mathbf{r}(k)$. So, loosely speaking, the minimization of $J(\mathbf{r},\mathbf{s}_\mathbf{r})$ yields a minimum entropy realization of $\mathbf{r}$, within a family of possible realizations of $\mathbf{r}$ that otherwise are equivalent in terms of matching to the measured data.

III. DECONVOLUTION OF SYNTHETIC DATA

To illustrate the properties of the proposed algorithm and the attenuation model we simulated A-scans using the model in Eq. (11) followed by deconvolution using the proposed algorithm. The impulse response used in the simulation was measured as the normal incidence pulse-echo response from an aluminum plate in the far field of an unfocused Panametric transducer with approximate center frequency 5 MHz. Throughout the simulations the attenuation model parameter was set to $a=0.06$. The frequency response of the corresponding cumulative attenuation impulse responses (CAIRs) are shown in Fig. 2. Before presentation, each CAIR$\rho_l(k)$ was compensated for the delay lT. Apart from this delay, the successive filtering with $\rho(k)$ introduced a group delay that for $a=0.06$ is asymptotically 0.06 for low frequencies. This delay is apparent for the CAIR corresponding to $200T$ in Fig. 2.

A reflection sequence was modeled as a zero mean, stationary white Gaussian noise with variance $\sigma_\mathbf{r}^2=0.01$. Three spikes with amplitudes 4, -4, and 8 were inserted at time indices 10, 30, and 200, respectively. In Fig. 3, we show a simulated reflection sequence (left) and the signal obtained using the model in Eq. (11) with the noise $\mathbf{e}$ modeled as zero mean, stationary white Gaussian noise with variance $\sigma_\mathbf{e}^2=100$.

In Fig. 4 we show $\hat{\mathbf{r}}^{\mathrm{it}}$ at iterations it=1,2,4,8. The minimum allowed standard deviation was set to $s_0=|\sigma_\mathbf{r}|$. The estimate at it=1 is the Wiener solution corresponding to a stationarity assumption. Note the ringing and the underestimation of the amplitudes of the estimated spikes in this estimate. At the subsequent iterations the variance is redistributed from first being-constant for all components at it=1, to getting larger at the time indices for the inserted spikes and smaller for the remaining indices. In Fig. 5 we show how this redistribution is evolving with the iterations. Note that the

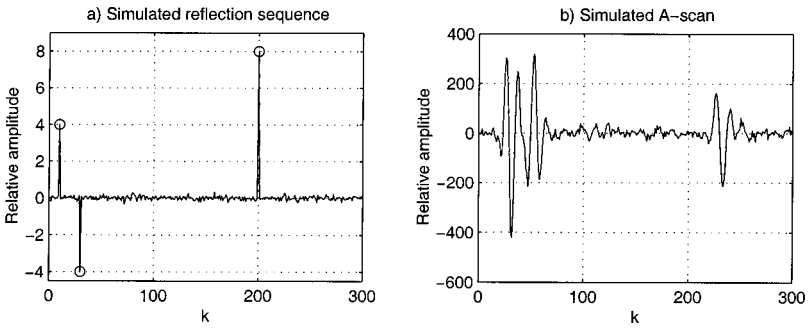

FIG. 3. Simulated signals. (a) Simulated reflection sequence, $r(k)$. (b) Simulated A-scan, $y(k)$.

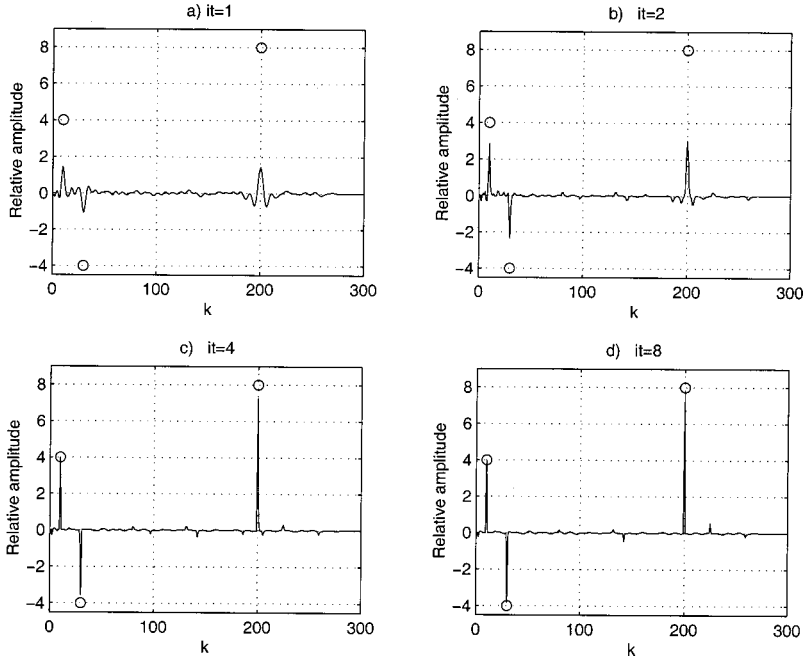

FIG. 4. Estimated reflection sequences. (a) Solution at iteration 1. (b) Iteration 2. (c) Iteration 4. (d) Iteration 8.

estimated reflection sequence at iteration it is based on standard deviation vectors at iteration it-1. Note also that the components in the standard deviation vector corresponding to the large amplitude components in $\mathbf{r}$ converge to the absolute values of the amplitudes of these components.

It can be seen in Fig. 3 that the heavy attenuation causes a strong decrease of the amplitude of the spike at $k=200$. The low-pass character of the signal caused by the attenuation, something which is especially evident at $k=200$, also causes the MAP estimate at it$=1$ to have low-pass character. As the standard deviations are redistributed this effect decreases.

IV. DECONVOLUTION OF REAL ULTRASONIC DATA

Immersion test pulse-echo data was acquired from a carbon fiber layered composite specimen using nonfocused transducers with diameters of 10 mm. The impulse responses of these transducers were measured as the normal incidence pulse-echo response from an aluminum plate in the far field. In order to obtain measurements with correct radiation coupling functions, the same distance between the transducer and the object was used as in the measurements from the composite objects. The deconvolution experiments were performed using a relatively narrow-band transducer, T_n, having an approximate center frequency 5 MHz.

To apply the model in Eq. (11), an estimate of the attenuation model parameter was needed. This parameter was found in an independent experiment, using a relatively broadband transducer T_b, having an approximate center frequency 10 MHz, by means of a variant of the frequency shift method. The front and back wall echoes (separated in time by approximately $60T$) were extracted and the

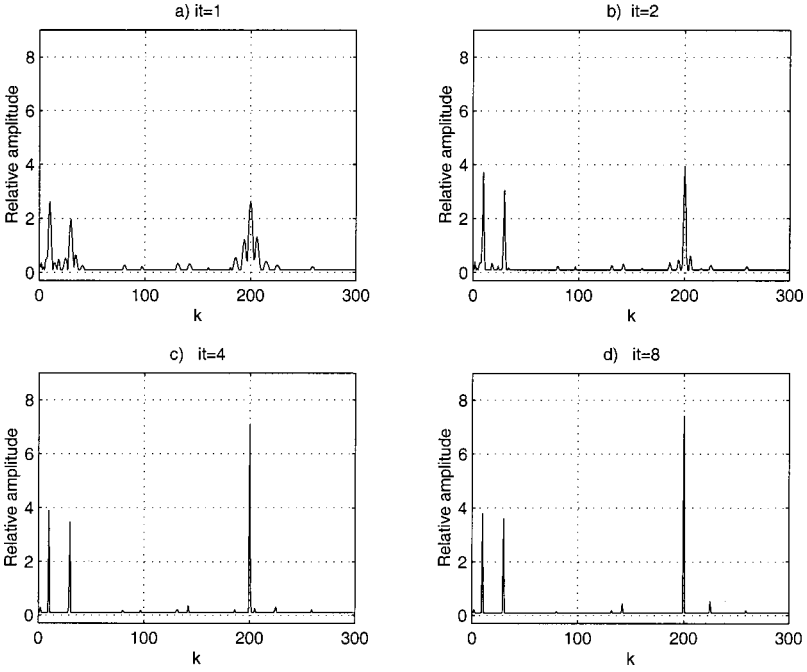

FIG. 5. Estimated standard deviations of the individual samples. (a) Solution at iteration 1. (b) Iteration 2. (c) Iteration 4. (d) Iteration 8.

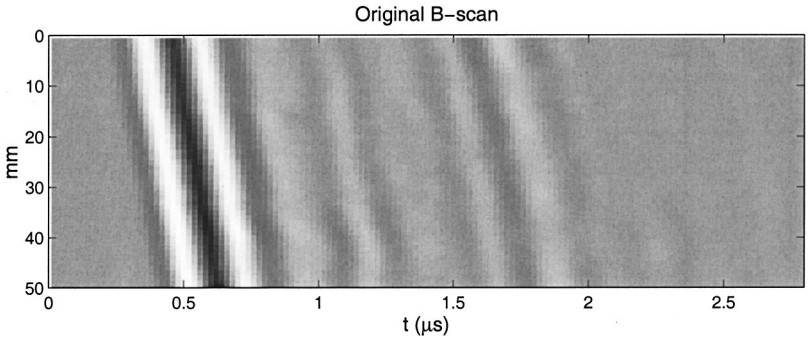

FIG. 6. Original B-scans obtained using transducer T_n. The front and back wall echoes start at time indices $k \approx 20$ and $k \approx 80$, respectively.

center of gravity of the corresponding amplitude spectra were calculated for these echoes. This was repeatedly done for 20 A-scans and the obtained values were averaged. The averaged frequency shift was found to be $\hat{S}_{fq} = 2.6\,\mathrm{MHz}$.

For simulated data we calculated the center of gravity of the amplitude spectrum of the impulse response of $T_b, h_b(k)$ as well as of a signal $w(k) = h_b(k) * \rho_{60}(k,a)$ where $\rho_{60}(k,a)$ is the simulated CAIR for a depth corresponding to a pulse-echo delay of $60T$. This was done for different choices of the parameter a. The estimate $\hat{a}$ was defined as the parameter that yielded the simulated frequency shift $\hat{S}_{fq}$. The described procedure yielded the estimate $\hat{a} = 0.065$.

In Fig. 6 we show a B-scan that was acquired using T_n. The B-scan was acquired from a carbon fiber reinforced epoxy composite having eight internal fiber layers. In Fig. 6 we see the front and back wall echoes at time indices $k \approx 20$ and $k \approx 80$, respectively. The internal fiber layers are difficult to recognize because of the ringing in the transducer.

In Fig. 7 we present the B-scan obtained by applying the proposed algorithm on the data presented in Fig. 6. Ten iterations were performed for each A-scan and no significant changes of the solution from iteration to iteration were observed at the last iterations. In Fig. 8, an example of an A-scan acquired at position 20 mm is presented.

The estimates obtained at iteration $\mathrm{it} = 1$, i.e., when implicitly assuming $r(k)$ to be stationary, are shown in Fig. 9 as a B-scan and in Fig. 10 the A-scan at position 20 mm is shown. By comparing these estimates with the estimates presented in Figs. 7 and 8 we see that the proposed algorithm yields, as was expected, estimates that are sparse in nature. We can also see that the reflection from the internal layers are more easily recognized in estimates obtained using the proposed algorithm than in the estimates based on a stationarity assumption.

Finally, in Fig. 11 the effects of neglecting the attenuation in the signal model are shown. The B-scan in the figure was obtained by applying the proposed algorithm on the data assuming simply $\mathbf{G} = \mathbf{H}$, i.e., $\mathbf{A} = \mathbf{I}$ [cf. Eq. (11)].

We note that estimates are still sparse in nature but the back wall echos shown in Fig. 11 are often seen to be estimated as two closely spaced spikes with the same sign instead of single sharp spikes. A possible explanation to this behavior is that when the attenuation is neglected in the model, this attenuation must instead be included in the reflection sequence, causing these sequences to contain a larger portion of low-frequency components. Since the proposed algorithm forces the solution to be sparse, this low-pass behavior is, suboptimally, modeled by these repetitive spikes with the same sign.

The above-mentioned negative effect points out a limitation of the proposed method. As with all algorithms based on a sparsity assumption on the data, the solution will become sparse. Either this is true or not. In this work we tried to solve this problem by introducing the user parameter s_0 by which we could control the amount of sparsity. It would, of course, be more convenient if this parameter could be entirely determined by the data. We have in this work not made any attempt to accomplish that.

One practical issue that should be mentioned is that the attenuation model should be synchronized with the front wall echo because the attenuation does not affect the measurements before the pulse has entered the attenuative medium. In this work we solved this problem by identifying for each A-scan the time index of the front wall echo, k_{fw}, in the estimates obtained at the first iteration of the algorithm. The matrix $\mathbf{A}$ was then modified by inserting an $k_{\mathrm{fw}} \times k_{\mathrm{fw}}$ identify matrix in the upper left corner of $\mathbf{A}$.

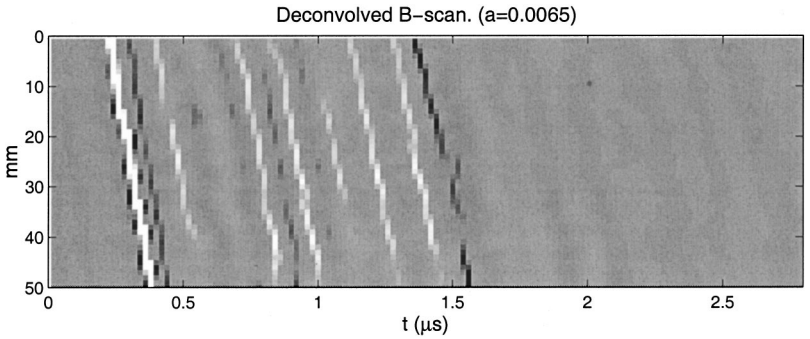

FIG. 7. B-scan obtained after ten iterations of the proposed algorithm. The attenuation model parameter was set to $a = 0.065$ and minimum allowed standard deviation $s_0 = 0.02$.

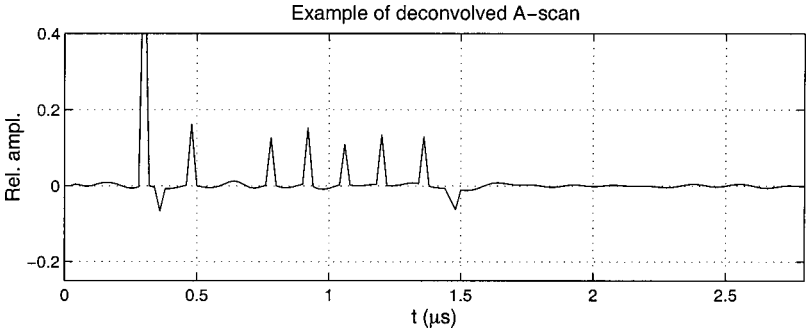

FIG. 8. Example of deconvolved A-scan from lateral position 20 mm in the B-scan in Fig. 7. The amplitude of the front wall echo at time index $k=15$ is 0.62.

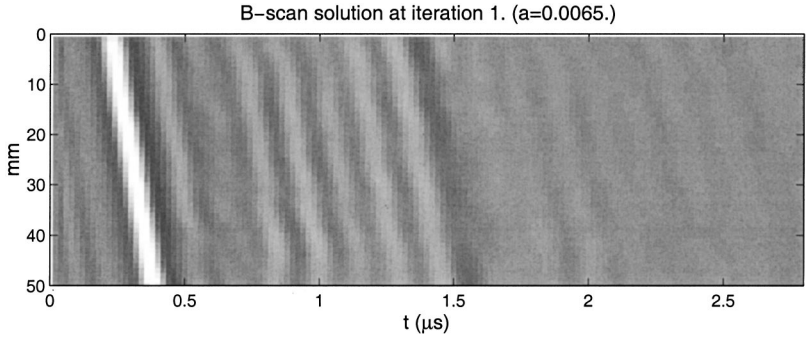

FIG. 9. B-scan obtained by performing one iteration of the proposed algorithm. The attenuation model parameter was set to $a=0.065$.

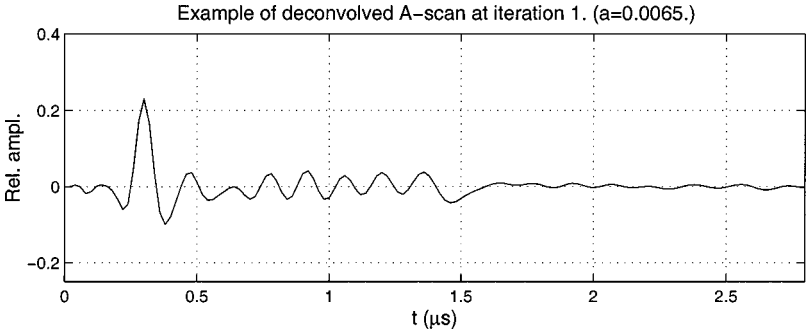

FIG. 10. Example of deconvolved A-scan from lateral position 20 mm in the B-scan in Fig. 9.

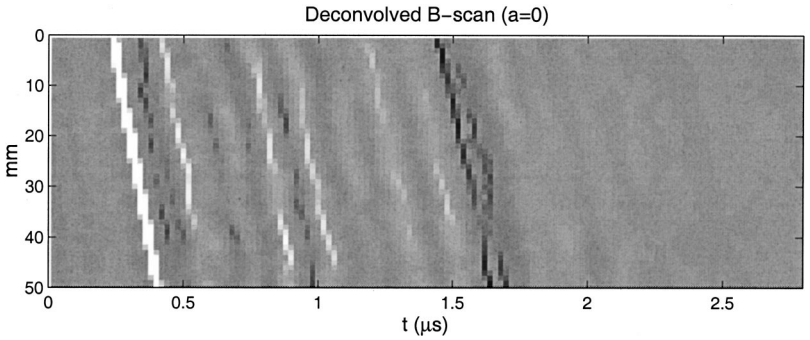

FIG. 11. B-scan obtained after ten iterations of the proposed algorithm. The attenuation was neglected in the signal model, i.e., $a=0$ and the minimum allowed standard deviation was set to $s_0=0.02$.

V. CONCLUSIONS AND POSSIBLE IMPROVEMENTS

We have presented an algorithm for deconvolution of ultrasonic pulse echo signals. The algorithm requires the signal to be dominated by a few echoes, i.e., the signal is required to be sparse (or semi-sparse). The algorithm is based on joint MAP estimation of the amplitudes in the reflection sequence and their corresponding standard deviation. It can be seen as a generalization of the noncausal Wiener filter adapting to nonstationarities in the input signal leading to sparse estimates. The sparsity can be controlled by means of a user parameter that controls the minimum standard deviation allowed for the amplitude pdf's and, thereby, the algorithm allows for treating a continuum between sparse and highly entropic (stationary Gaussian) reflection sequences.

The sparse signal model is based on the assumptions of a relatively thin material containing parallel layers that reflect echos that closely resemble a prototype echo acquired from a planar reflector. In some cases however, due to diffraction effects, the reflections from the layers will not have the same shape as the prototype. This can be observed, for instance, when the transducer is placed above an area that is close to the edge of the object.

In the article we also presented a simple but, for signal processing purposes, suitable discrete-time model for frequency-dependent attenuation. The distortion of the pulse wavelet as it travels through the medium was modeled as successive convolutions with a fixed kernel that is close to a delta function. By incorporating the attenuation in the signal generation model the assumption of sparsity of the reflection sequence becomes realistic.

Deconvolution results obtained by applying the algorithm on simulated data illustrated the properties of the algorithm and verified that the algorithm yields sparse solutions. Results obtained using real ultrasonic data showed the benefits of including the attenuation in the signal model. Neglecting attenuation in the model resulted in false spikes, especially at the strongly attenuated back wall echo, possibly compensating for the model error. The number of false spikes was reduced when including the attenuation in the model, and the interpretation of the estimates was thus simplified.

One limitation with the proposed algorithm is that the sparsity of the estimate at present is controlled by means of a user parameter. The choice of this parameter is somewhat subjective and we pointed out that it would be desirable to instead estimate this parameter using the measured data. Two other limitations, that in this work were not considered to be serious, are the need for an estimate of the attenuation model parameter and for synchronizing the attenuation model with the front echo. The first issue was solved by matching the model parameter to frequency shift data in an independent experiment and the second issue was solved by identifying the position of the front wall echo in an estimate obtained under stationarity assumptions.

ACKNOWLEDGMENTS

The authors wish to acknowledge Eider Martinez for performing the measurements and Dr. Ping Wu for valuable comments regarding attenuation modeling.

[1] S. Kay, *Fundamentals of Statistical Signal Processing: Estimation Theory* (Prentice Hall, Englewood Cliffs, NJ, 1993).
[2] J. Mendel, *Optimal Seismic Deconvolution, an Estimation Based Approach* (Academic, New York, 1983).
[3] C. Chi and J. Mendel, ''Viterbi Algorithm Detector for Bernoulli–Gaussian Processes,'' IEEE Trans. Acoust., Speech, Signal Process. **33**(3), 511–519 (1985).
[4] J. Goutsias and J. Mendel, ''Maximum Likelihood Deconvolution: An Optimization Theory Perspective,'' Geophysics **51**(6), 1206–1220 (1986).
[5] G. Giannakis, J. Mendel, and X. Zhao, ''A Fast Prediction Error Detector for Estimating Sparse-Spike Sequences,'' IEEE Trans. Geosci. Remote Sens. **27**(3), 344–351 (1989).
[6] F. Champagnat, Y. Goussard, and J. Idier, ''Unsupervised Deconvolution of Sparse Spike Trains Using Stochastic Approximation,'' IEEE Trans. Signal Process. **44**(12), 2988–2998 (1996).
[7] T. Pham and R. deFigueiredo, ''Maximum likelihood estimation of a class of non-Gaussian densities,'' IEEE Trans. Acoust., Speech, Signal Process. **37**(1), 73–82 (1989).
[8] I. Santamaría-Cabellero, C. Pantaleón, and A. Artés-Rodríguez, ''Sparse deconvolution using adaptive mixed-Gaussian models,'' Signal Process. **54**(2), 161–172 (1996).
[9] S. Azimi, A. Kalinin, V. Kalinin, and B. Pivovarov, ''Impulse and transient characteristics of media with linear and quadratic absorption laws,'' Izv. Earth Physics, 42–54 (1968).
[10] R. Weaver and Y.-H. Pao, ''Dispersion relations for linear wave propagation in homogeneous and inhomogeneous media,'' J. Math. Phys. **22**, 1909–1918 (1981).
[11] T. Szabo, ''Time domain wave equation for lossy media obeying a frequency power law,'' J. Acoust. Soc. Am. **96**, 491–500 (1994).
[12] K. Rasmussen, ''Maximum likelihood estimation of the attenuated ultrasound pulse,'' IEEE Trans. Signal Process. **42**(1), 220–222 (1994).
[13] N. Saffari and L. Svilainis, ''Signal Processing for Ultrasonic Imaging of Lossy Composites,'' Ultragarsas (Ultrasound), **2**(28), 7–11 (1997).
[14] T. Rhyne, ''Radiation coupling of a disk to a plane and back or a disk to a disk: An exact solution,'' J. Acoust. Soc. Am. **61**, 318–324 (1977).
[15] R. Fletcher, *Practical Methods of Optimization* (Wiley, New York, 1987).
[16] A. Papoulis, *Probability, Random Variables, and Stochastic Processes* (McGraw–Hill, New York, 1984).

A model for sound lateralization

Vered Aharonson[a] and Miriam Furst
Department of Electrical Engineering–Systems, Faculty of Engineering, Tel Aviv University, Tel Aviv 69978, Israel

(Received 3 December 1999; revised 18 July 2000; accepted 22 March 2001)

Recent studies of multiple sclerosis (MS) and stroke patients suggested a correlation between two patterns of abnormal performance in lateralization tasks and two sites of pontine lesions. Most patients who had lesions below or at the superior olivary complex (SOC) perceived all interaural differences in binaural stimuli as small, while most patients who had lesions above the SOC perceived all interaural differences as large. The two abnormal performance patterns occurred for interaural time differences (ITD) and/or for interaural level differences (ILD). The present model proposes a multi-level hierarchical brainstem structure that estimates ITD and ILD. The first level seeks dissimilarity between the left and right inputs and a second level looks for similarity between the two sides' inputs. Each level is modeled as an ensemble of neural arrays in which each unit performs a logic or arithmetic function. The inputs are simulations of auditory nerve responses to broadband stimuli. Simulations yield good correspondence to the effect of both locations of pontine lesions on binaural performance. © *2001 Acoustical Society of America.*
[DOI: 10.1121/1.1371756]

PACS numbers: 43.64.Bt [LHC]

I. INTRODUCTION

Recent psychophysical studies of multiple sclerosis (MS) and stroke patients (Furst *et al.*, 1995; Aharonson *et al.*, 1998) investigated lateralization performance of those patients. Stimuli with either interaural time differences (ITD) or interaural level differences (ILD) were introduced through earphones and the patients were asked to locate the perceived sound on a visual scale of nine positions. Two distinct patterns of abnormal performance were observed due to either of the tested pathologies, MS or stroke: Interaural differences (ITD and/or ILD) were perceived either only at the *sides* or only near the *center* of the head. The two performance types were labeled ''side-oriented lateralization'' and ''center-oriented lateralization,'' respectively.

In parallel to the psychoacoustical studies, Furst *et al.* (1995, 2000) also performed a magnetic resonance imaging (MRI) study in which the pontine lesions of the patients were detected and superimposed on a human auditory pathway atlas. The two abnormal lateralization patterns corresponded to two different anatomical locations of pontine lesions. Lesions at the trapezoid body (TB), a fiber tract leading to the superior olivary complex (SOC) nuclei, and/or lesions at the SOC, were correlated to center-orientated lateralization performance. Brainstem lesions at the lateral lemniscus (LL), a fiber tract leading to the inferior colliculus (IC) nuclei and/or at the IC, were correlated to a side-oriented performance. The lateralization performance of patients who had brainstem lesions in both anatomical sites, the TB/SOC and the LL/IC, was either center-oriented or side-oriented depending on the extent of the lesions in each site. All the patients that performed normally in the lateralization experiment did not have a detectable pontine lesion that involved the auditory pathway.

Most existing models of binaural mechanism in the brainstem were based on data from either animal studies or psychophysical evaluations of healthy subjects. Some models were qualitative but were stated in physiological terms (i.e., Jeffress, 1948, 1972; Bekesy, 1960; Van Bergeijk, 1962; Gaumond and Psdaltikidou, 1991). Other models were quantitative but predicted the binaural perception properties in terms of input-output functions, i.e., black-box models (i.e., Durlach, 1963, 1972; Osman, 1971, 1973). The most sophisticated quantitative models applied signal processing techniques on auditory nerve responses to binaural stimuli (i.e., Domnitz, 1973; Colburn, 1973, 1977; Domnitz and Colburn, 1977; Colburn *et al.*, 1990; Reed and Blum, 1991; Carney, 1993; Reed and Dubreck, 1995; Stern and Trahiotis, 1996; Brughera *et al.*, 1996; Cai *et al.*, 1998a, b). Some models suggested a single brainstem level structure located in the SOC nuclei that perform ITD or ILD estimation (e.g., Colburn, 1973, 1977). Other models suggested a multilevel structure whose first level was related to the SOC and where higher levels were not specifically expressed (e.g., Stern *et al.*, 1988; Shackleton *et al.*, 1992; Stern and Trahiotis, 1996). All the models could explain the lateralization performance of normal subjects. They might even be extended to explain an abnormality like center-oriented lateralization, when the SOC level is impaired. We are not aware, however, of any existing model that can explain the correlation between lesions at the LL/IC to side-oriented lateralization. In the present article we introduce a model that reproduces the experimental results and accounts for lateralization performance of both normal subjects and patients with brainstem lesions caused by both types of pathologies (MS and stroke).

[a]Author to whom correspondence should be addressed. Electronic mail: vered@eng.tau.ac.il

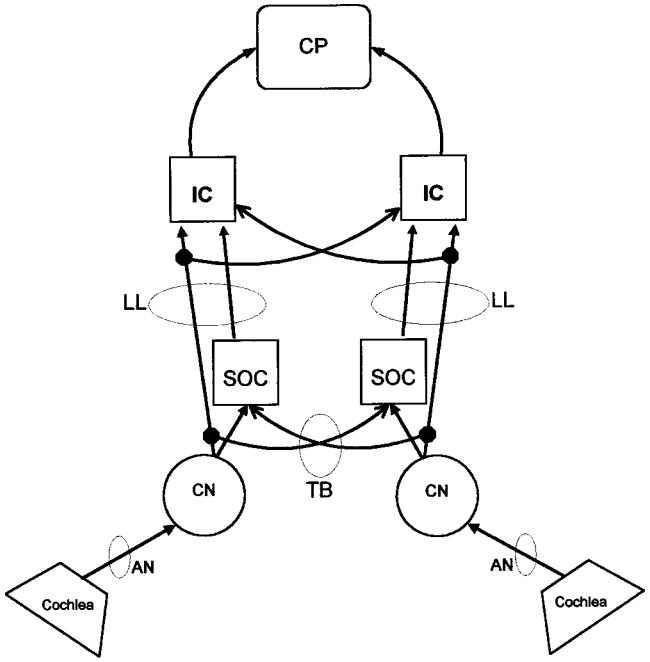

FIG. 1. A schematic drawing of the model nuclei and connections that perform lateralization. The SOC and IC nuclei are illustrated as rectangles, and the TB and LL fiber tracts are indicated by dotted circles. The block CP is the central processor, which reflects higher brain functions.

II. THE LATERALIZATION MODEL

A. Concept

The experimental results suggest that lesions at fiber tracts leading to the SOC can cause large interaural differences to be perceived as small, while lesions at fiber tracts leading to the IC, either unilaterally or bilaterally, can cause small interaural differences to be perceived as large. Both phenomena can be explained by a structure of two levels that estimate interaural differences in the brainstem: one level at the SOC, and a second level at or above the IC.

The first level detects *differences* between the left and right inputs. If no difference is detected, the default decision is that the two inputs are similar, and, consequently, small interaural difference will be estimated. The second level in the structure looks for *similarity* between the two inputs. If no similarity can be determined, the default decision is that the two inputs are different, and therefore large interaural difference will be estimated.

B. Model features and notations

The brainstem is modeled as a hierarchical structure of two levels: superior olivary complex (SOC) and inferior colliculus (IC), illustrated by square boxes in Fig. 1. The SOC is the first binaural processor that receives bilateral inputs, from both left and right cochlear nuclei (CN). The second binaural processing level in the brainstem is the IC. This level receives data from both the CN and from the SOC level. No binaural processing is performed at the CN (illustrated as circles in Fig. 1), since their input is unilateral. The model considers only feed forward links, or connections from lower levels to higher ones.

All the anatomical structures that were included in Fig. 1 have an anatomical basis, but by no means does Fig. 1 include all existing pathways in the auditory brainstem. We consider paths from each SOC to the ipsilateral IC and from each CN to both ipsilateral and contralateral IC. The latter path leads from the CN, without crossing at the SOC level, through the ipsilateral LL, where it bifurcates into both IC. Various studies have traced SOC-IC paths in the brainstem and bifurcations at the LL into both IC (Warr, 1966; Adams, 1979; Webster *et al.*, 1992; Li and Kelly, 1992; Faingold *et al.*, 1993; Bajo *et al.*, 1993; Merchan *et al.*, 1994). Although direct projections from the CN through the ipsilateral LL are very scarce (i.e., Warr, 1982), we included them in the model to account for backup monaural paths.

Nuclei at each level are modeled as ensembles of processing units. Each unit is identified by its level's name, i.e., SOC or IC. The term ''unit'' stands for an entity performing a function. The function can be realized either by a single neuron or by a group of neurons. The responses at all neural stages were modeled as trains of action potentials. This was done using functions that could take only the values 0 or 1:

$$f(t)=\begin{cases}0, & \text{when no action potential occurred,}\\ 1, & \text{when an action potential occurred.}\end{cases} \tag{1}$$

Those trains of action potentials can be described as stochastic processes that propagate information from one nucleus to another. Each nucleus is described by its input process and by the function it applies.

A binaural stimulus is transduced by both cochleae into two sets of neural spike trains that propagate through the two auditory nerves (AN) fiber to the brainstem. Since the tonotopic structure determined by the cochlea is preserved in the entire auditory pathway, each spike train will be labeled by a subscript ''n'' to denote its characteristic frequency.

The monaural signals transmitted by the AN fibers are labeled $\mathrm{MON}_{S,n}(t)$. The index n corresponds to a fiber out of N parallel fibers at the AN ($n=1,2,...,N$). The subscript S is the side-index, which stands for either left (''L'') or right (''R''). The signals $\mathrm{MON}_{L,n}(t)$ and $\mathrm{MON}_{R,n}(t)$ take a form described in Eq. (1). The signals enter the brainstem, pass through the CN at the ipsilateral side (L or R, respectively) and proceed towards the SOC level.

The SOC and IC levels contain two nuclei labeled ''left'' and ''right.'' The right model nuclei determine locations of a sound source in the left half space, while the left nuclei localize sound sources in the right half space. The integration of the left and right IC outputs into a single output is assumed to be performed by higher levels, above the brainstem. This process is implemented by a level labeled *central processor* (CP), which follows the IC (Fig. 1). The notations for all neural responses up to the CP include a subscript ''S,'' indicating left (''L'') or right (''R'') nuclei.

Processing of time and level cues in the signal is performed by separate, parallel mechanisms, in both SOC and IC levels. A notation ''T'' or ''L'' distinguishes responses for time or level, respectively. At the level of the CP the time and level pathways from both sides are merged to obtain a single decision as to where the sound source position is.

C. SOC model

The inputs $\mathrm{MON}_{L,n}(t)$ or $\mathrm{MON}_{R,n}(t)$ are transmitted from the left or right CN to the SOC level along two paths (Fig. 1). One path consists of fibers that do not pass through the midline of the brainstem, and carries data to the ipsilateral SOC. The second path is the trapezoid body (TB) that carries data to the contralateral SOC. The latter path consists of fast conducting fibers, connected to the left and right SOC, that are labeled $\mathrm{MON}_{R\to L,n}(t)$ and $\mathrm{MON}_{L\to R,n}(t)$, respectively.

Each input fiber enters two neural arrays in the SOC: a time processing array (ITD array) and a level processing array (ILD array). The SOC of each side thus consists of two ensembles of N arrays. In both ensembles, each array is identified by the same index n ($n=1,2,...,N$) which corresponds to the fiber characteristic frequency. Both array types contain M units, where each unit is characterized by an interaural difference, either ITD or ILD. The input fiber is connected to all the units of its destination array.

The structure and function of an ITD detection array were suggested by Jeffress (1948) and have been elaborated on in previous models (i.e., Colburn *et al.*, 1990). The present model implements ITD detection as follows: A contralateral and an ipsilateral fiber are connected to all the units in an ITD array. The connections of the contralateral fiber create a ladderlike structure that realizes delay lines, through fiber length (Smith *et al.*, 1991). The ipsilateral fiber's connections to the units have similar lengths. Each unit in the array detects coincidence between its ipsilateral and contralateral inputs. The M units are labeled by indices m, where $m=0,1,...,M-1$. A unit m is associated with a delay of $m\Delta\tau$ in the contralateral input, where $(M-1)\cdot\Delta\tau$ is the largest delay detectable by the array. A unit outputs ''1'' when two spikes—from the ipsilateral input fiber [i.e., $\mathrm{MON}_{R,n}(t)$ in the right SOC] and contralateral input fiber [i.e., $\mathrm{MON}_{L\to R,n}(t)$ in the right SOC]—arrive during an interval ε. The coincidence interval ε is short enough such that the probability for a monaural coincidence is insignificant. The output of a unit m in the right SOC ITD array n is given by the function:

$$\mathrm{TSOC}^{m}_{R,n}(t)=\begin{cases}1 & \text{when} \quad (\mathrm{MON}_{L\to R,n}(t')\wedge\mathrm{MON}_{R,n}(t''))>0,\\ & t-\varepsilon\leqslant t',t''<t,\\ 0 & \text{otherwise,}\end{cases} \tag{2}$$

where ''$\wedge$'' is a logical ''AND'' and ε is the coincidence time interval. $\mathrm{TSOC}^{m}_{L,n}(t)$ is similarly obtained, by substituting $(\mathrm{MON}_{R\to L,n}(t')\wedge\mathrm{MON}_{L,n}(t''))$ in Eq. (2).

Interaural level differences are calculated in ILD arrays. The structure and function of an ILD comparison array was suggested in previous models (i.e., Reed and Blum, 1991). The present model implements the ILD estimation mechanism as follows: A contralateral fiber and an ipsilateral fiber are connected to all the units in an ILD array. No delay lines are implemented in the ILD detection, hence, all contralateral connections are assumed to have similar lengths. A spike counting operator is applied as an ILD detector, where each contralateral input spike (i.e., $\mathrm{MON}_{L\to R,n}(t)$) increases the count by 1 and each ipsilateral input spike (i.e., $\mathrm{MON}_{R,n}$) decreases the count by 1. The counting is operated during an interval τ_{SOC}, and is then compared to threshold values. The spike counting operator is described as follows:

$$Lc(x,-y,\tau)=\log_{10}\frac{\mathrm{Count}(x(t),\tau)}{\mathrm{Count}(y(t),\tau)},$$

where x and y are excitatory and inhibitory spike trains, respectively, τ is the counting time interval and the function $\mathrm{Count}(x(t),\tau)$ is the number of spikes counted within an interval $[t,t+\tau]$.

For simplicity reasons, we define a similar number of units (M) for both ILD and ITD arrays. The M different units in an ILD array are labeled by indices m, where $m=0,1,...,M-1$. A unit m is associated with an element $C(m)$ from a vector C of length M, defined as follows: $C(0)=0$, $C(m)>0$ and $C(m+1)\geqslant C(m)$. M discrete ILD values are thus detectable by an array, where each ILD corresponds to a different $C(m)$ value. Specifically, the output of unit m at the right SOC ILD array n is given by the function

$$\mathrm{LSOC}^{m}_{R,n}(t)=\begin{cases}1 & \text{when} \quad C(m-1)\leqslant Lc(\mathrm{MON}_{L\to R,n},-\mathrm{MON}_{R,n},\tau_{\mathrm{SOC}})<C(m),\\ 0 & \text{otherwise.}\end{cases} \tag{3}$$

$\mathrm{LSOC}^{m}_{L,n}(t)$ is similarly obtained by substituting $\mathrm{MON}_{R\to L,n}(t)$ and $\mathrm{MON}_{L,n}$ in Eq. (3).

Since $C(m)$ are positively defined, ILD units yield no output when contralateral inputs are less intense than the ipsilateral ones. Analogously, ITD units can only yield output when the contralateral sound arrives at the ear before (or together with) the ipsilateral one. Each SOC can thus estimate interaural differences only when the signal at the contralateral side preceded or was more intense than the ipsilateral signal.

Both ITD and ILD arrays will not yield an output if the contralateral input was abnormally delayed or blocked (ITD$\gg M\Delta\tau$; ILD$\gg$C(M)).

D. IC model

The present model suggests a second lateralization level that follows the SOC level in the brainstem. The function of this second level is to produce interaural difference estimation if such estimation was not performed at the first level (SOC).

The IC arrays receive two data types: bilateral monaural inputs, directly from the CN level, that reach the IC level through both lemnisci (as can be seen in Fig. 1), and ipsilateral inputs from a SOC nucleus, carrying interaural difference estimations. If the SOC arrays and the TB and LL transmission paths are intact, the IC decision merely reproduces the SOC estimation and is thus redundant. If interaural difference estimation was not performed at the SOC level or was not transmitted to the IC, a crude estimation of ITD and/or ILD can still be made, based on the monaural inputs. The monaural paths are crucial for the system, since they indicate whether a signal was heard at either the left or the right peripheries or at both. An acute example is the case when only one ear is stimulated. In this case the SOC binaural units yield no output, and the stimuli location will be derived at the IC. Monaural right and left stimuli will be localized at the right and left sides, respectively. Such a backup system for lateralization is essential especially in a noisy environment, when the SOC might fail to transfer reliable information to the IC.

Each IC consists of ITD and ILD array matrices whose sizes are $M \times N$, and whose outputs are equal to the correspondent input SOC array matrices, i.e., $\mathrm{IC}^{m}_{S,n}(t) = \mathrm{SOC}^{m}_{S,n}(t)$; for $m=0,1,...,M-1$, $n=1,2,...,N$, where $\mathrm{SOC}^{m}_{S,n}(t')$ is an output from an ipsilateral SOC array n, either ITD or ILD. There are thus $4N$ interaural difference arrays at the IC level, and in an interval τ_{IC} each of them can provide a single output (only one of the M units in an array can be equal to 1). Thus, for every index n, four $\mathrm{IC}^{m}_{S,n}$ arrays can be characterized by four outputs: $m^{T}_{L,n}(t)$, $m^{T}_{R,n}(t)$, $m^{L}_{L,n}(t)$, and $m^{L}_{R,n}(t)$ that represent the left IC array for ITD, right IC array for ITD, left IC array for ILD, and right IC array for ILD, respectively.

Each IC array also includes three types of output units: $\mathrm{IC}^{I}_{S,n}$, $\mathrm{IC}^{II}_{S,n}$, and $\mathrm{IC}^{III}_{S,n}$. The unit $\mathrm{IC}^{I}_{S,n}$ indicates whether a response from any of the SOC outputs was received at the IC level. If $\mathrm{IC}^{I}_{S,n}=0$, which means no input from the SOC, then one of the other two units $\mathrm{IC}^{II}_{S,n}$ or $\mathrm{IC}^{III}_{S,n}$ can fire, either one but not both simultaneously. The $\mathrm{IC}^{II}_{S,n}$ unit indicates that inputs were received from both monaural paths, whereas $\mathrm{IC}^{III}_{S,n}$ indicates that only a crossed monaural input was received. Formally, the outputs of the IC units are defined as follows:

$$\mathrm{IC}^{I}_{S,n}(t)=\begin{cases} 1 & \text{when } \sum_{m=0}^{M-1} \mathrm{SOC}^{m}_{S,n}(t')>0, \quad t-\tau_{IC}\leqslant t'\leqslant t, \\ 0 & \text{otherwise,} \end{cases} \tag{4}$$

where ''Σ'' represents a logical OR and $\mathrm{SOC}^{m}_{S,n}(t')$ is an output from an ipsilateral SOC array n, either ITD or ILD:

$$\mathrm{IC}^{II}_{S,n}(t)=\begin{cases} 1 & \text{when } (\mathrm{MON}^{LL}_{S\to S,n}(t')\wedge \mathrm{MON}^{LL}_{S\to S,n}(t''))\wedge \overline{\mathrm{IC}^{I}_{S,n}(t''')}>0, \quad t-\tau_{IC}\leqslant t',t'',t'''<t, \\ 0 & \text{otherwise,} \end{cases} \tag{5}$$

where $\mathrm{MON}^{LL}_{S\to S,n}$ and $\mathrm{MON}^{\overline{LL}}_{S\to S,n}$ are the monaural ipsilateral and contralateral inputs that reach each IC, whose origins are at the ipsilateral and contralateral CN and their paths pass through the ipsilateral and contralateral LL, respectively (Fig. 1):

$$\mathrm{IC}^{III}_{S,n}(t)=\begin{cases} 1 & \text{when } (\mathrm{MON}^{LL}_{S\to S,n}(t')\wedge \overline{\mathrm{MON}^{LL}_{S\to S,n}(t'')})\wedge \overline{\mathrm{IC}^{I}_{S,n}(t''')}>0, \quad t-\tau_{IC}\leqslant t',t'',t'''<t, \\ 0 & \text{otherwise.} \end{cases} \tag{6}$$

Obviously, a response of IC^{III} unit indicates that only a crossed monaural input was received. It is clear from Eqs. (4)–(6) that in a time interval τ_{IC}, only one of the units $\mathrm{IC}^{I}_{S,n}$, $\mathrm{IC}^{II}_{S,n}$, or $\mathrm{IC}^{III}_{S,n}$ can be equal to 1.

The additional binaural processing at the level of the IC, as previously described, can advance the estimation of the interaural difference provided by the SOC in two manners. (1) It indicates that a binaural stimulus was presented $\mathrm{IC}^{II}_{S,n}=1$, which generates a default interaural delay at higher levels. (2) It indicates a monaural stimulus $\mathrm{IC}^{III}_{S,n}=1$. Those outputs are processed at higher levels of the auditory pathway to determine the perceived position of a sound.

E. CP model

A central processor (CP) follows the IC level and combines the two IC output estimations into a full range of both left and right interaural differences. The ITD and ILD that were separately estimated in the brainstem level are combined at the CP into a single position estimation in the central processor.

We assume that the CP integrates all IC inputs and ascertains consistencies between left and right inputs *and* ITD and ILD inputs. Inputs to the CP might have two main discrepancies: (1) left-right discrepancy and (2) level-time discrepancy. Left-right discrepancies arise from the dual structure of the SOC and the IC levels. When an interaural difference is presented, only the SOC at the side of the lagging, or less intense signal, is activated. The IC at that same side will then pass the correct estimation. The SOC at the other side, however, yields no output, and the IC output at that side will indicate a zero interaural delay because it receives only the monaural inputs from both sides. The CP task is to resolve this conflict.

A level-time discrepancy can arise in lateralization tests when *only* one of the interaural differences (ITD or ILD) is introduced. In this case, arrays that correspond to the intro-

duced interaural difference will indicate difference, while the arrays that correspond to the other interaural difference will indicate none. Since in lateralization experiments, normal subjects clearly perceive lateralization changes with only one type of interaural delay, it seems that the system prefers the ''difference'' decision over the ''similar'' decision.

In the present model we do not specifically relate the CP to a known anatomical structure. Therefore, we describe its function by using logical and arithmetic operations without a detailed description of how such a process is implemented.

Each CP array contains $2M-1$ units, labeled by indices k, where $k=-M+1,...,-1,0,1,...,M-1$. At each time interval τ_{CP}, only one of those units will be active (its output will be 1). The index of the active unit represents the perceived position; $k<0$ represents a left-side position; $k=0$ represents the center position; and right-side positions are presented by $k>0$. We divide the $2M-1$ different units in the CP array into three subgroups that correspond to three categories of interaural differences: small, intermediate, and large. Small interaural differences are represented by small values of k: $0\leqslant|k|\leqslant K_{II}$, where $K_{II}\ll M$. Intermediate interaural delays are represented by $K_{II}<|k|\leqslant K_{III}$, where $K_{III}\gg 0$. Large interaural delays are represented by $K_{III}<|k|\leqslant M-1$. Hence a center position is defined as one of the indices in the group: $\{-K_{II},\ldots,0,...,K_{II}\}$, and a side position is defined as one of the indices in the groups $\{K_{III},\ldots,M-1\}$ or $\{-M+1,...,-K_{III}\}$.

When both SOC and IC supply the CP with an estimation of ITD and ILD, then the CP will decide on k, the index of the active output, on basis of the 4 individual decisions obtained by the different IC arrays: $m^{T}_{L,n}(t)$, $m^{T}_{R,n}(t)$, $m^{L}_{L,n}(t)$, and $m^{L}_{R,n}(t)$. Let us define k_S as

$$k_S=\mathrm{sign}(S)\cdot(m^{T}_{S,n}+m^{L}_{S,n}), \tag{7}$$

when S indicates one of the sides R or L, and

$$\mathrm{sign}(S)=\begin{cases}1, & S=R,\\ -1, & S=L.\end{cases} \tag{8}$$

The perceived position k in this case will be

$$k=k_S+k_{\bar{S}}, \tag{9}$$

when $\bar{S}$ indicates the complement side of S. It is clear from the above equations that both cues ITD and ILD are taken into account. For example, a center position will be perceived when ITD cue will indicate right and ILD will indicate left.

In general, the CP array receives five input types from each side: time and level $\mathrm{IC}^{m}_{S,n}$ estimations: $m^{T}_{S,n}(t)$ and $m^{L}_{S,n}(t)$, and the additional three indications $\mathrm{IC}^{I}_{S,n}$, $\mathrm{IC}^{II}_{S,n}$, and $\mathrm{IC}^{III}_{S,n}$. From the definition of the latter three unit types [Eqs. (4)–(6)], it is clear that either none of the three are active (one option), or only one of them is active (another three options). These four possible inputs from each IC to the CP yield 16 input combinations where both IC are considered. However, due to the symmetry between the two IC, there are only ten different input combinations. Excluding the trivial case (no inputs from neither IC to the CP yields no output), we are left with nine different possible input combinations to the CP. We have listed those nine possibilities in Table I: The active inputs are indicated in the two left columns, and the index of the active output is indicated in the right column. The first row in Table I represents the case in which both $\mathrm{IC}^{I}_{L,n}(t)$ and $\mathrm{IC}^{I}_{R,n}(t)$ are active, and where the index of the active output output is given by Eq. (9).

TABLE I. CP input/output relations.

Active input to CP		Index of the active output
$\mathrm{IC}^{I}_{S,n}(t)$	$\mathrm{IC}^{I}_{\bar{S},n}(t)$	$k_S+k_{\bar{S}}$
$\mathrm{IC}^{I}_{S,n}(t)$	$\mathrm{IC}^{\mathrm{II}}_{\bar{S},n}(t)$	k_S
$\mathrm{IC}^{I}_{S,n}(t)$	$\mathrm{IC}^{\mathrm{III}}_{\bar{S},n}(t)$	$\begin{cases}k_S & \lvert k_S\rvert>K_{II}\\ \mathrm{side}_{\bar{S}} & \lvert k_S\rvert\leqslant K_{II}\end{cases}$
$\mathrm{IC}^{II}_{S,n}(t)$	$\mathrm{IC}^{II}_{\bar{S},n}(t)$	$\mathrm{rand}\{-K_{II},..,0,..,K_{II}\}$
$\mathrm{IC}^{II}_{S,n}(t)$	$\mathrm{IC}^{\mathrm{III}}_{\bar{S},n}(t)$	$\mathrm{side}_{\bar{S}}$
$\mathrm{IC}^{III}_{S,n}(t)$	$\mathrm{IC}^{\mathrm{III}}_{\bar{S},n}(t)$	$\mathrm{rand}\{\mathrm{side}_S,\mathrm{side}_{\bar{S}}\}$
$\mathrm{IC}^{I}_{S,n}(t)$	$\cdots$	$\begin{cases}k_S & \lvert k_S\rvert>K_{II}\\ \mathrm{side}_S & \lvert k_S\rvert\leqslant K_{II}\end{cases}$
$\mathrm{IC}^{II}_{S,n}(t)$	$\cdots$	side_S
$\mathrm{IC}^{III}_{S,n}(t)$	$\cdots$	side_S

As stated earlier, the CP strategy is to prefer ''difference'' decision over ''similarity'' decision. Thus a center position will be decided *only* if there is no contradiction between the different inputs to the CP. Let us define a side index as

$$\mathrm{side}_S=\mathrm{sign}(S)\cdot\mathrm{rand}\{K_{III},\ldots,M-1\}, \tag{10}$$

where $\mathrm{rand}\{G\}$ represents a random choice (based on a uniform distribution) of an element in the group G. The system will decide ''side'' on various cases, as can be seen in Table I. When only one ear is stimulated, $\mathrm{IC}^{III}_{S,n}(t)=1$, obviously the decision is ''side.'' When only one IC provides an estimate of a center position, and the opposite IC provides a contradictory information, then the CP decision will be side (rows 3, 5, 7, and 8 in Table I).

A center position will be decided only on the basis of receiving information from *both* IC. When both $\mathrm{IC}^{I}_{L,n}(t)$ and $\mathrm{IC}^{I}_{R,n}(t)$ are active (row 1 in Table I), a center position can be decided according to Eq. (9). The only other case that a center position will be decided is when both $\mathrm{IC}^{II}_{L,n}(t)$ and $\mathrm{IC}^{II}_{R,n}(t)$ are active (row 4 in Table I).

III. SIMULATION

A. Parameters and network performance representation

In order to evaluate the performance of the brainstem model, simulations were performed with the parameters cited in Table II. Since the model did not include auditory filters, we have tested the model performance for click stimuli, whose spectrum is wide band.

The network inputs $\mathrm{MON}_{L,n}(t)$ and $\mathrm{MON}_{R,n}(t)$, $n=1,2,...,N$, are realizations of a stochastic point process. As often used in simulation of neural systems, the point process

TABLE II. Parameters used in the simulation.

Parameter	Definition	Value
Δt	Simulation time step	5 μs
N	Number of parallel input fibers entering the network	2000
M	Number of units at an SOC array	36
ε	Coincidence detection interval of ITD array units at the SOC	15 μs
$M\Delta\tau$	Maximal interaural time difference at the SOC ITD array	900 μs
τ_{SOC}	Counting period of the SOC ILD array units	100 μs
τ_{IC}	Counting period of IC units	900 μs
τ_{CP}	Integration period of CP units	900 μs
K_{II}	The largest index among the IC units that can be activated when both monaural inputs are detected	10
K_{III}	The smallest index among the IC units that can be activated when monaural input is detected	25

is nonhomogenous Poisson with parameter $\nu(t)$. A simplified form of the rate function, $\nu(t;A)$ in spikes/second units, was chosen for the simulations, where A corresponds to the stimulus intensity in dB:

$$\nu(t;A)=\begin{cases}\nu_{\mathrm{spont}}, & A<30\ \mathrm{dB},\\ \nu_{\mathrm{spont}}+\alpha A, & 30\ \mathrm{dB}\leqslant A\leqslant 70\ \mathrm{dB},\\ \nu_{\mathrm{sat}}, & A>70\ \mathrm{dB}.\end{cases} \tag{11}$$

The reference intensity was chosen such that 50-dB stimulus level corresponds to a rate of 105 spikes/second. The values of the spontaneous and saturation rates for the simulation were $\nu_{\mathrm{spont}}=5$ spikes/second and $\nu_{\mathrm{sat}}=145$ spikes/second. The slope of the linear part of the function, between the two cut-off values was $\alpha=2[\mathrm{spikes}/(\mathrm{second}^*\mathrm{dB})]$. Simulations using these parameters were found sufficient to approximate PST histograms of AN responses to click stimuli recorded from the cat (i.e., Kiang *et al.*, 1965). Realizations of the stochastic point process were simulated by binary series of ''1'' for a spike (neural firing) and ''0'' for neural quiescence. A simulation of the network input, from a monaural single fiber $[\mathrm{MON}_{S,n}(t)]$ in response to a click stimulus, is shown in Fig. 2. The figure presents the simulated PST histogram of $\mathrm{MON}_{S,n}(t)$. The value of $\nu(t;A)$ in this simulation was 105 spikes/second. The histogram was obtained by repeating the simulation for 600 times.

Each monaural input bifurcates into two binaural processing paths, ITD and ILD arrays. The network thus contains 4^*N parallel arrays at the SOC and IC levels, 2^*N arrays in each side (right and left). At the CP level there are only N parallel arrays, since for every characteristic frequency all outputs, right, left, time and level are processed by a single CP array.

Since the inputs $\mathrm{MON}_{S,n}(t)$ are realizations of a stochastic point process and the processing involves logic and arithmetic functions, the outputs of the network's units are binary series as well and can be interpreted as realizations of different stochastic point processes. Figure 3 demonstrates three examples for the outputs of a SOC array. Figures 3(a) and (b) represent ITD arrays, and Fig. 3(c) represents ILD arrays. Both ITD and ILD arrays contain M units and thus

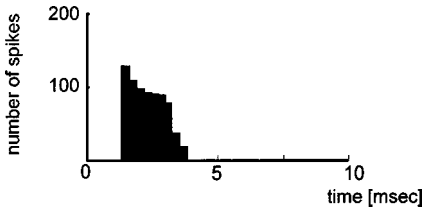

FIG. 2. A simulation of an auditory nerve fiber response to a click stimulus in PST histogram.

have M outputs, and they both receive similar bilateral monaural inputs. The input and outputs of the units are represented in Fig. 3 by their PST histograms. The input in Fig. 3(a) reflects no interaural difference, and the output shows response for units: $m=0$, $m=1$, and $m=2$ in both left and right SOC arrays. The input in Fig. 3(b) reflects an ITD of 675 μs with the left ear leading, and responses are seen for units $m=26$, 27, and 28 at the right SOC array; no units of the left SOC array have responded. The spike (logarithmic) count vector was chosen as $C(m)=m/2M$. The input in Fig. 3(c) reflects an interaural level difference of 7.5 dB with the left ear more intense; the responses are seen for units $m=25$, 26, 27, and 28 at the right SOC ILD array. Typically the number of units responded to different stimuli ranged from 1 to 15 units.

At the level of the central processor (CP) there are N arrays. Each array contains K units ($K=2^*M-1$). The output of the CP array's ensemble is represented by histograms for different ITD values in Fig. 4 [panels (a)–(e)]. The bins of the histograms are the indices of the CP units, k. The count in each bin, h_k, is the number of arrays in which the unit labeled k generated an output. All five histograms in Fig. 4 are manifestations of a Gaussian-like distribution whose mean is changing as a function of ITD. For ITD=0, the mean is at $k=0$ [Fig. 4(e)], while for ITD$=-0.9$ ms the mean is at $k=-31$ [Fig. 4(a)].

B. Simulation of pathologies

MS and stroke are two very different neural pathologies. However, the functional effect of both pathologies on signal processing in the brainstem can be similarly modeled. Both the destruction of fibers and/or neurons and the delayed transmission of neural signals can functionally cause a reception of incomplete data by the processing arrays. The use of similar simulations for the damage of both MS and stroke lesions can be justified by the fact that very similar behavioral abnormalities were detected in the lateralization tests for MS and stroke patients.

Both MS and stroke lesions were implemented in the simulations as an inactivation of fibers or neural arrays. A lesion involving either the auditory pathway below the SOC or at the SOC nuclei was implemented in the network as nonactivation of the TB fibers (modeled as contralateral conductors to the SOC). Nonactivation of SOC arrays yielded similar performance, since SOC array produces no output without a contralateral input. A TB lesion was simulated as affecting contralateral fibers to both the left and right SOC equally. According to the model, when TB fibers are not

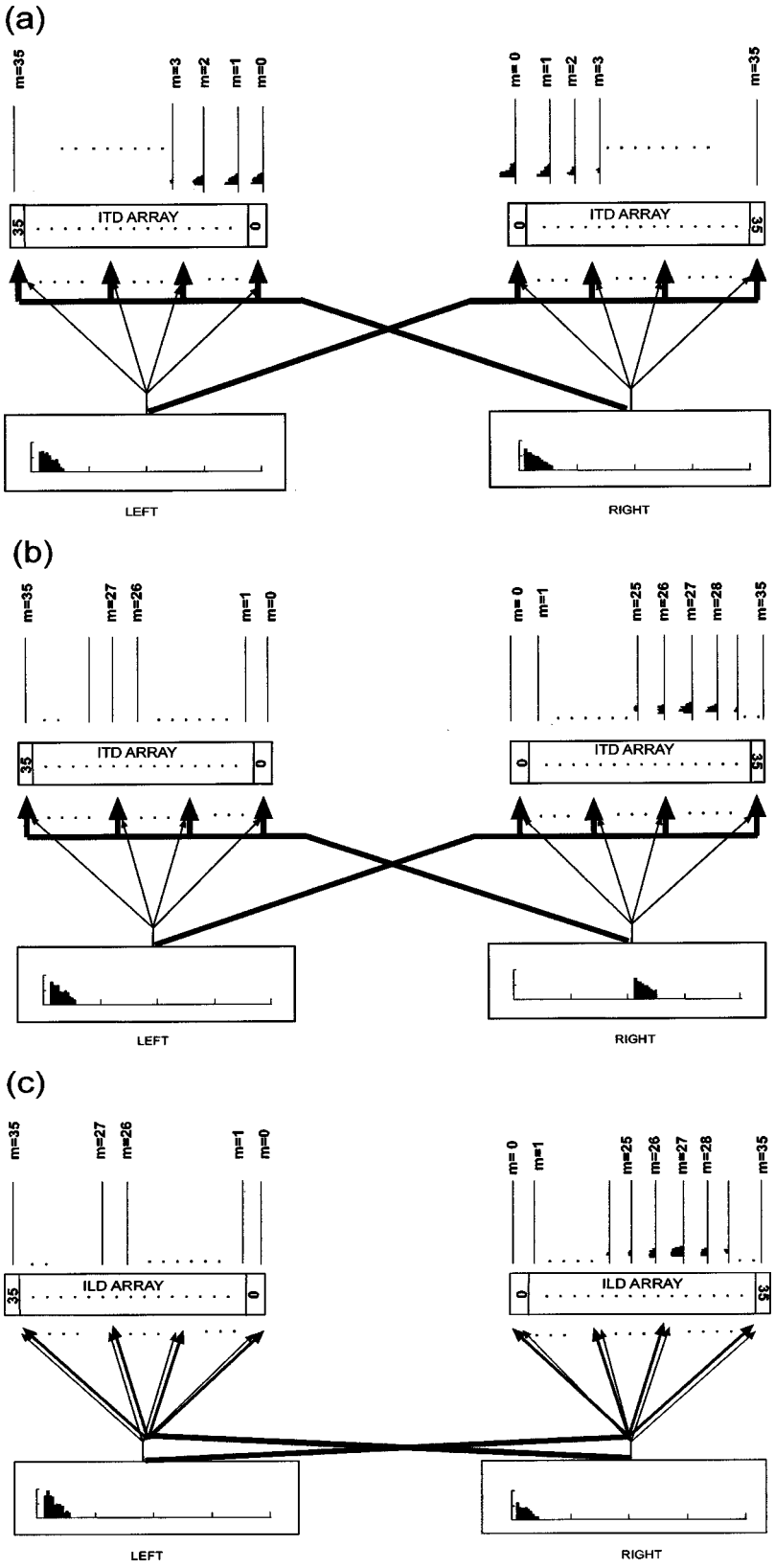

FIG. 3. A schematic structure of two SOC arrays at the left and right SOC, and PST histograms of their inputs and outputs. (a) Response of a pair of ITD arrays to an input where ITD $=0$ ms and ILD $=0$ dB. (b) Response of a pair of ITD arrays to an input where ITD $=-0.675$ ms and ILD $=0$ dB. (c) Response of a pair of ILD array to an input where ITD $=0$ ms and ILD $=-7.5$ dB.

activated, interaural differences cannot be detected at either SOC nuclei. The corresponding IC arrays then receive no SOC inputs but can still use the bilateral monaural inputs. Figure 5 demonstrates the performance of the network, for six cases of inactivated TB fibers, in histograms similar to the ones in Fig. 4. The six panels (a)–(f) demonstrate CP outputs for 0%, 25%, 50%, 65%, 80%, or 95% of the TB fibers inactivated, respectively. The stimulus for all cases was a binaural click with ITD $=0$ and ILD $=-5$ dB. Figure 5(a) represents the normal brainstem, in which the mean of the Gaussian-like distribution is at $k=-18$. When almost all TB fibers are not activated [panel (f), 95% of inactivation at the TB] the decision histogram has a uniform distribution for $-12<k<12$, with a mean at $k=0$. The distributions at pan-

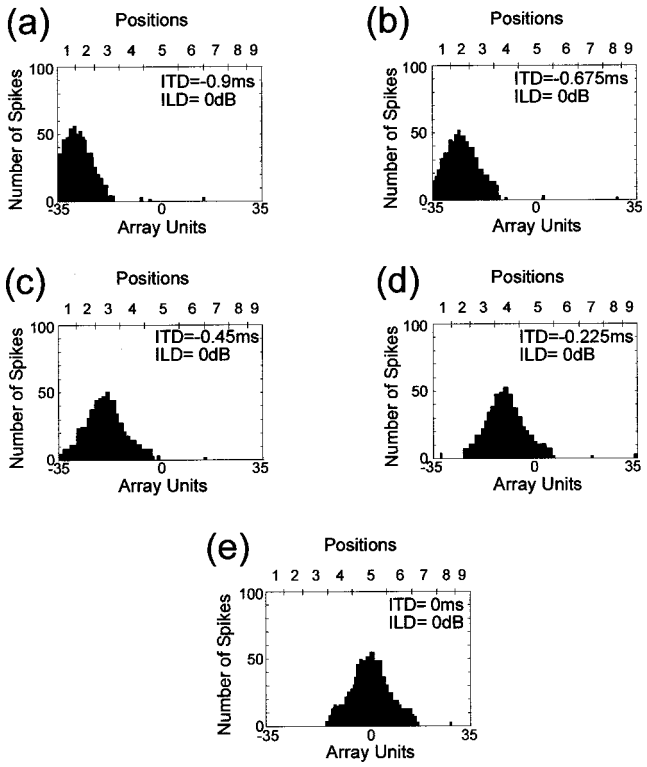

FIG. 4. Performance histograms representing the central processor decisions, for a binaural click with ITD values (a) −0.9 ms, (b) −0.675 ms, (c) −0.45 ms, (d) −0.225 ms, and (e) 0 ms.

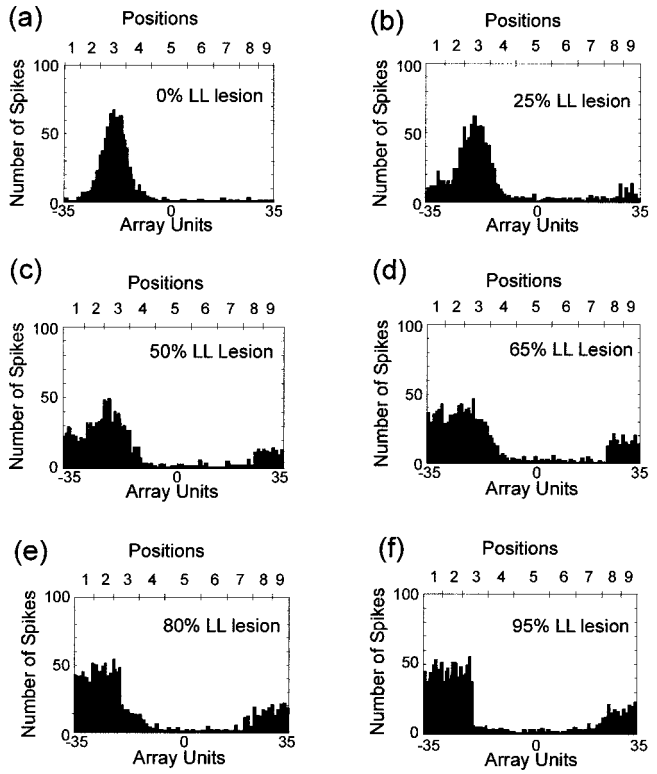

FIG. 6. Performance histograms representing the central processor decisions, for a binaural click with 0 ms ITD and −5 dB ILD, when a percentage of LL fibers were not activated: (a) 0%, (b) 25%, (c) 50%, (d) 65%, (e) 80%, and (f) 95%.

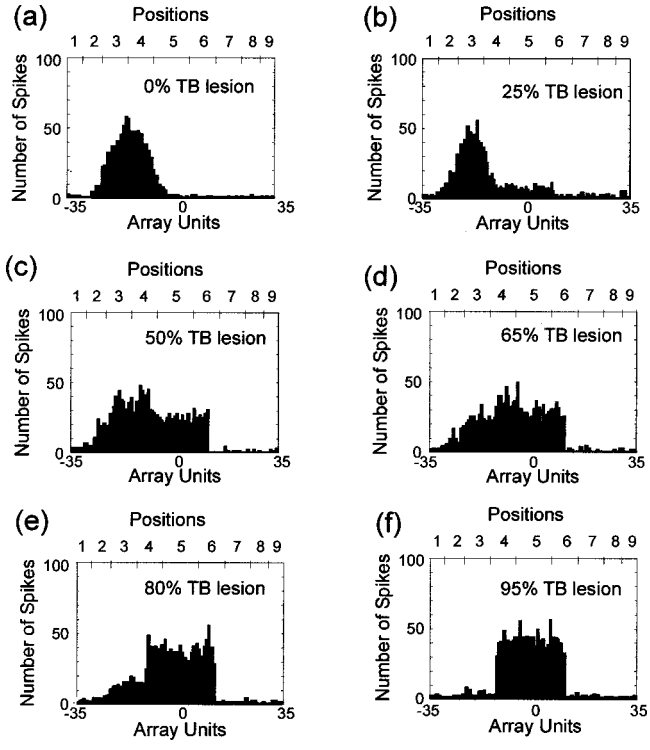

FIG. 5. Performance histograms representing the central processor decisions, for a binaural click with 0 ms ITD and −5 dB ILD, when a percentage of TB fibers (randomly distributed) were not activated: (a) 0%, (b) 25%, (c) 50%, (d) 65%, (e) 80% and (f) 95%.

els (b)–(e) undergo a progressive change from a Gaussian-like distribution to a uniformlike distribution.

IC lesions were modeled as damage to the LL. Figure 6 represents the CP output for a binaural click stimulus, with ILD$=-5$ dB and ITD$=0$, for different amounts of unilateral LL lesions. Figure 6(a) represents the normal brainstem with no lesions, and panels (b)–(f) represent the CP response with TB intact and different percentages of unilateral LL lesion from 25% [Fig. 6(b)] to 95% [Fig. 6(f)]. Figure 6(a) is similar to Fig. 5(a), a Gaussian-like distribution whose mean is at $k=-18$. In Fig. 6(f), the histogram has a bimodal uniform-like distribution centered around $-35<k<-24$ and around $28<k<35$. The dominant modal is centered at the negative values of k, which is the side of the mean of the histogram in Fig. 6(a). The distribution evolves from a Gaussian-like distribution to a bimodal uniform-like distribution with increasing percentage of LL lesion.

C. Comparison between patients' performance and model simulations

One of the main goals of this simulation is to compare the model predictions to lateralization performance obtained in psychophysical experiments by normal-hearing subjects and patients with different brainstem pathologies. We compared the model results to the lateralization experiments that are described in details in Furst *et al.* (1995) and Aharonson *et al.* (1998). In brief, the experiments included a set of stimuli with different interaural delays (ITDs) and interaural level differences (ILDs). Subjects were asked to match the

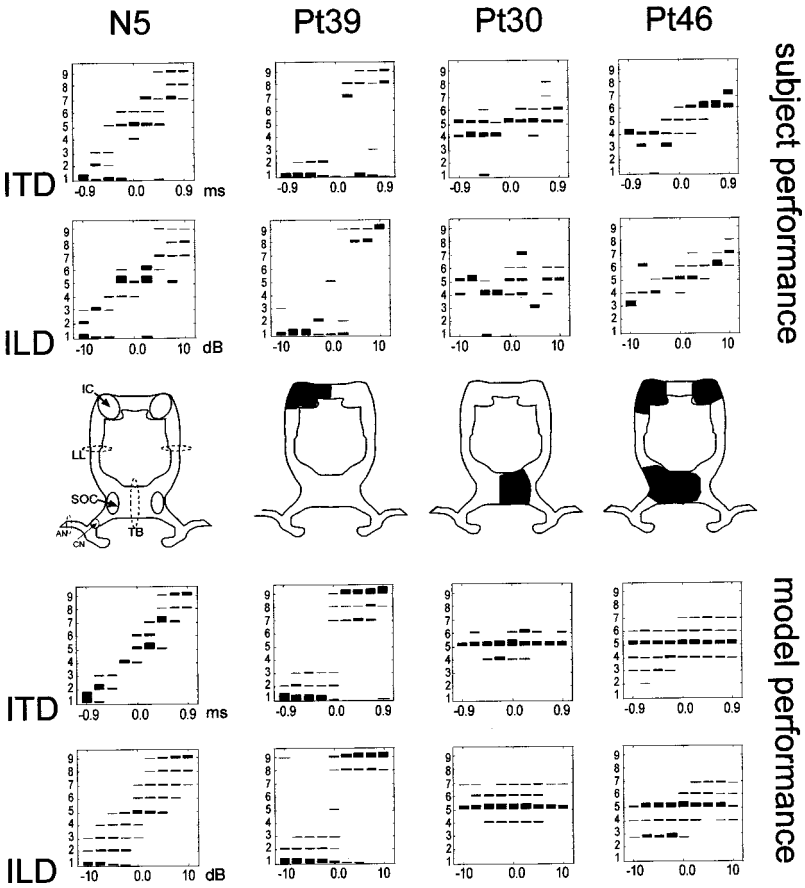

FIG. 7. Comparison between experimental data of different subjects' lateralization performance and the model predictions. The first and second rows represent the psychoacoustical performance of four subjects in a lateralization experiment (from Aharonson *et al.*, 1998) with ITD (first raw) and ILD (second raw). Each column represents a different subject. Schematic coronal drawing of the auditory pathways in the brainstem are shown in the third row. The locations of the lesions, as estimated by MRI analysis for the three patients (Furst *et al.*, 2000), are indicated in black. The fourth and fifth rows represent the lateralization performance predicted by the model for each subject (see details in text).

different stimuli to nine perceptual positions, POS $=1,2,...,9$. The middle position POS$=5$ indicated perception of a stimulus at the center of the head. Position 1 indicated perception of a stimulus at the left side of the head, and position 9 indicated perception at the right side of the head.

The model implements N^*K units that can fire in a response to a binaural click whose duration is 100 μs. Therefore, for each such stimulus, almost all N arrays respond, but in each array n, only one of the K units can fire. Thus the CP output can be presented as a random variable k, whose expected value ($E[k]$) is the estimated perceived position. To compare this estimation to the nine positions defined in the psychoacoustical experiments we use the following transformation:

$$\text{POS}=i \quad \text{if} \quad \overline{K_i} \leqslant E[k] < \overline{K_{i+1}} \quad \text{for} \quad i=1,2,...,9, \quad (12)$$

where the vector $\overline{K}$ is

$$\overline{K}=[\overline{K_1},\overline{K_2},\ldots,\overline{K_{10}}]$$
$$=[-35,-28,-21,-14,-5,6,15,22,29,26].$$

Since the density function of the perceived position is changing, as can be seen in Figs. 5 and 6, we used a heuristic approach for estimating $E[k]$: Repeating the simulation many times for the same stimuli, we counted the times that each k was selected. The k that yielded the maximum number of counts was considered as $E[k]$. In Figs. 4–6 POS is indicated in the upper axis of each panel, POS$=5$ corresponds to $k=0$, POS$=1$ corresponds to $k=-35$, POS$=9$ corresponds to $k=35$, etc.

Examples for click lateralization performance of four subjects are represented by histograms in the upper two rows of Fig. 7. The x axis in the histograms represents the interaural differences and the y axis represents the nine positions defined by the test procedure. The bins' heights in the histograms are the relative number of times a subject indicated a certain position (POS) for a given interaural difference, ITD or ILD. A performance histogram of a normal control subject, N5 (first column in Fig. 7) demonstrates high correlation between the indicated positions and the interaural differences. The second column in Fig. 7 demonstrates an example of a side-oriented performance. This stroke patient, Pt39, perceived all binaural stimuli only at the side positions (1, 2, 3 or 7, 8, 9) and never at the center positions (4, 5 and 6). The third and forth columns in the figure demonstrate a center-oriented lateralization performance of a stroke patient (Pt30) and a patient with multiple sclerosis (Pt46) who perceived most binaural stimuli at positions 4, 5, and 6.

The lesions of the three patients (Pt39, Pt30, and Pt46) relative to the brainstem auditory pathway are also shown in Fig. 7. Their locations are shown on a schematic drawing of the auditory pathway in the coronal plane. The locations of the brainstem nuclei are shown below the performance of subject N5. The location of the patients' lesions were obtained from their MRI scans and as a result of applying an algorithm that superimposed the auditory pathway on the MRI scans of each patient (Tenny, 1994; Tadmor *et al.*, 1994; Furst *et al.*, 2000). The percentage of fibers affected by the lesion was approximated by the ratio between a lesion size and the size of the fiber tracts or nuclei involved. The

performances of the simulations for the four subjects are shown in the fourth and fifth rows of Fig. 7, for ITD and ILD, respectively. The simulation was obtained with the following lesion percentage: Pt39−90% of left LL; Pt30 −90%TB; Pt46−90%TB, 90% left and right LL. As can be seen from Fig. 7, the model's simulation prediction and the actual behavioral performance are highly correlated.

In Aharonson *et al.* (1998), we have characterized patient's performance in the lateralization experiment by calculating the center lateralization index (Θ_C), which is the probability to perceive a center position (POS=4,5,6) in the lateralization experiment. Normal performance yielded $\Theta_C = 0.33$ for both ITD and ILD lateralization experiments. Θ_C was used to distinguish between the two abnormal performances; lateralization behavior was regarded as side-oriented if $\Theta_C < 0.2$ (the mean normal value -2.5^* s.d. of the normal values), and center-oriented if $\Theta_C > 0.5$ (the mean normal value $+2.5^*$ s.d. of the normal values). In order to estimate what is the lesion size that can account for the abnormal lateralization behaviors, we calculated Θ_C for different realizations of the model, i.e., different percentage of inactive fibers in either TB or LL. Due to the randomness property of the network, each network realization was simulated 100 times (Monte Carlo Method) to obtain reliable mean performance. Figure 8 demonstrates Θ_C as a function of inactivated fiber percentage for ITD and ILD experiments. In panel (a), Θ_C was calculated from simulations of LL lesions, and in panel (b) from simulations of TB lesions. The middle lines in both panels represent the mean values of Θ_C (solid symbols for ITD and empty symbols for ILD); the upper and lower lines are the mean ± 2.5 s.d. values of Θ_C.

Several features of the network performance can be derived from Fig. 8:

(1) Abnormal values for lateralization indices are observed at or above 70% of nonactivated fibers, for both interaural differences. This prediction of the model suggests that only very severe lesions can produce an abnormality like center-oriented or side-oriented lateralization.
(2) There is no significant difference between ITD and ILD in terms of mean lateralization indices.
(3) The standard deviation for center lateralization index is slightly larger for ILD than for ITD in small inactivation percentage (<50%). In this region the Θ_C values are in the normal range.
(4) For large inactivation percentages (>60%) the mean and s.d. of both ITD and ILD are similar, for TB and for LL inactivation.

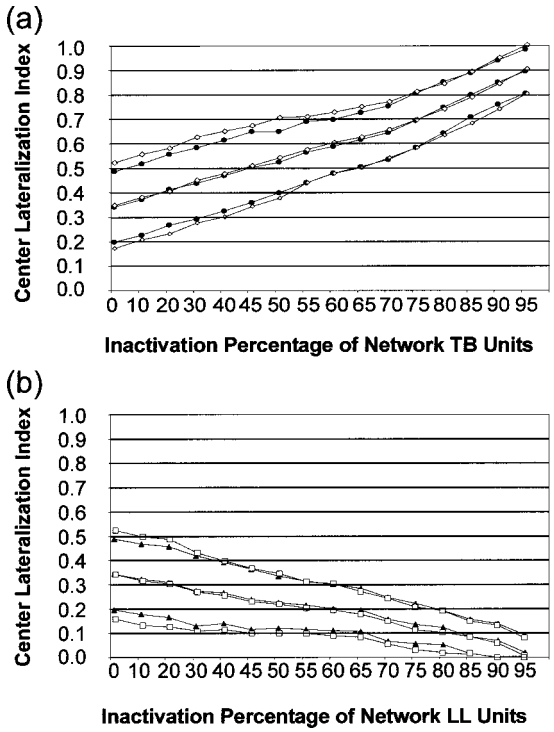

FIG. 8. Center lateralization index (Θ_C) as a function of inactivated fibers percentage in the network (lesion size) (a) for LL lesions and (b) for TB lesions. The middle line connects the mean CLI (solid symbols for ITD tests and empty symbols for ILD tests) and the upper and lower lines are the ± 2.5 s.d. range.

IV. DISCUSSION

A multi-level model for binaural processing was presented in this article. Only lateralization properties were currently evaluated, but the framework suggested in this article can be used to test other binaural properties. The model describes a feed-forward hierarchical structure of the CN, SOC, and IC. The model final decision is obtained by evaluating a large population of neurons, where each neuron carries its own decision. The model was designed so that its construction is consistent with anatomical structure of the brainstem auditory pathway. All the anatomical structures that were included in the model have an anatomical basis, but the strength of the various projections was not fully considered. The connections between brainstem nuclei were documented in many animal studies. Projections from both CN and SOC nuclei to the IC have been traced in various mammals. The projections from each SOC nucleus to the ipsilateral IC and from each CN nucleus to the contralateral IC are very prominent (i.e., Warr, 1966; Adams, 1979; Webster *et al.*, 1992). Anatomical evidence for direct projections from the CN to the ipsilateral IC is less conspicuous but still exists (i.e., Warr, 1982). We assumed the existence of axons that convey monaural information directly from the CN to the IC, without crossing in the lower brainstem (below the LL). The ipsilateral path, transmitting CN data to the IC, is crucial for the IC function in the model, in case that SOC data is missing. The functional effect of this transmission is an indication for sound in the ipsilateral hemifield. Indications for a sound in the contralateral hemifield arrive to the IC via the (well documented) contralateral projections from the CN. The scant evidence for ipsilateral projections in animals can be accounted for in two ways—either ipsilateral AN data does reach the IC from the CN level via other direct paths, or each IC communicates a monaural contralateral AN data to the other IC.

The model performance was evaluated based on testing the behavior of a population of neurons involved in the binaural process. A single-neuron model can represent a population of neurons only when all neurons are functioning properly. In order to model the effect of lesions on the per-

formance, a *population* of neural arrays must be considered: A lesion affects a portion of the neurons involved in a process and the performance differs with respect to both lesion location and size. The present model simulates large ensembles of neural arrays, performing similar processes, at each level. Lesions can thus be simulated as partial inactivation of the ensemble.

The robustness of the model is demonstrated by the fact that only inactivation of a very large percentage of networks ($>$70%) produced an abnormal lateralization performance.

The binaural processors SOC and IC are distinguished in the model by their purpose when comparing right and left inputs. SOC ''seeks dissimilarity'' and IC ''seeks similarity'' between the left and right inputs. Those assumptions are consistent with existing experimental data. Kavanagh and Kelly (1992) have shown that with SOC lesions in ferrets, the biggest impairment in sound localization is in the lateralmost part of the sound field, which means that a SOC lesion can produce sound lateralization in the central part of the sound field. Studies of SOC kainic acid lesions (Sally and Kelly, 1992; Kelly and Sally, 1993; Kelly *et al.*, 1996) have shown that large lesions of the SOC do not change the ILD sensitivity range seen in single neurons of the IC or the auditory cortex. It should be kept in mind that these studies only looked at a narrow performance range of the neurons and did not determine whether there was a quantitative difference in ILD sensitivity, or if there was any difference in ITD sensitivity. Ito *et al.* (1996) also found indications for sound localization at higher brainstem levels, while lower ones were damaged.

In the model, we defined a final stage (CP) where time and level or left and right conflicts are resolved, with a preference to the lateralized decisions over the center decisions. Human and animal behavioral studies support this hypothesis. Wightman and Kistler (1992) have shown that when normal subjects were presented with acoustic stimuli with conflicting time and intensity cues (time cues appropriate for a very lateral sound source and intensity cues over a wide range), they did not pick frontal midline sound localization. Middlebrooks and Knudsen (1987) have shown that conflicting time and level cues normally lead to a unitary estimate of source location.

The model suggests functions that are performed in the SOC and IC levels, but does not specify unit types within the nuclei. Brainstem unit recording thus cannot be directly compared to the suggested modules. However, cells in both MSO and LSO of mammals clearly present characteristic response to binaural stimuli (either EE or IE).

Based on our previous psychoacoustical results (Aharonson *et al.*, 1998; Furst and Algom, 1995; Levine *et al.*, 1993), we included different mechanisms for ITD and ILD estimations. Various physiological results support this assumption. Smith *et al.* (1991) have observed in the cat's brainstem a contralateral TB fibers projection to the SOC in ladderlike configuration. These projections can be related to the ITD comparison mechanism. Similarly, Beckius *et al.* (1999) have traced, in the cat, gradient of axonal length from the antroventral cochlear nuclei to the ipsi- and contralateral MSO, when a more significant gradient in length was found for fibers traveling to the contralateral side than to the ipsilateral side.

Cells that are mainly involved in ILD detection were found in animal's LSO (Boudreau and Tsuchitani, 1968; Tsuchitani and Boudreau, 1969; Guinan *et al.*, 1972; Joris and Yin, 1995). The LSO in mammals, however, consists mostly of high CF neurons and is practically nonexistent in humans (Moore, 1987). The function of ILD detection in humans, however, can be assumed to be located at the MSO. The ILD discrimination units at the model SOC respond when the sound is in the contralateral hemifield. The neurons at mammals' LSO, on the other hand, respond when sound is in the ipsilateral hemifield. However, in overall terms of the model, this difference is insignificant. The dual structures of left and right SOC and IC, where neurons at each side respond to stimuli precedence at the other side, were observed in experimental animals (i.e., Yin and Chan, 1990; Bruckner and Rubsamen, 1995). The sensitivity of brainstem neurons to either ITD or ILD cues in binaural stimuli were observed in many studies (i.e., Yin and Chan, 1990; Stanford *et al.*, 1992; Irvine *et al.*, 1995).

To conclude, the model describes unit arrays in simple logic or arithmetic functions that could be readily implemented. The functions of the different modules as well as the connections between them are simplification but consistent with experimental data. A further study is required to test the sensitivity of various parts of the model, in particular the weights that should be applied to the different pathways.

The central message of the model is the necessity and desirability of at least two levels of detailed interaural comparison, where the different levels perform different functions. Inactive cells below or at the first processing level result in the inability to localize stimuli with large ID, while inactive cells between the first and second processing levels deteriorate localization of small interaural ID.

Adams, J. C. (**1979**). ''Ascending projections to the inferior colliculus,'' J. Comp. Neurol. **183**, 519–538.

Aharonson, V., Furst, M., Levine, R. A., Chaigrecht, M., and Korczyn, A. D. (**1998**). ''Lateralization and binaural discrimination of patients with pontine lesions,'' J. Acoust. Soc. Am. **103**, 2624–2633.

Bajo, V. M., Merchan, M. A., Lopez, D. E., and Rouiller, E. M. (**1993**). ''Neuronal morphology and efferent projections of the dorsal nucleus of the lateral lemniscus in the rat,'' J. Comp. Neurol. **334**, 241–262.

Beckius, G. E., Batra, R., and Oliver, D. L. (**1999**). ''Axons from antroventral cochlear nucleus that terminate in medial superior olive of cat: Observations related to delay lines,'' J. Neurosci. **19**, 3146–3161.

Bekesy, G. V. (**1960**). *Experiments in Hearing*, translated and edited by E. G. Wever (McGraw-Hill, New York), Chap. 8.

Boudreau, J. C., and Tsuchitani, C. (**1968**). ''Binaural interactions in the cat superior olive S-segment,'' J. Neurophysiol. **31**, 442–454.

Bruckner, S., and Rubsamen, R. (**1995**). ''Binaural response characteristics in isofrequency sheets of the gerbil inferior coliculus,'' Hear. Res. **86**, 1–14.

Brughera, A. R., Stutman, E. R., Carney, L. H., and Colburn, S. H. (**1996**). ''A model with excitation and inhibition for cells in the medial superior olive,'' Aud. Neurosci. **2**, 219–233.

Cai, H., Carney, L. H., and Colburn, S. H. (**1998a**). ''A model for binaural response properties of inferior colliculus neurons. I. A model with interaural time difference-sensitive excitatory and inhibitory inputs,'' J. Acoust. Soc. Am. **103**, 475–493.

Cai, H., Carney, L. H., and Colburn, S. H. (**1998b**). ''A model for binaural response properties of inferior colliculus neurons. II. A model with interaural time difference-sensitive excitatory and inhibitory inputs and an adaptation mechanism,'' J. Acoust. Soc. Am. **103**, 475–493.

Carney, L. H. (**1993**). ''A model for the responses of low frequency auditory nerve fibers in cat,'' J. Acoust. Soc. Am. **93**, 401–417.
Colburn, S. C. (**1973**). ''Theory of binaural interaction based on auditodata. I. General strategy and preliminary results on interaural discrimination,'' J. Acoust. Soc. Am. **54**, 1458–1470.
Colburn, S. C. (**1977**). ''Theory of binaural interaction based on auditory-nerve data. I. Detection of tones in noise,'' J. Acoust. Soc. Am. **61**, 525–533.
Colburn, S. C., Han, Y., and Culotta, C. P. (**1990**). ''Coincidence model of MSO responses,'' Hear. Res. **49**, 335–346.
Domnitz, R. (**1973**). ''The interaural time jnd as a simultaneous function of interaural time and interaural amplitude,'' J. Acoust. Soc. Am. **53**, 1549–1552.
Domnitz, R., and Colburn, H. (**1977**). ''Lateral position and interaural discrimination,'' J. Acoust. Soc. Am. **61**, 1586–1598.
Durlach, N. I. (**1963**). ''Equalization and cancellation theory of binaural masking-level differences,'' J. Acoust. Soc. Am. **35**, 1206–1218.
Durlach, N. I. (**1972**). ''Binaural signal detection: equalization and cancellation theory,'' in *Foundations of Modern Auditory Theory*, edited by J. V. Tobias (Academic, New York), Vol. II.
Faingold, C. L., Anmderson, C. A., and Randall, M. E. (**1993**). ''Stimulation or blockage of the dorsal nucleus of the lateral lemniscus alters binaural and tonic inhibition in the contralateral inferior colliculus,'' Hear. Res. **69**, 98–106.
Furst, M., and Algom, D. (**1995**). ''Lateralization and discrimination of dichotic clicks: evidence from patients with brainstem lesions and normal cohorts,'' J. Basic Clinical Physiology Pharmacology **6**, 149–171.
Furst, M., Levine, R. A., Korczyn, A. D., Fullerton, B. C., Tadmor, R., and Algom, D. (**1995**). ''Brainstem lesions and click lateralization in patients with multiple sclerosis,'' Hear. Res. **82**, 109–124.
Furst, M., Aharonson, V., Levine, R. A., Fullerton, B. C., Tadmor, R., Pratt, H., Polyakov, A., and Korczyn, A. D. (**2000**). ''Sound lateralization and Interaural discrimination: Effects of brainstem infracts and multiple sclerosis lesions,'' Hear. Res. **143**, 29–42.
Gaumond, R. P., and Psdaltikidou, M. (**1991**). ''Models for the generation of the binaural difference response,'' J. Acoust. Soc. Am. **89**, 454–456.
Guinan, Jr., J. J., Guinan, S. S., and Noris, B. E. (**1972**). ''Single auditory units in the superior olivary complex, I: responses to sound and classification based on physiological properties,'' Int. J. Neurosci. **4**, 101–120.
Irvine, R. D. F., Park, V. N., and Mattingley, J. B. (**1995**). ''Responses of neurons in the inferior colliculus of the rat to interaural time and level differences in transient stimuli: implications for the latency,'' Hear. Res. **85**, 127–141.
Ito, M., van Adel, B., and Kelly, J. B. (**1996**). ''Sound localization after transection of the commissure of Probst in the albino rat,'' J. Neurophysiol. **76**, 3493–3502.
Jeffress, L. A. (**1948**). ''A place theory of sound localization,'' J. Comp. Physiol. Psychol. **41**, 35–39.
Jeffress, L. A. (**1972**). ''Binaural Signal Detection: Vector Theory'' in *Foundations of Modern Auditory Theory*, edited by J. V. Tobias (Academic, New York), Vol. II: Binaural Signal Detection: Vector Theory.
Joris, P. X., and Yin, C. T. (**1995**). ''Envelope coding in the lateral superior olive. I. Sensitivity to interaural time differences,'' J. Neurophysiol. **73**, 1043–1062.
Kavanagh, G. L., and Kelly, J. B. (**1992**). ''Midline and lateral field sound localization in the ferret (Mustela putorius): contribution of the superior olivary complex,'' J. Neurophysiol. **67**, 1643–1658.
Kelly, J. B., and Sally, S. L. (**1993**). ''Effects of superior olivary complex lesions on binaural responses in rat auditory cortex,'' Brain Res. **605**, 237–50.
Kelly, J. B., Li, L., and van Adel, B. (**1996**). ''Sound localization after kainic acid lesions of the dorsal nucleus of the lateral lemniscus in the albino rat,'' Behav. Neurosci. **110**, 1445–1455.
Kiang, N. Y. S., Watanabe, T., Thomas, E. C., and Clarke, L. F. (**1965**). *Discharge Patterns of Single Fibers in the Cat's Auditory Nerve* (MIT, Cambridge, MA).
Levine, R. A., Gardner, J. C., Stufflebeam, S. M., Fullerton, B. C., Carlisle, W. E., Furst, M., Rosen, R. B., Kiang, N. Y. S. (**1993**). ''Binaural auditory processing in multiple sclerosis subjects,'' Hear. Res. **68**, 59–72.
Li, L., and Kelly, J. B. (**1992**). ''Inhibitory influence of dorsal nucleus of the lateral lemniscus on binaural response in the rat's inferior colliculus,'' J. Neurosci. **12**, 4530–4539.
Merchan, M. A., Saldana, E., and Plaza, I. (**1994**). ''Dorsal nucleus of the lateral lemniscus in the rat: concentric organization and tonotopic projection to the inferior colliculus,'' J. Comp. Neurol. **342**, 259–278.
Middlebrooks, J. C., and Knudsen, E. I. (**1987**). ''Changes in external ear position modify the special tuning of auditory units in the cat's superior colliculus,'' J. Neurophysiol. **57**, 672–687.
Moore, J. K. (**1987**). ''The human auditory brainstem: a comparative view,'' Hear. Res. **29**, 1–32.
Osman, E. (**1971**). ''A correlation model of binaural masking-level differences,'' J. Acoust. Soc. Am. **50**, 1494–1511.
Osman, E. (**1973**). ''Correlation model of binaural detection: interaural amplitude ratio and phase variation for signal,'' J. Acoust. Soc. Am. **54**, 386–389.
Reed, M. C., and Blum, J. J. (**1991**). ''A model for the computation and encoding of azimuthal information by the lateral superior olive,'' J. Acoust. Soc. Am. **88**, 1442–1453.
Reed, M. C., and Dubreck, L. (**1995**). ''Delay lines and auditory processing,'' Comments Theoretical Biology **3**, 441–461.
Sally, L. S., and Kelly, J. B. (**1992**). ''Effects of superior olivary complex lesions in binaural responses in rat inferior colliculus,'' Brain Res. **572**, 5–18.
Shackleton, T. M., Meddis, R., and Hewett, M. J. (**1992**). ''Access frequency integration in a model of lateralization,'' J. Acoust. Soc. Am. **91**, 2276–2279.
Smith, P. H., Joris, L. H., and Yin, T. C. T. (**1991**). ''Projections of physiologically characterized spherical bushy cell axons from the cochlear nucleus of the cat: evidence for delay lines to the medial superior olivary,'' J. Comp. Neurol. **331**, 247–260.
Stanford, T. R., Kuwada, S., and Batra, R. (**1992**). ''A comparison of the interaural time sensitivity of neurons in the inferior colliculus and thalamus of the unanesthetized rabbit,'' J. Neurosci. **12**, 3200–3216.
Stern, R. M., and Trahiotis, C. (**1996**). ''Models of Binaural Perception,'' in *Binaural and Spacial Hearing in Real and Virtual Enviroments*, edited by R. H. Gilkey and T. R. Anderson (Erlbaum, Mahwah, NJ), pp. 499–531.
Stern, R. M., Zeiberg, A. S., and Trahiotis, C. (**1988**). ''Lateralization of complex binaural stimuli: A weighted image model,'' J. Acoust. Soc. Am. **84**, 156–165.
Tadmor R., Tenny, R., and Furst, M. (**1994**). ''Algorithm for Automatic Matching of Brainstem Atlas to MR Images,'' in *Proceedings of the XV Syposium Neroradiologicum*, edited by M. Takahashi, Y. Korogi, and I. Moseley (Springer, New York), pp. 34–36.
Tenny, R. (**1994**). ''Algorithm for matching brainstem atlas to MR images,'' M.Sc. thesis, Faculty of Engineering, Tel Aviv University.
Tsuchitani, C., and Boudreau, J. C. (**1969**). ''Stimulus level of dichotically presented tones and cat superior olive S-segment cell discharge,'' J. Acoust. Soc. Am. **46**, 979–988.
Van Bergeijk, W. A. (**1962**). ''Variation on a theme of Von Beseky: a model of binaural interaction,'' J. Acoust. Soc. Am. **34**, 1431–1437.
Warr, W. B. (**1966**). ''Fiber degeneration following lesions in the anterior-ventral cochlear nucleus of the cat,'' Exp. Neurol. **14**, 453–474.
Warr, W. B. (**1982**). ''Parallel ascending pathways from the cochlear nucleus: neuroanatomical evidence of functional specialization,'' in *Contributions to Sensory Physiology*, edited by W. D. Neff (Academic, New York), pp. 1–38.
Webster, D. B., Popper, A. N., and Fay, R. R. (**1992**). *The Mammalian Auditory Pathway: Neuroanatomy* (Springer-Verlag, New York).
Wightman, F. L., and Kistler, D. J. (**1992**). ''The dominant role of low-frequency interaural time differences in sound localization,'' J. Acoust. Soc. Am. **91**, 1648–1661.
Yin, T. C. T., and Chan, C. K. (**1990**). ''Interaural time sensitivity in medial superior olive of cat,'' J. Neurophysiol. **68**, 465–488.

A computational algorithm for computing nonlinear auditory frequency selectivity

Ray Meddis and Lowel P. O'Mard
Centre for the Neural Basis of Hearing at Essex, Department of Psychology, University of Essex, Colchester CO4 3SQ, United Kingdom

Enrique A. Lopez-Poveda
Facultad de Medicina, Universidad de Castilla-La Mancha, Campus Universitario, 02071 Albacete, Spain

(Received 26 September 2000; revised 6 March 2001; accepted 14 March 2001)

Computational algorithms that mimic the response of the basilar membrane must be capable of reproducing a range of complex features that are characteristic of the animal observations. These include complex input output functions that are nonlinear near the site's best frequency, but linear elsewhere. This nonlinearity is critical when using the output of the algorithm as the input to models of inner hair cell function and subsequent auditory-nerve models of low- and high-spontaneous rate fibers. We present an algorithm that uses two processing units operating in parallel: one linear and the other compressively nonlinear. The output from the algorithm is the sum of the outputs of the linear and nonlinear processing units. Input to the algorithm is stapes motion and output represents basilar membrane motion. The algorithm is evaluated against published chinchilla and guinea pig observations of basilar membrane and Reissner's membrane motion made using laser velocimetry. The algorithm simulates both quantitatively and qualitatively, differences in input/output functions among three different sites along the cochlear partition. It also simulates quantitatively and qualitatively a range of phenomena including isovelocity functions, phase response, two-tone suppression, impulse response, and distortion products. The algorithm is potentially suitable for development as a bank of filters, for use in more comprehensive models of the peripheral auditory system. [DOI: 10.1121/1.1370357]

PACS numbers: 43.64.Bt, 43.66.Ba [BLM]

I. INTRODUCTION

Using observations in chinchilla and guinea pig preparations, we evaluate an algorithm for simulating the nonlinear response of the cochlear partition in response to stapes motion. The algorithm is intended as a high-speed component in much larger models of the response of the whole auditory periphery to acoustic stimulation. It is not a model of cochlear mechanics, but rather a signal-processing algorithm. It is, however, an example of a recent tradition of nonlinear algorithms (e.g., Carney, 1993; Giguère and Woodland, 1994; Goldstein, 1990, 1995; Irino and Patterson, 1997; Lopez-Poveda *et al.*, 1998; Lyon, 1982; Meddis *et al.*, 1990; Robert and Eriksson, 1999). The aim of such models is to promote the evaluation of computational psychoacoustic theories based on the anatomy and physiology of the peripheral auditory system. Nonlinearity is an important characteristic of the response of the auditory partition (Rhode, 1971) and is relevant to a range of psychophysical phenomena. A high-speed nonlinear algorithm for simulating the nonlinear mechanical input to the inner hair cell transduction process is also essential to the rigorous modeling of the response of the auditory nerve (AN) and the auditory signal processing in the auditory brainstem (Winter *et al.*, 1990; Yates *et al.*, 1990).

The eventual aim is to construct a filter bank consisting of a series of such algorithms to represent as many locations along the cochlear partition as the modeller requires (cf. Lopez-Poveda and Meddis, 2000). Unfortunately, we only have detailed cochlear measurements of the input/output (I/O) functions at a limited number of sites. Below, we evaluate the algorithm at three sites for which detailed laser velocimetry observations are available. These three regions have best frequencies (BFs) of approximately 0.8, 10, and 18 kHz (Rhode and Cooper, 1996; Ruggero *et al.*, 1997; and Nuttall and Dolan, 1996). The development of a complete filter bank will be deferred so that this study can deal with the more focused question of the algorithm's ability to simulate, qualitatively and quantitatively, direct measurements of cochlear response functions. Future development of the filter bank will inevitably need to draw on observations of auditory nerve (AN) activity to fill in the gaps between the cochlear locations for which we have direct measurements. Unfortunately, nonlinear processes in the inner hair cell, the synapse, and AN dendrites intervene between the basilar membrane (BM) and AN fibers. As a result, AN data cannot be used as a *direct* test of the validity of the algorithm, even though such data will undoubtedly help tune the model once its value is established. In this study, we restrict our attention to the narrower question of whether the algorithm can generate a useful simulation of the complex, nonlinear behavior observed at those sites where physical measurements have been reported.

A particular challenge for the algorithm is the need to simulate the considerable differences in the appearance of the input/output (I/O) functions at different points along the cochlear partition [see Figs. 1(a), (c), and (e)], particularly the difference between basal and apical sites. We also need to know whether it can simulate a range of ancillary phe-

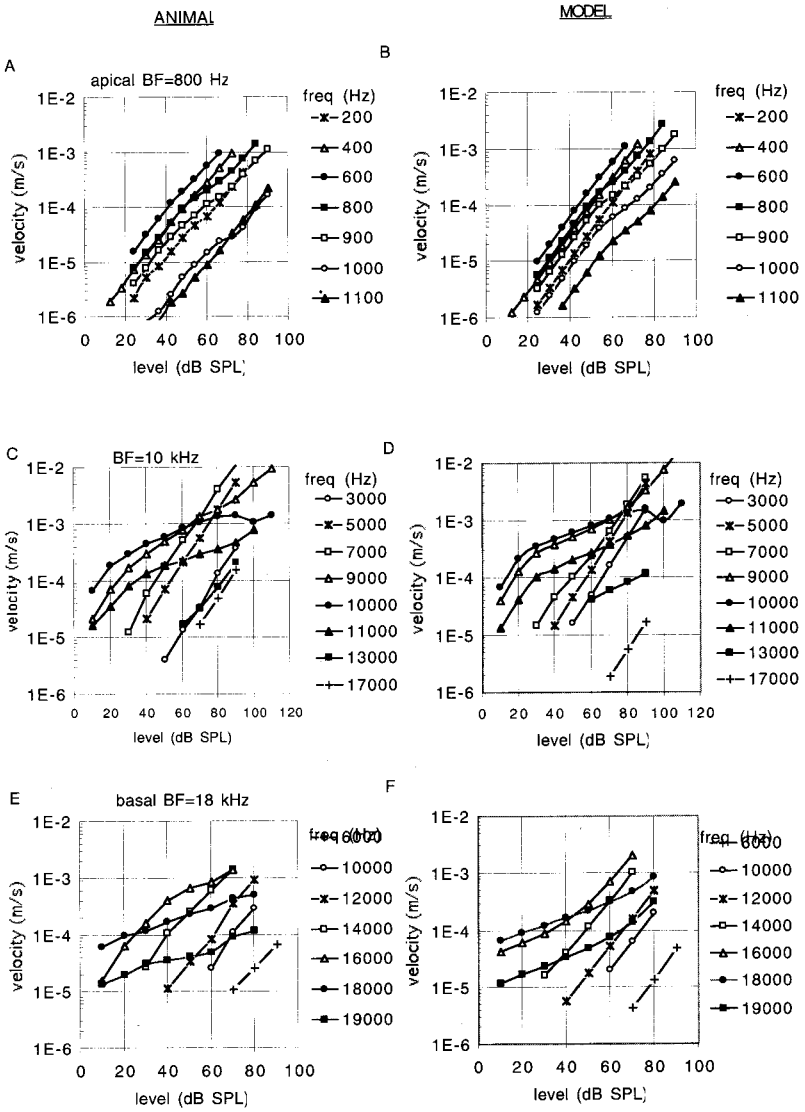

FIG. 1. Input/output functions; input is dB SPL corresponding to the stapes velocity used. Output is peak velocity of the basilar membrane (m/s). Legends show frequency of pure tone stimuli. Left column: animal observations. All data have been converted to velocity when necessary. Right column: model results corresponding to animal data immediately to left. (a) Data from Rhode and Cooper (1996, animal CH 16) for an apical site (BF ~800 Hz). (c) data from Ruggero *et al.* (1997, animal L113) (BF ~10 kHz). (e) data from Nuttal and Dolan (1996, animal GP 23-81). (b, d, and f). Corresponding algorithm results using parameters in Table I, cols 2 (CH 16), 4 and 5, respectively.

nomena including impulse responses showing frequency sweeps, filter functions that vary with signal level, two-tone suppression effects, and appropriate distortion products. All of these effects have been observed (see below) at the level of the cochlea. This model is not unique in attempting to simulate nonlinear responding, but it is probable that this is the first time that any nonlinear computational algorithm has been tested in such detail against a wide range of physical observations.

An important motivation for this research comes from the observations of Winter *et al.* (1990) and Yates *et al.* (1990) at the level of the auditory nerve. They demonstrated that the differences between low- and high-spontaneous rate fibers could be understood in terms of a nonlinear contribution to their driving force. Much of this nonlinearity probably originates at the level of the BM. It follows that the appropriate AN rate-intensity functions can only be reproduced in a composite model of the auditory periphery when an appropriate nonlinearity is present prior to the inner hair cell (IHC) stage. The principal has already been explored in computational models of IHC response (Lopez-Poveda *et al.*, 1998; Schoonhoven *et al.*, 1997).

Existing nonlinear models can be characterized in various ways; some are transmission-line models (Giguère and Woodland, 1994; Lyon, 1982) others are point models (Carney, 1993; Goldstein, 1990, 1995; Irino and Patterson, 1997). Point models simulate the response of the cochlear partition at a single site while transmission models simulate the flow of energy along the length of the partition. Most use feedback to control compression while Goldstein used an explicit compression function. Most use a single processing path while Goldstein used a dual resonance approach. The model to be evaluated below is a point model using an explicit compression function in a dual resonance configuration. It is, therefore, most similar to that of Goldstein's multiple bandpass nonlinear model and both derive their ''bandpass nonlinear'' method of compression from an idea by Pfeiffer (1970). However, there are important differences to note. For example, both use a linear ''tail'' and a nonlinear ''tip'' processing path, but the present algorithm has different center frequencies (CFs)[1] for the two paths. It is this difference that produces the shift in BF of the overall system as signal intensity rises. Like Goldstein, we use an explicit compression function, but we have found it possible to avoid the use of his expansive nonlinearity function. The use of dual resonance is also not new. Schoonhoven *et al.* (1994), for ex-

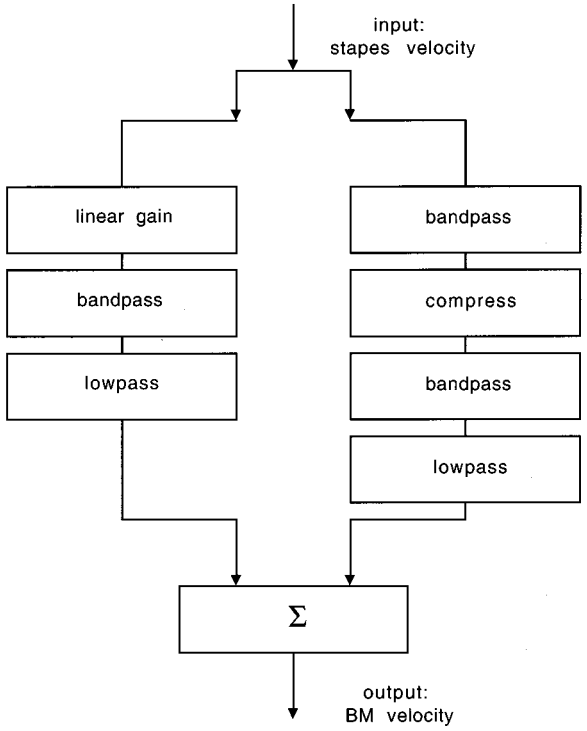

FIG. 2. Schematic diagram of the DRNL algorithm. The input is in the form of stapes velocity and is applied to two signal-processing paths: one linear and the other nonlinear. The outputs of the two paths are summed to form the output. The individual bandpass and low pass functions consist of cascades of bandpass and low pass functions (see the text and Fig. 3).

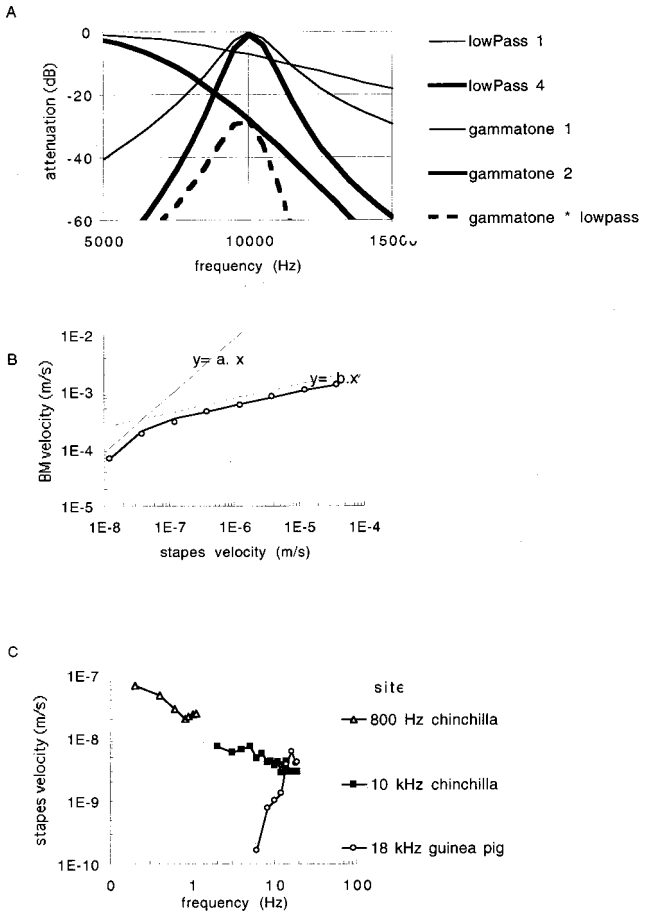

FIG. 3. (a) Examples of the gammatone and low pass filter used to construct the signal-processing units illustrated in Fig. 2. The gammatone filter shown has a CF of 10 kHz, a BW (3 dB down) of 1000 Hz and unit gain. A cascade of two gammatone filters is also shown. A low pass filter (6 dB down at 10 kHz) is also shown along with the result of four cascading identical filters. A cascade of the ''second-order'' gammatone filter and the ''fourth-order'' lowpass filter is shown to illustrate the effect of combining the components. (b) The compression effect is based on two functions (shown slightly displaced as dotted lines), one linear, y_a, and the other a power function, y_b. The individual data points are chinchilla peak velocity observations (Ruggero *et al.*, 1997, Fig. 6) and the continuous line is the model compression function, y (see the text). (c) Stapes velocity as a function of frequency used in the evaluation of the model. These data points are taken from animal measurements. White triangles: chinchilla data at the apical site (Rhode and Cooper, 1996, Fig. 4). Black squares: chinchilla data used at the ~10 kHz site (Ruggero *et al.*, 1990, Fig. 8). White circles: guinea-pig data used at the basal site (see note 3). All data points are scaled to 0-dB SPL. For modeling purposes, these are rescaled to the level of the stimulating tone.

ample, used a dual resonance model with different BFs to model threshold functions. Because they were concerned only with threshold functioning, they did not add a compression function.

The computational details of the model are presented in Sec. II while in Sec. III we evaluate the model against published input/output functions measured at three cochlear sites. In Sec. IV we review the response of the model to intensity changes, impulsive stimuli, and two-tone stimuli against physical measurements where these exist.

II. MODEL DESCRIPTION

The input to the algorithm is *stapes motion*, $x(t)$, and its output represents the vibration velocity,[2] $y(t)$, of a particular location along the cochlear partition. Each individual site is represented as a tuned system consisting of two parallel processes, one linear and the other nonlinear (Fig. 2). The linear path consists of a bandpass function, a low pass function, and a gain/attenuation factor, g, in a cascade. The nonlinear path is also a cascade consisting of a bandpass function, a compression function, a second bandpass function, and a low pass function, in that order. The output of the system is the sum of the outputs of the linear and the nonlinear paths. The complete unit is referred to below as a dual resonance nonlinear (DRNL) filter.

The three bandpass functions each consist of a cascade of two or more gammatone filters (Hartmann, 1997) with unit gain at CF. The low pass filters, likewise, consist of a cascade of second-order low pass filters. The low pass filters also have unit gain at low frequencies and a 6 dB down cutoff set to the CF of their matching bandpass functions. Figure 3(a) illustrates the shape of the gammatone and low pass filters both singly and in cascade. In the nonlinear path, the CFs and bandwidths (BW) of the two sets of gammatone filters are the same. The CF and BW of the gammatone filters in the linear path (CF_{nl} and BW_{nl}, respectively) are different from those in the nonlinear path (CF_{lin} and BW_{lin}). The parameters of the filters (including the number of elements in each cascade) for all three cochlear sites are specified in Table I.

The shape of the compressive function in the nonlinear path was chosen to agree with observations based on animal data. It is linear at low signal levels,

$$y_a[t] = a \cdot x[t],$$

TABLE I. Parameters of the DRNL algorithm used throughout the evaluation of the algorithm. The parameters were chosen to give an optimal fit to published input/output functions (see Fig. 1).

Simulated preparation	Apical (~800 Hz) CH 16	Apical (~800 Hz) CH 35	~10 kHz L113	Basal (~18 kHz) GP 23–81
Linear				
Gammatone cascade	2	2	2	2
Lowpass cascade	4	4	4	4
CF_{lin}	700 (Hz)	800	8000	15 500
BW_{lin}	130 (Hz)	800	2000	1400
Gain, g	83	25	100	500
Nonlinear				
Gammatone cascade	3	3	3	3
Lowpass cascade	3	3	3	3
CF_{nl}	750 (Hz)	850	9800	17 300
BW_{nl}	320 (Hz)	800	1400	1200
Compression				
Linear gain, a	50	100	12 000	90 000
Gain, b	0.008	0.01	0.057	0.03
Exponent, ν	0.25	0.25	0.25	0.25

where $x[t]$ is the output of the first filter in the nonlinear path and a is a parameter of the system. At higher signal levels, the response is nonlinear,

$$y_b[t] = b \cdot |x[t]|^{\upsilon} \operatorname{sign}(x[t]),$$

where b and υ are parameters of the model. At all signal levels, the *smaller* result of the two functions is chosen, i.e.,

$$y[t] = \operatorname{sign}(x[t]) \times \operatorname{MIN}(a|x[t]|, b|x[t]|^{\nu}),$$

Fig. 3(b) compares this function to the response of the chinchilla BM to a 10-kHz (BF) tone. Note that a and b are used to control the gain of the nonlinear path. Their relative value determines the compression threshold.

The output of the nonlinear path is linear at very low signal levels but is otherwise compressive. The output of the linear path is, of course, linear at all signal levels. At low signal levels, when both outputs are linear, the response of the linear path to tones near CF is typically weak and the response of the nonlinear path dominates the output of the system as a whole. At higher signal levels, the output of the nonlinear path will eventually be less than the output of the linear path because the former is subject to compression. As a consequence, the output of the system is typically linear at very high signal levels. This can be seen most easily in Fig. 1(b), where the response to 800-Hz tones is linear up to 60-dB SPL, then shows a mild compression up to 75-dB SPL when it again becomes linear. This return to linearity at high signal levels cannot be seen in at the basal sites featured in Figs. 1(d) and (f) because it occurs at signal levels greater than those displayed.

The parameters shown in Table I were obtained in the following manner. It was assumed that the output of the system, at very low stimulus levels, is dominated by the activity of the nonlinear filter, at least for frequencies close to BF. However, at the highest signal levels, it was assumed that the linear filter dominates the output of the system. This is because the output from the nonlinear path is compressed at high signal levels while the output from the linear path continues to increase linearly with the signal level. The CF and BW of the nonlinear gammatone filters were, therefore, adjusted to fit the animal data at low stapes velocities close to BF. The exercise was then repeated for the parameters of the linear path by fitting the system output to the animal data at the highest stapes velocities and paying special attention to frequencies well away from the CF of the nonlinear path. The compression parameters were then adjusted to give the best match at BF.

Various trials were made using gammatone filters of different ''orders'' (i.e., the number of filters in the cascade). Third order was generally best for the nonlinear path and second order for the linear path. These orders are used at all three cochlear sites in order to limit the number of free parameters in the model. Similarly, a compression exponent of 0.25 was found to be generally satisfactory at all three sites. This parameter was, therefore, fixed at an early stage in the research. The order of the low pass filtering was also fixed to be the same at all three sites. In the linear path the cascade was fixed at four second-order low pass filters. In the nonlinear path, three low pass filters were used. Small improvements can be achieved by varying these parameters between sites; the establishment of uniformity across sites was primarily to reduce the number of degrees of freedom in fitting the model.

III. EVALUATION OF THE MODEL

A. Methods

The algorithm is implemented using digital IIR filters. It was implemented in the Development System for Auditory Modeling (DSAM), a computational environment for evaluating auditory models.[3]

The input to the system is stapes velocity (m/s) and was sampled at a rate of 100 kHz, except where stated. Sinusoidal stimulation was used throughout testing except when a 20-μs wide pulse was used to evaluate impulse responses. Rhode and Cooper (1996) and Nuttall and Dolan (1996) measured activity at the stapes and their data (for chinchilla and guinea pig, respectively) were used to convert input sound pressure levels to stapes velocity directly. When modeling the data of Ruggero *et al.* (1997), it was necessary to

use a middle-ear transfer function of a different chinchilla measured previously in the same laboratory (Ruggero *et al.*, 1990, Fig. 10). Stapes velocity was interpolated from their figure up to 15 kHz. Above this frequency, the stapes velocity for 15 kHz was used as an approximation. All three sets of stapes functions are plotted together in Fig. 3(c). Note that the first two functions (800-Hz and 10-kHz sites) are for chinchilla and the third function is from a guinea pig (18-kHz site).

Input/output functions were computed using 50-ms pure tones. The output from the model is given in terms of *peak velocity* (m/s) measured during the last 25 ms of the tone. For the purpose of comparison, the published animal data were converted, where necessary, from displacement measurements to velocity. The model was evaluated using *only those stimuli for which corresponding animal data exist*.

B. Input/output functions

800-Hz site. Figure 1(a) shows measurements made using chinchilla at the apex of the cochlea in a region with BF around 800 Hz (Rhode and Cooper, 1996, preparation CH16). At this site, there is only limited evidence of nonlinearity. However, it can be seen at 800, 900, 1000 Hz as a bend in the function above 50-dB SPL followed by a return to linearity at around 70-dB SPL. Figure 1(b) shows the I/O functions generated by the model using the parameters given in Table I (CH16). The nonlinear effect seen in the animal data is reproduced both quantitatively and qualitatively. At this site, the CFs of the filters in the linear and nonlinear paths are almost the same (700 and 750 Hz, respectively) and the gain of the two paths (*g* and *a*) is also roughly equal at low signal levels (see Table I). At higher signal levels, the linear path is dominant because the output from the nonlinear path is compressed. As a result, all response are linear above 80-dB SPL. Compression is only briefly visible between the compression threshold at around 50-dB SPL and the level at which the linear resonance comes to dominate all channels at around 70-dB SPL.

10-kHz site. Figures 1(c) and (d) compare the animal data as measured by Ruggero *et al.* (1997) with input/output functions of the DRNL algorithm. For clarity, only the results for multiples of 2 kHz are shown even though the complete dataset of multiples of 1 kHz were used when fitting the model. Both the animal data and the model response are compressive at 10 kHz at high signal levels while the response to low frequencies are linear at all signal levels. The animal data show a notch in the 10-kHz response at 100-dB SPL. The model reproduces this notch at the same signal intensity. Notches occur (in the model) when the outputs of the linear and nonlinear paths have similar levels but different phases. Notches are frequently seen in animal data, particularly at low BF [cf. Rhode and Cooper, 1996, Fig. 7(a)].

18-kHz site. Figure 1(e) shows data obtained in the basal turn of the guinea pig cochlea (Nuttall and Dolan, 1996, animal GP #23.81[4]) at a site with BF close to 18 kHz. Figure 1(f) shows the results from the DRNL model for the corresponding data points. The model shows a good qualitative and reasonably good quantitative match to the guinea pig data. Below BF, the functions are largely linear and above BF they are highly compressed.

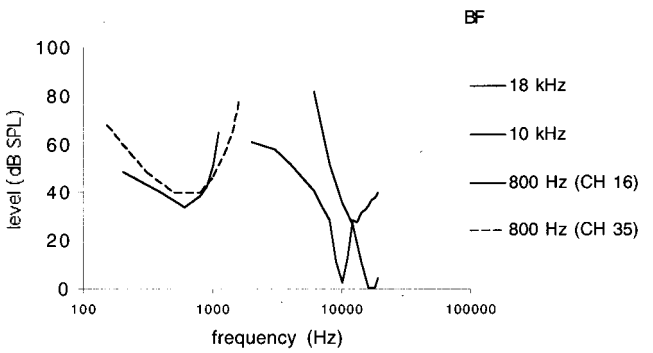

FIG. 4. Isovelocity contours for three sites computed with the algorithm and parameters given in Table I. Two contours are given for the ~800-Hz site (modeling data for animals CH 16 and 35, Rhode and Cooper, 1996). The criterion velocity is 3E-5 m/s.

The isovelocity contours for all three sites are plotted in Fig. 4 for a criterion output velocity of 3e-5 m/s (close to typical auditory nerve firing thresholds). They are not strictly comparable with each other because they are modeled on different animals from different species. However, they do show the characteristic broadening of the shape of the function at very low frequencies frequently seen in auditory nerve recordings. The high-frequency slopes may appear to be too shallow, particularly at the 10- and 18-kHz site. However, the inspection of Figs. 1(d) and (e) show that the model is underestimating the BM response at the highest frequencies. If anything, the high-frequency slope of the model result is steeper than the animal data allow.

Figure 4 shows an additional isovelocity contour derived using a second set of parameters shown in Table I. These parameters were derived by fitting I/O functions for a second animal studied by Rhode and Cooper (1996, CH 35). A simulated version of this unit will be required when evaluating the response to phase (see below).

C. Phase

In a linear system, we expect the phase to remain invariant with respect to intensity. The animal data show phase invariance at many frequencies, but not all. Phase shifts as a function of intensity are often observed for frequencies close to or above BF. The model data show a similar qualitative effect. When evaluating the phase response of the algorithm, no attempt was made to manipulate the model parameters. The parameters used are unchanged from those required to fit the I/O functions described above and are given in Table I.

Figures 5(a) and (b) compare the animal observations made by Rhode and Cooper (1996, preparation CH 35) with the algorithm results. The chinchilla phase-intensity functions were arranged by Rhode and Cooper in order of ascending frequency. The model data are presented alongside with a similar adjustment. In both animal and model data the phase is constant with respect to intensity for low frequencies. At high frequencies, an accumulating phase lag can be observed at high signal intensities. The shifts can be seen in the animal data at 800, 900, and 1000 Hz. In the model

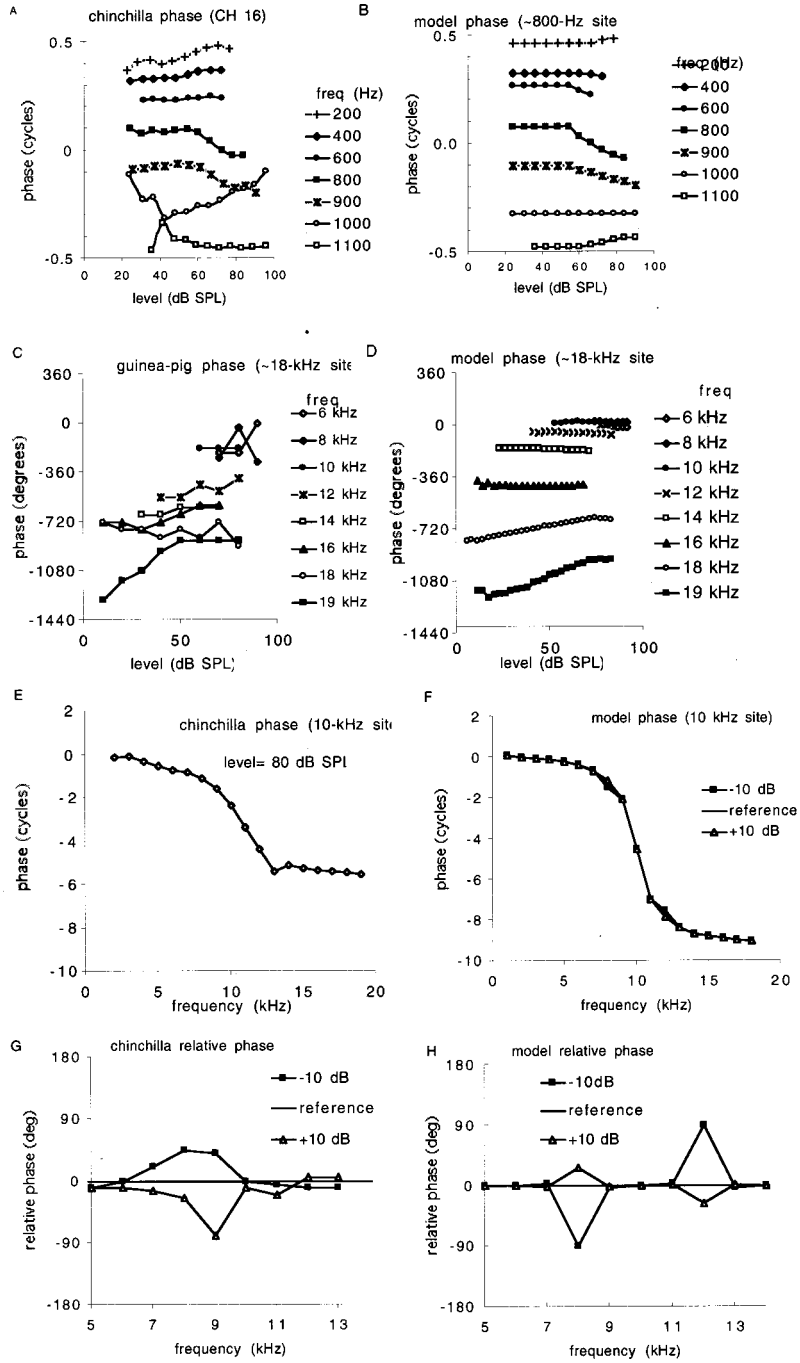

FIG. 5. A comparison of phase characteristics for animal and model data. (a) and (b) Phase as a function of the signal level at the apical, ~800-Hz site for chinchilla (Rhode and Cooper, 1996, Fig. 6, preparation CH 16) and model data, respectively. (c) and (d) Phase as a function of signal level at the basal, ~18-kHz site for a guinea pig. (Nuttall and Dolan, 1996, Fig. 8, preparation, GP#23-81) and model data, respectively. (e) and (f) Phase as a function of *frequency* at the 10-kHz site for chinchilla (Ruggero *et al.*, 1997, preparation L113, Fig. 13) and model data, respectively. Model parameters are given in Table I. The model data were computed using a 0.2-Pa, 20-μs-wide reference click (i.e., 80 dB *re* 20 μPa). Data are also shown for clicks 10 dB more and less intense than the reference. (g) and (h) Relative phase as a function of signal intensity for chinchilla (Ruggero *et al.*, 1997, preparation L113, Fig. 14). Two signal intensities are shown 10 dB above and below an 80-dB SPL reference. The corresponding model data are based on (f).

results the phase shifts can be seen at 800, 900, and 1100 Hz. At low intensities and close to BF, the model phase reflects the phase of the nonlinear path. At high intensity, the phase for all channels reflects the phase of the dominant linear path. The model phase response disagrees with the animal data at 1 kHz. This discrepancy matches the failure to reproduce the I/O function exactly in Fig. 1(b) at the same frequency.

A similar effect can be seen in the phase/intensity function for a more basal site in Fig. 5(c) (Nuttall and Dolan, 1996). The phase does not change significantly as a function of the signal level for frequencies at or below 14 kHz. Above this frequency, phase shifts as a function of intensity. Figure 5(d) shows the model response, which has a similar shift in phase at 19 kHz.

Figures 5(e) and (f) show how phase changes as a function of *frequency* at the 8-kHz site for the chinchilla and the model (Ruggero *et al.*, 1997). The chinchilla data were collected using pure tones. For computational convenience, the model data were evaluated using clicks. A 0.2-Pa, 20 μs-wide reference click (i.e., 80 dB *re* 20 μPa) was used for this purpose along with two other clicks; one 10 dB greater and one 10 dB smaller than the reference. No attempt was made to optimize the model's parameters to improve the fit. The slope of the model function is about three times that of the chinchilla data. This probably indicates that the filter bandwidths in the nonlinear path are too narrow. The total phase lag at high frequencies is also greater in the model response. The discontinuity in the animal function at 14 kHz suggests

that some of this difference may be the result of different methods used to unwrap phase.

The chinchilla data also show increasing phase lag with the stimulus level in a region below BF with a tendency in the opposite direction above BF. Figure 5(c) shows the phase response to tones at 70 and 90-dB SPL expressed relative to the response to a reference click at 80-dB SPL. No variation in phase lag is observed at BF for any intensity. The model shows a similar pattern with a change over around BF, except that the sign is reversed (i.e., increasing intensity produces less phase lag below BF). The reason for this discrepancy is unclear. Unfortunately, Ruggero *et al.* do not give full details of their phase unwrapping algorithm. Moreover, the idealized model clicks may not constitute the ideal comparison method.

D. Two-tone suppression

Two-tone suppression (2TS) was first observed at the level of the AN, where ''it has been shown that average discharge rate in response to a tone at a fiber's BF can be reduced by the addition of a second tone of appropriate frequency and sound pressure level'' (Abbas and Sachs, 1976). Ruggero *et al.* (1992) did find an analogous suppression in the velocity response of the BM. Cooper and Rhode (1996) did not find any overall suppression at an apical site but did observe a reduction in the response of the *spectral component* at BF when a second tone was added. Geisler and Nuttall (1997) also report no overall suppression at a basal site. These results leave open the question of how AN observations relate to BM observations and whether a second mechanism is required to complete the picture. However, the question for the present evaluation is simply whether the algorithm can simulate the observations made at the level of the BM.

The data of Cooper and Rhode (1996) are particularly useful in this respect because they measured both I/O and 2TS functions at the same site. Their measurement paradigm was replicated almost exactly in the evaluation of the algorithm. Figure 6(a) shows the chinchilla data (preparation CH35) at a site with an 800-Hz BF. In this experiment, a probe tone (f1) at 800 Hz (=BF) was presented at the same time as a suppressor tone (f2) at 1000 Hz. Cooper and Rhode did not observe a reduction in the amplitude of the peak displacement of Reisner's membrane, but they did observe a reduction in the *spectral component* of the displacement at f1 when f2 was added. Suppression is expressed as the ratio of the Fourier component at f1 in the presence and the absence of the f2 suppressor. Figure 6(a) shows the amount of suppression observed during an analysis using all combinations of levels (L1 and L2) of f1 and f2. Figure 6(b) shows the corresponding model functions using the parameters given in Table I (CH 35) for the 800-Hz site. The algorithm results agree with those of Cooper and Rhode in that they did not show any net suppression (not shown).

Ruggero *et al.* (1992) did observe total suppression at a site with a BF of 8.6 kHz. The peak BM velocity was observed to decrease when the suppressor was added. Figure 6(d) shows how the algorithm can simulate their main finding. In this example a probe tone is presented at BF (10 kHz)

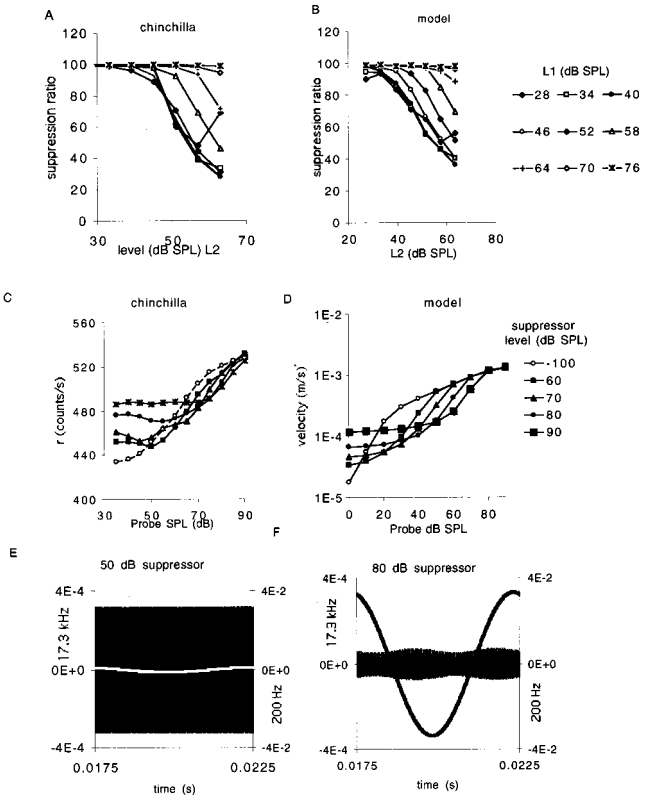

FIG. 6. Two-tone suppression. (a) and (b) Suppression ratio (suppressed/unsuppressed f1 Fourier component) for two tones (f1=800 Hz=BF and f2=1000 Hz) as a function of the level of f2 (L2). Each function represents a fixed level (L1) of f1. Animal data are taken from Cooper and Rhode (1996, Fig. 3, preparation CH 35). The model data use the parameters for CH 35 given in Table I. (c) and (d) Intensity functions for a BF probe tone alone and in the presence of a 1.2*BF suppressor tone at four suppressor levels (60–90-dB SPL). The animal observations are the average rates of gamma radiation. The model data are based on the parameters given in Table I and are for a 10-kHz BF site. (e) and (f) The effect of a 200-Hz suppressor tone (50-dB and 80-dB SPL, respectively) on the velocity response to a CF (17.3 kHz, 30-dB SPL) probe tone using the model parameters given in Table I for the 18-kHz site. The velocity has been processed using a very narrow filter at the suppressor and probe-tone frequencies and reflects the spectral component at that frequency. As the suppressor tone increases in amplitude, the velocity response to the probe tone decreases. The left *y* axis shows the scale for the probe tone; the right *y* axis shows the scale for the suppressor tone. The model data are similar to measurements reported by Geisler and Nuttall (1997, Fig. 5).

at a range of signal levels either alone or in the presence of a suppressor tone (12 kHz=1.2 BF) at four signal levels between 60- and 90-dB SPL, respectively). The suppressor tone clearly produces a reduction in the peak velocity of the output. Note that this is a net reduction in response level, and not just a reduction at the level of the spectral component. A similar pattern can be observed in the chinchilla data, where the *y* axis represents the raw physical measurement (''*r* counts'' or gamma-radiation energy) when using the Mössbauer method. Note that the algorithm parameters used are the same as those given in Table I (~10 kHz site) and are based on a different animal. This may explain differences in the signal level required to produce suppression.

Geisler and Nuttall (1997) reported observations at a basal site with a BF of around 17 kHz. They measured the effect of very low-frequency suppressors (f2) when added to

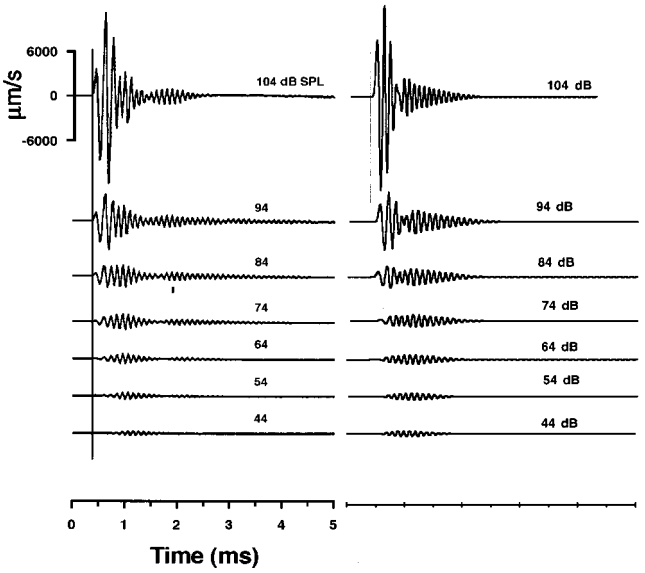

FIG. 7. (a) Basilar membrane velocity response to rarefaction clicks presented at several intensities (44–104 dB SPL), reproduced from Recio *et al.* (1998, Fig. 2). (b) Algorithm output in response to 20-μs clicks at corresponding signal levels.

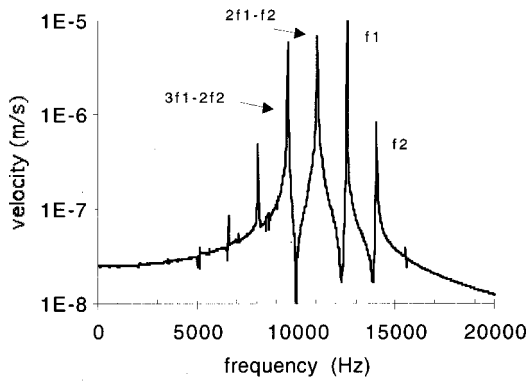

FIG. 8. Frequency spectrum of the response of the algorithm to two-tone stimuli (f1 = 12.5 kHz and f2 = 14 kHz, both at 50-dB SPL). Distortion products can be seen at 2f1-f2 and 3f1-f2. These results are comparable to measurements made of the response of the basilar membrane (Robles *et al.*, 1990, Fig. 2).

high-frequency (f1) stimuli presented at BF. Like Cooper and Rhode (1996), they also found no net suppression of the combined waveform but did observe suppression of the magnitude of the spectral component at f1. The response of the algorithm was computed using the parameters given in Table I for the 18-kHz site using their paradigm.

Geisler and Nuttall do not report comprehensive I/O measurements for their animal data and the parameters used are based on the model for the Nuttall and Dolan (1996) data. The algorithm produced no net suppression when the suppressor was added and this is similar to the Geisler and Nuttall data in this respect. Figures 6(e) and (f) shows the effect of a 200-Hz suppressor at two signal levels on the Fourier component at 17.3 kHz. The resulting figures are very similar to those of Geisler and Nuttall [1997, Figs. 5(a) and (d)]. Note that there is strong suppression at the BF frequency at two different points in the suppressor cycle, soon after both the highest and lowest suppressor-tone velocities.[5] This is a characteristic feature of the Geisler and Nuttall data, although there is an asymmetry in their compression that is not present in the model output.

E. Impulse response

Figure 7 shows the impulse response data from the chinchilla investigated using 20-μs wide clicks at different signal levels (Recio *et al.*, 1998). Comparable model results are shown alongside. The parameters of the model are the same as those used above (see Table I). In both the animal and the model data, it is possible to see at high signal levels a low-frequency rapid response that is not visible at low signal levels. This results in an apparent increase in the frequency of the impulse response during the first millisecond after the click. This low-frequency component has a very low amplitude at low click levels but increases linearly with click level. The higher-frequency component is prominent at low click intensities but shows little increase in amplitude over a 60-dB increase in click level. In the model, these two components are the outputs of two separate processing paths, linear and nonlinear. The linear path has a greater bandwidth and a lower CF resulting in an impulse response that peaks earlier and has a lower instantaneous frequency. The nonlinear path has a smaller bandwidth and a higher CF. This produces an impulse response that peaks later, lasts longer, and has a higher instantaneous frequency.

There are some differences between the animal and model impulse responses. In particular, the animal impulse response lasts considerably longer and shows amplitude modulations missing in the model response. This might be explained by the fact that the model parameters in Table I were tuned to the data from another animal in another study. Alternatively, it might be the case that the animal preparation has a third very narrowly tuned resonance at around BF that is not represented in the model. It should be noted that the model uses a perfect click stimulus that is not achievable using loudspeakers. The character of the model response changes when nonidealized clicks are used containing oscillations following the leading pulse (not shown). This alone may explain the discrepancies between the model and the animal observations.

F. Distortion products

Figure 8 shows the spectrum of the response of the model to a two-tone stimulus. The parameters of the pure tones are based on an experiment by Robles *et al.* (1990). They used two tones (f1 and f2) whose frequencies were chosen such that distortion products 2f1-f2 and 3f1-2f2 would be close to the BF of the site on the basilar membrane being measured. Their data showed clear frequency components in the response at f1, f2, 2f1-f2 and 3f1-2f2. The model was evaluated using two, 50-dB SPL test tones with frequencies of 12.5 and 14 kHz, respectively. The parameters of the DRNL model are given in Table I (~10-kHz site). The model output gives a distortion product at the 2f1-f2 frequency of 11 kHz and at the 3f1-2f2 frequency of 9.5 kHz. Other distortion products are also visible.

In the model, many distortion products are generated by the compression function in the nonlinear path. However, most of these are attenuated by the second bandpass filter (after the compression function) and are lost to the output. Pfeiffer (1970) first suggested this arrangement. It has frequently been used since then, most notably by Goldstein (1990 and 1995), who has also explored the strength of combination tones as a function of the level of the primaries.

IV. DISCUSSION

The signal-processing algorithm reproduces a wide range of phenomena that are desirable in a nonlinear filter bank to be used in more general models of the auditory periphery. The I/O functions show compression near BF but are linear at low and sometimes very high frequencies. As a consequence, the I/O functions cross at high signal levels and the BF of the system shifts as signal intensity increases. At least, this is true at the basal but not at the most apical sites, where both the animal and the algorithm show largely linear responses with only small shifts in BF. The model shows phase changes with intensity at frequencies above BF. Appropriate two-tone suppression effects mirror the results of animal observations. The impulse response is characterized by a shift in frequency with time. Distortion products are limited to a range of frequencies close to the site's BF. Most importantly, the model can produce reasonably good *quantitative* fits to the animal data.

While the algorithm has been tested against observations of motion in the cochlear partition, it is important to stress that this is *not* a model of the mechanics of the system. It is a high-speed simulation of cochlear response and is not intended as an explanation of cochlear phenomena. Its primary value will rest with its potential to act as a component in much larger-scale simulations of the response of the auditory periphery to arbitrary sounds. However, the similarities between the animal and model data do permit us to conclude that the animal responds *as if* a linear and nonlinear resonance were both involved. It is also the case that recent direct measurements of the apical cochlear partition in guinea pig have found two modes of vibration, not dissimilar to those implemented above when modeling chinchilla data below 1 kHz (Hemmert *et al.*, 2000). The model offers a close quantitative fit most of the time. However, there are some difficulties in reproducing, exactly, the full range of effects in the impulse response. Some I/O functions and phase characteristics could not be replicated exactly. These failures may indicated the need for more than two resonances. The Recio *et al.* (1998) impulse response measurements at 84- and 94-dB SPL are indicative of a very narrowly tuned resonance whose impulse response substantially outlasts that of the model. The Nuttall and Dolan data give another example of this. Their detailed isovelocity functions show a number of irregularities that could never be simulated with a double resonance (Nuttall and Dolan, 1996, Fig. 2). Their results show two minima close to CF (17 and 18 kHz, respectively) that could not be attributed to measurement error. The DRNL algorithm is a good match to most of the data published at these three sites but it could still be improved given a larger database.

There are limits as to what might be expected of a point model of cochlea filtering. Distortion products are known to migrate from their point of origin to be detected at remote locations. As a consequence, measurements on the BM must reflect the sum of such indirect contributions as well as purely local effects. A point model can only estimate the local effects. A desirable future development of the model would be to find a computational procedure for simulating the migration of distortion products among simulated sites.

Our aim in this study was to show that the basic algorithm is robust enough to be considered a useful candidate for inclusion in a filter bank arrangement. However, it is not possible to use the parameters in Table I as the basis of such a filter bank. The animal data are limited to a small number of sites along the cochlear partition within the human hearing range and these data were collected from two species, chinchilla and guinea pig. Given the technical difficulties of making these measurements, it is unlikely that many more locations at the apical end of the partition will be subjected to measurement in the near future and other routes will be required to develop a full filterbank representing all sites along the partition.

Auditory nerve data are not suitable for evaluating the model directly because additional nonlinearities intervene between the basilar membrane and the AN fibers. The I/O functions observed at the level of the AN fiber are characterized by firing thresholds and saturation of firing rates that are consequences of process that occur subsequent to mechanical frequency selectivity. Nevertheless, we might be able to use AN data to help define the parameters of the DRNL if used in conjunction with a good model of the inner hair cell and the IHC/AN synapse. Studies using REVCOR methods with low BF AN fibers for reconstructing the frequency response characteristics have shown frequency sweeps in the derived impulse responses (Carney *et al.*, 1999; Lin and Guinan, 2000). These parallel those found in BM measurements (see above) and these could be used to help define some of the details of the filter bank. Similarly, it is likely that AN measurements using off-BF frequencies can be used to infer some aspects of the I/O functions of the cochlear partition using methods indicated by Winter *et al.* (1990) and Yates *et al.* (1990).

Human psychophysical data can also be used to help define the way that parameters of the algorithm need to vary across cochlear sites. Moore *et al.* (1999), and Plack and Oxenham (1998, 2000) have used masking techniques to measure the degree of nonlinearity at different stimulating frequencies. As with the animal data, compression is severe at high frequencies but much weaker at very low frequencies. The transition appears to occur between 1 and 3 kHz. At its most severe, the slope of the compression is rarely less than 0.3. These two items of data suggest useful constraints on a filter bank to simulate mechanical frequency selectivity in the human cochlea. Alcantara and Moore (2000) have recently shown that a two-filter approach similar to that proposed above can be used to successfully model psychophysical frequency–selectivity measures of intensity-dependent changes in bandwidth. This suggests that our algorithm may benefit from the availability of extensive data on human fre-

quency selectivity in the design of a full filter bank suitable for use in models of human psychophysics but consistent with direct measurements of mechanical frequency selectivity in animals.

[1]CF is used throughout to represent the center frequency of digital filters that are components of the model. This is to distinguish it from BF which is used to specify observed best frequencies either in animal data or the response of the DRNL system as a whole when being compared to animal data.

[2]The model was explored using both displacement and velocity. Velocity was finally chosen because the threshold for compression at a particular site changed less with respect to signal frequency when velocity was used. However, opinions vary on this topic and the use of velocity in this project does not preclude the use of displacement as the metric of choice when the issue is decided using empirical methods. Published displacement observations were converted to velocity using the formula, $v = 2\pi fD$, where v is velocity, f is frequency, and D is the displacement measure. Velocity is always expressed as meters per second (ms^{-1}).

[3]O'Mard and Meddis (1997). The software platform and an application that can be used to run all of the tests in this paper is available through the internet at ''http://www.essex.ac.uk/psychology/hearinglab/dsam/index.htm.''

[4]The data were taken from files available in American Institute of Physics Auxiliary Publication Service (JASA PAPS) archive using AIP Document No. PAPS JASMA-99-1556. For further details, see Nuttall and Dolan (1996) or on the internet at ''http://ftp.aip.org/epaps/journ_acoust_soc/E-JASMA-99-1556-disk/.''

[5]Stapes velocity at 200 Hz was set to a value of 2e-6 m/s at 0-dB SPL. This is an arbitrary value as no measured stapes velocity was available at a frequency 200 Hz for the guinea pig. The value chosen is the one that would be required to yield a degree of suppression comparable to that observed by Geisler and Nuttall (1997). Note that the parameters in Table I are based on a different animal and a close quantitative correspondence is not expected nor claimed.

Abbas, P. J., and Sachs, M. B. (**1976**). ''Two-tone suppression in auditory-nerve fibers: extension of a stimulus-response relationship,'' J. Acoust. Soc. Am. **59**, 112–122.

Alcantara, J. I., and Moore, B. C. J. (**2000**). ''A psychoacoustic measure of level-dependent shifts in maximum cochlear excitation,'' Br. J. Audiol. **34**, 105.

Carney, L. H. (**1993**). ''A model for the responses of low-frequency auditory-nerve fibers in cat,'' J. Acoust. Soc. Am. **93**, 401–417.

Carney, L. H., McDuffy, M. J., and Shekhter, I. (**1999**). ''Frequency glides in the impulse responses of auditory-nerve fibers,'' J. Acoust. Soc. Am. **105**, 2384–2391.

Cooper, N. P., and Rhode, W. S. (**1996**). ''Two-tone suppression in apical cochlear mechanics,'' Aud. Neurosci. **3**, 123–134.

Geisler, C. D., and Nuttall, A. L. (**1997**). ''Two-tone suppression of basilar membrane vibrations in the base of the guinea pig cochlea using 'low-side' suppressors,'' J. Acoust. Soc. Am. **102**, 430–440.

Giguère, C., and Woodland, P. C. (**1994**). ''A computational model of the auditory periphery for speech and hearing research. I. Ascending path,'' J. Acoust. Soc. Am. **95**, 331–342.

Glasberg, B. R., Moore, B. C. J., and Stone, M. A. (**1999**). ''Modelling changes in frequency selectivity with level,'' in *Psychophysics, Physiology and Models of Hearing*, edited by T. Dau, V. Hohmann, and B. Kollmeier (World Scientific, River Edge, NJ).

Goldstein, J. L. (**1990**). ''Modeling rapid wave form compression on the basilar membrane as multiple-band-pass-nonlinearity filtering,'' Hear. Res. **49**, 39–60.

Goldstein, J. L. (**1995**). ''Relations among compression, suppression, and combination tones in mechanical responses of the basilar membrane: data and MBPNL model,'' Hear. Res. **89**, 52–68.

Hartmann, W. M. (**1997**). *Signals, Sound and Sensation* (Springer-Verlag, Berlin).

Hemmert, W., Zenner, H., and Gummer, A. W. (**2000**). ''Three-dimensional motion of the organ of Corti,'' Biophys. J. **78**, 2285–2297.

Irino, T., and Patterson, R. D. (**1997**). ''A time–domain level-dependent auditory filter: The gammachirp,'' J. Acoust. Soc. Am. **101**, 412–419.

Lin, T., and Guinan, J. J. (**2000**). ''Auditory-nerve-fiber responses to high-level clicks: Interference patterns indicate that excitation is due to the combination of multiple drives,'' J. Acoust. Soc. Am. **107**, 2615–2630.

Lopez-Poveda, E. A., O'Mard, L. P., and Meddis, R. (**1998**). ''A revised computational inner-hair cell model,'' in *Psychophysical and Physiological Advances in Hearing*, edited by A. R. Palmer, A. Rees, A. Q. Summerfield, and R. Meddis (Whurr, London).

Lopez-Poveda, E. A., and Meddis, R. (**2000**) ''A computational model for simulating basilar-membrane nonlinearity in subjects with normal and impaired hearing,'' International Hearing Aid Research Conference, PA9, Lake Tahoe, California.

Lyon, R. F. (**1982**). ''A computational model of filtering, detection, and compression in the cochlea,'' IEEE Proceedings, Paris, May 1982, pp. 1282–1285.

Meddis, R., Hewitt, M. J., and Shackleton, T. (**1990**). ''Nonlinearity in a computational model of the response of the basilar membrane,'' in *The Mechanics and Biophysics of Hearing*, edited by P. Dallos and C. D. Geisler (Springer-Verlag, Berlin).

Moore, B. C. J., Vickers, D. A., Plack, C. J., and Oxenham, A. J. (**1999**). ''Inter-relationship between different psychoacoustic measures assumed to be related to the cochlear active mechanism,'' J. Acoust. Soc. Am. **106**, 2761–2776.

Nuttall, A. L., and Dolan, D. F. (**1996**). ''Steady state sinusoidal velocity responses of the basilar membrane in guinea pig,'' J. Acoust. Soc. Am. **99**, 1556–1565.

O'Mard, L. P., and Meddis, R. (**1997**). ''Computer exploration of the auditory system with LUTear,'' Assoc. Res. Otolaryngol. Abs. **457**, p. 115.

Pfeiffer, R. R. (**1970**). ''A model for two-tone inhibition of single cochlear-nerve fibers,'' J. Acoust. Soc. Am. **48**, 1373–1378.

Plack, C. J., and Oxenham, A. J. (**1998**). ''Basilar membrane nonlinearity and the growth of forward masking,'' J. Acoust. Soc. Am. **103**, 1598–1608.

Plack, C. J., and Oxenham, A. J. (**2000**). ''Basilar membrane nonlinearity estimated by pulsation threshold,'' J. Acoust. Soc. Am. **107**, 501–507.

Recio, A., Rich, N. C., Narayan, S. S., and Ruggero, M. A. (**1998**). ''Basilar-membrane responses to clicks at the base of the chinchilla cochlea,'' J. Acoust. Soc. Am. **103**, 1972–1989.

Rhode, W. S. (**1971**). ''Observations of the vibration of the basilar membrane in squirrel monkeys using the Mössbauer technique,'' J. Acoust. Soc. Am. **49**, 1218–1231.

Rhode, W. S., and Cooper, N. P. (**1996**). ''Nonlinear mechanics in the apical turn of the chinchilla cochlea *in vivo*,'' Aud. Neurosci. **3**, 101–121.

Robert, A., and Eriksson, J. L. (**1999**). ''A composite model of the auditory periphery for simulating responses to complex sounds,'' J. Acoust. Soc. Am. **106**, 1852–1864.

Robles, L., Ruggero, M. A., and Rich, N. C. (**1990**). ''Two-tone distortion products in the basilar membrane of the chinchilla cochlea,'' in *Lecture Notes in Biomathematics*, edited by S. Levin, P. Dallos, C. D. Geisler, J. W. Matthews, M. A. Ruggero, and C. R. Steele (Springer-Verlag, Berlin).

Ruggero, M. A., Rich, N. C., Recio, A., Narayan, S. S., and Robles, L. (**1997**). ''Basilar membrane responses to tones at the base of the chinchilla cochlea,'' J. Acoust. Soc. Am. **101**, 2151–2163.

Ruggero, M. A., Rich, R. L., and Shivapuja, B. G. (**1990**). ''Middle-ear response in the chinchilla and its relationship to mechanics at the base of the cochlea,'' J. Acoust. Soc. Am. **87**, 1612–1629.

Ruggero, M. A., Robles, L., and Rich, N. C. (**1992**). ''Two-tone suppression in the basilar membrane of the cochlea: mechanical basis of auditory nerve suppression,'' J. Neurophysiol. **68**, 1087–1099.

Schoonhoven, R., Keizer, J., Versnel, H., and Prijs, V. F. (**1994**). ''A dual filter model describing single-fiber responses to clicks in the normal and noise-damaged cochlea,'' J. Acoust. Soc. Am. **95**, 2104–2121.

Schoonhoven, R., Prijs, V. F., and Frijns, J. H. M. (**1997**). ''Transmitter release in inner hair cell synapses: a model analysis of spontaneous and driven rate properties of cochlear nerve fibres,'' Hear. Res. **113**, 247–260.

Winter, I. M., Robertson, D., and Yates, G. K. (**1990**). ''Diversity of characteristic frequency rate-intensity functions in guinea pig auditory nerve fibers,'' Hear. Res. **45**, 191–202.

Yates, G. K., Winter, I. A., and Robertson, D. (**1990**). ''Basilar membrane nonlinearity determines auditory nerve rate-intensity functions and cochlear dynamic range,'' Hear. Res. **45**, 203–220.

Sources of distortion product otoacoustic emissions revealed by suppression experiments and inverse fast Fourier transforms in normal ears

Dawn Konrad-Martin,[a] Stephen T. Neely, Douglas H. Keefe, Patricia A. Dorn, and Michael P. Gorga
Boys Town National Research Hospital, 555 North 30th Street, Omaha, Nebraska 68131

(Received 28 October 2000; revised 6 March 2001; accepted 14 March 2001)

Primary and secondary sources combine to produce the $2f_1$-f_2 distortion product otoacoustic emission (DPOAE) measured in the ear canals of humans. DPOAEs were obtained in nine normal-hearing subjects using a fixed-f_2 paradigm in which f_1 was varied. The f_2 was 2 or 4 kHz, and absolute and relative primary levels were varied. Data were obtained with and without a third tone (f_3) placed 15.6 Hz below $2f_1$-f_2. The level of f_3 was varied in order to suppress the stimulus frequency otoacoustic emission (SFOAE) coming from the $2f_1$-f_2 place. These data were converted from the complex frequency domain into an equivalent time representation using an inverse fast Fourier transform (IFFT). IFFTs of unsuppressed DPOAE data were characterized by two or more peaks. Relative amplitudes of these peaks depended on overall primary level and on primary-level differences. The suppressor eliminated later peaks, but early peaks remained relatively unaltered. Results are interpreted to mean that the DPOAE measured in humans includes components from the f_2 place (intermodulation distortion) and DP place (in the form of a SFOAE). These findings build on previous work by providing evidence that multiple peaks in the IFFT are due to a secondary source at the DP place. [DOI: 10.1121/1.1370356]

PACS numbers: 43.64.Ha, 43.64.Jb [BLM]

I. INTRODUCTION

Distortion product otoacoustic emissions (DPOAEs) are sounds recorded in the ear canal in response to two closely spaced primary frequencies, f_1 and f_2, where $f_1<f_2$. Nonlinear interaction occurs between the basilar membrane displacement patterns corresponding to the two-tone stimulus, which gives rise to a set of distortion products (DPs). In the case of the $2f_1$-f_2 DP, energy at the site of its generation (near the f_2 place) propagates back toward the oval window (Brown and Kemp, 1984; Martin *et al.*, 1987; Harris *et al.*, 1992; Kummer *et al.*, 1995; Gaskill and Brown, 1996), as well as toward its own characteristic-frequency place (e.g., Goldstein and Kiang, 1967; Kim, 1980; Furst *et al.*, 1988). Presumably, the DP encounters small discontinuities near the place coding $2f_1$-f_2 causing the response, having been reinforced locally by the cochlear amplifier, to propagate back out of the cochlea in the form of a stimulus frequency otoacoustic emission (SFOAE) (Shera and Zweig, 1993). Higher order reflections arising through the same mechanisms as this second component could also be generated, depending on the amount of reflectance at the oval window and at the DP place. The SFOAE(s) arising at the DP place combines with the distortion-generated OAE to produce the $2f_1$-f_2 DPOAE measured in the ear canal (e.g., Kim, 1980; Kemp and Brown, 1983; Kemp, 1986; Furst *et al.*, 1988; Shera and Zweig, 1992; O'Mahoney and Kemp, 1995; Brown *et al.*, 1996; Kemp and Knight, 1999; Shera and Guinan, 1998, 1999a; Talmadge *et al.*, 1998; Knight and Kemp, 2000; Kalluri and Shera, 2001). The present study uses a temporal analysis of DPOAEs obtained with and without a suppressor-tone near $2f_1$-f_2 in order to test the multiple sources/reflections hypothesis previously described.

The dominant mode of $2f_1$-f_2 DPOAE generation appears to depend on the stimulus paradigm used during its measurement. For example, the change in DPOAE phase with respect to its frequency (group delay), determined using a primary frequency sweep in which the primary frequency ratio (f_2/f_1) is fixed, depends on f_2/f_1 (Kemp and Brown, 1983). It was suggested that an emission generating mechanism fixed to the traveling wave ensemble (''wave fixed'') might be responsible for the relatively constant DP phase obtained for ratios greater than 1.1 (Kemp, 1986; Brown *et al.*, 1996). A local reflection fixed to the basilar membrane (''place fixed'') was proposed to account for the rapidly varying phase observed for smaller f_2/f_1 ratios. In addition, SFOAE growth functions may begin to saturate at lower stimulus levels (Kemp and Chum, 1980) compared to DPs (e.g., Kummer *et al.*, 1998), suggesting that the relative strength of DPOAE sources also may vary as a function of stimulus level. Intermodulation distortion may dominate DPOAEs elicited by moderate and high levels of stimulation, whereas the component reflected at the DP place may dominate responses to low levels of stimulation (Fahey and Allen, 1997).

While there is increasing support for the hypothesis that two sources generate the $2f_1$-f_2 DPOAE, it is not known what their relative contributions are to the OAE measured in the ear canal. For example, a tone near $2f_1$-f_2 can reduce the overall DPOAE amplitude, even though frequencies near f_2 are more effective suppressors (Martin *et al.*, 1987; Harris

[a]Author to whom correspondence should be sent. Electronic mail: konradd@boystown.org

et al., 1992; Cianfron *et al.*, 1994; Kummer *et al.*, 1995; Gaskill and Brown, 1996; Brown *et al.*, 1996). Other evidence suggests that for some stimulus conditions in some subjects, the OAE arising near the DP place can be similar or larger in amplitude than the distortion component arising near f_2 (Kummer *et al.*, 1995; Fahey and Allen, 1997; Heitmann *et al.*, 1998; Siegel and Dreisbach, 1998; Dreisbach, 1999; Dreisbach and Siegel, 1999). Under these circumstances, one might expect that a suppressor near the DP frequency would have a large effect.

Models incorporating a distortion component and a reflection component predict that interaction between the two sources can be observed because their phase delays differ (reviewed in Talmadge *et al.*, 1999). Phase variations between two sources have been proposed to account for the quasi-parabolic functions generated by plotting DPOAE amplitude as a function of f_2/f_1 or DP frequency (''filter functions'') for lower side-band DPs (Brown *et al.*, 1992; Stover *et al.*, 1996, 1999; Kemp and Knight, 1999). Two-source/multiple reflection models have also been used to explain oscillatory fine structure in DPOAE amplitude and phase when either f_2/f_1 is varied by fixing one of the primaries while the other is swept in frequency, or when f_2/f_1 is held constant for a range of f_2 frequencies (Talmadge *et al.*, 1998; Mauermann *et al.*, 1999a). This has led to the hypothesis (Talmadge *et al.*, 1997, 1998), and the demonstration (Mauermann *et al.*, 1999a) that interaction between multiple sources (in the form of fine structure in the DPOAE level) is minimal for stimulus conditions dominated by either the relatively constant or the rapidly varying phase component.

Investigators have attempted to isolate contributions to the DPOAE arising near the f_2 and DP sites using subjects with well-defined hearing loss. Rapid excursions in DP level and/or phase with small changes in DP frequency (fine structure) were reduced when primaries were chosen such that $2f_1$-f_2 fell into a region of hearing loss (Mauermann *et al.*, 1999b), or when a third tone was introduced near the DP frequency in order to suppress the SFOAE arising at the DP place (Heitmann *et al.*, 1998; Kalluri and Shera, 2000, 2001). Filter functions obtained in subjects with hearing loss confined to the DP frequency region were not parabola shaped, but rather, resembled high-pass functions (i.e., DPOAE level decreased as a function of increasing separation between the two primary frequencies) (Stover *et al.*, 1999).

Investigators also have attempted to separate DPOAE components by exploiting differences in their temporal characteristics. Talmadge *et al.* (1999) used a stimulus paradigm in which one of the primaries was continuous and the other was pulsed. The f_2 was placed near notches in the DPOAE fine structure, which were thought to indicate strong destructive interaction between the two DPOAE sources and, therefore, conditions in which the two sources were similar in amplitude but out of phase. Consistent with other reports, DP phase changed shortly after the stimulus onset (Whitehead *et al.*, 1996; Martin *et al.*, 1998), presumably because the DP place component is delayed compared to the distortion component generated near the f_2 place. Talmadge *et al.* also found notches in DP level accompanied by rapid phase changes shortly after the stimulus offset. The introduction of a suppressor near the DP frequency minimized the excursions in the $2f_1$-f_2 level and phase response, suggesting that they were caused by transitions between the two components of the DPOAE.

Under conditions in which the relative contribution from the DP place is large, DP latencies estimated by the phase-slope method presumably would be influenced by multiple latency components. Using a fixed-f_2 stimulus paradigm, Stover *et al.* (1996) found evidence for multiple DPOAE reflections in the time-domain representation of filter-function data. The frequency and phase representations were transformed into an equivalent time representation using inverse fast Fourier transform (IFFT) techniques. The IFFT output was distributed in time rather than centered around a single delay. Stover *et al.* (1996) hypothesized that the multiple peaks in IFFTs (beyond two) were due to reflections off of the stapes footplate back into the cochlea that provided energy for additional reflected SFOAEs. For a given subject, latencies of individual peaks were constant with changes in stimulus level; however, their relative amplitudes varied systematically, with the earliest peak becoming more dominant as the stimulus level increased. These observations bring into question the validity of techniques that attempt to provide a single, overall estimate of DPOAE latency. For example, assuming a single-component signal, group delay is defined in the time domain as the latency of the center of energy of an impulse response (Papoulis, 1962). As was shown by Stover *et al.* (1996), the ''impulse response'' determined by IFFT of DPOAE filter functions contain multiple peaks, suggesting that an estimate of overall DPOAE latency will obscure contributions from individual components in the response.

Knight and Kemp (2000) obtained a set of DPOAEs by varying the primary frequencies while holding their ratio constant (fixed-f_2/f_1 paradigm). These data were used to construct DP phase versus DP frequency functions and were also transformed into the time domain using IFFT techniques. When the f_2/f_1 for the fixed-ratio sweep was 1.15, a suppressor presented near the DP frequency reduced the slope of the DP phase versus DP frequency profile and removed long-latency peak(s) from the IFFT envelope. Long-latency peaks, evident in the transform, presumably correspond to rapidly varying phase components in the DP sweep. Their selective removal by the suppressor was interpreted as a demonstration that the place-fixed DPOAE component is generated at the DP place. Kalluri and Shera (2001) used a time-windowing method, in which long-latency components of fixed-f_2/f_1 DPOAE data were removed in the time domain, and a suppression paradigm, in which energy near $2f_1$-f_2 was removed in the frequency domain. Both manipulations resulted in a DPOAE spectrum that was a smooth version of the original, linking the DP-place/long-latency component(s) of the DPOAE to the presence of emission fine structure.

The IFFT analysis of DPOAE data obtained using a fixed-f_2 paradigm in conjunction with a suppressor provides an opportunity to analyze multiple components of the DPOAE initiated at a particular f_2 location. It is generally assumed that the site of DP generation is the point of maximal overlap between the primaries, which occurs near the f_2

place. This point will shift with changes in f_1; however, given the steep slope of the apical side of the f_2 displacement pattern, DPOAEs arising from the f_1 sweep will, to a first approximation, share a primary generator site. Utilizing a range of f_2/f_1 ratios for a given f_2 ensures that the largest possible intermodulation-distortion and reflection components will be contained in the response. Thus, measurements in a fixed-f_2 paradigm allow for a more complete characterization of DPOAE response generation at an f_2 place compared to measurements in a fixed-f_1 paradigm.

The aims of this study were twofold: (1) to provide a more detailed explanation of the time-domain representation of DPOAE data by selectively suppressing the SFOAE originating at the DP place and (2) to examine the extent to which the relative contributions from sources at the primary and DP places depend on stimulus level and f_2 frequency. DPOAE filter functions were obtained in subjects with normal hearing using a fixed-f_2 stimulus paradigm. These data were obtained with and without a third suppressor tone (f_3) placed at a frequency just below $2f_1$-f_2. For fixed primary frequency and level conditions, the level of f_3 (L_3) was varied, and was used to suppress the SFOAE coming from the $2f_1$-f_2 place. Effects of L_3 on the DPOAE were examined in both frequency and time domains.

II. METHODS

A. Subjects

DPOAE data were collected from nine normal-hearing subjects age 18 to 32 years, while they were seated in a sound-treated booth. Normal hearing was defined as pure-tone audiometric thresholds $\leqslant$15 dB HL (ANSI, 1996) for half-octave frequencies from 250 Hz to 8 kHz. Normal middle-ear function, (compliance peak=0.2 to 1.4 cm^3 and pressure peak=$-$150 to 100 daPa) was confirmed by typanometric measurements (226-Hz probe tone) prior to each 2 to 3-h test session. Data collection for all conditions required approximately 15 h per subject.

B. Stimuli

For these measurements, f_2 was fixed at either 2 or 4 kHz, and f_1 was varied in 31-Hz steps. With this step size, the DP frequency ranged from 875 to 1813 Hz for f_2=2 kHz (15 points), and from 1750 to 3813 Hz for f_2=4 kHz (33 points). Absolute primary level and the level difference between primaries were manipulated as part of the experiment. In one series of experiments, L_2 was set to 25, 35, and 45 dB SPL, with $L_1=L_2+10$ dB. For L_2=25 and 35 dB SPL, additional L_1 conditions (L_1=49 and 53 dB SPL, respectively) were chosen in order to maximize DPOAE level (Whitehead *et al.*, 1995; Janssen *et al.*, 1998; Kummer *et al.*, 1998). Maximal DPOAE level for L_2=45 dB SPL is reportedly obtained where $L_1=L_2+12$ dB. Since this level ratio represents a small (2 dB) difference from the $L_1=L_2+10$ dB condition, it was not tested. Data were obtained with and without a third tone (f_3) at a frequency that was 15.6 Hz (2 frequency bins) below that of $2f_1$-f_2. Thus, f_3 tracked the DP frequency with changes in f_1. For a fixed primary-level combination, the level of f_3 (L_3) was varied ($L_3=L_2-20$ to L_2+30 dB).

C. Data collection

Stimulus presentation and OAE measurements were controlled by locally designed software (EMAV, Neely and Liu, 1993), which has been described elsewhere (Gorga *et al.*, 1994). The primary frequencies were generated using separate D/A channels of a signal processing board (Turtle Beach, Fiji), connected to separate digital attenuators, and presented through separate loudspeakers housed in a probe microphone system (Etymotic Research, ER-10C). When a third tone was presented, it was generated by the channel containing the lower-level primary, meaning that f_2 and f_3 were presented by the same loudspeaker. The system was calibrated every 1 to 1.5 h to adjust for any changes in the probe fit over time. If the stimulus level between calibrations varied by more than 3 dB, data collection was halted, the probe adjusted, and the system recalibrated.

DPOAEs were recorded using a probe microphone system (ER-10C microphone and preamplifier). The signal was sampled at a rate of 32 kHz, sent to the computer for dual time-domain averaging, and saved for further analysis. Half of the samples from the $2f_1$-f_2 FFT bin of the A/D converter were accumulated in one buffer, and the other half in a second buffer. The level of the response was determined by summing the subaverages obtained for the two buffers (in the complex frequency domain), and the level of the noise was determined by computing the difference between the two buffers. Thus, DPOAE and noise levels were estimated at the same frequency and the noise was defined as the average random component in the $2f_1$-f_2 frequency bin. Measurement-based stopping rules were used so that a condition terminated when the noise floor was $\leqslant -26$ dB SPL, or after 32 s of artifact-free averaging, whichever occurred first.

D. Data collection and analysis

1. Filter functions

For each f_2 and primary-level condition, DPOAE level and phase measurements were made over a range of f_1 frequencies. This is illustrated in Fig. 1 in the form of ''filter functions,'' in which DPOAE level is plotted as a function of f_2/f_1 (top *X*-axis) or DP frequency (bottom *X*-axis). Data are shown for f_2=2 and 4 kHz, and for L_2 ranging from 25 to 45 dB SPL. Open symbols represent data for conditions in which $L_1-L_2=10$ dB, and filled symbols represent data when primary-level separations were chosen to maximize DPOAE level (Gaskill and Brown, 1990; Whitehead *et al.*, 1995; Janssen *et al.*, 1998; Kummer *et al.*, 1998).

These plots show the characteristic filter-function shape that has been reported by others (Brown and Gaskill, 1990; Harris *et al.*, 1989); DPOAE level decreases as the two primary frequencies diverge, but also for closely spaced primary frequencies, with the largest levels centered at f_2/f_1 ratios near 1.2. The filter-function data were used in several off-line analyses (described below).

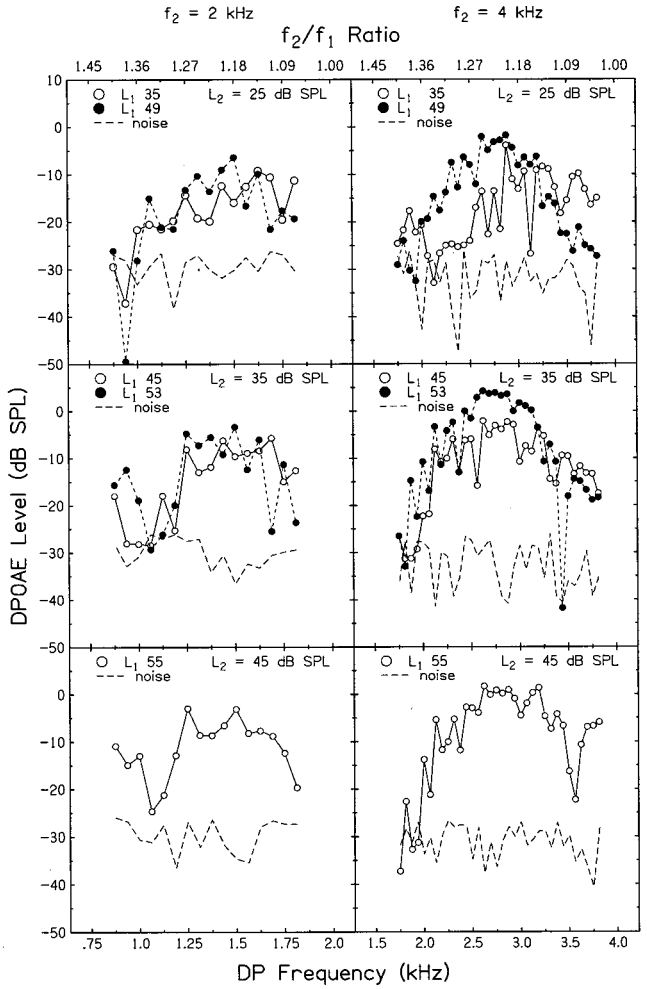

FIG. 1. DPOAE level plotted as a function of DP frequency and f_2/f_1 ratio (filter functions) for $f_2=2$ kHz (left) and $f_2=4$ kHz (right). Examples are for subject 99001, for L_2 ranging from 25 to 45 dB SPL. L_1 is either 10 dB above L_2 (open circles), or was presented at a level chosen to maximize DPOAE level (filled circles) (e.g., Kummer *et al.*, 1998). The ''optimal'' L_1 for an L_2 of 45 dB SPL is 57 dB SPL. Because it is similar to the $L_1=L_2+10$ dB condition, it was not measured.

2. IFFT analysis

DPOAE amplitude and phase responses at each point in an entire f_1-sweep (for a fixed f_2) were converted into complex values. The corresponding DP frequencies (described in Sec. II B) were placed into their correct frequency positions within a 1024-point buffer of zeros. The resulting ''spectrum'' of real and imaginary numbers served as the input to an IFFT, and the IFFT output was a complex function in the time domain. Thus, the IFFT output was an analytic signal representation of the DPOAE spectrum. The magnitude of the analytic signal with respect to derived time will be referred to as the ''IFFT envelope,'' with the duration of the time window (approximately 16 ms) determined by the f_1 step size.

It is important to note that certain methodological details have the potential to cause artifact in the IFFT when it is applied to the DPOAE filter function data. Sources of artifact include aliasing in the time domain, which would occur if the f_1 step sizes were insufficient to resolve DP phase changes as a function of frequency. This type of artifact would be manifested in wrap-around problems, i.e., early energy would end up at the end of the IFFT envelope and vice versa. Stover *et al.* (1996) used smaller step sizes compared to those used in the present study, resulting in a longer time window (20 ms). That study showed that, depending on the stimulus frequency and level, the IFFT envelope tended to ''sink'' into the noise floor between 12 and 15 ms, suggesting that aliasing artifact may have affected responses in the present study when f_2 was 2 kHz, but was less likely to contribute to 4-kHz responses.

Another potential source of artifact in IFFT analysis is windowing artifact, which would occur if the low and high frequency end-points of the DPOAE spectrum (i.e., the filter function) did not lie near the noise floor. This could happen if the range of frequencies tested was insufficient to include the entire filter function, or if filter functions did not display their characteristic peaked shape. The range of frequencies used here contained the entire filter function. However (as discussed in Sec. III B), filter functions for $f_2=2$ kHz at low stimulus levels sometimes did not have the characteristic peaked shape. These data, however, were excluded from further analyses.

3. Group delay

Three methods were used to estimate DPOAE group delay from each filter function. In order to compare results to previous studies, DPOAE group delay was determined using the DPOAE phase with respect to its frequency (phase-slope method). Phase-slope estimates were made by fitting the unwrapped phase (in cycles) with a linear regression across DP frequencies (in Hz). The fit was computed over the entire DPOAE spectrum; however, each point was weighted by the ratio of signal energy to noise energy (SNR), such that higher weighting was given to the filter function peak region. Two additional methods for estimating DPOAE group delay utilized data in the time domain. The median latency of the squared IFFT envelope was used as one latency estimate. This is equivalent to the 50% point on the cumulative distribution of envelope energy. Finally, the energy-weighted average latency of the IFFT envelope was determined. In this latency estimate, each point in time was weighted by its squared amplitude. Thus, the median and average latencies are calculated directly from the time-domain representation without phase unwrapping. As discussed earlier, deriving the temporal response from the DPOAE spectrum does not completely remove problems due to ambiguous phase responses. However, phase unwrapping at small SNRs greatly increases 2π phase ambiguity, in which case the median or average latency of the IFFT envelope might better describe the overall latency of the response than phase-slope group delay.

III. RESULTS

A. IFFT envelopes

DPOAEs measured in the ear canal potentially represent the complex interaction of multiple components. IFFT analysis of filter function data was used in order to separate DPOAE components based on their phase characteristics.

Figure 2 shows the effect of L_3 on corresponding time and frequency representations of DPOAEs for one subject. For this example, f_2 was 4 kHz and primaries were presented at a fixed low level. DPOAE level (first column) and phase (second column) are given as a function of DP frequency. The phase ($\Phi_{DP}-[2\Phi_{f1}-\Phi_{f2}]$) is given in fractions of a complete cycle. Increasing L_3 reduced the amount of fine structure present in level and phase responses (contrast the DP level and phase functions when $L_3=35$ and 45 dB SPL with those when $L_3=5$ dB SPL). Recall that f_3 was always 15.6 Hz below $2f_1-f_2$. The fact that fine structure was reduced by f_3 suggests that the fine structure results from the complex addition of the wave-fixed and place-fixed components, a conclusion reached by others (e.g., Heitmann *et al.*, 1998; Kalluri and Shera, 2000, 2001). For the example presented in Fig. 2, fine structure is visible over a wide range of DP frequencies for the lowest suppressor level ($L_3=5$ dB SPL) in the top row, and is reduced over a wide range of DP frequencies at higher suppressor levels. This observation suggests that the long latency components contributed to the DPOAE over a wide range of f_2/f_1 ratios.

IFFT magnitude is shown in the third column. These ''IFFT envelopes'' are the time-domain representations of the level and phase responses in each row. Multiple peaks in the envelope represent multiple group-delay components extracted from the fixed-f_2 data. Incrementing L_3 above 5 dB SPL reduced the amplitudes of all of the peaks in the IFFT envelope except the prominent early peak (vertical line at 3.2 ms). These results are consistent with the hypothesis that peaks in the IFFT, beyond the first, are most sensitive to increasing suppressor levels because they represent secondary source activity at the DP place. Thus, incrementing the level of the suppressor allows visualization of the transition from a DPOAE composed of multiple components, to one dominated by the distortion component from the f_2 place. The IFFT envelope corresponding to $L_3=45$ dB SPL represents almost complete suppression of later peaks, with minimal effect on the earliest peak. When $L_3=55$ dB SPL, the early peak is suppressed (presumably because the suppressor impinges on the emission generator near f_2).

The slope of the DPOAE phase with respect to its frequency can be used to estimate the DPOAE center of energy on a time axis (Papoulis, 1962). This measure of group delay has been used to estimate the DPOAE round-trip travel time, which has been correlated with travel time to the emission generator site (e.g., Kimberley *et al.*, 1993). Shorter DPOAE group delays are associated with emission generation at more basal cochlear locations compared to longer travel times. Phase-slope measures of group delay also depend on the mode in which the response is generated (Kemp and Brown, 1983). Moreover, $2f_1$-f_2 DPOAEs containing both distortion and reflection components have two source locations and modes of response generation (e.g., Knight and Kemp, 2000; Shera and Guinan, 1999a, 1999b; Talmadge *et al.*, 1999; Kalluri and Shera, 2001). The IFFT envelopes presented here separate the multiple latency components in the fixed-f_2 DPOAE data.

To illustrate this point, the symbols in the third column represent three measures of the overall group delay, in which a single delay estimate is assigned to the entire DP sweep. Comparing these symbols to the IFFT envelope, it can be seen that single-delay estimates correspond to the center of energy of single-component signals (for example, the IFFT envelope corresponding to $L_3=45$ dB SPL). However, single-delay estimates tend to obscure information about multi-component signals (for example, the IFFT envelope corresponding to $L_3=5$ dB SPL). Among the three measures of overall group delay shown here is the traditional phase-slope measure (triangles), and two additional estimates that are calculated from data in the time domain. These latter two estimates (shown as circles and asterisks) may better represent the center of energy of the IFFT, compared to phase-slope estimates. Circles represent estimates based on median IFFT peak energy, and asterisks represent estimates derived from average IFFT latency weighted by the energy at each peak. The vertical line bisecting the first prominent envelope peak is drawn to provide a point of reference. Two estimates of group delay (phase-slope and median-energy estimates) remain relatively constant as a function of L_3, indicating that these two measures of group delay are heavily weighted by the dominant early peak, which presumably arises from the wave-fixed, distortion-generator site. The asterisk tends to shift toward the reference line as later waves are suppressed (except at the highest suppressor level), indicating that the energy-weighted average of the time envelope is a better estimate of overall group delay, when all components are taken into account.

The last column of Fig. 2 shows the ''residual'' DPOAE component, which was derived in the complex frequency domain by subtracting the response (column 3) at each consecutive L_3 from the response corresponding to the case when the suppressor had no effect [envelope shown in panel (a)]. The magnitude of the residual is shown after being converted into its time-domain representation. Growth of suppression by L_3 is reflected in the progression down the column, which shows the residual becoming larger. Thus, for a given row, adding the suppressed IFFT envelope (column 3) to the residual (column 4) results in the control condition shown in panel (a), column 3. The residual response obtained where $L_3=45$ dB SPL is taken as the best estimate of the second-source activity for this example because it was characterized by a combination of the greatest reduction in later peaks and minimal reduction in the first peak.

In summary, the frequency (filter-function) representations show that DPOAE fine structure is reduced by introducing a suppressor near the DP frequency. Equivalent time domain (IFFT envelope) representations of the data show that the suppressor removed long-latency components of the response.

Introducing a third tone can potentially create a new array of distortion products with the potential to confound the interpretation of results. To address this issue, several unsuppressed IFFT envelopes were edited in the time domain such that rapidly varying phase components from the fixed-f_2 data were removed. The edited time-domain data were converted into the frequency domain so that fine structure in the filter function could be examined in the absence of long-latency envelope components without having to intro-

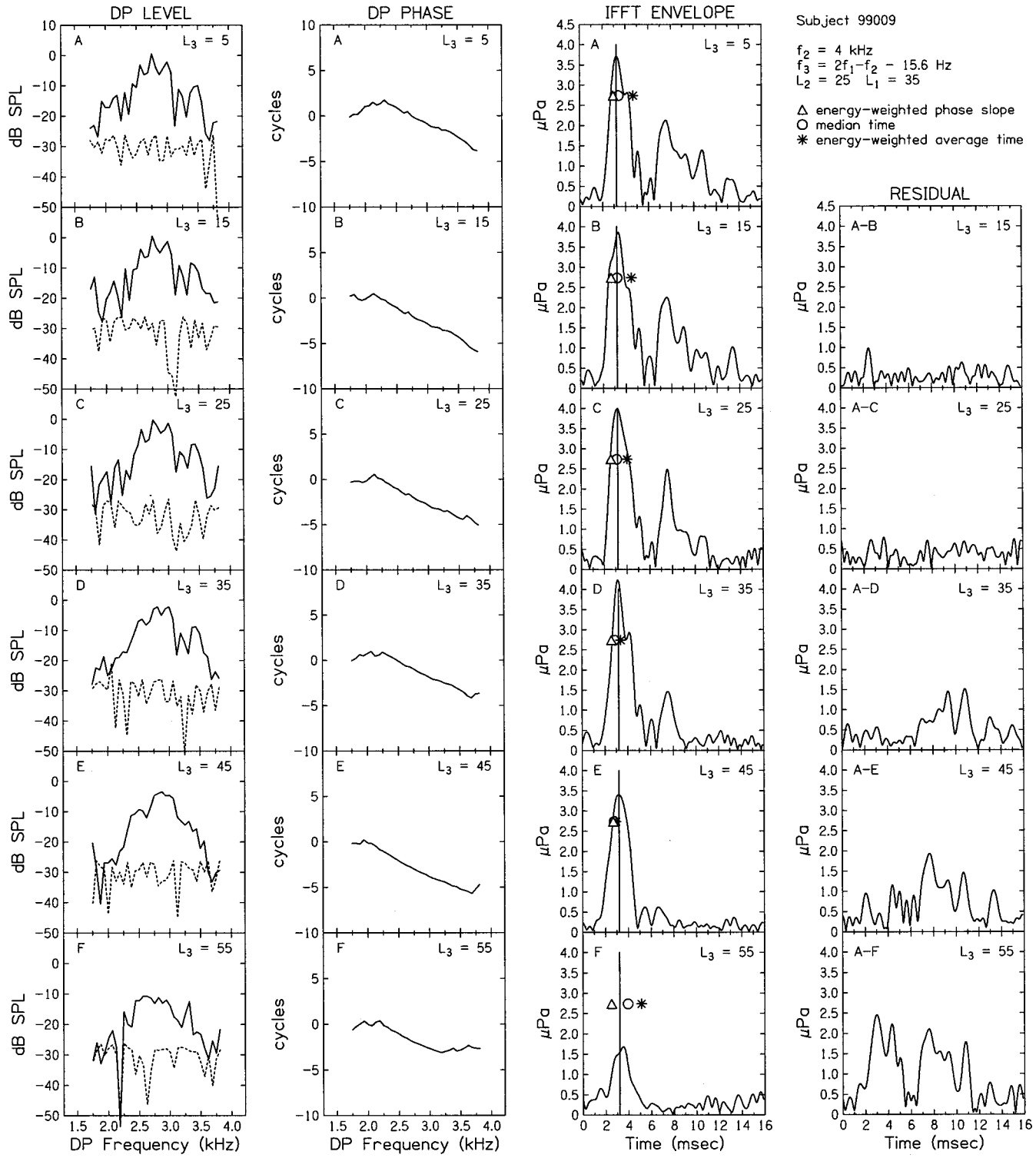

FIG. 2. Effect of L_3 on DPOAEs for subject 99009. Frequency and time representations of the data are shown for six suppressor levels (L_3) (ranging from 5 to 55 dB SPL from the top to bottom row, respectively). F_3 is always 15.6 Hz below $2f_1-f_2$. $F_2=4$ kHz. $L_2=25$ dB SPL, $L_1=35$ dB SPL. Column 1: DPOAE level as a function of DP frequency. Column 2: Phase ($\Phi_{DP}-[2\Phi_{f1}-\Phi_{f2}]$) in cycles as a function of DP frequency. Column 3: Magnitude of the IFFT as a function of derived time. Multiple peaks in the envelope represent the multiple group delay components extracted from the fixed-f_2 data. The symbols indicate the overall group delay. Triangles=group delay determined in the frequency domain using the phase slope method. Circles=median IFFT peak energy. Asterisks=average IFFT peak energy. Column 4: Time-domain representation of the ''residual'' component, derived in the complex frequency domain by subtracting the response at each consecutive L_3 from the response corresponding to the envelope shown in panel (a) (where L_3 had no effect). For a given row, the suppressed IFFT envelope (column 3) added to the residual (column 4), should equal the control condition shown in column 3, panel (a).

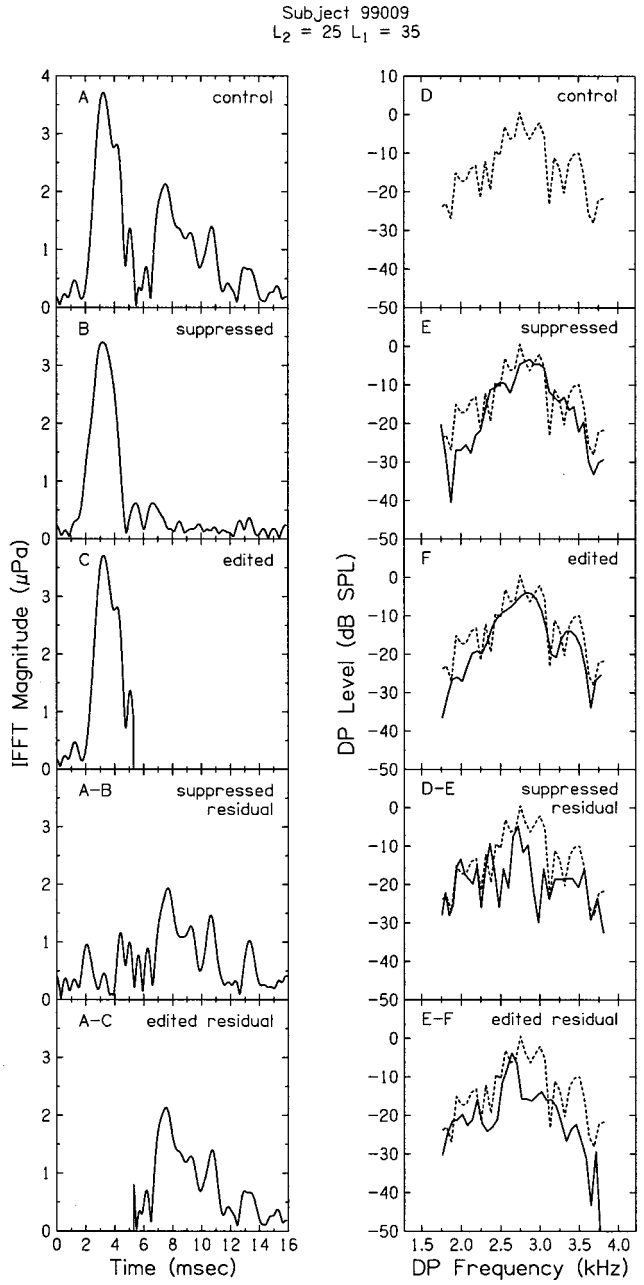

FIG. 3. Comparison of effects on the filter function of suppression and time-domain editing for subject 99009. (a) IFFT envelope introduced in Fig. 2(a); (d) the corresponding filter function. (b) Suppressed IFFT envelope introduced in Fig. 2(e); (e) the corresponding filter function. (c) Same IFFT envelope given in (a), except that complex values of points after the first peak were set to zero; (f) magnitude (in dB SPL) of FFT of the time envelope given in (c). (a-b) Time-domain representation of the residual response (control-suppressed); (d–e) frequency-domain representation of the residual response (control-suppressed). (a–c) Time-domain representation of the residual response obtained by zeroing the complex values of points in the IFFT comprising the first peak, or equivalently, by subtracting the edited response given in (c) from the control in (a). (e–f) Frequency-domain representation of the time-edited residual response.

duce a suppressor. This technique is similar to the ''time-windowing'' method used by Kalluri and Shera (2001), who found that removing long-latency components of the DPOAE response had the same effect on DPOAE microstructure as introducing a suppressor near the DP frequency.

Figure 3 shows corresponding time- and frequency-domain representations in the left and right columns, respectively. The IFFT envelope in Fig. 3(a) is the same as in Fig. 2(a). The optimally suppressed version of the response shown in Fig. 3(b) is re-plotted from Fig. 2(e). For the purpose of comparison, the ''control'' filter function (dotted line) is shown in each panel of the right column. The IFFT envelope shown in (c) was obtained by taking the control IFFT envelope and zeroing the values for times later than 5.3 ms. This edited envelope was used as input to a FFT in order to obtain the filter function shown in (f). Filter functions corresponding to the suppressed and time-edited data (which presumably reflect the distortion generator component) were relatively smooth versions of the control.[1]

For comparison to the presumed distortion component, the presumed DP-site component is presented in both frequency and time domains. A residual component was derived by vector subtraction of (b) from (a), and also was obtained by editing out the early component of the control time-domain envelope [or equivalently, subtracting (c) from (a)]. A FFT of the two residual IFFT envelopes resulted in filter functions (d-e and d-f), which had similar amplitudes. The residual filter functions were slightly lower in amplitude compared to those corresponding to the distortion component. Presumably, for this example, the contribution to the DPOAE by reflection(s) near the DP-site was slightly smaller than the contribution by intermodulation distortion.

B. Effect of suppressor level

Figure 4 shows the effect of L_3 on IFFT envelopes for four subjects, whose individual data are shown in separate columns. For each example, f_2 is 4 kHz, L_2 is presented at a low level (15 or 25 dB SPL), and $L_1 = L_2 + 10$ dB. Responses are shown in the absence of a suppressor (top row), and in the presence of a suppressor, increasing in level (L_3) as one descends each column. Unsuppressed IFFT envelopes were characterized by multiple peaks. Increasing the level of a suppressor located just below $2f_1$-f_2 systematically reduced the amplitude and eventually the number of peaks in the envelope until only an early peak (at about 3 ms) remained. The amplitude of this early peak sometimes increased slightly in the presence of a suppressor (for example, for L_3 of 15 to 35 dB SPL for subject 99009), which could represent normal variation in response amplitudes. For some subjects (for example, $L_3 = 55$ dB SPL for subject 99009), a high L_3 reduced the early peak relative to the unsuppressed condition, perhaps as a consequence of the suppressor-tone suppressing the emission generator located near f_2.

Figure 5 follows the same format as Fig. 4, for $f_2 = 2$ kHz. These examples include a number of L_2, L_1 combinations because for some subjects, high noise levels reduced SNRs, restricting the amount of reliable data at 2 kHz, particularly for low L_2's. In addition, the amount of reliable data at 2 kHz was reduced because filter functions obtained at $L_2 = 25$ dB SPL tended to have poorly defined peaks, which sometimes introduced a windowing artifact when data were transformed into the time domain.

At 2 kHz, the unsuppressed versions of IFFT envelopes usually included an early large peak (at 4–5 ms) and a second later peak (at 8–12 ms), in contrast to 4 kHz, where

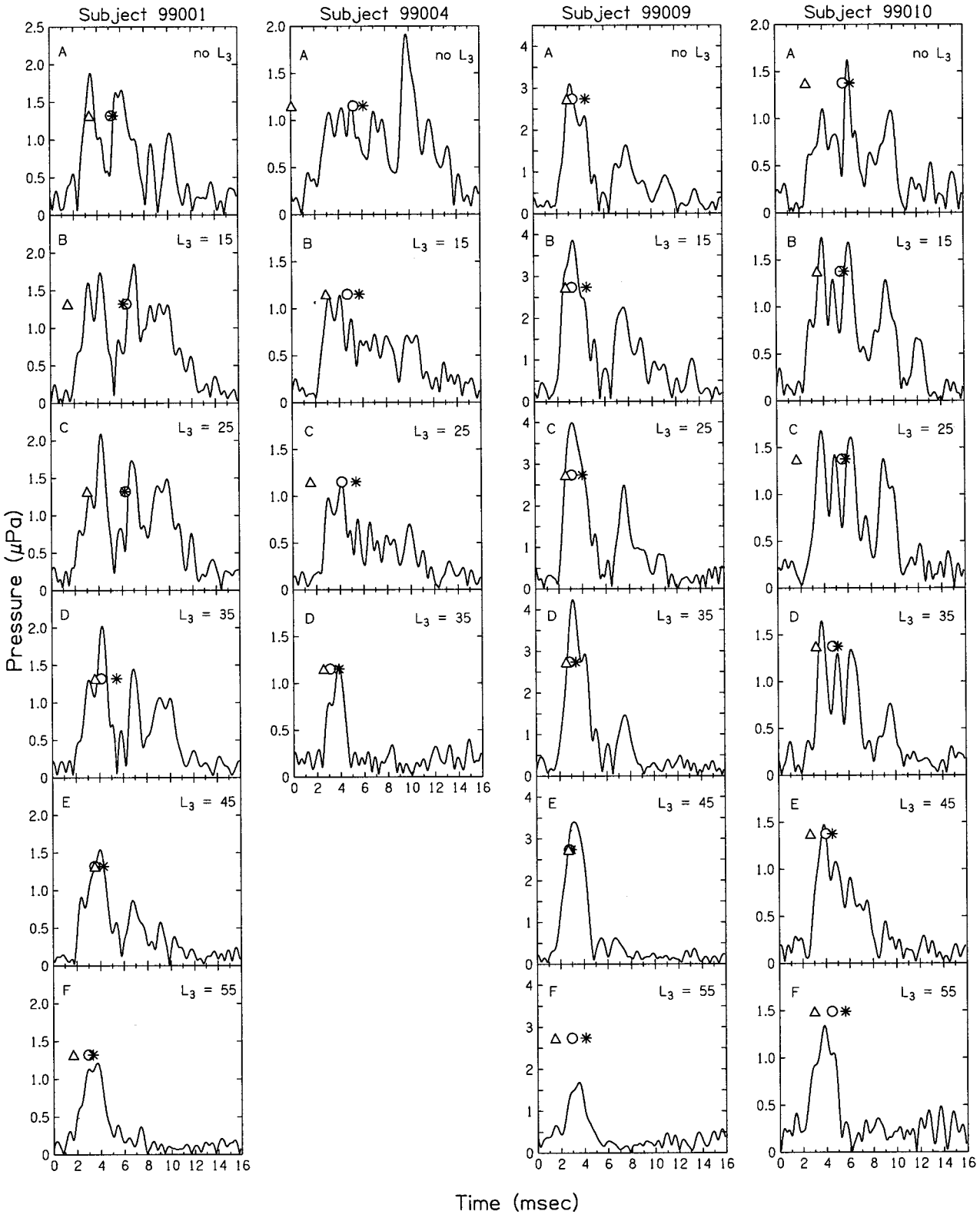

FIG. 4. Effect of L_3 on IFFT envelopes for four subjects. Individual data are shown in separate columns. $F_2=4$ kHz, $L_2=15$ or 25 dB SPL, $L_1=L_2+10$ dB. The suppressor is absent (top row), or present at the level (L_3) indicated. $F_3=15.6$ Hz below $2f_1$-f_2.

there were frequently more than two peaks. This is consistent with the results of Stover *et al.* (1996) who found fewer peaks at 2 and 8 kHz than at intermediate frequencies (3, 4, and 6 kHz). The latency of the earliest peak in the unsuppressed IFFT was longer for an f_2 of 2 kHz, compared to when f_2 was 4 kHz. When averaged across all primary levels, the mean first-peak latency at $f_2=2$ kHz was 4.7 ms (s.d.=0.84 ms, $N=25$), whereas the mean first-peak latency at $f_2=4$ kHz was 2.9 ms (s.d.=0.53 ms, $N=45$). This observation is consistent with the latency of the first peak reflecting the tonotopic representation of f_2. The overall effect of the suppressor at 2 kHz was similar to the observations made

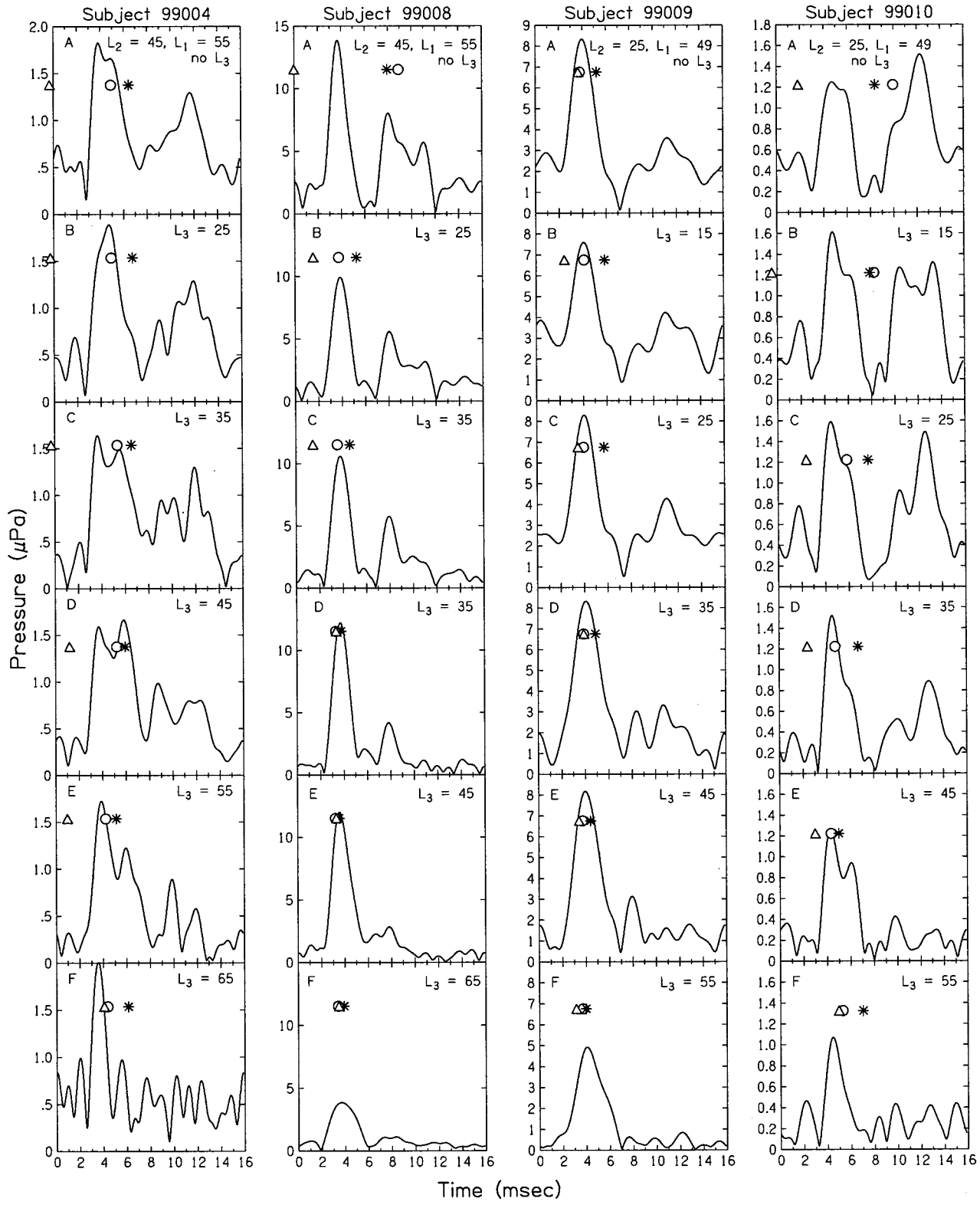

FIG. 5. Same as Fig. 4, but for $f_2=2$ kHz. Because signal-to-noise ratios (SNRs) were sometimes poor for $f_2=2$ kHz, particularly at low primary levels, examples shown here are for a number of L_2, L_1 combinations.

when $f_2=4$ kHz, in that the later peak was reduced more than the early peak.

Estimates of overall group delay are given by the symbols within each panel in Figs. 4 and 5 (following the convention used in Fig. 2, column 3) so that they can be compared to IFFT envelopes. Overall group-delay estimates were similar to the first-peak latency. However, phase-slope estimates (triangles) sometimes underestimated the latency of the earliest peak, and average IFFT latencies (asterisks) sometimes fell between major IFFT envelope peaks (for example, subject 99010 in Fig. 5). Estimates based on average IFFT latencies (asterisks), when compared to other group-

delay estimates, were more ''sensitive'' to the latencies of peaks other than the first peak.

The differential effect of the suppressor on the initial peak and on subsequent IFFT peaks was quantified by calculating the sum of the squared pressure (i.e., the energy) within these two divisions of the IFFT. For the purposes of this analysis, P_E was used to represent energy in the earliest peak and P_L was used to represent the energy in all later peaks. The unsuppressed condition and the condition in which later peaks were maximally suppressed while the initial peak was relatively unaffected were used as references to help determine the latency at which the early peak ended for each IFFT. For a given f_2 and L_2 combination, a dividing point was determined from the average across all subjects. For example, the dividing point was 5.3 ms when f_2 was 4 kHz and L_2 was 25 dB SPL, whereas, the dividing point was 7.6 ms when f_2 was 2 kHz and L_2 was 25 dB SPL. P_E and P_L values were normalized to those obtained under conditions in which the suppressor was present, but thought to have no effect ($L_3 = L_2 - 20$ dB). This was thought to be preferential to normalizing to the no-suppressor-condition because, for a given f_2 and L_2 condition, L_3 was varied consecutively. Conditions that did not contain a suppressor were run separately as a function of L_2, and thus were not always obtained during the same recording session.

Figure 6 shows individual and mean data for $f_2 = 2$ kHz, where L_2 was 25 or 45 dB SPL. Normalized P_E and P_L values are given for individual subjects in the top and middle rows, respectively. Mean data (P_E = open triangles; P_L = open circles) ± 1 s.d. are shown in the bottom row. Data below the line intersecting 1.0 on the *Y*-axis represent conditions in which response amplitude was reduced relative to that obtained when $L_3 = L_2 - 20$ dB. When $L_2 = 25$ dB SPL, the suppressor typically had an effect on both components regardless of its level, perhaps because unsuppressed response amplitudes were small. For one subject (99004), the effect of the suppressor on P_E (the earliest peak in the IFFT) was not as pronounced as the effect on P_L (peaks other than the first). This trend usually was observed at higher levels for this f_2 frequency.

Figure 7 follows the same format as was used in Fig. 6, for $f_2 = 4$ kHz. At this f_2, P_L was more susceptible to the suppressive effects of L_3 than was P_E, except at high L_3's where both components were reduced. There were a few individual cases for which the addition of a suppressor appeared to increase the amplitude of one of the DPOAE components, usually P_E. This observation may have been due to test/retest variations in the magnitude and phase of the emission. The suppressor level that eliminated the greatest proportion of P_L with minimal effect on P_E was usually 10–20 dB above L_2.

C. Effect of primary level

The relative amplitudes of early and later peaks in the unsuppressed IFFT envelope depended on absolute primary level and on primary-level ratio. Figure 8 illustrates the effects of stimulus level on the IFFT envelope. Comparing the solid lines (representing $L_1 = L_2 + 10$ dB) in a given column, it can be seen that the major difference among unsuppressed

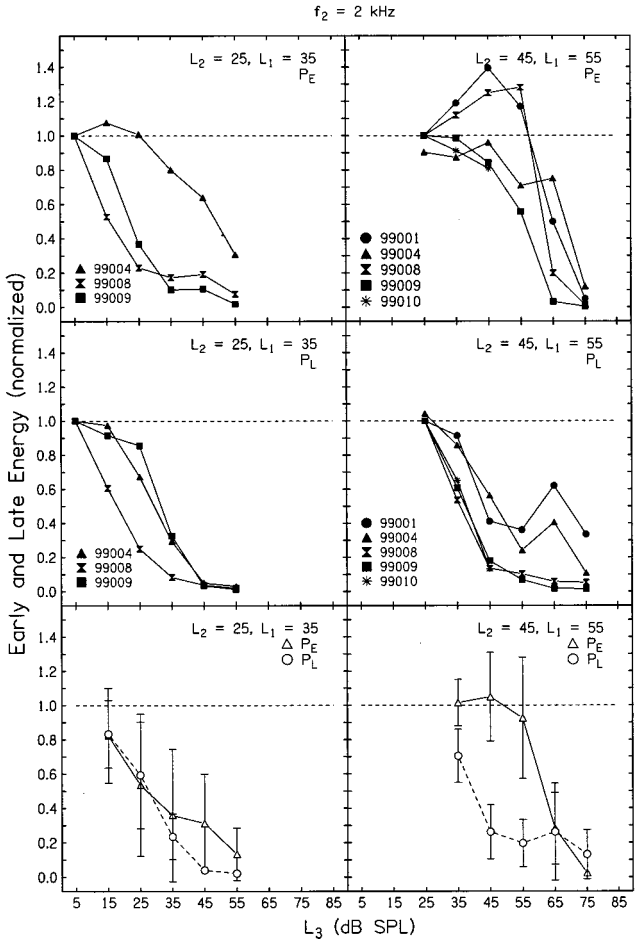

FIG. 6. Effect of L_3 on the earliest peak in the IFFT envelope (P_E) and on later peaks (P_L) shown by normalizing data to the lowest L_3 in a run ($L_3 = L_2 - 20$ dB) consisting of multiple suppressor-level conditions. Data were included if unsuppressed responses were at least 6 dB above the noise, and L_3 levels were able to be measured consecutively. P_E and P_L were calculated by taking the sum of the pressure within each of the two divisions of the IFFT. Prior to calculating these values, a nominal dividing point was established for a given f_2 and L_2 combination. Unsuppressed and maximally suppressed conditions were used as a reference, and the average dividing point was taken across all subjects. Data shown are for $f_2 = 2$ kHz. L_2 was either 25, with $L_1 = 35$ dB SPL (left), or L_2 was 45, with $L_1 = 55$ dB SPL (right). Top row: Normalized individual P_E values. Middle: Normalized individual P_L values. Bottom: Mean normalized P_E (triangles) and P_L (circles) values. Error bars indicate ± 1 standard deviation (s.d.).

IFFTs for three different L_2's was the amplitude of the first peak, which increased with level. By comparison, level-dependent changes in later peaks were smaller, particularly for $f_2 = 4$ kHz. These results are similar to those obtained by Stover *et al.* (1996), who showed that the earliest peak in the IFFT increased without apparent saturation for L_2's up to 65 dB SPL.

Within each of the four upper panels of Fig. 8, responses can be compared for different level ratios. At each L_2, the earliest IFFT envelope peak was larger when acquired using L_1 conditions that optimize DP level (dashed lines), compared to when $L_1 = L_2 + 10$ dB (solid lines). In contrast, the amplitude of later waves did not appear to depend on the relative level of L_1. Increasing L_2 (for either fixed or optimized level ratios) or increasing L_1 (optimizing level ratios for low L_2's) presumably increases the area of overlap be-

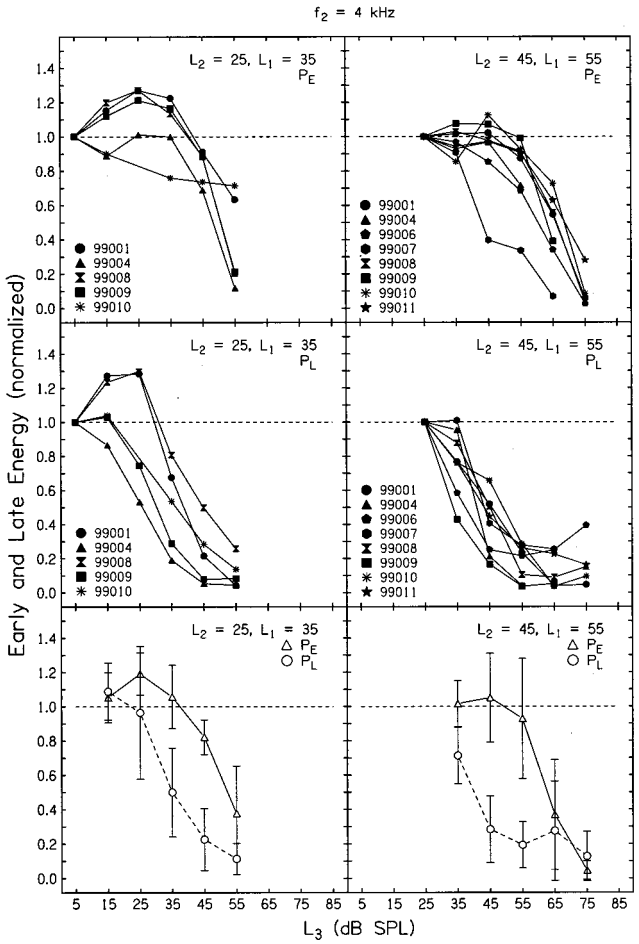

FIG. 7. Same as Fig. 6, except $f_2 = 4$ kHz.

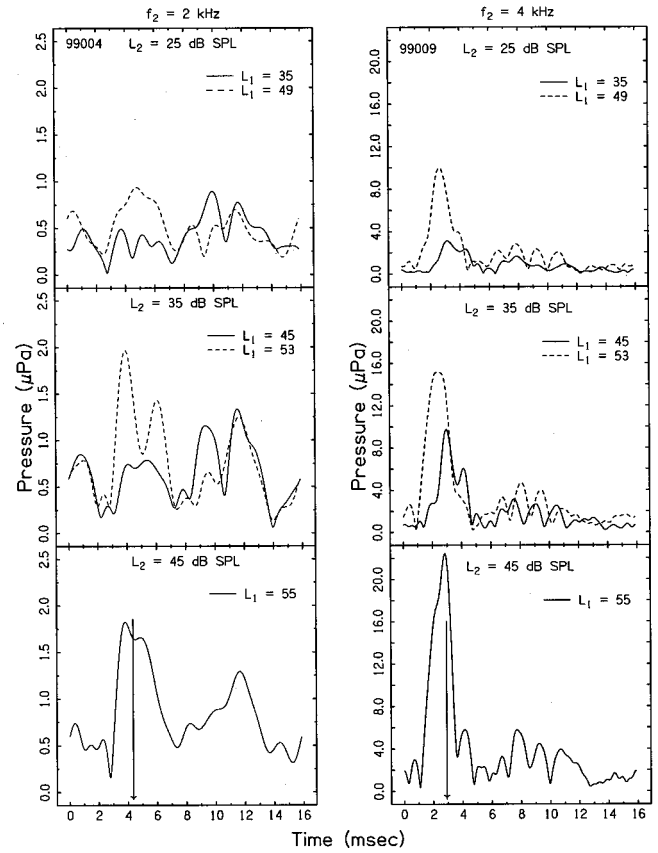

FIG. 8. Effect of primary level on IFFT envelopes for $f_2 = 2$ kHz (left) and $f_2 = 4$ kHz (right). Data from a single subject is shown for each frequency. L_2 increases with decreasing row. Solid lines represent data where $L_1 = L_2 + 10$ dB. Dashed lines represent data where L_1 was chosen in order to optimize DPOAE level. Only the $L_1 = L_2 + 10$ dB condition is shown for the case where $L_2 = 45$ dB SPL (solid line, bottom row), because the optimal and fixed primary level ratio conditions are nearly equivalent. Arrows indicate the latency of the first major peak for $L_2 = 45$ dB SPL.

tween the primary-driven excitation patterns, and results in more distortion being generated (implied by the increase in the first IFFT peak). A larger input to the SFOAE generator at the DP place (also implied by the increase in the first IFFT peak) did not alter its output as much, perhaps because the SFOAE component saturates at a relatively low level.

At 4 kHz, increases in the amplitude of the earliest peak were accompanied by slight decreases in its latency, consistent with increased displacement at the place of maximal overlap between the primaries. It is known from studies of the basilar membrane mechanical response that increases in the stimulus level produce a basal shift in the characteristic place, reduce the phase accumulation near the characteristic place, and decrease frequency tuning (e.g., Johnstone *et al.*, 1986; Ruggero *et al.*, 1997). Each of these mechanisms could translate into shorter OAE latencies. In contrast to the earliest peak, the latency of later peaks did not appear to shift as a function of primary level (within the resolution of these measures). This observation may be related to the different generating mechanisms of the first and subsequent peaks.

Figure 9 presents group data showing the effect of primary level on the energy in the early peak (P_E) and in the later peaks (P_L) of the IFFT envelope. As opposed to Figs. 6 and 7, data in Fig. 9 are given in absolute energy terms (in dB SPL).[2] With the exception of conditions when f_2 was 2 kHz and $L_1 = L_2 + 10$ dB (the upper left panel), mean P_E values (triangles) were larger than mean P_L values (circles). Both P_E and P_L values increased as a function of L_2. However, when L_1 was set to $L_2 + 10$ dB (top row), P_E increased more than P_L as a function of increasing L_2. Comparing values across rows, P_E was larger when L_1 was presented at an optimal level rather than at a level 10 dB above L_2. These results suggest that intermodulation distortion dominated DPOAE responses obtained using moderate-level primaries, or low L_2's presented together with a relatively high L_1. Comparing across columns in Fig. 9, mean P_E values were lower when f_2 was 2 kHz compared to conditions when f_2 was 4 kHz, and the reverse was true for mean P_L values. However, due to the overlapping distributions in these data, additional data are needed in order to determine whether a frequency effect exists.

D. Group delay

For conditions where $L_1 = L_2 + 10$ dB, the ratio of P_E to P_L tended to increase as a function of increasing L_2, and f_2. Based on a similar observation, Stover *et al.* (1996) hypothesized that level-dependent changes in the phase-slope group delay could be related to changes in the component that dominates the DPOAE as measured in the ear canal. In order to test this hypothesis, group delay in the absence of a sup-

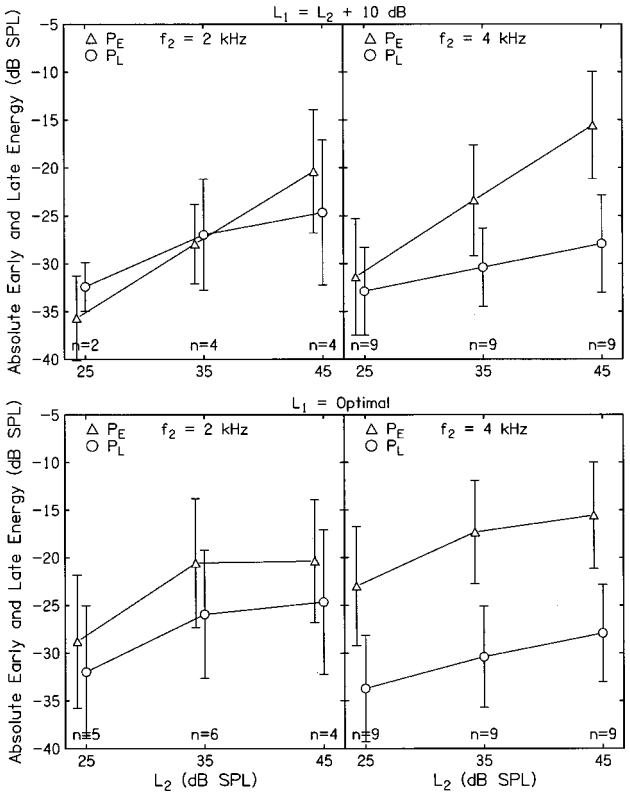

FIG. 9. Effect of primary level on the average pressure within the first peak (P_E) and subsequent peak (P_L) regions given in dB SPL. P_E values are indicated by triangles, and P_L values by circles. Mean data (± 1 s.d.) are shown as a function of L_2 for $f_2 = 2$ kHz (left) and $f_2 = 4$ kHz (right). Top row: $L_1 = L_2 + 10$ dB. Bottom row: L_1 chosen in order to optimize DPOAE level. The L_1 is similar for $L_2 = 45$ dB SPL whether L_1 is optimized or 10 dB greater than L_2. Therefore, for $L_2 = 45$, only $L_1 = L_2 + 10$ dB was used. These data are plotted in both rows. Sample size (N) is indicated in the figure for each stimulus condition.

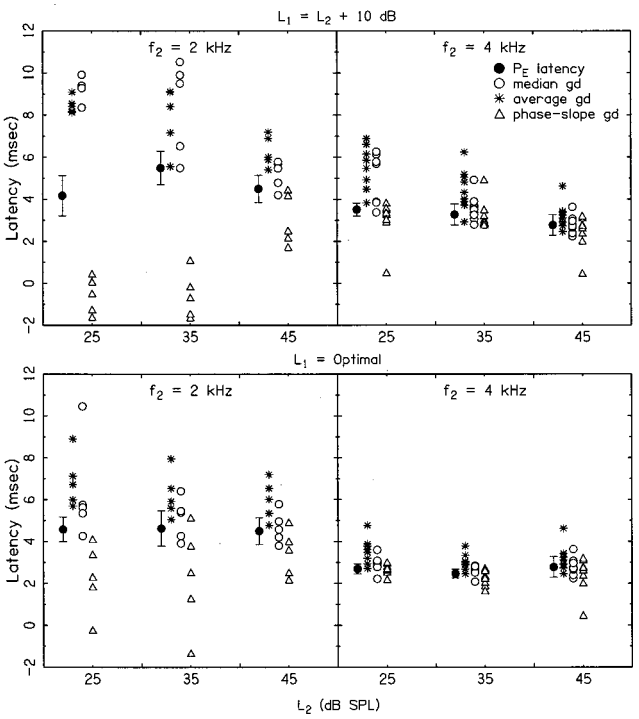

FIG. 10. Comparison of overall group delay and the latency of the earliest envelope peak as a function of L_2 for $f_2 = 2$ kHz (left) and $f_2 = 4$ kHz (right). Top row: $L_1 = L_2 + 10$ dB. Bottom row: L_1 chosen in order to optimize DPOAE level. Individual group delay data are given; triangles = phase-slope, open circles = median IFFT latency, asterisks = average IFFT latency. For ease in comparing the three group delay estimates to the latency of the first IFFT envelope peak, mean first peak latency is given (filled circles). Error bars are s.d.

pressor was compared with the latency of the earliest peak in the IFFT envelope, which was determined by eye for each unsuppressed envelope. The latency of the earliest peak is taken as the delay associated with the primary DP generator, whereas overall group delay may be influenced by secondary sources.

Figure 10 presents individual estimates of group delay in the absence of a suppressor. Overall group delay was estimated in three ways: phase-slope (triangles), median IFFT latency (open circles), and average IFFT latency (asterisks). For ease in comparing the three group-delay estimates to the latency of the earliest peak in the IFFT envelope, mean ''first-peak'' latency (± 1 s.d.) is shown as filled circles. Latency is plotted as a function of L_2, when $L_1 = L_2 + 10$ dB (top), and when L_1 was presented at an optimal level (bottom), as described previously.

Phase-slope group delays sometimes underestimated the latency of the earliest IFFT peak. This occurred most when f_2 was 2 kHz and L_2 was 25 or 35 dB SPL; in fact negative phase-slope group delays were sometimes observed. This reflects the fact that responses were close to the noise floor, causing level and phase estimates to be less reliable and, therefore, causing estimates of latency to be less reliable. It may be the case that when the response lies near the noise floor, selecting for inclusion only those points surrounding the amplitude peak (where more favorable SNRs are observed) would have provided a more reliable phase-slope estimate than the energy-weighted procedure used here.

When L_2 was 45 dB SPL, or when L_1 was presented at an ''optimal'' level, the three estimates of overall group delay tended to be similar to the first-peak latency, even in the presence of secondary source activity. However, for conditions in which L_1 was set to $L_2 + 10$ dB, there was a tendency for median (open circles) and average (asterisks) IFFT latencies to decrease with increasing L_2. Compared to these measures of overall group delay, the latency of the first IFFT peak was relatively constant with level. These results suggest that as stimulus level increases, the relative contribution from the DP place decreases and response latency, however estimated, is dominated by the source near the f_2 place. Therefore, level-dependent changes in secondary source activity may account for the commonly reported level-dependent changes in DPOAE group delay.

There is a relationship between place of generation and OAE delay, which was demonstrated in early transient OAE studies and has been taken as evidence for cochlear generation of the response (e.g., Kemp, 1978; Neely *et al.*, 1988). In the present study, group delay (and first-peak latency) in the absence of a suppressor was shorter at 4 kHz compared to 2 kHz. Tubis *et al.* [2000, Eq.(53)] recently proposed that the latency associated with the distortion component from fixed-f_2 data could be estimated as follows:

$$\tau_{\text{fixed}-f2}=\frac{k_o}{k_\omega}\left[\frac{1}{\sqrt{\omega_2^2-\omega_1^2}}+\frac{1}{\sqrt{\omega_2^2-\omega_{dp}^2}}\right]=\left(\frac{11.25}{f_2}\right), \quad (1)$$

where $k_o=31$ cm^{-1}, $k_\omega=1.382$ cm^{-1} (from Talmadge *et al.*, 1998, Table I), $f_1=1.2f_2$, and f_2 is in kHz. The theory is confirmed to within the accuracy of the experimental measures presented here. The mean first-peak latency obtained experimentally for $f_2=2$ kHz was 4.7 ms, whereas the predicted latency [Eq. (1)] was 5.6 ms, or 20% longer. The mean first-peak latency for conditions when $f_2=4$ kHz was 2.9 ms, whereas the predicted latency was 2.8 ms, or 3% shorter. Possible reasons for the discrepancy between measured and predicted values include a small term that was dropped by Tubis and colleagues [see Eq. (50) in Tubis *et al.*, 2000]. However, the amount that this would shorten the predicted latencies (0.25 ms) is thought to be small relative to uncertainty in the value of k_ω.

A feature of Eq. (1) is that $\tau_{\text{fixed-}f2}$ depends on f_1. This dependence appears to be demonstrated in the data presented here as a spread of energy associated with the various latency components of the IFFT envelope. (Broadening of peaks in the IFFT envelope was not thought to be due to aliasing artifacts because, as discussed earlier, most DPOAE filter functions began and ended in the noise floor.)

Latencies of the earliest IFFT peak also were similar to estimates of phase-slope group delays (5.4 ms for $f_2=2$ kHz, 3.4 ms for $f_2=4$ kHz) reported by others (Moulin and Kemp, 1996). These data were obtained using a fixed-f_2 paradigm, with a slightly higher stimulus level ($L_2=60$ and $L_1=65$ dB SPL) compared to that used here. Group delays, and latencies of the earliest peak in the IFFT in the present study, are shorter than round-trip travel times of tone burst-evoked OAEs estimated using onset latencies (Neely *et al.*, 1988; Brass and Kemp, 1991). Latency estimates described by Neely *et al.* (1988) for 2-kHz tone bursts presented at 25, 35, and 45 dB SPL were 13.0, 11.0, and 9.4 ms, respectively; estimates for 4-kHz tone bursts at corresponding levels were 9.7, 8.3, and 7.1 ms.

IV. DISCUSSION

A. Summary

For low-to-moderate stimulus levels, it was possible to resolve at least two main components in the time-domain representation of filter functions. A suppressor placed just below the $2f_1$-f_2 frequency reduced or eliminated later components in the time envelope, leaving the component with the shortest latency relatively unaffected. These results suggest that the components removed by the suppressor were due to secondary DPOAE source activity arising near the DP place. Introducing a suppressor-tone also reduced microstructure in DPOAE level and phase responses. This occurred mainly for low L_2's presented with $L_1=L_2+10$ dB. Results are consistent with the view that the DPOAE measured in the ear canal of humans includes components from the f_2 place (primary generation site) and from the DP place (in the form of a SFOAE), and that the relative contributions to ear-canal DPOAEs depend on overall and relative primary levels. These findings build on a previous study (Stover *et al.*, 1996) by providing evidence that multiple peaks in the IFFT are due to a secondary source at the DP place.

B. Origin of multiple peaks in the IFFT

Stover *et al.* (1996) proposed several hypotheses to account for multiple peaks in the time-domain representation of DPOAE filter functions. One hypothesis was that multiple IFFT peaks represent several reflections from a single source (for example, near f_2) as opposed to two sources. Data presented here are not consistent with that hypothesis. The effects of a suppressor-tone placed near the DP frequency were larger on later peaks compared to the earliest peak (see Figs. 2–7). Further, the relative contribution of later waves to the total response was largest at relatively low primary levels, consistent with previous data (Stover *et al.*, 1996). At low levels, later peaks were occasionally larger than the first peak, also suggesting that the first and subsequent IFFT peaks do not arise as multiple reflections from a single source.

A second hypothesis proposed by Stover *et al.* was that multiple peaks in the IFFT arise from a series of different distortion-generating places along the cochlea (i.e., each peak indicates a different place of generation). The effect of the suppressor on the multi-peaked IFFT at $f_2=4$ kHz is difficult to explain in the context of multiple DPOAE source locations. Specifically, all later peaks were suppressed by the suppressor tone, which was close to the frequency of the $2f_1$-f_2 DP. This observation, on the other hand, is consistent with a locus of generation for all later peaks at the DP place.

A third hypothesis proposed by Stover *et al.* was that two sources generate the first two major IFFT envelope peaks, and later peaks are higher order reflections arising through the same mechanism as the second zeroth-order component. The presence and number of higher order reflections would depend on the duration of the time window and the amount of reflectance at the oval window and DP place. Still, the fact that all components after the first peak were suppressed by f_3 is consistent with the view that all peaks after the initial peak were generated at the DP place. The different growth rates of phase-invariant and rapidly varying components, evident in the fixed-f_2 paradigm, are consistent with the hypothesis that more than one source contributes to the DPOAE. Peaks corresponding to these two components are expected to exhibit different rates of growth with increasing stimulus level, since SFOAEs appear to grow at a slower rate compared to DPOAEs (Kemp and Chum, 1980; Kummer *et al.*, 1998). The strongest argument linking specific envelope peaks to one of two sources is the finding that adding a suppressor near $2f_1$-f_2 diminished the later peaks (presumably, the second direct reflection and all higher order reflections) and, depending on its level, left the earliest peak (presumably the distortion component) relatively unaffected.

C. Proposed physical interpretation of the IFFT analysis of fixed-f_2 data

For this experiment, a ''spectrum'' was constructed by combining separate $2f_1$-f_2 DPOAE measurements for a range of f_1 frequencies when f_2 was fixed. A time envelope

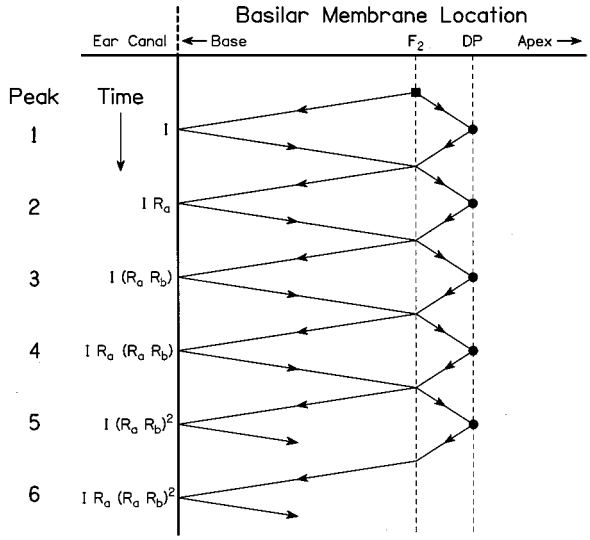

FIG. 11. Space-time diagram of the propagation of the DPOAE components produced at the f_2 place in the cochlea towards the base and apex, and subsequent multiple reflections from the basal footplate and DP place. These predicted trajectories, implicit from a two-source DPOAE model, are plotted as a function of distance along the cochlea (horizontal axis) and as a function of time (vertical axis). The filled square represents the generator site for intermodulation distortion (near the f_2 place). The filled circle represents the SFOAE generation site (at the DP place).

was derived from this spectrum using IFFT techniques. This envelope may be interpreted as an impulse response, in which DPOAE components are separated by their latencies. To gain insight into the nature of multiple-latency components within the IFFT envelope, it is helpful to consider the propagation of transient signals. A transient DPOAE experiment would consist of using the same f_2 as in the swept-f_1 experiment above, but substituting the swept-f_1 tone with a band-limited transient signal containing the same range of f_1 frequencies. Each frequency component in the transient signal would generate intermodulation distortion in the vicinity of the f_2 place, which would be recorded as a transient envelope in the ear canal. For the idealized case of an impulse with equal spectral density in the ear canal, this transient response envelope would be a complement to the IFFT envelope in the fixed-f_2 experiment, as has been noted by Piskorski (1997).

The intermodulation response in the transient DPOAE experiment can be analyzed in terms of multiple internal reflections within the cochlea, drawing from a class of cochlear models that incorporates roughness or discontinuities along the basilar membrane (e.g., Shera and Zweig, 1992; Talmadge *et al.*, 1998). DPOAE generation in these models involves the two sources/mechanisms proposed by others (e.g., Kemp and Brown, 1983; Shera and Zweig, 1992; Shera and Guinan, 1998). Figure 11 is a space-time diagram showing the predicted propagation of DPOAE components within the cochlea, which is implicit in a two-source DPOAE model.

The horizontal axis in Fig. 11 is the spatial location on the basilar membrane from base to apex, so that the left-hand edge represents the pressure signals measured in the ear canal (the effect of the middle ear, ear canal and probe are not represented in this figure). Relative to the normalized latency and amplitude of the initial pulse, the total microphone signal is

$$(1+R_a)[1+R_aR_b+(R_aR_b)^2+\cdots]=\frac{1+R_a}{1-R_aR_b} \qquad (2)$$

in which the right-hand side gives the spectral representation in the frequency domain after applying the geometric series (Shera and Zweig, 1992; Talmadge *et al.*, 1998), under the simplifying assumption that the nonlinearity in these reflectances can be neglected. The vertical axis in Fig. 11 denotes time, which increases with distance down the axis.

Because f_2 is on continuously, the source of the intermodulation component is in the vicinity of the f_2 location in the cochlea (filled square). The transient is assumed to be compact in time at this position, and the trajectories shown in Fig. 11 stem from this point. A pair of distortion transients propagates basally and apically away from the f_2 location. The basally propagating transient reaches the cochlear base (left edge of figure) travels through the middle ear and into the ear canal where it is recorded by the microphone. In the model, this initial distortion transient has a complex amplitude, I.

The apically propagating transient is reflected as a SFOAE from its tonotopic place (filled circle), and propagates basally, arriving at the microphone at a later time than the first component. R_a represents the apical trajectory from the f_2 place to the DP place and the basal trajectory from the DP place back to the f_2 place. The complex amplitude of this component is represented as $I\ R_a$. Note that in the absence of apical reflection ($R_a=0$), the above formula reduces to 1, representing an emitted transient with only a single pulse. This would be the case if all of the DPOAE energy measured in the ear canal came only from the f_2 place. R_b represents the reflectance (of the intermodulation component) that propagates from the f_2 place to the basal end of the cochlea, is reflected, and propagates back to the f_2 place. If no basal reflection is present ($R_b=0$), the emitted transient from this two-source model should have a pair of pulses (I and $I\ R_a$) with slightly different amplitudes and latencies. This would be the case if all of the energy from the intermodulation component (from the f_2 place) and the reflection component (from the DP place) were transmitted into the middle ear (i.e., no energy is reflected off of the stapes footplate back into the cochlea). If basal reflection is present, the transient envelope should have additional pairs of pulses at regular time intervals. This time interval should be approximately equal to the round-trip latency to the reflection source at the place associated with the DP frequency.

In the representation in Fig. 11, the initial pulse pair (I and $I\ R_a$) is partially transmitted through the middle ear and into the ear canal, and is partially reflected at the stapes footplate back into the cochlea, where it triggers a set of SFOAEs at the DP place, and the cycle is repeated. Each round trip associated with propagation from the cochlear base to the DP place changes the amplitude of the pulse by a factor R_aR_b, and the time variation encodes the round-trip latency. Thus, the complex value $I\ (R_aR_b)$ represents the propagation delays inherent in distortion generation near f_2

and SFOAE generation at the DP site, reflection characteristics at the SFOAE site and basal end of the cochlea, and concomitant changes in amplitude.

Information about traveling-wave phase accumulation as a function of basilar membrane place can be inferred from the neural population study of Kim *et al.* (1979). They measured the amplitude and phase of the synchronized neural response to a 1.6-kHz tone. Measurements in each experimental animal were made in many auditory nerve fibers representing a wide range of fiber characteristic frequencies (CFs) and, therefore, characteristic places. The phase delay of fibers with CFs one-half octave above the stimulating tone was approximately half that of fibers whose CF was equal to the stimulus frequency (Fig. 6 in Kim *et al.*, 1979). Trajectories shown in Fig. 11 are drawn to reflect the hypothesis that the phase accumulation of the apically traveling distortion component as it travels to the f_2 characteristic place is comparable to the apical journey from the f_2 place to the DP place. Stated differently, the time it takes for the traveling wave to come within one-half octave of the characteristic place is similar to the travel time for the remaining one-half octave.

Applying predictions from the two-source model depicted in Fig. 11 to the present data, the earliest IFFT peak provides an estimate of the latency associated with the distortion component coming directly out from the f_2 place. In addition, the interval between the first and third IFFT peaks should provide an estimate of the round-trip latency to the DP place [the time delay of I (R_aR_b) relative to I in the model]. Assuming that the basilar membrane travel time to the f_2 place is about half the travel time to the DP place, the second IFFT peak (I R_a) should occur half way between the first and third peaks.

The following equation describes round-trip travel time (in ms) to the DP reflection site based on Shera and Guinan's SFOAE phase-slope data, which was obtained in human ears (Shera and Guinan, 1999b, 2000):

$$\tau_{\mathrm{SFOAE}}=\frac{9}{\sqrt{f}}, \tag{3}$$

where f is DP frequency in kHz. For an f_2 of 2 kHz and a fixed-f_2 paradigm, the average DP frequency (the approximate peak of the DP filter function) equals 1.3 kHz. For an f_2 of 4 kHz, the average DP frequency in the same paradigm is 2.7 kHz. Using Eq. (3), the predicted round trip travel time to the DP place is 7.8 ms for a DP at 1.3 kHz ($f_2=2$ kHz) and 5.5 ms for a DP at 2.7 kHz ($f_2=4$ kHz). As anticipated from a two-source model, the predicted round-trip travel time corresponds to the interval between first and third IFFT peaks in Fig. 4 for $f_2=4$ kHz (mean=5.4 ms; range=4.7 to 5.8 ms), and the second peak (with the exception of one subject) falls roughly between the first and third peaks. It is important to note, however, that there is some circular reasoning in this comparison. For example, the second largest peak following the initial peak for subject 99009 (see Fig. 4) was viewed as peak 3 because its latency was consistent with model predictions. This problem highlights the difficulty associated with separating the multiple sources that may contribute to ear-canal DPOAEs in the unsuppressed condition.

It is also difficult to compare model predictions to IFFT data at 2 kHz without invoking circular arguments in order to label specific peaks in the IFFT. The predicted round-trip travel time corresponds to the interval between first and third IFFT peaks in Fig. 5 for $f_2=2$ kHz only if one interprets the second major peak in the IFFT response to be a combination of the second and third peaks (for example, see column 2, Fig. 5). In this case, the 2-kHz data would be interpreted as containing three components, including the first pulse pair and the first pulse of the second pulse pair.

Whatever the specific origin of IFFT peaks after the initial peak, their vulnerability to a suppressor near the DP frequency provides evidence that they are initiated near the DP place. The fact that there are late-component peaks in the IFFT envelope distributed over the entire time window is consistent with the existence of multiple internal reflections within the cochlea.

D. Relative IFFT peak magnitudes change with level and frequency

Increasing L_2 (for either fixed or optimized level ratios) or increasing L_1 (optimizing level ratios for low L_2's) presumably increases the displacement near the distortion generator region (near the point of maximal overlap between the primaries). As absolute or relative primary levels increased, the response became dominated by the earliest peak in the IFFT. In terms of later peaks in the IFFT envelope, these components represented a larger proportion of the DP measured in the ear canal for low primary levels, primarily when $L_1=L_2+10$ dB. One interpretation of these data is that increasing intermodulation near f_2 dominates the (perhaps already saturated) contribution by the DP place. Using an L_1 chosen to optimize DP level also increased the magnitude of the dip in the filter function corresponding to closely spaced primary frequencies, perhaps representing increased suppression of L_2 by L_1 for small f_2/f_1 ratios.

Energy contained in the first peak of the IFFT tended to be less for $f_2=2$ kHz than $f_2=4$ kHz (Fig. 9) at a given primary level, whereas the reverse was true for other envelope peaks. One interpretation of these findings is that the secondary DPOAE sources contributed more to responses elicited by $f_2=2$ kHz, compared to when $f_2=4$ kHz. This interpretation should be viewed cautiously, however, because response distributions across groups tended to overlap.

E. Group delay

Interpreting group delay is not straightforward because of the existence of multiple components arising at more than one place and/or through different modes of generation (cf. Tubis *et al.*, 2000). These interactions may explain why DPOAE group delays show a high degree of variability within and across studies. A consistent finding across many studies is that group delay decreases with increasing stimulus frequency and level (e.g., Kemp and Brown, 1983; Brown *et al.*, 1996; Kimberley *et al.*, 1993; O'Mahoney and Kemp, 1995; Moulin and Kemp, 1996). It was previously hypothesized that OAE group delay was dependent on traveling-

wave velocity (Neely *et al.*, 1988), or auditory-filter ''build-up time'' (Kimberley *et al.*, 1993), both of which might be expected to change as a function of frequency tuning at the OAE generation site. While these hypotheses may account for level-dependent changes in phase-slope estimates of SFOAE or transient-evoked OAE latency, the same mechanisms may not be reflected in estimates of DPOAE response delay. Studies have failed to demonstrate a systematic change in DPOAE group delay in subjects with transient (Engdahl and Kemp, 1996; Brown *et al.*, 1993) or permanent (Prijs and Schoonhoven, 1997) outer hair cell dysfunction. Further, it has been shown that DPOAE group delay obtained using a fixed-f_2 paradigm tends to be shorter than for a fixed-f_1 paradigm, for equivalent DP frequencies (e.g., O'Mahoney and Kemp, 1995; Moulin and Kemp, 1996). It was proposed that the fixed-f_2 paradigm ''reads'' the phase of f_2 at the place where the peak of the traveling wave produced by f_1 achieves maximum overlap with the traveling wave from f_2. Thus, for the fixed-f_2, the place of maximal overlap will correspond more closely to the f_2 peak for some f_2/f_1 ratios compared to others. In contrast to the fixed-f_2 paradigm, a fixed-f_1(f_2 sweep) paradigm will ''read'' the phase of f_2 near its peak, where the phase of the traveling wave builds up rapidly (e.g., Robles *et al.*, 1986; Zweig, 1991). Therefore, any level-dependent change in filter build-up time near the f_2 site might not be detectable using a fixed-f_2 paradigm. Alternatively, recent analyses (Tubis *et al.*, 2000; Shera *et al.*, 2000) indicate that the ratio of the latencies derived from fixed-f_2 and fixed-f_1 paradigms are mathematically predictable without taking into account cochlear mechanisms such as filter build-up times.

In the present study, DPOAE group delay tended to be level dependent for conditions in which $L_1 = L_2 + 10$ dB. However, the latency of the earliest IFFT peak changed only slightly with level, and these changes were small relative to within-group variability for a particular primary level. As a result, group delays were similar to the latency of the first peak in the IFFT at moderate stimulus levels, but increased relative to the latency of the first peak as stimulus level decreased. Thus, data presented here are consistent with the hypothesis that level-dependent changes in secondary source activity contribute to the commonly reported level-dependent changes in DPOAE group delay (Stover *et al.*, 1996).

V. CONCLUSION

It was found that multiple components of the $2f_1$-f_2 DPOAE could be separated by their individual latencies using a fixed-f_2 paradigm, and could be parsed by mode of generation (intermodulation distortion or reflection in the form of a SFOAE) using a suppressor tone placed near the DP frequency. These data support the existence of, and interplay between, two $2f_1$-f_2 DPOAE sources (one near the f_2 place and one at the DP place), and suggest that the relative contributions from these two sources change as a function of level and perhaps frequency. In particular, reflections at the DP place affect DPOAE latency and (to the extent that they are responsible for DPOAE fine structure) DPOAE level, at least for low-to-moderate primary levels when $f_2 = 2$ kHz and for low primary levels when $f_2 = 4$ kHz. It is possible that some of the variability in clinical DPOAE measurements could be reduced by reducing secondary-source activity (e.g., Heitmann *et al.*, 1998). For example, eliminating secondary-source activity reduced fine structure in the DPOAE signal (refer to Figs. 2 and 3). It may be important to note, however, that the relative contribution from the DP place decreased as primary level increased towards levels typically used under clinical conditions. Thus, one would anticipate less influence from the DP reflection source under the stimulus conditions in which DPOAEs are measured clinically.

ACKNOWLEDGMENTS

This work was supported by the NIH (Grant Nos. RO1 DC 02251 and T32 DC00013). The authors wish to thank Chris Neely for computer programming assistance, Beth O'Conner for help with preparation of the figures, and two anonymous reviewers for helpful comments on this manuscript.

[1]Interaction between two sources may contribute to the DPOAE filter-function shape (Stover *et al.*, 1996). However, the finding that filter functions corresponding to time-edited (distortion) data retained a band-pass shape suggests that two-source interaction does not completely account for this feature of the response (Dreisbach, 1999; Knight and Kemp, 2000).

[2]The apparent discrepancy between the dB SPL values in Fig. 9 and the measured DPOAE levels (for example, See Fig. 2, DP level) is due to taking an average across frequency when computing the IFFT envelope. An alternative definition of the IFFT envelope without this average would add 30 dB to the values shown in Fig. 9. In either case, the dB difference between P_E and P_L would not change.

ANSI 53.6-1996 (**1996**). Specifications for audiometers (American Institute of Physics, Woodbury, NY).

Brass, D., and Kemp, D. T. (**1991**). ''Time-domain observation of otoacoustic emissions during constant tone stimulation,'' J. Acoust. Soc. Am. **90**, 2415–2427.

Brown, A. M., and Gaskill, S. A. (**1990**). ''Measurement of acoustic distortion reveals underlying similarities between human and rodent mechanical responses,'' J. Acoust. Soc. Am. **88**, 840–849.

Brown, A. M., and Kemp, D. T. (**1984**). ''Suppressibility of the 2f1-f2 stimulated acoustic emissions in gerbil and man,'' Hear. Res. **13**, 29–37.

Brown, A. M., Gaskill, S. A., and Williams, D. M. (**1992**). ''Mechanical filtering of sound in the inner ear,'' Proc. R. Soc. London **250**, 29–34.

Brown, A. M., Harris, F. P., and Beveridge, H. A. (**1996**). ''Two sources of acoustic distortion products from the human cochlea,'' J. Acoust. Soc. Am. **100**, 3260–3267.

Brown, A. M., Williams, D. M., and Gaskill, S. A. (**1993**). ''The effect of aspirin on cochlear mechanical tuning,'' J. Acoust. Soc. Am. **93**, 3298–3307.

Cianfron, G, Atissimi, M., Cervellini, A., Musacchio, A., and Turchetta, R., (**1994**). ''Suppression tuning characteristics of $2f_1-f_2$ distortion product otoacoustic emissions,'' Br. J. Audiol. **28**, 205–212.

Dreisbach, L. E. (**1999**). ''Characterizing the $2f_1$-f_2 distortion-product otoacoustic emission and its generators measured from 2 to 20 kHz in humans,'' Ph.D. thesis, Northwestern University.

Dreisbach, L. E., and Siegel, J. H. (**1999**). ''Level and phase relationships of distortion-product otoacoustic emission sources with varied primary frequency ratios in humans,'' Midwinter Meeting of the Association for Research in Otolaryngology, Abstr. 392, p. 98.

Engdahl, B., and Kemp, D. T. (**1996**). ''The effect of noise exposure on the details of distortion product otoacoustic emissions in humans,'' J. Acoust. Soc. Am. **99**, 1573–1587.

Fahey, P. F., and Allen, J. B. (**1997**). ''Measurement of distortion product phase in the ear canal of the cat,'' J. Acoust. Soc. Am. **102**, 2880–2891.

Furst, M., Rabinowitz, W. M., and Zurek, P. M. (**1988**). ''Ear canal acoustic distortion at 2f1-f2 from human ears: Relation to other emissions and perceived combination tones,'' J. Acoust. Soc. Am. **84**, 215–221.

Gaskill, S. A., and Brown, A. M. (**1990**). ''The behavior of the acoustic distortion product, 2*f*1-*f*2, from the human ear and its relation to auditory sensitivity,'' J. Acoust. Soc. Am. **88**, 821–837.

Gaskill, S. A., and Brown, A. M. (**1996**). ''Suppression of human acoustic distortion product: dual origin of 2*f*1-*f*2,'' J. Acoust. Soc. Am. **100**, 3268–3274.

Goldstein, J. L., and Kiang, N-Y. S. (**1967**). ''Neural correlates of the aural combination tone 2*f*1-*f*2,'' Proc. IEEE, 1968; **56**, 981–992.

Gorga, M. P., Neely, S. T., Bergman, B. M., Beauchaine, K. L., Kaminski, J. R., and Liu, Z. (**1994**). ''Toward understanding the limits of distortion product otoacoustic emission measurements,'' J. Acoust. Soc. Am. **96**, 1494–1500.

Harris, F. P., Probst, R., and Xu, L. (**1992**). ''Suppression of the 2*f*1-*f*2 otoacoustic emission in humans,'' Hear. Res. **64**, 133–141.

Harris, F. P., Lonsbury-Martin, B. L., Stagner, B. B., Coats, A. C., and Martin, G. K. (**1989**). ''Acoustic distortion products in humans: Systematic changes in amplitude as a function of *f*2/*f*1 ratio,'' J. Acoust. Soc. Am. **85**, 220–229.

Heitmann, H. J., Waldmann, B., Schnitzler, H. U., Plinkert, P. K., and Zenner, H.-P. (**1998**). ''Suppression of distortion product otoacoustic emissions (DPOAE) near 2*f*(1)-*f*(2) removes dp-gram fine structure—evidence for a secondary generator,'' J. Acoust. Soc. Am. **103**, 1527–1531.

Janssen, T., Kummer, P., and Arnold, W. (**1998**). ''Growth behavior of the 2*f*1-*f*2 distortion product otoacoustic emission in tinnitus,'' J. Acoust. Soc. Am. **103**, 3418–3430.

Johnstone, B. M., Patuzzi, R., and Yates, G. K. (**1986**). ''Basilar membrane measurements and the traveling wave,'' Hear. Res. **22**, 147–153.

Kalluri, R., and Shera, C. A. (**2000**). ''Are DPOAEs a mixture of emissions generated by different mechanisms?'' Midwinter Meeting of the Association for Research in Otolaryngology, Abstr. 23, p. 480.

Kalluri, R., and Shera, C. A. (**2001**). ''Distortion-product source unmixing: A test of the two-mechanism model for DPOAE generation,'' J. Acoust. Soc. Am. **109**, 622–637.

Kemp, D. T. (**1978**). ''Stimulated acoustic emissions from the human auditory system,'' J. Acoust. Soc. Am. **64**, 1386–1391.

Kemp, D. T. (**1986**). ''Otoacoustic emissions, traveling waves and cochlear mechanisms,'' Hear. Res. **22**, 95–104.

Kemp, D. T., and Brown, A. M. (**1983**). ''An integrated view of cochlear mechanical nonlinearities observable from the ear canal,'' in *Cochlear Mechanics*, edited by E. de Boer and M. A. Viergever (Delft U.P., Delft), pp. 75–82.

Kemp, D. T., and Chum, R. A. (**1980**). ''Observations on the generator mechanism of stimulus frequency acoustic emissions-two tone suppression,'' in *Psychophysical, Physiological, and Behavioral Studies in Hearing: Proceedings of the 5th International Symposium on Hearing*, edited by G. Van den Brink and F. A. Bilsen, The Netherlands, pp. 34–42.

Kemp, D. T., and Knight, R. D. (**1999**). ''Virtual DP reflector explains DPOAE wave and place fixed dichotomy,'' Midwinter Meeting of the Association for Research in Otolaryngology, Abstr. 396, p. 99.

Kim, D. O. (**1980**). ''Cochlear mechanics: Implications of electrophysiological and acoustical observations,'' Hear. Res. **2**, 297–317.

Kim, D. O., Siegel, J. H., and C. E. Molnar (**1979**). ''Cochlear nonlinear phenomena in two-tone responses,'' in *Models of The Auditory System and Related Signal Processing Techniques*, edited by M. Hoke and E. de Boer (Scan. Audiol. Suppl.), pp. 63–81.

Kimberley, B. P., Brown, D. K., and Eggermont, J. J. (**1993**). ''Measuring human cochlear traveling wave delay using distortion product emission phase responses,'' J. Acoust. Soc. Am. **94**, 1343–1350.

Knight, R. D., and Kemp, D. T. (**2000**). ''Indications of different distortion product otoacoustic emission mechanisms from a detailed f1, f2 area study,'' J. Acoust. Soc. Am. **107**, 457–473.

Kummer, P., Janssen, T., and Arnold, W. (**1995**). ''Suppression tuning characteristics of the 2f1-f2 distortion-product otoacoustic emission in humans,'' J. Acoust. Soc. Am. **98**, 197–210.

Kummer, P., Janssen, T., and Arnold, W. (**1998**). ''The level and growth behavior of the 2f1-f2 distortion product otoacoustic emission and its relationship to auditory sensitivity in normal hearing and cochlear hearing loss,'' J. Acoust. Soc. Am. **103**, 3431–3434.

Martin, G. K., Jassir, D., Stagner, B. B., Whitehead, M. L., and Lonsbury-Martin, B. (**1998**). ''Locus of generation for the 2*f*1-*f*2 vs 2*f*2-*f*1 distortion-product otoacoustic emissions in normal-hearing humans revealed by suppression tuning, onset latencies, and amplitude correlations,'' J. Acoust. Soc. Am. **103**, 1957–1971.

Martin, G. K., Lonsbury-Martin, B. L., Probst, R., Scheinin, S. A., and Coats, A. C. (**1987**). ''Acoustic distortion products in rabbit ear canal. II. Sites of origin revealed by suppression contours and pure tone exposures,'' Hear. Res. **28**, 191–208.

Mauermann, M., Uppenkamp, S., van Hengel, P. W. J., and Kollimeier, B. (**1999a**). ''Evidence for the distortion product frequency place as a source of distortion product otoacoustic emission (DPOAE) fine structure in humans. I. Fine structure and higher-order DPOAE as a function of the frequency ratio *f*2/*f*1,'' J. Acoust. Soc. Am. **106**, 3473–3483.

Mauermann, M., Uppenkamp, S., van Hengel, P. W. J., and Kollmeier, B. (**1999b**). ''Evidence for the distortion product frequency place as a source of distortion product otoacoustic emission (DPOAE) fine structure in humans. II. Fine structure for different shapes of cochlear hearing loss,'' J. Acoust. Soc. Am. **106**, 3484–3491.

Moulin, A., and Kemp, D. T. (**1996**). ''Multicomponent acoustic distortion product otoacoustic phase in humans. II. Implications for distortion product otoacoustic emissions generation,'' J. Acoust. Soc. Am. **100**, 1640–1662.

Neely, S. T., and Liu, Z. (**1993**). ''EMAV: Otoacoustic emission averager,'' Tech. Memo No. 17 (Boys Town National Research Hospital, Omaha).

Neely, S. T., Norton, S. J., Gorga, M. P., and Jesteadt, W. (**1988**). ''Latency of auditory brain-stem responses and otoacoustic emissions using tone-burst stimuli,'' J. Acoust. Soc. Am. **83**, 652–656.

O'Mahoney, C. F., and Kemp, D. T. (**1995**). ''Distortion product otoacoustic emission delay measurement in human ears,'' J. Acoust. Soc. Am. **97**, 3721–3735.

Papoulis, A. (**1962**). *The Fourier Integral and its Applications* (McGraw–Hill, New York), p. 135.

Piskorski, P. (**1997**). ''The origin of the distortion product otoacoustic emission fine structure,'' Ph.D. thesis, Purdue University.

Prijs, V. F., and Schoonhoven, R. (**1997**). ''Mechanical delays in deteriorated cochleas,'' in *Psychophysical and Physiological Advances in Hearing*, edited by A. R. Palmer, A. Rees, A. Q. Summerfield, and R. Meddis (Whurr, London), pp. 53–58.

Robles, L., Ruggero, M. A., and Rich, N. C. (**1986**). ''Basilar membrane mechanics at the base of the chinchilla cochlea. I. Input-output functions, tuning curves, and response phases,'' J. Acoust. Soc. Am. **80**, 1364–1374.

Ruggero, M. A., Rich, N. C., Recio, A., Naranyan, S. S., and Robles, L. (**1997**). ''Basilar-membrane response to tones at the base of the chinchilla cochlea,'' J. Acoust. Soc. Am. **101**, 2151–2163.

Shera, C. A., and Guinan, J. J. (**1998**). ''Reflection emissions and distortion products arise by fundamentally different mechanisms,'' Midwinter Meeting of the Association for Research in Otolaryngology, Abstr. 21, p. 344.

Shera, C. A., and Guinan, J. J. (**1999a**). ''Evoked otoacoustic emissions arise by two fundamentally different mechanisms: A taxonomy for mammalian OAEs,'' J. Acoust. Soc. Am. **105**, 782–798.

Shera, C. A., and Guinan, J. J. (**1999b**). ''Reflection-emission phase: A test of coherent reflection filtering and a window on cochlear tuning,'' Midwinter Meeting of the Association for Research in Otolaryngology, Abstr. 545, p. 157.

Shera, C. A., and Guinan, J. J. (**2000**). ''Frequency dependence of stimulus-frequency-emission phase: Implications for cochlear mechanics,'' in *Proceedings of the International Symposium on Recent Developments in Auditory Mechanics*, edited by H. Wada, T. Takasaka, K. Ikeda, K. Ohyama, and T. Koike (World Scientific, Singapore), pp. 381–387.

Shera, C. A., and Zweig, G. (**1992**). ''Analyzing reverse middle-ear transmission: Noninvasive *Gedankenexperiments*,'' J. Acoust. Soc. Am. **92**, 1371–1381.

Shera, C. A., and Zweig, G. (**1993**). ''Order from chaos: Resolving the paradox of periodicity in evoked otoacoustic emission,'' in *Biophysics of Hair Cell Sensory Systems*, edited by H. Duifhuis, J. W. Horst, P. van Dijk, and S. M. van Netten (World Scientific, Singapore), pp. 54–63.

Shera, C. A., Talmadge, C. L., and Tubis, A. (**2000**). ''Interrelations among distortion-product phase-gradient delays: Their connection to scaling symmetry and its breaking,'' J. Acoust. Soc. Am. **108**, 2933–2948.

Siegel, J. H., and Dreisbach, L. E. (**1998**). ''Vector decomposition of distortion-product otoacoustic emission sources in humans,'' Midwinter Meeting of the Association for Research in Otolaryngology, Abstr. 347, p. 87.

Stover, L. J., Neely, S. T., and Gorga, M. P. (**1996**). ''Latency and multiple sources of distortion product otoacoustic emissions,'' J. Acoust. Soc. Am. **99**, 1016–1024.

Stover, L. J., Neely, S. T., and Gorga, M. P. (**1999**). ''Cochlear generation

of intermodulation distortion revealed by DPOAE frequency functions in normal and impaired ears,'' J. Acoust. Soc. Am. **106**, 2669–2678.
Talmadge, C., Piskorski, P., and Long, G. R. (**1997**). ''Modeling otoacoustic emission fine structure,'' in *Diversity in Auditory Mechanics*, edited by E. Lewis, G. Long, R. Lyon, P. Narins, and C. Steele (World Scientific, Singapore), pp. 462–471.
Talmadge, C. L., Long, G. R., Tubis, A., and Dhar, S. (**1999**). ''Experimental confirmation of the two-source interference model for the fine structure of distortion product otoacoustic emissions,'' J. Acoust. Soc. Am. **105**, 275–292.
Talmadge, C., Tubis, A., Long, G. R., and Piskorski, P. (**1998**). ''Modeling otoacoustic emission and hearing threshold fine structures in humans,'' J. Acoust. Soc. Am. **104**, 1517–1543.
Tubis, A., Talmadge, C. L., Tong, C., and Dhar, S. (**2000**). ''On the relationships between the fixed-*f*1, fixed-*f*2 and fixed-ratio phase derivatives of the 2*f*1-*f*2 distortion product otoacoustic emission,'' J. Acoust. Soc. Am. **108**, 1772–1785.
Whitehead, M. L., McCoy, M. J., Lonsbury-Martin, B. L., and Martin, G. K. (**1995**). '' Dependence of distortion product otoacoustic emissions on primary levels in normal and impaired ears. I. Effects of decreasing L2 below L1,'' J. Acoust. Soc. Am. **97**, 2346–2358.
Whitehead, M. L., Stagner, B. B., Martin, G. K., and Lonsbury-Martin, B. L. (**1996**). ''Visualization of the onset of distortion-product emissions and measurement of their latency,'' J. Acoust. Soc. Am. **100**, 1663–1679.
Zweig, G. (**1991**). ''Finding the impedance of the organ of Corti,'' J. Acoust. Soc. Am. **89**, 1229–1254.

Duration discrimination and subjective duration for ramped and damped sounds

Robert S. Schlauch, Dennis T. Ries, and Jeffrey J. DiGiovanni
Department of Communication Disorders, University of Minnesota, Minneapolis, Minnesota 55455

(Received 1 September 2000; revised 21 March 2001; accepted 26 March 2001)

The perception of stimuli with ramped envelopes (gradual attack and abrupt decay) and damped envelopes (abrupt attack and gradual decay) was studied in subjective and objective tasks. Magnitude estimation (ME) of perceived duration was measured for broadband noise, 1.0-kHz, and 8.0-kHz tones for durations between 10 and 200 ms. Damped sounds were judged to be shorter than ramped sounds. Matching experiments between sounds with ramped, damped, and rectangular envelopes also showed that damped sounds are perceived to be shorter than ramped sounds, and, additionally, the reason for the effect is a result of the damped sound being judged shorter than a rectangular-gated sound rather than the ramped sound being judged longer than a rectangular-gated sound. These matching studies also demonstrate that the size of the effect is larger for tones (factor of 2.0) than for broadband noise (factor of 1.5). There are two plausible explanations for the finding that damped sounds are judged to be shorter than ramped or rectangular-gated sounds: (1) the abrupt offset at a high level of the ramped sound (or a rectangular-gated sound) results in a persistence of perception (forward masking) that is considered in judgments of the subjective duration; and (2) listeners may ignore a portion of the decay of a damped sound because they consider it an ''echo'' [Stecker and Hafter, J. Acoust. Soc. Am. **107**, 3358–3368 (2000)]. In another experiment, duration discrimination for broadband noise with ramped, damped, and rectangular envelopes was studied as a function of duration (10 to 100 ms) to determine if differences in perceived duration are associated with the size of measured Weber fractions. A forced-choice adaptive procedure was used. Duration discrimination was poorer for noise with ramped envelopes than for noise with damped or rectangular envelopes. This result is inconsistent with differences in perceived duration and no explanation was readily apparent.
[DOI: 10.1121/1.1372913]

PACS numbers: 43.66.Ba, 43.66.Fe, 43.66.Jh, 43.66.Lj [MRL]

I. INTRODUCTION

Ramped sounds (gradual attack and rapid decay) and damped sounds (rapid attack and gradual decay) are perceived differently, even though the long-term spectra of these sounds are identical. A piano produces a damped sound when played in the normal manner, but playing a recording of piano music backwards produces ramped sounds. In other words, a ramped sound is simply a damped sound reversed in time. Despite this simple manipulation of the temporal envelope, the timbre of ramped and damped sounds is quite distinct.

Berger (1964) demonstrated that playing a recording of an instrument backwards not only reduces identification, but might actually shift the label to another category. An example of this shift in labeling is heard in a widely available auditory demonstration on compact disc (Houtsma *et al.*, 1987). In this recording, the notes from a Bach chorale played on a piano in the normal manner sound like notes produced by an accordion or organ when played backwards.

Patterson and his colleagues (Patterson, 1994a, b; Akeroyd and Patterson, 1995; Irino and Patterson, 1996; Lorenzi *et al.*, 1997, 1998; Patterson and Irino, 1998) have studied the perception of ramped and damped sounds to examine ways that the auditory system might code these sounds differently. They noted that concatenated ramped and concatenated damped sounds are perceived to have a continuous component and a transient component. Matching experiments between ramped and damped low-frequency tones show that the half life of a damped sinusoid has to be 4 times greater than that of a ramped sinusoid for the continuous segments to be perceived of equal strength (i.e., loudness) (Patterson and Irino, 1998). The same experiment with noise carriers showed that the perceptual asymmetry was about half that of low-frequency tones.

Stecker and Hafter (2000) measured the loudness of sounds with single-cycle envelopes with ramped and damped characteristics. On average, sounds with ramped envelopes were judged louder than sounds with damped envelopes. No statistical differences were noted for sinusoidal or broadband noise carriers.

Given this asymmetry in the strength of the continuous component for streams of ramped and damped sounds (Patterson and Irino, 1998) and in the loudness of single cycles of ramped and damped sounds (Stecker and Hafter, 2000), we decided to determine whether the temporal asymmetry in the acoustic waveform affected the perceived duration of single-cycle ramped and damped sounds.

The motivation for measuring subjective duration of ramped and damped sounds is a result of informal observations by the first author that ramped sounds are perceived to be longer than damped sounds. These observations were made while playing an ASA demonstration on compact disc (Houtsma *et al.*, 1987) of a recording of a Bach chorale

played forward and backwards during a hearing science class at the University of Minnesota.

II. EXPERIMENT 1: SUBJECTIVE DURATION OF RAMPED AND DAMPED STIMULI

A. Subjects

The listeners were young adults with hearing sensitivity of 15 dB HL or better at octave frequencies between 0.25 and 8.0 kHz. Listeners were paid for their participation. Initially, 12 listeners participated in the 1.0-kHz condition. These data were collected for a conference presentation along with intensity discrimination data for ramped and damped sounds (Schlauch *et al.*, 1998). At a later date, four additional listeners were recruited for the 1.0-kHz condition, and a second and third group of 16 listeners participated in the broadband-noise and 8.0-kHz conditions, respectively. Seven listeners from the group that judged 1.0-kHz tones also judged the noise stimulus, whereas five other listeners from the group that judged 1.0-kHz tones also judged 8.0-kHz tones.

B. Stimuli

Sounds were generated with a custom-designed 16-bit digital-to-analog converter. The sampling rates were 20 kHz for a broadband noise stimulus and a 1.0-kHz tone and 26 kHz for an 8.0-kHz tone. Antialiasing filters were set to 8.0 and 12.0 kHz for the 20.0 and 26.0-kHz sampling rates, respectively. Damped sounds were generated using a simple exponential decay with a time constant set to one-fifth the signal duration

$$x(t)=e^{(-5t/T)}w(t) \tag{1}$$

where t is time in s, w is a rectangular-gated noise or tone, and T is the duration of w. Ramped sounds were generated by simply reversing the order of the samples in the array for the damped sound prior to output. Stimulus durations were 10, 25, 50, 100, and 200 ms.

Our stimuli differ from those used by Patterson and his colleagues. Ramped and damped stimuli in Patterson and his colleagues' experiments were concatenated sequences of ramped or damped sounds with the amount of decay of damped sounds being limited by the onset of the envelope for the next sound in the sequence. For example, the 16-ms (half-life) damped stimulus in Irino and Patterson (1996) decayed 18.8 dB during its repeating, 50-ms envelope. By contrast, our 100-ms stimulus, with a half-life of 13.9 ms, decayed 42 dB over its duration, as did all of our stimuli. Our stimulus durations of 10, 25, 50, 100, and 200 ms have corresponding half-lives of 1.4, 3.5, 6.9, 13.9, and 27.7 ms, respectively.

C. Procedure

Before data collection began, potential subjects were screened with a magnitude estimation (ME) of line-length task. This line-scaling task was implemented to ensure subjects understood the instructions for the ME task and could use numbers appropriately. Subjects judged the length of 5 lines ranging in length from 0.64 to 447.35 cm. The lines were five pieces of tape located either on the wall of the laboratory or on the wall in the hallway outside the laboratory. Of the 51 subjects screened in this manner, only 3 were dropped from the study. These subjects either used negative numbers ($n=1$) or failed to use fractions or decimals (many lines were labeled with a ''1'' even though they differed by a large amount in length) ($n=2$).

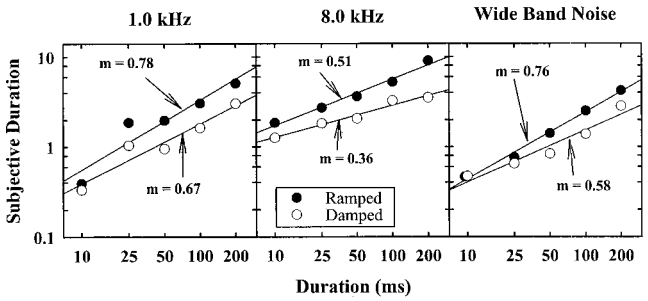

FIG. 1. ME of subjective duration for ramped (closed circles) and damped (open circles) sounds. The 1.0-kHz tones, 8.0-kHz tones, and broadband noise are shown in the left, middle, and right panels, respectively. Data points represent geometric means of assigned number for 16 listeners.

After completing the line-length screening test, subjects participated in the ME of duration task. Subjects assigned numbers to the stimuli that corresponded to their subjective impression of the duration. Numerical references or standards were not provided.

Subjects listened individually to stimuli through a headphone (Telephonics, TDH-39) during a single session while seated in a sound-isolated room. Tones were 70-dB SPL (peak), whereas the noise stimulus was 80 dB SPL. Stimulus type (ramped or damped) and durations were selected randomly within a session. There was a 5-s interval between successive stimuli. A 35-ms duration warning light appeared just prior to the presentation of a stimulus.

D. Results

Figure 1 shows subjective duration (assigned number) as a function of physical duration for the three different stimuli. The data are summarized by power functions of the form,

$$D=kT^{\beta}, \tag{2}$$

where D is subjective duration, T is the overall stimulus duration, and β and k are fitting constants. Power functions show the same general trend for each stimulus type. For all three stimuli, the slope of the function is steeper for ramped than for damped stimuli. On average, ramped stimuli were judged to be roughly 1.5 to 2.0 times longer than damped stimuli of the same physical duration. A Wilcoxon signed-ranks test (Siegel and Castellan, 1988) was used to examine the significance of the ramped–damped difference in subjective duration. For each ranked-sign significance test, comparisons were made for ramped and damped judgments within a subject for all 16 subjects and within duration for all 5 durations (a total of 80 pairs). The logarithm of the scaled values was used. For 1.0-kHz tones, ramped was judged longer than damped 55 times, damped was judged longer than ramped 13 times, and there were 12 ties ($z=5.0$; p

$<0.000\,000\,5$). For 8.0-kHz tones, ramped was judged longer than damped 58 times, damped was judged longer than ramped 7 times, and there were 15 ties ($z=6.0$; $p<0.000\,000\,5$). For wideband noise, ramped was judged longer than damped 50 times, damped was judged longer ramped 14 times, and there were 16 ties ($z=3.66$; $p=0.000\,25$). These results are significant at the 0.05 level after a Bonferroni correction (Hays, 1981) with $n=22$, the number of significance tests in this study.

E. Discussion

The differences in subjective duration observed in this study may be a consequence of a cognitive effect described by Stecker and Hafter (2000) to explain loudness differences between sounds with ramped and damped envelopes. They note that sounds with damped envelopes are perceived to have two distinct segments. Many naturally occurring sounds have the envelope of a damped sound and the perceptually different segments may represent direct and reverberant sound. They assume that direct sound provides information about the sound source and reverberant sound provides information about the listening environment. In judging the loudness of a damped sound presented in isolation, listeners may ignore the decay portion of the sound (i.e., the echo). Stecker and Hafter (2000) argue that this idea is consistent with their loudness data, and the same explanation could account for our findings that ramped sounds are judged to be longer than damped sounds.

Differences in subjective duration between ramped and damped sounds may be a result of physiological coding rather than a cognitive effect. Patterson and Irino (1998) and Stecker and Hafter (2000) have applied the ''auditory image model'' (AIM) to account for differences in the loudness of ramped and damped sounds. AIM models the auditory periphery, including basilar-membrane filtering, compression, and the neural response pattern (Patterson *et al.*, 1995). AIM responds asymmetrically to ramped and damped sounds. The output waveform for ramped sounds is extended in time because these sounds end abruptly, resulting in a ringing of the filter. By contrast, the abrupt onset of a damped sound results in a ringing of the filter which, when added out of phase to the decay portion of the damped sound, results in a more rapid decay of the filter output (Stecker and Hafter, 2000). This analysis is qualitatively consistent with the finding that ramped sounds are perceived to be longer than damped sounds. AIM also predicts that ramped sounds are louder than damped sounds, but this model incorrectly predicts that the loudness difference becomes smaller for high-frequency sounds (Stecker and Hafter, 2000). Although AIM does not predict all of the behavioral results, neural processing in the auditory periphery likely plays an important role in the perceptual differences between ramped and damped sounds. If the effect were entirely cognitive and a result of listeners ignoring the ''echo'' portion of a damped sound, the sequences of ramped and damped sounds used by Patterson and his colleagues would not show a loudness difference.

III. EXPERIMENT 2: DURATION MATCHING

The results of experiment 1 obtained with an ME procedure show that, on average, ramped sounds are judged to be about twice as long as damped sounds of the same physical duration.

A matching procedure provides an alternative means of quantifying the relative subjective impressions among different sounds. Matching functions have been derived from ME obtained for long-duration tones in quiet and in noise as a function of tonal level. These interpolated matching functions have been found to be virtually indistinguishable from the matching functions obtained directly from having listeners match the loudness of a tone presented alternately to an ear in quiet and an ear in background noise as a function of level (Hellman and Zwislocki, 1968).

On other occasions the results of matching experiments do not agree with those of scaling (Schlauch, 1992; Botte *et al.*, 1982). Experiments where the results of matching and scaling do not agree involve judgments requiring attention. Given that a cognitive effect may be responsible for the duration and loudness differences between sounds with ramped and damped envelopes, matching and scaling procedures may not agree in this case as well. More specifically, in a natural context, as in the ME experiment, listeners may have ignored the echo portion of the damped stimulus, but in the matching task, where standard and comparison stimuli can be compared in short-term memory repeatedly, the echo may be considered in judgments of duration. To test this hypothesis, duration-matching functions were obtained and the results were compared with those of the scaling data in experiment 1.

A. Subjects

Three subjects between the ages of 25 and 30 years old participated in this study. They had normal hearing (15 dB HL or better) at octave frequencies between 0.25 and 8.0 kHz.

B. Stimuli

The stimuli were 1.0-kHz tones and broadband noise. Ramped and damped stimuli were digitally generated using the methods described in experiment 1. A rectangular-gated stimulus, with a negligible rise and fall time, was also used in this matching task.

C. Procedure

Subjects listened to a standard stimulus followed by a comparison stimulus. For each judgment, the standard stimulus was fixed in duration. The initial duration of the comparison stimulus was selected at random from a wide range of durations. A slide controlled the duration of the comparison stimulus. The subject's task was to adjust the slide until the two stimuli were perceived to have the same duration. The standard stimulus was presented first and, following a 500-ms interstimulus interval, the comparison stimulus was presented (for one condition, rectangular vs rectangular, the standard followed the comparison for half of the matches and the comparison followed the standard for the remaining

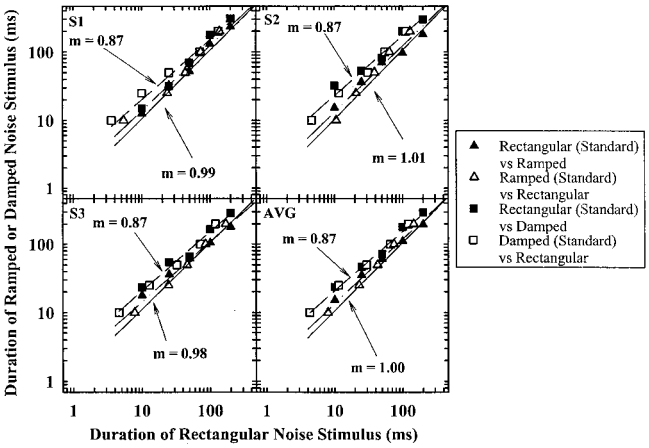

FIG. 2. Duration matching between a rectangular-gated noise and a ramped or damped noise. The dashed line is fitted to all of the data representing matches between damped noise and rectangular-gated noise. The dashed-dot line is fitted to the data representing matches for ramped and rectangular noise. The solid line represents a linear regression to data for a rectangular–rectangular condition for broadband noise (the actual data for this condition are shown in Fig. 4).

matches). The stimuli were presented continuously with about 1 s between the presentation of each standard and comparison pair. The duration of the comparison stimulus was changed during the intertrial interval, showing subjects the immediate impact of their adjustments. Subjects were instructed to bracket the point of subjective equality. When subjects perceived the durations of the standard and comparison to be equal, they pushed a button that recorded the value of the comparison duration in the computer.

Data for noise and for 1.0-kHz tones were collected for the following conditions: rectangular vs rectangular, rectangular vs damped, rectangular vs ramped, and ramped vs damped. For alternate runs, the sequence of the stimuli was reversed. Ten matches were completed by each subject for each condition. For example, in the condition comparing ramped vs damped tones, five matches were completed for the situation where the ramped tone was the standard and five were completed where the damped tone was the standard. The upper end of the range of possible comparison durations was jittered following each adjustment. A lower range offered durations from 1 to 256 ms. The upper limit varied for each adjustment between 171 and 256 ms. A higher range offered 100 to 610 ms. The upper limit for this higher range varied between 482 and 610 ms for each adjustment. Based on pilot data, the lower and upper ranges were selected for a particular condition so that the adjustments fell well within the range of possible values.

D. Results

Figure 2 illustrates data for the matching task for rectangular vs damped noise and rectangular vs ramped noise for three subjects (S1, S2, and S3) and, in the lower-right panel, the average data for these three subjects. Solid lines in each panel represent a linear regression to the matches for the rectangular vs rectangular condition. All of these lines have a slope close to 1.0 and with nearly equal values on the ordinate and abscissa for any given point on the line. For all subjects, the dashed line fitted to the damped vs rectangular condition (squares) falls above the slope-of-one line representing equal physical durations for subjective equality. This shows that the physical duration of the noise with the damped envelope was longer than the physical duration of the noise with the rectangular envelope when the durations were perceived to be equal. By contrast, the data for the ramped vs rectangular condition fall just above and in the vicinity of the slope-of-one line representing equal physical durations. The significance of these differences was evaluated with the Wilcoxon signed-ranks test. For each significance test, the sign of each match was determined based on which stimulus in the pair (standard and comparison) was judged to be longer. Ranked pairs were evaluated across subjects and across durations. These results, shown in Table I, indicate that broadband noise with damped envelopes or ramped envelopes is perceived to be statistically significantly shorter than noise with rectangular envelopes. A small bias in the rectangular–rectangular condition resulted in adjustments that were significantly larger than the standard when the second observation interval was adjusted by the listener.

The same pattern holds in Fig. 3, where duration-matching results are shown for tones with rectangular envelopes compared with those with ramped or damped envelopes. Significance tests, shown in Table I, indicate that tones with damped envelopes are perceived to be statistically significantly shorter than tones with rectangular envelopes, but the difference between ramped and rectangular envelopes did not reach significance.

Figure 4 illustrates the results of the duration-matching task for damped vs ramped noise. Table I shows that noise with damped envelopes is judged to be statistically significantly shorter than noise with ramped envelopes. That is, the damped noise was always adjusted to a longer duration than the ramped noise for subjective equality. The same result holds for tones as shown in Fig. 5. Table I shows that this difference is statistically significant as well.

A comparison was made between the duration-matching data and the ME data for noise and tones with ramped and damped envelopes. First, equal subjective durations were derived from the ME data for the ramped and damped noise in Fig. 1. For each datum in Fig. 1. (for the group data for 1.0-kHz tones and broadband noise), an equal subjective duration was interpolated from a line drawn between two adjacent points for the corresponding condition.[1] For example, if a ramped datum was used as a reference, the equal subjective duration was interpolated using a line drawn between two damped data points in the vicinity of the equal subjective duration. These interpolated ''matches'' from the ME data along with group data for the duration-matching procedure (individual data points from Fig. 5 for the average data) are shown in Fig. 6 in the upper panels and lower panels, respectively. To clarify the difference in duration between sounds with ramped and damped envelopes at equal subjective durations, the ratio of the durations for these sounds (damped/ramped) at equal subjective duration are plotted as a function of the duration of the ramped stimulus.

It is clear from Fig. 6 that the two experimental procedures produced similar results. This finding is reassuring be-

TABLE I. Various conditions from the matching experiment evaluated for statistical significance using the Wilcoxon signed-ranks test. Rectangular (Rect) vs rectangular is listed twice. For the first one listed the first observation interval was adjusted by the listener, whereas for the other measure the second interval was adjusted. Bold-faced *p* values are significant at the 0.05 level after considering a Bonferroni correction based on 22 tests.

Stimulus	Standard	Comparison	Standard perceived longer	Comparison perceived longer	Tie	*z*	*p*
Noise							
	Rect	Damp	68	1	1	6.97	**<0.000 000 5**
	Damp	Rect	1	74	0	7.52	**<0.000 000 5**
	Rect	Ramp	56	19	0	3.30	**0.000 9**
	Ramp	Rect	13	58	4	5.80	**<0.000 000 5**
	Rect	Rect	36	38	1	1.50	0.116
	Rect	Rect	55	17	3	3.88	**0.000 1**
	Ramp	Damp	60	14	1	5.94	**<0.000 000 5**
	Damp	Ramp	8	67	0	6.90	**<0.000 000 5**
Tone							
	Rect	Damp	69	6	0	7.12	**<0.000 000 5**
	Damp	Rect	3	72	0	7.49	**<0.000 000 5**
	Rect	Ramp	44	29	2	1.56	0.119
	Ramp	Rect	27	45	3	1.98	0.046
	Rect	Rect	48	18	9	3.67	**0.000 2**
	Rect	Rect	29	40	6	1.71	0.085
	Ramp	Damp	69	5	1	7.21	**<0.000 000 5**
	Damp	Ramp	2	72	1	7.45	**<0.000 000 5**

cause different nonsensory factors can influence the data from ME procedures and matching procedures. For instance, ME procedures can be influenced by an observer's nonlinear use of numbers (e.g., Schneider *et al.*, 1974). For the matching procedure, the possibility exists that listeners were adjusting the comparison stimulus until a rhythmic pattern was produced by the entire stimulus sequence (the two observation intervals separated by a short delay repeated after a longer delay).

Figure 6 also shows that the difference in subjective duration between ramped and damped sounds is larger for tones than for noise. A Wilcoxon signed-ranks test was run on the individual data for the matching procedure to assess the significance of this difference. Within a subject and for each duration, the number of cases where the ratio of damped/ramped at equivalent subjective duration for tones was larger than the ratio of damped/ramped at equivalent subjective duration for noise was evaluated. When the ramped stimulus was the standard, the ratio for tones was larger than for noise 60 times, the ratio for noise larger than for tones 14 times, and there was 1 tie ($z=-5.94$; $p<0.000\,000\,5$). When the damped stimulus was the standard, the ratio for tones was larger than for noise 73 times and the ratio for noise was larger than for tones 2 times ($z=7.5$; $p<0.000\,000\,5$).

E. Discussion

The results of the matching experiment are in agreement with those of magnitude estimation. Both experiments found

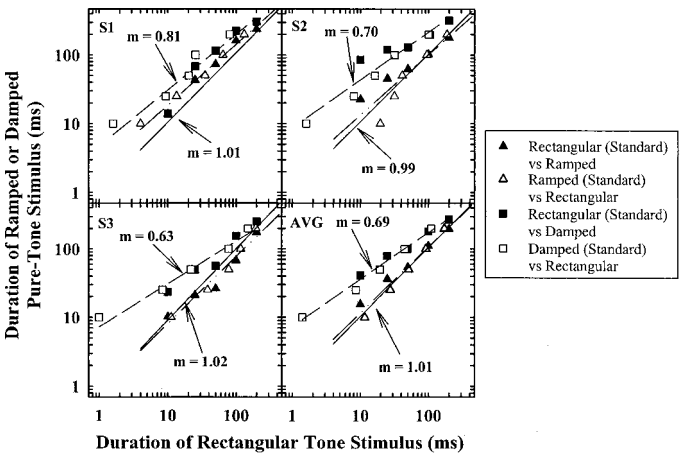

FIG. 3. Duration-matching behavior between ramped tones and rectangular-gated tones and damped tones and rectangular-gated tones. The data representation is identical to that of Fig. 2.

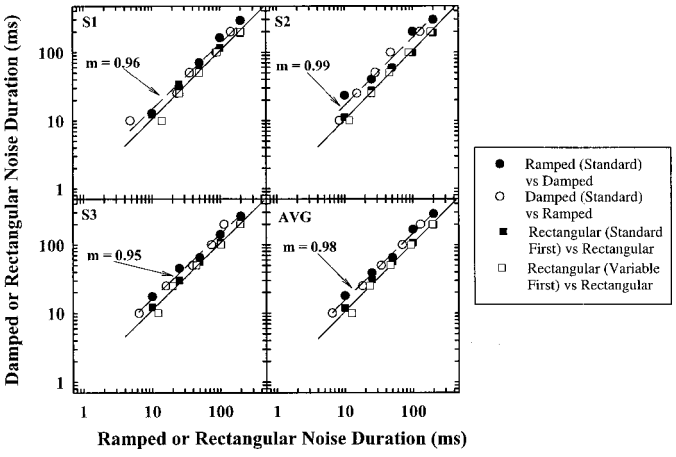

FIG. 4. Duration-matching data between ramped noise and damped noise along with data for a rectangular–rectangular control condition. The dashed line and solid line in this figure represent least-squares regression to all of the matches between ramped and damped noise and between rectangular–rectangular noise, respectively.

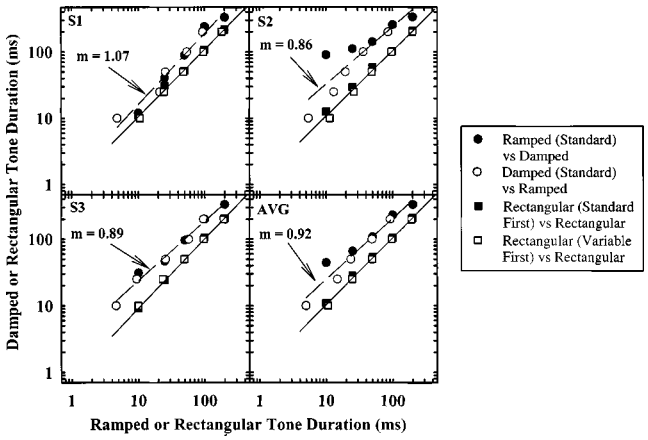

FIG. 5. Duration matching between ramped, 1.0-kHz tones and damped, 1.0-kHz tones. Also shown is a rectangular–rectangular control condition for 1.0-kHz tones. Data are represented in an identical manner as in Fig. 4 (but for 1.0-kHz tones instead of noise).

that sounds with damped envelopes are perceived to be shorter than sounds with ramped envelopes. These results are qualitatively consistent with the loudness data for ramped and damped stimuli and Stecker and Hafter's (2000) idea that listeners ignore the echo portion of a sound with a damped envelope. In other words, ignoring the echo renders a sound softer and shorter in duration than it would be if the echo were considered in the judgment. The finding of the matching experiment that sounds with damped envelopes are judged to be shorter than sounds with ramped and rectangular-shaped envelopes lends further support to this idea. A larger ramped–damped difference in the ME experiment than the matching experiment would have provided stronger support for Stecker and Hafter's (2000) cognitive explanation for this phenomenon, but the absence of a difference across experiments does not rule it out.

A more detailed comparison of the loudness and subjective duration of sounds with ramped and damped envelopes shows that these behaviors may be correlated for stimulus carrier type. Patterson and Irino (1998) found that noise produced a smaller loudness difference than tones. We found that differences in subjective duration were smaller for noise than for tones. By contrast, Stecker and Hafter (2000) reported no statistical difference in the loudness of noise with ramped or damped envelopes. Our results are consistent with those of Patterson and Irino (1998), but there is no obvious explanation for the difference between these stimulus carrier types in their subjective durations or loudness.

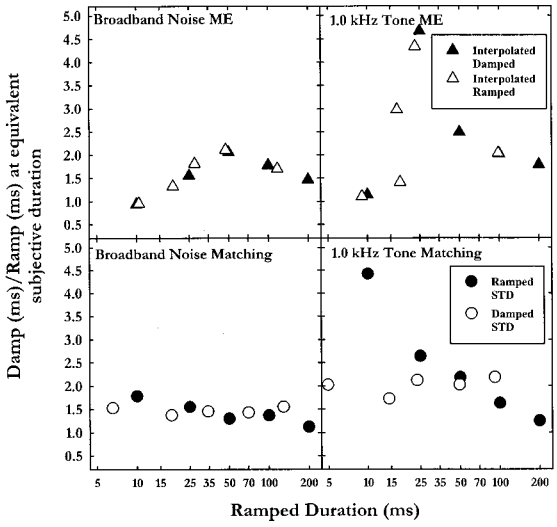

FIG. 6. The ratio of physical durations (damped/ramped) at equal subjective durations as a function of duration of the ramped stimulus. Data shown are from the matching experiment (lower panels) along with interpolated values from the ME experiment (upper panels). Data for noise (left panels) and 1.0-kHz tones (right panels) are shown for each stimulus type.

The matching experiment also demonstrates that the reason damped sounds are judged to be shorter than ramped sounds is due to an underestimation of the duration of the damped sound rather than an overestimation of the duration of the ramped sound. This result agrees with a recent finding by Grassi and Darwin (in press). They found that ramped sounds with durations between 250 and 1000 ms were about 30 percent longer than damped sounds for a number of stimuli: 1.0-kHz tones, a complex tone, and a vowel. This finding agrees favorably with our results for 200 ms, the longest duration we tested. Grassi and Darwin's (2001) results also show a trend for the ramped–damped difference to decrease as duration increases.

IV. EXPERIMENT 3: DURATION DISCRIMINATION AS A FUNCTION OF DURATION

Experiments 1 and 2 demonstrate that ramped sounds are perceived to be longer than damped sounds of the same physical duration. This prompted us to wonder whether the subjective difference in duration would be reflected in a difference in the just-noticeable difference (jnd) for duration. That is, would the damped stimuli, which are perceived to be shorter in duration, have a smaller jnd for duration in absolute terms than the ramped stimuli and/or the rectangular stimuli? This might be predicted on the basis of the fact that the jnd for duration is typically 10% of the duration of the stimulus for long duration stimuli (Abel, 1972).

To date, the only discrimination measurements for stimuli with asymmetric modulator shapes (Akeroyd and Patterson, 1995, 1997) have measured discrimination for gross changes in envelope shape (e.g., discrimination of ramped from damped).

A. Subjects

Four young adults with hearing within normal limits between 0.25 and 8.0 kHz participated. Subjects were paid for their participation.

B. Stimulus

A broadband noise was used to avoid spectral cues. The noise was generated using the same method as described in experiment 1. The noise level was 80 dB SPL (peak).

C. Procedure

Subjects listened individually in a sound-treated room through an earphone. A 3-AFC adaptive procedure that targeted 70.7% correct was used (Levitt, 1971). Two of the three intervals contained the standard duration (T) that was

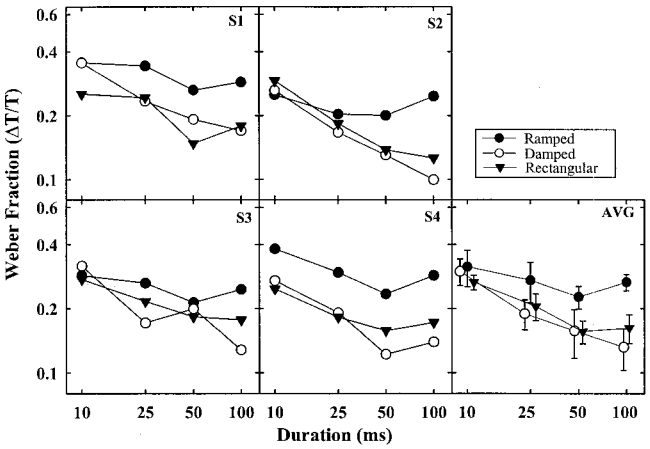

FIG. 7. Duration discrimination for ramped noise (closed circles), damped noise (open circles), and rectangular-gated noise (triangles) as a function of duration. Data are for four listeners (S1, S2, S3, and S4) and for the group (AVG). The abscissa values for the average condition were adjusted slightly for ease of viewing.

fixed within each block of 80 trials. The remaining interval of the 3-AFC task contained the standard duration plus an increment in duration $(T+\Delta T)$.[2] The position (one, two, or three) of the interval containing the increment was assigned randomly. The listeners' task was to select the interval thought to contain the increment by pushing a button corresponding to that interval. Correct-answer feedback was given following each trial.

After two consecutive correct responses, the duration of the increment was decreased. Each incorrect response resulted in an increase in the duration of the increment. Based on pilot data, the starting duration for the increment for a block of trials was set about a factor of 4 above the expected threshold. For the first two reversals, the duration of the increment changed by a factor of 2. For subsequent reversals, the duration of the increment was changed by a factor of the square root of 2. For each block of 80 trials, threshold was calculated based on the average of reversals in duration that occurred within that block. Average thresholds for each listener were based on the mean threshold for five blocks of trials.

D. Results

Figure 7 illustrates just-noticeable differences in duration as a function of duration for the four listeners as well as the average group data. All subjects show the same pattern of results. Notably, the Weber fractions for duration for rectangular and damped noise are nearly identical when evaluated for the same physical duration. By contrast, the Weber fractions are larger by about a factor of 2 for ramped noise for durations between 25 and 100 ms. An examination of data from Abel's (1972) experiment that presumably used rectangular-gated tones and noise bands shows results nearly identical to our results for rectangular-gated noise and damped noise. The Wilcoxon signed-ranks test showed that Weber fractions for duration for stimuli with ramped envelopes are statistically significantly different than those with rectangular $(z=6.29;\ p<0.000\,000\,5)$ or damped $(z=5.98;\ p<0.000\,000\,5)$ envelopes. The Weber fractions for rectangular-gated noise and damped noise were not significantly different $(z=0.566;\ p=0.571)$.

E. Discussion

These data suggest that there is not close coupling between subjective duration and duration discrimination. The perceived duration of noise with ramped and rectangular envelopes is judged to be longer than that of noise with damped envelopes. By contrast, Weber fractions are larger for noise with ramped envelopes than for noise with damped or rectangular envelopes.

V. GENERAL DISCUSSION

Damped sounds are perceived to be shorter than ramped sounds of the same duration. We found this result using two methods: ME and duration matching. The average data from the duration-matching experiment summarize the main effects from these studies. Duration matches between ramped and damped tones show that damped tones have to be a fairly constant factor of about 2.0 times the duration of a ramped sinusoid to produce a match (Fig. 5). When ramped and damped broadband noises are matched (Fig. 4), damped noise differs from ramped noise by a fairly constant factor of 1.5, a smaller effect than is observed for tones. Figure 3, which illustrates matches between ramped and rectangular-gated tones and damped and rectangular-gated tones, shows that the size of the effect is attributed to the damped sinusoid. That is, the rectangular-gated sinusoid and the ramped sinusoid are roughly equal for all durations. By contrast, the damped sinusoid differs from the rectangular-gated sinusoid by about a factor of 4.0 for short durations and this factor diminishes with duration until it reaches a factor of 1.5 for the longest duration examined (200 ms). Figure 2, which illustrates the corresponding matches for a noise carrier, shows the same finding but with a smaller effect. Namely, the ramped–damped difference is due to the damped noise differing from the rectangular-gated noise and ramped noise.

Two explanations come to mind to explain the finding that damped sounds are perceived to be shorter than ramped and rectangular-gated sounds. First, listeners may perceive the damped sound as sound source and its echo (Stecker and Hafter, 2000). The echo may not be considered as a part of the sound when judging its duration, or, as Stecker and Hafter report, its loudness. An alternative explanation for the difference in perceived duration for sounds with ramped and damped envelopes may be related to the asymmetrical nature of the temporal window. The temporal window has a gradual slope for times before its center than for times after its center, which accounts for the main features of forward and backward masking (Moore *et al.*, 1988). For modeling judgments of subjective duration, the temporal masking pattern for a stimulus, which includes segments of forward and backward masking, has proved important. Fastl (1977) found subjective duration grows at a slower rate than physical duration for rectangular-gated noise and that this difference can be accounted for by the temporal masking patterns for these sounds. The subjective duration for a given stimulus was determined by observing the times where the temporal masking pattern dropped to a critical value close to detection

threshold in quiet. These critical times mark the beginning and end of a stimulus for calculating subjective duration, and forward masking plays a large role in explaining discrepancies between physical duration and subjective duration for the rectangular-gated noise bands used in Fastl's (1977) study. Applied to sounds with ramped and damped envelopes, the abrupt offset of sounds with ramped envelopes would result in more forward masking than for sounds with damped envelopes. If this forward masking represents a persistence of perception, as assumed by Fastl (1977), the difference in perceived duration between ramped and damped sounds is qualitatively consistent with the asymmetrical shape of the temporal window that causes this forward masking.

The observed pattern of duration discrimination is difficult to explain based on the results for the subjective duration experiments. Noise with rectangular envelopes is judged to be about equal in duration with sounds with ramped envelopes, but the ramped condition produces much poorer discrimination performance than the rectangular condition. Noise with damped envelopes is perceived to be shorter than noise with rectangular or ramped envelopes, but discrimination performance is nearly identical for damped and rectangular noises. These results suggest that subjective duration and duration discrimination are not related for these stimuli.

The abrupt onset and offset of a stimulus might provide the decision processor a possible cue for duration discrimination. Abrupt changes in stimulus level would result in synchronous neural firing when these changes occur. From this, one would predict that rectangular envelopes would result in better duration discrimination than either ramped or damped envelopes. Given that damped envelopes yielded performance comparable to those of rectangular envelopes (rather than ramped and damped being roughly equal and poorer than rectangular), an explanation for the duration discrimination results remains a puzzle.

This difference in duration discrimination for noise with ramped and damped envelopes is in contrast to the result for intensity discrimination for 1.0-kHz tones (Schlauch *et al.*, 1998), where a difference was not observed. This finding may be due to peak amplitude of the waveform dominating the response for intensity discrimination for tones.

VI. CONCLUSIONS

(1) Sounds with damped envelopes are perceived to be shorter in duration than sounds with ramped envelopes. This is true for ME and duration-matching tasks.
(2) The difference in subjective duration between sounds with ramped envelopes and sounds with damped envelopes is larger for 1.0-kHz tones than for noise.
(3) Sounds with ramped envelopes have larger Weber fractions for duration than sounds with damped envelopes for identical durations for durations between 25 and 100 ms. This finding is not consistent with differences in perceived duration.

ACKNOWLEDGMENTS

This work was supported by NIH/NIDCD Grant No. R29 DC01542. We are grateful for the comments by Roy Patterson, Marjorie Leek, and an anonymous reviewer during the review process.

[1]The lines drawn between two adjacent data points for these interpolations make minimal assumptions about the overall shape of the function representing subjective duration as a function of duration. This would not be the case if we used the linear regression fitted to the entire data set. A consequence of this procedure is that variability in the average judgments for each datum is more likely to affect the interpolated values than a regression analysis involving the entire data set.

[2]The increment in duration was not appended directly to the standard. Instead, the total duration of the increment and standard ($T+\Delta T$) was calculated and this new value of T was used to generate the stimulus using Eq. (1).

Abel, S. M. (**1972**). ''Duration discrimination of noise and tone bursts,'' J. Acoust. Soc. Am. **51**, 1219–1223.
Akeroyd, M. A., and Patterson, R. D. (**1995**). ''Discrimination of wideband noises modulated by a temporally asymmetric function,'' J. Acoust. Soc. Am. **98**, 2466–2474.
Akeroyd, M. A., and Patterson, R. D. (**1997**). ''A comparison of detection and discrimination of temporal asymmetry in amplitude modulation,'' J. Acoust. Soc. Am. **101**, 430–439.
Berger, K. W. (**1964**). ''Some factors in the recognition of timbre,'' J. Acoust. Soc. Am. **36**, 1888–1891.
Botte, M. C., Canevet, G., and Scharf, B. (**1982**). ''Loudness adaptation induced by an intermittent tone,'' J. Acoust. Soc. Am. **72**, 727–739.
Fastl, H. (**1977**). ''Subjective duration and temporal masking patterns for broadband noise impulses,'' J. Acoust. Soc. Am. **61**, 162–168.
Grassi, M., and Darwin, C. J., ''Perception of the duration of sounds with increasing or decreasing amplitude,'' Br. J. Audiol. (in press).
Hays, W. L. (**1981**). *Statistics* (Holt, Rhinehart, & Winston, New York).
Hellman, R. P., and Zwislocki, J. J. (**1968**). ''Loudness determination at low sound frequencies,'' J. Acoust. Soc. Am. **43**, 60–64.
Houtsma, A. J. A., Rossing, T. D., and Wagenaars, W. M. (**1987**). ''Effect of tone envelope on timbre,'' in *Auditory Demonstrations* (Institute for Perceptual Research, Eindhoven, The Netherlands), p. 67.
Irino, T., and Patterson, R. D. (**1996**). ''Temporal asymmetry in the auditory stream,'' J. Acoust. Soc. Am. **99**, 2316–2331.
Levitt, H. L. (**1971**). ''Transformed up–down methods in psychoacoustics,'' J. Acoust. Soc. Am. **49**, 467–477.
Lorenzi, C., Gallego, S., and Patterson, R. D. (**1997**). ''Discrimination of temporal asymmetry in cochlear implantees,'' J. Acoust. Soc. Am. **102**, 482–485.
Lorenzi, C., Gallego, S., and Patterson, R. D. (**1998**). ''Amplitude compression in cochlear implants artificially restricts the perception of temporal asymmetry,'' Br. J. Audiol. **32**, 367–374.
Moore, B. C. J., Glasberg, B. R., Plack, C. J., and Biswas, A. K. (**1988**). ''The shape of the ear's temporal window,'' J. Acoust. Soc. Am. **83**, 1102–1116.
Patterson, R. D. (**1994a**). ''The sound of a sinusoid: Spectral models,'' J. Acoust. Soc. Am. **96**, 1409–1418.
Patterson, R. D. (**1994b**). ''The sound of a sinusoid: Time-interval models,'' J. Acoust. Soc. Am. **96**, 1419–1428.
Patterson, R. D., Allerhand, M. H., and Giguère, C. (**1995**). ''Time-domain modeling of peripheral auditory processing: a modular architecture and software platform,'' J. Acoust. Soc. Am. **98**, 1890–1894.
Patterson, R. D., and Irino, T. (**1998**). ''Modeling temporal asymmetry in the auditory system,'' J. Acoust. Soc. Am. **104**, 2967–2979.
Schlauch, R. S. (**1992**). ''A cognitive influence on the loudness of tones that change continuously in level,'' J. Acoust. Soc. Am. **92**, 758–765.
Schlauch, R. S., Ries, D. T., DiGiovanni, J. J., Elliot, S., and Campbell, S. (**1998**). ''Intensity discrimination of ramped and damped tones,'' Conference Proceedings of the International Congress on Acoustics and the Acoustical Society of America **2**, pp. 885–886.
Schneider, B., Parker, S., Ostrosky, D., Stein, D., and Kanow, G. (**1974**). ''A scale for the psychological scale of magnitude,'' Percept. Psychophys. **16**, 43–46.
Siegel, S., and Castellan, N. (**1988**). *Nonparametric Statistics for the Behavioral Sciences* (McGraw-Hill, New York).
Stecker, G. C., and Hafter, E. R. (**2000**). ''An effect of temporal asymmetry on loudness,'' J. Acoust. Soc. Am. **107**, 3358–3368.

Children's detection of pure-tone signals with random multitone maskers

Eunmi L. Oh, Frederic Wightman,[a] and Robert A. Lutfi[b]
Waisman Center, University of Wisconsin, Madison, Wisconsin 53705

(Received 15 June 2000; revised 12 January 2001; accepted 17 March 2001)

Preschoolers and adults were asked to detect a 1000-Hz signal, which was masked by a multitone complex. The frequencies and amplitudes of the components in the complex varied randomly and independently on each presentation. A staircase, cued two-interval, forced-choice procedure disguised as a ''listening game'' was used to obtain signal thresholds in quiet and in the presence of the multitone maskers. The number of components in the masker was fixed within an experimental condition and varied from 2 to 906 across experimental conditions. Thresholds were also measured with a broadband noise masker. Eight preschool children and eight adults were tested. Although individual differences were large, among both adults and children, there was little difference between the groups in the mean amount of masking produced by the maskers with large numbers of components (400 and 906). There was also a small but significant difference between adults and children in the mean amount of masking produced by the broadband noise. The difference between the groups was much larger with smaller numbers of components. Data obtained from the adults were basically similar to that previously reported [cf. Neff and Green, Percept. Psychophys. **41**, 409–415 (1987); Oh and Lutfi, J. Acoust. Soc. Am. **104**, 3489–3499 (1998)]: maskers comprised of 10–40 components produced as much as 30 to 60 dB of masking in some, but not all listeners. Those same maskers produced larger amounts of masking (70–83 dB) in many of the preschool children, although, as in the adult group, individual differences were large. The component-relative-entropy (CoRE) model [Lutfi, J. Acoust. Soc. Am. **94**, 748–758 (1993)] was used to describe the differences in performance between the children and adults. According to this model the average child appears to integrate information over a larger number of auditory filters than the average adult. © *2001 Acoustical Society of America.* [DOI: 10.1121/1.1371764]

PACS numbers: 43.66.Ba, 43.66.Dc [DWG]

I. INTRODUCTION

A child's ability to hear out relevant signals from a background of noise is essential in a classroom where the random or chaotic nature of noise can be very distracting. It has been well documented that young children perform poorly compared to adults in such detection tasks (Allen *et al.*, 1989; Allen and Wightman, 1992, 1994, 1995; Elfenbein *et al.*, 1993; Elliott and Katz, 1980; Irwin *et al.*, 1985; Schneider *et al.*, 1986; Trehub *et al.*, 1995). The fact that large within- and between-listener variability is reported, particularly in young children, might suggest that the differences involve not only auditory sensitivity but also more central, attentional aspects of auditory processing (Allen *et al.*, 1989; Jensen and Neff, 1993; Wightman and Allen, 1992).

Developmental changes in auditory detection threshold have been reported for conditions in which a pure tone or complex signal is presented either in quiet or in the presence of maskers such as wideband and narrowband noise. Most previous studies of developmental changes in threshold used maskers (e.g., broadband noise) that did not vary greatly from trial to trial. Allen and Wightman (1995) were among the first to examine the effect of masker uncertainty on signal detectability by preschool children. In their study, the signal to be detected was fixed in frequency. The masker consisted of a broadband noise plus a single pure tone, the frequency of which was randomly chosen (from a set of two frequencies) on each presentation. Since the frequency of the additional tone was far from the frequency of the signal, it seemed appropriate to refer to this tone as a ''distracter'' rather than a masker. The presence of the uncertain distracter, on average, increased the adults' thresholds by 11 dB and the children's thresholds by at least 24 dB. This suggests that when a signal is embedded in an uncertain acoustic background a child's ability to detect a tone is much more severely impaired than that of an adult.

The effect of stimulus uncertainty on detection has been extensively investigated in adult listeners (cf. Lutfi, 1993; Neff and Green, 1987; Spiegel *et al.*, 1981). A typical task requires the listener to detect a fixed-frequency signal in the presence of other tonal components (i.e., distracters) that vary in frequency and/or amplitude on each presentation. The frequencies of these distracter components are usually remote from the signal frequency. A key independent variable is the number of frequency components comprising the distracter. The usual results are that the total amount of masking depends in a nonmonotonic fashion on the number of distracter components and that there are large individual differences in the amount of masking and in the number of distracter components producing the maximum masking

[a]Also at Department of Psychology.
[b]Also at Department of Communicative Disorders.

(Neff and Dethlefs, 1995; Oh and Lutfi, 1998). Relatively few adult listeners are only slightly affected by the presence of the random multitone distracters. These ''low-threshold'' listeners seem to be able to focus attention on the signal and to ignore irrelevant information in the uncertain distracters. For most adult listeners, however, the uncertain tonal background does interfere with signal detection, especially when distracters are comprised of 10–40 components. The total amount of masking is as much as 50–60 dB for these multitone distracters (Neff and Green, 1987; Oh and Lutfi, 1998).

Some of this masking effect is almost certainly due to masker energy falling in close proximity to the signal frequency. This type of masking, called *energetic masking*, can be estimated from the signal-to-noise ratio at the output of the auditory filter centered at the signal frequency (cf. Patterson, 1976). Any additional masking is referred to as *informational masking* (Pollack, 1975) and is attributed to the distraction effect of the random frequency masker. Oh and Lutfi (1998) have used the component-relative-entropy (CoRE) model (Lutfi, 1993) to assess the relative contributions of energetic and informational masking and to describe individual differences in terms of two free parameters of the model. Their analysis suggests that the amount of informational masking obtained from adult listeners, which can be as much as 30 dB in so-called ''high threshold'' listeners, is related to the number of auditory filters over which information is integrated.

In the study reported here, the effect of multitone maskers with uncertain frequency content was investigated in preschool children. The task was to detect a 1000-Hz tone simultaneously presented with a multitone masker comprised of components whose frequencies and amplitudes varied randomly on each presentation. This task was disguised as a ''listening game'' in order to engage the attention and participation of young listeners. The amount of masking as a function of the number of masker components (the masking function) was estimated for each individual listener so that individual differences as well as age group differences could be quantified. The specific purposes of this study were to quantify each child's selective listening capability and to examine how children might differ from each other and from adults in uncertain listening conditions. We also attempt to describe individual differences in each age group and differences between adults and children by applying the CoRE model to the data obtained.

II. METHODS

A. Stimuli

The signal was a 1000-Hz tone presented simultaneously with random distracters. Distracters were derived from 100 samples of Gaussian noise, bandpass filtered from 0.1 to 10 kHz. The magnitude and phase spectra of each noise sample were analyzed into individual spectral components with a discrete Fourier transform (FFT). On each presentation, one of the noise samples was drawn at random, and a fixed number of its frequency components was selected, also randomly. The phases and amplitudes of the selected frequency components were then used to synthesize the multitone distracter. The number of distracter components (2, 10, 20, 40, 200, 400, or 906) was fixed within a given experimental condition and was varied across different experimental conditions. In a ''broadband noise'' condition, all available components of each noise sample (approximately 3700) were selected, thus producing bursts of true Gaussian noise. In all conditions (including the broadband noise condition) distracter components within a rectangular band centered at the signal frequency (920–1080 Hz) were excluded to reduce the contribution of energetic masking.

Both signal and distracter were gated on and off together with 10-ms, $\cos^2$ onset/offset ramps for a total duration of 370 ms. The RMS level of the distracter was 60 dB SPL regardless of the number of distracter components. The broadband noise distracter was also presented at 60 dB SPL overall (thus, its spectrum level was approximately 20 dB SPL). The dB levels of the individual distracter components were random, approximately normally distributed (component amplitudes were Rayleigh distributed) with a standard deviation of 5.6 dB. The maximum level of the signal was limited to 84 dB SPL. The signal and the distracter were computer generated and played over a 16 bit, digital-to-analog converter (Tucker Davis Technologies DD1) at a sampling rate of 44.1 kHz. All stimuli were presented monaurally, to the listener's right ear, through Sennheiser model HD-414 headphones. The sound levels produced by the Sennheiser headphones were estimated with a loudness balancing procedure using calibrated TDH-49 headphones and adult listeners.

B. Procedure

A staircase, cued two-interval, forced-choice procedure was used to estimate signal threshold in quiet and in the presence of both multitone and Gaussian noise distracters. Each trial was preceded by a cue, which consisted of the presentation of a bird picture on a computer screen and a simultaneous unmasked signal tone at 60 dB SPL. Two successive stimulus intervals were then presented with a 700-ms silent interval between them. Each stimulus interval was marked (on the computer screen) by a flashing square with the numeral ''1'' or ''2'' on it. One of the two intervals contained a distracter sample and the other contained a different distracter sample with the signal added to it. The signal occurred in the first or second interval with equal probability. The child's task was to select the interval that contained the signal. The instructions were, ''Listen to the two sounds presented with the two boxes and point to the box that has the bird sound.'' Correct responses were reinforced by presenting a few pieces of a picture puzzle. The child was allowed to choose pictures for the puzzle (cartoon characters, animals, his/her own pictures, etc.). The child's goal was to complete the puzzle within a block of trials.

The starting signal level was selected so as to make the signal clearly audible to the listener. On each of the next four trials the signal level was decreased in 8 dB steps and then was increased in 8 dB steps back to the starting level. This up–down pattern was continued for a total of 40 trials, producing 5 trials at the highest and lowest levels and 10 trials

at each of the three intermediate levels. The signal level was varied by a programmable attenuator (Tucker Davis Technologies PA4). At least three blocks of trials were completed for an experimental condition. If performance levels near 100% and 50% (chance) were not obtained for the highest and lowest signals levels, an additional block of trials was obtained with the starting level adjusted either up or down so that desirable performance levels were observed at both extremes. A logistic function relating percentage of correct responses to signal level was fit to the data from each condition using a maximum likelihood criterion [see Allen and Wightman (1994) for details on the fitting procedure]. The signal level at which performance was expected to be 75% correct was taken to be the threshold value.

Each listener was tested in a double-walled, sound-attenuating chamber. Two experimenters accompanied a child listener. One experimenter set up an appropriate starting level, initiated stimulus presentation when the child was ready for the next trial, and typed in ''1'' or ''2'' when the child made a response by touching one of the boxes on the screen or by calling out the number. The other experimenter was present to satisfy local security rules. The experimenters interacted with the child in an attempt to hold his/her interest during the session.

Practice trials were given until the listener appeared familiar with the task. The children completed three or fewer blocks of 40 trials each day, depending on their willingness to continue and time availability. It took the children 8–10 minutes to complete a block of trials and they participated for no longer than 30 minutes on any single day. The children were tested several times until all experimental conditions were completed. Adults were tested in the same conditions as the children and required approximately 5 minutes to complete each block of 40 trials. The adult listeners participated for 1.5 hours on each day. All listeners first completed the condition in which the signal was presented alone (quiet threshold), and then the condition involving the broadband noise masker. Next they completed the experimental conditions in which the signal was presented with the multitone distracters. These latter experimental conditions were presented in random order.

C. Listeners

Eight preschool children and eight adults participated in this study. The children were selected from the Waisman Center Early Childhood Program on the basis of their willingness to participate and both parent and teacher consent. Their age at the time of the first session ranged from 4 years 1 month to 5 years 7 months. The children appeared to have enjoyed the listening games, and they were rewarded with a toy or some other item (e.g., a Ty™ Beanie Baby) at the end of each session. The adults were students at the University of Wisconsin who were paid at an hourly rate for their participation, except for SNK (the first author of this article).

The listeners' audiometrically determined pure tone thresholds were less than 15 dB HL (ANSI, 1989) at octave frequencies from 250 to 4000 Hz. Middle-ear problems, which may increase detection thresholds, are common in young children. Thus, tympanometry was performed on each child prior to each session using a screening tympanometer (Grason–Stadler, GSI-27A Auto-Tymp), calibrated to ANSI specifications (ANSI, 1987). Peak-compensated static acoustic admittance was measured, and the child permitted to continue only if these results were normal.

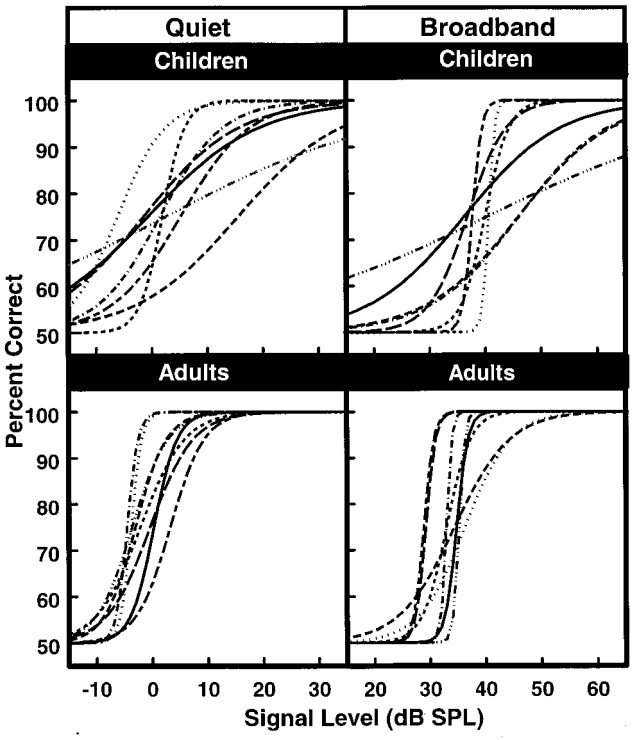

FIG. 1. Fitted psychometric functions for individual children (top panels) and adults (bottom panels). The label ''Quiet'' indicates the condition where the signal was presented in quiet, and the label ''Broadband'' indicates the condition where the signal was simultaneously presented with a broadband noise.

III. RESULTS

Figure 1 shows psychometric functions fitted to the data of individual children and adults where the signal was presented in quiet and in broadband noise. Thresholds for individual children and adults in these conditions are given in Tables I and II along with the means and 95% confidence intervals. Quiet thresholds in both groups seem low, and this

TABLE I. Children's thresholds (dB SPL) in quiet and broadband noise and CoRE model parameters, *n* (number of auditory filters) and *W* (attentional bandwidth in kHz) for best fits to the thresholds from the random, multitone masker conditions.

ID	Quiet	Noise	*n*	*W*
STC	15.6	46.1	7	4
SSR	5.1	37.6	9	10
STJ	2.8	40.2	12	4
STU	−1.4	36.2	4	6
SST	−6.1	39.4	7	10
SSQ	1.9	40.0	9	10
SSU	−0.8	36.3	8	4
SSP	1.4	46.0	7	10
Mean	2.3	40.2		
95% C.I.	−3.0–7.6	37.0–43.5		

TABLE II. Adults' thresholds (dB SPL) in quiet and broadband noise and CoRE model parameters, *n* (number of auditory filters) and *W* (attentional bandwidth in kHz), for best fits to the thresholds from the random, multitone masker conditions.

ID	Quiet	Noise	*n*	*W*
SSJ	0.4	34.7	1	2
SSH	−4.5	32.5	1	1
SQW	−3.8	36.2	1	1
SUA	−2.3	32.9	1	2
SSX	−3.1	34.3	1	2
SUC	−0.2	29.3	5	3
SNK	3.2	29.1	1	1
SSO	−3.6	35.1	1	1
Mean	−1.7	33.0		
95% C.I.	−3.9;0.5	30.8;35.2		

is most likely a result of slight errors in the headphone calibration procedure. [There are several features of the headphone calibration procedure that could lead to small errors in absolute SPL levels. First, it involved loudness balancing, a subjective procedure, and reference was made to a different headphone (TDM-49) that had been calibrated on a coupler, not on either an adult or child's ear. At the target frequency of 1000 Hz, we feel these errors would be less than 5 dB.] Since most results from these experiments are reported in terms of differences between thresholds (amount of masking), these calibration issues are inconsequential. It is also the case that in terms of signal-to-noise ratio (sometimes expressed as E/No), the noise-masked thresholds are also lower than previously reported (e.g., Allen and Wightman, 1994), and this is probably a result of the fact that the noise spectrum excluded frequencies in a band around the signal frequency. As Tables I and II show, the children's quiet thresholds were not significantly different from those of adults, but the children's noise-masked thresholds were significantly higher (about 7 dB on average).

As reported in previous studies, individual differences in the slopes and thresholds of the psychometric functions were larger for the children than for the adults (Allen and Wightman, 1994; Allen and Wightman, 1995). Some children's psychometric functions were adultlike. Most of the children produced shallower psychometric functions and higher thresholds. The psychometric functions of two children did not always asymptote at 100%, which implies that they may simply have been inattentive on some proportion of the trials (Schneider and Trehub, 1992; Wightman and Allen, 1992).

Thresholds (and 95% confidence limits) obtained in the presence of multitone distracters are plotted in Figs. 2 (Children) and 3 (Adults). The listener's age at the time of the first session is indicated in each panel. The filled symbols indicate total masking (dB difference between signal threshold in quiet and in the presence of the distracter) for a fixed number of distracter components. Horizontal lines represent total masking when the signal was presented in broadband noise. The open symbols shown in Fig. 2 for two of the listeners represent data from a retest series of sessions conducted approximately one month after the first series of sessions had been completed. Only two of the children were available for such retests.

The data from both adults and children are characterized by large individual differences. Consider first the data from the children (Fig. 2). Note that the maximum amount of masking varies over at least a 20 dB range (roughly 65–85 dB), and although the maximum occurs with from 10–100 distracter components for each listener, there are dramatic differences in the shape of the function relating masking to number of distracter components. It seems clear that even eight listeners cannot adequately represent the range of possible performance in preschool children. Note also that the replications suggest improved performance (smaller amounts of masking) in both cases. This result is consistent with previous observations (Oh and Lutfi, 1998) and probably represents a practice effect. For the adults, the maximum total amount of masking ranges from 30 to 60 dB for those same distracters.

Next consider the results from the adult listeners (Fig. 3). Just as in the group of children, maximum masking varies over at least a 20 dB range and there are large individual differences in the shape of the function relating masking to number of distracter components. Most remarkable in the adult data is the fact that half of the listeners appear to be the kind of ''low-threshold'' listeners described by Neff and Dethlefs (1995) and by Oh and Lutfi (1998). These listeners do not demonstrate masking with random multitone complexes in excess of that produced by a broadband noise. In Fig. 3, these are the listeners (SSO, SNK, SQW, and SSH) who produced functions that remained at or below the horizontal line. In the previous studies the proportion of ''low-threshold'' listeners was relatively low, but in this study at least half of the listeners appeared to be in the ''low-threshold'' category. The reasons for this might relate to the combination of two procedural features in this study that could allow listeners to focus attention on the target stimulus. First, an unmasked cue was presented on every trial, and second, the stimulus level did not change adaptively, hovering near threshold, but according to a staircase rules that guarantee a large proportion of suprathreshold trials. Of course, given the small number of listeners tested, it is also possible that the results reflect nothing more than sampling variability.

Finally, consider the differences between the data produced by the children and by the adults. The children demonstrated only slightly (about 3 dB on average) greater amounts of masking with the broadband noise (horizontal lines) than the adults. Since masking with a fixed, broadband noise masker is assumed to involve primarily energetic masking, this result suggests some similarity between adults and children in energetic masking. However, in most conditions involving a random, multitone distracter, children produced considerably more masking than the adults. One striking difference can be observed for distracters consisting of only two components. All of the adult listeners showed masking less than that produced by the broadband noise, but all but one of the children show masking more than 20 dB greater than that produced by broadband noise. A similar statement could be made about distracters consisting of 200 components. It is also important to note the potential impact of procedural factors on the results from the children. Chil-

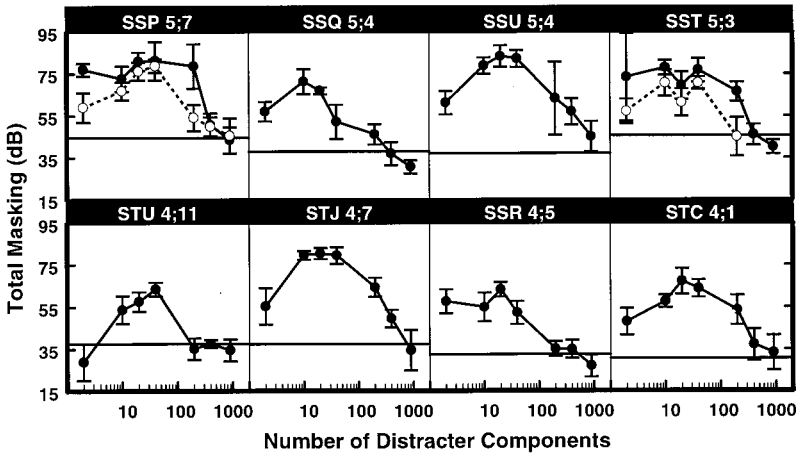

FIG. 2. Individual masking functions for eight preschool children. Each circle represents total masking (masked threshold minus quiet threshold) for a fixed number of distracter components. Error bars indicate 95% confidence intervals estimated according to maximum likelihood techniques described by Bush (1963). Horizontal lines represent total masking for broadband noise samples. The unfilled circles and dashed lines indicate data from conditions replicated one month after the completion of the main experiment. The age of the child at the time of first session is specified in each panel.

dren and adults were tested with the same procedure. Thus, it is possible that the cue and the nonadaptive trial structure might have helped both children and adults to focus attention on the target and in this way reduce informational masking. The implication is that without those procedural features both children and adults might have produced more informational masking. Unfortunately the data presented here do not allow resolution of this issue.

Figure 4 summarizes the data. Mean amounts of masking are shown (* symbols) for both adults (dashed line) and children (solid line), along with means from a related study (Oh and Lutfi, 1998, dotted line). Data from each individual listener in the present study are also shown (filled symbols for children and open symbols for adults). This figure highlights three features of the data from this study. First, the large individual differences are obvious. In many conditions the range of masking is more than 30 dB for both adults and children. Although there is little overlap of the data from children and adults, it is clear that conclusions based on mean data are not warranted. Second, the differences between the adult and child data are greatest with distracters consisting of small numbers of components. Third, the adult data from this study are different from the data obtained in previous studies, especially for distracters consisting of small numbers of components.

IV. DISCUSSION

This study measured the ability of preschool children to detect a fixed frequency tone embedded in a multitone distracter with frequencies that varied randomly on each presentation. The fact that nearly all psychometric functions asymptoted at 100% correct attests to the attentiveness of the children. Nevertheless, large elevations in thresholds with random distracters were observed in all children. The distracters produced 65–83 dB of masking when they were comprised of 10–40 components. With adult listeners the threshold elevations were generally much lower, although individual differences were quite large.

As reported in previous studies, young children's thresholds are higher than those from adult listeners in most auditory detection and discrimination tasks. The rather surprising result of this study is the magnitude of this difference when a signal is presented with a distracter that varies randomly on each presentation. When a pure tone or complex signal is presented in quiet or in the presence of stationary narrowband or wideband noise, adult–child detection threshold differences are relatively small, ranging from 4 dB to 10 dB (Allen and Wightman, 1992; Allen *et al.*, 1989; Elliott and Katz, 1980; Jensen and Neff, 1993). When a single, fixed level, random frequency distracter tone is added to a broad-

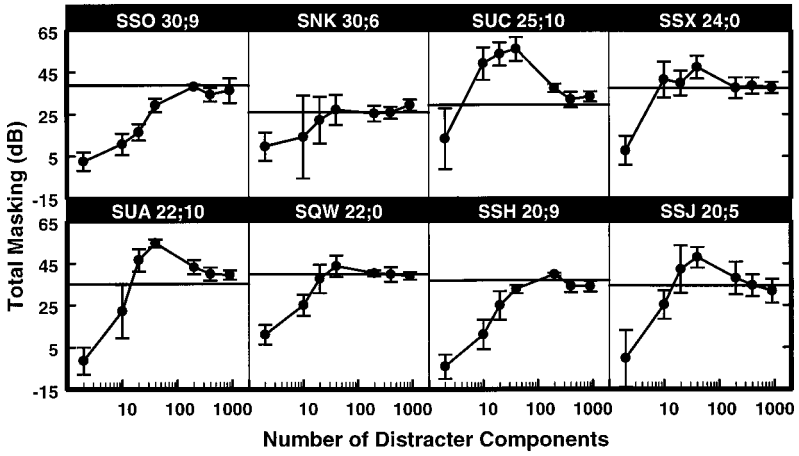

FIG. 3. Individual masking functions for eight adults. Each circle represents total masking (masked threshold minus quiet threshold) for a fixed number of distracter components. Error bars indicate 95% confidence intervals computed as for Fig. 2. Horizontal lines represent total masking for broadband noise samples. The listener's age is provided in each panel.

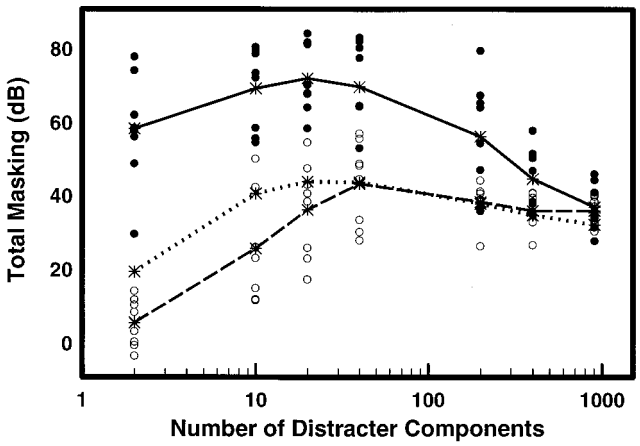

FIG. 4. The total masking for individual listeners in each age group (children: filled circles, adults: open circles). The mean functions are indicated by the solid and dashed lines (with means marked by *) for children and adults, respectively. The dotted line represents the mean data obtained from 11 adults reported in Oh and Lutfi (1998).

band noise, adult–child differences are at least 25 dB (Allen and Wightman, 1995). The result from this study show that adult–child differences can be more than 50 dB when a multitone distracter varies at random on each presentation.

In this section, we examine possible sources for the adult–child differences. Age-dependent changes in anatomy of physiology seem improbable. There is some evidence that the auditory system continues developing after birth. For instance, animal studies suggest that there are systematic changes in the tonotopic organization in the cochlea as a function of age (Lippe and Rubel, 1983). Also, there are age-dependent changes in the anatomy of the ear (e.g., ear canal size) that continue even after age five (Schneider *et al.*, 1986). Nevertheless, these anatomical developments occur early and most auditory structures are adult-like at birth. It appears unlikely, therefore, that the large differences we obtained between preschool children and adults (and the large differences within groups) could derive from structural and functional immaturities in the auditory peripheral system. Also, given the fact that most estimates of the bandwidth of the auditory filter do not seem to change from preschool to adulthood (Hall and Grose, 1991; Schneider *et al.*, 1990), we expect relatively small adult–child differences in energetic masking, those being caused by differences in the ''efficiency'' parameter of the common filter model of masking. Rather we suspect that the differences between adults and preschool children in performance in this study mainly result from differences in informational masking. In order to quantify these differences, we applied a model that has been used successfully to quantify differences in informational masking in adults.

The component-relative-entropy (CoRE) model: Results from studies similar to that reported here have been shown to be well predicted by the CoRE model (Lutfi, 1993). In the model, listeners are assumed to adopt a maximum-likelihood decision rule. Informational masking is thought to result from an imperfect implementation of the decision rule, which can be described as a failure to ignore irrelevant information that varies on each presentation. The CoRE model

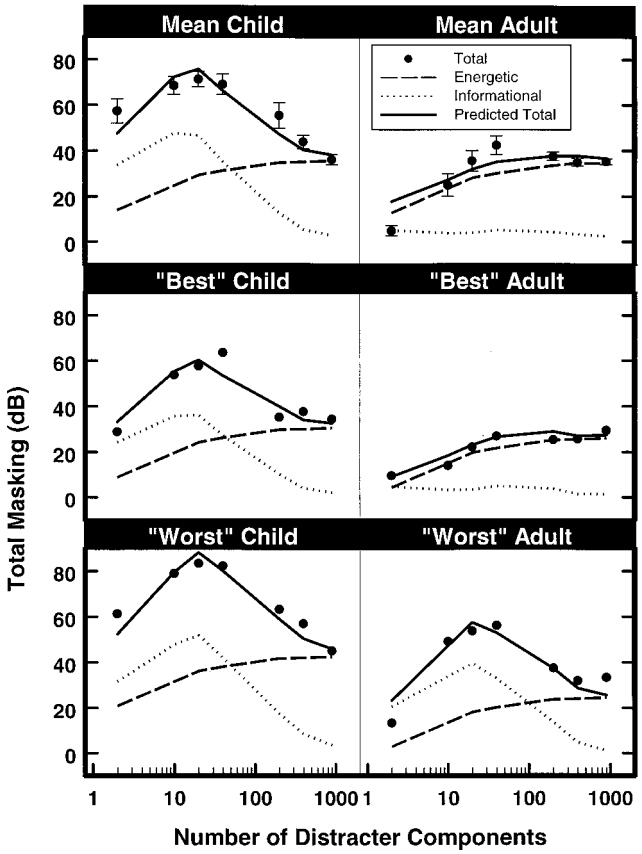

FIG. 5. The total masking and the predictions of the CoRE model for the average child (upper left panel) and average adult (upper right panel). The total masking and predictions for the ''best'' (STU and SNK) and ''worst'' (SSU and SUC) listeners in each age group are in the middle and lower panels, respectively. For the purpose here, ''best'' and ''worst'' refer to least and most amounts of informational masking. The error bars indicate 1 standard error. The predictions of the model for the total masking (solid line) are given by adding the estimates of energetic (dashed line) and informational masking (dotted line).

was applied to the mean data in the present study. Figure 5 (top panels show mean data) shows the agreement between the predictions of the model and the total masking averaged over individual listeners in each age group. The total masking predicted by the CoRE model (solid line) is the dB sum of the estimates of energetic (dashed line) and informational masking (dotted line). The process of estimating energetic and informational masking is described in detail in the analysis section of Oh and Lutfi (1998). Briefly, a three-parameter ROEX filter (Patterson *et al.*, 1982) was applied to estimate the amount of energetic masking produced by distracters in a given experimental condition. The same values of filter parameters are used for the children and the adults, since the bandwidth of the auditory filter does not seem to change from preschool to adulthood (Hall and Grose, 1991; Schneider *et al.*, 1990). The differences in the estimates of energetic masking between the adults and children are assumed to arise from differences in the efficiency of the detection process (K). For our purposes here the value of K was chosen such that the signal threshold predicted by the model would converge near the mean threshold obtained from the listeners for the broadband noise condition (cf. Patterson

et al., 1982). As shown in this figure, the estimates of energetic masking (dashed line) from the mean data in the two age groups are similar.

The estimates of informational masking (dotted line) depend on two free parameters of the model [see Eq. (8) in Oh and Lutfi (1998)]. They are the width of the ''attentional band'' (W), and the number of independent auditory filters (n) from which information is integrated within the attentional band. The attentional bandwidth determines the basic shape of the masking function (function relating total masking to number of distracter components). The number of auditory filters serves as a scaling factor on the masking function: larger amounts of informational masking are predicted as n increases. With best-fitting choices for the two parameter values, informational masking estimated by the CoRE model is 30–50 dB in the children and less than 5 dB in the adults. The best fitting parameter values are $W=7$ kHz and $n=7$ for the children, while they are $W=1$ kHz and $n=1$ for the adults. Since the basic shape of the masking function is the same for children and adults, the results suggest that children may monitor the outputs of many auditory filters that are irrelevant to the task. The masking functions for half of the adults (low-threshold listeners) show little informational masking. Thus, those results are consistent with the predictions of the traditional auditory filter model wherein masking is determined by the energy at the output of a single auditory filter centered at the signal frequency (see Patterson, 1976). Overall, the agreement between the obtained and the predicted amount of total masking is good in both groups. This suggests that the discrepancy between children and adults derives primarily from differences in attentional factors rather than differences in the functioning of the auditory periphery (e.g., Viemeister and Schlauch, 1992; Wightman and Allen, 1992). The extent to which those attentional factors may have interacted with procedural details (e.g., the presence of the cue and the nonadaptive trial structure) is unclear.

Care must be taken in interpreting the values of W reported here as an estimate of the listener's true attentional bandwidth. For a number of reasons, large changes in the value of W have a relatively small effect on the predicted shape of the masking function; in effect, serving to shift the peak of the function slightly to the right or left. Because of the relative insensitivity of W as an estimate of listener attention, we refrain from drawing any inferences about child–adult differences in performance based on this parameter.

The model was also applied to the individual data. Fits of the model to the data from two adults and two children are shown in Fig. 5. These specific listeners were selected from each group to represent the most (''worst'') and least (''best'') amounts of informational masking obtained from the group. The model fits reveal that the difference between the children and the adults can be explained primarily by differences in the parameter n, the number of auditory filters over which the listener integrates information within the attentional band. The best fitting values of n and W for individual adult and child listeners are given in Tables I and II. Compared to the adults the children seem to integrate information over a larger number of auditory filters.

The modeling results are encouraging since they allow us to quantify the reduced auditory processing capabilities of children that are often attributed to immaturity of attentional mechanisms or poor attentional control (Allen and Wightman, 1994; Allen and Wightman, 1995; Stellmack *et al.*, 1997; Wightman and Allen, 1992).

V. SUMMARY

(1) A preschool child's ability to listen selectively to a fixed-frequency signal in the presence of multitone distracters was severely degraded in conditions in which the distracters varied on each presentation. The total masking observed in children was as much as 83 dB for distracters with 10–40 components.

(2) Data from both children and adults were characterized by large individual differences, such that statements about overall adult–child differences in performance in any one condition seem unwarranted.

(3) Both the individual and the group masking functions were well described by the CoRE model with two free parameters, suggesting a means by which the effects of attentional factors in children and adults can be quantified.

ACKNOWLEDGMENTS

The authors would like to thank Dr. Doris Kistler, Sara Conzemius, Jen Junion Dienger, and the teachers at the Waisman Center Early Childhood Program for their contributions to the research. This research was supported by grants from the National Institutes of Health (Grants Nos. R01 HD23333 and R01 CD01262-9).

ANSI (**1989**). ANSI S3.9-1989, ''American National Standard specification for audiometers'' (American National Standards Institute, New York).

ANSI (**1987**). ANSI S3.9-1987, ''American National Standard specification for instruments to measure aural acoustic impedance and admittance (aural acoustic immittance)'' (American National Standards Institute, New York).

Allen, P., Wightman, F. L., Kistler, D. L., and Dolan, T. R. (**1989**). ''Frequency resolution in children,'' J. Speech Hear. Res. **32**, 317–322.

Allen, P., and Wightman, F. L. (**1992**). ''Spectral pattern discrimination by children,'' J. Speech Hear. Res. **35**, 222–233.

Allen, P., and Wightman, F. L. (**1994**). ''Psychometric functions for children's detection of tones in noise,'' J. Speech Hear. Res. **37**, 205–215.

Allen, P., and Wightman, F. L., (**1995**). ''Effects of signal and masker uncertainty on children's detection,'' J. Speech Hear. Res. **38**, 503–511.

Bush, R. R. (**1963**). ''Estimation and evaluation,'' in *Handbook of Mathematical Psychology: Volume I*, edited by R. D. Luce, R. R. Bush, and E. Galanter (Wiley, New York), p. 441.

Elfenbein, J. L., Small, A. M., and Davis, J. M. (**1993**). ''Developmental patterns of duration discrimination,'' J. Speech Hear. Res. **36**, 842–849.

Elliott, L. L., and Katz, D. R. (**1980**). ''Children's pure tone detection,'' J. Acoust. Soc. Am. **67**, 343–344.

Hall, J. W., III, and Grose, J. H. (**1991**). ''Notched-noise measures of frequency selectivity in adults and children using fixed-masker-level and fixed-signal-level presentation,'' J. Speech Hear. Res. **34**, 651–660.

Irwin, R., Ball, A., Kayt, N., Stillman, J., and Rosser, J. (**1985**). ''The development of auditory temporal acuity in children,'' Child Dev. **56**, 614–620.

Jensen, J. K., and Neff, D. L. (**1993**). ''Development of basic auditory discrimination in preschool children,'' Psychol. Sci. **4**, 104–107.

Lippe, W., and Rubel, E. W. (**1983**). ''Development of the place principle: Tonotopic organization,'' Science **219**, 514–516.

Lutfi, R. A. (**1993**). ''A model of auditory pattern analysis based on component-relative-entropy,'' J. Acoust. Soc. Am. **94**, 748–758.

Neff, D. L., and Dethlefs, T. M. (**1995**). ''Individual differences in simultaneous masking with random-frequency, multicomponent maskers,'' J. Acoust. Soc. Am. **98**, 125–134.
Neff, D. L., and Green, D. M. (**1987**). ''Masking produced by spectral uncertainty with multicomponent maskers,'' Percept. Psychophys. **41**, 409–415.
Oh, E. L., and Lutfi, R. A. (**1998**). ''Nonmonotonicity of informational masking,'' J. Acoust. Soc. Am. **104**, 3489–3499.
Patterson, R. D. (**1976**). ''Auditory filter shapes derived with noise stimuli,'' J. Acoust. Soc. Am. **59**, 640–654.
Patterson, R. D., Nimmo-Smith, I., Weber, D. L., and Milroy, R. (**1982**). ''The deterioration of hearing with age: Frequency selectivity, the critical ratio, the audiogram, and speech threshold,'' J. Acoust. Soc. Am. **72**, 1788–1803.
Pollack, I. (**1975**). ''Auditory informational masking,'' J. Acoust. Soc. Am. **57**, S5.
Schneider, B. A., and Trehub, S. E. (**1992**), ''Source of developmental changes in auditory sensitivity,'' in *Developmental Psychoacoustics*, edited by L. A. Werner and E. W. Rubel (APA, Washington, DC), pp. 3–46.
Schneider, B. A., Trehub, S. E., Morrongiello, B. A., and Thorpe, L. A. (**1986**). ''Auditory sensitivity in preschool children,'' J. Acoust. Soc. Am. **79**, 447–452.
Schneider, B. A., Morrongiello, B., and Trehub, S. E. (**1990**). ''The size of the critical band in infants, children, and adults,'' J. Exp. Psychol. **16**, 642–652.
Spiegel, M. F., Picardi, M. C., and Green, D. M. (**1981**). ''Signal and masker uncertainty in intensity discrimination,'' J. Acoust. Soc. Am. **70**, 1015–1019.
Stellmack, M. A. Willihnganz, M. S., Wightman, F. L., and Lutfi, R. A. (**1997**). ''Spectral weights in level discrimination by preschool children: Analytic listening conditions,'' J. Acoust. Soc. Am. **101**, 2811–2821.
Trehub, S. E., Schneider, B. A., and Henderson, J. L. (**1995**). ''Gap detection in infants, children, and adults,'' J. Acoust. Soc. Am. **98**, 2532–2541.
Viemeister, N. F., and Schlauch, R. S. (**1992**). ''Issues in infant psychoacoustics, in *Developmental Psychoacoustics*, edited by L. A. Werner and E. W. Rubel (APA, Washington, DC), pp. 191–209.
Wightman, F. L., and Allen, P. (**1992**). ''Individual differences in auditory capability among preschool children,'' in *Developmental Psychoacoustics*, edited by L. A. Werner and E. W. Rubel (APA, Washington, DC), pp. 113–133.

Using statistical decision theory to predict speech intelligibility. I. Model structure

Hannes Müsch and Søren Buus
Communications and Digital Signal Processing Center, Department of Electrical and Computer Engineering (442 DA) and Institute for Hearing, Speech, and Language, Northeastern University, Boston, Massachusetts 02115

(Received 6 March 2000; accepted for publication 23 March 2001)

This article introduces a new model that predicts speech intelligibility based on statistical decision theory. This model, which we call the speech recognition sensitivity (SRS) model, aims to predict speech-recognition performance from the long-term average speech spectrum, the masking excitation in the listener's ear, the linguistic entropy of the speech material, and the number of response alternatives available to the listener. A major difference between the SRS model and other models with similar aims, such as the articulation index, is this model's ability to account for synergetic and redundant interactions among spectral bands of speech. In the SRS model, linguistic entropy affects intelligibility by modifying the listener's identification sensitivity to the speech. The effect of the number of response alternatives on the test score is a direct consequence of the model structure. The SRS model also appears to predict the differential effect of linguistic entropy on filter condition and the interaction between linguistic entropy, signal-to-noise ratio, and language proficiency. © *2001 Acoustical Society of America.* [DOI: 10.1121/1.1371971]

PACS numbers: 43.66.Ba, 43.71.An, 43.71.Es [RVS]

I. INTRODUCTION

Macroscopic models of speech recognition are tools for research and engineering. They aim to predict the average intelligibility of a large amount of speech input from measurable parameters of the transmission system, the hearing acuity of the listener, and the linguistic entropy (van Rooij and Plomp, 1991) of the speech material. Macroscopic models are distinguished from microscopic models, which look at details of the signal such as voice-onset time and formant transitions. Macroscopic models analyze the long-time-average power spectrum of the speech, where the average is taken across many talkers and speech materials. Most macroscopic models disregard all phase information and only analyze power spectra of signals that are considered to be stationary. One exception is the speech transmission index (Steeneken and Houtgast, 1980; see also clause 5.2 in ANSI S3.5, 1997), which analyzes the modulation spectrum in addition to the power spectrum.

Whereas macroscopic models may seem crude, they have proven to be extremely useful in the design of communication systems. The successful development of the American telephone system in the first decades of the last century was based in part on a macroscopic model of speech recognition that became known as the articulation index (AI; French and Steinberg, 1947; Beranek, 1947; Fletcher and Galt, 1950). The need for reliable communication under adverse listening conditions, as encountered in military applications, was the driving force behind efforts to simplify and standardize the articulation index. As a result, an easily applicable method was devised (Kryter, 1962a) and tested (Kryter, 1962b). This method became the basis for the standardized AI procedure (ANSI S3.5, 1969). More recently, the standard has been replaced by the speech intelligibility index, SII (ANSI S3.5, 1997), which reintroduced some of the concepts embodied in earlier AI models and implemented new ones. One other model, the speech transmission index (STI; Steeneken and Houtgast, 1980), is based on the AI, but derives speech-to-noise ratios from modulation-transfer functions. The STI is frequently used in room acoustics.

The usefulness of macroscopic speech-recognition models in other fields is still under debate. Rankovic (1991) studied whether the AI could be used for hearing-aid fitting. She found that maximizing the AI resulted in suboptimal fits. However, her finding may only reflect that the AI in its current form is not suitable for this application (Dubno *et al.*, 1989; Kamm *et al.*, 1985). A more appropriate model of speech intelligibility may allow the selection of an ''optimal'' hearing-aid setting. Finally, macroscopic speech-recognition models may influence the development of automatic-speech-recognition algorithms by directing attention to the fact that speech does not have to be broadband to be highly intelligible (Allen, 1994; Lippmann, 1996).

Although the articulation-index-based procedures are very successful in predicting intelligibility in many listening conditions, they have several shortcomings that warrant a search for alternatives. As discussed further below, one such shortcoming is the AI model's inability to account for synergetic and redundant interactions among the various spectral regions of the speech spectrum. This article introduces the structure of a model that was designed to account for these synergetic and redundant interactions. To appreciate the utility of the new model, it is useful to contrast it with the established AI models. In doing so, the meaning of synergetic and redundant band interaction will be explained.

The main purpose of AI models is to predict performance in speech-recognition tests in which the speech signal's audibility is manipulated by filtering, masking, and/or

adjustments of the overall speech level. As part of the prediction, the AI—an intermediate variable that is a measure of speech intelligibility—is derived from the audibility of the speech signal in a number of adjacent spectral regions (speech bands). Each band makes a contribution to the AI that is independent from the AI contributions of the other bands. Speech-test scores expressed as percentage of correct responses are derived from the AI through a transformation that is test-material and test-format specific. Different transformations must be used when the number of items in the set of test stimuli changes. Different transformations must also be used for different levels of constraints placed upon the message set. For example, low-predictability sentences require a different transformation than high-predictability sentences. Consequently, a large set of transformation functions is needed to accommodate the large number of possible speech-material/test-format combinations. With the exception of a transformation for open-set phoneme recognition in a nonsense context (Fletcher and Galt, 1950), all of these transformations are derived empirically.

The idea that frequency bands contribute independently to AI results from the observation that the probability of erring in the recognition of a phoneme in a broadband listening condition is (nearly) equal to the product of the error probabilities that are measured when the speech bands that form the broadband condition were tested in isolation. A combination rule that is based on multiplication of the error probabilities indicates that the errors in the individual bands are independent. When the error probability in a broadband condition is less than the product of the error probabilities in the individual subbands, the bands interact with synergy. Conversely, when the error probability in the broadband condition is larger than the product of the error probabilities in the individual bands, the bands are considered to carry redundant information.

The articulation index has been developed and verified for listening situations in which the speech signal is audible in one contiguous frequency region, as in low-pass, high-pass, or single-bandpass filtered speech. It is not valid for multiple disjoint passbands. The ANSI (1969) standard states that the articulation index will not provide a valid estimate of intelligibility when the long-term speech spectrum goes through a series of peaks and valleys with average slopes exceeding 18 dB/oct. Similarly, sharply filtered noises that create disconnected speech bands are excluded from the scope of the revised ANSI standard (ANSI, 1997). When the audible speech spectrum is partitioned into two or more spectrally disjoint frequency bands (e.g., when the mid-frequency part of the speech spectrum is blocked out by a band-stop filter) intelligibility systematically exceeds the predictions made by AI models (Kryter, 1962b; Grant and Braida, 1991). Moreover, Ching *et al.* (1998) found that in hearing-impaired listeners the measured intelligibility in a broadband condition is larger than predicted from the summed contributions of octave bands within the same bandwidth. However, the same was not true in normals. Together, these findings indicate that synergetic interactions may occur among spectrally disjoint bands of speech.

One particularly impressive example of synergetic interaction was reported by Warren *et al.* (1995). They tested the intelligibility of everyday sentences filtered into single speech bands or into two widely separated bands. When the speech was presented in a $\frac{1}{20}$-oct-wide band centered at 370 Hz, only 0.9% of all keywords were reported back correctly. When the speech was presented in a $\frac{1}{20}$-oct-wide band centered at 6000 Hz, 10.4% of all keywords were recognized correctly. When both bands were presented simultaneously, the score increased dramatically to 27.8% correct keyword recognition. Multiplication of the error rates for the two individual bands yields a predicted recognition of just 11.2% for the two bands presented together. Clearly, the low-frequency band, whose intelligibility contribution in isolation is very small, contributes significantly to intelligibility when presented in conjunction with the high-frequency band. Articulation index models cannot produce synergy by raising the AI value because the total AI is the sum of the band AIs, which are determined independently. Therefore, AI models attempt to account for synergetic interaction by adjusting the form of the transformation between AI and test score. However, the transformation cannot be adjusted freely to account for synergetic interaction between speech bands because the form of the transformation must also account for the increase in test score that results from audibility increases in any given band. Such constraints ultimately led to the exclusion of listening conditions that produce strong synergetic interactions from the scope of the AI.

Recently, Steeneken and Houtgast (1999) proposed a modification of the speech transmission index (STI) that is equally applicable to the articulation index. In this modification, the contribution to the articulation index by each octave band of speech can be lowered depending on the contribution of the adjacent lower-frequency band. Whereas this approach can model the redundant band interaction between adjacent octave bands, it cannot account for the synergetic band interaction discussed above.

The goal of the present work is to develop a model that can accurately predict intelligibility in listening conditions with multiple, spectrally disjoint speech bands—conditions excluded from the scope of AI models. To do so, the model must be able to predict synergetic interaction between speech bands. In addition, the model should account for the dependence of test scores on the number of response alternatives given to the listener without having to resort to empirical correction functions. Finally, the effect of linguistic entropy on the test score should be modeled by simple, intuitive relations.

To these ends, a model structure based on statistical decision theory was examined. The application of statistical decision theory to speech recognition was first investigated by Green and Birdsall (1958). The current model combines their ideas with the framework of a model for discrimination of broadband signals, which was described by Durlach *et al.* (1986). For brevity, the model to be introduced in this article will be referred to as the speech recognition sensitivity (SRS) model, because it involves the calculation of a sensitivity index that describes the listeners' identification sensitivity to speech.

The next section of this article outlines the structure of

the SRS model. In Sec. III we discuss the model behavior and show that the model can predict several phenomena described in the literature. In particular, it will be shown that the SRS model predicts (a) synergetic interaction between frequency bands as measured by Warren *et al.* (1995), (b) interactions between listening condition, test material, and size of the response set as described by Kryter (1962a), and (c) interactions between linguistic entropy and filter condition as measured by Hirsh *et al.* (1954). The SRS model also appears to predict the interaction among linguistic entropy, signal-to-noise ratio (SNR), and language proficiency of the listener. Results of SRS-model fits to data collected by the authors are presented in a companion article (Müsch and Buus, 2001).

II. MODEL STRUCTURE

Durlach *et al.* (1986) suggested a model structure for the discrimination of stationary broadband sounds. The emphasis of their model was on cross-channel processing, with a focus on processing central to the auditory periphery. Durlach *et al.*'s (1986) model was cast in the framework of statistical decision theory and their ideas are applicable to a macroscopic model of speech recognition. The speech signal is considered to be stationary, because only the long-term average of the speech spectrum is analyzed. In general, the speech signal is broadband and the model combines the speech information across different bands. Signal processing central to the auditory periphery is included in the model to account for the effects of linguistic entropy on speech intelligibility. The modeling of peripheral and central auditory processes is facilitated by statistical decision theory, which Green and Birdsall (1958) have shown to be an appropriate framework for speech recognition models. Their reasoning is outlined below.

A. Applicability of statistical decision theory to speech recognition

The concept of statistical decision theory implies the existence of an ''ideal'' signal, which is the speech waveform the listener expects to hear. If the talker and listener share the same linguistic background, the talker will attempt to produce an ''ideal'' signal. However, due to limitations in the accuracy of articulation, the actual speech only approximates this ideal signal. The difference between the ideal signal and the signal actually produced is a production-related noise. Together with noises introduced in the transmission channel and/or the listener's auditory system, this noise determines the intelligibility of the signal. Intelligibility depends on the relation between the power of the ideal signal and the power of the combined noises.

Green and Birdsall (1958) verified the appropriateness of this approach by showing that performance in a closed-set word-recognition task changes with the number of response alternatives as predicted by optimal decision theory. They proposed a simple model in which each word of the test set is represented by a unique waveform, the ideal signal. All word-defining waveforms are assumed to be orthogonal to one another. The receiver cross correlates the received word with a template of every expected word. If the talker produced the ideal signal and the transmission channel and the receiver did not add noise to the signal, the correlation between the presented waveform and any template would be zero with the exception of the correlation between the signal and the template of the target word, which would be one. This results because the waveforms in the test set are all orthogonal. In this example, listeners were expected to discriminate among words and only words were valid response alternatives. Because each test item to be recognized is thought to be represented by a unique template, the templates were at the word level. Had the test been to discriminate among speech sounds of a different level (e.g., if the listeners had to discriminate among phonemes or among syllables), the templates would have been at the corresponding level (i.e., phoneme or syllable templates).

In practice, however, the receiver only has access to a noise-degraded version of the ideal representation. As a consequence, the correlations will vary from presentation to presentation. Each correlation becomes a random variable. These correlations can be transformed such that all random variables have zero means, except for the correlation between the signal and the target template, whose mean is greater than zero (Green and Birdsall, 1958). The variance of all random variables is constant and is determined by the power of the interfering noises. These simple concepts allow statistical decision theory to be used for determining how well the signals can be discriminated. According to Green and Birdsall's (1958) model, which assumes an optimal detector, the probability that the presented word is identified correctly is equal to the likelihood that the transformed correlation between the signal and the target template is larger than the transformed correlation between the signal and any other template. Clearly, this likelihood diminishes as the noise power increases and decreases as the number of templates with which the signal is correlated increases.

If the noises, whose origin will be described later, have Gaussian distributions, listeners' performance is described by their sensitivity, d', which is the mean of the distribution of the transformed correlations for the target word measured in units of standard deviation of the random variables. The dependence of performance on the number of templates, M, for any d' is easily quantified (Hartmann, 1998) as

$$P_c = \int_{-\infty}^{\infty} f_{SN}(x,d',1) \cdot F_N^{M-1}(x,0,1)\, dx, \tag{1}$$

where P_c is the proportion of test items identified correctly, $f_{SN}(\cdot,d',1)$ is the Gaussian probability density function with mean d' and unit variance, and $F_N(\cdot,0,1)$ is the cumulative Gaussian probability function with zero mean and unit variance. The sensitivity index d' is the ratio of the mean of the transformed correlation between the signal and the target template to the standard deviation of the performance-limiting noise. Examples of transformations generated by Eq. (1) are shown in Fig. 1. If Eq. (1) predicts how measured performance changes with the number of templates, M, one would conclude that Green and Birdsall's (1958) assumption of mutually orthogonal ideal signals is appropriate for the prediction of speech intelligibility.

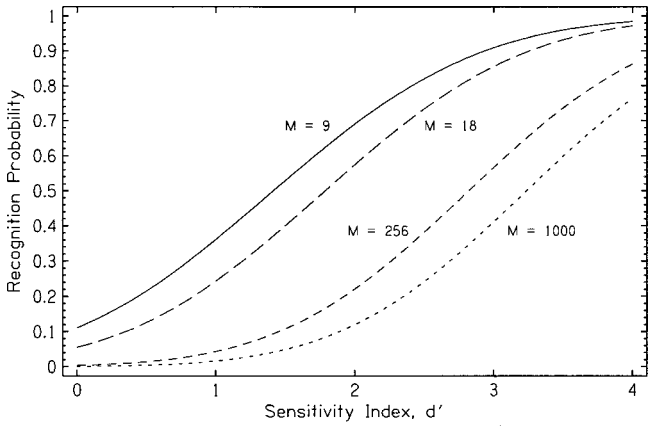

FIG. 1. The relation between the sensitivity index, d', and the probability, p, of correct recognition. This relation is described by Eq. (1). The parameter is the number of response alternatives, M.

Miller *et al.* (1951) measured the proportion of monosyllabic words identified correctly as a function of SNR for various sizes of the test set. As expected, Miller *et al.*'s (1951) data show that performance increases with SNR and that performance at any given SNR increases as the size of the test set decreases. For example, 27% of all words drawn from a known set of 256 words were reported back correctly at a SNR of -9 dB. The proportion of correct responses increased to 63% and 97% when the size of the stimulus set was reduced to 32 and 2, respectively. Green and Birdsall (1958) assumed that the number of templates with which the listeners correlated the perceived signal was equal to the number of test items in the word list. They inverted Eq. (1) to find, for each SNR and stimulus-set size M, the d' that corresponded to the measured performance. When the d's for the various test-set sizes were plotted as a function of SNR, Green and Birdsall (1958) found that the data points could be summarized by a single curve. This indicates that Eq. (1) provides a good description of the effect of test-set size. Accordingly, Green and Birdsall (1958) concluded that the one-of-M-orthogonal-signals hypothesis was a good approximation of a forced-choice speech-recognition task.

An evaluation of the one-of-M-orthogonal-signals hypothesis was necessary, because it is known that the presumed ideal speech waveforms are not orthogonal. If the waveforms were in fact orthogonal, all incorrect responses for any target would be distributed uniformly among all incorrect alternatives, which they are not (Miller and Nicely, 1954). Instead, confusions in discrimination tests show distinct clusters, indicating that some items are more often confused than others. This implies that the ideal waveforms are partially correlated, and that the correlation between some waveforms is higher than the correlation between others. Correlations between the ideal signals are equivalent to nonzero means of the decision variables for some nontargets when a given target is presented. Green and Birdsall's (1958) results indicate that these deviations are small compared to the variances of the variables and can be ignored as long as one is only interested in the overall percentage of correct recognition.

The structure of the proposed model as well as the presumed sources of the performance-limiting noises will be described in the remainder of this section. The SRS model can be divided into three stages. The first stage models information processing in the auditory periphery. Here, the mean of the transformed correlation between the signal and the target template as well as the powers of the production-related noises, acoustic maskers, and noises generated in the auditory periphery are derived from the listening condition and the listener's hearing acuity. The second stage models the effects of linguistic entropy on speech intelligibility. The third stage models the effect of the number of response alternatives in the test on test results. In the following, each stage will be discussed in detail.

B. First stage of the model: Auditory periphery

The SRS model assumes that the auditory representation of the received signal is correlated with internal templates of every expected word. The correlations are random variables that can be transformed such that their mean is zero for correlations between the signal and nontarget templates and greater than zero for the correlation between the signal and the target template. The mean transformed correlation between the signal and the target template is an important variable in the SRS model and will be called the congruence index, Δ. It is a measure of how well, on average, the auditory representation of the received waveform matches the listener-internal template. In the signal-detection framework, the congruence index can be considered to be the expected value of the decision variable for the target.

Note that development of the model does not require specification of the internal representation, nor does it require the transformation between correlation coefficient and decision variable to be known. As long as equal-variance, normally distributed decision variables corresponding to each possible response can be assumed to exist and these variables are mutually orthogonal, signal-detection theory provides a framework for predicting the overall percentage of correct responses. Green and Birdsall (1958) showed that correlations between the speech signal's time waveform and the template can be transformed into random variables. We used their argument to motivate the model presented in the previous subsection and will, for the sake of a consistent terminology, continue to refer to the property that gives rise to the random variable as the correlations between the signal and the templates. Of course, the internal representation is unlikely to be a simple waveform, because similar percepts can result from very different waveforms. A more likely model for deriving the correlation coefficients may be template matching with frequency-specific envelope patterns as proposed by Dau *et al.* (1996) in their auditory-processing model. However, even such a complex representation does not offer provisions for normalizing the templates and/or the internal representation of the signal in frequency and time, which is necessary to accommodate different speakers and speaking rates. A complete model of speech perception remains elusive and is far beyond the scope of the present work. The important point is that the internal representation of each speech token reasonably can be described by a set of

normally distributed random variables that are, at least approximately, orthogonal.

Speech is a broadband signal whose energy is distributed over most of the audible frequency range. Accordingly, the SRS model assumes that contributions to the congruence index, Δ, are distributed in frequency. Its density along the critical-band-rate scale is described by a congruence-index density function, $\delta(z)$. Thus, the congruence index in the frequency band i that extends from $z_L(i)$ to $z_H(i)$ is

$$\Delta(i)=\int_{z_L(i)}^{z_H(i)}\delta(z)\,dz. \tag{2}$$

Because $\delta(z)$ describes the distribution of speech cues across frequency, we assume it to be proportional to the importance density function of articulation theory. In particular, $\delta(z)$ is assumed to be proportional to the SII's band-importance function for ''various nonsense syllable tests where most of the English phonemes occur equally often'' (ANSI, 1997, p. 19, function ''NNS'' in Table B.1). Specifically, the congruence-index density is defined as $\delta(z)=19^{*}\mathrm{NNS}(z)$, where $\mathrm{NNS}(z)$ is the continuous importance-density function on a critical-band-rate scale that is derived from the critical-band importance function of Table B.1, ANSI (1997). The scale factor was chosen so that the average of the congruence indexes in 1-Bark-wide bands is unity.

One source of variance is assumed to be the speaker's production of the speech. Although the speaker attempts to produce the ''ideal'' signal, deviations occur due to limitations of the speaker's articulatory apparatus. These deviations from the ideal signal can be modeled as noise, which is added to the ideal signal. We call this noise the production noise. The power of the production noise, σ_p^2, is also distributed across frequency. This noise was introduced in Sec. II A. Its power-spectrum density, $\sigma_p^2(z)$, is assumed to be proportional to the square of the density of the congruence index:

$$\sigma_p^2(z)=K\delta^2(z). \tag{3}$$

Note that if the production noise is Gaussian, the proportionality constant can be interpreted as a sensitivity index: $d_p'=\sqrt{1/K}$. The assumption of proportionality between the congruence index and the production noise amplitude reflects the idea that any articulation errors that change the information in a particular narrow frequency region will be reflected to a similar extent in adjacent frequency regions. Accordingly, the information in adjacent narrow frequency bands will be redundant, which dictates that an ideal, noiseless receiver should not improve its performance when the width of a narrow band is increased slightly. The constancy of d_p' reflects this notion.

The production-noise components at different critical-band rates are assumed to be partially correlated. Their correlation is high when the components are spectrally close and decreases with increasing spectral separation. The correlation between two noise components at z_1 and z_2 is described by

$$r(z_1,z_2)=e^{-\alpha(z_2-z_1)^2} \tag{4}$$

where $\alpha>0$. Accordingly, the power of the production noise in a spectral band extending from $z_L(i)$ to $z_H(i)$ is

$$\sigma_p^2(i)=K\int_{z_L(i)}^{z_H(i)}\int_{z_L(i)}^{z_H(i)}r(z_1,z_2)\,\delta(z_1)\,\delta(z_2)\,dz_1\,dz_2. \tag{5}$$

As bandwidth increases, the production-noise power in the band also increases. The rate at which $\sigma_p^2(i)$ increases with bandwidth diminishes with increasing bandwidth because $r(z_1,z_2)$ decreases with $|z_2-z_1|$.

For any frequency band, the ratio $\Delta(i)/\sigma_p(i)=d_p'(i)$, which describes the speech band's inherent potential for intelligibility, can be calculated. For narrow bands, the congruence-index density is nearly constant over the width of the band and the correlation between the majority of the noise components in the band is nearly unity. For such bands the band sensitivity is nearly independent of bandwidth $[d_p'(i)\approx d_p']$ and independent of the band's location in the spectrum. Thus, although the congruence-index density varies across frequency, the inherent potential for intelligibility, $d_p'(i)$, of narrow bands does not. This reflects our assumption that the accuracy with which speech is produced is constant across frequency. It should be noted that this assumption does not prevent the full model from predicting a frequency dependency of the intelligibility of a narrow band with constant width. As will be shown later, the noises that arise from other sources modify the relation between $\Delta(i)$ and the intelligibility.

The dependence of the correlations between production noises on band separation [Eq. (4)] implies that the intelligibility contributions of two bands are combined less effectively when the bands are spectrally close than when they are spectrally remote. This trend is in agreement with experimental results (e.g., Kryter, 1960; Müsch and Buus, 2001) and has been the target of a recent proposal for a modified STI (Steeneken and Houtgast, 1999).

Clearly, speech intelligibility is affected by the audibility of speech. Numerous experiments have shown that for any given bandwidth, intelligibility increases with audibility over a dynamic range of approximately 30 to 36 dB (e.g., French and Steinberg, 1947; Kryter, 1962a). In the SRS model, the dependence of intelligibility on audibility is a result of an additional variance, σ_N^2, in the representation of the signal. This variance is the result of a combination of external acoustical noise and noise generated in the auditory periphery. It is large when the SNR, as defined later, is low and small when the SNR is high. The SNR is a function of critical-band rate. At any critical-band rate, the SNR is the difference in dB between the excitation level generated by speech energy at that critical-band rate and the excitation level generated by the combination of masking sounds and an internal noise floor that accounts for the absolute threshold of hearing. The variance associated with these noises in a frequency band extending from $z_L(i)$ to $z_H(i)$ is calculated as

$$\sigma_N^2(i)=\int_{z_L(i)}^{z_H(i)}f^2(\mathrm{SNR}(z))\,dz, \tag{6}$$

where $f^2(\cdot)$ is a function that decreases monotonically with increasing SNR and is zero for SNRs exceeding 30 dB.

C. Second stage of the model: Linguistic entropy

The sensitivity index at the output of the first stage is determined entirely by the audibility of the speech signal and the accuracy with which it is produced. It is independent of the linguistic entropy of the speech signal and of the size of the response set.

It is well known that speech-recognition performance depends on the phonological, semantic, contextual, and situational constraints placed upon the spoken message. The audibility needed to achieve a given recognition performance increases systematically as the entropy of the speech material increases (van Rooij and Plomp, 1991). High-predictability sentences are recognized more accurately than low-predictability sentences (Kalikow *et al.*, 1977). Words in sentences are better understood than words in isolation (Miller *et al.*, 1951). In general, intelligibility increases as the constraints placed upon the message increase. The SRS model seeks to account for this effect by modifying the variance of the distributions of the decision variables such that the distributions get wider as the message entropy increases. The variance of the distributions is manipulated by introducing an additional noise. Because the effect of message entropy on intelligibility is thought to be related to cognitive processes, the noise is referred to as cognitive noise. Its power, σ_{cog}^2, is large when there are few constraints on the speech signal (e.g., nonsense syllables) and small when there are many constraints (e.g., high-predictability sentences). Notice that the power of the cognitive noise is determined only by the linguistic entropy of the speech signal. It is independent of the listening condition and size of the response set.

The assumption of a central (or ''cognitive'') noise has been made in other contexts (Durlach and Braida, 1969; Durlach *et al.*, 1986; Oxenham and Buus, 2000). It is a reasonable assumption in the context of speech recognition. Pollack (1959a,b) concluded that word recognition in a task that involved memorization was better described by a model that assumed a fading trace of a sensory impression than by a model that assumed categorization. The fading of the memory is often assumed to be the result of noise during rehearsing. Accordingly, the finding of a ''trace mode'' implies the existence of cognitive noise in the context of speech recognition.

In a different study, Pollack (1964) investigated why words with a high *a priori* probability of occurrence were recognized better than words with a low *a priori* probability of occurrence. He found that the performance differences did not result from a response bias, but reflected a genuine sensitivity difference ($\Delta d'$) that resulted from the different *a priori* probabilities of occurrence. The d' for words with high *a priori* probability of occurrence was higher than the d' for words with low *a priori* probability of occurrence. This finding is reminiscent of the effects of a decision variance that depends on the entropy of the speech material. Based on information gained from the speech signal preceding a certain passage, the listener has an expectation as to what the signal of that passage might be. Given that this expectation is correct, it will increase the recognition of the passage. This situation is equivalent to Pollack's (1964) study, in which the knowledge of an increased *a priori* probability of one word increased the listener's ''readiness'' for recognizing that word (reflected in an increased d'). The SRS model achieves such increases in d' by varying the cognitive-noise power. A high degree of phonological and contextual constraints, corresponding to a high *a priori* probability of occurrence, requires a small cognitive-noise power to yield a high d'. Cases with few constraints in the speech signal are modeled by a high cognitive-noise power, which reduces the d'.

D. Third stage of the model: Optimal detector

As was observed by Miller *et al.* (1951), listeners' performance in any given listening condition increases as the number of response alternatives decreases [see also Kryter (1962a) and Pollack (1959a)]. This effect is modeled in the third stage of the model, which is an optimal detector that predicts performance from the sensitivity index at the output of the second stage of the model. The detector's performance is described by Eq. (1) and illustrated in Fig. 1. This stage is independent of the listening condition and the test material used and depends entirely on the number of response alternatives.

It should be noted that the noise power's dependence on the congruence index does not preclude the use of d' to characterize recognition performance. Clearly, the sensitivity index is only a valid measure of detectability if the noise power that is observed when the signal is present equals the noise power when the signal is absent. This restriction is met in the present model. For a certain listening condition and response-set size, M, the classifier calculates the decision variable in each of M dimensions. The noise powers are assumed to be equal in all dimensions and are determined by the listening condition. They are independent of the item presented. Because the classifier compares the decision variables across the individual dimensions, and all dimensions are exposed to the same noise, the assumptions that underlie the use of d' are likely to be valid. The noise power changes only when the listening condition changes—i.e., when the signal audibility changes and/or when the cognitive-noise power changes due to the use of different test materials.

E. Discrete approximation

It is often convenient to approximate the integrals in Eqs. (2), (5), and (6) by summations across contributions of discrete frequency channels. When a discrete approximation is made, the d' at the input to the detector [Eq. (1)] can be expressed as

$$d' = \frac{\Sigma_i \Delta(i)}{\sqrt{\Sigma_i \sigma_N^2(i) + \Sigma_i \Sigma_j (r(i,j)\sigma_p(i)\sigma_p(j)) + \sigma_{\mathrm{cog}}^2}}, \qquad (7)$$

where the summation indexes i and j cover all channels that contribute signal and noise to the sensitivity index. In general, only bands that make significant contributions to intelligibility will be used by the listener. To decide which channels will be included in the formation of d', several criteria are conceivable. A particularly simple one that allows good

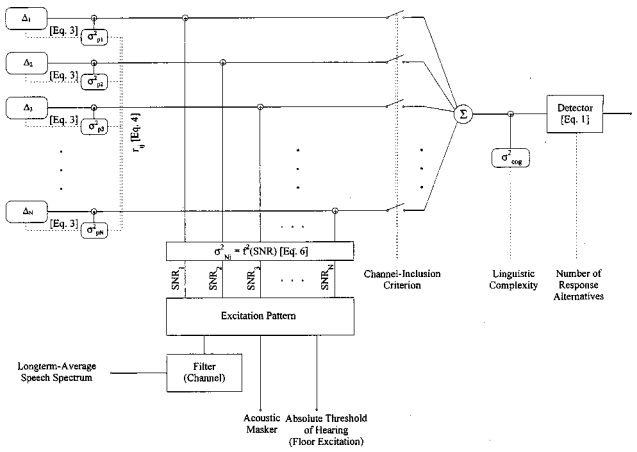

FIG. 2. Model structure (N-channel discrete approximation). In each of N channels, there is a congruence index, $\Delta(i)$, and a production-related variance, $\sigma_p^2(i)$, whose power is derived from the congruence index by means of Eq. (3). The difference in dB between the long-term average excitation evoked by the speech signal and the excitation evoked by the combination of external acoustic maskers and the internal excitation-noise floor is transformed by Eq. (6) into a sensory variance, $\sigma_N^2(i)$. In each channel, this variance is added to the congruence indexes and the production-related variance. According to some criterion, a subset of the channels is selected and their congruence indexes and noise components are combined. The variance introduced by the cognitive processes involved in speech recognition is added to the combined signals. The power of this cognitive noise is determined by the linguistic entropy of the speech. An optimal detector [Eq. (1)] correlates the ideal signal with each of M templates (the response alternatives).

predictions of the data by Müsch and Buus (2001) includes all channels whose SNR exceeds a specified critical value.

In this approximation, the production-noise components within one channel are assumed to be 100% correlated and $\delta(z)$ is assumed to be constant across the width of a channel. With this assumption, $\Delta(i)=\delta(i)\cdot(z_H(i)-z_L(i))$ [see Eq. (2)] and $\sigma_p(i)=\Delta(i)/d_p'$ [see Eq. (5)]. The error introduced by this approximation will be small when the channels are not wider than the equivalent rectangular width of the correlation function [Eq. (4)]. The coefficients $r(i,j)$ of the between-channel correlations are determined by Eq. (4), where z_1 and z_2 are the critical-band rates of the channels' center frequencies. The model structure is illustrated in Fig. 2.

F. Model parameters

As evident from the preceding discussion, the SRS model has a number of functions and parameters that must be determined to provide predictions of the performance obtained with a given transmission system, speech material, and response paradigm. They include (a) the congruence-index density function, $\delta(z)$; (b) the inherent potential for intelligibility, d_p'; (c) the frequency range across which the production noises are correlated as characterized by α in Eq. (4); (d) the relation between signal-to-noise ratio and the audibility-related noise power, $f^2(\mathrm{SNR}(z))$; and (e) the cognitive-noise power, σ_{cog}^2. Initial fits to the data discussed in Sec. III provided parameter estimates that varied relatively little across data sets. Although the fits necessarily are somewhat better if parameters are varied as needed to obtain the best possible fit for each individual study, the parameters must be fixed to provide a model that is generally useful. Therefore, a single set of parameters is used to fit the data from all these studies and a data set presented in a companion article (Müsch and Buus, 2001), except that σ_{cog}^2 and the number of response alternatives are allowed to vary as dictated by the different speech materials and response paradigms used in these studies.

Throughout this article and the companion article (Müsch and Buus, 2001), predictions by the SRS model were obtained with $\delta(z)=19^*\mathrm{NNS}(z)$, where $\mathrm{NNS}(z)$ is SII's band-importance function for phonetically balanced nonsense syllable tests (ANSI, 1997), as discussed in Sec. II B. The inherent potential for intelligibility, d_p' is set to 3.5 and the equivalent rectangular bandwidth of the correlation function given by Eq. (4) is set to 3.2 Barks, corresponding to a $\alpha=0.0766$.

The function governing the audibility-related noise power, $f^2(\mathrm{SNR}(z))$, was approximated by a piecewise linear function: $f^2(\mathrm{SNR}(z))=a[\min\{\mathrm{SNR}(z),30\,\mathrm{dB}\}-30\,\mathrm{dB}]$, where $a=-0.032$. If the SNR in a particular band is very poor, the audibility-related noise may become so large that including it in the decision decreases performance. To avoid this artifact, the model predictions exclude bands with SNRs less than -20 dB. It should be noted that these functions and parameters may change as the SRS model is applied to data from new experiments designed to test the validity of specific functions and parameter values. Nevertheless, the present set of functions and parameters provide good fits to the data examined so far and are likely to be useful for predicting the outcome of a variety of speech-recognition experiments.

III. MODEL PREDICTIONS

A. Synergy

The structure of the SRS model differs considerably from that of AI models. Whereas it maintains some premises underlying AI models—such as frequency specificity and the assumption that intelligibility is determined by audibility—the SRS model combines information across frequency in a way that is fundamentally different from that used in AI models. As outlined in the Introduction, the AI works on the assumption that the probability of incorrectly identifying a phoneme in a broadband condition can be described by the product of the error probabilities in the speech bands comprised by the broadband condition. This implies that the speech bands are assumed to contribute independently to phoneme recognition.[1] In contrast, the SRS model combines the *information* available in the channels prior to making any decision. In general, this strategy will lead to predictions that differ from those derived by combining *decisions* that were based on the information in individual bands.

The assumption of independent band contributions prevents AI models from predicting redundant or synergetic interaction. In contrast, synergy and redundancy can be simulated by the SRS model, even in the absence of band interactions that result from spread of masking.

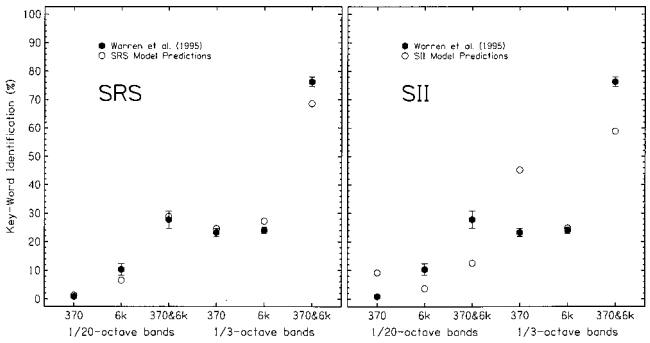

FIG. 3. Percentage of correctly identified keywords in everyday sentences. The black hexagons are scores reported by Warren *et al.* (1995). The error bars span ± one standard error. The open circles in the left panel represent predictions by the SRS model. The open circles in the right panel represent predictions by the SII model. The listening conditions were either single bands, centered at 370 and 6000 Hz, or dual bands, composed of the two single bands. The bandwidth of the individual bands was either $\frac{1}{20}$ octave or $\frac{1}{3}$ octave. The dual-band conditions show large amounts of synergetic interaction.

1. Method

To show the SRS model's ability to account for synergetic interaction, data presented by Warren *et al.* (1995) are predicted. As outlined in the Introduction, they found that a narrow speech band centered at 370 Hz, whose intelligibility in isolation is very low, increases the intelligibility of a narrow speech band centered at 6000 Hz dramatically when the bands are presented simultaneously. The mean scores (black hexagons) and standard errors obtained by Warren *et al.* (1995) are replotted in Fig. 3.

Warren *et al.* (1995) presented listeners with unknown everyday sentences and instructed them to repeat each sentence as accurately as possible. The reported scores are the proportions of correctly identified keywords. Because listeners were free to choose any word, the number of response alternatives equals the size of the listeners' active vocabulary. Both this data set and the data described in Sec. III B are well described if we assume the size of the listener's active vocabulary to be 8000. The power of the audibility-related noise was set to zero because the presentation level was assumed to be such that the entire dynamic range of the speech signal was audible. Two parameters will be freely adjusted to fit the six data points. One parameter is the power of the cognitive noise, σ_{cog}^2. The other is a factor that seeks to compensate for the finite slopes of the filters used by Warren *et al.* (1995). Warren and Bashford (1999) showed that a considerable number of speech cues are provided by signal components on the skirts of the filters (i.e., outside the nominal bandwidth). To account for the contribution of the filter skirts, the congruence indexes derived by integrating the congruence-index density function over the nominal width of the bands was increased by a constant factor, which was chosen to optimize the fit to the data.

The data were also predicted using the SII model (ANSI, 1997). It should be noted that this listening condition is beyond the stated scope of the SII, because it contains multiple sharply filtered bands of speech. The level in the speech bands was assumed to be high enough so that the entire dynamic range of the speech signal was audible. The SII could therefore be calculated as the integral of the importance *density* function over the widths of the speech bands. The width of the speech bands was assumed to be the nominal width of the bands widened by a constant factor. Both assumptions are in agreement with those made for the SRS model predictions. The importance density function was derived from the importance function for ''short passages of easy reading material'' (ANSI, 1997, Table B.1, p. 18). The transformation between SII and intelligibility, which is not specified in the standard, was modeled by

$$Pc = 100 \cdot (1 - 10^{-\mathrm{SII}/p}). \tag{8}$$

The parameter p was selected to minimize the mean-squared error between the predicted and the measured scores.

2. Results

As shown by the open circles in the left panel of Fig. 3, the SRS model provides an excellent account of the large amount of synergetic band interaction seen in Warren *et al.*'s (1995) data. For the $\frac{1}{20}$-oct bands, the predictions are close to the data and the synergy is at least as large as that observed. For the $\frac{1}{3}$-oct bands, the SRS model predicts a very large synergy, but it is slightly less than that observed. Nevertheless, the good agreement between the data and predictions indicates that the SRS model is capable of predicting even quite extreme cases of synergy obtained with widely separated bands of speech.

The predictions shown in the left panel of Fig. 3 were obtained by multiplying the Δ_i for the nominal passbands by a factor of 1.41. The finding that the effective bandwidth is larger than the nominal bandwidth is consistent with Warren and Bashford's (1999) finding that information at frequencies on the skirts of the filter contributes considerably to the recognition performance. The best-fitting cognitive noise power is $\sigma_{\mathrm{cog}}^2 = 0.0056$.

The open circles in the right panel of Fig. 3 show the predictions of the SII model. Because of the shape of the importance function for easy reading material, the SII predicts that the band at 6 kHz should contribute less to intelligibility than the band centered at 370 Hz. Moreover, the amount of synergy predicted by the SII model is much smaller than that predicted by the SRS model and that seen in the data. The best-fitting p in Eq. (8) was 0.4. The choice of the broadening factor did affect the SII predictions, but did not substantially affect the goodness of fit achievable. Thus the broadening factor was set equal to that used in the SRS predictions.

B. Performance as a function of response-set size, speech material, and SNR

Because the SRS model is developed to predict intelligibility in listening conditions for which AI models are not suitable, differences between predictions with the SRS model and AI models are expected in some listening conditions. The general trends predicted by AI models, however, should also be reflected in the SRS model's behavior. In this

section it will be shown that the SRS model can predict a set of empirically derived transformation functions that are used in AI models.

An important step in intelligibility predictions with AI models is the transformation of the calculated AI value into a predicted performance level. This transformation depends heavily on the speech material used and the size of the response set. It is always determined empirically, except for open-set phoneme recognition in a nonsense-syllable context, where the transformation is a direct result of the assumption that the speech bands contribute independently to intelligibility. Because the transformations are so dependent on the details of the test, many—sometimes conflicting—transformations have been published. Perhaps the most-widely accepted set of transformations is published in Fig. 15 of Kryter (1962a). That set encompasses transformations to be applied when the speech material is a phonetically balanced (PB) word list with 32, 256, or 1000 items, as well as transformations to be used in nonsense-syllable tests in which the syllables are drawn from a list of 1000 syllables.[2]

1. Method

To examine whether the SRS model can predict the transformations obtained by Kryter (1962a), the model was made to predict performances encompassing nine AI values by manipulating the SNR of unfiltered speech that is presented in speech-shaped noise. A low SNR corresponds to a small AI and a high SNR corresponds to a large AI.

Whereas the response-set size is given for at least some of the conditions examined by Kryter (1962a), the cognitive-noise powers have to be estimated. A cognitive-noise power of $\sigma^2_{\mathrm{cog}}=0.0056$ accounted for Warren *et al.*'s (1995) data. They used everyday sentences. The variance introduced by the cognitive processes involved in the recognition of isolated words is expected to be larger and is arbitrarily set to $\sigma^2_{\mathrm{cog}}=0.01$. The variance introduced by the cognitive processes involved in the recognition of nonsense syllables is expected to be even larger and is arbitrarily set to $\sigma^2_{\mathrm{cog}}=1$.

In the SRS model, different SNRs are reflected by different values of $\sigma^2_N(i)$. A high SNR corresponds to a small $\sigma^2_N(i)$ and a low SNR corresponds to a high $\sigma^2_N(i)$. To ensure that possible errors in the values $\sigma^2_N(i)$ would not obscure the ability of the SRS model to account for the recognition performance obtained with different speech materials and response-set sizes, $\sigma^2_N(i)$ were estimated directly from Kryter's transformation functions. For nine AI values (AI $=0.1$ to 0.9) the percentage of correctly understood PB words drawn from a list of 256 PB words was read from Kryter's (1962a) Fig. 15 and the corresponding d's were found by inverting Eq. (1). Subsequently, the audibility-related noise powers, $\sigma^2_N(i)$, that yielded these d's were determined. Because one $\sigma^2_N(i)$ can be selected for each AI value, the fit can be made perfect. These audibility-related noise powers are related to their corresponding SNRs by Eq. (6). It should be noted that when $f^2(\mathrm{SNR}(z))$ is chosen as described in Sec. II F (i.e., $f^2(\mathrm{SNR}(z))=a[\min\{\mathrm{SNR}(z),30\,\mathrm{dB}\}-30\,\mathrm{dB}]$, where $a=-0.032$), the resulting SNRs are significantly smaller than SNRs usually associated with this range of AIs. This indicates that a piecewise-linear representation of $f^2(\mathrm{SNR}(z))$ may be too simple to account for the relation between SNR and the power of the audibility-related noise. With all parameters in stage one and two fixed, performances in recognition tests involving PB-word lists of length $M=32$, 1000, and 8000 are predicted by setting the parameter M in Eq. (1) (stage three) to its correct value. The prediction for $M=8000$ was made to account for the possibility that listeners may be unable to maintain a response set that matches the stimulus set when the number of stimulus words is large, e.g., 1000, or even unknown to the listener. In these cases, the response set may consist of the listener's entire active vocabulary, possibly excluding items that do not match lexical constraints implied by the stimulus set. To predict the performance in a nonsense-syllable recognition task, the power of the cognitive noise is set to $\sigma^2_{\mathrm{cog\_nonsense}}=1$ while all other parameters remain unchanged.

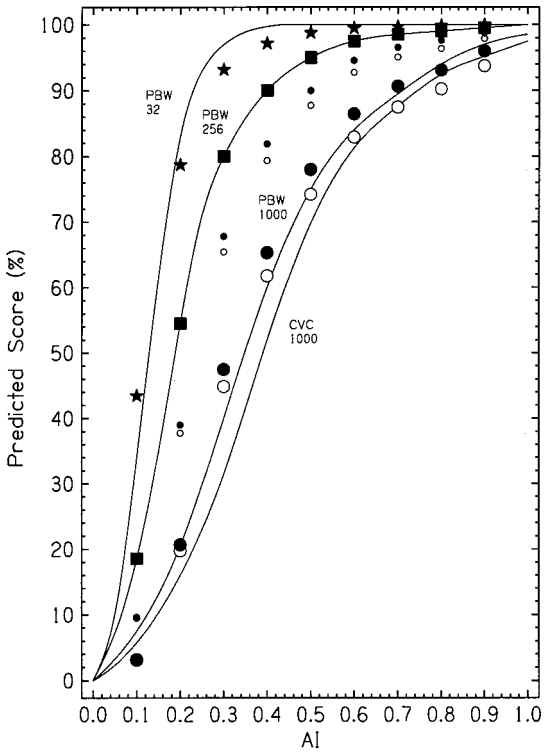

FIG. 4. Transformation between AI and predicted test performance for phonetically balanced words (PBW) and nonsense syllables drawn from lists with 32, 256, and 1000 items. The curves are replotted from Fig. 15 of Kryter (1962a). The symbols indicate predictions by the SRS model. See text for details.

2. Results

Figure 4 shows the predictions obtained in this manner (symbols) together with the transformations in Kryter's (1962a) Fig. 15 (lines). The black squares indicate the predictions for PB words drawn from a list of 256. Because one free parameter—the masking-noise power, $\sigma^2_N(i)$—was available for each predicted value, the fit could be made perfect and the symbols fall exactly on the curve. The stars show the predictions for PB-word recognition when $M=32$. Considering that there were no free parameters to obtain these fits, the agreement between the predictions and the

curve is impressive. The predictions for PB-word recognition when $M=1000$ are shown by the small black circles. These predictions are substantially above the curve for 1000 PB words. When the calculations are repeated with $M=8000$, the predictions indicated by the large black circles are obtained. These predictions approximate Kryter's (1962a) transformation for lists of 1000 PB words quite well. Although there are clear differences between the predictions and the curve, the trend of Kryter's (1962a) transformation is captured by the model predictions.

When the cognitive noise power is increased to model the recognition of nonsense syllables, the predictions indicated by the small open circles ($M=1000$) and large open circles ($M=8000$) are obtained. Again, the predictions for $M=8000$ match Kryter's (1962a) curve reasonably well. The difference between the SRS-model predictions for PB words ($M=8000$) and nonsense syllables ($M=8000$) is comparable to the differences between Kryter's (1962a) curves for 1000 test stimuli, except that the difference predicted by the SRS model appears slightly smaller than that between Kryter's curves at AIs of 0.1 and 0.2. Considering that Kryter's ''relations are only approximate'' (Kryter, 1962a, p. 1697), the SRS-model predictions are very good. Slightly different fits could have been obtained had different model parameters been selected, but the overall quality of the fit would not have changed substantially.

3. Discussion

Listeners' performance in speech-recognition tasks with large stimulus sets appears to be described better when M is assumed to be larger than the stimulus set. No significant discrepancy between M and the size of the stimulus set is found when small stimulus-set sizes are used. A similar effect was observed by Green and Birdsall (1958). They offered the explanation that performance may be determined by the number of response alternatives rather than the number of stimulus alternatives. When the stimulus set is small and known to the listener, the listener will only consider responses that are members of the stimulus set. When tested with a test list of 1000 words, the list is not known to the listener. The listener's active vocabulary contains all words on the list, but also other words. Because the listener is unfamiliar with the list, the received signal is compared with representations of the entire active vocabulary, which effectively makes the response set open. Some incorrect responses will not be members of the stimulus set. This implies that the number of response alternatives will often be larger than the number of stimulus alternatives when the listener is unfamiliar with the stimulus set. In Eq. (1), the parameter M represents the number of response alternatives considered by the listener. When the SRS model is applied to open-set or quasi-open set speech recognition, the number of response alternatives available to the listener must be estimated. The simulation of Kryter's (1962a) transformations suggests that the size of the listener's active vocabulary is approximately 8000 words. This is in agreement with the assumption made in Sec. III A to model Warren *et al.*'s (1995) data.

Supporting evidence for this interpretation has been found by Pollack (1959a), who showed that performance in a closed-set word-recognition task is determined by the number of response alternatives rather than the number of stimulus alternatives. In addition, data presented in a companion paper (Müsch and Buus, 2001) indicate that the same is true for consonant discrimination.

C. Effect of interaction between filter condition and linguistic entropy on performance

The present model also predicts a phenomenon that cannot be explained easily by AI-based models. The transformations in Fig. 4 reflect the AI models' assumption that every level of linguistic entropy (e.g., nonsense syllables, meaningful words, and sentences) has its own fixed relation between test score and AI. This assumption implies the existence of fixed relations among the test scores obtained with speech materials that differ in linguistic entropy. In other words, if two different listening conditions yield identical percentages of correct responses for one kind of material—e.g., nonsense syllables—they should also yield identical performance for another kind of speech material—e.g., words.

This implication is in conflict with data by Hirsh *et al.* (1954), who measured the intelligibility of nonsense syllables and polysyllabic words under two types of listening conditions. In one type, unfiltered speech was presented in a fixed-level white-noise masker. Intelligibility was manipulated by adjusting the speech level to different SNRs. In the second type of listening condition, fixed-level speech was presented in quiet and intelligibility was manipulated by high-pass and low-pass filtering the speech signal. When word-recognition scores were plotted as a function of syllable-recognition scores, the data showed that filtering produced a different relation between the two test scores than did masking. A masking condition and a filtering condition that yielded identical syllable-recognition scores yielded quite different word-recognition scores. The curves Hirsh *et al.* (1954) used to summarize the data in their Fig. 10 are replotted in Fig. 5. The dashed curve summarizes the data for the filter conditions and the solid curve summarizes the data obtained in the wideband masking condition. The need for two different curves indicates that the relation between AI and predicted score depends not only on the speech material and size of the response set, but also on the listening condition. Such a dependence, of course, runs counter to the AI's objective of being an intelligibility descriptor that is independent of listening condition. The speech intelligibility index, SII (ANSI, 1997), attempted to remedy this shortcoming by using different band-importance functions for different speech materials (Pavlovic, 1993). Consequently, the SII model does predict that the SII of any listening condition—except those with a SII of unity—changes when a different test material is used.

To test whether different band importance functions can account for the interaction between filter condition, linguistic entropy, and performance, the SII model was applied the data by Hirsh *et al.* (1954). Two SII values were calculated for each filter (or masking) condition. One SII value was based on the importance function for the W-22 word list (ANSI, 1997). The other was based on the importance func-

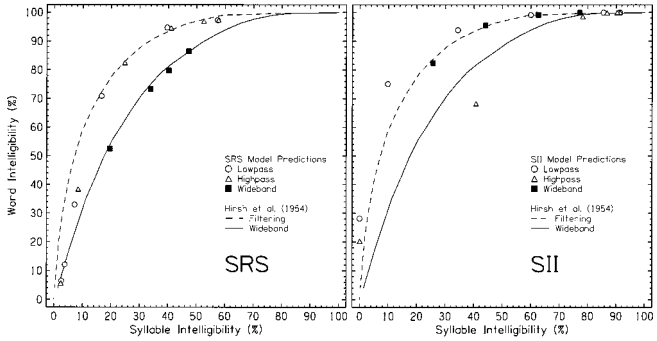

FIG. 5. The intelligibility of polysyllabic words in various listening conditions is plotted as a function of nonsense-syllable intelligibility. The curves are replotted from Fig. 10 of Hirsh *et al.* (1954). They used the dashed curve to summarize the data obtained under high-pass and low-pass filtering, and the solid curve to summarize the data obtained under masking. The symbols indicate model predictions. The left panel shows predictions with the SRS model and the right panel shows predictions with the SII model. Open circles represent low-pass filtering, triangles represent high-pass filtering, and black squares represent wideband conditions. The shaded area in the lower left indicates the performance range that is below chance performance.

tion for nonsense syllables (ANSI, 1997). The resulting SII values were transformed into their corresponding intelligibility scores and plotted in the right panel of Fig. 5. Because the transformation between SII and intelligibility is not specified in the ANSI standard, the transformations were derived from the data.[3] The SII predicted that the low-pass condition (open circles) and the broadband condition (black squares) should be summarized by one function and the high-pass condition (open triangles) by a separate function. This is at odds with the data, which show that the high- and low- conditions were summarized by the same function (dashed line) and the wideband condition by a separate function (solid line). Clearly, the predictions with the SII model do not reflect the trend in the data.

1. Analytical derivation

The interaction between linguistic entropy and listening condition observed by Hirsh *et al.* (1954) can be explained by the SRS model. First consider a qualitative analysis.

To demonstrate that the SRS model can account for the phenomena observed by Hirsh *et al.* (1954), one needs to show that equality between the d's for nonsense-syllable recognition in filter and wideband conditions,

$$d'^{\text{nonsense}}_{\text{filter}} = d'^{\text{nonsense}}_{\text{wideband}} \tag{9}$$

implies that in a word-recognition task d's are larger in the filter conditions than in the wideband conditions. That is,

$$d'^{\text{word}}_{\text{filter}} > d'^{\text{word}}_{\text{wideband}}. \tag{10}$$

Using the discrete approximation in Eq. (7) together with the fact that σ_{cog} is fixed for a given speech material, squaring and simplifying, allows Eqs. (9) and (10) to be written as

$$\sigma^2_{\text{cog}_{\text{nonsense}}}(\Delta_F^2 - \Delta_W^2) = \Delta_W^2\sigma_F^2 - \Delta_F^2\sigma_W^2, \tag{11}$$

and

$$\sigma^2_{\text{cog}_{\text{word}}}(\Delta_F^2 - \Delta_W^2) > \Delta_W^2\sigma_F^2 - \Delta_F^2\sigma_W^2, \tag{12a}$$

respectively, when the substitutions

$$\sigma_F^2 = \sum_{i\in F\subset W}\sum_{j\in F\subset W}(\sigma_{p_i}\sigma_{p_j}r_{ij}) + \sum_{j\in F\subset W}\sigma_{N_j}^2, \tag{12b}$$

$$\sigma_W^2 = \sum_{i\in W}\sum_{j\in W}(\sigma_{p_i}\sigma_{p_j}r_{ij}) + \sum_{j\in W}\sigma_{N_j}^2, \tag{12c}$$

$$\Delta_F^2 = \sum_{j\in F\subset W}\Delta_j^2, \tag{12d}$$

and

$$\Delta_W^2 = \sum_{j\in W}\Delta_j^2 \tag{12e}$$

are made. Because the transmission systems (F for a filtered system, W for a broadband system with added noise) are the same for the two speech materials, Δ_F and Δ_W maintain their values between Eq. (11) and Eq. (12a). The set W encompasses all channels of the model and the set F encompasses only those channels that fall into the filter's passband (i.e., F is a subset of W, $F\subset W$). If $\sigma^2_{\text{cog\_word}} = A\sigma^2_{\text{cog\_nonsense}}\,(A>0)$ is substituted in Eq. (12a) one can solve for A and show that

$$A < \frac{\Delta_W^2\sigma_F^2 - \Delta_F^2\sigma_W^2}{\sigma^2_{\text{cog}_{\text{nonsense}}}(\Delta_F^2 - \Delta_W^2)}, \tag{13}$$

where the fact that $F\subset W$, which implies $(\Delta_F^2 - \Delta_W^2) < 0$, was used. Combining Eqs. (11) and (13), it follows that $A<1$, which indicates that the power of the cognitive noise in tests involving word material is smaller than the power of the cognitive noise in tests involving nonsense syllables. This is in agreement with the assumptions of the SRS model.[4] Thus, a qualitative explanation for Hirsh *et al.*'s (1954) results is inherent in the structure of the SRS model.

2. Quantitative analysis

a. Method. The curves used by Hirsh *et al.* (1954) to summarize their results will be predicted with the SRS model. They tested six high-pass and six low-pass conditions. The high-pass filters and the low-pass filters had the same cutoff frequencies, which were $f_c = 200$, 400, 800, 1600, 3200, and 6400 Hz. The level of the unfiltered speech was 95 dB SPL. For the purpose of modeling, it is assumed that the filters' cutoff was infinitely steep so that channels in the filter's stop bands contribute neither signal nor noise to the overall sensitivity index. Hirsh *et al.* (1954) also tested speech in white-noise maskers of four different levels at four SNRs (+5, −1, −7, and −13 dB). They found that the test score obtained for any fixed SNR varied with overall masker level. Recently, Dubno *et al.* (2000a,b) showed that the decrease in intelligibility that occurs when the masker level is increased while the SNR is kept constant is accounted for by increased masking. Thus, if audibility is kept constant, performance appears to be independent of level over a wide range of levels. In keeping with this finding, the SRS model predicts an effect of masker level only to the extent that spread of masking increases with level, as long as the masker levels are high enough to elevate the absolute threshold over the entire range of speech frequencies. Because we are more

interested in testing the model structure of Fig. 2 than the excitation pattern model used to derive the excitation SNR in the SRS model, we made predictions for only one masker level (50 dB SPL). To fit the curves in Fig. 5, the powers of the cognitive noises, $\sigma^2_{\text{cog\_nonsense}}$ and $\sigma^2_{\text{cog\_ward}}$, were used as free parameters.

b. Results. The predictions shown by the symbols in Fig. 5 were obtained with $\sigma^2_{\text{cog\_nonsense}}=50$ and $\sigma^2_{\text{cog\_word}}=8$. They follow the general trend of the curves very well. Clearly, the SRS model can account for the finding that the relation between scores obtained with nonsense syllables and with words depends on whether recognition performance is reduced by filtering or by masking.

c. Discussion. Although the two values for cognitive variances used to account for Hirsh *et al.*'s (1954) data follow the expectation that the cognitive noise should increase with the entropy of the speech material, they are significantly higher than the variances obtained in the other fits. This may have to do with the test paradigm used in Hirsh *et al.*'s (1954) study. They used lists of 25 polysyllabic words and 50 nonsense syllables, which were shuffled and interspersed with 50 monosyllabic words, 75 bisyllabic words, and several sentences. The predictions of polysyllabic-word recognition and nonsense-syllable recognition are made with M set to 25 and 50, respectively. To take advantage of the restricted response-set sizes, the listener had to decide in every trial to which list the speech token belonged. The cognitive effort involved in making this decision may explain the enlarged cognitive variances.

The shaded area in the lower left corner of Fig. 5 shows the area of the plot in which performance is worse than expected from guessing alone. Hirsh *et al.*'s (1954) curves start at the origin of the graph and pass through this area. The curves one would draw to summarize the model predictions, on the other hand, start more nearly at the upper right corner of the shaded area and would be more in line with expectations from chance performance. Thus, it appears that the deviation between Hirsh *et al.*'s (1954) curves and the predictions reflect that the SRS model accounts for chance performance, whereas the curves drawn by Hirsh *et al.* (1954) do not. Altogether it is clear that the SRS model is capable of predicting how the relation between recognition scores for words and for nonsense syllables depends on whether the intelligibility is degraded by noise or by filtering.

D. Interaction between linguistic entropy, SNR, and language proficiency

The SRS model also explains interactions between linguistic entropy and SNR in native and non-native listeners. These effects were not yet modeled quantitatively and only a discussion of the qualitative effects is presented here.

Pollack (1964) measured the recognition accuracy of words with high and low *a priori* probability of occurrence in a closed-set word-recognition test. As mentioned earlier, he found that the d' for words with high *a priori* probability of occurrence is higher than the d' for words with a low *a priori* probability of occurrence. Moreover, he observed that the rate at which d' increases with *a priori* probability of occurrence depends on the SNR. At low SNRs, when speech is barely audible, the *a priori* probability of occurrence has only a very small effect on d'. The effect of *a priori* probability on d' increases as the SNR increases. This trend is predicted by the SRS model. As SNR decreases, the variance in the auditory periphery, $\sigma_p^2(i)+\sigma_N^2(i)$, increases due to an increased $\sigma_N^2(i)$. Consequently, the total variance at the input of the detector, $\sigma_p^2(i)+\sigma_N^2(i)+\sigma_{\text{cog}}^2$ is affected less in relative terms by a given change in σ_{cog}^2 when the SNR is low than when it is high. The reduced effect of changes in σ_{cog}^2 on the overall variance is reflected in a smaller change of d'. A similar trend was observed by Dubno *et al.* (2000a), who measured recognition of words embedded in sentences with high- and low-contextual constraints as a function of SNR. Their results show that performance increases faster with SNR in the high-predictability condition than in the low-predictability condition. The performance difference is smallest at the low SNRs and increases with SNR. The SRS model predicts this trend owing to the assumption of a cognitive noise.

Further support comes from a study by Mayo *et al.* (1997), who measured the intelligibility of words in high- and low-predictability sentences as a function of SNR in native and non-native listeners. Using speech babble as a masker, they also found that in any listening condition their native listeners performed better with the high-predictability sentences than with the low-predictability sentences. The performance-intensity functions for high-predictability sentences were steeper than the performance-intensity functions for low-predictability sentences, and the functions were more nearly equal at the low SNRs. This is in agreement with Dubno *et al.*'s (2000a) finding and with predictions of the SRS model.

In addition, Mayo *et al.* (1997) measured the intelligibility of words in high- and low-predictability sentences as a function of SNR in non-native listeners, who were highly proficient in English. At any SNR, native listeners performed better than non-native listeners. The slopes of the non-native listeners' performance-intensity functions for low- and high-predictability sentences did not differ significantly and were shallower than the slopes of the native listeners' performance-intensity functions for low-predictability sentences. This indicates that non-native listeners were less able than native listeners to take advantage of contextual information in adverse listening conditions. Similar findings were reported by Florentine (1985).

These relationships can be explained by the SRS model if it is assumed that the power of the cognitive noise is larger in non-native listeners than in native listeners. When the cognitive noise is increased, the relative change in the overall noise power caused by any given change in the power of the audibility-related noise is reduced. Thus, increased cognitive noise produces a reduced rate of improvement of recognition performance with increasing SNR. In other words, the performance-intensity functions are predicted to be shallower in non-native listeners than in native listeners if the cognitive noise is enlarged in non-native listeners.

There are several reasons to assume that the noise power is larger in non-native listeners than in native listeners. An

obvious assumption is that non-native listeners are less familiar with the lexicon and the linguistic constraints of the language than native listeners. This causes them to devote more cognitive effort to the speech recognition task, which introduces a larger cognitive variance. Experiments with speech recognition under divided attention appear to support this interpretation (Boothroyd, 2000).

Regardless of where the additional noise originates, the assumption of increased noise in non-native listeners' speech perception allows the SRS model to predict qualitatively the differential effect of linguistic entropy, SNR, and language proficiency on speech-recognition performance.

IV. CONCLUSIONS

The SRS model, which is presented in this article, appears capable of predicting a wide range of data in the literature. None of these data are easily predicted in the framework of the articulation index. The primary strengths of the SRS model are that it can predict interactions between listening condition and the linguistic entropy of the speech material, account for redundancy in the speech signal, and predict synergetic interaction among disjoint bands of speech. The latter listening conditions are excluded from the scope of the AI (ANSI, 1969) and the SII (ANSI, 1997). The effect of linguistic entropy on intelligibility is modeled by a single variable, which is a measure of the variance introduced by the cognitive processes involved in speech recognition. In addition, the structure of the SRS model accounts for the effect of the number of available response alternatives on test performance.

Approximate values of the parameters contained in the SRS model can be derived from the data considered in this article and the companion paper (Müsch and Buus, 2001):

(1) The inherent discriminability of the phonetic information in naturally produced speech appears to be well described by a sensitivity index of $d'_p = 3.5$ within some narrow band.
(2) The contribution to the congruence index appears to be well described by the importance-density function for nonsense syllables of the SII (ANSI, 1997). The SRS model employs a scaled version with a scale factor chosen to make the average congruence-index in a 1-Bark-wide band equal to unity. The scale factor can be chosen arbitrarily, because the model's predictions are unaltered if δ, σ_{cog}, σ_N, and σ_p are all multiplied by the same factor.
(3) The fit to Warren *et al.*'s (1995) data indicates that the variance introduced by the cognitive processes involved in the recognition of everyday sentences is around $\sigma^2_{\mathrm{cog\_sentences}} = 0.006$. Kryter's (1962a) transformations between AI and intelligibility are well described by the SRS model when it is assumed that variances introduced by the cognitive processing of isolated words and nonsense syllables are $\sigma^2_{\mathrm{cog\_PW\text{-}words}} = 0.01$ and $\sigma^2_{\mathrm{cog\_nonsense}} = 1$, respectively. These values are internally consistent and provide an estimate of the cognitive variances involved in speech recognition.
(4) The cognitive variances needed to account for Hirsh *et al.*'s (1954) data are significantly higher than those obtained in the other fits. This may have to do with the test paradigm used in Hirsh *et al.*'s (1954) study.
(5) The fits to the data of Warren *et al.* (1995) and the transformations of Kyter (1962a) indicate that in open-set recognition tasks listeners match the received signal to a set of $M = 8000$ templates.

ACKNOWLEDGMENTS

This work was supported by NIH/NIDCD. The authors wish to thank Mary Florentine, Joanne Miller, and Chaslav Pavlovic, as well as two anonymous reviewers for their helpful comments.

[1]Independence is meant in an information-theoretical sense. There might be band interaction due to a physical interaction between the bands that results from the spread of excitation. At low levels, where there is no spread of excitation, all AI models—with the exception of Fletcher and Galt's (1950) method—assume that the bands are truly independent. The AI model by Fletcher and Galt (1950) does predict that synergetic interaction between bands may exist. In Fletcher and Galt's (1950) model, the sum of the AIs obtained in two single-band conditions does not equal the AI obtained in the dual-band condition, even in the absence of mutual masking. However, this interaction is too small to account for the synergetic interaction observed in speech tests.

[2]A transformation for sentence material, also included in Kryter's (1962a) Fig. 15, could not be modeled because the size of the response set was unclear.

[3]To derive the transformation between SII and intelligibility, which is not specified in the standard, the measured word intelligibility scores of Hirsh *et al.* (1954) were plotted as a function of SII calculated with the W-22 importance function. Equation (8) was fitted to these points and taken as the transformation between SII and intelligibility for word material (best-fitting $p = 0.22$). Likewise, the measured intelligibility scores for nonsense syllables (Hirsh *et al.*, 1954) were plotted as a function of the SII calculated with the importance function for nonsense syllables (ANSI, 1997), and the function generated by the best-fitting p ($p = 0.81$) was taken as the transformation between SII and intelligibility of nonsense syllables.

[4]To satisfy $A > 0$, one needs $1 < \Delta^2_W/\Delta^2_F < \sigma^2_W/\sigma^2_F$, which is the only constraint on the model parameters.

Allen, J. B. (**1994**). ''How do humans process and recognize speech,'' IEEE Trans. Speech Audio Process. **2**, 567–577.
ANSI (**1969**). ANSI S3.5-1969 ''Methods for the calculation of the articulation index'' (American National Standards Institute, New York).
ANSI (**1997**). ANSI S3.5-1997 ''Methods for calculation of the speech intelligibility index'' (American National Standards Institute, New York).
Beranek, L. L. (**1947**). ''The design of speech communication systems,'' Proc. IRE **35**, 880–890.
Boothroyd, A. (**2000**). Personal communication.
Ching, T. Y., Dillon, H., and Byrne, D. (**1998**). ''Speech recognition of hearing-impaired listeners: Predictions from audibility and the limited role of high-frequency amplification,'' J. Acoust. Soc. Am. **103**, 1128–1140.
Dau, T., Püschel, D., and Kohlrausch, A. (**1996**). ''A quantitative model of the 'effective' signal processing in the auditory system. II. Simulations and measurements,'' J. Acoust. Soc. Am. **99**, 3623–3631.
Dubno, J. R., Dirks, D. D., and Schaefer, A. B. (**1989**). ''Stop-consonant recognition for normal-hearing listeners and listeners with high-frequency hearing loss. II: Articulation index predictions,'' J. Acoust. Soc. Am. **85**, 355–364.
Dubno, J. R., Ahlstrom, J. B., and Horwitz, A. R. (**2000a**). ''Use of context by young and aged adults with normal hearing,'' J. Acoust. Soc. Am. **107**, 538–546.
Dubno, J. R., Horwitz, A. R., and Ahlstrom, J. B. (**2000b**). ''Speech recognition in noise at higher-than-normal levels: Decreases in scores and increases in masking,'' in Proc. IHCON (Int. Hear. Aid. Res. Conf.) 2000, p. 58.

Durlach, N. I., and Braida, L. D. (**1969**). ''Intensity perception. I. Preliminary theory of intensity resolution,'' J. Acoust. Soc. Am. **46**, 372–383.
Durlach, N. I., Braida, L. D., and Ito, Y. (**1986**). ''Towards a model for discrimination of broadband signals,'' J. Acoust. Soc. Am. **80**, 63–72.
Fletcher, H., and Galt, R. H. (**1950**). ''The perception of speech and its relation to telephony,'' J. Acoust. Soc. Am. **22**, 89–151.
Florentine, M. (**1985**). ''Non-native listeners' perception of American English in noise,'' in *Proceedings of Inter-Noise '85*, pp. 1021–1024.
French, N. R., and Steinberg, J. C. (**1947**). ''Factors governing the intelligibility of speech sounds,'' J. Acoust. Soc. Am. **19**, 90–119.
Grant, K. W., and Braida, L. D. (**1991**). ''Evaluating the articulation index for auditory-visual input,'' J. Acoust. Soc. Am. **89**, 2952–2960.
Green, D. M., and Birdsall, T. G. (**1958**). ''The effect of vocabulary size on articulation score,'' Technical Memorandum No. 81 and Technical Note AFCRC-TR-57-58, University of Michigan: Electronic Defense Group.
Hartmann, W. M. (**1998**). *Signals, Sound, and Sensation* (Springer Verlag, New York).
Hirsh, I. J., Reynolds, E. G., and Joseph, M. (**1954**). ''Intelligibility of different speech materials,'' J. Acoust. Soc. Am. **26**, 530–538.
Kalikow, D. N., Stevens, K. N., and Elliot, L. L. (**1977**). ''Development of a test of speech intelligibility in noise using sentence materials with controlled word predictability,'' J. Acoust. Soc. Am. **61**, 1337–1351.
Kamm, C. A., Dirks, D. D., and Bell, T. S. (**1985**). ''Speech recognition and the Articulation Index for normal and hearing-impaired listeners,'' J. Acoust. Soc. Am. **77**, 281–288.
Kryter, K. D. (**1960**). ''Speech bandwidth compression through spectrum selection,'' J. Acoust. Soc. Am. **32**, 547–556.
Kryter, K. D. (**1962a**). ''Methods for the calculation and use of the articulation index,'' J. Acoust. Soc. Am. **34**, 1689–1697.
Kryter, K. D. (**1962b**). ''Validation of the articulation index,'' J. Acoust. Soc. Am. **34**, 1698–1702.
Lippmann, R. P. (**1996**). ''Accurate consonant perception without mid-frequency speech energy,'' IEEE Trans. Speech Audio Process. **4**, 66–69.
Mayo, L. H., Florentine, M., and Buus, S. (**1997**). ''Age of second-language acquisition and perception of speech in noise,'' J. Speech Hear. Res. **40**, 686–693.
Miller, G. A., and Nicely, P. E. (**1954**). ''An analysis of perceptual confusion among some English consonants,'' J. Acoust. Soc. Am. **27**, 338–352.
Miller, G. A., Heise, G. A., and Lichten, W. (**1951**). ''The intelligibility of speech as a function of the context of the test material,'' J. Exp. Psychol. **41**, 329–335.
Müsch, H., and Buus, S. (**2001**). ''Using statistical decision theory to predict speech intelligibility. II. Measurement and prediction of consonant-discrimination performance,'' J. Acoust. Soc. Am. **109**, 2910–2920.
Oxenham, A. J., and Buus, S. (**2000**). ''Level discrimination of sinusoids as a function of duration and level for fixed-level, roving-level, and across-frequency conditions,'' J. Acoust. Soc. Am. **107**, 1605–1614.
Pavlovic, C. V. (**1993**). ''Problems in the prediction of speech recognition performance of normal-hearing and hearing-impaired individuals,'' in *Acoustical Factors Affecting Hearing Aid Performance*, edited by G. A. Studebaker and I. Hochberg (Allyn and Bacon, Needham Heights, MA), pp. 221–234.
Pollack, I. (**1959a**). ''Message uncertainty and message reception,'' J. Acoust. Soc. Am. **31**, 1500–1508.
Pollack, I. (**1959b**). ''Message repetition and message reception,'' J. Acoust. Soc. Am. **31**, 1509–1515.
Pollack, I. (**1964**). ''Message probability and message reception,'' J. Acoust. Soc. Am. **36**, 937–945.
Rankovic, C. M. (**1991**). ''An application of the articulation index to hearing aid fitting,'' J. Speech Hear. Res. **34**, 391–402.
Steeneken, H. J. M., and Houtgast, T. (**1980**). ''A physical method for measuring speech-transmission quality,'' J. Acoust. Soc. Am. **69**, 318–326.
Steeneken, H. J. M., and Houtgast, T. (**1999**). ''Mutual dependence of octave-band weights in predicting speech intelligibility,'' Speech Commun. **28**, 109–123.
van Rooij, J. C. G. M., and Plomp, R. (**1991**). ''The effect of linguistic entropy on speech perception in noise in young and elderly listeners,'' J. Acoust. Soc. Am. **90**, 2985–2991.
Warren, R. M., and Bashford, J. J. A. (**1999**). ''Intelligibility of $\frac{1}{3}$-octave speech: Greater contribution of frequencies outside than inside the nominal passband,'' J. Acoust. Soc. Am. **106**, L47–L52.
Warren, R. M., Riener, K. R., Bashford, J. J. A., and Brubaker, B. S. (**1995**). ''Spectral redundancy: Intelligibility of sentences heard through narrow spectral slits,'' Percept. Psychophys. **57**, 175–182.

Using statistical decision theory to predict speech intelligibility. II. Measurement and prediction of consonant-discrimination performance

Hannes Müsch and Søren Buus
Communications and Digital Signal Processing Center, Department of Electrical and Computer Engineering (442 DA) and Institute for Hearing, Speech, and Language, Northeastern University, Boston, Massachusetts 02115

(Received 6 March 2000; accepted for publication 23 March 2001)

The speech recognition sensitivity (SRS) model [H. Müsch and S. Buus, J. Acoust. Soc. Am. **109**, 2896–2909 (2001)] was tested by applying it to consonant-discrimination data collected in this study. Normally hearing listeners' abilities to discriminate among 18 consonants were measured in 58 filter conditions using two test paradigms. In one paradigm, listeners chose among all 18 stimuli. In the other, response alternatives were restricted to the correct response and eight consonants that were randomly selected among the 17 incorrect response alternatives. The effect of the number of response alternatives on performance can be described by statistical decision theory. Most filter conditions included one or more sharply filtered narrow bands of speech. Depending on the selection of bands, listeners' performance in multi-band conditions falls short of, equals, or exceeds the performance expected from multiplication of the error rates in the individual bands. The performance advantage in multi-band conditions increases with average band separation. The SRS model provides a good fit to the data and predicts the data more accurately than does the speech intelligibility index. © *2001 Acoustical Society of America.* [DOI: 10.1121/1.1371972]

PACS numbers: 43.66.Lj, 43.71.Es, 43.71.Gv [RVS]

I. INTRODUCTION

In a companion article, Müsch and Buus (2001) introduced the speech recognition sensitivity (SRS) model, which uses statistical decision theory to predict speech intelligibility from the audibility spectrum of the speech signal, the linguistic entropy (van Rooij and Plomp, 1991) of the speech, and the number of response alternatives. They showed that the SRS model accounts for several sets of data from the literature that cannot be explained easily with articulation-index-(AI) based models (French and Steinberg, 1947; Beranek, 1947; Fletcher and Galt, 1950; Kryter, 1962; ANSI, 1969, 1997). The SRS model and AI-based models combine the information in distinct spectral bands in fundamentally different ways. As a result, the SRS model can predict synergetic band interactions that AI-based models cannot account for. The SRS model also predicts the effects of interactions between linguistic entropy and filter condition on test scores. In addition, the SRS model appears to predict the effects of interactions among linguistic entropy, signal-to-noise ratio, and language proficiency on test scores. These effects cannot be explained by the AI models. Finally, the effect of the number of response alternatives on test performance, which must be determined empirically in articulation-index-based models, is described by the model structure. In short, the SRS model appears able to account for several phenomena that the articulation-index-based models, at best, have difficulty explaining.

A detailed explanation of the SRS model and its underlying assumptions is given in Müsch and Buus (2001). Briefly, the SRS model assumes that listeners correlate an auditory representation of the received signal with memorized templates of ''ideal'' representations of speech signals. All ideal signal templates are assumed to be mutually orthogonal. The ideal signal matches exactly one of the templates, and the correlation between this template and the ideal signal is unity. The correlation between the ideal signal and all other templates is zero. If the listener received the ideal signal, performance would be perfect. In practice, however, only a noise-degraded version of the signal is available and the correlations between the noise-degraded signal and the templates become random variables. These random variables can be transformed into decision variables with equal variances and means that are zero for the nontarget templates and larger than zero for the target template. In the following, the mean value of the transformed correlation between the auditory representation of the signal and the target template is called the congruence index, Δ. After correlating the representation of the received signal with all templates, the detector selects the template with the highest congruence index as the received signal. Performance depends, among other things, on the relation between the variance of the transformed random variables and the congruence index.

The model includes three sources of performance-limiting noises. One is related to the speech-production process. It arises because any utterance produced by a speaker only approximates the ideal template. The difference between the ideal signal that the talker attempts to produce and the waveform actually produced is a production-related noise.

The second noise source is related to the audibility of the speech signal. When the speech signal is clearly audible (i.e., more than 30 dB above threshold) intelligibility is maximal and no additional variance is introduced. As audi-

bility decreases, an additional variance is introduced to model the associated decrease of intelligibility.

The third noise source models the effect of linguistic entropy on intelligibility. Spoken messages with a high degree of sequential redundancy (e.g., sentences) require less audibility than messages with little redundancy (e.g., isolated words) to be recognized with equal accuracy (Miller *et al.*, 1951). To account for this effect, the model assumes an additional variance whose magnitude depends on the linguistic entropy of the speech material. The additional variance is small when the message has a high degree of redundancy and the variance is large when the redundancy in the message is small.

Predicted performance also depends on the number of response alternatives considered by the listener. For any listening condition, performance increases as the number of response alternatives decreases (Miller *et al.*, 1951). In forced-choice, *M*-alternative speech-recognition tests, the number of response alternatives is assumed to be equal to the number of stimulus alternatives if the listener is aware of all possible stimuli. In open-set recognition tasks, or if the listener is unaware of the test set, the number of response alternatives is assumed to equal the size of the listener's active vocabulary, possibly reduced to include only groups of items (e.g., nouns or two-syllable words) from which the stimuli are chosen.

One reason for adopting this model structure is its ability to account for redundant and synergetic interactions among spectral components of speech (speech bands). When evaluating redundancy or synergy, we will follow classical AI concepts, according to which speech bands are considered to contribute independently to intelligibility. Independence means that the probability of erring in the recognition of a phoneme in a broadband listening condition equals the product of the error probabilities that are measured when the speech bands that form the broadband condition are tested in isolation. When the error probability in a broadband condition is less than the product of the error probabilities in the individual subbands, the bands interact with synergy. Conversely, when the error probability in the broadband condition is larger than the product of the error probabilities in the individual bands, the bands are considered to carry redundant information.

Articulation-index-based models of speech intelligibility (French and Steinberg, 1947; Beranek, 1947; Fletcher and Galt, 1950; Kryter, 1962; ANSI, 1969, 1997) provide little flexibility to account for synergetic and redundant interactions among speech bands, because they are based on the assumption that speech bands contribute independently to the AI. Because band interactions are most noticeable when the speech spectrum is restricted to a few, spectrally disjoint speech bands, such conditions are excluded from the scope of the standardized AI models. To test the validity of the SRS model, which was designed to overcome this limitation, the experiment reported in this article focuses primarily on listening conditions that fall outside the stated scope of standardized AI models (ANSI, 1969, 1997).

To test the dependence of intelligibility on the number of response alternatives that is inherent in the SRS model structure, the experiments were performed with two response paradigms, which differed only in the number of response alternatives available to the listener. The second part of this article considers the ability of the SRS model and the speech intelligibility index (SII, ANSI, 1997) to account for the data.

II. MATERIAL AND PROCEDURE

Listeners' ability to discriminate among 18 consonants presented in a consonant-vowel (CV) context was tested in 58 filter conditions. Listeners were instructed to ignore the vowel identity and to report only the perceived consonant. In the first part of the experiment, all 18 possible consonants were offered as response alternatives. In the second part of the experiment, the same stimulus set was tested under the same filter conditions, but the number of response alternatives was reduced to nine consonants by eliminating nine response alternatives selected at random among all 17 incorrect response alternatives on any given trial. Therefore, all 18 consonants were equally likely to be valid responses. This response paradigm allows distinguishing between the effects of stimulus-set size and response-set size.

A. Test conditions

Each filter condition is composed of one or more one-critical-band-wide passbands. With a few exceptions, the bands in multiple-band conditions are spectrally separated by stopbands that are one or more critical bands wide. The speech level in each band is expressed by means of the band attenuation introduced by the filter. The long-term average speech level of the *unfiltered* speech at the input of the filter was held constant at 80 dB SPL throughout the experiment.

The audibility of any speech band was desired to be independent of the presence or absence of other speech bands. To this end, those parts of the speech spectrum that were removed by filtering were replaced by noise whose spectrum was shaped to match the average speech spectrum for normal vocal effort as defined in ANSI (1997) standard S3.5. The masking produced by the noise can only approximate the masking that the speech bands it replaces would have caused, because the masker must be steady in order not to encode any speech information (Shannon *et al.*, 1995). Therefore, the masking excitation caused by the noise is steady, whereas the masking excitation caused by speech covaries with the short-term level of the masked speech band. To avoid masking the low-level consonants, the constant masker level must be lower than the long-term average speech level, which is dominated by the level of the vowels. On the other hand, the masker level should approximate the long-time average speech level to simulate the spread of excitation that would have resulted during vowel presentation. To balance these opposing goals, the level of the speech-shaped noise masker was set to 40 dB SPL.

This masker was modified for every filter condition by inserting spectral notches that mirrored the passbands of the speech in that filter condition. The speech spectrum and the masker spectrum in each condition were complements that spanned the entire range of the speech spectrum without overlapping.

The edge frequencies of the passbands, as well as the band attenuations for every filter condition, are listed in Table I. Each row, identified by a condition number, represents one filter condition. The header specifies the edge frequencies of the passbands. The critical-band rates at the lower and upper edge frequencies are noted left and right of the slash, respectively.[1] Note that the bands listed in the header are adjacent and range from 1 to 21.2 Barks (100 to 8000 Hz).

The bands represented by each column are 1 Bark wide, with the exception of the bands corresponding to the left-most and right-most columns, which are 3 and 2.2 Barks wide, respectively. The numbers in the table represent the attenuation in dB of the speech signal in the bands relative to the level of the original speech within that band. Empty cells indicate that the speech in these bands was removed and replaced by speech-shaped noise. For example, in filter condition 25, the speech signal is restricted to the critical-band rates between 9 and 10 Barks and between 15 and 16 Barks. The speech level in these bands is attenuated 8 dB in the low band and 10 dB in the high band relative to the levels in these bands when the overall speech level is 80 dB SPL. Listening conditions marked with an asterisk were tested with twice as many repetitions as the unmarked conditions.

B. Test material

The test material was provided by researchers at the University of California, Los Angeles (UCLA), who recorded 18 consonants in the context of three vowels for two male and two female talkers (16-bit resolution and 16-kHz sampling frequency). The consonants are listed in Table II. Each talker spoke each consonant eight times in conjunction with the vowels /a/, /i/, and /u/. Thus, 1728 tokens were recorded. All tokens were rms equalized so that the unfiltered speech was always at the same level. The rms equalization keeps the intensity of the vowels nearly constant and the natural differences among the intensities of the consonants are maintained. The masker duration in each trial was 2046 ms, and the syllables, which were shorter than the masker, were temporally centered in the masker.

C. Test procedure

Listeners sat in a sound-attenuating booth wearing headphones through which the speech and masker were presented to the right ear. Each experiment was divided into 280 blocks ([58 unique filter conditions plus one repetition of 12 filter conditions]$\times$4 talkers). Each block consisted of 54 trials (18 consonants$\times$3 vowels). Within a block of trials, every consonant was presented three times, once with each vowel. All tokens within a block of trials were spoken by the same talker and processed by the same filter condition. For each trial, the syllable that was presented was chosen at random among the eight recordings of that syllable. After a consonant-vowel pair had been presented, all valid response alternatives were displayed on a computer screen inside the booth. The response alternatives were represented by transcriptions of the associated consonants (see Table II). The listeners indicated their selections by moving a cursor over the appropriate response and hitting a key. Listeners were given practice with unfiltered speech to ensure that they could associate the perceived phoneme with the transcription on the computer screen (see Table II).

D. Listeners

Five young female adults whose first language is American-English were recruited for the study. Their audiograms, acoustic reflexes, and tympanograms were clinically normal. To be admitted to the study, listeners' performance for unfiltered speech presented in the quiet had to exceed 90% correct responses. One listener, who could not meet this criterion after 2 h of practice, was not accepted into the study. Thus, the data presented are for four listeners, who participated in both parts of the experiment. All listeners were paid for their time.

E. Signal processing

The signal was filtered digitally in the frequency domain (TDT AP2) with a FIR filter whose coefficients were derived in a two-step process. First, the filter's transfer function was specified in the frequency domain. The filter slopes were linear on a critical-band-rate scale with slopes of -100 dB/Bark towards low critical-band rates and 50 dB/Bark towards high critical-band rates. To reduce the temporal distortion introduced by the filters, the impulse response was windowed in the time domain by a 20-ms Hanning window and transformed back into the frequency domain where it was multiplied with the discrete Fourier transform of the speech signal. As a result of the windowing, the frequency response is smoothed, but the deviations from the ideal transfer function are small.

The masker was generated digitally and mixed with the signal before D/A conversion (TDT DD1). The overall level of the analog signal was adjusted (TDT PA4) and led to a headphone buffer (TDT HB6), which fed the right earpiece of a Sony MDR-V6 headset.

III. RESULTS AND DISCUSSION

A. Effect of response-set size

1. Results

The filter conditions were selected to encompass a wide range of performances and the average results span the range from just above chance for the low-level single-band conditions to near perfect in the wideband conditions. The scores in all 58 filter conditions, averaged across all four listeners, are listed in Table III for the two response paradigms. The results for the individual listeners, together with the group average, are shown in Fig. 1. The percentage of correct consonant identifications is plotted as a function of the sensitivity index, d'. The solid lines show the theoretical relation between d' and the percentage of correct responses. This relation is described by

$$P_c = \int_{-\infty}^{\infty} f_{SN}(x,d',1) \cdot F_N^{M-1}(x,0,1)\, dx \tag{1}$$

TABLE I. Listing of the filter conditions used. Each row represents one filter condition. Each column specifies one potential passband. In each column heading, the numbers to the left and right of the slashes specify the critical-band rates at the passbands' lower and upper edges, respectively. The numbers in the table represent the attenuation in dB of the signal in the bands relative to the unfiltered speech level. Empty cells indicate that the speech in these bands was filtered out and replaced by speech-shaped noise. See text for details.

Filter condition	Critical-band rates at band edges																
	1/4	4/5	5/6	6/7	7/8	8/9	9/10	10/11	11/12	12/13	13/14	14/15	15/16	16/17	17/18	18/19	19/21.2
1	25																
2*			25														
3			16														
4*			8														
5			0														
6					25												
7*							25										
8							16										
9*							8										
10							0										
11									25								
12											30						
13													40				
14*													30				
15													20				
16*													10				
17													0				
18															30		
19																	30
20							25		25								
21							25				30						
22*							25						30				
23							25						10				
24							8						30				
25*							8						10				
26							25								30		
27							25										30
28					25		25										
29*			25				25										
30			8				25										
31			25				8										
32*			8				8										
33	25						25										
34													30				30
35													30		30		
36											30		30				
37									25				30				
38					25								30				
39*			25										30				
40			8										30				
41			25										10				
42*			8										10				
43	25												30				
44							25		25		30						
45			25						25						30		
46			25				25						30				
47			8				8						10				
48							25		25		30		30				
49	25						25						30				30
50	25						8						10				30
51					25		25		25		30		30		30		
52	25				25				25				30				30
53	25	25	25														
54	30	30	30	30	30												
55													30	30	30	30	30
56	10	10	10	10	10	10	10	10	10	10	10	10	10	10	10	10	10
57							20	20	20	20							
58				10	10	10	10				25	25	25	25			

TABLE II. Consonants used in the discrimination task in notation of the International Phonetics Association (upper row) and the corresponding representations on the response screen (bottom row).

IPA symbol																	
b	d	g	p	t	k	m	n	s	z	ʃ	ʒ	f	v	θ	ð	dʒ	tʃ
Representation on response screen																	
b	d	g	p	t	k	m	n	s	Z	sh	SH	f	V	th	TH	j	ch

(Hartmann, 1998), where P_c is the proportion of consonants identified correctly, $f_{SN}(\cdot,d',1)$ is the Gaussian probability density function with mean d' and unit variance, and $F_N(\cdot,0,1)$ is the cumulative Gaussian probability function with zero mean and unit variance. The relation depends on the number of available response alternatives, M. The upper curve is for $M=9$ and the lower is for $M=18$.

The filled circles show data obtained with the unrestricted response set of 18 consonants (part one of the experiment) and the unfilled circles show the data obtained when the response set is restricted to nine response alternatives (part two of the experiment). The error bars show plus and minus one standard error. Each graph holds 58 pairs of data points. Each pair corresponds to one filter condition. The SRS model predicts that for a given listener, the two members of any pair have the same sensitivity index (i.e., they are aligned vertically), because they differ only in the number of response alternatives, which has no effect on the congruence index or the powers of the performance limiting noises. Each pair is plotted at the d' that minimizes the sum of the weighted squared vertical distances between the data points and the solid lines. The weights were inversely proportional to the standard error of the measurement.

Note that the d's shown in Fig. 1 were not calculated by the SRS model, but were selected for each listening condition to minimize the difference between the measured performances and those predicted by Eq. (1). This is justified, because in this section we are only concerned with the accuracy of the transformation between d' and percent correct and its dependence on the number of response alternatives. In Sec. IV the data will be compared with predictions obtained from the full SRS model; for the present discussion,

TABLE III. Consonant-identification performance in percent averaged across four listeners. The condition identifier (column headed ''ID'') corresponds to the filter condition in the left-most column of Table I. Scores in the column $M=18$ were obtained with the full response set, and scores in the column $M=9$ were obtained when the response set was limited to nine alternatives.

	Average consonant-identification performance (%)				
ID	$M=18$	$M=9$	ID	$M=18$	$M=9$
1	17.4	32.2	30	30.0	46.1
2	11.5	19.5	31	34.6	48.4
3	18.4	31.6	32	35.6	50.5
4	23.7	38.0	33	32.2	43.9
5	25.2	42.6	34	56.7	66.2
6	10.4	16.3	35	51.7	60.9
7	13.9	21.6	36	40.5	51.5
8	21.2	30.1	37	44.7	55.3
9	27.0	42.5	38	41.0	51.7
10	28.9	41.0	39	44.5	55.3
11	18.4	25.5	40	48.4	62.8
12	19.7	28.4	41	47.5	64.1
13	20.9	29.7	42	54.9	69.6
14	33.3	45.4	43	50.3	60.5
15	35.5	54.2	44	45.4	56.7
16	37.9	53.8	45	51.5	63.3
17	35.0	51.3	46	52.5	67.7
18	30.2	42.6	47	65.4	79.4
19	26.6	38.1	48	64.2	74.2
20	25.9	39.0	49	77.3	84.6
21	34.5	43.3	50	80.6	89.7
22	43.8	56.1	51	78.9	84.8
23	52.4	65.7	52	79.7	88.9
24	53.6	64.4	53	29.6	44.6
25	60.9	73.1	54	30.6	48.6
26	42.6	54.4	55	68.9	80.3
27	43.6	53.2	56	92.7	96.6
28	16.7	27.5	57	55.1	66.0
29	20.8	35.0	58	78.5	86.7

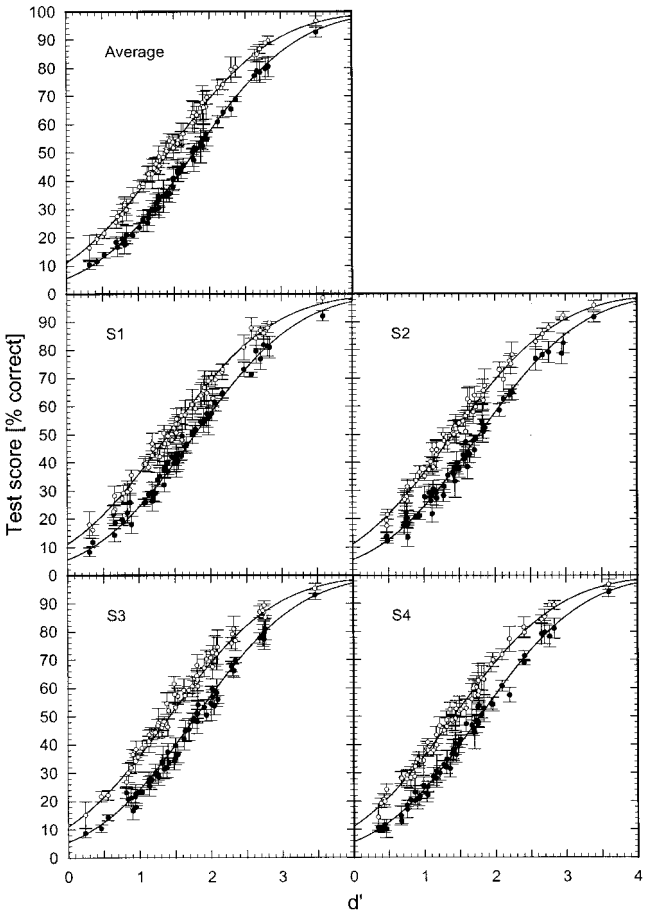

FIG. 1. Consonant-recognition scores as a function of identification sensitivity, d'. The top panel shows average data for the four listeners; the lower panels show data for individual listeners. The unfilled symbols are for $M=9$ and the filled symbols are for $M=18$. The lines are graphical representations of Eq. (1) [$M=9$ (upper line) and $M=18$ (lower line)]. See text for details.

the important point is that the effect of changing the number of response alternatives clearly is modeled very well by changing M in Eq. (1).

2. Discussion

An important assumption of the SRS model is that the speech recognition sensitivity is related to test performance by Eq. (1) and that the parameter M in Eq. (1) is the number of response alternatives considered by the listener. The data presented here support this assumption. The SRS model predicts that for any given sensitivity (i.e., listening condition and test material), the performance decreases when the number of possible responses considered by the listener increases, as described by Eq. (1). This idea was first proposed by Green and Birdsall (1958), who applied it successfully to data by Miller *et al.* (1951). Miller *et al.* (1951) measured the intelligibility of words drawn from phonetically balanced lists of different sizes. For any listening condition, performance decreased as the length of the list increased. For lists with 2, 4, 8, 16, 32, and 256 words, Eq. (1) accounted well for the performance change when M equaled the length of the list. For a list length of 1000 words, however, Eq. (1) described performance better when M was set to 4000 rather than 1000. Green and Birdsall (1958) suggested that the performance depended on the number of response alternatives rather than on the number of stimulus alternatives. When the stimulus set is small and known to the listener, the stimulus set and the set of response alternatives considered by the listener are identical. However, these sets dissociate when the list is unknown to the listener or is so large that listeners cannot memorize it accurately. In these cases, they compare the internal representation of the received signal with the representations of their entire active vocabulary, possibly reduced by lexical constraints implied by the test list. When the list encompassed 1000 items, listeners were likely to respond as if the response set were open. In these conditions, therefore, M in Eq. (1) must equal the size of the listener's active vocabulary, which was estimated to be 4000. Likewise, Müsch and Buus (2001), who used the SRS model to predict Kryter's (1962) transformations between AI and performance for different test-set sizes, concluded that conditions employing test lists with 1000 items clearly were modeled better when M in Eq. (1) was 8000 instead of 1000.

Green and Birdsall's (1958) suggestion that intelligibility is determined by the number of response alternatives considered by the listener is supported by data from Pollack (1959). He varied the stimulus- and response-set sizes in a word-recognition task independently and found that performance depends strongly on the size of the response set and much less on the size of the stimulus set.

The results of this study corroborate Pollack's (1959) finding. Because the stimulus sets were the same in both parts of the experiment, the performance difference between the two experimental conditions shows that the number of response alternatives considered by the listener has a strong influence on performance. Moreover, Eq. (1) appears to account for the effect of response alternatives on performance. This is seen in Fig. 1, which shows that the difference in performance between the two response paradigms are well summarized by Eq. (1). The ability of Eq. (1) to account for the effect of the number of response alternatives on performance is further illustrated in Fig. 2, which shows the d's derived from scores obtained with 18 response alternatives plotted as a function of the d's derived from the scores obtained with nine response alternatives. The d's were related to the test scores by inverting Eq. (1). The proximity of the points to the diagonals in Fig. 2 indicates that the performance differences between the two test paradigms can be explained by Eq. (1) if the parameter M is set to the number of response alternatives given to the listener. This finding, which holds for individual listeners as well as for the average across listeners, indicates that the d' in each filter condition is independent of the number of response alternatives, which is a basic assumption of the SRS model. Equation (1) is based on the assumption that the mental templates of the internal representations of the ''ideal'' signals are mutually orthogonal. The fact that Eq. (1) can model the effect of the number of response alternatives on performance also implies that deviations from this assumption are small and can be ignored if one is only interested in the overall identification performance.

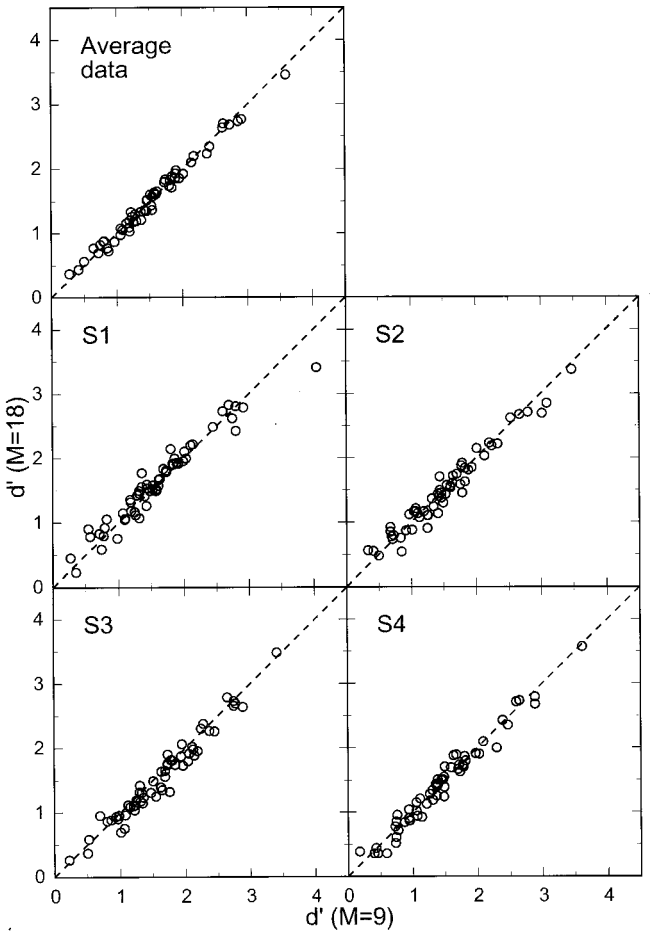

FIG. 2. Sensitivity index in the test condition with $M=18$ response alternatives as a function of the sensitivity index with $M=9$ response alternatives for 58 filter conditions. The sensitivity index is derived from the observed proportion of correct identifications by inverting Eq. (1). The top panel shows data derived from the average percentages of correct responses across the four listeners. The lower four panels show data for individual listeners.

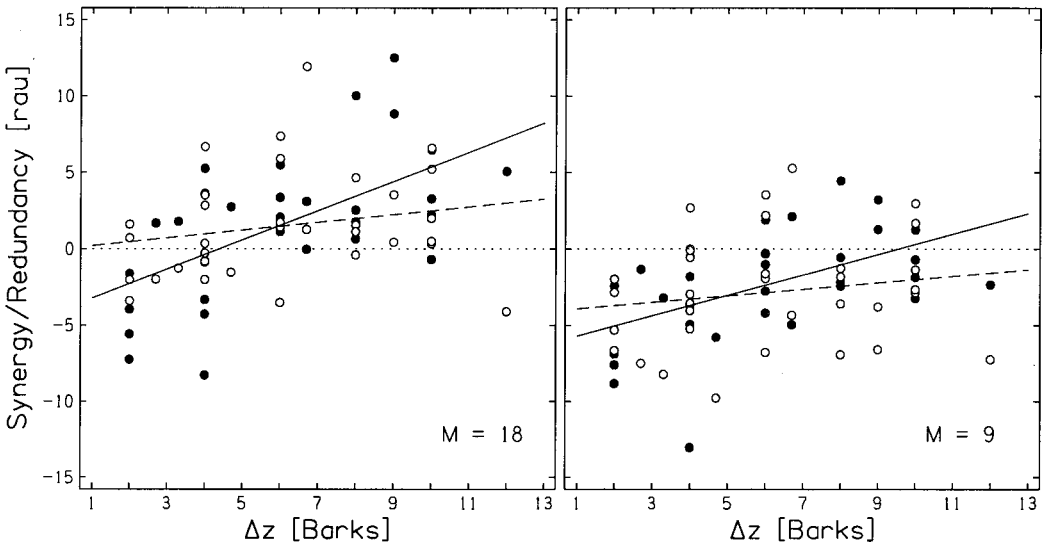

FIG. 3. The difference (ordinate) between the performance obtained in a multi-band condition and that calculated by multiplication of the error probabilities obtained for the individual bands is plotted as a function of average band separation (abscissa). Performances are in *rau*. Positive differences indicate that the bands interacted with synergy; negative values indicate that they carried redundant information. The filled circles show the redundancy/synergy calculated from the *measured* performances. The unfilled circles show the redundancy/synergy calculated from the *SRS model predictions*. The left and right panels are for 18 and 9 response alternatives, respectively. The lines are the best-fitting regression lines. The solid lines are for the measured performances (filled circles) and the dashed lines are for the SRS model predictions (unfilled circles). The trends indicate that synergy increases with band separation. See text for details.

B. Synergetic and redundant band interactions

1. Results

The effect of redundant and synergetic band interaction in the data collected for this study can be seen in Fig. 3, which shows the extent to which the performances obtained in the multi-band filter conditions (20 through 52) differ from those calculated from the performances obtained for the constituent single bands under the assumption that their error probabilities multiply. The calculated performances were transformed into rationalized arcsine units (rau; Studebaker, 1985) and subtracted from the actual multi-band performance scores, which were also transformed into rau. This difference is plotted as a function of the average spectral-band separation for two sets of data. The filled circles show data calculated from the average data for our four listeners. The unfilled circles show the data calculated from predictions by the SRS model. Positive differences indicate that the bands interacted with synergy and negative differences indicate that the bands carried redundant information. The regression line for the listeners' data (solid line) shows that redundancy tends to decrease and synergy tends to increase as the average band separation grows. The redundancy appears to be larger when the response-set size is small ($M=9$) than when the response-set size is large ($M=18$). These trends also are apparent in the data calculated from predictions by the SRS model. (The SRS-model predictions used to calculate the values for the unfilled circles in Fig. 3 are described in Sec. IV.)

2. Discussion

Figure 3 shows that disjoint speech bands combine with synergy in some filter conditions but with redundancy in other conditions. The likelihood that bands interact with synergy increases with their frequency separation.

Two factors are likely to be responsible for the shift from redundant to synergetic interaction that accompanies an increase in average band separation. The first factor pertains to spread of masking and explains why redundant interaction decreases as band separation increases. Although the bands in the single-band condition were embedded in masking noise to approximate the masking caused by the additional bands in the multi-band condition, the effective masking of any target band was likely to be stronger in the multi-band condition than in the single-band condition. The difference in effective masking between the two conditions decreases with increasing band separation. If masking in the multi-band condition exceeds masking in the single-band conditions, the bands will appear to carry redundant information. Because the masking difference decreases with increasing band separation, the apparent redundancy produced by masking also decreases with increasing band separation.

The second factor is related to the speech-production process. The SRS model postulates the existence of a production-related noise, whose spectral components are partially correlated. As will be explained in the next section, the correlation is assumed to decrease with increased spectral separation. The power of a noise composed of partially correlated components decreases as the correlation among its components decreases. Therefore, increased band separation results in reduced overall variance. Reduced overall variance, in turn, leads to improved performance. Therefore, any two bands with a given intelligibility will yield a higher dual-band score when the bands are widely separated than when they are close together.

This is reflected in Fig. 3, in which the multi-band advantage (calculated as the difference from the score obtained by combining the single-band scores under the assumption of band independence) increases with the average band separa-

tion. A two-way analysis of covariance [ANCOVA; Δz (continuous variable) by number of response categories (two levels: $M=9$ and $M=18$)] showed that the amount of synergy increased significantly as the average frequency separation between the disjoint speech bands increased [$F(1,62)=28.3$; $p<0.0001$].

Although the effect of the number of response categories and the interaction between the number of response categories and frequency separation were not significant ($p>0.05$), the band interaction appears to depend on test format. The synergy seems larger when the number of response alternatives is 18 than when it is nine. The explanation for this phenomenon is likely to be found in the shape of the curve that relates d' to performance [Eq. (1) and Fig. 1]. When the local slope of the curve increases over the range of d's encompassed by the single- and multi-band conditions, synergy will tend to be larger than when the slope is nearly constant over the region of d's encompassed by the single- and multi-band conditions. Specifically, when the d's for the single bands fall onto the shallow part of the curve and the d' for the dual-band condition—which is always larger than the d' for the most intelligible single band—falls on the steep part, the predicted intelligibility in the dual-band condition will be larger than when the slope of the transformation function does not increase. Consequently, synergy is more likely to be observed when the transformation function steepens in the range of d' predicted by the model. As M in Eq. (1) increases, the curves become shallower at small d's and steeper at d's that correspond to medium performance levels. Consequently, the likelihood that bands interact with synergy increases with the number of response alternatives given the listening conditions used in the present study.

Steeneken and Houtgast (1999) recently proposed a modification of the Articulation Index in which the contribution to the Articulation Index by each octave band of speech can be lowered depending on the contribution of the adjacent lower-frequency band. This approach might model the redundant band interaction between adjacent octave bands, but it cannot account for the synergetic band interaction seen in Fig. 3.

IV. MODEL PREDICTIONS

In this section, the discrete approximation of the SRS model (Müsch and Buus, 2001) and the SII model (ANSI, 1997) will be applied to the data.

A. Method

1. SRS model

The discrete approximation of the SRS model requires that the speech spectrum be described by the band levels of a set of adjacent spectral bands. Accordingly, the speech spectrum is divided into 19 bands. All bands are one critical band wide, with the exception of the band at the highest frequencies, which is 2.2 Barks wide. The SRS model derives the recognition sensitivity, d', as

$$d'=\frac{\Sigma_i \Delta(i)}{\sqrt{\Sigma_i \sigma_N^2(i)+\Sigma_i \Sigma_j (r(z(i),z(j))\sigma_p(i)\sigma_p(j))+\sigma_{\mathrm{cog}}^2}}, \quad (2)$$

where the summation indexes i and j run over all bands. For every band the congruence index, $\Delta(i)$, the power of the production noise, $\sigma_p^2(i)$, and the power of the audibility-related noise, $\sigma_N^2(i)$, must be determined. In addition, the power of the cognitive noise, σ_{cog}^2, and the correlation, $r(i,j)$, between the production noises in the bands centered at $z(i)$ and $z(j)$ must also be defined. The SRS model assumes that the correlation is described by the formula

$$r(z(i),z(j))=e^{-\alpha(z(i)-z(j))^2}, \quad (3)$$

where the parameter α can be adjusted freely. In the present article and the companion article (Müsch and Buus, 2001), α is set equal to 0.0766, which yields a 3.2-Bark equivalent rectangular bandwidth of the correlation function.

The congruence indexes, $\Delta(i)$, in the individual bands are derived from the congruence-index density, $\delta(z)$, as

$$\Delta(i)=\int_{z_L(i)}^{z_H(i)} \delta(z)\,dz. \quad (4)$$

The congruence-index density is comparable to the frequency-importance function of the articulation index. As in the companion article, $\delta(z)$ is assumed to be proportional to the band-importance function ''NNS'' (ANSI, 1997, Table B.1), which is valid for ''various nonsense syllable tests where most of the English phonemes occur equally often'' (ANSI, 1997, p. 19). In particular, $\delta(z)=19*\mathrm{NNS}(z)$, where $\mathrm{NNS}(z)$ is the continuous importance-density function on a critical-band-rate scale that is derived from the critical-band importance function of Table B.1, ANSI (1997). The scale factor is convenient because it ensures that the average congruence index of a one-critical-band-wide band of speech is one.

The power of the production-related noises in any band is determined by the congruence index and the band articulation sensitivity, $d_p'(i)$:

$$\sigma_p^2(i)=(\Delta(i)/d_p'(i))^2. \quad (5)$$

The band articulation sensitivity, $d_p'(i)$, is assumed to be independent of frequency when the bands are narrower than the 3.2-Bark equivalent rectangular width (ERW) of the correlation function [Eq. (3)], as is true for the present data. Consequently, the production-related noises in all bands are defined by specifying only one free parameter, d_p', which is set equal to 3.5 in accordance with the value used in the companion paper.

The audibility-related noise powers in the bands are derived from the signal-to-noise ratios (SNR) in the bands. In any band, the SNR is taken as the difference in dB between the excitation generated by the average speech energy in that band and the masking excitation in the band. The overall masking excitation in a band is calculated as the intensity

sum of three component excitations. One component is the excitation generated by any acoustic masker that is presented together with the speech. The masker can have spectral components in the target band (direct excitation) and/or in remote bands (spread of excitation). Another masking component is the excitation generated by speech in neighboring bands that spreads into the target band. The third component is the excitation of an internal noise floor, which is included to account for the absolute threshold of hearing.

An excitation-pattern model that employed RoEx filters (Patterson, 1976; Glasberg and Moore, 1990) spaced at 0.1-Bark intervals was used to calculate the band excitations. The excitation caused by the acoustic masker was calculated separately from the masking excitation generated by the speech in neighboring bands. The excitation pattern of the speech signal was calculated from the average speech spectrum of the test syllables. The average was taken across all recorded syllables.

When the SNR is larger than 30 dB, the intelligibility predicted by the model is determined only by production accuracy, bandwidth, and the variance introduced by the cognitive processes involved in speech recognition. Audibility-related variance is assumed to be absent because the entire dynamic range of the signal is audible. As the SNR decreases, additional variance is introduced to model the intelligibility reduction that is associated with the reduced audibility. Below 30 dB SNR, the power of the audibility-related variance is assumed to be linearly related to the SNR. As SNR decreases, σ_N^2 increases:

$$\sigma_N^2(i) = a[\min(\mathrm{SNR}(i), 30) - 30]. \tag{6}$$

The rate, a, at which σ_N^2 changes with SNR is the same as that used in the companion article, -0.032. Finally, the power of the cognitive noise, σ_{cog}^2, was set to unity, which is the same value used to predict Kryter's (1962) transformation functions between A1 and nonsense-syllable recognition performance in the companion article (Müsch and Buus, 2001).

2. SII model

The SII model is defined in ANSI (1997), which states that ''the scope of the standard is limited to [...] communication conditions which do not include multiple, sharply filtered bands of speech or sharply filtered noise'' (ANSI, 1997, p. 1). Although the standard does not define sharply filtered bands of speech, it seems reasonable to assume that most of the filter conditions tested in this article are excluded from the scope of the SII model. Despite this limitation, the SII model is applied to the data in order to provide a reference for judging the fitting accuracy of the SRS model.

The SII was calculated with the $\frac{1}{3}$-oct-band procedure in accordance with the ANSI standard, except that the actual speech spectrum rather than the standard speech spectrum was used. The same importance-density function that was used to form the congruence-density function of the SRS model was used for the SII calculation.

B. Results

Figure 4 shows the predictions obtained with the SRS model together with predictions by the SII model. The symbols in the panels on the left show the measured scores as a function of calculated SII. The symbols in the panels on the right show the measured scores as a function of the calculated recognition sensitivity. The filled symbols are for listening conditions with only one passband. The unfilled symbols are for listening conditions with multiple, spectrally disconnected passbands. These conditions are excluded from the scope of the SII.

Because the SII and the recognition sensitivity, d', both are independent of the number of response alternatives, every data point in the upper panels has a corresponding data point at the same SII (or d') in the lower panels. A similar correspondence exists in the horizontal direction. Every data point in the left column, in which test scores are plotted as a function of SII, can also be found in the right column, in which the same scores are plotted as a function of d'.

The solid lines are the transformations that relate SII (left panels) and d' (right panels) to the predicted performance. The scatter of the data points around these lines is a measure of the models' prediction accuracy. For the SRS model, the curves are graphical representations of Eq. (1) for $M=18$ (top) and $M=9$ (bottom). These transformations are specified by the SRS-model's structure and cannot be adjusted to match the data. Transformations between SII and predicted test score, on the other hand, are left unspecified by the ANSI (1997) standard and must be defined by the user to match the data. The transformations used here are modifications of transformations between AI and open-set phoneme identification in a nonsense-syllable context that were proposed by Fletcher and Galt (1950). These transformations are a direct result of the assumption that bands contribute independently to intelligibility. They were modified to account for correct guessing. The lowest expected performance depends on the size of the response set, M. The proportion, P_c, of correctly identified consonants is

$$P_c = 1 - \left(1 - \frac{1}{M}\right) \cdot 10^{-(\mathrm{SII}/p)}, \tag{7}$$

where M is the size of the response set and p is a fitting constant, which is presumed to account for the listener's proficiency in speech recognition (Ching *et al.*, 1998). Two curves, one for $M=9$ and one for $M=18$, were fitted to minimize the mean squared error between the predictions and the curves. Because the same group of listeners served in both parts of the experiment, the parameter p is the same for both curves ($p=0.82$).

C. Discussion

The SRS model appears to account better for this set of data than the SII model. The data points scatter more widely around the transformation curves for the SII model than for the SRS model. The root-mean-square difference between the measured scores and the predicted scores, expressed in rationalized arcsine units (rau; Studebaker, 1985), is 6.5 rau for the SRS model and 11.3 rau for the SII model. Thus, the

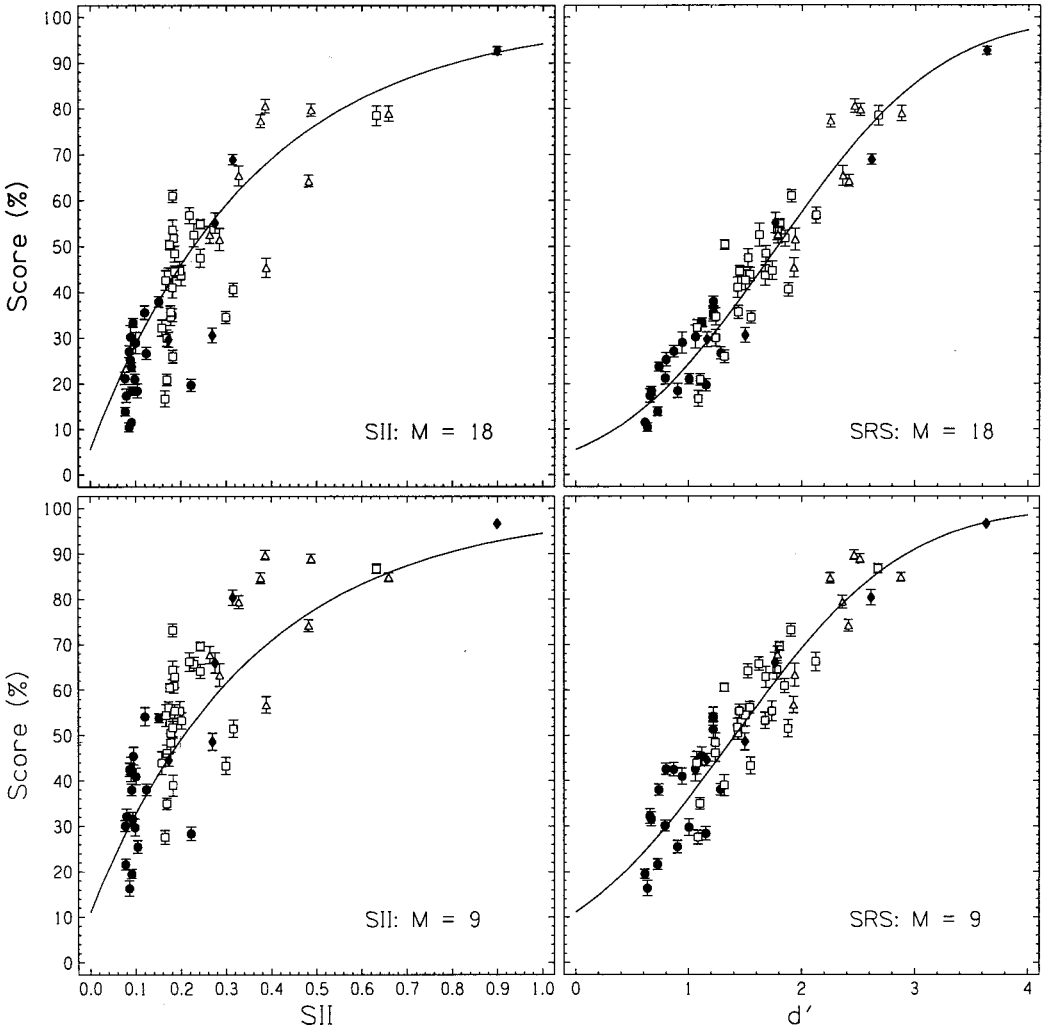

FIG. 4. Predictions of consonant discrimination in 58 listening conditions with two response paradigms. The left column shows predictions with the SII model and the right column shows predictions with the SRS model. The top panels are for the first part of the experiment in which the full response set of 18 consonants was available on every trial. The bottom panels are for the second part of the experiment in which the response set was restricted to nine consonants. The lines in the left panels are transformation functions between SII and percentage of correct responses. The lines in the right panels are transformation functions between d' and percentage of correct responses calculated from Eq. (1). The filled circles represent filter conditions with one narrow passband. The unfilled squares represent filter conditions with two disjoint passbands. The unfilled triangles are for conditions with three or more disjoint passbands. The filled diamonds are for wideband conditions. Accordingly, all unfilled symbols show data that are outside the scope of the SII. The error bars show ± 1 standard error. See text for further explanation.

SRS model almost halves the average difference between measured and predicted performance in the SII model.

Both models show significant differences between the predictions and the measured scores. The 95%-confidence interval (two-sided one-sample t test) of 35 data points includes the transformation of the SRS model, whereas in the SII model the same is true for only 31 data points. If the discrepancies between the measured scores and the predictions were due only to measurement error, the 95% confidence intervals of 110 data points were expected to overlap with the transformation curves. Significant differences between measured and predicted scores were expected because both the SRS and the SII model are macroscopic models that do not use the time course of the signal for their predictions. Nevertheless, based on the long-term average power spectrum of the speech alone, the SRS model predicts average intelligibility to within 6.5 rau of its measured value. This means that the predicted intelligibility generally will be within 6.5% of the obtained performance when the performance is moderate (30 to 70% correct) and even closer for performances outside this range.

The SRS model's better performance is not surprising, because the SII is only expected to account for listening conditions with one contiguous passband. This restriction is met only in the filter conditions that are represented by the filled symbols in Fig. 4. The conditions represented by the unfilled symbols are excluded from the scope of the SII. Moreover, only one parameter, specified in Eq. (7), could be adjusted freely for the SII prediction, whereas four parameters were varied to produce the fit for the SRS model. Of course, many aspects of the SII model are based on empirical fits of that model's structure to other sets of data during the development of the SII model. These implicit parameters include the rate at which SII grows with SNR and the importance-density function. The corresponding parameters in the SRS model had to be selected based on the data of this study and

a study presented in the companion article (Müsch and Buus, 2001).

Altogether, the SRS model predicts a large set of data points with few parameters. The data obtained in the present study together with a variety of data from the literature (see Müsch and Buus, 2001) has yielded a preliminary set of parameter values, which allow it to make good predictions of the present data as well as a variety of data from the literature. Some of these data cannot be predicted easily with AI-based models (Müsch and Buus, 2001). Moreover, the prediction accuracy of the SRS model surpasses that of the SII model for the present data.

V. CONCLUSIONS

Consonant-discrimination performance was measured in 58 filter conditions using two test paradigms. Most filter conditions included two or more sharply filtered narrow bands of speech. The test paradigms differed only in the number of response alternatives available to the listener. The measured performance was modeled using the SII model (ANSI, 1997) and the discrete approximation of the SRS model (Müsch and Buus, 2001).

The consonant-discrimination data show that listeners extract cues from speech in distinct spectral bands that are either redundant, independent, or interact with synergy as defined by the relation between measured error rates and error rates obtained as the product of error rates for individual narrow bands. The likelihood that listeners combine speech cues in different bands synergistically increases with the spectral separation between the bands and with the number of response alternatives available to the listener.

The data confirm that when the number of stimulus alternatives is fixed, changing the number of response alternatives strongly affects recognition performance. The data also show that changes in recognition performance caused by changes in the number of response alternatives are well described by the 1-of-M decision rule [Eq. (1)] that is part of the SRS model.

Four model parameters of the SRS model were chosen to give good fits to the data presented here and to data from the literature (Müsch and Buus, 2001). The present data appear to be modeled better by the SRS model than by the SII model. The model's ability to predict a wide range of data with a consistent set of model parameters makes it likely that universal model parameters, which could be used in any listening condition, can be found. To establish this set of universal parameters, the model must be fit to a wider range of speech materials, response paradigms, and listening conditions.

ACKNOWLEDGMENTS

We would like to thank Brian Strope for allowing us to use his speech recordings. Thanks are also due to Mary Florentine and Joanne Miller as well as to two anonymous reviewers for their helpful comments. This work was supported by NIH/NIDCD and by Sigma Xi Grants-in-Aid for Research.

[1]Critical bands are converted into frequency by the following relation (Buus, 1997):

$$f(z)=\left(\frac{9800\ \text{Hz}^{0.81}\ \text{Barks}}{0.81(28.32\ \text{Barks}-z)}\right)^{1/0.81}-1750\ \text{Hz}.$$

[Note that this formula corrects a typographical error in Buus's (1997) Eq. 3.]

ANSI (**1969**). ANSI S3.5-1969 ''Methods for the calculation of the articulation index'' (American National Standards Institute, New York).

ANSI (**1997**). ANSI S3.5-1997 ''Methods for calculation of the speech intelligibility index'' (American National Standards Institute, New York).

Beranek, L. L. (**1947**). ''The design of speech communication systems,'' Proc. IRE **35**, 880–890.

Buus, S. (**1997**). ''Auditory masking,'' in *Encyclopedia of Acoustics, Vol. 3*, edited by M. J. Crocker (Wiley, New York), pp. 1427–1445.

Ching, T. Y., Dillon, H., and Byrne, D. (**1998**). ''Speech recognition of hearing-impaired listeners: Predictions from audibility and the limited role of high-frequency amplification,'' J. Acoust. Soc. Am. **103**, 1128–1140.

Fletcher, H., and Galt, R. H. (**1950**). ''The perception of speech and its relation to telephony,'' J. Acoust. Soc. Am. **22**, 89–151.

French, N. R., and Steinberg, J. C. (**1947**). ''Factors governing the intelligibility of speech sounds,'' J. Acoust. Soc. Am. **19**, 90–119.

Glasberg, B. R., and Moore, B. C. J. (**1990**). ''Derivation of auditory filter shapes from notched-noise data,'' Hear. Res. **47**, 103–138.

Green, D. M., and Birdsall, T. G. (**1958**). ''The effect of vocabulary size on articulation score,'' Technical Memorandum No. 81 and Technical Note AFCRC-TR-57-58, University of Michigan: Electronic Defense Group.

Hartmann, W. M. (**1998**). *Signals, Sound, and Sensation* (Springer Verlag, New York).

Kryter, K. D. (**1962**). ''Methods for the calculation and use of the Articulation Index,'' J. Acoust. Soc. Am. **34**, 1689–1697.

Miller, G. A., Heise, G. A., and Lichten, W. (**1951**). ''The intelligibility of speech as a function of the context of the test material,'' J. Exp. Psychol. **41**, 329–335.

Müsch, H., and Buus, S. (**2001**). ''Using statistical decision theory to predict speech intelligibility. I. Model structure,'' J. Acoust. Soc. Am. **109**, 2896–2909.

Patterson, R. D. (**1976**). ''Auditory filter shapes derived with noise stimuli,'' J. Acoust. Soc. Am. **59**, 640–654.

Pollack, I. (**1959**). ''Message uncertainty and message reception,'' J. Acoust. Soc. Am. **31**, 1500–1508.

Shannon, R. V., Zeng, F. G., Kamath, V., Wygonski, J., and Ekelid, M. (**1995**). ''Speech recognition with primarily temporal cues,'' Science **270**, 303–304.

Steeneken, H. J. M., and Houtgast, T. (**1999**). ''Mutual dependence of octave-band weights in predicting speech intelligibility,'' Speech Commun. **28**, 109–123.

Studebaker, G. A. (**1985**). ''A 'rationalized' arcsine transformation,'' J. Speech Hear. Res. **28**, 455–462.

van Rooij, J. C. G. M., and Plomp, R. (**1991**). ''The effect of linguistic entropy on speech perception in noise in young and elderly listeners,'' J. Acoust. Soc. Am. **90**, 2985–2991.

Psychophysical recovery from single-pulse forward masking in electric hearing

David A. Nelson[a] and Gail S. Donaldson
Clinical Psychoacoustics Laboratory, University of Minnesota, MMC 396, 420 Delaware St. S.E., Minneapolis, Minnesota 55455

(Received 10 October 2000; revised 9 March 2001; accepted 20 March 2001)

Psychophysical single-pulse forward-masking (SPFM) recovery functions were measured for three electrodes in each of eight subjects with the nucleus mini-22 cochlear implant. Masker and probe stimuli were single 200-μs/phase biphasic current pulses. Recovery functions were measured at several masker levels spanning the electric dynamic range of electrodes chosen from the apical, middle, and basal regions of each subject's electrode array. Recovery functions were described by an exponential process in which threshold shift (in μA) decreased exponentially with increasing time delay between the masker and probe pulses. Two recovery processes were observed: An initial, rapid-recovery process with an average time constant of 5.5 ms was complete by about 10 ms. A second, slow-recovery process involved less masking than the rapid-recovery process but encompassed much longer time delays, sometimes as long as several hundred milliseconds. Growth-of-masking slopes for the rapid process depended upon time delay, as expected in an exponential recovery process. Unity slopes were observed at a time delay of 0 ms, whereas progressively shallower slopes were observed at time delays of 2 ms and 5 ms. Many recovery functions demonstrated nonmonotonicities or ''facilitation'' at very short masker-probe delays (1–2 ms). Such nonmonotonicities were usually most pronounced at low masker levels. Time constants for the rapid-recovery process did not vary systematically with masker level or with electrode location along the implanted array. Most subjects demonstrated rapid-recovery time constants less than 7 ms; however, the subject with the longest duration of deafness prior to implantation exhibited clearly prolonged time constants (9–24 ms). Time constants obtained on basal electrodes were inversely related to word recognition scores.
[DOI: 10.1121/1.1371762]

PACS numbers: 43.66.Dc, 43.66.Mk, 43.66.Ts, 43.64.Me [SPB]

I. INTRODUCTION

This paper describes psychophysical forward-masking recovery functions obtained in human cochlear implant listeners using a specific stimulus paradigm in which both masker and probe stimuli are single, biphasic current pulses. We refer to this paradigm as ''single-pulse forward masking'' (SPFM). SPFM recovery functions are of interest because they are thought to reflect the refractory characteristics of underlying peripheral auditory nerve fibers (ANFs). Because neural degeneration is likely to alter ANF refractory properties, SPFM recovery functions may provide an indication of peripheral auditory neural status in cochlear implant patients and may help to explain differences in subjects' performance on psychophysical and speech recognition tasks. It is important to distinguish SPFM from pulse-train forward masking (PTFM), which uses longer duration probe and masker signals, since the two paradigms yield recovery functions with quite different characteristics (Donaldson and Nelson, 1999). Although differences between SPFM and PTFM are not well understood, it is likely that SPFM provides a more direct measure of short-term recovery processes than PTFM (Donaldson and Nelson, 1999) and that SPFM is less affected than PTFM by central auditory phenomena such as temporal pattern recognition (Blamey and Dooley, 1993).

Physiological SPFM recovery functions have been reported in animals with implanted electrode arrays (Stypulkowski and van den Honert, 1984; Miller *et al.*, 1993; Zhou *et al.*, 1995) and in human cochlear implant listeners (Brown *et al.*, 1990; Abbas and Brown, 1991; Brown *et al.*, 1996; Hong *et al.*, 1998). Such functions are obtained by presenting two identical current pulses in close succession and measuring the amplitude of the neural response to the second pulse as a function of inter-pulse time delay. In general, reported functions follow an exponential time course of recovery with time constants less than 5 ms. Animal studies indicate that recovery time constants vary with spike-initiation site and with the morphological characteristics of fibers in deafened ears (Stypulkowski and van den Honert, 1984; Miller *et al.*, 1993; Zhou *et al.*, 1995). An intriguing aspect of some physiologic SPFM functions is the existence of level-dependent nonmonotonicities at very short time delays (<2 ms) (Stypulkowski and van den Honert, 1984; Miller *et al.*, 1993).

Brown *et al.* (1996) obtained both physiological and psychophysical SPFM functions in a group of human cochlear implant listeners. Psychophysical and physiological functions had similar recovery characteristics in many subjects, suggesting that psychophysical SPFM measures are

[a]Author to whom correspondence should be addressed. Electronic mail: dan@tc.umn.edu

TABLE I. Subjects. Subject identifying code, gender, age when tested for the present study, etiology of deafness (implanted ear), duration of bilateral severe-to-profound hearing loss prior to implantation, depth of electrode array insertion (mm from the round window, with 25 mm representing complete insertion), duration of implant use prior to the study, and percent-correct score on the NU-6 monosyllabic word test in quiet. NU-6 scores were obtained at a presentation level of 65 dB SPL with subjects using their own speech processor programmed in the MPEAK (subject EJQ) or SPEAK (all other subjects) speech processing strategy.

Subject code	M/F	Age	Etiology of deafness	Dur. (years)	Depth (mm)	CI use (years)	NU-6 (% C)
AGF	m	79	Noise exposure; progressive SNHL	25	20	8	6
AMB	m	56	Familial progressive SNHL	1	25	7	68
CJP	m	31	Maternal rubella; progressive SNHL	<1	23	2	70
DAW	f	59	Otosclerosis	10	25	1	40
EJQ	f	54	Mumps; progressive SNHL	9	22	10	0
GPB	m	59	Meningitis	<1	25	2	28
JPB	m	61	Progressive SNHL	4	24	9	70
RFM	m	66	Meniere's disease	1	22	10	24

primarily determined by mechanisms operating at the level of the eighth nerve. In some subjects, psychophysical recovery was slower than physiological recovery, suggesting that central factors may secondarily affect psychophysical measures of SPFM in some listeners.

In an earlier study, Brown and Abbas (1990) demonstrated an inverse correlation between recovery time constants obtained from physiological SPFM functions and scores on word and sentence recognition tasks, although a later report failed to confirm that relationship (Brown *et al.*, 1999). These interesting findings suggests that SPFM time constants could provide an index of peripheral auditory status in individual cochlear implant patients. To our knowledge, the relationship between psychophysical SPFM recovery characteristics and speech recognition has not yet been evaluated.

In summary, the existing literature indicates that SPFM is a potentially important phenomenon in electric hearing and warrants further investigation. The present study was designed to examine characteristics of psychophysical SPFM recovery functions, including the general form of the SPFM recovery function, the dependence of recovery function shapes on masker level, and the extent to which recovery characteristics vary across cochlear implant listeners and regions of the implanted array. Recovery functions were obtained from apical, middle and basal electrodes in each subject for masker levels ranging from 25 to 75% of the masker dynamic range, and were analyzed using an exponential model of recovery. Slopes of growth-of-masking functions derived from SPFM recovery functions were also evaluated.

II. METHODS

A. Subjects

Subjects were eight post-lingually deafened adults implanted with the Nucleus mini-22 electrode array and receiver/stimulator. Table I displays relevant information for each subject, including age at implantation, etiology of deafness, duration of hearing loss prior to implantation, duration of implant use prior to participation in the study, and performance on the NU-6 monosyllabic word test in quiet.

Psychophysical recovery functions were measured for each of three test electrodes per subject. Test electrodes were distributed across the electrode array, with one electrode near the apical end of the array, one electrode near the middle of the array, and a third electrode near the basal end of the array.[1] All subjects were stimulated in bipolar mode, using an electrode separation of 1.5 mm (BP+1 mode) or the narrowest separation greater than 1.5 mm that would allow maximum acceptable loudness to be achieved at realizable current amplitudes. Table II lists the specific electrode pairs evaluated in each subject and corresponding bipolar separations.

B. Stimuli and procedures

1. SPFM recovery functions

Experiments were controlled by a microcomputer connected through a parallel port to a specialized cochlear implant interface (Shannon *et al.*, 1990). Stimuli were single, biphasic current pulses with a per-phase duration of 200 μs, and a delay between phases of 44 μs. Figure 1 illustrates the stimulation protocol used to obtain SPFM recovery functions. As shown in the figure, a single ''masker'' pulse was presented first, followed at some time delay by a single

TABLE II. Test electrodes. Subject identifying code, test electrodes and their bipolar separations. Electrode numbers increase from apex to base (research electrode numbering system, denoted by an ''r'' before electrode number). Each electrode pair is referred to in the text by the higher-numbered (more basal) electrode. Bipolar separation refers to the distance between the active and reference electrodes in a given electrode pair. These separations were 1.5 mm (BP+1), 2.25 mm (BP+2), 3.0 mm (BP+3) or 3.75 mm (BP+4).

Subject code	Test electrodes (Bipolar separation)		
AGF	r12 (BP+2)	r16 (BP+1)	r21 (BP+1)
AMB	r06 (BP+2)	r12 (BP+2)	r20 (BP+2)
CJP	r05 (BP+2)	r12 (BP+2)	r19 (BP+2)
DAW	r04 (BP+1)	r17 (BP+1)	r21 (BP+3)
EJQ	r06 (BP+3)	r11 (BP+3)	r17 (BP+3)
GPB	r05 (BP+1)	r12 (BP+1)	r20 (BP+1)
JPB	r07 (BP+4)	r11 (BP+4)	r16 (BP+4)
RFM	r05 (BP+1)	r15 (BP+1)	r20 (BP+1)

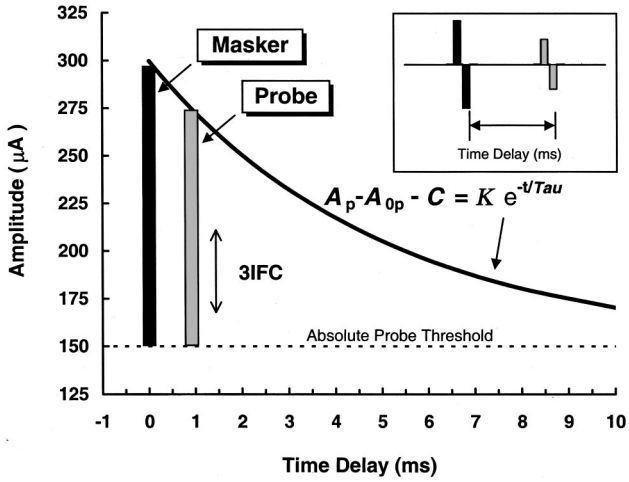

FIG. 1. Schematic diagram of the stimulus protocol used to measure single-pulse forward-masking recovery functions.

''probe'' pulse. The current amplitude of the masker pulse was fixed, and for a particular time delay, the amplitude of the probe pulse was varied adaptively to determine masked threshold. By varying the time delay between masker and probe pulses in different adaptive tracks, a recovery function was defined. In this report, time delay (ms) is measured between masker offset and probe offset (Fig. 1 inset), masker and probe amplitudes are specified in microamperes (μA) of current, and masked thresholds for the probe are specified in terms of threshold shift (TS) in μA, i.e., the amplitude difference between the masked threshold of the probe (A_p) and the unmasked threshold of the probe in quiet (A_{0p}).[2]

2. Absolute thresholds and maximum acceptable loudness levels

Prior to obtaining recovery functions for a particular electrode, absolute detection threshold (THS) and maximum acceptable loudness level (MAL) were determined for the single-pulse stimuli. THS was measured with a 3-interval forced choice (3IFC) adaptive procedure similar to that used for measuring masked thresholds (described below). MAL was measured with an ascending method of limits procedure in which single pulses, presented at a rate of 2/s, were slowly increased in amplitude until the subject indicated that loudness had reached a ''maximum acceptable'' level. Estimates for two consecutive ascending runs were averaged to obtain a single measure of MAL. THS and MAL were measured at the start of each test session for the particular electrode to be evaluated in that session. Values reported here represent the average of all measures obtained across sessions.

3. Masked thresholds

Forward-masked thresholds were obtained using a 3IFC adaptive procedure. The masker pulse was presented in each of three listening intervals. The probe pulse was presented in one of the three intervals, chosen randomly from trial to trial, at some fixed time delay following the masker pulse. The subject's task was to choose the ''different'' interval by pressing the appropriate button on a three-button computer mouse. Stimulus intervals were cued on a video monitor, and correct-answer feedback was provided after each trial. The amplitude of the probe pulse was initially set 0.5 dB to 4 dB (depending on the dynamic range of the test electrode) above the anticipated masked threshold. For the first four reversals, probe level was altered according to a 1-down/1-up stepping rule, with step size equal to 1 dB (about 6 current step units {CSUs}).[3] These initial reversals quickly moved the adaptive procedure into the target region for masked threshold. After the fourth reversal, step size was reduced, typically to one-fourth of the initial step size, and a 3-down/1-up stepping rule was assumed. This stepping rule estimates the stimulus level corresponding to 79.4% correct discrimination (Levitt, 1971). Step size was constant for all remaining trials. Trials continued until a total of 12 reversals occurred. The mean of the final 8 reversals was taken as the masked threshold estimate.

Masked thresholds were determined in this manner for 9 time delays from 1 ms to 256 ms, in octave steps, to define a complete forward-masking recovery function. Each point on the recovery function was based on the average of 3 to 5 forward-masked threshold estimates. Data were obtained in sets, where a single set included one adaptive track at each time delay. Three to five sets were obtained with the order of time delays alternated for consecutive sets (short-to-long time delays alternated with long-to-short). This allowed any learning effects to be distributed across time delays. Most recovery functions were completed within a single test session. At the end of a session, absolute threshold for the probe pulse was re-measured to insure that no significant shifts in unmasked threshold had occurred due to auditory fatigue.

Recovery functions were obtained in this manner at several masker levels distributed across each electrode's dynamic range. Four or five masker levels were assessed for electrodes with large dynamic ranges; fewer masker levels were assessed when dynamic ranges were small. Only 1 or 2 masker levels were tested in five electrodes. For one subject (AMB), three masker levels were tested per electrode but only one or two of these produced sufficient threshold shift to allow fitting with exponential functions.

III. RESULTS

A. Characteristics of individual SPFM recovery functions

1. Exponential function fits

Least-squares regression procedures were used to fit individual recovery functions with the equation

$$(A_p - A_{0p} - C) = K \cdot e^{-t/\tau}, \tag{1}$$

where A_p is the forward-masked threshold of the probe (μA), A_{0p} is the unmasked probe threshold (μA), t is the masker-probe time delay (ms), τ is the time constant of recovery from forward masking (ms), and K and C are constants. The constant C was included in Eq. (1) to accommodate residual masking (incomplete recovery) observed in some recovery functions at moderate or long masker-probe delays. Such residual masking is commonly observed in acoustic forward-masking experiments (Abbas and Gorga, 1981; Markman,

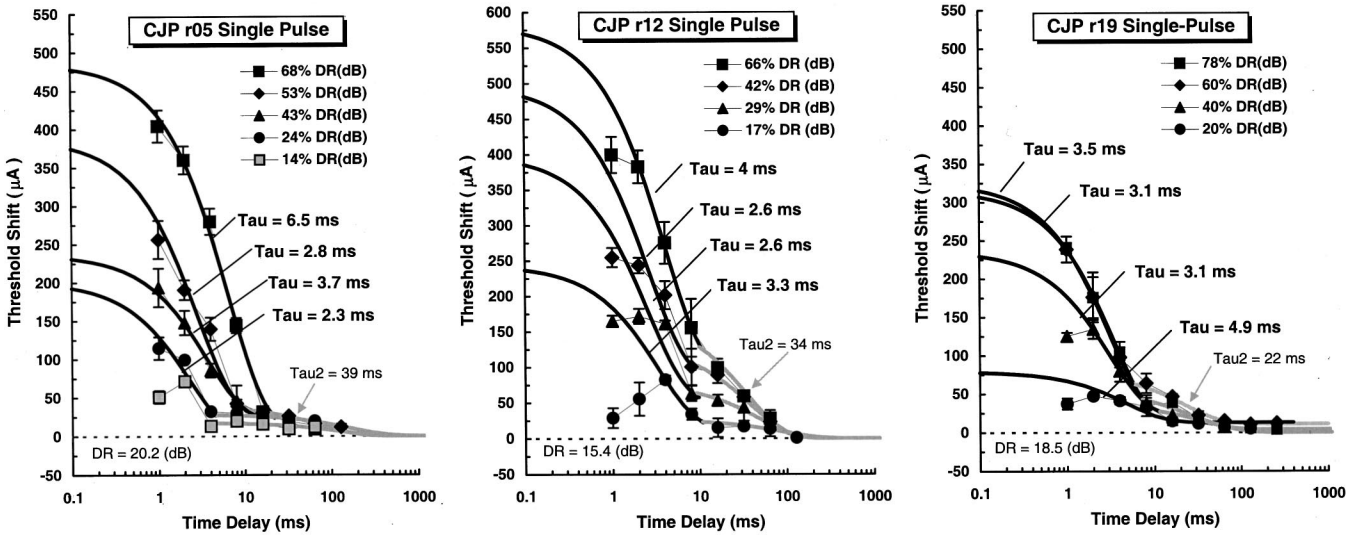

FIG. 2. Single-pulse forward-masking recovery functions as a function of the time delay between masker offset and probe offset. Data are from subject CJP, who demonstrated short time constants for the rapid-recovery process ($\tau < 7$ ms) as well as relatively short time constants for the slow-recovery process. Each panel contains recovery functions for a single electrode (apical, middle, and basal electrodes, from left to right). Error bars indicate 1 standard deviation from the mean. The parameter is masker level, expressed in the legend as the percentage of the dynamic range available on each electrode. Dynamic range for each electrode is given within the panel. Time constants are indicated by τ for each rapid-recovery function and by $\tau 2$ for the slow-recovery function obtained at the highest masker level.

1989; Oxenham and Moore, 1995), but is not well understood.

As described below, many recovery functions in the present study exhibited two separate components, one at short time delays ($t < 10$ ms) and the other at longer time delays ($t > 10$ ms). In later descriptions of the data, these components are referred to as the ''rapid'' and ''slow'' recovery processes, respectively. Equation (1) was used to fit each process independently over the subset of time delays for which it appeared to dominate the overall recovery function. In most cases, the break-point between processes occurred at a time delay of about 10 ms. For convenience, fitting parameters for the rapid-recovery process are specified τ, *K, and C*, and fitting parameters for the slow-recovery process are specified $\tau 2$, $K2$, and $C2$.

2. Rapid- and slow-recovery processes

SPFM recovery functions for one subject (CJP) are shown in Fig. 2. These functions are typical of functions obtained from five of the eight subjects tested in the present study (CJP, DAW, EJQ, JPB, and RFM). Several general characteristics are demonstrated by recovery functions in the left panel of Fig. 2, which were obtained from CJP's apical test electrode (r05). First, note that two distinct recovery processes are evident, a rapid-recovery process at short time delays (<10 ms), and a slower process at longer time delays (>10 ms). Both the rapid and slow components are well described by the exponential recovery process given in Eq. (1). Time constants for the rapid process (τ) range from 2.3 ms to 6.5 ms for masker levels ranging from 14 to 68% of dynamic range. This particular electrode has a large dynamic range (20.2 dB); thus, masker levels encompass a large range of current amplitudes (183–576 μA). Only a small amount of masking is involved in the slow-recovery process, and there is almost no residual masking at the longest time delays. Fitted time constants for the slow-recovery process ($\tau 2$) varied from approximately 40 ms to 120 ms for different masker levels. Only the time constant (39.5 ms) for the highest masker level (68% DR) is indicated in the figure.

The center and right panels of Fig. 2 show corresponding data for subject CJP's middle and basal test electrodes, respectively. Note that the amount of masking for the slow-recovery process varies across electrodes, even though all three electrodes show similar time constants (3–6 ms) for the rapid-recovery process. This suggests that the rapid- and slow-recovery processes are independent or only weakly related, and may stem from different physiological mechanisms.

3. Facilitation at short time delays

For most electrodes, the rapid-recovery process was well described by a decaying exponential function defined by Eq. (1); however, clear departures were sometimes observed. The most common departure was a nonmonotonicity at short time delays (1–2 ms) that resulted in masked thresholds that were lower than those predicted by the exponential function. We refer to this nonmonotonic behavior as ''facilitation.'' As discussed later, facilitation could stem from the same peripheral phenomenon underlying nonmonotonicities in 8th nerve SPFM recovery functions (Stypulkowski and van den Honert, 1984; Miller *et al.*, 1993), or could reflect subjects' use of loudness cues at very short masker-probe delays. Facilitation is demonstrated by CJP on electrode r05 at the lowest masker level (left panel in Fig. 2), on electrode r12 at all masker levels but more so at the lower levels (center panel), and on electrode r19 at the two lowest masker levels (right panel). Nineteen of the twenty-four electrodes tested in the present study exhibited facilitation at the shortest time delays for one or more masker levels, with the largest facilitation usually occurring at the lowest masker levels. When

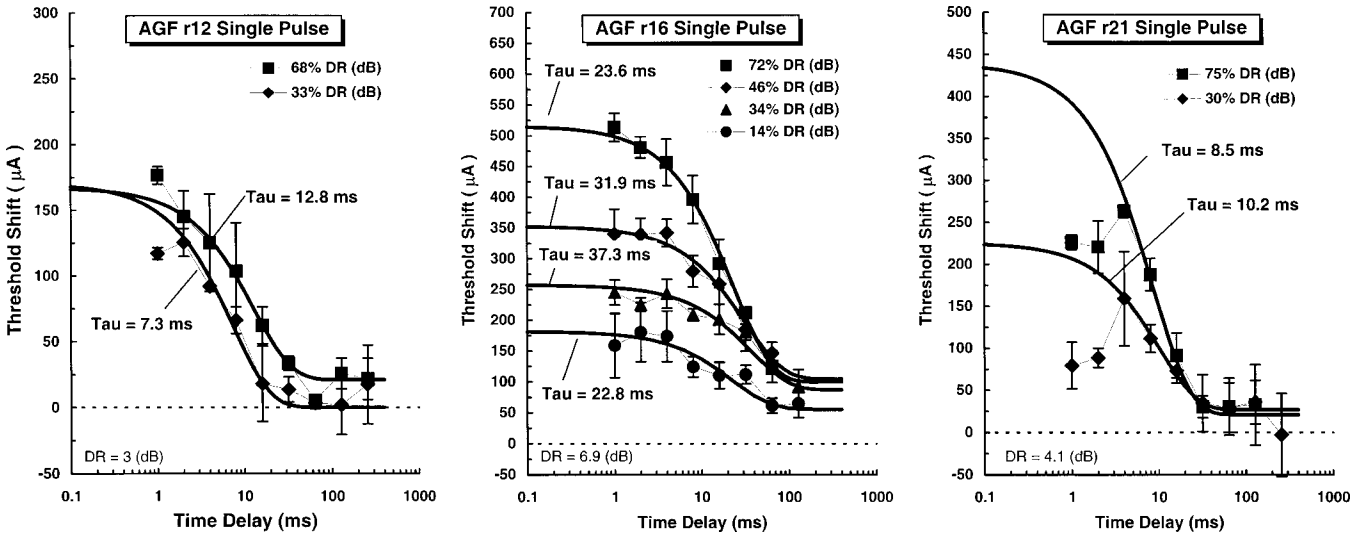

FIG. 3. Single-pulse forward-masking recovery functions, as in Fig. 2. Data for subject AGF, who demonstrated long time constants for the rapid-recovery process (>7 ms), and no clear slow-recovery process. Residual masking is evident at long time delays, which may reflect a slow-recovery process with an exceptionally long time constant.

facilitation was clearly present, masked thresholds at the shortest time delays were excluded from exponential curve fits. This occasionally left too few remaining data points at short masker-probe delays to permit meaningful fits to be obtained, as was the case for electrode CJPr05 at the lowest masker level.

4. Atypical functions

Although five of eight subjects demonstrated recovery functions similar to those shown in Fig. 2, three subjects demonstrated distinctly different SPFM recovery characteristics. Figure 3 shows the recovery functions for one such subject, AGF, who demonstrated unusually long time constants for the rapid-recovery process, especially on his middle electrode, r16 (τ=23–37 ms). Slow-recovery processes were not evident in this subject's data; however, electrode r16 showed substantial residual masking at long time delays. This could indicate that a slow-recovery process existed, but was not well defined within the range of time delays evaluated. Note that considerable facilitation was observed on r21. Also note that subject AGF has very poor word recognition (Table I), suggesting a possible relationship between prolonged SPFM time constants and poor speech recognition.

Figure 4 shows data for a second subject, GPB, who exhibited atypical recovery functions. GPB's time constants for the rapid-recovery process were not unusual (2–7 ms); however, time constants for the slow-recovery process were prolonged (>200 ms) for all three electrodes, and there was substantial residual masking present at long time delays for the apical and middle electrodes (r05 and r12). Note that strong facilitation was evident for both the apical and basal electrodes (r05 and r20) and that these electrodes exhibited extremely small dynamic ranges (3.2 and 2.3 dB, respectively). Also notice that there is a clear demarcation between rapid- and slow-recovery processes on the middle electrode (r12).

Figure 5 shows data for the third subject who demonstrated unusual recovery functions, subject AMB. The notable aspect of these functions is the amount of facilitation demonstrated at low masker levels and the fact that masked thresholds were clearly lower than unmasked thresholds for some conditions involving low masker levels and short time delays. Time constants for the rapid-recovery process were similar to those for CJP and other ''typical'' subjects. A second recovery process was evident on the middle electrode (r12) at the highest masker level, but there was no evidence of a second recovery process on electrodes r06 or r20, or at lower masker levels on r12.

B. Growth of masking

If an exponential model with a level-independent time constant is appropriate for describing the single-pulse recovery process, then the model should accurately predict the rate at which single-pulse forward masking grows with masker level at all time delays. To evaluate characteristics of growth of masking (GOM) for the rapid-recovery process, parameter K in Eq. (1) was expressed as a linear function of masker sensation level $(A_m - A_{0m})$, as follows:

$$K = b + n \cdot (A_m - A_{0m}). \tag{2}$$

Substituting Eq. (2) for K in Eq. (1) yields the following:

$$(A_p - A_{0p} - C) = [b + n(A_m - A_{0m})] \cdot e^{-t/\tau}. \tag{3}$$

This shows that for a time delay of $t = 0$ ms, the growth rate of masking is equal to n, and the sensitivity to masking is equal to b. For other values of t, Eq. (3) shows that the rate of growth of masking is inversely related to τ. Growth of masking slopes were evaluated for several values of t in order to determine if the expected dependence of growth rate on τ was actually reflected in the data.

The y-intercept, K (value at $t = 0$), of recovery functions fitted with Eq. (3) provides a measure of response growth rate that is independent of the time constant. In Fig. 6(A),

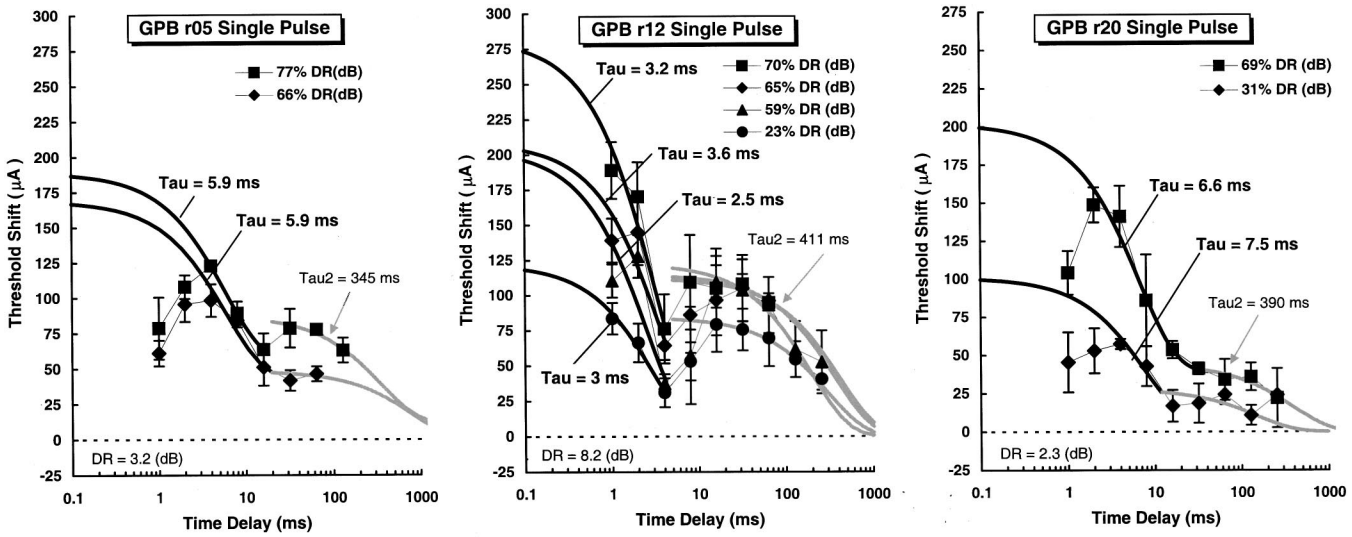

FIG. 4. Single-pulse forward-masking recovery functions, as in Fig. 2. Data for subject GPB, who demonstrated typical, short time constants for the rapid-recovery process, but demonstrated unusually large amounts of masking at longer time delays together with extended time constants for the slow-recovery process.

values of K for subjects' rapid-recovery processes are plotted as a function of masker level in μA to obtain growth-of-masking (GOM) functions at a time delay of 0 ms. A solid line with a slope of 1.0 is shown for reference. Data for most electrodes can be described by straight line functions with unity slopes over a wide range of masker levels, but in some cases the measurement detail (only two data points) is insufficient to obtain a valid determination of slope. Although the individual GOM functions in Fig. 6(A) tend to have similar slopes, their origins vary considerably due to differences in absolute threshold. Such differences are reduced by expressing masker level relative to absolute threshold, in sensation-level units, as shown in Fig. 6(B). Each GOM function in Fig. 6(B) was fitted with Eq. (3) to determine its slope, n, and sensitivity constant, b. The average slope, n, across electrodes was 1.01 and the average sensitivity constant, b, was 66 μA.[4] The average slope indicates that effective masking due to a single-pulse masker tends to grow linearly with the sensation level of the masker (in μA). The average sensitivity constant suggests, by extrapolation, that single-pulse forward masking begins when masker amplitude is slightly below absolute threshold.

For time delays greater than 0 ms, Eq. (3) predicts that GOM slopes will be shallower than the unity slope observed at zero time delay, with slopes depending both upon the time delay (t) and the time constant for recovery (τ). Figures 6(C) and (D) show threshold shifts predicted by the fitted recovery curves at time delays of 2 and 5 ms. In these panels, both threshold shift and masker level are expressed as a percentage of the dynamic range (%DR) available on the test electrode. This normalization, accomplished by dividing both threshold shift and masker level by the dynamic range in μA, makes changes in GOM slope more apparent across electrodes with widely different dynamic ranges.

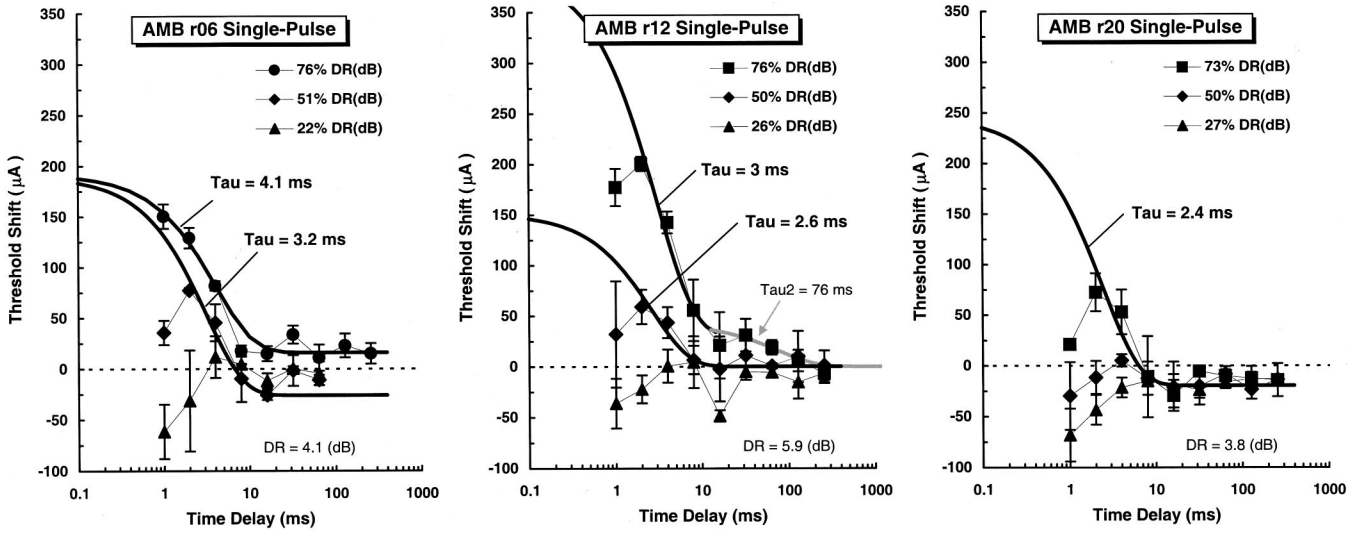

FIG. 5. Single-pulse forward-masking recovery functions, as in Fig. 2. Data for subject AMB, who demonstrated typical, short time constants for the rapid-recovery process, but demonstrated particularly large facilitation effects at the shortest time delays, especially for the lower two masker levels. The facilitation effect can be seen as an improvement in masked threshold as time delay becomes shorter than 2–4 ms, depending upon masker level.

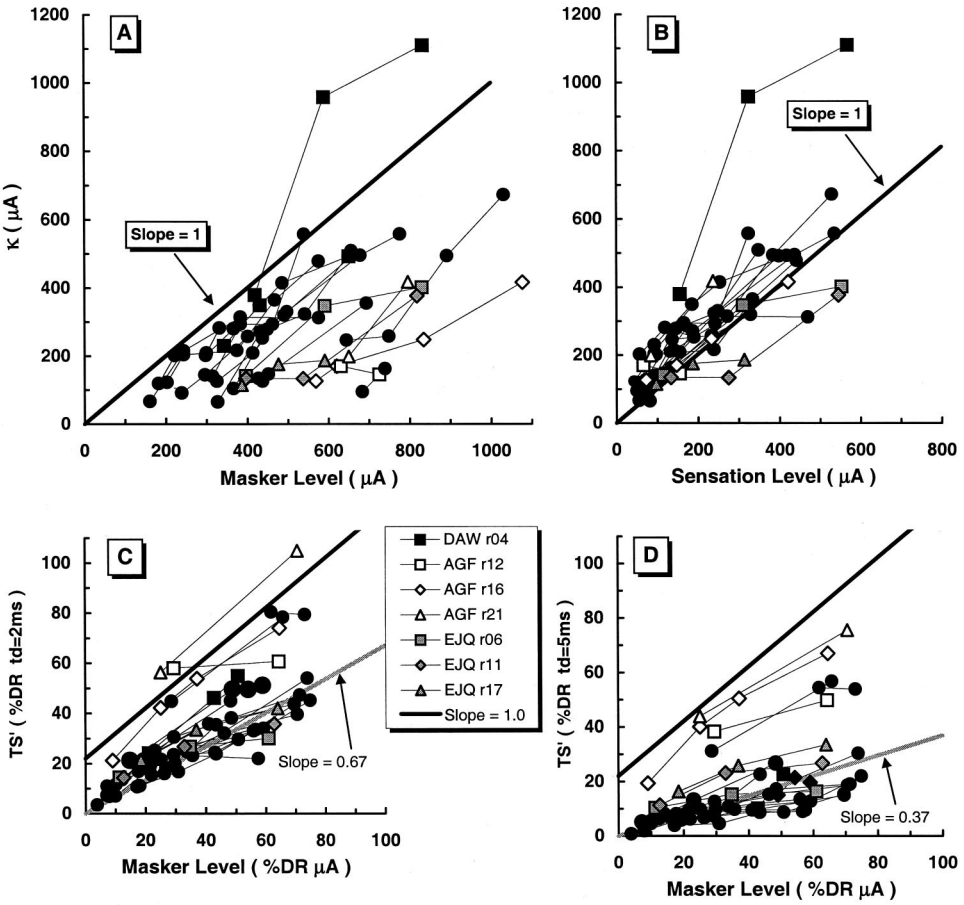

FIG. 6. Amount of masking as a function of masker level. Amount of masking (threshold shift in μA) at a time delay of 0 ms was obtained from the intercepts (K) of exponential fits to the rapid-recovery process of single-pulse forward masking. *Panel (A)*: Amount of masking (K) as a function of the physical masker level in μA. A slope of 1.0 is shown by the wide line. *Panel (B)*: Amount of masking (K) as a function of the relative level of the masker above absolute threshold. The average slope of the growth of masking at td=0 ms is shown by the wide line. *Panel (C)*: Amount of masking (TS' in % DR) calculated for a time delay of 2 ms, as a function of masker sensation level expressed as % DR (μA). The average slope of the growth of masking at td=2 ms (0.67) is shown by the gray line. A slope of 1 is shown by the black line. *Panel (D)*: Amount of masking (TS' in % DR) calculated for a time delay of 5 ms, as a function of masker sensation level expressed as % DR (μA). The average slope of the growth of masking at a time delay of 5 ms (0.37) is shown by the gray line. A slope of 1 is shown by the black line.

Average GOM slopes were 0.67 at $t=2$ ms [panel (C)] and 0.37 at $t=5$ ms [panel (D)]. Values of τ that would yield these average slopes were computed to be 5.1 ms at both time delays, which is close to the average measured τ of 5.5 ms. Conversely, this average value of $\tau=5.5$ ms predicts GOM slopes of 0.69 and 0.40, respectively, at time delays of 2 and 5 ms [Eq. (3)]. These predicted slopes are very close to the average slopes of 0.67 and 0.37 shown in Figs. 6(C) and (D). The similarity of predicted and measured values indicates that the exponential recovery process adequately describes the data. Notice that the subject with the longest time constant, AGF, exhibits the steepest GOM slope and the greatest amount of threshold shift at 2 and 5 ms [Figs. 6(C) and (D)]. The steep GOM slope is a direct consequence of this subject's prolonged time constant, but the greater amount of masking seems to be related to a relatively narrow dynamic range. This suggests the possibility that subjects with narrow dynamic ranges may be more susceptible to prolonged recovery from SPFM than those with wider dynamic ranges.

C. Group tendencies in SPFM recovery functions

1. Summary of fitting parameters

Table III summarizes recovery function parameters for all subjects and electrodes, for SPFM data obtained at the highest masker level (>60% DR). For each test electrode (denoted by research electrode number, rEL), threshold and dynamic range for the single-pulse probe (or masker) stimulus are shown, together with fitting parameters τ, K, and C for the rapid-recovery process. Exponential fits to the initial rapid-recovery process were excellent, as evidenced by coefficients of determination (r^2) that averaged 0.98 across all three masker levels (−2 s.e.=0.965). Values for $\tau 2$ are shown for 19 (out of 24) electrodes that clearly demonstrated a second slow-recovery process. Exponential fits to the slow-recovery process were not as good, as evidenced by coefficients of determination that averaged 0.82 across all three masker levels (−2 s.e.=0.757). Table III also shows the relative amounts of masking present at a time delay of 2 ms, which were estimated from the fitted recovery functions. Amount of masking is expressed in terms of a percentage of the dynamic range existing on each electrode (%DR).

2. Masker level effects

The exponential model used to describe these data resulted in time constants for the rapid-recovery process (τ) that were independent of masker level. As shown in Fig. 7, values for τ varied considerably across subjects, from 1.5 ms to 37.3 ms, but for individual electrodes did not vary systematically with masker level. Thus, the exponential recovery model defined by Eq. (1), with a level-independent time constant, appears to adequately describe the SPFM recovery process. The average value of τ across all subjects and electrodes was 5.5 ms. Only two subjects (AGF and EJQ) consistently demonstrated time constants that were longer than 7 ms, the value 2 standard errors above the mean (dashed line in Fig. 7). As will be discussed later, these two subjects also performed poorest on the NU-6 word recogni-

TABLE III. Recovery function parameters. Parameters obtained from exponential fits to single-pulse forward-masked thresholds for each electrode at the highest masker level (Lm>60% DR). (See text.)

Subject rEL	THS (dB μA)	DR (dB)	Lm (% DR)	τ (ms)	κ (μA)	C (μA)	r^2	$\tau 2$ (ms)	C2 (μA)	%DR (td=2ms)
AGF r12	55.1	3.1	68.3%	12.8	146.2	21.0	0.995		0.0	61
AGF r16	56.3	6.0	71.9%	23.6	416.0	100.0	0.990		100.0	74
AGF r21	55.0	4.1	75.2%	8.5	417.9	21.1	0.997		0.0	105
AMB r06	52.9	4.5	75.6%	4.1	176.0	13.0	0.990		0.0	41
AMB r12	51.0	6.3	75.8%	3.0	361.1	31.0	0.984	75.7	0.0	58
AMB r20	53.6	4.1	72.5%	2.4	265.6	−19.5	0.943		−19.5	34
CJP r05	42.6	18.6	67.9%	6.5	478.3	7.0	0.994	39.5	0.0	35
CJP r12	47.3	13.5	66.4%	4.0	492.5	89.5	0.999	34.2	0.0	45
CJP r19	40.5	18.8	78.2%	3.5	311.9	4.0	1.000	25.6	4.0	22
DAW r04	48.4	14.4	69.3%	3.4	1110.0	0.0	0.994	50.0	0.0	55
DAW r17	46.7	11.2	70.8%	1.7	556.8	23.0	0.997	55.8	0.0	34
DAW r21	47.6	12.4	82.3%	2.0	557.3	95.4	0.999	43.8	13.1	40
EJQ r06	48.8	12.6	75.5%	4.7	402.1	10.2	0.989	75.5	0.0	30
EJQ r11	48.7	12.4	76.7%	10.4	377.2	0.0	0.956	98.5	0.5	36
EJQ r17	48.9	8.8	74.3%	9.4	186.7	55.0	0.949	87.7	24.0	42
GPB r05	50.0	3.4	76.7%	5.9	134.4	23.0	1.000	345.3	0.0	79
GPB r12	44.0	9.1	70.5%	3.2	282.4	0.0	0.949	411.0	0.0	51
GPB r20	55.6	2.5	69.0%	6.6	162.8	39.0	0.989	389.5	0.0	78
JPB r07	47.8	6.5	76.7%	2.4	252.6	9.3	0.973	83.9	0.0	44
JPB r11	48.2	11.5	70.5%	2.0	491.4	57.2	0.999	23.5	1.6	33
JPB r16	49.8	8.2	79.7%	1.8	508.6	60.0	0.983	14.7	2.1	47
RFM r05	54.0	8.0	78.1%	2.6	672.3	18.5	1.000	43.1	0.0	44
RFM r15	44.2	11.4	84.6%	2.6	319.7	49.2	0.978	74.6	⋯	45
RFM r20	51.2	7.0	80.7%	5.2	355.0	0.0	0.994	48.8	0.4	54

tion test (see Table I). One subject (GPB) demonstrated time constants close to 7 ms on one electrode, but time constants for his other two electrodes were closer to the mean.

3. Effects of electrode location

To examine whether recovery function parameters differed for electrodes located in the apical, middle, or basal regions of the electrode array, single factor repeated-measures ANOVAs were performed for the measures τ, K, $\tau 2$ and threshold shift at $t=2$ ms and $t=5$ ms. None of the resulting F ratios approached statistical significance. This indicates that neither the recovery from SPFM nor the amount of masking at any time delay varied consistently according to electrode region. Repeated-measures ANOVAs similarly showed that neither absolute threshold nor dynamic range varied systematically with electrode location.

4. Correlations among fitting parameters

Comparisons were made between measures of dynamic range (DR), absolute threshold (THS), maximum acceptable loudness level (MAL), and parameters of the SPFM recovery functions (τ, K, C, $\tau 2$, $K2$, and threshold shift at different delay times). There was a significant negative correlation ($R=-0.99$; $p<0.01$) between DR and THS for the basal electrodes, but that relationship was weaker for the middle and apical electrodes ($R=-0.63$ and -0.78, respectively). Correlations between DR and MAL were positive but not significant for apical, middle, and basal electrodes ($R=0.71$, 0.10, and 0.57, respectively). This suggests that larger dynamic ranges are primarily determined by lower THS levels rather than higher MAL levels. There were no significant relations among the other parameters. The lack of significant correlations between parameters of the rapid-recovery process (τ, K, C) and the slow-recovery process ($\tau 2$, $K2$) supports our earlier speculation that these two processes operate independently and are governed by different physiological mechanisms.

5. Correlations with word recognition scores

As mentioned earlier, Brown *et al.* (1990) demonstrated an inverse correlation between recovery time constants measured with an electrophysiological SPFM procedure and

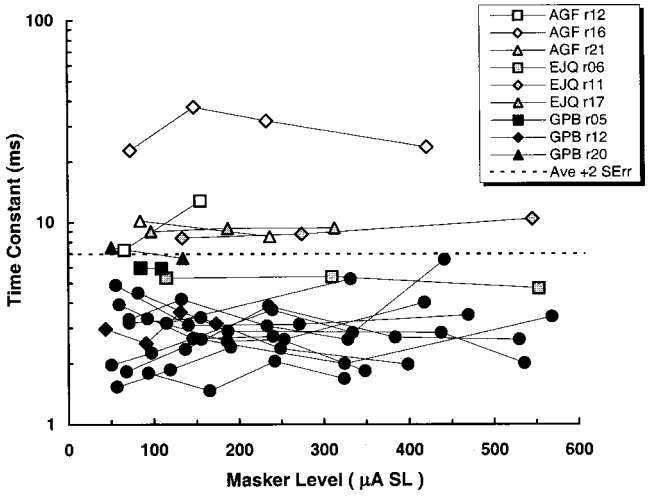

FIG. 7. Time constants for the rapid-recovery process as a function of masker level. Time constants were obtained from exponential fits of single-pulse forward-masking recovery functions. The dashed line indicates two standard errors above the mean. Time constants for outlying subjects are identified in the legend with separate symbols, those for the rest of the subjects are plotted as filled circles.

speech recognition scores in a group of 10 users of the Ineraid cochlear implant. To determine whether a similar relationship existed for the present subjects, NU-6 word recognition scores (Table I) were compared with SPFM time constants for subjects' apical, middle, and basal electrodes (Table III). An inverse relationship between word recognition and τ was observed for all electrode locations; however, a statistically significant correlation coefficient was obtained only for the basal location ($R=-0.89$, $p<0.01$). A scatterplot of the basal electrode data is shown in Fig. 8(A). Comparable data are replotted from Brown *et al.* (1990) in Fig. 8(B).

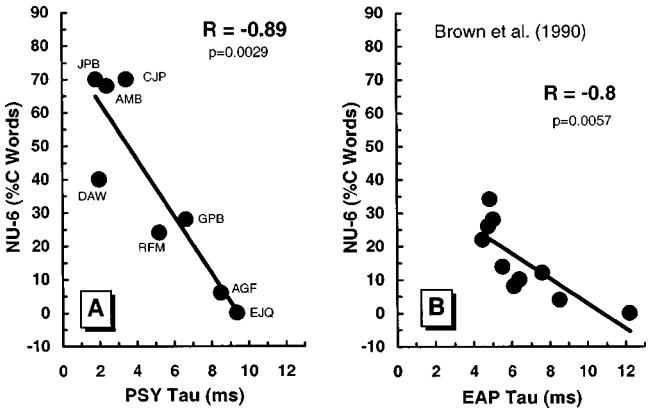

FIG. 8. Scattergrams of speech scores and time constants (τ) of SPFM recovery functions. Panel (A) Data for basal electrodes of subjects in the present study, for whom time constants were measured using a psychophysical (PSY) SPFM procedure. Panel (B) Data for subjects from Brown *et al.* (1990), for whom time constants from monopolar basal electrodes of an Ineraid cochlear implant were obtained using an electrically evoked action potential (EAP) measure of SPFM recovery.

IV. DISCUSSION

A. Exponential recovery process

An important finding of this study was that recovery from psychophysical single-pulse forward masking can be accurately described by recovery processes in which the amount of threshold shift produced by a masker pulse recovers exponentially in time. Two recovery processes were observed, a rapid-recovery process and a slow-recovery process. Our findings indicate that the rapid-recovery process was dominant and could be measured from all test electrodes. The rapid-recovery process required only a single time constant to account for recovery data obtained over a wide range of masker amplitudes. The average rapid-recovery time constant across 24 electrodes in eight subjects was 5.5 ms, with a standard error of 0.75 ms. This means that approximately 95% of electrodes in a similar cochlear implant population would be expected to demonstrate time constants shorter than 7 ms. The slow-recovery process was inconsistent across subjects and electrodes, with time constants ranging from 20 to 400 ms, and in some cases was not evident at all.

In this study, threshold shift was specified in terms of microamperes of current. That is, the effect of the masker was specified as a difference in μA between the forward-masked threshold and absolute threshold. This differs from the traditional approach in acoustic hearing that specifies threshold shift as a ratio of masked threshold to absolute threshold, i.e., in decibels. In electric hearing, dynamic ranges are small and, therefore, threshold shift in decibels is also small ($<$10 dB). This predicts that good exponential fits can be obtained whether threshold shift is expressed in decibels or in μA. In fact, refitting the present data using decibels of threshold shift produced similar time constants with only slightly poorer fits. Even so, it seems appropriate to specify threshold shift in terms of linear μA of current, since the compressive nonlinearities in acoustic hearing are a product of cochlear processes that are absent in electric hearing.

Loudness matches obtained in listeners with acoustic hearing in one ear and electric hearing in the opposite ear suggest that linear changes in μA of current are proportional to decibels of acoustic sound pressure (Eddington *et al.*, 1978; Zeng and Shannon, 1992). Thus, the use of linear μA of current as the input to a more central adaptation mechanism in electric hearing is consistent with the use of decibels as the input to the same central adaptation mechanism in acoustic hearing (Duifhuis, 1973; Nelson and Freyman, 1987; Nelson and Pavlov, 1989).

Also note that we chose to describe the recovery process as an *effect* of the masker that recovers over time and not as a decay in the physical amplitude of the masker. This is because the recovery curves all tended to asymptote at absolute threshold. None of the rapid- or slow-recovery curves were well fit using an equation that described exponential decay as a function of masker amplitude.

The exponential recovery process used to fit SPFM recovery curves, described by Eq. (3), is essentially identical to the recovery process used by Brown *et al.* to describe their physiological (1990, 1996) and psychophysical (1996) recovery curves. The principal difference is that Brown *et al.* normalized their functions to the masked threshold at some short time delay, thereby eliminating differences in the amount of masking across subjects (normalization does not affect time-constant estimates), and they did not include a constant (C) to describe residual masking at longer time delays. Time constants (inverses of reported recovery slopes) for their physiological data ranged from 4.5 to 12.2 ms across 10 subjects. Time constants for their psychophysical data for six electrodes in four subjects, estimated with our fitting procedures, ranged from 2.2 to 14.7 ms.

In summary, both the form of the recovery curve described by Eq. (3) and the range of time constants obtained across subjects and electrodes in the present study, are consistent with data from previous physiological and psychophysical studies. About three-fourths of recovery functions reported in existing studies have time constants shorter than 7 ms, roughly similar to eighth-nerve refractory time constants measured in normal and acutely deafened ears. The remaining psychophysical functions have time constants longer than 7 ms, perhaps indicating unusual amounts or types of auditory nerve degeneration.

B. GOM slopes

GOM slopes in this study decreased with time delay as expected in an exponential recovery process. Our analyses

indicate that effective masking (amount of masking at zero time delay) grows linearly with masker sensation level expressed in μA, and that GOM slope is determined by the recovery time constant, τ, and the time delay, t. This finding, that GOM slopes can be predicted from the recovery time constant, supports the validity of an exponential model for describing SPFM recovery.

C. Residual threshold shift and the slow-recovery process

One of the differences between previous work and the present study is our use of a C constant to reflect residual threshold shift and improve exponential fits to the SPFM recovery curves. As indicated in Table III, C constants for the rapid-recovery process ranged from 0 to 100 μA. These constants were typically associated with a clearly defined slow-recovery process (e.g., CJP in Fig. 2). In some cases, however, substantial residual masking existed but no second recovery process was apparent, perhaps because sufficiently long time delays were not evaluated (e.g., AGF in Fig. 3). Examination of the Brown *et al.* (1996) psychophysical recovery functions suggests that the use of an additive constant might have improved some of their exponential fits (e.g., IS24 3–4 in their Fig. 12). This was not true of their EAP (electrically evoked action potential) recovery functions, however, suggesting that threshold shifts at long masker-probe time delays (residual masking or a well-defined slow-recovery process) represent some form of adaptation originating central to the eighth nerve. Further evidence for this is provided by the Brown *et al.* (1996) finding that psychophysical SPFM functions exhibited slower recovery than EAP SPFM functions in some subjects at time delays longer than 2–5 ms. Although procedural differences in psychophysical and EAP forward-masking procedures could contribute to such differences, both their findings and ours are consistent with the existence of two recovery processes, an initial rapid process associated with eighth-nerve relative refractoriness, and a second slower process that may be associated with more central adaptation.

D. Level-independent time constants

The present study represents the first thorough examination of the level dependence of the recovery time constant in SPFM. From Fig. 7 it is clear that there were no systematic changes in time constant across masker levels, either within or across subjects and electrodes. That is, time constants in this study were level independent. A similar finding was recently reported by Hong *et al.* (1998), who found that recovery time constants were unaffected by masker level as long as masker level exceeded probe level. This was generally the case in our study, and in those instances where probe level did exceed masker level the differences were small. Thus, findings of the two studies are consistent. Note, however, that it would not be surprising to observe a masker-level effect under conditions in which probe level substantially exceeded masker level. In that circumstance, the probe could excite a significantly larger population of auditory nerve fibers than the masker and recovery functions might be less affected by the refractory characteristics of individual neurons excited by the masker than by the recruitment of new fibers by the probe. Under more typical conditions in which masker level exceeds or is similar to probe level, our data indicate that an exponential recovery process with a level-independent time constant adequately describes the rapid process of SPFM recovery.

E. Electrode location effects

In the present study, SPFM recovery parameters did not vary systematically with electrode location, suggesting that underlying neural characteristics did not vary consistently with cochlear location across subjects. This finding agrees with Brown's findings for EAP recovery functions (Brown *et al.*, 1996). Note, however, that for individual subjects in the present study, rapid-process time constants sometimes showed large differences for apical, middle and basal test electrodes (Table III). Four subjects exhibited time constants that were 2–2.7 times larger on one electrode than another (AGF, GPB, RFM, and EJQ), suggesting local differences in neural survival along the cochlear partition. Additional evidence for local effects of neural survival is provided by a recent comparison of EAP recovery curves obtained with monopolar and bipolar stimulation (Brown *et al.*, 1996). Monopolar stimulation produced nearly identical recovery functions in a group of nine subjects, whereas bipolar stimulation produced more variable function shapes in a group of 13 subjects (see their Fig. 8). One interpretation of this finding is that bipolar stimulation sampled more discrete regions of the cochlear partition than monopolar stimulation, thereby allowing local differences in neural survival to have a greater influence on results.

F. Comparison with eighth-nerve recovery functions

Examination of physiological data from animals supports the hypothesis that the rapid-recovery process seen in human SPFM functions reflects refractory properties of the eighth-nerve response. Stypulkowski and van den Honert (1984) measured EAP recovery functions in normal-hearing and short-term deafened cats, and identified two components of the EAP on the basis of latency-intensity characteristics: The shorter-latency $N0$ component was thought to arise from stimulation of auditory nerve fibers' central processes (axons), whereas the longer-latency $N1$ component was thought to arise from fibers' peripheral processes (dendrites). Refractory functions were examined for $N1$ responses in normal-hearing and ototoxically-deafened animals who were presumed to have normal dendrites and axons, and for $N0$ responses in laminectomized animals who were presumed to have functional axons but no dendrites. Both $N1$ and $N0$ recovery functions showed complete or near-complete recovery at masker-probe delays of 4 ms, consistent with recovery time constants of about 2–3 ms. Miller *et al.* (1993) identified two wave I components in the guinea pig EABR, analogous to the $N0$ and $N1$ responses studied by Stypulkowski and van den Honert (1984). Recovery was significantly faster for wave Ia (similar to $N0$, axonal stimulation) than for wave Ib (similar to $N1$, dendritic stimulation), but exponential time

constants for both waves were always less than 5 ms. Recovery functions for short-term deafened animals in the Miller *et al.* study were similar to those in normal-hearing animals, but showed greater variability across individuals. Zhou *et al.* (1995) measured EABR recovery functions in mice with myelin-deficient auditory nerve fibers. The myelin-deficient mice demonstrated slightly but significantly slower recovery than normal controls; however, recovery time constants were again about 2–3 ms for both myelin-impaired and normal animals.

The similarity of SPFM time constants in normal and short-term deafened animals, as well as most human subjects, suggests that recovery characteristics at the level of the eighth nerve are relatively insensitive to deafness-related changes in fiber morphology and density. As discussed below, an important exception to this may occur in the case of long-term deafness. The human psychophysical data do not allow differentiation of axonal versus dendritic excitation mechanisms, as there are not clear differences among functions with time constants less than 5 ms. However, the distribution of psychophysical time constants across electrodes and subjects (mean 5.5 ms, with a standard error of 0.75 ms) is broader than that seen in animals (typical range 2–3 ms). This could imply that the proportion of neural responses stemming from axonal versus dendritic excitation varies across subjects and electrodes, and that SPFM functions with the shortest time constants involve only axonal excitation.

G. Extended time constants and long-term deafness

Most of Brown and Abbas' subjects (Brown *et al.*, 1990; Abbas and Brown, 1991; Brown *et al.*, 1996) evaluated with physiological and psychophysical measures of SPFM showed complete recovery at time delays of 4–6 ms ($\tau < 5$ ms), consistent with animal data described above. However, a few showed noticeably slower recovery ($\tau > 10$ ms), similar to that shown psychophysically by subject AGF in the present study. It is possible that prolonged recovery times are indicative of severe neural degeneration associated with long-term deafness. Information regarding individual subjects' duration of deafness is not provided in Brown and Abbas' studies; however, our subject AGF was profoundly deaf for 25 years prior to cochlear implantation, far longer than other subjects in this study. Subject AGF was also the oldest of our group (79 years), suggesting that age could be another factor contributing to prolonged recovery.

Physiologic factors that could account for prolongation of SPFM time constants in long-term deafness involve the recovery time constants of individual auditory nerve fibers and the density of residual neurons in the region of electrical stimulation. Recovery rates of individual fibers affect the likelihood that fibers responding to the masker pulse will respond again to the probe pulse at short time delays. In subjects with long-term deafness, it is conceivable that demyelination of fibers' axonal processes (Leake and Hradek, 1988) or reduced fiber diameters could prolong individual fiber time constants (Paintal, 1966), thereby contributing to prolonged SPFM time constants. Neural density is likely to influence the proportion of stimulated fibers that respond to the masker and are in a refractory state when the probe pulse occurs. The proportion of refractory fibers should vary inversely with the time constants measured in SPFM and, at least intuitively, should vary inversely with neural density. Thus, reduced neural density may also be associated with prolongation of SPFM time constants. A number of human and animal studies have shown that the density of functional auditory neurons decreases following deafness, and that the number of viable fibers may be severely reduced in some cases of long-term deafness. Subjects with severe neural depletion would also be those most likely to exhibit morphological changes resulting in prolonged recovery for individual fibers, suggesting that both factors may operate in tandem to prolong SPFM time constants. Subject EJQ's hearing loss was attributed to mumps, one of several viruses that can cause severe cochlear damage (Schuknecht, 1974) and associated neural degeneration. EJQ also demonstrated prolonged rapid-recovery constants for two electrodes (τ's more than two standard errors above the mean), consistent with the idea that prolonged time constants are indicative of neural degeneration. An evaluation of SPFM recovery functions in a larger population of cochlear implantees with varying durations of deafness and etiologies of hearing loss is needed to further address this possibility.

H. Facilitation

The effect that we refer to a psychophysical facilitation was observed for nearly all electrodes evaluated in the present study at one or more masker levels. In general, facilitation was stronger at lower masker levels than at higher masker levels; however, masker level did not have a systematic effect on the amount of facilitation observed for individual electrodes.

It is interesting that nonmonotonicities similar to the facilitation seen here exist in the eighth-nerve measures of SPFM described earlier, suggesting that facilitation may reflect some physiological phenomenon at the level of the eighth nerve. Stypulkowski and van den Honert (1984) propose two mechanisms to explain this phenomenon with respect to their $N1$ recovery functions (p. 220), both of which depend on the existence of intact dendrites. However, it is not clear whether the mechanisms they propose are consistent with the Miller *et al.* data (1993), in which nonmonotonicities at 1–2 ms were observed for both wave Ia (presumed axonal) and wave Ib (presumed dendritic) responses.

A second possible explanation for facilitation in the present data involves loudness summation. White *et al.* (1984) observed in one subject that the loudness of two equal-amplitude pulses increased considerably as inter-pulse separation was reduced from 6 ms to 0.5 ms. This implies that significant loudness summation can occur when two pulses are presented in close succession. Consistent with this, our subjects frequently reported using a loudness cue to discriminate the signal interval at short time delays (1–2 ms), but reported different perceptual cues (e.g., hearing two separate pulses) at longer time delays. Because loudness summation decreases with interpulse interval, this explanation is consistent with our observation that facilitation was greatest at the shortest time delays.

Loudness summation can also account for the fact that facilitation tended to be larger at lower masker levels than at higher masker levels. At the short time delays where facilitation is observed, refractoriness prevents individual nerve fibers from responding to both the masker and probe pulses; thus, loudness summation can only occur when different groups of fibers respond to the two stimuli. High-level maskers elicit responses from a large proportion of stimulated fibers, leaving few fibers to respond to the probe. In contrast, low-level maskers excite a smaller proportion of fibers, with the result that many fibers are available to respond to the probe. Presuming that loudness summation increases with the number of fibers responding to the probe, then greater loudness summation should occur at low masker levels, as seen in the present data. A similar relationship between probability of response and loudness summation was recently proposed by McKay and McDermott (1998).

A related phenomenon has been observed in single-unit neural responses to subthreshold pulse pairs (Eddington *et al.*, 1978; Butikofer and Lawrence, 1979; Dynes and Delgutte, 1995; Eddington *et al.*, 1995). When subthreshold pulses are presented in pairs, with a short time delay between them (<4 ms), they can elicit a neural response even though the pulses are up to 6 dB below their individual neural excitation thresholds. Whether the physiological mechanisms underlying the present demonstrations of suprathreshold facilitation are the same as those responsible for such subthreshold facilitation is not known. However, it is interesting that the largest suprathreshold facilitation is seen at lower masker levels. Additional studies are needed to quantify the facilitation effects observed here in SPFM, to determine whether they are related to subthreshold facilitation, and to determine how such facilitation effects might modify the perceptions of longer pulse trains.

I. Correlations with word recognition

A significant negative correlation was obtained in this study between SPFM recovery time constants for basal electrodes and word recognition scores. This finding echoes results previously reported for EAP measures of refractoriness (Brown *et al.*, 1990), but is primarily due to the data for two subjects (AGF and EJQ) who demonstrated the lowest speech scores. In addition, it is not clear why correlation coefficients were not significant for middle and apical electrodes. Evaluation of similar measures in a much larger population of cochlear implant listeners is needed to clarify possible relationships between SPFM time constants and performance on speech recognition tests.

V. CONCLUSIONS

Recovery from single-pulse psychophysical forward masking can be described by an exponential recovery process in which the amount of threshold shift (in μA) produced by a single-pulse masker recovers exponentially in time. Time constants average 5.5 ms across subjects and electrodes, with a standard error of 0.75 ms. Time constants are independent of masker level and do not vary systematically with electrode location. However, they can differ significantly with electrode location in individual subjects.

Response to the masker grows linearly with masker level (in μA) at a time delay of 0 ms. Growth rates at longer time delays are shallower than 1, and are determined by the level-independent time constant. This behavior is consistent with an exponential recovery process.

The addition of a constant residual threshold shift improves the exponential fit to most SPFM recovery curves, consistent with the existence of a second, slower recovery process. In some cases, the slower recovery process is sufficiently well defined to be fitted with a second exponential process with a longer time constant.

The rapid-recovery process of psychophysical SPFM has a time constant less than 5–7 ms, consistent with eighth-nerve refractoriness. The slower recovery process exhibits time constants that are too long to attribute to eighth-nerve refractoriness and likely reflects more central processes.

Prolonged time constants for the rapid-recovery process (>7 ms) may reflect altered mechanisms of neural excitation associated with long-term deafness.

There is some evidence that prolonged SPFM time constants are associated with poor speech recognition; however, a larger data set is needed to better evaluate this possibility.

ACKNOWLEDGMENTS

This work was supported by NIDCD grant DC00110 and by the Lions 5M International Hearing Foundation. John Van Essen converted Robert Shannon's computer software into the *C* language and made modifications to that software for carrying out the present research. Tanya Grann, Shanna Allen, Tara Khetrepal, and Ying-Yee Kong assisted with data collection, and Magda Wojtczak provided helpful comments on an earlier version of the paper. Cochlear Corporation provided subjects' calibration tables. The authors would like to extend special thanks to the eight subjects who participated in this work.

[1]Facial nerve stimulation restricted electrode selection in two subjects (AGF and DAW). For these subjects, test electrodes were distributed across the range of stimulable electrodes.

[2]The ordinate in Fig. 1 is shown in linear units (μAmps) of threshold shift to illustrate that masked threshold recovers asymptotically to absolute probe threshold, i.e., the recovery process involves the recovery of an *effect* (threshold shift) to zero, not the recovery of a physical stimulus down to some physical reference. All later figures express masked thresholds in this way (i.e., they show threshold shift in μAmps on the ordinate). The abscissa in Fig. 1 is shown in linear units of time delay between masker and probe to illustrate the exponential nature of the recovery process. Because the range of time delays evaluated in this experiment is large, later figures use a logarithmic scale to show time delay on the abscissa.

[3]A CSU is the smallest change in current realizable with the implanted stimulator. The decibel step size corresponding to one CSU varies slightly across the dynamic range and among individual implanted stimulators, but is usually between 0.1 and 0.3 dB.

[4]Fittable SPFM recovery curves at two or more masker levels were obtained from only seven of the subjects, because AMB's recovery curves were only well fit for the highest masker level. Of those seven subjects, one electrode exhibited a negative slope (AGFr12), which was not included in the averages across electrodes reported here.

Abbas, P. J., and Brown, C. J. (**1991**). ''Electrically evoked auditory brainstem response: Refractory properties and strength-duration functions,'' Hear. Res. **51**, 139–148.

Abbas, P. J., and Gorga, M. P. (**1981**). ''AP responses in forward-masking paradigms and their relationship to responses of auditory-nerve fibers,'' J. Acoust. Soc. Am. **69**, 492–499.

Blamey, P. J., and Dooley, G. J. (**1993**). ''Pattern recognition and masking in cochlear implant patients,'' in *Progress in Brain Research*, edited by J. H. J. Allison, D. J. Allison-Mecklenburg, F. P. Harris, and R. Probst (Elsevier Science, New York), Vol. 97, pp. 271–278.

Brown, C. J., Abbas, P. J., Borland, J., and Bertschy, M. R. (**1996**). ''Electrically evoked whole nerve action potentials in Ineraid cochlear implant users: Responses to different stimulating electrode configurations and comparison to psychophysical responses,'' J. Speech Hear. Res. **39**, 453–467.

Brown, C. J., Abbas, P. J., and Gantz, B. J. (**1990**). ''Electrically evoked whole-nerve action potentials: Data from human cochlear implant users,'' J. Acoust. Soc. Am. **88**, 1385–1391.

Brown, C. J., Abbas, P. J., Hughes, M. L., Parkinson, A., and Tyler, R. (**1999**). ''Relationship between EAP growth and recovery functions measured using the Nucleus neural response telemetry software and psychophysical measures of loudness and speech perception,'' presented at the Conference on implantable auditory prostheses, Asilomar Conference Center, Pacific Grove, California.

Butikofer, R., and Lawrence, P. D. (**1979**). ''Electrocutaneous nerve stimulation: II. Stimulus waveform selection,'' Izv. Akad. Nauk SSSR, Ser. Geogr. Geofiz. **26**, 69–75.

Donaldson, G. S., and Nelson, D. A. (**1999**). ''Single-pulse and pulse-train forward masking functions: Do they reflect different neural recovery processes,'' presented at the 1997 Conference on Implantable Auditory Prostheses, Pacific Grove, California.

Duifhuis, H. (**1973**). ''Consequences of peripheral frequency selectivity for nonsimultaneous masking,'' J. Acoust. Soc. Am. **54**, 1471–1488.

Dynes, S., and Delgutte, B. (**1995**). ''Temporal interactions of electric pulses in the auditory nerve: experiments and modeling,'' presented at the Proceedings of the 1995 Conference on Implantable Auditory Prostheses, Pacific Grove, California.

Eddington, D. K., Doebelle, W. H., Brackmann, D. E., Mladejovsky, M. G., and Parkin, J. L. (**1978**). ''Auditory prostheses research with multiple channel intracochlear stimulation in man,'' Ann. Otol. Rhinol. Laryngol. **87**, 5–39.

Eddington, D. K., Long, C. J., Rubinstein, J. T., and Whearty, M. E. (**1995**). ''Minimizing nonsimultaneous interactions,'' presented at the Proceedings of the 1995 Conference on Implantable Auditory Prostheses, Pacific Grove, California.

Hong, S. H., Brown, C. J., Hughes, M. L., and Abbas, P. J. (**1998**). ''Electrically evoked compound action potentials using neural response telemetry in CI24M: Refractory recovery function of the auditory nerve,'' ARO Abstracts, #288.

Hong, S. H., Hughes, M. L., Abbas, P. J., Brown, C. J., Gervais, J. P., Wolaver, A. A., and Gantz, B. J. (**1998**). ''Temporal response measures of the electrically evoked compound action potential (EAP) using the neural response telemetry system of the Nucleus CI24M device,'' presented at the 7th Symposium on Cochlear Implants in Children, Iowa City.

Leake, P. A., and Hradek, G. T. (**1988**). ''Cochlear pathology of long term neomycin induced deafness in cats,'' Hear. Res. **33**, 11–34.

Levitt, H. (**1971**). ''Transformed up-down methods in psychoacoustics,'' J. Acoust. Soc. Am. **49**, 467–477.

Markman, N. D. (**1989**). ''Recovery from forward masking in listeners with normal hearing, sensorineural hearing loss, and simulated hearing loss,'' Masters thesis, University of Minnesota.

McKay, C. M., and McDermott, H. J. (**1998**). ''Loudness perception with pulsatile electrical stimulation: The effect of interpulse intervals,'' J. Acoust. Soc. Am. **104**, 1061–1074.

Miller, C. A., Abbas, P. J., and Robinson, B. K. (**1993**). ''Characterization of wave I of the electrically evoked auditory brainstem response in the guinea pig,'' Hear. Res. **69**, 35–44.

Nelson, D. A., and Freyman, R. L. (**1987**). ''Temporal resolution in sensorineural hearing-impaired listeners,'' J. Acoust. Soc. Am. **81**, 709–720.

Nelson, D. A., and Pavlov, R. (**1989**). ''Auditory time constants for off-frequency forward masking in normal-hearing and hearing-impaired listeners,'' J. Speech Hear. Res. **32**, 298–306.

Oxenham, A. J., and Moore, B. C. J. (**1995**). ''Additivity of masking in normally hearing and hearing-impaired subjects,'' J. Acoust. Soc. Am. **98**, 1921–1934.

Paintal, A. S. (**1966**). ''The influence of diameter of medulated nerve fibers of cat on the rising and falling phases of the spike and its recovery,'' J. Physiol. (London) **184**, 791–811.

Schuknecht, H. F. (**1974**). *Pathology of the Ear* (Harvard University Press).

Shannon, R. V., Adams, D. D., Ferrel, R. L., Palumbo, R. L., and Grandgenett, M. (**1990**). ''A computer interface for psychophysical and speech research with the Nucleus cochlear implant,'' J. Acoust. Soc. Am. **87**, 905–907.

Stypulkowski, P. H., and van den Honert, C. (**1984**). ''Physiological properties of the electrically stimulated auditory nerve. I. Compound action potential recordings,'' Hear. Res. **14**, 205–223.

White, R. L., Merzenich, M. M., and Gardi, J. N. (**1984**). ''Multichannel cochlear implants. Channel interactions and processor design,'' Arch. Otolaryngol. **110**, 493–501.

Zeng, F. G., and Shannon, R. V. (**1992**). ''Loudness balance between electric and acoustic stimulation,'' Hear. Res. **60**, 231–235.

Zhou, R., Abbas, P. J., and Assouline, J. G. (**1995**). ''Electrically evoked auditory brainstem response in peripherally myelin-deficient mice,'' Hear. Res. **88**, 98–106.

Effects of temporal envelope modulation on acoustic signal recognition in a vocal fish, the plainfin midshipman

Jessica R. McKibben
Department of Neurobiology and Behavior, Cornell University, Ithaca, New York 14853

Andrew H. Bass[a)]
Department of Neurobiology and Behavior, S. G. Mudd Hall, Cornell University, Ithaca, New York 14853 and University of California, Bodega Marine Laboratory, Bodega Bay, California 94923

(Received 19 September 2000; revised 19 March 2001; accepted 24 March 2001)

Amplitude modulation is an important parameter defining vertebrate acoustic communication signals. Nesting male plainfin midshipman fish, *Porichthys notatus*, emit simple, long duration hums in which modulation is strikingly absent. Envelope modulation is, however, introduced when the hums of adjacent males overlap to produce acoustic beats. Hums attract gravid females and can be mimicked with continuous tones at the fundamental frequency. While individual hums have flat envelopes, other midshipman signals are amplitude modulated. This study used one-choice playback tests with gravid females to examine the role of envelope modulation in hum recognition. Various pulse train and two-tone beat stimuli resembling natural communication signals were presented individually, and the responses compared to those for continuous pure tones. The effectiveness of pulse trains was graded and depended upon both pulse duration and the ratio of pulse to gap length. Midshipman were sensitive to beat modulations from 0.5 to 10 Hz, with fewer fish approaching the beat than the pure tone. Reducing the degree of modulation increased the effectiveness of beat stimuli. Hence, the lack of modulation in the midshipman's advertisement call corresponds to the importance of envelope modulation for the categorization of communication signals even in this relatively simple system. © *2001 Acoustical Society of America.* [DOI: 10.1121/1.1373441]

PACS numbers: 43.66.Gf, 43.80.Lb [WA]

I. INTRODUCTION

Patterns of amplitude variation are known to play an important role in bioacoustic communication (Bradbury and Vehrencamp, 1998). Vocalizations typically can be described by amplitude fluctuations in the temporal envelope, defining features such as call duration and inter-call intervals, as well as the division of a vocalization into subunits (e.g., syllables). Behavioral responses to acoustic signals often depend on such species- or call-specific amplitude modulations. Examples range from preferences for specific call repetition rates in various frog species (review Gerhardt, 1988) to the inherent information content of the temporal envelope in human speech (e.g., Shannon *et al.*, 1995).

In this paper we address the importance of envelope modulation from a novel perspective. Nesting male plainfin midshipman fish, *Porichthys notatus*, produce essentially unmodulated, very long duration calls known as hums [Fig. 1(A)]. Hums are spectrally simple signals, consisting of a fundamental (around 80–120 Hz) and several higher harmonics. Hum fundamental frequency is linearly related to temperature, and the variation among individuals at the same site is quite small (mostly <4 Hz; Brantley and Bass, 1994; Bodnar and Bass, 1997; Bass *et al.*, 1999). A single hum can last for an hour or more and durations on the order of several minutes are typical (Brantley and Bass, 1994; Bass *et al.*, 1999). Not only is the temporal envelope of a hum flat (following its onset ramp), but the hum's long duration makes it probable that neither patterns of onsets and offsets nor the entirety of a single hum is necessary for evoking a response. Therefore, if envelope modulation plays a role in hum recognition, it is expected to be the absence of modulation rather than any characteristic rate or shape that is important.

Hums attract gravid females to a male's nest, where spawning occurs (Ibara *et al.*, 1983; Brantley and Bass, 1994). In playback experiments, gravid females quickly approached, touched, and circled underwater loudspeakers playing hum-like continuous tones (McKibben and Bass, 1998). This robust phonotactic response provides a readily observable behavioral measure for recognition of a signal as a hum.

Although an individual hum has an essentially flat envelope, midshipman acoustic communication does include at least two distinct types of envelope modulation. First, nesting males emit trains of short (50–200 ms) pulsed sounds, known as grunts [Fig. 1(C); Brantley and Bass, 1994]. Grunts are associated with agonistic contexts and presumably signal aggression. While only nesting males produce grunt trains, both sexes sometimes produce isolated single grunts. The second type of envelope modulation results from the frequent occurrence of overlap between the hums of nearby males. When two hums with slightly different fundamental frequencies overlap, the acoustic waveforms interfere to produce beats at their difference frequency [df, Fig. 1(B)]. Beats are amplitude and phase modulations that result from the continual shifting in and out of phase of the two fundamentals. In this natural listening situation, a receiver would

[a)]Author to whom correspondence should be addressed. Electronic mail: ahb3@cornell.edu

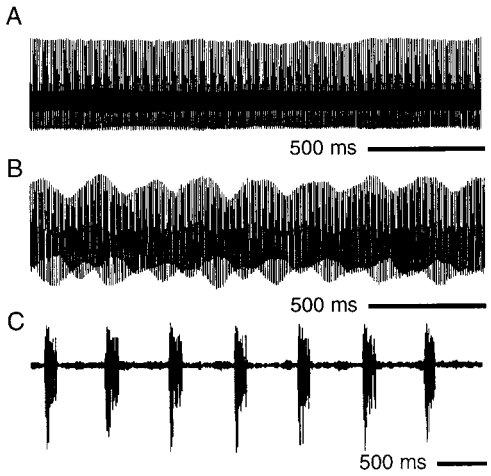

FIG. 1. Midshipman acoustic communication signals. (A) Segment of individual hum envelope (2 s). (B) Beats resulting from concurrent hums (2 s). df is approximately 4 Hz. (C) Segment of grunt train (5 s).

hear the summated beating waveform instead of the flat envelope of an individual hum.

A previous study demonstrated that certain pulse train and beat stimuli can be recognized and responded to as if they were hums (McKibben and Bass, 1998). However, grunt trains and pulsed stimuli timed to approximate a grunt train were not effective. Also, the effectiveness of single-source beat stimuli appeared to be limited by both beat rate and depth of modulation. Here we build upon those results by presenting a range of pulse train and beat stimuli and testing the sufficiency of each to evoke a response. The specific goals are to examine functional behavioral sensitivity to envelope modulation in midshipman and to determine the role of envelope modulation or lack thereof in defining a hum.

II. METHODS

A. Experimental animals

Gravid female midshipman fish were collected from nests along Tomales Bay and San Quentin Point in Marin County, California. Females enter nests only to spawn and may have begun egg laying when collected. The fish used in tests were sexed according to external morphology (see Brantley and Bass, 1994; McKibben and Bass, 1998) and had the swollen abdomens typical of gravid females. Individual females ($n=123$) were measured and tagged with a numbered plastic tab sutured just rostral to the dorsal fin. Standard length ranged from 10.2–17 cm (mean 13.3 ± 1.3 cm) and mass ranged from 14.7–66.8 g (mean 31.8 ± 9.8 g). Fish were maintained, and all tests were conducted, at the UC Bodega Marine Laboratory, Bodega Bay, CA. Fish were kept in running seawater tanks at temperatures that varied with the incoming water (9–12 °C) and offered live brine shrimp and goldfish as food.

B. Experimental setup

The experimental set up and methods are generally the same as previously described (McKibben and Bass, 1998). Tests were performed in an outdoor, 4-m diameter, concrete tank with a water depth of 0.75 m. An underwater loudspeaker (UW-30, University Sound) was placed near the center of the tank facing the perimeter, 1.4 m from the front wall, in order to minimize effects of reflections. The loudspeaker was suspended from a PVC frame so that the center of its face was 11 cm above the tank bottom. A second ''dummy'' speaker stood adjacent to the active speaker (32 cm center-to-center), and was used only as a silent control.

Experiments took place during the midshipman breeding season (May–August) and at night (20:26–03:30 hours), which is when midshipman are normally most active. Two red floodlights symmetrically placed on either side of the tank permitted responses to be observed and videotaped. During tests, the water temperature was 13.4–15.8 °C. However, for any given night and stimulus set presentation, the temperature range was only 0.4 to 1.2 °C.

TABLE I. Experimental stimuli. Pulse train stimulus durations are given in columns B–E as *pulse duration* [gap duration] in ms.

Experiment	Experiment type	Stimulus A	B	C	D	E
1	Pulse	Tone	500 [10]	500 [50]	500 [100]	500 [250]
2	Pulse	Tone	750 [25]	500 [10]	500 [25]	250 [10]
3	Pulse	Tone	900 [100]	800 [200]	700 [300]	
4	Beat 100% modulation	Tone	2-Hz df	4-Hz df	6-Hz df	10-Hz df
5	Beat 100% modulation	Tone	0.5-Hz df	1-Hz df	2-Hz df	
6	Beat 50% modulation	Tone	2-Hz df	4-Hz df	6-Hz df	10-Hz df
7	Beat 25% modulation	Tone	2-Hz df	4-Hz df	6-Hz df	10-Hz df

C. Stimuli

Stimuli were synthesized and played using SoundEdit 16 (Macromedia) running on a Macintosh 540c portable computer. The signal was amplified with a battery-powered amplifier (Nagra/Kudelski) and played through the UW-30 loudspeaker. Sound in the experimental tank was recorded for analysis and calibration using a hydrophone (Cornell Bioacoustics Research Program, Laboratory of Ornithology, CBRP; response flat ±1 dB from 60 to >500 Hz) connected to an AC voltmeter for direct output measurements and to a portable computer (Macintosh Powerbook G3) for spectral analysis (using Canary, a sound analysis program from CBRP). Source levels were adjusted so that the sound pressure was approximately 140 dB *re* 1 μPa (measuring only the ''on'' portion of the stimulus for pulse trains) 20 cm in front of the speaker. This signal level is in the range of the highest levels recorded from midshipman nests in the field (Bass and Clark, in press; A. Bass and M. Marchaterre, unpublished observations). In the experimental tank, sound pressure attenuated quickly with distance from the source, however, the gradient was continuous, with no apparent nulls or maxima (McKibben, 1998; McKibben and Bass, 1998).

The stimulus sets used in each of the seven experiments are outlined in Table I. Pulsed stimuli (Experiments 1–3) were constructed from 90 Hz tone segments of the specified

duration with a linear ramp (approximately 30 ms) applied at each end. The specified silent gap was appended to the pulse and the resulting signal looped to produce an ongoing pulse train. In Table I and figures, pulsed stimuli are given the notation: pulse duration [gap duration]. The continuous tone stimulus consisted of a continuous loop of the same 90-Hz signal used to construct the pulses. Starting and ending voltages for the looped segment were precisely matched so there were no transients on playback.

Beat stimuli were synthesized by digitally mixing two tones (f1 and f2) with a difference frequency (df) equal to f2 minus f1. The beat stimulus was then played out of a single speaker. For all stimuli, f1 was 90 Hz; f1 and f2 synthesis amplitudes were adjusted to compensate for the frequency response of the speaker. For Experiments 4 and 5, f1 and f2 were equal in amplitude, resulting in a combined signal with 100% envelope modulation (peaks cancelled out at nulls and summed to twice f1's amplitude at maxima). For Experiment 6, beats were synthesized with f2 attenuated by 50% (−6 dB re f1). This reduced the envelope modulation correspondingly. For Experiment 7, f2 was attenuated by 75% (−12 dB re f1), resulting in 25% envelope modulation. For all four beat experiments, the single tone stimulus consisted of f1 presented alone. Thus, the beat stimuli were higher in average amplitude than the tone stimulus, approximately 3 dB, 1.8 dB, and 1 dB higher for the 100%, 50%, and 25% modulation stimuli, respectively. Each stimulus was looped for continuous playback.

D. Testing protocol

In preparation for testing, fish were held in buckets of water from the test tank and allowed to acclimate for at least 20 minutes. During the course of the night, water in the holding buckets was repeatedly refreshed from the test tank to maintain temperature and quality. Fish were tested individually with a set of four or five stimuli, depending on the experiment. Each stimulus of a set was presented in a separate trial and repeat trials with the same fish were separated by at least 30 minutes. The order of stimulus presentation followed a randomized block design, so that the same or similar numbers of fish were tested with each stimulus in each temporal order.

For each trial, a fish was placed in a cylindrical mesh release cage (30-cm diameter, approximately 60-cm from the speakers) while the test signal was playing. When the fish was near the bottom and facing toward the center of the tank (in the direction of the speaker) it was released by manually raising the cylinder. Responses were noted, and the movements of the fish were described and videotaped for future analysis. Scoring of positive responses followed a previously established protocol (McKibben and Bass, 1998). Most positive responses were unambiguous, involving touching of the speaker and prolonged circling around and under the speaker. Simply approaching the speaker or swimming through the speaker frame were not clearly reactions to the sound and were not considered responses. Trials ended either when the fish had been at the speaker for several seconds and the sound was turned off (an attempt to avoid habituation) or when the fish swam out of the area between the release site and the speakers.

E. Analysis

Final scoring of responses was based on analysis of the videotapes by a person blind to the stimulus being presented. Ninety-nine fish (80.5% of all gravid females tested) responded to at least one stimulus (''responsive'' fish) and were used in the analysis. Most fish were used for just one experiment, however, six were used in two of the experiments, but not for data that were combined or compared. For each experiment, the Cochran Q test for related samples (Siegel and Catellan, 1988) was applied to determine if there was an overall significant effect of stimulus type on response likelihood. Where such an effect existed, the McNemar change test (Siegel and Catellan, 1988) was then used to make comparisons between individual stimuli.

III. RESULTS

A. Pulse train stimuli

Results for Experiment 1 are shown in Fig. 2(A). The five stimuli consisted of a continuous tone and four different pulse trains. The pulse trains were composed of 500-ms pulses separated by silent gaps of 10, 50, 100 or 250 ms. All 18 fish responded to the continuous tone. Of these, 11 (61%) responded to the pulsed stimulus with 10-ms gaps, two to the stimulus with 50-ms gaps, and one to the stimuli with the two longest gap lengths. (This subject responded to all five stimuli.) Overall, responses varied significantly with stimulus type (Cochran Q test, $Q=51.8$, $df=4$, chi-square $p<0.001$). The tone attracted a significantly higher number of fish than any of the pulsed stimuli, and the 10-ms gap stimulus was more effective than the pulsed stimuli with longer gaps (McNemar change test, $p<0.01$).

Experiment 2 also tested fish with four different pulsed stimuli and a continuous tone. In order to fill-in the region of intermediate stimulus effectiveness, pulse durations were 250, 500 or 750 ms with gaps of 10 or 25 ms [Fig. 2(B)]. The proportion of fish responding depended on the stimulus (Cochran Q test, $Q=24.3$, $df=4$, chi-square $p<0.001$). All 15 fish approached the tone and, as was the case in Experiment 1, fewer fish responded to 500-ms pulses with 10-ms gaps (8 fish, 53%; McNemar change test, $p<0.01$). The three other pulsed stimuli also attracted a smaller proportion of fish than the tone (McNemar change test, $p<0.02$). Among pulse train stimuli, the 750 [25] and 500 [10] stimuli were more effective than the 250 [10] ($p<0.05$). Figure 2(C) plots the combined results from Experiment 1 and Experiment 2. The proportion of fish responding to 500-ms pulses decreased as the gaps increased from 10 to 100 and 250 ms. Also, shorter pulses tended to attract fewer fish when the gap duration was kept constant (e.g., 500-ms vs 750-ms pulses with 25-ms gaps; 250-ms vs 500-ms pulses with 10-ms gaps).

The final pulse experiment, Experiment 3, presented three pulse train stimuli with varying pulse and gap durations but all with 1-s periods. The fourth stimulus was a continuous tone. Again, effectiveness varied across stimuli [Fig. 2(D); Cochran Q test for related samples, $Q=29.4$, $df=3$,

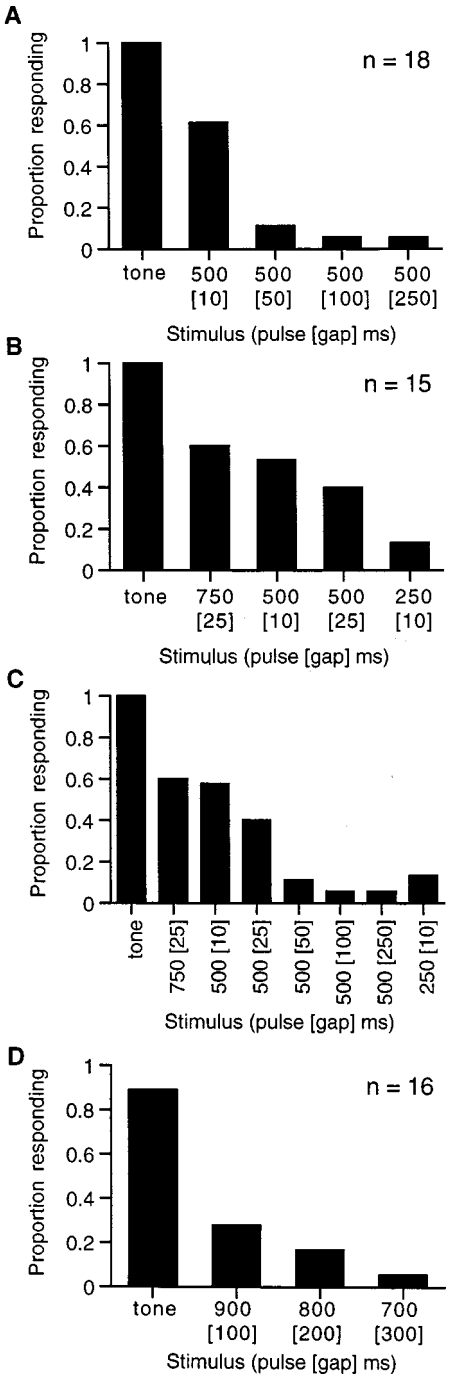

FIG. 2. Proportion of fish responding to a continuous tone and to pulse trains in Experiments 1–3. Notation for pulsed stimuli is pulse duration [gap duration] in ms. (A) Experiment 1 with 500-ms pulses ($n=18$ responsive fish). (B) Experiment 2 with 250-, 500-, and 750-ms pulses ($n=15$ responsive fish). (C) Results from Experiments 1 and 2 combined and arranged in order of decreasing pulse, then increasing gap, duration ($n=15$–33 depending on stimulus; each fish was used in only one experiment). (D) Experiment 3 with 1-s periods and pulse durations of 700, 800, or 900 ms ($n=16$ responsive fish).

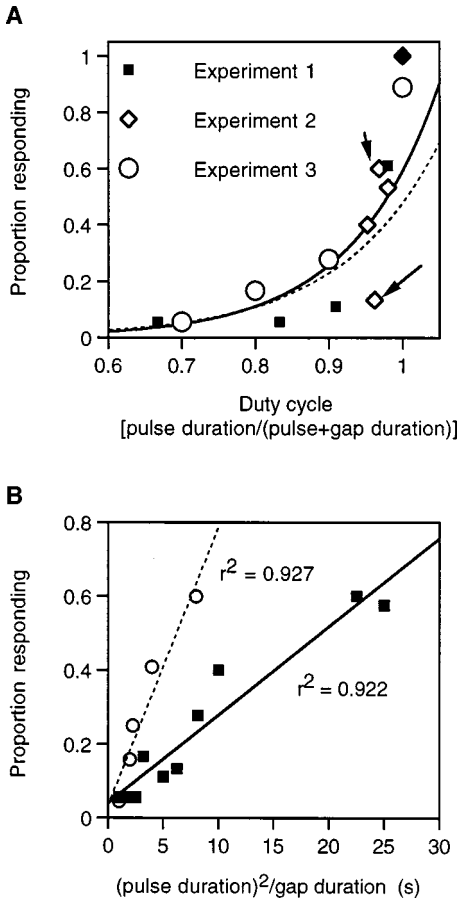

FIG. 3. (A) Proportion of fish responding plotted according to stimulus duty cycle for Experiment 1 (filled squares), Experiment 2 (open diamonds), and Experiment 3 (open circles). A duty cycle of one corresponds to the continuous tone. Exponential curves are fitted to all data points (solid line, $r^2=0.724$) or to data combined such that there is only one point per stimulus (dashed line, $r^2=0.666$). (B) Combined data for all pulsed stimuli (Experiments 1–3, filled squares, solid line) quantified as (pulse duration)^2/gap duration in order to take both the relative and absolute pulse and gap durations into account. Data from a previous study are also shown (open circles, dashed line; McKibben and Bass, 1998).

chi-square $p<0.001$]; and the tone was the most effective stimulus (McNemar change test, $p<0.002$), attracting 15 of the 16 responsive fish. While the number of fish responding to the pulsed stimuli followed the relative pulse duration, these differences were not statistically significant.

Results for Experiments 1–3 are replotted in Fig. 3(A) in terms of stimulus duty cycle [pulse duration/(pulse+gap duration)]. Stimuli which had the sound on for a greater proportion of time (i.e., larger duty cycle) tended to be more effective; however, some stimuli with similar duty cycles had quite different effectiveness [e.g., the 750-ms and 250-ms pulses in Experiment 2, which had duty cycles of 0.968 and 0.962, respectively; arrows in Fig. 3(A)]. The relationship between duty cycle and stimulus effectiveness can be roughly approximated by an exponential curve. The upper curve (solid line, $r^2=0.724$) in Fig. 3(A) is based on all the data points from Experiments 1–3 (as shown), whereas the lower curve (dashed line, $r^2=0.666$) is fitted to the data from Experiments 1–3 combined such that each pulse train stimulus is represented only once, even if used in more than one experiment. For combined data, proportions responding were calculated by dividing the total number of responses to a stimulus across experiments by the total number of fish tested with that stimulus. This was done to eliminate weighting the curves by, for example, having three points for a duty cycle of one (the continuous tone).

An alternative way of quantifying the pulsed stimuli takes into account both the ratio of pulse to gap duration and

the absolute values involved. Plotting responses according to (pulse duration^2/gap duration), yields a linear relationship [Fig. 3(B); solid line, $r^2=0.922$]. As was the case for the lower exponential curve in Fig. 3(A), results from Experiments 1–3 are combined such that there is only one data point per stimulus. The pure tone is left out of this analysis because a value cannot be calculated from a gap duration of zero. Data from a previous set of pulse train experiments also show a linear relationship, although the slope is different (open circles, dashed line, $r^2=0.927$; McKibben and Bass, 1998). Considering this metric as having two components [i.e., pulse duration*(pulse duration/gap duration)], makes clear its correspondence with observations already made based on comparisons between individual stimuli: stimuli become more effective when either the pulse duration is increased or the ratio of pulse to gap duration is increased.

B. Beat stimuli

Experiments 4 and 5 tested responses to beat stimuli with the two component tones (f1 and f2) of equal amplitude. This results in sounds with maximal (100%) envelope modulation. The stimulus set for Experiment 4 consisted of beats with difference frequencies (dfs=f2–f1) of 2, 4, 6, and 10 Hz, as well as a single tone at 90 Hz (f1). Fourteen of fifteen fish responded to the single tone, whereas only one to three fish responded to the 2-, 6-, and 10-Hz df beats, and no fish to the 4-Hz beat [Fig. 4(A)]. Thus, the tone was more effective than the beat stimuli (Cochran Q test for related samples, Q=38, df=4, chi-square $p<0.001$), but there was no distinction among beat stimuli with different dfs (McNemar change test, $p>0.1$).

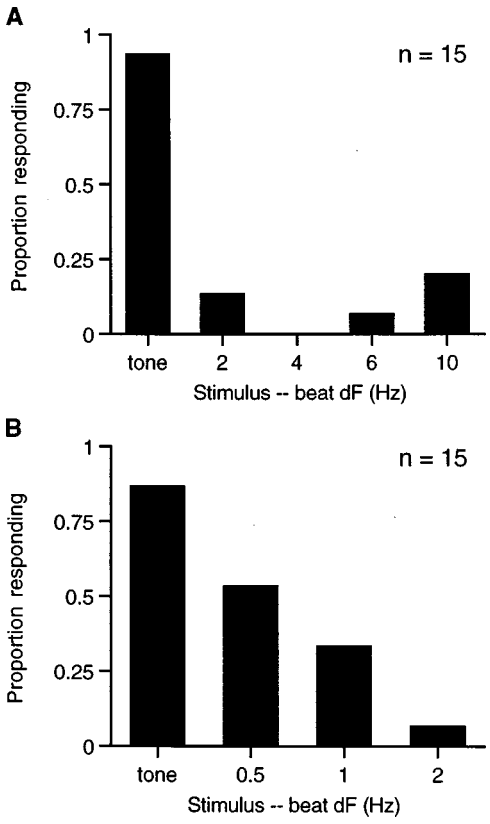

FIG. 4. Beat stimuli with 100% envelope modulation (f1 and f2 equal amplitude). Proportion of fish responding to a single tone (f1=90 Hz) and to beat stimuli. Results are plotted according to difference frequency (df=f2–f1). (A) Experiment 4: dfs of 2, 4, 6, and 10 Hz. (B) Experiment 5: dfs of 0.5, 1, and 2 Hz.

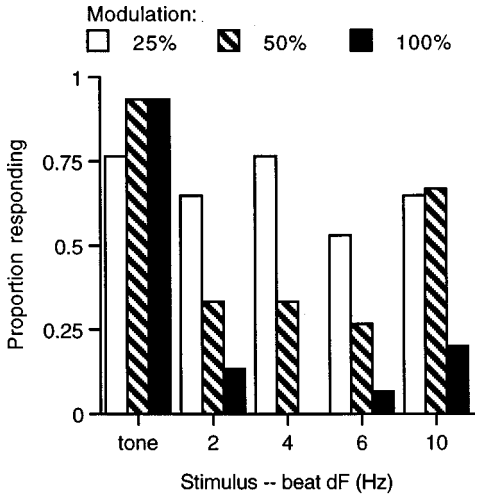

FIG. 5. Beat stimuli with f2 attenuated and reduced envelope modulation (Experiments 6 and 7). Proportion of fish responding to tone and each of four beat stimuli is shown for 25% modulation (open bars; $n=17$), 50% modulation (hatched bars; $n=15$), and 100% modulation [filled bars; $n=15$, same as Fig. 4(A)].

Experiment 5 tested fish with a single tone and three beat dfs: 0.5, 1, and 2 Hz. While the tone again attracted the most fish (13 of 15 responsive fish), the smallest dfs also evoked several responses, eight and five to the 0.5-Hz and 1-Hz dfs, respectively [Fig. 4(B)]. Consistent with Experiment 4, the 2-Hz df beat was not very effective, eliciting only one response, and that from one of two fish that approached all three other stimuli. Overall, probability of response clearly depended on the stimulus (Cochran Q test for related samples, Q=19.6, df=3, chi-square $p<0.001$).

The remaining two beat experiments presented stimuli with f2 attenuated by 50% or 75%, resulting in envelope modulation of 50% and 25%, respectively. Responses for Experiment 6 (50% modulation) and Experiment 7 (25% modulation) are plotted in Fig. 5. With 50% modulated beats, 5–10 fish (33–67 %) responded to each of the beat stimuli (Fig. 5, hatched bars). However, the tone still attracted the most fish (14 of 15), and the stimulus dependence of response probability was statistically significant (Cochran Q test for related samples, Q=21.5, df=4, chi-square $p<0.001$). The 10-Hz df beat elicited at least twice as many responses as any of the other beat stimuli and was significantly more effective than the 6-Hz df beat (McNemar change test, $p<0.05$). When beat modulation was reduced to 25% (Fig. 5, open bars), fish responded to all four beat stimuli (53–76 % of fish at each df, $n=15$) and to the tone; there was no overall effect of stimulus type on probability of response (Cochran Q test for related samples, Q=4.9, df=4, chi-square $p>0.2$). Results from Experiment 4 (100% modulation) are replotted for comparison (Fig. 5, filled bars).

IV. DISCUSSION

A. Envelope modulation in midshipman acoustic communication

The hum emitted by nesting male plainfin midshipman is a remarkably simple signal, consisting of an essentially unmodulated fundamental frequency and a series of higher harmonics (Brantley and Bass, 1994; Bass *et al.*, 1999). A single hum can be continuous for minutes up to an hour or more, and detection of onsets or offsets is not necessary for evoking behavioral responses (McKibben and Bass, 1998). The lack of amplitude modulation on such an extended time scale is perhaps the most unique aspect of a midshipman hum. Here we have examined the role of temporal envelope modulation—or lack thereof—in hum recognition by midshipman.

Two different types of envelope amplitude modulation were used in this study: pulse trains and two-tone beats. Both of these classes of stimuli correspond to natural features in the midshipman acoustic social environment. All adult midshipman morphs are known to produce grunts. These are short duration pulses, which, though spectrally noisier than a hum, have the same basic frequency profile. Nesting males emit trains of grunts that can consist of dozens of typically 50-ms to 150-ms grunts separated by gaps of several hundred ms [Fig. 1(C); Brantley and Bass, 1994; M. Marchaterre unpublished observations]. Aquarium observations suggest that grunts are aggressive signals and are directed at conspecifics (Brantley and Bass, 1994).

Beats are a second form of envelope modulation that midshipman routinely encounter. These amplitude and phase fluctuations result from slight differences in fundamental frequency between the hums of adjacent males. An analysis of a sample of field recordings of concurrent hums showed dfs were all less than 8 Hz with the majority less than 4 Hz (Bodnar and Bass, 1997). In a previous playback study, both beat df and depth of beating affected signal preference when gravid females were given a choice between a beat signal from one speaker and a single tone from another (McKibben and Bass, 1998).

All beat stimuli presented in this study consisted of two tones combined electronically and emitted from a single source. This differs from the natural situation in which the beat waveform would result from acoustic combination of hums from distinct sources. However, at a distance from the sources, a fish is likely to perceive a single beating waveform. Single-source beats can be thought of as one extreme on a continuum of spatial overlap (McKibben and Bass, 1998). While single-source beats may be less effective than beats that resolve into individual tones at the sources, they are well suited for defining the boundaries of hum recognition at close range.

B. Signal recognition

In this study, fish were presented one sound at a time, thus the question addressed was signal recognition rather than choice or preference. Recognition of a signal as a hum was assessed by whether a behavioral response comparable to that for a continuous pure tone was seen. Continuous single tones at hum fundamental frequencies effectively mimic hums and elicit robust phonotaxis by gravid females (McKibben and Bass, 1998). The use of a behavioral measure for recognition presumed that motivation to respond was the same in all experimental contexts.

Recognition, as used here, implies detection of the signal and a (neurally based) decision that the signal should be responded to as a hum. In a natural behavioral context, the recognition would be of a potential mate: a conspecific male with an established nest (Brantley and Bass, 1994). Recognition can be considered to require that each signal parameter falls within a limited range. Preferences could then be expressed based on the relative values of parameters within the range of recognition. Recognition and preference would therefore reflect the same underlying filtering process (Ryan and Rand, 1993). In this framework, a certain hypothetical signal would be the most hum-like and the most preferred. Changing a signal parameter in any direction would result in a less preferred signal and, if the change was continued, eventually a perceptual switch from a recognized hum to something other than a hum. This ''switch'' is assumed to be probabilistic with more recognizable signals expected to evoke responses with a higher probability than less recognizable signals. By comparing responses of individual fish across several stimuli, subjects served as their own controls and the population probabilities of response to specific stimuli could be compared.

C. Response to pulse trains

Pulse train stimuli were designed to determine the limits of hum recognition. Therefore, stimuli with various short duration pulses and interpulse gap lengths were used. The difference in response between pulse trains with the shortest duration gaps (10 ms) and continuous tones indicates that the gaps clearly were detected. A study in another teleost, the goldfish, demonstrated that, although goldfish have relatively long thresholds for gap detection in noise (around 35 ms), they are very sensitive to decrements as short as 10 ms in tones (Fay, 1972, 1985). While the low frequency (90 Hz) of the pulses in the current study might be expected to decrease temporal envelope resolution (Moore *et al.*, 1993), the gradual modulation made for a longer amplitude change. Including the pulse offset and onset ramps, the amplitude decrement for the 10-ms gaps lasted for approximately 70 ms.

Experiments 1 and 2 (Fig. 2) demonstrated that pulses as short as 250–500 ms could evoke responses, although, even with the minimum gap duration, they were not as effective as a continuous tone. The pulse durations used, on the order of several hundred milliseconds, are within the range where temporal integration might affect perception of signal strength. Fay and Coombs (1983) found that goldfish show improvements in threshold for tones as duration increases up to around 300–600 ms (also see Hawkins, 1981). This temporal integration could be based on simple summation of energy over time or the improvement in information possible when stimulus duration permits multiple ''looks'' (Viemeister and Wakefield, 1991). However, in the current tests sound levels were high enough that all pulses are assumed to have been well above the threshold for detection. Therefore,

even though the longer pulses contained more energy, duration itself seems likely to be the more relevant factor for recognition. Further studies could address the role of pulse energy directly by looking for amplitude-duration tradeoffs (i.e., whether increased pulse amplitude could compensate for decreased duration either compared to other pulses or to a continuous tone). Of course, pulses in this study were not considered in isolation but as part of pulse trains where gap length also affected response. For example, as gaps were lengthened from 10 to 250 ms a graded decrease in the acceptability of 500 ms pulses was seen [Fig. 2(C)].

In Experiment 3, the periodicity of the pulse train was held constant at 1 s, while the pulse and gap durations were varied. The pulse durations of 700–900 ms were longer than most of those used in Experiments 1 and 2, however the gaps were also large. It is probable that the long gaps (100–300 ms) accounted for the limited effectiveness of these stimuli. The 1-s periodicity is comparable to that of the 1-Hz df beat stimulus that attracted 33% of the gravid females [Fig. 4(B)], and the relation between these stimuli is discussed below.

Overall, the pulse train data show that stimulus effectiveness can be increased either by increasing pulse duration or decreasing gap duration. Pulse and gap duration can be combined to give stimulus duty cycle, the proportion of the stimulus period that the pulse occupies [pulse duration/(pulse +gap duration)]. This is a measure of signal energy, which varied among the stimuli. Only stimuli with relatively large duty cycles (approximately 0.9 or greater) were generally effective [Fig. 3(A)]. This is expected if hum recognition depends on hearing a sound that is mostly on. Considering all the pulse train stimuli together, there was a clear trend for stimuli with larger duty cycles to be more effective [Fig. 3(A)]. The pattern of responses suggests that there may be a threshold duty cycle, above which responses increase to a maximum at a duty cycle of one (a continuous tone). However, duty cycle does not explain all the variation in the proportion of fish responding. For example, responses were quite different for the 750-ms and 250-ms pulses in Experiment 2, despite similar duty cycles [arrows in Fig. 3(A)].

Duty cycle indicates only the relative pulse and gap durations and does not incorporate their absolute values (i.e., the stimulus period). Therefore, a metric that takes into account both the ratio of pulse to gap duration and the absolute pulse duration was also used to quantify the stimuli [Fig. 3(B)]. This measure combines absolute pulse duration and the ratio of the pulse to gap durations in the form of pulse duration*(pulse/gap duration) or, simply, pulse^2/gap. Over the range of stimuli presented pulse^2/gap is a good predictor of stimulus effectiveness [Fig. 3(B); filled squares, solid line $r^2=0.922$]. Data from a previous study are also shown [Fig. 3(B), open circles, dashed line $r^2=0.927$; McKibben and Bass, 1998]. While the slopes of the two regressions are different, the fact that both data sets fall along approximately straight lines supports the predictive value of the pulse^2/gap measure. The differences between the two data sets could be due to differences in overall responsiveness between the groups of fish or to subtle differences in the stimulus presentation. Future experiments could specifically test the predictive value of duty cycle or pulse^2/gap by varying pulse and gap durations while holding the measure of interest constant.

There are two general ways in which a pulse train—an amplitude modulated signal—could achieve the perceptual value of a hum—a long duration, unmodulated signal. Either the individual pulses could be perceptually fused into segments long enough to be considered hums (i.e., the modulation is within the range of acceptability for recognition of a hum) or each pulse could be of sufficient duration to be perceived as a hum on its own (i.e., the pulse train is effectively a succession of separate hums).

Under certain conditions, pulsed signals are known to induce perceptions of continuity in human listeners. For example, when the gaps in a train of tone pulses are filled with noise containing the tone frequency, a listener may perceive an ongoing tone overlain by pulses of noise (Bregman, 1990). This has been related to a natural context in which a signal (e.g., the tone) is intermittently interrupted by other sounds in the environment (Bregman *et al.*, 1999). The expectation of continuity allows the listener to piece together a continuous tone from the audible fragments. Midshipman could face a similar problem in listening to hums. Fluctuations in apparent sound level or transient interference from other hums could result from complexities of sound transmission in very shallow water (Jensen *et al.*, 1994), or perhaps even from acceleration of the fish itself.

It is possible that the recognition of pulsed signals as hums depends on the listener's proximity to the source, as has been suggested for certain beat stimuli (McKibben and Bass, 1998). Because the behavioral response measured here required both approaching the loudspeaker and exhibiting response-specific circling or touching at the speaker, recognition had to be maintained both at a distance and at the source. While this is a subtle point, perceptual processes that allow for transmission-dependent modulation at a distance from the source, might be superceded by more restrictive recognition criteria at the source.

Likewise, the behavioral test used here does not allow determination of the absolute minimum duration for recognition of a hum. This is because the response itself takes time, and midshipman stop responding almost immediately when a hum-like signal stops. Thus, while a train of 500-ms pulses can evoke phonotaxis, a single 500-ms pulse probably would not. It is therefore not possible to say definitively whether positive responses to pulse trains reflect tolerance of within-signal modulation, continued response to a succession of short but recognized signals, or some combination thereof. The dependence on an ongoing signal for an ongoing response is itself an interesting difference between midshipman and the other well-studied toadfish, *Opsanus tau*. Nesting *O. tau* males also attract females with vocal signals, but in that system the calls, known as boatwhistles, are intermittent pulses (review Fine *et al.*, 1977).

D. Response to beats

Responses to beat stimuli showed that hum recognition can be disrupted by even very slow or shallow modulations. Fish that responded strongly to single tones largely ignored strong (100% modulated) beat stimuli with dfs of 2–10 Hz [Fig. 4(A)]. Reducing the df below 2 Hz restored some of the

stimulus effectiveness. With a df of only 0.5 Hz (a 2-Hz period), the beat stimulus still attracted a smaller proportion of fish than did a single tone, although the difference was not quite significant [McNemar change test, $p = 0.06$; Fig. 4(B)]. Comparably small dfs can affect the ability to identify concurrent harmonic signals (i.e., vowels) in humans. However, the effect is not large and may be limited to ideal rather than real world listening situations (de Cheveigné, 1999). A major difference between vowel perception experiments and the current study is stimulus duration.

While fine waveform cues (phase modulation) associated with beats are likely to play a role in discriminating concurrent vowels (see de Cheveigné, 1999), in the case of midshipman, the relatively long duration of the signals may make envelope cues more salient. Consider that synthetic vowel stimuli are typically shorter than the beat period when very small dfs are used, but for the study presented here, stimuli were long enough to include multiple beat cycles. Both midshipman auditory afferents and midbrain neurons encode df in their firing patterns (McKibben, 1998; McKibben and Bass, in press; Bodnar and Bass, 1997, 2001).

Beat stimuli with shallower modulations were constructed by keeping the f1 component the same and attenuating f2. These shallow beats are probably more typical of the naturally occurring beats a fish would encounter [e.g., Fig. 1(B)], since beat modulation will be maximal only if the amplitudes of concurrent hums are the same at the listener's location. More often, one signal will dominate the summed waveform, either because the source is closer, or more intense, or both. Reducing the depth of modulation increased the effectiveness of beat stimuli at all dfs tested (2–10 Hz).

In tests with 50% modulated beats, the tone response was still significantly greater than beat responses at 2- to 6-Hz dfs, but not at the 10-Hz df. This sensitivity to 50% modulated beats is consistent with detection data from midbrain auditory neurons, which still show significant synchronization to the df with 50% modulation (Bodnar and Bass, 2001). The 10-Hz df stimulus attracted a greater proportion of fish than the other beat stimuli, although this difference was only statistically significant between the 10-Hz and 6-Hz dfs.

The trend toward greater response to a 10-Hz df seen at 50% and 100% modulation suggests a couple of hypotheses. One is that hum recognition depends at least in part on envelope modulation being outside of the range of modulation in other midshipman calls, including agonistic grunts. Grunt trains tend to have periodicities of 1 to 3 Hz (Brantley and Bass, 1994; Bass *et al.*, 1999). A second hypothesis is that the perceived depth of beating is less at the 10-Hz df. Midshipman show clear frequency preferences for signals that differ by 10 Hz, and these frequency preferences are temperature dependent (McKibben and Bass, 1998). At a 10-Hz df, the frequency separation of the components may be great enough to skew their perceptual weighting.

Fay (1998) showed that, in goldfish, the perceptual similarity between beat stimuli and a single tone changes with df such that there is a range of dfs over which the beat stimulus is most unlike a tone. Although he did not condition fish with tones below 200 Hz, the current data on hum recognition are consistent with what he reported, with slow and fast beats tending to be more tone-like than beats with intermediate dfs.

With 25% modulated beats the difference between tone and beats was no longer significant, and there were no significant differences among dfs (2–10 Hz) in the proportion of fish responding. Because the apparent depth of beating will change as a fish swims nearer to one particular calling male, beats could serve as a cue for localizing a male and his nest (McKibben and Bass, 1998). The increased response to shallower beats, using the fixed depth beat stimuli in this study, would be predicted by this hypothesis. Beats with greater modulation could potentially be recognized as hums at a distance only to be rejected once they failed to diminish on approach to the source (and in this study response at the source was required for recognition to be scored).

The reduced modulation stimuli were constructed by attenuating f2, so they differed in amplitude and waveform fine structure (i.e., phase modulation), as well as in degree of envelope modulation. Amplitude seems unlikely to have been responsible for any differences in stimulus effectiveness, since the trend was for lower amplitude signals to be more effective. Also, even the 100% modulated beats (the least effective stimuli) were only 3 dB more intense than the single tone (the most effective stimulus). While fine structure cannot be ruled out as a potential contribution to the differential responses, the long stimulus durations made envelope modulation an obvious cue. Also, the extremely small differences in component period at the slowest beats (e.g., less than 0.1 ms at 0.5 Hz) made for even smaller variations in fine structure peak intervals. Midshipman hum recognition has been shown to be tolerant of some degree of fine structure ''jitter'' (FM stimuli in McKibben and Bass, 1998). Also, midshipman auditory afferent synchronization to beat envelopes predicts the greater disruption of response at higher dfs, whereas synchronization to the component frequencies (fine structure) does not (McKibben, 1998; McKibben and Bass, in press).

A previous two-choice playback study tested female midshipman preference for beat or tone stimuli. Fish favored individual tones over beat stimuli at a larger df (5 Hz) but not at a df of 2 Hz (McKibben and Bass, 1998). These were two-choice tests and, hence, looked at preference rather than simple recognition of the beat stimuli. One potential reason for the greater response to 2 Hz beats relative to the current study is that for the two-choice tests the beat was always heard against a backdrop of the continuous tone. The summation of these two sources may have reduced the perceived strength of the beat modulation. There may also have been subtle differences in the stimulus presentation or in fish responsiveness between years. Similar to the findings presented here, that study also showed that attenuating the f2 component tended to make responses to beat stimuli more similar to those to tones.

E. Envelope shape for pulse and beat

One-hundred percent modulated beat stimuli resemble pulse trains in that the amplitude minima could be thought of as ''gaps'' separating above threshold sound pulses. The fir-

ing rates of midshipman auditory neurons typically follow the envelope modulation of beat stimuli, with the greatest probability of firing at beat maxima (McKibben, 1998; McKibben and Bass, in press). This often results in regular bursts of action potentials separated by silent gaps. Thus, the neural input in response to beat stimuli is pulsatile, and could be the basis for perceptual similarity between strongly modulated beat stimuli and pulse trains.

In terms of envelope shape, however, the pulse and beat stimuli used here are markedly different. Whereas the pulses had relatively abrupt rises to a sustained amplitude, the amplitude of a beat envelope changes continuously over the beat cycle. Envelope risetime and slope were not specifically addressed in this study, but they may have significant effects on signal perception (e.g., Gerhardt and Schul, 1999). Beats with a 1-Hz dF attracted approximately 33% of the fish, but only one of the 1-s period pulsed tones was similarly effective. The 0.9 ms pulses attracted 28% of the fish. The higher effectiveness of slower beats and the difference in response between beats and pulse trains, may result from slower beats having more gradual slopes and thus modulating neural input less than either pulses or faster beats (McKibben, 1998; McKibben and Bass, in press).

V. SUMMARY AND CONCLUSIONS

As in other vertebrates, temporal envelope modulation may be important for discrimination between different types of acoustic signals in midshipman. However, hums themselves can appear modulated, as a result of acoustic interference with concurrent hums. Thus, hum recognition would be expected to incorporate some tolerance of envelope modulation. In one-choice tests, pulse trains were less effective than continuous tones at attracting gravid female midshipman. Response to pulse trains was graded, with longer pulses and greater pulse to gap duration ratios resulting in more effective signals. This probably reflects both duration minima for initial hum recognition and the time required for the response behavior, which depends on an ongoing signal. Midshipman are not simply responding to the relative amount of energy in a signal (i.e., duty cycle), although for fixed pulse lengths, duty cycle can predict stimulus effectiveness. Across a variety of pulse and gap length combinations, the proportion of fish responding to a signal was closely approximated by pulse*pulse/gap duration. While it is unclear what specific underlying perceptual mechanisms account for this relationship, it does confirm the observed effects of pulse length and pulse to gap ratio.

Midshipman were sensitive to even very slow beat modulations. While the slowest, 0.5–1 Hz, and fastest, 10 Hz, beats had intermediate effectiveness, beats from 2–6 Hz attracted almost no fish. Reducing the depth of modulation by attenuating one of the beat components restored signal effectiveness. However, responses to 50% modulated beats were still less than that to an unmodulated tone. This suggests that natural beats could affect signal recognition even when the interfering hums differ in amplitude at the listener's location. Because this study tested unconditioned responses to sounds, differences in response presume differences in perception but do not establish perceptual limits. It would be interesting to know, within this communication context, whether there is generalization across modulation types and envelope shapes.

ACKNOWLEDGMENTS

This research was supported by NIH Grant No. DC-00092 to A.H.B. Margaret Marchaterre provided field recordings of midshipman calls, and Charles E. McCulloch gave statistical advice. This is contribution 2144 from the Bodega Marine Laboratory, University of California at Davis.

Bass, A. H., Bodnar, D. A., and Marchaterre, M. A. (**1999**). ''Complementary explanations for existing phenotypes in an acoustic communication system,'' in *Neural Mechanisms of Communication*, edited by M. Hauser and M. Konishi (MIT Press, Cambridge, MA), pp. 493–514.

Bass, A. H., and Clark, C. (**in press**). ''The physical acoustics of underwater sound communication,'' in *Springer Handbook of Auditory Research*, edited by A. M. Simmons, A. Popper, and R. Fay (Springer-Verlag, New York).

Bodnar, D. A., and Bass, A. H. (**1997**). ''Temporal coding of concurrent acoustic signals in auditory midbrain,'' J. Neurosci. **17**, 7553–7564.

Bodnar, D. A., and Bass, A. H. (**2001**). ''Coding of concurrent vocal signals by the auditory midbrain: Effects of stimulus level and depth of modulation,'' J. Acoust. Soc. Am. **109**, 809–825.

Bradbury, J. W., and Vehrencamp, S. L. (**1998**). *Principles of Animal Communication* (Sinauer Associates, Inc., Sunderland).

Brantley, R. K., and Bass, A. H. (**1994**). ''Alternative male spawning tactics and acoustic signals in the plainfin midshipman fish, *Porichthys notatus* (Teleostei, Batrachoididae),'' Ethology **96**, 213–232.

Bregman, A. S. (**1990**). *Auditory Scene Analysis: The Perceptual Organization of Sound* (MIT Press, Cambridge, MA).

Bregman, A. S., Colantonio, C., and Ahad, P. A. (**1999**). ''Is a common grouping mechanism involved in the phenomena of illusory continuity and stream segregation?'' Percept. Psychophys. **61**, 195–205.

de Cheveigné, A. (**1999**). ''Waveform interactions and the segregation of concurrent vowels,'' J. Acoust. Soc. Am. **106**, 2959–2972.

Fay, R. R. (**1972**). ''Perception of amplitude modulated auditory signals by the goldfish,'' J. Acoust. Soc. Am. **52**, 660–666.

Fay, R. R. (**1985**). ''Sound intensity processing by the goldfish,'' J. Acoust. Soc. Am. **78**, 1296–1309.

Fay, R. R. (**1998**). ''Perception of two-tone complexes by the goldfish (*Carassius auratus*),'' Hear. Res. **120**, 17–24.

Fay, R. R., and Coombs, S. (**1983**). ''Neural mechanisms in sound detection and temporal summation,'' Hear. Res. **10**, 69–92.

Fine, M. L., Winn, H. E., and Olla, B. L. (**1977**). ''Communication in fishes,'' in *How Animals Communicate*, edited by T. A. Sebeok (Indiana University Press, Bloomington), pp. 472–518.

Gerhardt, H. C. (**1988**). ''Acoustic properties used in call recognition by frogs and toads,'' in *The Evolution of the Amphibian Auditory System*, edited by B. Fritzsch (Wiley, New York), pp. 455–483.

Gerhardt, H. C., and Schul, J. (**1999**). ''A quantitative analysis of behavioral selectivity for pulse rise-time in the gray treefrog, *Hyla versicolor*,'' J. Comp. Physiol. A **185**, 33–40.

Hawkins, A. D. (**1981**) ''The hearing abilities of fish,'' in *Hearing and Sound Communication in Fishes*, edited by W. Tavolga, A. Popper, and R. Fay (Springer-Verlag, New York), pp. 109–138.

Ibara, R. M., Penny, L. T., Ebeling, A. W., Van Dykhuizen, G., and Cailliet, G. (**1983**). ''The mating call of the plainfin midshipman fish, *Porichthys notatus*,'' in *Predators and Prey in Fishes*, edited by D. L. G. Noakes, D. G. Lindquist, G. S. Helfman, and J. A. Ward (Dr. W. Junk Publishers, The Hague, The Netherlands), pp. 205–212.

Jensen, F. B., Kuperman, W. A., Porter, M. B., and Schmidt, H. (**1994**). *Computational Ocean Acoustics* (American Institute of Physics, New York).

McKibben, J. R. (**1998**). ''A neuroethological analysis of acoustic communication in the plainfin midshipman fish, *Porichthys notatus*.'' Ph.D. thesis, Cornell University, Ithaca, NY.

McKibben, J. R., and Bass, A. H. (**1998**). ''Behavioral assessment of acous-

tic parameters relevant to signal recognition and preference in a vocal fish,'' J. Acoust. Soc. Am. **104**, 3520–3533.
McKibben, J. R., and Bass, A. H. (**in press**). ''Peripheral encoding of behaviorally relevant acoustic signals in a vocal fish: Harmonic and beat stimuli,'' J. Comp. Physiol. A.
Moore, B. C. J., Peters, R. W., and Glasberg, B. R. (**1993**). ''Detection of temporal gaps in sinusoids: Effects of frequency and level,'' J. Acoust. Soc. Am. **93**, 1563–1570.
Ryan, M. J., and Rand, A. S. (**1993**). ''Species recognition and sexual selection as a unitary problem in animal communication,'' Evolution (Lawrence, Kans.) **47**, 647–657.
Shannon, R. V., Zeng, F., Kamath, V., Wygonski, J., and Ekelid, M. (**1995**). ''Speech recognition with primarily temporal cues,'' Science **270**, 303–304.
Siegel, S., and Catellan, J. N., Jr. (**1988**). *Nonparametric Statistics for the Behavioral Sciences*, 2nd ed. (McGraw-Hill, New York).
Viemeister, N. F., and Wakefield, G. H. (**1991**). ''Temporal integration and multiple looks,'' J. Acoust. Soc. Am. **90**, 858–865.

Pitch strength and pitch dominance of iterated rippled noises in hearing-impaired listeners

Marjorie R. Leek[a] and Van Summers
Army Audiology and Speech Center, Walter Reed Army Medical Center, 6900 Georgia Avenue, NW, Washington, DC 20307-5001

(Received 12 August 2000; revised 13 December 2000; accepted 20 March 2001)

Reports using a variety of psychophysical tasks indicate that pitch perception by hearing-impaired listeners may be abnormal, contributing to difficulties in understanding speech and enjoying music. Pitches of complex sounds may be weaker and more indistinct in the presence of cochlear damage, especially when frequency regions are affected that form the strongest basis for pitch perception in normal-hearing listeners. In this study, the strength of the complex pitch generated by iterated rippled noise was assessed in normal-hearing and hearing-impaired listeners. Pitch strength was measured for broadband noises with spectral ripples generated by iteratively delaying a copy of a given noise and adding it back into the original. Octave-band-pass versions of these noises also were evaluated to assess frequency dominance regions for rippled-noise pitch. Hearing-impaired listeners demonstrated consistently weaker pitches in response to the rippled noises relative to pitch strength in normal-hearing listeners. However, in most cases, the frequency regions of pitch dominance, i.e., strongest pitch, were similar to those observed in normal-hearing listeners. Except where there exists a substantial sensitivity loss, contributions from normal pitch dominance regions associated with the strongest pitches may not be directly related to impaired spectral processing. It is suggested that the reduced strength of rippled-noise pitch in listeners with hearing loss results from impaired frequency resolution and possibly an associated deficit in temporal processing.
[DOI: 10.1121/1.1371761]

PACS numbers: 43.66.Hg, 43.66.Sr [SPB]

I. INTRODUCTION

In its simplest form, pitch is the perceptual attribute corresponding to the frequency of a pure tone. However, the perception of the pitch of more complex sounds, containing many component frequencies, involves other auditory functions in addition to frequency analysis. Contributions to pitch analysis include spectral information provided by the spatial location of stimulation along the basilar membrane and the temporal characteristics of the time wave forms that are coded in neural firing patterns. The clear perception of pitch in complex sounds is one of several cues to the accurate understanding of speech and the enjoyment of music. The abilities to perceive voice pitch and to track small changes in that pitch have been shown to provide assistance to lip readers (Grant *et al.*, 1985) and to aid in the separation of voices in a multitalker environment (Assman and Summerfield, 1990). Further, the perception of voice pitch may be instrumental in normalizing the changes in formant structure specific to individual talkers, thereby aiding in the accurate perception of vowels and vowel transitions (Syrdal and Gopal, 1986; Miller, 1989; Johnson, 1990). Pitch also provides suprasegmental cues to speech understanding, including primary information concerning intonation and stress on certain portions of the speech signal (Lehiste, 1976). To the extent that pitch perception is impaired, altered, or distorted by a sensorineural hearing loss, these cues may not be available to the listener.

In studies of both simple and complex pitch, hearing-impaired (HI) listeners demonstrate a weaker, more imprecise percept than is usually experienced by normal-hearing (NH) listeners. Larkin (1983) argued that cochlear hearing impairment results in a poorer and more unstable perception of the pitch of pure tones. Hearing-impaired subjects were more susceptible to a biasing tone that tended to shift their pitch match, which Larkin attributed to an inability by hearing-impaired listeners to maintain a constant perception of pitch. He concluded that pitch perception in hearing-impaired listeners was generally more ambiguous and subject to external influences, such as the biasing tone used in his experiment. Burns and Turner (1986) reported that subjects with hearing impairment tended to show exaggerated downward shifts in the pitch of pure tones with increasing stimulus level, especially for tones lower in frequency than 1 kHz. They reported further that pitch matches were more variable than for normal-hearing listeners. Burns and Turner suggested that these results were reflections of a general and widespread ambiguity of pitch in the presence of cochlear damage.

These reports of indistinct pure-tone pitch are complemented by similar reports involving the pitch of more complex sounds, such as speech or harmonic complexes, in which the pitch percept experienced by hearing-impaired listeners is typically impoverished relative to perception by normal-hearing listeners. This may be seen in the poorer-

[a]Author to whom correspondence should be addressed.

than-normal performance of hearing-impaired listeners on both pure-tone frequency discrimination and fundamental frequency discrimination within harmonic complexes, both tasks reported by Moore and Peters (1992). Although there were large individual differences in performance, hearing-impaired listeners generally required larger-than-normal pitch differences for both pure-tone stimuli and periodic complex stimuli. Moore and Peters found some indication that the temporal aspects of the stimuli provided important pitch information to both normal-hearing and hearing-impaired listeners, with a lesser role for spectral analyses provided by the resolved harmonics. There was not a strong relationship in their hearing-impaired listeners between frequency resolution, as reflected in measures of auditory filter bandwidths, and frequency discrimination of pure tones, suggesting that temporal aspects of these stimuli contributed more to pitch perception than did results of a spectral analysis. Further evidence that pitch discrimination in complex sounds relied more on temporal characteristics than spectral characteristics was seen in that the lower (i.e., resolved) harmonics contributed less to the pitch percept than did the higher, unresolved harmonics, for both normal-hearing and hearing-impaired subjects. Interestingly, Moore and Peters reported that, in some cases, including low-frequency harmonics in a stimulus resulted in poorer pitch performance than if those harmonics were filtered out. The authors suggested that such low harmonics interfered with the clear temporal picture at the outputs of the broadened auditory filters centered at the higher harmonics in their hearing-impaired listeners. A final argument for the pre-eminence of temporal over spectral cues to pitch was made relative to the importance of component phases in determining pitch. A purely spectral pitch analysis would not be affected by component phases in the stimuli, and yet differences in phases generally resulted in alterations of pitch.

Arehart (1994) reported that temporal information extracted from high-frequency unresolved harmonics provided the basis for pitch discrimination of harmonic complexes for many hearing-impaired subjects. This was, however, not true for all subjects, as some were able to base their judgments on low-frequency harmonics. As in most studies of pitch processing in hearing-impaired listeners, there was considerable variability in performance across subjects, that could not be readily attributed either to degree or configuration of the hearing loss. This suggests that deficits in spectral or temporal processing reflected in pitch perception are not homogenous across listeners with hearing loss, and therefore it is difficult to attribute the poorer pitch performance usually observed in these listeners to a clear loss of processing ability along either dimension. In general, however, Arehart's data supported the view that temporal processing was primarily responsible for complex pitch discrimination in these listeners, and specifically, that pitch was determined by the periodicity in the stimulus. Also noted for some subjects were slight improvements in pitch discrimination as stimulus level was increased, suggesting a stronger and less variable percept of pitch at higher levels.

In a more recent study reporting the ability of hearing-impaired listeners to make musical interval judgments in response to two-harmonic complex tones, Arehart and Burns (1999) found that musicians with high-frequency hearing loss showed reductions in their ability to identify musical intervals placed in regions of their hearing losses, although at lower frequencies, where their sensitivity was near normal, this ability was unimpaired. However, the poorer performance at high frequencies could not be attributed either to the lower sensation level (SL) of the stimuli nor to impaired frequency resolution, because all stimuli were presented at equal SLs, and performance was similar whether the two tones in the stimuli were presented to the same ear or dichotically. The authors interpreted their findings, taken along with other reports of reduced temporal processing in hearing-impaired listeners (summarized in Moore, 1995), as evidence that the source of the reduced performance can be found in reduced temporal processing abilities.

These studies of complex pitch discrimination suggest that a number of possible correlates of cochlear damage may underlie altered pitch perception in listeners with sensorineural hearing loss. A reduced ability to detect the basic frequency and temporal information within a complex sound may result from increased auditory thresholds, i.e., the sound may not be sufficiently audible. Although care has been taken to present stimuli at above-threshold levels, still there are some indications that the SLs of the stimuli may affect the perception of pitch, at least in some listeners (see, e.g., Arehart, 1994). In addition to reduced sensitivity, it is known that frequency resolution typically is altered in the presence of cochlear impairment (Glasberg and Moore, 1986; Leek and Summers, 1993), suggesting that the initial spectral analysis stage of pitch processing will be abnormal in these individuals. Such impaired frequency selectivity could interfere with pitch perception that may rely on normally resolved stimulus components, in that the lower limits of resolution might be reduced due to broader auditory channels. To the extent that complex pitch may be dependent on within-channel temporal analysis, impaired frequency resolution could degrade pitch perception by altering the temporal outputs of auditory channels, complicating the temporal analysis [see Moore and Peters (1992) for more of this argument]. Arehart (1994), Arehart and Burns (1999), and Moore and Peters (1992) have related the poorer pitch discrimination of complex sounds shown by hearing-impaired listeners to deficits in temporal processing. Further, there are other indications of reduced temporal processing abilities accompanying sensorineural hearing loss in some hearing-impaired subjects in studies of gap detection in noise (e.g., Florentine and Buus, 1984), and temporal integration (e.g., Carlyon *et al.*, 1990), although most of the deficits in temporal processing are related to other known accompaniments to sensorineural hearing loss (Moore, 1995). For example, Bacon and Viemeister (1985) argued that hearing-impaired listeners showed reduced sensitivity to high rates of amplitude modulation because the bandwidths of the stimuli were limited by the subjects' sensitivity losses.

A further source of altered or more indistinct pitch perception in hearing-impaired listeners may be that the frequency regions that provide the strongest basis for pitch analysis in normal-hearing listeners may be damaged and, as

a result, cannot support pitch perception in a normal manner. Ritsma (1967) showed that, for harmonic complexes with fundamental frequencies between 100 and 400 Hz, the frequency region of the third to the fifth harmonic provided the strongest pitch percept. Plomp (1976) reviewed other studies that confirm the notion that, for complexes with fundamental frequencies less than about 1000 Hz, the frequency region that dominates the perception of pitch for normal-hearing listeners tends to fall around these harmonics. Plomp pointed out that this region approximately marks the limit of critical bands, and suggested that this supports the importance of frequency resolution to the perception of complex pitch.

Given the importance of a dominance region in the perception of the pitch of complex sounds, listeners with cochlear damage may experience pitch weakness or alteration because of either a loss of sensitivity or a loss of resolution. Although Ritsma (1967) reported that, above a minimum level, the SL of the stimuli does not affect the perception of pitch, nonetheless, cochlear damage in regions of dominant harmonics may not produce the strength of pitch that normal-hearing listeners obtain, and therefore, the dominant regions may not support a strong pitch percept. Further, to the degree that the pitch strength may be dependent on frequency resolution, it might be expected that listeners with broader auditory channels would have reduced regions of resolved harmonics, perhaps lowering the region of pitch dominance relative to that shown by normal-hearing listeners. Either reduced sensitivity or reduced frequency selectivity in the dominant regions might underlie a weaker pitch percept by these listeners. Subsequent temporal processing mechanisms may also be impaired.

These studies of complex pitch perception in hearing-impaired listeners used periodic stimuli in order to examine the relative contributions of spectral and temporal analyses. The periodicity in the stimuli may be eliminated as a cue by employing noise stimuli, modified to produce defined peaks in their amplitude spectra. Yost and colleagues (Yost, 1982; Yost and Hill, 1978, 1979; Yost, Hill, and Perez-Falcon, 1978) as well as Fastl and colleagues (Fastl, 1988; Fastl and Stoll, 1979) have reported studies of pitch perception using such aperiodic stimuli, typically generated by adding a delayed version of a noise to itself. Called a rippled noise, this stimulus is characterized by concentrations of energy in regularly spaced frequency regions of the amplitude spectrum, similar in some respects to the spectrum of a harmonic complex, but with a flat-envelope waveform without any periodicity as is present in harmonic complexes. By varying some of the characteristics of the rippled noise, both its pitch and the strength of the pitch percept can be manipulated experimentally. The rippled-noise pitch (also called a ''repetition'' pitch) is typically matched by subjects to a pure tone with a frequency equal to the inverse of the delay. For example, if the re-added noise is delayed by 4 ms, a pitch equivalent to 250 Hz will be heard. There are a number of variations on this general procedure of adding noise to itself that produce more or less strong perceptions of a pitch. If the delayed portion of the noise is added more than once to the original noise, the stimulus is termed ''iterated rippled noise'' (IRN). The strength of the pitch percept is related to the number of iterations used in creating the noise: Pitch strength grows as the same delays within the noise are repeated, increasing the temporal regularities in the waveform fine structure (Yost, 1996; Yost *et al.*, 1996; Patterson *et al.*, 1996). Increasing the iterations not only creates a waveform with more representations of the same delay, thereby creating a stronger regularity in the temporal waveform, but also increases the peak-to-valley amplitude differences in the rippled spectrum of the noise, and narrows the spectral peaks. Although both the temporal and spectral changes associated with increasing numbers of iterations might underlie the greater pitch strength, Yost and Patterson and their colleagues (e.g., Yost *et al.*, 1994) have shown repeatedly that the processing of pitch in IRN is more likely mediated through temporal rather than spectral factors, and that the strength of IRN pitch is reflected in the height of the first peak in the autocorrelation function of the noise waveforms. Spectral bases for IRN pitch would require the presence in the stimuli of resolved frequency regions, and it has been shown by Patterson *et al.* (1996) that both the pitch and the pitch strength are little affected by high-pass filtering the stimuli above the region of resolved harmonics.

Even though rippled noise is a broadband stimulus, with energy over a wide range of frequencies, Yost (1982), using bandpass filtered versions of the noise, determined that the frequency region that contributes most to the strength of the pitch percept corresponds to about four times the inverse of the delay. This corresponds well with pitch dominance regions within complex tones, and lends support to the notion that the pitch of complex tones and the pitch of rippled noise are generated by the same mechanisms in the auditory system. Yost (1982) has argued that pitch dominance for rippled noise may be modeled as a weighting function, with the greatest weight located in the region of 3 to 5 times the inverse of the delay, followed by a temporal analysis of the energy found within the weighting region. Thus, although both the spectral dominance theories and the weighting theories include the concept of an emphasis in particular frequency regions within a stimulus, the weighting theories attribute the ultimate pitch strength to a temporal analysis of noise energy falling within the dominant frequency region.

Dominant frequency regions for complex pitch perception may be disrupted or altered in listeners with hearing loss, perhaps resulting in abnormal pitch processing. In addition to the general auditory processing deficits mentioned above, such as sensitivity loss and impaired frequency and temporal resolution, the hearing loss typically is not equal across frequencies. Therefore, cochlear mechanisms supporting temporal and frequency analysis might be nearly normal in frequency regions below 500 Hz, for example, yet be significantly abnormal at higher frequencies. A listener with such a configuration of hearing loss might match the pitch of a complex stimulus to a pure-tone frequency nearly the same as a normal-hearing listener, but the pitch dominance region might be abnormal and the strength of the pitch percept reduced. This would be consistent with the findings of less clarity in pitch perception by hearing-impaired listeners.

The two questions addressed in this study are whether the pitch of iterated rippled noise is equally strong or clear in

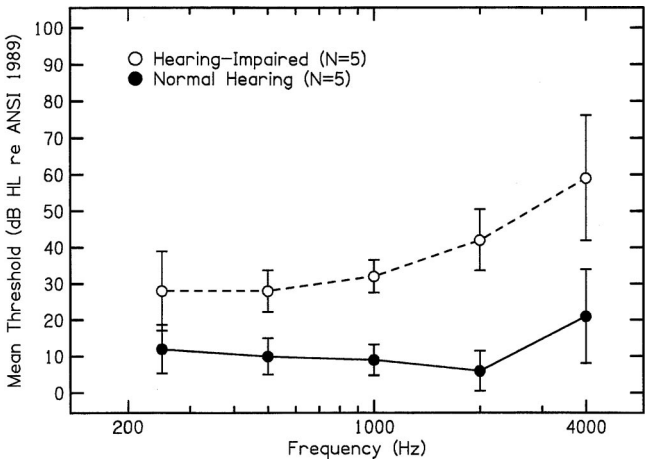

FIG. 1. Mean audiograms for normal-hearing and hearing-impaired subjects. Error bars represent standard deviations for each mean.

hearing-impaired listeners as in normal-hearing listeners, and whether the dominant frequency regions supporting the strongest pitch perception for normal-hearing listeners are the same for hearing-impaired listeners. For a given delay, the maximum pitch strength occurs when the delayed noise and the original noise are equal in amplitude. Pitch strength fades as the gain of the delayed noise decreases, and eventually the pitch is lost. The strength of a given iterated rippled noise may be measured reliably by determining the gain in the delayed portion of two rippled noises having slightly different delays that is necessary to discriminate them.

II. METHODS

A. Subjects

Five normal-hearing and five hearing-impaired subjects participated in the experiment. Means and standard deviations of the audiometric thresholds of the subject groups are shown in Fig. 1. The hearing-impaired subjects had mild-to-moderate sensorineural hearing losses. Cochlear site of lesion was identified for each subject based on agreement between air- and bone-conduction thresholds and normal middle ear function as determined by immittance audiometry. Subjects in this group ranged in age from 61 to 75, with a mean age of 70 years. Normal-hearing subjects ranged in age from 41 to 76, with a mean age of 64. Each subject participated in approximately 9 h of testing, carried out over several experimental sessions. All subjects provided informed consent and were compensated for their participation in the experiment if eligible according to institutional policy.

B. Stimuli

Stimuli were constructed digitally. A Gaussian noise was digitally copied and then added to itself after a specified delay (T), and with an attenuation ranging between 0 and 1.0. This combined noise was then delayed and attenuated and added again into the original noise. [The construction of the rippled noise follows the ''add-original'' network described in Yost *et al.* (1996).] The delay, attenuate, and add sequence was continued nine times. When the delayed noise portions are unattenuated, nine iterations produces a stimulus with a fairly strong pitch (Yost *et al.*, 1996; Patterson *et al.*, 1996). Rippled noise stimuli were 300 ms in duration, including 20-ms cosine-squared rise–fall times.

For each experimental trial, a standard noise stimulus and a comparison stimulus were produced. The standard and comparison noises were constructed anew (i.e., starting with a new sample of Gaussian noise) for each trial. Standard delay times were 1, 2, 4, and 8 ms, producing stimuli with pitches corresponding to about 1000, 500, 250, and 125 Hz, respectively. Comparison stimuli differed in delay from the standard stimuli by 12%, producing comparison pitches about 12% (two semitones) lower than the standard pitches. This is a large pitch change, and produces a clear difference between stimuli when the original and delayed noise have the same amplitude (see Fig. 2). The strengths of the pitches of both standard and comparison noises on each trial were varied by attenuating the delayed part of the noise stimulus before adding it to the original noise. The gain is applied during construction of the IRN at each iteration stage, after the appropriate delay and before adding into the original noise. Figure 2 shows waveforms and amplitude spectra for two standard and two comparison stimuli used in the study. The two top noises were created with a gain of 1.0 (0 dB) and delays of 4.5 and 4.0 ms. For these two delays, the peaks in the spectrum are spaced 223 and 250 Hz apart. The bottom two noises have a gain of 0.5 (-6 dB), again with delays of 4.5 and 4.0 ms. Note that the effect of attenuating (i.e., gain <1.0) the delayed version of the noise is to reduce the peak-to-valley differences in the rippled noise spectra. Greater attenuations used in construction of the stimuli produce increasingly flattened spectra, and poorer representations of temporal regularities in the fine structure. The pitch strength of the rippled noise is reflected by the extent to which discrimination continues to be possible with increasing attenuation.

For some parts of the experiment, the rippled noises were filtered through octave-band digital filters (TDT PF1) centered at frequencies corresponding to harmonics of the pitch generated by each rippled noise. The TDT built-in functions were used, which provide a Butterworth filter of order 10 at center frequencies of 1000 Hz and higher, and order 6 below 1000 Hz. The overall levels of the noises after bandpass filtering were not adjusted, although this meant that the levels covaried with filter center frequency because of absolute differences in filter bandwidths. However, because the goal of this part of the experiment was to determine the relative pitch strengths of several frequency regions within the unfiltered stimulus, adjusting the levels might alter relative strengths, and so they were not adjusted.

Stimuli were played from a TDT DD1 D/A converter at a rate of 25K samples per second, low-pass filtered at 8.5 kHz (TDT FT5), passed through a programmable filter (TDT PF1) to provide octave-band filtering as called for, attenuated (TDT PA4), and played through a headphone buffer to one earpiece of TDH-49 earphones.

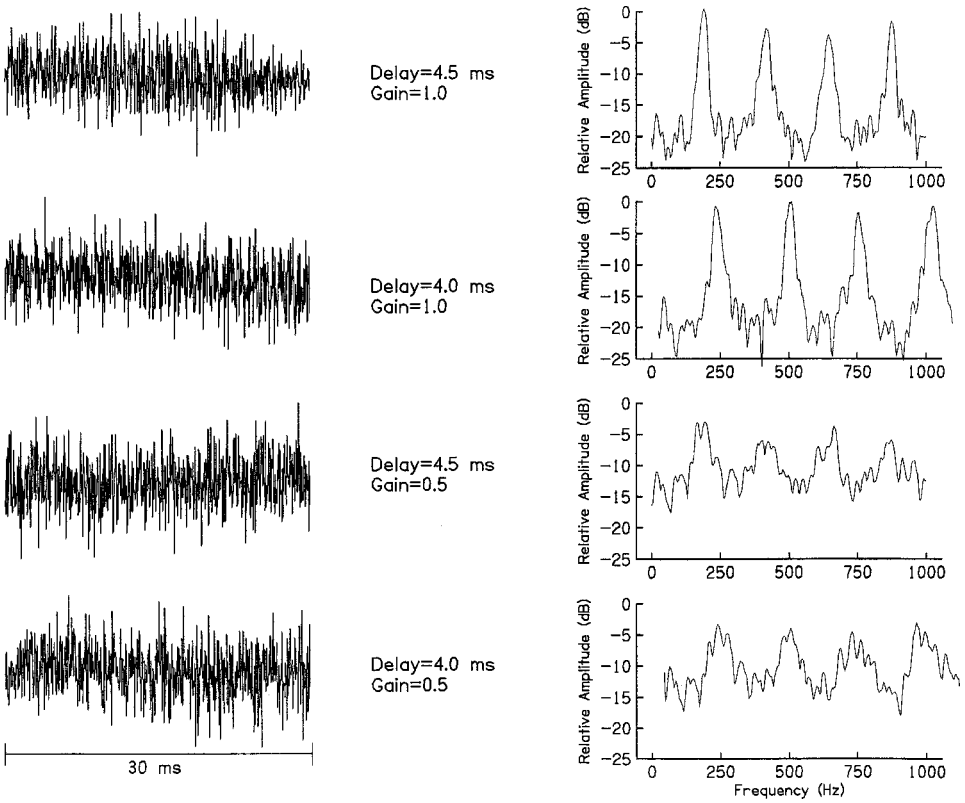

FIG. 2. Examples of the waveforms and spectra of four iterated rippled noises. The top panels have a gain of 1.0 (0 dB), and delays of 4 and 4.5 ms, corresponding to peak spacing in the spectrum of 250 Hz or 223 Hz, respectively. The bottom panels show the same two delays, but with a gain of 0.5 (−6 dB).

C. Procedures

Listeners were seated comfortably in a sound-treated booth, wearing earphones and facing a touch-screen response terminal. The threshold amount of attenuation of the delayed noise was determined in a standard/two-alternative forced-choice (S/2AFC) procedure over a number of stimulus trials. On each trial, the standard presentation was a rippled noise with one of four delays and with an attenuation determined by the level of an adaptive track. This stimulus was repeated in one of two presentations to follow. The other stimulus was the comparison noise, identical to the standard except for the 12% difference in delay. Presentations on each trial were separated by 400-ms interstimulus intervals. The listener's task on each trial was to indicate whether the first or second comparison presentation differed in pitch from the standard stimulus by touching a defined area on the terminal. Correct-answer feedback was provided after each response.

An adaptive tracking procedure was used to determine a threshold level of gain that would support 79% correct discriminations of rippled noises differing in delay by 12% (Levitt, 1971). As the gain of the delayed noise decreases, the peaks and valleys in the noise spectrum flatten, approaching a flat-spectrum wideband noise for each stimulus. The strength of the perceived pitch is related to the peak-to-valley differences. Therefore, the smallest magnitude of peak-to-valley difference in the stimuli that supports a discrimination in pitch between the comparison and standard stimuli provided a measure of the strength of the pitch percept for a given noise condition. For each noise condition, the adaptive track started with a gain of 0 dB. If a subject correctly discriminated the two pitches on three consecutive trials, the gain was decreased on the next trial by 3 dB. One incorrect response led to an increase in gain of 3 dB on the next trial, producing a stronger pitch percept for both the standard and comparison stimuli. After three turnarounds in the adaptive track, the step size changed to 1 dB, and the track continued until eight more turnarounds had occurred. The threshold was calculated as the mean of the turnaround points in the track over trials with a step size of 1 dB, and will be reported in dB [i.e., 20*log(gain)].

Stimuli were played to listeners at an overall level of 90 dB SPL, plus or minus a 3-dB amplitude rove. Yost and Hill (1978) showed that roving the levels provided an important control so that listeners would not be cued to the discrimination by a change in intensity in one part of the frequency spectrum, rather than pitch itself. Yost and Hill used a 4-dB overall amplitude rove; later studies have typically included amplitude roves ranging from 4 to 10 dB. The imposition of the small 6-dB amplitude rove here was meant to reduce possible loudness cues, while staying within the comfort range of the hearing-impaired listeners.

Thresholds were determined for rippled noise at four different standard delays, in separate blocks of trials. On each block, one of the four delay conditions was selected at random, with the constraint that all four were presented before any were repeated. Three separate estimates for each condition were made, and the final value averaged. Rest breaks were provided at regular intervals within each session to reduce fatigue.

Thresholds were determined first for the stimuli with full bandwidths. Then the same procedures were used to measure the pitch strength of the rippled noises when they were octave-band filtered. From four to seven octave-band stimuli were presented for each delay, centered at frequencies from

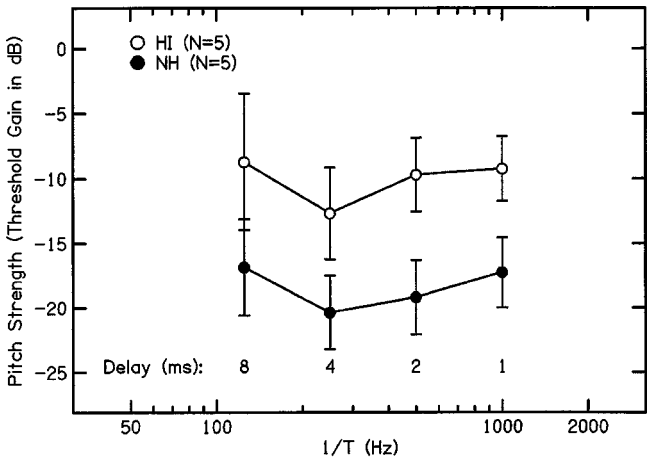

FIG. 3. Mean pitch strength measured as gain of the delayed noise for two groups of listeners. The abscissa shows the inverse of the delay, which generally corresponds to the perceived pitch in Hz. Delay in ms is shown on the figure. Error bars represent standard deviations. Smaller threshold gains (downward on the graph) are associated with noises having stronger pitches.

250 to 4000 Hz at the harmonics of the pitches generated by the rippled noises.

III. RESULTS

A. Pitch strength of iterated rippled noise

The first questions to be addressed here are whether the average pitch strength measured for hearing-impaired subjects is less than that for normal-hearing subjects, and whether the same patterns of pitch strength across delay times are observed for the two groups. Figure 3 shows the amount of attenuation of the delayed portion of the rippled noise that could be tolerated while still allowing subjects to discriminate between a standard and a comparison delay (pitch), as a function of the inverse of the delay in Hz. The delay times are shown on the figure, and the abscissa shows the pitch typically assigned to the noise. The greater the attenuation, i.e., the smaller the gain in dB, the more resistent is the stimulus to losing its pitch-like quality, and hence, the greater the pitch strength. Pitches are weaker at all tested delay times for hearing-impaired listeners than for normal-hearing listeners by about 8–10 dB. The pattern of pitch strengths across delay times was similar for the two groups, with less strength at the shortest and longest delays, and a minimum attenuation, or greatest strength, at 4 ms, associated with a pitch of 250 Hz. Yost and Hill (1978) found the strongest pitch for a delay of 2 ms (500 Hz), but their data show a broad minimum with little difference in pitch strength between 2 and 4 ms.

B. Pitch dominance

Figure 4 shows pitch strength as a function of the center frequency of the filtered stimuli. Each panel represents a delay time, and average data from the two groups of listeners are shown. To the right on each panel is the full-bandwidth pitch strength. As was seen for the full-bandwidth pitch strengths in Fig. 3, in all filtered conditions, the pitches were stronger in the normal-hearing listeners than for the hearing-impaired listeners. At each delay, some filters resulted in a stronger pitch percept than others. Each curve on these panels shows a more or less well-defined point of greatest pitch strength (shown as the minimum threshold gain), but some of the minima are fairly broad. For the normal-hearing subjects, at delays of 1 and 2 ms, there is a clear pitch dominance for the third and sixth harmonic, respectively, at 3000 Hz in each instance. At 4 and 8 ms, the dominance is not as clear, but pitch strength appears to decrease above about the fifth or sixth harmonic. For the hearing-impaired subjects, a minimum can be identified around the third to fifth harmonics at delays of 4 and 8 ms, with less obvious dips in the functions for 1 and 2 ms. In most cases, the minimum is most clearly seen by reference to the upper frequency side; the lower frequency sides change much more gradually. Yost (1982) also observed that the dominance region was defined

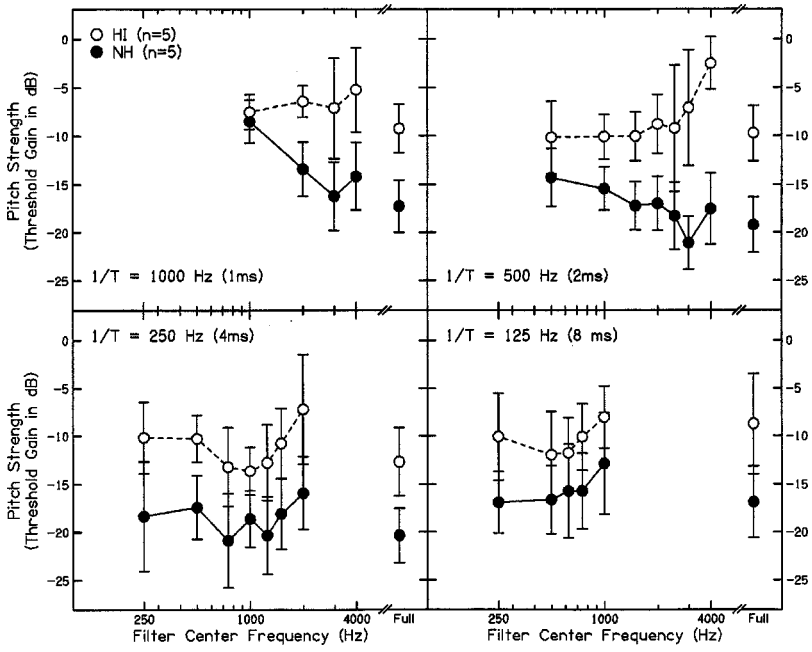

FIG. 4. Mean pitch strength and standard deviations for two groups of listeners for rippled noises filtered into octave bands. Each panel shows threshold gains for a different rippled noise. The abscissa indicates the center frequency of each filter. On each panel, the points at the far right indicate pitch strength for the full bandwidth, unfiltered rippled noises.

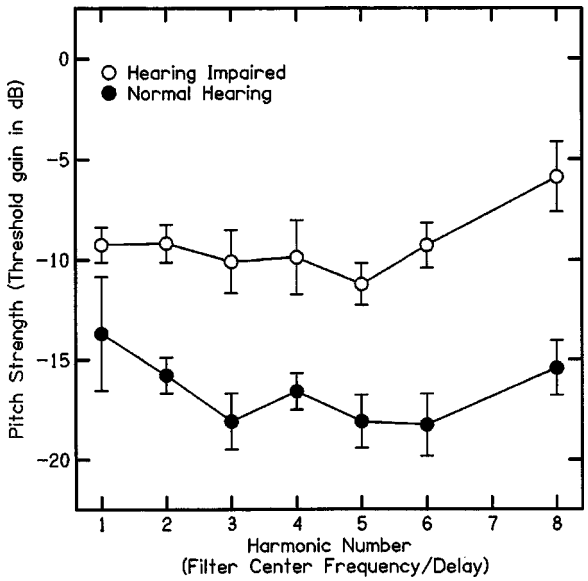

FIG. 5. Pitch strength of iterated rippled noises filtered into octave bands for normal-hearing and hearing-impaired listeners. Values are averages across rippled noises for each whole-number multiple (''harmonic'') of $1/T$.

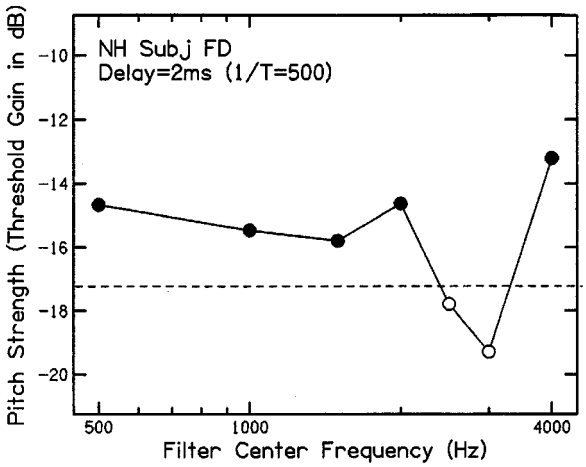

FIG. 6. Classification of ''dominant'' frequencies for one NH subject and delay. The standard deviation across the seven data points is 2.07. Dashed line indicates 1 standard deviation above the minimum data point. Frequencies indicated by the open circles are identified as dominant in this example.

more steeply on the high-frequency side, with a low-frequency side that changed little in pitch strength.

Yost (1982) identified a broad region of dominance for filtered stimuli that showed the strongest pitches in the third to sixth harmonic range. The present results may be compared qualitatively with Yost's data by collapsing the threshold gains over all four delay times, and plotting the average pitch strength across delay times and subjects within groups. The result, shown in Fig. 5, is a very broad U-shaped curve for both groups of listeners, with the strongest pitches associated with the middle harmonic numbers. There is, as seen before, a substantial difference in pitch strength between the two groups. The smallest and largest delay times for normal-hearing listeners show a clear decrease in pitch strength, but the pattern is somewhat different for the hearing-impaired group. For the lower harmonic numbers, the pitch strength does not decrease quite so clearly as observed in the normal-hearing group. On the higher harmonic side there is also a difference between the groups. The hearing-impaired data show a sharp reduction in pitch strength at harmonics above the fifth harmonic.

These mean data indicate general patterns of responses across subjects and conditions. Dominant harmonics may also be observed in individual subject responses. To estimate the range of dominant harmonics in the individual subject thresholds, a procedure based roughly on an analysis described by Shofner and Yost (1997) was carried out on these data. The goal of the procedure was to estimate dominant harmonics using a criterion based on variability in the threshold gain measures. The analysis was carried out separately for each subject and delay. An example for one normal-hearing subject for a 2-ms delay is shown in Fig. 6. First, an estimate of variability specific to an individual subject and delay was determined by calculating the standard deviation of threshold estimates across all filter bandwidths (seven values in the example). A harmonic was deemed ''dominant'' if its threshold gain was within one standard deviation of the minimum gain measured for that subject and delay. In the example, a filter centered at 3000 Hz is a dominant harmonic, as is one other harmonic, whose threshold gain falls within one standard deviation of the minimum. This determination of dominant harmonics differs somewhat from that implemented by Shofner and Yost (1997), who used a different task and metric. They implemented this procedure with a criterion of two times the estimate of variability, which has the effect of designating more harmonics as dominant. Using that less stringent criterion for the data here does result in more dominant harmonics, but does not materially affect the overall patterns of results discussed below.

Figure 7 shows the number of subjects registering a ''dominant'' harmonic for each delay. Normal-hearing subjects are shown with solid bars and hearing-impaired listeners with striped bars. This analysis demonstrates that there is considerable overlap in the dominance estimates for the normal-hearing and hearing-impaired groups at the two largest delays ($1/T = 125$ and 250 Hz), but a greater separation

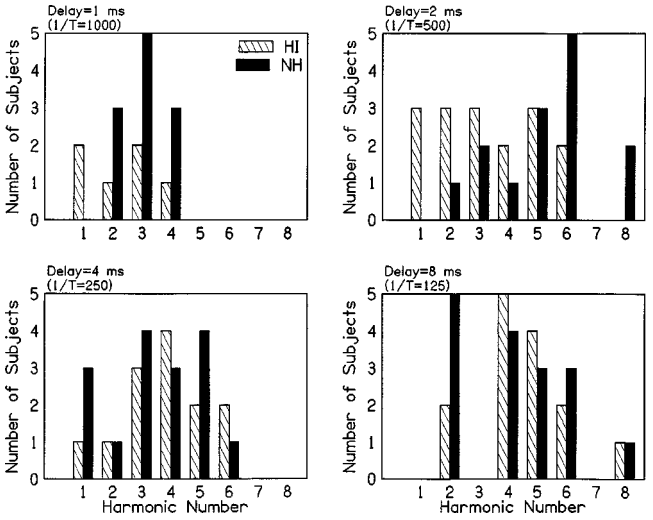

FIG. 7. Number of subjects (out of 5) within each group with a dominant pitch associated with each ''harmonic'' number. Each panel shows data for a different delay.

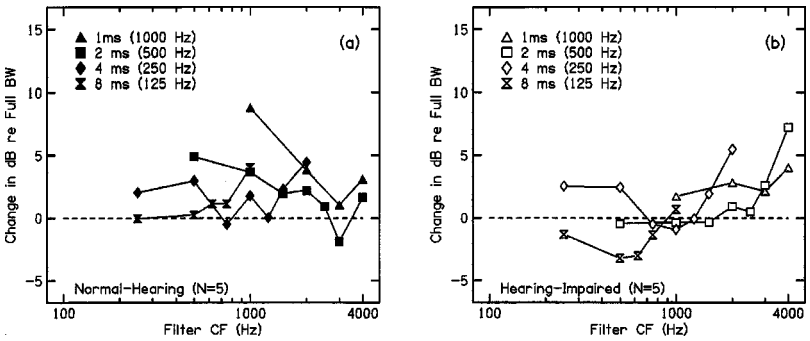

FIG. 8. Pitch strength in dB for each subject relative to full bandwidth for each unfiltered rippled noise. Left panel shows data for normal-hearing subjects; right panel shows data for hearing-impaired subjects. Different symbols refer to the different delay times. Points greater than 0 indicate a filtered noise weaker than the full bandwidth; points less than 0 represent filtered noises stronger than the full bandwidth.

when the delay was less ($1/T = 500$ and 1000 Hz). Most of the NH subjects at all delays fell within the third to fifth harmonic generally accepted as a dominant region for pitch. For the longer delay times, shown in the bottom two panels, there is complete overlap in dominance regions for the two groups. At the two shortest delays, corresponding to the highest pitches, most hearing-impaired subjects show their strongest pitches at lower harmonics than the dominant harmonics for normal-hearing subjects. This suggests that, when the ''normal'' dominant harmonics (i.e., third to fifth) fall in a region of more hearing loss (e.g., 3000–5000 Hz), the dominant regions tend to shift downward into a region of less hearing loss. However, when the dominant regions are in a lower frequency, more normal-sensitivity region, they remain similar to dominant regions of normal-hearing listeners. This pattern of results is further indication that the hearing loss in the higher frequencies for hearing-impaired subjects interferes with the usual dominance effects, with a shift in dominance perhaps into regions of milder hearing loss. For stimuli created with longer delay times, filters located in regions dominant for normal-hearing listeners do not intrude into regions of significant hearing loss and so the patterns of dominance are more normal for those longer delays and lower pitches. However, even though the pattern of dominance may be similar at these lower pitches to normal-hearing patterns, it must be remembered that the pitch strength is always considerably weaker for the hearing-impaired listeners, as shown in Fig. 4.

C. Does pitch dominance relate to full-bandwidth pitch strength?

Hearing-impaired listeners appear to find less pitch strength in regions of hearing loss, and to shift the pattern of pitch dominance in response to hearing loss in the higher frequencies. By translating the dominant harmonic numbers, we may more readily see the contribution to pitch of the frequency region of the filtered stimuli.

Figure 8 shows the change in pitch strength from the full-bandwidth stimuli as a function of frequency region of the filtered stimuli. Within each panel, average data across subjects are shown for each delay of noise. These plots indicate how much each filtered bandwidth contributes to the perception of pitch produced in these listeners by the unfiltered stimulus. Values above zero on these axes indicate a pitch strength that is less than the strength of the full-bandwidth pitch. Numbers less than zero indicate stronger pitches in the filtered stimuli than those observed in the full-bandwidth stimuli. For the normal-hearing listeners shown in the left-hand panel, note that nearly all the filtered conditions for all the delay times show pitches either weaker than or nearly equal in strength to pitches of the full-bandwidth stimuli. Contributions to overall pitch strength are not systematically related to frequency region: the correlation based on all data points shown in Fig. 8(a) between frequency of the filter and change in pitch strength relative to the full bandwidth strength was -0.01. The right-hand panel [Fig. 8(b)], showing the data for the hearing-impaired listeners, however, does indicate a strong relationship between contribution to the full pitch percept and frequency of the octave-band filter ($r = 0.59$, $p = 0.003$). Although for most conditions, there is still more pitch strength in the full bandwidth, there are more instances than observed for normal-hearing listeners where the stronger pitch is associated with one of the filtered stimuli, as indicated by those points falling below the zero line. The strength of the pitch percept begins to fade for these listeners as the center frequency of the filter increases. This reduction in pitch strength is probably related to the hearing-loss configurations of these listeners, with greater losses as frequency increases. In fact, the correlation between individual hearing-impaired subjects' audiometric thresholds at a given filter frequency and their average pitch strength measure obtained for that filter (averaged across noises) is even greater: $r = 0.69$ ($p = 0.0001$), with poorer absolute sensitivity related to reduced pitch strength.

IV. DISCUSSION

A. Effect of hearing loss on pitch strength

In all of the measurements reported here, the hearing-impaired subjects demonstrated reductions in pitch strength relative to normal-hearing subjects. These differences amounted to on average some 8–10 dB for the full-bandwidth stimuli. It is possible that this reduction in pitch strength is related to the overall lower SL of the stimuli for hearing-impaired listeners. However, although previous findings of the effects of level on pitch strength of rippled noise are somewhat contradictory, generally there is little influence of level, as long as the level of the stimuli is greater than about 25 dB SL (Bilsen and Ritsma, 1970; Yost and Hill, 1978). Recall that stimuli in this study were played at 90 dB SPL (full-bandwidth level). This level is about 70 dB SL for the normal-hearing listeners, and about 40–50 dB SL for the hearing-impaired listeners. SLs at frequencies above 1000 Hz, where thresholds are increased in the hearing-impaired

subjects, may actually be 15–20 dB less for those listeners. (Note that these estimates are not based on spectrum levels or outputs of auditory filters, but should simply be regarded as rough estimates of the SLs in these listeners.) Thus, even for the full-bandwidth noises, an effective low-pass filtering may occur when listeners have reduced high-frequency sensitivity. Such an internally narrowed bandwidth has been implicated in studies of temporal modulation transfer functions in hearing-impaired listeners. Bacon and Viemeister (1985) reported that hearing-impaired listeners were unable to perceive high rates of modulation as well as listeners with normal hearing. However, low-pass filtering of the stimuli also impaired performance in normal-hearing listeners, suggesting that the deficit associated with hearing impairment was at least in part a result of a narrowed internal bandwidth. As seen in Fig. 4, larger differences between subject groups were generally observed in the filtered stimuli when frequency bands were located in regions above 1000 Hz. These higher frequency regions correspond to regions of greater hearing loss in the hearing-impaired listeners, suggesting that the reductions in pitch strength for those listeners is related to the loss. The weakening of pitch for the full-bandwidth stimuli, as well as the alteration of pitch dominance regions for the two smallest delays (1 and 2 ms) points to an effect of the hearing loss, either in terms of a reduction in audible bandwidth due to reduced sensitivity, or perhaps to distortions in the normal dominance regions due to cochlear damage.

In addition to SL decreases in the hearing-impaired listeners, other cochlear processing mechanisms are likely to be impaired. Most notably, the frequency analyzing bandwidths are almost certainly broader than those found in normal-hearing listeners, even at these relatively high stimulus levels (Glasberg and Moore, 1986; Leek and Summers, 1993). Broader auditory filters in the hearing-impaired listeners would serve to smear the peaks in the internal cochlear excitation pattern. Such a reduction in spectral contrast imposed by smearing of the excitation patterns would have to be compensated by increasing the contrast in the stimulus, e.g., by increasing the gain of the delayed noise. Reductions in internal spectral contrast have been implicated in a number of measures involving hearing-impaired subjects, such as the discrimination of a rippled spectrum from a flat spectrum described by Summers and Leek (1994). In the absence of any other deficit, a reduction in the spectral contrast of the rippled noise used in this study by the hearing-impaired people of about 10 dB would correspond to filters increasing in width by about 2–3 times relative to normal filters, which is quite consistent with the broadening actually observed in listeners with moderate sensorineural hearing loss (Moore, 1995).

B. How does hearing loss affect pitch dominance?

Even though there is a clear reduction in pitch strength for hearing-impaired listeners for nearly all conditions of iterated rippled noise, the dominance region around the third to sixth ''harmonics'' (of $1/T$) remains the strongest for these listeners. This may be seen averaged across all delays in Fig. 5, and for individual delay conditions in Fig. 7. However, there is some indication of an effect of the hearing loss on the individual listeners' most dominant harmonic. For the two shortest delay times (1 and 2 ms), resulting in the highest frequencies of the filtered stimuli, the dominant harmonics for individuals in the two subject groups show less overlap than for stimuli with longer delays (see Fig. 7). This is likely due to the greater hearing losses in the higher frequency regions for the hearing-impaired group. For the longer delay conditions, in which the third to sixth harmonics fall in frequencies up to only 1500 Hz, the distributions of the two subject groups are nearly indistinguishable. These patterns of dominance suggest that hearing-impaired listeners experience the same regions of pitch dominance as their normal-hearing counterparts, except when those dominance regions fall in regions of moderate hearing loss. In those cases, the dominance regions shift downward to frequencies with milder hearing loss.

C. How do different frequency regions contribute to pitch of the full-bandwidth stimuli?

As shown in Fig. 8, for normal-hearing listeners, pitch strength is greater for the full-bandwidth noise than for almost all the octave-band conditions, with most of the data points from the filtered conditions falling above the full-bandwidth line. However, for three of the four delay conditions, at least one filter condition does match or exceed the pitch strength of the full-bandwidth signal. It may be that the full-bandwidth pitch is mediated most strongly by those frequency regions (i.e., the dominant regions), and that the contribution from the other frequency regions (reflected in the filtered noise data) are less important.

In contrast to normal-hearing listeners, Fig. 8 indicates that listeners with hearing impairment experience a greater pitch strength for several octave-band stimuli than for the full-bandwidth stimuli. In particular, stronger pitches are associated with several octave bands centered below about 1000 Hz, and for the longest delayed noises ($T=8$ ms). This suggests that contributions to pitch strength are dominated by lower frequency regions when they are represented by peaks in the spectrum (as for the 8-ms delay), and in fact, to some extent, the presence of higher frequencies for those delays may actually interfere by decreasing the pitch strength when the full bandwidth is present. That is, the reduced pitch strength in some frequency regions may, when combined with stronger pitch regions, serve to make the pitch percept less clear than when the ''best'' pitch regions are presented alone. The contribution of each filtered bandwidth to the pitch strength of these noises in hearing-impaired listeners is, however, strongly related to the frequency of the band, as seen in Fig. 8, with greater contributions from lower frequencies and lesser contributions at higher frequencies.

The patterns of pitch strength and pitch dominance observed in hearing-impaired individuals may reflect abnormal spectral processing mechanisms, typically accompanying sensorineural hearing loss, coupled with more normal temporal pitch processing. If, as argued by Yost and his colleagues (Yost, 1997; Yost *et al.*, 1994), the pitch of iterated rippled noise is mediated primarily by temporal processes, the frequency location of pitch dominance might not be al-

tered except in regions of greatest sensitivity loss. However, because pitch strength is related to the peak-to-valley depth of the amplitude spectrum, and such spectral contrast is smeared by abnormal frequency resolution, hearing-impaired listeners would not tolerate as much attenuation (i.e., negative gain) in the creation of the rippled noises. The pitch of rippled noise is weaker in hearing-impaired than in normal-hearing subjects. In studies of pitch perception in listeners with low-frequency hearing loss, Florentine and Houtsma (1983) and Turner *et al.* (1983) also suggested a deficit in the spectral aspects of pitch processing in hearing-impaired listeners, with greater reliance on cues provided by temporal analysis. The data reported here might suggest, however, that adequate temporal processing may only occur in the presence of normal spectral analysis, at least for these types of complex stimuli.

V. CONCLUSIONS

Listeners with sensorineural hearing impairment experience weaker pitches when listening to iterated rippled noises than do normal-hearing listeners. This may be a result of a lower SL of the stimuli as absolute thresholds increase, or, perhaps more likely, it may be related to broader-than-normal auditory filters smearing the spectral representation of the rippled noise. Such spectral flattening would effectively reduce peak-to-valley amplitude differences and may contribute to a less well-defined pitch.

Some frequency regions apparently are weighted more heavily than other frequencies in determining the pitch of most iterated rippled noises in normal-hearing listeners, as reported earlier. Frequency regions that dominate the perception of pitch of iterated rippled noise generally are the same for normal-hearing and hearing-impaired listeners, except when those regions involve significant sensitivity loss. If the frequency region that is expected to dominate the pitch falls in a region of moderate hearing loss, pitch dominance shifts to frequencies with more normal sensitivity.

The pitch strength of unfiltered (full-bandwidth) noise may be mediated primarily by energy in the dominant frequencies. Pitch strength in other frequency regions was generally less than that of the full-bandwidth stimulus, suggesting less contribution to the overall pitch by those regions. Listeners with hearing loss show even less ability to combine contributions to pitch strength from several frequency regions. The strength of pitches in the lower frequency regions is somewhat greater in isolation for those listeners than when combined into a full-bandwidth stimulus.

The most common and debilitating difficulty expressed by listeners with sensorineural hearing loss is the inability to understand speech, especially in the presence of competing voices or other environmental noise. A number of underlying causes for these problems have been identified, including poor frequency resolution, reduced audibility for low-amplitude speech sounds, and impaired temporal processing. The weaker pitches experienced by hearing-impaired listeners in this study provide further confirmation that pitch in these listeners is generally less precise, and possibly less accessible as a percept than in normal-hearing listeners. To the extent that the pitch percept contributes to the recognition of speech, the segregation of competing voices and other signals, and the enjoyment of music, the weaker representation of pitch identified here imposes yet another auditory liability resulting from sensorineural hearing loss.

ACKNOWLEDGMENTS

This research was supported by Grant No. DC 00626 from the National Institute on Deafness and Other Communication Disorders, and by the Department of Clinical Investigation, Walter Reed Army Medical Center, under Work Unit #2552. All subjects participating in this research provided written informed consent prior to beginning the study. The opinions or assertions contained herein are the private views of the authors and are not to be construed as official or as reflecting the views of the Department of the Army or the Department of Defense.

Arehart, K. H. (**1994**). ''Effects of harmonic content on complex-tone fundamental-frequency discrimination in hearing-impaired listeners,'' J. Acoust. Soc. Am. **95**, 3574–3585.

Arehart, K. H., and Burns, E. M. (**1999**). ''A comparison of monotic and dichotic complex-tone pitch perception in listeners with hearing loss,'' J. Acoust. Soc. Am. **106**, 993–997.

Assman, P. F., and Summerfield, Q. (**1990**). ''Modeling the perception of concurrent vowels: vowels with different fundamental frequencies,'' J. Acoust. Soc. Am. **88**, 680–697.

Bacon, S. P., and Viemeister, N. F. (**1985**). ''Temporal modulation transfer functions in normal-hearing and hearing-impaired subjects,'' Audiology **24**, 117–134.

Bilsen, F. A., and Ritsma, R. J. (**1970**). ''Some parameters influencing the perceptibility of pitch,'' J. Acoust. Soc. Am. **47**, 469–475.

Burns, E. M., and Turner, C. (**1986**). ''Pure-tone pitch anomalies. II. Pitch-intensity effects and diplacusis in impaired ears,'' J. Acoust. Soc. Am. **79**, 1530–1540.

Carlyon, R. P., Buus, S., and Florentine, M. (**1990**). ''Temporal integration of trains of tone pulses by normal and by cochlearly impaired listeners,'' J. Acoust. Soc. Am. **87**, 260–268.

Fastl, H. (**1988**). ''Pitch and pitch strength of peaked ripple noise,'' in *Basic Issues in Hearing*, edited by H. Duifhuis, J. W. Horst, and H. P. Wit (Academic, London), pp. 370–379.

Fastl, H., and Stoll, G. (**1979**). ''Scaling of pitch strength,'' Hear. Res. **1**, 293–301.

Florentine, M., and Buus, S. (**1984**). ''Temporal gap detection in sensorineural and simulated hearing impairments,'' J. Speech Hear. Res. **27**, 449–455.

Florentine, M., and Houtsma, A. J. M. (**1983**). ''Tuning curves and pitch matches in a listener with a unilateral, low-frequency hearing loss,'' J. Acoust. Soc. Am. **73**, 961–965.

Glasberg, B. R., and Moore, B. C. J. (**1986**). ''Auditory filter shapes in subjects with unilateral and bilateral cochlear impairments,'' J. Acoust. Soc. Am. **79**, 1020–1033.

Grant, K. W., Ardell, L. H., Kuhl, P. K., and Sparks, D. W. (**1985**). ''The contribution of fundamental frequency, amplitude envelope, and voicing duration cues to speechreading in normal-hearing subjects,'' J. Acoust. Soc. Am. **77**, 671–677.

Johnson, K. (**1990**). ''Contrast and normalization in vowel perception,'' J. Phonetics **18**, 229–254.

Larkin, W. D. (**1983**). ''Pitch vulnerability in sensorineural hearing impairment,'' Audiology **22**, 480–493.

Leek, M. R., and Summers, V. (**1993**). ''Auditory filter shapes of normal-hearing and hearing-impaired listeners in continuous broadband noise,'' J. Acoust. Soc. Am. **94**, 3127–3137.

Lehiste, I. (**1976**). ''Suprasegmental features of speech,'' in *Contemporary Issues in Experimental Phonetics*, edited by N. J. Lass (Academic, New York), pp. 225–239.

Levitt, H. (**1971**). ''Transformed up-down methods in psychoacoustics,'' J. Acoust. Soc. Am. **49**, 467–477.

Miller, J. D. (**1989**). ''Auditory-perceptual interpretation of the vowel,'' J. Acoust. Soc. Am. **85**, 2114–2134.
Moore, B. C. J. (**1995**). *Perceptual Consequences of Cochlear Damage* (Oxford University Press, Oxford).
Moore, B. C. J., and Peters, R. W. (**1992**). ''Pitch discrimination and phase sensitivity in young and elderly subjects and its relationship to frequency selectivity,'' J. Acoust. Soc. Am. **91**, 2881–2893.
Patterson, R. D., Handel, S., Yost, W. A., and Datta, A. J. (**1996**). ''The relative strength of tone and noise components of iterated rippled noise,'' J. Acoust. Soc. Am. **100**, 3286–3294.
Plomp, R. (**1976**). *Aspects of Tone Sensation* (Academic, New York).
Ritsma, R. J. (**1967**). ''Frequencies dominant in the perception of the pitch of complex sounds,'' J. Acoust. Soc. Am. **42**, 191–198.
Shofner, W. P., and Yost, W. A. (**1997**). ''Discrimination of rippled-spectrum noise from flat-spectrum noise by chinchillas: evidence for a spectral dominance region,'' Hear. Res. **110**, 15–24.
Summers, V., and Leek, M. R. (**1994**). The internal representation of spectral contrast in hearing-impaired listeners. J. Acoust. Soc. Am. **95**, 3518–3528.
Syrdal, A. K., and Gopal, H. S. (**1986**). ''A perceptual model of vowel recognition based on the auditory representation of American English vowels,'' J. Acoust. Soc. Am. **79**, 1086–1100.
Turner, C. W., Burns, E. M., and Nelson, D. A. (**1983**). ''Pure-tone pitch perception and low-frequency hearing loss,'' J. Acoust. Soc. Am. **73**, 966–975.
Yost, W. A. (**1982**). ''The dominance region and ripple noise pitch: A test of the peripheral weighting model,'' J. Acoust. Soc. Am. **72**, 416–425.
Yost, W. A. (**1996**). ''Pitch strength of iterated rippled noise,'' J. Acoust. Soc. Am. **100**, 3329–3335.
Yost, W. A. (**1997**). ''Pitch strength of iterated rippled noise when the pitch is ambiguous,'' J. Acoust. Soc. Am. **101**, 1644–1648.
Yost, W. A., and Hill, R. (**1978**). ''Strength of pitches associated with ripple noise,'' J. Acoust. Soc. Am. **64**, 485–492.
Yost, W. A., and Hill, R. (**1979**). ''Models of the pitch and pitch strength of ripple noise,'' J. Acoust. Soc. Am. **66**, 400–410.
Yost, W. A., Hill, R., and Perez-Falcon, T. (**1978**). ''Pitch and pitch discrimination of broadband signals with rippled power spectra,'' J. Acoust. Soc. Am. **63**, 1166–1173.
Yost, W. A., Sheft, S., and Patterson, R. D. (**1994**). ''Iterated rippled noise: testing theories of complex pitch,'' J. Acoust. Soc. Am. **95**, 2966.
Yost, W. A., Patterson, R. D., and Sheft, S. (**1996**). ''A time domain description for the pitch strength of iterated rippled noise,'' J. Acoust. Soc. Am. **99**, 1066–1078.

Aging and temporal discrimination in auditory sequences[a)]

Peter J. Fitzgibbons[b)]
Department of Audiology and Speech Language Pathology, Gallaudet University, 800 Florida Avenue NE, Washington, DC 20002

Sandra Gordon-Salant
Department of Hearing and Speech Sciences, University of Maryland, College Park, Maryland 20742

(Received 28 August 2000; revised 23 January 2001; accepted 19 March 2001)

This study examined age-related changes in temporal sensitivity to increments in the inter-onset intervals (IOI) of successive components in tonal sequences. Temporal discrimination was examined using reference stimulus patterns consisting of five 50-ms, 4000-Hz components with equal tonal IOIs selected from the range 100–600 ms. Discrimination was examined in separate conditions by measuring the relative difference limen (DL) for increments of tonal IOI in comparison sequences. In some conditions, comparison sequences featured equal increments of all tonal IOIs to examined listener sensitivity to uniform changes of sequence rate, or tempo. Other conditions measured the DL for increments of a single target IOI within otherwise uniform-rate comparison sequences. For these measurements, the single target IOI was either fixed in sequence location, or randomized in location across listening trials. Listeners in the study included four groups of young and elderly adults with and without high-frequency hearing loss. The results for all listeners showed the relative DL for rate discrimination to decrease from a maximum at the 100-ms IOI to a smaller stable value across the range of longer sequence IOI. All listeners also exhibited larger relative DLs for discrimination of single target intervals compared to rate discrimination for equivalent reference IOI values. Older listeners showed poorer performance than younger listeners in all conditions, with the largest age differences observed for discrimination of brief single intervals that were varied randomly in sequence location. None of the results revealed significant effects of hearing loss on performance of younger and older listeners. [DOI: 10.1121/1.1371760]

PACS numbers: 43.66.Mk, 43.66.Sr [SPB]

I. INTRODUCTION

This paper describes experiments that compared the ability of younger and older listeners to discriminate changes in the timing of successive events within auditory sequences. For many years, research on cognitive aging has provided evidence that elderly persons exhibit a generalized decline in the rate of information processing, with factors such as stimulus complexity and task demands having an important influence on performance Meyerson *et al.*, 1990; Cerella, 1990; Salthouse, 1991). The contribution of sensory and perceptual influences on the cognitive tasks is not usually considered, and has only recently become an area of enhanced investigation. For example, it is generally known that high-frequency sensorineural hearing loss is a primary consequence of aging that can interact with temporal processing deficits to influence speech recognition in older listeners. This is particularly evident in experiments that utilize rapid or time-compressed speech stimuli, where both hearing loss and listener age independently influence recognition performance (e.g., Gordon-Salant and Fitzgibbons, 1993; Wingfield, 1996). Other studies report that older listeners have difficulty in processing the temporal order of nonspeech stimuli presented in sequential auditory patterns (Trainor and Trehub, 1989; Humes and Christopherson, 1991; Fitzgibbons and Gordon-Salant, 1998). The source of age effects observed with sequential patterns, speech or nonspeech, is not clearly understood, but may be related to a loss of sensitivity to changes in sequential component durations or the timing structure of the pattern as a whole.

Evidence providing support for the existence of age-related changes in temporal sensitivity comes primarily from psychophysical data. Some of it relates to measures of the minimum detectable duration of a temporal gap separating successive acoustic markers, either pairs of tone or noise bursts. Recent studies report that gap thresholds measured with elderly listeners are about twice the magnitude of those observed for younger listeners (Schneider *et al.*, 1994, 1998; Snell, 1997; Snell and Frisina, 2000). Stimulus factors also appear to be important, with other studies finding that age effects in gap detection are evident primarily for short duration stimuli (Schneider and Hamstra, 1999) or for gaps located near onsets and offsets of longer signals (He *et al.*, 1999). Other temporal sensitivity measures reveal that older listeners exhibit greater difficulty than younger listeners in discriminating changes in the duration of simple noise or tone bursts, or silent intervals separating a pair of stimulus markers (Abel *et al.*, 1990; Fitzgibbons and Gordon-Salant, 1994). These duration discrimination results were reported to be largely independent of sensorineural hearing loss, indicating that cochlear mechanisms are not the principal source of the age-related differences in temporal sensitivity. Alterna-

[a)]Portions of this work were presented in ''Discrimination of tonal sequence tempo by young and elderly listeners,'' Association for Research in Otolaryngology, St. Petersburg Beach, FL, February, 2000.
[b)]Author to whom correspondence should be addressed.

tively, Schneider and Pichora-Fuller (2000) suggest that diminished performance on tasks such as gap detection and duration discrimination may be linked in part to an age-related loss of synchrony in the neural firing response to stimulus markers, as suggested by findings from evoked-response studies on aging conducted with gerbils (Hellstrom and Schmiedt, 1990; Boettcher *et al.*, 1993, 1996).

In a recent experiment (Fitzgibbons and Gordon-Salant, 1995) we extended the study of aging and temporal processing to more complex stimulus patterns that featured tonal sequences with varying degrees of spectral complexity. The study compared difference limens (DLs) for changes in the duration of a single tonal component of the stimulus pattern to those measured for the same component presented in isolation. The older listeners in the study exhibited large reductions in discrimination ability for target stimuli embedded within the sequences, whereas younger listeners produced duration DLs that were about the same for the embedded and isolated target stimuli. Additionally, the discrimination performance of younger listeners was relatively unaffected by variations of spectral complexity within stimulus patterns, or the uncertainty introduced by randomization of sequence location for the embedded target component. There were some indications from the experiment suggesting that younger listeners were able to resolve changes in the duration of embedded pattern components, regardless of location, simply by attending to changes in the overall rhythm or tempo of the stimulus sequence. By contrast, older listeners appeared to be less sensitive to overall changes in pattern tempo, and their performance was diminished significantly by variations of spectral complexity and randomization of target location within sequences.

The present study is designed to examine more directly the hypothesis that elderly listeners exhibit diminished sensitivity to changes in the rhythm and timing pattern within tonal sequences. The perceived rhythmic characteristics of sequential patterns can be influenced by a large number of stimulus factors including variation in component frequency and intensity, as well as durations and interval spacings among successive events (Hirsh *et al.*, 1990). To minimize some of this complexity, the present investigation is restricted in scope to the examination of listener sensitivity to changes in the time intervals separating successive onsets of tones within sequences. The stimulus patterns included sequences of brief tone bursts of equal frequency, intensity, and duration.

Stimulus patterns of this type have been utilized in a number of earlier investigations of temporal processing, both in musical and psychoacoustic research. For example, Hirsh *et al.* (1990) studied temporal sensitivity in young listeners using sequences of tones equally separated in time (isochronous sequences). The stimuli were six or ten 20-ms 1000-Hz tones separated equally by silent intervals to produce uniform toner inter-onset intervals (IOIs) corresponding to different sequence presentation rates. Using these as reference patterns in discrimination trials, Hirsh *et al.* examined listener sensitivity to displacement of a tonal component within sequences introduced by the lengthening of a single IOI. The measured DLs for tonal displacement, expressed as a percentage of the reference IOI, were observed to be about the same as expected for discrimination of IOI changes between a pair of tones presented in isolation, that is about 10% for reference intervals of at least 100 ms or so. Additionally, the sequence location of the imposed interval change seemed to have little influence on discrimination performance for all but the fastest sequence presentation rates.

Whereas Hirsh *et al.* reported similar discrimination results for single intervals and sequences, other results indicate that temporal sensitivity for sequences is more acute than that observed for simple stimuli. Drake and Botte (1993) used a large set of isochronous sequences featuring 50-ms 440-Hz tones uniformly separated by silent intervals to produce a range of presentation rates for sequence lengths of 2–7 tones. In this experiment, sequence tempo discrimination was examined by measuring the DL for IOI changes when all sequence intervals were covaried equally and simultaneously to effect a uniform change of presentation rate. Their results, also reported as relative DLs for sequence IOI, showed a similar trend for all sequences with discrimination being fairly stable for reference IOIs in the range of about 200–800 ms, and poorer for shorter and longer reference IOI values. Of particular interest was the observation that for a given value of sequence IOI, discrimination improved progressively as the number of intervals in a sequence increased from two to six. For example, with a reference IOI of 400 ms, the relative DL was observed to decrease from about 6% for a two-tone sequence to about 2% for a seven-tone sequence. Drake and Botte suggested that this outcome might be attributed to a multiple-look mechanism that listeners use to enhance their temporal sensitivity for regularly spaced intervals in a sequential context.

Less is known about the consequences of aging as it pertains to temporal processing of extended sequential patterns. From the available evidence reported for simple sounds, it is anticipated that older listeners would be disadvantaged in their sensitivity to temporal spacings within a tonal sequence. This would be the case particularly for rapid presentation rates where any effects of reduced speed of processing, or perhaps loss of neural synchrony, would be expected to be most evident. The present study examines some potential age effects by assessing the ability of younger and older listeners to discriminate changes of presentation rate in tonal sequences. The study also examines the magnitude of age-related differences in temporal sensitivity for multiple versus single changes of interval spacing within stimulus sequences. Towards this goal, the DLs for rate discrimination are compared to those for single-interval discrimination under conditions of both low and high experimental certainty regarding sequence location of a target interval. Additionally, because hearing loss is prevalent among many older listeners, another purpose of the experiments is to examine the independent and interactive effects of age and hearing loss in each discrimination condition. This is accomplished by testing groups of listeners who were matched according to age and degree of hearing loss. All testing was restricted to a high-frequency region that coincided with a region of threshold elevation in those listeners with hearing loss.

TABLE I. Mean audiometric thresholds in the test ear (from 0.25–8.0 kHz, in dB HL *re*: ANSI, 1996), word recognition scores (Northwestern University Auditory Test No. 6) and ages of the four listener groups. Standard deviations are included in parentheses.

Group	Age	Audiometric thresholds						Word recognition % Correct
		0.25 kHz	0.5 kHz	1.0 kHz	2.0 kHz	4.0 kHz	8.0 kHz	
Young, norm hrg	25.3 (4.6)	5.3 (4.0)	3.7 (4.0)	5.3 (3.5)	3.7 (4.4)	5.0 (5.3)	5.3 (5.8)	97.6 (2.9)
Elderly, norm hrg	67.6 (2.0)	9.6 (4.3)	6.5 (3.1)	6.1 (3.0)	7.3 (6.0)	13.4 (5.5)	26.5 (11.3)	97.8 (2.6)
Young, hrg loss	30.3 (10.8)	23.0 (17.0)	29.0 (20.5)	37.5 (21.2)	41.5 (18.9)	51.0 (14.1)	54.0 (17.1)	92.0 (5.3)
Elderly, hrg loss	70.7 (2.6)	20.3 (7.9)	22.7 (11.0)	26.3 (13.4)	39.7 (12.7)	58.0 (7.5)	72.7 (7.0)	89.3 (6.0)

II. METHODS

A. Subjects

A total of 52 listeners participated in the experiments. These included a group of 15 younger listeners (18–40 years of age) with normal hearing (YNH: pure tone thresholds from 250–4000 Hz between 0 and 15 dB HL, *re*: ANSI, 1996), a group of 13 older listeners (65–76 years of age) with normal hearing (ONH), a group of 10 younger listeners with hearing loss (YHL: sloping, mild-to-moderate sensorineural hearing losses), and a group of 14 older listeners with hearing loss (OHL: sloping, mild-to-moderate sensorineural hearing losses). Additional audiometric criteria for participant selection were monosyllabic word recognition scores $\geqslant$80% (Northwestern University Auditory Test No. 6) and normal acoustic immittance results (i.e., normal tympanograms, acoustic reflex thresholds elicited within the 90th percentile range for normal hearing or cochlear hearing loss, and negative acoustic reflex adaptation). Table I presents the mean ages, audiometric thresholds, and word recognition scores of the four listener groups. The etiology of hearing loss for listeners in the YHL group included heredity and noise exposure. The etiology of hearing loss for listeners in the OHL group was assumed to be presbycusis, based on an absence of a significant otologic history and gradual onset and progression of hearing loss during the sixth and seventh decade of life. Additionally, all listeners passed a screening test of cognitive function (Pfeiffer, 1975). Students at the University of Maryland were recruited to serve as participants in the YNH group. Clients of the University of Maryland Hearing Clinic and their family members were invited by letter to participate in the other three listener groups. All listeners were paid for their participation in the experiments.

B. Stimuli

All tonal sequences for the experiments were generated using an inverse fast-Fourier-transform (FFT) procedure with a digital signal processing board (Tucker–Davis Technologies, AP2) and a 16-bit D/A converter (Tucker–Davis Technologies DD1, 20-kHz sampling rate) that was followed by low-pass filtering (Frequency Devices 901F, 6000-Hz cutoff, 90dB/oct). Stimulus sequences were constructed with five 4000-Hz tone bursts separated in time by equal-duration silent intervals. Each tone burst in a sequence had a fixed duration of 50 ms that included 5-ms cosine-squared rise/fall envelopes, with all tone and silent-interval durations specified between zero-voltage points on the electrical wave forms. Within these isochronous sequences, the silent intervals between tones were adjusted to establish the desired sequence inter-onset interval (IOI), an interval that includes both the tone and silent interval. Adjustments of sequence IOI also produced shifts in overall sequence duration. For some conditions of the experiment, tone sequences with equal IOI values of 100, 200, 400, and 600 ms were created to serve as the reference stimuli for examining rate discrimination. For these conditions, the comparison sequences used in discrimination trials were the same as the reference sequences except that all sequence IOIs were lengthened equally by increasing the inter-tone silent intervals, and covaried to determine the duration DL for increments of sequence IOI. In other discrimination conditions, a DL was measured for changes in the duration of a single IOI within an otherwise isochronous sequence. The reference stimuli used for these measures were the isochronous sequences with uniform IOIs of either 100 ms or 600 ms, representing the fastest and slowest rates for the tonal patterns, respectively. The comparison sequences were the same as the reference sequences except one tonal IOI was longer than the others and was varied to measure a duration DL. For these single-interval conditions, some stimulus patterns featured minimal uncertainty in which the single variable IOI always preceded the third tone of the sequence, and was known to the listener. Other single-interval measures were collected for sequences featuring greater stimulus uncertainty in which the single variable IOI occurred in random fashion preceding the 2nd, 3rd, or 4th sequence tone across listening trials, with the selection of these particular intervals being arbitrary. The variation of single IOIs was accomplished while preserving other sequence IOIs at their original values, thus increasing overall sequence duration.

C. Procedures

The measurement of DLs for the tonal inter-onset intervals was obtained using an adaptive three-interval, two-alternative forced-choice discrimination procedure. Each discrimination trial contained three observation intervals spaced 750 ms apart. The first listening interval of each trial contained a sample of the reference stimulus sequence, with the second and third intervals containing samples of the reference and comparison sequence in either order selected randomly across listening trials. Measurements of sequence rate discrimination were collected for each of four reference IOI values of 100, 200, 400, and 600 ms. For each of these conditions, the reference and comparison stimulus sequences of a listening trial differed only by the duration of the tonal IOIs, which were always longer in the comparison sequence.

Measurements of single-interval discrimination were also collected in four conditions, for reference IOI values of 100 ms and 600 ms, each tested under two degrees of stimulus certainty regarding target-interval location. For single-interval conditions, the reference and comparison sequences of a listening trial were the same, except for a single longer target IOI in the comparison sequence. This single target interval in the comparison sequence was either fixed or randomized in sequence location, respectively, across listening trials in the minimal and maximal uncertainty conditions. Listeners used a keyboard to respond to the comparison stimulus in the second or third observation interval of each trial. All listening intervals were marked by a visual display that also provided correct-interval feedback for each trial.

Estimates for all duration DLs were obtained using an adaptive rule for varying comparison sequence IOI such that the IOI decreased in magnitude following two consecutive correct responses by the listener and increased in magnitude following each incorrect response. Threshold estimates derived by this adaptive rule corresponded to values associated with 70.7% correct discrimination (Levitt, 1971). Testing in each condition was conducted in 50-trial blocks with an IOI starting value of 1.4 times reference value, and a step size for IOI changes that decreased logarithmically over trials to produce rapid convergence on threshold values. Following the first three reversals in direction of IOI change, a threshold estimate was calculated by averaging reversal-point IOI values associated with the remaining even-numbered reversals. An average of six threshold estimates was used to calculate a final DL for IOI with each listener in each condition. Prior to data collection, each listener received 2–3 hours of practice for sequence discrimination, with all listeners showing performance stability after 3–4 trial blocks in each condition.

The listeners were tested individually in a sound-treated booth. The eight discrimination conditions (rate discrimination at four reference IOI values, and four single-interval measures) were tested in a different order for each listener. Stimulus levels were 85–90 dB SPL in order to provide adequate audibility and produce minimum sensation levels of 25–30 dB at 4000 Hz for the listeners with hearing loss. Testing was monaural through an insert earphone (Etymotic ER-3A) that was calibrated in a 2-cm^3 coupler (B&K, DB 0138). All listening was conducted in 2-hour sessions over the course of several weeks. Total test time (not including practice) varied across listeners, but averaged about 8 hours.

III. RESULTS

For the purpose of analysis and comparison with previous findings, all duration DLs collected in the experiment were converted to relative values expressed as a percentage of sequence IOI, the interval representing the reciprocal of sequence rate for each of the reference stimulus patterns. Results from the sequence rate discrimination conditions are shown in Fig. 1, which displays the mean relative DLs in percent as a function of sequence IOI for each of the four listener groups, with vertical bars in the figure representing the positive standard error of the mean. Performance variability among the older listeners was equivalent to that of the younger listeners for 100-ms IOI, but was about twice that of

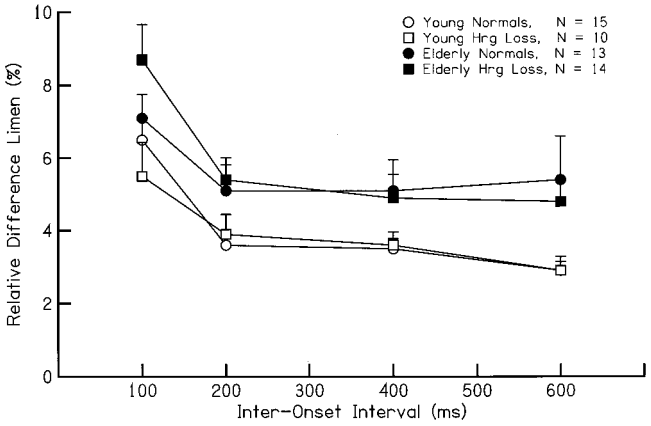

FIG. 1. Mean relative difference limen (DL) in percent as a function of sequence inter-onset interval (IOI) in ms (100 ms, 200 ms, 400 ms, and 600 ms); all conditions involved uniform changes in inter-onset interval. Vertical bars represent the positive standard error of the mean. The four listener groups are Young Normals (young adult listeners with normal hearing, $M=15$), Young Hrg Loss (young adult listeners with mild-to-moderate sensorineural loss, $N=10$), Elderly Normal (elderly listeners with normal hearing, $N=13$), and Elderly Hrg Loss (elderly listeners with mild-to-moderate sensorineural hearing loss, $N=14$).

the younger listeners across the range of longer IOI values. Among younger listeners, most of the performance variability was attributed to listeners with hearing loss. Among older listeners the reverse was true, with the normal-hearing listeners showing greater variability than those with hearing loss. The mean relative and absolute DL values (in parentheses) for younger listeners (collapsed across hearing loss groups) for IOIs of 100, 200, 400, and 600 ms were 6% (6 ms), 3.8% (7.6 ms), 3.5% (14.1 ms), and 2.9% (17.5 ms), respectively. Corresponding average values for the older listeners for the same IOIs were 7.9% (7.9 ms), 5.3% (10.5 ms), 5.0% (20 ms), and 5.1% (30.6 ms). Thus, younger and older listeners exhibited a similar trend in average threshold values across the IOIs examined here.

An analysis of variance (ANOVA) was performed on the individual data for relative DLs using a split-plot factorial design with two between-subjects factors (age and hearing status) and one within-subjects factor (sequence IOI). Results of the analysis revealed significant main effects of sequence IOI $[F(3,48)=36.85,\ p<0.01]$ and listener age $[F(1,48)=10.75,\ p<0.01]$ with no significant interaction effects. Multiple comparison testing (Scheffé) revealed that the effect of IOI was primarily attributed to the larger DL values for the 100-ms IOI, with no significant differences observed across conditions of longer IOIs ($p<0.05$). The performance of the older listeners was significantly poorer than that of younger listeners across the range of sequence IOIs. None of the data analyses revealed systematic or significant influences of hearing loss within the groups of older and younger listeners.

A second analysis compared the relative DLs measured for the single-interval discrimination condition with the corresponding DLs measured for rate discrimination with the same reference sequence IOI. These results are displayed in Figs. 2 and 3, respectively, for the reference sequence IOIs of 100 ms and 600 ms. Each figure shows the mean relative

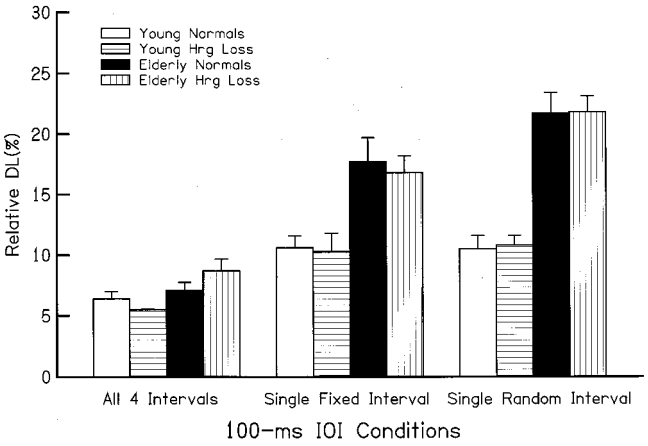

FIG. 2. Mean relative DL in percent for each listener group in stimulus sequence conditions with 100-ms IOI. The three conditions are uniform increments in all four intervals (All 4 Intervals), single increments in one fixed-location interval (Single Fixed Interval), and single increments in one random-location interval (Single Random Interval). Vertical bars represent the standard error of the mean. The four groups are the same as those described for Fig. 1.

DL for each listener group for a single interval that was either fixed (Single Fixed Interval) or randomized (Single Random Interval) in sequence location, together with the corresponding rate discrimination DL from Fig. 1 measured with covariation of all sequence intervals (All 4 Intervals). Error bars in the figures represent standard errors of the mean. Each figure shows that relative DLs for the single-interval conditions were larger than corresponding values for the four-interval conditions, with DLs of the older listeners being larger than DLs of the younger listeners. Additionally, relative DLs for 100-ms IOIs are larger than corresponding values for 600-ms IOIs, reflecting the same trend seen for the rate-discrimination results of Fig. 1. For the younger listeners, mean single-interval relative and absolute values (in parentheses) of DLs for the fixed- and random-location conditions, respectively, were 10.5% (10.5 ms) and 10.7% (10.7 ms) for 100-ms IOIs, and 4.3% (26.1 ms), and 3.9% (23.2 ms) for 600-ms IOIs. Corresponding mean single-interval DLs for the older listeners were 17.3% (17.3 ms) and 21.8% (21.8 ms) for 100-ms IOIs, and 6.1% (36.4 ms) and 8.3% (49.2 ms) for 600-ms IOIs.

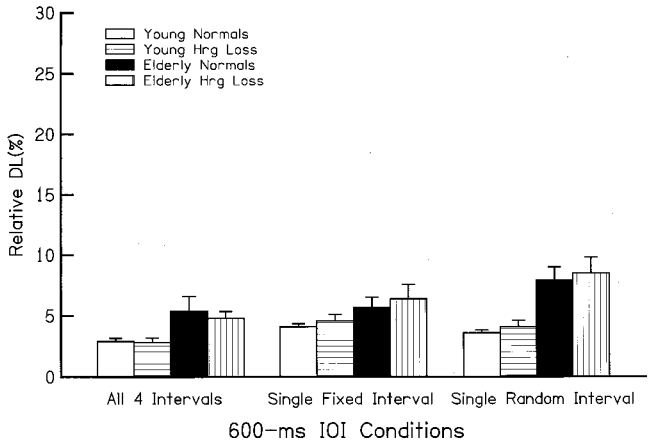

FIG. 3. Same as for Fig. 2, but for a 600-ms IOI.

Separate ANOVAs were conducted with the individual relative DLs for the 100-ms and 600-ms IOI conditions shown in Figs. 2 and 3, each using a split-plot factorial design with two between-subjects factors, age, and hearing status, and one within-subjects factor, stimulus condition. Each analysis revealed significant main effects of age [$F(1,47) > 10.0$, $p < 0.01$], IOI condition [$F(2,94) > 17.6$, $p < 0.01$], and an age by condition interaction [$F(2,94) > 9.6$, $p < 0.01$], with no significant effect of hearing loss. Analysis of simple effects in these data revealed that relative DLs of the older listeners were significantly larger than those of the younger listeners ($p < 0.01$) in each condition for both IOIs. Additionally, all listeners produced significantly smaller relative DLs for the four-interval conditions compared to the single-interval conditions. However, for single intervals, younger listeners performed about the same for the fixed- and random-location conditions, whereas older listeners showed significantly larger DLs for the random-location versus fixed-location conditions ($p < 0.01$).

IV. DISCUSSION

The experiments compared the abilities of younger and older listeners to discriminate changes in the timing between successive components within simple tone sequences. In some conditions, listeners were asked to respond to uniform changes in tonal onset intervals that altered the presentation rate, or tempo, of the sequential stimulus patterns. In other conditions, listeners responded to changes in the magnitude of a single sequence interval that produced a localized disruption of timing within the tonal patterns. The results showed that listeners' sensitivity to changes of temporal intervals depends on both the magnitude and number of sequence intervals that are subjected to change. The results also indicated that older listeners were less sensitive than younger listeners to both single and multiple changes of sequence intervals. The magnitude of age-related performance deficits also differed for conditions featuring single and multiple timing cues.

A. Younger listeners

Results for the single-interval conditions revealed that younger listeners were able to discriminate interval changes with a degree of accuracy that was as good as, or better than, results reported in several earlier studies of duration discrimination for simple stimuli presented in isolation. Collective results from these earlier investigations indicate that, for a broad range of reference durations for filled and unfilled stimulus intervals (about 200–2000 ms), listeners can reliably discriminate duration increments exceeding 10–20 % of the reference interval, with larger values seen for much briefer reference intervals (Creelman, 1962; Small and Campbell, 1962; Abel, 1972; Divenyi and Danner, 1977; Allen, 1979). Younger listeners of the present study produced mean relative DLs of 4.3% and 10.5%, respectively, for single IOI intervals of 600 ms and 100 ms that were presented in a fixed mid-sequence location. By comparison, for a sequence IOI of 100 ms Hirsh *et al.* (1990) reported a

relative DL of 11.6% for single-interval discrimination, and Drake and Botte (1993) measured a relative DL for a single 600-ms IOI of about 5.4%. These values agree closely with the present single-interval estimates collected using stimulus patterns quite similar to those of the earlier studies. The single-interval DL estimates of the present investigation are smaller than those reported in our earlier study of duration discrimination for an embedded target tone or silent gap in tonal stimulus sequences (Fitzgibbons and Gordon-Salant, 1995). These earlier results, however, were collected using stimulus patterns that featured a high degree of spectral complexity, a factor that can exert a strong influence on discrimination performance. Despite the stimulus differences, the present results, like those of our earlier study, revealed that single-interval discrimination performance of the younger listeners was largely unaffected by stimulus uncertainty introduced by randomization of sequence location for the target interval. This outcome suggests that the younger listeners are able to attend to the timing characteristics of the pattern as whole, rather than attempting to focus on changes of a specific target interval.

The measurements for rate discrimination were collected by varying all sequence intervals by an equivalent amount at each of the four sequence presentation rates. As mentioned previously, the average performance of the younger listeners, as displayed in Fig. 1, revealed that the relative DL decreased from a maximum value for the 100-ms IOI to a smaller fairly stable value for each of the longer sequence IOIs tested. Additionally, the relative DLs for rate discrimination are smaller than those measured for single-interval discrimination for the same reference IOI. It could be argued that observed differences in DLs for rate and single-interval discrimination were a consequence of listeners attending to changes in overall sequence duration to perform the discrimination tasks. In this event, however, we would expect an equivalent increment in overall sequence duration at discrimination threshold, whether the sequence increment resulted from the lengthening of single or multiple sequence IOIs. Results show this not to be case. Sequence durations for the reference tonal patterns ranged from 450 ms with 100-ms IOI to 2450 ms for 600-ms IOI. For younger listeners, increases in duration for the 450-ms sequence at discrimination threshold were 10.4 ms for increments of a single interval and 24 ms for increments of multiple intervals (i.e., four times absolute DL of 6 ms). Corresponding duration increases for the 2450-ms reference pattern were 26.1 ms for a single-interval increment and 70 ms for multiple-interval increments. These differences indicate that it is unlikely that overall stimulus duration was a useful cue for sequence discrimination. Drake and Botte (1993) also provided convincing evidence that interval discrimination by their listeners was not based on changes of overall sequence duration. Additionally, the close agreement between the present single-interval DLs and those reported by Hirsh *et al.* (1990) is apparent despite differences in procedure wherein Hirsh *et al.* lengthened a single sequence IOI by tonal displacement without consequent changes in overall sequence duration.

Results for the rate discrimination measurements in the present investigation display the same trends seen in the tempo discrimination data reported by Drake and Botte across a similar range of sequence IOIs. One characteristic of rate discrimination thresholds is the apparent constancy of the observed relative DLs across the range of longer IOIs from about 200–600 ms, a range corresponding to sequence durations of 850–2450 ms for tonal patterns of the present study. Thus it appears that a relatively constant Weber ratio for duration discrimination seen in the earlier studies with simple isolated sounds also extends to more complex sequential patterns, at least within the range of durations examined here. The Hirsh *et al.* experiments did not specifically measure rate discrimination, although the collective findings from that investigation suggested that discrimination of a repeated sequence interval would be about the same as that measured for a single interval. However, the present rate-discrimination data support those of Drake and Botte in showing that temporal sensitivity for changes of multiple intervals is more acute than that observed for single intervals, presented as either isolated targets or as an embedded component of an extended sequence. For example, in the present results for younger listeners the relative DLs for sequence rate at IOIs of 100 ms and 600 ms are smaller by 4.5% and 1.5%, respectively, than the corresponding DL values for single-interval discrimination.

Drake and Botte postulated a multiple-look hypothesis to account for the better temporal sensitivity seen for multiple- versus single-interval discrimination. This hypothesis argues that for an isochronous sequence, multiple repetitions of the same interval leads to a strengthening of memory trace for the reference interval and thus greater sensitivity to temporal deviations. In their examination of the hypothesis, Drake and Botte predicted that, for independent observations of each sequence interval, the absolute DL for sequences with a given number (N) of intervals should be equal to that measured for a single interval divided by the square root of N. Similar predictions, that are derived from the logic of signal-detection theory (Green and Swets, 1966), were examined earlier by Hafter and Dye (1983) to account for listeners' ability to lateralize click sequences that varied in duration and size of the inter-click interval. In applying the multiple-look model to the temporal discrimination data, Drake and Botte found approximate agreement between observed and predicted DLs for IOI, at least for a limited range of IOI and sequence length. For stimulus sequences with four intervals, as used in the present experiment, a multiple-look strategy would predict absolute DLs for rate discrimination to be about half those measured for a single interval. Inspection of the data for the younger listeners reveals that the observed differences between DLs for rate and single-interval discrimination are sizeable, but not quite as large as predicted. It should be noted, however, that our single-interval DLs were also measured within a sequential context that itself included multiple repetitions of the reference IOI. Thus, it is possible that the single-interval DLs measured here reflect better discrimination performance than would be expected for a pair of tones presented in isolation. We suspect this to be the case because some of our earlier measures (Fitzgibbons and Gordon-Salant, 1995) for duration discrimi-

nation with isolated stimuli produced larger relative DLs (about 20%) for single intervals than observed here for single intervals within sequences. Nevertheless, it is clear from the present results that multiple repetition of the same sequence interval leads to improve temporal sensitivity.

B. Older listeners

The older listeners exhibited reduced ability to discriminate temporal intervals. Additionally, like the younger groups of listeners, hearing loss among the older listeners was shown to have little influence on discrimination performance. For older listeners, the mean relative DLs for the fixed-location single interverals were 17.3% and 6.1%, respectively, for baseline IOIs of 100 ms and 600 ms. Each of these values is significantly larger than corresponding values measured for the younger listeners, with the absolute magnitude of the age-related difference being greatest for the 100-ms IOI. Unlike the younger listeners, the older listeners were significantly affected by the procedure of randomizing the sequence location of the single target interval that was subjected to variation in duration. For example, relative to their performance with fixed target locations, the relative DLs of older listeners increased by 4.5% and 2.1%, respectively, with randomization of the 100-ms and 600-ms target intervals. It is conceivable that the target randomization effects simply reflect differences in temporal sensitivity as a function of sequence location of the target interval, a possibility that was not specifically examined in the experiments. However, a sequence-location effect would necessarily apply to elderly listeners only, as the young listeners were largely unaffected by target randomization, and no sequence location effects for single intervals were observed in the discrimination experiments conducted by Hirsh *et al.* (1990). Thus, it seems reasonable to assume that the influence of target randomization on the performance of the older listeners was primarily a consequence of stimulus uncertainty. These age-related performance decrements associated with target randomization are similar to those observed earlier with the spectrally complex tonal patterns that produced larger temporal DLs (Fitzgibbons and Gordon-Salant, 1995).

The older listeners also exhibited less sensitivity than the younger listeners for rate discrimination, although the shifts in performance as a function of sequence IOI tended to parallel those observed with the younger listeners. For the older listeners, mean relative DLs for rate discrimination shifted from a value of about 8% for the 100-ms IOI to a relatively stable value of 5.1% across longer IOIs, where the Weber ratio was also fairly constant for younger listeners. For rate discrimination, the magnitude of the age-related decrement was reasonably uniform in degree across the range of sequence IOI that was examined.

Explanations for the age-related differences observed in temporal discrimination performance are not straightforward. On the basis of previous accounts of an age-related slowing in auditory processing, it was anticipated that the largest deficits among older listeners in the present experiments would be evident for the shorter temporal intervals associated with the fast sequence presentation rates. The rate discrimination results did not show a substantially larger age-related deficit at the fastest sequence rate. However, it was apparent that the greatest age-related deviations from the performance of younger listeners were associated with the shortest reference interval (100-ms IOI) when presented as a single target interval. Thus the degree of improvement in temporal sensitivity from single-interval to multiple-interval discrimination was greatest among elderly listeners, but only for the brief reference intervals. This could imply more efficient utilization of a multiple-look strategy among elderly listeners, but this was not evident in the results for the slower stimulus rates featuring longer IOI values. Alternatively, an age-related loss of neural synchrony (Schneider and Pichora-Fuller, 2000) that is required to mark successive tonal onsets might be expected to impact discrimination of brief intervals more so than much longer reference intervals. As such, multiple repetition of the same brief stimulus interval might be expected to enhance the neural coding of stimulus onsets in the same manner as signal averaging reveals a robust onset response characteristically seen in the post-stimulus-time histograms of single VIII N. fibers (Kiang *et al.*, 1965). One outcome of this clearly defined onset marking would be to improve sensitivity to duration cues.

The results of the experiments provide additional evidence for age-related temporal processing deficits that are unrelated to the presence of sensorineural hearing loss. It is possible that a central timing mechanism is inherently involved for listening tasks requiring a judgment about stimulus duration, as postulated for some time in a theoretical model developed initially by Creelman (1962), and subsequently modified by Abel (1972) and Divenyi and Danner (1977). The theoretical accounts for duration discrimination postulate a central counter that essentially sums neural firings produced during the extent of stimulation, with a larger count resulting for the longer of two signals. Other elements of the model include a memory factor for the neutral pulse count, and a factor indicating the degree of precision in marking of stimulus onsets and offsets. Earlier studies have demonstrated the utility of the model in describing the general trends and level of performance exhibited in a large body of discrimination data collected from young, trained listeners.

Consideration of the model components can provide a useful framework for examining possible sources of the age-related performance differences observed in the present investigation. A first consideration involves the possibility that age effects in duration discrimination are partially the result of reduced precision in marking signal onset/offset boundaries. For younger listeners, precision in marking signal boundaries is a factor that is primarily influenced by signal level, and Divenyi and Danner (1977) showed that levels of about 25 dB SL are sufficient to minimize uncertainty in registering signal onsets. This requirement was met in the present experiment for all listeners except three in the elderly hearing-loss group, who had thresholds of 65 dB HL at 4 kHz and may have listened at sensation levels below 25 dB. However, the discrimination performance of these three listeners was better than that of several others in the same elderly group of listeners. Another factor that could influence the coding of signal boundaries in elderly listeners is a loss

of synchrony in the neural response to stimulation, as suggested previously by Schneider and Pichora-Fuller (2000). However, the primary effects of this factor would be expected for the discrimination of brief intervals, with progressively less influence at longer reference durations, as noted by Divenyi and Danner. The present results did show the largest age-related deficit for single-interval discrimination of the shortest reference IOI of 100 ms, but for rate discrimination the age differences were similar in degree for all reference IOIs. Thus, there is no consistent trend in the present results indicating that lack of precision of the coding of stimulus boundaries was a primary source of age-related deficits. Of course, the shortest 100-ms reference interval of the current study may have been too long to observe any strong effects related to a loss of neural synchrony, a possibility that we are currently investigating by examining discrimination within a range of briefer reference intervals.

Other components of the Creelman model that could undergo changes with aging include the central counting mechanism itself, or the memory for accumulated counts that is required to compare durations of two or more signals in a discrimination task. For example, the density of neural pulses feeding a central counter may be diminished simply as a consequence of a reduction in the number of neural fibers with aging (Willott, 1990). In this event, longer increments of signal duration would be required for discrimination by elderly listeners compared to younger listeners. This factor could account for the uniform deficit with aging observed across the range of reference IOIs. Alternatively, a difference in memory for the clock count between younger and older listeners for accumulated pulse counts could also produce age-related differences in discrimination performance. In this case, an age-related memory deficit should produce more exaggerated performance differences between younger and older subjects at the longer reference intervals. The rate discrimination data shown in Fig. 1 do not provide strong evidence in support of this hypothesis. However, the larger variability observed for the elderly listeners across the range of longer reference IOIs suggest that the memory factor could have contributed to performance deficits in some of the elderly listeners. Additional testing with longer reference intervals than employed in the present study may show stronger influences of memory differences between younger and older listeners.

Finally, the observed age-related performance differences with single intervals for fixed- and random-location targets implicate a cognitive factor that deteriorates with aging but remains robust in younger listeners. Possible sources of this cognitive factor are auditory attention, auditory search capacity, or working memory capacity. However, the fact that a similar pattern of age-related performance deficits was observed at the 100-ms IOI and the 600-ms IOI argues somewhat against working memory as the likely candidate of the cognitive factor. These considerations of the model components suggest a number of factors that can be investigated independently in subsequent studies of aging and temporal processing: accuracy of marking of stimulus onsets, number of observation intervals, memory load, and the consequences of cognitive demands in specific discrimination tasks.

C. Summary

The experiments measured the ability of younger and older listeners with and without hearing loss to discriminate changes in the temporal intervals separating components of simple tonal sequences. Sequence rate discrimination was assessed by varying the inter-onset intervals of all tonal components in a uniform manner at each of four reference sequence rates. The relative DLs observed for rate discrimination for all listeners were larger for fast sequence rates, and smaller but equivalent at the slower rates tested. The rate DLs for the older listeners were larger than DLs of the younger listeners at each sequence rate. Temporal DLs were also measured for changes of a single sequence interval that was either fixed or randomized in sequence location in separate test conditions. For all listeners, the temporal DLs for single-interval changes were larger than corresponding DLs for multiple-interval changes. The older listeners also produced larger single-interval DLs than younger listeners, particularly for short reference intervals. The performance of the young listeners was unaffected by randomization of target interval location, whereas older listeners exhibited large performance decrements with target randomization. None of the results revealed a significant influence of sensorinueral hearing loss. Collectively, the results indicate age-related differences in sensitivity to both localized and overall changes in the timing of components within sequential tone patterns.

ACKNOWLEDGMENTS

This research was supported by a grant from the National Institute of Aging (AG R0109191). The authors are grateful to Leslie McCreight and Jennifer Lantz for their assistance with the collection of data for this project. We are also indebted to Dr. Karen Snell and Dr. Pierre Divenyi for their many helpful and insightful comments on an earlier version of this paper.

Abel, S. M. (**1972**). ''Duration discrimination of noise and tone bursts,'' J. Acoust. Soc. Am. **51**, 1219–1223.

Abel, S. M., Krever, E. M., and Alberti, P. W. (**1990**). ''Auditory detection, discrimination, and speech processing in ageing, noise-sensitive and hearing-impaired listeners,'' Scand. Audiol. **19**, 43–54.

Allen, L. G. (**1979**). ''The perception of time,'' Percept. Psychophys. **26**, 340–354.

ANSI (**1996**). S3.6-1996, ''Specifications for audiometers'' (American National Standards Institute, New York).

Boettcher, F. A., Mills, J. H., and Norton, B. L. (**1993**). ''Age-related changes in auditory evoked potentials of gerbils: I. Response amplitudes,'' Hear. Res. **71**, 137–145.

Boettcher, F. A., Mills, J. H., Swerdloff, J. L., and Holley, B. L. (**1996**). ''Auditory evoked potentials in aged gerbils: responses elicited by noises separated by a silent gap,'' Hear. Res. **102**, 167–178.

Cerella, J. (**1990**). ''Aging and information processing rate,'' in *Handbook of the Psychology of Aging*, edited by J. E. Birren and K. W. Schaie (Academic, San Diego), pp. 201–221.

Creelman, C. D. (**1962**). ''Human discrimination of auditory duration,'' J. Acoust. Soc. Am. **34**, 582–593.

Divenyi, P. L., and Danner, W. F. (**1977**). ''Discrimination of time intervals marked by brief acoustic pulses of various intensities and spectra,'' Percept. Psychophys. **21**, 125–142.

Drake, C., and Botte, M-C. (**1993**). ''Tempo sensitivity in auditory sequences: Evidence for a multiple-look model,'' Percept. Psychophys. **54**, 277–286.

Fitzgibbons, P. J., and Gordon-Salant, S. (**1994**). ''Age effects on measures of auditory duration discrimination,'' J. Speech Hear. Res. **37**, 662–670.

Fitzgibbons, P. J., and Gordon-Salant, S. (**1995**). ''Age effects on duration discrimination with simple and complex stimuli,'' J. Acoust. Soc. Am. **98**, 3140–3145.
Fitzgibbons, P. J., and Gordon-Salant, S. (**1998**). ''Auditory temporal order perception in younger and older adults,'' J. Speech Hear. Res. **41**, 1052–1060.
Gordon-Salant, S., and Fitzgibbons, P. J. (**1993**). ''Temporal factors and speech recognition performance in young and elderly listeners,'' J. Speech Hear. Res. **36**, 1276–1285.
Green, D. M., and Swets, J. A. (**1966**). *Signal Detection Theory in Psychophysics* (Wiley, NewYork).
Hafter, E. R., and Dye, R. H., Jr. (**1983**) ''Detection of interaural differences of time in trains of high-frequency clicks as a function of interclick interval and number,'' J. Acoust. Soc. Am. **73**, 644–651.
He, N.-J., Horwitz, A. R., Dubno, J. R., and Mills, J. H. (**1999**). ''Psychometric functions for gap detection in noise measured from young and aged subjects,'' J. Acoust. Soc. Am. **106**, 966–978.
Hellstrom, L. L., and Schmiedt, R. A. (**1990**). ''Compound action potential input/output functions in young and quite-aged gerbils,'' Hear. Res. **50**, 163–174.
Hirsh, I. J., Monahan, C. B., Grant, K. W., and Singh, P. G. (**1990**). ''Studies in auditory timing: I. Simple patterns,'' Percept. Psychophys. **47**, 215–226.
Humes, L., and Christopherson, L. (**1991**). ''Speech identification difficulties of hearing-impaired elderly persons: The contribution of auditory processing deficits,'' J. Speech Hear. Res. **34**, 686–693.
Kiang, N. Y. S., Watanabe, T., Thomas, E. C., and Clark, L. F. (**1965**). *Discharge Patterns of Fibers in the Cat's Auditory Nerve* (MIT Press, Cambridge, MA).
Levitt, H. (**1971**). ''Transformed up-down methods in psychoacoustics,'' J. Acoust. Soc. Am. **49**, 467–477.
Meyerson, J., Hale, S., Wagstaff, D., Poon, L. W., and Smith, C. A. (**1990**). ''The information-loss model: A mathematical theory of age-related cognitive slowing,'' Psychol. Rev. **97**, 475–487.
Pfeiffer, E. (**1975**). ''A short portable mental status questionnaire for the assessment of organic brain deficit in elderly patients,'' J. Am. Geriatric Soc. **23**, 433–441.
Salthouse, T. A. (**1991**). *Theoretical Perspectives on Cognitive Aging* (Lawrence Erlbaum Associates, Inc., Hillsdale, NJ).
Schneider, B. A., Pichora-Fuller, M. K., Kowalchuk, D., and Lamb, M. (**1994**). ''Gap detection and the precedence effect in young and old adults,'' J. Acoust. Soc. Am. **95**, 980–991.
Schneider, B. A., Speranza, F., and Pichora-Fuller, M. K. (**1998**). ''Age-related changes in temporal resolution: Envelope and intensity effects,'' Can. J. Psychol. **52**, 184–191.
Schneider, B. A., and Hamstra, S. J. (**1999**). ''Gap detection thresholds as a function of tonal duration for younger and older listeners,'' J. Acoust. Soc. Am. **106**, 371–380.
Schneider, B. A., and Pichora-Fuller, M. K. (**2000**). ''Implications of perceptual deterioration for cognitive aging research,'' in *The Handbook of Aging and Cognition*, 2nd ed., edited by F. I. Craik and T. A. Salthouse (Lawrence Erlbaum Associates, Inc., Mahwah, NJ), pp. 155–219.
Small, A. M., and Campbell, R. A. (**1962**). ''Temporal differential sensitivity for auditory stimuli,'' Am. J. Psychol. **75**, 401–410.
Snell, K. B. (**1997**). ''Age-related changes in temporal gap detection,'' J. Acoust. Soc. Am. **101**, 2214–2220.
Snell, K. B., and Frisina, D. R. (**2000**). ''Relationships among age-related differences in gap detection and word recognition,'' J. Acoust. Soc. Am. **107**, 1615–1626.
Trainor, L. J., and Trehub, S. E. (**1989**). ''Aging and auditory temporal sequencing: Ordering the elements of repating tone patterns,'' Percept. Psychophys. **45**, 417–426.
Willott, J. F. (**1990**). *Aging and the Auditory System* (Singular Publishing Group, San Diego).
Wingfield, A. (**1996**). ''Cognitive factors in auditory performance: Context, speed of processing, and constraints of memory,'' J. Am. Acad. Audiol. **7**, 175–182.

The effects of compression ratio, signal-to-noise ratio, and level on speech recognition in normal-hearing listeners

Benjamin W. Y. Hornsby[a] and Todd A. Ricketts
Dan Maddox Hearing Aid Research Laboratory, Vanderbilt Bill Wilkerson Center, 1114 19th Avenue South, Nashville, Tennessee 37212

(Received 24 August 2000; revised 17 January 2001; accepted 6 March 2001)

Previous research has demonstrated reduced speech recognition when speech is presented at higher-than-normal levels (e.g., above conversational speech levels), particularly in the presence of speech-shaped background noise. Persons with hearing loss frequently listen to speech-in-noise at these levels through hearing aids, which incorporate multiple-channel, wide dynamic range compression. This study examined the interactive effects of signal-to-noise ratio (SNR), speech presentation level, and compression ratio on consonant recognition in noise. Nine subjects with normal hearing identified CV and VC nonsense syllables in a speech-shaped noise at two SNRs (0 and +6 dB), three presentation levels (65, 80, and 95 dB SPL) and four compression ratios (1:1, 2:1, 4:1, and 6:1). Stimuli were processed through a simulated three-channel, fast-acting, wide dynamic range compression hearing aid. Consonant recognition performance decreased as compression ratio increased and presentation level increased. Interaction effects were noted between SNR and compression ratio, as well as between presentation level and compression ratio. Performance decrements due to increases in compression ratio were larger at the better (+6 dB) SNR and at the lowest (65 dB SPL) presentation level. At higher levels (95 dB SPL), such as those experienced by persons with hearing loss, increasing compression ratio did not significantly affect speech intelligibility. [DOI: 10.1121/1.1369105]

PACS numbers: 43.66.Ts, 43.71.Es [SPB]

I. INTRODUCTION

With the increased use of digital signal processing in commercial hearing aids, the number of processing parameters available for adjustment has grown substantially. Some multichannel systems allow for very precise frequency-specific and level-dependent application of gain. These systems may have specific control, in multiple channels, over parameters such as overall gain, compression threshold, compression ratio, and attack and release times. There has been substantial research examining the effects of many of these parameters on speech recognition as a function of speech input level (see Dillon, 1996 for review). In contrast, very little work has been done examining the effects of various hearing aid parameters as a function of output level at the ear. It is not clear how specific changes to some hearing aid parameters, such as compression ratio, will affect speech recognition at high output levels. In this paper the terms ''output level'' and ''presentation level'' of speech will be used interchangeably to refer to the in situ level of the signal (measured in a Zwislocki coupler).

High presentation levels influence several facets of auditory processing, including speech recognition and discrimination, frequency and temporal resolution and upward spread of masking (Egan and Hake, 1950; Dorman and Dougherty, 1981; Moore and Glasberg, 1987; Studebaker *et al.*, 1999). Several researchers have shown that speech recognition is degraded when speech is presented at high levels (French and Steinberg, 1947; Pollack and Pickett, 1958; Goshorn and Studebaker, 1994; Studebaker *et al.*, 1999). Studebaker and colleagues (1999) reported decreases in speech intelligibility at presentation levels above 69 dB SPL at some signal to-noise ratios (SNRs). In addition, SNR appears to interact with presentation level to affect speech recognition performance. Larger and more rapid decrements in speech intelligibility are observed at poorer SNRs as speech levels increase (Pollack and Pickett, 1958; Studebaker *et al.*, 1999). Based on these and other findings (French and Steinberg, 1947; Fletcher and Galt, 1950; Pollack and Pickett, 1958; Goshorn and Studebaker, 1994), it appears that when a speech-shaped noise is present, higher-than-normal speech presentation levels reduce speech understanding. Persons with hearing loss are forced to listen to speech at these levels to ensure audibility and are therefore subject to these negative effects. In addition, using different techniques, Studebaker *et al.* (1999) and Ching *et al.* (1998) found that high levels similarly affected hearing-impaired and normal-hearing subjects once audibility was taken into account. In all the experiments cited above, however, performance was assessed with linearly amplified speech. Appropriately fit amplification for persons with hearing loss often results, however, in the presentation of compressed speech at high levels. Determining the effect of high presentation level on the perception of compressed speech is the focus of the current study.

The compression literature has a long history of mixed findings regarding the efficacy of compression. In this paper we focus solely on the use of fast-acting compression (see Dillon, 1996, for a broader discussion of various types of compression). Wide dynamic range compression (WDRC),

[a]Author to whom correspondence should be addressed. Electronic mail: ben.hornsby@vanderbilt.edu

defined here as fast-acting (attack times <5 ms, release times <50 ms), low threshold compression (compression threshold <60 dB SPL), can provide persons with hearing loss more gain for soft sounds than for loud sounds. Consequently, this processing has the potential to increase audibility without exceeding loudness discomfort levels. Several investigators have advocated the use of fast-acting compression. Using fast-acting compression, particularly in multiple frequency channels, allows for increased gain of low-level consonants following a more intense sound such as a vowel. This increase in audibility and consonant sensation level has the potential of improving speech understanding for some hearing-impaired subjects (Yund and Buckles, 1995a, 1995b; Verschuure *et al.*, 1998; Souza and Bishop, 1999). Moore and colleagues found fast-acting compression, compared to linear amplification, provided small but significant benefits for hearing-impaired subjects particularly when listening to speech in a noise background that contained temporal and spectral dips (Moore *et al.*, 1999). The fast-acting compression was able to improve the audibility of speech in the temporal and spectral dips in the noise.

Research also suggests, however, that in certain conditions the use of fast-acting, multichannel compression may degrade speech intelligibility (Nabelek, 1983; Plomp, 1994; Hohmann and Kollmeier, 1995). When compression is applied independently in multiple frequency channels the spectrotemporal variations of speech can be severely altered, particularly at high compression ratios. This may have a large negative impact on speech recognition (Plomp, 1994).

Boike and Souza (2000) measured sentence recognition and sound quality at a fixed level of 80 dB SPL using speech processed through a simulated single-channel compression system with compression ratios ranging from 1:1 to 10:1. In one condition the speech was mixed with a speech babble noise (+10 dB SNR) prior to compression. In this condition, no decrease in speech recognition was observed for the normal-hearing subjects. In contrast, performance for the hearing-impaired group fell by about 30% as the compression ratio was increased from 1:1 to 10:1. Hohmann and Kollmeier (1995) reported a negative effect of fast-acting compression, compared to linear processing, on speech intelligibility under some conditions. These authors used a 23-band phonemic compressor to examine the effects of multiband compression, compression ratio and SNR on speech intelligibility. They showed only a small decrease in intelligibility, compared to linear processing, with a SNR of −2 dB and compression ratios up to 3:1. At a SNR of −8, however, performance dropped by over 20% when the compression ratio increased from linear (1:1) up to 3:1. This study is unusual, however, in that only the speech (and not the noise) was compressed. Crain and Yund (1995) found stop-consonant discrimination decreased, compared to linear processing, when normal-hearing subjects listened to speech processed at a 4:1 compression ratio using an eight-channel fast-acting compression system. The previous research indicates that increasing presentation levels and compression ratios can, independently, have a negative effect on speech recognition. It has also been demonstrated that both level and compression ratio interact with other factors (e.g., SNR) to affect speech intelligibility (Yund and Buckles, 1995b; Studebaker *et al.*, 1999). What is not clear is how output levels and compression ratios interact to affect speech recognition.

Much of the existing research on compression has focused on the benefits and limitations of compression for subjects with hearing loss. Clearly this is important, as findings from work using normal-hearing subjects are not always similar in hearing impaired. For example, Verschuure and colleagues have argued, and have some experimental support for the idea, that fast-acting compression may limit the impact of poorer temporal resolution in subjects with hearing loss by restoring audibility to low level consonants (Verschuure *et al.*, 1994; Verschuure *et al.*, 1996; Verschuure *et al.*, 1998).

Interpreting the impact of changes in compression parameters on speech recognition based on results from persons with hearing loss, however, is complicated by the changes in audibility that occur following compression. The use of normal-hearing subjects reduces this confound of increased audibility when assessing the effects of level and compression ratio. Using subjects with normal hearing allows us to vary presentation level and compression ratio without affecting audibility. Therefore no improvements in speech recognition based solely on audibility would be expected (Yund and Buckles, 1995b). Any changes in speech recognition performance could then be attributed solely to the variable(s) under investigation (e.g., compression ratio, SNR or level). This allows us to estimate the degradation in speech scores that must be overcome to make multichannel compression an appropriate choice for a given hearing loss. In addition, since the direction of the interaction between these factors is unclear, some existing research using normal-hearing subjects as controls may underestimate (or inflate) the negative effects of compression by presenting speech at levels much lower than those required by a hearing-impaired subject (Plomp, 1994; Crain and Yund, 1995). It is for these reasons that this study uses subjects with normal hearing to assess the interactive effects of level and compression ratio on speech recognition.

In summary, knowledge about compression ratio and presentation levels (such as those experienced by persons with hearing loss) is important because these factors may interact to affect speech recognition. The use of amplitude compression may have both negative (e.g., reduced temporal and spectral contrasts; Plomp, 1994) and positive effects (e.g., increased audibility of speech; Souza and Turner, 1998). Since the magnitude of these effects may be dependent on level, there is the potential for interaction between compression parameters and output level. For example, the negative effects of compression may be exacerbated at high output levels, resulting in substantially poorer performance with compressed speech as opposed to noncompressed speech. This study systematically investigated the interactive effects of compression ratio and output level on speech recognition with speech processed through a simulated 3-channel WDRC compression system.

TABLE I. Classification of consonants by acoustic-phonetic features. Place coding: 1=labial, 2=dental, 3=alveolar, 4=palatal, 5=back. Manner coding: 1=stop, 2=fricative, 3=affricate, 4=nasal, 5=glide.

Feature	/p/	/t/	/k/	/f/	/θ/	/s/	/ʃ/	/b/	/d/	/g/	/v/	/ð/	/z/	/ʒ/	/m/	/n/	/ŋ/	/tʃ/	/dʒ/	/w/	/r/	/j/	/l/
Voicing	0	0	0	0	0	0	0	1	1	1	1	1	1	1	1	1	0	1	1	1	1	1	
Frication	0	0	0	1	1	1	1	0	0	0	1	1	1	1	0	0	0	1	1	0	0	0	0
Duration	0	0	0	0	0	1	1	0	0	0	0	0	1	1	0	0	0	0	0	0	0	0	0
Nasality	0	0	0	0	0	0	0	0	0	0	0	0	0	0	1	1	1	0	0	0	0	0	0
Place	1	3	5	1	2	3	4	1	3	5	1	2	3	4	1	3	5	4	4	5	4	4	3
Sonorance	0	0	0	0	0	0	0	0	0	0	0	0	0	0	1	1	1	0	0	1	1	1	1
Manner	1	1	1	2	2	2	2	1	1	1	2	2	2	2	4	4	4	3	3	5	5	5	5

II. METHODS

A. Subjects

Nine subjects (2 males and 7 females), between the ages of 23 to 39 years (mean=28.3), with normal hearing and no history of otologic pathology participated in this study. All subjects had pure-tone air-conduction thresholds of 20 dB or less at octave frequencies of 250–8000 Hz (ANSI S3.6, 1996b), and normal middle ear function. Normal middle ear function was defined as normal pressure (−150 to +100 daPa) and compliance (0.2 to 1.8 ml) functions. In addition, all subjects showed the presence of an ipsilateral acoustic reflex in response to 500 and 2000 Hz pure tones presented at 90 dB HL. Speech recognition ability for all subjects was good with a minimum performance of 92% on a 25-item Northwestern University (NU-6) word list (Tillman and Carhart, 1966) presented at 50 dB HL. In addition, prior to data collection each subject was screened to ensure that presentation levels used in the study did not exceed loudness discomfort levels. Subjects listened to the same speech stimuli used during the data collection phase (0 dB SNR) as the presentation level was increased from 65 to 95 dB. Subjects were allowed to listen to as many stimuli as needed to determine if levels were uncomfortably loud. All subjects screened for enrollment reported no difficulty in listening to stimuli at the levels used in this study.

B. Stimuli

Eighty-six syllables (44 CV and 42 VC syllables) from the UCLA recording of the NST or Nonsense Syllable Test (Levitt and Resnick, 1978) were used as stimuli for this study. Nonsense syllables were used to limit linguistic contributions to speech recognition. The 23 consonants shown in Table I were paired with the vowels /i/ and /*a*/. Stimulus context was consistent with what occurs in conversational English. Therefore the consonant /ŋ/ occurred only in the VC position while the consonants /w/ and /j/ occurred only in the CV position. Stimuli were natural tokens spoken by a single male speaker. Speech and noise stimuli were digitally recorded using a 33 kHz sampling rate with 16-bit quantization.

Each stimulus was digitally mixed with a 1200-ms segment of speech-shaped noise (Byrne *et al.*, 1994) prior to compression. Since the maximum duration of a single syllable was 950 ms and each syllable was centered within the 1200-ms segment, noise was present for at least 125 ms prior to the onset and following the offset of each syllable. The rms level of the noise was digitally adjusted to equal the rms level of all test syllables concatenated together for a 0 dB SNR, and adjusted to 6 dB less for a +6 dB SNR. These SNRs were chosen because they represent a range of everyday difficult listening situations (Pearsons, Bennett, and Fidell, 1977) and performance at these SNRs exhibited limited floor and ceiling effects. Two concatenated files (0 dB and +6 dB SNRs) consisting of all test syllables were used as input files for the compression algorithm.

C. Compression system

The focus of this study was on the interaction between compression and output level. To this end the amount of compression in each condition was fixed and only the amount of attenuation or SNR was varied. This situation is analogous to providing varying amounts of gain following compression. This method results in some conditions that would not usually occur when fitting compression hearing aids to individuals with hearing loss. For example, a person with a mild loss would not normally be provided with fast-acting compression incorporating a compression ratio of 4:1. A subject with a more severe loss, however, may be fit in this fashion. Thus in order to limit confounding variables and focus on the interaction of interest, we chose to fix the compression ratio and vary the output level of the speech at the ear.

The rms levels of the uncompressed concatenated stimuli were digitally adjusted to a level 25 dB above compression threshold (e.g., with input stimuli adjusted to 65 dB SPL the compression threshold was 40 dB SPL). Compression threshold was constant across frequency (octave frequencies from 250 to 4000 Hz). Compression ratio varied somewhat as a function of frequency. The nominal values of 1:1, 2:1, 4:1, and 6:1 are based on rounded average values measured across octave frequencies of 250–4000 Hz. Frequency-specific compression ratios, for inputs over the maximum dynamic range of our stimuli (22 dB), are shown in Table II.

It was assumed that the stimuli compressed at a 1:1 ratio were equivalent to unprocessed stimuli. However, these stimuli were also processed through the compression algorithm at a 1:1 ratio, in order to ensure that any artifacts introduced by the compression program would be equivalent for all stimuli. Informal listening revealed no differences between the unprocessed stimuli and stimuli compressed at a 1:1 ratio. Attack and release times at 1000 Hz were fixed at 5 and 20 ms, respectively (ANSI S3.22, 1996a). Attack and

TABLE II. Desired and actual compression ratios as a function of frequency for the compression algorithm used in this study.

Frequency	CR1:1	CR2:1	CR4:1	CR6:1
250 Hz	1.0	2.0	3.9	7.2
500 Hz	1.0	1.9	3.0	4.1
1000 Hz	1.0	2.0	3.9	7.4
2000 Hz	1.0	1.9	3.3	4.6
3000 Hz	1.0	1.9	3.3	4.8
4000 Hz	1.0	2.0	4.1	8.6
Average	1.0	1.9	3.6	6.1

release times, as measured by ANSI S3.22, vary as a function of compression ratio. Therefore the nominal input values for attack and release were varied to achieve measured attack and release times of 5 and 20 ms, independent of compression ratio.

Signal processing was performed offline using a digital algorithm. A 3-channel compression system was implemented. The concatenated speech and noise files were first filtered into three channels prior to compression. Filtering was performed digitally using three, 100th order FIR filters. Filter shapes are shown graphically in Fig. 1. Compression was then applied independently in each frequency channel with the compressed output of each band recombined and scaled to maximize the dynamic range of the D–A converter. Following compression, the rms levels of the compressed concatenated stimulus files were digitally adjusted to equalize their levels. When played out through the test earphone (Etymotic ER4), the average rms levels in a Zwislocki coupler for all concatenated stimulus files, at all SNRs and compression ratios, were equivalent to within approximately 1 dB. Following compression each compressed concatenated stimulus was separated into the 86 individual 1200-ms CV and VC stimuli.

D. Calibration

Calibration levels were set so that the rms level of a 1000-Hz pure tone measured in a Zwislocki coupler was equivalent to the rms level for the concatenated stimuli also measured in the coupler. The output of the calibration tone in the Zwislocki coupler was set to 95 dB SPL as measured with a sound level meter (Larson–Davis 814) using *C* weighting and slow averaging. A programmable attenuator was employed to control the presentation level (65, 80, or 95 dB SPL) of the processed speech.

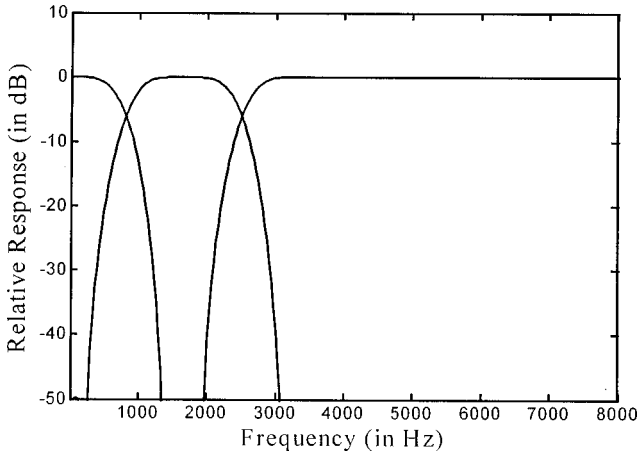

FIG. 1. Frequency response of the 100th order FIR filters used in the 3-channel simulated hearing aid. Nominal cutoff frequencies were 800 Hz for the lowpass filter, 800 and 2500 Hz for the bandpass filter and 2500 Hz for the high-pass filter.

E. Procedure

Prior to data collection subjects were trained by listening monaurally in quiet, to all 86 stimuli, at a 65 dB SPL presentation level. Practice sessions continued until asymptotic performance (better than 90% performance on two sequential practice sessions) was reached. This typically took three to five practice sessions. During the data collection phase subjects listened to two runs of 24 conditions (two SNRs, three presentation levels, and four compression ratios) over four test sessions. Each session lasted approximately 1.5 hours with breaks provided as needed. The SNR remained constant during a session, and subjects listened to 12 randomly presented conditions (four compression ratios at three presentation levels) during each session. The order of SNR was randomized across subjects. Eighty-six syllables were presented in each condition and each condition was repeated once. Subject scores for each condition were then based on a total of 172 syllables. Stimuli were presented monaurally (right ear) via an insert earphone (Etymotic ER4). Subjects listened to stimuli while viewing the 86 response alternative on a computer screen and indicated their response by clicking on the appropriate syllable. All possible response options were present on the screen during each trial and no correct answer feedback was given during practice sessions or during actual data collection.

F. Data analysis

Percentage correct scores for each SNR, level, and compression condition were converted to Rationalized Arcsine Transform Units (RAUs) to stabilize the error variance prior to statistical analysis (Studebaker, 1985). Results were initially examined using a four-factor repeated-measures analysis of variance (ANOVA) with SNR, level, compression ratio and test session as independent variables and RAU score as the dependent variable. Post hoc analysis was performed using a Newman–Keuls test. All results are reported with a statistical significance level of $p<0.05$ unless otherwise noted.

Results were also examined as a function of speech feature. The features used for analysis in this study followed those suggested by Kent *et al.* (1979). The authors suggested using five binary features [voicing, frication, duration, and nasality from Miller and Nicely (1955), and sonorance], and a five-value feature for place of articulation (labial, dental, alveolar, palatal, and back). An additional five-value feature for manner of articulation (stop, fricative, affricate, nasal, and glide) was also included. Previous research has demonstrated the perceptual relevance of these features and shown that discrimination of these features is important for speech

TABLE III. Results from three-way ANOVA. *P*-values less than 0.05 are shown in boldface (SNR, signal-to-noise ratio; PL, presentation level, and CR, compression rato).

Effect	*df*	*F*	*p* level
SNR	1,8	291.97	**<0.001**
PL	2,16	54.99	**<0.001**
CR	3,24	18.81	**<0.001**
PL×SNR	2,16	0.61	0.543
SNR×CR	3,24	3.58	**0.031**
PL×CR	6,48	4.96	**0.005**
SNR×PL×CR	6,48	2.25	0.052

sound discrimination (Miller and Nicely, 1955; Wang and Bilger, 1973). Table I shows a breakdown of consonants by acoustic–phonetic features.

Individual subject confusion matrices for the entire set of 23 consonants (collapsed across vowel context and type) were added together to create a single matrix for each experimental condition. These matrices were then analyzed using the Feature Information Transfer (FIX) program to determine the unconditional percent information transmitted as a function of feature for each level, SNR and compression ratio (Miller and Nicely, 1955; Wang and Bilger, 1973). This transformation provided an estimate of how susceptible a particular feature was to the effects of level, compression ratio and SNR. Because of the limited number of consonants presented to an individual subject in each condition, statistical analysis of confusion matrix data was not performed.

III. RESULTS

A. Constant recognition

Experimental data were initially examined using a four-factor, repeated-measures ANOVA to explore potential practice effects. Along with SNR, level, and compression ratio, test session was included as an independent variable. A significant main effect of session was observed ($F_{1,8}=16.16$, $p<0.0038$). Overall performance was slightly better during the second session (56% vs 58% for the first and second sessions, respectively), suggesting a small but significant practice effect. However, no significant interaction effects were observed between test session and other variables. Therefore data between test days were collapsed for further analysis. The results from the three-way ANOVA used to examine the main and interaction effects of SNR, presentation level, and compression ratio on consonant recognition are displayed in Table III.

Main effects of SNR, presentation level and compression ratio were observed. Figure 2 shows mean consonant recognition values as a function of presentation level for both SNRs and all four compression ratios. As expected, consonant recognition worsened at the poorer SNR. Also, consistent with previous research, consonant recognition scores on average decreased as presentation levels increased (Pollack and Pickett, 1958; Studebaker *et al.*, 1999). This decrease was consistently observed across subjects, with all nine subjects showing poorer average performance at 95 dB than at 65 dB. In addition, a small but significant effect of compression ratio was observed. Consonant recognition, averaged

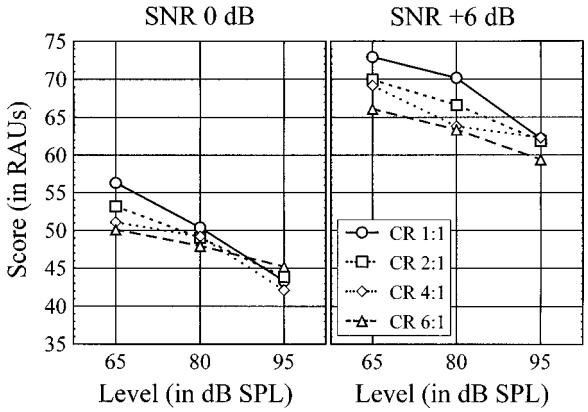

FIG. 2. Effect of SNR, presentation level and compression ratio on consonant recognition in RAUs.

across SNR and level, decreased systematically as compression ratio increased. An average decrease of approximately 4% occurred as compression ratio increased from 1:1 to 6:1. This decrease was also consistent across subjects. In 26 of 27 conditions (nine subjects and three compression ratios) subjects showed poorer speech recognition performance when listening to compressed speech (2:1, 4:1, or 6:1) as compared to speech processed at a 1:1 ratio.

Significant interaction effects between compression ratio and SNR, as well as between level and compression ratio were also observed. In addition, the three-way interaction between SNR, compression ratio, and level approached significance ($p<0.052$). Post hoc analyses using a Newman–Keuls test were performed to compare performance between compression conditions. A portion of the analysis results comparing linearly processed speech to speech compressed at ratios of 2, 4 and 6:1 are shown in Table IV. The general findings were that consonant recognition was most negatively affected at lower presentation levels, and the negative effect of increasing compression ratio was more apparent at a better SNR.

The effect of compression ratio at the lowest level tested (65 dB) is discussed first. A negative effect of increasing compression ratio was observed *consistently* only at this lowest level. At the 65 dB level, across both SNRs, consonant recognition performance was significantly higher for linearly processed speech, as opposed to speech compressed at a 4:1 or 6:1 compression ratio. In addition, at the +6 dB SNR, performance decreased significantly as the compression ratio increased from 4:1 to 6:1 ($p<0.048$), while no differences among the 2, 4 or 6:1 compression conditions were observed

TABLE IV. *P* values from Neuman–Keuls post hoc testing of consonant recognition for linearly (compression ratio 1:1) processed speech compared to recognition for speech compressed at a ratio of 2, 4 or 6:1. *P* levels less than 0.05 are shown in boldface.

	SNR: 0 dB			SNR: +6 dB		
Level	65 dB	80 dB	95 dB	65 dB	80 dB	95 dB
CR 2:1	**0.020**	0.703	0.668	0.053	**0.033**	0.806
CR 4:1	**<0.001**	0.606	0.346	**0.021**	**<0.001**	0.931
CR 6:1	**<0.001**	0.309	0.293	**<0.001**	**<0.001**	0.076

TABLE V. Unconditional proportion of information transmitted as a function of speech feature, level, SNR and compression ratio.

	CR 1:1			CR 2:1			CR 4:1			CR 6:1		
Feature	65 dB	80 dB	95 dB	65 dB	80 dB	95 dB	65 dB	80 dB	95 dB	65 dB	80 dB	95 dB
						SNR 0 dB						
Voicing	0.672	0.607	0.596	0.622	0.64	0.591	0.685	0.63	0.596	0.684	0.591	0.626
Frication	0.248	0.199	0.145	0.235	0.179	0.139	0.203	0.191	0.127	0.189	0.193	0.164
Duration	0.364	0.284	0.211	0.295	0.243	0.18	0.322	0.218	0.186	0.288	0.24	0.199
Nasality	0.538	0.465	0.367	0.535	0.474	0.339	0.435	0.478	0.376	0.513	0.49	0.435
Place	0.334	0.261	0.213	0.306	0.25	0.195	0.288	0.248	0.194	0.291	0.244	0.23
Sonorance	0.572	0.505	0.361	0.567	0.499	0.395	0.511	0.498	0.383	0.525	0.507	0.465
Manner	0.451	0.368	0.285	0.413	0.353	0.291	0.391	0.361	0.291	0.376	0.353	0.333
						SNR +6 dB						
Voicing	0.849	0.848	0.803	0.795	0.811	0.791	0.843	0.789	0.829	0.849	0.812	0.782
Frication	0.486	0.435	0.364	0.439	0.4	0.381	0.467	0.376	0.346	0.375	0.362	0.323
Duration	0.553	0.543	0.453	0.55	0.503	0.425	0.563	0.417	0.412	0.53	0.373	0.364
Nasality	0.823	0.787	0.673	0.75	0.719	0.625	0.713	0.77	0.654	0.72	0.73	0.682
Place	0.555	0.506	0.41	0.512	0.465	0.414	0.516	0.417	0.403	0.462	0.423	0.385
Sonorance	0.836	0.824	0.734	0.788	0.783	0.721	0.781	0.788	0.743	0.77	0.775	0.742
Manner	0.661	0.644	0.552	0.642	0.605	0.562	0.642	0.587	0.548	0.584	0.582	0.536

at the 0-dB SNR. In other words, at low levels and with a positive SNR, increasing the compression ratio above 4:1 continued to negatively affect consonant recognition. This was not true for the 0-dB SNR condition.

In contrast, at the highest level tested (95 dB), no significant differences were observed between any compression conditions at either SNR. That is, at high levels increasing compression ratio did not negatively affect speech recognition. At the 80-dB level, however, performance differences due to compression were dependent on SNR, with the negative effect of increasing compression ratio exacerbated at the better SNR. At this level (80 dB) no effect of compression was observed at the 0-dB SNR, while at the +6 dB SNR performance was significantly poorer for compressed speech (2, 4 or 6:1), than for linearly processed speech (see Table IV).

These data were further examined as a function of vowel type (/*a*/ or /i/) and context (CV versus VC) to determine if the trends that were observed in the overall analysis were consistent across conditions. Scores were derived separately for CV and VC stimuli as well as for consonants paired with /*a*/ and /i/. As in the overall analysis, 3-factor ANOVAs were performed on the data from each of these four conditions. The trend across conditions was similar to that observed in the averaged data. At a low level (65 dB) consonant recognition tended to decrease as the compression ratio increased. At higher levels (95 dB) no such consistent decrease was observed.

B. Feature analysis

It was also of interest to examine the impact of compression ratio and output levels as a function of speech feature. An analysis of speech features might provide some insight into mechanisms responsible for the trends observed in the averaged consonant recognition data. It was possible that the observed trends were due to deficits in specific feature sets as opposed to more global deficits across features. Data were pooled across subjects to create a single consonant confusion matrix for each condition. These combined matrices included 72 responses for each syllable (except for /ŋ/, /w/ and /j/ which had only 36 responses because they occurred only in a single syllable position). Using these combined matrices, proportion of information transmitted as a function of feature was determined for the group data. The results are shown in Table V.

The pattern of results across features varied, although the general trend observed in the consonant recognition analysis was also observed in at least one SNR condition for all speech features except voicing. In general, information transmission decreased with increases in compression at low, but not high levels. Specifically, the features of place, manner and frication demonstrated this trend at both SNRs while the voicing feature was resistant to the negative effects of level and compression ratio at both SNRs.

To further clarify the interactive effects of level and compression a difference in percent information transmitted between linear and compressed speech was derived. First, confusion matrices for compressed speech at a given SNR and level were derived by adding the matrices from the 2, 4 and 6:1 compression conditions together. This resulted in a compression confusion matrix for each level and SNR condition. The percent information transmitted for compressed and linearly processed speech was then determined for each feature set. Difference scores were obtained by subtracting the percent information transmitted for compressed speech, at a given level and SNR, from that obtained with linearly processed speech in the same condition. In Fig. 3 difference scores as a function of feature are shown for all levels and for both SNR conditions. A positive difference score is indicative of greater information transmission by linearly processed speech than by compressed speech.

The effect of level on feature transmission is most clearly shown at the poorer SNR. At the 0-dB SNR, difference values across all features were more positive at low (65 dB) than at high (80 or 95 dB) intensity levels. In fact, at the 95-dB level difference values for some features, for example sonorance, were negative. This suggests that at this SNR (0

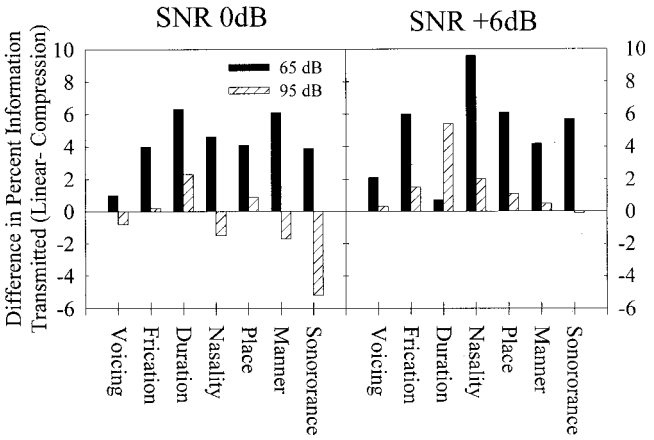

FIG. 3. Difference values for percent information transmitted as a function of speech feature with linearly processed speech as compared to speech compressed at a ratio of 2, 4, or 6:1. A positive value suggests more information was transmitted by the linearly processed speech.

dB) the effect of compression on speech feature recognition at high levels is either negligible or positive. At the +6 dB SNR the linear advantage was again present across most features (except for duration) at low (65 and 80 dB levels) as compared to high (95 dB) levels.

IV. DISCUSSION

The purpose of this research was to examine the effects of SNR, level and compression ratio on speech recognition. Previous research has demonstrated that speech recognition performance breaks down when speech is presented at higher-than-normal levels, particularly when the speech is presented in a background of speech-shaped noise (Studebaker *et al.*, 1999). In addition, the use of multichannel compression in conjunction with a high compression ratio may reduce speech recognition performance in some conditions (Plomp, 1994). It has not been clear, however, how these two factors would interact to affect speech recognition. One possible scenario is that high compression ratios and high presentation levels would interact to further reduce speech recognition. The results from the current study, however, suggest that the opposite is true. The negative impact of increasing compression ratio was most apparent at speech levels approximating unamplified conversational speech (e.g., 65 dB SPL) rather than at the highest presentation levels (95 dB SPL) used in this study. This finding suggests that for subjects with normal hearing, the application of compression to speech presented at higher-than-normal levels does not add to the existing speech recognition deficits already observed at high levels. This effect is robust in that it is present across vowel types and contexts as well as across multiple speech features. The cause of the interaction between presentation level and compression ratio observed in this study is unknown. The application of multichannel fast-acting compression to speech in noise may reduce spectrotemporal variations important for speech recognition. It is not clear why this reduction in spectrotemporal variations would vary as a function of output level.

An alternative way of describing the data is that the negative effect of increasing presentation level was less for compressed than for uncompressed speech. This is evidenced by the relatively shallow slopes of the functions for compressed speech as opposed to uncompressed speech seen in Fig. 2. Previous research has suggested that upward spread of masking and temporal (forward and backward) masking may play a role in the observed decreases in speech recognition at high levels (Goshorn and Studebaker, 1994). If this were true, the high-frequency emphasis provided by compression may make compressed speech less susceptible to the deleterious effects of increasing presentation level.

To investigate this hypothesis, speech intelligibility index (SII) calculations (ANSI S3.5, 1997) were made. The current SII standard is an update of a previous standard (ANSI S3.5, 1969), which was then referred to as the Articulation Index (AI). Although the SII, as described in the ANSI standard, is not appropriate for predicting the dynamic effects of compression on speech understanding, it is useful for predicting the effects of static changes in frequency response on speech understanding. Our motivation for using the SII is to examine the latter (static) effect of the high-frequency emphasis provided by compression processing. In other words, is speech with a high-frequency emphasis (whether obtained via linear frequency-shaping or fast-acting compression) less susceptible to spread of masking effects observed at high levels?

Briefly, the SII is a mathematical method for deriving a single measure that is highly correlated with speech intelligibility and can be defined as the algebraic sum:

$$\mathrm{SII} = \sum_{i=1}^{n} I_i A_i ,$$

where n refers to the number of individual bands used for computation (ranging from 6 bands for the octave method to 21 bands for the critical band procedure), I_i refers to the importance of a given band in terms of speech understanding and A_i refers to the audibility of a given band. The values I_i are derived empirically for a given speech stimulus. The values A_i indicate the *effective* proportion of speech cues that are audible in a given frequency band. The current ANSI standard includes calculations to account for spread of masking effects (upward and downward spread of masking as well as self-speech masking) and the negative effects of high presentation levels. These factors may reduce the A_i value of a given band and hence SII values will also be reduced. The following calculations were made to determine if reductions in SII values with increasing level were less for speech stimuli with a high-frequency emphasis (due to compression processing) than unprocessed speech in noise.

To calculate the SII, frequency-specific levels of both speech and noise as well as the auditory thresholds of the listener are required. It was not possible to derive frequency-specific measures of our compressed speech and noise because they were mixed prior to compression. Therefore estimates were made of the effects of compression on our speech and noise signals based on the changes in frequency spectrum observed in the mixed speech and noise as a function of compression ratio. One-third octave band levels were deter-

TABLE VI. SII values based on the estimated frequency response of the speech and noise stimuli for each compression ratio (CR) and signal-to-noise ratio (SNR). Presentation levels refer to the output in dB SPL in a Zwislocki coupler. The difference value refers to the difference in SII values for the 65 dB level minus the 95 dB level.

	SNR 0 dB				SNR +6 dB			
Level (dB)	CR 1:1	CR 2:1	CR 4:1	CR 6:1	CR 1:1	CR 2:1	CR 4:1	CR 6:1
65	0.432	0.429	0.423	0.42	0.633	0.653	0.654	0.659
80	0.397	0.39	0.383	0.38	0.591	0.602	0.601	0.605
95	0.34	0.335	0.329	0.327	0.518	0.527	0.527	0.53
Difference	0.092	0.094	0.094	0.093	0.115	0.126	0.127	0.129

mined for the mixed then compressed speech-plus-noise stimuli (for both SNR conditions). The changes in the 1/3-octave band levels due to compression were then applied to the original unprocessed speech and noise. These adjusted levels were used in the SII calculations. Results from these calculations are shown in Table VI.

As expected, SII values for the unprocessed speech and noise decreased as presentation level increased across both SNR conditions. This decrease also occurred, however, across all compression ratio conditions in an essentially equivalent manner. In other words, the small high-frequency emphasis, provided by the compression processing, did not substantially impact SII values as level increased.

Although the high-frequency emphasis provided by compression is not responsible for the reduced effect of compression at high levels, at least as calculated by the SII, reduced spread of masking may still be involved. Dubno *et al.* (2000) examined the effects of presenting speech at higher-than-normal levels on monosyllabic word recognition in noise. The long-term rms spectrum of the noise was spectrally shaped to match the 1% levels of their speech stimuli. In addition, they measured auditory thresholds in the presence of their speech-shaped masking noise and used these measured thresholds to make AI predictions of speech recognition performance as a function of level. Their results showed linear growth-of-masking slopes in the low frequencies but nonlinear growth of masking, consistent with upward spread of masking, in the high-frequency regions. In addition, the peaks in growth-of-masking functions in the high frequencies appeared to coincide with spectral peaks in the masking noise. The steepest growth-of-masking occurred in the 2000-Hz region which also coincided with a peak in the frequency importance function for the speech stimuli they used. Differences between observed and predicted scores were minimized when the measured thresholds, which accounted for spread of masking effects, were used in the AI calculations. The authors argue that the poorer speech recognition observed at high levels could be explained largely by reductions in the effective audibility of the speech stimuli resulting from upward spread of masking. Given that peaks in growth of masking functions coincided with peaks in the frequency response of the masker it is possible that the spectral flattening resulting from multichannel compression may reduce these peaks and consequently reduce nonlinear growth of masking in the high frequencies. This may explain, in part, the reduced impact of level on compressed speech. Further work in this area is needed to better understand these processes and how they may affect persons with hearing loss.

Another finding of interest was the interaction between compression ratio and SNR. When averaged across levels, increasing compression ratio caused performance to decrease more at the better (+6 dB) SNR as opposed to the poorer (0 dB) SNR. In addition, the three-way interaction between level, compression ratio and SNR approached statistical significance ($p<0.052$). An examination of this three-way interaction provides a better understanding of how SNR and compression ratio interact to affect consonant recognition. As can be seen in Fig. 2, at the better (+6 dB) SNR increasing compression ratio had a negative effect at both the 65-dB and 80-dB levels. In contrast, performance at the 0-dB SNR was affected by increasing compression ratios only at the lowest level (65-dB) tested. There was no effect of increasing compression ratio at either SNR for stimuli presented at a 95-dB level. Thus the effect of increasing compression ratio appears to be similar across SNR for both the 65- and 95-dB levels but not the 80-dB level. The interaction appears to be due, in large part, to the more rapid decrease in scores as level increases at the poorer (0-dB) SNR for uncompressed speech. Speech scores for uncompressed speech fall more rapidly at the 0-dB SNR than the +6-dB SNR, particularly as the level increased from 65 to 80 dB. The changes in speech scores for compressed speech, however, were similar across SNR conditions as level increased. In other words, at the +6-dB SNR the negative effect of increasing compression ratio was observed at the 80-dB level primarily because the effect of level on the uncompressed speech was less. This is consistent with previous research that indicates the negative effects of increasing level are reduced as SNR improves, and are minimal in a quiet environment (Studebaker *et al.*, 1999). Based on this trend, the negative effects of increasing compression ratio may become apparent at even higher levels (e.g., 95 dB) if the SNR continued to improve above +6 dB.

Drawing conclusions about the efficacy of multichannel fast-acting compression based on study results using subjects with normal hearing is clearly difficult. Previous research has demonstrated substantial differences in the psychoacoustic abilities of persons with normal and impaired hearing (see Moore, 1996, for review). Consequently, the impact of multichannel compression on speech recognition may be different for these groups. That said, it is still of interest to examine these findings as applied to listeners with hearing loss. When adjusted appropriately, multichannel compression can

improve audibility and consequently speech recognition performance (Souza and Turner, 1998). If at high levels, such as those experienced by persons with hearing loss, the negative effect of increasing compression ratios were large then the increase in audibility provided by compression would also need to be large to overcome this deficit. The current study, however, does not support this hypothesis.

This study reports data suggesting that the amount of degradation in speech understanding due to fast-acting compression depends, in part, on speech output levels as well as SNR. At higher presentation levels, such as those experienced by persons with hearing loss, the negative impact of 3-channel, fast-acting compression is minimal. The contrasting findings of the current study and those reporting much larger negative effects for subjects with hearing loss (e.g., Boike and Souza, 2000), may be due to differences in the psychoacoustic abilities of normal-hearing and hearing-impaired subjects. In addition, procedural differences in the implementation of compression, the application of frequency shaping and/or the type of speech materials (nonsense syllables versus sentences) used may also play a role. Previous research has demonstrated sentence intelligibility may be more susceptible to the negative effects of compression than nonsense syllables (Van Tasell and Trine, 1996).

In summary, these study results support the following conclusions. For subjects with normal hearing a significant interaction exists between output level and compression ratio. Increasing compression ratio at lower (65 dB) presentation levels results in reduced consonant recognition. In contrast, increasing compression ratio at higher (95 dB) levels has only a minimal effect on consonant recognition. In addition, the negative effects of increasing compression ratio are more apparent at a better SNR (+6 dB). Future work should extend this research by further varying compression parameters, hearing aid characteristics such as frequency shaping, incorporating sentence materials, and including subjects with hearing loss.

ACKNOWLEDGMENTS

We want to thank D. Wesley Grantham, Ph.D. for his thoughtful comments and support during this project. In addition, our thanks go to the associate editor, Sid Bacon, Ph.D. and two anonymous reviewers for their helpful criticisms of an earlier version of this paper. Thanks also go to William Woods, Ph.D. at Starkey Laboratories, Inc. for writing and making available the compression algorithm used in this study and Stuart Rosen at University College London for providing the Feature Information Transfer program.

ANSI (**1996a**). ANSI S3.22-1996, ''Specification of hearing aid characteristics'' (American National Standards Institute, New York).

ANSI (**1996b**). ANSI S3.6-1996, ''Specification for Audiometers'' (American National Standards Institute, New York).

ANSI (**1969**). ANSI S3.5-1969, ''Methods for the calculation of the articulation index'' (American National Standards Institute, New York).

ANSI (**1997**). ANSI S3.5-1997, ''The calculation of the speech intelligibility index'' (American National Standards Institute, New York).

Boike, K., and Souza, P. (**2000**). ''Effect of compression ratio on speech recognition and speech-quality ratings with wide dynamic range compression amplification,'' J. Speech Hear. Res. **43**, 456–468.

Byrne, D., Dillon, H., Tran, K., Arlinger, S., Wilbraham, K., Cox, R., Hagerman, B., Hetu, R., Kei, J., Lui, C., Kiessling, J., Kotby, M. N., Nasser, H. A., Wafaa, A. H., Nakanishi, Y., Oyer, H., Powell, R., Stephens, D., Meredith, R., Sirimanna, T., Tavartkiladze, G., Frolenkov, G., Westerman, S., and Ludvigsen, C. (**1994**). ''An international comparison of long-term average speech spectra,'' J. Acoust. Soc. Am. **96**, 2108–2120.

Ching, T., Dillon, H., and Byrne, D. (**1998**). ''Speech recognition of hearing-impaired listeners: Predictions from audibility and the limited role of high-frequency amplification,'' J. Acoust. Soc. Am. **103**, 1128–1140.

Crain, T. R., and Yund, E. W. (**1995**). ''The effect of multichannel compression on vowel and stop-consonant discrimination in normal hearing and hearing-impaired subjects,'' Ear Hear. **16**, 529–543.

Dillon, H. (**1996**). ''Compression? Yes, but for low or high frequencies, for low or high intensities, and with what response times?,'' Ear Hear. **17**, 287–307.

Dorman, M. F., and Dougherty, K. (**1981**). ''Shifts in phonetic identification with changes in signal presentation level,'' J. Acoust. Soc. Am. **69**, 1439–1440.

Dubno, J., Horowitz, A., and Ahlstrom, J. (**2000**). ''Speech recognition in noise at higher than-normal levels: Decreases in scores and increases in masking,'' Poster presented at the International Hearing Aid Research Conference (IHCON 2000), Lake Tahoe, CA, August, 2000.

Egan, J. P., and Hake, H. W. (**1950**). ''On the masking pattern of a simple auditory stimulus,'' J. Acoust. Soc. Am. **22**, 622–630.

Fletcher, H., and Galt, R. H. (**1950**). ''The perception of speech and its relation to telephony,'' J. Acoust. Soc. Am. **22**, 89–151.

French, N. R., and Steinberg, J. C. (**1947**). ''Factors governing the intelligibility of speech sounds,'' J. Acoust. Soc. Am. **10**, 90–119.

Goshorn, E. L., and Studebaker, G. A. (**1994**). ''Effects of intensity of speech recognition in high- and low-frequency bands,'' Ear Hear. **15**, 454–460.

Hohmann, V., and Kollmeier, B. (**1995**). ''The effect of multichannel dynamic compression on speech intelligibility,'' J. Acoust. Soc. Am. **97**, 1191–1195.

Kent, R. D., Wiley, T. L., and Strennen, M. L. (**1979**). ''Consonant discrimination as a function of presentation level,'' Audiology **18**, 212–224.

Levitt, H., and Resnick, S. B. (**1978**). ''Speech reception by the hearing impaired: Methods of testing and the development of new tests,'' Scand. Audiol. Suppl. **6**, 107–130.

Miller, G. A., and Nicely, P. A. (**1955**). ''An analysis of perceptual confusions among some English consonants,'' J. Acoust. Soc. Am. **27**, 338–352.

Moore, B. C. J., and Glasberg, B. R. (**1987**). ''Formulae describing frequency selectivity as a function of frequency and level and their use in calculating excitation patterns,'' Hear. Res. **28**, 209–225.

Moore, B. C. J. (**1996**). ''Perceptual consequences of cochlear hearing loss and their implications for the design of hearing aids,'' Ear Hear. **17**, 133–160.

Moore, B. C. J. (**1999**). ''Benefits of linear amplification and multichannel compression for speech comprehension in backgrounds with spectral and temporal dips,'' J. Acoust. Soc. Am. **105**, 400–411.

Nabelek, I. (**1983**). ''Performance of hearing-impaired listeners under various types of amplitude compression,'' J. Acoust. Soc. Am. **74**, 776–791.

Pearsons, K. S., Bennett, R. L., and Fidell, S. (**1977**). ''Speech levels in various noise environments'' (Bolt, Beranek and Newman, Inc. Contract No. 68-01-2466), Washington, DC (Environmental Protection Agency EPA-600/1-77-025).

Plomp, R. (**1994**). ''Noise, amplification, and compression: Considerations of three main issues in hearing aid design,'' Ear Hear. **15**, 2–12.

Pollack, I., and Pickett, J. M. (**1958**). ''Masking of speech by noise at high sound levels,'' J. Acoust. Soc. Am. **30**, 127–130.

Souza, P. E., and Bishop, R. D. (**1999**). ''Improving speech audibility with wide dynamic range compression in listeners with severe sensorineural hearing loss,'' Ear Hear. **20**, 461–470.

Souza, P. E., and Turner, C. W. (**1998**). ''Multichannel compression, temporal cues, and audibility,'' J. Speech Hear. Res. **41**, 315–326.

Studebaker, G. (**1985**). ''A ''rationalized'' arcsine transform,'' J. Speech Hear. Res. **28**, 455–462.

Studebaker, G. A., Scherbecoe, R. L., McDaniel, D. M., and Gwaltney, C. A. (**1999**). ''Monosyllabic word recognition at higher-than-normal speech and noise levels,'' J. Acoust. Soc. Am. **105**, 2431–2444.

Tillman, T., and Carhart, R. (**1966**). ''An expanded test for speech discrimination utilizing CNC monosyllabic words: Northwestern University Audi-

tory Test No. 6,'' Technical Report No. SAM-TR-66-55, USAF School of Aerospace Medicine, Brooks Air Force Base, TX.
Van Tasell, D., and Trine, T. (**1996**). ''Effects of single-band syllabic amplitude compression on temporal speech information in nonsense syllables and in sentences,'' J. Speech Hear. Res. **39**, 912–922.
Verschuure, J., Benning, F., Van Cappellen, M., Dreschler, W., and Boeremans, P. (**1998**). ''Speech intelligibility in noise with fast compression hearing aids,'' Audiology **37**, 127–150.
Verschuure, J., Maas, A. J. J., Stikvoort, E., de Jong, R. M., Goedegebure, A., and Dreschler, W. A. (**1996**). ''Compression and its effect on the speech signal,'' Ear Hear. **17**, 162–174.
Verschuure, H., Prinsen, T. T., and Dreschler, W. A. (**1994**). ''The effects of syllabic compression and frequency shaping on speech intelligibility in hearing impaired people,'' Ear Hear. **15**, 13–21.
Wang, M. D., and Bilger, R. C. (**1973**). ''Consonant confusions in noise: a study of perceptual features,'' J. Acoust. Soc. Am. **54**, 1248–1266.
Yund, E. W., and Buckles, K. M. (**1995a**). ''Multichannel compression hearing aids: Effect of number of channels on speech discrimination in noise,'' J. Acoust. Soc. Am. **97**, 1206–1223.
Yund, E. W., and Buckles, K. M. (**1995b**). ''Enhanced speech perception at low signal-to-noise-ratios with multichannel compression hearing aids,'' J. Acoust. Soc. Am. **97**, 1224–1240.

Modeling the motion of the internal tongue from tagged cine-MRI images

Maureen Stone[a)]
Division of Otolaryngology, University of Maryland School of Medicine, 16 South Eutaw Street, Room 525, Baltimore, Maryland 21201

Edward P. Davis and Andrew S. Douglas
Department of Mechanical Engineering, Johns Hopkins University, 3400 North Charles Street, Baltimore, Maryland 21218

Moriel NessAiver and Rao Gullapalli
Department of Radiology, University of Maryland School of Medicine, 22 North Greene Street, Baltimore, Maryland 21201

William S. Levine
Department of Electrical Engineering, University of Maryland, A. V. Williams Building, College Park, Maryland 20740

Andrew Lundberg
Department of Computer Science, Johns Hopkins University, 3400 North Charles Street, Baltimore, Maryland 21218

(Received 19 April 1999; accepted for publication 30 November 2000)

A new technique, tagged Cine-Magnetic Resonance Imaging (tMRI), was used to develop a mechanical model that represented local, homogeneous, internal tongue deformation during speech. The goal was to infer muscle activity within the tongue from tissue deformations seen on tMRI. Measurements were made in three sagittal slices (left, middle, right) during production of the syllable /kɑ/. Each slice was superimposed with a grid of tag lines, and the approximately 40 tag line intersections were tracked at 7 time-phases during the syllable. A local model, similar to a finite element analysis, represented planar stretch and shear between the consonant and vowel at 110 probed locations within the tongue. Principal strains were calculated at these locations and revealed internal compression and extension patterns from which inferences could be drawn about the activities of the Verticalis, Hyoglossus, and Superior Longitudinal muscles, among others. © *2001 Acoustical Society of America.* [DOI: 10.1121/1.1344163]

PACS numbers: 43.70.Aj, 43.70.Bk [AL]

I. INTRODUCTION

It is difficult to measure the movements of local regions within the human tongue during speech and determine their effect on the tongue surface. It is useful to do so, however, because the human tongue has a complicated musculature that is not easily reconciled with the deformation patterns seen on the tongue surface during speech. Moreover, the relationship between muscle activity and surface deformation is an important component in understanding how speech is controlled and how it is disrupted in various disorders. As a first step, the model and data presented here are intended to add details about the local kinematics of the tongue during speech. By interpolating the deformation of the tongue between observed MRI tag-points in a reference (consonant) and deformed (vowel) state, detailed information on the (2D) strain and in-plane muscle contraction was obtained. This allowed us to investigate tissue deformation patterns and infer related muscle activity.

There is a small body of material detailing the activity of the internal tongue using tagged Magnetic Resonance Imaging. These data have been used to predict tongue muscle contractions for rest-to-vowel motion (Niitsu *et al.*, 1992; Kumada *et al.*, 1992; Dang and Honda, 1997) and nonspeech movements (Napadow *et al.*, 1999a, 1999b). Some anatomical information on tongue muscles is also available from dissections and histological studies (Abd-El Malek, 1939; Carpentier and Pajoni, 1989; Doran, 1975; Miyawaki, 1974; Shawker *et al.*, 1984; Takemoto, 2001).

Electromyography (EMG) data are another source of muscle information (Miyawaki, 1975; MacNeilage and Sholes, 1964; Sauerland and Mitchell, 1975). Within the tongue, however, EMG data are difficult to collect and interpret due to substantial muscle interdigitation, cross-talk, diffuse fiber distribution of the muscle of interest (Perlman *et al.*, 1989) and fatigue (Faber and Raphael, 1989). Promising work has used EMG to predict articulator movements

[a)]Electronic mail: mstone@umaryland.edu

from speech motor commands (Honda and Kusakawa, 1997), and has compared EMG to tongue configurations (MacNeilage and Sholes, 1964; Maeda and Honda, 1994; Niimi *et al.*, 1994), and acoustic spectra in vowels (Maeda and Honda, 1994; Baer *et al.*, 1988). Nonetheless, EMG is not a commonly used instrument, because it is unpleasant, invasive, and difficult to interpret. Tagged MRI could supplement EMG if it successfully represented tongue muscle contraction.

Soft tissue such as tongue musculature is generally regarded as volume preserving (Fung, 1993). Therefore, tongue motion is the result of local tissue distortion (without volume change). Since muscle activation is contractile in nature, there is an associated elongation of tissue in the direction transverse to the primary contraction. By measuring the local tongue deformation, principal stretches and their associated directions can be determined. Using our knowledge of tongue anatomy, these directions can be compared with the orientation of the musculature to deduce which muscles locally are active during a particular phase of tongue motion. These inferences can provide important information about the neural control and muscle activation in both normal and disordered speakers. In the present study, a simple model of one plane of the tongue was developed based on a finite-element type mesh derived from the movement of tagged Cine-Magnetic Resonance Imaging (tMRI) tag-points. The modeled plane could be probed at regions of any size and principal strains could be calculated for that region.

Four concepts are necessary to keep in mind when examining how MRI tagging is accomplished. First, only the spins aligned along the Z axis can become excited by the applied rf energy. Second, only the spins on the XY or transverse plane can produce an MRI signal. Third, the signal that corresponds to a single pixel in the image is actually the vector sum of more than 1015 spins. That signal can be destroyed by causing the spins in a single pixel to lose phase coherency. Fourth, the time necessary for the spins to realign along the Z axis is measured in hundreds of milliseconds (ms). Tag lines are stripes of tissue that have been tipped onto the XY plane and then forced to become dephased, temporarily destroying their ability to produce a coherent signal. A simplified description of how this is accomplished follows.

First, apply an rf pulse that tips all spins in a plane by 45°. Next apply a linear magnetic gradient along one direction in the imaging plane, temporarily changing the resonance frequency of these excited spins, resulting in an accumulation of phase along that direction, say ten complete cycles across the field of view (FOV). There are now ten lines that have the same phase (call it 0°) immediately after the 45° rf pulse and ten lines in between that are 180° out of phase. Now apply a second rf pulse of $-45°$. Those spins with 0° phase will be tipped back up to the Z axis, those with 180° phase will be tipped a total of $-90°$ down onto the XY plane. Finally, another large gradient is applied that totally dephases all of the spins on the XY plane. These spins are no longer producing a coherent signal and cannot be re-excited until they have recovered a significant portion of their Z magnetization. The process lasts on the order of a few ms, producing alternating regions of tissue that produce no signal or full signal. The number of bands, and hence the distance between dark stripes, is determined by the strength and duration of the gradient between the two rf pulses. A dark grid is applied by first laying down horizontal lines (x axis) followed by vertical lines (y axis). Once these tag lines of little or no signal have been created, a standard cine (motion) imaging sequence can be used to track the motion and deformation of the tag lines.

Deformation models have been developed for the heart, which include circumferential shortening and stretching of the ventricles, allowing tagged Cine-MRI (tMRI) to study myocardial deformation (cf. McVeigh, 1996; McVeigh and Atalar, 1992). tMRI of the heart provides displacement and motion of discrete points, allowing computation of principal strains and directions. The heart differs from the tongue, however, in important ways. The heart has relatively simple, repetitive, kinematics that do not vary much with cardiac contractility, stroke volume, preload, or afterload. Consequently there is no regional variation (except in the case of infarction). Heart beats are highly repeatable and are independent of the rate of contraction (Douglas *et al.*, 1991). Heart beat cycles are easily synchronized temporally to the electrocardiogram (ECG) because the heart produces a large electrical depolarization (R-wave peak) immediately prior to contraction.

What is different about this study of the tongue is that it examines a soft tissue structure with highly variable and complex deformation caused by the differential stimulation of an anatomically highly complex (architecturally) musculature. The small rapid internal movements of the tongue used in speech provide a challenge for the tMRI procedure, since it has a fairly poor temporal (18 Hz) and spatial (1.9 mm$\times$1.9 mm$\times$7.0 mm) resolution. This study, therefore, was an experimental application of tMRI to speech, to determine the extent to which small speech movements could be resolved. Measurements were made of the small deformations internal to the tongue during CV syllables for evidence of regional activity that reflected specific muscle contractions.

The goal of this study was to show the application of tMRI and a fairly simple model of tongue deformation as a means of illustrating internal tongue stretch and inferring muscle activity during speech. The tMRI procedure and local model presented here identified the direction and extent of stretch at local tissue points. From the stretch and shear data local principal strains were calculated and underlying muscle contraction patterns were inferred. Because of the experimental nature of this method the model was applied only to a limited, preliminary data set.

II. METHODS

A. Subject and speech materials

A 19-year-old male, native speaker of English demonstrated the application of the model. The subject had no den-

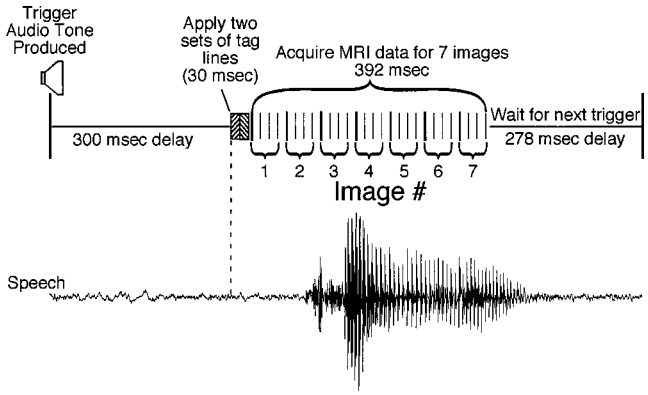

FIG. 1. Procedure for producing a tag and measuring seven time-phases during each repetition.

tal fillings that might interfere with the MRI magnetic field. The speech materials were the syllable /kɑ/. A standard MRI head coil was used to record the MRI data and also position the head. There appeared to be no extraneous head motion (see Sec. I D below). Three tMRI slice sequences were collected in the left, middle, and right sagittal planes. The syllable /kɑ/ was repeated 32 times per slice, or 96 times in total. The spatial quality of the image depended on the ability of the subject to repeat the syllable accurately 96 times on cue, at one per second. An ECG simulator triggered a tonal cue at the *R*-wave peak of the ECG simulator and created the tags 300 ms later (Fig. 1). At a later date, an audio recording was made as the subject repeated the syllable 16 times to the beat of a metronome. Acoustic analysis showed that the /k/ release occurred a mean of 534 ms (s.d. 37) after the acoustic cue, suggesting that the first data frame was collected within or before the stop, with the tongue pre-positioned in consonantal position. Visual inspection of the tMRI data during collection indicated that the tongue began moving downward in the second or third time-phase, with the maximum tongue position always in the first time-phase.

B. Instrumentation and data collection

A Picker 1.5 Tesla Edge System collected the data using tagged Cine-MRI. The subject lay supine in the MRI scanner with the neck coil positioned to image the area from the lower nasal cavity to the upper trachea. Three sagittal slices, left (L), middle (M), and right (R), were collected. During each syllable repetition, 7 time-phases were recorded at 56 ms per time-phase, or the equivalent of 18 samples per second (Fig. 1). The signal emitted by the protons, in a single time-phase in a single slice, was summed across multiple repetitions of the same syllable producing a single image-sequence of 7 time-phases per syllable, i.e., a cyclic sequence of the C-to-V motion. The first four time-phases are displayed in Fig. 2, showing the movement from /k/ to /ɑ/.

A SPAMM-like procedure (Spatial Modulation of Magnetization prior to imaging) (Axel and Dougherty, 1989a, 1989b) was used with the following parameters: a gradient echo with an echo time of 4.6 ms and a repetition time of 14 ms, a phase encode group size of 4, a field of view of 24 cm, and a slice thickness of 7 mm. A series of five rf pulses was used, with relative amplitudes of $[+1-4+6-4+1]$ to produce sharp dark tag lines separated by a distance of 11 mm. This complex rf pulse was applied sequentially to the *x* and *y* axis taking a total time of 30 ms, and resulting in a grid of horizontal and vertical tag lines. Seven time-phases (56 ms each) were recorded during the succeeding 392 ms as the tongue moved into the vowel (see Fig. 1). Therefore, the one second repetition time is allotted to a time lag of 300 ms between the trigger and the tag, a period of tag onset and decay lasting about 420 ms (which includes creating the tags and the 7 time-phases), and a final period (about 280 ms) devoted to looking for the next trigger.

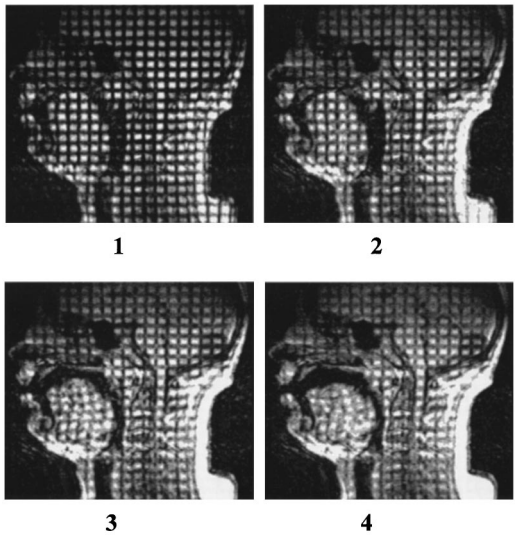

FIG. 2. MRI image sequence of the first four frames in the /k/ to /ɑ/ motion. (a) is the /k/ and (d) is the /ɑ/. (b) and (c) are the transitional frames.

Thirty-two repetitions were needed for reconstruction of the 7 time-phases in a single plane, because only 4 of the 128 lines of *k*-space were acquired per repetition $(128/4=32)$. It should be noted that *k*-space is Fourier or frequency-based space. The third line in each group of four contained the high frequency or edge definition material. By not collecting fewer lines of *k*-space at each sweep we sacrificed some edge definition and temporal resolution. The gain was reduced syllable repetitions and subject fatigue. A similar collection process was done without tagging by Masaki *et al.* (1999). That study differed from the present one in three ways. First, their temporal resolution was 25 ms and ours 56 ms. Second, their acquisition required 128 repetitions for each slice while ours used 96 repetitions for three slices. Third, they were only able to look at gross anatomical features; the use of tagging lines in this paper enabled us to look at deformation of the tongue tissue with a resolution of roughly 2 mm.

In tMRI images, the intersection of the tag lines are material points that move with the tissue. Based on the motion of these discrete points, the motion of the entire tongue was interpolated using the same low-order polynomials that are employed in finite element analysis (Cook *et al.*, 1989). Movement of the tongue normal to the sagittal plane was assumed to be insignificant at midline, and indeterminate in the parasagittal slices without 3D data.

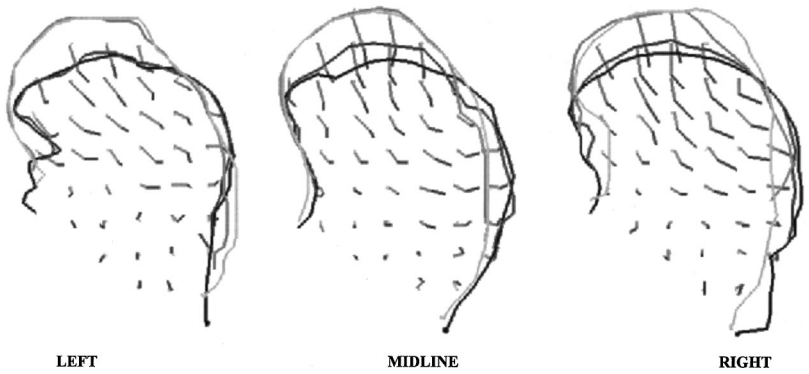

FIG. 3. Time course of tag movement for first four time-phases of the /k/ to /ɑ/ movement. Line color progresses from light gray (/k/) to black (/ɑ/) over time. All MRI based figures are oriented with the tongue tip on the left.

C. Internal measurement and modeling

The intersections of tag-lines with each other and with the tongue surface were measured for all time-phases between the consonant and vowel and stored as *xy* coordinates. There were about 40 intersections or ''tag-points'' in each image. The lowest anterior point of the tongue was defined as the intersection of the inferior-posterior edge of the jaw (black) and the nearest horizontal tag line in the tongue [Fig. 2(a)]. The bone of the jaw is black and the marrow within the jaw is light gray. It is possible that the black region anterior to the tongue included air from the sublingual cavity. If the black area were air (i.e., soft tissue unattached) more motion would be expected in the adjacent tongue region than if the black were bone (soft tissue attached). Air cannot be distinguished from bone on MRI images, so the black area could not be better defined. Movement of the lower tongue, especially the anterior region, was quite small (Fig. 3) suggesting a bony attachment. The lowest posterior point was defined similarly as the intersection of the inferior–posterior surface of the epiglottis with the nearest horizontal tag line.

Once the anterior and posterior tag-points were specified at the base of the tongue, all the tags were tracked across the sequence. We were consistent in the points chosen across time-phases. The experimenter was assisted in tracking the points by (1) observing tag position in the preceding and following time-phases and (2) digitally superimposing the reference tag-points on the current image. Measured points were within the tongue proper, that is, above the jaw-opening muscles, which were brighter than the tongue. As the tags decayed, muscle distinctions became clearer. Therefore, after all the time-phases were measured, the base of the tongue was determined on the vowel images [Fig. 2(d)]. Tags on previous time-phases were then added or deleted to equalize the number of points on all images within a single image sequence. The vowel frame was defined as the last time-phase before the posterior tongue surface changed direction back toward the consonant, and was typically the third, fourth, or fifth time-phase. Different portions of the tongue do not reach maximum vowel position at the same time. Our criterion was for the back of the tongue to reach maximum. Due to the long time-phase, 56 ms, the entire tongue usually appeared to reach maximum in a single frame.

As the tongue moved between two sounds the tags deformed, reflecting the internal tissue deformation. Principal strains were calculated on the extreme consonant and vowel shapes, because the intervening movements were too small to rule out measurement error.

1. Deformation model

The extreme consonant (reference) and vowel (deformed) tag-points were modeled using principal strains. While these intersection points were treated as tissue points in the plane, they actually represent the motion of a volume with a depth of 7 mm perpendicular to the image plane. Nodal motion therefore represented an average of the tongue motion across that region. In the reference state the nodes had coordinates (X_j, Y_j). In the deformed state k (where $k=1,...,7$ indicating which of the time phases was being examined) the nodes had coordinates $(x_j^{(k)}, y_j^{(k)})$.

The two in-plane displacement components, $u_j = u(X_j, Y_j) = x_j^{(k)} - X_j$ and $v_j = v(X_j, Y_j) = y_j^{(k)} - Y_j$, were calculated at each node. A finite-element type mesh, made up of triangular and quadrilateral elements, was created from these nodes. The details of the node point identification algorithms and point-tracking procedures can be found in Davis (1999). Displacement of any arbitrary points within the tongue was calculated from the finite-element type basis functions, $\phi_j(X,Y)$ and the displacements measured (u_j, v_j) at each associated node. These basis functions have the characteristic that $\phi_i(X_j, Y_j) = \delta_{ij}$, where δ_{ij} is the Kronecker delta defined by $\delta_{ij}=1$ if $i=j$ and $\delta_{ij}=0$ if $i \neq j$.

First the number of closest nodes, N, was found which defined the quadrilateral $(N=4)$ or triangular $(N=3)$ element in which any generic point was located. Second, the N closest nodes, (X_j, Y_j), $j=1,...,N$, were used to define the basis functions, $\phi_j(X,Y)$ in that element (Cook *et al.*, 1989). The displacement of any point in an element could then be found using the known displacements, u_j and v_j, and the basis functions $\phi_j(X,Y)$ from

$$u(X,Y) = \sum_{j=1}^{N} u_j \phi_j(X,Y)$$

and (1)

$$v(X,Y) = \sum_{j=1}^{N} v_j \phi_j(X,Y).$$

2. Computing deformation, stretch and strain

This principal strain model gives the simplest possible kinematic interpretation to local tongue deformations. The tag displacements can be computed from Eq. (1), and we can find the in-plane components of the displacement gradient tensor, **H**, namely

$$
\begin{aligned}
H_{11} &= \frac{\partial u(X,Y)}{\partial X} = \sum_{j=1}^{N} u_j \frac{\partial \phi_j(X,Y)}{\partial X}, \\
H_{22} &= \frac{\partial v(X,Y)}{\partial Y} = \sum_{j=1}^{N} v_j \frac{\partial \phi_j(X,Y)}{\partial Y}, \\
H_{12} &= \frac{\partial u(X,Y)}{\partial Y} = \sum_{j=1}^{N} u_j \frac{\partial \phi_j(X,Y)}{\partial Y}, \\
H_{21} &= \frac{\partial v(X,Y)}{\partial X} = \sum_{j=1}^{N} v_j \frac{\partial \phi_j(X,Y)}{\partial X},
\end{aligned}
\tag{2}
$$

where $\phi_j(X,Y)$ and the derivatives of $\phi_j(X,Y)$ are known everywhere in any element.

Principal strains and their directions can be computed from the two eigenvalues, E_i, and their associated eigenvectors, $\mathbf{N}_i$, of the in-plane Lagrangian strain tensor, $\mathbf{E} = \frac{1}{2}[\mathbf{H}\mathbf{H}^T + \mathbf{H}^T\mathbf{H}]$. The stretch, $\lambda_{\mathbf{M}}$, in any direction, **M**, can be computed from the relationship $\lambda_{\mathbf{M}} = \sqrt{2\mathbf{M}\cdot\mathbf{E}\mathbf{M}+1}$ (Lai *et al.*, 1993, p. 134).

D. Measurement error and repeatability

Three possible sources of error affect the MRI measurements. The first source is image quality, and includes spatial and temporal resolution of the image, as well as magnetic distortion due to tagging. The second is human measurement error, and the third is speaker variation, specifically speech precision and head movement.

Spatial resolution of the acquired MRI image, was based on a 128×128 pixel grid. Resolution was increased to 256 ×256 in the raw image by zero filled Fourier interpolation. Pixel to mm conversion was calculated by dividing the field of view (240 mm) by the number of pixels (256). One displayed pixel, therefore, equaled 0.95 mm. Thus the minimum resolvable movement, absent gray scale, was 2 pixels or 1.9 mm.

The temporal resolution was reduced by the large time window. The time window (56 ms/time-phase) meant that tongue movement might cause blurring of the surface in an image. The magnetic disturbance of the tags caused frames with newly laid tags (consonants) to have better tag quality, and poorer surface clarity, than later frames (vowels) where the tags have decayed (see Fig. 2). Poor image clarity increases human measurement error. Human measurement error was assessed by having a second judge re-measure the tag-points in the midline /k/ and /ɑ/ time-phases. For the consonant frame, the average (maximum) error value was $x = 0.5$ (0.95) mm, and $y = 0.5$ (1.9) mm. For the vowel frame the average and maximum errors were larger: $x = 1.4$ (4.8) and $y = 1.8$ (6.6) mm. These numbers reflect human measurement error, image resolution and speaker precision.

Speaker contributions to error included temporal precision (discussed in Sec. II A above) and extraneous head motion. The latter was considered, because the head coil limited but did not preclude head motion. Six specific tag-points, three vertical and three horizontal, were measured in the brain portion of the image of the consonant and vowel time-phases. Five of the six points differed by one pixel, the sixth differed by one in each direction. These differences were within the measurement error indicating no evidence of C-to-V head motion.

III. DATA APPLICATION

A natural use of the principal strain model is to infer activity of tongue muscles from regions of compression. This is done by measuring the tag-points consistent with the muscles' lines of action in the consonant (reference) and vowel (deformed) time-phases. A wire mesh of both data sets is created by applying the deformation model and calculating in-plane principal strains throughout the tongue. The patterns of compression are then examined for patterns reflective of muscle contraction.

A. Tag-point measurements

Tag-points were measured in all four time-phases from /k/ to /ɑ/ (Fig. 3). In all images the tongue tip is on the left. The figures show time-lapse movement of the individual tags with the first time-phase (/k/) in gray and the last (/ɑ/) in black. The tag trajectories depict local differences in motion. For example, the midsagittal slice shows directional differences; the top third moves downward and the central third backward. The local motion also differed in range; the top moved farther than the center.

B. Wire mesh deformation grids

Tag-point wire mesh grids for left, middle and right slices of the /k/-to-/ɑ/ deformation appear below (Fig. 4). This figure, and the derived strains (Fig. 5), cannot be directly compared to Fig. 3. These figures present deformations of tag grid cells (four points), not single tag-points, and are observed only at the extreme consonant and vowel position. The intervening time-phases are not considered. The grids are made by connecting with straight lines all the tag-points, including surface tag-points, which are the intersections of the tag lines with the surface. This is why the surfaces of Fig. 4 look angular. The in-plane grids for the /k/ and /ɑ/ contain the same tissue points; the differences are due to changes in the shape of the tongue. For viewing convenience, four cells have been shaded on each grid, indicating local deformation at the top, central, back, and bottom regions. An uncompressed cell is 1.1 cm per side.

In Fig. 4 the top lowered substantially in all three slices (gray to black). The posterior tongue moved backward about half that amount. The upper-back was lower for /k/-L,M than /k/-R (gray). The shaded cells in the center exhibit horizontal expansion, shear, and vertical compression, especially on the right (black square). The topmost cells compressed and lowered vertically, while the upper-back rotated. The bottom showed some horizontal expansion.

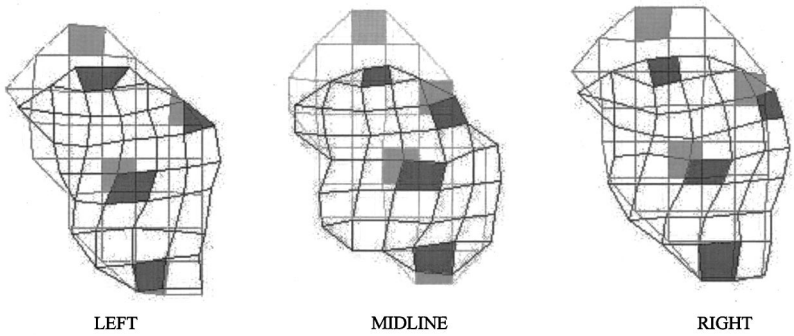

FIG. 4. Wire mesh representations of /k/ (gray) and /ɑ/ (black) for left, middle, and right slices.

C. Principal strains

Once the model was developed, principal strains could be calculated for any portion of the tongue, cover any size area, and reflect the strain at that location. Principal strains were computed at 110 locations in the tongue. The strain at each location was derived from the tag-based model. Principal strains for /kɑ/ appear in Fig. 5. Gray indicates extension and black compression.

The lower third of the tongue compressed primarily downward and backward accompanied by upward and backward extension. The middle tongue compressed vertically and extended horizontally a small amount; the top compressed inwardly. In all three slices the tip extended: forward at midline, forward/upward at left and right. On the left a band of tags just below the tongue surface compressed lengthwise, parallel to the tongue surface (black lines). On the right the two surface tag rows also were distinct from the deeper tags by being more greatly compressed (see Fig. 5). The location and direction of local compression could be compared to the anatomy seen in Fig. 6.

IV. DISCUSSION

The present study is the first to use tagged Cine-MRI to mathematically model tongue muscle activity during speech, although Napadow *et al.* (1999a, b) used a similar procedure to study the midsagittal tongue during swallowing and nonspeech movements. Several features of the present study differ from other speech studies. First, previous studies have examined the midsagittal plane and inferred muscle action through visual inspection. Niimi *et al.* (1994) visually inspected midsagittal MRI tag line deformations and hypothesized muscle contraction. Kumada *et al.* (1992) and Niitsu *et al.* (1994) drew lines manually on midsagittal slices to connect deformed tag-points. From these they inferred active muscles. In the present study, principal strains modeled regional homogeneities and allowed inference of underlying muscle contraction patterns. The second feature was the choice of a consonant as the reference shape. The above studies used rest as the reference position, but rest position is variable, because it is not constrained by any acoustic requirements, and the starting position of the tongue affects what muscles are used to achieve the end position. The present study used /k/ because it is an extreme shape and requires a specific downward movement into the vowel. The third feature is that the present study used Cine-MRI, which allowed us to choose the target frame from an actual motion sequence, rather than examine the deformation from one sustained position to another.

A. Internal segments and muscle activity

This study extracted principal strains for small local tongue regions in an effort to expose compression patterns consistent with lines of action of possible tongue muscle contractions. The wire mesh grids (Fig. 4) depict local deformations; the principal strains (Fig. 5) reflect local tissue compression and expansion. Muscle lengthening (expansion) must always be passive, because active muscle contraction causes shortening. Muscle shortening, however, can be due to active muscle contraction, or to passive compression of the tissue. In addition, the tongue is globally and locally volume preserving, i.e., tissue cannot be increased or decreased, only relocated. Therefore, when both in-plane strains at a single point indicate compression, extension must have occurred orthogonally to the slice, i.e., in the cross-sectional, or lateral plane.

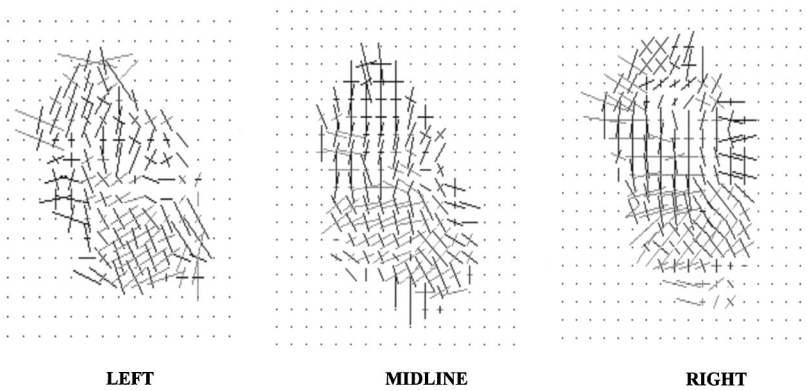

FIG. 5. Principal strains for the /k/ to /ɑ/ deformation for left middle and right slices. Black lines indicate local tissue compression and gray indicate local expansion.

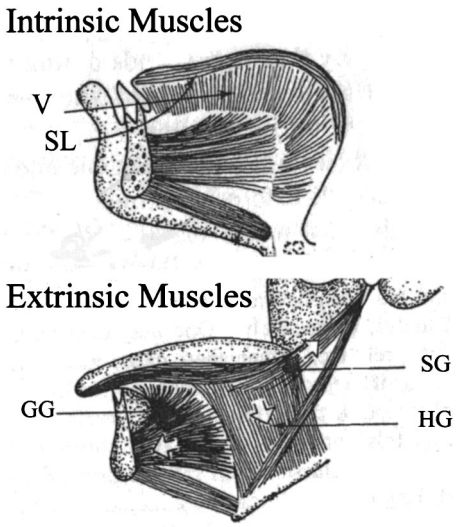

FIG. 6. Muscles of the tongue: Superior Longitudinal (SL), Verticalis (V), Genioglossus (GG), Styloglossus (SG), and Hyoglossus (HG). From Dew and Jenson, *Phonetic Processing*, 1977, pp. 92–93.

In Fig. 5, the principal strains isolated several local regions: the lower third, the upper tongue and the circumference. These regions were used to predict the role of specific muscles in the deformation. First, consider the lower third of the tongue. The downward and backward compression seen in the lower third of the tongue (Fig. 5) is consistent with Hyoglossus (HG) muscle contraction (Fig. 6). Next consider the upper tongue in Fig. 5. Compression here was almost uniformly vertical, particularly at midline and right, consistent with Verticalis contraction (Fig. 6). Verticalis fibers interdigitate completely with several other muscles and so cannot be isolated using EMG. As a result, the muscle does not always appear in tongue muscle models (cf. Dang and Honda, 1997; Honda and Kusakawa, 1997), or its role is based on anatomy, not physiology (Perkell, 1974; Wilhelms-Tricarico, 1995). The vertical compression in the middle and upper tongue was sharply separated spatially from the backward compression of the lower third. This spatial distinction greatly reduces the likelihood that HG alone lowered and backed the tongue, and strongly supports Verticalis contraction as a part of a rapid tongue lowering gesture for /kɑ/. Contracting both muscles would increase the rate and distance of surface lowering compared to HG alone.

The third region that acted as a unit was the circumference of the tongue—the outer two rows of tags. On the left particularly, circumferential shortening of the tongue surface was consistent with contraction of the Superior Longitudinal muscle (SL), as can be seen in the strains of the left side (Fig. 5). SL (see Fig. 6) may have as many as three roles in tongue movement. First, SL contraction shortens the tongue, because it is a lengthwise muscle (Kier and Smith, 1985). Since the tongue surface is curved in the sagittal plane, SL contraction should shorten tongue length circumferentially from the tongue tip to the hyoid. Second, SL, in combination with Genioglossus Anterior, can elevate the tongue tip (Napadow *et al.*, 1999b, p. 4; Smith and Kier, 1989; Thexton *et al.*, 1998). To cause upward curling, GGA contraction would locally stiffen the tongue behind the tip, which is consistent with the small concavity often seen in /ɑ/. At the same time, SL would compress the upper surface longitudinally. This must be done without simultaneous compression of the lower surface (Inferior Longitudinal) or the tongue will merely shorten (Kier and Smith, 1986). In the present data, the tongue tip expanded horizontally at midline, and obliquely on the sides, orthogonal to and consistent with SL activity. This expansion, however, did not result in tongue tip protrusion or elevation (Fig. 4), because other muscles pulled the entire tongue backward and downward. As a third role for SL, we propose that contraction of the orthogonal SL and Verticalis fibers might create a ''belt'' that stiffens the tongue circumference and reduces its degrees of freedom. A belt could be used to resist outward expansion. Resistance to expansion was inferred from the strains in the back two rows of the rear tongue, which rarely extended horizontally despite the backward movement of /ɑ/ (Fig. 5). One cannot completely discount, however, the possibility that this, or any of the other strains, is due to passive compression created indirectly by the contraction of other muscles or to the supine position.

Genioglossus anterior (GGA) has long been associated with local depressions of the anterior tongue. For example, in tMRI images, Niimi *et al.* (1994) attributed downward motion from rest-to-/ɑ/ to GGA. Their data exhibited a depression posterior to the tip. Considerable ultrasound data has shown the same depression in /ɑ/ (cf. Stone and Lundberg, 1996). More importantly, Davis *et al.* (1996) found that for steady state /ɑ/ the local depression behind the tip could be modeled as a shear deformation consistent with GGA contraction. Anatomy studies also have found that GGA fibers do not curve forward or extend into the tip (Takemoto, 2001). Contraction of fibers oriented vertically and inserting behind the tip will lower the surface immediately posterior to the tip, facilitating tip elevation. Figure 4, in the current data, showed vertical compression behind the tongue tip that was in agreement with GGA fiber direction. Inspection of the midsagittal compression lines (Fig. 5), however, did not disclose trajectories directly following the fibers of GGA. The strains did not distinguish the local depression from the general lowering of the upper surface, perhaps because the direction of action of Verticalis and GGA are virtually identical in the midline upper tongue. In the lower tongue, some support for GGA involvement was seen. Backward compression, due to HG contraction, was less pronounced in the anterior two-thirds of the lower midline tongue than in the left and right slices. GGA activity may have caused this attenuation. Measurement of additional tasks and subjects, and increased tMRI resolution, will create a database of internal tongue strains that can be interpolated and interpreted with more confidence.

B. Does the tongue surface reflect internal tag deformation patterns?

The surface and tag movements of Fig. 3 were compared. The tags tracked movement of specific tissue points at the surface and within the tongue. The upper surface of the tongue moved downward and the posterior surface moved backward. The internal tag movements of the upper tongue

were consistent with the movement of the upper surface and the tag movements of the middle tongue with the back surface. With a larger quantity of data and consistent associations, surface and internal relationships might be compiled in a standard reference table. Such a table would be useful in mapping normal muscle-to-surface relationships, and as baseline data for comparison with articulatory disorders of various origins.

Two characteristics of the internal tissue point motion supplement the knowledge gained from 2D models. The first characteristic was left-to-right asymmetry in the tag trajectories (Fig. 3). On the left, the upper tongue moved in a fairly linear path downward and backward. On the right, it moved downward and then backward. Because the data did not include the coronal and axial planes, asymmetries like this were difficult to interpret. Some asymmetries are found in normal human anatomy. Additionally, functional asymmetries could result if a muscle on one side of the tongue contracted more forcefully, or a passive pull on the tissue modified its path asymmetrically. The second characteristic of note was that the surface and tag motions were not always simultaneous. For example, in Fig. 3 the movement of the left and right tongue surface occurred primarily between time-phases 2 and 3. The upper tags, however, moved quite a bit between time-phases 3 and 4 (black). This movement may have been a passive response to the rapid surface lowering at phase 3 or a reflection of activity in other planes. True 3D volumetric data are needed to get a fully accurate representation of the internal-to-surface relationships.

V. CONCLUSIONS

This preliminary study supports the continued use of tagged Cine-MRI as a method of examining muscle activity between phonemes during speech. Data such as these can supplement EMG data, and the procedure is noninvasive. From tags measured at the intersection of horizontal and vertical tag lines, the deformation of tissue-points within the tongue were measured with a resolution of about 0.95 mm. Principal strains detailed regions of compression and extension in the tongue and were interpreted in relation to internal tongue muscle activity. Two muscles, from which it is difficult (Superior Longitudinal) or impossible (Verticalis) to acquire accurate EMG data, appeared to contract in /k/-to-/ɑ/ tongue lowering. Some evidence for GGA contraction was seen in the anterior tongue consistent with surface lowering and depression formation.

This local homogeneous model for deriving principal strains from tMRI tongue images appears promising for future examination of the tongue musculature. It enabled us to examine stretch independently from translation, to infer contraction of muscles that are difficult to access with EMG, and to hypothesize new roles for muscles from the data. We expect predictive models and additional data to improve the accuracy of these inferences.

Since this data set was collected on a single subject, and contains simplified speech material, these results cannot be generalized. Rather, they are presented to illustrate the valuable information that can be derived from a principal strain model.

ACKNOWLEDGMENTS

The authors would like to thank Michael Cohen, Rafael Laboissiere, Heni Yehia, Anders Lofqvist, and one anonymous reviewer for their helpful comments on this paper. This project was supported in part by Grant No. DC025681 from the National Institute of Deafness and Other Disorders, and Northrop Grumman, Inc.

Abd-El Malek, S. (**1939**). ''Observations on the morphology of the human tongue.'' J. Anatomy **73**, 201–210.

Axel, L., and Dougherty, L. (**1989**). ''MR imaging of motion with spatial modulation of magnetization.'' Radiology **171**, 841–849.

Axel, L., and Dougherty, L. (**1989**). ''Heart wall motion: Improved method of spatial modulation of magnetization for MR imaging.'' Radiology **172**, 349–350.

Baer, T., Alfonso, P., and Honda, K. (**1988**). ''Electromyography of the tongue muscles during vowels in /əpVp/ environment,'' Annual Bulletin of the Research Institute of Logopedics and Phoniatrics, U. of Tokyo, Vol. 22, pp. 7–19.

Carpentier, P., and Pajoni, D. (**1989**). ''The tongue: A complex muscular array,'' Rev. Orthop. Dento. Faciale **23**, 19–28 (in French).

Cook, R., Malkus, D., and Plesha, M. (**1989**). *Concepts and Applications of Finite Element Analysis* (Wiley, New York).

Dang, J., and Honda, K. (**1997**). ''A physiological model of the tongue and jaw for simulating deformation in the midsagittal and parasagittal planes,'' J. Acoust. Soc. Am. **102**, 3167(A).

Davis, E. (**1999**). ''Measurement and Kinematic Modeling of the Human Tongue,'' Ph.D. Dissertation, Department of Mechanical Engineering, Johns Hopkins University, Baltimore, MD.

Davis, E., Douglas, A., and Stone, M. (**1996**). ''A continuum mechanics representation of tongue motion in speech,'' Proceedings of the 4th International Conference on Spoken Language Processing, Philadelphia, PA, Vol. 2, pp. 788–792.

Dew, D., and Jensen, P. (**1977**). *Phonetic Processing* (Charles E. Merrill, Columbus, OH), pp. 92–93.

Doran, G. A. (**1975**). ''Review of the evolution and phylogeny of the mammalian tongue,'' Acta Anat. **91**, 118–129.

Douglas, A., Rodriguez, E., O'Dell, W., and Hunter, W. (**1991**). ''Unique strain history during ejection in canine left ventricles,'' Am. J. Physiol. **260**, H1596–H1611.

Faber, A., and Raphael, L. (**1989**). ''Relationship of recorded EMG signals to within- and cross-utterance acoustic variation,'' J. Acoust. Soc. Am. Suppl. 1 **85**, S58.

Fung, Y. C. (**1993**). *Biomechanics, Mechanical Properties of Living Tissues* (Springer Verlag, New York).

Honda, K., and Kusakawa, N. (**1997**). ''Compatibility between auditory and articulatory representations of vowels,'' Acta Oto-Laryngol., Suppl. **532**, 103–105.

Kier, W., and Smith, K. (**1985**). ''Tongues, tentacles and trunks: The biomechanics of movement in muscular-hydrostats,'' Zoological Journal of the Linnean Society **83**, 307–324.

Kumada, M., Niitsu, M., Niimi, S., and Hirose, H. (**1992**). ''A study on the inner structure of the tongue in the production of the 5 japanese vowels by tagging snapshot MRI,'' Annual Bulletin of the Research Institute of Logopedics and Phoniatrics, U. of Tokyo, Vol. 26, pp. 1–13.

Lai, W., Rubin, D., and Krempl, E. (**1993**). *Introduction to Continuum Mechanics*, 3rd ed. (Pergamon, New York).

MacNeilage, P., and Sholes, G. (**1964**). ''An electromyographic study of the tongue during vowel production,'' J. Speech Hear. Res. **7**, 209–232.

Maeda, S., and Honda, K. (**1994**). ''From EMG to formant patterns of vowels: The implications of vowel spaces,'' Phonetica **51**, 17–29.

Masaki, S., Tiede, M., Honda, K., Shimada, Y., Fujimoto, I., Nakamura, Y., and Ninomiya, N. (**1999**). ''MRI based speech production study using a synchronized sampling method,'' J. Acoust. Soc. Jpn. (E) **20**, 375–379.

McVeigh, E. (**1996**). ''MRI of myocardial function: Motion tracking techniques,'' Magn. Reson. Imaging **14**, 137–150.

McVeigh, E., and Atalar, E. (**1992**). ''Cardiac tagging with breath-hold Cine-MRI,'' Magn. Reson. Imaging **28**, 318–327.

Miyawaki, K. (**1974**). ''A study on the musculature of the human tongue,'' Annual Bulletin of the Research Institute of Logopedics and Phoniatrics, U. of Tokyo, Vol. 8, pp. 23–49.
Miyawaki, K. (**1975**). ''A preliminary report on the electromyographic study of the activity of lingual muscles,'' Annual Bulletin of the Research Institute of Logopedics and Phoniatrics, U. of Tokyo, Vol. 9, pp. 91–106.
Napadow, V. J., Chen, Q., Wedeen, V. J., and Gilbert, R. J. (**1999a**). ''Biomechanical basis for lingual muscular deformation during swallowing.'' Am. J. Physiol. **277**, G695–G701.
Napadow, V. J., Chen, Q., Wedeen, V. J., and Gilbert, R. J. (**1999b**). ''Intramural mechanics of the human tongue in association with physiological deformations,'' J. Biomech. **32**, 1–12.
Niimi, S., Kumada, M., and Niitsu, M. (**1994**). ''Functions of tongue-related muscles during production of the five Japanese vowels,'' Annual Bulletin of the Research Institute Logopedics and Phoniatrics, U. of Tokyo, Vol. 28, pp. 33–40.
Niitsu, M., Kumada, M., Niimi, S., and Itai, Y. (**1992**). ''Tongue movement during phonation: A rapid quantitative visualization using tagging snapshot MRI imaging,'' Annual Bulletin of the Research Institute Logopedics and Phoniatrics, U. of Tokyo, Vol. 26, pp. 149–156.
Perkell, J. (**1974**). ''A physiologically oriented model of tongue activity in speech production,'' Ph.D. Dissertation, Massachusetts Institute of Technology, Cambridge, MA.
Perlman, A., Luschei, E., and Dumond, C. (**1989**). ''Electrical activity from the superior pharyngeal constrictor during reflexive and nonreflexive tasks,'' J. Speech Hear. Res. **32**, 749–754.
Sauerland, E. K., and Mitchell, P. (**1975**). ''Electromyographic activity of intrinsic and extrinsic muscles of the human tongue,'' Texas Reports on Biology and Medicine **33**, 445–455.
Shawker, T., Sonies, B., and Stone, M. (**1984**). ''Sonography of speech and swallowing,'' in *Ultrasound Annual* (Raven, New York), pp. 237–260.
Smith, K. K., and Kier, W. M. (**1989**). ''Trunks, tongues, and tentacles: Moving with skeletons of muscle,'' Am. Sci. **77**, 29–35.
Stone, M., and Lundberg, A. (**1996**). ''Three-dimensional tongue surface shapes of English consonants and vowels,'' J. Acoust. Soc. Am. **99**, 3728–3737.
Takemoto, H. (**2001**). ''Morphological analyses of the human tongue musculature for three-dimensional modeling,'' J. Speech Hear. Res. (in press).
Thexton, A. J., Crompton, A. W., and German, R. Z. (**1998**). ''Transition from suckling to drinking at weaning: a kinematic and electromyographic study in miniature pigs,'' J. Exp. Zool. **280**, 327–343.
Wilhelms-Tricarico, R. (**1995**). ''Physiological modeling of speech production: Methods for modeling soft-tissue articulators,'' J. Acoust. Soc. Am. **97**, 3085–3098.

Verifying a vocal tract model with a closed side-branch

Michel Tah-Tung Jackson,[a] Carol Espy-Wilson, and Suzanne E. Boyce[b]
Department of Electrical and Computer Engineering, Boston University, 8 St. Mary's Street, Boston, Massachusetts 02215

(Received 27 January 1999; revised 3 March 2001; accepted 13 March 2001)

In this article an implementation of a vocal tract model and its validation are described. The model uses a transmission line model to calculate pole and zero frequencies for a vocal tract with a closed side-branch such as a sublingual cavity. In the validation study calculated pole and zero frequencies from the model are compared with frequencies estimated using elementary acoustic formulas for a variety of vocal tract configurations. © *2001 Acoustical Society of America.*
[DOI: 10.1121/1.1370526]

PACS numbers: 43.70.Bk, 43.70.Fq [AL]

I. INTRODUCTION

Our purpose in this article is to describe a vocal tract model using a branching transmission line to model a sublingual cavity, and its validation. As research on the acoustics of speech production proceeds, models necessarily become more complex and detailed; the verification of these models also becomes more difficult. Thorough validation of the models is required before model-based inferences (e.g., ''analysis by synthesis'') can be accepted.

The construction of the model was motivated by a desire to test the hypothesis that a sublingual cavity plays a crucial role in determining the acoustics of various apical, retroflex, and rhotic speech sounds. This hypothesis has been advanced separately in the literature for /s/ (Perkell, Boyce, and Stevens, 1979), for retroflex and sublingual stops (Ladefoged and Bhaskararao, 1983), and retroflex American English /r/ (Stevens, 1999) and is addressed further in Espy-Wilson, Boyce, Jackson, Narayanan, and Alwan (2000). As in Espy-Wilson *et al.* (2000), we assume that the sublingual cavity behaves acoustically like a ''side-branch'' off the vocal tract, at least for relatively low frequencies.

II. DESCRIPTION OF THE MODEL

The branching transmission-line model is implemented as a MATLAB-callable routine called AFSB2XFB. It is based on the VTCALCS program described by Maeda (1982), as modified for use with MATLAB numerical analysis software by Dr. Ronan Scaife at Dublin City University. It is intended to calculate the acoustic behavior of a vocal tract that includes a side-branch such as a sublingual cavity. The AFSB2XFB routine, given section lengths and area functions of the ''main'' glottis-to-lips portion of the vocal tract and a side-branch, calculates the vocal tract transfer function. The transfer function may then be searched, using numerical peak-picking routines, to determine peak (pole) frequencies. The acoustic behavior of the ''main'' tract and the side-branch is approximated using the transmission-line analog sections specified in Maeda (1982) and Espy-Wilson *et al.* (2000), Fig. 6. Each section includes terms for viscous losses, heat-conduction losses, and vocal tract wall losses, as specified in Maeda (1982). For the purposes of this Letter, the glottal end of the vocal tract was modeled with a closed termination, and an R–L circuit model was used to approximate the effect of radiation at the lips.

III. VERIFICATION PROCEDURE

In order to verify the performance of the AFSB2XFB implementation of this model, the pole and zero frequencies of two groups of tube configurations were estimated using simple tube models. The first group of configurations tests the model when the side-branch is strongly coupled to the rest of the vocal tract because the vocal tract has no constriction. These configurations are similar to some configurations observed in r-colored vowels in American English [see, for example, the cineradiographic data in Lindau (1985), especially speaker P5, Fig. 11.5]. The second group of configurations tests the model when the vocal tract has a constriction that decouples the side-branch from the back cavity of the vocal tract. These configurations are similar to the configurations observed in some /r/'s in American English [for example, Lindau (1985), especially speaker P4, Fig. 11.5; and Espy-Wilson *et al.* (2000), Fig. 3]. Unlike VTCALCS, these estimates neglect radiation effects and the effects of vibrating vocal tract walls.

Then, the model was used to calculate the frequency response of the same tube configurations, and peak and zero frequencies were determined from this frequency response. The model's *calculated* peak and zero frequencies are compared with the *estimated* pole and zero frequencies from simple tubes. The results from the model are also compared with the results from VTCALCS, since the model results from side-branches tending toward zero length and zero cross-sectional area should converge to the same results as VTCALCS.

IV. RESULTS FOR VARIOUS TUBE CONFIGURATIONS

A. Side-branch strongly coupled to main tract

This configuration is schematized in Fig. 1(a). A uniform tube with the ''glottal'' end closed and the ''labial'' end open has a side-branch (with a closed end) attached. The position, length, and cross-sectional area of the side-branch vary.

[a]Current address: 86 Spring Ave., Arlington, MA 02476. Electronic mail: ladmttj@ix.netcom.com
[b]Currently at Department of Communication Sciences and Disorders, Mail Location 379, University of Cincinnati, Cincinnati, OH 45221.

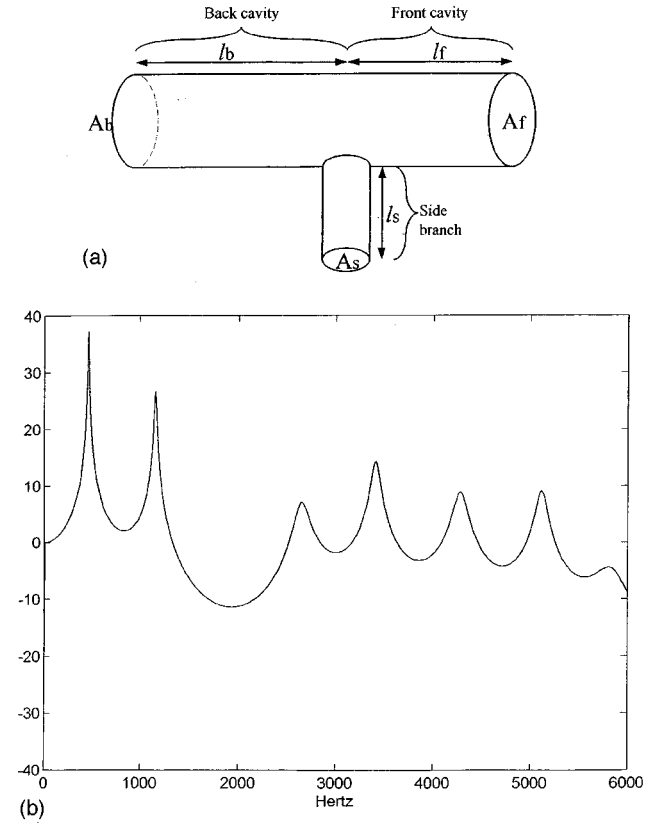

FIG. 1. (a) The tube configuration simulated in the ''strongly coupled'' models. (b) A sample plot of the calculated transfer function.

The acoustic impedance of ideal, hard-walled tubes in this configuration, as seen from the branching point, is given by Eq. (1), in which wall and other losses are neglected. The resonances of the glottis-to-lips transfer function are given by the zeros of Eq. (1),

$$Z(\omega)=A_b\tan(\omega l_b/c)+A_s\tan(\omega l_s/c)-A_f\cot(\omega l_f/c). \quad (1)$$

[Here, $Z(\omega)$ is the vocal tract impedance at the angular frequency ω, A_b, A_s, and A_f are the cross-sectional areas of the back tube, side-branch tube, and front tube, respectively; l_b, l_s, and l_f are the lengths of the same; and c is the speed of sound. In this Letter, c will be taken as 35 000 cm/s for the warm, humid air in the vocal tract.]

The side-branch produces zeros in the glottis-to-lip transfer function at the frequencies at which the acoustic impedance of the side-branch goes to zero, i.e., at the frequencies that would be the resonant frequencies of the isolated side-branch tube. This series of zero frequencies ζ_n is given by the well-known formula (2),

$$\zeta_n=(2n-1)c/4l_s. \quad (2)$$

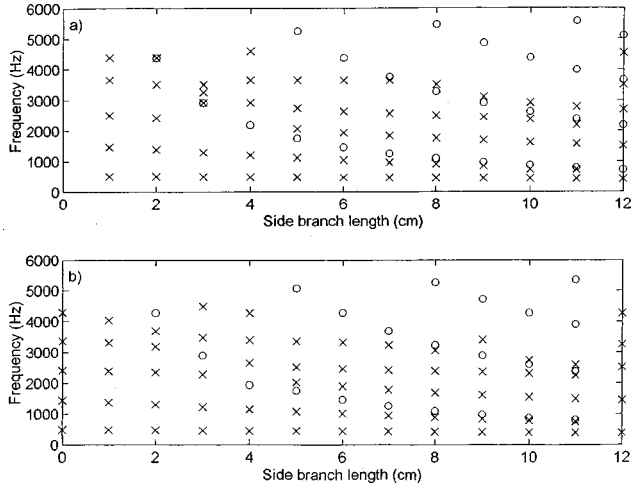

FIG. 2. (a) Estimated pole and zero frequencies of the tube configuration in Fig. 1 as l_s varies from 1 to 12 cm. In this and subsequent figures, ''×'' represents a pole frequency and ''○'' represents a zero frequency. (b) Calculated pole and zero frequencies.

For example, given a 17-cm vocal tract with a uniform cross-sectional area $A_b=A_s=A_f=4$ cm^2, with a back cavity length $l_b=12$, a side-branch length $l_s=4$, and a front cavity length $l_f=5$, the zeros of Eq. (1) can be numerically evaluated. The estimated resonant frequencies are ≈495, 1205, 2925, 3655, and 4605 Hz. An estimated zero frequency of 2190 Hz is found from Eq. (2). Figure 1(b) shows a plot of the glottis-to-lips transfer function calculated by the model for this configuration. It can be seen that there are peaks near 450, 1150, 2650, 3400, and 4300 Hz. In addition, there is a possible zero at 2000 Hz.

Table I summarizes the strongly coupled configurations tested. The results are presented as nomograms in Figs. 2–4, and summarized in Tables III and IV. The first two rows of Table I summarize configurations in which the side-branch length varied from 1 to 12 cm (with the minor variation of using 0.5-cm sections for the 1-cm side-branch and 1.0-cm sections for the rest). The third row of Table I summarizes configurations in which the cross-sectional area of the side-branch varied from 0.5 to 4 cm^2. The fourth row of Table I summarizes configurations in which the location of the side-

TABLE I. ''Strongly coupled'' model configurations tested. ''Fig.'' is the figure in which the results are presented. n_b, n_s, n_f: the number of tube sections (circuit elements) used to model the back, side, and front cavities, respectively. x_b, x_s, x_f: length in cm of tube sections used to model the back, side, and front cavities. Other symbols are as in the text.

	Back cavity				Side-branch				Front cavity			
Fig.	l_b	A_b	n_b	x_b	l_s	A_s	n_s	x_s	l_f	A_f	n_f	x_f
2	12.0	4.0	12	1.0	1.0	4.0	2	0.5	5.0	4.0	5	1.0
2	12.0	4.0	12	1.0	2.0→12.0	4.0	2→12	1.0	5.0	4.0	5	1.0
3	12.0	4.0	12	1.0	6.0	0.5→4.0	6	1.0	5.0	4.0	5	1.0
4	2.0→15.0	4.0	2→15	1.0	6.0	4.0	6	1.0	15.0→2.0	4.0	15→2	1.0

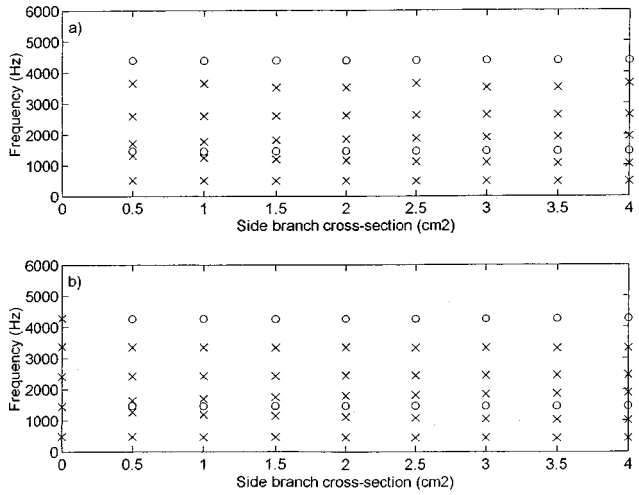

FIG. 3. (a) Estimated pole and zero frequencies of the tube configuration in Fig. 1 as A_s varies from 0.5 to 4 cm^2. (b) Calculated pole and zero frequencies.

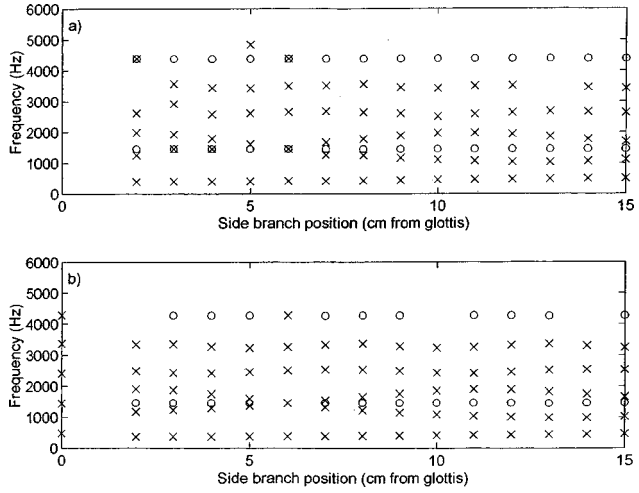

FIG. 4. (a) Estimated pole and zero frequencies of the tube configuration in Fig. 1 as l_b varies from 2 to 15 cm while l_b+l_f (the overall tract length) is held constant at 17 cm. (b) Calculated pole and zero frequencies.

branch (its distance from the glottal end of the model) varied from 2 to 15 cm.

Figure 2(a) shows a nomogram of the pole and zero frequencies beneath 5.5 kHz estimated from Eqs. (1) and (2) as the length of the side-branch varies. Figure 2(b) shows the (first five) pole and zero frequencies measured from the calculated transfer function, together with the limiting pole frequencies for a tube with no side-branch (i.e., the column of pole frequencies plotted on the y axis, at $l_s=0$ cm), as calculated by VTCALCS.

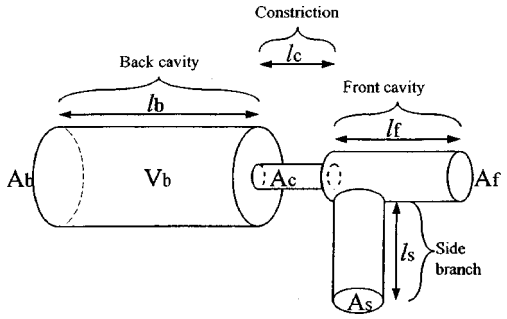

FIG. 5. The tube configuration simulated in the ''weakly coupled'' models.

Qualitative features of the nomogram, such as the abrupt decrease in the number of poles in the transfer function of the model vocal tract at $l_b=l_s=12$ cm, are seen in both Figs. 2(a) (estimated) and (b) (determined from model transfer functions.) In addition, the pole frequencies calculated by the model as the side-branch length tends to zero clearly converge to the pole frequencies for a tube with no side branch.

Figure 3 shows nomograms of the estimated and calculated (model) pole and zero frequencies as a function of the cross-sectional area of the side-branch together with the limiting pole frequencies for a tube with no side-branch. Figure 4 shows nomograms of the estimated and calculated pole and zero frequencies as a function of the position of the side-branch together with the limiting pole frequencies.

B. Side-branch weakly coupled to back cavity

This configuration is schematized in Fig. 5. In these configurations, a back cavity opens, through a constriction of length l_c and cross-sectional area A_c, into a front cavity with a side branch. Configurations in which l_s and A_s varied were tested. In addition, configurations in which l_s varied inversely with l_f were tested.

A lumped vocal tract resonance exists in these configurations because the back cavity is separated from the front cavity of the vocal tract by a constriction. This resonant frequency is approximately the Helmholtz, or cavity resonance frequency F_{H} given by Eq. (3) (again, the radiation impedance and vocal tract losses are neglected),

$$F_{\mathrm{H}}=(c/2\pi)\sqrt{(A_c/(V_b l_c))}. \tag{3}$$

[In (4), A_c is the cross-sectional area of the constriction; $V_b=A_b*l_b$ is the back cavity volume, and l_c is the constriction length.]

The combination of the side-branch and front cavity gives rise to a series of quarter-wave resonant frequencies F_n given by Eq. (4); see Espy-Wilson *et al.* (2000), p. 345 ff,

TABLE II. ''Weakly coupled'' model configurations tested. n_c: number of tube sections (circuit elements) used to model the constriction. x_c: length in cm of tube sections used to model the constriction. Other symbols are as in the previous table.

	Back cavity				Constriction				Side-branch				Front cavity			
Fig.	l_b	A_b	n_b	x_b	l_c	A_c	n_c	x_c	l_s	A_s	n_s	x_s	l_f	A_f	n_f	x_f
6	12.0	4.0	12	1.0	1.0	0.2	1	1.0	0.75→6.0	2.0	2→16	3/8	4.0	2.0	4	1.0
7	12.0	4.0	24	0.5	1.0	0.2	2	0.5	2.5	0.25→2.0	5	0.5	4.0	2.0	8	0.5
8	12.0	4.0	24	0.5	1.0	0.2	2	0.5	1.0→6.0	2.0	2→12	0.5	7.0→2.0	2.0	14→4	0.5

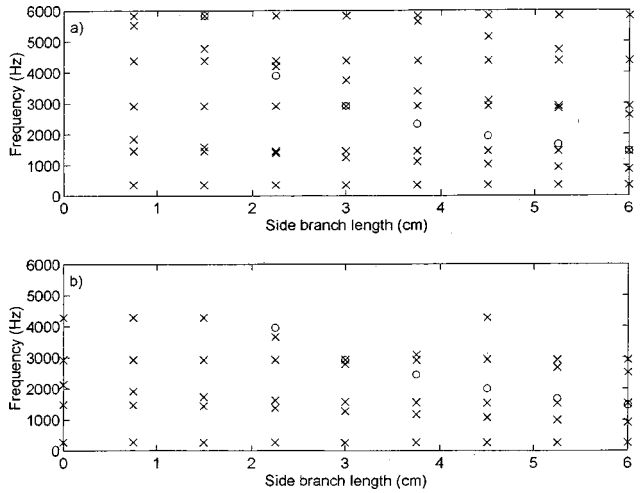

FIG. 6. (a) Estimated pole and zero frequencies of the tube configuration in Fig. 5 as l_s varies from 0.75 to 6 cm. (b) Calculated pole and zero frequencies.

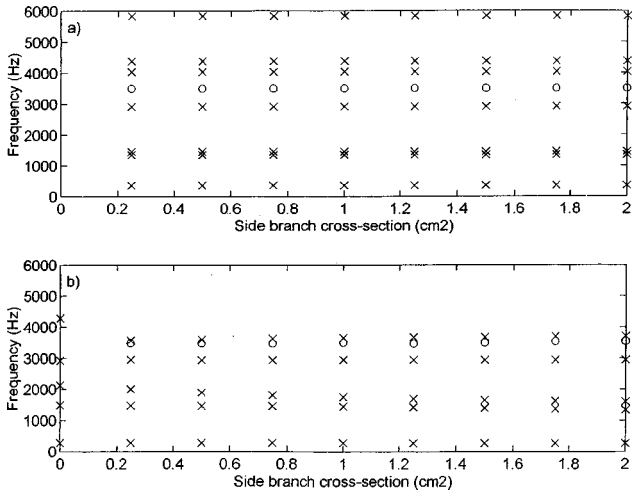

FIG. 7. (a) Estimated pole and zero frequencies of the tube configuration in Fig. 5 as A_s varies from 0.25 to 2 cm. (b) Calculated pole and zero frequencies.

$$F_n=(2n-1)c/4(l_s+l_f). \tag{4}$$

The back cavity contributes a half-wave resonance with the series of resonant frequencies given in (5):

$$F_n=nc/2l_s. \tag{5}$$

Finally, the side-branch causes zeros in the transfer function at the frequencies given in (2).

Table II summarizes the weakly coupled configurations tested. The results are presented as nomograms in Figs. 6–8, and summarized in Tables III and IV. The first row of Table II summarizes configurations in which the side-branch length l_s varied from 0.75 to 6 cm. The second row summarizes configurations in which the side-branch cross-sectional area A_s varied from 0.25 to 2.0 cm^2. The third row summarizes configurations in which the side-branch length l_s varied from 1 to 6 cm while the front cavity length l_f varied inversely from 7 to 2 cm (thus keeping the total length l_s+l_f constant at 8 cm).

Figure 6 shows nomograms of the estimated and calculated (model) pole and zero frequencies as the length of the side-branch varies, together with the limiting pole frequencies for a tube with no side-branch, as calculated by VTCALCS. Figure 7 shows the estimated and calculated pole and zero frequencies as the cross-sectional area of the side-branch varies, together with the limiting pole frequencies. Figure 8 shows the estimated and calculated pole and zero frequencies as the lengths of the side-branch and front cavity vary inversely, together with the limiting pole frequencies.

Table III reports the rms differences between the estimated and model pole frequencies in Hz and in percent (of the average pole or zero frequency) for each series of configurations. Table IV reports the rms differences between the estimated and model zero frequencies.

V. DISCUSSION AND CONCLUSIONS

The patterns of pole and zero frequencies calculated by the model are in good qualitative agreement with the patterns of pole and zero frequencies estimated from simple tube models. Many details are seen in both the estimated and the calculated nomograms. For example, Figs. 2(a) and (b) both show an exact pole-zero cancellation at $l_s=3$ cm; in Fig. 2(b), F_5 at $l_s=3$ cm appears to be 1 kHz greater than F_5 at $l_s=2$ cm because a peak ''expected'' for F_4 at about 3 kHz has been cancelled. Finally, the calculated pole frequencies when the side-branch length or cross-sectional area are close to zero do in fact converge to the pole frequencies calculated by VTCALCS for a tube with no side-branch.

In many cases, the pole frequencies calculated by VTCALCS and this model implementation (AFSB2XFB) are lower than the estimated values. The model pole frequencies are from 5%–10% lower than the estimated ones, with the smallest discrepancies generally in F_2. The discrepancy is due to the fact that VTCALCS and the side-branch model take into account viscous, heat conduction, and wall losses and radiation loads that the simple tube models neglect. In addition, it is possible that (3), which estimates the lumped

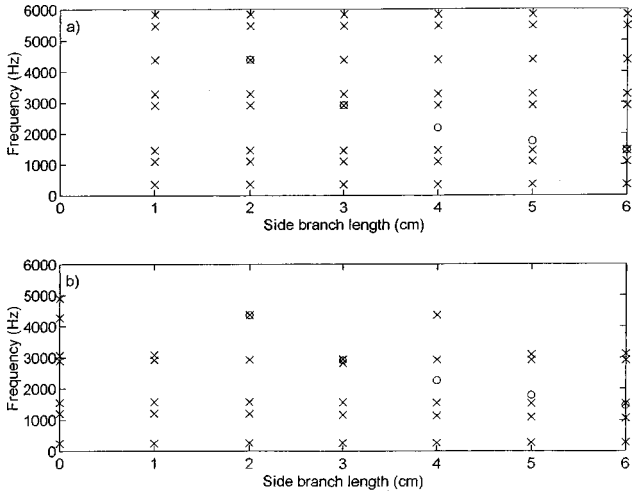

FIG. 8. (a) Estimated pole and zero frequencies of the tube configuration in Fig. 5 as l_s varies from 2 to 7 cm while l_s+l_f (the ''overall front cavity length'') is held constant at 8 cm. (b) Calculated pole and zero frequencies.

TABLE III. Root-mean-square differences between estimated and model pole frequencies in Hz, and in % of the mean pole frequency, for each series of configurations.

Varying parameter	F_1 [Hz (%)]	F_2 [Hz (%)]	F_3 [Hz (%)]	F_4 [Hz (%)]	F_5 [Hz (%)]
			''Strongly coupled''		
l_s	37.2(7.8)	51.5(4.7)	216.9(10.0)	207.8(7.1)	451.7(12.1)
A_s	37.3(7.5)	37.5(3.3)	52.3(2.8)	175.9(6.7)	253.8(7.1)
l_b, l_f	34.4(7.6)	108.5(8.7)	287.3(14.6)	321.1(11.6)	568.1(15.5)
			''Weakly coupled''		
l_s	84.3(23.4)	37.9(3.2)	113.0(7.4)	79.1(2.8)	559.5(15.4)
A_s	83.3(23.2)	95.2(7.1)	328.0(22.5)	33.7(1.2)	386.9(9.6)
l_s, l_f	88.6(24.6)	76.7(7.0)	104.3(7.2)	38.6(1.3)	654.7(20.0)

vocal tract resonant frequency from the back cavity volume and the dimensions of the constriction, unduly neglects the load due to the front cavity and side-branch.

In summary, these results demonstrate that the pole and zero frequencies produced by the side-branch model, as implemented by the AFSB2XFB routine, are plausible for /r/-like consonants produced by forming an acoustic side-branch in the vocal tract.

TABLE IV. Root-mean-square differences between estimated and model zero frequencies in Hz, and in % the mean zero frequency, for each series of configurations.

Varying parameter	ζ_1 [Hz (%)]	ζ_2 [Hz (%)]	ζ_3 [Hz (%)]	ζ_4 [Hz (%)]
		''Strongly coupled''		
l_s	85.4(4.8)	83.3(2.4)	140.8(3.0)	220.0(4)
A_s	4.1(0.3)	105.7(2.4)		
l_b, l_f	5.6(0.4)	103.7(2.4)		
		''Weakly coupled''		
l_s	85.1(3.0)			
A_s	21.4(0.6)			
l_s, l_f	41.3(1.6)			

ACKNOWLEDGMENTS

This work was supported primarily by Grant No. NIH IR03-C2576-01 to Dr. Suzanne E. Boyce. Further support was provided by National Science Foundation Grant No. IRI-9310518 and NIH Grant No. 1 K02 DC00149 to Carol Espy-Wilson. The general strategy for verification was suggested by Dr. Ken Stevens, of MIT. The authors would also like to thank Dr. Ronan Scaife, of Dublin City University, for the original MATLAB-callable code implementing VTCALCS.

Espy-Wilson, C. Y., Boyce, S. E., Jackson, M. T.-T., Narayanan, S., and Alwan, A. (**2000**). ''Acoustic modeling of American English /r/,'' J. Acoust. Soc. Am. **108**, 343–356.

Ladefoged, P., and Bhaskararao, P. (**1983**). ''Non-quantal aspects of consonant production: A study of retroflex consonants,'' J. Phonetics **11**, 291–302.

Lindau, M. (**1985**). ''The story of /r/,'' in *Phonetic Linguistics: Essays in Honor of Peter Ladefoged*, edited by V. A. Fromkin (Academic, Orlando), pp. 157–168.

Maeda, S. (**1982**). ''A digital simulation method of the vocal-tract system,'' Speech Commun. **1**, 199–229.

Perkell, J. S., Boyce, S. E., and Stevens, K. N. (**1979**). ''Articulatory and acoustic correlates of the [s-š] distinction,'' J. Acoust. Soc. Am. Suppl. 1 **65**, S24.

Stevens, K. N. (**1999**). *Acoustic Phonetics* (MIT Press, Cambridge, MA).

The acoustic bases for gender identification from children's voices

Theodore L. Perry, Ralph N. Ohde,[a] and Daniel H. Ashmead
Department of Hearing and Speech Sciences, Vanderbilt Bill Wilkerson Center for Otolaryngology and Communication Sciences, Vanderbilt University Medical Center, Nashville, Tennessee 37232

(Received 20 August 1999; revised 28 February 2001; accepted 14 March 2001)

The purpose of this study was to examine the acoustic characteristics of children's speech and voices that account for listeners' ability to identify gender. In Experiment I, vocal recordings and gross physical measurements of 4-, 8-, 12-, and 16-year olds were taken (10 girls and 10 boys per age group). The speech sample consisted of seven nondiphthongal vowels of American English (/æ/ ''had,'' /ɛ/ ''head,'' /i/ ''heed,'' /I/ ''hid,'' /ɑ/ ''hod,'' /ʌ/ ''hud,'' and /u/ ''who'd'') produced in the carrier phrase, ''Say /hVd/ again.'' Fundamental frequency (f_0) and formant frequencies ($F1$, $F2$, $F3$) were measured from these syllables. In Experiment II, 20 adults rated the syllables produced by the children in Experiment I based on a six-point gender rating scale. The results from these experiments indicate (1) vowel formant frequencies differentiate gender for children as young as four years of age, while formant frequencies and f_0 differentiate gender after 12 years of age, (2) the relationship between gross measures of physical size and vocal characteristics is apparent for at least 12- and 16-year olds, and (3) listeners can identify gender from the speech and voice of children as young as four years of age, and with respect to young children, listeners appear to base their gender ratings on vowel formant frequencies. The findings are discussed in relation to the development of gender identity and its perceptual representation in speech and voice. © *2001 Acoustical Society of America.* [DOI: 10.1121/1.1370525]

PACS numbers: 43.70.Ep, 43.71.Bp [AL]

I. INTRODUCTION

Differences between male and female speech and voice are an important aspect of gender identity. These differences are in part a result of anatomical structures such as vocal fold size and vocal tract length as well as learned characteristics of vocal production such as intonation contour (Cruttenden, 1986; Crystal, 1982; Ohde and Sharf, 1992). Thus, prosodic features that are overlaid (suprasegmentals) upon sound segments in words, phrases, or sentences and include intonation, stress, duration, and juncture may be important in gender identification. It is well known that a typical f_0 for an adult male is around 120 Hz, while a typical f_0 for an adult female is around 200 Hz. Moreover, an average adult male will have lower formant frequencies than an average adult female, because of longer vocal tracts in the former than latter speakers (Ladefoged and Broadbent, 1957; Laver and Trudgill, 1979; Peterson and Barney, 1952; Lee, Potamianos, and Narayanan, 1999; Tecumseh Fitch and Giedd, 1999).

The acoustic differences between male and female voices are also influenced by behavioral factors. It has been noted that adult males will often speak with an unnaturally lower vocal pitch and women will often speak with an unnaturally higher vocal pitch in order to conform to stereotypical views of vocal production characteristics (Sachs, Lieberman, and Erickson, 1973). In studies of the perception of maleness or femaleness in a transsexual's voice, it was demonstrated that listeners were more likely to rate a voice as being female sounding with increasing variability in the intonation contour (i.e., the relative rising and falling of f_0) of the speech sample (Oates and Dacakis, 1983; Spencer, 1988; Wolfe, Ratusnik, Smith, and Northrop, 1990).

There have been several previous investigations of gender-specific vowel formant frequency characteristics of preadolescent children (Eguchi and Hirsh, 1969; Hasek, Singh, and Murry, 1980; Bennett, 1981; Busby and Plant, 1995; Lee, Potamianos, and Narayanan, 1999). Bennett (1981) analyzed the vocal productions of 7- to 8-year-old children for five vowels in a fixed phonetic context. The vowel resonances of boys were consistently lower than those of the girls, and several measures of body size were related to formant frequencies. The findings were consistent with the conclusion that boys had larger vocal tracts than girls. Busby and Plant (1995) examined the acoustic features of Australian vowels produced by preadolescent children. Five boys and five girls from each of four age groups (5-, 7-, 9-, and 11-year olds) vocalized 11 test words representing the nondiphthong vowels of Australian English. Fundamental frequency, the first three formant frequencies, amplitudes of the first three formants, and vowel duration were measured. The results revealed that there was no difference in f_0 between boys and girls within each age group, the values of the first three formant frequencies for the girls were higher than those for the boys, the formant amplitudes for the boys were higher than those for the girls, and there was no consistent variation in vowel duration values across age and/or gender. For f_0 and formant frequencies ($F1$,$F2$), Eguchi and Hirsh (1969) reported similar gender results for boys and girls between 11 and 13 years of age. Overall, these findings are consistent with the notion that boys have larger vocal tracts than girls. The specific age at which this distinction occurs is controversial (Lee *et al.*, 1999).

[a]Electronic mail: ohdexxrn@ctrvax.vanderbilt.edu

The above studies show that there are differences between boys and girls, particularly in resonance characteristics of vowels. Because of these production differences, there has been an interest in determining their role in perceiving gender from children's speech and voice. Weinberg and Bennett (1971) presented adult listeners with recorded samples of spontaneous speech produced by 5- and 6-year-old children. The listeners correctly identified speaker gender for 78% of the boys and 71% of the girls. An acoustic analysis revealed a large overlap in the f_0 ranges of the boys and girls. This result suggested that gender identification of children's speech and voice must be based not only on fundamental frequency, but on other acoustic properties as well. Sachs, Lieberman, and Erickson (1973) studied the speech and voice of 26 preadolescent children (4–14 years). Adult listeners made correct gender identifications of 81% of the speakers. Acoustically, the boys had a higher average f_0 than the girls, although the boys did have lower resonance frequencies than the girls. Due to the counterintuitive finding that the boys had a higher average f_0 than the girls, Sachs *et al.* (1973) suggested that gender identifications were based on the differences in the formant frequencies between the boys and the girls.

Other research has also suggested that, although f_0 provides the most dominant cue for gender identification from the voices of adults, other vocal properties may be important, especially in children. For example, listeners are able to identify gender: (1) when f_0 is filtered (e.g., Lass, Almerino, Jordan, and Walsh, 1980) or suppressed (e.g., Coleman, 1971, 1973) within the speech signal, (2) when speech samples are whispered (e.g., Bennett and Weinberg, 1979), and (3) when the frequency range of f_0 is very similar, like that of preadolescent boys and girls (e.g., Bennett, 1981; Ingrisano, Weismer, and Schuckers, 1980). In light of this evidence, it appears that adults are accustomed to using acoustic properties other than f_0 alone as a basis for gender identification. In addition to understanding the development of gender, there is recent information underscoring the importance of the voice in processing phonetic (vowels and consonants) information (Johnson, 1990a, 1990b; Haley and Ohde, 1996). Moreover, it has been claimed that the perceptual representation of gender is auditory based and qualitatively different from phonetic information (Mullennix *et al.*, 1995).

Although previous research has provided information on the importance of f_0 and formant frequencies in the acoustic and perceptual differentiation of gender, there is no study employing a consistent production/perceptual methodology to examine gender development in production, along with an adults' perception of gender throughout the period ranging from pre- to post-adolescence. For example, studies assessing an adults' perception of gender frequently have employed sentential material (Bennett and Weinberg, 1979; Ingrisano *et al.*, 1980), which could provide listeners with gender-specific prosodic cues other than f_0 and formant frequencies (Wolfe *et al.*, 1990). Since formant frequencies may contribute to gender differentiation, there is a potential relationship between vocal tract resonances and indices of body size, even for very young children. Previous findings show such a relationship between measures of body size and formant frequencies, but these findings were limited to 7- to 8-year-old children (Bennett, 1981). Because the perception of gender appears to depend on several acoustic factors, including f_0, formant frequencies, and breathiness (Klatt and Klatt, 1990), an evaluation of these properties in development is important for an understanding of both gender and the potential integration of source (f_0) and transfer function (formant frequencies) as cues to gender identification. Thus, the general purpose of this research was to examine f_0 and formant frequencies to assess their developmental role in the production and perception of gender. The two experiments were designed to answer the following questions.

(1) Do f_0 and vowel formant frequencies differentiate gender in 4-, 8-, 12-, and 16-year-old boys and girls?
(2) Is there a developmental relationship between gross measures of physical size and the vocal characteristics of these children?
(3) Is there a perceptual differentiation of gender between 4 and 16 years of age that parallels differences in production?

II. EXPERIMENT I: ACOUSTIC PROPERTIES OF GIRLS' AND BOYS' SPEECH AND VOICE

Anatomical properties of the vocal tract as well as learned speech characteristics influence the identification of gender from speech and voice. These speech characteristics include changes in mouth opening, lip rounding, and larynx height. The acoustic parameters considered most influential are f_0 and vocal tract resonances (Abercrombie, 1967; Eguchi and Hirsh, 1969; Kent, 1976; Liberman, Cooper, Shankweiler, and Studdert-Kennedy, 1967; Nolan, 1983). The focus of experiment I is on the salience of f_0 and formant frequencies as acoustic predictors of gender.

A. Method

1. Subjects

Twenty children in each of the age groups, 4-, 8-, 12-, and 16-year olds, participated with 10 girls and 10 boys per age group. The mean (and age range) ages (years:months) were 4:3 (4:1 to 4:8), 8:7 (8:5 to 9:5), 12:4 (12:2 to 12:9), and 16:4 (16:3 to 16:10) years. Age ranges computed for boys and girls separately were very similar, and varied between 1 to 4 months. All children spoke Standard American dialect, and none had a known speech disorder. A hearing screening at 20-dB HL for the octave frequencies between 500 and 4000 Hz was performed on children.

2. Speech sample and recording procedure

The speech sample consisted of seven nondiphthongal vowels of American English (/æ/ ''had,'' /ɛ/ ''head,'' /i/ ''heed,'' /I/ ''hid,'' /ɑ/ ''hod,'' /ʌ/ ''hud,'' and /u/ ''who'd'') produced in the neutral context of /hVd/. Each /hVd/ syllable was embedded in the carrier phrase, ''Say /hVd/ again.'' The children listened to a tape recording of an adult female vocalizing each syllable seven times within the carrier phrase according to a randomized schedule. There was a 3-s interval between presentations of the syllables, during which the chil-

dren repeated the phrase last heard. For each child, five of the seven syllables produced for each vowel were chosen as token utterances by the experimenter on the basis of clarity of recording and correctness of the vowel sound. All speech recordings were made at the children's schools in a portable sound-treated booth (noise level approximately 35–40 dBA) using a Tascam reel-to-reel tape recorder (Model 22-2) and a Signet unidirectional electret condenser recording microphone (Model RK 201). The microphone was placed in a microphone stand and positioned 8–10 in. from the speaker's mouth. The recording procedure took approximately 15–20 min for each child to complete.

3. Perceptual verification of vowels

Perceptual verification tests of the speech samples were conducted to determine that the vowels were consistent with their intended targets. Five phonetically experienced adult native speakers of English with no known speech or hearing disorder identified the 2800 syllables in random order from all experimental syllables (5 syllables$\times$7 vowels$\times$80 speakers). A criterion of 80% agreement (four out of five listeners) was used to consider the vowels as judged to be the intended targets. One-hundred fourteen of the syllables were judged at 80% agreement, while the remainder of the syllables were judged at 100% agreement. Consequently, all of these syllables were used.

4. Physical measurements

Body size measurements of the children similar to those obtained by Bennett (1981) were taken. Standing height, sitting height, body weight, and neck circumference were measured with the children's shoes removed. Standing height and body weight were measured using a medical scale, while sitting height and neck circumference were measured by a tape measure. Sitting height was measured as children sat on a stool. The distance from the seat of the stool to the vertex of the head was measured. Neck circumference was measured at the angle of the thyroid cartilage. This point was determined by palpation, and the measurement was taken just above the thyroid (laryngeal) prominence.

5. Formant frequency and fundamental frequency analyses

The speech samples were analyzed on a microcomputer system (CSL—Computerized Speech Lab, Model 4300, Software Version 5.0, Kay Elemetrics Corp.) at a 20-kHz sampling rate. Each syllable was isolated and removed from the sentence, ''Say /hVd/ again,'' by determining the onset of aspiration in /h/ and the point of the stop-gap in /d/. This was accomplished by producing a spectrogram of the sentence and segmenting the syllable from the phrase. In order to ensure capture of the entire vowel, segmentation was made 5–10 ms into the stop-gap of each syllable. Measurements of formant frequencies of children's speech can be difficult because of their high f_0's and unusual voice types (Kent, 1978). To minimize difficulties in formant frequency measurement, an analysis procedure similar to Sussman, Minifie, Buder, Stoel-Gammon, and Smith (1996) was adopted. $F1$, $F2$, and $F3$ were measured from the spectrogram of each syllable at the duration midpoint of the vowel. Furthermore, LPC (linear predictive coding) analyses were obtained with a 10-msec Triangular window at approximately the same point at which the formant values were determined from the spectrogram by placing the cursor at the midpoint of $F2$ stability. In the LPC analysis, the number of coefficients employed varied between 14 and 20 to derive the best estimate of formant frequencies. Both formant values from the spectrogram and the LPC analysis were recorded, and the specific frequency was determined as the average for a valid criterion measure (Sussman *et al.*, 1996). There was no more than 150-Hz difference between the values recorded from the spectrogram and the LPC analysis.

Fundamental frequency of the vowel was determined with the CSL pitch extraction program. Fundamental frequency is computed as the inverse of the time between glottal impulse markers. In addition to the absolute formant and f_0 frequency values, frequency scale factors (K factors) were used to show the percentage relationship of male and female f_0 and formant frequencies (Fant, 1973).

6. Statistical analyses

Since the major emphasis in Experiment I was to measure acoustic differences in children's speech as a function of gender, these data were analyzed using repeated measures analysis of variance (ANOVA), simple correlations, and multiple regression analysis (Kirk, 1982). All *post-hoc* tests were made using Tukey HSD comparisons at $p<0.05$. Separate analyses were conducted on data for f_0, $F1$, $F2$, and $F3$ as well as measures of physical size.

Several vowels were included in these analyses to represent the comprehensive range of productions in the oral cavity. Based on previous research (Bennett, 1981), gender differences for specific formants were likely to interact with specific vowel productions. However, the overall gender effects were of greatest interest, and the interactions of gender and vowel type entail complexities that do not have a clear theoretical basis. Therefore, the statistical interactions involving a vowel are reported, but not examined in detail.

B. Results and discussion

1. Reliability measures

Interjudge reliability was determined by having a second examiner sophisticated in acoustic analyses measure 10% of the speech sample. All four age groups were represented in these analyses. An equal number of samples from boys and girls were analyzed. The speakers and vowels were randomly selected. Interjudge reliability was high for both f_0 and formant frequency measures. Correlations of the two experimenters were computed for the two measures. The mean and range of the f_0 correlations across the speaker age groups were 0.91, and 0.86–0.99, respectively. The mean and range of the formant frequency correlations were 0.93, and 0.87–0.97, respectively.

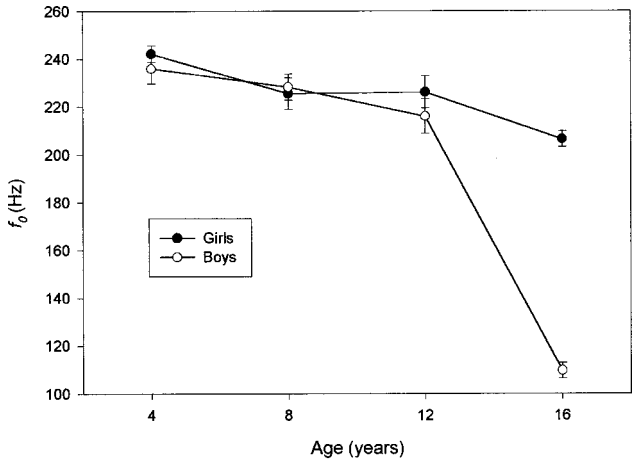

FIG. 1. Mean fundamental frequency (f_0) across the CVC syllables for 4-, 8-, 12-, and 16-year-old speakers. Error bars show ±1 standard error.

2. Fundamental frequency

The f_0 means averaged across vowel type are illustrated in Fig. 1. There were gender differences between the f_0 values of girls and boys only in the 16-year-old age group. In an Age (4) × Gender (2) × Vowel (7) analysis of variance, there were main effects of age [$F(3,72)=86.96$; $p<0.0001$], gender [$F(1,72)=50.44$; $p<0.0001$], vowel [$F(6,432)=10.27$; $p<0.0001$], and a significant interaction of age×gender [$F(3,72)=35.72$; $p<0.0001$]. Within each age group, the only significant gender difference was for the 16-year olds.

The finding that f_0 was similar for girls and boys at 4, 8, and 12 years is consistent with previous research (e.g., Bennett, 1983; Busby and Plant, 1995; Kent, 1976), although Hasek *et al.* (1980) found gender differences in f_0 for 7- to 10-year-old children. Nevertheless, the data from the current study suggest that there is little or no difference in f_0 between boys and girls 12 years old or younger. Therefore, it is unlikely that f_0 provides sufficient information to differentiate speaker gender in young children. Because most acoustic studies of children's speech have shown little difference in f_0 between boys and girls under 13 years of age, it appears that vocal fold size increases modestly throughout middle childhood (Kent, 1976; Hollien, Green, and Massey, 1994; Kent and Vorperian, 1995).

K factors were calculated for these children to determine the pattern of gender differences in f_0 and formant frequencies using the formula Kn% = 100[(Fn female/Fn male) − 1] where Fn is either f_0, $F1$, $F2$, or $F3$ (Fant, 1973; Bennett, 1981; Nordstrom, 1997). These values represent the percentage difference between the vocal and speech characteristics of the boys and girls. K factors were calculated for mean f_0, $F1$, $F2$, and $F3$ values within each age group for the boys and girls referred to as K0, K1, K2, and K3, respectively.

The extent of gender differences in f_0 within the younger age groups was very small (K0: 2.6% for 4-year olds, −1.2% for 8-year olds, and 4.7% for 12-year olds). The negative value for the 8-year olds reflects a slightly lower mean f_0 for the girls than the boys. However, the difference between f_0 of the 16-year-old boys and girls was substantial (88.2%).

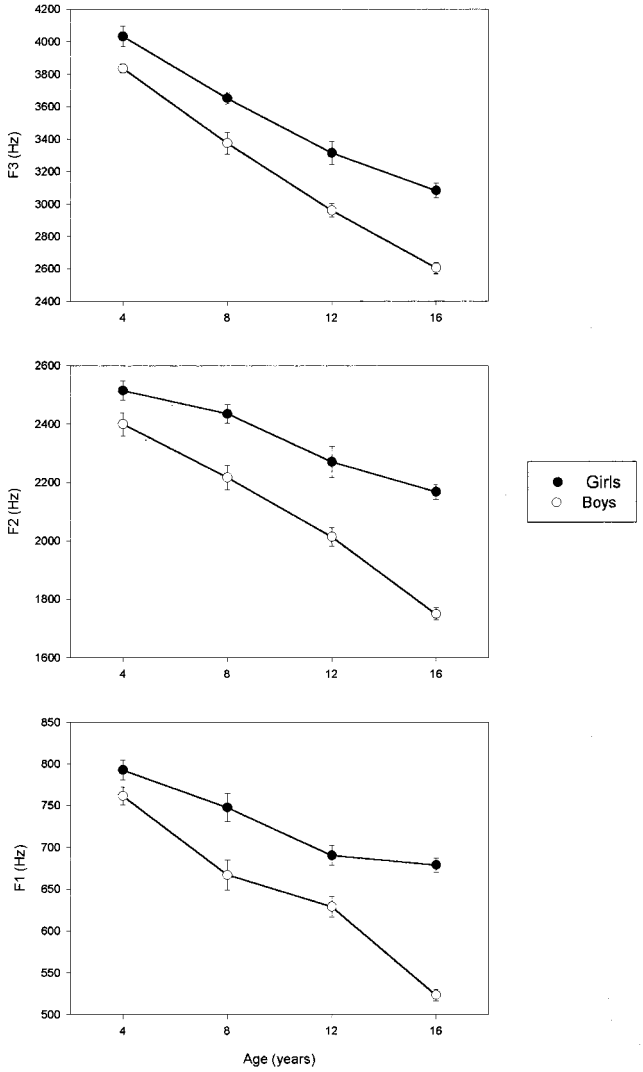

FIG. 2. Mean $F1$, $F2$, and $F3$ values across the CVC syllables for 4-, 8-, 12-, and 16-year-old speakers. Error bars show ±1 standard error.

3. Vowel formant frequency

The above analyses suggest that f_0 does not provide the information necessary to differentiate gender until after 12 years of age. However, gender differences may exist in the vowel formant frequencies of these children. The three panels of Fig. 2 illustrate the $F1$, $F2$, and $F3$ means collapsed across the vowels. Separate Age(4)×Gender(2)×Vowel(7) analyses of variance were performed on the $F1$, $F2$, and $F3$ values. The results of the analysis for $F1$ values showed main effects of age [$F(3,72)=69.74$; $p<0.0001$], gender [$F(1,72)=84.45$; $p<0.0001$], and vowel [$F(6,432)=1008.19$; $p<0.0001$]. A significant age×gender interaction was found [$F(3,72)=8.87$; $p<0.0001$].[1] The analysis for $F2$ values showed the main effects of age [$F(3,72)=73.15$; $p<0.0001$], gender [$F(1,72)=98.20$; $p<0.0001$], and vowel [$F(6,432)=980.69$; $p<0.0001$], and a significant age×gender [$F(3,72)=6.16$; $p<0.001$] interaction.[2] The analysis for $F3$ values showed the main effects of age [$F(3,72)=175.70$; $p<0.0001$], gender [$F(1,72)=84.18$; p

<0.0001], and vowel [$F(6,432)=167.94$; $p<0.0001$] and a significant age×gender [$F(3,72)=2.78$; $p<0.05$] interaction.

According to Tukey tests, $F1$ values for the boys were significantly lower than those for the girls within each age group except the 4-year olds. The same pattern held for the $F2$ values. $F3$ values for the boys were significantly lower than for the girls within each age group (Tukey HSD, $p<0.05$). These results suggest that there may be adequate information available from $F1$, $F2$, and $F3$ values to differentiate gender of the 8-, 12-, and 16-year olds. Differences between $F1$ and $F2$ values for the 4-year olds were not significant. However, since $F3$ differences between 4-year-old boys and girls were significantly different, it is conceivable that this information may also be sufficient to differentiate gender.

Computation of K factors in this study revealed that the percentage of differences between boys and girls in $F1$ (K1: 2.6%, 11.4%, 9.1%, and 27.5% for 4-, 8-, 12-, and 16-year olds, respectively), $F2$ (K2: 4.6%, 10.3%, 12.5%, and 23.8% for 4-, 8-, 12-, and 16-year olds, respectively) and $F3$ (K3: 5.2%, 8.3%, 12.0%, and 18.4% for 4-, 8-, 12-, and 16-year olds, respectively) values within each age group remained very similar, and these formant frequencies were lower for the boys than for the girls. Busby and Plant (1995) also showed that vowel formant frequencies were consistently lower for boys than girls, and that $F1$, $F2$, and $F3$ decreased in value with age. Though Bennett (1981) only examined 7- and 8-year olds, she found that vowel formant frequencies for the boys were, on average, 10% lower than those for the girls. Similar data from the 8-year olds in the present study revealed that the boys' formant frequencies were approximately 9% lower than those for the girls. Thus, gender differences in formant frequencies increase with age and are apparent, even in very young children. If gender identification from young children's speech is possible, then listeners may utilize this difference in formant frequencies.

4. Relationship between physical size and formant frequencies

Bennett (1981) suggested that gender differences in formant frequencies of children may be attributable to vocal tract size, and in particular the pharynx (Kent and Vorperian, 1995). Bennett does not define vocal tract size, but it is reasonable to assume that the length and width of the vocal tract would vary as a function of gross changes in body size. For purposes of this paper, size will include the length and width of the vocal tract. Because it was not possible to obtain exact measurements of vocal tract size, various measurements of physical size were taken. Findings for height, weight, sitting height, and neck circumference are contained in Table I. The difference between the physical size of boys and girls increased with age but became readily apparent only at 16 years of age. On average, the 4-, 8-, and 12-year-old boys were 2 cm taller, 2 kg heavier, and had neck circumferences 2 cm larger than the girls. Separate analyses of variance (age×gender) were carried out for each of the four physical size measures. As expected, all four analyses showed significant main effects of age and gender, as well as significant interactions of age and gender. Since these results were highly predicted based on anatomical development (Kent and Vorperian, 1995), the details of these analyses are not reported. These analyses were run principally to provide the error terms used for Tukey tests of gender differences at each age level. The pattern of the Tukey tests was simple. At age 16 years, boys were significantly larger than girls on all four measures. At age 12 years, boys had significantly larger neck circumferences than girls. None of the other comparisons of boys versus girls within age groups were significant. The measurements employed in the current research are similar to Bennett's (1981) measurements for 7- and 8-year olds (mean age=7 years 11 months), though her measurements showed that the boys were slightly taller (7 cm) and heavier (4 kg) than the girls in her study.

TABLE I. Means and standard deviations (SD) for measures of physical size for 4-, 8-, 12-, and 16-year-old males and females (H=height, W=weight, SH=sitting height, and NC=neck circumference).

Age group	H (cm)	W (kg)	SH (cm)	NC (cm)
4 years				
Male				
mean	106.8	17.8	60.1	26.1
SD	2.8	1.2	2.6	1.2
Female				
mean	106.9	17.9	58.6	24.9
SD	5.1	2.5	3.6	1.1
8 years				
Male				
mean	134.9	34.4	74.3	29.0
SD	8.0	9.1	4.9	1.8
Female				
mean	132.8	33.8	73.7	27.9
SD	4.7	8.2	2.9	2.1
12 years				
Male				
mean	158.4	49.7	83.9	32.2
SD	5.9	5.8	3.9	1.6
Female				
mean	155.5	44.1	84.7	29.4
SD	6.1	4.6	3.5	1.5
16 years				
Male				
mean	179.8	79.1	96.1	38.0
SD	4.8	10.2	2.7	2.9
Female				
mean	164.7	60.8	90.1	31.4
SD	6.1	7.6	2.5	1.2

Figure 3 shows scatter plots of the relationship between body weight and the formant measures. The measures of body size were highly correlated with one another and all showed similar relationships with formant values, so only body weight is shown for illustrative purposes. The formant values are averaged across all speech tokens for each individual child speaker. The symbols in Fig. 3 indicate the age and gender of each child. Linear regression lines are shown separately for the boys and girls (each regression was computed on all 40 children of a given gender, that is, on children from all four age groups). There are two points to emphasize with respect to Fig. 3. First, physical size is strongly

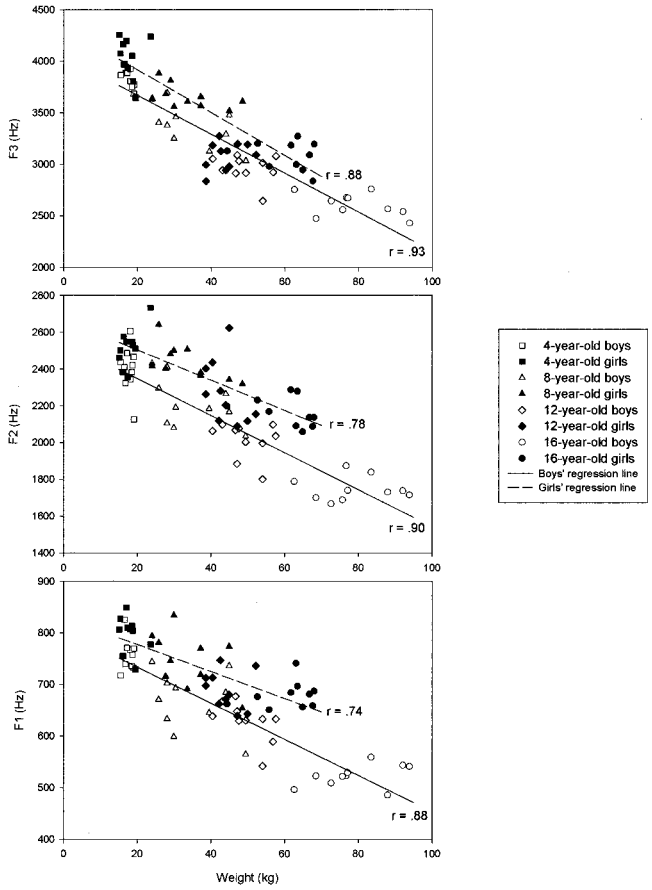

FIG. 3. Average formant frequencies versus body weight for individual children.

correlated with formant frequencies, as would be expected if vocal tract size grows along with grosser measures of size such as body weight. All the correlations indicated in Fig. 3 were statistically significant, and the slope values for boys and girls were similar, as can be seen in the figure. The second point about Fig. 3 is that there are gender differences in formant frequencies even when physical size is taken into account. The girls' formant frequencies tended to be higher than the boys,' especially for $F1$ and $F2$.

This gender difference in formant frequencies was further analyzed with stepwise multiple regression. The logic of each regression analysis, which was done separately for $F1$, $F2$, and $F3$, was to enter predictors of the formant frequency in the following order: physical size measures (body weight, neck circumference, sitting height, standing height); age group (4, 8, 12, or 16 years); and gender (boy, girl). If gender has a unique effect on formant frequencies, over and above physical size and age, then the addition of gender as a predictor on the last step should produce a significant increase in the R^2 value. The gender-related increase in R^2 was significant for all three formants: [$F1$—R^2 increment$=0.054$, $F(1,73)=21.052$; $p<0.0001$], [$F2$—R^2 increment$=0.088$, $F(1,73)=35.484$; $p<0.0001$], and [$F3$—R^2 increment $=0.049$, $F(1,73)=43.645$; $p<0.0001$]. The overall R^2 values with all predictors in the model were 0.902, 0.905, and 0.918 for $F1$, $F2$, and $F3$, respectively, so the variance in formant frequencies was accounted for quite well by these predictors. In summary, formant frequencies were strongly correlated with body size measures for both boys and girls, but there were gender differences in formant frequencies, even after the body size measures used in this study were taken into account. These remaining gender differences could reflect differences in vocal tract size between boys and girls that were not captured by the body size measures taken, but the difference could also reflect variations in articulatory postures of lip rounding and jaw opening for boys and girls (Lindblom and Sundberg, 1971; Fant, 1973; Bennett and Weinberg, 1979; Bennett, 1981).

III. EXPERIMENT II: PERCEPTION OF GIRLS' AND BOYS' SPEECH AND VOICE

The acoustic data from Experiment I showed that f_0 was only slightly different between the 4-, 8-, and 12-year-old boys and girls, while f_0 was significantly lower for the 16-year-old boys than for the 16-year-old girls. However, all formant frequency values were lower for the 8-, 12-, and 16-year-old boys than for the girls. As for the 4-year olds, there were only small gender differences in $F1$ and $F2$ values, but $F3$ was lower for the boys than for the girls. Because acoustic gender differences were observed in all age groups, it was of interest to determine if adult listeners could differentiate gender from the CVC syllables, and to see whether this identification varied with speaker age. Since the magnitude of acoustic differences as a function of gender differed across age groups, it was important to employ a scaling technique, which would be a more sensitive identification procedure than a two category response choice.

A. Method

1. Subjects and listening procedure

The subjects for this experiment were 20 undergraduate students (equal numbers of men and women) with no known speech or hearing disorders by self-report. All subjects spoke general American dialect.

Perceptual tests were performed in an IAC booth over headphones (TDH-49) at a comfortable listening level (75-dB SPL). Before beginning a series of trial blocks, listeners were informed by the experimenter that they would hear speech sounds from either 4-, 8-, 12-, or 16-year-old boys and girls and that they would make gender ratings of each vocalization based on a six-point scale described below. Though listeners were not told the age of the speakers to be heard, they were informed that all voices in a single session were from the same age group. On-line data collection as well as the generation of random orderings of the vowel sounds within each trial block was performed by a computer. Listeners were not given any feedback as to the actual gender of the speakers.

Listeners used a six-point rating scale to indicate gender. Ratings were entered via a six-button response box. The categories were as follows:

1 positively a female;

2 appeared to be a female;

3 unsure, may have been a female;

4 unsure, may have been a male;

5 appeared to be a male;

6 positively a male.

The rating scale numbers were written on the response box, and a copy of the rating scale was always within view. This scale allowed listeners to make judgments based upon their certainty of gender, unlike previous studies that permitted only binary male and female responses (Bennett and Weinberg, 1979; Ingrisano *et al.*, 1980; Sachs *et al.*, 1973; Weinberg and Bennett, 1971).

The events in a trial consisted of a 300-ms warning light, a 300-ms delay, the stimulus, and a response light indicating that it was time to make a rating. There was a four-second interval between trials. Subjects were presented five trial blocks per session, with all five trial blocks consisting of stimuli from only one speaker age group. There were four listening sessions, with the order of speaker age group counterbalanced (each listener had a different one of the 24 possible orders). No more than one session was conducted per day, and there were no more than ten days between sessions.

The stimuli consisted of the CVC syllables from Experiment I. Each of the seven vowel sounds was produced five times by the 20 speakers within each of the four age groups (4-, 8-, 12-, and 16-year olds), yielding a total of 2800 syllables. There were 700 stimuli for each of the four age groups. These 700 stimuli were divided into 5 trial blocks per speaker group. Within each age group, a trial block consisted of the 140 utterances produced by 20 children, each saying 7 vowel sounds once. For reliability purposes, four of the utterances within each vowel sound were presented twice. Thus, each of the 5 trial blocks consisted of 168 trials, 140 trials corresponding to seven vowels from each of 20 children in a single age group plus 28 repetition trials.

2. Reliability

In order to determine the test–retest reliability, one syllable per speaker was chosen at random for each of the seven vowel sounds within each speaker age group for a total of 560 (80 speakers$\times$7 vowels) reliability tokens for each listener. Kappa (Cohen, 1969; Fleiss, 1981) was used to determine the chance-corrected reliability of the gender ratings for the two presentations of the same stimuli for the listeners within each trial block. Two categories were used in this analysis. A rating of ''1,'' ''2,'' or ''3'' was considered as ''female sounding,'' and a rating of ''4,'' ''5,'' or ''6'' was considered as ''male sounding.'' The kappa value was 0.64, which according to Fleiss (1981) reflects good agreement.

B. Results and discussion

1. Gender ratings

Previous data suggested that female listeners were better than male listeners in determining gender from children's speech and voice (Ingrisano *et al.*, 1980). Preliminary analyses of the data in which ratings were collapsed categorically as female (''1,'' ''2,'' ''3'') and male (''4,'' ''5,'' ''6'') indicated no differences in the rating responses by listener gender. Thus, listener gender was excluded as a variable in further analyses.

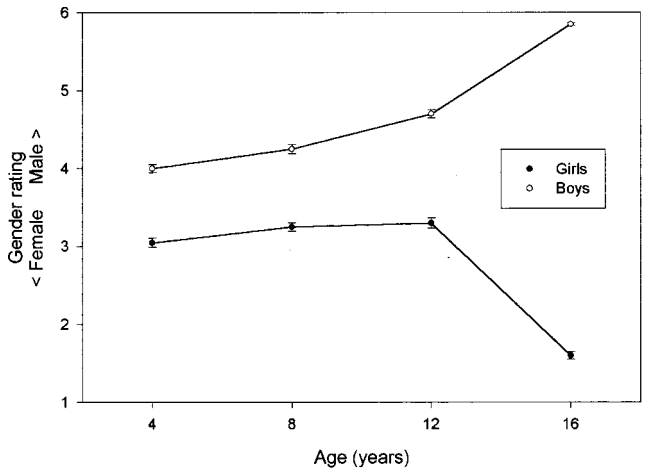

FIG. 4. Mean gender ratings (1=girl; 6=boy) for 4-, 8-, 12-, and 16-year-old speakers. Error bars show ± 1 standard error.

Based on the six-point gender rating scale, listeners' mean ratings are shown in Fig. 4. In a Speaker Age (4) $\times$Speaker Gender (2)$\times$Vowel (7) repeated measures analysis of variance, there were main effects of speaker age [$F(3,57)=8.70$; $p<0.001$], speaker gender [$F(1,19)=683.69$; $p<0.0001$], and vowel [$F(6,114)=57.88$; $p<0.0001$], and a significant speaker age$\times$speaker gender [$F(3,57)=328.61$; $p<0.0001$] interaction.[3] As illustrated, gender ratings were significantly different between boys' and girls' speech and voice within each age group (Tukey HSD, $p<0.05$). However, the gender ratings were clearly more similar at the three younger speaker ages than at 16 years.

To obtain an overall measure of whether gender was rated appropriately, the six-point rating scale was collapsed into a dichotomous scale, where 1, 2, or 3 was ''female'' and 4, 5, or 6 was ''male.'' The rating of each utterance by each listener was then scored as correct or not, based on whether the collapsed rating corresponded to the gender of the speaker. The percentages of utterances rated for which a correct gender rating was made were as follows: 4-year-olds (boys 67%, girls 62%); 8-year olds (boys 74%, girls 56%); 12-year-olds (boys 82%, girls 56%); and 16-year olds (boys 99.7%, girls 95%). Each of these percentages was based on 7,000 ratings, so that even the modest values of 56% for the 8- and 12-year-old girls exceeded the 50% chance level according to binomial tests. Nevertheless, listeners were better able to assign a correct gender to utterances spoken by boys than by girls in the 4-, 8-, and 12-year age groups.

Listeners in this study responded to CVC syllables based on a six-point gender rating scale. Overall, results indicated that listeners were able to rate vocalizations as either male of female sounding, even for the youngest children. Similarly, Weinberg and Bennett (1971) reported an identification rate of 78% for boys and 71% for girls in 5- and 6-year olds. Ingrisano *et al.* (1980) reported a gender identification rate of 71% for 4- and 5-year olds, and Bennett and Weinberg (1979) reported an identification rate of approximately 65%

TABLE II. Simple correlations between f_0, $F1$, $F2$, $F3$ and listener gender ratings for 4-, 8-, 12-, and 16-year-old boys and girls.

Age group	f_0	$F1$	$F2$	$F3$
4 years	-0.60^a	-0.47	-0.33	-0.82^a
8 years	-0.52^a	-0.81^a	-0.84^a	-0.86^a
12 years	-0.56^a	-0.89^a	-0.78^a	-0.83^a
16 years	-0.98^a	-0.96^a	-0.95^a	-0.90^a

[a]$p<0.05$.

for 6- and 7-year olds. Overall, listeners in this study correctly identified the speaker gender of 74% of the utterances averaged across the four age groups. This is comparable to the 81% identification rate reported by Sachs *et al.* (1973) for children between 4 and 14 years of age. Differences in gender identification between the current study and previous research may be due to the kind of speech material that was used. The current research used the CVC syllable, whereas all previous studies employed sentences. The sentence material may have contained additional prosodic cues to gender identification.

2. Relationship between voice/speech characteristics and gender ratings

To investigate the relationship between acoustic measures and gender ratings, simple correlations were performed. Table II shows the simple correlation coefficients between the average listener gender rating across all utterances for each child speaker, and f_0, $F1$, $F2$, and $F3$. Note that a negative correlation means that a higher frequency was associated with ''girl-ness'' (since the gender rating scale had lower values for girls and higher values for boys). This table suggests that listeners gave considerable emphasis to $F3$ for the 4-year olds, to all three formants for the 8- and 12-year olds, and to f_0 as well as all the formants for the 16-year olds.

It has been shown that f_0 provides the most salient cue to gender perception from the voices of adults (e.g., Coleman, 1971, 1973; Lass, Hughes, Bowyer, Waters, and Bourne, 1976; Schwartz, 1968). However, even in the absence of f_0, listeners are able to make correct gender identifications from adults' speech (e.g., Lass *et al.*, 1976; Schwartz, 1968). As for children's voices, this study as well as others (e.g., Bennett, 1983; Bennett and Weinberg, 1979; Busby and Plant, 1995; Kent, 1976; Weinberg and Bennett, 1971) indicate that there is little or no difference in f_0 between boys and girls under the age of 12. Since f_0 probably does not play a large role in the determination of gender from children's voices in the four to 12 year age range, the contribution of vocal tract resonance characteristics to gender identification appears important.

IV. GENERAL DISCUSSION

The main objective of this study was to examine children's acoustic characteristics that account for listeners' ability to identify gender from the voice and speech. To accomplish this, vocal recordings of 4-, 8-, 12-, and 16-year-old boys and girls were made, and acoustic analyses of these recordings were performed. These speech tokens were then used in a gender perceptual rating task. Results from these acoustic and perceptual experiments have provided information about the developmental bases for listeners' ability to identify gender from speech and voice.

A. Acoustic correlates of gender

Adult listeners were able to determine gender from the speech and voice of children as young as four years of age. Since f_0 is very similar for young girls and boys between 4- and 12-years-old, it is unlikely that this property was utilized by the listeners. Instead, listeners must have attended to other acoustic correlates of gender such as formant frequencies.

The average formant frequency ($F1$, $F2$, $F3$) functions revealed consistently lower values for boys than girls. Vocal tract length is one determinant of formant frequencies. Several anatomical studies have provided support for gender differences in vocal tract length. Fant (1973) found differences in both oral and pharyngeal dimensions for male female vocal tracts, but the distinction was largest for the pharynx. In a cephalometric study, King (1952) found that the pharyngeal portion extending from the hard palate to the hyoid bone was longer for boys than girls ranging from one to 16 years. The difference in vocal tract length values for boys and girls ranged from 2% to 13%, with the smaller value for the 1-year olds and the larger value for the 16-year olds. Based on these anatomical data, it would be predicted that differences in formant frequencies of boys and girls would increase as a function of age. The results of the current study clearly support this prediction. Across $F1$, $F2$, and $F3$, gender differences were greatest for the 16-year-old group and smallest for the 4-year-old group.

The computation of K factors in this study revealed that the percentage of differences between boys and girls in $F1$, $F2$, and $F3$ values within each age group remained very similar, and these formant frequencies were lower for the boys than for the girls. Busby and Plant (1955) also showed that vowel formant frequencies were consistently lower for boys than girls, and that $F1$, $F2$, and $F3$ decreased in value with age. The formant frequency K factors were computed as an average across vowel contexts. An examination of specific vowels showed that for 8-, 12-, and 16-year olds, average formant frequencies were always lower for boys than girls. Previous studies employing K-factor analyses of adult formant frequencies have shown that sexual distinctions are vowel and formant dependent (Fant, 1973). For example, Fant determined that male/female differences were largest for $F2$ and $F3$ of the front vowels, and $F1$ of [æ]. These differences were smaller for $F1$ and $F2$ of back vowels. Thus, certain vowels may have a larger impact of gender differentiation than other vowels.

One obvious implication of the current findings showing lower vocal tract resonances for young boys than girls is that sexual differences exist in vocal tract length. Although direct estimates of vocal tract size are difficult to obtain for children, at least one previous study estimated more gross measures of vocal tract dimensions (Bennett, 1981). Bennett measured standing height, sitting height, weight, and neck circumference in 7- to 8-year-old boys and girls. Simple cor-

relations between each of the measures of body size and the various vowel formants revealed that 93% of these correlations were significant. All of the correlations were negative, indicating that an increase in a physical dimension was associated with a decrease in formant frequency. These same physical dimensions were measured in the current study for a population of children similar in age. The majority of the correlations were negative, and the correlations for body weight were in the same range as those reported by Bennett. Moreover, these findings are consistent with the K-factor analyses revealing that the average formant frequency difference between 7- to 8-year-old boys and girls was 10% and 9% for the Bennett and current studies, respectively. Thus, the acoustic analyses and measures of gross vocal tract dimensions were comparable across studies.

In a recent study (Tecumseh Fitch and Giedd, 1999), magnetic resonance imaging (MRI) was used to quantify the vocal tract morphology of subjects between 2 and 25 years of age. The MRI results revealed positive correlations between vocal tract length and either body height or weight. As illustrated in Fig. 3 of the current study, the relationship between body weight and formant frequency change was similar for boys and girls. Thus, an increase in weight resulted in lower formant frequencies for both boys and girls. Although it would be reasonable to predict that vocal tract length contributed to lower formant frequencies of boys compared to girls at a given age level in the current research, the MRI data only partially support this prediction. Tecumseh Fitch and Giedd found that vocal tract length was significantly longer in boys than girls after 10 years of age. These findings indicate that vocal tract length contributes to differences in formant frequencies between boys and girls after age 10. However, the results also suggest that formant frequency differences between boys and girls before age 10 come from anatomical and/or articulatory sources other than vocal tract length.

B. Perceptual correlates of gender

It is plausible that listeners in this study based their gender rating of the younger children on information from vowel formant frequencies. The third formant values accounted for the highest percentage of the total variance in listener rating behavior for the 4- and 8-year olds, while $F1$ accounted for the highest percentage of the total variance in listener rating behavior for the 12-year olds. Across all age groups, boys tended to have lower vowel formant frequencies than girls. Bennett and Weinberg (1979) and Ingrisano *et al.* (1980) found similar results for 4- to 7-year olds. We conclude that vowel formant frequencies most likely played a primary role in listener rating behavior of the younger children.

It is generally assumed that the perception of gender from speech and voice is dependent upon several acoustic correlates of sound such as f_0 and formant frequencies (Mullennix *et al.*, 1995). Even though gender is characterized by various acoustic properties, our perceptual system is able to adapt to and compensate for different types of acoustic information (e.g., in the absence of f_0), which provide cues as to speaker gender. In a series of experiments, Mullennix *et al.* (1995) investigated the perceptual representation of gender from the voice. In one experiment, listeners were presented synthetic vowel sounds designed to range from male to female voices and were asked to rate each stimulus on a six-point scale similar to the one used in the current study. There was a gradual identification function between male and female voices, as well as good discrimination between voices within each gender category. They concluded that the perceptual representation of gender from the voice is auditory based, not categorical. Though the current study did not directly examine the perceptual mode (i.e., categorical versus auditory perception) for identifying gender from speech and voice, the results indicate that listeners were attending to various f_0 and formant acoustic cues in order to make their gender ratings.

Since the focus of the current research was on the role of formant frequencies and f_0 in gender identification, a CVC production unit was used to minimize other prosodic cues to gender. However, gender-specific prosodic differences have been shown to provide listeners with cues as to speaker gender (e.g., Spencer, 1988; Wolfe *et al.*, 1990). For example, typical female speech patterns generally show greater tonal variability (i.e., more upward intonations) than male speech patterns (Crystal, 1975). Wolfe *et al.* (1990) found when listeners were presented voices with similar f_0 ranges, they tended to identify voices that were less monotonous (i.e., more f_0 variability) as female sounding. There is a strong possibility that the results from several studies that examined the gender perception of children's speech were influenced by this type of prosodic effect, because listener responses were based on sentence stimuli (e.g., Bennett and Weinberg, 1979; Ingrisano *et al.*, 1980). Nevertheless, it is unlikely that prosodic effects influenced listener ratings in the current study. The CVC syllables in this study were of very short duration (mean duration was 200 ms), and stressed with typical rhythmic and intonational patterns.

V. CONCLUSIONS

In the present study we showed clear gender differences in both children's vowel productions, and adults' perception of children's speech and voice. The acoustic as well as the perceptual data from this study clarify the role of f_0 and formant frequency properties in the production and perceptual differentiation of gender across a large age range of child speakers. Moreover, the current research also provides directions for future research. Although a number of production studies, including the present, have examined the role of f_0 and formant frequency in gender identification, there is a need for research on the role of voice quality and particularly breathiness in sex differentiation. In the perception of gender, future research should examine the contribution of the auditory mode of perception through appropriate discrimination conditions of sound continua. As in the current research, the inclusion of a rating scale in conjunction with the discrimination paradigm may provide additional information on the mode of gender identification (Mullennix *et al.*, 1995). Further perceptual studies should examine variations in prosody as cues to gender perception.

The conclusions supported by the results of this research are as follows.

(1) Vowel formant frequencies differentiate gender for very young children, whereas formant frequencies and f_0 differentiate gender after 12 years of age.
(2) Adults can perceive the gender of children as young as four years of age, and the magnitude of the difference between boy and girl perceptual ratings is large by age 16. Adults' perception of gender from children's speech and voice is strongly related to formant frequencies for children aged 4 to 12 years, whereas f_0 plays a key role by 16 years.

ACKNOWLEDGMENTS

This article is based on a Ph.D. dissertation completed at Vanderbilt University by the first author under the direction of the second and third authors. The research was supported by NIH Grant Nos. DC00464 and DC00523, and a Vanderbilt University Research Council grant. We express our sincere gratitude to the children who participated in this study, to their parents, and to the adult listeners. The authors express their appreciation to William Caul, Jeffery Franks, Joseph Lappin, and Maureen Powers for their discussions, interest, and advice about this work. The authors thank Anders Lofqvist, Eugene Buder, and two anonymous reviewers for comments on this manuscript.

[1]Other significant interactions for $F1$ were as follows: vowel×age [$F(18,432)=7.66$; $p<0.0001$], vowel×gender [$F(6,432)=18.81$; $p<0.0001$], and vowel×age×gender [$F(18,432)=2.29$; $p<0.01$].

[2]Other significant interactions for $F2$ and $F3$ were as follows: $F2$—vowel×age [$F(18,432)=13.21$; $p<0.0001$], vowel×gender [$F(6,432)=4.84$; $p<0.001$], and vowel×age×gender [$F(18,432)=3.65$; $p<0.01$]; $F3$—vowel×age [$F(18,432)=3.10$; $p<0.0001$].

[3]Other significant interactions were as follows: vowel×speaker age [*Frs(18,342)=11.60*, $p<0.0001$], vowel×speaker gender [$F(6,114)=28.58$, $p<0.0001$], and vowel×speakerage×speakergender [$F(18,432)=5.80$, $p<0.0001$].

Abercrombie, D. (**1967**). *Elements of General Phonetics* (Edinburgh University Press, Edinburgh).
Bennett, S. (**1981**). ''Vowel formant frequency characteristics of preadolescent males and females,'' J. Acoust. Soc. Am. **69**, 321–238.
Bennett, S. (**1983**). ''A 3-year longitudinal study of school-aged children's fundamental frequencies,'' J. Speech Hear. Res. **26**, 137–142.
Bennett, S., and Weinberg, B. (**1979**). ''Sexual characteristics of preadolescent children's voices,'' J. Acoust. Soc. Am. **66**, 989–1000.
Busby, P., and Plant, G. (**1995**). ''Formant frequency values of vowels produced by preadolescent boys and girls,'' J. Acoust. Soc. Am. **97**, 2603–2606.
Cohen, J. (**1969**). *Statistical Power Analysis for the Behavioral Sciences* (Academic, New York).
Coleman, R. (**1971**). ''Male and female voice quality and its relationship to vowel formant frequencies,'' J. Speech Hear. Res. **14**, 565–577.
Coleman, R. (**1973**). ''Speaker identification in the absence of inter-subject differences in glottal source characteristics,'' J. Acoust. Soc. Am. **53**, 1741–1743.
Cruttenden, A. (**1986**). *Intonation* (Cambridge, University Press, Cambridge).
Crystal, D. (**1975**). *The English Tone of Voice* (St. Martin's Press, New York).
Crystal, D. (**1982**). *Clinical Linguistics* (Springer-Verlag, Vienna).
Eguchi, S., and Hirsh, I. (**1969**). ''Development of speech sounds in children,'' Acta Oto-Laryngol. Suppl. **257**, 2–51.
Fant, G. (**1973**). ''A note on vocal tract size factors and nonuniform F-pattern scalings,'' in *Speech Sounds and Features* (MIT Press, Cambridge, MA), pp. 84–93.
Fleiss, J. (**1981**). *Statistical Methods for Rates and Proportions* (Wiley, New York).
Haley, K. L., and Ohde, R. N. (**1996**). ''Stimulus uncertainty and speaker normalization processes in the perception of nasal consonants,'' Phonetica **53**, 185–199.
Hasek, C., Singh, S., and Murry, T. (**1980**). ''Acoustic attributes of preadolescent voices,'' J. Acoust. Soc. Am. **68**, 1262–1265.
Hollien, H., Green, R., and Massey, K. (**1994**). ''Longitudinal research on adolescent voice change in males,'' J. Acoust. Soc. Am. **96**, 2646–2654.
Ingrisano, D., Weismer, G., and Schuckers, G. (**1980**). ''Sex identification of preschool children's voices,'' Folia Phoniatr. **32**, 61–69.
Johnson, K. (**1990a**). ''The role of perceived speaker identity in f_0 normalization of vowels,'' J. Acoust. Soc. Am. **88**, 642–654.
Johnson, K. (**1990b**). ''Contrast and normalization in vowel perception,'' J. Phonetics **18**, 229–254.
Kent, R. (**1976**). ''Anatomical and neuromuscular maturation of the speech mechanism: Evidence from acoustic studies,'' J. Speech Hear. Res. **19**, 421–447.
Kent, R. D. (**1978**). ''Imitation of synthesized vowels by preschool children,'' J. Acoust. Soc. Am. **63**, 1193–1198.
Kent, R., and Vorperian, H. (**1995**). *Development of the Craniofacial–oral–laryngeal Anatomy* (Singular Publishing, San Diego).
King, E. (**1952**). ''A roentgenographic study of pharyngeal growth,'' Angle Orthod. **22**, 23–37.
Kirk, R. (**1982**). *Experimental Design: Procedures for the Behavioral Sciences* (Wadsworth, Belmont, CA).
Klatt, D., and Klatt, L. (**1990**). ''Analysis, synthesis, and perception of voice quality variations among female and male talkers,'' J. Acoust. Soc. Am. **87**, 820–857.
Ladefoged, P., and Broadbent, D. (**1957**). ''Information conveyed by vowels,'' J. Acoust. Soc. Am. **29**, 98–104.
Lass, N., Almerino, C., Jordan, L., and Walsh, J. (**1980**). ''The effect of filtered speech on speaker race and sex identifications,'' J. Phonetics **8**, 101–112.
Lass, N., Hughes, K., Bowyer, M., Waters, L., and Bourne, V. (**1976**). ''Speaker sex identification from voiced, whispered, and filtered isolated vowels,'' J. Acoust. Soc. Am. **59**, 675–678.
Laver, J., and Trudgill, P. (**1979**). ''Phonetic and linguistic markers in speech,'' in *Social Markers in Speech*, edited by K. Scherer and H. Giles (Cambridge University Press, Cambridge), pp. 1–32.
Lee, S., Potamianos, A., and Narayanan, S. (**1999**). ''Acoustics of children's speech: Developmental changes of temporal and spectral parameters,'' J. Acoust. Soc. Am. **105**, 1455–1468.
Liberman, A., Cooper, F., Shankweiler, D., and Studdert-Kennedy, M. (**1967**). ''Perception of speech code,'' Psychol. Rev. **74**, 431–461.
Lindblom, B., and Sundberg, J. (**1971**). ''Acoustical consequences of lip, tongue, jaw, and larynx movement,'' J. Acoust. Soc. Am. **50**, 1166–1179.
Mullennix, J., Johnson, K., Topcu-Durgun, M., and Farnsworth, L. (**1995**). ''The perceptual representation of voice gender,'' J. Acoust. Soc. Am. **98**, 3080–3095.
Nolan, F. (**1983**). *The Phonetic Bases of Speaker Recognition* (Cambridge University Press, Cambridge).
Nordstrom, P. (**1997**). ''Female and infant vocal tracts simulated from male area function,'' J. Phonetics **5**, 81–92.
Oates, J., and Dacakis, G. (**1983**). ''Speech pathology considerations in the management of transsexualism—A review,'' Br. J. Comm. Dis. **18**, 139–151.
Ohde, R., and Sharf, D. (**1992**). *Phonetic Analysis of Normal and Abnormal Speech* (McMillan, Columbus, OH).
Peterson, G., and Barney, H. (**1952**). ''Control methods used in a study of the vowels,'' J. Acoust. Soc. Am. **24**, 175–184.
Sachs, J., Lieberman, P., and Erickson, D. (**1973**). ''Anatomical and cultural determinants of male and female speech,'' in *Language Attitudes*, edited by R. W. Shuy and R. W. Fasold (Georgetown University Press, Washington, DC), pp. 74–83.
Schwartz, M. (**1968**). ''Identification of speaker sex from isolated, voiceless fricatives,'' J. Acoust. Soc. Am. **43**, 1178.
Spencer, L. (**1988**). ''Speech characteristics of male-to-female transsexuals: A perceptual and acoustic study,'' Folia Phoniatr. **40**, 31–42.
Sussman, H., Minifie, F., Buder, E., Stoel-Gammon, C., and Smith, J. (**1996**). ''Consonant-vowel interdependencies in babbling and early

words: Preliminary examination of a locus equation approach,'' J. Speech Hear. Res. **39**, 424–433.
Tecumseh Fitch, W., and Giedd, J. (**1999**). ''Morphology and development of the human vocal tract: A study using magnetic resonance imaging,'' J. Acoust. Soc. Am. **106**, 1511–1522.
Weinberg, B., and Bennett, S. (**1971**). ''Speaker sex recognition of 5- and 6-year-old children's voices,'' J. Acoust. Soc. Am. **50**, 1210–1213.
Wolfe, V., Ratusnik, D., Smith, F., and Northrop, G. (**1990**). ''Intonation and fundamental frequency in male-to-female transsexuals,'' J. Speech-Hear. Res. **55**, 43–50.

Providing low- and mid-frequency speech information to listeners with sensorineural hearing loss

Christopher W. Turner[a] and Shea L. Brus
Department of Speech Pathology and Audiology, University of Iowa, Iowa City, Iowa 52242

(Received 2 October 2000; accepted for publication 21 March 2001)

The present study examined the benefits of providing amplified speech to the low- and mid-frequency regions of listeners with various degrees of sensorineural hearing loss. Nonsense syllables were low-pass filtered at various cutoff frequencies and consonant recognition was measured as the bandwidth of the signal was increased. In addition, error patterns were analyzed to determine the types of speech cues that were, or were not, transmitted to the listeners. For speech frequencies of 2800 Hz and below, a positive benefit of amplified speech was observed in every case, although the benefit provided was very often less than that observed in normal-hearing listeners who received the same increase in speech audibility. There was no dependence of this benefit upon the degree of hearing loss. Error patterns suggested that the primary difficulty that hearing-impaired individuals have in using amplified speech is due to their poor ability to perceive the place of articulation of consonants, followed by a reduced ability to perceive manner information. [DOI: 10.1121/1.1371757]

PACS numbers: 43.71.Ky, 43.66.Sr, 43.66.Ts [KRK]

I. INTRODUCTION

Sensorineural hearing loss is often accompanied by reduced understanding of speech. Elevated sensitivity thresholds, leading to the inaudibility of conversational speech, is a major contributing factor. Numerous investigators have demonstrated that speech recognition for persons with mild to moderate hearing loss is often the same as that of normal-hearing listeners for equivalent amounts of audible speech information (e.g., Dubno *et al.*, 1989; Humes *et al.*, 1986; Kamm *et al.*, 1985; Zurek and Delhorne, 1987). Restoring speech audibility, usually accomplished by hearing aid amplification, is the most common form of rehabilitation for persons with sensorineural hearing loss.

On the other hand, evidence exists that reduced audibility is not the only factor contributing to speech recognition deficits in persons with sensorineural hearing loss. For listeners with more severe hearing loss, providing equivalent speech information at suprathreshold levels to both normal-hearing and hearing-impaired listeners often results in poorer speech understanding for the impaired listeners (e.g., Kamm *et al.*, 1985; Pavlovic, 1984; Ching *et al.*, 1998; Hogan and Turner, 1998; Turner and Cummings, 1999). Specifically, these studies demonstrated that when the hearing loss is more severe (greater than 50–80 dB HL) in the higher frequencies, the benefits of audible speech were, on average, negligible. In fact, for some patients, adding audible speech to regions of severe high-frequency hearing loss sometimes produced decreases in speech scores (Rankovic, 1991; Ching *et al.*, 1998; Hogan and Turner, 1998). Thus it may not always be beneficial to amplify certain frequency regions of speech for some patients.

For the most part, the above studies looked at listeners who exhibited substantial amounts of sensorineural hearing loss only in the higher frequencies. For example, the Hogan and Turner (1998) study employed only one listener with greater than 50 dB of hearing loss below 1000 Hz. Turner and Cummings (1999) showed data from one listener with a severe low-frequency hearing loss who did receive benefit from low-frequency amplification. Data from these two studies do not provide much information regarding the benefits of amplifying low-frequency speech information and its possible relation to the degree of hearing loss. The Ching *et al.* (1998) study is a notable exception to this pattern. In their study, a large proportion of the subjects had substantial hearing losses for frequencies less than 1500 Hz. In their data analysis, providing audible speech information to frequency regions of 1500 Hz and below resulted in improvements in speech recognition for the majority of subjects; however, some subjects did show zero or negative changes in speech scores when audible speech was provided to low-frequency regions. There was, on average, no obvious effect of the degree of hearing loss upon the benefit of audible low-frequency speech. Their work suggests that the benefits of audible speech are linked more closely to the degree of hearing loss in the higher frequencies than in the lower frequencies. The present study was undertaken in part to further investigate if the degree of hearing loss is an important factor in whether or not there is a benefit in providing audible speech to lower-frequency regions of hearing loss.

Why might there be differences between the benefits provided to low- versus high-frequency regions of the speech signal in terms of their dependence upon degree of hearing loss might arise? One might hypothesize that the types of speech cues located in the high versus low frequencies are different, and therefore might be differentially affected by cochlear damage. For example, place of articulation cues, which are usually located in the higher-frequency regions and tend to be signaled by the specific frequency spectrum of

[a]Author to whom correspondence should be addressed. Electronic mail: christopher-turner@uiowa.edu

the speech signal, may not be transmitted effectively by a cochlea containing regions of substantial inner hair cell loss. In contrast, cues for the presence or absence of voicing, which presumably are encoded by amplitude variations common across large regions of the speech spectrum, may not be affected by regions of inner hair cell loss as long as some intact inner hair cells remain.

The present study was designed to provide additional data on the benefits of low-frequency speech audibility for listeners with sensorineural hearing loss in that frequency region. This was accomplished by specifically selecting subjects with a wide range of hearing losses in the lower frequencies. Listeners' error patterns were also analyzed to determine if the perception of some speech features are more affected than others by the degree of hearing loss. Specifically, the present study asks the following questions.

(1) Does the benefit of providing audible speech information below 2800 Hz to listeners with sensorineural hearing loss depend upon the degree of hearing loss in those frequency regions? If so, are there situations where providing audible low-frequency speech information is not beneficial?
(2) When speech is made audible, are the perception of certain features of speech more affected than others by the degree of sensorineural hearing loss?

II. METHODS

A. Subjects

Eighteen subjects participated in the present study. Five females with a mean age of 24 years (ranging from 23 to 27 years) had hearing within normal limits with pure tone thresholds better than 20 dB HL [*re*: ANSI (1996)] for the octave frequencies from 125 to 8000 Hz. Thirteen hearing-impaired listeners (nine females and four males) also participated; their mean age was 65 years (ranging from 53 to 80 years). Subjects were selected in order to achieve a range of hearing losses in the low-frequency region. Although the majority of subjects had pure-tone thresholds poorer than 20 dB HL for the frequencies of 1000 Hz and below, a few individuals were included who had thresholds better than 20 dB HL at some of these lower frequencies. Figure 1 depicts the individual audiograms of the subjects with hearing impairment and the average hearing thresholds of the subjects with normal hearing. The hearing-impaired listeners' threshold curves are divided into two groups (open squares versus filled circles) based upon whether their pure-tone average amount of hearing loss (PTA) for 0.5, 1.0 and 2.0 kHz was better or worse than 40 dB HL, respectively.

B. Stimuli

For purposes of articulation index calculations, pure-tone thresholds were measured at the center frequency of one-third octaves from 250 to 5000 Hz, with 1000 Hz tested twice for reliability purposes. Test tones were 500 ms in duration with 25-ms rise/fall times. All testing was done in a sound booth using Sennheiser HD 25-SP circumaural headphones. All sound levels reported in these experiments are referenced to the levels developed by these headphones in the NBS-9A coupler. Participants were tested using the same ear throughout the experiment.

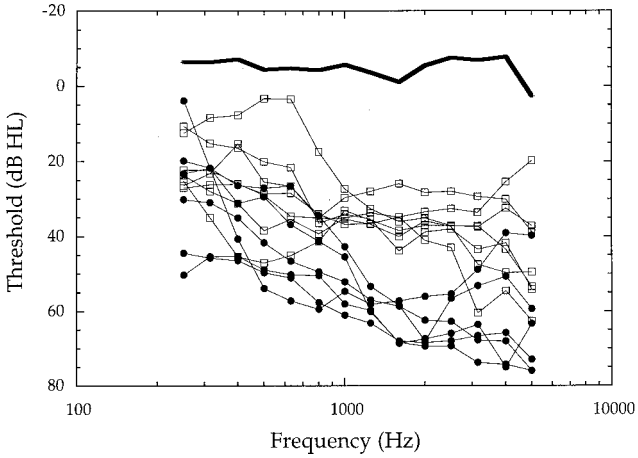

FIG. 1. The pure-tone detection thresholds at one-third octave test frequencies for the hearing-impaired listeners in this study. The heavy, solid line represents laboratory norms for a group of young, normal-hearing listeners. The lighter lines with symbols each represent one of the hearing-impaired individuals. Open squares represent subjects with pure-tone averages at 0.5, 1.0 and 2.0 kHz less than 40 dB HL, and the filled circles represent those subjects with PTA greater than 40 dB HL.

The 12 lists of the Nonsense Syllable Test (NST, UCLA version) were used to obtain measures of consonant recognition. These speech materials consist of six consonant-vowel (CV) lists and six vowel-consonant (VC) lists. Each list consisted of target consonants paired with a vowel which remained fixed throughout the list (either /u/, /i/, or /a/). Half the lists were spoken by a male talker and the other half by a female talker. The consonant phonemes used were /b/, /t/, /d/, /ʒ/, /z/, /f/, /g/, /k/, /l/, /m/, /h/, /n/, /p/, /r/, /s/, /ʃ/, /ø/, /ð/, /v/, /w/, /y/, and /z/. These speech materials were identical to those used in the Hogan and Turner (1998) study. One hundred randomly chosen stimuli were presented for each list.

The speech stimuli were stored in a digital form on a Power Macintosh 9500/150 computer after being transferred from a DAT recording. The stimuli were presented through a 16-bit, digital-to-analog converter (AudioMedia III, DigiDesign, Inc.) at a sampling rate of 44.1 kHz. The speech materials were presented using either unshaped or high-pass emphasis shaping (with an Altec-Lansing spectrum shaper), depending upon each subject's degree and configuration of hearing loss. The high-pass shaping provided approximately 20 dB of gain for frequencies above 1000 Hz. The subject was allowed to choose whether or not they desired the high-pass shaping and also to choose their presentation level in initial practice sessions listening to the NST materials in a broadband condition The experimenter instructed the subject to choose the speech level that ''provided the most information about the speech sounds yet was not uncomfortably loud.'' The chosen settings and levels were then used throughout the study for that subject. For the actual data collection portion of the experiment, the speech materials were low-pass filtered with the cutoff frequencies of 560, 700, 900, 1120, 1400, 1800, 2250, or 2800 Hz. The filter slopes were measured at approximately 30 dB/oct. For each

subject across the various filtering conditions, the levels of speech for frequency bands below the filter cutoff frequency remained the same as they were in the subject's chosen broadband settings.

C. Procedures

Pure tone stimuli for threshold testing were generated using a Power Macintosh 9500/150 computer and attenuated by a Tucker-Davis Programmable attenuator (model PATT). Each subject's air conduction thresholds were obtained in a one-up, two-down, four-alternative forced-choice method, with threshold defined as the 70.7% point in the psychometric function for each subject, using 2-dB steps.

At their first visit, subjects were trained to associate the different phonemes with specific response buttons and live-voice examples were given to demonstrate any they had difficulty identifying. After this introduction, subjects participated in the computer-controlled NST recognition procedure. Subjects were instructed to respond following each stimulus presentation by pushing the button labeled with the correct phoneme. The subjects were instructed to guess if they were unsure at any time of an answer. Feedback in the form of a correct-answer light located above the button labels was provided for these first practice runs. Each run consisted of 100 randomly chosen syllables (phoneme/vowel combination) of a particular list. Data collection was begun once the subject was able to perform consistently on the broadband speech testing (recognition scores grouped within 10 percentage points of each other on three consecutive 100-item runs). Final data for each condition for each subject consisted of 12 runs of 100 trials each, corresponding to the 12 lists of the NST materials. No trial-by-trial feedback was provided to the subject during the actual data collection, however subjects were informed of their score on each list if they were interested.

For the subjects with normal hearing, the speech recognition material was administered at 70 dB SPL (for the broadband condition), without any spectrum shaping, at eight low-pass cutoff frequencies, and also in the broadband condition. For the subjects with hearing loss, presentation level and the choice whether or not to use the spectrum shaper was individually determined for each listener, as described earlier. These levels ranged from 85 to 110 dB SPL across hearing-impaired listeners. A complete set of data for each listener consisted of all 12 lists at all of the filter cutoff frequency conditions. The order of filter cutoff conditions was randomized separately for all listeners with the exception that the practice testing was first administered at the broadband setting to familiarize the subjects with the speech materials.

III. RESULTS

A. Data analysis

Both the original articulation index, or AI (ANSI, 1969), and the revision of the AI method, known as the speech intelligibility index, or SII (ANSI, R1997), were used to quantify the audible speech information available to each subject for the various filter settings. These calculations take into account the subject's hearing loss and the level at which the speech signal was presented, along with the importance of speech information in each frequency band, giving a value ranging from 0.0 to 1.0 for each experimental condition for each subject, which represents the proportion of speech information (the AI or SII) available to the listener. Frequency-importance functions specifically measured for our recordings of the NST speech materials were provided by the UCLA group. In our application of the SII, we used speech dynamic ranges of $+12$ and -18 dB re: long-term rms level of the speech to make the two methods equivalent except for the high-presentation level corrections. The original AI procedure makes no corrections for overall speech presentation level, whereas the newer SII ''corrects'' the calculated SII value for the reduced speech information available at higher presentation levels. Thus comparing the results of the data analyzed using the original AI versus the newer SII procedures allows us to estimate the contributions of high presentation levels to the performance of the hearing-impaired listeners separate from the effects of cochlear damage in those listeners.

Data were further analyzed using FIX, a ''SINFA'' Analysis Suite (Department of Phonetics and Linguistics, University College of London). SINFA, or ''Sequential Information Analysis,'' determines the relative amount of information transferred to the listener based upon phoneme error patterns (Wang and Bilger, 1973). The analysis separates the features of speech, such that manner, voicing, and place are given individual values. The 12 files for each filter cutoff frequency for each subject were collapsed into a confusion matrix, then analyzed for the relative transmitted information (RTI) for place, voicing, and manner. RTI is a number between 0.0 and 1.0 that represents the proportion of information transmitted for each distinctive feature. In this analysis, the order of feature analysis was held fixed for voicing, manner, followed by place.

B. Normal-hearing listeners

All normal-hearing listeners scored 95% or above for the broadband condition. Their recognition scores decreased as the higher frequency regions of speech were removed by decreasing the low-pass filter cutoff. Recognition scores in each condition for each normal-hearing subject were transformed to rationalized arcsin units (RAU, Studebaker, 1985) to normalize the variance of the speech scores, and were plotted as a function of the degree of audible speech information (AI or SII). These data were then fit with a second-order polynomial curve which then served as a comparison for the hearing-impaired listeners. The second-order polynomial was chosen as the simplest curve fit that allowed for the possibility of fitting hearing-impaired data that may show a ''rollover'' as speech audibility was increased [as was found in the previous work of Hogan and Turner (1998) and Ching *et al.* (1998)]. Ninety-five percent confidence intervals about this average curve were calculated based upon the residuals of the curve fit. In Fig. 2, the average normal articulation function and its associated confidence intervals are shown by the heavy solid line (without symbols) and the surrounding lighter solid lines, respectively. As one moves from left to

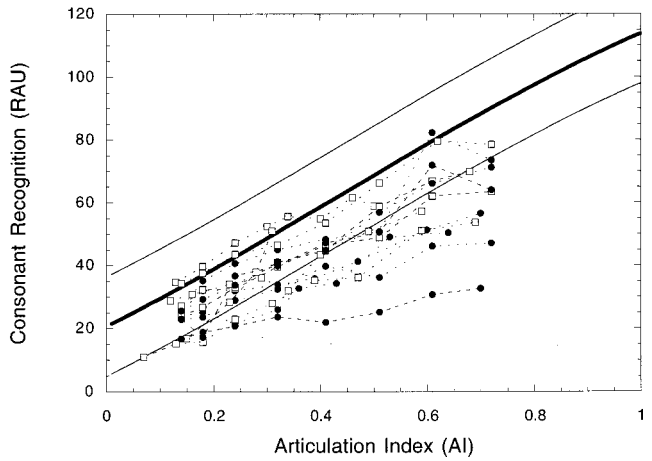

FIG. 2. Articulation functions for the individual hearing-impaired listeners. The speech recognition scores in rationalized arcsin units (RAU) are plotted as a function of the articulation index (ANSI, 1969) for each listening condition. The heavy solid line depicts the fitted curve (see text) to the average performance for the normal-hearing listeners, and the two surrounding lighter solid lines show the 95%-confidence intervals for the normal performance. The individual hearing-impaired data are shown by the lines with symbols. As in Fig. 1, the open squares represent subjects with PTA less than 40 dB HL, and the filled circles represent subjects with PTA greater than 40 dB HL.

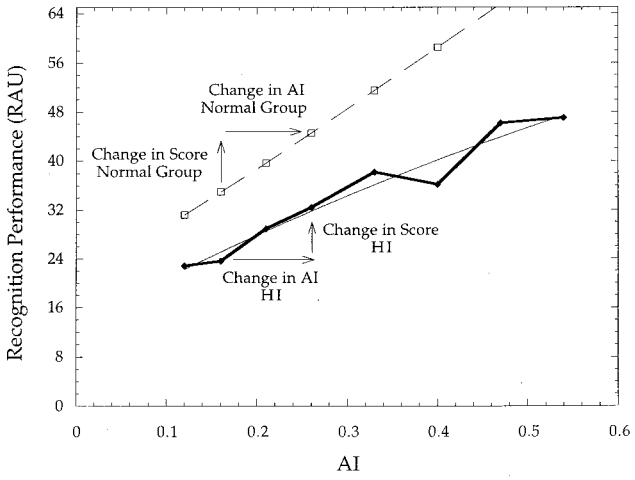

FIG. 3. An example of the method used for calculation of the efficiency measure for one hearing-impaired subject at one listening condition. The increase in speech recognition (predicted by the curve fit) for the hearing-impaired listener for a given increase in speech audibility (AI) is divided by the corresponding increase in score predicted by a curve fit to the normal-hearing data for an equivalent increase in audible speech information.

right along the fitted function, the low-pass frequency cutoff of the speech was increased. The normal data and curve fits of the present study were similar to, but slightly different from, the normal-hearing articulation function published in Hogan and Turner (1998), even though that study used the same speech materials. We speculate that these differences most likely arose from (1) the use of different normal subject populations and (2) the fact that the present data were collected using different (lower-frequency) filter cutoffs than the previous study.

C. Hearing-impaired listeners

In Fig. 2 the articulation functions obtained under the various filtering conditions are displayed for the individual hearing-impaired listeners (data also transformed into RAU). The two symbol types represent the two general groupings of subject's as in Fig. 1; those with pure-tone average better than 40 dB HL are shown by open squares, those poorer than that by filled circles. As a group, the hearing-impaired listeners performed somewhat more poorly than the normals for equivalent degrees of audible speech information, however a large number of the data points (70 out of 117) fell within the 95%-confidence intervals of the normal curve. In particular, for the leftmost points on each hearing-impaired listener's data (representing the conditions of speech low-pass filtered at 560, 700, and 900 Hz), the scores lie almost entirely within the range of normally predicted performance. This may be a ''floor'' effect, in that neither the normal-hearing or the hearing-impaired listeners performed well for these conditions. When the presented speech included the higher frequencies (the rightmost data points), the performances of the individual hearing-impaired listeners were overwhelmingly located below the normal range. However, it is not possible to clearly separate the effects of speech-band frequency from the confounding factor of the degree of hearing loss from this figure, due to the fact that most of the subjects had greater amounts of hearing loss at the higher frequencies than at the lows.

In order to examine the question of whether adding low-frequency audible speech is beneficial or not for a hearing-impaired listener, and if this depends upon the degree of hearing loss, the data for the hearing-impaired listeners were analyzed in terms of the ''efficiency'' of adding each frequency increment of the speech range. Efficiency is defined as the ratio of improvement in a speech score resulting from providing an increment in audible speech for an individual as compared to providing an equivalent increment in audible speech to normal-hearing listeners. This same measure was used in the Hogan and Turner (1998) paper in looking at the higher-frequency regions of speech. Figure 3 gives an example of a typical calculation of the efficiency for one hearing-impaired listener. For each listener with hearing loss, a second-order polynomial curve was fitted to their articulation function data. For each frequency increment of audible speech information (AI) added for a hearing-impaired subject, an equal increment in AI corresponding to the same point on the articulation function was chosen on the average function for the normal-hearing subjects. The increase in score from the fitted curve for the hearing-impaired subject was divided by the corresponding increase in the normal-hearing fitted curve to yield the efficiency measure. An efficiency of 1.0 means that the patient received the same benefit of an increment of audible speech information as a normal-hearing listener, whereas an efficiency of 0.0 means no benefit was received.

Since the pure-tone threshold was known for each listener at the center frequency of each speech frequency increment added as the filter cutoff was raised, it is possible to associate each calculated efficiency with a degree of hearing loss, as was done in the Hogan and Turner (1998) paper. A similar analysis, using a related ''proficiency'' factor as a

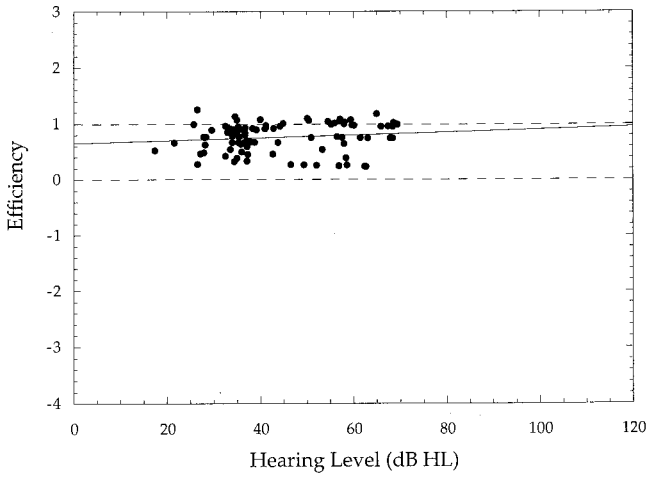

FIG. 4. The efficiency of adding audible speech for each hearing-impaired listener and each listening condition plotted as a function of the degree of hearing loss at the center frequency of the upper band of speech frequencies added in that condition. The efficiency measures in this figure are based upon calculation using the older ANSI (1969) method, in which higher presentation levels of speech are not accounted for. The fitted line is a linear regression fit to the data.

function of degree of hearing loss, was used in the Ching *et al.* (1998) study. The degree of hearing loss was calculated from the individual hearing-impaired subjects' pure-tone thresholds as compared to our laboratory norms for the one-third octave test frequencies, which were based upon a group of young, normal-hearing individuals. For all filter cutoff frequencies of 2800 Hz and below, these data are displayed in Fig. 4. One should keep in mind that since the low-pass filter slopes in this experiment were not infinite, when speech was low-pass filtered with a stated filter cutoff, some speech information from the next few higher one-third octave bands was often also audible to the listener. Thus the ''effective'' cutoff frequency for the low-pass speech was somewhat higher than the nominal cutoff frequency used in each condition. This ''effective'' cutoff frequency depended upon the subject's hearing thresholds and also upon the presentation level of the speech, but in all cases additional audible information was calculated to be present in only one or two one-third-octave bands above the nominal cutoff frequency. In Fig. 4, the efficiencies were calculated using the ANSI (1969) standards for calculation of the AI, meaning that the higher presentation levels for speech for the hearing-impaired listeners will contribute to the calculated efficiency. Since hearing-impaired individuals have no choice but to listen to speech at higher presentation levels, this analysis depicts the benefit that they might expect listening to amplified speech.

Figure 4 shows that for hearing losses up to approximately 75 dB HL, and for speech information at approximately 2800 Hz and below, all efficiencies were positive. However, many efficiency values for the hearing-loss subjects were less than 1.0, indicating that they did not receive full benefit from audible speech. There was no relation between the degree of hearing loss and the efficiency when the data were collapsed across all frequencies. A linear regression line fit to the data yielded a slightly positive slope, however the correlation coefficient of $r=0.13$ was not significant ($p>0.05$). While the average efficiency was less than 1.0, and there was considerable scatter in the data, it is still the case that providing amplified, audible speech for the lower-frequency regions of the spectrum was beneficial in every case.

In Fig. 5, the efficiencies from Fig. 4 are plotted separately by frequency, corresponding to the center frequencies of the added speech bands for six of the filter cutoff frequencies. The seventh condition (1000 Hz center frequency) was omitted from this figure to conserve space; however the 1000-Hz data was very similar to the data shown in the six panels of Fig. 5. Linear regression lines are fit to each of these data subsets, and a slight positive slope was found in six of the seven cases. None of the correlations were significant ($p<0.05$), with correlation coefficients ranging from $r=-0.02$ to $r=0.29$. With the limited number of data points in each panel, these slope estimates are, however, not particularly reliable. The general pattern of results in the panels of Fig. 5 is similar across frequency; in each case, the efficiency is greater than zero, and there is no tendency for the benefits of amplification at these lower frequencies to decrease as a function of degree of hearing loss.

In Fig. 6, the efficiencies across all frequencies [as calculated using the newer SII standards (ANSI, R1997)] are plotted. In these calculations, the SII contains a correction for ''loud'' speech levels, resulting in an estimate of the benefit of audible speech that would be obtained if the speech could have been presented audibly to the hearing-impaired listeners at lower sound levels. If these ''loud speech'' corrections are accurate, then any deficits in speech recognition for our hearing-impaired patients seen in this figure would be due to the damage to the auditory system accompanying sensorineural hearing loss, without a negative contribution from ''loud speech.'' By comparing the pattern of results in Fig. 4 with those of Fig. 6, we can estimate the contribution of ''loud'' speech to amplification benefit for these lower frequencies. There is a slight tendency for some of the efficiencies to be higher when corrected for loud speech; however, the important trends of the data remain unchanged. There are no negative efficiencies when they are calculated using the older AI or the newer SII standards. In Fig. 6, there is also no significant correlation between the amount of benefit provided by audible speech and the degree of hearing loss for frequencies of approximately 2800 Hz and below ($r=-0.18$; $p<0.5$). As in Figs. 4 and 5, the amount of benefit provided by making speech information audible to the hearing-loss listeners was often less than that obtained by providing a similar increment in audible speech information to normal-hearing listeners.

D. Distinctive features of speech

In order to determine what types of speech cues are transmitted most effectively to listeners with sensorineural hearing loss when they are provided with audible speech, the relative transmitted information (RTI) was calculated for each condition and each listener for the features of voicing, manner, and place. For each calculation of RTI, the degree of audible speech information (AI) was also calculated [using the older, ANSI (1969) standards]. One caution is that the AI

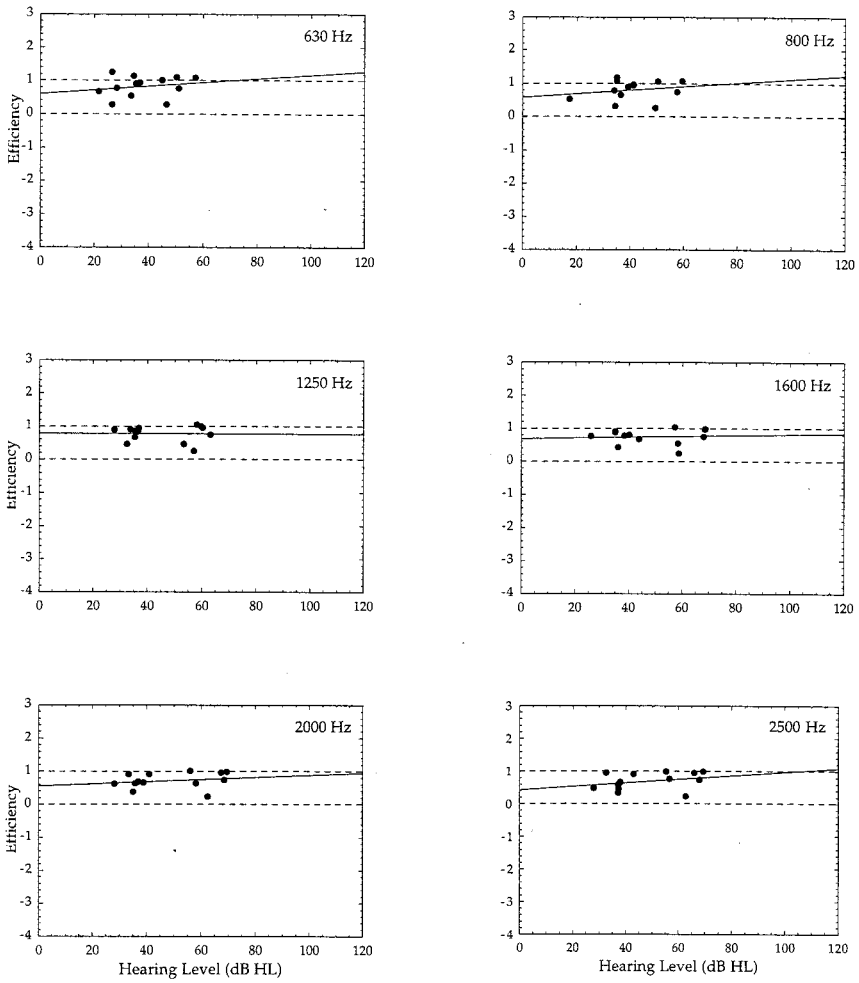

FIG. 5. The individual panels represent the efficiency data from Fig. 4, separated by the center frequency of the speech band added.

and its frequency-importance functions were not specifically designed to be used with feature analysis data; Duggirala *et al.* (1988) showed that the frequency-importance functions for several of the distinctive features of speech were different from frequency-importance functions based upon overall recognition score. However, the present calculations provide a reasonable first approximation of speech audibility for this comparison. In particular, the same AI procedures are used for the normal-hearing and the hearing-impaired listeners.

In Fig. 7, the RTI for voicing information is plotted as a function of AI for the group normal data as well as for the individual hearing-impaired listeners. The average normal data are indicated by the heavy solid line, and the 95%-confidence intervals are indicated by the lighter surrounding solid lines. The hearing-impaired individuals' data are shown by the individual lines with symbols. Figure 7 shows that considerable voicing information is available to normal-hearing listeners when only the lowest frequency portions of speech are presented (left side of the heavy solid lines). As the frequency cutoff of the low-pass filter was increased, very little increase in voicing information is even possible. The hearing-impaired listeners, as a group, performed slightly poorer than the normal group for the lower values of AI, and increasing speech audibility by providing higher-frequency speech information provided only small gains in the perception of voicing. The present results suggest that most individuals with sensorineural hearing loss have a small deficit in the perception of voicing even when speech information is made audible, and that this small deficit is not compensated for by increasing the frequency bandwidth of speech made available to the listener. One hearing-impaired subject (the lowest set of data in Fig. 7) seemed to be an exception to this trend. This subject performed poorly for the perception of voicing in all conditions. This same subject was the poorest performer for all analyses of the data including the overall performance measures presented in previous figures, as well as in the following analyses of manner and place. No specific characteristics of this subject's audiogram were noted that would seem to distinguish him/her from the other more severe hearing-loss subjects however.

In Fig. 8, the RTI for the perception of manner as a function of audible speech information is displayed. For this feature of speech, increasing the amount of high-frequency speech information provides a substantial increase in the perception of the manner feature for the normal-hearing listeners. The listeners with hearing loss perform at the lower end of the normal range for the lowest frequencies of speech, and as additional high frequencies of speech are added, their perception of manner continues to lag behind that of the normals.

Figure 9 displays RTI for place of articulation information as a function of AI. The normal-hearing listeners receive

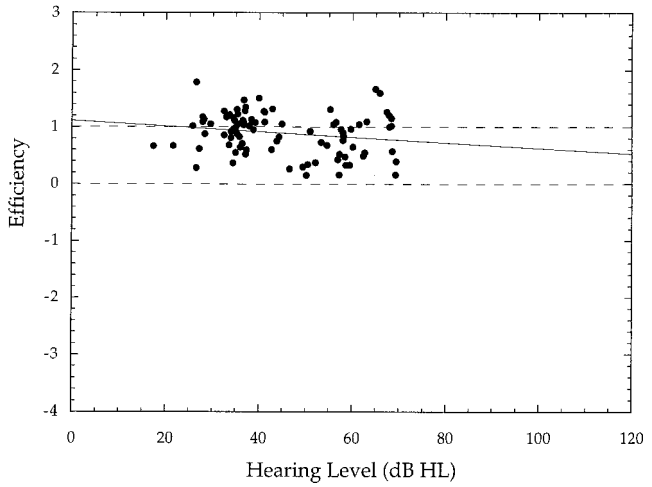

FIG. 6. The efficiency of adding audible speech for each hearing-impaired listener and each listening condition plotted as function of the degree of hearing loss at the center frequency of the speech frequencies added in that condition. The efficiency measures in this figure are based upon calculation using the newer SII ANSI (1997) method, in which higher presentation levels of speech are corrected for. The fitted line is a linear regression fit to the data.

almost no place information from the lowest frequencies of speech, and as the higher frequencies are added, their perception of the place feature increases rapidly. The listeners with hearing loss perform considerably poorer than the normals for the perception of place as the higher frequencies of speech are added. It is also very evident that those listeners with more severe hearing losses (filled circles) perform considerably poorer than those with lesser amounts of hearing loss (open circles) as the higher frequencies of speech are added to the signal.

IV. DISCUSSION

In the present study, all listeners received some benefit from amplified speech in the lower-frequency regions of the spectrum. There was no dependence upon the degree of hearing for the hearing losses employed in this study (up to 70 dB HL). The present study provides further support for the previously reported conclusions of Ching *et al.* (1998), in which they found that the majority of hearing-impaired listeners received benefit for amplified speech for frequencies of approximately 2800 Hz and below, even when hearing losses were as great as 90–100 dB HL. These conclusions for the lower frequencies of the speech range are in contrast to the case of higher frequencies (above 3000 Hz). Hogan and Turner (1998), as well as Ching *et al.* (1998), found that for higher frequencies the amount of benefit received from amplification did depend upon the degree of hearing loss, such that when the hearing loss exceeded approximately 50–80 dB HL, a substantial number of patients received no

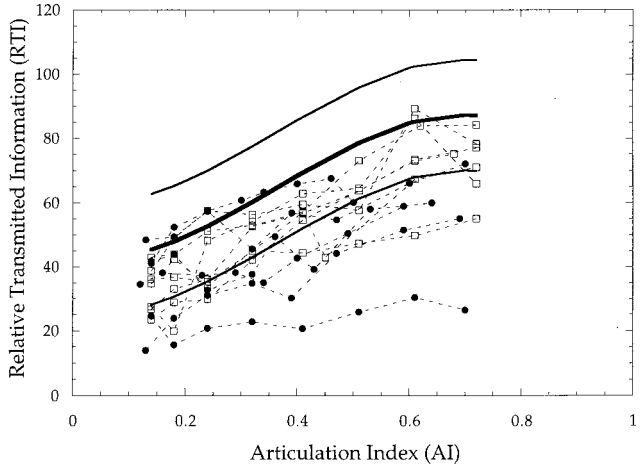

FIG. 8. The relative information transmitted for the feature of manner for all subjects plotted as a function of the degree of audible speech information (AI) for each listening condition. The heavy solid line represents the average performance of the normal-hearing group, and the surrounding lighter, solid lines are the 95%-confidence intervals of the normal data. Individual hearing-impaired listeners' data are shown by the lines with symbols as in previous figures.

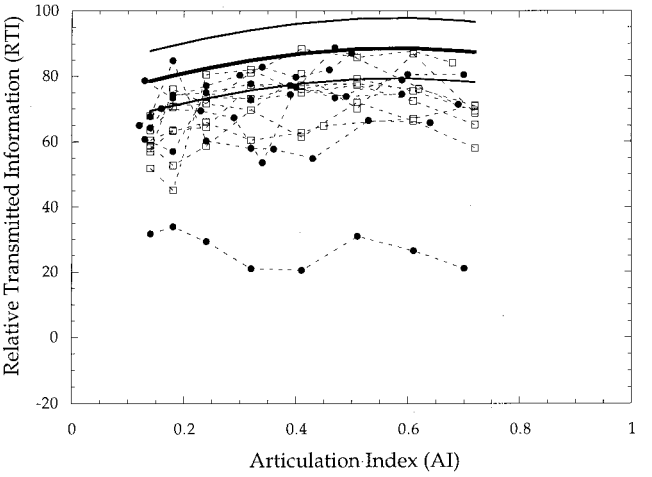

FIG. 7. The relative information transmitted for the feature of voicing for all subjects plotted as a function of the degree of audible speech information (AI) for each listening condition. The heavy solid line represents the average performance of the normal-hearing group, and the surrounding lighter, solid lines are the 95%-confidence intervals of the normal data. Individual hearing-impaired listeners' data are shown by the lines with symbols as in previous figures.

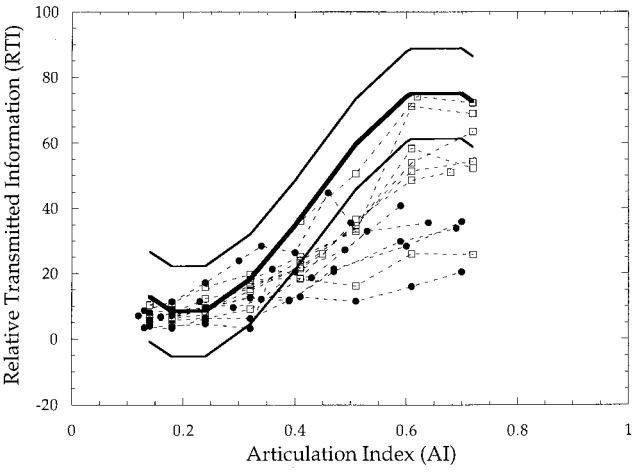

FIG. 9. The relative information transmitted for the feature of place for all subjects plotted as a function of the degree of audible speech information (AI) for each listening condition. The heavy solid line represents the average performance of the normal-hearing group, and the surrounding lighter, solid lines are the 95%-confidence intervals of the normal data. Individual hearing-impaired listeners' data are shown by the lines with symbols as in previous figures.

benefit from amplification. While all listeners in the present study did receive some benefit from amplification in the lower frequencies, in most cases the amount of benefit was less than that observed in normal-hearing listeners for equivalent increases in audible speech information. The implications of these results are that in most cases providing audible speech to lower frequency regions will be beneficial, however, even providing fully audible speech will usually not restore speech recognition abilities to completely normal capabilities. For higher-frequency regions in hearing-impaired listeners, amplification may not always be beneficial. In both cases (high and low frequencies), the general pattern of results did not change when the data were analyzed using newer SII procedures that ''corrected'' for the higher-than-normal presentation levels of speech that are required to make speech audible for hearing-impaired listeners. This implies that the underlying causes of these deficits are primarily due to the consequences of more severe cochlear damage in the basal end of the cochlea, and not merely to high presentation levels.

Why the apparent differences between high- and low-frequency regions of the audiogram? It appears that this is a result of the types of speech cues residing in the different regions of the speech spectrum, as well as the consequences of severe hearing loss upon the transmission of the various types of speech cues. Miller and Nicely (1955), among others, demonstrated that place of articulation information for speech is located primarily in the frequencies of 1000 Hz and above, whereas a great deal of voicing information is present at lower frequencies. In the present data, we observed the same pattern of results in our measures of normal-hearing listeners. Our hearing-impaired listeners showed only a slight deficit for voicing information for all frequency-cutoff conditions. On the other hand, perception of place of articulation information by our hearing-impaired listeners was considerably poorer than that of the normal-hearing group, and this deficit began to appear almost as soon as mid- to high-frequency regions of speech were presented. It was also the case that the more severe the hearing loss, the more severe the deficit for place perception. The pattern of results for the perception of manner lay somewhere in between those of voicing and manner. This suggests that the unique nature of place of articulation (and to a lesser extent, manner) cues of speech as opposed to those for voicing, in combination with the inability of more severe degrees of hearing loss to transmit these cues, results in the differential pattern of results for high versus low-frequency regions, even when speech information is made audible to the listener. Thus, a reasonable goal for future types of sensory aids for hearing-impaired individuals should be to increase the transmission of place (and to a lesser degree, manner) cues of speech which are generally located in the higher-frequency regions of the audiogram.

ACKNOWLEDGMENTS

This research project is based in part upon a Master's thesis in Audiology by the second author. Support for this work was provided by the National Institute of Deafness and other Communicative Disorders (1R01 DC00377). Helpful comments on an earlier draft of the paper were provided by Ruth Bentler and Belinda Henry.

ANSI (**1969**). ANSI S3.5-1969, ''American National Standard: Methods for the Calculation of the Articulation Index'' (American National Standards Institute, New York).

ANSI (**1996**). ANSI S3.6-1996, ''American National Standard: Specification for Audiometers'' (American National Standards Institute, New York).

ANSI (**R1997**). ANSI S3.6-1997, ''American National Standard: Methods for the Calculation of the Articulation Index'' (American National Standards Institute, New York).

Ching, T., Dillon, H., and Bryne, D. (**1998**). ''Speech recognition of hearing-impaired listeners: Predictions from audibility and the limited role of high-frequency amplification,'' J. Acoust. Soc. Am. **103**, 1128–1140.

Dubno, J. R., Dirks, D. D., and Schaeffer, A. B. (**1989**). ''Stop-consonant recognition for normal-hearing listeners and listeners with high-frequency hearing loss II. Articulation Index predictions,'' J. Acoust. Soc. Am. **85**, 355–364.

Duggirala, V., Studebaker, G. A., Pavlovic, A. V., and Sherbecoe, R. L. (**1988**). ''Frequency-importance functions for a feature recognition test material,'' J. Acoust. Soc. Am. **83**, 2372–2382.

Hogan, C., and Turner, C. W. (**1998**). ''High-frequency amplification: Benefits for hearing-impaired listeners,'' J. Acoust. Soc. Am. **104**, 432–441.

Humes, L. E., Dirks, D. D., Bell, T. S., Ahlstrom, C., and Kincaid, G. E. (**1986**). ''Applications of the Articulation Index and the speech transmission index to the recognition of speech by normal-hearing and hearing-impaired listeners,'' J. Speech Hear. Res. **29**, 447–462.

Kamm, C. A., Dirks, D. D., and Bell, T. D. (**1985**). ''Speech recognition and the articulation index for normal and hearing-impaired listeners,'' J. Acoust. Soc. Am. **77**, 281–288.

Miller, G. A., and Nicely, P. E. (**1955**). ''An analysis of perceptual confusions among some English consonants,'' J. Acoust. Soc. Am. **27**, 338–352.

Pavlovic, C. V. (**1984**). ''Use of the Articulation Index for assessing residual auditory function in listeners with sensorineural hearing impairment,'' J. Acoust. Soc. Am. **75**, 1253–1258.

Rankovic, C. M. (**1991**). ''An application of the Articulation Index to hearing aid fitting,'' J. Speech Hear. Res. **34**, 391–402.

Studebaker, G. A. (**1985**). '' A 'rationalized' arcsine transform,'' J. Speech Hear. Res. **12**, 455–462.

Turner, C. W., and Cummings, K. J. (**1999**). ''Speech Audibility for Listeners with High-Frequency Hearing Loss,'' Am. J. Audiol. **8**, 47–56.

Wang, M. D., and Bilger, R. C. (**1973**). ''Consonant confusions in noise: a study of perceptual features,'' J. Acoust. Soc. Am. **54**, 1248–1266.

Zurek, P. M., and Delhorne, L. A. (**1987**). ''Consonant recognition in noise by listeners with mild and moderate sensorineural hearing impairment,'' J. Acoust. Soc. Am. **82**, 1548–1559.

Audio-visual enhancement of speech in noise

Laurent Girin,[a] Jean-Luc Schwartz,[b] and Gang Feng[c]
Institut de la Communication Parlée, INPG/Université Stendhal/CNRS UMR 5009, Université Stendhal, Domaine universitaire, 38040 Grenoble, France

(Received 5 November 1998; revised 26 May 2000; accepted 29 January 2001)

A key problem for telecommunication or human–machine communication systems concerns speech enhancement in noise. In this domain, a certain number of techniques exist, all of them based on an acoustic-only approach—that is, the processing of the audio corrupted signal using audio information (from the corrupted signal only or additive audio information). In this paper, an audio-visual approach to the problem is considered, since it has been demonstrated in several studies that viewing the speaker's face improves message intelligibility, especially in noisy environments. A speech enhancement prototype system that takes advantage of visual inputs is developed. A filtering process approach is proposed that uses enhancement filters estimated with the help of lip shape information. The estimation process is based on linear regression or simple neural networks using a training corpus. A set of experiments assessed by Gaussian classification and perceptual tests demonstrates that it is indeed possible to enhance simple stimuli (vowel-plosive-vowel sequences) embedded in white Gaussian noise. [DOI: 10.1121/1.1358887]

PACS numbers: 43.72.Ew, 43.71.Ma [DOS]

I. INTRODUCTION

The bimodal nature of speech is now acknowledged as a basic characteristic, both for understanding speech perception (Summerfield, 1987) and for developing tools for human–human and human–machine communication (Bernstein and Benoît, 1996). One of the most well-known paradigms for the study of audio-visual speech perception is the identification of speech in noise (Sumby and Pollack, 1954; Erber, 1975; MacLeod and Summerfield, 1987; Benoît *et al.*, 1994; Grant and Walden, 1996; Robert-Ribes *et al.*, 1998). In the field of speech technologies, there is an increasing number of works on automatic audio-visual speech recognition systems, evaluated in general through their performance in recognizing speech in adverse conditions (e.g., Stork and Hennecke, 1996).

In all these studies, a common assumption is that the audio and visual sensors process information *independently* for parameter estimation, feature extraction or category estimation (according to the various architectures proposed, see Schwartz *et al.*, 1998) before they are fused by the human brain or the decision recognition algorithm for achieving an audio-visual identification task. The question of the dependence versus independence of processing is seldom addressed (although see Massaro, 1989) but independence is implicit in all recognition systems and cognitive models of audio-visual speech identification.

At the same time, it is obvious that there is some dependence between the *content* of the sensory inputs, that is audio and visual speech, since they are both consequences of one physical cause, the articulatory gestures: e.g., spread lips may be associated in French with the sound of an [i] or a [ti] but not an [y] or a [by], while open lips are compatible with almost nothing but the sound of an [a]. This means that some *predictions about the sound* should be feasible from the image. Indeed, it seems that the visual information coming from a speaker is able to improve the auditory *detection* of speech in noise (Grant and Seitz, 2000). Hence it is likely that audio and video processing are not independent in human perception. This could result in an additional contribution to audio-visual speech perception, in which the visual stream would not only provide an intrinsic benefit through lipreading, but also, at an earlier level, help the extraction of audio cues necessary for identification (Barker *et al.*, 1998). This idea receives some confirmation through data obtained by Driver (1996) which show that seeing a speaker improves the identification of a message produced by *another* unseen speaker, the audio component of which has been mixed with the audio component of the seen speaker's message.

All these facts lead us to suggest that sound enhancement could exploit the information contained in the coherent visible movements of the speaker's face. The objective of this study was to demonstrate the technical feasibility of audio-visual speech enhancement—that is, the enhancement of noisy speech sounds, using the video input—which, to our knowledge, has never before been attempted. We developed a prototype system that generates enhanced speech sounds from noisy speech plus visual information. It is based on a *fusion-and-filtering* algorithm that combines the information provided by the noisy audio and video channels to estimate the parameters of an enhancement filter—in this case, a Wiener filter—and then processes the noisy audio input with this filter.

This study focused on degradations due to additive, stationary, white Gaussian noise. Obviously, such ''simple'' degradations of the audio input could be efficiently removed using classical pure audio enhancement systems, such as spectral subtraction based on noise estimation in silent periods of speech (Boll, 1979; McAulay and Malpass, 1980;

[a]Electronic mail: girin@icp.inpg.fr
[b]Electronic mail: schwartz@icp.inpg.fr
[c]Electronic mail: feng@icp.inpg.fr

Kang and Fransen, 1989; Le Bouquin-Jeannès and Faucon, 1995), multi-microphone techniques (Widrow *et al.*, 1975; Sambur, 1978; Boll and Pulsipher, 1980; Ferrara and Widrow, 1981; Harrison *et al.*, 1986; Feder *et al.*, 1989), or blind source separation (Comon *et al.*, 1991; Jutten and Hérault, 1991; for an overview of basic acoustic speech enhancement methods, see Lim, 1983). However, our aim was to demonstrate that enhancement may be improved through the use of the video channel. Therefore, we focused on a mono-microphone technique, and special care was given to implement three variants within the fusion-and-filtering process: that is, filter parameters were estimated from only the audio sensor, only the video sensor, or both sensors. The enhancement results were then compared systematically. This enabled us to determine if the system was able to exploit the partial complementarity of the audio and video signals in speech perception: that is, the phonetic contrasts least robust in auditory perception in acoustical noise are the most visible ones, both for consonants (Summerfield, 1987) and vowels (Robert-Ribes *et al.*, 1998). In the future, our project will be to combine the audiovisual technique—if successful—with the previously mentioned pure audio mono- or multi-microphone algorithms to improve speech enhancement: this will be discussed further in Sec. V.

This paper is organized into five sections. In Sec. II, we introduce the basic components of the system: the architecture for estimating filter parameters from audio and video inputs, the filter design, and the nature of these audio and video inputs. In Sec. III, we describe the experimental conditions in more detail and present the main results obtained with an early version of the system. In Sec. IV, we present a second version in which we implemented more powerful (and more successful) processing tools to eliminate difficulties encountered with plosives. Both objective tools such as classification experiments and subjective tools involving perceptual data from identification tests were used to assess the enhancement effect. Finally, in Sec. V, we evaluate the achievements of the system and propose a number of directions for future development.

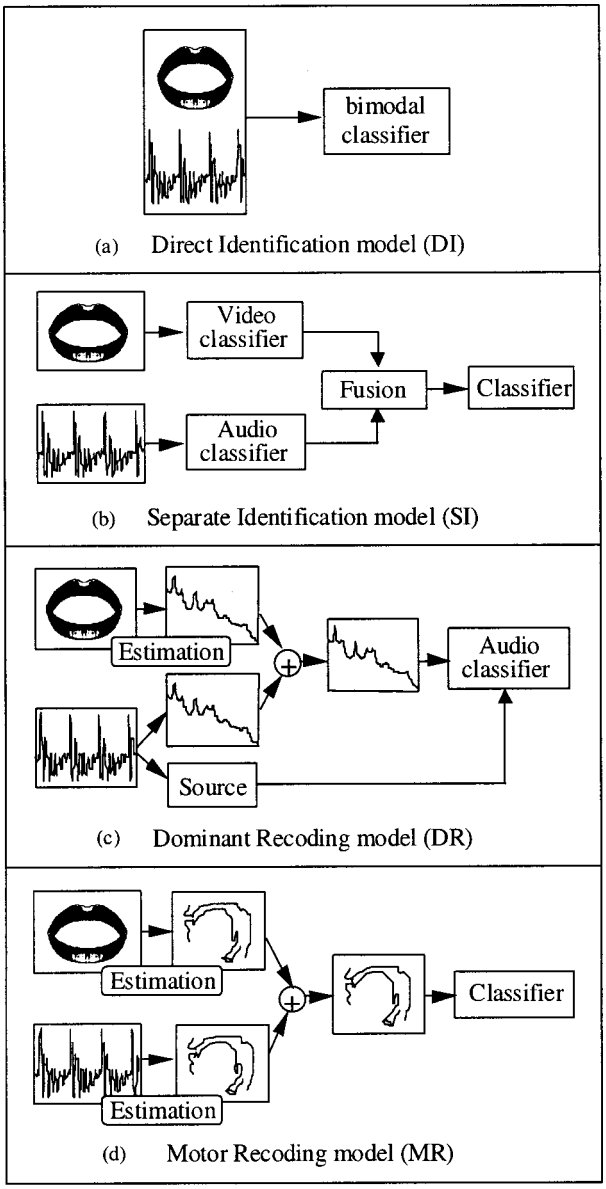

FIG. 1. Four integration models for audiovisual speech identification.

II. ARCHITECTURE OF THE SPEECH ENHANCEMENT SYSTEM

A. Audio-visual fusion for speech enhancement

Audio-visual speech enhancement is a multi-channel enhancement problem. Most classical multi-sensors noise canceling systems are based on the calculation of correlation functions between the samples of different audio inputs. In our case, the two sensors, that is, the audio and the video input, are quite different in nature. Indeed, the visual input, which is restricted to lip characteristics, has a low sampling frequency compared to the audio one, and it provides only partial information about the vocal tract shape, and no information at all about the source. Hence no usual correlation function can be computed, and we cannot exploit these noise canceling systems as they are. However, the partial information provided by the lips about the vocal tract shape corresponds to some information on the spectral shape of the speech signal. Hence it can be used to define the spectral parameters of an enhancement filter designed to process the audio noisy channel. As additional spectral information should be available from the audio channel, even degraded, the audio and video inputs must be integrated for an accurate estimation of the filter.

Since the problem of mixing an audio and a video speech stream has been addressed extensively in automatic speech recognition, it may be interesting to analyze the proposed solutions. It appears that there exist four basic architectures for fusing sounds and images toward the identification of the speech message (Schwartz *et al.*, 1998). We shall review them briefly, before attempting to study their adaptation to the speech enhancement problem.

In speech recognition, the problem is to estimate a phonetic class from audio and video parameters. In the Direct Identification model (DI), the input stimuli are recognized by a bimodal classifier, which works with vectors of concatenated audio-visual parameters [Fig. 1(a)]. In the Separate Identification model (SI), the audio and video inputs are clas-

sified separately before a late-integration fusion process occurs on the separate classification results [Fig. 1(b)]. In contrast, the last two models are based on early-integration (i.e., before classification). In the Dominant Recoding model (DR), audition is supposed to be the dominant modality for speech perception and the visual input is recoded into an auditory representation. Then, classification takes place inside this auditory integration space [Fig. 1(c)]. In the Motor Recoding model (MR), both inputs are projected into an amodal motor representation of articulatory gestures before fusion and classification [Fig. 1(d)].

In this speech enhancement problem, the parameters of an enhancement filter $H(\theta)$ must be estimated from audio and video parameters. The noisy acoustic input is then processed by this filter to provide an enhanced audio signal. By adapting the previous taxonomy to audio-video fusion for filter estimation, four possible architectures can be defined: Direct Estimation (DE) of the filter from the audio+video parameters [Fig. 2(a)]; Separate Estimations (SE) of spectral characteristics of the filter from each input, followed by a fusion process [Fig. 2(b)]; Dominant Recoding (DR) of the video input into spectral characteristics of the filter [Fig. 2(c)]; or implementation of a complete audio-visual inversion process followed by a resynthesis of the filter (Motor Recoding, MR) [Fig. 2(d)].

Within these four architectures, the last one, MR, while quite appealing for theoretical and technical reasons, seems not feasible at present. Indeed, articulatory data are sorely lacking, and neither audiovisual-to-articulatory inversion, nor articulatory-to-acoustic synthesis are sufficient (although see promising advances in, e.g., Bailly *et al.*, 1991; Schroeter and Sondhi, 1994; Yehia *et al.*, 1998). The DR structure, which is the simplest one, has already been tested (Girin *et al.*, 1996). Although preliminary results on vowel enhancement were interesting, they were limited by the fact that the filter was estimated only from the visual input. Therefore, it seems necessary to combine audio and video inputs for filter estimation, which is the case of the two other architectures, SE and DE. Using DE seems to provide a more general framework than SE and requires fewer *a priori* assumptions about audio-visual fusion; this is the one which was selected in this study. In this architecture, the filter estimation is realized from both the video and the noisy audio input. We compared this audio-visual (AV) version with an audio-only (A) condition and with a video-only (V) condition in which only the noisy audio input or only the video input was used for filter estimation. Notice that the V condition is similar to both the DR architecture and the video branch of SE, while the A condition is a special case of the audio branch of SE. This provided a basic homogeneous framework for a comparison with the audio techniques. Such comparisons enabled us to evaluate the true benefit of the video input for speech enhancement, and the role of the audio-visual synergy in this process. In the following, the synergy criterion will be the test of the inequality AV$\geqslant$(A or V), that is, performances should be better with two inputs than with one.

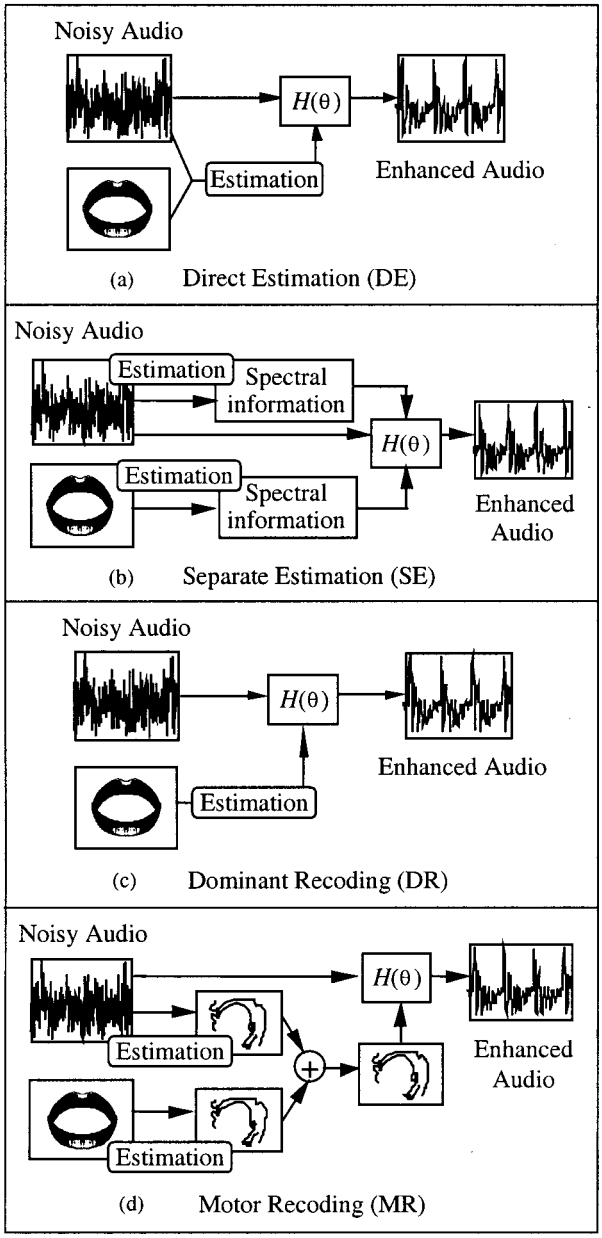

FIG. 2. Four derived integration models for audiovisual speech enhancement.

B. Filter estimation

The sensor fusion process in the DE architecture converges on the estimation of the filter frequency response $H(\theta)$ [Fig. 2(a)]. We shall now specify our choice for this filter and its estimation process. Let us denote, respectively, the speech signal $s(t)$, the noise $v(t)$ [white, Gaussian and assumed to be uncorrelated with $s(t)$], and the observed noisy signal $x(t)=s(t)+v(t)$. The linear, optimal estimator of the signal according to the mean square error criterion is obtained by filtering $x(t)$ with the Wiener filter, of which the expression in the (normalized) frequency domain is (Lim, 1983):

$$H(\theta)=\frac{P_s(\theta)}{P_x(\theta)}, \tag{1}$$

where $P_s(\theta)$ and $P_x(\theta)$ denote, respectively, the power

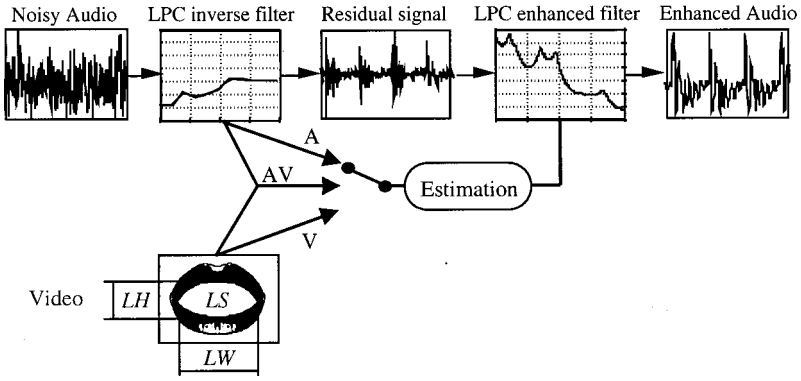

FIG. 3. General schema for the audio-visual speech enhancement system. AV, A, and V correspond, respectively, to the audiovisual, audio-only, and visual-only conditions. The *LW*, *LH*, and *LS* lip contour parameters are defined in Sec. III A 2.

spectral densities (PSD) of the signal and the observed noisy signal.

$P_x(\theta)$ can be estimated directly from the observed noisy signal with classical spectral analysis techniques. The major problem is the estimation of $P_s(\theta)$ since the signal is corrupted by noise. In the present system, $P_s(\theta)$ was estimated using an associative algorithm (henceforth ''associator'') trained on data from a training corpus. This corpus contained clean audio stimuli and their associated video input. The audio stimuli were mixed with noise in a controlled way, so that both clean and noisy spectra (PSD) were available. Then, we used this training set to tune the following three associators:

- an audio-only associator A estimating $P_s(\theta)$ from $P_x(\theta)$ only;
- a video-only associator V estimating $P_s(\theta)$ from the video input only;
- an audio-visual associator AV estimating $P_s(\theta)$ from both $P_x(\theta)$ and the video input.

Concerning the representation of the PSDs, a linear prediction (LP) model was used (Markel and Gray, 1976). There are several justifications for this choice. Since the lip contour provides no information about the source, only the global shape of the short-time spectral amplitude (STSA) of the signal can be estimated from a labial shape, rather than any information on the fine (temporal) structure of the signal.[2] It so happens that the LP model is an efficient method for coding the STSA envelope with a small number of coefficients that can be used by the associators. Furthermore, the LP model has the form of an all-poles transfer function, that is to say a numeric filter, which can be easily used to build the enhancement filter.

Thus the A, V, or AV associators deliver an estimated spectrum of the signal modeled by LP equations, that is,

$$\hat{S}_s(z)=\frac{\hat{G}_s}{1+\Sigma_{i=1}^{p}\hat{a}_{si}z^{-i}}=\frac{\hat{G}_s}{\hat{A}_s(z)}, \tag{2}$$

where $\hat{A}_s(z)=1+\Sigma_{i=1}^{p}\hat{a}_{si}z^{-i}$ is the polynomial of the estimated LP signal model and $\hat{G}_s$ is its gain (the detailed protocol for this estimation will be described in the methodology sub-sections). Then, the PSD $P_s(\theta)$ can be estimated by $|\hat{S}_s(e^{j\theta})|^2$. The observation spectrum is estimated with the LP model calculated directly on the noisy signal, that is,

$$S_x(z)=\frac{G_x}{1+\Sigma_{i=1}^{p}a_{xi}z^{-i}}=\frac{G_x}{A_x(z)}, \tag{3}$$

and $P_x(\theta)$ can be estimated by $|S_x(e^{j\theta})|^2$. Now, the enhancement filter is defined by

$$H(z)=\frac{|\hat{S}_s(z)|^2}{|S_x(z)|^2}=\frac{\hat{G}_s^2}{G_x^2}\frac{A_x(z)A_x(z^{-1})}{\hat{A}_s(z)\hat{A}_s(z^{-1})}. \tag{4}$$

This filter was implemented with the two following restrictions. First, since no information about the source energy can be estimated from the lip shape, $\hat{G}_s$ remained unknown. In other words, only the $\hat{a}_{si}$ coefficients could be estimated from the lip shape (i.e., the coefficients that describe the global shape of the spectrum but not its energy level). Thus the filter was defined without its gain, and the output signal was renormalized in energy with the same energy as the input signal. Second, to simplify the model, only the causal factorized part of the filter was considered, that is,

$$H(z)=\frac{A_x(z)}{\hat{A}_s(z)}. \tag{5}$$

Hence, the filtering can be considered as a two-step process, summarized in Fig. 3. In the first step, an LP analysis was performed on the noisy signal and the noisy residual signal was extracted by filtering through the inverse noisy LP filter $A_x(z)$. Then, a new signal was synthesized by filtering the residual through the LP filter $1/\hat{A}_s(z)$, estimated by the associators. Enhancement was expected, provided that the estimated spectrum was close enough to the true spectrum of the signal, or at least, closer than the noisy spectrum $1/A_x(z)$. For continuous speech, the processing was performed frame-by-frame in synchrony with the extraction period of the video parameters. A trapezoidal window was applied to frame junctions to ensure the continuity of the filtered signal.

III. A, V, AND AV ENHANCEMENT OF VOWEL-PLOSIVE-VOWEL SEQUENCES

A. Stimuli

1. Phonetic content and predictions

To evaluate the feasibility of the method and to assess its potential advantages and drawbacks, we worked on a simple corpus consisting of single speaker French vowel–consonant sequences of the form $V_1CV_2CV_1$, where V_1 and

TABLE I. Phonetic features for the vowel set [a,i,y,u] (a) and the plosive set [p,t,k,b,d,g] (b). Only the height feature is required for the vowel [a]. The [a] stimuli/answers were not used in the computation of transmitted information for the rounding and backness features.

(a) Vowel	Height	Rounding	Backness
a	−	?	?
i	+	−	−
y	+	+	−
u	+	+	+

(b) Consonant	Place	Voicing
p	labial	unvoiced
t	dental	unvoiced
k	velar	unvoiced
b	labial	voiced
d	dental	voiced
g	velar	voiced

V_2 were within the set [a,i,y,u] and C was within [p,t,k, b,d,g]. The 96 $V_1CV_2CV_1$ sequences ($4\times V_1$, $6\times C$, $4\times V_2$) were repeated twice, once for training, the second time for testing. The advantage of this corpus is that it enables us to make a number of predictions based on previous experiments on audio-visual speech perception. Indeed, the vowel set displays the three basic phonetic contrasts for vowels, namely height (e.g., [a] vs [i]), backness (e.g., [y] vs [u]), and rounding (e.g., [i] vs [y]), these last two contrasts being independent in French (Table Ia). It is well-known that rounding and height are visible while backness is not. It has also been shown (Robert-Ribes *et al.*, 1998) that the auditory information of these vowels is distributed in a manner complementary to the visual information: the most visible contrast [i y] is the least robust in acoustical noise. We expected that this complementarity of the audio and video channels should play an important role in the comparison of the AV speech enhancement process with the A-alone or V-alone processes. The same kind of pattern holds for the plosive set, including a visible place contrast (bilabials vs dentals/velars); an almost invisible one, at least when only the lip information is provided (dentals vs velars); and an invisible but quite audible mode contrast between voiced and unvoiced consonants (Table I b). Once more, the audio and video channels are complementary (see Summerfield, 1987), and the AV enhancement process should be expected to increase place intelligibility, if not voicing.

2. Audiovisual characteristics

The video parameters used in this work were geometric parameters describing the lip contour. The choice of such parameters is justified by three main reasons. (i) Lip shape provides the main contribution to visual speech information. By isolating the lip movements in speech perception tests, Summerfield (1979) and Le Goff *et al.* (1996) have shown that lip information represents about two-thirds to three-fourths of the total intelligibility gain obtained when seeing the speaker's face. (ii) It happens that the most relevant information is at the same time the easiest to extract. Different video lip shape tracking systems have been elaborated to focus on this particular region of the face. The lip shape extraction process is usually based on texture contrast with the background skin. Such a system has been developed in our laboratory to record and analyze synchronized sounds and lip movements (Lallouache, 1990). This system, which is used in the present study, can automatically extract basic parameters of the lip shape contour in two steps. First, the lip contour is isolated from the remainder of the image using blue lipstick and a Chroma-Key system. Second, classical pixel-based contour tracking algorithms are applied.[1] (iii) These parameters represent an efficient ''coding'' of the visual input, since information is well concentrated in a small number of coefficients. Several studies have been completed that efficiently characterize lip shape in French (Abry and Boë, 1980, 1986; Benoît *et al.*, 1992). We chose the three parameters that appear to be the most informative, namely interolabial width (LW), height (LH), and area (LS) (see Fig. 3). Notice that LS is highly correlated with the product $LW.LH$, which provided an indirect way to introduce a quadratic term into the linear associator defined later.

Each audio-visual stimulus consisted of an audio segment with a duration around 500 ms, sampled at 16 kHz, paired with a video matrix of $[LW\,LH\,LS]$ vectors extracted every 20 ms, according to the 50 frames-per-second camera sampling.

B. Noise degradation and LP model generation

Stationary white Gaussian noise (generated by computer) was added to each audio stimulus of both the training and test sets with signal-to-noise ratios (SNR) in the set $\{\infty$, 18, 12, 6, 0, −6, −12, −18 dB$\}$ (SNR$=\infty$ means that no noise was added).

Then, all (clean and noisy, training and test) audio stimuli were cut into 32 ms frames synchronized with the video parameters. This involved an audio window overlap of 12 ms to synchronize with the 20 ms video period. For each audio frame, a 20-order LP spectrum was calculated using the autocorrelation method and the Durbin–Levinson algorithm (Markel and Gray, 1976).

On the one hand, the LP spectra of the training corpus were used for the training of the associators (see Sec. C), and the LP spectra of the test corpus were used for the Gaussian classification test of Sec. E. On the other hand, the noisy stimuli of the test set were processed by the system (in the same configuration as above in what concerns synchronization, overlap, and LP model calculation) and used in the perceptual test of Sec. F. Note that when generating the noisy stimuli, the SNR was defined as the ratio of the signal energy and the noise energy on each entire stimulus so that the noise was stationary over its entirety. But when generating the LP spectra, the SNR was defined as the ratio of the signal energy and the noise energy on each frame. In this latter case, the noise was added frame by frame, so that the complete set of eight SNRs was well controlled in the training process and classification test (see the following sections).

C. Associators for filter parameter estimation

For each noisy frame of the signal to be processed, the A, V, and AV associators were designed to estimate the $1/\hat{A}_s(z)$ spectrum from either $1/A_x(z)$, or the corresponding set of video parameters $[LW\,LH\,LS]$, or both.

The first tool chosen for performing the estimation was linear regression. Its efficiency has already been demonstrated in different works involving estimation of speech spectral parameters from characteristics of the speaking face (Robert-Ribes *et al.*, 1996; Teissier *et al.*, 1999; Yehia *et al.*, 1998). The principle is simply to estimate each output spectral parameter as a linear combination of the input (audio and video) parameters. The regression matrix $\mathbf{M}$ of linear combination coefficients was obtained by minimizing the mean square error $e=\|\mathbf{M}_I\mathbf{M}-\mathbf{M}_O\|_2$, where $\mathbf{M}_I$ and $\mathbf{M}_O$ were two matrices concatenating the input and corresponding output parameter sets contained in the training corpus.

As far as the input/output LP parameters are concerned, preliminary tests based on spectral distances and classification tests (as described in Sec. E) showed that the best estimation performances were obtained with a spectral amplitude representation, consisting of the logarithmic values of the amplitudes of the LP spectrum taken for 50 values spaced equally on the upper-half unit circle. To obtain the $1/\hat{A}_s(z)$ filter from the 50 output spectral parameters, an inverse FFT was processed on the squared linear-scale coefficients, and a 20-order Levinson procedure was performed on the resulting estimated autocorrelation coefficients.

The A, V, and AV linear associators were trained on the 96 stimuli in the training set, with altogether about 2400 audio-visual vectors (about 25 frames per stimulus). In each condition (A, V, or AV), the associator output consisted of the set of the 50 values of $1/\hat{A}_s(z)$ for each training frame. In the A condition, these values were estimated from $1/A_x(z)$ only. Each input was hence a vector concatenating the 50 values of $1/A_x(z)$ and the value 1 (thereby ensuring that the intercept value of the regression need not be zero). Thus the associator $\mathbf{M}$ was a 51×50 matrix. In the V condition, $1/\hat{A}_s(z)$ was estimated from the $[LW\,LH\,LS]$ triplet, and $\mathbf{M}$ was a 4×50 matrix. In the AV condition, $1/\hat{A}_s(z)$ was estimated from both the 50 values of $1/A_x(z)$ and from $[LW\,LH\,LS]$, resulting in a 54×50 matrix for $\mathbf{M}$.

In the A and AV conditions, the associator training was realized with audio inputs corrupted at different noise levels for better generalization with respect to SNR. Then the association process combined two associators tuned under two different training/processing conditions. One was dedicated to stimuli with ''large'' SNRs: in the training phase, the stimuli frames were presented at frame SNRs of ∞, 18, 12, 6, and 0 dB. The other one was dedicated to stimuli with ''small'' SNRs: the stimuli frames were presented at frame SNRs of 6, 0, −6, −12, and −18 dB. During the enhancement process, each frame was submitted to a linear discriminant analysis (trained on the same corpus) to decide whether it belonged to the large or small SNR condition, so that the corresponding associator could be applied. Pilot tests carried out on the complete training corpus showed that this linear discriminant analysis could separate frames with SNR lower than 0 dB or higher than 6 dB with less than 1% errors. Between 0 and 6 dB, the two associators provided quite similar outputs.

D. Filtered stimuli

Once the three associators had been trained, the 768 stimuli in the test set (96 sequences, 8 SNRs) were processed in the following way. First, for each 32 ms video-synchronous frame, the LP normalized spectrum $1/A_x(z)$ and the residual signal were computed, and the 50 values of the spectrum log amplitude were extracted. Second, these values and/or the video input $[LW\,LH\,LS]$ were used to estimate the 50 values of $1/\hat{A}_s(z)$ (in the A or AV condition, each frame was first submitted to the linear discriminant analysis to select the large or small SNR associator). Then, an inverse FFT was performed on the linearized 50 estimated values of $1/\hat{A}_s(z)$, providing autocorrelation coefficients; the filter parameters were obtained from these coefficients by a 20-order LP model. Last, the residual signal was processed in this filter; energy was normalized and a trapezoidal windowing was used for frame continuity. This provided us with three sets of filtered stimuli, in the A, V, and AV conditions. The evaluation of these filtered stimuli together with the unprocessed noisy stimuli was made objectively, by a classification test, and subjectively, by a perceptual identification test.

E. Gaussian classification test

1. Methodology

The objective evaluation of the process was made by a classification test performed separately on the vowel and plosive spectra. For each of the 96 sequences in both the training and test corpus, we first manually selected two frames within the vocalic nuclei of each vowel and two frames containing or just preceding the burst of each consonant. Altogether, this provided us with 576 vowel frames in both the training and test corpus (96 stimuli×3 vowels per stimulus×2 frames per vowel)—that is to say 144 per vowel category (four categories)—and 384 consonant frames (96 stimuli×2 plosives per stimulus×2 frames per plosive)—that is to say 64 per plosive category (six categories).

From the frames selected in the training corpus, we found the Gaussian distribution associated with the four vowels and the six plosives. Since the number of data were small compared to the number of input parameters, the number of audio parameters was reduced from 50 to 10 by means of a principal component analysis (PCA). Both the PCA and the Gaussian distribution parameters for the ten classes (means and covariance matrices) were determined with the audio data selected in the training corpus and presented at the three largest SNRs (∞, 18, 12 dB). The ten first components in the PCA represented 97% of the whole variance in this training set.

Then the selected vowel frames in the test set were submitted to Gaussian classification. This means that for each frame, ten PCA spectral components were computed, and *a priori* probabilities of this vector of ten components were calculated for each of the four vowel Gaussian distributions estimated from the training set. The frame was identified as

belonging to the category providing the highest *a priori* probability. Similarly, the selected plosive frames in the test set were classified in reference to the six plosive Gaussian distributions. Both unfiltered frames and A, V, and AV filtered frames (that is, the spectra at the output of the A, V, and AV associators) were submitted to the classification process for the eight selected SNRs.

Results are presented in terms of classification scores and transmitted information scores. The classification scores were normalized with respect to chance performance according to the formula

$$\text{Corrected score} = 100\,\frac{\dfrac{\text{correct responses}}{\text{total responses}} - \dfrac{1}{\text{number of categories}}}{1 - \dfrac{1}{\text{number of categories}}}. \quad (6)$$

The numbers of classification of each phoneme i for presentation of each phoneme j were gathered into confusion matrices. From these matrices, the transmitted information (Miller and Nicely, 1955; Breeuwer and Plomp, 1986; Robert-Ribes *et al.*, 1998) was computed for the three vocalic phonetic features introduced in Sec. A 1, namely height, rounding, and front–back contrast, and the two consonantic phonetic features, namely voicing and place (see Table I). The percentage of transmitted information is defined by:

$$T = 100\,\frac{H(s,r)}{H(s)}, \quad (7)$$

with $H(s,r)$ the transmitted information from stimuli s to answers r, and $H(s)$ the existing information in the stimuli. These values are defined by:

$$H(s,r) = -\sum_i \sum_j p(s_i,r_j)\log_2\left(\frac{p(s_i)p(r_j)}{p(s_i,r_j)}\right)$$

$$H(s) = -\sum_i p(s_i)\log_2(p(s_i)),$$

with $p(s_i)$ the probability of occurrence of feature s_i in the stimuli, $p(r_j)$ the probability of occurrence of feature r_j in the answers, $p(s_i,r_j)$ the probability of shared occurrence of feature s_i in the stimuli and feature r_j in the answers. If we denote n the total number of stimuli and n_i the number of occurrences of stimulus s_i (both fixed), and n_j the number of occurrences of answer r_j and n_{ij} the number of occurrences of stimulus s_i with answer r_j (both provided by the confusion matrices), then $p(s_i)$ is known as n_i/n; and $p(r_j)$ and $p(s_i,r_j)$ are not known but can be estimated by n_j/n and n_{ij}/n.

2. Results

The correct classification scores are displayed in Fig. 4(a) for the unfiltered and filtered vowel frames. First, we notice that the scores in the unfiltered condition decreased

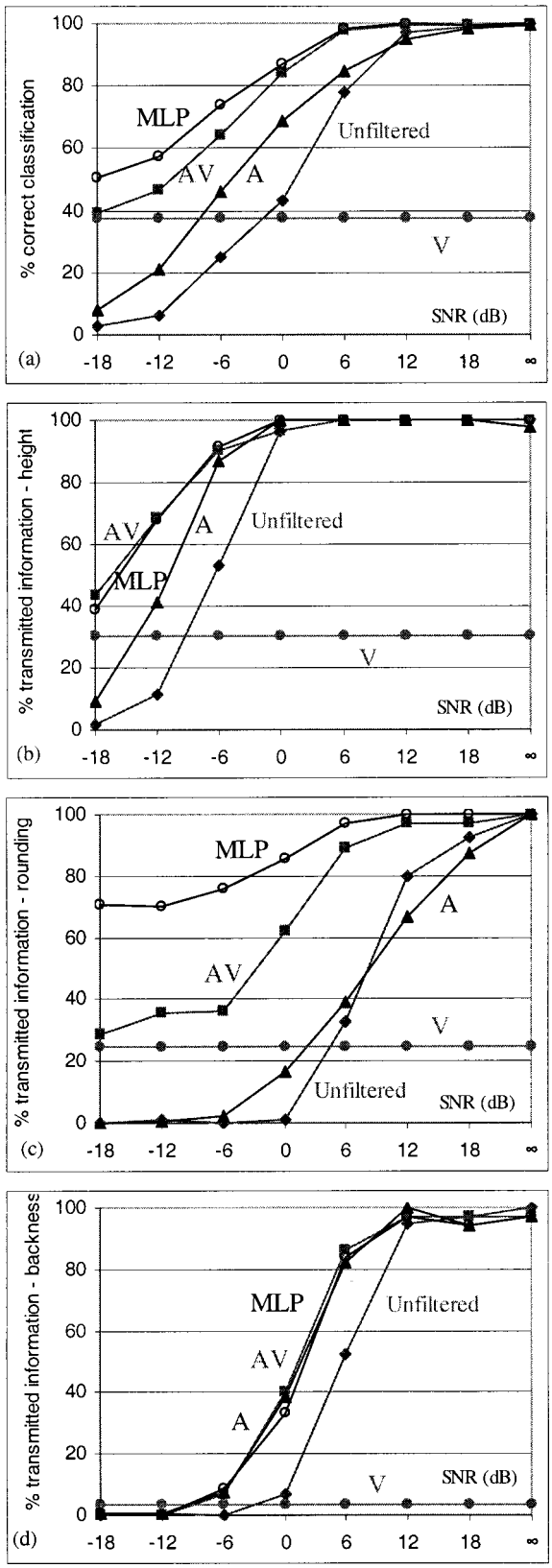

FIG. 4. Gaussian classification scores for the four vowels, in the unfiltered condition and AV, A, and V filtered conditions. MLP stands for the Multi-Layer Perceptron used in Sec. IV. (a) Corrected percentage of correct classification; percentage of transmitted information for the height, (b), rounding, (c), and backness, (d) features.

from 100% with clean stimuli to close to 0% for SNR=−18 dB. At such a small SNR value, all spectra were roughly flat, hence identification became impossible. From this baseline, we observe that the A filtered stimuli were better identified, with a gain up to 20% or more around −6 dB to 0 dB [at 0 dB, 43% vs 69%, $\chi^2(1)=77.1$, $p<0.001$]. This shows that the associator did learn some helpful relationship between noisy and clean audio spectra. More interestingly, we notice that the V filtered stimuli were partly recognizable, with a score around 40%. Finally, the AV filtered condition shows the efficiency of the system, with an increase in recognition score around 40% at SNRs lower than 0 dB [at 0 dB, 43% vs 84%, $\chi^2(1)=211.3$, $p<0.001$]. The scores in the AV condition were higher than in the A condition for SNRs below 18 dB [e.g., at 0 dB, 84% for AV vs 69% for A, $\chi^2(1)=38.5$, $p<0.001$] and similar above 18 dB. The AV scores were always higher than the V scores for all SNRs except −18 dB where the AV and V scores were similar. The superiority of AV over V holds even at very low SNRs where the audio information is very poor [e.g., at −12 dB, 46.5% for AV vs 37% for V, $\chi^2(1)=10.1$, $p<0.005$]. To summarize, the inequality AV≥(A or V) was verified for the classification scores. This shows the ability of the AV system to ''reshape'' vowel spectra, and to efficiently exploit the complementarity of the A and V sensors.

In terms of individual phonetic features, the transmitted information scores for the vowel features [Figs. 4(b)–(d)] show that each feature was improved by the process in the AV condition. The rounding and height contrasts were well maintained up to the largest amounts of noise in the AV filtered condition compared to the unfiltered (and the A and V filtered) condition(s). The only surprise comes from the low score for the rounding feature in the V condition (and AV condition at SNR=−18 dB), since this feature is considered highly visible. We shall come back on this in Sec. IV. For the front–back feature, the AV condition was similar to the A condition, which was expected since the video information is quite poor for this feature, as shown by the V score close to 0%. Altogether, the inequality AV≥(A or V) was confirmed for the different features. These results are a first indication of the efficiency of the DE architecture to combine the video and audio information for vowel enhancement.

The results for consonants are more disappointing. Absolute scores were quite poor, but they must be taken cautiously, since it is well known that local information is too restricted. Hence Gaussian classifiers were not powerful enough to achieve fully acceptable performances. However, compared scores are relevant, and they demonstrate that the consonants were poorly improved by the AV filtering process (which was again more efficient than the A or V processes). The scores for large SNRs were even decreased by the filtering procedure while the gains for the small SNRs were less than 15% [max at 0 dB, 5% for unfiltered vs 19% for AV, $\chi^2(1)=36.7$, $p<0.001$] [Fig. 5(a)]. The transmitted information scores [Figs. 5(b)–(c)] show that the voicing feature was severely degraded by both the A and AV filtering procedure at large SNRs. The place feature was degraded by the A filtering over 6 dB SNR and was slightly or not enhanced by the AV filtering for almost all SNRs (some degradation is even induced at 18 dB), in spite of the high visibility of the labial versus nonlabial contrast.

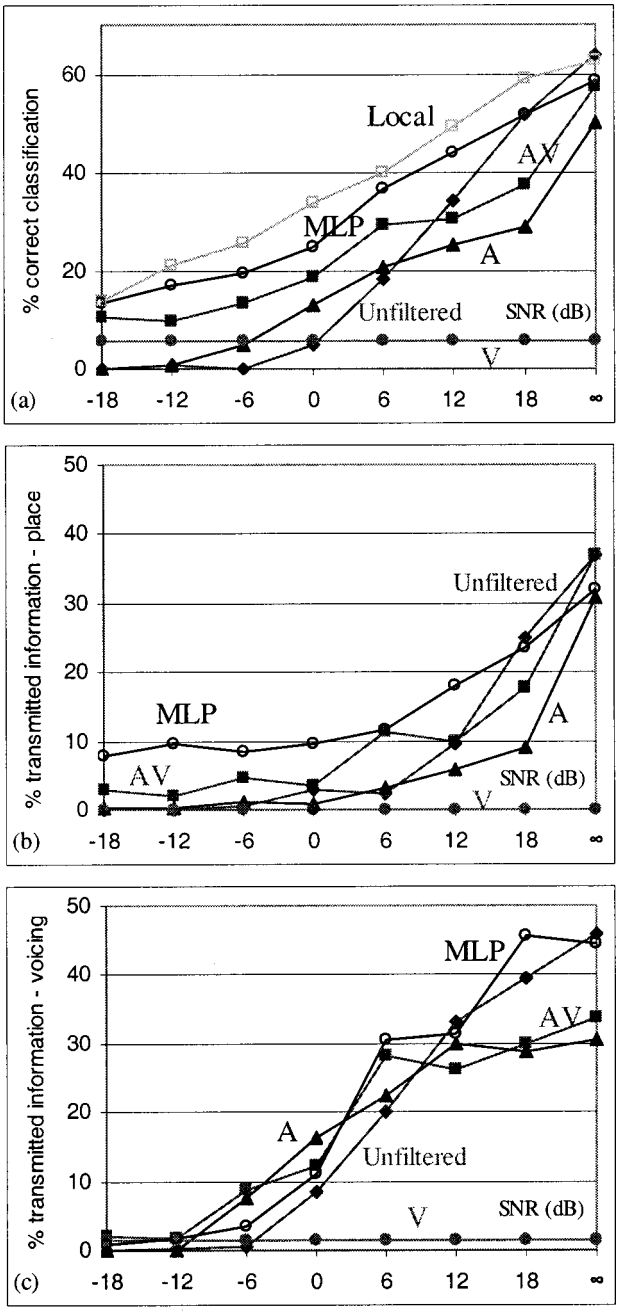

FIG. 5. Gaussian classification scores for the six plosives, in the unfiltered condition and AV, A, and V, filtered conditions. ''Local'' stands for the local consonant associator introduced in Sec. III G, and MLP stands for the Multi-Layer Perceptron used in Sec. IV. (a) Corrected percentage of correct classification; percentage of transmitted information for the place, (b) and voicing (c) features.

F. Perceptual test

1. Methodology

To perform a complete assessment of the system, a perceptual identification experiment was carried out on the 96 stimuli of the test corpus. Sixteen French native subjects, aged from 22 to 31, were tested. They displayed no known problem of hearing and speech production/perception. They

were asked to identify both vowels and consonants of the stimuli presented in the unfiltered and A, V, and AV filtered conditions, for the eight SNRs. It should be remembered that in this test, the SNR was defined as the ratio of the signal energy and the noise energy over the complete stimulus (and no longer for each frame).

The $V_1CV_2CV_1$ stimuli were segmented manually into V_1CV_2 and V_2CV_1 items so that the subjects would hear V_1 and C only once for each presentation. The total of 6144 sounds (96 stimuli×2 segments×8 SNRs×4 conditions) was randomized and divided between the 16 subjects. For each stimulus, they were asked to give a response between the four possible vowels for both V_1 and V_2, and between the six possible plosives for C. There were altogether 384 vowel responses and 192 consonant responses for each noise level and each condition (96 stimuli, two VCV segments per stimulus, 2 vowels and 1 plosive per segment), that is to say 96 responses per vowel category (4 categories) and 32 responses per consonant category (6 categories). These responses were analyzed separately for the vowels and the plosives and processed in the same way as for the Gaussian classification test, that is, with corrected global scores, confusion matrices, and transmitted information scores for the individual phonetic features.

2. Results

The results are presented in Fig. 6 for the vowels and Fig. 7 for the plosives. Concerning the vowels, we first notice that the degradation of identification scores for the unfiltered stimuli with low SNRs was similar to classification scores. However, the A filtering was not very efficient: the gain was low at low SNRs [at SNR=−12 dB, 20% for unfiltered vs 29% for A, $\chi^2(1)=7.8$, $p<0.005$]. There was even some degradation due to filtering at high SNRs [at SNR=18 dB, 96% for unfiltered vs 91% for A, $\chi^2(1)=9.6$, $p<0.005$]. The V filtering provided some information, with an intelligibility around 20%–30%. Notice that the fluctuations in score with SNR were due to differences in the residual form (see Fig. 3). However, the results in the AV condition were quite good, although less so than in the Gaussian classification test, with an increase in identification scores compared with unfiltered stimuli at all SNRs below 18 dB. The gains reach 5.5% at 12 dB [$\chi^2(1)=9.2$, $p<0.005$], 9% at 6 dB [$\chi^2(1)=12.6$, $p<0.001$], 17.5% at 0 dB [$\chi^2(1)=24.6$, $p<0.001$], 16% at −6 dB [$\chi^2(1)=20$, $p<0.001$], and about 22% at −12 dB [$\chi^2(1)=41.7$, $p<0.001$], and −18 dB [$\chi^2(1)=77.8$, $p<0.001$]. Once more, the AV condition was systematically better than the A and V conditions.

The percentages of transmitted information, given in Figs. 6(b)–(d), confirm these results and the ones of the classification test. The scores for the A condition were close to the scores in the unfiltered condition with some improvement for low SNRs and some degradation for high SNRs. The V condition, while providing some information on the height contrast, was surprisingly deceptive for the rounding contrast. However, in the AV condition the system provided much better performances that can be summarized as follows. (i) There was an efficient reinforcement of the round-

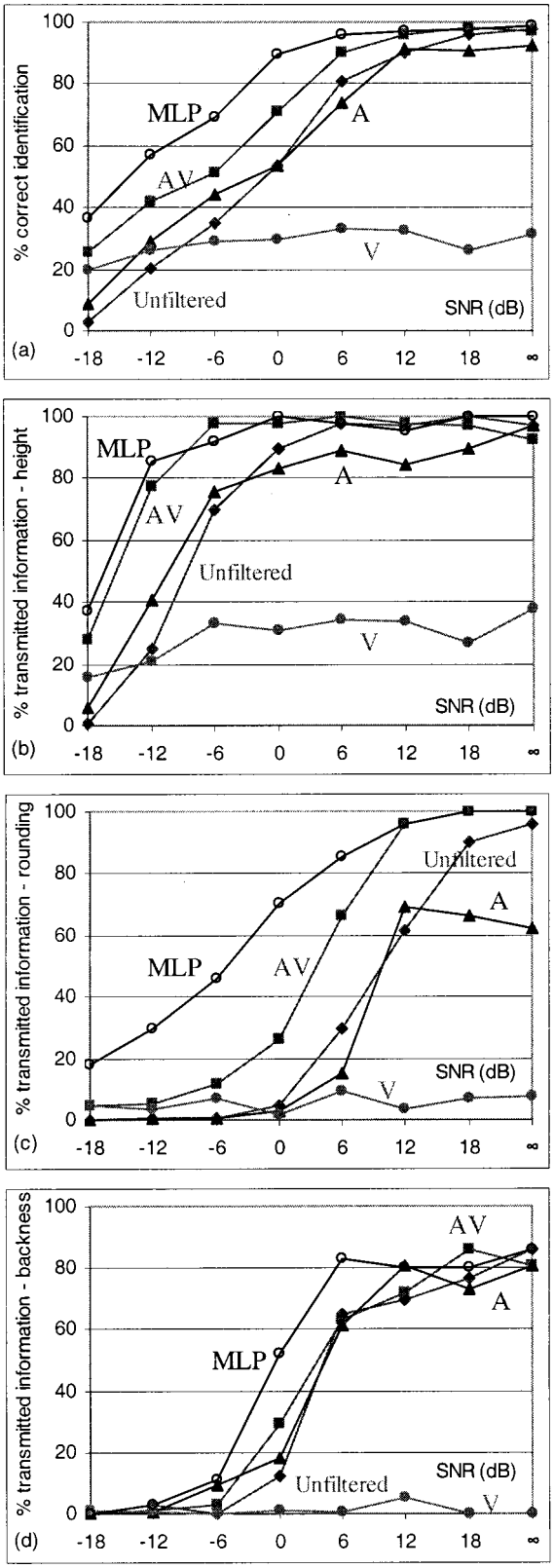

FIG. 6. Perceptual test scores for the vowels, in the unfiltered condition and in the AV, A, and V filtered conditions. MLP stands for the Multi-Layer Perceptron used in Sec. IV. (a) Corrected percentage of correct identification; percentage of transmitted information for the height (b), rounding (c), and backness (d) features.

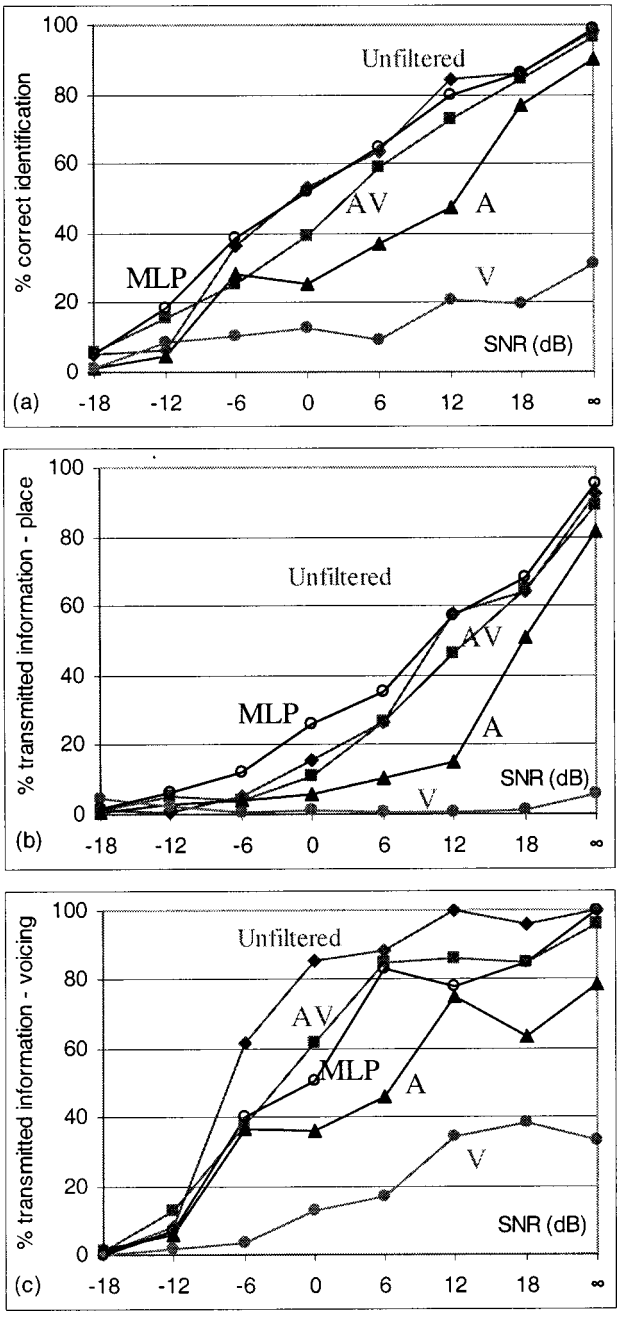

FIG. 7. Perceptual test scores for the consonants, in the unfiltered condition, and in the AV, A, and V filtered conditions. MLP stands for the Multi-Layer Perceptron used in Sec. IV. (a) Corrected percentage of correct identification; percentage of transmitted information for the place (b) and voicing (c) features.

ing feature: the [i,y] contrast, which was rapidly and strongly degraded in noise before enhancement, was well recovered. This case represents a good example of the audio/video complementarity of speech (robust video distinction while it is the weakest audio contrast in noise; see Robert-Ribes *et al.*, 1998). (ii) Contrary to the rounding feature, the height [a] versus [i y u] contrast was robust in the unfiltered condition (until 0 dB SNR). This is due to the good audibility of the first formant region in white noise. Below 0 dB, the AV filtering produced a large improvement of the height feature scores. (iii) At last, the front–back [y,u] contrast, not very robust in the unfiltered condition, was not improved by the AV process.

For consonants, the perceptual results were poor and confirmed the classification test results. While still better than in the A and V conditions, the identification scores [Fig. 7(a)] in the AV condition remained lower than those for unfiltered stimuli [e.g., at SNR=0 dB, 53% for unfiltered vs 39.5% for AV, $\chi^2(1)=7.3$, $p<0.01$], except for the two weakest SNRs [e.g., at SNR=−12 dB, 6% for unfiltered vs 15.5% for AV, $\chi^2(1)=8.7$, $p<0.005$]. This shows that at this point the system produced some degradation of the consonants. As shown by Figs. 7(b)–(c), the voicing feature was degraded by the process, while the place feature was not improved despite the labial information available in the data (the V condition seemed unable to exploit this information as well).

G. Discussion

The Gaussian classification tests on single frames and the perceptual identification of whole sequences provided a consistent pattern of results. AV filtering produced a strong enhancement of vowels, at all SNRs, and always much stronger than both the A and the V filtering. The results for consonants were much more disappointing: A, V, or AV enhancement filters failed to improve on consonant identification or classification except at the poorest SNR conditions, and often resulted in lower scores than those obtained when no filter was applied. Our interpretation is that in the present implementation, the linear associator was more adapted to vowel spectra than to plosives. There are two reasons for this. First, vowellike spectra (consisting of well-defined formant patterns) occurred more frequently in the corpus than plosivelike spectra (including silence, consonantal voicing and bursts). Second, vowel spectral contrasts were larger than plosive ones. Therefore, the intrinsic ''averaging'' process characteristic of linear regression resulted in estimated plosive spectra that looked quite similar to vowels! This was obvious through visual inspection of the filtered stimuli.

To confirm this hypothesis, we carried out a complementary experiment where the training corpus for the AV associator training was restricted to only plosive frames (the two frames per consonant defined in Sec. E 1). In this case, the linear regression algorithm was focused on the available information: it appeared that the plosive test frames filtered by this local AV association process provided much higher scores in the Gaussian classification test. Indeed, these scores, displayed in Fig. 5, were this time systematically better than those of unfiltered stimuli, with a gain close to 30% at 0 dB [5% for unfiltered vs 34% for local associator, $\chi^2(1)=104$, $p<0.001$]. This shows that the poor scores obtained previously were not due to a lack of information in the A and V sensors but to an under-representation of this information in the filtering process. The aim of the next experiment was to exploit an association tool more powerful than linear regression.

IV. NONLINEAR ASSOCIATORS FOR IMPROVING PLOSIVE ENHANCEMENT

A. Improving the association process: From linear regression to perceptrons

The previous section revealed the need for more powerful associators than linear regression (LR in the following), in order to better take into account the plosive parts of the corpus. We decided to look for nonlinear associators in the most efficient condition of the previous experiment, that is, the AV one. Neural Networks have been used extensively for classification tasks in speech recognition, including audio-visual recognition (Stork and Hennecke, 1996). In addition, they are theoretically able to approximate any nonlinear function. Therefore we used classical Multi-Layer Perceptrons (MLP) based on error gradient back-propagation with momentum (Rumelhart *et al.*, 1986), with one hidden layer and sigmoidal neuronal threshold functions.

Different values for the number of neurons in the hidden layer were tested from 20 to 200, using both Gaussian classification and listening tests. It appeared that performances improved slightly above 40 neurons. The following results were obtained with 120 hidden neurons, which was a good compromise between performances and calculation cost. The complete experimentation protocol of Sec. III concerning training and testing was preserved, so that the new results can be compared with the results obtained with linear regression. The training phase involved 200 iterations with the whole training set, which was enough to ensure convergence of the network (i.e., low error and no overtraining).

B. Gaussian classification test

The output spectra obtained with the MLP on the selected frames defined in Sec. III E 1 were presented to the Gaussian classifier of the same section and the results are displayed in Figs. 4 and 5.

For vowels, the classification scores for the MLP were improved compared to the linear regression below 6 dB. The gain reached more than 10% at -18 dB [39.5% vs 51%, $\chi^2(1)=15$, $p<0.001$] and at -12 dB [46.5% vs 57.5%, $\chi^2(1)=14.2$, $p<0.001$]. The transmitted information scores show that this gain was provided by a quite large improvement of the rounding feature, while the height and backness features were not noticeably modified. This provides an interesting correction to the surprisingly low score for the rounding feature noticed in Sec. III E 2.

For consonants, the recognition scores were also increased compared to linear associators, and reached a value almost always higher than the scores for unfiltered stimuli. The gain reached 14% to 20% from -18 dB to 6 dB [at 0 dB, 5% for unfiltered vs 25% for MLP, $\chi^2(1)=62.7$, $p<0.001$], with only a small and not significant loss at SNR$=\infty$ [64% for unfiltered vs 58.5% for MLP, $\chi^2(1)=2.3$, $p>0.1$]. However, the scores of the ''local'' associator described in Sec. III G were not reached. Hence, the available information was not exploited completely. At the phonetic features level, transmitted information scores were almost always higher with the MLP than with linear regression. Consequently, the voicing feature was more or less at the same level for MLP filtered and unfiltered spectra, while the place feature was much improved by the MLP filtering below 18 dB SNR. These encouraging results led us to perform a complementary perceptual test for a final evaluation of the system on this corpus.

C. Perceptual test

The MLP-processed stimuli were presented to the 16 subjects in the same condition as the unfiltered or linear regression filtered stimuli. Global results confirm the important progress from LR to MLP estimation (Figs. 6 and 7). In the MLP condition, the increase of vowel intelligibility with respect to the unfiltered condition was quite large [about 35% for SNRs lower than 0 dB: e.g., at -12 dB, 20% for unfiltered vs 57% for MLP, $\chi^2(1)=110$, $p<0.001$]. These results correspond to a gain in SNR around 9 to 12 dB (Fig. 6). At the phonetic features level, transmitted information scores reveal a large improvement from LR to MLP for vowel rounding below 12 dB SNR, and also some improvement for the vowel backness feature between -6 and $+12$ dB [Fig. 6(d)]. This demonstrates the ability of the MLP-DE structure to efficiently combine the video and audio information for vowel enhancement.

For consonants, there was also a significant improvement from LR to MLP [13% at SNR$=-6$ dB: 26% for LR vs 39% for MLP, $\chi^2(1)=7.6$, $p<0.01$, and 12.5% at 0 dB: 39.5% for LR vs 52% for MLP, $\chi^2(1)=6$, $p<0.025$]. As a result, the identification scores of the MLP-processed plosives reached the values for unfiltered stimuli, and the average score across the whole SNR range was almost the same as the one obtained in the unfiltered condition: 55.5% for MLP filtered vs 54.1% for unfiltered stimuli [the difference is not significant, $\chi^2(1)=0.6$, $p>0.4$]. In comparison the LR scores only reached 49.8%, showing an average degradation of about 4% compared with the unfiltered condition [$\chi^2(1)=5.7$, $p<0.025$] [Fig. 7(a)]. The voicing feature was still quite degraded in the MLP filtered condition compared with the unfiltered condition [Fig. 7(c)]. In contrast, the place feature was quite improved by the MLP-based process, especially from -12 to 6 dB SNR [Fig. 7(b)], which explains why the identification scores were comparable with the unfiltered condition. This shows that some visible information (notably on the [p,b] closures) was used efficiently by the filtering process.

V. DISCUSSION

A. Summary of the main achievements

We defined in Sec. III an architecture for audio-visual speech enhancement, expecting some predictability of the audio spectrum from the video input, and based on a fusion-and-filtering procedure in three steps:

(1) separate the sound source from the spectral transfer function characteristics using an LP analysis of the input audio signal;
(2) combine the noisy spectral characteristics and the visual

input parameters to estimate the transfer function of the clean speech sound, using either a linear or a nonlinear associator;

(3) filter the estimated source through the estimated transfer function.

We assessed this system on a vowel-plosive-vowel corpus with both an objective Gaussian classification test and a subjective perceptual identification procedure, and we obtained the following results:

(1) the linear-regression filter estimation provided much better global results when both the audio and the video streams participated to the filter estimation (AV filtered stimuli) than in the audio-only (A filtered stimuli) or video-only (V filtered stimuli) conditions. In more detail, the AV scores were better than the A scores for low SNRs; better than the V scores for high SNRs; better than both the A and V scores for medium SNRs; and in no case lower. This demonstrates the efficiency of the visual contribution and the good exploitation of the audio-visual synergy for speech enhancement by the DE architecture;

(2) in the AV condition, vowels displayed a very large enhancement for both assessment tools, with a significant improvement of the enhancement efficiency from the linear to the nonlinear associator. This was largely due to a better enhancement of the rounding feature. The best filtering algorithm, involving AV nonlinear estimation, provided an increase in recognition and perception scores corresponding to a 9–12 dB gain along the entire SNR range for the vowels;

(3) plosives were not enhanced, and were even degraded by the use of the linear associator. However, the results with the nonlinear associator were less clearcut. Indeed, Gaussian classification displayed a significant enhancement of the stimuli through nonlinear estimation, while perceptual tests showed the same global intelligibility for unfiltered and filtered plosives. At the feature level, voicing was quite degraded for linear and nonlinear estimation, while place was enhanced only for nonlinear estimation.

B. Audio-visual interdependencies

Given this pattern of results, we can return to some issues raised in the introductory sections. The departure point of this study was the assumption that there was some interdependency between the audio and the video streams. The experimental results provide strong support to this assumption. Indeed, it appears that the AV filtering condition produces a gain of about 6 dB in SNR compared with the A condition for both vowels (Fig. 6) and plosives (Fig. 7). Hence the video stream does contain a significant deal of information on the audio spectrum, which is evidence for a statistical dependence. Notice that in this AV versus A comparison, the A condition provides a baseline which is similar to the unfiltered condition for vowels, but unfortunately lower for plosives. In this latter case, the AV associator helped at best to remove the degradation introduced by the A associator.

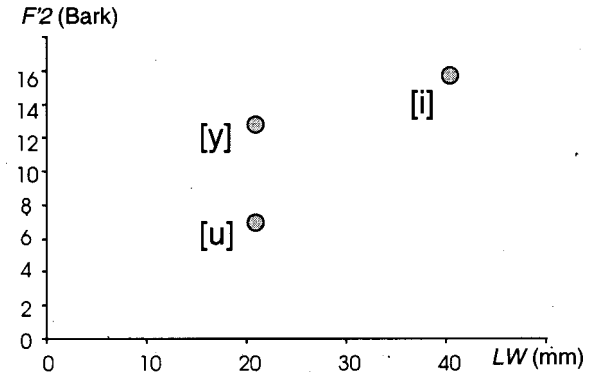

FIG. 8. Typical pattern of distribution of the auditory parameter $F'2$ and the visual parameter LW for the set of high French vowels [i y u].

Audio-visual complementarity is also demonstrated in this work. It enables the poorest audio feature to benefit greatly from audio-visual enhancement, as it was clearly demonstrated for vowels. For example, the rounding feature for unfiltered vowels provided low perceptual intelligibility scores compared to the front–back feature: 5% vs 12% at 0 dB, 30% vs 65% at 6 dB; but the MLP-AV filtered stimuli displayed the inverse pattern: 46% vs 11% at −6 dB, 71% vs 52% at 0 dB, and 100% vs 80% at 18 dB [Figs. 6(b)–(c)].

Finally, it is of interest to notice the importance of introducing nonlinear processes in audio-visual fusion. Indeed, it is commonly considered that linear association between audio and video speech parameters captures a great deal of the information (see, e.g., Yehia *et al.*, 1998; Robert-Ribes *et al.*, 1996). However, it is clear that only gross audio-visual correlations can be captured by linear regression, while audio-visual complementarity is intrinsically associated to a basic nonlinear property of the audio-visual relationship. Consider, for example, the [i,y,u] set of French high vowels. The major auditory parameter characterizing this set would be $F'2$, the ''perceptual second formant,'' while interolabial width LW provides a major correlate of the rounding contrast between [i] and [y] or [u]. In Fig. 8, typical values of $F'2$ and LW for [i y u] for a French male speaker display audio-visual complementarity: in LW, [i] is well separated from [y] and [u] which are almost confounded, while in $F'2$ [i] and [y] are close together and well separated from [u]. Linear regression between LW and $F'2$ would lose this complementary pattern, hence the success of nonlinear association in Sec. IV, particularly for enhancing the rounding feature for vowels.

C. Future directions

Although these results fulfill the initial objective of this study, they are not a final achievement. Indeed, the framework was quite controlled and simple. It will be necessary now to explore new directions. Three main directions can be mentioned.

First, the estimation tools were quite basic. A first effort to switch from linear regression to nonlinear MLPs led to significant progress (see Fig. 6). However, the comparison of LR, MLP, and local associators for plosive enhancement in Fig. 7 shows that all the local information is still not exploited: the MLP went more or less halfway toward what can be considered optimum under the corresponding evaluation tool. More powerful tools, such as multi-expert systems (Jordan and Jacobs, 1994) or neural gas (Fritzke, 1994), could fill this gap. Another important objective will be to explore dynamic associators, able to exploit the regularities in the evolution of audio and video parameters. Hidden Markov Models could provide a natural basis for this, as they do for pure audio enhancement of speech in noise (Ephraim, 1992). This kind of tool is likely to be crucial for plosive enhancement, since it is quite well-known that plosive characterization cannot be achieved correctly without considering spectral dynamics (Kewley-Port *et al.*, 1983; Sussman *et al.*, 1991). More generally, such tools will be also necessary for dealing with more complex conditions, involving extended corpora and noise degradations, and multi-speaker applications. This is part of a global program that will be of increasing interest in the future: i.e., to systematically explore the statistical relationship between sound and image, using such tools as mutual information between groups of parameters in the audio and the video streams.

Second, though it was chosen for this initial demonstration to ignore pure audio enhancement techniques, it will be necessary to re-introduce them in the following of this work. This will be important for dealing with nonstationary noises, and particularly with variations in the spectral patterns of the competing sources, as is the case with ''cocktail-party'' speech. We will study how to extend the so-called DE architecture to a multi-channel framework including various audio and video sensors for performing the filter estimation: we are beginning to explore a generalization of the blind separation approach to multi-modal speech sources (Girin *et al.*, 2000).

Finally, the ''joint processing of the audio and video streams,'' which was applied here to speech enhancement, could be generalized to various problems in the field of human–machine communication and telecommunication. The natural coherence and complementarity of these two data streams are already exploited in speech recognition systems, and in the development of speech synthesis systems. They could also be of benefit to audio-visual compression in videophone technology: in another study, vector quantization algorithms were applied either separately to audio and video data, or to audio-visual vectors (Girin *et al.*, 1998). The latest results showed that it was possible to save 3 bits out of 15 in the second case. This provides a quantitative estimate of the amount of redundancy in the audio and video streams.

Altogether, one can foresee the elaboration of a global platform for audio-visual speech communication, which would involve preprocessing (localization, enhancement, scene analysis...), recognition, coding, transmission and synthesis of audio-visual speech. In any case, the main objective remains to maintain the intrinsic coherence of sound and image at the heart of all the speech processing algorithms.

[1]A new generation of lip contour extraction systems without blue make-up is currently being studied in our laboratory (Revéret and Benoît, 1998). These systems are based on the fitting of a lip model with the speaker's natural lips.

[2]More complete specification of the vocal tract, and even of the source, could be available from facial parameters: see, e.g., Yehia *et al.* (2000).

Abry, C., and Boë, L. J. (**1980**). ''A la recherche de corrélats géométriques discriminants pour l'opposition d'arrondissement vocalique en français,'' in *Labialité et Phonétique*, edited by C. Abry, L. J. Boë, P. Corsi, R. Descout, M. Gentil, and P. Graillot (Publications de l'Université des Langues et Lettres, Grenoble), pp. 217–237.

Abry, C., and Boë, L. J. (**1986**). ''Laws for lips,'' Speech Commun. **5**, 97–104.

Barker, J., Berthommier, F., and Schwartz, J. L. (**1998**). ''Is primitive AV coherence an aid to segment the scene?,'' Proc. AVSP'98, Sydney.

Bailly, G., Laboissière, R., and Schwartz, J. L. (**1991**). ''Formant trajectories as audible gestures: An alternative for speech synthesis,'' J. Phonetics **19**, 9–23.

Benoît, C., Mohamadi, T., and Kandel, S. D. (**1994**). ''Effects of phonetic context on audio-visual intelligibility of French,'' J. Speech Hear. Res. **37**, 1195–1203.

Benoît, C., Lallouache, T., Mohamadi, T., and Abry, C. (**1992**). ''A set of visual French visemes for visual speech synthesis,'' in *Talking Machines: Theories, Models and Designs*, edited by G. Bailly, C. Benoît, and T. R. Sawallis (Elsevier, Amsterdam), pp. 485–504.

Bernstein, L. E., and Benoît, C. (**1996**). ''For speech perception by humans or machines, three senses are better than one,'' Proc. ICSLP'96, 1477–1480.

Boll, S. F. (**1979**). ''Suppression of acoustic noise in speech using spectral subtraction,'' IEEE Trans. Acoust., Speech, Signal Process. **29**, 113–120.

Boll, S. F., and Pulsipher, D. C. (**1980**). ''Suppression of acoustic noise in speech using two microphones adaptive noise cancellation,'' IEEE Trans. Acoust., Speech, Signal Process. **28**, 752–753.

Breeuwer, M., and Plomp, R. (**1986**). ''Speechreading supplemented with auditorily presented speech parameters,'' J. Acoust. Soc. Am. **79**, 481–499.

Comon, P., Jutten, C., and Hérault, J. (**1991**). ''Blind separation of sources, Part II: Problems statement,'' Signal Process. **24**, 11–20.

Driver, J. (**1996**), ''Enhancement of selective listening by illusory mislocation of speech sounds due to lip-reading,'' Nature (London) **381**, 66–68.

Ephraim, Y. (**1992**). ''A Bayesian estimation approach for speech enhancement using Hidden Markov Models,'' IEEE Trans. Acoust., Speech, Signal Process. **40**, 725–735.

Erber, N. P. (**1975**). ''Auditory-visual perception of speech,'' J. Speech Hearing Disorders **40**, 481–492.

Feder, M., Oppenheim, A. V., and Weinstein, E. (**1989**). ''Maximum likelihood noise cancellation using the EM algorithm,'' IEEE Trans. Acoust., Speech, Signal Process. **37**, 204–216.

Ferrara, E. R., and Widrow, B. (**1981**). ''Multi-channel adaptive filtering for signal enhancement,'' IEEE Trans. Acoust., Speech, Signal Process. **29**, 766–770.

Fritzke, B. (**1994**). ''Growing cell structures—A self-organizing network for unsupervised and supervised learning,'' Neural Networks **7**, 1441–1460.

Girin, L., Feng, G., and Schwartz, J.-L. (**1996**), ''Débruitage de parole par un filtrage utilisant l'image du locuteur: Une étude de faisabilité,'' Traitement du Signal **13**, 319–334.

Girin, L., Foucher, E., and Feng, G. (**1998**). ''An audio-visual distance for audio-visual vector quantization,'' Proc. IEEE Workshop Multimedia Signal Process., Los Angeles.

Girin, L., Allard, A., Feng, G., and Schwartz, J-L. (**2000**). ''Séparation de sources de parole: Une nouvelle approche utilisant la cohérence audio-visuelle des signaux,'' Proc. XXIII Journées d'Etudes sur la Parole, Aussois, France, pp. 57–60.

Grant, K. W., and Walden, B. E. (**1996**). ''Evaluating the articulation index for auditory-visual consonant recognition,'' J. Acoust. Soc. Am. **100**, 2415–2424.

Grant, K. W., and Seitz, P. F. (**2000**). ''The use of visible speech cues for improving auditory detection of spoken sentences,'' J. Acoust. Soc. Am. **108**, 1197–1208.

Harrison, W. A., Lim, J. S., and Singer, E. (**1986**). ''A new application of adaptive noise cancellation,'' IEEE Trans. Acoust., Speech, Signal Process. **34**, 21–27.

Jordan, M. I., and Jacobs, R. A. (**1994**). ''Hierarchical mixtures of experts and the EM algorithm,'' Neural Comput. **6**, 181–214.
Jutten, C., and Hérault, J. (**1991**). ''Blind separation of sources, Part I: An adaptive algorithm based on neuromimetic architecture,'' Signal Process. **24**, 1–10.
Kang, G. S., and Fransen, L. J. (**1989**). ''Quality improvement of LPC-processed noisy speech by using spectral subtraction,'' IEEE Trans. Acoust., Speech, Signal Process. **37**, 939–943.
Kewley-Port, D., Pisoni, D. B., and Studdert-Kennedy, M. (**1983**). ''Perception of static and dynamic acoustic cues to place of articulation in initial stop consonants,'' J. Acoust. Soc. Am. **73**, 1779–1793.
Lallouache, M. T. (**1990**). ''Un poste 'visage-parole'. Acquisition et traitement de contours labiaux,'' Proc. XVIII Journées d'Études sur la Parole, Montréal, pp. 282–286.
Le Bouquin-Jeannès, R., and Faucon, G. (**1995**). ''Study of a voice activity detector and its influence on a noise reduction system,'' Speech Commun. **16**, 245–254.
Le Goff, B., Guiard-Marigny, T., and Benoît, C. (**1996**). ''Analysis-synthesis and intelligibility of a talking face,'' in *Progress in Speech Synthesis*, edited by J. P. H. Van Santen, R. W. Sproat, J. P. Olive, and J. Hirschberg (Springer-Verlag, New York), pp. 235–244.
Lim, J. S. (**1983**). *Speech Enhancement* (Prentice-Hall, Englewood Cliffs, NJ).
MacLeod, A., and Summerfield, Q. (**1987**). ''Quantifying the contribution of vision to speech perception in noise.'' Br. J. Audiol. **21**, 131–141.
McAulay, R. J., and Malpass, M. L. (**1980**). ''Speech enhancement using a soft-decision noise suppression filter,'' IEEE Trans. Acoust., Speech, Signal Process. **28**, 137–145.
Markel, J. D., and Gray, A. H. (**1976**). *Linear Prediction of Speech* (Springer-Verlag, New York).
Massaro, D. W. (**1989**). ''Multiple book review of speech perception by ear and eye: A paradigm for psychological inquiry,'' Behav. Brain Sci. **12**, 741–794.
Miller, G. A., and Nicely, P. E. (**1955**). ''An analysis of perceptual confusions among some English consonants,'' J. Acoust. Soc. Am. **27**, 338–358.
Revéret, L., and Benoît, C. (**1998**). ''A new 3D lip model for analysis and synthesis of lip motion in speech production,'' Proc. AVSP'98, 207–212.
Robert-Ribes, J., Piquemal, M., Schwartz, J. L., and Escudier, P. (**1996**). ''Exploiting sensor fusion architectures and stimuli complementarity in AV speech recognition,'' in *Speechreading by Man and Machine: Models, Systems and Applications*, edited by D. G. Stork and M. Hennecke (Springer-Verlag, Berlin), pp. 193–210.
Robert-Ribes, J., Schwartz, J. L., Lallouache, T., and Escudier, P. (**1998**). ''Complementarity and synergy in bimodal speech: Auditory, visual, and audio-visual identification of French oral vowels in noise,'' J. Acoust. Soc. Am. **103**, 3677–3689.
Rumelhart, D. E., Hinton, G. E., and Williams, R. J. (**1986**). ''Learning representations by back-propagating errors,'' Nature (London) **323**, 533–536.
Sambur, M. R. (**1978**). ''Adaptive noise canceling for speech signals,'' IEEE Trans. Acoust., Speech, Signal Process. **26**, 419–423.
Schroeter, J., and Sondhi, M. M. (**1994**). ''Techniques for estimating vocal-tract shapes from the speech signal,'' IEEE Trans. Speech Audio Process. **2**, 133–150.
Schwartz, J. L., Robert-Ribes, J., and Escudier, P. (**1998**). ''Ten years after Summerfield... A taxonomy of models for AV fusion in speech perception,'' in *Hearing by Eye, II. Perspectives and Directions in Research on Audio-visual Aspects of Language Processing*, edited by R. Campbell, B. Dodd, and D. Burnham (Erlbaum/Psychology Press, Hillsdale, NJ), pp. 85–108.
Stork, D. G., and Hennecke, M., Eds. (**1996**). *Speechreading by Man and Machine: Models, Systems and Applications* (Springer-Verlag, Berlin).
Sumby, W. H., and Pollack, I. (**1954**). ''Visual contribution to speech intelligibility in noise,'' J. Acoust. Soc. Am. **26**, 212–215.
Summerfield, Q. (**1979**). ''Use of visual information for phonetic perception,'' Phonetica **36**, 314–331.
Summerfield, Q. (**1987**). ''Some preliminaries to a comprehensive account of audio-visual speech perception,'' in *Hearing by Eye: The Psychology of Lipreading*, edited by B. Dodd and R. Campbell (Lawrence Erlbaum, London), pp. 3–51.
Sussman, H. M., McCaffrey, H. A., and Matthews, S. A. (**1991**). ''An investigation of locus equations as a source of relational invariance for stop place categorization,'' J. Acoust. Soc. Am. **90**, 1309–1325.
Teissier, P., Robert-Ribes, J., Schwartz, J. L., and Guérin-Dugué, A. (**1999**). ''Comparing models for audio-visual fusion in a noisy-vowel recognition task,'' IEEE Trans. Speech Audio Process. **7**, 629–642.
Widrow, B., Glover, J. R., McCool, J. M., Kaunitz, J., Williams, C. S., Hearn, R. H., Zeidler, J. R., Dong, E., and Goodlin, R. C. (**1975**). ''Adaptive noise cancelling: principles and applications,'' Proc. IEEE **63**, 1692–1716.
Yehia, H., Kuratate, T., and Vatikiotis-Bateson, E. (**2000**). ''Facial animation and head motion driven by speech acoustics,'' Proc. 5th Seminar on Speech Production: Models and Data, Munich, pp. 265–268.
Yehia, H., Rubin, P., and Vatikiotis-Bateson, E. (**1998**). ''Quantitative association of vocal-tract and facial behavior,'' Speech Commun. **26**, 23–43.

The speed of pitch resolution in a musical context

R. Ranvaud
Departamento de Fisiologia e Biofisíca, Instituto de Ciências Biomédicas, Universidade de São Paulo, Avenida Lineu Prestes 1524, São Paulo, SP 05508-900, Brazil

W. F. Thompson[a)]
Department of Psychology, Atkinson College, York University, 4700 Keele Street, Toronto, Ontario M3J 1P3, Canada

L. Silveira-Moriyama
Departamento de Fisiologia e Biofisíca, Instituto de Ciências Biomédicas, Universidade de São Paulo, Avenida Lineu Prestes 1524, São Paulo, SP 05508-900, Brazil

L.-L. Balkwill
Department of Psychology, Atkinson College, York University, 4700 Keele Street, Toronto, Ontario M3J 1P3, Canada

(Received 19 April 2000; revised 5 January 2001; accepted 5 March 2001)

In five experiments, we investigated the speed of pitch resolution in a musical context. In experiments 1–3, listeners were presented an incomplete scale (doh, re, mi, fa, sol, la, ti) and then a probe tone. Listeners were instructed to make a rapid key-press response to probe tones that were relatively proximal in pitch to the last note of the scale (valid trials), and to ignore other probe tones (invalid trials). Reaction times were slower if the pitch of the probe tone was dissonant with the expected pitch (i.e., the completion of the scale, or doh) or if the probe tone was nondiatonic to the key implied by the scale. In experiments 4 and 5, listeners were presented a two-octave incomplete arpeggio, and then a probe tone. In this case, listeners were asked to make a rapid key-press response to probe tones that were relatively distant in pitch from the last note of the arpeggio. Under these conditions, registral direction and pitch proximity were the dominant influences on reaction time. Results are discussed in view of research on auditory attention and models of musical pitch. [DOI: 10.1121/1.1367254]

PACS numbers: 43.75.Cd [RDA]

I. INTRODUCTION

Attention is of paramount importance in guiding the behavior of human beings. In recent years, empirical research has focused on attention in the visual system. Visual attention must rapidly and continuously shift between different spatial locations in response to environmentally significant events. Shifts in visual attention are not dependent on eye movements, but they occur in real time (Posner, 1985). In particular, there is evidence that the time taken to shift visual attention from one spatial location to another is proportional to the angular separation of these two points (Tsal, 1983; Downing and Pinker, 1985). This finding suggests that visual attention moves within an analog representation, and that spatial relations and distance information are directly represented by the structure of that representation.

Similar principles apply to auditory attention. Rhodes (1987) found that the time taken to shift auditory attention in three dimensional space was a linearly increasing function of the angular distance moved, at least for distances up to 90 degrees. This finding suggests that both visual and auditory spatial information are represented analogically, and that similar constraints apply to movements of visual and auditory attention within these representations. Another location-based characteristic known in visual attention, inhibition of return (Posner and Cohen, 1984), was recently demonstrated for auditory attention by Mondor *et al.* (1998) and by Spence and Driver (1998), further illustrating parallel features in visual and auditory attentional shifts.

In this investigation, we further examined shifts in auditory attention. However, rather than examine shifts from one spatial location to another, we examined shifts in attention between different pitches. Our investigation was motivated by two theoretical considerations. First, the analysis of pitch by the auditory system is, in an important sense, analogous to spatial analysis by the visual system. The analysis of visual space occurs early in processing. Responses at different parts of the retina are mapped retinotopically onto the primary visual cortex. In contrast, the analysis of spatial information may occur quite late in auditory processing, only after information from the two ears is combined. Rather than spatial location, it is frequency that is analyzed at early stages of auditory processing. Different acoustic frequencies create vibrations at different segments of the basilar membrane, leading to a tonotopic organization of pitch in the primary auditory cortex.

A second consideration was that there is an extensive body of research concerned with musical pitch resulting in several models describing psychological relationships between pitches as they occur in musical contexts (e.g., Deut-

[a)]Author to whom correspondence should be addressed. Electronic mail: billt@yorku.ca

sch, 1982; Krumhansl, 1990). These models, and the empirical work supporting them, provided a solid foundation upon which to make predictions about the speed with which pitches can be resolved in a musical context. In particular, when attention is focused on one pitch (the attended pitch), the speed with which a new pitch is resolved may be influenced by the psychological distance between the attended pitch and the new pitch.

One early model of pitch—the helical model—considers two dimensions: pitch height, which is proportional to the logarithm of the fundamental frequency of a complex tone, and pitch chroma, which treats as equivalent those tones whose fundamental frequencies are separated by an octave. More recent models of pitch have acknowledged the importance of other dimensions of pitch relationships, such as pitch contour, and tonal function (for reviews, see Dowling and Harwood, 1986; Krumhansl, 1990).

It is widely agreed that proximity in pitch height—or ''pitch proximity''—has a significant influence on perceived relationships between pitches. Tones that are proximal in pitch height are perceived to be highly related, listeners expect melodic patterns in which sequential tones are proximal in pitch height, and proximal tones tend to form perceptual groups when played consecutively. Pitch proximity may have a greater influence than spatial location on auditory grouping. Deutsch (1975) presented musical materials to listeners in a manner such that location information suggested one grouping of sounds, while pitch proximity suggested a conflicting grouping of sounds. She presented two major scales simultaneously to listeners, one ascending and the other descending. Successive tones in each of the two scales were presented alternately to the left and right ears, such that when a tone from the ascending scale was presented to the right ear, a tone from the descending scale was presented to the left ear. Listeners did not accurately perceive the location of pitches. Rather, listeners grouped the tones in a way that preserved pitch proximity. This effect, known as the ''scale illusion,'' indicates that pitch proximity may override spatial location in auditory grouping.

Musical context may introduce a number of other properties that may influence perceived relationships between pitches, such as scale membership, contour, harmony, and tonality. Sensitivity to these properties arises through exposure to music organized along discrete sets of pitches known as scales. Research suggests that listeners readily abstract underlying scales (Cohen, 1991), and that perceived relationships among pitches in a musical context are influenced by whether or not those pitches are members of the scale (Krumhansl, 1979). Tones whose pitches are members of the scale are called diatonic tones. Tones whose pitches are not members of the scale are called nondiatonic tones. The most common scale in Western music is the major scale, which has seven pitches per octave (doh, re, mi, fa, sol, la, ti). The first note of the scale is referred to as the tonic, and serves as a point of perceived stability in music. Other notes vary in their perceived stability, resulting in a *tonal hierarchy* (Krumhansl and Kessler, 1982). Sensitivity to the scale and the tonal hierarchy will be collectively referred to as *tonality*.

Melodic contour, which we refer to as *registral direction* (the up/down pattern of notes in a melody), also may influence the speed of pitch resolution. If a melody involves part of an ascending scale, for example, listeners may expect that ascending motion to continue. The latter prediction is based on the Gestalt principle of ''good continuation,'' which has been examined extensively in studies of music (e.g., Deutsch, 1999; Narmour, 1990). Scale and contour are thought to be among the most significant influences on memory for melodies (Dowling, 1978).

Harmony also may influence perceived pitch relationships. The perception of harmony is influenced by sensory dissonance, but is also shaped by long term knowledge of music (Bharucha and Stoeckig, 1986, 1987; Tekman and Bharucha, 1992). Only the sensory aspect of harmony was addressed in this investigation. When two or more tones are sounded simultaneously, their combination may result in physical beating among partials. An excess of such beating patterns is perceived as dissonance; an absence of such beating is perceived as consonance (Plomp and Levelt, 1965).[1] Pitches that are consonant with each other may be perceived as psychologically related, even when they are presented in sequence (Krumhansl, 1995; Thompson and Stainton, 1998). The latter effect may reflect sensitivity to the degree of spectral overlap among such tones, or result from an evaluation of sensory interactions that arise when the memory trace of one tone is combined with physically occurring properties of a subsequent tone.

To summarize, psychological relationships between pitches are influenced by several factors including pitch proximity, tonality, registral direction, and dissonance. In this study, we examined whether these factors affect the time it takes to shift auditory attention between pitches. Listeners were induced to focus on one pitch, and were then presented a probe tone. They were asked to respond rapidly to certain probe tones (''valid'' trials) while ignoring others (''invalid'' trials). We focused on four factors that may influence psychological pitch distance, and, therefore, the time required to shift auditory attention through pitch space. Specifically, we predicted that the time taken to resolve the pitch of a probe tone would be more rapid when

(1) the pitch of the probe tone is proximal to the expected pitch (proximity);
(2) the probe tone is not dissonant with the expected tone (dissonance);
(3) the probe tone is stable within the key defined by the preceding context (tonality); and
(4) the probe tone continues the registral direction suggested by the preceding context (registral direction).

There is precedent for using reaction time to evaluate pitch perception in a musical context. Janata and Reisberg (1988) examined the reaction time of listeners who were instructed to indicate as quickly as possible whether probe tones were diatonic to the scale defined by a preceding musical context. Reaction times were significantly faster for more stable tones within the key. The authors argued that differences in reaction time reflected listeners' internal representation of the tonal hierarchy. One question addressed in our investigation is whether such an influence is observed

when responses to pitch are not contingent on an explicit (conscious) assessment of tonality.

We report the results of five experiments. The design of all experiments was adapted from studies of visual attention, in which participants responded rapidly to visual stimuli presented at varying distances from an initial fixation point (Umiltá, 1988; Hikosaka *et al.*, 1996; Egeth and Yantis, 1997; Steinman and Steinman, 1998). In experiments 1–3, listeners were presented an incomplete major scale, which directed their attention to the note that would complete that scale. Reaction times were obtained for different probe tones. In experiments 4 and 5, an incomplete arpeggio was used to direct the attention of listeners to a certain note. Responses were obtained for the same set of probe tones used in experiments 2 and 3. The results for scale and arpeggio contexts were compared to explore how psychological distances between pitches are affected by musical context.

II. EXPERIMENT 1

In experiment 1, we examined the speed with which listeners can resolve pitches following an incomplete major scale. Participants were first exposed to an incomplete major scale (doh, re, mi, fa, sol, la, ti) in order to direct their attention to a specific pitch (the completion of the scale, or ''doh''). A major scale was adopted because it is well established that this context generates strong expectations for the pitch that completes the scale, i.e., doh (Krumhansl and Shepard, 1979; Krumhansl, 1990). The incomplete scale was followed by one of eight probe tones, and participants were instructed to make a key-press response as soon as they detected the pitch of the probe tone.

To ensure that participants responded to the pitch of the probe tone, rather than to other dimensions of the probe tone (e.g., onset), a go–no-go procedure was adopted in which the response criterion was specifically determined by pitch. Listeners were instructed that if the probe tone was less than three semitones from the tone that would complete the scale, they should respond as quickly as possible (valid probe tones), but if the probe tone was seven or more semitones from the tone that would complete the scale, they should not respond (invalid probe tones). Thus, the decision to respond was contingent on an analysis of pitch, and reaction times should be affected by the psychological distance between the expected pitch (next tone on the major scale) and the pitch of the (valid) probe tone.

A. Method

1. Participants

Fourteen participants (nine males, five females) with at least three years of musical training were recruited for experiment 1 among the staff and student community at the Institute of Biomedical Sciences at the University of São Paulo. All participants were volunteers, their ages ranged from 19 to 50 (mean=26.4, s.d.=9), and all reported normal hearing.

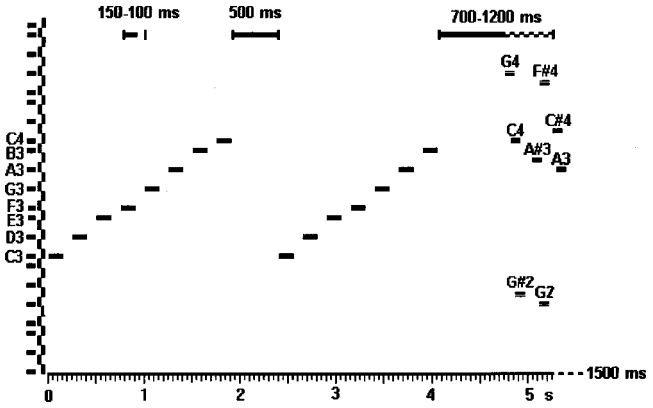

FIG. 1. The experimental design of experiment 1. The vertical axis represents frequencies on a logarithmic scale; the horizontal axis represents time (s). The letters at the right indicate the probe tones for a C major scale beginning at C3. Valid probe tones are shown as a solid line and invalid probe tones are shown as a double line. Horizontal bars at the top indicate the duration of tones and intervals between tones.

2. Materials and tone construction

The tones to which participants were exposed were generated using MEL Professional V2.0 software acquired from Psychology Software Tools (PST, Inc., Pittsburgh; see Schneider, 1988), on an IBM-PC compatible Pentium computer. Tones were sine waves, and were each 150 ms in length including 30 ms of onset and 30 ms of offset. Participants heard the stimuli through high-quality speakers at a comfortable listening level (approximately 70 dB) in a sound-attenuated booth with reduced lighting. Participants were tested individually, and responded by pressing a button on a joystick with their thumb, directly entering the data into the computer.

3. Conditions and procedure

Details of the experimental design are shown, to scale, in Fig. 1. To avoid habituation, the first pitch of the scale was one of four pitches, determined randomly for each trial: C3 (523 Hz), A2 (440 Hz), G2 (391 Hz) or F2 (349 Hz). There were four valid probe tones for the C3 scale: C4, C♯4, A3 and A♯3. There were four invalid probe tones for the C3 scale: F♯4, G4, G2 and G♯2. Valid and invalid probe tones of the A2, F2, and G2 scales were transpositions of the example given.

After each response, participants were provided feedback on their performance, as shown in Table I. If errors were committed in the course of a block, new tests were presented to the participants at the end of the block, such that the number of correct responses was the same for all conditions. Altogether, each participant had to provide correct re-

TABLE I. Feedback (in italics) given to participants in experiment 1, according to their response in the different conditions.

Reaction time	Valid probe tone	Invalid probe tone
RT<130	*Anticipated*	*Error & anticipated*
130<RT<1000	*RT displayed*	*Error*
RT>1000	*Slow*	*Error*
No response	*Slow*	*Correct*

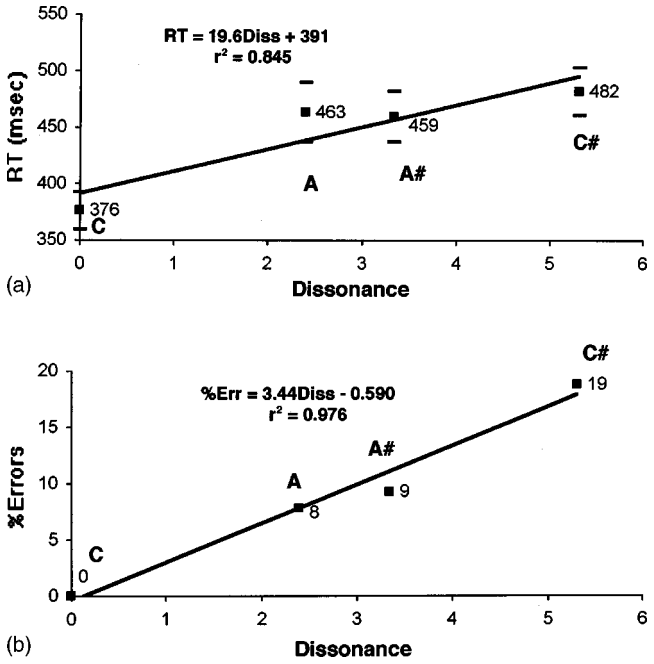

FIG. 2. (a) Mean reaction times (RT) for the four valid probe tones of experiment 1, plotted as a function of dissonance relative to the expected probe tone. According to Plomp and Levelt (1965), the values of dissonance are as follows: C4=0, A3=2.40, A♯3=3.34, C♯4=5.32. The bars indicate standard errors. Regression equations and squared correlations are shown. (b) Percentage of errors committed by subjects in response to valid probe tones in experiment 1, plotted as a function of dissonance relative to the expected probe tone. Regression equations and squared correlations are shown.

sponses to 192 tests (16 blocks of 12 tests each), of which half were valid, and half were invalid. The results presented were thus based on 96 reaction times per participant, 24 for each one of the four valid probe tones. The number of errors committed was also recorded.

Participants were tested on three separate experimental sessions. On the first day, they were given instructions for the task, and participated in a training session in which they were informed ahead of time whether the probe tone would be valid or invalid. After completing the training session, all participants took part in a practice experiment, the reaction times of which were discarded. On the second and third days, participants went through another practice experiment (the data being again discarded) before participating in the experiment (8 random blocks of 12 tests each, 6 valid and 6 invalid, plus repeats to make up for mistaken responses, with pauses after the third block and the sixth block to avoid excessive fatigue).

B. Results and discussion

The mean reaction times for the four valid probe tones are shown in Fig. 2(a). A one-way analysis of variance showed a significant effect of probe tone, $F(3,39)=28.41$, $p<0.001$). Planned comparisons were conducted to assess the predictions. First, reaction times for the expected probe tone, C4 (mean=376 ms), were significantly faster than reaction times across other valid probe tones (mean=468 ms), $F(1,39)=81.35$, $p<0.001$. This result suggests that the scale context indeed focused auditory attention on the pitch of C4, so that no shift in auditory attention was required to resolve that pitch, leading to shortest reaction times for this probe tone.

A second planned comparison revealed that reaction times for the probe tone C♯4 (mean=482 ms) were significantly longer than reaction times across other probe tones (mean=433 ms), $F(1,39)=23.51$, $p<0.001$. This finding is consistent with predictions based on dissonance and tonality, as this pitch is perceived as dissonant with the expected pitch (C4) and it is not diatonic to the scale. Yet this finding is inconsistent with predictions based on proximity and registral direction: the pitch of C♯4 is only one semitone away from the expected pitch and is in the expected registral direction. According to the analysis of Plomp and Levelt (1965), C♯4 has a greater degree of perceived dissonance with the expected pitch, C4, than any other probe tone. The quantitative values of dissonance obtained by these authors were used to plot values of the abscissa in Fig. 2(a).

The remaining two probe tones, A3 and A♯3, showed intermediate reaction times, which were statistically indistinguishable (463 and 459 ms, respectively). These two probe tones have similar levels of dissonance with the expected probe tone at C4. The tones also have similar tonal hierarchy values as quantified by Krumhansl and Kessler (1982), even though only one of these probe tones (A3) is diatonic to the established key. As shown in Table II, regressions of reaction times as a function of dissonance [shown in Fig. 2(a)] and tonality both show a high correlation coefficient ($r^2=0.845$ and 0.895 respectively, $p<0.05$).

In addition to analyzing reaction times, we also examined the proportion of incorrect responses for each valid probe tone. This analysis was performed to assess whether psychological distance influenced the accuracy with which

TABLE II. Squared correlations (r^2) between mean reaction times and % errors as a function of dissonance, pitch proximity, and tonality. An asterisk indicates statistical significance at the 0.05 level.

	Reaction time			% Errors		
Experiment No.	Dissonance	Pitch proximity	Tonality	Dissonance	Pitch proximity	Tonality
1	**0.845***	0.429	**0.895***	**0.976***	0.053	**0.747**
2	**0.949***	0.101	**0.729**	**0.886***	0.000	**0.576**
3	**0.710**	0.055	**0.469**	**0.989***	0.067	**0.789**
4	0.331	**0.667**	0.005	0.016	**0.980***	0.161
5	0.001	**0.968***	0.276	0.009	**0.997***	0.780

listeners classified probe tones. The distribution of incorrect responses among the four valid probe tones was consistent with the reaction time data, as shown in Fig. 2(b). Errors were highly nonrandom (chi squared (3)=66.9, 3 $p < 0.001$). The pattern of errors suggests that processing the expected tone, C4, was a much easier task than processing tones at A3 or A♯3, and C♯4 (in the order). As shown in Table II, the percentage of correct responses was strongly related to dissonance ($r^2 = 0.976$, $p < 0.01$).

III. EXPERIMENTS 2 AND 3

Experiment 1 indicated that listeners responded more quickly to a probe tone with an expected pitch than to a probe tone with an unexpected pitch. In addition, reaction times increased linearly with dissonance relative to the expected probe tone, and decreased with the tonal stability of the probe tone relative to the key established by the preceding scale. The slowest reaction time, observed for the probe tone at C♯4, was expected on the basis that it is psychologically distant from the expected note of C4. Although C4 and C♯4 are proximal in pitch (separated by only one semitone), they are highly dissonant with each other, and psychologically distant from each other in a C major context (Krumhansl, 1990). Overall, dissonance and tonality were strong predictors of the reaction time.

Experiments 2 and 3 were conducted for three reasons. First, listeners in experiment 1 were extensively trained to respond to valid probe tones within 1 s, and several responses were measured for each probe tone. It is possible that such extensive training may have encouraged listeners to develop explicit strategies of responding that are not typically invoked when shifting auditory attention between pitches under normal conditions of music listening, and which might mask the automatic pitch encoding processes under investigation. Experiments 2 and 3 were designed to verify whether the results of experiment 1 would be obtained without elaborate training and exposure to the experimental protocol. Second, the tones used in experiment 1 were sine waves, but pitch perception in most musical contexts involves more familiar timbres. We considered the possibility that pitch resolution for sine tones may be influenced by somewhat different factors than pitch resolution for more familiar timbres. Thus, the stimuli used in experiments 2 and 3 consisted of sampled piano tones.

Third, it is possible that the large reaction time observed for the probe tone at C♯4 was partially related to the asymmetric distribution of valid and invalid probe tones (see method section, experiment 1). Valid probe tones were more distant in pitch from invalid probe tones in the lower register (between 13 and 18 semitones) than from invalid probe tones in the upper register (between 5 and 10 semitones). This asymmetry may have made it more difficult to distinguish between higher pitched valid and invalid probe tones than between lower pitched valid and invalid probe tones. Thus, the large reaction time at C♯4 may have resulted, in part, from a difficulty in discriminating this pitch from upper invalid pitches. Experiments 2 and 3 eliminated this asymmetry.

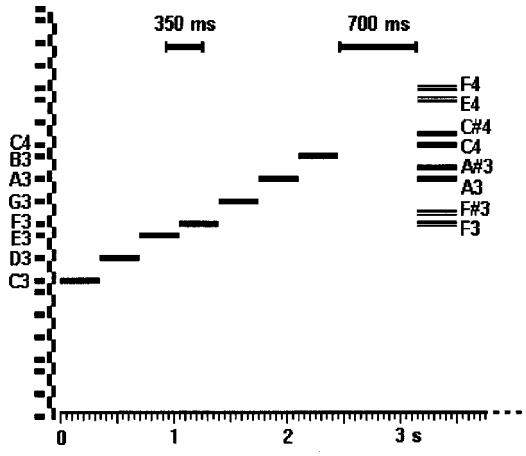

FIG. 3. The experimental design of experiments 2 and 3.

We noted that reaction times for the first two responses to each probe tone in experiment 1 illustrated the same trend as the mean reaction time for the full set of 24 responses (386, 448, 474 and 490 ms versus 376, 463, 460 and 482 ms, respectively, for probe tones C4, A3, A♯3, and C♯4). Thus, experiments 2 and 3 limited the number of responses to two.

A. Method

1. Participants

Twelve women and eight men from the York University community, ranging in age from 19 to 31 (mean=24.3) participated in experiment 2. Ten received undergraduate course credit for their participation, and ten were volunteers. Twelve women and three men, aged between 18 and 54 (mean 23.1) participated in experiment 3. Twelve received undergraduate credit for their participation and three were volunteers. The number of years of formal musical training of participants ranged from zero to greater than ten (mean =6.8 years) in experiment 2 and from zero to ten (mean=3.4 years) in experiment 3. All participants reported normal hearing.

2. Materials and tone construction

Tones were taken from the internal timbre set of a Power Macintosh computer. The timbre of all tones was the sampled piano sound of the Roland piano (for an acoustic description, see Fletcher and Rossing, 1991), with fundamental frequencies set to equal temperament tuning. Stimuli were presented to listeners in a sound attenuated booth through Sennheiser HD-480 headphones. Responses were entered directly onto a computer.

3. Conditions and procedure

The stimuli used for experiments 2 and 3 were identical and are illustrated in Fig. 3. Listeners were presented an incomplete C major scale, followed by a pause of 700 ms, and then a probe tone in each trial. The seven notes of the incomplete scale, C3, D3, E3, F3, G3, A3, B3, were each 350 ms in duration, as was the duration of the probe tone. There were eight probe tones.

Participants were instructed to make a rapid key-press response if the probe tone was two or fewer semitones from the last tone of the incomplete scale (ti); otherwise they should make no response, and wait for the next trial. The four valid probe tones were A3, A♯3, C4, and C♯4. For both experiments 2 and 3, the maximum reaction time acceptable was set to 2000 ms. The four invalid probe tones were F3, F♯3, E4, and F4. Upper and lower probe tones were symmetric in pitch distance from the reference tone: valid probe tones were exactly 1 or 2 semitones above or below the reference tone (ti), and invalid probe tones were 5 or 6 semitones above or below the reference tone.

In experiment 2 each probe tone was presented just twice, regardless of whether correct responses were obtained, thus minimizing participant exposure to the experimental procedure. In experiment 3, each invalid probe tone was presented twice, but each valid probe tone was presented as many times as needed to obtain two valid key-press responses (i.e., responses under 2000 ms). Thus, if no response to a valid probe tone was made by 2000 ms, that trial was repeated at a randomly determined position later in the experimental session. The order in which probe tones were presented was randomized independently for each participant.

Experiments 2 and 3 also differed in the following ways. In experiment 2, listeners were given minimal training, with an emphasis on accuracy, and proceeded to the experiment as soon as they succeeded in correctly classifying (unspeeded) 16 probe tones in a row (i.e., each possible probe tone, twice). Once the experiment began, there were no trial replacements for mistaken responses, and therefore the number of correct responses was not always the same for all probe tones or participants.

In experiment 3, participants were trained with one set of practice trials involving all valid probe tones, and another set of practice trials involving all invalid probe tones. Participants were given the opportunity to switch back and forth between these two practice sets until they felt comfortable with the distinction between valid and invalid probe tones. Emphasis was on speed, and participants were given feedback on their performance during the practice trials (reaction time in ms).

B. Results and discussion

The mean reaction times obtained in experiments 2 and 3, shown in Fig. 4(a), illustrate the same trend observed in experiment 1. Figures 4(a) and (b) illustrate linear fits of mean reaction times and error-rates for valid probe tones, respectively, as a function of dissonance. These analyses generally suggest that longer reaction times and higher error rates occurred for probe tones that were more dissonant with the expected probe tone. Table II illustrates that reaction times in experiment 2 also supported the importance of tonality. Asymmetry in pitch distance of valid and invalid probe tones about the reference tone, or the development of explicit strategies following extensive training, were thus not likely to have been essential to the results of experiment 1. Details of the experimental design, the instructions, and the training procedures appeared to influence absolute values of

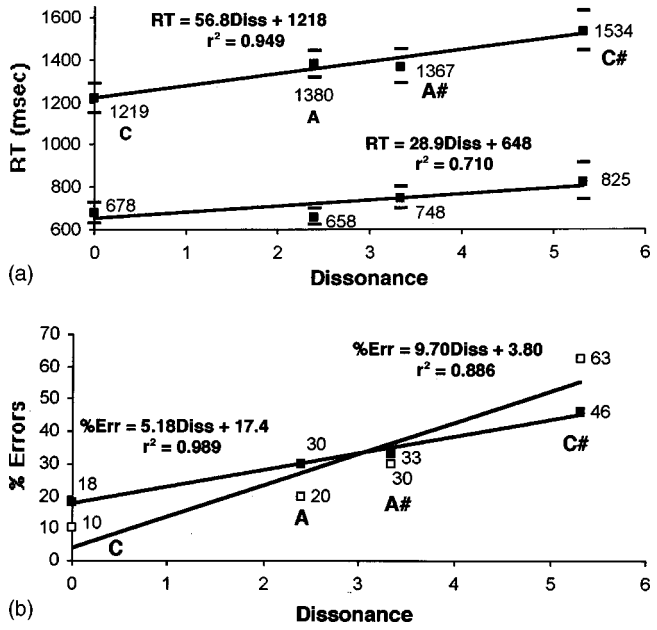

FIG. 4. (a) Mean reaction times (RT) for the four valid probe tones of experiments 2 (upper line) and 3 (lower line). The values of dissonance are as follows: C4=0, A3=2.40, A♯3=3.34, C♯4=5.32. (b) Percentage of errors committed by subjects in response to valid probe tones in experiments 2 (unfilled squares) and 3 (filled squares), plotted as a function of dissonance relative to the expected probe tone. Regression equations and squared correlations are shown.

reaction times and error rates, but the essential pattern of reaction times, and how they related to dissonance, was preserved. In all three experimental contexts, reaction times were more strongly related to dissonance and tonality than to pitch proximity and registral direction.

The design of experiment 2 meant that responses were not always obtained when a valid probe tone was presented, and different probe tones elicted a different number of responses (0, 1, or 2). The number of responses made to each of the eight probe tones of experiment 2 was recorded as 0, 1, or 2, and a repeated measures ANOVA was conducted on the resultant data. As expected, there were significantly more responses made to valid probe tones (mean=1.54 responses per probe tone) than to invalid probe tones (mean=0.39 responses per probe tone), $F(1,19)=128.04$, $p<0.0001$. This finding indicates that participants were sensitive to the difference between valid and invalid probe tones.

Among valid probe tones, there were significantly more responses made to the expected note, C4, than to other valid probe tones, $F(1,19)=15.17$, $p<0.001$. Among unexpected valid probe tones, there were significantly more responses made to A3 than to A♯3 or C♯4, $F(1,19)=16.05$, $p<0.001$. Finally, there were significantly more responses made to A♯3 than to C♯4, $F(1,19)=16.38$, $p<0.001$. These findings parallel the reaction time data obtained in experiment 1, and suggest that as the psychological distance between probe tones and the expected note increased, participants tended to overestimate the distance in semitones between the probe tone and the last note of the scale.

Reaction times obtained in experiment 3 were assessed in a two-way ANOVA, with repeated measures on probe tone (four valid probe tones) and example (two responses for

each probe tone). As expected, there was a main effect of probe tone, $F(3,42)=2.8508$, $p=0.05$, but no main effect of example, $F(1,14)=1.0547$, ns, and no interaction between probe tone and example, $F(3,42)=1.3413$, ns. These findings, summarized in Fig. 4(a), illustrate that the time taken to respond to different probe tones depended on the pitch of those probe tones.

As in experiment 1, the mean reaction time for the expected note, C4 (mean=678.37 ms), was lower than the mean reaction time for other probe tones (mean=743.84 ms), but in this case the difference was not significant, $F(1,42)=1.60$, ns. However, the mean reaction time for diatonic notes (C4 and A3, mean=668.32 ms) was significantly lower than the mean reaction time for nondiatonic notes (A♯3 and C♯4, mean=786.62 ms), $F(1,42)=6.95$, $p=0.02$. This finding supports the importance of one aspect of tonality in determining reaction times: scale membership. In addition, the mean reaction time for the probe tone at C♯4 (mean=825.47 ms), the most dissonant note with respect to the expected note, was significantly longer than the mean reaction time for all other notes (mean=694.80 ms), $F(1,42)=6.36$, $p=0.02$. This finding supports the importance of dissonance in determining reaction times. Taken together, the results again suggest that the time taken to shift attention from one pitch to another is proportional to the psychological distance between pitches, and that this distance is influenced by tonality and the degree of dissonance between pitches.

IV. EXPERIMENTS 4 AND 5

Experiments 1–3 indicated that listeners respond more slowly to unexpected notes than to expected notes following an incomplete major scale. Experiments 4 and 5 were conducted to examine the effect for another musical context—one that generates an expected note that is not proximal to the last note of the context. Listeners were presented an incomplete two-octave arpeggio (E2, G♯2, B2, E3, G♯, B3) followed by a probe tone. In this case, listeners were instructed to make a rapid key-press response to probe tones that were greater than three semitones from the last tone (the reference tone) of the arpeggio. Thus, the distance of valid and invalid probe tones from the reference tone was inverted. The arpeggio was used to direct the attention of participants to the next expected note of the arpeggio, E4. Again two experimental approaches were taken, paralleling the approaches of experiments 2 and 3. The approach of experiment 4 was to minimize training (preventing the development of complex strategies in responding to the probe tones) and to emphasize accuracy. The approach of experiment 5 was to increase training and emphasize speed of response.

A. Method

1. Participants

Twelve women and eight men from the York University community, ranging in age from 19 to 31 (mean=24.3), participated in experiment 2. Ten received undergraduate course credit for their participation, and ten were volunteers. Sixteen women and three men, aged between 18 and 54 (mean 23.0) participated in experiment 3 thirteen received undergraduate credit for their participation and six were volunteers. The number of years of formal musical training of participants ranged from zero to greater than ten (mean=6.8 years) in experiment 2 and from zero to ten (mean=2.9 years) in experiment 3. All but four of these participants also took part in experiments 2 and 3. All participants reported normal hearing.

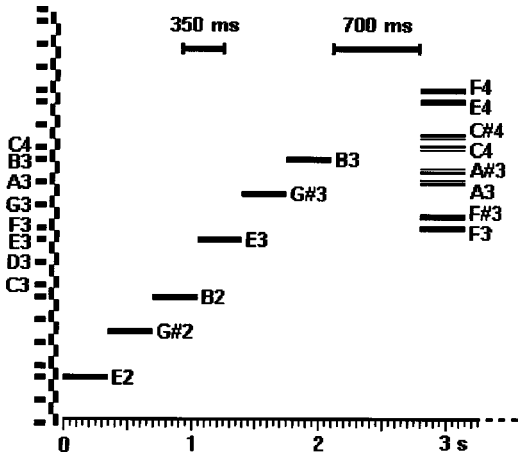

FIG. 5. The experimental design of experiments 4 and 5.

2. Materials and tone construction

The materials and tone construction were the same as those used in experiments 2 and 3.

3. Conditions and procedure

The stimuli used for experiments 4 and 5 are illustrated in Fig. 5. Listeners were presented an incomplete E major arpeggio, followed by a pause of 700 ms, and then a probe tone. The six notes of the arpeggio, E2, G♯2, B2, E3, G♯3, B3, were each 350 ms in duration, as was the duration of the probe tone. There were eight probe tones. Participants were instructed to make a rapid key-press response if the probe tone was three or more semitones from the last note of the arpeggio; otherwise they should make no response, and wait for the next trial. Thus, the response criterion was reversed with respect to that used in experiments 2 and 3. That is, participants in experiments 3 and 4 were instructed that they should not respond to probe tones whose pitch was proximal to the final tone of the arpeggio.

The four valid probe tones were F3, F♯3, E4, and F4. For both experiments 4 and 5, the maximum reaction time acceptable was set to 2000 ms. The four invalid probe tones were A3, A♯3, C4, and C♯4. As in experiments 2 and 3, upper and lower probe tones were symmetric in pitch distance from the reference tone: valid probe tones were exactly 5 and 6 semitones above or below the reference tone, and invalid probe tones were 1 and 2 semitones above or below the reference tone.

In experiment 4, each probe tone was presented twice, regardless of whether correct responses were obtained. In experiment 5, each invalid probe tone was presented twice, but each valid probe tone was presented as many times as needed to obtain two valid key-press responses (i.e., responses under 2000 ms). Thus, if no response to a valid

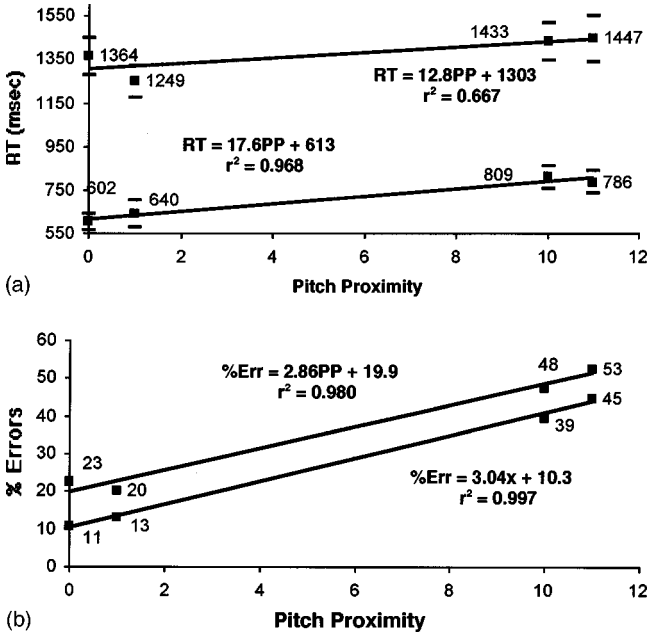

FIG. 6. (a) Mean reaction times (RT) for the four valid probe tones of experiments 4 (upper line) and 5 (lower line) plotted as a function of pitch proximity relative to the expected probe tone, E4. Values of pitch proximity were E4=0, F4=1, F♯3=10, F3=11; the units are semitones. (b) Percentage of errors committed by subjects in response to valid probe tones in experiments 4 (upper line) and 5 (lower line) as a function of pitch proximity.

probe tone was made by 2000 ms, that trial was repeated later in the experimental session. The order in which probe tones were presented was randomized independently for each participant. Other differences between experiments 4 and 5 were the same as those described for experiments 2 and 3.

B. Results and discussion

Mean reaction times and the percentage of errors obtained in experiments 4 and 5 are shown in Figs. 6(a) and (b), plotted as a function of pitch proximity relative to the expected note. Table II summarizes regression analyses conducted on both mean reaction times and error-rates for valid probe tones. These analyses suggest that reaction times and error-rates were not strongly related to dissonance and tonality, but rather, were more strongly related to pitch proximity and registral direction.

As in experiment 2, different probe tones elicted a different number of responses in experiment 4 (0, 1, or 2). Significantly more responses were made to valid probe tones (mean=1.46 responses per probe tone) than to invalid probe tones (mean=0.70 responses per probe tone), $F(1,19) = 23.26$, $p<0.0001$. This finding indicates that, as with the scale context, participants were sensitive to the difference between valid and invalid probe tones. Among valid probe tones, there were significantly more responses made to probe tones in the expected registral direction (E4 and F4) than to probe tones in the unexpected registral direction, $F(1,19) = 18.67$, $p<0.001$. This finding suggests that the arpeggio, unlike the scale, directed attention in an upward direction. There were no other significant effects.

Reaction time data obtained in experiment 5 were assessed in a two-way ANOVA, with repeated measures on probe pone (four valid probe tones) and example (two examples). As expected, there was a main effect of probe tone, $F(3,54)=6.43$, $p<0.001$, but no main effect of example, $F(1,18)<1.0$, ns, and no interaction between probe tone and example, $F(3,54)<1.0$, ns. Planned comparisons showed that the mean reaction time was lower for the expected probe tone, E4 (mean=601.82 ms), than for the other three probe tones (mean=745.03 ms), $F(1,54)=9.20$, $p<0.005$. This result suggests that the arpeggio context focused auditory attention on the pitch of E4, so that no shift in auditory attention was required to resolve that pitch, leading to shortest reaction times for this probe tone.

The mean reaction time was also significantly lower for probe tones in the same registral direction (E4 and F4, mean =620.86 ms) than for probe tones in the opposite registral direction (F3 and F♯3, mean=797.61 ms), $F(1,54)=18.69$, $p<0.0001$. Finally, among the three unexpected probe tones (F3, F♯3, F4), the two extreme notes (furthest away from the last note of the context, F3 and F4, mean=712.92 ms) had marginally lower reaction times than the note that was closer in pitch (F♯3, mean=809.26 ms), $F(1,54)=3.70$, $p<0.06$. The latter finding suggests that pitch proximity may influence reaction times following an incomplete arpeggio.

Overall, the results of experiments 4 and 5 support the notion that the time taken to resolve pitch depends on the psychological distance between the attended pitch and a presented pitch. In this case, however, registral direction and pitch proximity appeared to influence the psychological distance between pitches.

V. GENERAL DISCUSSION

The results of this investigation indicate that the time taken to respond to probe tones varies significantly depending on the pitch of that probe tone. In particular, pitch resolution in a musical context was determined by the psychological distance between the expected and actual pitch of the probe tone. This finding is analogous to effects reported for the visual system: response times for different visual cues are proportional to the distance between the location of the initial visual focus and the location of the target cue. In this case, the focus of auditory attention was established by generating a strong expectation for the completion of a pitch pattern (scale or arpeggio), which is a location in pitch space. Delays in responding to different pitches are interpreted as the time taken for participants to shift auditory attention from the expected pitch to the pitch of the probe tone.

The experimental designs illustrated in Figs. 1, 3, and 5 allowed an evaluation of four influences on pitch distance. Pitch proximity was defined in terms of a log frequency scale (number of semitones). Measures of dissonance and tonality were drawn from the work of Plomp and Levelt (1965) and Krumhansl (1990), respectively. Regression curves of reaction times as a function of these factors were determined and evaluated for their goodness of fit (Table II). Another parameter, registral direction, was assessed by comparing reaction times for probe tones in the expected registral direction with

reaction times for probe tones in the opposite registral direction.

The process of shifting attention between pitches appears to be constrained by different factors depending on whether the preceding context is an incomplete major scale or an arpeggio. Perceived dissonance and tonality played an important role in the scale context, while neither of these parameters were significant factors in the arpeggio context. For the arpeggio context, reaction times were significantly faster for probe tones that continued the registral direction of the arpeggio than for probe tones that reversed the registral direction of the arpeggio. There was also moderate support for an influence by pitch proximity following the arpeggio context.

One interpretation of these results is that expectancies following the arpeggio context are most strongly associated with general (gestalt) principles of pitch relationships, whereas expectancies following the scale context are more strongly associated with harmony and tonality. Thus, the scale context may have invoked a more musical representation of pitch distance, which then determined reaction times. The arpeggio, in contrast, did not appear to invoke a rich musical representation of pitch distance, and judgments were therefore based on more general auditory principles (see Bregman, 1990; Deutsch, 1999).

This interpretation may appear to conflict with research conducted by Krumhansl and her associates, who found that harmonic materials induce a strong sense of tonality (Krumhansl, 1990). Two aspects of the harmonic stimuli used in those studies should be borne in mind, however. First, those studies involved minimizing effects of pitch height by using circular tones (Shepard, 1964). In contrast, we used noncircular tones (sine tones or piano tones), and thus did not inhibit influences from pitch proximity. Second, the harmonic materials in studies reviewed by Krumhansl (1990) were chord sequences, whereas we used an ascending arpeggio that extended across two octaves.

There are other possible explanations for the differences observed for the scale and arpeggio contexts. First, whereas the scale context involved stepwise melodic motion (i.e., intervals no greater than two semitones), the arpeggio involved leaps between successive notes, and also extended across a greater range of frequencies. The involvement of melodic leaps and the large extent of movement in the arpeggio context may have conveyed a strong sense of direction, distance, and momentum, thus overwhelming any influences by harmony and key.

Another factor may be the distance between the expected pitch and the valid probe tones. In the arpeggio context, the expected pitch (Fig. 5) was either the same or 1 semitone removed from the higher pitched valid probe tones, but 10 and 11 semitones away from the lower pitched valid probe tones. In the scale context, this difference was considerably reduced (0 and 1 semitone away from the higher pitched valid probe tones; 2 and 3 semitones away from the lower pitched valid probe tones). Thus, any effects of registral direction for the arpeggio context may have been bolstered by proximity to the attended pitch. That is, low-pitched valid and invalid probe tones may have been difficult to discriminate because both categories are distant in pitch from the expected pitch.

A notable feature of the scale results is a proportional increase of mean reaction times over experiments 1–3. Taking into account the details of the experimental designs, these three experiments might be classified as easiest (experiment 1), of intermediate difficulty (experiment 3), and most difficult (experiment 2). Mean reaction times increase accordingly at a ratio of 1:1.6:3.1. Interestingly, the slopes of the fits of reaction times as a function of dissonance increase across these experiments in the same way, the coefficient-ratios being 1:1.5:2.9. Moreover, these linear fits, when extrapolated backwards, all cross the abscissa at about the same point (reaction time$=0$, dissonance$=-20$, approximately). This finding suggests that the cognitive processes involved in recognizing the expected valid probe tone (doh), which take longer in more difficult situations, continue at a constant rate in the search and analysis of the remaining valid probe tones.

VI. CONCLUSIONS

The organization of pitch space and of shifts of auditory attention in this space depend on musical context, which shapes this space and directs auditory attention to a given position within the space. A familiar scale produces a pitch space in which yardsticks calibrated with dissonance and tonality are the best instruments to measure psychological distance. An arpeggio, in contrast, creates a pitch space in which psychological distances are determined more by registral direction and proximity.

ACKNOWLEDGMENTS

We are grateful to Luiz Eduardo Ribeiro do Valle, Marcus Vinícius C. Baldo and Luiz Renato Carreiro for assistance with software and several fruitful discussions especially concerning experiment 1. Tais Silveira Moriyama helped perform experiment 1 and Doug Gifford provided technical support for experiments 2–5. The research was supported by a grant from the Natural Sciences and Engineering Research Council of Canada, awarded to the second and fourth authors. The third author was awarded a scholarship from the Conselho Nacional de Desenvolvimento Científico e Tecnológico and travel grants from the Fundação Faculdade de Medicina da Universidade de São Paulo and the Association of Universities and Colleges of Canada in the course of this work. Part of this research was presented at the annual meeting of the Canadian Society for Brain, Behavior and Cognitive Science, Ottawa, June 1998.

[1]Dissonance, as described by Plomp and Levelt (1965), is a complex concept that involves perceptual judgment, sensory organization of the cochlea and physical beats between harmonics of complex tones. Quantitative values of dissonance between complex tones were obtained by these authors by summing the separate contributions of dissonance between the closest pairs of the pure tones that constituted the first six harmonics of each complex tone. The values of dissonance for pure tones were extracted from measurement of the percentage of listeners who described two pure tones as consonant.

Bharucha, J. J., and Stoeckig, K. (**1986**). ''Reaction time and musical expectancy: Priming of chords,'' J. Exp. Psychol. **12**(4), 403–410.

Bharucha, J. J., and Stoeckig, K. (**1987**). ''Priming of chords: Spreading activation or overlapping frequency spectra?'' Percept. Psychophys. **41**(6), 519–524.
Bregman, A. S. (**1990**). *Auditory Scene Analysis* (MIT, Cambridge, MA).
Cohen, A. J. (**1991**). ''Tonality and perception: Musical scales primed by excerpts from 'The Well Tempered Clavier' of J. S. Bach,'' Psychol. Res. **53**, 305–314.
Deutsch, D. (**1975**). ''Two-channel listening to musical scales,'' J. Acoust. Soc. Am. **57**, 1156–1160.
Deutsch, D. (**1982**). ''The internal representation of information in the form of hierarchies,'' Percept. Psychophys. **31**, 596–598.
Deutsch, D. (**1999**). ''Grouping mechanisms in music,'' in *The Psychology of Music*, 2nd ed., edited by D. Deutsch (Academic, New York), pp. 299–348.
Dowling, W. J. (**1978**). ''Scale and contour: Two components of a theory of memory for melodies,'' Psychol. Rev. **85**, 341–354.
Dowling, W. J., and Harwood, D. L. (**1986**). *Music Cognition* (Academic, Orlando, FL).
Downing, C. J., and Pinker, S. (**1985**). ''The spatial structure of visual attention,'' in *Attention and Performance XI*, edited by M. I. Posner and O. S. M. Marin (Erlbaum, Hillsdale, NJ).
Egeth, H. E., and Yantis, S. (**1997**). ''Visual attention: Control, representation and time course,'' Annu. Rev. Psychol. **48**, 269–297.
Fletcher, N. H., and Rossing, T. D. (**1991**). *The Physics of Musical Instruments* (Springer-Verlag, New York).
Hikosaka, O., Miyauchi, S., and Shimojo, S. (**1996**). ''Orienting of spatial attention—its reflexive, compensatory, and voluntary mechanisms,'' Cognitive Brain Research **5**, 1–9.
Janata, P., and Reisberg, D. (**1988**). ''Response-time measures as a means of exploring tonal hierarchies,'' Music Perception **6**(2), 161–172.
Krumhansl, C. L. (**1979**). ''The psychological representation of musical pitch in a tonal context,'' Cogn. Psychol. **11**, 346–374.
Krumhansl, C. L. (**1990**). *Cognitive Foundations of Musical Pitch* (Oxford U.P., Oxford, England).
Krumhansl, C. L. (**1995**). ''Effects of musical context on similarity and expectancy,'' Systematische Musikwissenschaft (Systematic Musiology) **3**(2), 211–250.
Krumhansl, C. L., and Kessler, E. (**1982**). ''Tracing the dynamic changes in perceived tonal organization in a spatial representation of musical keys,'' Psychol. Rev. **89**, 334–368.
Krumhansl, C. L., and Shepard, R. N. (**1979**). ''Quantification of the hierarchy of tonal functions within a diatonic context,'' J. Exp. Psychol. **5**, 579–594.
Mondor, T. A., Breau, L. M., and Milliken, B. (**1998**). ''Inhibitory processes in auditory selective attention: Evidence of location-based and frequency-based inhibition of return,'' Percept. Psychophys. **60**(2), 296–302.
Narmour, E. (**1990**). *The Analysis and Cognition of Basic Melodic Structures* (Univ. of Chicago, Chicago).
Plomp, R., and Levelt, W. J. M. (**1965**). ''Tonal consonance and critical bandwidth,'' J. Acoust. Soc. Am. **38**, 548–560.
Posner, M. I. (**1985**). *Chronometric Explorations of the Mind* (Oxford U.P., New York).
Posner, M. I., and Cohen, Y. (**1984**). ''Components of visual orienting,'' in *Attention and Performance X*, edited by H. Bouma and D. G. Bowhuis (Erlbaum, Hillsdale, NJ), pp. 531–555.
Rhodes, G. (**1987**). ''Auditory attention and the representation of spatial information,'' Percept. Psychophys. **42**(1), 1–14.
Schneider, W. (**1988**). ''Micro Experimental Laboratory: An integrated system for IBM-PC compatibles,'' Behav. Res. Methods Instrum. Comput. **20**, 206–217.
Shepard, R. N. (**1964**). ''Circularity in judgments of relative pitch,'' J. Acoust. Soc. Am. **36**, 2346–2353.
Spence, C., and Driver, J. (**1998**). ''Auditory and audiovisual inhibition of return,'' Percept. Psychophys. **60**(1), 125–139.
Steinman, S. B., and Steinman, B. (**1998**). ''Vision and Attention. I: Current Models of Visual Attention,'' Optom. Vision Sci. **75**(2), 146–155.
Tekman, H. G., and Bharucha, J. J. (**1992**). ''Time course of chord priming,'' Percept. Psychophys. **51**(1), 33–39.
Thompson, W. F., and Stainton, M. (**1998**). ''Expectancy in Bohemian folk song melodies: Evaluation of Implicative Principles for implicative and closure intervals,'' Music Perception **15**, 231–252.
Tsal, Y. (**1983**). ''Movements of attention across the visual field,'' J. Exp. Psychol. **9**, 523–530.
Umiltá, C. (**1988**). ''Orienting of attention,'' in *Handbook of Neuropsychology*, edited by F. Boller and J. Grafman, Vol. 1, pp. 175–193.

In situ source level and source position estimates of biological transient signals produced by snapping shrimp in an underwater environment

Brian G. Ferguson[a] and Jane L. Cleary
Maritime Operations Division, Defence Science and Technology Organisation, P.O. Box 44, Pyrmont NSW 2009, Australia

(Received 26 February 2000; accepted for publication 13 November 2000)

Biological transient signals produced by snapping shrimp are sensed underwater by a wide aperture array. The instantaneous range and bearing of the source position of each snap is estimated along with a source level equal to the peak-to-peak amplitude of the pressure impulse generated by the snap at a standard distance of 1 m from its point of origin. For a sample of 1000 snaps recorded in Sydney Harbour, the distribution of peak-to-peak sound pressure levels has a mean value of 187 dB (*re* 1 μPa) and an interquartile range of 185–189 dB (*re* 1 μPa). Plotting the Cartesian coordinates of the source positions of the biological transient signals over a period of time maps the two-dimensional spatial distribution of the local snapping shrimp population. The principal habitat is found to be geocoincident with a 120-m-long wharf, the closest point of which is 60 m from the middle of the receiving array. The passive ranging performance of the wide aperture array is evaluated by generating mechanical transient signals at selected positions along the wharf. Precise estimates of the relative times-of-arrival of the acoustic wavefronts lead to source range and bearing estimates with standard deviations of only 0.1 m and 0.005 degrees (respectively), in agreement with theoretical predictions. [DOI: 10.1121/1.1339823]

PACS numbers: 43.80.Ka, 43.60.Gk [WA]

I. INTRODUCTION

High levels of ambient noise can affect the performance of high frequency sonar systems used by humans and marine mammals. Snapping shrimp are small crustaceans that produce high levels of ambient noise in those marine environments where the water is both warm (>11 °C) and shallow (<55 m deep).[1–5] A snapping shrimp has one enlarged claw[6] that produces a short acoustic transient signal when snapped closed.[7] The frequency response of the click is extremely wide-band with frequency components up to 200 kHz.[2–4] When snapping shrimp congregate, the superposition of their sound impulses leads to a sustained background noise resembling a distinctive sizzling or crackling sound. In temperate and tropical waters, the dominant source of biological noise in shallow bays, harbours and inlets is attributed to snapping shrimp.[1–5,7]

Previous observations of snapping shrimp sound ensembles have concentrated on measuring the autospectral density function of the biological noise and reporting the measurements as time-averaged noise spectra of spatially distributed impulsive sound sources.[2–4] Recently, sound pressure source level measurements of single snaps have been measured in a controlled environment by housing a single specimen in a small cage in a test tank.[7] The specimen was located at a standard distance of 1 m from a calibrated wide-band hydrophone.

However, an *in situ* measurement of the source level in open waters requires a reliable estimate of the range to the individual shrimp responsible for the snap so that the source level can be referenced to the standard distance. Knowledge of the source level is necessary for any modeling of the function of the sounds produced by snapping shrimp, since it determines the range at which the sounds have an effect. This is the case whether the sounds are used for stunning and killing prey,[8] or territorial defense.[9]

This article uses a passive ranging technique based on wavefront curvature to estimate both the range and bearing of the source of each snapping sound recorded during a high-frequency sonar experiment in Sydney Harbour, where *Alpheus euphrosyne richardsoni* and *Alpheus edwardsii* are the dominant snapping shrimp species.[6] The biological transient signals produced by snapping shrimp are sensed by a line array of three widely spaced hydrophones. Such a sensor configuration is commonly referred to as a wide aperture array because the sensor separation distance is considerably larger than the acoustic wavelengths that compose the received signal. Measuring the relative (or differential) times of arrival of the acoustic transient's wavefront at each pair of adjacent sensors enables the instantaneous range and bearing of the source position of the transient to be estimated. The source range, which is equal to the radius of curvature of the wavefront, is required to calculate the attenuation of the signal in traveling from the source to the middle sensor of the array. Once the attenuation is known, the source level can be estimated. In the present experiment, the source level represents the peak-to-peak amplitude of the pressure impulse generated by a snap at a standard distance of 1 m from its point of origin. This approach enables a comparison of the peak-to-peak source levels of individual snaps recorded in harbour waters with the peak-to-peak sound pressure levels

[a]Electronic mail: brian.ferguson@dsto.defence.gov.au

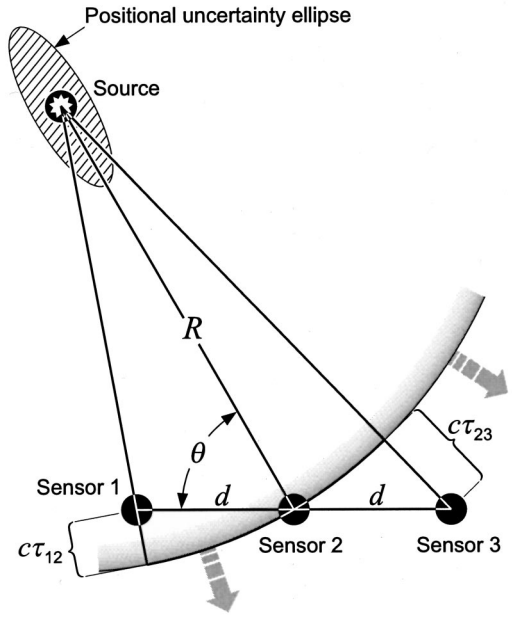

FIG. 1. Source-sensor geometry for passive ranging using wavefront curvature. The source is at a range R and bearing θ from the middle sensor of the array. The outputs of three widely separated but equally spaced collinear hydrophones are correlated to provide estimates of the signal delay times τ_{12} and τ_{23} from which the range and bearing estimates of the source position are calculated.

reported recently for snapping sounds from individual specimens recorded in a test tank.[7]

II. PASSIVE RANGING WITH A WIDE APERTURE ARRAY

A. Range and bearing estimation

The wavefront curvature passive ranging technique uses a linear array of three widely separated but equally spaced sensors to estimate the range and bearing of an acoustic source. The source-sensor array geometry is shown in Fig. 1. The range R and bearing θ are the polar coordinates of the source with the position of the middle sensor of the array coinciding with the origin. If d and c denote the intersensor spacing and the iso-speed of sound travel (respectively), then the range to the source from the middle sensor is given by[10]

$$R=\frac{2d^2-c^2(\tau_{12}^2+\tau_{23}^2)}{2c(\tau_{12}-\tau_{23})}, \tag{1}$$

where τ_{12} and τ_{23} are the time delays defined by the signal wavefront traversing the array. [Note that the (relative) time delay $\tau_{ij}=\tau_i-\tau_j$, where τ_i and τ_j are the absolute times-of-arrival of the wavefront at sensors i and j, respectively.] Also, the bearing of the source measured at the middle sensor with respect to the array axis is given by[10]

$$\theta=\cos^{-1}\left[\frac{c}{2d}(\tau_{12}+\tau_{23})+\frac{c^2}{4Rd}(\tau_{12}^2-\tau_{23}^2)\right]. \tag{2}$$

If the sound speed and sensor spacings are known, then the source range and bearing can be estimated by replacing the time delays τ_{12} and τ_{23} by their estimates in Eqs. (1) and (2).

B. Time delay estimation

The time delay is estimated by cross-correlating the outputs of a pair of sensors, $x_i(t)$ and $x_j(t)$, over an observation period of T. The cross-correlation function is given by

$$r_{ij}(\tau)=\int_{-T/2}^{T/2}x_i(t-\tau)x_j(t)dt. \tag{3}$$

If the acoustic source of interest emits a transient signal $s(t)$, and $n_i(t)$ and $n_j(t)$ represent uncorrelated additive zero-mean noise terms, then the outputs of the two sensors can be modeled as

$$x_i(t)=s(t)+n_i(t), \tag{4a}$$

$$x_j(t)=\alpha s(t-\tau_d)+n_j(t), \tag{4b}$$

where α is an attenuation factor and τ_d is the time delay between the two sensors. Substituting Eqs. (4a) and (4b) into Eq. (3) and assuming that the observation period is infinitely long ($T\to\infty$) so that the effect of noise is reduced to zero, then the cross-correlation function becomes

$$r_{ij}(\tau)=\alpha\int_{-\infty}^{\infty}s(t-\tau)s(t-\tau_d)dt=\alpha r_{ss}(\tau-\tau_d), \tag{5}$$

where $r_{ss}(\tau)$ is the autocorrelation function of $s(t)$ defined by

$$r_{ss}(\tau)=\int_{-\infty}^{\infty}s(t-\tau)s(t)dt. \tag{6}$$

Since $r_{ss}(\tau)\leqslant r_{ss}(0)$, it follows from Eq. (5) that $r_{ij}(\tau)$ attains its global maximum at $\tau=\tau_d$. Thus, the time lag value that maximizes $r_{ij}(\tau)$ is an estimate of the time delay τ_d.

C. Variances of range and bearing estimates

Using the far-field approximation (i.e., $R\geqslant 10d$), Eqs. (1) and (2) become

$$R\cong\frac{d^2\sin^2\theta}{c(\tau_{12}-\tau_{23})}, \tag{7}$$

$$\theta\cong\cos^{-1}\left[\frac{c}{2d}(\tau_{12}+\tau_{23})\right]. \tag{8}$$

The major source of error in estimating the range is the error in the time delay difference estimate, $(\tau_{12}-\tau_{23})$, in the denominator of Eq. (7). The variance of the range estimate, σ_R^2, is related to the variance of the time delay *difference* estimate, $\sigma^2_{\tau_{12}-\tau_{23}}$, by[11]

$$\sigma_R^2\cong c^2\left(\frac{R}{d\sin\theta}\right)^4\sigma^2_{\tau_{12}-\tau_{23}} \tag{9}$$

or, in terms of standard deviations,

$$\sigma_R\cong c\left(\frac{R}{d\sin\theta}\right)^2\sigma_{\tau_{12}-\tau_{23}}. \tag{10}$$

Similarly, the variance in the bearing estimate, σ_θ^2, is related to the variance of the time delay *sum* estimate, $\sigma^2_{\tau_{12}+\tau_{23}}$, by

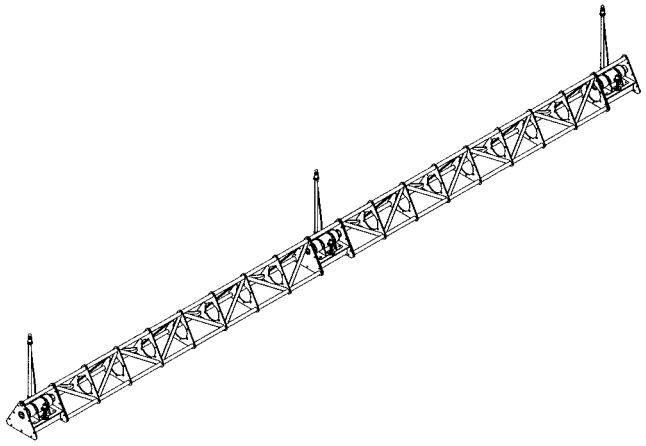

FIG. 2. Isometric drawing of the wide aperture array structure. The inter-element spacing of the three-hydrophone line array is 9.7 m with the sensors being 1.3 m above the sea floor.

$$\sigma_\theta^2 \cong \frac{c^2}{(2d\sin\theta)^2}\sigma^2_{\tau_{12}+\tau_{23}} \tag{11}$$

or, in terms of standard deviations

$$\sigma_\theta \cong \frac{c}{2d\sin\theta}\sigma_{\tau_{12}+\tau_{23}}, \tag{12}$$

where σ_θ is in radians.

Unlike the bearing error variance σ_θ^2 (which is independent of range), the range error variance σ_R^2 depends on the *fourth* power of the ratio of the source range to the half-length of the array's effective baseline ($d\sin\theta$). Figure 1 shows a range-bearing error ellipse depicting the uncertainty in localizing the source position using the wavefront curvature passive ranging method. In comparison with the range estimate, the bearing estimate is much less sensitive to time delay estimation errors especially when the source is far from the array. Hence, an ellipse bounds the area of uncertainty in the source position with the elongation of the major (range) axis with respect to the minor (bearing) axis reflecting the larger variance of the range estimates when compared with the variance of the bearing estimates. [Note that close agreement between theory and experiment for the variation of the range and bearing error variances with the effective half-length of the array ($d\sin\theta$) has been reported recently for broadband sources of continuous sound in air.[12]]

III. RANGE AND BEARING ESTIMATES OF MECHANICAL ACOUSTIC TRANSIENTS

A wide aperture array consisting of a line array of three calibrated hydrophones is deployed in Sydney Harbour, where high-frequency sonar experiments are conducted in very shallow water (<10 m deep). An additional (fourth) hydrophone is deployed in a direction that is broadside to the wide aperture array axis so as to resolve the left-right ambiguity problem common to line arrays. The operation of the system is controlled from the shore and the digital data acquisition system samples each sensor output at the rate of 1 million samples/s. Figure 2 is an isometric drawing of the wide aperture array where the intersensor separation distance

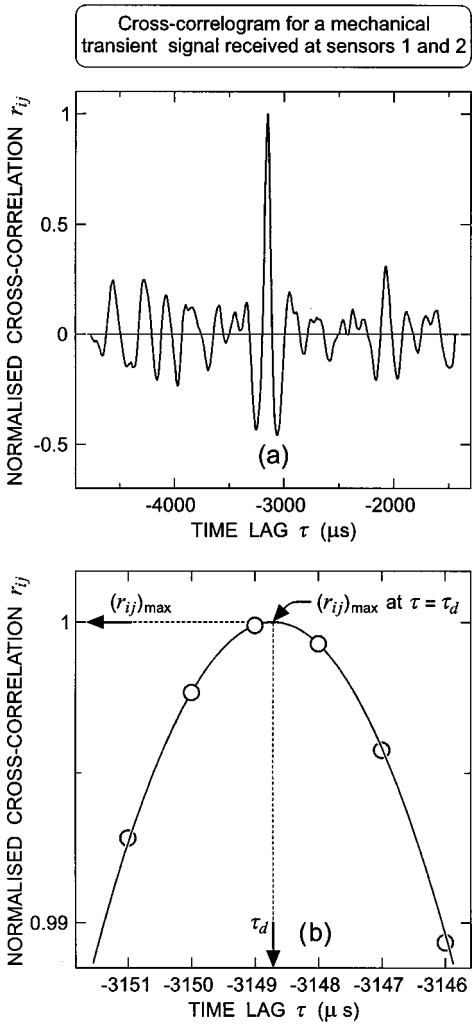

FIG. 3. (a) The cross-correlogram of a mechanical transient signal obtained by cross correlating the outputs of sensors 1 and 2 of the wide aperture array and (b) a zoom of the cross-correlogram in the neighborhood of the peak where the time delay estimate is refined by quadratic interpolation.

is 9.7 m. The sensors are 1.3 m above the sea floor, which is composed of sand. At the experimental site, the water depth is 6.1 m plus the height of the tide, which varies from 0.1 to 1.9 m. For the present experiment, the measured speed of sound propagation in the underwater medium is 1520 m/s.

The passive ranging performance of the system is tested by generating mechanical transient signals underwater from a known position and using the wide aperture array to localize the source. Striking a metal tube that is attached to a wharf produces the mechanical transient signal; the tube protrudes 0.3 m below the sea surface at high tide. Each adjacent pair of sensor outputs is cross-correlated and the relative times-of-arrival of the signal estimated as the acoustic wavefront traverses the array. The cross-correlation is implemented in the frequency domain using a rectangular frequency window between 1 and 100 kHz. Each time lag increment ($\delta\tau$) is equal to one sampling period, that is, 1 μs. Figure 3(a) shows a typical example of the cross-correlation function for a mechanical transient signal. Figure 3(b) is a zoom of the cross-correlogram peak in the neighborhood of its maximum. The time delay estimate is refined by (three-point) quadratic interpolation, which is equivalent to inverse

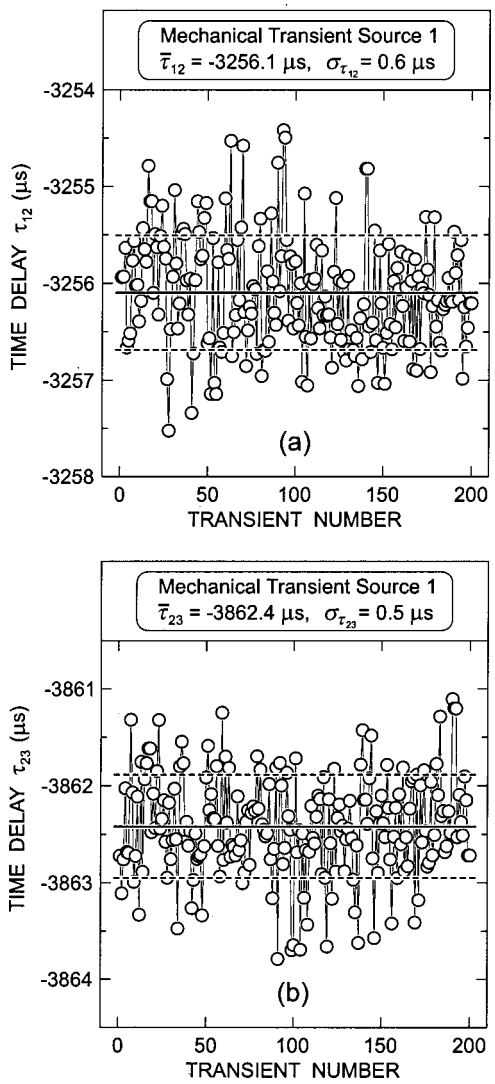

FIG. 4. Time delay estimates for a sequence of 200 mechanical transient signals generated at source position 1 (P1) using (a) sensors 1 and 2, and (b) sensors 2 and 3.

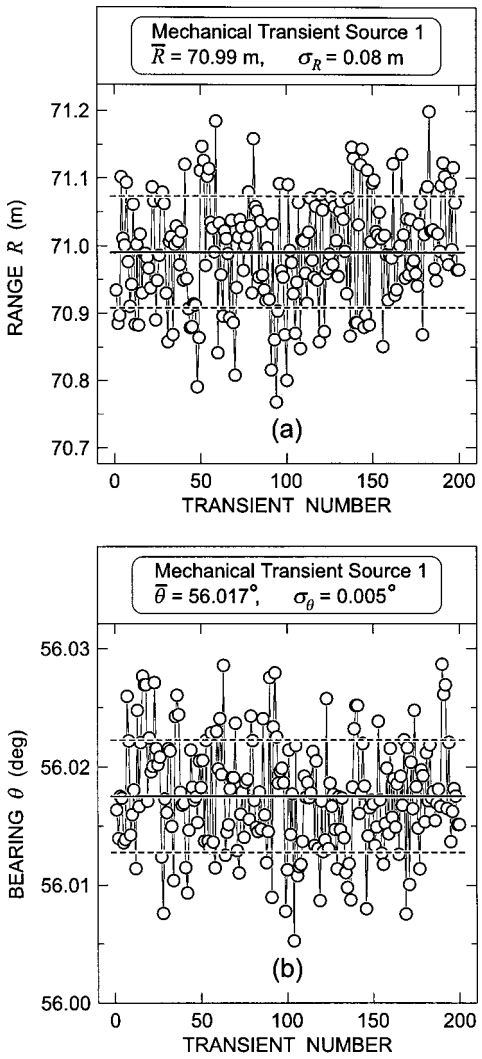

FIG. 5. (a) Range and (b) bearing estimates of the source position for the same sequence of 200 mechanical transient signals generated at source position 1 (P1).

parabolic interpolation. Refining the time delay estimate is a two-step process:[13]

Step 1—Determine the initial (coarse) estimate of the time delay, which is equal to the argument $(m\,\delta\tau)$ that maximizes the sequence $r_{ij}(k\,\delta\tau)$, $1 \leqslant k \leqslant K$.

Step 2—Calculate the refined (subsample) estimate (τ_d) which is given by

$$\tau_d = m\,\delta\tau - \frac{\delta\tau}{2}\,\frac{r_{ij}(m\,\delta\tau+\delta\tau)-r_{ij}(m\,\delta\tau-\delta\tau)}{r_{ij}(m\,\delta\tau+\delta\tau)-2r_{ij}(m\,\delta\tau)+r_{ij}(m\,\delta\tau-\delta\tau)}. \tag{13}$$

In Fig. 3(b), $m=-3149$, $\delta\tau=1$ μs and $\tau_d=-3148.7$ μs.

The time delay estimates for each pair of adjacent sensors are shown in Fig. 4 for a sequence of 200 mechanical transient signals generated at the first source position. The scatter in each sequence of time delay estimates is small (respective standard deviations of 0.6 and 0.5 μs), implying the signal-to-noise ratio is high and the bandwidth of the mechanical transient signal is wide. Simultaneous (refined) time delay estimates (one for each pair of adjacent sensors) are substituted for τ_{12} and τ_{23} in Eqs. (1) and (2) to calculate (respectively) the instantaneous range and bearing of the source. The range and bearing estimates of the source position are shown in Fig. 5 for the sequence of 200 mechanical transients. The high precision of the source localization method is reflected in the small scatter of the range and bearing estimates: the standard deviations of the range and bearing estimates are 0.08 m and 0.005 degrees, respectively. [Note that if the far-field approximation is invoked, then Eqs. (7) and (8) provide range and bearing estimates to within 0.2% of the values calculated using the exact Eqs. (1) and (2).]

The polar coordinates of each of the estimated source positions shown in Fig. 5 are transformed to Cartesian coordinates (with the middle sensor of the array as the origin) and the results presented in Fig. 6. The predicted range-bearing positional uncertainty ellipse is superimposed on the two-dimensional spatial distribution of the observed acoustic source positions. The ellipse has major and minor axes equal to $\pm 3\sigma_R$ and $\pm 3\sigma_\theta$, where σ_R and σ_θ are calculated using Eqs. (10) and (12).

Similar results are obtained for a longer sequence of

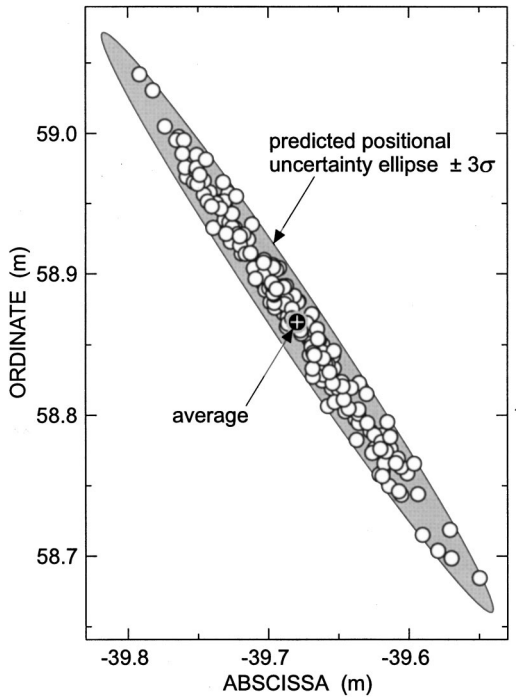

FIG. 6. The two-dimensional spatial distribution in Cartesian coordinates of the estimated source positions for the same 200 mechanical transient signals generated at source position 1 (P1). The range-bearing ellipse depicts the uncertainty in localizing the source position of the mechanical transient signals using the wavefront curvature passive ranging method.

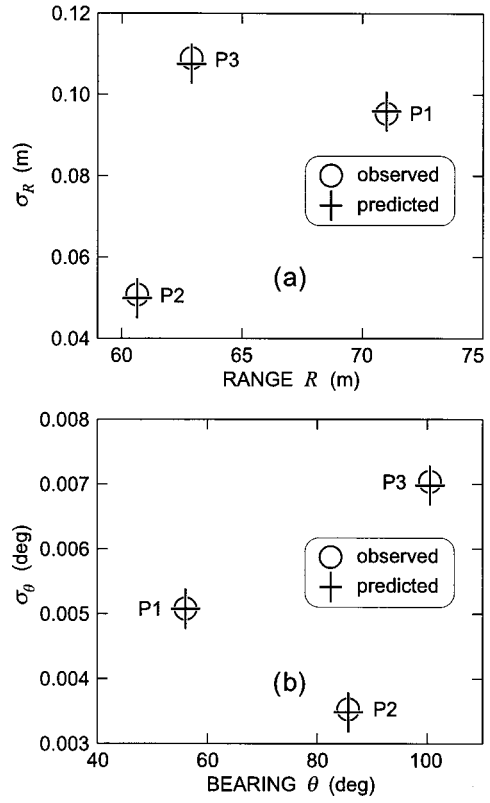

FIG. 7. Predicted and observed standard deviations in (a) range and (b) bearing for each of the three source positions (P1, P2, P3) of the mechanical transient signals.

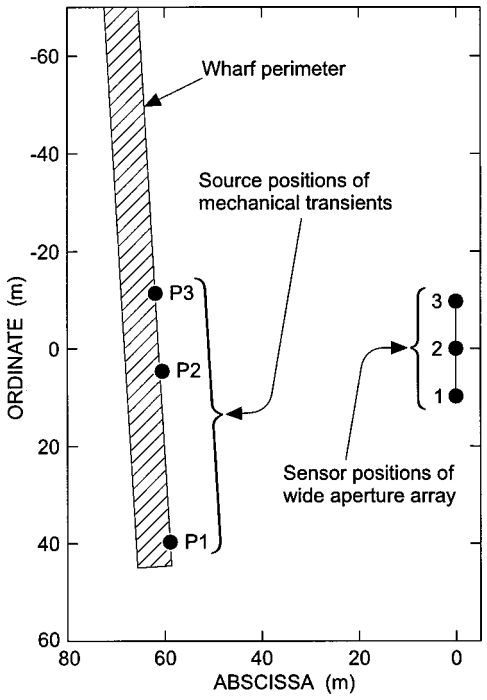

FIG. 8. Plan view of the sensor positions of the wide aperture array and the estimated positions of the three sources of mechanical transient signals distributed along a wharf.

(600) mechanical transients at the same position, and at two other positions along the wharf. The observed and predicted standard deviations in the range and bearing estimates are shown in Fig. 7 where the experimental results match the theoretical values calculated using Eqs. (10) and (12).

Figure 8 is a plan view of the sensor–source geometry showing the mean acoustic position estimates of the three sources (P1, P2, P3) of mechanical transient signals and the position of each of the sensors that comprise the wide aperture array. The origin coincides with the position of the middle sensor of the wide aperture array. The perimeter and hatched area of the rectangle represent the naval wharf along which the three mechanical transient source positions are distributed.

IV. RANGE AND BEARING ESTIMATES OF BIOLOGICAL ACOUSTIC TRANSIENTS

The acoustic sensor data for the biological transient signals produced by snapping shrimp are processed in the same way as the mechanical transient signals. Only single snaps, which are both free of multipath effects and occur in isolation in the 25-ms data window, are selected for processing. Figure 9 shows the source position estimates of 1000 biological transient signals together with the source position estimates of the mechanical transients and the position of the wharf. Most of the source positions of the snapping sounds are geocoincident with the position of the naval wharf. The two-dimensional distribution of the source positions of the biological transient signals delineates the extent of the wharf.

Figure 10 is a wireframe mesh showing the spatial density of the source position estimates of the 1000 biological transients over an area 100×100 m^2; each mesh cell is 1×1 m^2. The mesh height is proportional to the number of snaps

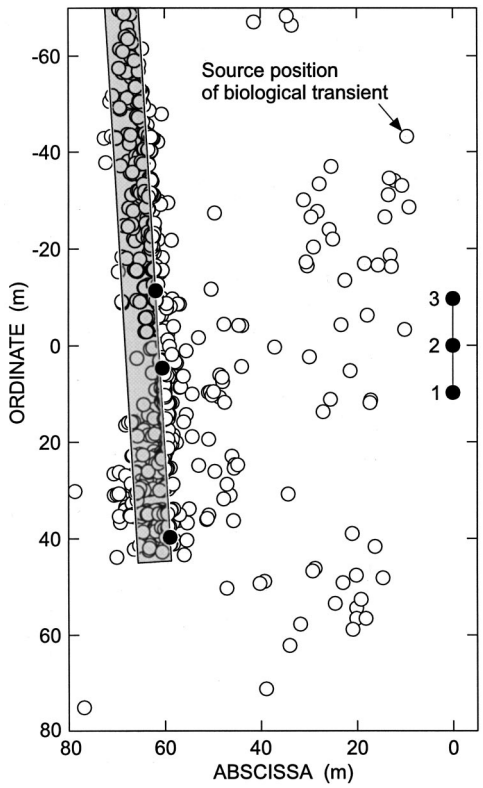

FIG. 9. Similar to Fig. 8 but with the inclusion of the estimated source positions of 1000 biological transient signals.

per unit area over the rectangular grid. The mesh plot confirms that the principal habitat of the local snapping shrimp population is the subsurface structure of the wharf, indicating that it is conducive to snapping shrimp habitation.

Although the passive ranging method is applied here to the localization of snapping shrimp transients, it has general application to the localization of other underwater biological transient signals. The duration of the experiment was of sufficient length to enable the extent of the habitat to be localized. A longer-term experiment could provide data on diurnal and seasonal variations in the spatial distribution of the snapping shrimp colony. Passive ranging is a nonintrusive method for monitoring the underwater acoustic environment and could be a useful tool for marine park management.

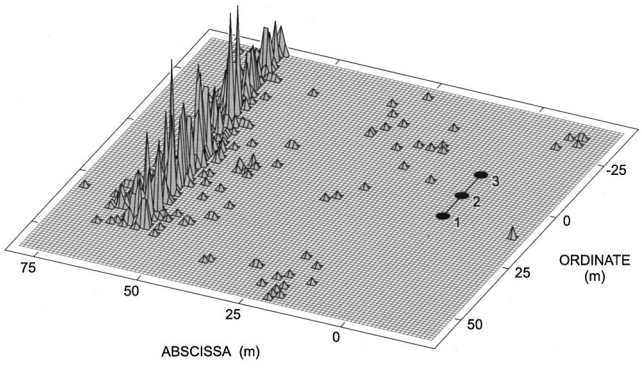

FIG. 10. Spatial distribution of the source position density of the biological transient signals. The positions of the three sensors that comprise the wide aperture array are also shown.

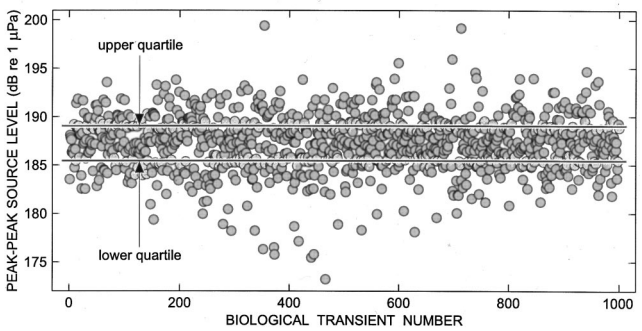

FIG. 11. Peak-to-peak source levels for 1000 biological transient signals.

V. SOURCE LEVEL ESTIMATES OF BIOLOGICAL TRANSIENTS

The peak-to-peak voltage level at the output of the middle receiver is converted to peak-to-peak source level using the calibrated receiving response of the middle hydrophone, the known gain of the receiving system and the spreading loss (calculated using the range estimate of the source.) For the present experiment, the absorption loss is ignored, as it is less than the system measurement uncertainty (± 1 dB). Figure 11 shows the peak-to-peak source levels for the 1000 snaps. The median value of the source level distribution is 187 dB (*re* 1 μPa) with the lower quartile [$\sim$185 dB (*re* 1 μPa)] and the upper quartile [$\sim$189 dB (*re* 1 μPa)] bounding the interquartile range, which includes half the source level estimates. This result for harbour waters is in agreement with the range of peak-to-peak source levels [183–190 dB (*re* 1 μPa)] reported for a tank experiment in which the source levels were averaged over ten snaps from each of the 40 snapping shrimp specimens.

VI. CONCLUSIONS

Passive ranging using a wide aperture array and the wavefront curvature method provides reliable range and bearing estimates of source positions of underwater acoustic transient signals. The observed standard deviations of the range and bearing estimates of the mechanical transient source positions match the values predicted by theory. Plotting the source positions of a long sequence of snapping sounds enables snapping shrimp habitats to be localized and mapped. The *in situ* peak-to-peak source level measurements of the snapping sounds recorded in harbour waters agree with those reported for a controlled experiment conducted in a test tank.

ACKNOWLEDGMENTS

The authors gratefully acknowledge the contributions of their colleagues—Doug Cato, Lionel Criswick, Chris Halliday, Kam Lo, Angus MacInnes, Bill Martin, Anthony Quach, Mark Readhead, John Shaw, Gary Speechley, Ross Susic, Neil Tavener and Ranjit Thuraisingham. The authors also appreciate the support and assistance provided during the experiment by the Royal Australian Navy's Clearance Diving Team One (HMAS Waterhen) and LCDR Sue Smith RAN (Executive Officer, HMAS Penguin). The Royal Australian Navy Missile Maintenance Establishment—ARMLO

expertly machined the mechanical subassemblies of the array structure. Shane Ahyong of the Marine Invertebrate Department of the Australian Museum provided information on the snapping shrimp species in Sydney Harbour.

[1] F. A. Everest, R. W. Young, and M. W. Johnson, ''Acoustical characteristics of noise produced by snapping shrimp,'' J. Acoust. Soc. Am. **20**, 137–142 (1948).
[2] D. Cato, ''The biological contribution to the ambient noise in water near Australia,'' Acoust. Australia **20**, 76–80 (1993).
[3] M. L. Readhead, ''Snapping shrimp noise near Gladstone, Queensland,'' J. Acoust. Soc. Am. **101**, 1718–1722 (1996).
[4] D. H. Cato and M. J. Bell, ''Ultrasonic ambient noise in Australian shallow waters at frequencies up to 200 kHz,'' MRL Technical Report MRL-TR-91-23 (1991).
[5] United States Navy Electronics Laboratory, ''Underwater noise caused by snapping shrimp,'' University of California Division of War Research publication no. U337, San Diego (1946), pp. 1–74.
[6] D. M. Banner and A. H. Banner, ''The alpheid shrimp of Australia. Part III: The remaining alpheids, principally the genus *Alpheus* and the family Ogyrididae,'' Records of the Australian Museum **34**, No. 1, 235–241, 270–274 (1982).
[7] W. L. Au and K. Banks, ''The acoustics of the snapping shrimp *Synalpheus parnoeomeris* in Kaneohe Bay,'' J. Acoust. Soc. Am. **103**, 41–47 (1998).
[8] M. Versluis, B. Schmitz, A. von der Heydt, and D. Lohse, ''How snapping shrimp snap: through cavitating bubbles,'' Science **289**, 2114–2117 (2000).
[9] B. A. Hazlett and H. E. Winn, ''Sound production and associated behaviour of Bermuda crustaceans (*Panulirus*, *Gonodactylus*, *Alpheus*, and *Synalpheus*),'' Crustaceana **4**, 25–38 (1962).
[10] J. C. Hassab, B. W. Guimond, and S. C. Nardone, ''Estimation of location and motion parameters of a moving source observed from a linear array,'' J. Acoust. Soc. Am. **70**, 1054–1061 (1981).
[11] W. R. Hahn, ''Passive ranging accuracies of an idealized sonar compared to theoretical bounds,'' U.S. Navy J. Underwater Acoust. **23**, 513–522 (1973).
[12] B. G. Ferguson, ''Variability in the passive ranging of acoustic sources in air using a wavefront curvature technique,'' J. Acoust. Soc. Am. **108**, 1535–1544 (2000).
[13] G. Jacovitti and G. Scarano, ''Discrete time techniques for time delay estimation,'' IEEE Trans. Signal Process. **SP-41**, 525–533 (1993).

Localization and visual verification of a complex minke whale vocalization[a)]

Jason Gedamke[b)]
Ocean Sciences Department, A316 Earth & Marine Sciences, University of California, Santa Cruz, California 95064

Daniel P. Costa
Biology Department, A316 Earth & Marine Sciences, University of California, Santa Cruz, California 95064

Andy Dunstan
UNDERSEA EXPLORER, P.O. Box 615, Port Douglas, Queensland 4871, Australia

(Received 10 September 2000; revised 7 March 2001; accepted 17 March 2001)

A recently described population of minke whales (*Balaenoptera acutorostrata*) offered a unique opportunity to study its acoustic behavior. The often-inquisitive dwarf minke whale is seen on the Great Barrier Reef nearly coincident with its suspected calving and breeding seasons. During drifting encounters with whales, a towed hydrophone array was used to record sounds for subsequent localization of sound sources. Shipboard and in-water observers linked these sounds to the closely circling minke whale. A complex and stereotyped sound sequence, the ''star-wars'' (SW) vocalization, was recorded during a series of visual and acoustic observations. The SW vocalization spanned a wide frequency range (50 Hz–9.4 kHz) and was composed of distinct and stereotypically repeated units with both amplitude and frequency-modulated components. Broadband source levels between 150 and 165 dB *re* 1 μPa at 1 m were calculated. Passive acoustic studies can utilize this distinct vocalization to help determine the behavior, distribution, and movements of this animal. While the SW vocalization's function remains unknown, the regularly repeated and complex sound sequence was common in low latitude, winter month aggregations of minke whales. At this early stage, the SW vocalization appears similar to the songs of other whale species and has characteristics consistent with those of reproductive advertisement displays.
 [DOI: 10.1121/1.1371763]

PACS numbers: 43.80.Ka, 43.30.Sf [WA]

I. INTRODUCTION

Marine mammals have developed intricate acoustic systems of communication utilizing the efficient sound propagating properties of the ocean. Baleen whales produce a wide range of sounds from simple tonal calls to harmonically rich frequency and amplitude modulated sounds, as well as clicks, pulses, knocks, and grunts (Clark, 1990). The identified acoustic repertoires of many whales, however, remain incomplete and the function or communicative value of most sounds is unknown. Common behaviors have emerged among species, though, including the production of a sequence of notes repeated in a predictable pattern, or song (Payne and Webb, 1971; Clark, 1990; Smith, 1991; Tyack, 1999). Humpback, bowhead, fin, and blue whales all produce stereotypical, patterned, and regularly repeated vocalizations of varying complexity that have been characterized as ''song'' (Payne and Webb, 1971; Ljunblad *et al.*, 1982; Watkins *et al.*, 1987; Helweg *et al.*, 1992; Clark and Ellison, in press). Humpback whale song is produced by males primarily on breeding grounds and is likely used as a reproductive advertisement display (Helweg *et al.*, 1992; Tyack, 1999). Preliminary evidence indicates that fin whale song may serve a similar reproductive purpose (Watkins *et al.*, 1987).

Due to the paucity of detailed observations of vocalizing whales (Clark, 1990; Edds-Walton, 1997; Tyack, 1999), the functional significance of sound has been difficult to assess for most species. Even simultaneous sighting and recording from minke whales (*Balaenoptera acutorostrata*) has proven challenging (Folkow and Blix, 1991; Edds-Walton, 2000; Mellinger *et al.*, 2000). Minke whales are difficult to sight. They produce small, inconspicuous blows that are easily missed even in calm conditions (Thompson *et al.*, 1979; Stewart and Leatherwood, 1985). They are typically pelagic and encountered in groups of one to two animals. There has been limited success in both high-latitude, spring/summer recordings of minke whales, where the animals feed, and low-latitude, winter month recordings, where the animals are believed to calve and breed (Horwood, 1990; Kasamatsu *et al.*, 1995; Boyd *et al.*, 1999).

Mid- to high-latitude recordings have yielded simple, short sounds. Vocalizations sweeping down in frequency (130–60 Hz) over 0.2–0.3 s have been described from minke whales in the Ross Sea, Antarctica (Schevill and Watkins, 1972; Leatherwood *et al.*, 1981). Similar sounds spanning a wider frequency range (396–42 Hz) have subsequently been

[a)]Portions of this work were presented in ''Minke whale acoustic behavior and remote tracking,'' 13th Biennial Conference on the Biology of Marine Mammals, Maui, Hawaii, November–December, 1999, and ''New vocalization definitively linked to the minke whale,'' 134th Meeting of the Acoustical Society of America, San Diego, CA, December, 1997.

[b)]Author to whom correspondence should be addressed; electronic mail: jgedamke@cats.ucsc.edu

reported as the almost exclusive (98% of 360) vocalization recorded from minke whales in the St. Lawrence Estuary (Edds-Walton, 2000). Short, mid-frequency clicks (3–12 kHz, 1–20 ms) were also recorded in the presence of one animal south of Newfoundland (Beamish and Mitchell, 1973), but it now appears that these sounds may have been produced by another unseen species (Tyack and Clark, 2000).

Only Winn and Perkins (1976) described sounds recorded in the presence of whales at low latitudes in winter months. Low-latitude, winter recordings are particularly important because of the likelihood of sound production associated with reproductive behavior. A mid-frequency ratchet (850 Hz, 1–6 ms) and clicks (3–12 kHz, 1–20 ms), and low-frequency (centered at or below 200 Hz) grunts (165–320 ms) and patterned thump trains (50–70 ms/thump, 2-3 thumps/s) were recorded in the West Indies (Winn and Perkins, 1976). Very similar thump or pulse trains have often been recorded in low-latitude, winter settings, but have not typically been associated with visual observations of minke whales (Folkow and Blix, 1991; Mellinger *et al.*, 2000). The pulse trains are loud, repetitive and patterned sequences (Mellinger *et al.*, 2000), and therefore share characteristics with the songs of fin, blue, humpback, and bowhead whales. Recent studies have called for further recordings from this animal (Edds-Walton, 2000), particularly from known congregations during the breeding season (Mellinger *et al.*, 2000).

A low-latitude, winter concentration of dwarf minke whales has recently been reported (Arnold, 1997). The dwarf or diminutive form of the minke whale is a slightly smaller form found widely throughout the Southern Hemisphere (Best, 1985; Arnold *et al.*, 1987; Zerbini *et al.*, 1996). Despite its Southern Hemisphere distribution, the dwarf minke whale is more similar genetically and morphologically to the Northern Hemisphere minke whale (*Balaenoptera acutorostrata*) than to the Southern Hemisphere form (*Balaenoptera bonaerensis*) (Best, 1985; Arnold *et al.*, 1987; Rice, 1999). In austral winter months, a concentration of dwarf minke whales occurs on the east coast of Australia and the Great Barrier Reef (GBR) (Arnold *et al.*, 1987). They are seen from May to September on the northern GBR, with nearly 80% of sightings occurring in June and July (Arnold, 1997). Dwarf minke whale occurrence in the area coincides with peaks in the Southern Hemisphere minke whale calving (May–June) (Boyd *et al.*, 1999) and breeding seasons (August–September) (Horwood, 1990; Kasamatsu *et al.*, 1995; Boyd *et al.*, 1999). Preliminary evidence indicates the dwarf form shares similar reproductive seasons (Birtles and Arnold, 2000). Increased sighting effort has resulted in greater reports of mother–calf pair sightings (Arnold and Birtles, 1999), but the extent of breeding or calving in this area remains unclear.

Whales in this GBR population are particularly inquisitive and actively seek out vessels. The curious nature of these whales nearly eliminated many common difficulties in positively linking an underwater sound with the species that produced it. They routinely circle a drifting or moored boat for hours. In this study, animals remained with the boat for up to 10 h, 45 min, consistently circling within 200 m. They often approached to within 1–5 m of the boat and skin divers, and sometimes remained in such close proximity for minutes (Fig. 1). During extended encounters, animals typically remained circling until the vessel motored away. This offered the unique opportunity to simultaneously observe and record animals at extremely close range for hours. Such unusual circumstances provided explicit associations between minke whale vocal activity and visual observations. Here, a complex and repetitive sound sequence produced by minke whales on the northern GBR is described.

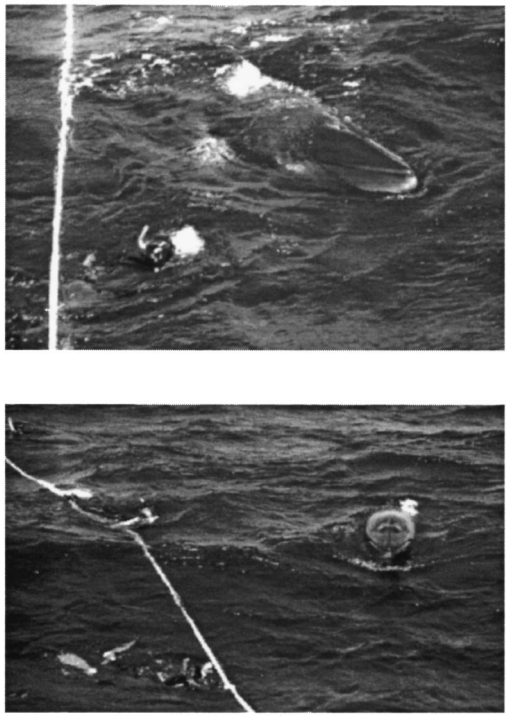

FIG. 1. Inquisitive whales approaching skin divers on observer lines.

II. METHODS

A. Recording

Research was conducted on the UNDERSEA EXPLORER, a 25-m research and ecotourism vessel, for 4–5 weeks each June–July of 1997–1999. Six-day trips were conducted in the back-reef waters (20–35 m depth) of the northern GBR, between approximately 14.5 and 17 °S. When minke whales were sighted, the vessel stopped and drifted with the wind abeam. In most cases, the whale(s) would approach the vessel and begin circling. Once animals were near, the engines were shut down and monitoring began from a single hydrophone. If vocalizations were heard, immediately, or after a behavioral control period, a hydrophone array was deployed.

The linear array consisted of four calibrated hydrophones (High Tech, Inc. SSQ-41b, Gulfport, MS, sensitivity -171 dBV *re* 1 V/μPa$\pm$2dB 10 Hz–32 kHz) spaced 50 m apart and suspended separately on 15 m of cable. A small sea anchor at the trailing end kept the array in a straight line extending from the drifting boat (Fig. 2). The array was marked with brightly colored floats every 10 m for simple and accurate determination of the array's orientation and a

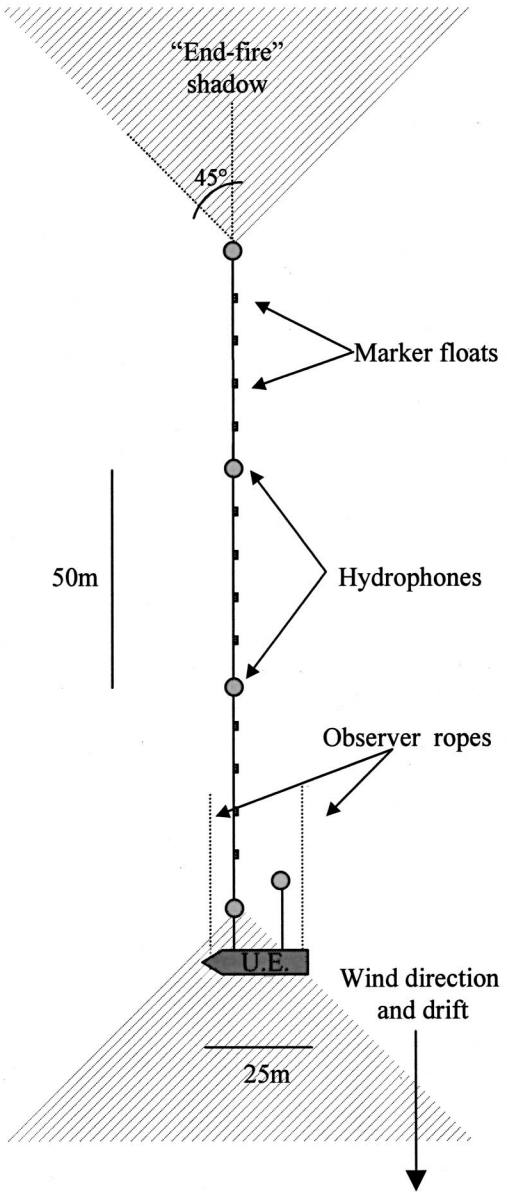

FIG. 2. View from above of the UNDERSEA EXPLORER (U.E.), the hydrophone array, and in-water observer ropes. Shipboard observations were made from the deck of the UNDERSEA EXPLORER. Up to 10 skin diving observers held ropes (5 per line) trailing the bow and stern. Marker floats spaced every 2.5–10 m were used to describe whale locations with X/Y coordinates. ''End-fire'' shadows (<45° from array axis) covered regions that were not used for location or source level data due to potentially increased range error.

whale's position relative to the boat and individual hydrophones. The 50 m of array nearest to the boat were additionally marked every 2.5–5 m for more accurate visual determination of whale positions. Using the colored floats, positions and behavior of whales were described with X/Y coordinates relative to hydrophones on the array. To resolve the left–right ambiguity of the linear array, a fifth hydrophone was laterally offset by 10–15 m and was used exclusively for this purpose.

The signals from the five hydrophones were amplified on a Spirit Protracker mixing deck (Soundcraft Electronics Ltd., Hertfordshire, UK) and recorded onto a Tascam DA-38 digital audio, 8-channel recording deck (48-kHz/channel sampling rate) (Teac Corp., Montebello, CA). A 100-Hz high-pass filter (12 dB/octave) was used on the mixing deck when needed to reduce flow noise. At least one track was always left unfiltered to inspect spectral energy below 100 Hz. A sixth audio track recorded observers' comments (i.e., number of whales, positions, behaviors, etc.) from the deck of the vessel. Calibration tones (500 Hz) of a known rms voltage were recorded onto each track to determine accurate received sound pressure levels.

When an encounter with whales began, two ropes were also trailed from the bow and stern for two to ten skin-diving observers. The ropes permitted underwater visual observations within the first 45–50 m of the array, in addition to shipboard observations of the entire area (Fig. 2). Water visibility was typically 15–25 m. Time-stamped underwater video was also recorded for the duration of the encounter from one or both of the observer ropes. The number and location of observers was noted.

B. Control recordings

Control recordings were made to ensure that the sounds were only associated with the presence of whales. On six occasions (including three from the recent 2000 field season), totaling 3.5 h, the vessel drifted in open water with no whales immediately present and the array deployed. On four of these occasions one or more skin divers were in the water with the observer lines deployed. Twice, observers were asked specifically to clang gear, pull on lines, or do anything that might reproduce sounds recorded in the presence of the whales. In addition, 8 h of recordings from 1-2 hydrophones were made while drifting in the same open waters from a small (7-m) diesel research vessel (Lizard Island Research Station, Lizard Island, Australia). Finally, 32 h from 1-2 hydrophones were either recorded or monitored by ear while the UNDERSEA EXPLORER was moored or anchored.

C. Analysis and localization

Acoustic recordings were analyzed in Canary 1.2 (Charif *et al.*, 1995). Spectral and temporal characteristics and received levels of sounds were determined. For individual vocalizations, hydrophone tracks were cross correlated to determine time of arrival differences. Two-dimensional locations of vocal animals were determined based on time-of-arrival differences using methods described in Clark and Ellison (2000). A three-dimensional array of similar dimensions (30 m between four hydrophones) was capable of localizing nearby sound sources to within 1 m (Watkins and Schevill, 1972). In this study, as the water depth in the back-reef of the GBR is shallow (20–35 m), depth of the sound source was assumed to have only a small effect on the accuracy of the two-dimensional location given. ''End-fire'' vocalizations produced beyond either end of the array and close to the array's linear axis were not used in analysis of location or source level data (Fig. 2). Sounds produced within 30° of the array's axis (<45° was conservatively chosen here) have inherently large range errors associated with small uncertainties in arrival times of the sound (Cummings and Holliday, 1987; Clark and Ellison, 2000).

Sound speed was calculated with temperature and salinity measurements made from the shallow and well-mixed GBR waters throughout the study. Positions of hydrophones were verified with a series of short, broadband calibration sounds produced at the end of the array by a skin diver hitting two metal wrenches together. Localization accuracy was also tested with calibration sounds produced at seven locations along the array.

During analysis, the localized position of a sound's source was compared with a sighted location of a whale from the recorded voice track or underwater video. A verified match between visual and acoustic locations was considered to have occurred if one or more whales were sighted within 15 s and 10 m of where the sound source was subsequently acoustically located.

D. Source levels

Broadband source levels (SLs) of sounds were calculated using methods described in Cummings and Holliday (1987), and Watkins and Schevill (1972). Multiple (up to 4 array hydrophones) received levels (RLs) of individual localized vocalizations were measured and plotted against range to determine an average transmission loss (TL) of $18\log(R)$ within 200 m of the source. Source levels were calculated using the measured received levels, a calculated source location, and average transmission loss (SL=RL+TL). Source levels of individual vocalizations were verified with comparative calculations from each of the array hydrophones. If a hydrophone was less than 15 m from where a sound was produced, it was not used for SL measurements because slight differences in range caused large changes in these calculated SLs.

III. RESULTS

A. Sounds recorded

During the three field seasons (1997–1999) 92 h were recorded during 49 encounters. Recordings were made while groups of 1 to at least 10 animals circled the vessel, totaling 150 or more animals. These are very conservative estimates of maximum group size and total number of animals based on the number of whales sighted simultaneously by underwater (generally within 20–30 m) or shipboard observers.

A particularly striking sound sequence was recorded often and described as the ''star-wars'' (SW) vocalization or sequence due to its unusual and synthetic-sounding characteristics (Fig. 3). The component units of the sequence (A, B, C) are composed of both amplitude-modulated (AM) and frequency-modulated (FM) sounds that can be discerned with the careful spectral and temporal analysis described by Watkins (1967). The individual units of the SW vocalization were produced in this stereotypical pattern (AAABC). The sequence, as a whole, was repeated over consistent intervals that ranged from 1–2 s to 3–4 min. To illustrate, during three bouts of vocalizations from one encounter, lasting 7 ($n=13$), 10 ($n=18$), and 8 ($n=15$) minutes, the mean interval between SW vocalizations was 32.0 ($\pm$1.6 s.d.), 33.2 ($\pm$1.7 s.d.), and 32.9 ($\pm$2.2 s.d.) s, respectively. The low standards of deviation for each bout illustrate the sequence's potentially rigid, patterned repetition.

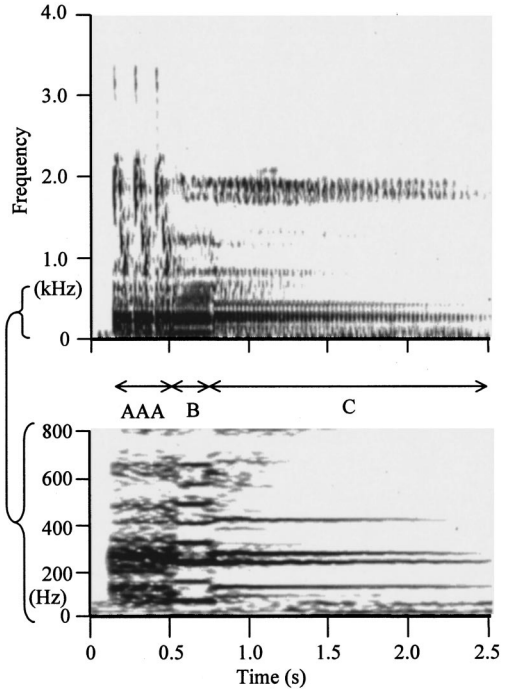

FIG. 3. Two-part spectrogram of the ''star-wars'' (SW) vocalization. The sound sequence is composed of discrete units (AAABC) that are repeated in this stereotypical pattern. *Top*: Spectrogram spans a wide frequency range (0–4 kHz) and has high temporal [frame length (fl)=21.3 ms] but low-frequency resolution [analysis bandwidth (ab)=190 Hz]. *Bottom*: Expanded view of the low-frequency portion (0–800 Hz) with low temporal (fl=128 ms), but higher frequency resolution (ab=31.7 Hz). The individual AM pulses of the A units are not easily discernible because of the low temporal resolution of this spectrogram. Note the evenly spaced harmonics of the 80-Hz tonal signal (unit B) and the characteristic spacing of ''harmonics'' around the 140-Hz tone (unit C) caused by amplitude modulation (Watkins, 1967).

The vocalization shown in Fig. 3 is typical of what was recorded in all three seasons. It began with three identical pulses of approximately 100-ms duration, with 20-ms pauses between pulses (AAA in Fig. 3). These pulses had sharp onsets and energy that sometimes extended from 50 Hz up to 9.4 kHz. Within each pulse, there was a multicomponent downward sweep of sound from 2.3 to 0.8 kHz. Harmonics of these sweeps comprised the energy that sometimes reached over 9 kHz. Simultaneously, there were three broad AM low-frequency pulses with peak energy at 250 Hz (50–750 Hz).

Following the three pulses, two different sounds began (B in Fig. 3). One, a broadband sound (range 1.65–1.95 kHz), was centered at 1.8 kHz and was amplitude modulated at approximately 22 pulses/s. The second sound was tonal (80 Hz fundamental, 240 ms duration) with a harmonic series (B, bottom of Fig. 3). At the beginning of C, this tonal sound shifted in frequency to a 140 Hz fundamental and simultaneously became amplitude modulated at a rate of 38 pulses/s. When this shift in frequency to 140 Hz occurred, the 1.8-kHz sound became more distinctly pulsed (at 22 pulses/s). Finer scale temporal analysis also showed additional pulsing of the 1.8-kHz sound at 140 pulses/s, indicat-

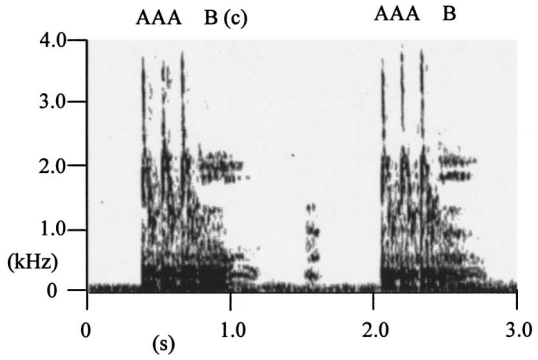

FIG. 4. Spectrogram (ab=174.9 Hz, fl=23.2 ms) of truncated SW vocalization showing a shortened or missing C unit. This pattern of pairs of vocalizations separated by a short ''grunt,'' was heard in numerous situations with rapid vocal activity.

ing possible modulation by the lower-frequency sound in unit C. Both the high- (1.8-kHz) and low- (140-Hz) frequency tails (C) lasted up to 2 s. These units were always repeated in the stereotypical AAABC pattern. Interestingly, during rapid rates of vocal activity the sound sequence was often truncated, with unit C shortened and occasionally completely absent (Fig. 4).

In addition to the vocalization described previously, other FM and AM sounds were also recorded during encounters but are beyond the scope of this paper. A commonly recorded sound is briefly mentioned, however, because it supports that these animals were indeed vocally active. This vocalization swept down in frequency (variable sweeps ranged from 250 to 50 Hz) over 0.2–0.3 s and was heard in at least 59% (29/49) of recorded encounters (Fig. 5). These sweeps are very similar to downward sweeps that have been recorded from both Northern and Southern Hemisphere minke whales (Schevill and Watkins, 1972; Leatherwood *et al.*, 1981; Edds-Walton, 2000).

B. Control recordings

During 3.5 h of control recordings from the drifting UNDERSEA EXPLORER, no sounds attributed to whales were heard or localized nearby. The ship and the divers did produce sounds that were readily identified and had distinct characteristics that could not be confused with the minke whale vocalizations. Notably, during four of the six control sessions, whales appeared at the boat and began circling within 15 min to 1 h—limiting the ability to conduct lengthy controls. Eight hours of recordings were also made while drifting in these waters from a small vessel and 32 h were recorded or monitored from the UNDERSEA EXPLORER while moored. Although the SW vocalization was heard in the distance (its distinct characteristics were easily recognizable over ambient noise), no vocalizations were ever received at levels that indicated the close presence of a vocalizing animal when no dwarf minke whales were present.

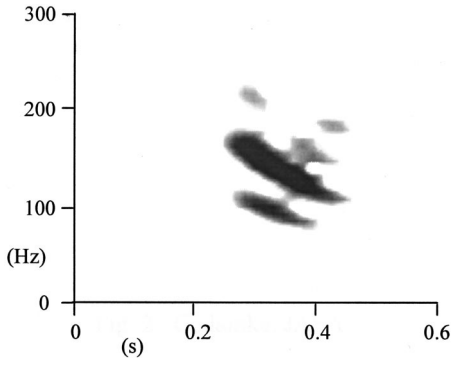

FIG. 5. Spectrogram of down-sweep (ab=31.7 Hz, fl=128 ms) filtered below 100 Hz.

C. Localization accuracy

Forty-seven calibration sounds from seven locations along the array were localized. Calculated positions of different sounds from the same location were generally consistent and clustered (±0.3–5.0 m s.d.). The acoustically calculated positions differed from visually observed locations by averages of 2.0–7.1 m at the different locations. The accuracy of calculated positions increased when sound sources were located small distances from the axis of the array. Five calibration locations were directly along the axis of the array ($X=0$) and had increased lateral (X coordinate) uncertainty and a higher mean displacement between acoustic and visual locations (4.8 m, ±2.80 m s.d.). The two locations at least 5–10 m from the axis of the array, and more indicative of the majority of vocalization locations, had a smaller mean displacement of 3.0 m and were more tightly clustered (±1.44 m s.d.).

D. Localization in detail: A vocal encounter

In one encounter, a group of up to at least 10 whales surrounded the vessel for over 5.5 h and a drift of 18 km. There were 3 h and 40 min of nearby (<200 m) and rapid SW vocalizations (averaging between 4 and 9/min). Two long pauses in vocalizations (22 and 44 min) occurred breaking the vocally active sections into 51-, 92-, and 77-min periods. During 110 min of analyzed vocal activity, 558 SW vocalizations were localized to within 200 m of the vessel (a conservative range over which sounds were assumed nearly equally localizable). The vessel drifted a distance of 5.4 km over this time.

Despite the long drift, 89% (498 of 558) of these vocalizations were localized to within 100 m of the center of the vessel, and 61% (341 of 558) were produced within 50-m range (Figs. 6 and 7). Only 11% were produced at more distant ranges of 100–200 m from the vessel. The ''end-fire'' shadows caused the large decrease in the number of vocalizations at less than 20-m range (Figs. 2, 6, and 7). Plotted sound source locations show that the behavior of the vocalizing animals was centered on the vessel for the period of nearly 2 h and vessel drift of 5.4 km. If the animal(s) producing the vocalizations was not associated with the vessel, a random distribution of ranges and a mean range of 100 m would be expected. A highly significant chi-square value for range categories unaffected by ''end-fire'' shadows ($20\,\text{m}<r<170\,\text{m}$) confirms the nonrandom distribution of vocalizations ($\chi^2=633.27$, df=29, $n=497$, $p<0.001$). A

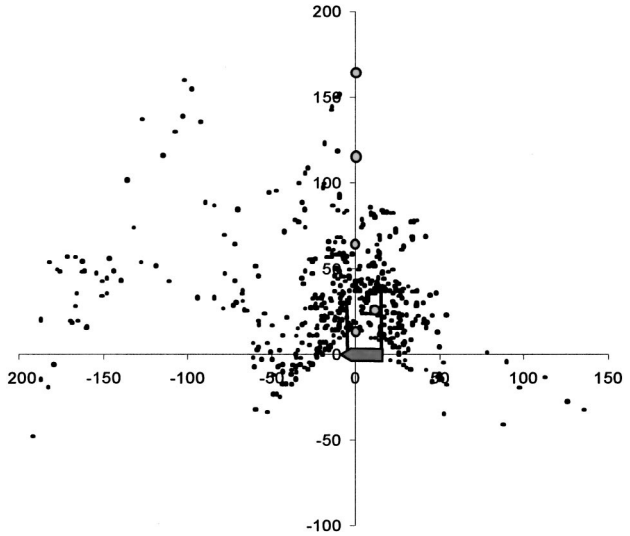

FIG. 6. View from above (as in Fig. 2 on a smaller scale) of all localizable SW source locations (plotted points, $n=558$) from 110 min of vocal activity showing the clustering around the vessel. This occurred over 5.4 km of drift. Values on X/Y axes are meters.

mean range of 55.3 and median of 42.6 m demonstrate the close association of the vocalizing animals with the boat.

Visual verification of minke whales as the source of the vocalizations occurred at ranges of 1–100 m. Throughout the entire encounter, including all vocal periods (totaling over 1500 SW vocalizations), minke whales were consistently located within 50–100 m of the boat, matching the distribution of the sound sources. No more than a few minutes passed between shipboard sightings, and even less time passed between in-water sightings (A. Birtles, private communication). Additionally, in 110 min of analyzed vocal activity, 132 vocalizations (23.7%) were produced within 10 m of underwater observer ropes. Water visibility ranged from 15 to 25 m. Underwater observers sighted only minke whales, with the brief exception of a shark. Finally, verified matches between shipboard sighted whale positions and acoustic locations (within 10 m and 15 s) occurred 42 times during 70 min of shipboard observations (Fig. 8).

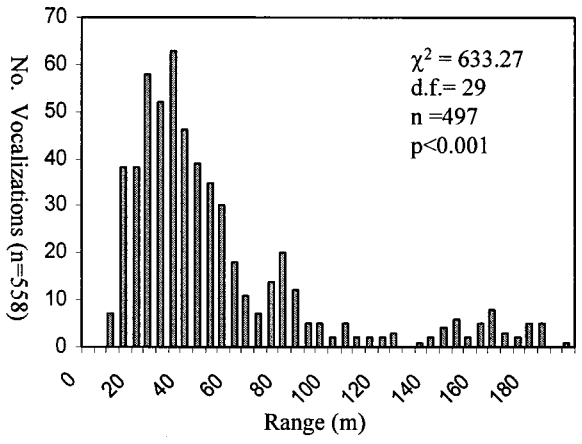

FIG. 7. Number of SW vocalizations ($n=558$) vs range from the vessel during 110 min of vocal activity. Eighty-nine percent (498/558) were produced within 100 m of the vessel and 52% (341/558) were produced within a 50-m range. The apparent drop in vocalizations below 20 m occurs because these fell predominantly in the ''end-fire'' shadow. Range categories affected by end-fire shadows ($20\text{ m}>r>170\text{ m}$) were therefore not used in the chi-square test.

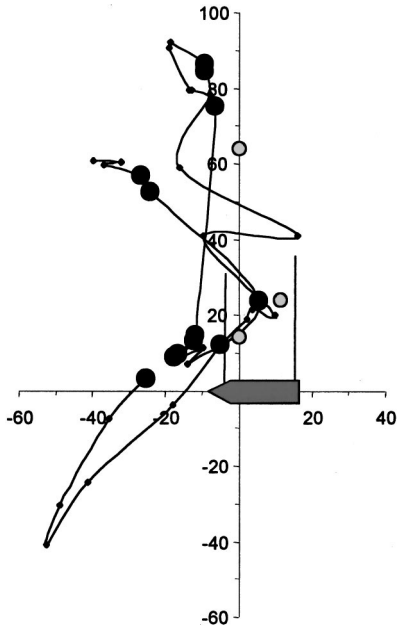

FIG. 8. View from above (as in Figs. 2 and 7—note larger scale so only half of the array is visible) of a 7-min track of successive sound source locations. Values on X/Y axes are meters. Small points represent acoustically calculated locations, while the larger dark circles indicate acoustic locations that matched observed whale locations within 10 m and 15 s.

During periods of high vocal activity (4–9 SW vocalizations/minute), an individual animal's vocalizations appeared distinguishable from others if the individuals were sufficiently separated in location. A single animal was assumed to be the source of nearby successive vocalizations when certain criteria were met: (1) No overlapping vocalizations were received at similar levels indicating two nearby vocalizing animals. (2) Vocalizations occurred in a consistent temporal pattern. (3) Successive vocalizations were received at similar levels. (4) Successive source locations indicated small, directed movements with no erratic location changes. In fact, with 4–9 vocalizations per minute, successive sound source locations were often spaced less than 10 m apart and near continuous tracks of individual vocalizing animals were obtained (Fig. 8).

When the successive sound source locations were plotted, clear circling patterns emerged. These were identical to the horizontal circling behavior of whales seen by visual observers. From shipboard observations and in-water video records, whales were reported in the same positions and moving in the same direction as indicated by the acoustic tracks (Fig. 8). Animals were also acoustically tracked for up to 30 min as they moved toward or away from the vessel (to distances greater than 500 m). Individual animals, therefore, appear to be the source of successive vocalizations and if repeated rapidly enough, allow relatively continuous tracking of two or more individual animals' movements.

E. Localization summary of three seasons

Over the three analyzed seasons, the SW vocalization was localized within 200 m of the vessel during 10 separate

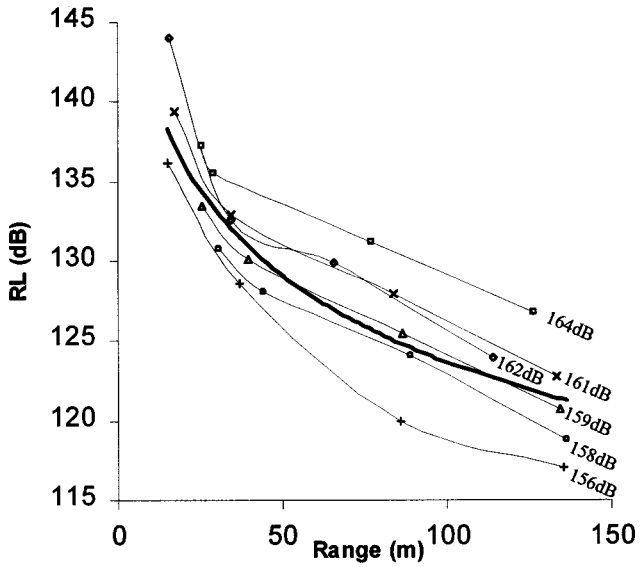

FIG. 9. Plot of range versus received level (RL) for six SW vocalizations (+, △, ○, ×, ◇, □). RLs from the four array hydrophones are plotted for each SW vocalization. Extrapolated source levels (dB *re* 1 μPa at 1 m) are indicated to the right of each vocalization. The bold superimposed line is a plot of the average transmission loss, 18 log(R) for a sound with a source level of 160 dB at 1 m. All dB values are *re* 1 μPa.

encounters. In 9 of these encounters, the sequence was additionally localized within 50 m of the freely drifting boat, illustrating the tendency of these animals to closely associate with the vessel. During all of these encounters the minke whale's close presence was visually verified and matched the distribution of sound source locations. Both sound source locations and whales were consistently less than 100 m from the boat as it drifted distances up to 18 km. On five occasions, a fast repetition rate permitted small-scale acoustic tracking of an individual vocalizing animal as it circled the drifting vessel. During all encounters, even nonvocal ones, only minke whales were seen circling. On four separate occasions, shipboard observations placed whales in the same positions (within 10 m) and times (within 15 s) as calculated sound source locations. Shipboard observations and the video record also provided consistent visual verification of whales when sound sources were acoustically tracked moving near or beneath the in-water observers.

F. Source levels

Using the average measured transmission loss (TL) of 18 log(R), source levels were calculated for 30 localized SW vocalizations from four encounters (Fig. 9). The broadband (100 Hz–10 kHz) received sound pressure levels of the three ''A'' units of the sequence (Fig. 3) and were measured either singly (~100-ms sample) or together (~360-ms sample). Received levels of analyzed sounds reached 145 dB *re* 1 μPa. Source levels between 150 and 165 dB *re* 1 μPa at 1 m were calculated. For comparison, broadband (100 Hz–10 kHz) source levels of 10 downsweeps (100- to 200-ms sample) were additionally calculated and ranged from 148 to 160 dB *re* 1 μPa at 1 m.

IV. DISCUSSION

A. The vocalization and its source

Through three field seasons, the most striking sound recorded was the ''star-wars'' (SW) vocalization. The SW vocalization is complex, finely structured, and sounds almost synthetic, metallic, or mechanical. Its distinct units (A, B, C) contain multiple components that span a wide frequency range and are intricately frequency and amplitude modulated. These units are produced in a stereotypical sequence that is loud and regularly repeated.

The vocalization's acoustic characteristics are unusual for a baleen whale, and similar sounds have not been reported from other *Balaenoptera spp*. (fin, blue, minke, sei, and Bryde's whales). Fin whale sounds are well documented and are typically short (about 1 s), very low frequency to infrasonic (10–150 Hz), and tonal or FM in structure (Watkins *et al.*, 1987; Thompson *et al.*, 1992). Blue whales produce simple FM or AM (3.85–7.7 pulses/s) sounds in a similar frequency range (12.5–200 Hz) that last up to 36 s (Cummings and Thompson, 1971; Thompson *et al.*, 1996). Sei and Bryde's whales have both been recorded very infrequently. Sounds recorded from sei whales consist of a series of ''metallic sounding'' FM sweeps lasting 0.5–0.8 s in the 1.5- to 3.5-kHz range (Thompson *et al.*, 1979; Richardson *et al.*, 1995). FM tonal moans (70–245 Hz, averaging 0.4 s) (Cummings *et al.*, 1986) and pulsed FM and AM sounds (primarily 100–500 Hz with 50–160 pulses/s) (Edds *et al.*, 1993) have been recorded from Bryde's whales.

The majority of these *Balaenoptera spp*. sounds are simple calls, defined as low-frequency, narrow-band FM signals (Clark, 1990). Complex calls are typically broadband (bandwidths in the 500- to 5000-Hz range), pulsive signals with variable mixtures of amplitude and frequency modulation. They have generally been recorded from bowhead, humpback, and right whales (Clark, 1990), but there is a report of complex pulsed sounds from surface-active Bryde's whales (Edds *et al.*, 1993; Edds-Walton, 1997). The SW vocalization is another complex vocalization from a member of the genus *Balaenoptera*. Unlike the Bryde's whale sounds, this vocalization is a patterned sequence that appears to be a consistent and stereotypical part of the dwarf minke whale's vocal repertoire.

The vocalization's complexity is due in part to the simultaneous production of two harmonically unrelated sounds. The separate 80-Hz tonal sound and AM (22 pulses/s) 1.8-kHz centered sound can be seen in Fig. 3, unit B. Their simultaneous presence implies that the whale may have two sound producing mechanisms, as has been suggested in bowhead whales (Wursig and Clark, 1993; Clark, 1990). Passerine birds can produce two simultaneous, unrelated sounds with their double syrinx (Catchpole and Slater, 1995) but the sound production mechanism in baleen whales remains poorly understood. Notably, in unit C (Fig. 3), the separate high- (1.8 kHz, 22 pulses/s) and low- (140 Hz, 38 pulses/s) frequency components show a potential coupling through the 1.8-kHz sound's additional pulsing at 140 pulses/s. The complex nature of this vocalization raises fur-

ther questions about the sound production mechanism in baleen whales.

Due to the complex nature of the SW vocalization, recordings were analyzed from three seasons, and extensive measures were taken to verify that the minke whale was the source of this sound sequence. Dwarf minke whales were exclusively identified as the source by the acoustic location and visual verification evidence collected in this study. The vocalizing animals consistently centered their behavior around the vessel during encounters where drifts of over 18 km occurred. Acoustic movement tracks were identical to the observed whales' circling behavior. Vocalizations were repeatedly localized to within meters of the boat and in-water observers for hours. Only minke whales were sighted. Shipboard observations repeatedly verified whales in positions less than 10 m from sound source locations during four separate encounters. In addition, the SW vocalization and the low-frequency downsweep, a previously reported minke whale sound, were produced at similar source levels between 148 and 165 dB *re* 1 μPa. Finally, the vocalization has been recorded spanning a wide range of latitudes during times when minke whales have been observed in these areas (see the following). The evidence points solely toward the minke whale as the source of this vocalization.

B. Distribution of vocalization: Known and potential

While its source was previously unknown, the SW vocalization has been recorded in June/July off Stradbroke Island (27.5 °S, Queensland) (Cato, private communication) and Coff's Harbor (30 °S, New South Wales) (Gill and Eyre, private communication). These locations are approximately 1700 km south of our research site on the east Australian coast. The dwarf minke whale has been sighted from Victoria to northern Queensland in winter months (Arnold *et al.*, 1987), over approximately the same range and seasons that the SW vocalization has been recorded. Broader use of passive acoustic study, therefore, appears promising to assess spatial and temporal distribution of dwarf minke whales.

While the SW vocalization has not yet been reported from anywhere other than the east Australian coast, dwarf minke whales have been sighted off Brazil, New Zealand, S. Africa, and in the Indian Ocean (Best, 1985; Arnold *et al.*, 1987; Zerbini *et al.*, 1996). To date, there have not been reported efforts to study the sounds of other populations of dwarf minke whales, but it would be useful to know if the SW vocalization is produced elsewhere. Previous reports of Southern Hemisphere minke whale sounds have not included the SW vocalization or any similar sounds (Schevill and Watkins, 1972; Leatherwood *et al.*, 1981). Both of these reports, however, describe Antarctic minke whales (*Balaenoptera bonaerensis*), and were recorded at high latitudes in summer months. The SW sequence is also very different from the repetitive, patterned thump trains recorded in the winter, low-latitude Atlantic (Mellinger *et al.*, 2000). The differences in sounds recorded could be due to either behavioral/contextual or taxonomic factors. The vocalization's absence from previous reports could also be due to the limited nature of recordings that have been made from most populations of minke whale (e.g., little is known about Northern Pacific minke whale sounds).

Interestingly, a similar sound with an unknown source has been recorded in the north Pacific since the late 1950s. The ''boing'' sounds mechanically produced with strong-pulsed modulation (Wenz, 1964; Thompson *et al.*, 1979). It consists of a pulse of sound centered at 1.4 kHz and is followed by a long AM 1.4-kHz tail (up to 4.5 s) that is pulsed at a rate of 115 pulses/s (Thompson and Friedl, 1982). The fundamental component (115 Hz) of the modulation frequency is sometimes prominent. The boing is regularly repeated (8 s–6 min intervals) and was estimated to be produced at source levels of over 150 dB *re* 1 μPa. These characteristics and its winter occurrence in Hawaiian waters have led to speculation that the source may be a whale (Wenz, 1964; Thompson and Friedl, 1982; Thompson *et al.*, 1979). While minke whale sightings are rare in Hawaiian waters (Horwood, 1990), the boing exhibits many similarities to the SW vocalization. Considering the dwarf minke whale's closer evolutionary relationship to the Northern Hemisphere minke whale (*Balaenoptera acutorostrata*) than the Southern Hemisphere form (*Balaenoptera bonaerensis*) (Arnold *et al.*, 1987; Rice, 1999), and the absence of reports of minke thump trains in the Pacific Ocean, the potential link between these sounds is intriguing.

C. Conclusions

The evidence presented in this paper establishes the dwarf minke whale as the source of the SW vocalization. The sound sequence's unique characteristics can now be utilized for passive acoustic study of this animal. The repetitive and pulsed nature of the SW vocalization is ideal for localization and tracking study. While small-scale tracking (hundreds of meters) has been conducted in this study, the loud source levels and the presence of distant SW vocalizations indicate the feasibility of larger-scale (km s) acoustic tracking. Large-scale hydrophone arrays could be used to determine how vocalizing whales are behaving toward each other over long distances. Passive acoustics could also be used in conjunction with visual surveys to determine seasonal and spatial distribution, and movement patterns of individuals and populations of dwarf minke whales. Acoustic study could also help assess the conflicting biases to boat-based surveys posed by these curious, but typically difficult to sight whales.

The SW vocalization is stereotypically patterned and regularly repeated (AAABC, AAABC, AAABC), similar to the varied ''songs'' of humpback, bowhead, fin, and blue whales (Payne and Webb, 1971; Ljungblad *et al.*, 1982; Watkins *et al.*, 1987; Helweg *et al.*, 1992; Clark and Ellison, in press). Since a nearly identical SW vocalization was recorded within and through all three seasons, it appears to have the relatively low variability of other *Balaenoptera spp.* (fin and blue whale) songs, as opposed to the more fluid and changing songs of humpback and bowhead whales. Humpback, fin, and blue whale song have been recorded during the breeding season, often in low latitudes (Watkins *et al.*, 1987; Helweg *et al.*, 1992; Clark and Charif, 1998; Stafford *et al.*, 1999). While the breeding ground acoustic behavior of bow-

head whales is unstudied, it is also suspected to be acoustically rich based on the song heard during migration (Clark and Johnson, 1984; Wursig and Clark, 1993). Watkins *et al.* (1987) suggested fin whale song was a possible reproductive display produced by males based on a direct correlation of sounds with the breeding season, but this role has not been confirmed. The reproductive advertisement role of humpback whale song is, however, supported by years of study. It is complex, regularly repeated, and produced by males primarily during the breeding season (Tyack, 1999). Studies of spacing between animals have revealed a likely role mediating male–male interactions, and while there is a lack of direct evidence, the elaborate nature of the song is indicative of a potential role mediating female choice (Tyack, 1981; Helweg *et al.*, 1992; Frankel *et al.*, 1995; Tyack, 1999).

At this stage, any statement about the function of the SW vocalization is purely speculative. The sex, size, and behavior of the vocalizing whales are unknown. The acoustic behavior of the dwarf minke whale outside this time of year is also unknown. The SW sequence, however, was the most distinct and complex vocalization recorded in this study. It was produced repeatedly and regularly during the breeding and calving seasons in low-latitude concentrations of this animal. The dwarf minke whale's ''star-wars'' vocalization has the repetitive and stereotypical traits of songs produced by other whales. Its complexity and presence during the breeding season are also consistent with qualities expected in reproductive advertisement displays. Further study of this animal's acoustic behavior will help elucidate the functional role of SW vocalization and assess it in the broader context of the dwarf minke wale's system of communication.

ACKNOWLEDGMENTS

This study was made possible by the research and ecotourism vessel UNDERSEA EXPLORER. Funding was provided by the Office of Naval Research Grant Nos. N00014-98-1-2859 and N00014-97-1-1005, and National Geographic Committee for Research and Exploration Grant Nos. 6323-98 and 6864-00 to Dan Costa and Jason Gedamke. Supplemental support was provided by the American Cetacean Society, the David Gaines Award, the UCSC Department of Ocean Sciences, a Lizard Island Research Station Augmentative Grant, and an NDSEG fellowship to J. G. We are especially grateful to Dr. Peter Arnold and Dr. Alastair Birtles for the collaborative research team we have formed with the UNDERSEA EXPLORER, and for allowing us to work under their research permits (Environment Australia research Permit Nos. P1996/043, P1997/049, P1998/055, P1999/02 to Peter Arnold). Thanks to Sean Hayes and Dave Mellinger for continued logistical, practical, and analytical support. We thank Dave Mellinger and Bill Watkins for their help with initial analyses of the SW vocalization. Chris Clark, Doug Cato, Mark McDonald, and Adam Frankel provided excellent advice. Burney Tershy, Chris Clark, Don Croll, Peggy Edds-Walton, Peter Arnold, and Mark McDonald provided excellent comments on various versions of the manuscript. We also wish to thank: the Rumneys, Monique Matthews, Bob Gisiner, Peter Gill, Elizabeth Eyre, Jay Barlow, John Hildebrand, Bill Cummings, and all the crew and passengers of the UNDERSEA EXPLORER for their help, advice, and support.

Arnold, P. W. (**1997**). ''Occurrence of dwarf minke whales (*Balaenoptera acutorostrata*) on the northern Great Barrier Reef, Australia,'' Rep. Int. Whal. Comm. **47**, 419–424.

Arnold, P. W., and Birtles, R. A. (**1999**). ''Towards sustainable management of the developing dwarf minke whale tourism industry in northern Queensland,'' CRC Reef Research Centre Technical Report No. 27, CRC Reef Research Centre, Townsville, Queensland, 30 pp.

Arnold, P. W., Marsh, H., and Heinshon, G. (**1987**). ''The occurrence of two forms of minke whales in east Australian waters with a description of external characters and skeleton of the diminutive or dwarf form,'' Sci. Rep. Whales Res. Inst. **38**, 1–46.

Beamish, P., and Mitchell, E. (**1973**). ''Short pulse length audio frequency sounds recorded in the presence of a minke whale (*Balaenoptera acutorostrata*),'' Deep-Sea Res. Oceanogr. Abstr. **20**, 375–386.

Best, P. B. (**1985**). ''External characters of southern minke whales and the existence of a diminutive form,'' Sci. Rep. Whales Res. Inst. **36**, 1–33.

Birtles, A. (private communication).

Birtles, R. A., and Arnold, P. W. (**2000**). ''Commercial swim program with dwarf minke whales, *Balaenoptera acutorostrata sensu lato* on the northern Great Barrier Reef, Australia: A case study,'' paper SC/52/WW13 presented to the IWC Scientific Committee, June 2000 (unpublished), 11 pp.

Boyd, I. L., Lockyer, C. L., and Marsh, H. D. (**1999**). ''Reproduction in marine mammals,'' in *The Biology of Marine Mammals*, edited by J. E. Reynolds III and S. A. Rommel (Smithsonian Institution Press, Washington, DC), pp. 218–286.

Catchpole, C. K., and Slater, P. J. B. (**1995**). *Bird Song, Biological Themes and Variations* (Cambridge University Press, New York), Chap. 2, pp. 21–28.

Cato, D. (private communication).

Chariff, R. A., Mitchell, S., and Clark, C. W. (**1995**). *Canary 1.2 User's Manual* (Cornell Laboratory of Ornithology, Ithaca, NY), p. 229.

Clark, C. W. (**1990**). ''Acoustic behavior of mysticete whales,'' in *Sensory Abilities of Cetaceans*, edited by J. A. Thomas and R. A. Kastelein (Plenum, New York), pp. 571–583.

Clark, C. W., and Charif, R. A. (**1998**). ''Acoustic monitoring of large whales to the west of Britain and Ireland using bottom-mounted hydrophone arrays, October 1996–September 1997,'' Joint Nature Conservation Committee Report No. 281.

Clark, C. W., and Ellison, W. T. (**2000**). ''Calibration and comparison of the acoustic location methods used during the spring migration of the bowhead whale *(Balaena mysticetus)*, off Pt. Barrow, Alaska, 1984–1993,'' J. Acoust. Soc. Am. **107**, 3509–3517.

Clark, C. W., and Ellison, W. T. (**in press**). ''Potential use of low-frequency sounds by baleen whales for probing the environment: Evidence from models and empirical measurements,'' in *Advances in the Study of Echolocation in Bats and Dolphins*, edited by J. A. Thomas and R. A. Kastelein (Plenum, New York).

Clark, C. W., and Johnson, J. H. (**1984**). ''The sounds of the bowhead whale, *Balaena mysticetus*, during the spring migrations of 1979 and 1980,'' Can. J. Zool. **62**, 1436–1441.

Cummings, W. C., and Holliday, D. V. (**1987**). ''Sounds and source levels from bowhead whales off Pt. Barrow, Alaska,'' J. Acoust. Soc. Am. **82**, 814–821.

Cummings, W. C., and Thompson, P. O. (**1971**). ''Underwater sounds from the blue whale, *Balaenoptera musculus*,'' J. Acoust. Soc. Am. **50**, 1193–1198.

Cummings, W. C., Thompson, P. O., and Ha, S. J. (**1986**). ''Sounds from Bryde, *Balaenoptera edeni*, and finback, *Balaenoptera physalus*, whales in the Gulf of California [Mexico],'' U.S. National Marine Fisheries Service Fishery Bulletin **84**, 359–370.

Edds, P. L., Odell, D. K., and Tershy, B. R. (**1993**). ''Vocalizations of a captive juvenile and free-ranging adult-calf pairs of Bryde's whales, *Balaenoptera edeni*,'' Mar. Mammal Sci. **9**, 269–284.

Edds-Walton, P. L. (**1997**). ''Acoustic communication signals of mysticete whales,'' Bioacoustics **8**, 47–60.

Edds-Walton, P. L. (**2000**). ''Vocalizations of minke whales (*Balaenoptera acutorostrata*) in the St. Lawrence Estuary,'' Bioacoustics **11**, 31–50.

Folkow, L. P., and Blix, A. S. (**1991**). ''Norwegian whale sighting and acoustic surveys in the Atlantic Ocean during the winter of 1989/90,'' Rep. Int. Whal. Commn. **41**, 531–538.
Frankel, A. S., Clark, C. W., Herman, L. M., and Gabriele, C. M. (**1995**). ''Spatial distribution, habitat utilization, and social interactions of humpback whales, *Megaptera noveangliae*, off Hawaii, determined using acoustic and visual techniques,'' Can. J. Zool. **73**, 1134–1146.
Gill, P. C., and Eyre, E. (private communication).
Helweg, D. A., Frankel, A. S., Mobley, J. R., and Herman, L. M. (**1992**). ''Humpback whale song: Our current understanding,'' in *Marine Mammal Sensory Systems*, edited by J. A. Thomas, R. A. Kastelein, and A. Ya. Supin (Plenum, New York), pp. 459–483.
Horwood, J. (**1990**). *Biology and Exploitation of the Minke Whale* (CRC Press, Boca Raton, FL), pp. 21–59.
Kasamatsu, F., Nishiwaki, S., and Ishikawa, H. (**1995**). ''Breeding areas and southbound migrations of southern minke whales (*Balaenoptera acutorostrata*),'' Mar. Ecol.: Prog. Ser. **119**, 1–10.
Leatherwood, S., Thomas, J. A., and Awbrey, F. T. (**1981**). ''Minke whales off northwestern Ross Island,'' Antarctic J. **16**, 154–156.
Ljungblad, D. K., Thompson, P. O., and Moore, S. E. (**1982**). ''Underwater sounds recorded from migrating bowhead whales, *Balaena mysticetus*, in 1979,'' J. Acoust. Soc. Am. **71**, 477–482.
Mellinger, D. K., Carson, C. D., and Clark, C. W. (**2000**). ''Characteristics of minke whale (*Balaenoptera acutorostrata*) pulse trains recorded near Puerto Rico,'' Marine Mammal Sci. **16**, 739–756.
Payne, R. S., and Webb, D. (**1971**). ''Orientation by means of long range acoustic signaling in baleen whales,'' Ann. N.Y. Acad. Sci. **188**, 110–141.
Rice, D. W. (**1999**). *Marine Mammals of the World. Systematics and Distribution*, Special Publication Number 4 of the Society for Marine Mammalogy (Allen Press, Lawrence), pp. 69–71.
Richardson, W. J., Greene, C. R., Jr., Malme, C. I., and Thomson, D. H. (**1995**). *Marine Mammals and Noise* (Academic, San Diego), pp. 159–204.
Schevill, W. E., and Watkins, W. A. (**1972**). ''Intense low-frequency sounds from an Antarctic minke whale (*Balaenoptera acutorostrata*),'' Breviora **388**, 1–8.
Smith, W. J. (**1991**). ''Singing is based on two markedly different kinds of signaling,'' J. Theor. Biol. **152**, 241–253.
Stafford, K. M., Nieukirk, S. L., and Fox, C. G. (**1999**). ''Low-frequency whale sounds recorded on hydrophones in the eastern tropical Pacific,'' J. Acoust. Soc. Am. **106**, 3687–3698.
Stewart, B. S., and Leatherwood, S. (**1985**). ''Minke whale: *Balaenoptera acutorostrata* (Lacepede, 1804),'' in *Handbook of Marine Mammals, Vol. 3: The Sirenians and Baleen Whales*, edited by S. H. Ridgway and R. Harrison (Academic, New York), pp. 91–136.
Thompson, P. O., Findley, L. T., and Cummings, W. C. (**1996**). ''Underwater sounds of blue whales, *Balaenoptera musculus*, in the Gulf of California, Mexico,'' Marine Mammal Sci. **12**, 288–293.
Thompson, P. O., Findley, L. T., and Vidal, O. (**1992**), ''20-Hz pulses and other vocalizations of fin whales, *Balaenoptera physalus*, in the Gulf of California, Mexico,'' J. Acoust. Soc. Am. **92**, 3051–3057.
Thompson, P. O., and Friedl, W. A. (**1982**). ''A long term study of low frequency sounds from several species of whales off Oahu, Hawaii,'' Cetology **45**, 1–19.
Thompson, T. J., Winn, H. E., and Perkins, P. J. (**1979**), ''Mysticete sounds,'' in *Behavior of Marine Animals, Current Perspectives in Research, Volume 3: Cetaceans*, edited by H. E. Winn and B. L. Olla (Plenum, New York), pp. 403–431.
Tyack, P. L. (**1981**). ''Interactions between singing Hawaiian humpback whales and conspecifics nearby,'' Behav. Ecol. Sociobiol. **8**, 105–116.
Tyack, P. L. (**1999**). ''Communication and Cognition,'' in *The Biology of Marine Mammals*, edited by J. E. Reynolds III and S. A. Rommel (Smithsonian Institution Press, Washington, DC), pp. 287–323.
Tyack, P. L., and Clark, C. W. (**2000**). ''Communication and acoustic behavior of dolphins and whales,'' in *Springer Handbook of Auditory Research: Hearing by whales and dolphins*, edited by W. W. L. Au, A. N. Popper, and R. R. Fay (Springer-Verlag, New York), pp. 156–224.
Watkins, W. A. (**1967**). ''The harmonic interval: Fact or artifact in spectral analysis of pulse trains,'' in *Marine Bioacoustics*, edited by W. N. Tavolga (Pergamon, New York), pp. 15–43.
Watkins, W. A., and Schevill, W. E. (**1972**), ''Sound source location by arrival-times on a non-rigid three-dimensional hydrophone array,'' Deep-Sea Res. Oceanogr. Abstr. **19**, 691–706.
Watkins, W. A., Tyack, P., and Moore, K. E. (**1987**), ''The 20-Hz signals of finback whales (*Balaenoptera physalus*),'' J. Acoust. Soc. Am. **82**, 1901–1912.
Wenz, G. M. (**1964**). ''Curious noises and the sonic environment in the ocean,'' in *Marine Bioacousics*, edited by W. N. Tavolga (Pergamon, New York), pp. 101–119.
Winn, H. E., and Perkins, P. J. (**1976**), ''Distribution and sounds of the minke whale with a review of mysticete sounds,'' Cetology **19**, 1–12.
Wursig, B., and Clark, C. W. (**1993**). ''Behavior,'' in *The Bowhead Whale*, edited by J. J. Burns, J. J. Montague, and C. J. Cowles, Special Publication Number 2 of the Society for Marine Mammalogy (Allen Press, Lawrence), pp. 157–199.
Zerbini, A. N., Secchi, E. R., Siciliano, S., and Simoes-Lopes, P. C. (**1996**). ''The dwarf form of the minke whale, *Balaenoptera acutorostrata Lacepede*, 1804, in Brazil,'' Rep. Int. Whal. Commn. **46**, 333–340.

Ultrasound detection by clupeiform fishes

David A. Mann
Mote Marine Laboratory, 1600 Ken Thompson Parkway, Sarasota, Florida 34236 and Tucker-Davis Technologies, 4637 NW 6th Street, Gainesville, Florida 32653

Dennis M. Higgs
Department of Biology, University of Maryland, College Park, Maryland 20742

William N. Tavolga
Mote Marine Laboratory, 1600 Ken Thompson Parkway, Sarasota, Florida 34236

Marcy J. Souza and Arthur N. Popper[a)]
Department of Biology, University of Maryland, College Park, Maryland 20742

(Received 18 December 2000; revised 26 February 2001; accepted 5 March 2001)

It has previously been shown that at least one species of fish (the American shad) in the order clupeiforms (herrings, shads, and relatives) is able to detect sounds up to 180 kHz. However, it has not been clear whether other members of this order are also able to detect ultrasound. It is now demonstrated, using auditory brainstem response (ABR), that at least one additional species, the gulf menhaden (*Brevoortia patronus*), is able to detect ultrasound, while several other species including the bay anchovy (*Anchoa mitchilli*), scaled sardine (*Harengula jaguana*), and Spanish sardine (*Sardinella aurita*) only detect sounds to about 4 kHz. ABR is used to confirm ultrasonic hearing in the American shad. The results suggest that ultrasound detection may be limited to one subfamily of clupeiforms, the Alosinae. It is suggested that ultrasound detection involves the utricle of the inner ear and speculate as to why, despite having similar ear structures, only one group may detect ultrasound. [DOI: 10.1121/1.1368406]

PACS numbers: 43.80.Lb, 43.66.Cb [WA]

I. INTRODUCTION

Until recently, all studies of hearing in fishes have reported that the hearing bandwidth generally extends from below 100 Hz to approximately 1000 Hz in fishes without specializations for sound detection and to perhaps as high as 5000 to 7000 Hz in species that have specializations that enhance bandwidth and sensitivity (e.g., Fay, 1988; Popper and Fay, 1999). However, a number of peer reviewed and ''gray literature'' reports over the past 10 years have suggested that certain fishes, including a number of members of the taxonomic order clupeiforms (herrings, shads, anchovies, and relatives), may be able to detect ultrasonic signals to as high as 126 kHz (ESEERCO, 1991; Dunning *et al.*, 1992; Nestler *et al.*, 1992; Con Edison, 1994; Ross *et al.*, 1995, 1996). Other studies on the Atlantic cod (*Gadus morhua*), a species in a different taxonomic order (Gadiformes), suggested that this species could detect ultrasound at almost 40 kHz (Astrup and Møhl, 1993, 1998; Astrup, 1999).

We previously performed a set of classical conditioning experiments on one of the species reportedly capable of detecting high frequencies, the American shad (*Alosa sapidosomma*), and demonstrated that it could detect pure tones to over 180 kHz (Mann *et al.*, 1997, 1998). We suggested that ultrasound detection may be associated with a specialization of the utricle in the clupeiform ear (also see Nestler *et al.*, 1992). The utricular specializations include a unique arrangement of the utricular sensory epithelium and the presence of an air-filled bulla closely associated with this ear region.

One of the issues related to ultrasound detection is the extent to which it is found among the clupeiforms. Several of the earlier papers suggested, based on nonquantitative measures, that other members of the genus *Alosa* are able to detect ultrasound. However, there is also some evidence that two other clupeiforms, the bay anchovy (*Anchoa mitchilli*) and possibly the Atlantic herring (*Clupea haregus*), may not respond to these high frequencies (Schwarz and Greer, 1984; Dunning *et al.*, 1992; Nestler *et al.*, 1992; Con Edison, 1994). Since all of these species have air-filled auditory bullae in the utricle, it became important to test whether ultrasound detection is ubiquitous among this order, or whether it remains a specialization of only a few species.

In order to test the hypothesis that not all clupeiforms can detect ultrasound, we used the auditory brainstem response (ABR) to measure sound detection abilities of several taxonomically diverse members of this order. The ABR technique has been used successfully with fishes and shows thresholds for sound detection that are generally similar to those measured by traditional classical conditioning tests (Kenyon *et al.*, 1998; Yan *et al.*, 2000). We chose to perform ABR measurements rather than classical conditioning because the fragility of many clupeiforms makes it difficult to keep the fish alive long enough to complete classical conditioning training and recording. We also tested goldfish (*Carassius auratus*) as a control to determine if ABR responses were to spurious signals associated with the ultrasonic stimulus. The goldfish is a good control for the acoustic system

[a)]Author to whom correspondence should be addressed. Electronic mail: AP17@umail.umd.edu

since this species does not detect sounds above about 3 kHz, and this has been confirmed in many studies (Jacobs and Tavolga, 1967; Fay, 1988), including our earlier studies on American shad (Mann *et al.*, 1997, 1998).

II. METHODS

A. Fish

The species used in this study were the bay anchovy (*Anchoa mitchilli*) ($n=15$; 25–30 mm standard length), scaled sardine (*Harengula jaguana*) ($n=16$, 80–120 mm standard length), gulf menhaden (*Brevoortia patronus*) ($n=10$; 37–54 mm standard length), Spanish sardine (*Sardinella aurita*) ($n=2$; 90–110 mm standard length), American shad ($n=11$; 75–90 mm standard length), and goldfish (*Carassius auratus*) ($n=2$, 60 mm standard length). Large numbers of scaled sardine and bay anchovy were used because we were not always able to get an entire audiogram from an individual fish. We were only able to collect two Spanish sardines, but neither of these showed a response to ultrasound.

American shad were obtained from the PEPCO Chalk Point Generating Station (Chalk Point, MD) aquaculture facility and held at the University of Maryland fish colony, while the other species were obtained at the Mote Marine Laboratory, Sarasota, FL. Work on American shad and goldfish was approved by the Institutional Animal Care and Use Committee (IACUC) of the University of Maryland (UMD). Procedures with the other species were approved by the IACUC of the Mote Marine Laboratory (MML).

B. ABR testing

Testing of American shad and goldfish was performed at UMD, while work on the other species was performed at MML. It was not possible to do all of the studies at one location since the fish were obtained at different sites and transporting fish between locations would have been impossible due to the difficulty in keeping the fish alive. However, in order to ensure comparable procedures at both sites, ABR testing was carried out using identical hardware systems from Tucker-Davis Technologies using the BioSig software. The most significant difference in the two setups was tank size (19-liter circular tank, 30 cm deep at UMD) and (40 $\times$50-cm^2 rectangular tank, 30 cm deep at MML). However, this difference is not likely to have affected the data since the signals were calibrated in the same manner, as described later in this work. In addition, one of us (DAM) participated in the experiments at both locations in order to make sure that there were no differences in experimental detail. It is important to note that sound was calibrated as sound pressure level, and that acoustics in small tanks are different from free-field where there are presumably fewer reflections.

Auditory brainstem response were collected in response to repeated presentations of tone pip stimuli. Low-frequency tones ($<$20 kHz) were generated with an underwater speaker (University Sound UW-30). High-frequency tones ($>$20 kHz) were generated with an ITC-1042 underwater transducer. Signals were amplified with either a McIntosh amplifier (UMD) or with a Hafler amplifier (MML). Tone pips were 20 ms in duration, gated on and off with a Hanning window, and presented at 9 per second with the TDT system. Low-frequency tone pips were generated with a 6-μs sample period. Ultrasonic tone pips were generated with a 5.2-μs sample period. At UMD tone pips were calibrated with an LC-10 hydrophone (calibration sensitivity of -208.6 *re*: 1 V/μPa; ± 3 dB 0.1–180 kHz, omnidirectional). At MML, calibrations were performed with a Reson TC4013 hydrophone (calibration sensitivity of -211 dB *re*: 1 V/μPa; $\pm$ 3 dB 1 Hz to 170 kHz, omnidirectional). The hydrophone was positioned in the fish holder without the fish and the output was calibrated on an oscilloscope. Calibrations of the tone pips were performed by peak equivalent calibration. This entailed first calibrating continuous tones as rms SPL, and then the tone pips were presented using the identical signal parameters. Spectral analyses were also performed on acquired signals to ensure that there was no significant harmonic distortion (total harmonic distortion was less than 2% at all frequencies).

For ABR testing the fish was held approximately 10 cm underwater and a recording electrode was placed subcutaneously along the midline just behind the brain, and a reference electrode was placed subcutaneously along the midline just behind the eyes. A ground electrode was either placed in the muscle behind the reference electrode, or in the water adjacent to the fish. Signals from the electrodes were amplified using a digital biological amplifier (TDT DB4/HS4) and low-pass filtered at 10 kHz, high-pass filtered at 8 Hz, and notch-filtered at 60 Hz. Amplification was typically between 50 000 and 100 000.

The ABR responses were acquired by averaging 50 ms of the signal from the electrode from the onset of the tone pip. The ABRs were obtained after 50–200 averages depending on the species. ABRs with 50 averages were used for the bay anchovy, because they did not survive more than about 15 min in the tank. ABRs with 100–200 averages were used for the gulf menhaden, scaled sardine, Spanish sardine, American shad, and goldfish.

C. ABR threshold calculation

Auditory brainstem response thresholds were determined from the data by measuring the peak response at each frequency and level. A threshold criterion was determined based on an estimation of background noise from trials to low sound level presentations (all trials less than 100 dB SPL at both experimental sites). The criterion was set at the level of the 95th percentile for these nondetection trials (i.e., the level below which 95% of the trials fell), or if few trials were run at low levels, at the maximum positive or negative peak for these nondetection trials. To be considered above threshold, the peak level had to be higher than the criterion on two consecutive trials. Linear interpolation between the level before and after the criterion was used to calculate the threshold. Thresholds from 5 of the 11 American shad were measured by hand as the lowest sound pressure level that gave a repeatable response, because the signal-to-noise ratio did not allow an accurate measurement using the peak method de-

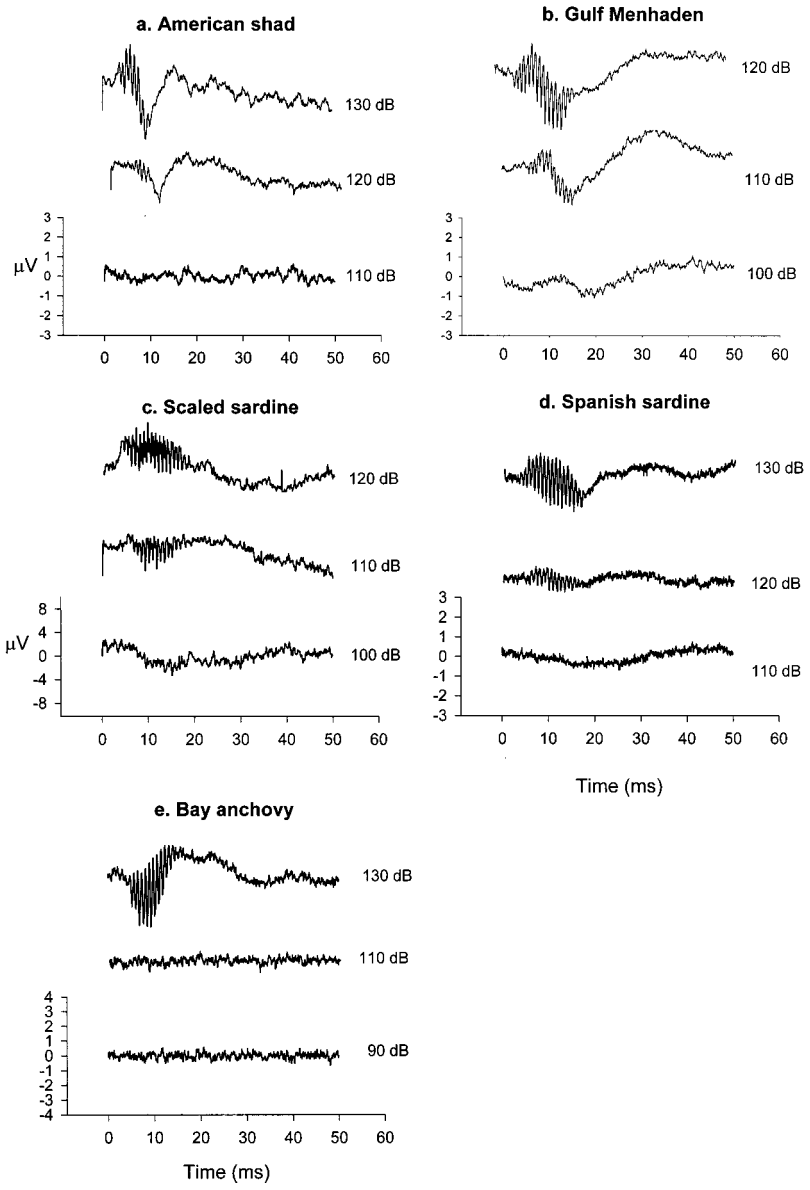

FIG. 1. ABR waveforms in response to 600-Hz sounds presented at several levels for (a) American shad, (b) gulf menhaden, (c) scaled sardine, (d) Spanish sardine, and (e) bay anchovy.

scribed above. The thresholds from these fish were not significantly different than those measured from the other six American shad using the peak method.

III. RESULTS

The ABR waveforms obtained in response to low-frequency sound and ultrasound presentation all show a negative trough at about 10 ms after the beginning of sound presentation. The ABR from the low-frequency sound presentation also has a higher-frequency component that is twice the frequency of the tone stimulus, which is typical of fish ABRs.

All species responded to low-frequency sound presentation (Fig. 1), while only American shad and gulf menhaden showed responses to ultrasound presentation from 40 to 80 kHz (Figs. 2 and 3). The other species did not respond to ultrasound presentation at sound pressure levels up to 180 dB SPL, but they showed a consistent ABR to low-frequency stimulation. The voltage of the ABR in response to ultrasound in the American shad and gulf menhaden was about the same as the voltage of the ABR to low-frequency sound for all species tested (Figs. 1 and 2). Therefore, we should have been able to detect a response to ultrasound in the other species had the ability to detect such sounds been present.

The low-frequency thresholds (below 10 000 Hz) were similar for all species, with thresholds around 120–130 dB SPL (Figs. 4 and 5). The ultrasonic thresholds for American shad were around 155 dB SPL and the ultrasonic thresholds for gulf menhaden were about 180 dB SPL (Fig. 4).

The ABR thresholds obtained for the American shad were in the range of 0 to 15 dB higher than the behavioral thresholds obtained in a previous study (Figs. 4 and 5), but showed a similar trend of better sensitivity at low frequencies than at ultrasonic frequencies. However, some of the lowest thresholds to ultrasound presentation (e.g., one American shad showed thresholds at 40 kHz of 130 dB) were as low as the detection thresholds for low frequency sound (Figs. 1 and 2).

Trials with low-frequency stimulation were run both before and after trials with ultrasound to ensure that the low-

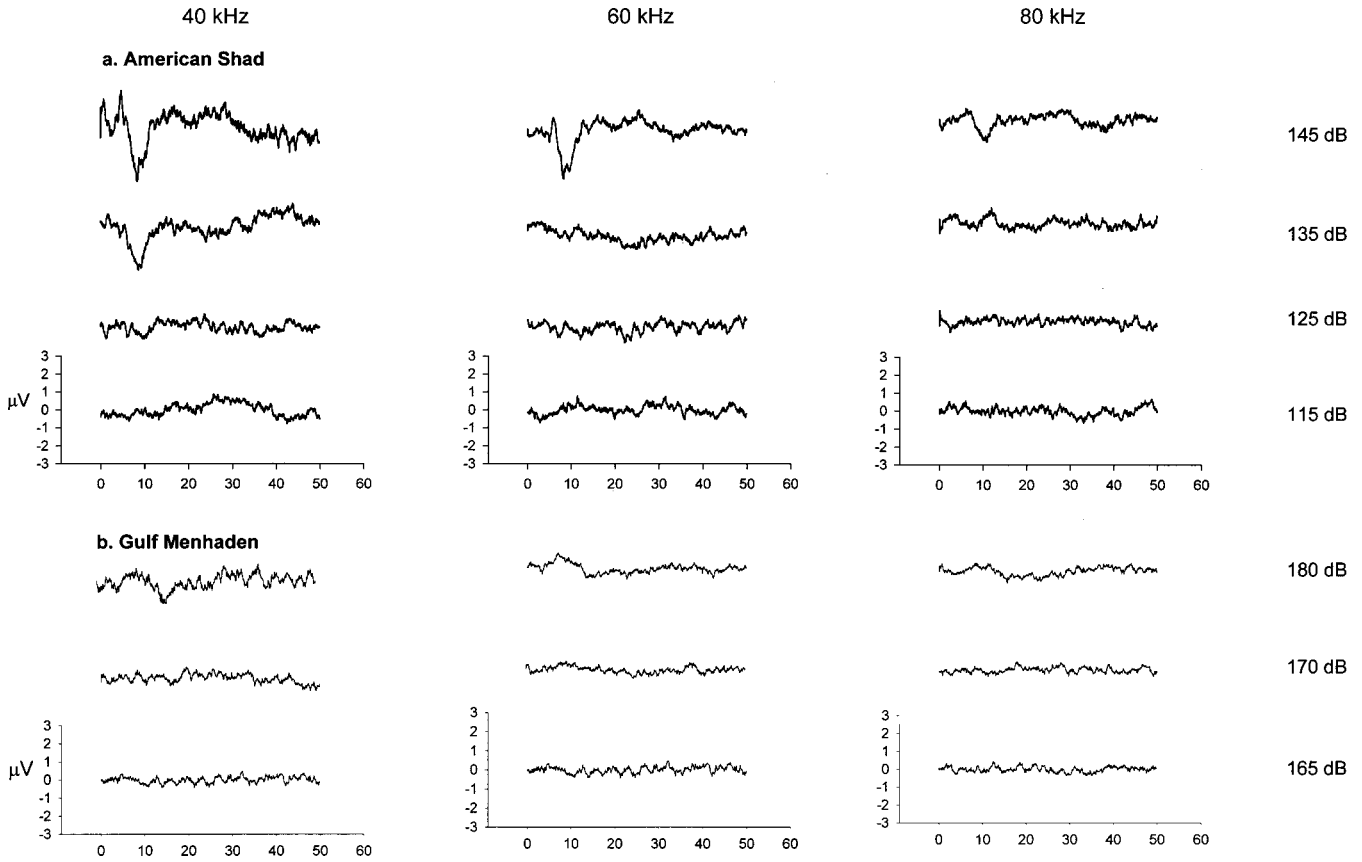

FIG. 2. ABR waveforms in response to 40-, 60-, and 80-kHz ultrasound presented at several levels for species that are able to detect ultrasound: (a) American shad and (b) gulf menhaden.

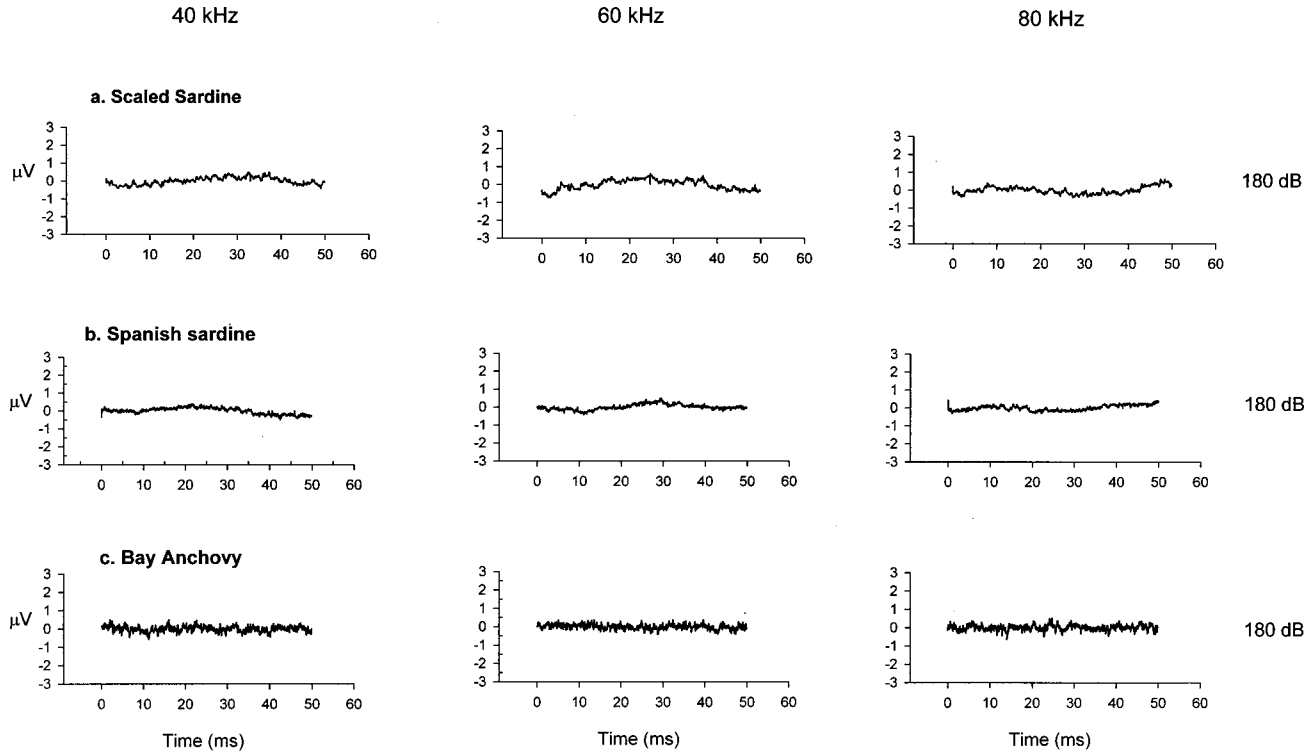

FIG. 3. ABR waveforms in response to 40, 60, and 80 kHz and at 180 dB for species that do not detect ultrasound: (a) scaled sardine, (b) Spanish sardine, and (c) bay anchovy. Arrows at 10 ms indicate troughs in ABR.

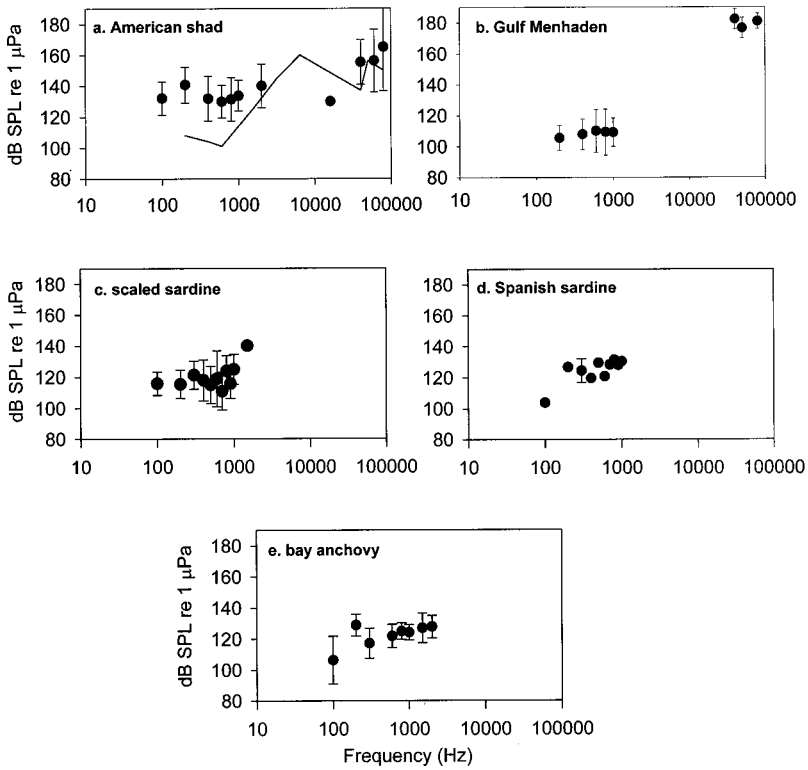

FIG. 4. Audiogram for (a) American shad, (b) gulf menhaden, (c) scaled sardine, (d) Spanish sardine, and (e) bay anchovy determined from ABRs. Data shown are mean values ±1 standard deviation. The behavioral audiogram for American shad determined by classical conditioning is plotted as a solid line in (a) (Mann *et al.*, 1998).

frequency ABR was consistent. Controls were also run with goldfish and dead clupeiform fishes to confirm that the ABR responses were not artifacts. There was never a positive ABR with dead fish, and goldfish controls did not respond above 4 kHz. Only two goldfish controls were run because there was no evidence of artifacts with dead fish or either of the goldfish. Also, the clupeoids that did not respond to ultrasound serve as a control for artifactual responses to ultrasound presentation.

IV. DISCUSSION

This study has demonstrated that a member of a second genus of clupeiform fish, the gulf menhaden, is able to detect ultrasonic signals, and it has also demonstrated that there are members of other genera of this order that cannot detect ultrasound. This study also demonstrated that even those species that do not detect ultrasound are able to detect sound to at least 4000 Hz (although they are not particularly sensitive), putting them into the general classification of hearing ''specialist'' (Popper and Fay, 1973, 1999). This is noteworthy since several other investigators have suggested that clupeiforms could only detect sounds to around 1–2 kHz (e.g., Enger, 1967; Sorokin *et al.*, 1988).

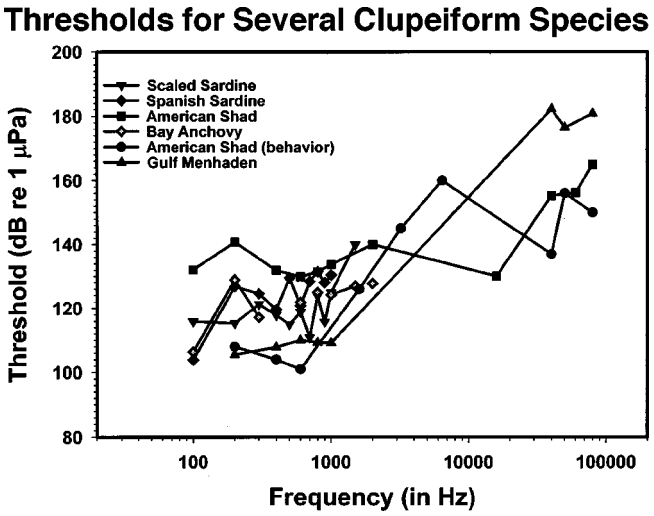

FIG. 5. Combined plot of audiograms for each of the species studied with ABR as well as behavioral data for the American shad (Mann *et al.*, 1998).

A. Evolution of ultrasound detection

One of the most interesting questions related to the discovery of ultrasound detection in fishes is how and why this capability arose. We previously hypothesized that this ability may have been an exaptation (= preadaptation) that evolved before there were echolocating predators, because all clupeids have the auditory bullae and specializations in the utricle (Mann *et al.*, 1997). We had assumed, incorrectly, that all clupeoids could detect ultrasound. These new findings of clupeoids that cannot detect ultrasound are important because they will allow us to investigate the mechanism and evolution of ultrasound detection in closely related species.

While we can only speculate, it is possible that the bulla and specialized utricle arose early in the evolution of clupeiforms and may have been a mechanism by which these fish could detect relatively higher frequency sounds (in the range of 1–4 kHz) than fishes without such specializations, or aided the fish in some other way, as suggested by Denton *et al.* (1979). An analogous event is likely to have occurred in the Otophysan fishes where the presence of the Weberian ossicles enables most of these species (e.g., goldfish and catfish) to detect sounds to 3 kHz or a bit higher (Fay, 1988). The detection of these higher frequencies may have been in response to the ancestors of both groups of fishes living in

shallow waters where low-frequency sounds attenuate very rapidly, but where higher frequencies carry greater distances (Rogers and Cox, 1988). In order for these fishes to glean information from any significant distance, they would only have been able to use higher frequencies, and this would have been a strong selective pressure for the evolution of specializations that enabled the fish to detect the biologically relevant sounds.

Since we now have shown that not all clupeiforms detect ultrasound, it is reasonable to suggest that while the evolution of the specialized utricle may have been responsible for hearing specializations, these adaptations do not immediately lead to the ability to detect ultrasound. Thus, we propose that the evolution of ultrasound detection in a number of clupeiforms of the subfamily Alosinae, including American shad and gulf menhaden, could have been under the selective pressures of echolocating *Tursiops*, which produce high-level (up to 220 dB *re* 1 μPa at 1 m) ultrasonic echolocation clicks (Au, 1993). In effect, the presence of the specialized utricle, if this is indeed the structure involved with ultrasound detection, may be viewed as an exaptation that could readily evolve into an ultrasound-detecting device, at least in some clupeiforms. It is interesting to question, however, why all members of this order did not evolve the same capability given that they are also prey of echolocating cetaceans. It is also important to note that there are several other subfamilies in the Clupeidae that remain to be tested.

B. Mechanism of ultrasound detection

One of the most interesting questions to ask is how ultrasound detection is performed in American shad and gulf menhaden. While we are not yet able to directly answer this question, the ABR data do provide us some potential insight into this issue. We previously argued (Mann *et al.*, 1997, 1998) that while it is possible that these fishes have evolved a new mechanism for ultrasound detection not involving an ear, the parsimonious argument is that detection involves the ear (see also Nestler *et al.*, 1992). The ABRs to both low-frequency sound and ultrasound showed a similar trough at 10 ms, suggesting that they are utilizing at least some of the same brain pathways. Furthermore, virtually all other animals, vertebrate and invertebrate, that detect ultrasound use an ear or earlike structure for ultrasound detection (e.g., Sales and Pye, 1974; Au, 1993; Grinnell, 1995; Hoy, 1999). Cod, *Gadus morhua*, is reported to be able to detect ultrasound, but only at high sound levels (185–200 dB *re* 1 μPa), and it has been suggested that receptors other than the ear are potentially being overstimulated (Astrup, 1999).

Clearly the potential mechanism thought to be involved in the cod is possible for clupeids. However, the clupeiform utricle has several unique features as compared to all other vertebrates and so it becomes a candidate for ultrasound detection in these species (e.g.,Wohlfhart, 1936; O'Connell, 1955; Denton *et al.*, 1979; Popper and Platt, 1979). The utricular sensory epithelium in the clupeiforms is divided into three distinct regions, the middle of which is suspended above a fluid-filled space that is separated by a thin membrane from an otic air bubble known as the auditory bulla that connects via a thin tube to the swim bladder (e.g., Denton *et al.*, 1979; Blaxter *et al.*, 1981a, b; Best and Gray, 1982). While earlier investigators suggested that this specialization may be associated with detection of changes in pressure as the fish moved to different depths (e.g., Denton *et al.*, 1979; Gray and Denton, 1979), it has been suggested that, instead, it may be an adaptation for high-frequency hearing (e.g., above 20 kHz) (Nestler *et al.*, 1992; Mann *et al.*, 1997, 1998). Moreover, we have suggested that the middle of the three sensory regions may be involved in ultrasound detection (Mann *et al.*, 1998), and this is supported by observations that there are defined differences in the utricular epithelium and its support in the American shad, an ultrasound detector, and the bay anchovy, a species that does not detect ultrasound (e.g., the middle macula of shad is more loosely suspended in shad than in anchovy; Higgs and Popper, in prep.). Ultimately, direct neurophysiological recordings from the ear and brain will be needed to prove the mechanism of ultrasound detection.

C. Practical applications

The behavioral response of various *Alosa* species to ultrasound presentation has been observed in the field and used to repel them from power plant intakes (e.g., Dunning *et al.*, 1992; Nestler *et al.*, 1992; Ross *et al.*, 1996). Our results showing that other clupeiforms, such as the bay anchovy, do not respond to ultrasound suggest that behavioral responses to ultrasound may be limited to a few species, perhaps only to members of the subfamily Alosinae, and thus limit the broad applicability of ultrasound in controlling clupeiform impingement.

The response of several *Alosa* species to ultrasound may also impact the fishing industry. There is evidence that acoustic sound sources (known as pingers) placed on fishing nets to reduce the by-catch of harbor porpoises (pingers presumably ''alert'' the porpoise to the presence of the nets) also reduced the catch of clupeids (Kraus *et al.*, 1997; see also Goodson, 1997). Kraus *et al.* (1997) suggested that the reason the harbor porpoise by-catch was reduced may have been because they were chasing clupeids that were deterred from the nets, and that the pingers were only indirectly influencing dolphin by-catch by reducing the number of clupeids in the vicinity of the nets. This becomes particularly important since Gulf and Atlantic menhaden are among the most important commercial fishes. In 1997–1998, 1.7 billion pounds were caught in the United States, accounting for 21% of all fish landings, and making menhaden the second largest commercial catch in the United States (NMFS, 1999). Given that these fishes account for such a large proportion of the fish catch, pingers on these nets might be very useful for deterring dolphins, although they may also serve to deter menhaden and ultimately affect the commercial catch of these species.

ACKNOWLEDGMENTS

This work was supported by Grant No. DC03936 from the National Institute of Deafness and Other Communicative Disorders of NIH. We thank Randy Wells and Doug Nowacek for help with organizing fish testing at MML. All

experiments comply with the ''Principles of animal care,'' Publication No. 86-23, revised 1995, of the National Institutes of Health and were under the supervision of the Institutional Animal Care and Use Committees of each institution involved in the study.

Astrup, J. (**1999**). ''Ultrasound detection in fish—a parallel to the sonar-mediated detection of bats by ultrasound-sensitive insects?'' Comp. Biochem. Physiol. A **124**, 19–27.

Astrup, J., and Møhl, B. (**1993**). ''Detection of intense ultrasound by the cod *Gadus morhua*,'' J. Exp. Biol. **182**, 71–80.

Astrup, J., and Møhl, B. (**1998**). ''Discrimination between high and low repetition rates of ultrasonic pulses by the cod,'' J. Fish Biol. **52**, 205–208.

Au, W. W. L. (**1993**). *The Sonar of Dolphins* (Springer-Verlag, New York).

Best, A. C. G., and Gray, J. A. B. (**1982**). ''Morphology of the utricular recess in the sprat,'' J. Mar. Biol. Assoc. U.K. **60**, 703–715.

Blaxter, J. H. S., Denton, E. J., and Gray, J. A. B. (**1981a**). ''Acousticolateralis systems in clupeid fishes,'' in *Hearing and Sound Communication in Fishes*, edited by W. N. Tavolga, A. N. Popper, and R. R. Fay (Springer, New York), pp. 39–59.

Blaxter, J. H. S., Denton, E. J., and Gray, J. A. B. (**1981b**). ''The auditory bullae-swimbladder system in late stage herring larvae,'' J. Mar. Biol. Assoc. U.K. **61**, 315–326.

Con Edison (**1994**). ''Evaluation of underwater sound to reduce impingement at the Arthur Kill Station, final report'' (Consolidated Edison Co., New York).

Denton, E. J., Gray, J. A. B., and Blaxter, J. H. S. (**1979**). ''The mechanics of the clupeid acousticolateralis system, frequency responses,'' J. Mar. Biol. Assoc. U.K. **59**, 27–47.

Dunning, D. J., Ross, Q. E., Geoghegan, P., Reichle, J. J., Menezes, J. K., and Watson, J. K. (**1992**). ''Alewives in a cage avoid high-frequency sound,'' North Am. J. Fish. Man. **12**, 407–416.

Enger, P. S. (**1967**). ''Hearing in herring,'' Comp. Biochem. Physiol. **22**, 527–538.

ESEERCO (Empire State Electric Energy Research Corporation) (**1991**). ''Responses of white perch, striped bass, alewives, spottail shiners, golden shiners, and Atlantic tomcod in a cage to high and low frequency underwater sounds generated by an electronic fish startle system,'' ESEERCO Project EP89-30, Amherst, New York.

Fay, R. R. (**1988**). ''Hearing in vertebrates, a psychophysics databook'' (Hill-Fay Assoc., Winnetka, IL).

Goodson, A. D. (**1997**). ''Developing deterrent devices designed to reduce the mortality of small cetaceans in commercial fishing nets,'' Mar. Fresh. Behav. Physiol. **29**, 211–236.

Gray, J. A. B., and Denton, E. J. (**1979**). ''The mechanics of the clupeid acoustico-lateralis system, low frequency measurements,'' J. Mar. Biol. Assoc. U.K. **59**, 11–26.

Grinnell, A. D. (**1995**). ''Hearing in bats, An overview,'' in *Hearing by Bats*, edited by A. N. Popper and R. R. Fay (Springer, New York), pp. 1–36.

Hoy, R. R. (**1999**). ''Acute as a bug's ear, An informal discussion of hearing in insects,'' in *Comparative Hearing, Insects*, edited by R. R. Hoy, A. N. Popper, and R. R. Fay (Springer, New York), pp. 1–17.

Jacobs, D. W., and Tavolga, W. N. (**1967**). ''Acoustic intensity limens in the goldfish,'' Anim. Behav. **15**, 324–335.

Kenyon, T. N., Ladich, F., and Yan, H. Y. (**1998**). ''A comparative study of hearing ability in fishes, the auditory brainstem response approach,'' J. Comp. Physiol. A **182**, 307–318.

Kraus, S. D., Read, A. J., Solow, A., Baldwin, K., Spradlin, T., Anderson, E., and Williamson, J. (**1997**). ''Acoustic alarms reduce porpoise mortality,'' Nature (London) **388**, 525.

Mann, D. A., Lu, Z., and Popper, A. N. (**1997**). ''A clupeid fish can detect ultrasound,'' Nature (London) **389**, 341.

Mann, D. A., Lu, Z., Hastings, M. C., and Popper, A. N. (**1998**). ''Detection of ultrasonic tones and simulated dolphin echolocation clicks by a teleost fish, the American shad (*Alosa* sapidissima),'' J. Acoust. Soc. Am. **104**, 562–568.

National Marine Fisheries Service (NMFS) (**1999**). ''Fisheries of the United States, 1998,'' NMFS Office of Science and Technology/Fisheries Statistics and Economics Division.

Nestler, J. M., Ploskey, G. R., Pickens, J., Menezes, J., and Schilt, C. (**1992**). ''Responses of blueback herring to high-frequency sound and implications for reducing entrainment at hydropower dams,'' N. Am. J. Fish. Man. **12**, 667–683.

O'Connell, C. P. (**1955**). ''The gas bladder and its relation to the inner ear in *Sardinops caerulea* and Engraulis mordax,'' Fish. Bull. **56**, 505–533.

Popper, A. N., and Fay, R. R. (**1973**). ''Sound detection and processing by fish, A critical review,'' J. Acoust. Soc. Am. **53**, 1515–1529.

Popper, A. N., and Fay, R. R. (**1999**). ''The auditory periphery in fishes,'' in *Comparative Hearing, Fish and Amphibians*, edited by R. R. Fay and A. N. Popper (Springer, New York), pp. 43–100.

Popper, A. N., and Platt, C. (**1979**). ''The herring ear has a unique receptor pattern,'' Nature (London) **280**, 832–833.

Rogers, P. H., and Cox, M. (**1988**). ''Underwater sound as a biological stimulus,'' in *Sensory Biology of Aquatic Animals*, edited by J. Atema, R. R. Fay, A. N. Popper, and W. N. Tavolga (Springer-Verlag, New York), pp. 131–149.

Ross, Q. E., Dunning, D. J., Menezes, J. K., Kenna, M. J., Tiller, G. (**1995**). ''Reducing impingement of alewives with high-frequency sound at a power plant on Lake Ontario,'' N. Am. J. Fish. Man. **15**, 378–388.

Ross, Q. E., Dunning, D. J., Thorne, R., Menezes, J. K., Tiller, G. W., and Watson, J. K. (**1996**). ''Response of alewives to high-frequency sound at a power plant intake on Lake Ontario,'' N. Am. J. Fish. Man. **16**, 548–559.

Sales, G., and Pye, D. (**1974**). *Ultrasonic Communication by Animals* (Chapman and Hall, London).

Schwarz, A. L., and Greer, G. L. (**1984**). ''Responses of Pacific Herring, *Clupea harengus pallasi*, to some underwater sounds,'' Can. J. Fish. Aquat. Sci. **41**, 1183–1192.

Sorokin, M. A., Donskoi, S. V., and Lebedeva, A. N. (**1988**). ''Sound reception in clupeidae,'' Biologiya Morya **2**, 34–40.

Wohlfhart, T. A. (**1936**). ''Das ohrlabyrinth der sardine (*Clupea pilchardus* Walb.) und seine beziehungen zur zchwimmblase und seitenlinie,'' Z. Morphol. Oekol. Tiere **31**, 371–410.

Yan, H. Y. Y., Fine, M. L., Horn, N. S., and Colón, W. E. (**2000**). ''Variability in the role of the gasbladder in fish audition,'' J. Comp. Physiol. A **186**, 435–445.

Ultrasound phased arrays for prostate treatment

Joseph S. Tan and Leon A. Frizzell
Bioacoustics Research Laboratory, Department of Electrical and Computer Engineering, University of Illinois, 405 North Mathews Avenue, Urbana, Illinois 61801

Narendra Sanghvi, Shih-jeh Wu,[a] and Ralf Seip
Focus Surgery, Inc., 3940 Pendleton Way, Indianapolis, Indiana 46226

Jeffrey T. Kouzmanoff[b]
Labthermics Technologies, Inc., 701 Devonshire Drive, Champaign, Illinois 61820

(Received 6 June 2000; accepted for publication 26 March 2001)

The effect of array geometry on the steering performance of ultrasound phased arrays is examined theoretically, in order to maximize array performance under the given anatomical constraints. This paper evaluates the performance of arrays with spherical and cylindrical geometry, determined by using computer simulations of the pressure fields produced at various extremes of steering. The spherical segment arrays were truncated for insertion into the rectum, and contained either annular or linear elements. The cylindrical arrays were either flat or had a variable curvature applied along their length. Fields were computed by dividing the array elements into many point sources. The effectiveness of an array configuration when steered to a particular focal location was assessed by defining a parameter, G, as the ratio of the intensity at the desired focus to the maximum intensity of any unwanted lobes. The performance of truncated spherical arrays with annular elements was evaluated for focal steering along the array axis (in depth, in the z direction). When steered 15 mm toward the source, these truncated spherical annular arrays exhibited excellent performance, with $G>5.7$ for arrays containing more than 10 elements. Similarly, the spherical arrays with linear elements performed well when steered along the array axis to the same degree, with $G>7$ (for element widths up to 3 λ), though many more array elements were required. However, when these arrays were steered 15 mm laterally, along the length of the prostate (the y direction), the value for G fell below 1 for element widths greater than about 1.6 λ. It was found that the cylindrical arrays performed much better for y-direction steering ($G>4$, for 60 mm arrays with an element width of 1.75 λ), but their performance was poorer when steered in the z direction ($G\cong 4$ for an element width of 1.5 λ). In order to find a compromise between these extremes, a curved cylindrical array was examined, which was a cylindrical array with additional curvature along its length. These curved cylindrical arrays yielded performance between that of spherical linear arrays and cylindrical arrays, with better steering along the y direction than the spherical arrays and better z-direction steering than the cylindrical arrays. © *2001 Acoustical Society of America.*
[DOI: 10.1121/1.1373444]

PACS numbers: 43.80.Sh, 43.80.Vj [FD]

I. INTRODUCTION

Two diseases of the prostate, benign prostatic hyperplasia (BPH) and cancer of the prostate (PC), are problems that are increasingly afflicting our male population. The incidence of both conditions increases with age and concern about these diseases is reflected in increased exposure in the popular[1–3] as well as in the medical literature.[4] Current treatment options can be fairly expensive, and are associated with a high incidence of impotence, frequent urinary incontinence, as well as the risks associated with surgical procedures.[5] Since none of these treatment options are ideal, alternative therapies are currently being sought.[1,4–6]

In recent years, ultrasound has been increasingly investigated for use in thermal or ablative therapy.[7–20] When focused, ultrasound can produce well-defined regions of thermal necrosis for treatment of prostate disease.[7,9,19–25] In the treatment of the prostate, focused ultrasound is applied via a probe inserted into the rectum, in order to minimize the amount of intervening tissue while providing an adequate acoustic window for treatment. This allows higher frequencies to be used, increasing the ultrasonic absorption coefficient and resulting in more efficient heating of the treatment region.[15] Additionally, transrectal treatment avoids undesired heating of the pelvic bone. Preliminary findings have demonstrated that ultrasonic ablation can successfully control localized prostate cancer with low morbidity.[19,25] This approach has been shown not to enhance metastatic spread,[26,27] and avoids damage to the rectal wall.[28]

Transrectal ultrasonic therapy of the prostate imposes geometric constraints on the transducer utilized in the treatment, because the ultrasound probe containing the array must fit within the patient's rectum. This limits the practical array

[a]Current address: I-Shou University, Section 1, Hsueh-Cheng Rd., Ta-Hsu Hsiang, Kaohsiung County, Taiwan, 84008, Republic of China.
[b]Current address: Cisco Systems, Inc., 2302 Fox Drive, Champaign, IL 61820.

width. The ability to move the focal point is essential, since the treatment region is larger in volume than the ultrasonic focus. With a steerable focus, the focus can be placed at various locations in a controlled manner, in order to ablate the entire treatment volume.[13,18,29,30] Current devices in clinical trials use a single spherical transducer with a fixed focus.[16,19,20] Variation of the focal position is achieved through mechanical movement of the transducer, and variation of focal depth can only be accomplished by using a different transducer with a different radius of curvature. Because mechanical components are subject to failure due to wear, and because changing transducers requires time both to switch transducers and to reposition the new transducer relative to the prostate, it would be advantageous to employ a phased array transducer system, and steer the focus electronically. The phased array would offer the advantages of steering the focal region very rapidly with minimal mechanical movement of the transducer and the possibility of modifying the focal size by electronic means.[17,30,31] These capabilities would facilitate the efficient treatment of large tumor volumes. The inevitable disadvantages of phased arrays include the need to manufacture arrays with many small, acoustically isolated elements; the associated large number of electrical leads, amplifiers and phasing circuits; and the existence of unwanted lobes, including grating lobes in the field, which might be of sufficient intensity to cause unintended damage to normal tissue. More intense unwanted lobes also result in longer treatment times, as greater waiting periods between sonications are required in order to allow for thermal dissipation, to prevent heat build-up in normal tissue regions.

A number of methods have been investigated in order to improve the performance of surgical phased arrays. These methods have, for the most part, involved modifications occurring at the level of the array elements, for example, element size randomization in linear arrays,[23] adaptive aperture techniques,[32] permutations in element layout,[33,34] or novel phasing schemes.[17,30,31,35] A few have involved the introduction of new phased array shapes, such as spherical-section arrays[36,37] and a cylindrical array.[38] In this theoretical study, a number of transducer array configurations were examined in order to elucidate the effects of array geometry on performance. This was conducted with the intent of determining which of these configurations would be optimal in terms of using the fewest elements while providing acceptable ultrasonic fields and flexible focusing capability for prostate therapy through the rectum. Thus, the goal was not to eliminate unwanted lobes entirely but to insure that they were of acceptably low amplitude while steering the focus over the intended range, so as to minimize unintended heating elsewhere in the field. To this end, only arrays containing element widths larger than a wavelength were examined. Although sparsely filled, randomized spherical arrays have been shown to be highly effective in suppressing unwanted lobes,[11,12,33] the limited surface area available in transrectal prostate therapy precludes the use of a sparsely filled array.

The first transducer array examined was a truncated spherical segment with annular elements for steering the focus in depth along the axis of the transducer. A second spherical array with linear elements was investigated for steering the focus both axially and laterally along the length of the prostate. In order to improve steering along the length of the prostate, a cylindrical array geometry was then examined. Finally, a novel transducer array design was examined, which involved the addition of curvature along the length of the cylindrical array. This curved cylindrical array can be considered a hybrid of the truncated spherical array and the cylindrical array. For array configurations fitting within the geometric constraints mentioned earlier, computational studies were performed, in order to assess their effectiveness in delivering high intensity ultrasonic energy to specified focal positions. The effectiveness of an array configuration when steered to a particular focal location was assessed by defining a parameter, G, as the ratio of the intensity at the desired focus to the maximum intensity of any unwanted lobes. The focal positions employed in the studies correspond to the anticipated steering extremes required during clinical use of the array for prostate therapy.

II. METHODS

The pressure fields produced by the arrays examined in this study were calculated using the point radiator method, which subdivides the elements of the array into subelements that are small enough that they produce fields approximating that from a point radiator.[39–41] The total pressure at any given point in the field is the sum of the complex pressures contributed from each of the subelements across the entire active surface of the array, taking into account the relative phase of the signal applied to the transducer element to which the subelement belongs. The pressure field produced by a given array configuration (geometry, element width and element spacing) could be calculated for the focus steered to any specified location. The origin of the coordinate system was taken as 45 mm from the center of the array with the positive z axis directed away from the array, the y axis was directed along the length of the array and the x axis across the array, as shown in Fig. 1. This point was chosen as the origin because it represents a typical distance between the transducer face located in the rectum and the deepest extent of the treatment region into the prostate. Additionally, the origin corresponds to the geometric focus of the spherical arrays. Signals applied to the elements of the array were phased so as to result in constructive interference at the intended focal point.

The pressure field was calculated at points in the region of interest using the following equation:

$$p(x,y,z) \cong j \frac{\rho c k U_0 \Delta A}{2\pi} \sum_{\text{array surface}} \frac{e^{-(\alpha + jk)R}}{R}, \tag{1}$$

where the summation is over the active surface of the array, i.e., the surface of the elements of the array, $p(x,y,z)$ is the total acoustic pressure at the point (x,y,z), ρ is the density and c is the speed of sound of the loading medium, k is the acoustic propagation constant (calculated from $k=2\pi/\lambda$, where λ is the wavelength), U_0 is the velocity amplitude of the surface of the source in m/s [calculated from $U_0 = (2I_0/\rho c)^{1/2}$, where $I_0 = 10\,000\ \text{W/m}^2$], $R=[(x-x_s)^2+(y-y_s)^2+(z-z_s)^2]^{1/2}$ is the distance from the center of the

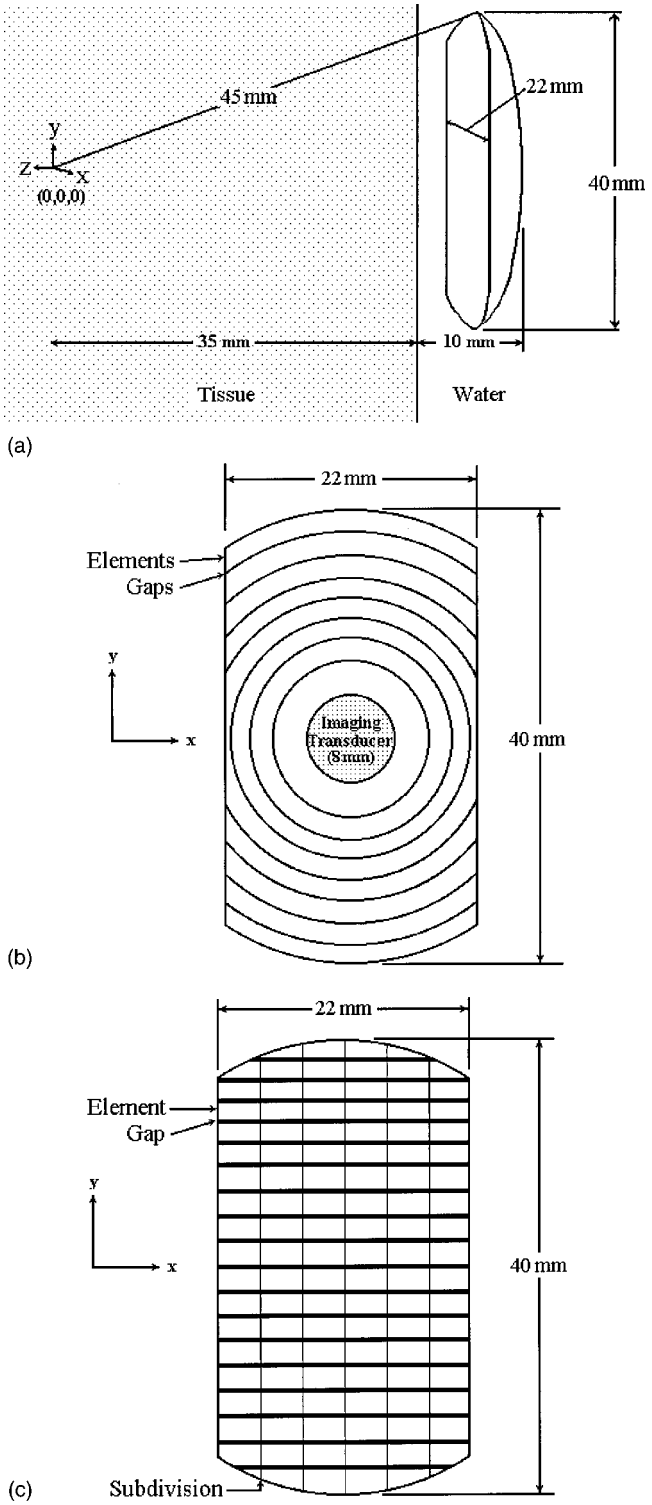

FIG. 1. (a) Truncated spherical array side view with water and tissue, (b) truncated spherical annular array front view, (c) truncated spherical linear array front view.

subelement of the source (x_s, y_s, z_s) (i.e., point radiator) to the field point being calculated, ΔA is the area of the subelement, and α is the attenuation coefficient. The simulations were run at a frequency of 4 MHz (see Table I for parameter values used), which has been shown to be appropriate for this depth of treatment.[42] The calculation requires that the dimensions of the subelements be small relative to a wavelength; in these simulations the subelements were modeled as squares with dimensions of a tenth of a wavelength on a side. Note that each element of the array was excited with equal amplitude, i.e., there was no apodization.

TABLE I. Properties used for the simulations, all at 4 MHz.

Material	Density (kg/m^3)	Speed (m/s)	Absorption coefficient (cm^{-1})
Water	1000	1500	0
Tissue	1000	1500	0.3224

Simulations were carried out with a 10 mm water standoff between the center of the array and a planar boundary with the tissue (at $z_{\text{Interface}} = -35$ mm), as shown in Fig. 1(a). Thus the origin of the coordinate system, located 45 mm from the center of the array, was separated from the center of the array by 10 mm of water, followed by 35 mm of tissue. For each point radiator-field point pair, the path in water and in tissue was calculated in order to account for the attenuation along the tissue portion of the path. The equation used to calculate the pressure field was thus modified:

$$p(x,y,z) \cong j \frac{\rho c k U_0 \Delta A}{2\pi} \sum_{\text{array surface}} \frac{e^{-[\alpha_W R_W + \alpha_T R_T + jkR_{\text{tot}}]}}{R_{\text{tot}}}, \qquad (2)$$

where α_W is the attenuation coefficient in water, α_T is the attenuation coefficient in tissue, R_W is the distance that the beam traveled through water, R_T is the distance that the beam traveled through tissue, and $R_{\text{tot}} = R_W + R_T$ is the total distance that the beam traveled along the straight line from source subelement to field point, see Fig. 1(a).

Since the intent of this study was the fundamental comparison of the performance of different array configurations, not all of the detailed aspects of the sound propagation were required. For example, the speed and density for both tissue and water were taken to be the same so that the analysis was not complicated by reflection and refraction. Additionally, the effects of nonlinear propagation were not incorporated to simplify the extensive and time consuming calculations of the fields. Studies that might be conducted in the future involving the calculation of temperature rise associated with the fields from these sources would need to consider nonlinear propagation.

The calculations were performed using programs written in Visual C++4.1 and executed on several Pentium-type personal computers. The fields were calculated for different cases of focal steering: no steering, steering -15 mm in the y direction (along the prostate), and steering -15 mm in the z direction (towards the transducer). The transducer element size (width) was varied. The array configurations and ranges of parameters examined are listed in Table II.

The performance of the arrays under each steering condition was assessed by first calculating the acoustic intensity at each field point, using the equation $I = p^2/2\rho c$, and then finding the ratio of intensity at the focus to the intensity of the largest unwanted lobe, G:

$$G = \frac{I_{\text{focus}}}{I_{\text{max,unwanted}}}. \qquad (3)$$

This G value provided a means to reduce the large amount of data contained in each calculated field to a single number to

TABLE II. Configurations and ranges of array parameters.

Array geometry	Element description	Element gap	Focal location(s)	Parameter(s) varied
TSA	Annular equal area	1/2 λ	(0,0,−15)	Number of elements: 6 to 14
TSL	Linear	1/2 λ	(0,0,0) (0,−15,0) (0,0,−15)	(a) Element width: 1 to 3 λ (b) Number of elements in *x*: 2, 4, 6, 12, 24
Cylindrical	Linear	1/2 λ	(0,0,0) (0,−15,0) (0,0,−15)	(a) Element width: 1 to 3 λ (b) Array length: 40, 50, or 60 mm
Curved cylindrical	Linear	1/2 λ	(0,0,0) (0,−15,0) (0,0,−15)	(a) Element width: 1 to 3 λ (b) Array length: 50 or 60 mm (c) Radius of array curvature: 50, 60, 75, or 90 mm

facilitate comparison among the numerous arrays and steering conditions. Although no thermal calculations were done as a part of this study, it is the authors' opinion that a *G* value of 4 or greater would be sufficient to prevent unintended damage to normal tissue, when used in conjunction with a properly planned therapy regimen and active rectal wall cooling.

The fields produced by the arrays were initially investigated at a low spatial resolution (1 mm=8/3 λ). This resulted in irregular (nonmonotonic) behavior of the *G* values as a function of the element size.[43] Since this phenomenon was discovered, simulations with higher spatial resolution (0.25 mm=2/3 λ) of the field have been performed, with the spatial resolution being limited by the practical consideration of simulation time. The results of these higher-resolution simulations did not show these irregularities and are presented here.

III. RESULTS AND DISCUSSION

A. Truncated spherical annular (TSA) array

The truncated spherical annular (TSA) array consisted of a truncated spherical shell divided into annular elements of equal area, with a gap λ/2 wide between adjacent elements. A center region of 8 mm diameter was considered inactive as it was reserved for an imaging transducer, see Fig. 1(b). The spherical shell had a 45 mm radius of curvature, with a face diameter of 40 mm which was truncated in the *x* direction to a width of 22 mm to allow passage through the rectum, as has been done for fixed focus transducers currently used by Focus Surgery, Inc.,[20] as well as in the studies by Curiel *et al.*[44] and Chapelon *et al.*[7] The spherical design, first proposed by Ebbini and Cain,[36] has the advantage of possessing a geometric focus, but the phase of signals applied to the transducer elements can be varied in order to steer the focus electronically from the geometric focus along the transducer axis, the *z* direction.

In Fig. 2 the results of steering to (0,0,−15) mm is shown for annular arrays containing various numbers of elements. An annular array of 6 annuli performed very poorly, the unwanted lobes in the field were numerous and almost the same intensity as the intended focus. An annular array of 8 annuli displayed improved performance, with a clearly discernable focus and a *G* value of 2.4. With 10 annuli, the *G* value increased to 5.7 (well above the $G>4$ criterion), which would provide adequate performance for clinical application.

Truncated spherical annular arrays with different dimensions and operating frequency were investigated earlier by Chapelon *et al.*[7] When the simulation parameters were modified to match those used by Chapelon *et al.*, the results agreed closely with theirs, supporting the validity of the present calculations.

B. Truncated spherical linear (TSL) array

The truncated spherical linear (TSL) array consisted of a truncated spherical shell transducer as used for the TSA array except that the transducer was divided into linear elements along the *y* direction with gaps (λ/2 width) between the elements, see Fig. 1(c). In addition, these linear elements were divided into six elements in the *x* direction, as indicated by the ''subdivision'' lines in the figure. This was required because, for these curved transducers, the appropriate phase

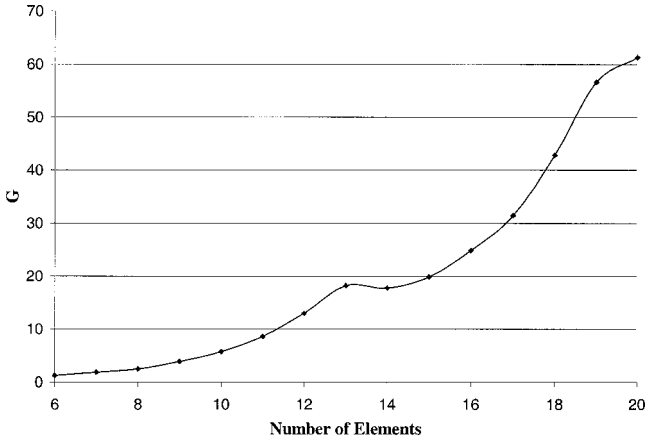

FIG. 2. Ratio of intensity at the focus to intensity of the maximum unwanted lobe versus number of elements for the annular array steered to (0,0,−15). Tissue was present and the gap between elements was 0.5 λ for all these calculations.

for steering also varies along the x direction. This study showed six elements in the x direction (symmetric elements in the $+$ and $-x$ directions have a common phase) were adequate for the steering desired and results shown are for this case only. This was the first design used to investigate the feasibility of focal steering in both the y and z directions.

Focal steering in the x direction was attempted using different numbers of subdivisions in the x direction (6, 12, and 24). The G values were extremely low even when 24 subdivisions were used (resulting in a very large number of elements in the array) and the beam could only be steered 5 mm off center. Based on these results, the current study was limited to examination of steering in only the y and z directions for all arrays studied.

Typical intensity field plots produced by the TSL array with an element width of λ are shown in the $y-z$ plane in Figs. 3(a)–3(c). When the array was focused at its geometric focus the unwanted lobe intensities were found to be much lower than the intensity at the focus (the G values were very large) as seen in Fig. 3(a). When the focus was steered to $(0,-15,0)$ mm, Fig. 3(b), significant unwanted lobes appeared, even for the smaller element widths (λ in this case). Better performance was obtained when steering to $(0,0,-15)$ mm; unwanted lobes can barely be seen in Fig. 3(c) The $x-z$ plane was also examined and it was found that unwanted grating lobes did appear as the array was steered in the z direction. However, these lobes were very close to the focus, so that they had the desirable effect of enlarging the focal region in this direction, which would decrease treatment time. Therefore, in the remainder of this paper the G value is based on an examination of unwanted lobes appearing in the $y-z$ plane.

Results in terms of the value for G versus the element width for the TSL array, unsteered and steered to $(0,-15,0)$ and $(0,0,-15)$ mm, are shown in Fig. 4. These results show that G decreased as the element width increased when the focus was steered away from the geometric focus. When the focus was not steered away from the geometric focus, (0,0,0) mm, the performance was superb, even at the larger element widths. In fact, the performance was approximately the same for all element widths examined. This makes sense since, when the specified focus coincided with the geometric focus, the array geometry dictated the focal position, and the phasing of the elements played no role. From the results for steering to $(0,0,-15)$ mm (i.e., decreasing the depth of the focus by 15 mm), it is apparent that the value for G was much greater than its value for steering the same distance in the y direction. The G value stayed above 7 for all element widths up to 3 λ, resulting in performance that was quite acceptable even at larger element widths. When steering to $(0,-15,0)$ mm, the value for G was low for all element widths, falling below 1 for element widths greater than about 1.6 λ, which was clearly unacceptable. Thus the performance of the TSL array was very poor when steered in the y direction, along the prostate, making it clearly unsuitable for steering in the $y-z$ plane.

A 1.5 D phased array of a similar form was investigated by Curiel *et al.*[44] Their array differed in dimensions and operating frequency, and, in the 1.5 D array, gaps were present between all of the elements except the central pairs, and all elements were of equal area. In agreement with this study, Curiel *et al.* concluded that having five elements in the x direction (achieved by combining the two middle elements of the TSL array into one) was necessary for adequate steering in the y and z directions, and did not attempt to steer in the x direction. However, their calculations differed from this

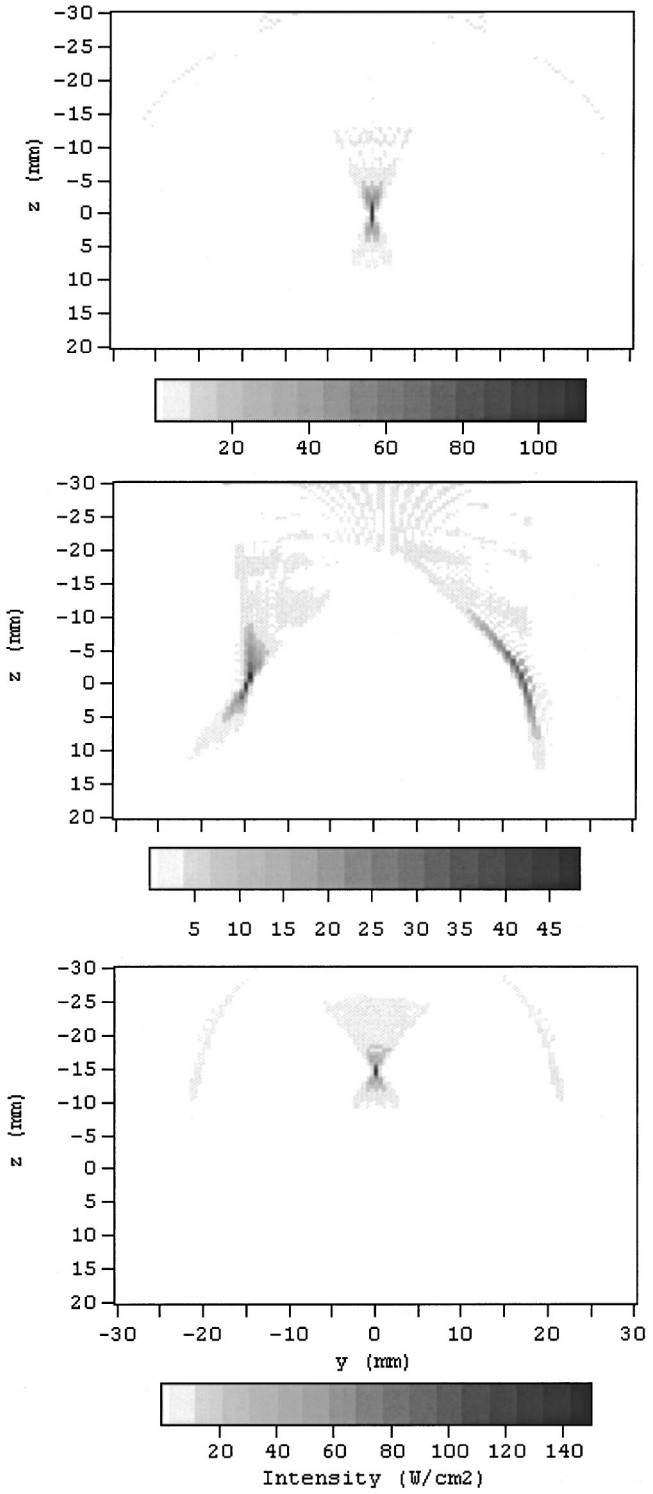

FIG. 3. Intensity as a function of field position for a TSL array with 1 λ wide elements, 0.5 λ gap between elements in the y direction, and 6 elements in the x direction. (a) With no steering; (b) steered to $(0,-15,0)$ mm, (c) steered to $(0,0,-15)$ mm.

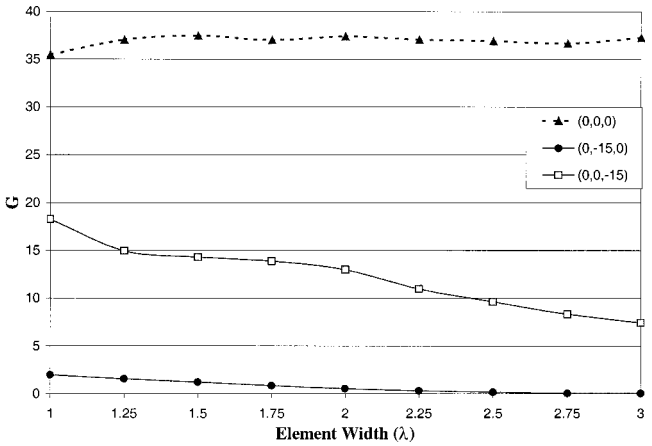

FIG. 4. *G* versus the element width for the TSL array focused at (0,0,0), (0,−15,0) mm, and (0,0,−15) mm.

study in that no tissue was included in their simulation, and the steering extremes were limited to 10 mm from the geometric focus. Another important difference was that they attempted to steer the focus deeper in the *z* direction than the geometric focus, whereas in this study it was found that the performance degraded rapidly when this was attempted. However, overall, the results obtained with the TSL array were in good agreement with their results.

C. Cylindrical array

The cylindrical array provided a line focus along the *y* direction. Note that the origin of the coordinate system for studies involving this array was located on the geometric line focus (i.e., 45 mm away from the center of the array in the *z* direction), and centered on the array in the *y* direction, see Fig. 5. The cylindrical array had a width of 22 mm to allow access through the rectum, and the length was varied from 40 mm to 60 mm. As with the TSL array, six elements were present along the *x* direction, as delineated by the ''subdivisions'' in the figure, in order to improve the focal steering.

Figure 6(a) shows that, for no steering, the value of *G* decreased steadily as the element width increased. The *G* value stayed above 4 for element widths of up to 1.75 λ. The use of larger array lengths appeared to have very little effect on *G* in this case, especially at larger element sizes, where the performance of arrays of different lengths was indistinguishable. In comparing these results to those obtained for the TSL array, the cylindrical array was seen to perform more poorly when the focus was not steered away from the origin. This was because, unlike a spherical array, the cylindrical array produced a geometric line focus rather than a point focus, and therefore required phasing of its elements in order to produce a point focus at the origin. This also led to the fact that the performance of the cylindrical array showed a definite dependence on element size.

The *G* values that resulted from steering the focus of the cylindrical array to (0,−15,0) mm are shown in Fig 6(b). In comparing these results to previous results obtained for the truncated spherical shell array (Fig. 4), the cylindrical array performed better when steered in the *y* direction, staying above 1 for all element widths examined. Furthermore, as the length of the array increased, there was a steady improvement in the performance of the cylindrical array. In fact, the *G* value stayed above 4 for the 60 mm arrays for element widths up to 1.75 λ.

However, the performance of the cylindrical array was much poorer than that for the truncated spherical linear array when steered in the *z* direction, see Fig. 6(c). This was due to the existence of much larger unwanted lobes than were exhibited for the truncated spherical arrays. Relative to earlier results with the TSL arrays (where $G>7$ for all element widths examined), the cylindrical shell displayed a drastic and disappointing decrease in performance when the focus was steered in the *z* direction. The *G* value fell below 4 for element widths greater than 1.5 λ. Increasing the length of the array appeared to provide only a minimal improvement in performance, which disappeared at larger element sizes.

Thus, it was found that the cylindrical array, while

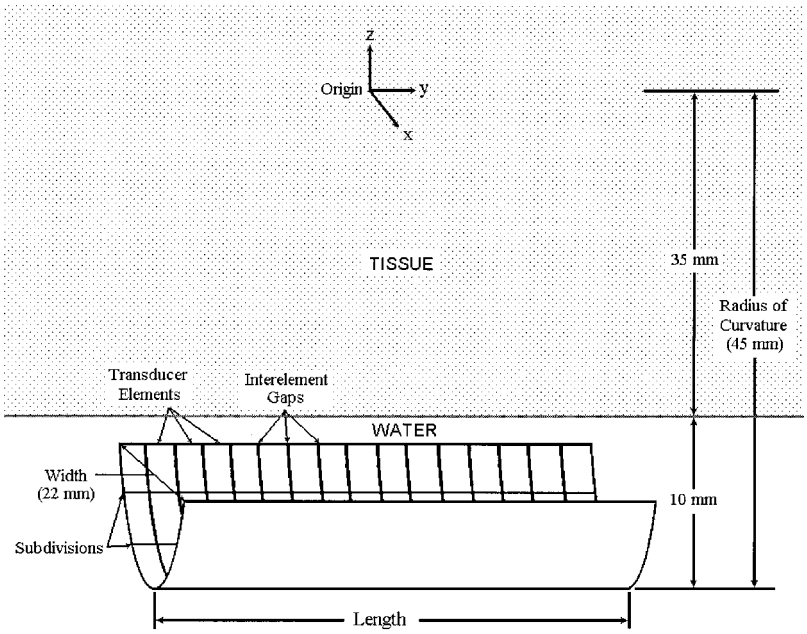

FIG. 5. Side view of cylindrical transducer array.

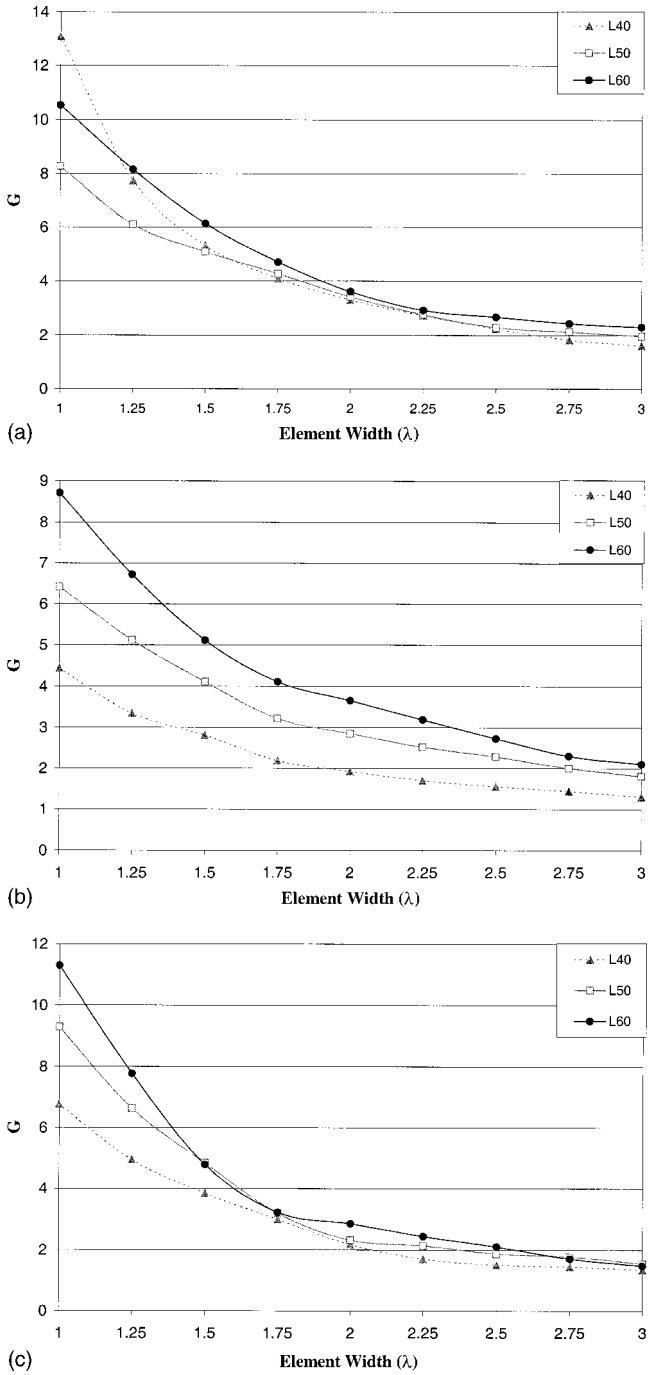

FIG. 6. *G* versus the element width for the cylindrical array with tissue present focused at (0,0,0) mm (a), (0,−15,0) mm (b), and (0,0,−15) mm (c).

showing some improvement in steering in the *y* direction, especially with increased array length, exhibited a drastic increase in the intensity level of unwanted lobes while steering in the *z* direction.

At this point, two transducer array geometries had been examined, which represented opposite extremes of a particular geometric spectrum. The spherical array, with equal curvature in the *x* and *y* directions, behaved poorly when steered in the *y* direction but performed well when steered in the *z* direction. On the other hand, the cylindrical array, which had no curvature in the *y* direction, exhibited improved behavior when steered in the *y* direction but performed much more poorly when steered in the *z* direction. The cylindrical array had the additional advantage that its length could be increased, improving its performance when steered in the *y* direction. Even though these results might have been expected, the present analysis shows just how much performance degrades for the particular array size and configuration.

D. Curved cylindrical (CC) array

The performance of a curved cylindrical (CC) array was examined as a compromise between the spherical and cylindrical arrays. This array, as shown in Fig. 7, was a cylindrical array that had curvature added in the *y* direction. When the radius of curvature of the CC array in the *y* direction equaled the radius of curvature in the *x* direction, the result was an array geometry similar to, but not exactly the same as, a truncated spherical array. With an infinite radius of curvature in the *y* direction, a cylindrical array was obtained. The effects on array performance of varying the radius of curvature in the *y* direction and the array length were investigated. The maximum length of the array was determined by the curvature in the *y* direction, since the ends of the array would eventually extend into the tissue, which was unacceptable. The smaller the radius of curvature, the shorter the maximum array length that could be used.

Figures 8(a)–(c) show the values for *G* as a function of element width, for curved cylindrical arrays for just one of the lengths investigated (50 mm) and for four different radii of curvature (50, 60, 75, and 90 mm). Note that the 50 mm radius of curvature corresponds to the greatest amount of curvature, most like a spherical array, while the 90 mm radius of curvature corresponds to a more gently curved, flatter array, most like a cylindrical array.

In Fig. 8(a), the *G* value is plotted against element width with the focus located at the origin, for 50 mm length arrays of varying curvature. As with the cylindrical array, since the curved cylindrical array lacked a geometric point focus, phasing of the elements was required for focusing at the origin, and therefore performance decreased with increasing element size. It is also apparent that performance (*G* value) decreased with increasing radius of curvature. Since the larger radius of curvature corresponded to a flatter array, these results agree quite well with the previous conclusion that the performance of the flat cylindrical array was inferior to that of the spherical array when the focus was located at the origin. Also, for the same radius of curvature, the *G* values for 60 mm length arrays (not shown in Fig. 8) were slightly lower than those for the 50 mm length arrays, showing a modest decrease in performance with increased array length. In comparing Fig. 8(a) with Fig. 6(a), there was a definite improvement in performance of the CC array over that of the cylindrical array, especially for arrays with shorter radii of curvature, whose performance exceeded even that of the TSL array for small element sizes. In all cases examined, the *G* value remained above 4, even for the largest element widths examined.

The results obtained when steering the curved cylindrical array to (0,−15,0) mm are shown in Fig. 8(b). There was a modest improvement in performance with increasing radius

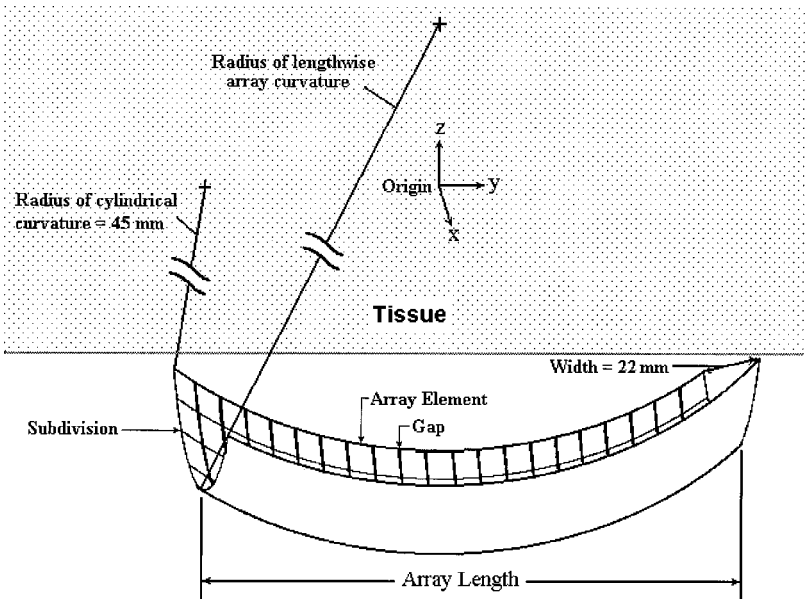

FIG. 7. Diagram of the curved cylindrical (CC) array.

of curvature. These results agreed with the conclusion that the flatter cylindrical array performed better than the truncated spherical array when steered to $(0,-15,0)$ mm. Also, the G values for the 60 mm array length curves, not shown, were higher than for the corresponding 50 mm array length curves, indicating improved performance with increased length, a characteristic which was also seen with the cylindrical array. Although the performance in all cases was not as good as with the cylindrical array of the same length, it was consistently better than that of the truncated spherical array, since G values stay above 1 for element widths as great as 2.25 λ. However, G values above 4 were obtained only for element widths less than 1.25 λ.

Figure 8(c) contains results obtained when the CC array was steered to $(0,0,-15)$ mm. Here, a trend opposite to that seen when steering in the y direction occurs. Performance generally decreased with increasing radius of curvature. These results agree quite well with the earlier conclusion that the spherical array performed better than the cylindrical array when steered in the z direction. Improved performance was obtained when the array length was increased from 50 mm to 60 mm [not shown in Fig. 8(c)], for the same radius of curvature. The performance in all cases was not nearly as good as with the truncated spherical arrays; however, it was consistently better than that of the cylindrical array, especially at larger element widths. In this case, G values above 4 can be achieved at all curvatures for element widths up to 2 λ.

IV. CONCLUSIONS

An analysis of the variation in G value with element size and geometry was conducted, with a G value greater than 4 as a cutoff for clinical applicability. The TSA array was able to electronically steer effectively in the z direction even with a small number of elements ($G>4$ for 10 elements). However, mechanical steering would still be required to move the focus in the x and y directions.

The TSL array was examined as a possible design to provide steering in the y and z directions. (Rotation of the array would still be necessary for steering in the x direction.) Like the TSA array, it was found to perform superbly when steered in the z direction. However, it performed poorly for steering in the y direction.

These results suggest that it is not possible to avoid mechanical steering of transducer arrays along the length of the prostate for transrectal treatment using the truncated spherical array geometry investigated. However, probe replacement during treatment to vary the depth of the focus can be eliminated from current treatments by using either the TSA or TSL arrays. The TSA array would be used for this purpose because it contains far fewer elements.

Results with the TSL array led to the consideration of using cylindrical arrays. The cylindrical array exhibited improved steering in the y direction, relative to the truncated spherical array. However, its performance when steered in the z direction was drastically reduced, relative to the truncated spherical array. Also, taking advantage of the ability to increase the length of the array improved results for y direction steering, and provided minimal improvement for z direction steering.

The curved cylindrical array was devised as a compromise, in order to take advantage of the best features of the spherical and cylindrical arrays. As hoped, the performance of the curved cylindrical array in all cases was between that of the truncated spherical array and the cylindrical array. Because of its variable curvature and length, the curved cylindrical array design may be optimized for steering in both the y and z directions.

In light of the $G>4$ criterion, it would appear that, of the geometries examined, both the 50 mm and 60 mm cylindrical arrays would satisfy this criterion for all focal steering cases examined with element widths as large as 1.5 λ. This was mainly due to superior performance when steering in the y direction, which was the worst steering scenario for the other two array geometries.

This study has investigated the effects of overall array geometry on array performance. In order to further improve the performance of the arrays, a number of other methods

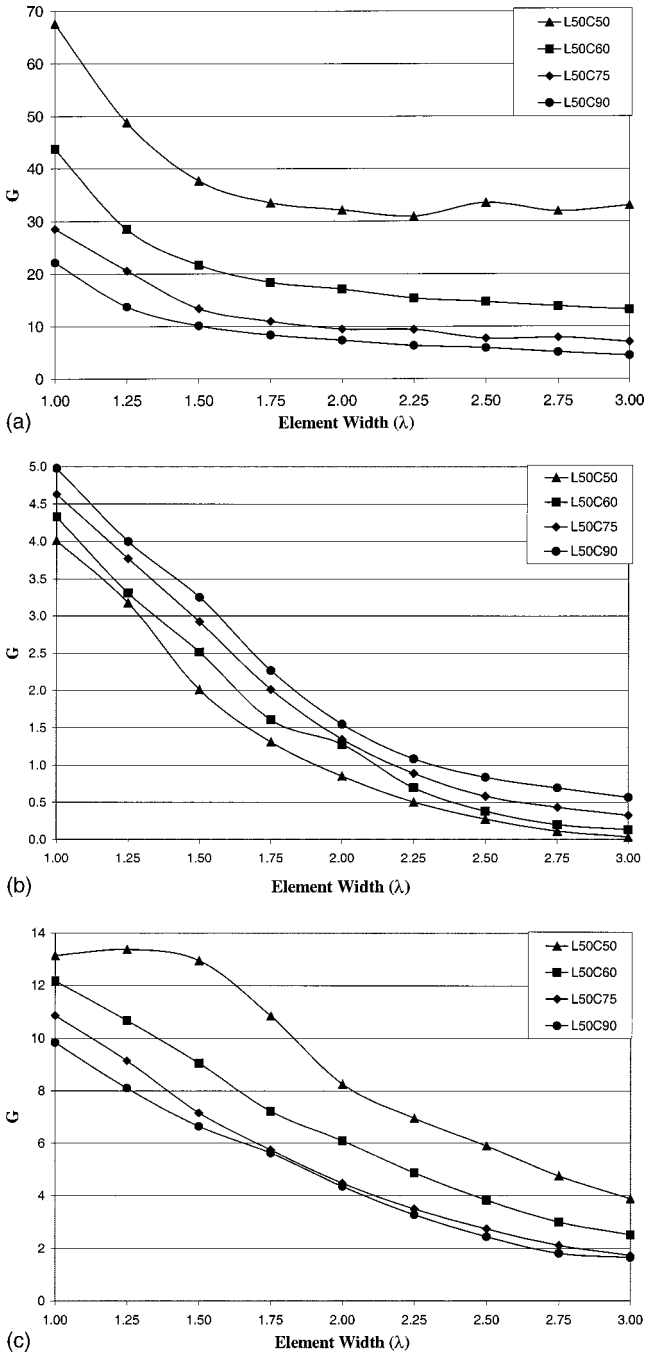

FIG. 8. *G* versus the element width for the CC array focused at (0,0,0) mm (a), (0,−15,0) mm (b), (0,0,−15) mm (c), with tissue present. Results are shown for a 50 mm length and different curvatures in the *y* direction.

may be employed. The randomization of element sizes may be used to decrease the intensity of unwanted lobes.[23] Use of only the portion of the array that contributes most directly to the intended focus can improve results by diminishing the amount of energy going into unwanted lobes.[32]

ACKNOWLEDGMENTS

The authors gratefully acknowledge help developing the early software by Rabin Pirakitti. This work was supported in part by U.S. Public Health Service Grants Nos. R43 CA 81340 and T32 CA 09067, awarded by the National Cancer Institute DHHS.

[1] A. Grove, ''Taking on prostate cancer,'' Fortune **133**, 54–56 (1996).
[2] L. Jaroff, ''The man's cancer,'' Time **147**, 58–65 (1996).
[3] J. Henkel, ''Prostate cancer: no one answer for testing or treatment,'' FDA Consum. **32**, 22–27 (1998).
[4] J. J. M. C. H. De la Rosette, F. C. H. D'ancona, and F. M. J. Debruyne, ''Current status of thermotherapy of the prostate,'' J. Urol. (Baltimore) **157**, 430–438 (1997).
[5] T. Parkins, ''Concern grows over prostate cancer treatment options,'' J. Natl. Cancer Inst. **86**, 897–898 (1994).
[6] T. R. Williams and N. Love, ''Treatment of localized prostate cancer,'' Postgrad Med. **100**, 105 (1996).
[7] J. Y. Chapelon, P. Faure, M. Plantier, D. Cathignol, R. Souchon, F. Gorry, and A. Gelet, ''The feasibility of tissue ablation using high intensity electronically focused ultrasound,'' Proc.-IEEE Ultrason. Symp., 1211–1214 (1993).
[8] F. L. Lizzi, ''High-precision thermotherapy for small lesions,'' Eur. Urol. **23**, 23–28 (1993).
[9] G. ter Haar, ''Ultrasound focal beam surgery,'' Ultrasound Med. Biol. **21**, 1089–1100 (1995).
[10] C. J. Diedrich and E. C. Burdette, ''Transurethral ultrasound array for prostate thermal therapy: initial studies,'' IEEE Trans. Ultrason. Ferroelectr. Freq. Control **UFFC-43**, 1011–1021 (1996).
[11] L. A. Frizzell, S. A. Goss, J. T. Kouzmanoff, and J. M. Yang, ''Sparse random ultrasound array for focal surgery,'' Proc.-IEEE Ultrasonics Symp. 1319–1323 (1996).
[12] S. A. Goss, L. A. Frizzell, J. T. Kouzmanoff, J. M. Barich, and J. M. Yang, ''Sparse random ultrasound phased array for focal surgery,'' IEEE Trans. Ultrason. Ferroelectr. Freq. Control **43**, 1111–1121 (1996).
[13] A. L. Malcolm and G. R. ter Haar, ''Ablation of tissue volumes using high intensity focused ultrasound,'' Ultrasound Med. Biol. **22**, 659–669 (1996).
[14] R. J. McGough, M. L. Kessler, E. S. Ebbini, and C. A. Cain, ''Treatment planning for hyperthermia with ultrasound phased arrays,'' IEEE Trans. Ultrason. Ferroelectr. Freq. Control **UFFC-43**, 1074–1084 (1996).
[15] I. H. Rivens, R. L. Clarke, and G. R. ter Haar, ''Design of focused ultrasound surgery transducers,'' IEEE Trans. Ultrason. Ferroelectr. Freq. Control **UFFC-43**, 1023–1031 (1996).
[16] N. T. Sanghvi, K. Hynynen, and F. L. Lizzi, ''New developments in therapeutic ultrasound,'' IEEE Eng. Med. Biol. Mag. **15**, 83–92 (1996).
[17] H. Wan, P. VanBaren, E. S. Ebbini, and C. A. Cain, ''Ultrasound surgery: comparison of strategies using phased array systems,'' IEEE Trans. Ultrason. Ferroelectr. Freq. Control **UFFC-43**, 1085–1097 (1996).
[18] F. Prat, J. Y. Chapelon, A. Arefiev, D. Cathignol, R. Souchon, and Y. Theilliere, ''High-intensity focused ultrasound transducers suitable for endoscopy: feasibility study in rabbits,'' Gastroint. Endoscop. **46**, 348–351 (1997).
[19] A. Gelet, J. Y. Chapelon, R. Bouvier, C. Pangaud, and Y. Lasne, ''Local control of prostate cancer by transrectal high intensity focused ultrasound therapy: preliminary results,'' J. Urol. (Baltimore) **161**, 156–162 (1999).
[20] N. T. Sanghvi, R. S. Foster, R. Bihrle, R. Casey, T. Uchida, M. H. Phillips, J. Syrus, A. V. Zaitsev, K. W. Marich, and F. J. Fry, ''Noninvasive surgery of prostate tissue by high intensity focused ultrasound: an updated report,'' Eur. J. Ultrasound **9**, 19–29 (1999).
[21] N. T. Sanghvi, R. S. Foster, F. J. Fry, R. Bihrle, C. Hennige, and L. V. Hennige, ''Ultrasound intracavity system for imaging, therapy planning and treatment of focal disease,'' Proc.-IEEE Ultrasonics Sym., 1249–1253 (1992).
[22] S. Madersbacher, M. Pedevilla, L. Vingers, M. Susani, and M. Marberger, ''Effect of high-intensity focused ultrasound on human prostate cancer in vivo,'' Cancer Res. **55**, 3346–3351 (1995).
[23] E. B. Hutchinson, M. T. Buchanan, and K. Hynynen, ''Design and optimization of an aperiodic ultrasound phased array for intracavitary prostate thermal therapies,'' Med. Phys. **23**, 767–776 (1996).
[24] E. B. Hutchinson and K. Hynynen, ''Intracavitary ultrasound phased arrays for noninvasive prostate surgery,'' IEEE Trans. Ultrason. Ferroelectr. Freq. Control **UFFC-43**, 1032–1042 (1996).
[25] J. Y. Chapelon, M. Ribault, F. Vernier, F. R. Souchon, and A. Gelet, ''Treatment of localised prostate cancer with transrectal high intensity focused ultrasound,'' Eur. J. Ultrasound **9**, 31–38 (1999).
[26] J. Y. Chapelon, J. Margonari, F. Vernier, F. Gorry, R. Ecochard, and A. Gelet, ''In vivo effects of high-intensity ultrasound on prostatic adenocarcinoma,'' Cancer Res. **52**, 6353–6357 (1992).
[27] G. O. Oosterhof, E. B. Cornel, G. A. Smits, F. M. Debruyne, and J. A.

Schalken, ''Influence of high-intensity focused ultrasound on the development of metastases,'' Eur. Urol. **32**, 91–95 (1997).
[28] A. Gelet, J. Y. Chapelon, J. Margonari, Y. Theillere, F. Gorry, D. Cathignol, and E. Blanc, ''Prostatic tissue destruction by high-intensity focused ultrasound: experimentation on canine prostate,'' J. Endourol. **7**, 249–253 (1993).
[29] C. Damianou and K. Hynynen, ''Focal spacing and near-field heating during pulsed high temperature ultrasound therapy,'' Ultrasound Med. Biol. **19**, 777–787 (1993).
[30] X. Fan and K. Hynynen, ''Ultrasound surgery using multiple sonications—treatment time considerations,'' Ultrasound Med. Biol. **22**, 471–482 (1996).
[31] E. S. Ebbini and C. A. Cain, ''Multiple-focus ultrasound phased-array pattern synthesis: optimal driving-signal distributions for hyperthermia,'' IEEE Trans. Ultrason. Ferroelectr. Freq. Control **UFFC-36**, 540–548 (1989).
[32] L. R. Gavrilov and J. W. Hand, ''Design and experimental evaluation of an endocavitary linear phased array for ultrasound surgery of prostate,'' Acoust. Phys. **46**, 144–152 (2000).
[33] L. R. Gavrilov and J. W. Hand, ''A theoretical assessment of the relative performance of spherical phased arrays for ultrasound surgery,'' IEEE Trans. Ultrason. Ferroelectr. Freq. Control **UFFC-47**, 125–139 (2000).
[34] C. A. Cain and S. Umemura, ''Concentric-ring and sector-vortex phased-array applicators for ultrasound hyperthermia,'' IEEE Trans. Microwave Theory Tech. **MTT-34**, 542–551 (1986).
[35] J. W. Hand, E. Ebbini, D. O'Keeffe, D. Israel, and S. Mohammadtaghi, ''An ultrasound linear array for use in intracavitary applicators for thermotherapy of prostatic diseases,'' Proc.-IEEE Ultrason. Symp., 1225–1228 (1993).
[36] E. S. Ebbini and C. A. Cain, ''A spherical-section ultrasound phased array applicator for deep localized hyperthermia,'' IEEE Trans. Biomed. Eng. **38**, 634–643 (1991).
[37] P. VanBaren, C. Simon, R. Seip, T. Solf, C. Cain, and E. Ebbini, ''Image-guided phased array system for ultrasound thermotherapy,'' Proc.-IEEE Ultrason. Symp., 1269–1272 (1996).
[38] M. Bechtold, B. Granz, H. P. Heindel, and K. Newerla, ''A linear phased array for prostate therapy,'' Proc.-IEEE Ultrason. Symp., 1385–1388 (1997).
[39] J. Zemanek, ''Beam behavior within the nearfield of the vibrating piston,'' J. Acoust. Soc. Am. **49**, 181–191 (1970).
[40] D. A. Hutchins, H. D. Mair, P. A. Puhach, and A. J. Osei, ''Continuous-wave pressure fields of utrasonic transducers,'' J. Acoust. Soc. Am. **18**, 1–12 (1986).
[41] K. B. Ocheltree and L. A. Frizzell, ''Sound field calculation for rectangular sources,'' IEEE Trans. Ultrason. Ferroelectr. Freq. Control **UFFC-36**, 242–248 (1989).
[42] N. T. Sanghvi, F. J. Fry, R. Bihrle, R. S. Foster, M. H. Phillips, J. Syrus, A. V. Zaitsev, and C. W. Hennige, ''Noninvasive surgery of prostate tissue by high-intensity focused ultrasound,'' IEEE Trans. Ultrason. Ferroelectr. Freq. Control **UFFC-43**, 1099–1110 (2000).
[43] J. S. Tan, L. A. Frizzell, N. T. Sanghvi, R. Seip, J. S. Wu, and J. T. Kouzmanoff, ''Design of focused ultrasound phased array for prostate treatment,'' Proc.-IEEE Ultrason. Symp., 1247–1251 (2000).
[44] L. Curiel, F. Chavrier, R. Souchon, A. Birer, and J. Y. Chapelon, ''1.5D multi-elements phased array applied to high intensity focused ultrasound,'' Proc.-IEEE Ultrason. Symp., 1451–1454 (1999).

Enhanced weak integral formulation for the mixed ($\underline{u}$,$\underline{p}$) poroelastic equations

Noureddine Atalla
Mechanical Engineering Department, GAUS, Université de Sherbrooke, Québec J1K 2R1, Canada

M. A. Hamdi
Université de Technologie de Compiègne, Compiègne, France

Raymond Panneton
Mechanical Engineering Department, GAUS, Université de Sherbrooke, Québec J1K 2R1, Canada

(Received 14 July 2000; revised 23 February 2001; accepted 24 February 2001)

Recently Atalla *et al.* [J. Acoust. Soc. Am. **104**, 1444–1452 (1998)] and Debergue *et al.* [J. Acoust. Soc. Am. **106**, 2383–2390 (1999)] presented a weak integral formulation and the general boundary conditions for a mixed pressure-displacement version of the Biot's poroelasticity equations. Finite element discretization was applied to the formulation to solve 3D vibro-acoustic problems involving elastic, acoustic, and poroelastic domains. In this letter, an enhancement of the weak integral formulation is proposed to facilitate its finite element implementation. It is shown that this formulation simplifies the assembly process of the poroelastic medium, the imposition of its boundary conditions, and its coupling with elastic and acoustic media. © *2001 Acoustical Society of America.* [DOI: 10.1121/1.1365423]

PACS numbers: 43.20.Gp, 43.50.Gf, 43.55.Dt [CBB]

I. INTRODUCTION

Consider the problem depicted in Fig. 1. A primary poroelastic domain Ω is supported and excited on its bounding surface Γ. This primary poroelastic domain is surrounded by elastic, acoustic, and secondary poroelastic domains. It may include an impervious screen. Atalla *et al.*[1] presented a mixed pressure-displacement formulation of the Biot's poroelasticity equations and Debergue *et al.*[2] presented the associated boundary and coupling conditions to solve the problem depicted in Fig. 1. Assuming harmonic time dependence, the integral equations governing the harmonic behavior of a poroelastic medium are given by Atalla *et al.*:[1]

$$\int_\Omega \hat{\underline{\underline{\sigma}}}^s(\underline{u}):\underline{\underline{\epsilon}}^s(\delta\underline{u})d\Omega-\omega^2\int_\Omega \tilde{\rho}\underline{u}\cdot\delta\underline{u}\,d\Omega-\int_\Omega \tilde{\gamma}\underline{\nabla}p \cdot \delta\underline{u}\,d\Omega-\int_\Gamma[\hat{\underline{\underline{\sigma}}}^s\cdot\underline{n}]\cdot\delta\underline{u}\,dS=0,\quad \forall(\delta\underline{u}), \tag{1}$$

$$\int_\Omega\left[\frac{\phi^2}{\omega^2\tilde{\rho}_{22}}\underline{\nabla}p\cdot\underline{\nabla}\delta p-\frac{\phi^2}{\tilde{R}}p\,\delta p\right]d\Omega-\int_\Omega\tilde{\gamma}\underline{\nabla}\delta p\cdot\underline{u}\,d\Omega+\int_\Gamma\left[\tilde{\gamma}u_n-\frac{\phi^2}{\tilde{\rho}_{22}\omega^2}\frac{\partial p}{\partial n}\right]\delta p\,dS=0\quad\forall(\delta p). \tag{2}$$

Here, Ω and Γ refer to the poroelastic domain and its bounding surface. ϕ is the porosity of the porous material. $\underline{u}$ and p are the solid phase displacement vector and the interstitial fluid pressure of the poroelastic medium, respectively, while $\delta\underline{u}$ and δp refer to their admissible variation. $\underline{n}$ is the unit external normal vector around the bounding surface Γ, and subscript n denotes the normal component of a vector. The effective densities $\tilde{\rho}$, $\tilde{\rho}_{22}$ and the coupling coefficient $\tilde{\gamma}$ are given by Atalla *et al.*[1] where the tilde symbol is used to indicate that a quantity is complex. $\underline{\underline{\epsilon}}^s$ is the strain tensor of the solid phase and $\hat{\underline{\underline{\sigma}}}^s$ is the modified stress tensor of the solid phase (it represents the stress tensor of the solid phase *in vacuo* for acoustic materials where the porosity is close to one) that is related to the total stress tensor $\underline{\underline{\sigma}}^t$ of the material by the following relation:[1]

$$\hat{\underline{\underline{\sigma}}}^s(\underline{u})=\underline{\underline{\sigma}}^t(\underline{u},\underline{U})+\phi[1+(\tilde{Q}/\tilde{R})]p\cdot\underline{\underline{1}}, \tag{3}$$

where $\underline{u}$ and $\underline{U}$ refer to the solid and fluid macroscopic displacement vectors, $\tilde{Q}$ is an elastic coupling coefficient between the two phases, and $\tilde{R}$ may be interpreted as the bulk modulus of the air occupying a fraction ϕ of a unit volume of aggregate. Elastic coefficients $\tilde{Q}$ and $\tilde{R}$ are related to K_b, the bulk modulus of the porous material *in vacuo*, to K_s, the bulk modulus of the elastic solid from which the skeleton is made, and to $\tilde{K}_f$, the effective bulk modulus of the air in the pores by the following relations:[3]

$$\tilde{Q}=\frac{[1-\phi-K_b/K_s]\phi K_s}{1-\phi-K_b/K_s+\phi K_s/\tilde{K}_f}, \tag{4}$$

$$\tilde{R}=(\phi^2K_s)/(1-\phi-K_b/K_s+\phi K_s/\tilde{K}_f). \tag{5}$$

To simplify the formulation and its coupling with elastic, porous, and acoustic media, Atalla *et al.*[1] used the fact that for the majority of porous materials used in acoustics, the bulk modulus of the porous material is negligible compared to the bulk modulus of the material from which the skeleton is made: $K_b/K_s\ll1$,[3] thus:

$$\phi[1+(\tilde{Q}/\tilde{R})]=1-(K_b/K_s)\cong1. \tag{6}$$

Using this assumption, the coupling of the ($\underline{u}$,p) formulation with elastic, acoustic, and porous elastic media becomes simple. A detailed derivation and discussion of these cou-

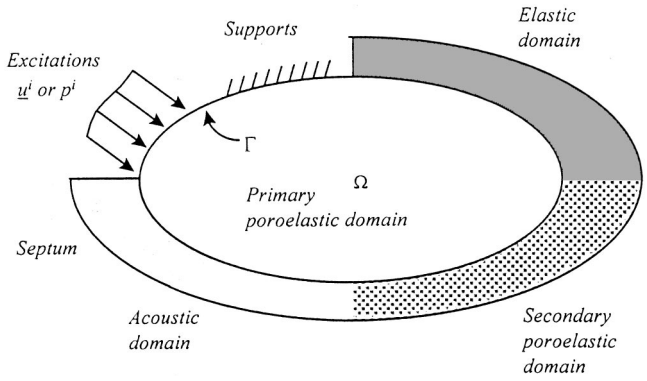

FIG. 1. Typical boundary conditions on a poroelastic domain.

pling conditions are given by Debergue *et al.*[2] It shows that, in this formulation, a poroelastic medium couples naturally with acoustic and poroelastic media; and couples through a classical fluid-structure coupling matrix with elastic media (solids, septa, etc.). The objective of this letter is to present an improved formulation that eliminates the need of approximation (6) and couples naturally with elastic and poroelastic media, thus making the numerical implementation accurate and easier.

II. ENHANCED ($\underline{u}$,p) WEAK FORMULATION

Using Eq. (3) and the relation between the fluid phase displacement vector $\underline{U}$ and the pressure gradient $\underline{\nabla} p$:[1]

$$\underline{U} = (h/\tilde{\rho}_{22}\omega^2)\underline{\nabla} p - (\tilde{\rho}_{12}/\tilde{\rho}_{22})\underline{u}, \tag{7}$$

and the expression of the coupling coefficient $\tilde{\gamma}$ given by[1]

$$\tilde{\gamma} = \phi\left(\frac{\tilde{\rho}_{12}}{\tilde{\rho}_{22}} - \frac{\tilde{Q}}{\tilde{R}}\right). \tag{8}$$

Equations (1) and (2) rewrite, $\forall(\delta p)$, $\forall(\delta\underline{u})$:

$$\int_\Omega \hat{\underline{\underline{\sigma}}}^s(u):\underline{\underline{\epsilon}}^s(\delta\underline{u})\,d\Omega - \omega^2\int_\Omega \tilde{\rho}\underline{u}\cdot\delta\underline{u}\,d\Omega - \int_\Omega \tilde{\gamma}\underline{\nabla} p\cdot\delta\underline{u}\,d\Omega - \int_\Gamma (\underline{\underline{\sigma}}^t\cdot\underline{n})\cdot\delta\underline{u}\,dS - \int_\Gamma \phi\left(1+\frac{\tilde{Q}}{\tilde{R}}\right) p\,\delta u_n\,dS = 0, \tag{9}$$

$$\int_\Omega \left[\frac{\phi^2}{\omega^2\tilde{\rho}_{22}}\underline{\nabla} p\cdot\underline{\nabla}\delta p - \frac{\phi^2}{\tilde{R}} p\,\delta p\right] d\Omega - \int_\Omega \tilde{\gamma}\underline{\nabla}\delta p\cdot\underline{u}\,d\Omega - \int_\Gamma \phi(U_n - u_n)\,\delta p\,dS - \int_\Gamma \phi\left(1+\frac{\tilde{Q}}{\tilde{R}}\right) u_n\delta p\,dS = 0. \tag{10}$$

Assuming a homogeneous medium, application of the divergence theorem on the last surface integral of Eqs. (9) and (10) with the use of the vector identity, $\underline{\nabla}\cdot(\beta\underline{\mathbf{b}}) = \beta\underline{\nabla}\cdot\underline{\mathbf{b}} + \underline{\nabla}\beta\cdot\underline{\mathbf{b}}$, lead to the following set of equations:

$$\int_\Omega \hat{\underline{\underline{\sigma}}}^s(u):\underline{\underline{\epsilon}}^s(\delta\underline{u})\,d\Omega - \omega^2\int_\Omega \tilde{\rho}\underline{u}\cdot\delta\underline{u}\,d\Omega - \int_\Omega \left(\tilde{\gamma}+\phi\left(1+\frac{\tilde{Q}}{\tilde{R}}\right)\right)\underline{\nabla} p\cdot\delta\underline{u}\,d\Omega - \int_\Omega \phi\left(1+\frac{\tilde{Q}}{\tilde{R}}\right) p\underline{\nabla}\cdot\delta\underline{u}\,d\Omega - \int_\Gamma (\underline{\underline{\sigma}}^t\cdot\underline{n})\,\delta\underline{u}\,dS = 0,$$

$$\int_\Omega \left[\frac{\phi^2}{\omega^2\tilde{\rho}_{22}}\underline{\nabla} p\cdot\underline{\nabla}\delta p - \frac{\phi^2}{\tilde{R}} p\,\delta p\right] d\Omega - \int_\Omega \left(\tilde{\gamma}+\phi\left(1+\frac{\tilde{Q}}{\tilde{R}}\right)\right)\times\underline{\nabla}\delta p\cdot\underline{u}\,d\Omega - \int_\Omega \phi\left(1+\frac{\tilde{Q}}{\tilde{R}}\right)\delta p\underline{\nabla}\cdot\underline{u}\,d\Omega - \int_\Gamma \phi(U_n-u_n)\,\delta p\,dS = 0.$$

Noting that $\tilde{\gamma}+\phi(1+\tilde{Q}/\tilde{R}) = \phi/\tilde{\alpha}$, where $\tilde{\alpha}$ is the dynamic tortuosity, and summing the two previous equations, the new expression of the ($\underline{u}$,p) weak formulation reads, $\forall(\delta p)$, $\forall(\delta\underline{u})$:

$$\int_\Omega \hat{\underline{\underline{\sigma}}}^s(u):\underline{\underline{\epsilon}}^s(\delta\underline{u})\,d\Omega - \omega^2\int_\Omega \tilde{\rho}\underline{u}\cdot\delta\underline{u}\,d\Omega + \int_\Omega \left[\frac{\phi^2}{\omega^2\tilde{\rho}_{22}}\underline{\nabla} p\cdot\underline{\nabla}\delta p - \frac{\phi^2}{\tilde{R}} p\,\delta p\right] d\Omega - \int_\Omega \frac{\phi}{\tilde{\alpha}}\delta(\underline{\nabla} p\cdot\underline{u})\,d\Omega - \int_\Omega \phi\left(1+\frac{\tilde{Q}}{\tilde{R}}\right)\delta(p\underline{\nabla}\cdot\underline{u})\,d\Omega - \int_\Gamma (\underline{\underline{\sigma}}^t\cdot\underline{n})\cdot\delta\underline{u}\,dS - \int_\Gamma \phi(U_n-u_n)\,\delta p\,dS = 0. \tag{11}$$

This form shows that the coupling between the two phases is volumetric and of two natures: (i) kinetic (or inertial), $\int_\Omega(\phi/\tilde{\alpha})\,\delta(\underline{\nabla} p\cdot\underline{u})\,d\Omega$, and (ii) potential (or elastic), $\int_\Omega \phi(1+\tilde{Q}/\tilde{R})\,\delta(p\underline{\nabla}\cdot\underline{u})\,d\Omega$. It is shown in the next section, that this new formulation couples naturally to elastic and porous media with no recourse to approximation (6).

III. COUPLING CONDITIONS

Considering the generic problem depicted in Fig. 1, the coupling conditions applied on the bounding surface Γ are of four types: (i) poroelastic–elastic, (ii) poroelastic–acoustic, (iii) poroelastic–poroelastic, and (iv) poroelastic–septum. This section discusses these coupling conditions together with two loading conditions, imposed surface pressure and imposed surface displacement, using the new ($\underline{u}$,p) formulation.

A. Poroelastic–elastic coupling condition

In the presented form of the ($\underline{u}$,p) formulation, the porous media couples to other media through the following boundary terms:

$$I^p = -\int_\Gamma (\underline{\underline{\sigma}}^t\cdot\underline{n})\,\delta\underline{u}\,dS - \int_\Gamma \phi(U_n-u_n)\,\delta p\,dS. \tag{12}$$

The elastic medium is described in terms of its displacement vector $\underline{u}^e$. If the weak formulation of the poroelastic medium is combined with the one of the elastic medium, the boundary integrals of the assembly rewrite:

$$I^p + I^e = -\int_\Gamma (\underline{\underline{\sigma}}^t \cdot \underline{n}) \cdot \delta \underline{u}\, dS - \int_\Gamma \phi (U_n - u_n) \cdot \delta p\, dS + \int_\Gamma (\underline{\underline{\sigma}}^e \cdot \underline{n}) \cdot \delta \underline{u}\, dS, \tag{13}$$

where $\underline{\underline{\sigma}}^e$ represents the stress tensor of the elastic medium. The positive sign of the third term is due to the direction of the normal vector $\underline{n}$ which is inwards to the elastic medium. The coupling conditions at the interface Γ are given by

$$\underline{\underline{\sigma}}^t \cdot \underline{n} = \underline{\underline{\sigma}}^e \cdot \underline{n}, \quad \phi (U_n - u_n) = 0, \quad \underline{u} = \underline{u}^e. \tag{14}$$

The first equation ensures the continuity of the total normal stresses at the interface. The second equation expresses the fact that there is no relative mass flux across the impervious interface. The third equation ensures the continuity of the solid displacement vectors. Substituting Eq. (14) into Eq. (13), one obtains: $I^p + I^e = 0$; this equation shows that the coupling between the poroelastic and the elastic media is natural. Only the kinematic boundary condition $\underline{u} = \underline{u}^e$ will have to be explicitly imposed on Γ. In a finite element implementation, this may be done automatically through assembling between the solid phase of the porous media and the elastic media.

B. Poroelastic–acoustic coupling condition

The acoustic medium is described in terms of its pressure field p^a. Combining both the weak formulations of the poroelastic and acoustic media the boundary integrals can be rewritten:

$$I^p + I^a = -\int_\Gamma (\underline{\underline{\sigma}}^t \cdot \underline{n}) \cdot \delta \underline{u}\, dS - \int_\Gamma \phi (U_n - u_n) \cdot \delta p\, dS + \int_\Gamma \frac{1}{\rho_0 \omega^2} \frac{\partial p^a}{\partial n} \cdot \delta p^a\, dS, \tag{15}$$

where ρ_0 refers to the density of the acoustic medium. The positive sign of the last term of $I^p + I^a$ is due to the direction of the normal vector $\underline{n}$, inwards to the acoustic medium. The coupling conditions at the interface Γ are given by

$$\underline{\underline{\sigma}}^t \cdot \underline{n} = -p^a \underline{n}, \quad \frac{1}{\rho_0 \omega^2} \frac{\partial p^a}{\partial n} = (1-\phi) u_n + \phi U_n = u_n + \phi (U_n - u_n), \quad p = p^a. \tag{16}$$

The first equation ensures the continuity of the normal stresses on Γ. The second equation ensures the continuity between the acoustic displacement and the total poroelastic displacement on Γ. The third equation refers to the continuity of the pressure across the boundary. Substituting Eq. (16) in the boundary integral, Eq. (15), leads to

$$I^p + I^a = \int_\Gamma \delta (p^a u_n) dS. \tag{17}$$

This equation shows that the poroelastic medium will be coupled to the acoustic medium through the classical structure–cavity coupling term. This coupling occurs naturally between the solid phase normal displacement and the acoustic pressure on Γ. In addition to this surface coupling term, the kinematic boundary condition $p = p^a$ will have to be explicitly imposed on Γ. Once again, in a finite element implementation, this may be done automatically through assembling.

C. Poroelastic–poroelastic coupling condition

Let indices 1 and 2 denote the primary and secondary poroelastic media, respectively. Here, $\underline{n}$ is the normal vector outwards to the primary poroelastic medium. Both media are described in terms of their solid phase displacement vector $\underline{u}$ and pore fluid pressure p. Combining the weak integral formulations of both poroelastic media, the boundary integrals rewrite:

$$I_1^p + I_2^p = -\int_\Gamma (\underline{\underline{\sigma}}_1^t \cdot \underline{n}) \cdot \delta \underline{u}_1 dS - \int_\Gamma \phi_1 (U_{1n} - u_{1n}) \cdot \delta p_1 dS + \int_\Gamma (\underline{\underline{\sigma}}_2^t \cdot \underline{n}) \cdot \delta \underline{u}_2 dS + \int_\Gamma \phi_2 (U_{2n} - u_{2n}) \cdot \delta p_2 dS, \tag{18}$$

where subscripts 1 and 2 refer to the primary and secondary poroelastic media, respectively. The opposite signs between the two first terms and the two last terms are due to the direction of the normal vector $\underline{n}$, outwards to the primary poroelastic medium. The coupling equations at the interface Γ are given by

$$\underline{\underline{\sigma}}_1^t \cdot \underline{n} = \underline{\underline{\sigma}}_2^t \cdot \underline{n}, \quad \phi_1 (U_{1n} - u_{1n}) = \phi_2 (U_{2n} - u_{2n}), \quad \underline{u}_1 = \underline{u}_2, \quad p_1 = p_2. \tag{19}$$

The first condition ensures the continuity of the total normal stresses. The second equation ensures the continuity of the relative mass flux across the boundary. The two last equations ensure the continuity of the solid phase displacement and pore fluid pressure fields across the boundary, respectively. Using these boundary conditions, the boundary integral reduces to $I^p + I^e = 0$, showing that the coupling between the two poroelastic media is natural. Only the kinematic relations $\underline{u}_1 = \underline{u}_2$ and $p_1 = p_2$ will have to be explicitly imposed on Γ. In a finite element implementation, this may be done automatically through assembling.

D. Poroelastic–septum coupling condition

Here, the septum is represented by the surface domain $\underline{S}$. It is assumed to be a limp and thin impervious layer having a surface density m. The septum is described in terms of its displacement vector $\underline{u}^s$. One side of the septum is in contact with the poroelastic domain (i.e., surface $S^- = \Gamma$), and the other side supports a given load (i.e., surface S^+).

The hypothesis of a thin layer supposes that $\underline{S}$ and Γ are virtually the same. The principle of virtual work applied to the septum leads to

$$I^s = \int_S \omega^2 m \underline{u}^s \cdot \delta \underline{u}^s \, dS + \int_{S^- \cup S^+} \underline{t} \cdot \delta \underline{u}^s \, dS = 0. \tag{20}$$

The first term corresponds to the virtual work of the inertial forces while the second term corresponds to the virtual work of the exterior traction forces. Combining the weak integral formulations of the poroelastic media and the septum, the boundary integrals can be rewritten:

$$\begin{aligned} I^p + I^S = & - \int_\Gamma (\underline{\underline{\sigma}}^t \cdot \underline{n}) \cdot \delta \underline{u} \, dS - \int_\Gamma \phi (U_n - u_n) \delta p \, dS \\ & - \int_S \omega^2 m (\underline{u}^s \cdot \delta \underline{u}^s) dS - \int_{S^-} \underline{t} \cdot \delta \underline{u}^s \, dS \\ & - \int_{S^+} \underline{t} \cdot \delta \underline{u}^s \, dS. \end{aligned} \tag{21}$$

The exterior forces acting on the septum are written as follows:

$$\begin{aligned} & \underline{t}^- = - \underline{\underline{\sigma}}^t \cdot \underline{n} \quad \text{on} \quad S^-, \\ & \underline{t}^+ = \underline{F} \quad \text{on} \quad S^+, \end{aligned} \tag{22}$$

where $\underline{\underline{\sigma}}^t$ is the total stress tensor of the poroelastic medium, and $\underline{F}$ is the traction force vector applied on the septum. Also, since the septum is assumed thin and impervious, the following conditions have to be verified at the septum-poroelastic interface:

$$\phi (U_n - u_n) = 0, \quad \underline{u} = \underline{u}^s.$$

The first relation indicates that there is no mass flux across the boundary Γ, and the second relation expresses the continuity of the displacement vectors. By considering the hypothesis of a thin layer, $\Gamma = S = S^- = S^+$ and using these boundary conditions, the coupling term can be rewritten:

$$I^p + I^S = - \int_\Gamma m \omega^2 (\underline{u} \cdot \delta \underline{u}) \, dS - \int_\Gamma \underline{F} \cdot \delta \underline{u} \, dS. \tag{23}$$

Therefore, the effect of the impervious screen on the poroelastic medium consists in an added mass and excitation terms.

E. Case of an imposed pressure field

In the case of an imposed pressure field p^i applied on Γ (used in some cases to simulate an acoustic plane wave—in this case the blocked pressure is used), the boundary conditions are

$$\underline{\underline{\sigma}}^t \cdot \underline{n} = - p^i \underline{n}, \quad p = p^i, \tag{24}$$

which express the continuity of the total normal stress and the continuity of the pressure (i.e., no pressure drop) through the interface Γ. Since the pressure is imposed, the admissible variation δp will fall to zero. Consequently, the surface integrals of (11) simplify to

$$I^p = \int_\Gamma p^i \, \delta \underline{u} \, dS. \tag{25}$$

This equation indicates that, in addition to the kinematic condition $p = p^i$ on Γ, only a pressure excitation on the solid phase, given by (25), is to be applied.

F. Case of an imposed displacement field

In the case of an imposed displacement field $\underline{u}^i$ applied on Γ (used in some cases to simulate a piston motion), the boundary conditions are

$$u_n^i = (1 - \phi) u_n + \phi U_n \Rightarrow \phi (U_n - u_n) = 0, \quad \underline{u} = \underline{u}^i. \tag{26}$$

The first condition expresses the continuity of the normal displacements between the solid phase and the fluid phase. The second equation expresses the continuity between the imposed displacement vector and the solid phase displacement vector. Since the displacement is imposed, the admissible variation $\delta \underline{u} = 0$. Consequently, the surface integrals of Eq. (11) simplify to

$$I^p = 0. \tag{27}$$

This equation indicates that for an imposed displacement, the boundary conditions reduce to the kinematic condition $\underline{u} = \underline{u}^i$ on Γ.

IV. CONCLUSION

The new mixed pressure-displacement formulation has several advantages compared to the initial version given by Atalla *et al.*[1] With no recourse to any assumption regarding the modeled porous material, the formulation couples naturally with elastic, acoustic, and porous media and handles naturally acoustic and mechanical loads. Moreover, the new $(\underline{u}, p)$ formulation can easily handle ''nonhomogeneous'' complex medium made up from arbitrary arrangements of homogeneous elastic, acoustic, and porous media as found in automotive and aircraft applications.[4] Finally, the numerical implementation of this formulation is straightforward since it can be done easily within a classical finite element code using its solid and acoustic elements library. Since this formulation is theoretically equivalent to the initial version given by Atalla *et al.*,[1] examples showing its validation and performances can be found elsewhere.[1,3,5]

[1] N. Atalla, R. Panneton, and P. Debergue, ''A mixed pressure-displacement formulation for poroelastic materials,'' J. Acoust. Soc. Am. **104**, 1444–1452 (1998).

[2] P. Debergue, R. Panneton, and N. Atalla, ''Boundary conditions for the weak formulation of the mixed (u,p) poroelasticity problem,'' J. Acoust. Soc. Am. **106**, 2383–2390 (1999).

[3] J.-F. Allard, *Propagation of Sound in Porous Media: Modeling Sound Absorbing Materials* (Elsevier, New York, 1993).

[4] M. A. Hamdi, N. Atalla, L. Mebarek, and A. Omarni, ''Novel mixed finite element formulation for the analysis of sound absorption by porous materials,'' Proceedings of Internoise 2000, Nice, France.

[5] F. Sgard, N. Atalla, and J. Nicolas, ''A numerical model for the low frequency diffuse field sound transmission loss of double-wall sound barriers with elastic porous linings,'' J. Acoust. Soc. Am. **108**, 2865–2872 (1999).

Absorption of sound in the Martian atmosphere

Henry E. Bass
Department of Physics and Astronomy, The University of Mississippi, University, Mississippi 38677-1848

James P. Chambers
National Center for Physical Acoustics, The University of Mississippi, University, Mississippi 38677-1848

(Received 1 March 2000; revised 16 October 2000; accepted 21 February 2001)

Future missions to the planet Mars might include microphones to listen for sounds in the tenuous Martian atmosphere. The chemical composition of the atmosphere is well established by previous missions and ground based observations. The dominant constituent is CO_2 with a minor amount of N_2 and Argon and smaller amounts of H_2O. The factors important to compute the absorption of sound in a gas are reasonably well known, the most uncertain being the relaxation time of CO_2 at the low temperatures encountered (200–300 K). By extrapolating higher temperature measurements of relaxation times, analytical expressions have been developed for the absorption due to viscosity and thermal conduction (classical absorption), rotational relaxation, and vibrational relaxation. Calculations are presented for a surface level pressure of 6 millibars (600 Pa). The absorption at mid-audio frequencies (500 Hz) is 0.03 (200 K) to 0.1 (300 K) Np/m. This is about 100–500 times greater than for the earth's atmosphere (depending upon relative humidity).
 [DOI: 10.1121/1.1365424]

PACS numbers: 43.35.Ae, 43.35.Fj, 43.20.Hq [SGK]

I. INTRODUCTION

Development of analytical expressions for sound absorption in the Martian atmosphere closely follows that used for absorption of sound in air.[1,2] The typical atmospheric pressure on Mars is much different from that on earth but the critical factor which influences the following analytical expressions is the difference in atmospheric composition. We will assume that the composition of the Martian atmosphere is 95.3% CO_2, 2.7% N_2, 1.6% Argon, and a variable but small amount of water vapor.[1] There is a smaller concentration of O_2 (about 0.13%)[1] but O_2 is not very effective in relaxing CO_2 so it can be ignored. The concentration of H_2O is lower than that of O_2 even at high relative humidity but its effect on the relaxation of CO_2 may be important.

Following the development of Ref. 2, the first step will be to develop analytical expressions for classical absorption that is due to viscosity and thermal conduction. Next, the effect of rotational then vibrational relaxation will be included. Because of the overwhelming concentration of CO_2, diffusion terms will be ignored.

II. CLASSICAL ABSORPTION

The general form for absorption due to viscosity and thermal conduction is

$$\alpha=[\omega^2/(2\rho^0 c^3)][4\mu/3+(\gamma-1)\kappa/(\gamma C_v)] \tag{1}$$

in Np/m, where $\omega=2\pi f$ and f is the frequency in Hz, ρ^0 is the equilibrium density in kg/m^3, c is the speed of sound in m/s, μ is the coefficient of viscosity in kg/m, γ is the ratio of specific heats, κ is the coefficient of thermal conductivity in J(kg kmol)$^{-1}$K^{-1}kg m^{-1}s^{-1}, and C_v is the specific heat at constant volume in J (kg kmol)$^{-1}$K^{-1}.

At pressures important in the Martian atmosphere, gas should follow the ideal gas law. At frequencies above a few Hz, the sound wave can be considered an adiabatic disturbance. With these assumptions, the speed of sound becomes

$$c=(\gamma RT/M)^{1/2}, \tag{2}$$

where R is the gas constant equal to 8.31432×10^3 J (kmol)$^{-1}$K^{-1}, M is the molecular weight in kg (kmol)$^{-1}$ and T is the ambient temperature. For the concentrations assumed here, this gives a low frequency sound velocity of 227.3 m/s at 200 K and 272.9 m/s at 300 K. Making further use of the ideal gas law to write $\rho^0=\gamma P/c^2$, where P is the atmospheric pressure in N/m^2, reduces Eq. (1) to

$$\alpha_{\rm cl}=[\omega^2/(2\gamma Pc)][4\mu/3+(\gamma-1)\kappa/(\gamma C_v)]. \tag{3}$$

The Eucken expression,[3]

$$\kappa=(15R\mu/4)[4C_v/(15R)+3/5] \tag{4}$$

in J (kmol)$^{-1}$K^{-1}kg m^{-1}s^{-1}, can be used to relate κ and μ. Combining Eqs. (3) and (4),

$$\alpha_{\rm cl}=[2\pi^2 f^2/(\gamma Pc)]\mu \times\{4/3+[(\gamma-1)/\gamma](15/4)[4/15+3R/(5C_v)]\}. \tag{5}$$

In Ref. 2, the term in braces was found to be constant over the range of atmospheric conditions one would expect to encounter in the Earth's atmosphere. We will now evaluate this term for the Martian atmosphere.

The terms in the braces of Eq. (5) are not very dependent on pressure; the temperature is the important term. The temperature of the Martian atmosphere varies between 140–300 K (218 K average).[4] At 200 K (the lowest temperature considered in Ref. 5), $C_p/R=C_v/R+1=3.85$ (at low pressure). At 300 K, $C_p/R=4.477$. Over the same range, γ goes from 1.351 to 1.299. The term in braces ranges from 2.59 at low temperatures (200 K) to 2.27 at high temperatures (300

K). This variation exceeds 10% (the target accuracy of these calculations) so we will maintain the form of Eq. (5) rather than try to approximate the term in braces.

It should be noted that the term in braces varies due to the temperature dependence of C_v. That dependence is well described by the Plank–Einstein relation,[2]

$$C_v/R = 3/2 + 1 + C_j'/R, \tag{6}$$

where the 3/2 term is due to translation of the molecules, the 1 is due to rotation (CO_2 and N_2 are both linear), and

$$C_j'/R = [X_j(\theta_j/T)^2 \exp(-\theta_j/T)]/[1-\exp(-\theta_j/T)]^2, \tag{7}$$

where X_j is the mole fraction of the component considered and θ_j is the characteristic temperature of a vibrational mode.

In the Martian atmosphere, the only two molecules with significant concentrations are CO_2 and N_2. The vibrational temperature, θ_j, for N_2 vibration is sufficiently large so that it can be ignored in comparison to CO_2. In CO_2, most of the specific heat due to vibration (at least at low temperatures) is due to the doubly degenerate bending mode with $\theta_j = 960$ K. As a result,

$$C_v/R = 3/2 + 0.98 + [2.0 \times 0.95 \times (960/T)^2 \times \exp(-960/T)]/[1-\exp(-960/T)]^2. \tag{8}$$

The 0.98 term comes from the rotation of CO_2, N_2, and O_2, all of which are linear with a contribution to the rotational specific heat of R. The sum of concentrations of CO_2, N_2, and O_2 is about 0.98. The multiplication by 2 expresses the double degeneracy of the bending mode which doubles the contribution to the specific heat. The 0.95 term reflects the CO_2 concentration.

The remaining terms in Eq. (5) required to compute α_{cl} are c and μ. The speed of sound can be computed from Eq. (2) with γ from Eq. (8) and

$$M = 0.953 \times 44.011 + 0.027 \times 28.016 + 0.02 \times 39.944 = 43.5. \tag{9}$$

The viscosity, μ, can be determined from the Sutherland equation,

$$\mu = \beta T^{1/2}/[1+(S/T)], \tag{10}$$

where β and S are empirical parameters. For CO_2, the parameters are $\beta = 1.49 \times 10^{-6}$ kg m^{-1}K$^{-1/2}$ s^{-1} and $S = 217$ K determined by fitting the data in Ref. 5 to Eq. (10). Equation (10) should be applicable as the gas can be treated as ideal.

We now have all the equations necessary to compute α_{cl}. Figures 1(a) and (b) show α_{cl} as a function of frequency for an assumed pressure of 6 millibars (ground level average on Mars) and temperatures of 200 and 300 K.

III. ROTATIONAL RELAXATION ABSORPTION

Again, following the development of Ref. 2, the form for α_{rot} should be essentially the same as that in air,

$$\alpha_{rot} = [2\pi^2 f^2/(\gamma P c)]\mu[\gamma(\gamma-1)R/(1.25C_p^0)]Z_{rot}, \tag{11}$$

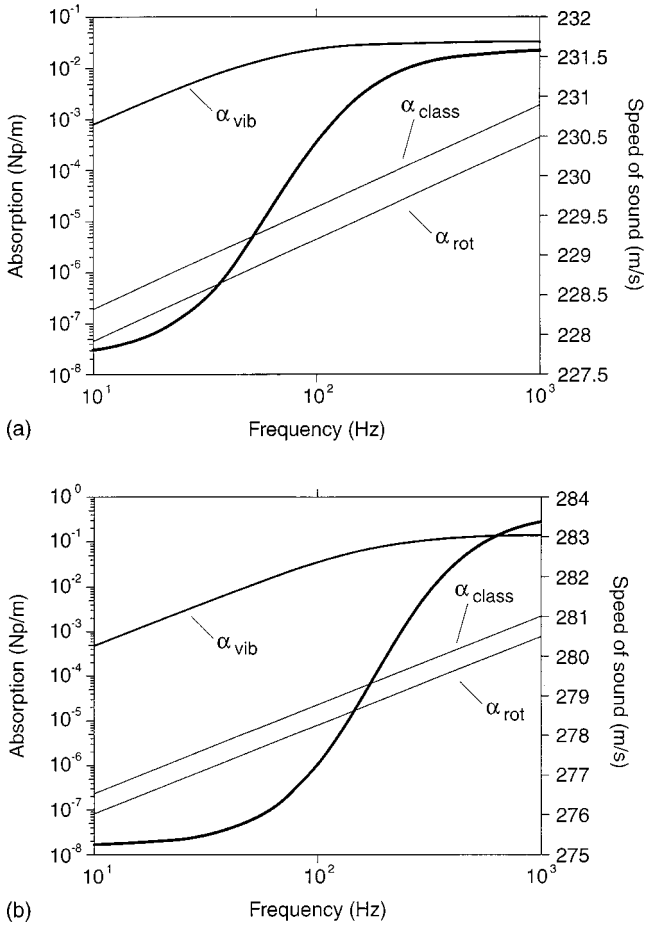

FIG. 1. Rotational, classical, and vibrational absorption (identified) and phase speed (bold line) as a function of frequency for (a) $T = 200$ K and (b) $T = 300$ K.

where C_p^0 is the specific heat at constant pressure at a frequency low enough for rotation to fully contribute but above the relaxation frequency for vibration ($C_p^0 = 7/2$) and Z_{rot} is the rotational collision number. In this case, the value of γ should also exclude the vibrational contribution ($\gamma = 7/5$). The rotational collision number for CO_2 depends upon the speed of motion and the rotational energy level spacing. Based upon those considerations, the rotational collision numbers for CO_2, O_2, and N_2 should be very close. Based upon measurements for the later two,

$$Z_{rot} = 61.1 \exp(-16.8/T^{1/3}). \tag{12}$$

Equation (12) reflects experimental data over the temperature range 293–690 K. Extrapolation to 200 K should be reasonable since the rotational energy level spacing is much less than $k_B T$ (where k_B is Boltzman's constant). Rotational relaxation absorption is shown in Figs. 1(a) and (b) at temperatures of 200 and 300 K at a pressure of 6 millibar.

IV. VIBRATIONAL RELAXATION ABSORPTION

Almost all of the vibrational energy in the gaseous mixture that makes up the Martian atmosphere is due to CO_2. At temperatures of 300 K and below, more than 90% of the vibrational specific heat is due to the doubly degenerate bending mode of $CO_2(\nu_2)$. This feature makes vibrational

relaxation absorption in the Martian atmosphere simpler than for the terrestrial atmosphere that has two molecules (O_2 and N_2) with almost equal contributions to the specific heat. The relaxation path for $CO_2(\nu_2)$ in collisions with CO_2, N_2, and H_2O are well established, at least near room temperature. There are no $v-v$ energy transfer pathways to complicate the calculation of relaxation times in the mixture.

The rate, k, at which $CO_2(\nu_2)$ will transfer vibrational energy, can be written as

$$k = X_{CO_2} k_{CO_2} + X_{N_2} k_{N_2} + X_{Argon} k_{Argon} + X_{H_2O} k_{H_2O} \quad (13)$$

in s^{-1}, where X_{CO_2}, X_{N_2}, X_{Argon}, and X_{H_2O} are the mole fractions of CO_2, N_2, Argon, and H_2O, respectively, and k_{CO_2}, k_{N_2}, k_{Argon}, and k_{H_2O} are the rate of energy transfer from $CO_2(\nu_2)$ during collisions with CO_2, N_2, Argon, and H_2O, respectively. The rate constants, k, are typically given at a pressure of one atmosphere. Since the rate is directly proportional to the collision frequency, the rate is proportional to pressure.

The relaxation time at constant volume and temperature, τ'_{vT}, is related to the difference between the forward rate of the reaction, k, and the reverse reaction rate, k_b, by the equation,

$$1/\tau'_{vT} = k - k_b \quad (14)$$

in s^{-1}. From detailed balance, $k_b = k \exp(-\theta_j/T)$. For a single energy-transfer reaction,

$$\tau'_{vs} = (C_p^\infty / C_p^0)\tau'_{vT} \quad (15)$$

in s^{-1}, where C_p^∞ is the constant pressure specific heat at frequencies well above the relaxation frequency, $f_r = 1/(2\pi\tau'_{vs})$, and C_p^0 is the value well below f_r. Since k and k_b are directly proportional to pressure, τ'_{vs} is inversely proportional to pressure.

Again, following Ref. 2, the absorption due to vibrational relaxation can be written as

$$\alpha_{vib} = (\pi s/c)(f^2/f_r)/[1 + (f/f_r)^2] \quad (16)$$

in Np/m, where the relaxation strength, $s = C'_j R/[C_p^\infty (C_v^\infty + C'_j)]$.

The only remaining unknown to calculate α_{vib} is k that, in turn, depends upon k_{CO_2}, k_{N_2}, k_{Argon}, and k_{H_2O}. These quantities cannot be reliably calculated from first principles; some type of experimental guidance is required. Fortunately, the most important of these, k_{CO_2} is well established at 300 and 600 K. The simple treatment by Landau and Teller[7] suggests that the transition probability P^{10} should vary as $\exp(-C/T^{1/3})$. The rate, k, is related to the transition probability P^{10} through the collision frequency $v = 1.25P/\mu$. Using this temperature dependence and the experimental results of Ref. 8, k_{CO_2} was determined to be

$$k_{CO_2} = 1.25P/\mu P^{10} = 0.219P/\mu \exp(-60.75/T^{1/3}). \quad (17)$$

A similar process leads to

$$k_{N_2} = 1.25P/\mu P^{10} = 1.44P/\mu \exp(-78.29/T^{1/3}). \quad (18)$$

Data are not available for collisions with Argon so we assume that $k_{Argon} = k_{N_2}$. Theory suggests that such an assumption will not lead to significant errors. The final rate that might be important is k_{H_2O}. Lewis and Lee[9] made measurements of CO_2 relaxation by H_2O and concluded that P^{10} is temperature independent and approximately equal to 4×10^{-2}. Shields and Burke[10] explain this unusual lack of temperature dependence in terms of a vibration to rotation energy transfer step. We will write

$$k_{H_2O} = 1.25P/\mu P^{10} = 6 \times 10^{-2} P/\mu. \quad (19)$$

We now have all the information required to compute f_r and α_{vib} from Eq. (16).

Figures 1(a) and (b) show the absorption due to vibrational relaxation at 200 and 300 K in the audible frequency range. When the fraction of H_2O is increased from 0% to 1%, there are no noticeable changes in Figs. 1(a) and (b).

V. CONCLUSIONS

The most remarkable feature of Fig. 1 is the magnitude of the absorption. On Earth at a frequency of 500 Hz, a typical absorption might be 10^{-4} Np/m compared to 10^{-2} Np/m for the Martian atmosphere. The large absorption in the Martian atmosphere is due to two factors. First, the pressure is very low (1/150 atm). When computing absorption, a decrease in pressure has the same result as an increase in frequency and as the frequency increases so does absorption. The second factor is the large concentration of CO_2. Absorption due to vibrational relaxation dominates that due to classical and rotational processes at audible frequencies. Vibrational relaxation absorption is directly proportional to the specific heat of the relaxing mode. The vibrational specific heat of CO_2 is about 20 times greater than for N_2 at 300 K. The combined effect will make it very difficult to transmit information via sound waves at audible frequencies in the Martian atmosphere.

ACKNOWLEDGMENTS

This interesting problem was suggested by Lou Sutherland and Paul Soderman.

[1] Eric Chaisson and Steve McMillan, *Astronomy Today* (Prentice-Hall, Upper Saddle River, NJ, 1999), p. 235.
[2] H. E. Bass, L. C. Sutherland, Joe Piercy, and Landon Evans, ''Absorption of sound by the atmosphere,'' in *Physical Acoustics*, edited by Warren P. Mason and R. N. Thurston (Academic, New York, 1984), Vol. XVII, pp. 145–232.
[3] Joseph O. Hirschfelder, Charles F. Curtiss, and R. Byron Bird, *Molecular Theory of Gases and Liquids* (Wiley, New York, 1964), p. 534.
[4] Paul T. Soderman, private communication.
[5] ''Tables of Thermal Properties of Gases,'' National Bureau of Standards Circular 564, reprinted as *Tables of Thermodynamic and Transport Properties of Air, Argon, Carbon Dioxide, Carbon Monoxide, Hydrogen, Nitrogen, Oxygen, and Steam* (Pergamon, Oxford, 1960).
[6] Same as Ref. 2, p. 550.
[7] L. Landau and E. Teller, Phys. Z. Sowjetunion **10**, 34–43 (1936).
[8] F. Douglas Shields, C. Cayce Warf, and H. E. Bass, ''Acoustical method of obtaining vibrational transition rates tested on CO_2/N_2 mixtures,'' J. Chem. Phys. **58**, 3837–3840 (1973).
[9] James W. L. Lewis and K. P. Lee, ''Vibrational relaxation in carbon dioxide/water-vapor mixtures,'' J. Acoust. Soc. Am. **38**, 813–816 (1965).
[10] F. Douglas Shields and James Alton Burks, ''Vibrational relaxation in CO_2/D_2O mixtures,'' J. Acoust. Soc. Am. **43**, 510–515 (1968).

Dynamic behavior of multistep cracked beams with varying cross section

Q. S. Li
Department of Building and Construction, City University of Hong Kong, Kowloon, Hong Kong

(Received 22 February 2000; revised 5 September 2000; accepted 9 September 2000)

An analytical method for free-vibration analysis of a multistep nonuniform cracked beam is presented. Special solutions for five different types of nonuniform beams are given first. The procedure for determining the fundamental solutions that satisfy the normalization conditions is proposed. The problem of free vibration of a multistep beam, each step beam being nonuniform and having an arbitrary number of cracks and concentrated masses, can be conveniently solved based on the fundamental solutions and recurrence formulas developed in this paper. The eigenvalue equation of such a multistep cracked beam with any kind of two end supports can be established from a determinant of order 2. © *2001 Acoustical Society of America.* [DOI: 10.1121/1.1322565]

PACS numbers: 43.40.Cw, 43.40.Le [CBB]

I. INTRODUCTION

Cracks that are often found to exist in structural members certainly lower the structural integrity and should be considered in dynamic analysis for such structures. In order to study dynamic behavior of beams with cracks, the evaluation of changes in natural frequencies of a simple cantilever beam due to the presence of one or, at most, two cracks was addressed in several papers. Rizos *et al.* (1990) developed an approach for identification of crack location and magnitude in a cantilever beam from the vibration modes. Their approach leads to a system of $(4n+4)$ equations for establishing the eigenvalue equation in the case of n cracks inside a beam. An improved analytical method for calculating natural frequencies of a uniform beam with an arbitrary number of cracks was proposed by Shifrin and Ruotolo (1999). This method was based on the use of massless rotational springs to represent the cracks and, as a main feature, leads to a system of $(n+2)$ linear equations, for a beam with n cracks. A review of technical literature dealing with the title problem by analytical methods indicates that the authors of the previous studies have generally directed their investigations to a one-step uniform beam with cracks. More work is thus required for investigating dynamic behavior of multistep nonuniform beams with cracks.

Although the problem of free vibration of a multistep cracked beam, where each step beam is nonuniform and has an arbitrary number of cracks and concentrated masses, is complicated, it can be conveniently solved based on the fundamental solutions and recurrence formulas developed in this paper. The eigenvalue equation of such a multistep cracked beam with varying cross section can be conveniently established from a determinant of order 2. As a consequence, due to the decrease in the determinant order as compared with previously developed procedures (e.g., Rizos *et al.*, 1990; Shifrin and Ruotolo, 1999), the computational time required by the present method for solving the title problem can be reduced significantly.

II. THEORY

A multistep beam with an arbitrary number of cracks is shown in Fig. 1. Now, we consider a general case where the mass intensity and flexural stiffness of each step are continuous variables and can be described by continuous real-valued functions. It is assumed that the number of cracks in the ith step beam is n_i, and the n_i cracks are located at points $x_{i1}, x_{i2}, \ldots, x_{in_i}$, such that $0<x_{i1}<x_{i2}<\cdots<x_{in_i}<l_i$, l_i is the length of the i-step beam. The effect of the ijth crack can be idealized as a massless rotational spring (Liang *et al.*, 1992; Shifrin and Ruotolo, 1999) as shown in Fig. 1. Because the difference between a beam with a crack (the ijth crack) and the corresponding beam without any crack is that the rotation at the ijth point has a jump, in order to study the dynamic characteristics of a cracked beam, it is useful to investigate the dynamic behavior of the corresponding uncracked beam first.

The differential equation for mode shape function, $X_i(x)$, of the ith step uncracked beam can be written as

$$(d^2/dx^2)[K_i(x)(d^2X_i(x)/dx^2)]-\omega^2\bar{m}_i(x)X_i(x)=0, \tag{1}$$

where $K_i(x)$ and $\bar{m}_i(x)$ are the flexural stiffness and mass intensity of the ith step beam, respectively. ω is the circular natural frequency.

The general solution of Eq. (1) can be expressed as

$$X_i(x)=\sum_{j=1}^{4} D_{ij}S_{ij}(x), \tag{2}$$

where S_{ij} and D_{ij} $(j=1,2,3,4)$ are the linearly independent solutions and integral constants of Eq. (1), respectively.

It is obvious that the exact solutions of Eq. (1) are dependent on the distributions of mass and stiffness. As suggested by Li *et al.* (1994), the functions that can be used to approximate the variation of mass and stiffness are algebraic polynomials, exponential functions, trigonometric series, or their combinations. Five different types of nonuniform beams are considered herein.

Case 1. $K_i(x)=K_i, \quad \bar{m}_i(x)=\bar{m}_i,$ (3)

where K_i and $\bar{m}_i$ are constants.

The solutions, $S_{ij}(x)$, for this case are given by

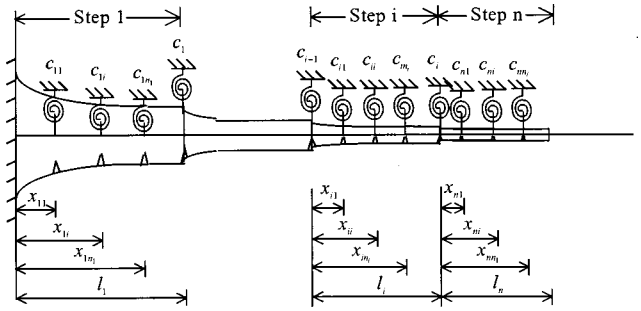

FIG. 1. A fixed-free multistep beam.

$$S_{i1}(x)=e^{k_i x},\quad S_{i2}(x)=e^{-k_i x},\quad S_{i3}(x)=\sin k_i x,$$
$$S_{i4}(x)=\cos k_i x,\quad k_i^4=\overline{m}_i\omega^2/K_i. \tag{4}$$

Case 2. $K_i(x)=\alpha_i(1+\beta_i)^{\gamma_i+2}$, $\overline{m}_i(x)=a_i(1+\beta_i)^{\gamma_i}$, (5)

where α_i, β_i, γ_i, and a_i are constants which can be determined from the distributions of $K_i(x)$ and $\overline{m}_i(x)$ (Li, 1999).

The solutions, $S_{ij}(x)$, for case 2 are as

$$S_{i1}(x)=(1+\beta_i x)^{-\gamma_i/2}J_{\gamma_i}[\lambda_i(1+\beta_i x)^{1/2}],$$
$$S_{i2}(x)=(1+\beta_i x)^{-\gamma_i/2}Y_{\gamma_i}[\lambda_i(1+\beta_i x)^{1/2}],$$
$$S_{i3}(x)=(1+\beta_i x)^{-\gamma_i/2}I_{\gamma_i}[\lambda_i(1+\beta_i x)^{1/2}], \tag{6}$$
$$S_{i4}(x)=(1+\beta_i x)^{-\gamma_i/2}K_{\gamma_i}[\lambda_i(1+\beta_i x)^{1/2}].$$
$$\lambda_i=(2/|\beta_i|)(a_i\omega^2/\alpha_i)^{1/2},$$

where $J_{\gamma_i}(\cdot)$, $Y_{\gamma_i}(\cdot)$, $I_{\gamma_i}(\cdot)$, and $K_{\gamma_i}(\cdot)$ are Bessel functions of order γ_i.

Case 3. $K_i(x)=\alpha_i(1+\beta_i x)^{\gamma_i+4}$, $\overline{m}_i(x)=a_i(1+\beta_i x)^{\gamma_i}$. (7)

The solutions, $S_{ij}(x)$, for case 3 are as follows:

$$S_{ij}(x)=e^{-\lambda_{ij}\ln(1+\beta_i x)}$$
$$\lambda_{ij}=-\tfrac{1}{2}(\gamma_i+1\pm\sqrt{\gamma_i-3\pm 4k_i}),\quad i=1,2,3,4, \tag{8}$$
$$k_i^2=((\gamma_i+2)/2)^2+\frac{a_i\omega^2}{\alpha_i}.$$

Case 4. $K_i(x)=\alpha_i(1+\beta_i x)^4$, $\overline{m}_i(x)=a_i(1+\beta_i x)^4$. (9)

The solutions, $S_{ij}(x)$, for this case are

$$S_{i1}(x)=(1+\beta_i x)^{-2}e^{c_i x},\quad S_{i2}(x)=(1+\beta_i x)^{-2}e^{-c_i x},$$
$$S_{i3}(x)=(1+\beta_i x)^{-2}\sin c_i x,$$
$$S_{i4}(x)=(1+\beta_i x)^{-2}\cos c_i x, \tag{10}$$
$$c_i^4=a_i\omega^2/\alpha_i.$$

Case 5. $K_i(x)=\alpha_i e^{-\beta_i x}$, $\overline{m}_i(x)=a_i e^{-\beta_i x}$. (11)

The solutions, $S_{ij}(x)$, for this case are

$$S_{ij}(x)=e^{-\lambda_{ij}\ln x}$$
$$\lambda_{ij}=\tfrac{1}{2}(\gamma_i\pm\sqrt{\beta_i^2\pm 4d_i^2}),\quad j=1,2,3,4 \tag{12}$$
$$d_i^4=a_i\omega^2/\alpha_i.$$

In order to deal with any kind of boundary condition at the end of each step of the beam, based on the linearly independent solutions $S_{ij}(x)$ $(j=1,2,3,4)$, the linearly independent fundamental solutions denoted by $\overline{S}_{ij}(x)$ $(j=1,2,3,4)$ satisfying the following normalization condition at the origin of the co-ordinate system, which is set at the left end of the ith step beam (Fig. 1)

$$\begin{bmatrix}\overline{S}_{i1}(0) & \overline{S}'_{i1}(0) & \overline{S}''_{i1}(0) & \overline{S}'''_{i1}(0)\\ \overline{S}_{i2}(0) & \overline{S}'_{i2}(0) & \overline{S}''_{i2}(0) & \overline{S}'''_{i2}(0)\\ \overline{S}_{i3}(0) & \overline{S}'_{i3}(0) & \overline{S}''_{i3}(0) & \overline{S}'''_{i3}(0)\\ \overline{S}_{i4}(0) & \overline{S}'_{i4}(0) & \overline{S}''_{i4}(0) & \overline{S}'''_{i4}(0)\end{bmatrix}=\begin{bmatrix}1&0&0&0\\0&1&0&0\\0&0&1&0\\0&0&0&1\end{bmatrix}, \tag{13}$$

can be easily constructed by

$$\begin{bmatrix}\overline{S}_{i1}(x)\\ \overline{S}_{i2}(x)\\ \overline{S}_{i3}(x)\\ \overline{S}_{i4}(x)\end{bmatrix}=\begin{bmatrix}S_{i1}(0) & S'_{i1}(0) & S''_{i1}(0) & S'''_{i1}(0)\\ S_{i2}(0) & S'_{i2}(0) & S''_{i2}(0) & S'''_{i2}(0)\\ S_{i3}(0) & S'_{i3}(0) & S''_{i3}(0) & S'''_{i3}(0)\\ S_{i4}(0) & S'_{i4}(0) & S''_{i4}(0) & S'''_{i4}(0)\end{bmatrix}^{-1}\times\begin{bmatrix}S_{i1}(x)\\ S_{i2}(x)\\ S_{i3}(x)\\ S_{i4}(x)\end{bmatrix}. \tag{14}$$

The primes in Eqs. (13) and (14) denote differentiation with respect to the coordinate variable x.

Using the fundamental solutions, $\overline{S}_{ij}(x)$, the mode shape function of the ith step beam with n_i cracks and n_i concentrated masses can be expressed as

$$X_i(x)=X_i(0)\overline{S}_{i1}(x)+X'_i(0)\overline{S}_{i2}(x)-\frac{M_i(0)}{K_i(0)}\overline{S}_{i3}(x)$$
$$-\frac{1}{K_i(0)}[Q_i(0)-\mu_i(0)M_i(0)]\overline{S}_{i4}(x)$$
$$+\sum_{j=1}^{n_i}C_{ij}X''_i(x_{ij})\overline{S}_{i2}(x-x_{ij})H(x-x_{ij})$$
$$+\sum_{j=1}^{n_i}K_{mij}X_i(x_{ij})\overline{S}_{i4}(x-x_{ij})H(x-x_{ij}), \tag{15}$$

where

$$\mu_i(0)=K'_i(0)/K_i(0),\quad K_{mij}=m_{ij}\omega^2/K(x_{ij}). \tag{16}$$

$X_i(0)$, $X'_i(0)$, $M_i(0)$, and $Q_i(0)$ are the displacement, slope, bending moment, and shear force of this ith step beam at $x=0$, respectively. $H(\cdot)$ is the Heaviside function. m_{ij} is the concentrated mass attached at the point x_{ij}. Cracks sometimes occur at the same sections as those to which the concentrated masses are attached.

The last two terms on the right-hand side of Eq. (15) represent the jumps of the rotation and the shear force, respectively, at the point x_{ij} where a crack and a concentrated mass are located. C_{ij} $(j=1,2,...,n_i)$ are the flexibilities of the

rotational springs which are functions of the crack depth and beam height. For a one-sided crack, C_{ij} can be expressed as (Shifrin and Ruotolo, 1999)

$$C_{ij}=5.346h_{ij}f(\xi_{ij}), \tag{17}$$

where h_{ij} is the height of cross section of the ith step beam at $x=x_{ij}$.

$$\xi_{ij}=a_{ij}/h_{ij}. \tag{18}$$

a_{ij} is the depth of the ijth crack and

$$f(\xi_{ij})=1.862\xi_{ij}^2-3.95\xi_{ij}^3+16.375\xi_{ij}^4-37.226\xi_{ij}^5+76.81\xi_{ij}^6 -126\xi_{ij}^7+172\xi_{ij}^8-143.97\xi_{ij}^9+66.56\xi_{ij}^{10}. \tag{19}$$

The displacement, slope, bending moment, and shear force at the common interfaces of two neighboring step beams are required to be continuous, i.e.,

$$X_i(0)=X_{i-1}(l_{i-1}),\quad X_i'(0)=X_{i-1}'(l_{i-1}),$$
$$M_i(0)=M_{i-1}(l_{i-1}),\quad Q_i(0)=Q_{i-1}(l_{i-1}). \tag{20}$$

If there is a crack at the left end of the ith step beam, then

$$X_i'(0)=X_{i-1}'(l_{i-1})+C_{i-1}X_{i-1}''(l_{i-1}), \tag{21}$$

where C_{i-1} is the flexibility of the rotational spring given by Eq. (17), in which h_{ij} should be changed to h_{i-1}, which is the height of cross section at the right end of the $(i-1)$th step beam.

Substituting Eq. (20) into Eq. (15) leads to

$$\begin{aligned}X_i(x)=&X_{i-1}(l_{i-1})\overline{S}_{i1}(x)+[X_{i-1}'(l_{i-1})+C_{i-1}X_{i-1}''(l_{i-1})]\\&\times\overline{S}_{i2}(x)-[M_{i-1}(l_{i-1})]/K_i(0)\,\overline{S}_{i3}(x)\\&-\frac{1}{K_i(0)}[Q_{i-1}(l_{i-1})-\mu_i(0)M_{i-1}(l_{i-1})]\overline{S}_{i4}(x)\\&+\sum_{j=1}^{n_i}C_{ij}X_i''(x_{ij})\overline{S}_{i2}(x-x_{ij})H(x-x_{ij})\\&+\sum_{j=1}^{n_i}K_{mij}X_i(x_{ij})\overline{S}_{i4}(x-x_{ij})H(x-x_{ij}),\\&i=2,3,\ldots,n.\end{aligned} \tag{22}$$

This is a recurrence formula. Using this formula and $X_1(x)$, which has only two unknown parameters for any type of boundary conditions at the left end of the first step beam, we can determine the mode shape function of the ith step ($i=2,\ldots,n$) which has the same two unknown parameters as $X_1(x)$.

The frequency equation of a multistep nonuniform beam can be established by using the two boundary conditions of the last step beam, the nth one, at $x=l_n$. For example, if the left end of the first step beam is fixed and the first step beam has n_l cracks located at $x_{11},x_{12},\ldots,x_{1n_1}$, then

$$\begin{aligned}X_1(x)=&-\frac{M_1(l_{i-1})}{K_1(0)}\overline{S}_{13}(x)-\frac{1}{K_1(0)}[Q_1(0)-\mu_1(0)M_1(0)]\\&\times\overline{S}_{14}(x)+\sum_{j=1}^{n_1}C_{1j}X_1''(x_{1j})\overline{S}_{12}(x-x_{1j})H(x-x_{1j}).\end{aligned} \tag{23}$$

Using Eqs. (22) and (23) one obtains $X_i(x)$ $(i=2,3,\ldots,n)$.

Using the boundary conditions at the right end of the nth step beam, one obtains

$$\begin{aligned}&X_{n-1}(l_{n-1})\overline{S}_{n1}''(l_n)+[X_{n-1}'(l_{n-1})+C_{n-1}X_{n-1}''(l_{n-1})]\\&\quad\times\overline{S}_{n2}''(l_n)-[M_{n-1}(l_{n-1})]/K_n(0)\,\overline{S}_{n3}''(l_n)\\&\quad-\frac{1}{K_n(0)}[Q_{n-1}(l_{n-1})-\mu_n(0)M_{n-1}(l_{n-1})]\overline{S}_{n4}''(l_n)\\&\quad+\sum_{j=1}^{n_n}C_{nj}X_n''(x_{nj})\overline{S}_{n2}''(l_n-x_{nj})\\&\quad+\sum_{j=1}^{n_n}K_{mnj}X_n(x_{nj})\overline{S}_{n4}''(l_n-x_{nj})=0,\\&X_{n-1}(l_{n-1})\overline{S}_{n1}'''(l_n)+[X_{n-1}'(l_{n-1})+C_{n-1}X_{n-1}''(l_{n-1})]\\&\quad\times\overline{S}_{n2}'''(l_n)-[M_{n-1}(l_{n-1})]/K_n(0)\overline{S}_{n3}'''(l_n)\\&\quad-\frac{1}{K_n(0)}[Q_{n-1}(l_{n-1})-\mu_n(0)M_{n-1}(l_{n-1})]\overline{S}_{n4}'''(l_n)\\&\quad+\sum_{j=1}^{n_n}C_{nj}X_n''(x_{nj})\overline{S}_{n2}'''(l_n-x_{nj})\\&\quad+\sum_{j=1}^{n_n}K_{mnj}X_n(x_{nj})\overline{S}_{n4}'''(l_n-x_{nj})=0,\end{aligned} \tag{24}$$

Since $X_1(x)$ has only two unknown parameters, $M_1(0)$ and $Q_1(0)$, $X_i(x)$ $(i=2,\ldots,n)$ have the same two unknown parameters only. Setting the determinant consisting of the coefficients of $M_1(0)$ and $Q_1(0)$ in Eq. (24) equal to zero establishes the frequency equation.

III. NUMERICAL EXAMPLE

This numerical example will show how to determine the natural frequencies and mode shapes of a three-step beam. The width of cross section of this beam is a constant; only the height of cross section varies linearly along the length of the beam.

A. Determination of the distributions of flexural stiffness and mass intensity

These distributions are found to be described reasonably well by the following functions:

$$\begin{aligned}&\overline{m}_i(x)=a_i(1+\beta_i),\quad K_i(x)=\alpha_i(1+\beta_i)^3,\\&a_1=5.80\times10^2\ \text{kg/m},\quad a_2=4.10\times10^2\ \text{kg/m},\\&a_3=3.12\times10^2\ \text{kg/m},\quad \alpha_1=9.65\times10^7\ \text{N/m}^2,\\&\alpha_2=3.85\times10^7\ \text{N/m}^2,\quad \alpha_3=1.84\times10^7\ \text{N/m}^2,\\&\beta_1=0.045,\quad \beta_2=0.04,\quad \beta_3=0.\end{aligned} \tag{25}$$

TABLE I. The fundamental mode shape. The values in parentheses represent the mode shape of the uncracked beam.

x/l_i	0	0.1	0.2	0.3	0.4	0.5	0.6	0.7	0.8	0.9	1.0
The first step	0	0.0059	0.0141	0.0184	0.0367	0.0448	0.0567	0.0814	0.1066	0.1318	0.1699
	(0)	(0.0051)	(0.0104)	(0.0169)	(0.0301)	(0.0434)	(0.0562)	(0.0810)	(0.1054)	(0.1302)	(0.1627)
The second step	0.1669	0.1994	0.2480	0.2751	0.3194	0.3460	0.3751	0.4149	0.4586	0.5001	0.5476
	(0.1627)	(0.1952)	(0.2281)	(0.2633)	(0.2987)	(0.3340)	(0.3742)	(0.4145)	(0.4550)	(0.4952)	(0.5335)
The third step	0.5476	0.5893	0.6519	0.6794	0.7431	0.7618	0.5092	0.8561	0.9031	0.9520	1.0000
	(0.5355)	(0.5760)	(0.6213)	(0.6668)	(0.7124)	(0.7596)	(0.5071)	(0.8547)	(0.9029)	(0.9512)	(1.0000)

x_{ij} and the heights, h_{ij}, of the cross sections at x_{ij} where cracks occur are given by $x_{11}=x_{21}=x_{31}=1$ m, $x_{12}=x_{22}=x_{32}=2$ m, $x_{20}=x_{30}=0$, $h_{11}=0.6685$ m, $h_{12}=0.6370$ m, $h_{20}=0.4950$ m, $h_{21}=0.4800$ m, $h_{22}=0.4650$ m, $h_{30}=h_{31}=h_{32}=0.3500$ m.

B. Determination of the fundamental solutions

Since the distributions of flexural stiffness and mass intensity of the first and second step beam belong to case 2 discussed previously, the solutions are

$$\begin{aligned} S_{i1}(x)&=(1+\beta_i x)^{-1/2}J_1[\lambda_i(1+\beta_i x)^{1/2}],\\ S_{i2}(x)&=(1+\beta_i x)^{-1/2}Y_1[\lambda_i(1+\beta_i x)^{1/2}],\\ S_{i3}(x)&=(1+\beta_i x)^{-1/2}I_1[\lambda_i(1+\beta_i x)^{1/2}],\\ S_{i4}(x)&=(1+\beta_i x)^{-1/2}K_1[\lambda_i(1+\beta_i x)^{1/2}],\quad i=1,2. \end{aligned} \tag{26}$$

Because the third step beam is uniform, the solutions are the same as those given in Eq. (4). The fundamental solutions, $\overline{S_{ij}}$ $(i=1,2,3;\ j=1,2,3,4)$ can be determined from Eq. (14).

C. Evaluation of the natural frequencies and mode shapes

The mode shape of the first step beam can be found from Eq. (23) by setting $i=1$, $n_1=2$, $x_{11}=1$, $x_{12}=2$, $X_1(0)=0$, $M_1(0)=0$. Using the recurrence formula, Eq. (15), and letting $K_{mij}=0$ obtains $X_2(x)$ and $X_3(x)$. The frequency equation is established by using Eq. (24) and setting $n=3$. All C_1, C_2, and C_{11}, C_{12}, C_{21}, C_{22}, C_{31}, C_{32} are determined from Eqs. (17)–(19).

Here, we consider three cases of the depths of the cracks. When the depths of all the cracks are $0.1h_{ij}$, h_{ij} is the height of the cross section where the ijth crack is located; then, the fundamental natural frequency is found as $\omega_1=5.9943$ rad/s.

When the depths of all the cracks are $0.2h_{ij}$, $\omega_1=5.7968$ rad/s. When the depths of all the cracks are $0.3h_{ij}$, $\omega_1=5.0961$ rad/s.

If the beam has three cracks and each step beam has only one crack which occurs at $x_{i1}=1$ m, 2 m $(i=1,2,3)$, respectively, the depths of all the cracks are $0.3h_{ij}$; then, we find $\omega_1=5.3786$ rad/s; for $x_{i1}=1$ m $(i=1,2,3)$; $\omega_1=5.5194$ rad/s; for $x_{i1}=2$ m $(i=1,2,3)$. The fundamental circular natural frequency of the corresponding uncracked beam is found as 6.3701 rad/s.

It can be seen from the above results that the effects of the number, depth, and location of cracks on natural frequencies of the multistep beam are significant.

After ω_1 is determined, using Eqs. (23) and (24) we can determine the fundamental mode shape for the case of eight cracks inside the beam shown in Fig. 1 $(i=3)$; the depths of all the cracks are $0.3h_{ij}$ for this case. The fundamental mode shape of the cracked beam is compared with that of the corresponding uncracked beam in Table I. Because the slope of the cracked section has a jump, the effect of cracks on the mode shapes is also obvious.

IV. CONCLUSIONS

A new exact approach for determining free vibrations of a multistep nonuniform beam with cracks is presented in this paper. Special solutions for free vibrations of five different types of nonuniform beams are given first. The procedure for determining the fundamental solutions that satisfy the normalization conditions is proposed. Using the fundamental solutions and recurrence formulas developed in this paper leads to the eigenvalue equation of a multistep nonuniform beam with any kind of two end supports, any finite number of cracks and concentrated masses that can be expressed in terms of a determinant of order 2. As a consequence, due to the decrease in the determinant order as compared with previously developed procedures, the computational time required by the present method for solving the title problem can be reduced significantly. The numerical example shows that the effects of the number, depth, and location of cracks on natural frequencies and mode shapes of a nonuniform beam are significant and the proposed procedure is an efficient method.

Li, Q. S. (**1999**). ''Flexural Free Vibration of Cantilevered Structures of Variable Stiffness and Mass,'' Struct. Eng. Mech. **8**(3), 243–256.

Li, Q. S., Cao, H., and Li, G. (**1994**). ''Analysis of Free Vibrations of Tall Buildings,'' ASCE, J. Eng. Mech. **120**(9), 1861–1876.

Liang, R. H., Hu, J., and Choy, F. (**1992**). ''Theoretical Study of Crack-induced Eigenfrequence Changes on Beam Structures,'' ASCE, J. Eng. Mech. **118**(2), 384–396.

Rizos, R. F., Aspragotos, N., and Dimarogonas, A. D. (**1990**). ''Identification of Crack Location and Magnitude in a Cantilever Beam from The Vibration Modes,'' J. Sound Vib. **138**, 381–388.

Shifrin, and Ruotolo, R. (1999). ''Natural frequencies of a beam with arbitrary number of cracks,'' J. Sound Vib. **222**(3), 409–423.

Hyperbolic location errors due to insufficient numbers of receivers

John L. Spiesberger[a)]
Department of Earth and Environmental Science, 240 South 33rd Street, University of Pennsylvania, Philadelphia, Pennsylvania 19104-6316

(Received 12 December 2000; revised 7 March 2001; accepted 29 March 2001)

Animal locations are sometimes estimated by measuring the difference in travel times of their sounds at pairs of receivers. Ideally, each difference specifies the animal's location to a hyperboloid, and sufficient numbers of intersecting hyperboloids specify the location. Most bioacoustic publications state that one needs three receivers to locate animals in two spatial dimensions and four receivers in three spatial dimensions. However, the actual numbers of receivers required for locations in two and three dimensions are four and five, respectively. Significant location errors can result from using insufficient numbers of receivers. Methods are provided for determining locations of ambiguous source-location regions. © *2001 Acoustical Society of America.*
[DOI: 10.1121/1.1373442]

PACS numbers: 43.80.Ev, 43.30.Sf, 43.10.Ln [WA]

I. INTRODUCTION

Animals are sometimes located from their sounds when it is difficult to assess their positions using other methods. Such locations may be used for conservation and the study of animal behavior. One location technique uses the difference in travel time of the sound at pairs of widely separated receivers to confine the animal to a hyperbola in two spatial dimensions or a hyperboloid in three dimensions. By adding sufficient numbers of receivers, the intersecting hyperbolas or hyperboloids yield locations. An overwhelming majority of publications in this and other journals state that locations can be made in two and three dimensions with three and four receivers, respectively. For example, Spiesberger and Fristrup[1] mistakenly stated that three receivers are sufficient for two-dimensional locations. While this may be true if the animals are forbidden on physical grounds from occurring in certain locations, it is untrue in general. As shown here, ambiguous location solutions are neither unusual nor so far away from the receivers to be of no practical interest. In fact, two- and three-dimensional locations generally require four and five receivers, respectively, to avoid ambiguous location solutions.

An insufficient number of receivers is one of many causes for imperfect locations. Other causes include measurement error, deviations of acoustic paths from straight lines due to gradients in the sound speed and wind fields, and imperfect estimates of the locations of the receivers. The influence of these and other effects have been discussed.[1,2] This paper discusses only location errors derived from insufficient numbers of receivers.

Hyperbolic techniques for navigating ships and aircraft began in WWII through the development of LORAN.[3] Most engineering publications state that locations can be made with three receivers. In 1972, Schmidt[4] recognized that one requires four receivers for two-dimensional locations. Because this is perhaps not recognized anywhere in the bioacoustics literature, an example is provided. Let t_i denote the travel time of sound from a source to receiver i. The travel-time difference between receivers i and j is $\tau_{ij} \equiv t_i - t_j$. With three receivers, one has three travel-time differences available for location, τ_{12}, τ_{13}, and τ_{23}. Without measurement error, τ_{23} adds no information concerning location because it can be predicted without error from the identity $\tau_{23} = \tau_{13} - \tau_{12}$. To see why four receivers may be required for two-dimensional locations, first consider that two receivers confine the animal to a hyperbola specified by the receiver positions and τ_{12}. Adding a third receiver introduces a second hyperbola through τ_{13} that may intersect the first hyperbola at two points. Because τ_{23} can be derived from the identity above, its hyperbola does not resolve the ambiguity of the two points. A fourth receiver is then needed to resolve the ambiguity.

For a typical atmospheric sound speed of $330\,\mathrm{m\,s^{-1}}$, there are two locations at Cartesian coordinates $(0.7184, 0.5511)$ and $(-10.1506, -9.4319)$ m that yield identical travel time differences, $\tau_{12} = -0.025\,431\,9$, $\tau_{13} = -0.025\,902\,0$, $\tau_{23} = -0.000\,470\,148$ s [Fig. 1(a)]. Both locations are plausible in terrestrial environments. Many other regions exhibit significant ambiguities in location [Fig. 1(b)]. If one adds a fourth receiver, its attendant travel-time difference resolves the ambiguity (Sec. III). Schmidt[4] showed that hyperbolas delineate regions where ambiguous source-location solutions occur. These hyperbolas are evident in Fig. 1(b). On the sides of the hyperbolas where ambiguities appear, all regions have ambiguous location solutions, except at the receiver. The other sides of the hyperbolas have no source-location ambiguities unless crossing another hyperbola's boundary.

In three dimensions, one generally needs five receivers for unique locations for the following reason. Two receivers confine the estimate of the animal's location to a hyperboloid using τ_{12}. A third receiver adds another hyperboloid using τ_{13}, which can intersect the first hyperboloid along an el-

a)Electronic mail: johnsr@sas.upenn.edu

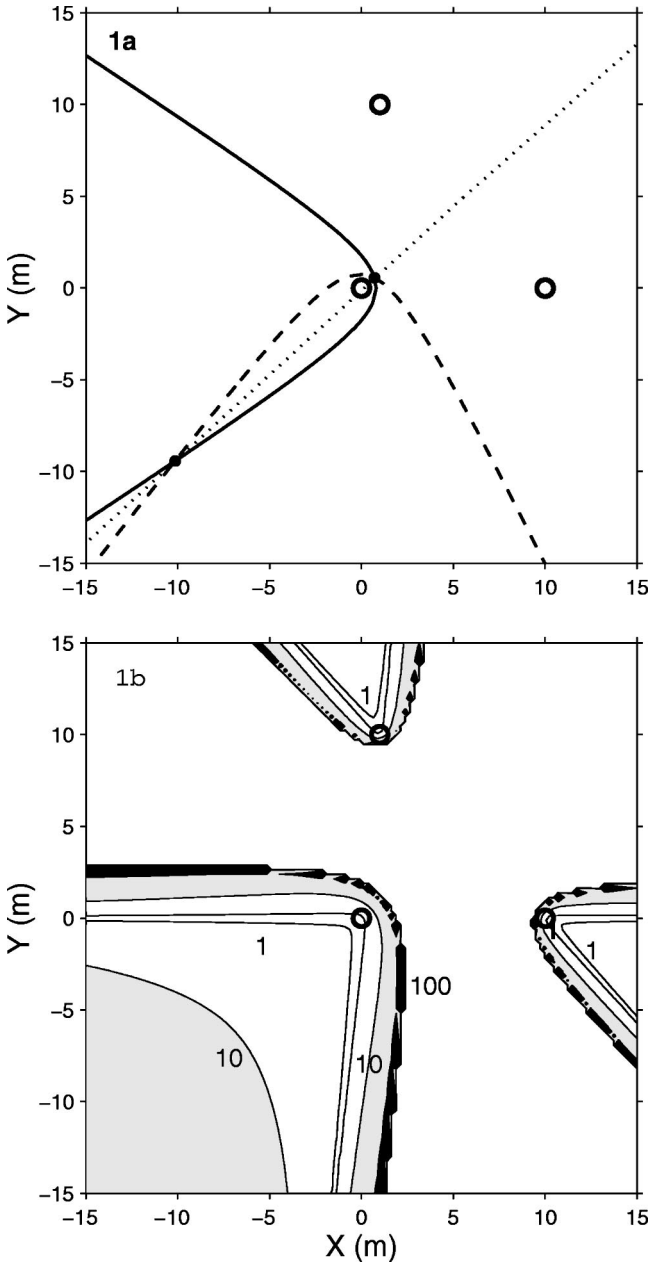

FIG. 1. (a) Example of two source locations (dots) that have identical differences in travel times at each of three receivers (circles). The Cartesian coordinates of the receivers are (0,0), (10,0), and (1,10) m, respectively. The ambiguity in source location is not due to any near symmetry in the positions of the receivers but instead is a consequence of using three receivers instead of four. There are an infinite number of source-location pairs yielding identical differences in travel times. (b) shows the distances (m) between pairs of sources having the same travel-time differences at each of the three receivers (circles) for this two-dimensional geometry. Contours are 0, 1, 10, and 100 m. The black regions denote 100 m or greater. The contours are drawn from a grid spacing of 0.25 m. Ambiguous source locations only occur in regions bounded by the hyperboloids. Sources located in the central white region can be located without ambiguity.

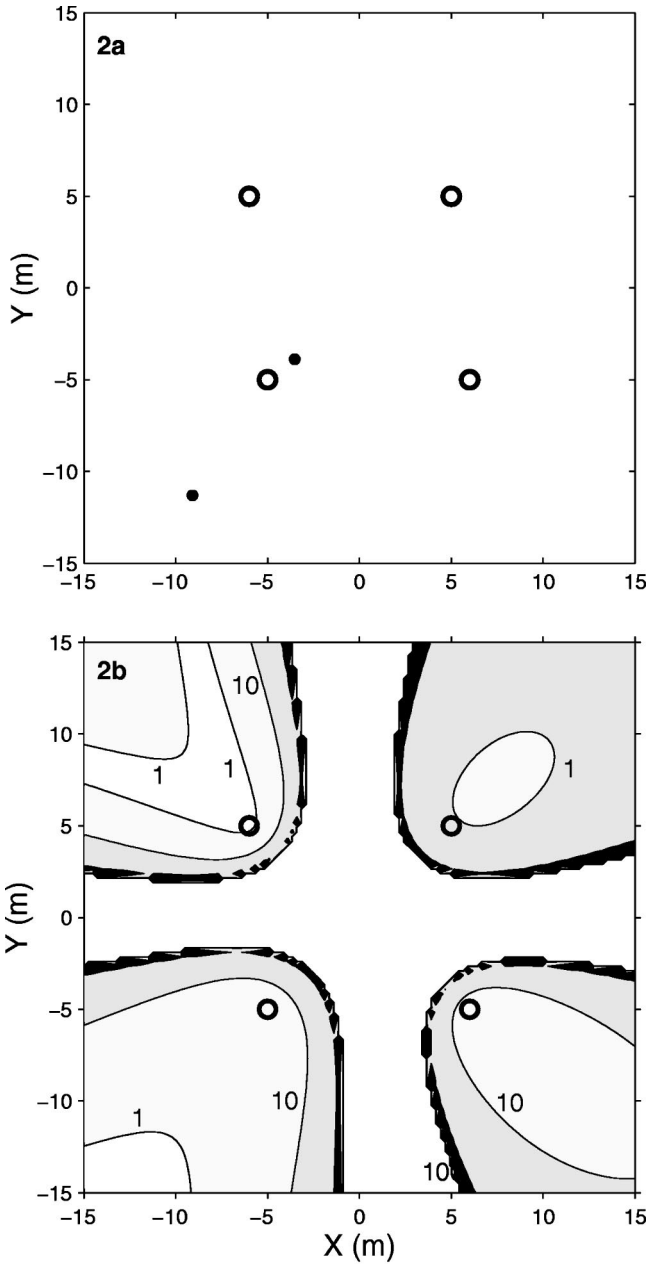

FIG. 2. (a) An example of two source locations (dots) that have identical differences in travel time at each pair of receivers (circles). The Cartesian coordinates of the receivers are $(-5,-5,0)$, $(-6,5,1)$, $(5,5,-1)$, $(6,-5,2)$ m. The vertical coordinate of the source near $x=-4$ and $y=-4$ is 1 m. The vertical coordinate of the other source is -11.1635 m. (b) Distances (m) between two source locations that have identical travel-time differences at all receiver pairs when one source is at the indicated $x-y$ coordinate and at $z=1$ m. Ambiguous source locations that yield identical travel-time differences can be resolved if one adds a fifth receiver. The distance is zero in the broad white cross running through the middle of the figure. The contours are at 0, 1, 10, and 100 m. The black regions indicate 100 m or more. The contours are drawn from a grid spacing of 0.25 m.

lipse. A fourth receiver introduces τ_{14} and one has a third hyperboloid which can intersect the ellipse at two points. A fifth receiver uses τ_{15} and a fourth hyperboloid, which intersects one of the two points. The other hyperboloids from the cross terms such as τ_{23} are redundant because these cross terms are predicted without error from τ_{1r}; $r=2,3,4$, and 5. The 1964 paper in the bioacoustics literature by Tyrrell[5] correctly states that five receivers are sometimes required to avoid ambiguous solutions for locations.

For example, consider four receivers and a speed of sound of $330\,\mathrm{m\,s^{-1}}$ [Fig. 2(a)]. The two source locations with Cartesian coordinates of $(-3.527\,80, -3.878\,60, 1.000\,00)$ and $(-9.098\,89, -11.2931, -11.1633)$ m yield identical travel-time differences, $\tau_{12}=-0.021\,554\,0$, $\tau_{13}=-0.031\,419\,8$, and $\tau_{14}=-0.022\,854\,5$ s. Both loca-

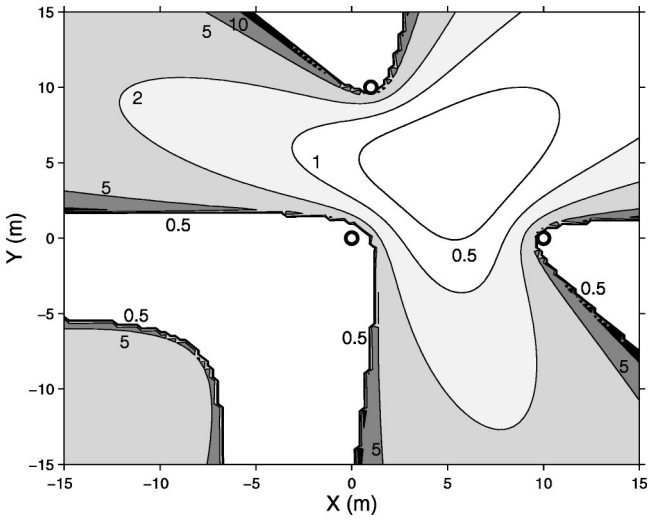

FIG. 3. Three receivers in an $x-y$ plane are used to locate a source that is somewhere from 0 to 3 m above the plane containing the receivers. The location algorithm assumes a two-dimensional geometry, so the source is mathematically assumed to be in the plane of the receivers. The plot shows the horizontal error (m) in the two-dimensional algorithm due to the fact that the source is not exactly in the plane of the receivers. Receiver locations are identical to Fig. 1.

tions are plausible in terrestrial environments. There are regions both near and far from the receivers where ambiguous source locations yield identical travel-time differences [Fig. 2(b)]. The addition of a fifth receiver resolves the ambiguity and the errors vanish (Sec. III). As in two dimensions, the regions where source-location ambiguities appear are delineated by hyperbolas for a given value of the vertical coordinate. The broad central white region in Fig. 2(b) has no source-location ambiguities.

II. LOCATION ERRORS WHEN USING THREE MICROPHONES IN ALMOST TWO-DIMENSIONAL SETTINGS

Sometimes physical barriers prevent animals from occupying areas that contain ambiguous solutions for locations. A design study can be done beforehand to ensure that animals cannot be located in these ambiguous regions. Then, one can use three receivers to locate animals in two dimensions without error. However, real situations are rarely two-dimensional in an exact sense. A design study can be done to estimate the errors incurred by using three receivers when the animals are not in the plane of the receivers.

Figure 1(b) shows no location errors if the animal is located in the central white region. The three receivers are in the $z=0$ plane. Now suppose the animal is almost in this plane, but could actually be between $z=0$ and $z=3$ m. Suppose one generates travel-time differences from a calling animal anywhere from $z=0$ to 3 m, and calculates where the animal is located *assuming* the animal is at $z=0$. This is the two-dimensional approximation. Figure 3 shows the resulting horizontal error between the actual and estimated position of the animal. The central white region without error in Fig. 1(b) now has errors of about a meter or two. These errors come from the two-dimensional approximation alone. Whether such errors are significant depends on the scientific question or conservation issue of interest.

III. MATHEMATICAL METHODS OF SOLUTION

Several authors provide mathematical approaches for locating a source from travel-time differences.[4,6–10] The approach by Watkins and Schevill[11] is used to show how ambiguous solutions arise with insufficient numbers of receivers.

Suppose the speed of sound is a known constant, c, and there are no winds. The distance between the ith receiver at $\mathbf{r}_i$ and a source at $\mathbf{s}$ is $\|\mathbf{r}_i-\mathbf{s}\|$ so we have $\|\mathbf{r}_i-\mathbf{s}\|^2=c^2t_i^2=c^2(\tau_{i1}+t_1)^2$. Putting the first receiver at the origin of the coordinate system, one subtracts the equation for $i=1$ from $i>1$ to get

$$r_x(i)s_x+r_y(i)s_y+r_z(i)s_z = \tfrac{1}{2}[r_x^2(i)+r_y^2(i)+r_z^2(i)-c^2\tau_{i1}^2]-c^2\tau_{i1}t_1,$$

which simplifies to

$$\mathbf{s}=\mathbf{R}^{-1}\mathbf{b}/2-c^2t_1\mathbf{R}^{-1}\boldsymbol{\tau}, \tag{1}$$

where for four receivers,

$$\mathbf{R}\equiv\begin{pmatrix} r_x(2) & r_y(2) & r_z(2)\\ r_x(3) & r_y(3) & r_z(3)\\ r_x(4) & r_y(4) & r_z(4)\end{pmatrix};\quad \boldsymbol{\tau}\equiv\begin{pmatrix}\tau_{21}\\ \tau_{31}\\ \tau_{41}\end{pmatrix};$$
$$\mathbf{b}\equiv\begin{pmatrix}\|\mathbf{r}_2\|^2-c^2\tau_{21}^2\\ \|\mathbf{r}_3\|^2-c^2\tau_{31}^2\\ \|\mathbf{r}_4\|^2-c^2\tau_{41}^2\end{pmatrix}, \tag{2}$$

and $\mathbf{R}^{-1}$ is the inverse of $\mathbf{R}$. The Cartesian coordinates of receiver i and the source are $\mathbf{r}_i=[r_x(i),r_y(i),r_z(i)]$ and $\mathbf{s}=(s_x,s_y,s_z)$, respectively. Use $t_1^2=\|\mathbf{s}\|^2/c^2$ in the square of Eq. (1) to solve for t_1 to get

$$t_1=\frac{ca_2\pm\sqrt{c^2a_2^2-(c^2a_3-1)a_1}}{2c(c^2a_3-1)}, \tag{3}$$

where

$$a_1\equiv(\mathbf{R}^{-1}\mathbf{b})^T(\mathbf{R}^{-1}\mathbf{b}),\quad a_2\equiv(\mathbf{R}^{-1}\boldsymbol{\tau})^T(\mathbf{R}^{-1}\mathbf{b}),$$
and
$$a_3\equiv(\mathbf{R}^{-1}\boldsymbol{\tau})^T(\mathbf{R}^{-1}\boldsymbol{\tau}), \tag{4}$$

and the superscript T denotes transpose. The solution for $\mathbf{s}$ is obtained by substituting this into Eq. (1). Two positive solutions are found when the square root and the numerator from Eq. (3) are positive, which can occur in reality. The addition of a fifth receiver adds an additional travel-time difference, and this resolves this ambiguity because only one of the source locations gives this new travel-time difference.

For two spatial dimensions and three receivers, one obtains these same equations except one drops receiver four and drops all the z coordinates of the sources and receivers. The same ambiguity can occur as before. The addition of a fourth receiver determines which source location is correct. The figures in this paper were generated using these equations.

When one has five receivers, the solution to Eqs. (1) and (3) with the correct value of t_1 given by the information from the fifth receiver, is identical to that given in Ref. 1 for five receivers:

$$\mathbf{m}=\mathbf{A}^{-1}\mathbf{d}, \tag{5}$$

where

$$\mathbf{A}\equiv 2\begin{pmatrix} r_x(2) & r_y(2) & r_z(2) & c^2\tau_{21} \\ r_x(3) & r_y(3) & r_z(3) & c^2\tau_{31} \\ r_x(4) & r_y(4) & r_z(4) & c^2\tau_{41} \\ r_x(5) & r_y(5) & r_z(5) & c^2\tau_{51} \end{pmatrix},$$
$$\mathbf{d}\equiv\begin{pmatrix} \|\mathbf{r}_2\|^2-c^2\tau_{21}^2 \\ \|\mathbf{r}_3\|^2-c^2\tau_{31}^2 \\ \|\mathbf{r}_4\|^2-c^2\tau_{41}^2 \\ \|\mathbf{r}_5\|^2-c^2\tau_{51}^2 \end{pmatrix}, \tag{6}$$

because the solutions come from identical sets of equations.

Some bioacoustic publications use Eq. (5) to locate a source in three dimensions using only *four* receivers. However, this equation was designed to use five or more receivers. With four receivers, this equation usually yields incorrect answers. For example, suppose $c=330\,\mathrm{m\,s^{-1}}$, $\mathbf{s}=(0.45,23.04,29.13)$ m, and $\mathbf{r}_1=(10.60,13.62,12.06)$, $\mathbf{r}_2=(12.81,9.22,1.01)$, $\mathbf{r}_3=(4.18,11.36,8.31)$, and $\mathbf{r}_4=(7.60,15.88,6.10)$ m. The solution from Eq. (5) for these four receivers yields $\mathbf{s}=(6.44,14.65,12.06)$ m, which is incorrect. When Eq. (5) is solved using the data from five receivers, it yields the correct solution.

IV. CONCLUSIONS

Ambiguous solutions for the locations of a calling animal can be avoided for two and three spatial dimensional problems by using four and five receivers, respectively. It may not be necessary to use this many receivers if a design study shows that ambiguous locations cannot occur because physical barriers prevent the animal from occupying ambiguous regions. Alternatively, one can use $N+1$ receivers for an N-dimensional geometry if one chooses to only use sounds without ambiguous location solutions. For example, if one uses sounds whose locations fall in the broad white-central region of Fig. 1(b), then three receivers are sufficient in this two-dimensional geometry. Ambiguous locations may also be resolved if animal tracks can be followed from unambiguous to ambiguous regions. Even when one has a nearly two-dimensional problem, it may be desirable to conduct a design study to estimate location errors due to the use of three receivers in a situation which is really three-dimensional (Fig. 3).

It may be possible to use signal amplitudes to rule out ambiguous locations when one location is very near the receivers and the other is very far away. However, amplitudes may not be as stable as travel-time differences because amplitudes may be sensitive to destructive and constructive interference, as well as focusing and defocusing effects. Perhaps amplitude information is easier to use when the signals have a broad bandwidth, because there will be fewer cases in which the signals will temporally interfere with one another in the cross correlation domain, when cross correlation is used to estimate differences in travel time.

ACKNOWLEDGMENTS

The author thanks Magnus Wahlberg, Mary E. Putt, and the reviewers for their comments.

[1] J. L. Spiesberger and K. M. Fristrup, ''Passive localization of calling animals and sensing of their acoustic environment using acoustic tomography,'' Am. Nat. **135**, 107–153 (1990).
[2] M. D. Collins and W. A. Kuperman, ''Focalization: Environmental focusing and source localization,'' J. Acoust. Soc. Am. **90**, 1410–1422 (1991).
[3] J. P. Van Etten, ''Loran C system and product development,'' Electrical Commun. **45**, 100–115 (1970).
[4] R. O. Schmidt, ''A new approach to geometry of range difference location,'' IEEE Trans. Aerosp. Electron. Syst. **AES-8**, 821–835 (1972).
[5] W. A. Tyrrell, ''Design of acoustic systems,'' in *Marine Bioacoustics*, edited by W. N. Tavolga (Pergamon, Oxford, U.K., 1964), pp. 65–86.
[6] H. C. Schau and A. Z. Robinson, ''Passive source localization employing intersecting spherical surfaces from time-of-arrival differences,'' IEEE Trans. Acoust., Speech, Signal Process. **ASSP-35**, 1223–1225 (1987).
[7] N. Marchand, ''Error distributions of best estimate of position from multiple time difference hyperbolic networks,'' Aerosp. Navigational Electron. **11**, 96–100 (1964).
[8] H. B. Lee, ''A novel procedure for assessing the accuracy of hyperbolic multilateration systems,'' IEEE Trans. Aerosp. Electron. Syst. **AES-11**, 2–15 (1975).
[9] W. H. Foy, ''Position-location solutions by Taylor-series estimation,'' IEEE Trans. Aerosp. Electron. Syst. **AES-12**, 187–194 (1976).
[10] J. M. Delosme, M. Morf, and B. Friedlander, ''Source location from time differences of arrival: Identifiability and estimation,'' IEEE Int. Conf. Acoust., Speech, Signal Process., 818–824 (1980).
[11] W. A. Watkins and W. E. Schevill, ''Four hydrophone arrays for acoustic three-dimensional location,'' Woods Hole Oceanographic Technical Report No. 71–60 (1971).

Ants are deaf

Flavio Roces[a] and Jürgen Tautz[b]
Theodor-Boveri-Institut der Universität Würzburg, Lehrstuhl für Zoologie II, Biozentrum, Am Hubland, D-97074 Würzburg, Germany

(Received 15 January 2001; revised 1 March 2001; accepted 7 March 2001)

Workers of a number of ant species produce vibrational signals, a phenomenon called ''stridulation,'' with a specialized organ located on their gasters. Even though stridulation can be heard by humans as faint air-borne sound, it has repeatedly been shown that ants are insensitive to the air-borne components of such signals. Instead, they are highly responsive to their substrate-borne components. Contrary to this view, it has recently been claimed that fire ants can hear stridulatory signals produced by nest mates as near-field sound, and that there is no evidence of signal transmission through the substrate in ants. In the present letter, this view is challenged by calculating the amplitude of the near-field particle oscillation around a stridulating ant, and by comparing it with the sensitivity threshold of the ant sensory receptors. The amplitude is shown to be at least 50 times lower than the sensitivity threshold, a fact that precludes the perception of the signals with the stiff antennal sensilla (and Johnston organ) so far described for ants. Finally, published data and our own findings on vibrational communication in ants are summarized, clearly showing that they are highly responsive to the substrate-borne components of stridulatory signals, and insensitive to near-field sound.
[DOI: 10.1121/1.1370085]

PACS numbers: 43.80.Lb [WA]

In the October issue of *JASA*, Hickling and Brown claimed, based on theoretical considerations and empirical data they obtained from work with fire ants, that ants can hear stridulatory signals produced by nest mates as near-field sound (Hickling and Brown, 2000). Moreover, they argued that communication via substrate-borne vibrations in ants is unlikely and that there is no evidence for ant responses to the substrate-borne components of vibrational signals (stridulation), maintaining that ''there is a strong belief among myrmecologists that the signals are transmitted through the substrate'' (Hickling and Brown, 2000, p. 1923). In our opinion, the authors' arguments contradict all previous communication-behavioral experiments in ants, and also disagree with published studies on sensory physiology of insect receptor sensilla which are relevant for the issues being discussed.

We do not intend here to review the bulk of literature on ant vibrational communication, but merely point out some aspects that indicate that ants are insensitive to air-borne sound. That ants are highly sensitive to substrate-borne vibrations in the absence of air-borne sound was demonstrated as early as 1936 by Autrum, who was able to separate the effects of sound and substrate vibration on ant responses in a series of clear-cut designed experiments.

But what about the ant responses to sound in the absence of substrate-borne vibrations? Hearing is based on the reception of either sound pressure or the oscillation of air particles around a sound source. Sound pressure is received by ear drums, particle oscillation by highly moveable levers, both linked to mechanosensory neurons. Indeed, some ant species can produce sounds by a process called stridulation in which a series of cuticular edges are rubbed against a scraper (Markl, 1968). Ants have no ear drums; when exposed to a standing sound wave the ants do not show any behavioral reaction in the sound pressure maxima. However, they exhibit behavioral reactions at positions in which particle oscillation is maximal (Autrum, 1936). At first glance this seems to support the recent published claim that ants can hear (Hickling and Brown, 2000), yet a closer inspection of the physical and physiological circumstances shows this to be incorrect.

The air particle oscillation around a sound field is the so-called near field. The strength and the spatial structure of this near field depends on the size of the sound source, on the mode of sound generation (monopole, dipole), and on the sound frequency produced. The most effective near-field sound source is a so-called monopole, i.e., a pulsating sphere. Based on measurements of the sound pressure generated by a stridulating *Solenopsis* fire ant, which averaged 2 mPa, Hickling and Brown (2000) calculated the particle velocity at 100 mm of the ant gaster as being 3.1×10^{-3} mm/s (their Fig. 7). They hypothesized that the steep gradient of the particle velocity around the source would affect the response of the trichoidea sensilla on the ant antennae, which were supposed to be the structures responsible for sound perception, and they even discussed on theoretical grounds the possibility that ants use the relative differences in sound velocity between both antennae to sense the steepness of the sound gradient.

Their arguments, however, overlooked the *amplitude* of the particle oscillation around the stridulating ant, and, also, to what extent the generated particle oscillation amplitudes match the sensitivity threshold of the sensory receptors so far

[a]Electronic mail: roces@biozentrum.uni-wuerzburg.de
[b]Electronic mail: tautz@biozentrum.uni-wuerzburg.de

studied in ants. To evaluate Hickling and Brown's arguments, we use their data on *Solenopsis* fire ants for our calculation of the amplitudes of the particle oscillation around a stridulating ant: basic stridulation frequency: 700 Hz; size of the ant gaster: 1 mm radius. For the calculations of the particle displacement amplitudes in the near field of an ant we also assume the ant gaster (''abdomen'') to behave as a monopole during signal production, simply because if the data show for a monopole that the stimulus is too weak to be detected by the ants, then it must be true for all higher-order sound sources.

Any sound source has the properties of a monopole as long as $k^*a_0<1$ ($k=2\pi/\lambda$, $a_0=$radius of sound source, $\lambda=$wavelength). Taking for the ant gaster (from where the sound is being radiated) a radius of 1 mm, and λ being 300 mm at 1 kHz, the conditions for a monopole are fulfilled. The near-field particle displacement amplitude drops from a zeroth-order sound source with increasing distance following $1/r^2$ ($r=$distance to the center of the sphere); from a first-order sound source with $1/r^3$, etc. The near-field particle displacement amplitude (d) for a zeroth-order sound source can be calculated according to

$$d=a_0^2*\Delta d/r^2 \tag{F1}$$

(where $\Delta d=$displacement amplitude of the surface of the sphere).

For the amplitude of the oscillation at the gaster surface (i.e., the amplitude resulting from a pulsating movement of a sphere at 700 Hz), which represents the *particle displacement amplitude* (*pda*), we take 4 μm as measured for *Atta* leaf-cutting ants (Masters *et al.*, 1983), even though the gaster of *Solenopsis* ants has a volume about six to eight times smaller than that of leaf-cutting ants, so that the value likely represents an overestimate.

According to *F*1 we calculate a $pda=2$ μm at 1 mm, 0.04 μm at 10 mm, and 0.0004 μm at 100 mm distance from the stridulating ant. Using the data reported by Hickling and Brown (2000), i.e., a particle velocity of 3.1 μm/s generated by a stridulating *Solenopsis* ant at 100 mm, we obtained a $pda=0.0007$ μm.

Do ants possess sensory receptors which can detect stimuli of such low amplitudes? Near-field receptors so far described and analyzed in insects are sensory hairs or antennae. Both are connected to sensory neurons and function as levers driven by the air oscillation. Specialized mechanosensory hairs are extremely sensitive to slightest air movements. The most sensitive arthropod hairs known were described in spiders, caterpillars, and the cercal system of crickets (Barth, 2000; Kumagai *et al.*, 1998; Tautz, 1977).

With regard to ants, such high-sensitive mechanosensory hairs, which would be physically responsive to slight air movements in a sound field, have not been detected in any species investigated so far. All ant mechanoreceptor hairs are stiff contact sensilla, morphologically different from the mechanosensory hairs mentioned earlier (Dumpert, 1972).

How about the antennae as a whole? In the joint between the pedicel and flagellum of the antenna the so-called Johnston organ is located, a structure composed of up to several hundred of mechanosensory cells responding to movement of antennal flagellum. While a recent paper reported an extremely high sensitivity for the mosquito antenna, lying in the nanometer range of air particle displacement in the sound field (Göpfert and Robert, 2000), behavioral experiments in ants showed that sound intensities starting from 100 dB (corresponding to displacement amplitudes of the air particles of 2 μm at 810 Hz) can oscillate the antennal flagellum, evoking ant behavioral responses (Autrum, 1936). However, these values are 50 times greater than any sound field ants are able to generate as short as in 10 mm distance. Ants did not respond to sounds of lower intensities. Taking all these insights together, it is not surprising that no one has discovered behavioral reactions in ants to physiologically relevant sound stimuli.

How do ants perceive stridulatory signals? Stridulatory vibrations are transmitted from the ant body to the substratum (sand they are surrounded by or vegetation they stand on). The energy is traveling as substrate vibrations from sender to receiver, eliciting a particular response or influencing their probability of occurrence. This has been demonstrated using several different experimental designs (Markl, 1965, 1967; Markl and Hölldobler, 1978; Baroni Urbani *et al.*, 1988; Roces *et al.*, 1993). In the case of foraging leaf-cutting ants, the production of stridulatory vibrations correlates with the actual mandibular movements during leaf-cutting, so that most of the energy is led into the substrate through the mandibles (Tautz *et al.*, 1995). In fact, play-back experiments clearly showed that ants responded to the substrate-borne signals (Roces *et al.*, 1993). With regard to signal perception, insects possess so-called subgenual organs (SGO), highly sensitive mechanoreceptors that respond to substrate vibrations. In electrophysiological experiments, it was shown for leaf-cutting ants that the SGOs respond to substrate vibrations produced by ant stridulatory signals (Markl, 1970).

In sum, ant stridulation can be heard by humans as faint air-borne sound, but cannot be detected by ants either as sound pressure or as particle oscillation. However, if the energy is sent through the substrate, ants are not only sensitive to the signal, but also show particular, even context-specific, reactions (Roces and Hölldobler, 1995).

Autrum, H. (**1936**). ''Uber Lautäusserungen und Schallwahrnehmung bei Arthropoden. 1. Untersuchungen an Ameisen. Eine allgemeine Theorie der Schallwahrnehmung bei Arthropoden (On sound production and perception by arthropods. 1. Investigations on ants. A general theory of sound perception by arthropods),'' Z. vergl. Physiol. **23**, 332–373.

Baroni Urbani, C., Buser, M. W., and Schilliger, E. (**1988**). ''Substrate vibration during recruitment in ant social organization,'' Insectes Soc. **35**, 241–250.

Barth, F. G. (**2000**). ''How to catch the wind: spider hairs specialized for sensing the movement of air,'' Naturwissenschaften **87**, 51–58.

Dumpert, K. (**1972**). ''Bau und Verteilung der Sensillen auf der Antennengeissel von *Lasius fuliginosus* (Latr.) (Hymenoptera, Formicidae) [Structure and distribution of sensilla on the antennae of *Lasius fuliginosus* (Latr.) (Hymenoptera, Formicidae)],'' Z. Morphol. Oekol. Tiere **73**, 95–116.

Göpfert, M. C., and Robert, D. (**2000**). ''Nanometre-range acoustic sensitivity in male and female mosquitoes,'' Proc. R. Soc. London, Ser. B **267**, 453–457.

Hickling, R., and Brown, R. L. (**2000**). ''Analysis of acoustic communication by ants,'' J. Acoust. Soc. Am. **108**, 1920–1929.

Kumagai, T., Shimozawa, T., and Baba, Y. (**1998**). ''Mobilities of the cercal wind-receptor hairs of the cricket, *Gryllus bimaculatus*,'' J. Comp. Physiol. A **183**, 7–21.
Markl, H. (**1965**). ''Stridulation in leaf-cutting ants,'' Science **149**, 1392–1393.
Markl, H. (**1967**). ''Die Verständigung durch Stridulationssignale bei Blattschneiderameisen. I. Die biologische Bedeutung der Stridulation (Communication by stridulatory signals in leaf-cutting ants. I. The biological function of stridulation),'' Z. vergl. Physiol. **57**, 299–330.
Markl, H. (**1968**). ''Die Verständigung durch Stridulationssignale bei Blattschneiderameisen. II. Erzeugung und Eigenschaften der Signale (Communication by stridulatory signals in leaf-cutting ants. II. Production and characteristics of the signals),'' Z. vergl. Physiol. **60**, 103–150.
Markl, H. (**1970**). ''Die Verständigung durch Stridulationssignale bei Blattschneiderameisen. III. Die Empfindlichkeit für Substratvibrationen (The communication through stridulatory signals in leaf-cutting ants. III. The sensitivity to substrate vibrations),'' Z. vergl. Physiol. **69**, 6–37.
Markl, H., and Hölldobler, B. (**1978**). ''Recruitment and food-retrieving behavior in *Novomessor* (Formicidae, Hymenoptera). II: Vibration signals,'' Behav. Ecol. Sociobiol. **4**, 183–216.
Masters, W. M., Tautz, J., Fletcher, N. H., and Markl, H. (**1983**). ''Body vibration and sound production in an insect (*Atta sexdens)* without specialized radiating structures,'' J. Comp. Physiol. A **150**, 239–249.
Roces, F., and Hölldobler, B. (**1995**). ''Vibrational communication between hitchhikers and foragers in leaf-cutting ants (*Atta Cephalotes*),'' Behav. Ecol. Sociobiol. **37**, 297–302.
Roces, F., Tautz, J., and Hölldobler, B. (**1993**). ''Stridulation in leaf-cutting ants: short-range recruitment through plant-borne vibrations,'' Naturwissenschaften **80**, 521–524.
Tautz, J. (**1977**). ''Reception of medium vibration by thoracal hairs of caterpillars of *Barathra brassicae L.* (Lepidoptera, Noctuidae). I. Mechanical properties of the receptor hairs,'' J. Comp. Physiol. **118**, 13–31.
Tautz, J., Roces, F., and Hölldobler, B. (**1995**). ''Use of a sound-based vibratome by leaf-cutting ants,'' Science **267**, 84–87.

Response to "Ants are deaf" [J. Acoust. Soc. Am. 109, 3080 (2001)]

Robert Hickling
Sonometrics, Inc., 8306 Huntington Road, Huntington Woods, Michigan 48070

Richard L. Brown
Department of Entomology and Plant Pathology, Mississippi State University, Mississippi State, Mississippi 39762

(Received 20 February 2001; revised 5 March 2001; accepted 7 March 2001)

[DOI: 10.1121/1.1370086]

PACS numbers: 43.80.Lb [WA]

In our article (Hickling and Brown, 2000) we believe we have given an objective account of acoustic communication by ants that fits all of the available data, not just our own. That stridulatory communication is prevalent among ants appears to be beyond debate. Obviously it is needed in highly organized ant societies, in addition to chemical communication. We hope we have created an increased interest in an area that appears to have become moribund because of the excessive emphasis on chemical communication. We expect that future work will more clearly demonstrate the significance of sounds made by ants.

The principal concern of Roces and Tautz appears to be our conclusion that the stridulatory signals of ants are generally transmitted through the air and not through the substrate. Like other animals, ants are sensitive to vibrations in the substrate but, of course, this does not mean that their stridulatory signals are transmitted this way. Substrate transmission of stridulatory signals is currently an article of faith among myrmecologists and, in recent years, the paper by Roces *et al.* (1993) appears to have become a cornerstone of this belief. However, the paper only demonstrates transmission through the flexible leaves and stems of a plant, and only when the mandibles of the ant are in contact with the leaf. Nonstridulating insects, such as the treehopper (Cocroft *et al.*, 2000), also transmit signals in this way. Thus, although the paper by Roces *et al.* appears to provide evidence for substrate transmission in this particular instance, it does not provide evidence for substrate transmission of stridulatory signals in general, especially when, as is usually the case, the substrate is soil and only the tarsi (feet) of the ant are in contact with it. Since this is a question of fundamental importance it was discussed carefully in our paper and there is no need to repeat all the arguments here.

We would have liked to respond in detail to the comments of Roces and Tautz because they obviously have gone to some trouble preparing them. However we feel that their arguments are overly tendentious and we would prefer to leave it to knowledgeable readers to compare our paper with their statements. The following two examples illustrate why we think this. In general, ant mechanoreceptor hairs are known to have a membranous base that allows the hair to bend, so that their statement ''All ant mechanoreceptor hairs are stiff contact sensilla'' is clearly misleading. Their use of theory also appears to be under-informed. Very small sound sources do not always have the characteristics of a monopole.

Probably what this correspondence demonstrates most clearly is the need for greater common-sense understanding and cooperation between disciplines, particularly between biological science, mechanics, and signal processing.

Cocroft, R. B., Tieu, T. D., Hoy, R. R., and Miles, R. N. (**2000**). ''Directionality in the mechanical response to substrate vibration in a treehopper (Hemiptera: Membracidae: *Umbonia crassicornis*),'' J. Comp. Physiol. A **186**, 7/8, 695–705.

Hickling, R., and Brown, R. L. (**2000**). ''Analysis of acoustic communication by ants,'' J. Acoust. Soc. Am. **108**, 1920–1929.

Roces, F., Tautz, J., and Hölldobler, B. (**1993**). ''Stridulation in leaf-cutting ants: short range recruitment through plant-borne vibrations,'' Naturwissenschaften **80**, 521–524.